



**T. Pradeep**

**Publications 2019**



# **Contents**

1. Publications
2. Lectures Delivered
3. Patents/Technology
4. Media Reports

# Journal Papers Published in 2019\*

1. Nanocellulose reinforced organo-inorganic nanocomposite for synergistic and affordable defluoridation of water and an evaluation of its sustainability metrics, Sritama Mukherjee, Haritha Ramireddy, Avijit Baidya, A. K. Amala, Chennu Sudhakar, Biswajit Mondal, Ligy Philip, and, Thalappil Pradeep, *ACS Sustain. Chem. Eng.*, 2019. (DOI: 10.1021/acssuschemeng.9b04822) (ARTICLE ASAP).
2. Formation of cubic ice via clathrate hydrate, prepared in ultrahigh vacuum under cryogenic conditions, Jyotirmoy Ghosh, Radha Gobinda Bhui, Gaurav Vishwakarma, and, Thalappil Pradeep, *J. Phys. Chem. Lett.*, 11 (2020), 26-32. (DOI: 10.1021/acs.jpcllett.9b03063).
3. Intercluster reactions resulting in silver-rich trimetallic nanoclusters, Esma Khatun, Papri Chakraborty, Betsy Jacob, Ganesan Paramasivam, Mohammad Bodiuzzaman, Wakeel Dar, and, Thalappil Pradeep, *Chem. Mater.*, 2019. (DOI: 10.1021/acs.chemmater.9b04530) (Just Accepted).
4. Internalization of a preformed atomically precise silver cluster in proteins by multistep events and emergence of luminescent counterparts retaining bioactivity, Debasmita Ghosh, Mohammad Bodiuzzaman, Anirban Som, Sebastian Raja, Ananya Baksi, Atanu Ghosh, Jyotirmoy Ghosh, Akshayaa Ganesh, Priyanka Samji, Sundarasamy Mahalingam, Devarajan Karunakaran, and, Thalappil Pradeep, *J. Phys. Chem. C*, 123 (2019), 48, 29408-29417. (DOI: 10.1021/acs.jpcc.9b07765).
5. Metal ion-induced luminescence enhancement in protein protected gold clusters, Jyoti Mohanty, Kamallesh Chaudhari, Chennu Sudhakar, and, Thalappil Pradeep, *J. Phys. Chem. C*, 123 (2019) 28969–28976. (DOI: 10.1021/acs.jpcc.9b07370).
6. Interparticle reactions between silver nanoclusters leading to product co-crystals by selective co-crystallization, Wakeel Ahmed Dar, Mohammad Bodiuzzaman, Debasmita

- Ghosh, Ganesan Paramasivam, Esma Khatun, Korath Shivan Sugi, and, Thalappil Pradeep, *ACS Nano*, 13 (2019) 13365–13373 (DOI: 10.1021/acsnano.9b06740).
7. Mechanistic elucidation of the structure and reactivity of bare and hydride protected  $\text{Ag}_{17}^+$  clusters, Ananya Baksi, Madhuri Jash, Soumabha Bag, Sathish Mudedla, Mohammad Bodiuzzaman, Debasmita Ghosh, Ganesan Paramasivam, Venkatesan Subramanian, and Thalappil Pradeep, *J. Phys. Chem. C*, 123 (2019) 28494-28501. (DOI: 10.1021/acs.jpcc.9b09465).
  8. Enhancing the sensitivity of point-of-use electrochemical microfluidic sensors by ion concentration polarisation - A case study on Arsenic, Vidhya Subramanian, Sangjun Lee, Sanjoy Jena, Sourav Kanti Jana, Debductta Ray, Sung Jae Kim, and Thalappil Pradeep, *Sensors & Actuators: B. Chemical*, 304 (2020) 127340 (DOI: 10.1016/j.snb.2019.127340).
  9. Ambient electrospray deposition Raman spectroscopy (AESD RS) using soft landed preformed silver nanoparticles for rapid and sensitive analysis, Tripti Ahuja, Atanu Ghosh, Sandip Mondal, Pallab Basuri, Jenifer Shantha Kumar, Pillalamarri Srikrishnarka, Jyoti Sarita Mohanty, Sandeep Bose, and Thalappil Pradeep, *Analyst*, 144 (2019) 7412-7420 (DOI: 10.1039/C9AN01700C).
  10. Crystallization of a supramolecular coassembly of an atomically precise nanoparticle with a crown ether, Papri Chakraborty, Abhijit Nag, Korath Shivan Sugi, Tripti Ahuja, Babu Varghese, and Thalappil Pradeep, *ACS Materials Lett.*, 1 (2019) 534–540 (DOI: 10.1021/acsmaterialslett.9b00352).
  11. Tribochemical degradation of polytetrafluoroethylene in water and generation of nanoplastics, Abhijit Nag, Ananya Baksi, Jyotirmoy Ghosh, Vishal Kumar, Soumabha Bag, Biswajit Mondal, Tripti Ahuja, and Thalappil Pradeep, *ACS Sustain. Chem. Eng.*, 7 (2019) 21, 17554-17558 (DOI: 10.1021/acssuschemeng.9b03573).
  12. Waterborne fluorine-free superhydrophobic surfaces exhibiting simultaneous  $\text{CO}_2$  and humidity sorption, Avijit Baidya, Anagha Yatheendran, Tripti Ahuja, Chennu Sudhakar,

- Sarit Kumar Das, Robin H.A. Ras, and Thalappil Pradeep, *Adv. Mater. Interfaces*, 6 (2019) 9990–10000 (DOI: 10.1002/admi.201901013).
13. In-situ monitoring of electrochemical reactions through CNTs-assisted paper cell mass spectrometry, Rahul Narayanan, Pallab Basuri, Sourav Kanti Jana, Ananthu Mahendranath, Sandeep Bose and Thalappil Pradeep, *Analyst*, 144 (2019) 5404 (DOI: 10.1039/C9AN00791A).
  14. Highly-sensitive As<sup>3+</sup> detection using electrodeposited nanostructured MnO<sub>x</sub> and phase evolution of the active material during sensing, Tanvi Gupte, Sourav Kanti Jana, Jyoti Sarita Mohanty, Srikrishnarka Pillalamarri, Sritama Mukherjee, Tripti Ahuja, Chennu Sudhakar, Tiju Thomas, and Thalappil Pradeep, *ACS Appl. Mater. Interfaces*, 11 (2019) 28154–28163 (DOI: 10.1021/acsami.9b06023).
  15. Conformational changes of protein upon encapsulation of noble metal clusters: An investigation by hydrogen/deuterium exchange mass spectrometry, Debasmita Ghosh, Sathish Kumar Mudedla, Md Rabiul Islam, Venkatesan Subramanian, and Thalappil Pradeep, *J. Phys. Chem. C*, 123 (2019) 17598–17605 (DOI: 10.1021/acs.jpcc.9b04009).
  16. Spontaneous formation of tetrahydrofuran hydrate in ultra-high vacuum, Jyotirmoy Ghosh, Radha Gobinda Bhuin, Gopi Ragupathy, and Thalappil Pradeep, *J. Phys. Chem. C*, 123 (2019) 16300–16307 (DOI: 10.1021/acs.jpcc.9b04370).
  17. Geologically-inspired monoliths for sustainable release of essential minerals into drinking water, Swathy Jakka Ravindran, Ananthu Mahendranath, Srikrishnarka Pillalamarri, Anil Kumar Avula, Md Rabiul Islam, Sritama Mukherjee, Ligy Philip, and Thalappil Pradeep, *ACS Sustain. Chem. Eng.*, 7 (2019) 11735–11744 (DOI: 10.1021/acssuschemeng.9b01902).
  18. Surface treated nanofibers as high current yielding breath humidity sensors for wearable electronics, Sathvik Iyengar, Srikrishnarka Pillalamarri, Sourav Jana, Md Rabiul Islam, Tripti Ahuja, Jyoti Sarita Mohanty, and Thalappil Pradeep, *ACS Appl. Electron. Mater.*, 1 (2019) 951–960 (DOI: 10.1021/acsaelm.9b00123).

19. Reply to Choukroun et al.: IR and TPD data suggest the formation of clathrate hydrates in laboratory experiments simulating ISM, Jyotirmoy Ghosh, Rabin Rajan J. Methikkalam, Radha Gobinda Bhuin, Gopi Ragupathy, Nilesh Choudhary, Rajnish Kumar, and Thalappil Pradeep, *Proc. Natl. Acad. Sci. U.S.A.*, 29 (2019) 14409-14410 (DOI: 10.1073/pnas.1905894116).
20. The emerging interface of mass spectrometry with materials, Papri Chakraborty, and Thalappil Pradeep, *NPG Asia Materials*, 11 (2019) 1095 (DOI: 10.1038/s41427-019-0149-3).
21. Formation of a NIR emitting  $\text{Ag}_{34}\text{S}_3\text{SBB}_{20}(\text{CF}_3\text{COO})_6^{2+}$  cluster from a hydride protected silver cluster, C. K. Manju, Debasmita Ghosh, Mohammad Bodiuzzaman, and Thalappil Pradeep, *Dalton Trans.*, 48 (2019) 8664-8670 (DOI: 10.1039/C9DT01533G).
22. Sub-ppt level detection of analytes by superhydrophobic pre-concentration paper spray ionization mass spectrometry (SHPPSI MS), Pallab Basuri, Avijit Baidya and Thalappil Pradeep, *Anal. Chem.*, 91 (2019) 7118-7124 (DOI: 10.1021/acs.analchem.9b00144).
23. Confining an  $\text{Ag}_{10}$  Core in an  $\text{Ag}_{12}$  Shell: A Four-Electron Superatom with Enhanced Photoluminescence upon Crystallization, Esma Khatun, Md Bodiuzzaman, Korath Sugi, Papri Chakraborty, Ganesan Paramasivam, Wakeel Dar, Tripti Ahuja, Sudhadevi Antharjanam, and Thalappil Pradeep, *ACS Nano*, 13 (2019) 5753-5759 (DOI: 10.1021/acsnano.9b01189).
24. A covalently linked dimer of  $[\text{Ag}_{25}(\text{DMBT})_{18}]$ , Md Bodiuzzaman, Abhijit Nag, Raghu Narayanan Pradeep, Ankush Chakraborty, Ranjit Bag, Paramasivam Ganesan, Ganapati Natarajan, G. Sekar, Sundargopal Ghosh and Thalappil Pradeep, *Chem. Commun.*, 55 (2019) 5025-5028 (DOI: 10.1039/C9CC01289C).
25. Electrospray deposition-induced ambient phase transition in copper sulphide nanostructures, Arijit Jana, Sourav Kanti Jana, Depanjan Sarkar, Tripti Ahuja, Pallab Basuri, Biswajit Mondal, Sandeep Bose, Jyotirmoy Ghosh, and Thalappil Pradeep, *J. Mater. Chem. A*, 7 (2019) 6387-6394 (DOI: 10.1039/C9TA00003H).

26. Spatial distribution mapping of molecules in the grains of different rice landraces, using desorption electrospray ionization mass spectrometry, Arunan Suganya, Debal Deb and Thalappil Pradeep, *Rapid Commun. Mass Spectrom.*, 33 (2019) 727–736 (DOI: 10.1002/rcm.8397).
27. Clathrate hydrates in interstellar environment, Jyotirmoy Ghosh, Rabin Rajan J. Methikkalam, Radha Gobinda Bhuin, Gopi Ragupathy, Nilesh Choudhary, Rajnish Kumar, and Thalappil Pradeep, *Proc. Natl. Acad. Sci. U.S.A.*, 116 (2019) 1526-1531 (DOI: 10.1073/pnas.1814293116).
28. Approaching materials with atomic precision using supramolecular cluster assemblies, Papri Chakraborty, Abhijit Nag, Amrita Chakraborty and Thalappil Pradeep, *Acc. Chem. Res.*, 52 (2019) 2–11 (DOI: 10.1021/acs.accounts.8b00369).
29. Rapid isotopic exchange in nanoparticles, Papri Chakraborty, Abhijit Nag, Ganapati Natarajan, Nayanika Bandyopadhyay, Ganesan Paramasivam, Manoj Kumar Panwar, Jaydeb Chakrabarti and Thalappil Pradeep, *Science Advances*, 5 (2019) eaau7555 (DOI: <https://doi.org/10.1126/sciadv.aau7555>).
30. UPLC and ESI-MS analysis of metabolites of *Rauvolfia tetraphylla* L. and their spatial localization using desorption electrospray ionization (DESI) mass spectrometric imaging, P. Mohana Kumara, R. Uma Shaanker and Thalappil Pradeep, *Phytochemistry*, 159 (2019) 20-29 (DOI:10.1016/j.phytochem.2018.11.009).

## **PUBLICATIONS WITH OTHER GROUPS**

31. Effects of chloride concentration on the water disinfection performance of silver containing nanocellulose-based composites, Janika Lehtonen, Jukka Hassinen, Riina Honkanen, Avula Anil Kumar, Heli Viskari, Anu Kettunen, Nikolaos Pahimanolis, Thalappil Pradeep, Orlando J. Rojas, and Olli Ikkala, *Sci. Rep.*, 9 (2019) 19505 (DOI: 10.1038/s41598-019-56009-6).

32. Nano-Gymnastics: Visualisation of inter-cluster reactions by high resolution trapped ion mobility mass spectrometry, Ananya Bakshi, Erik Schneider, Patrick Weis, Kumaranchira Krishnadas, Debasmita Ghosh, Horst Hahn, Thalappil Pradeep, and, Manfred Kappes, *J. Phys. Chem. C*, 121 (2019) 13421–13427 (DOI: 10.1021/acs.jpcc.9b08686).

\*Some of these papers will appear in 2020. Some were listed in the publications of 2018, without page numbers but appeared in 2019.

# Journal Papers



# Nanocellulose-Reinforced Organo-Inorganic Nanocomposite for Synergistic and Affordable Defluoridation of Water and an Evaluation of Its Sustainability Metrics

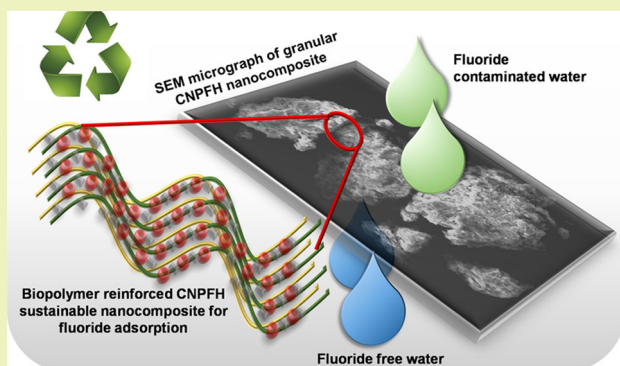
Sritama Mukherjee,<sup>†,‡</sup> Haritha Ramireddy,<sup>†</sup> Avijit Baidya,<sup>†,§</sup> A. K. Amala,<sup>†</sup> Chennu Sudhakar,<sup>†</sup> Biswajit Mondal,<sup>†</sup> Ligy Philip,<sup>‡,§</sup> and Thalappil Pradeep<sup>\*,†,§</sup>

<sup>†</sup>DST Unit of Nanoscience (DST UNS) and Thematic Unit of Excellence (TUE), Department of Chemistry and <sup>‡</sup>EWRE Division, Department of Civil Engineering, Indian Institute of Technology Madras, Chennai 600036, India

## S Supporting Information

**ABSTRACT:** Fluoride ( $F^-$ ) is one of the common naturally occurring anions present in groundwater worldwide that may be beneficial or detrimental depending on the total amount ingested and the duration of exposure. Among all the remediation techniques, adsorption using nanomaterials shows superior efficiency and the process can be eco-friendly and economical. We report cellulose nanofiber-polyaniline (PANI)-templated ferrihydrite nanocomposite synthesized by a green one-pot process where the iron precursor not only acts as an oxidant for the polymerization of aniline to give emeraldine base–emeraldine salt (EB–ES) form of PANI but also forms 2-line ferrihydrite ( $FeOOH$ ) nanoparticles in situ. These nanoparticles get embedded into the cellulose–PANI blend to give a granular nanocomposite having double action sites for adsorption and robustness which also prevent nanoparticle leaching. Doped PANI and  $FeOOH$  act as synergistic adsorption sites for  $F^-$  removal which results in an enhanced uptake capacity. The materials' adsorption mechanism and removal performance have been evaluated by diverse analytical techniques. The investigations led to the conclusion that the material is suitable to be used as adsorption media in the form of simple cartridges for gravity-fed water purification. In addition, the impact of such materials on the environment has been assessed by evaluating the relevant sustainability metrics and socio-economic parameters.

**KEYWORDS:** fluoride, cellulose nanofiber, polyaniline, ferrihydrite, synergy, sustainability metrics



## 1. INTRODUCTION

Fluorine is the lightest halogen and the most electronegative element of the periodic table. It ranks 13th in terrestrial abundance and 625 mg/kg of it can be found in the earth's crust.<sup>1</sup> In nature, it exists as fluoride anion ( $F^-$ ) and occurs mainly as sedimentary rocks like fluorspar, apatite, and so forth.<sup>2</sup> These fluoride minerals are mostly insoluble in water, unless factors like high alkalinity, temperature, and low fluoride and high bicarbonate concentrations in the water medium cause its mobilization, thereby resulting in fluoride contamination.<sup>1,3</sup> The hydrogeochemical factors give rise to natural  $F^-$  in groundwater in the range of 0.5–50 ppm, keeping the latter's color, smell, and taste intact. Although a concentration up to 1–1.5 mg/L is the requirement for good dental health, prolonged exposure to water consisting  $F^-$  in the range of 1.5–4 and 4–10 mg/L is known to cause dental and skeletal fluorosis, respectively.<sup>2,4,5</sup> Fluorosis is known to affect over 200 million people, from about 25 countries across the globe, making  $F^-$  one of the deadliest inorganic pollutants of natural origin in groundwater.<sup>6–8</sup> The risk of fluorosis because of

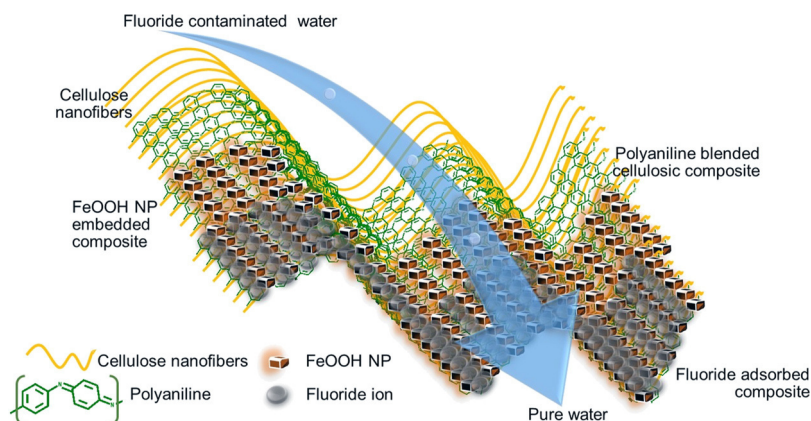
human consumption of such water is faced by many countries, notably India, Sri Lanka, China, Chile, Mexico, and Hungary, the Rift Valley countries in East Africa, Turkey, and parts of South Africa.<sup>7,9</sup> Solution for  $F^-$  contamination is suggested to be an affordable removal method with simplicity in design and operation.

Defluoridation can be carried out at household and community levels.<sup>6</sup> Conventionally, coagulation and precipitation on activated alumina, alum, and calcium hydroxide have been widely employed which results in an unpleasant taste for the resultant water and increase in the residual ion concentration.<sup>10–15</sup> Other methods like membrane filtration, reverse osmosis, electrocoagulation, dialysis, and ion exchange are efficient but expensive and cumbersome, and also require high maintenance.<sup>16–21</sup> Adsorption is a widely used process which is economical as well as simple to use.<sup>6,22</sup> It gives

Received: August 16, 2019

Revised: October 24, 2019

Scheme 1. Illustration of CNPFH used For Fluoride Removal from Water



satisfactory results with less operation time by means of mechanisms like external mass transfer, surface adsorption, and intraparticle diffusion. Many low cost adsorbents have also been employed for fluoride removal like alumina, red mud, clays, fly ash, activated carbon, calcite, brick powder, activated coconut-shell, oxide ores, and bone char, which exhibit varying uptake capacities.<sup>3,6</sup> Activated alumina is popular amongst other adsorbents because of its high surface area, which induced greater uptake while maintaining its structural stability without shrinkage, swelling, or disintegration in water.<sup>2,23,24</sup>

Other metal oxide- and hydroxide-based adsorbents prepared in micro and nanoforms include modified ferric oxide/hydroxide, hydroxyapatite, magnesium, zirconium, and cerium-modified materials, titanium-derived adsorbent, schwertmannite, zeolite, and so forth; all of them show higher uptake and selectivity toward fluoride.<sup>21,25–30</sup> Biopolymer-derived adsorbents like chitosan, chitosan derivatives, and metal (Mg, Al, Fe, Zr, Ce, La, and Nd) impregnated chitosan have been thoroughly studied giving adsorption capacities ranging from 1.39 mg/g for raw chitosan to 44.4 mg/g for silica-coated chitosan.<sup>31,32</sup> Although, chitosan is environmentally friendly, it is derived from crustacean shells and is a less sustainable option as compared to plant sources. Its polycrystalline nature reduces uptake capacities as adsorption takes place only on the amorphous region available on the surface. On the other hand, nanocellulose, derived from cotton or wood pulp, having hydrophilic surface chemistry, high strength, chemical inertness, and high surface area is a promising material to be used as a matrix for adsorbent synthesis.<sup>33</sup> Cellulose nanofibers (CNFs), typically in the range of 2–20 nm in diameter and 1–100  $\mu\text{m}$  in fiber length and is exposed with hydroxyl groups in the process of production.<sup>34,35</sup> Polymer-based nanocomposites have become a prominent area of research in the field of water purification because of the advantages like film forming ability, dimensional variability, and availability of various tunable functional groups. Polyaniline (PANI), polypyrrole (PPy), polythiophene, and their derivatives/analogues, have gained popularity as chemical adsorbents because of their facile synthesis, porous structure, good electrorheological property, and insolubility in water.<sup>36</sup> With the advancement in nanoscience and nanotechnology, it is now easy to engineer the polymeric composites with specific nanoparticles to enhance efficiency, as per the requirement.

In this work, a cellulose nanofiber-PANI-templated ferrihydrite (CNPFH) nanocomposite was prepared by a one pot synthesis process via an in situ polymerization method. The

simple synthesis yielded a sustainable composite which was used for  $\text{F}^-$  removal from water by means of adsorption. This is an eco-friendly adsorbent with high  $\text{F}^-$  uptake capacity. Iron oxyhydroxide (FeOOH) is already reported as an efficient arsenic (As) remover but a poor performer in the case of  $\text{F}^-$ .<sup>29,37</sup> PANI shows unique, yet simple doping/dedoping and redox chemistry, and it is cost-effective and nonhazardous in pure form.<sup>38</sup> It also has been reported as a  $\text{F}^-$  remover but with a meager uptake capacity of 0.8 mg/g.<sup>35</sup> Here, FeOOH and PANI were blended together and trapped in the CNF matrix to get a robust composite for an improved synergistic performance toward  $\text{F}^-$  removal. Both of these entities together not only give a greater number of surface active sites but also enhance the kinetics of adsorption. Our previous studies have brought out synergy in the performance of several nanostructures in water adsorption (Scheme 1).

## 2. EXPERIMENTAL SECTION

**2.1. Materials.** Native CNF gel (2.8 wt %) was purchased from BioPlus. Ferric chloride hexahydrate ( $\text{FeCl}_3 \cdot 6\text{H}_2\text{O}$ ) and NaOH were purchased from RANKEM Glasswares and Chemicals Pvt. Ltd., India. Aniline (extrapure, AR 99.5%) was purchased from SRL Pvt. Ltd. Sodium fluoride Emparta was purchased from Merck. Deionized (DI) water was used throughout the experiments unless otherwise mentioned.

**2.2. Methods: Synthesis of the CNPFH Nanocomposite.** Aniline (2 mL) was taken in 60 mL DI water and was kept stirring for 30 min. CNF slurry (5 g) was mixed in 10 mL of water which was then added to the aniline solution. After another 30 min stirring, 1.5 g of  $\text{FeCl}_3 \cdot 6\text{H}_2\text{O}$  was added to the reaction mixture. The resultant pH of the mixture was about 1.2 which was adjusted to 4 by dropwise addition of 2 M NaOH. The resultant slurry was stirred for 12 h, followed by filtration and washing with DI water. The precipitate collected was dried at 50  $^\circ\text{C}$  to get shiny black chunks. The chunks were crushed mechanically and sieved to get the granular adsorbent media. The product obtained was about 1.8 g.

**2.3. Batch Adsorption Studies.** In a typical batch adsorption experiment, 25 mg of the granular media were shaken with 100 mL of  $\text{F}^-$  spiked distilled water of 10 mg/L concentration in a 250 mL polypropylene vessel. The vessels were agitated at 200 rpm in a thermostatic shaker at room temperature ( $25 \pm 2$   $^\circ\text{C}$ ). The water sample was collected to measure the leftover  $\text{F}^-$  concentration in treated water as a function of time and dosage, using a fluoride-ion-selective electrode (ISE). The maximum uptake of  $\text{F}^-$  ( $q_e$ ) by CNPFH was calculated using the eq S1.

**2.4. pH Effect.** To know the pH effect on  $\text{F}^-$  adsorption, 25 mg of granular media were added to 25 mL of  $\text{F}^-$  spiked water, adjusted to the required pH by 1 M HCl/1 M NaOH and shaken for 3 h. The treated water sample was analyzed by ISE.

**2.5. Interfering Ions.** To understand the effect of interfering ions on As adsorption, the ions of interest which generally exist in ground water, like calcium ( $\text{Ca}^{2+}$ ), magnesium ( $\text{Mg}^{2+}$ ), potassium ( $\text{K}^+$ ), sodium ( $\text{Na}^+$ ), chloride ( $\text{Cl}^-$ ), carbonate ( $\text{CO}_3^{2-}$ ), bicarbonate ( $\text{HCO}_3^-$ ), nitrate ( $\text{NO}_3^-$ ), silicate ( $\text{SiO}_3^{2-}$ ), and sulfate ( $\text{SO}_4^{2-}$ ) were spiked in 25 mL of distilled water in separate conical flasks, with concentrations relevant to ground water. This water was treated with 25 mg of CNPFH for 3 h and ISE measurements were conducted. The relevant water quality parameters are listed (Table S2, Supporting Information).

### 3. INSTRUMENTATION

Transmission electron microscopy (TEM) and high-resolution TEM (HRTEM) were performed at an accelerating voltage of 200 kV on a JEOL 3010, 300 kV instrument equipped with a UHR polepiece. The accelerating voltage was kept low to ensure that the beam-induced damage on the material was low. The samples for HRTEM were prepared as the dispersions which were drop casted on carbon-coated copper grids and allowed to dry under ambient conditions. Surface morphology, elemental analysis, and elemental mapping studies were carried out using a scanning electron microscope (SEM) equipped with energy-dispersive spectroscopy (EDS) (FEI Quanta 200). For the SEM and EDS measurements, the samples were spotted on an aluminum sample stub. X-ray photoelectron spectroscopy (XPS) measurements were done using an ESCAprobe TPD spectrometer of Omicron Nanotechnology. Polychromatic Mg  $K\alpha$  was used as the X-ray source ( $h\nu = 1253.6$  eV). The samples were spotted as drop cast films on a sample stub. A constant analyzer energy of 20 eV was used for the measurements. Binding energy was calibrated with respect to C 1s at 284.8 eV. Residual fluoride concentration in water was measured (using TISAB) by a fluoride-ISE (ION 2700, Eutech Instruments). Iron concentration in water was detected using a PerkinElmer NexION 300X ICPMS (inductively coupled plasma mass spectrometry) with appropriate standards. Brunauer–Emmett–Teller (BET) surface area was measured using a Micromeritics ASAP 2020. The samples were degassed at 200 °C for 4 h under a vacuum and analyzed at 77 K with an ultrahigh pure nitrogen gas. Thermogravimetric measurements were done with a TA Instruments Q500 Thermogravimetric Analyzer (TGA) under air and  $\text{N}_2$  atmosphere from room temperature to 900 °C, with 10 min scan rate. All the uptake capacity studies in the batch mode were done in 250 mL polypropylene conical flasks.

### 4. RESULTS AND DISCUSSION

**4.1. Characterization of CNPFH before and after  $\text{F}^-$  Uptake.** The nanocomposite has been characterized by HRTEM, powder X-ray diffraction (XRD), SEM, EDS, mapping, and TG to know about its structural features, surface and morphological properties, composition, and thermal stability. Figure 1 presents SEM images of the CNPFH nanocomposite having rough and granular surface morphology which does not change upon exposure to various  $\text{F}^-$  concentrated solutions implying that the process of interaction is adsorption. This also suggests that the composite possesses very good mechanical strength which makes it suitable for use in a water purification cartridge. The granular size is about  $150 \pm 50$   $\mu\text{m}$ . The absence of fibrillar structures confirms the complete transformation of polymeric reagents to the product. The elemental composition of CNPFH showed C, O, Fe, and N as major constituents. High carbon content is due to

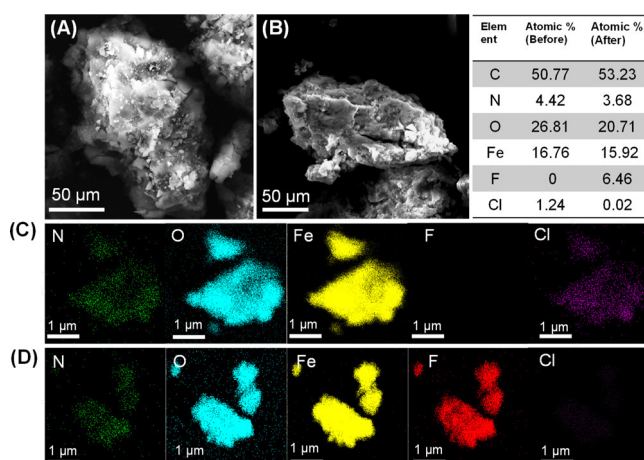
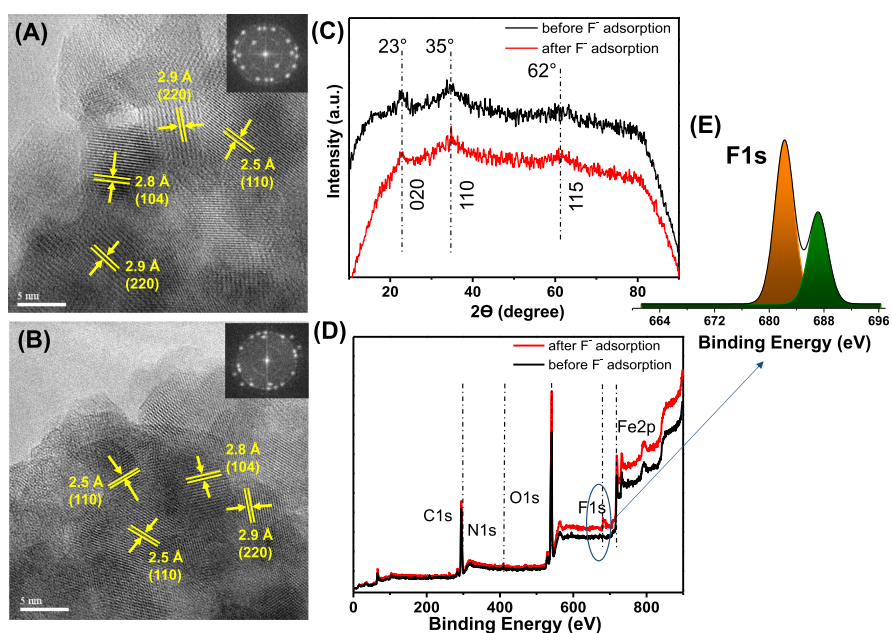


**Figure 1.** (A,B) show SEM of CNPFH before and after  $\text{F}^-$  adsorption, respectively. (C,D) EDS elemental mapping of N, O, Fe, F, and Cl of CNPFH before and after  $\text{F}^-$  adsorption, respectively, along with EDS quantification of elements.

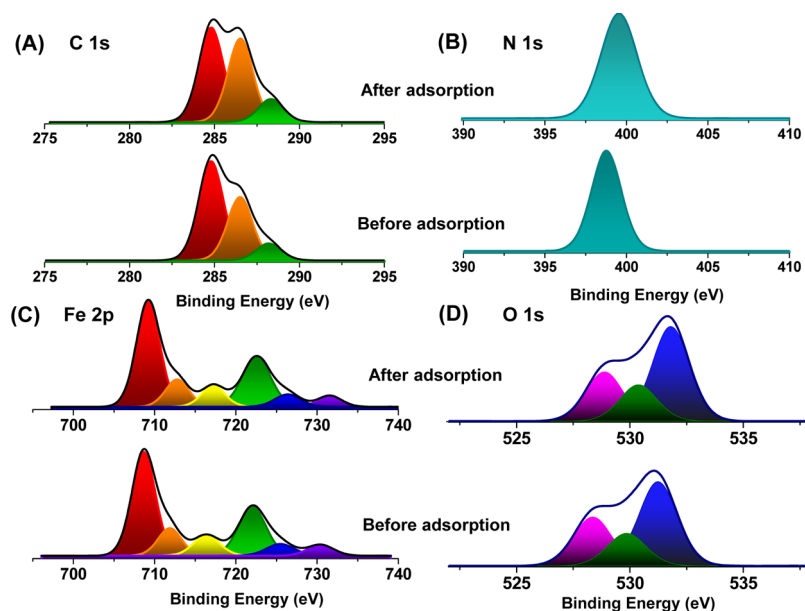
nanocellulose and PANI forming the backbone of the composite structure while N and O (partly) come from the major functional groups of the respective polymers. Fe and O constitute the presence of iron oxide content in the composite. Mapping shows the uniform distribution of each element throughout the surface, specifically  $\text{F}^-$  in the adsorbed sample. Further, we note the presence of Cl which decreases in the adsorbed sample, when compared to the parent composite.

Figure 2 illustrates the HRTEM images of the CNPFH composite at a 5 nm scale where iron oxyhydroxide nanoparticles are embedded in the CNF–PANI blend matrix, confirming composite formation. The structure is largely amorphous but nanoscale polycrystalline domains appear upon beam irradiation for a few minutes, depicted by the fast Fourier transform (FFT) diffraction pattern shown in the inset (Figure 2A). Lattice planes were resolved and matched with hematite ( $\alpha\text{-Fe}_2\text{O}_3$ ) and goethite ( $\alpha\text{-FeOOH}$ ) and they appeared because of gradual conversion of metastable iron oxyhydroxide to more stable iron oxides upon beam irradiation for a few minutes. XRD spectra (Figure 2C) show characteristic broad peaks of 2-line ferrihydrite at 35 and 62° which correspond to a metastable form of iron oxyhydroxide. A weak peak at 23° corresponds to the (020) plane of PANI constituting the amorphous nanocomposite. The physical properties of the nanocomposite do not change before and after  $\text{F}^-$  removal which indicates that the process involved is adsorption. XPS survey spectra (Figure 2D) confirm the presence of C, N, O, and Fe in CNPFH before and after  $\text{F}^-$  uptake. The  $\text{F}^-$  saturated sample showed a feature for F 1s which was deconvoluted to get a clearer idea. The deconvoluted F 1s spectra (Figure 2E) show 2 peaks at 682.2 and 687.1 eV indicating two different binding sites on CNPFH for  $\text{F}^-$  adsorption. Figure 3A shows the deconvoluted C 1s peaks at 284.8, 286.5, and 288.1 eV belonging to  $\text{sp}^3$  C–C/C–H,  $\text{sp}^3$  C–O/ $\text{sp}^2$  C–N, and  $\text{sp}^3$  C–N of the parent CNPFH which has a backbone of cellulose and PANI. Figure 3C shows the Fe 2p peaks at 708.6, 711.9, and 716.3 eV because of  $-\text{Fe}-\text{O}-\text{Fe}-$ ,  $>\text{Fe}-\text{OH}$  and a satellite peak. The peaks at 528.3, 529.9, and 531.2 eV in O 1s correspond to  $\text{Fe}-\text{OH}$ ,  $\text{Fe}-\text{O}$  groups, and adsorbed water of parent CNPFH, respectively. They show an expected shift to 528.8, 530.4, and 531.7 eV, respectively, upon  $\text{F}^-$  adsorption. While C 1s and Fe 2p did





**Figure 2.** (A,B) HRTEM showing various crystallographic planes of CNPFH by beam-induced crystallization along with a FFT of the images before and after  $F^-$  adsorption. (C) Powder XRD patterns of CNPFH before and after  $F^-$  adsorption. (D) XPS survey spectra of CNPFH before and after  $F^-$  adsorption. Deconvoluted F 1s peaks are expanded in (E).



**Figure 3.** Deconvoluted XPS spectra of (A) C 1s, (B) N 1s, (C) Fe 2p, and (D) O 1s regions of CNPFH before and after  $F^-$  adsorption.

not show any shift in binding energy before and after adsorption, N 1s and O 1s deconvoluted peaks got shifted to higher binding energies upon  $F^-$  adsorption indicating that they bind via N- and O- sites of CNPFH (Figure 3).

To explore the mechanism of  $F^-$  adsorption in detail, we conducted an experiment where a sample of CNPFH was exposed to low  $F^-$  concentration for 5 min and the other CNPFH sample of the same weight was exposed to high  $F^-$  concentration for 3 h. This helped us understand the affinity of  $F^-$  ions toward different sites available on the composite. Figure 4A shows the F1s XPS peaks at 687.3 eV after 5 min of  $F^-$  adsorption which corresponds to  $F^-$  binding through the N<sup>+</sup> site of PANI. Whereas, when it was left exposed to high amount of  $F^-$  for 3 h, apart from the 687.3 eV, a peak at 682.5

eV emerges which is due to F binding at the FeOOH site.<sup>29</sup> This has been confirmed by analyzing the  $F^-$  adsorbed cellulose–ferrihydrite composite (Figure S4) which shows a peak at 682.1 eV. Late activity of FeOOH sites may be due to the sandwiched nature of nanoparticles embedded in the PANI–cellulose blend matrix that can be reached by  $F^-$  ions, high concentrations only. Hence, N sites of PANI are better exposed at the surface than the iron oxide nanoparticles, and the former initiates the adsorption process, but the latter shows large uptake capacity. Adsorption on PANI occurs by the ion exchange mechanism where  $F^-$  replaces  $Cl^-$  which is the dopant to quaternary N of PANI leading to a peak at higher binding energy of N 1s in the adsorbed sample compared to the parent sample. Similarly,  $F^-$  was adsorbed through the ion

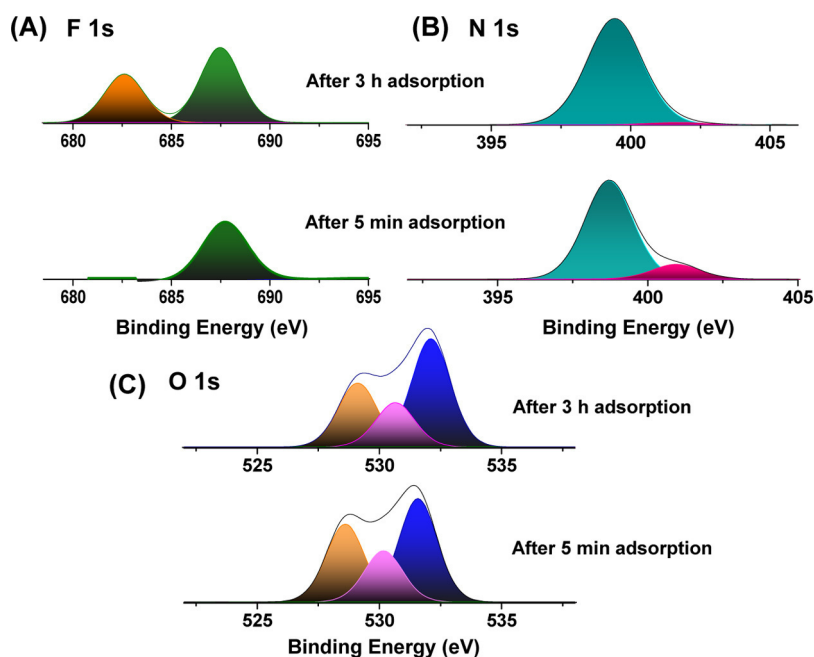


**Figure 4.** Deconvoluted XPS spectra of (A) F 1s, (B) N 1s, and (C) O 1s regions of CNPFH after 5 min and 3 h of  $F^-$  adsorption giving insights about the mechanism of adsorption.

exchange process with the surface hydroxyl groups of FeOOH (Figure 4C). The O 1s peaks at 530.1 and 528.6 eV corresponding to Fe–OH and Fe–O groups of parent CNPFH got shifted to 530.6 and 529.1 eV with decreased intensity for the adsorbed sample. This is supported by the Langmuir isotherm which gave a high correlation coefficient in this case (to be discussed in Figure 5).

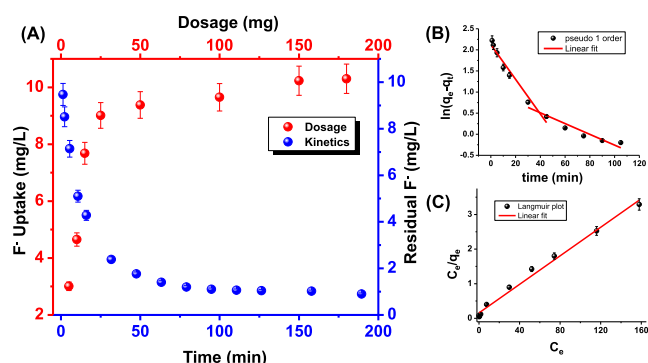


**Figure 5.** Batch studies for the performance of CNPFH (A) as a function of dosage and contact time, (B) pseudo first order, and (C) Langmuir isotherm model for fluoride adsorption from water.

**4.2. Batch Studies of  $F^-$  Adsorption on CNPFH.** It is observed that CNPFH exhibited superior performance where 50 mL of 10 mg/L  $F^-$  spiked water was treated with different dosages ranging from 5 to 180 mg, as shown in Figure 5A. About 50 mg of the composite was sufficient for bringing down the  $F^-$  concentration below 1 mg/L within 3 h of exposure time. It also shows the fast uptake kinetics of the composite where the initial 10 mg/L concentration of  $F^-$  was rapidly reduced to 1.5 mg/L within 60 min of incubation, by virtue of availability of the maximum number of free surface sites. At the end of 3 h, the residual concentration of  $F^-$  decreased further to 1 mg/L, following a relatively slower kinetics because of high surface coverage. Analyzing the kinetic data with the Lagergren's pseudo-first-order model (Figure 5B), two different slopes corresponding to  $F^-$  adsorption at two different sites belonging to PANI and FeOOH, respectively, which were in agreement with the XPS analysis of the adsorption mechanism discussed in Figure 4. Other adsorption mechanisms also are in broad agreement with the data, although they may not be strictly explainable for a two site model (Figure S1).

Figure 5C shows the linear form of the Langmuir isotherm model (eq S2) which gives a maximum adsorption capacity of 50.8 mg/g for CNPFH with a high correlation coefficient ( $R^2$ ) 0.96 using eq S2. It indicates monolayer adsorption, also known as chemisorption which agrees with the ion-exchange mechanism discussed in Figure 4A.<sup>10,39</sup> This is further

**Table 1.** Comparison of CNPFH Adsorption Capacity with Other PANI/PPy-Based Adsorbents

sl no.	materials	uptake capacity (mg/g)	max wt % PANI/PPy	optimum pH	references
1	PANI	0.8	100	3	40
2	PANI/chitosan	5.5	8–10	3–4	39
3	PANI/alumina	6.6	11.6	3	24
4	FeOOH	23.8	0	7	29
5	PPy/ $Fe_3O_4$	17.6–22.3	83	6.5	41
6	PPy/ $TiO_2$	33.17	9.3	7	42
7	CNF/PANI/FeOOH	50.8	14.1	3–4	this study

supported by the lower  $R^2$  value of the Freundlich isotherm (eq S11) and a low BET surface area of 111.1 m<sup>2</sup>/g of the composite and median pore width of 11.321 Å which do not play a major role in the adsorption process. The low surface area can be attributed to the ionic sites of the material as shown by XPS analysis, which cannot be completely picked up by N<sub>2</sub> adsorption, used for surface area evaluation. By using the Dubinin–Radushkevich isotherm (eq S12), we determined the  $E$  value (adsorption energy) to be 2500 kJ/mol (Figure S3). The correlation coefficient ( $R^2$ ) was 0.96. The  $E$  value (>16 kJ/mol) shows chemisorption taking place in the medium. The outcome of various isotherms and kinetic parameters is summarized in Table S1. The maximum F<sup>−</sup> uptake capacity of various other PANI/Ppy-based composites is compared with that of CNPFH, in Table 1. CNPFH shows higher removal efficiency even with lesser wt.% PANI because it exhibits synergistic performance because of simultaneous availability of FeOOH sites as well. Moreover, the adsorption of F<sup>−</sup> on the CNPFH surface is also thermodynamically feasible and is a spontaneous process with a negative  $\Delta G$  value. Using eqs S13 and S14, the thermodynamic parameters ( $\Delta H$  and  $\Delta S$ ) with the  $R^2$  value as 0.87 were derived. The  $\Delta H$  and  $\Delta S$  gave positive values which indicated that the adsorption is endothermic in nature giving rise to randomness at the solid solution interface during the adsorption of F<sup>−</sup> species at the active sites of the composite.

**4.2.1. Control Studies.** The control studies were carried out by using only CNF for fluoride uptake. It showed a meager removal of 200–300 ppb of F<sup>−</sup> out of 10 ppm which may be due to its porous structure. Hence, CNF can be considered as a platform having a high surface area which can favor blending with PANI and can embed the ferrihydrite nanoparticles in such a way that the active sites are available for adsorption of the surface of the mechanically stable composite.

CNPFH shows F<sup>−</sup> removal more than 80% in the presence of the most interfering anions like carbonate (CO<sub>3</sub><sup>2−</sup>), bicarbonate (HCO<sub>3</sub><sup>−</sup>), nitrate (NO<sub>3</sub><sup>−</sup>), silicate (SiO<sub>3</sub><sup>2−</sup>), sulfate (SO<sub>4</sub><sup>2−</sup>), and chloride (Cl<sup>−</sup>) in higher concentrations, except for SO<sub>4</sub><sup>2−</sup>, where F<sup>−</sup> removal is about 60%. This may be because of the competing nature for both the ions to form inner-sphere complexes with functional groups at the adsorption sites. The uptake of F<sup>−</sup> by CNPFH stays unaffected by the interfering cations like calcium (Ca<sup>2+</sup>), magnesium (Mg<sup>2+</sup>), potassium (K<sup>+</sup>), and sodium (Na<sup>+</sup>) (Figure 6A). It is able to maintain about 90% removal efficiency in a wide range of pH, that is, 3–9, but starts showing a decreased uptake when tested above pH 9 as shown in Figure 6B. This is because the decrease in surface positive charges of the adsorbent at higher pH levels (9–11) shown by zeta potential measurements, which adversely effects the coulombic interaction between the F<sup>−</sup> ion and the adsorbent surface (Figure 6C). Also, in the presence of excess hydroxyl ions in the medium, they start competing with F<sup>−</sup> ions for adsorption.

TGA of CNPFH in Figure 7A shows early weight loss of about 7% because of moisture below 250 °C. The weight loss of about 26% is due to the burning for carbon backbone of the cellulose and PANI polymers used in the composite between 220 and 350 °C. Next 15% weight loss is due to the loss of PANI functional groups and its dopants above 400 °C. Rest of the composite consists of iron oxide contributing 51% of the weight of the nanocomposite that stays stable till 900 °C. The iron oxide content in the composite is further studied by IR spectroscopy where Fe–O vibrations appear at 600–700 cm<sup>−1</sup>,

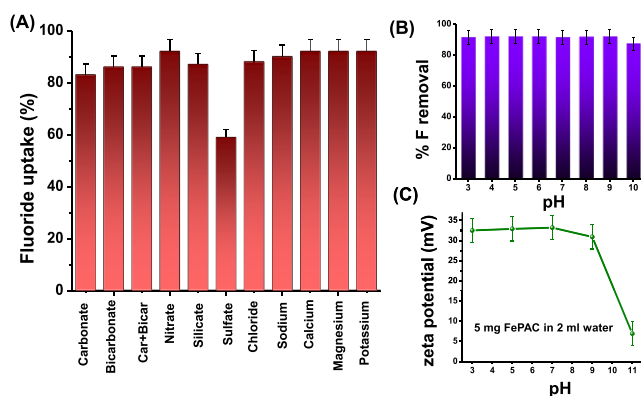


**Figure 6.** Batch studies for the performance of CNPFH (A) in the presence of interfering ions, (B) in the pH range of 3–10 for fluoride removal from water, and (C) zeta potential of CNPFH in the pH range of 3–11.

overlapping with a broad peak of O–H bending as shown in Figure 7B. The region between 1100 and 1600 cm<sup>−1</sup> corresponds to C–O stretching of cellulose, characteristic peaks of aromatic C–N stretching, C=C, C–H, and C=N stretching of the benzenoid ring and quinoid ring that confirms the emeraldine form of PANI.<sup>40</sup> A band around 1570 cm<sup>−1</sup> corresponding to the N–H bending of the amine salts and strong band in the 1100 cm<sup>−1</sup> region corresponding to the dopant suggest the presence of the mixed (EB–ES) salt form of PANI in the nanocomposite. N–H stretching at 3378 cm<sup>−1</sup> of the parent CNPFH gets broadened and shifted to 3410 cm<sup>−1</sup> upon F<sup>−</sup> adsorption.

From the perspective of environmental safety, CNPFH was tested for its leaching behavior. TOC (total organic carbon) and TN (total nitrogen) were measured of the adsorbent-soaked water. About 1.8 and 0.1 mg/L were the TOC and TN values before F<sup>−</sup> adsorption, while 1.7 and 0.08 mg/L were the TOC and TN values of CNPFH after F<sup>−</sup> adsorption, respectively. Iron leaching was also checked (20 and 12 μg/L before and after F<sup>−</sup> adsorption, respectively) but all these values are below MCL (maximum contaminant levels) in drinking water, that is, 10 mg/L for TN and 300 μg/L for iron according to the United States Environmental Protection Agency (USEPA). This can be attributed to the mechanical stability imparted to the nanocomposite by the cellulose backbone. Thus, the granular material can be packed in a prototype cartridge through which contaminated water can be passed continuously in an antigravity fashion for a larger contact time without using any external energy.

**4.3. Environmental Impact Assessment.** This technology was assessed qualitatively and quantitatively by evaluating some of the relevant mass-based sustainability and socioeconomic parameters, to determine the extent of “greenness” of the material and its manufacturing process.<sup>43–45</sup> The calculations were done using equations listed in an earlier paper.<sup>46</sup> They are also listed in the Supporting Information (eqs S4–S8) and the outcomes are summarized in Table 2.

**4.3.1. Raw Materials.** A major raw material includes cellulose which is renewable and biodegradable. Processing of CNFs usually involves mechanical extrusion and defibration for homogenization and chemical treatment by enzymes or strong acids and those manufacturers who use mild processing techniques for lignocellulosic fibers should be preferred for the supply of the raw material. Iron salt and aniline are used in

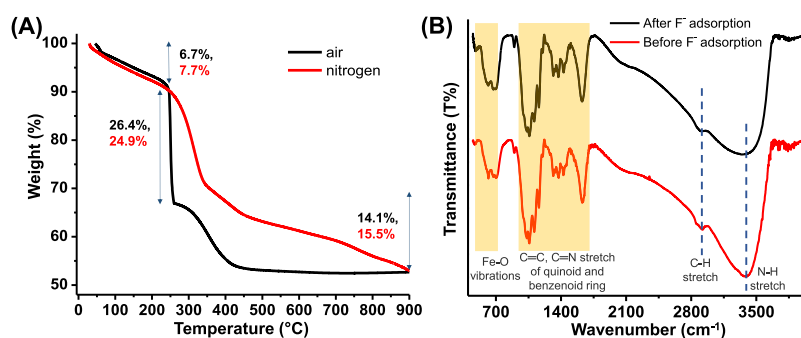


Figure 7. (A) TGA of CNPFH in an air and nitrogen atmosphere and (B) IR spectroscopy of CNPFH before and after  $F^-$  adsorption.

Table 2. Mass-Based Sustainability Metrics Evaluation for the Manufacturing Process of the CNPFH Nanocomposite

material	size ( $\mu\text{m}$ )	mass intensity (MI) (kg/kg)	solvent intensity (SI) (kg/kg)	reaction mass efficiency (RME) %	energy consumption (kW·h/kg)	E-factor
CNPFH nanocomposite	$150 \pm 50$	1.84	38.80	54	1.78	0.6

small quantities. Water is used as the solvent. The mass intensity (excluding water) was calculated to be 1.84, while the water intensity came as 38.8. Reaction mass efficiency was 54%. Large amounts of water were used because of moderate solubility of aniline which is 3.6 g per 100 mL water at 20 °C. Reaction mass efficiency can be improved by further optimization of reactant masses and avoiding the use of excess reagents.

**4.3.2. Energy Consumption.** Electricity was used for operating the pH meter, stirrer, and vacuum filtration settings. The composite was dried under the sun and no electrical energy was involved in the operation of the technology. Energy intensity was calculated to be 1.78 kW·h/kg of the composite, in a lab scale synthesis set up. The energy intensity can be reduced effectively by increasing the scale of production.

**4.3.3. Resulting Emissions.** No harmful solvents/fumes or side products were discharged during the synthesis of the composite. Use of extra oxidants to polymerize aniline was avoided in the synthesis. The E factor (environmental factor) was calculated to be 0.6 which indicates minimum emissions. The unreacted salts coming out with wash water discharge can be removed, and water can be recycled. The method of preparation of the composite is water positive by 1–2 orders of magnitude; that is, it produces about 200 L of fluoride-free water for every 1 L of water consumed for its production.<sup>47</sup>

**4.3.4. Toxicity Potential.** As per European Chemicals Agency (ECHA),  $\text{FeCl}_3$  and NaOH are classified as a skin sensitizer and corrosive, respectively, while aniline is toxic on repeated exposure to humans and aquatic life. While the first two reagents are nonflammable and stable at room temperature, aniline is in situ polymerized to PANI during composite formation and gets blended with cellulose, thereby preventing any leaching as shown by TOC analysis. PANI is not a hazardous substance or mixture according to regulation (EC) no. 1272/2008.  $\text{FeCl}_3$ , NaOH, and aniline show acute oral toxicity ( $\text{LD}_{50}$ ) at 900 mg/kg, 280–680 and  $\geq 102$  mg/kg in mice, respectively. Therefore, the manufacturing process has to be undertaken with some simple precautionary measures.

**4.3.5. Disposal of Waste.** Fluoride-adsorbed composites can be subjected to multiple regenerations for subsequent adsorption cycles by suitable base treatment like  $\text{NH}_4\text{OH}$ . They can be finally disposed off in leach-free landfills.

**4.3.6. Affordability.** Taking 5 mg/L as the average  $F^-$  concentration in accessible water in affected communities, reagents procured at bulk industrial rates and when the same composite synthesis is optimized with the industrial grade bulk cellulose, this technology can provide fluoride-free water under \$ 0.7/1000 L of clean water.

**4.3.7. Social Acceptability.** It depends on various criteria such as whether a technology is economical, requires low operational effort, acceptable for the users as a product, and can treat the contaminated water with the expected societal impact. The CNPFH-based technology is eco-friendly, simple, cost-effective, and does not incur excessive operational cost. The technology does not require trained manpower for implementation and maintenance. Thus, it is expected to be highly acceptable by the affected communities.

## 5. CONCLUSIONS

We report a green method for preparing highly efficient and sustainable cellulose/PANI-based nanocomposite and CNPFH for defluoridation of water. The 2-line ferrihydrite nanoparticles incorporated in the polymeric confinement of CNFs and doped N sites of the blended PANI function as active sites which operate synergistically for enhanced  $F^-$  removal. This also results in faster kinetics of adsorption. Therefore, the cooperation between such functional groups produce a combined performance that is greater than the sum of their separate capacities. SEM, HRTEM, XPS, and IR studies confirm that the surface, physical, and chemical properties of CNPFH remain intact even after  $F^-$  exposure till saturation. Moreover, the nanocomposite works efficiently in a wide range of pH with fast adsorption kinetics. The maximum  $F^-$  adsorption capacity of CNPFH is 50.8 mg/g which is higher than other PANI-based composites reported so far. Moreover, the robustness of the composite keeps it free from leaching, which makes it a superior option for an industrially feasible and green material for delivering affordable water in  $F^-$  affected communities worldwide. Lastly, further insights related to the environmental impact of such materials was developed by assessing relevant sustainability metrics.



## ■ ASSOCIATED CONTENT

### ● Supporting Information

The Supporting Information is available free of charge at <https://pubs.acs.org/doi/10.1021/acssuschemeng.9b04822>.

Equations used in the main text; TEM and SEM–EDS of CNPFH before and after  $F^-$  adsorption; pseudo second-order reaction kinetic plots for the adsorption of  $F^-$ ; table summarizing isotherm and kinetics parameters; Freundlich and Dubinin–Radushkevich isotherm models for  $F^-$  adsorption; XPS of F 1s for  $F^-$  adsorbed FeOOH; calculations for thermodynamic parameters related to adsorption; and physicochemical characteristics of influent natural drinking water (PDF)

## ■ AUTHOR INFORMATION

### Corresponding Author

\*E-mail: [pradeep@iitm.ac.in](mailto:pradeep@iitm.ac.in). Phone: +91-44 2257 4208. Fax: +91-44 2257 0545/0509.

### ORCID ●

Avijit Baidya: 0000-0001-5215-2856

Ligy Philip: 0000-0001-8838-2135

Thalappil Pradeep: 0000-0003-3174-534X

### Notes

The authors declare no competing financial interest.

## ■ ACKNOWLEDGMENTS

The authors thank Sandeep Bose and Krithika for EDS and TOC measurements, Department of Chemistry and Department of Civil Engineering, respectively, of IIT Madras. The authors also thank the Common facility, Department of Chemistry, IIT Madras for BET and TGA measurements. The authors thank the Department of Science and Technology, Government of India and project no. DST/TM/WTI/WIC/2k17/82(G) for supporting our research program on nanomaterials.

## ■ REFERENCES

- (1) Mukherjee, I.; Singh, U. K. *Groundwater Fluoride Contamination, Probable Release, and Containment Mechanisms: A Review on Indian Context*; Springer Netherlands, 2018; Vol. 40.
- (2) Jagtap, S.; Yenkie, M. K.; Labhsetwar, N.; Rayalu, S. Fluoride in Drinking Water and Defluoridation of Water. *Chem. Rev.* **2012**, *112*, 2454–2466.
- (3) Mohapatra, M.; Anand, S.; Mishra, B. K.; Giles, D. E.; Singh, P. Review of Fluoride Removal from Drinking Water. *J. Environ. Manage.* **2009**, *91*, 67–77.
- (4) Trieu, A.; Mohamed, A.; Lynch, E. Silver Diamine Fluoride versus Sodium Fluoride for Arresting Dentine Caries in Children: A Systematic Review and Meta-Analysis. *Sci. Rep.* **2019**, *9*, 2115.
- (5) Jia, B.; Zong, L.; Lee, J. Y.; Lei, J.; Zhu, Y.; Xie, H.; Clemens, J. L.; Feller, M. C.; Na, Q.; Dong, J.; et al. Maternal Supplementation of Low Dose Fluoride Alleviates Adverse Perinatal Outcomes Following Exposure to Intrauterine Inflammation. *Sci. Rep.* **2019**, *9*, 2575.
- (6) Ali, I. New Generation Adsorbents for Water Treatment. *Chem. Rev.* **2012**, *112*, 5073–5091.
- (7) Ali, S.; Thakur, S. K.; Sarkar, A.; Shekhar, S. Worldwide Contamination of Water by Fluoride. *Environ. Chem. Lett.* **2016**, *14*, 291–315.
- (8) Kheradpisheh, Z.; Mirzaei, M.; Mahvi, A. H.; Mokhtari, M.; Azizi, R.; Fallahzadeh, H.; Ehrampoush, M. H. Impact of Drinking Water Fluoride on Human Thyroid Hormones: A Case-Control Study OPEN. *Sci. Rep.* **2018**, *8*, 2674.
- (9) Kimambo, V.; Bhattacharya, P.; Mtalo, F.; Mtamba, J.; Ahmad, A. Fluoride occurrence in groundwater systems at global scale and status of defluoridation—State of the art. *Groundw. Sustain. Dev.* **2019**, *9*, 100223.
- (10) Maliyekkal, S. M.; Anshup, Antony, K. R.; Pradeep, T. High Yield Combustion Synthesis of Nanomagnesia and Its Application for Fluoride Removal. *Sci. Total Environ.* **2010**, *408*, 2273–2282.
- (11) Jadhav, S. V.; Bringas, E.; Yadav, G. D.; Rathod, V. K.; Ortiz, I.; Marathe, K. V. Arsenic and Fluoride Contaminated Groundwaters: A Review of Current Technologies for Contaminants Removal. *J. Environ. Manage.* **2015**, *162*, 306–325.
- (12) Bhatnagar, A.; Kumar, E.; Sillanpää, M. Fluoride Removal from Water by Adsorption—A Review. *Chem. Eng. J.* **2011**, *171*, 811–840.
- (13) Cherukumilli, K.; Maurer, T.; Hohman, J. N.; Mehta, Y.; Gadgil, A. J. Effective Remediation of Groundwater Fluoride with Inexpensively Processed Indian Bauxite. *Environ. Sci. Technol.* **2018**, *52*, 4711–4718.
- (14) Nayak, B.; Samant, A.; Patel, R.; Misra, P. K. Comprehensive Understanding of the Kinetics and Mechanism of Fluoride Removal over a Potent Nanocrystalline Hydroxyapatite Surface. *ACS Omega* **2017**, *2*, 8118–8128.
- (15) Wan, S.; Lin, J.; Tao, W.; Yang, Y.; Li, Y.; He, F. Enhanced Fluoride Removal from Water by Nanoporous Biochar-Supported Magnesium Oxide. *Ind. Eng. Chem. Res.* **2019**, *58*, 9988.
- (16) Cadiau, A.; Belmabkhout, Y.; Adil, K.; Bhatt, P. M.; Pillai, R. S.; Shkurenko, A.; Martineau-Corcios, C.; Maurin, G.; Eddaoudi, M. Hydrolytically Stable Fluorinated Metal-Organic Frameworks for Energy-Efficient Dehydration. *Science* **2017**, *356*, 731–735.
- (17) Pistner, A. J.; Lutterman, D. A.; Ghidui, M. J.; Ma, Y.-Z.; Rosenthal, J. Synthesis, Electrochemistry, and Photophysics of a Family of Phlorin Macrocycles That Display Cooperative Fluoride Binding. *J. Am. Chem. Soc.* **2013**, *135*, 6601.
- (18) Zhao, H.; Zhao, B.; Yang, W.; Li, T. Effects of  $Ca^{2+}$  and  $Mg^{2+}$  on Defluorination in the Electrocoagulation Process. *Environ. Sci. Technol.* **2010**, *44*, 9112–9116.
- (19) Moran Ayala, L. I.; Paquet, M.; Janowska, K.; Jamard, P.; Quist-Jensen, C. A.; Bosio, G. N.; Mártire, D. O.; Fabbri, D.; Boffa, V. Water Defluorination: Nanofiltration vs Membrane Distillation. *Ind. Eng. Chem. Res.* **2018**, *57*, 14740–14748.
- (20) Pan, B.; Xu, J.; Wu, B.; Li, Z.; Liu, X. Enhanced Removal of Fluoride by Polystyrene Anion Exchanger Supported Hydrous Zirconium Oxide Nanoparticles. *Environ. Sci. Technol.* **2013**, *47*, 9347–9354.
- (21) Zhang, J.; Kong, Y.; Yang, Y.; Chen, N.; Feng, C.; Huang, X.; Yu, C. Fast Capture of Fluoride by Anion-Exchange Zirconium-Graphene Hybrid Adsorbent. *Langmuir* **2019**, *35*, 6861–6869.
- (22) Sreeprasad, T. S.; Maliyekkal, S. M.; Lisha, K. P.; Pradeep, T. Reduced graphene oxide-metal/metal oxide composites: Facile synthesis and application in water purification. *J. Hazard. Mater.* **2011**, *186*, 921–931.
- (23) Meenakshi; Maheshwari, R. C. Fluoride in Drinking Water and Its Removal. *J. Hazard. Mater.* **2006**, *137*, 456–463.
- (24) Karthikeyan, M.; Satheesh Kumar, K. K.; Elango, K. P. Conducting Polymer/Alumina Composites as Viable Adsorbents for the Removal of Fluoride Ions from Aqueous Solution. *J. Fluorine Chem.* **2009**, *130*, 894–901.
- (25) Dou, X.; Zhang, Y.; Wang, H.; Wang, T.; Wang, Y. Performance of Granular Zirconium-Iron Oxide in the Removal of Fluoride from Drinking Water. *Water Res.* **2011**, *45*, 3571–3578.
- (26) Chen, L.; He, B.-Y.; He, S.; Wang, T.-J.; Su, C.-L.; Jin, Y. Fe—Ti oxide nano-adsorbent synthesized by co-precipitation for fluoride removal from drinking water and its adsorption mechanism. *Powder Technol.* **2012**, *227*, 3–8.
- (27) Deng, S.; Liu, H.; Zhou, W.; Huang, J.; Yu, G. Mn-Ce Oxide as a High-Capacity Adsorbent for Fluoride Removal from Water. *J. Hazard. Mater.* **2011**, *186*, 1360–1366.
- (28) Kanno, C. M.; Sanders, R. L.; Flynn, S. M.; Lessard, G.; Myneni, S. C. B. Novel Apatite-Based Sorbent for Defluorination: Synthesis and Sorption Characteristics of Nano-Micro-Crystalline



Hydroxyapatite-Coated-Limestone. *Environ. Sci. Technol.* **2014**, *48*, 5798–5807.

(29) Zhu, B.-S.; Jia, Y.; Jin, Z.; Sun, B.; Luo, T.; Kong, L.-T.; Liu, J.-H. A Facile Precipitation Synthesis of Mesoporous 2-Line Ferrihydrite with Good Fluoride Removal Properties. *RSC Adv.* **2015**, *5*, 84389–84397.

(30) Navío; Hidalgo; Colón, G.; Botta, S. G.; Litter, M. I. Preparation and Physicochemical Properties of ZrO<sub>2</sub> and Fe/ZrO<sub>2</sub> Prepared by a Sol–Gel Technique. *Langmuir* **2001**, *17*, 202.

(31) Sairam Sundaram, C.; Viswanathan, N.; Meenakshi, S. Fluoride Sorption by Nano-Hydroxyapatite/Chitin Composite. *J. Hazard. Mater.* **2009**, *172*, 147–151.

(32) Liao, X.-p.; Shi, B. Adsorption of Fluoride on Zirconium(IV)-Impregnated Collagen Fiber. *Environ. Sci. Technol.* **2005**, *39*, 4628.

(33) Chen, W.; Yu, H.; Lee, S.-Y.; Wei, T.; Li, J.; Fan, Z. Nanocellulose: A Promising Nanomaterial for Advanced Electrochemical Energy Storage. *Chem. Soc. Rev.* **2018**, *47*, 2837–2872.

(34) Thomas, B.; Raj, M. C.; Athira, K. B.; Rubiyah, M. H.; Joy, J.; Moores, A.; Drisko, G. L.; Sanchez, C. Nanocellulose, a Versatile Green Platform: From Biosources to Materials and Their Applications. *Chem. Rev.* **2018**, *118*, 11575–11625.

(35) Peng, B. L.; Dhar, N.; Liu, H. L.; Tam, K. C. Chemistry and Applications of Nanocrystalline Cellulose and Its Derivatives: A Nanotechnology Perspective. *Can. J. Chem. Eng.* **2011**, *89*, 1191–1206.

(36) Baker, C. O.; Huang, X.; Nelson, W.; Kaner, R. B. Polyaniline Nanofibers: Broadening Applications for Conducting Polymers. *Chem. Soc. Rev.* **2017**, *46*, 1510–1525.

(37) Kumar, A. A.; Som, A.; Longo, P.; Sudhakar, C.; Bhuin, R. G.; Gupta, S. S.; Sen, A.; Anshup, M. U.; Sankar, M. U.; Chaudhary, A.; et al. Confined Metastable 2-Line Ferrihydrite for Affordable Point-of-Use Arsenic-Free Drinking Water. *Adv. Mater.* **2017**, *29*, 1604260.

(38) MSDS—576379 <https://www.sigmaaldrich.com/MSDS/MSDS/DisplayMSDSPage.do?country=IN&language=en&productNumber=576379&brand=ALDRICH&PageToGoToURL=https%3A%2F%2Fwww.sigmaaldrich.com%2Fcatalog%2Fproduct%2Faldrich%2F576379%3Flang%3Den> (accessed Oct 24, 2019).

(39) Karthikeyan, M.; Kumar, K. K. S.; Elango, K. P. Batch Sorption Studies on the Removal of Fluoride Ions from Water Using Eco-Friendly Conducting Polymer/Bio-Polymer Composites. *Desalination* **2011**, *267*, 49–56.

(40) Karthikeyan, M.; Satheeshkumar, K. K.; Elango, K. P. Defluoridation of Water via Doping of Polyanilines. *J. Hazard. Mater.* **2009**, *163*, 1026–1032.

(41) Bhaumik, M.; Leswif, T. Y.; Maity, A.; Srinivasu, V. V.; Onyango, M. S. Removal of Fluoride from Aqueous Solution by Polypyrrole/F<sub>3</sub>O<sub>4</sub> Magnetic Nanocomposite. *J. Hazard. Mater.* **2011**, *186*, 150–159.

(42) Chen, J.; Shu, C.; Wang, N.; Feng, J.; Ma, H.; Yan, W. Adsorbent Synthesis of Polypyrrole/TiO<sub>2</sub> for Effective Fluoride Removal from Aqueous Solution for Drinking Water Purification: Adsorbent Characterization and Adsorption Mechanism. *J. Colloid Interface Sci.* **2017**, *495*, 44–52.

(43) Sheldon, R. A. Metrics of Green Chemistry and Sustainability: Past, Present, and Future. *ACS Sustainable Chem. Eng.* **2018**, *6*, 32–48.

(44) Jiménez-González, C.; Constable, D. J. C.; Ponder, C. S. Evaluating the “Greenness” of Chemical Processes and Products in the Pharmaceutical Industry—a Green Metrics Primer. *Chem. Soc. Rev.* **2012**, *41*, 1485–1498.

(45) Starkl, M.; Anthony, J.; Aymerich, E.; Brunner, N.; Chubilleau, C.; Das, S.; Ghangrekar, M. M.; Kazmi, A. A.; Philip, L.; Singh, A. Interpreting Best Available Technologies More Flexibly: A Policy Perspective for Municipal Wastewater Management in India and Other Developing Countries. *Environ. Impact Assess. Rev.* **2018**, *71*, 132–141.

(46) Mukherjee, S.; Kumar, A. A.; Sudhakar, C.; Kumar, R.; Ahuja, T.; Mondal, B.; Srikrishnarka, P.; Philip, L.; Pradeep, T. Sustainable and Affordable Composites Built Using Microstructures Performing Better than Nanostructures for Arsenic Removal. *ACS Sustainable Chem. Eng.* **2019**, *7*, 3222–3233.

(47) Sankar, M. U.; Aigal, S.; Maliyekkal, S. M.; Chaudhary, A.; Anshup, A. A.; Kumar, A. A.; Chaudhari, K.; Pradeep, T. Biopolymer-Reinforced Synthetic Granular Nanocomposites for Affordable Point-of-Use Water Purification. *Proc. Natl. Acad. Sci. U.S.A.* **2013**, *110*, 8459–8464.

## Supporting Information

### **Nanocellulose reinforced organo-inorganic nanocomposite for synergistic and affordable defluoridation of water and an evaluation of its sustainability metrics**

*Sritama Mukherjee<sup>†‡</sup>, Haritha Ramireddy<sup>†</sup>, Avijit Baidya<sup>†</sup>, A. K. Amala<sup>†</sup>, Chennu Sudhakar<sup>†</sup>,  
Biswajit Mondal<sup>†</sup>, Ligy Philip<sup>‡</sup>, Thalappil Pradeep<sup>\*,†</sup>*

<sup>†</sup>DST Unit of Nanoscience (DST UNS) and Thematic Unit of Excellence (TUE), Department of Chemistry, Indian Institute of Technology Madras, Chennai 600036, India.

<sup>‡</sup>EWRE Division, Department of Civil Engineering, Indian Institute of Technology Madras, Chennai 600036, India.

\*Corresponding author

E-mail: [pradeep@iitm.ac.in](mailto:pradeep@iitm.ac.in)

Thalappil Pradeep, DST Unit of Nanoscience (DST UNS) and Thematic Unit of Excellence (TUE), Department of Chemistry, Indian Institute of Technology Madras, Chennai 600036, India.

Tel.: +91-44 2257 4208; Fax: +91-44 2257 0545/0509

#### **SUPPORTING INFORMATION CONTENT**

Total number of pages: 14

Total number of figures: 8

Total number of tables: 2

Total number of equations: 14

## TABLE OF CONTENTS

<b>Supporting items</b>	<b>Title</b>	<b>Page no.</b>
E1-E14	Equations used in main text	S3-S4
Figure S1	Large area SEM images of CNPFH (a) before and (b) after F <sup>-</sup> adsorption	S5
Figure S2	TEM images of CNPFH (a) before and (b) after F <sup>-</sup> adsorption, corresponding to elemental mapping	S6
Figure S3	TEM images of as-synthesized CNPFH composite (a) before and (b) after F <sup>-</sup> adsorption.	S7
Figure S4	Pseudo second-order reaction kinetic plots for the adsorption of F <sup>-</sup> on CNPFH	S8
Figure S5	Freundlich isotherm plot for the adsorption of F <sup>-</sup> on CNPFH	S9
Figure S6	Dubinin–Radushkevich isotherm model for F <sup>-</sup> adsorption on CNPFH	S11
Figure S7	Deconvoluted XPS spectra of F 1s for F <sup>-</sup> adsorbed FeOOH-cellulose composite	S12
Figure S8	Thermodynamic plot for the adsorption of F <sup>-</sup> on CNPFH	S13
Table S1	Summary of isotherms and kinetic parameters of F <sup>-</sup> adsorption on CNPFH	S10
Table S2	Physicochemical characteristics of influent natural drinking water	S14

**Equation (1):** The maximum uptake of F<sup>-</sup> ( $q_e$ ) by cellulosic composites was calculated using the equation given below:

$$Uptake (q_e) = \frac{(C_o - C_e)V}{m}$$

where  $q_e$  is the amount of F<sup>-</sup> ions adsorbed per gram of the adsorbent (mg/g) at equilibrium,  $C_e$  is the equilibrium concentration of As(III)/As(V) in the bulk solution (mg/L),  $C_o$  is the initial F<sup>-</sup> concentration (mg/L),  $V$  is the volume of solution (L) and  $m$  is the mass of the adsorbent (g).

**Equation (2):** The linearized form of Langmuir equation used in this work is defined as,

$$\frac{C_e}{q_e} = \frac{C_e}{q_{max}} + \frac{1}{bq_{max}}$$

where  $q_e$  is the amount of adsorption at the surface of the adsorbent (mg/g),  $C_e$  is the equilibrium concentration of the solution (mg/L),  $q_{max}$  is the maximum surface density at monolayer coverage and  $b$  is the Langmuir adsorption constant (L/mg) related to the free energy of adsorption and  $1/q_{max}$  and  $1/bq_{max}$  are the Langmuir constants.

**Equation (3):** The removal % of F<sup>-</sup> was calculated using the equation mentioned below:

$$Removal \% = \frac{C_o - C_e}{C_o} \times 100$$

where  $C_o$  and  $C_e$  are the initial and equilibrium concentrations of the metal ions, respectively.

Sustainability metrics equations

**Equation (4):**  $Mass\ intensity = \frac{mass\ of\ all\ reactants\ used\ excluding\ water}{mass\ of\ product} kg/kg\ product$

**Equation (5):** 
$$\text{Water intensity } (W_p) = \frac{\text{mass of all water used}}{\text{mass of product}} \text{ kg/kg product}$$

**Equation (6):** 
$$\text{Reaction mass efficiency (RME)} = \frac{\text{mass of product}}{\text{mass of all reactants}} \times 100\%$$

**Equation (7):** 
$$\text{Energy Intensity} = \frac{\text{amount of non renewable energy used}}{\text{mass of product}} \text{ kW.h/kg}$$

**Equation (8):** 
$$E \text{ factor} = \frac{[\text{kg}(\text{raw materials}) - \text{kg}(\text{desired product})]}{\text{kg}(\text{total product including water})}$$

**Equation (9):** 
$$\text{Lagergren pseudo-first-order model: } \ln(q_e - q_t) = \ln q_e - k_1 t$$

**Equation (10):** 
$$\text{Ho's pseudo-second-order model: } \frac{t}{q_e} = \frac{1}{k_2 q_e^2} + \frac{1}{q_e} t$$

**Equation (11):** 
$$\text{Freundlich adsorption isotherm model: } \log Q_e = \log K_f + \frac{1}{n} \log C_e$$

**Equation (12):** 
$$\text{Dubinin-Radushkevich isotherm model: } \ln Q_e = \ln Q_s - K_{ad} \varepsilon^2$$

**Equation (13):** 
$$\text{Gibbs free energy equation: } \Delta G^\circ = \Delta H^\circ - T \Delta S^\circ$$

**Equation (14):** 
$$\text{Equation for thermodynamic parameters: } \ln k = (-\Delta H^\circ)/RT + (\Delta S^\circ)/R$$

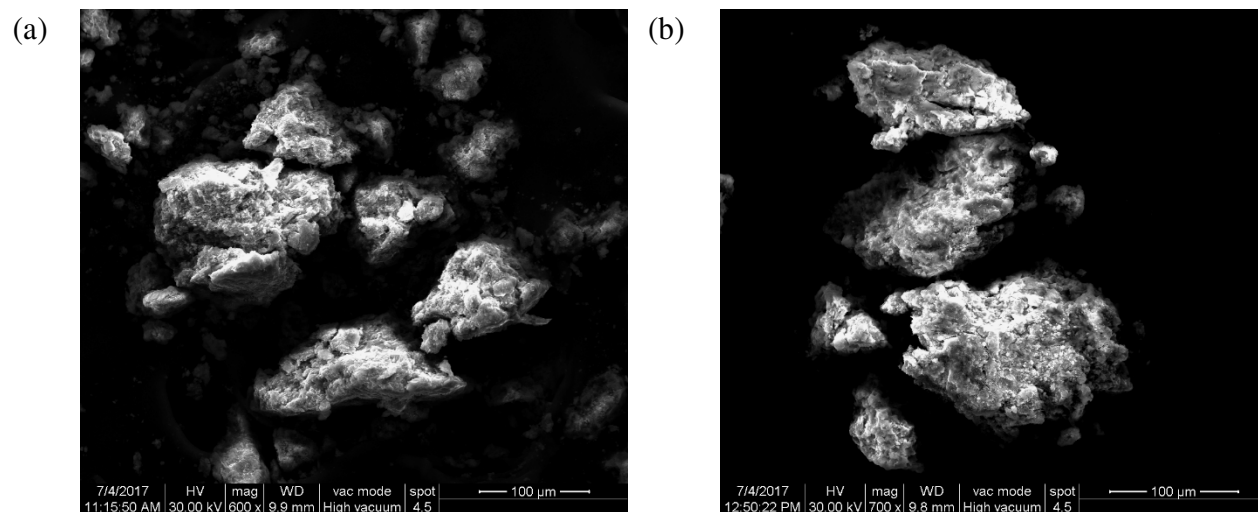


**Figure S1:** Large area SEM images of CNPFH (a) before and (b) after F- adsorption.

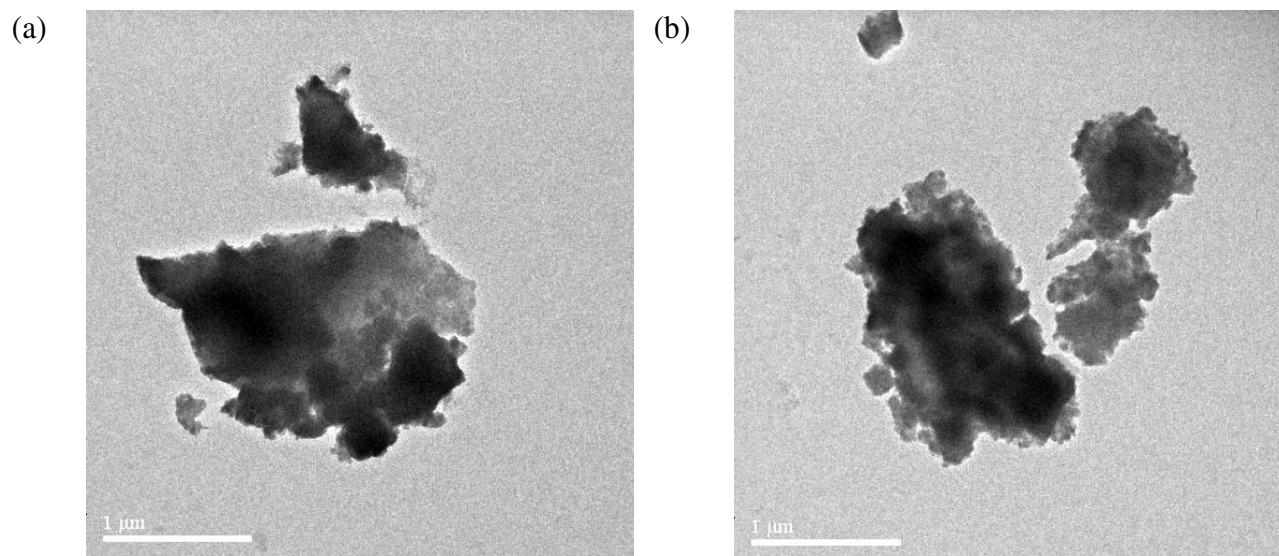


**Figure S2:** TEM images of CNPFH (a) before and (b) after F<sup>-</sup> adsorption, corresponding to elemental mapping shown in Figure 1 (C) and (D).

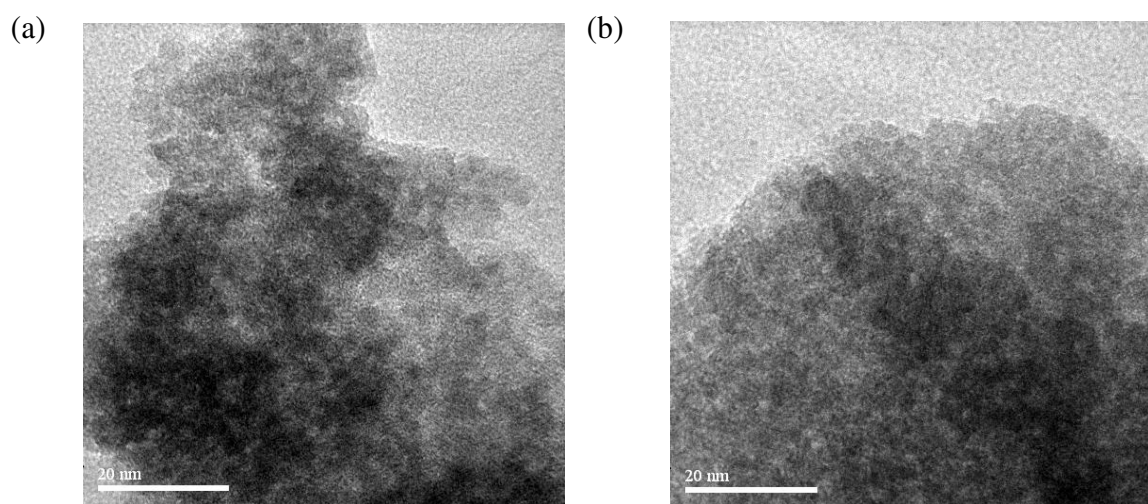


**Figure S3.** TEM images of as-synthesized CNPFH composite (a) before and (b) after F-adsorption.



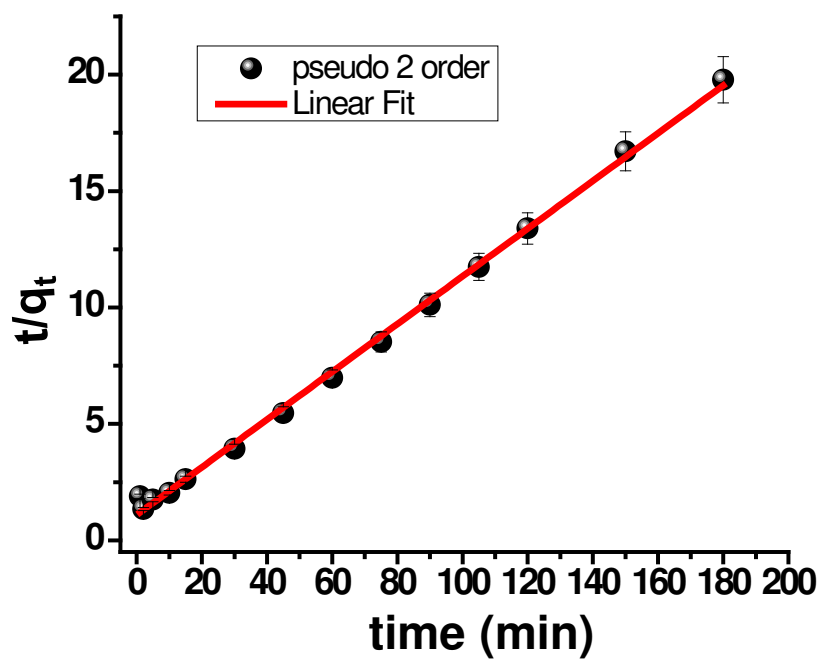


**Figure S4.** Pseudo second-order reaction kinetic plot for the adsorption of F<sup>-</sup> on CNPFH, fitted with Eq. 10.

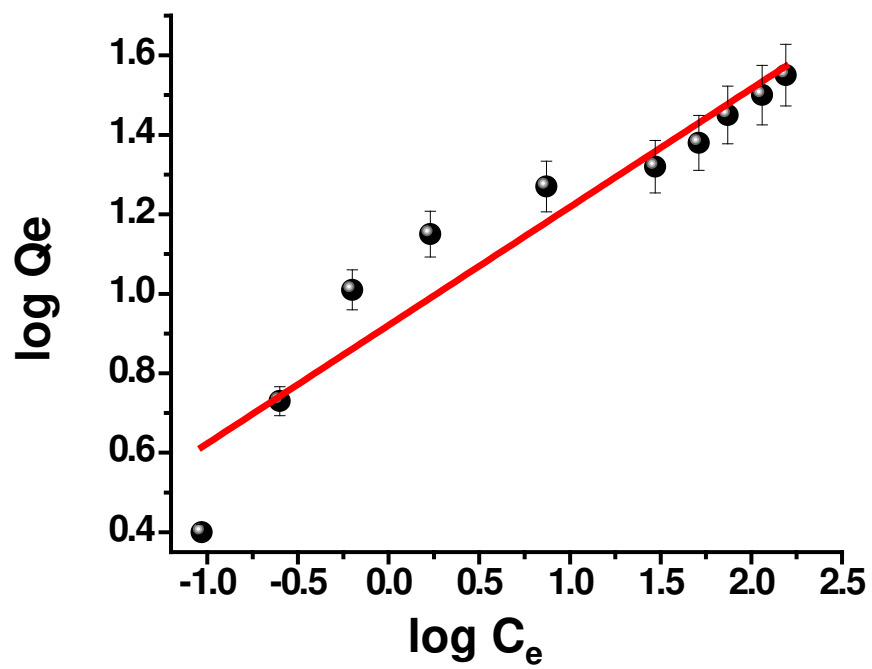
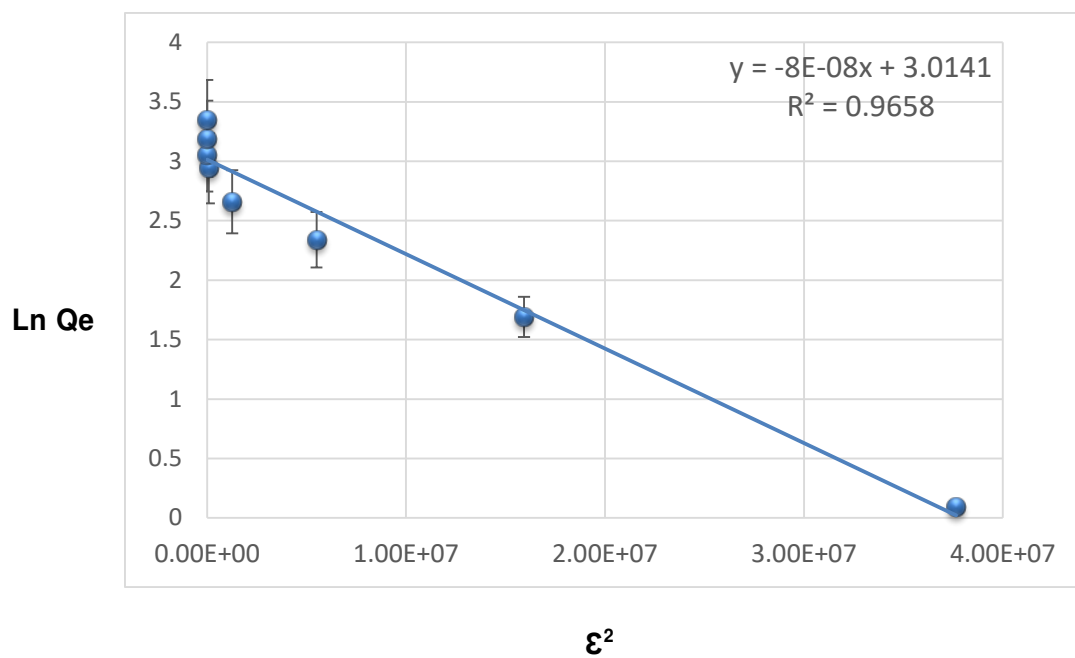


**Figure S5.** Freundlich isotherm plot for the adsorption of  $F^-$  on CNPFH, fitted with Eq. 11.

**Table S1.** Summary of isotherms and kinetic parameters of F<sup>-</sup> adsorption on CNPFH.

	Model	Formulae	k (rate constant)	q <sub>e</sub> (Adsorption capacity) (mg/g)	R <sup>2</sup>
Kinetics	Pseudo 1 <sup>st</sup> order	$\ln(q_e - q_t) = \ln q_e - k_1 t$	0.02	6.5	0.891
	Pseudo 2 <sup>nd</sup> order	$\frac{t}{q} = \frac{1}{k_2 q_e^2} + \frac{1}{q_e} t$	0.01	9.8	0.997
	Model	Formulae	n (isotherm constant)	Adsorption capacity	R <sup>2</sup>
Isotherm	Langmuir	$\frac{C_e}{q_e} = \frac{C_e}{q_{max}} + \frac{1}{n q_{max}}$	0.04	50.8 mg/g	0.969
	Freundlich	$\log q_e = \log K_f + \frac{1}{n} \log C_e$	3.3	8.3 (mg <sup>1-1/n</sup> L <sup>1/n</sup> /g)	0.899



$$E_{DR} = 2500 \text{ kJ/mol}, R^2 = 0.96$$

**Figure S6.** Dubinin–Radushkevich isotherm model for F- adsorption on CNPFH using Eq. 12.

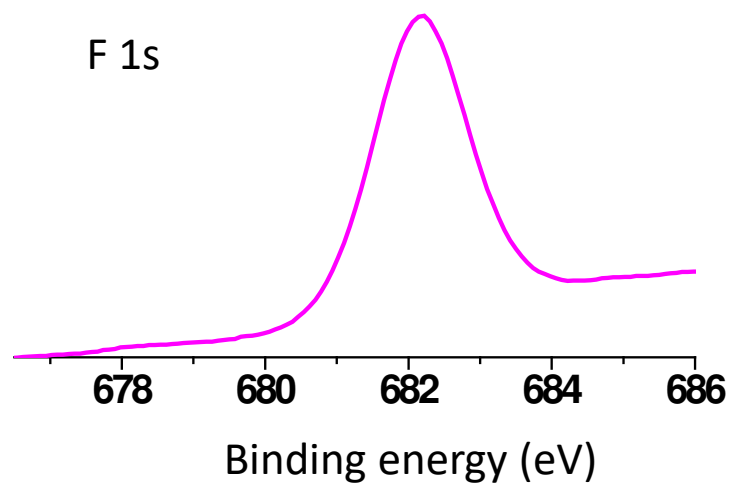


**Figure S7.** Deconvoluted XPS spectrum of F 1s for F<sup>-</sup> adsorbed FeOOH-cellulose composite.

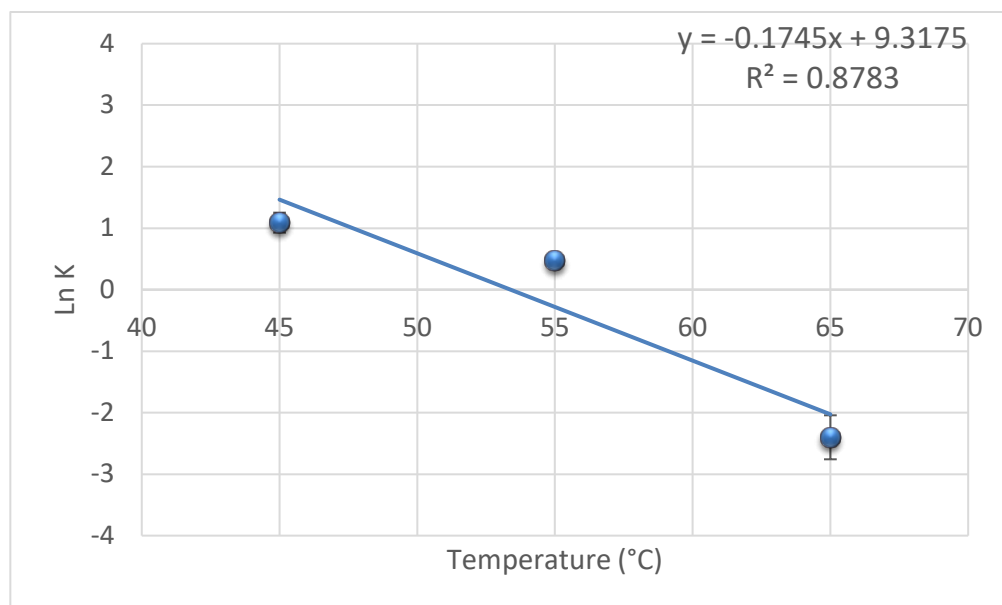


**Figure S8.** Thermodynamic plot for the adsorption of  $F^-$  on CNPFH, using Eq. 14.

$\Delta S = 0.077 \text{ kJ/mol} \cdot \text{K}$ ,  $\Delta H = 0.002 \text{ kJ/mol}$

**Table S2.**

Physicochemical characteristics of influent natural water.

Sl no.	Parameters	Value
1	Total coliforms (CFU/ml)	1-2 * 10 <sup>3</sup>
2	pH at 25°C	7.8
3	Conductivity (µS/cm)	640.0
4	Fluoride (mg/L)	0.57
5	Chloride (mg/L)	86.34
6	Nitrate (mg/L)	1.84
7	Sulfate (mg/L)	32.41
8	Silicate (mg/L)	15.87
9	Phosphate (mg/L)	55.83
10	Sodium (mg/L)	53.74
11	Potassium (mg/L)	2.33
12	Magnesium (mg/L)	14.34
13	Calcium (mg/L)	28.72

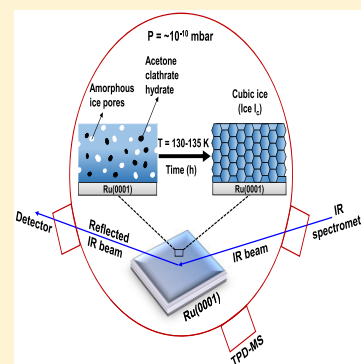
# Formation of Cubic Ice via Clathrate Hydrate, Prepared in Ultrahigh Vacuum under Cryogenic Conditions

Jyotirmoy Ghosh, Radha Gobinda Bhui,† Gaurav Vishwakarma, and Thalappil Pradeep\*<sup>‡</sup>

DST Unit of Nanoscience (DST UNS) and Thematic Unit of Excellence (TUE), Department of Chemistry, Indian Institute of Technology Madras, Chennai 600036, India

## Supporting Information

**ABSTRACT:** Cubic ice (ice  $I_c$ ) is a crystalline phase of solid water, which exists in the earth's atmosphere and extraterrestrial environments. We provide experimental evidence that dissociation of acetone clathrate hydrate (CH) makes ice  $I_c$  in ultrahigh vacuum (UHV) at 130–135 K. In this process, we find that crystallization of ice  $I_c$  occurs below its normal crystallization temperature. Time-dependent reflection absorption infrared spectroscopy (RAIRS) and reflection high-energy electron diffraction (RHEED) were utilized to confirm the formation of ice  $I_c$ . Associated crystallization kinetics and activation energy ( $E_a$ ) for the process were evaluated. We suggest that enhanced mobility or diffusion of water molecules during acetone hydrate dissociation enabled crystallization. Moreover, this finding implied that CHs might exist in extreme low-pressure environments present in comets. These hydrates, subjected to prolonged thermal annealing, transform into ice  $I_c$ . This unique process of crystallization hints at a possible mechanistic route for the formation of ice  $I_c$  in comets.



Ices are ubiquitous in the universe, planets, and interstellar medium (ISM)<sup>1</sup> and can exist in different amorphous and crystalline forms.<sup>2,3</sup> At ambient conditions, only hexagonal ice (ice  $I_h$ ) can be obtained, out of more than 17 known crystalline ice polymorphs.<sup>4–6</sup> Recently, in 2019, a new crystalline superionic ice phase was discovered,<sup>7</sup> termed ice XVIII, which indicates the diverse and exciting nature of this field. Cubic ice (ice  $I_c$ ), a metastable ice phase, was discovered by König<sup>8</sup> in electron diffraction experiments.<sup>3</sup> Subsequently, many experiments were performed to produce ice  $I_c$ .<sup>9,10</sup> Such studies include vapor deposition on cooled substrates,<sup>9,11–13</sup> freezing of water in confined geometries,<sup>14–16</sup> supercooling of water droplets,<sup>17–20</sup> freezing of high-pressure ice phases (phase II to IX) followed by annealing to 120–170 K,<sup>3,21–24</sup> annealing of amorphous ices,<sup>25,26</sup> dissociation of clathrate hydrates (CHs),<sup>27–30</sup> etc.

Formation of ice  $I_c$  by dissociation of CHs is intriguing among the several methods mentioned above. It was shown that dissociation of CO<sub>2</sub> hydrates can lead to ice  $I_c$ .<sup>27,29</sup> The dissociation experiments were carried out at 6 mbar and 170–190 K, simulating the Martian surface and subsurface conditions.<sup>27</sup> However, the applicability of this unique transformation route in more exotic environments (comets and ISM), where the pressure is extremely low ( $\sim 10^{-10}$  mbar), is still an open question. Note that ice  $I_c$  is predicted to exist in comets.<sup>31,32</sup> This is possible as CH, the precursor of ice  $I_c$  in this transformation, can exist in cometary conditions.<sup>33</sup> Moreover, ice  $I_c$  is also known to form in the earth's atmosphere.<sup>19,34–36</sup> Calculation of dissociation pressures of different hydrates suggests their stability at low pressures and low temperatures.<sup>37</sup> We have shown recently that methane and CO<sub>2</sub> can form CHs at  $\sim 10^{-10}$  mbar and  $\sim 10$  K, conditions

relevant to ISM.<sup>38</sup> However, there has been no experimental evidence to our knowledge for the formation of ice  $I_c$  upon dissociation of CHs in ultrahigh vacuum (UHV) conditions.

Comets are assumed to be the most primitive bodies of the solar system and impart essential information on its formation. The nuclei of comets are mostly composed of rock, dust, and water-ice along with other volatile substances. The structures and phases of ice in comets play crucial roles in the entrapment of volatile gases,<sup>39</sup> as well as in different cometary activities such as cometary outbursts, heat balance of the cometary nuclei, etc.<sup>39</sup> Patashnick et al.<sup>40</sup> proposed that the heat evolved during crystallization (amorphous to ice  $I_c$ ) may be the driving force for these outbursts. Again, it was speculated that the change of thermal conductivity during this crystallization may alter the heat balance of the cometary nucleus.<sup>39,41–43</sup> Amorphous ice is a poor heat conductor in comparison to ice  $I_c$ , and thermal conductivity rises by a factor of 10 upon phase transition.<sup>39</sup> The comets composed of ice  $I_c$  show low volatile outburst activity in comparison to comets with amorphous ice.<sup>39</sup> Enhanced thermal conductivity of ice  $I_c$  increases the overall temperature of the cometary nucleus, resulting in the escape of volatile species at one time. In contrast, the comets with amorphous ice continuously show outburst activity every time the surface is sufficiently heated by solar radiation. This phenomenon may occur in an erratic manner until all the ice is transformed into the cubic state.<sup>39</sup>

**Received:** October 24, 2019

**Accepted:** December 5, 2019

**Published:** December 5, 2019



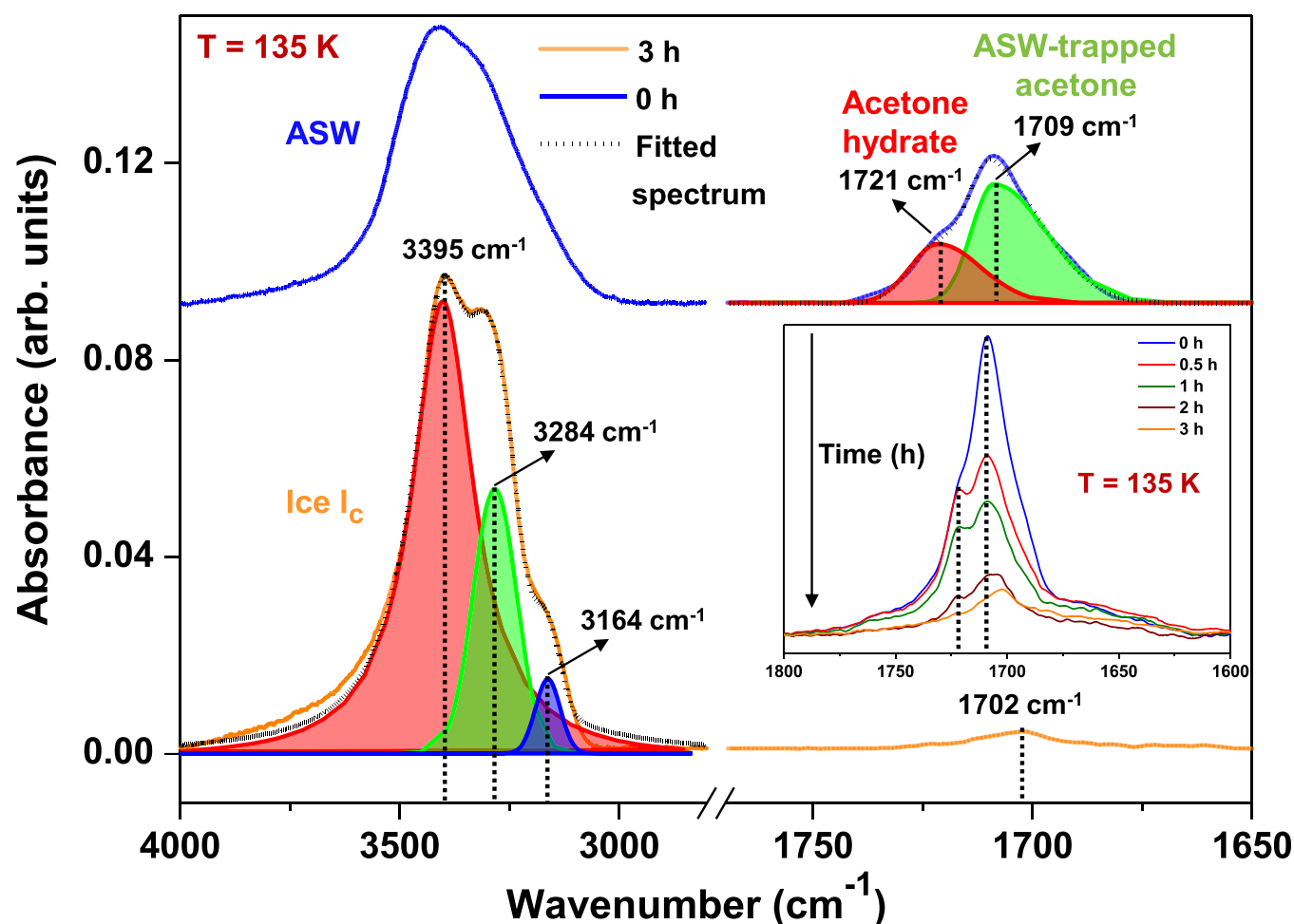


**Figure 1.** RAIR spectra of 300 MLs of acetone:H<sub>2</sub>O (1:1) at 135 K in the O–H and C=O stretching regions. The mixture was codeposited on Ru(0001) substrate at 10 K and annealed at a rate of 2 K·min<sup>−1</sup> to 135 K. The C=O stretching band was deconvoluted to show the concentration of acetone trapped in the hydrate cage and ASW pores. The inset focuses on the change in C=O stretching band upon dissociation of acetone hydrate over time. The O–H band changed after crystallization, and different features were resolved upon deconvolution.

Acetone, a precursor of prebiotic species,<sup>44</sup> was found on comet 67P/Churyumov-Gerasimenko, for the first time, in 2015.<sup>45</sup> Recent measurements by the ROSINA (Rosetta Orbiter Spectrometer for Ion and Neutral Analysis) instrument onboard Rosetta suggested the possible existence of CHs in this comet.<sup>46</sup> Here, we have shown that acetone could form CH because of its interaction with amorphous solid water (ASW) in conditions analogous to those of the comets. Extensive studies<sup>47–50</sup> on the interactions of acetone with ASW or crystalline ice film exist in the literature. At higher temperatures, acetone can escape the hydrate cage to form empty hydrate. The empty hydrate is usually regarded as unstable because the guest species stabilize the host framework.<sup>51</sup> Falenty et al. reported the formation of an “empty” hydrate after 5 days of continuous vacuum pumping of neon hydrate at 110–145 K, which they attributed to ice XVI.<sup>51</sup> Here, we demonstrate that acetone hydrate formed in UHV can transform into ice I<sub>c</sub> upon in situ dissociation of the former at 130–135 K.

Ice I<sub>c</sub> via acetone hydrate was prepared by annealing a codeposited ~300 MLs acetone:H<sub>2</sub>O (1:1) film to 135 K and maintaining it there in UHV for 3 h (additional experimental details are given in the Supporting Information). Figure 1 shows the RAIR spectra obtained immediately after annealing

the codeposited film at 135 K (blue trace; 0 h) and after 3 h (orange trace; 3 h). The inset of Figure 1 shows the time-dependent RAIR spectra of the same system in the C=O stretching region. In Figure 1, only the O–H (2800–4000 cm<sup>−1</sup>) and C=O (1650–1770 cm<sup>−1</sup>) stretching regions are displayed as these two regions are important for the acetone:H<sub>2</sub>O system where major changes were observed. At 135 K, the O–H bending band became featureless, and therefore, it was neglected in the spectra. The C=O stretching band at 0 h shows two features at ~1721 and ~1709 cm<sup>−1</sup>, which are attributed to acetone hydrate<sup>52–54</sup> and ASW-trapped acetone,<sup>55</sup> respectively, based on previous IR studies. These two features were deconvoluted to predict the actual amount of acetone in the hydrate form with respect to the total acetone present. Taking the area under the 1721 cm<sup>−1</sup> peak, the amount of acetone in the hydrate form was estimated to be 32.59% of the total acetone. Isothermal time-dependent RAIR spectra of 150 MLs of pure acetone (Figure S1), measured at different temperatures (115, 120, and 125 K), showed a major feature at ~1718 cm<sup>−1</sup> due to bulk acetone.<sup>49,55,56</sup> This confirmed that the 1721 cm<sup>−1</sup> peak is entirely a new feature and arises only because of acetone hydrate and not because of bulk acetone or its aggregates. Temperature-dependent RAIR

spectra shown in Figure S2 suggest that acetone hydrate starts to form at 130 K.

However, it is not stable in this condition and dissociated within 3 h. The inset of Figure 1 shows the reduction of C=O stretching band with time and resulted in a weak feature at  $\sim 1702\text{ cm}^{-1}$ . This feature is assigned to a dilute mixture of acetone and water (1:20), which was separately examined (Figure S3).

Acetone is a relatively less abundant molecule in the cometary environment. We have performed time-dependent RAIR spectra for dilute mixtures (1:10 and 1:20) of acetone:H<sub>2</sub>O at 135 K (Figure S4). They also resulted in ice I<sub>c</sub> in processes as described. Therefore, it is confirmed that acetone hydrate could be formed even with a very dilute mixture of acetone:H<sub>2</sub>O, which may have direct relevance from the cometary science perspective. However, to present the results in a clear and consistent way, a 1:1 mixture was used, which allowed us to obtain better quality spectra and monitor the changes distinctly in the spectra.

The O–H stretching band also underwent a profound change with time. The featureless broad O–H stretching band at 0 h is a characteristic feature of ASW (blue trace in Figure 1). However, this particular band is red-shifted with respect to the O–H stretching band of an ASW film, reflecting the increase in the order and number of H-bonded water molecules with time.<sup>57</sup> The unit cells of hydrates are complex, and the water molecules reside in several inequivalent sites, which results in the broadening of the O–H stretching band of the host ice network.<sup>58</sup> This band became sharp and split partially after 3 h (orange trace in Figure 1). Splitting and sharpening of O–H stretching of the IR spectrum are associated with the crystallization of the ice film. This O–H band was deconvoluted to three distinct features as shown in Figure 1. The features at 3164, 3284, and 3395  $\text{cm}^{-1}$  correspond to  $\nu_1$  in-phase band,  $\nu_3$  TO band, and the overlapped  $\nu_3$  LO and  $\nu_1$  out-of-phase bands of ice I<sub>c</sub>. These assignments were made based on the previous IR studies of ice I<sub>c</sub>.<sup>59,60</sup> It is evident that acetone hydrate in UHV slowly (within 3 h) dissociates at 135 K, leading to ice I<sub>c</sub>. We carried out a similar time-dependent RAIR study of the same system at 130 and 120 K. These results are shown in Figures S5 and S6, respectively. We see that acetone hydrate formed at 130 K (Figure S5) got converted to ice I<sub>c</sub> after 9 h. However, the formation of acetone hydrate and subsequent crystallization to ice I<sub>c</sub> were not observed at 120 K, even after 48 h (Figure S6). This observation indicates that the thermal motion of acetone molecules is responsible for the formation of acetone CH. At low temperature ( $\leq 120\text{ K}$ ), these motions are restricted; however, they became significant near the acetone desorption temperature ( $\sim 130\text{ K}$ ) in UHV. Earlier studies<sup>38</sup> also suggest that molecular mobility plays a vital role in the entrapment of guest molecules into the hydrate cages; therefore, the temperature near the desorption of guest species used here is crucial for the observed phenomenon.

A similar time-dependent study was carried out with 300 MLs of acetone:D<sub>2</sub>O (1:1) at 140 K, and cubic D<sub>2</sub>O ice was formed upon dissociation of acetone hydrate (Figure S7). The requirement of a slightly higher temperature of 140 K is understandable because D<sub>2</sub>O is a heavier molecule than H<sub>2</sub>O, whose rearrangement required a higher temperature.<sup>61</sup>

Thin films of ASW (<30 MLs) grown by vapor deposition below 110 K are known to have intrinsic ferroelectricity<sup>62</sup> and negative surface potential.<sup>63</sup> However, in our study, the

contribution of these effects of ice may be disregarded, because all the experiments were performed with higher coverage of ice (300 MLs) and above 120 K when such properties disappear. Time-dependent studies of pure 150 MLs of H<sub>2</sub>O were carried out at 120 and 130 K (Figure S8), and self-crystallization of ice was not observed. It proved that dissociation of acetone hydrate alone produced the ice I<sub>c</sub>, even at a lower temperature.

The structure of the ice formed is crucial to be investigated by more direct measurements. Figure 2 shows the time-

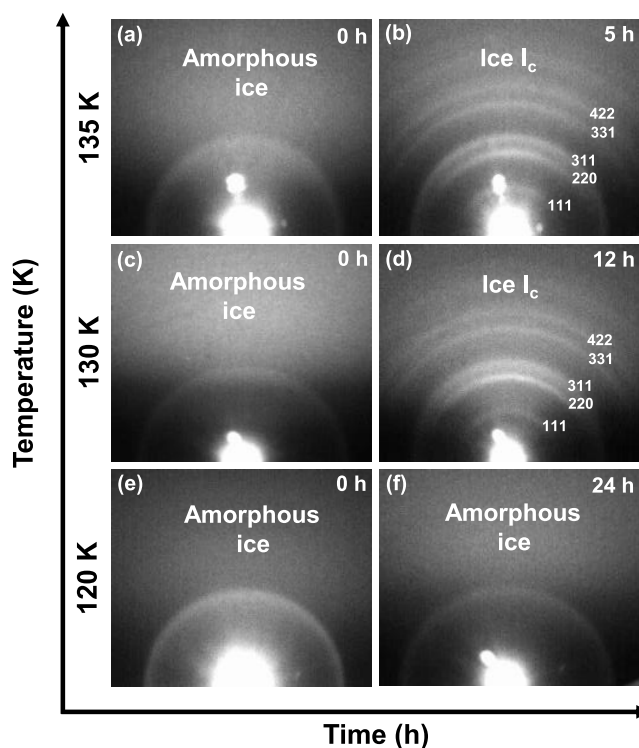


**Figure 2.** Time-dependent RHEED images of 300 MLs of acetone:H<sub>2</sub>O (1:1) at 120, 130, and 135 K. Here, a codeposition was done on the Ni(111) substrate at 20 K by following a method similar to that in a RAIRS study. After deposition, the mixtures were annealed at  $2\text{ K}\cdot\text{min}^{-1}$  to reach the required temperatures. RHEED images were collected at 135 K for (a) 0 h and (b) 5 h, 130 K for (c) 0 h and (d) 12 h, or 120 K for (e) 0 h and (f) 24 h.

dependent reflection high-energy electron diffraction (RHEED) images of 300 MLs of acetone:H<sub>2</sub>O (1:1) at different temperatures as indicated. These experiments were conducted in a separate chamber by depositing 300 MLs of mixed ice on a Ni(111) substrate at 20 K. After deposition, the mixture was annealed (heating rate =  $2\text{ K}\cdot\text{min}^{-1}$ ) to the experimental temperatures and kept for the required time, as shown in the figure. Here, it must be noted that all of the experiments were performed under multilayer deposition conditions, and therefore, the substrate does not play a role in the morphology of the deposited ice systems.<sup>64,65</sup> The RHEED image in Figure 2a, which was taken immediately after annealing the acetone:H<sub>2</sub>O system at 135 K, does not show any pattern indicating the amorphous nature of the mixture. However, after 5 h, several diffraction rings were observed (Figure 2b). Notably, these diffraction patterns originate from the water ice film. In this particular condition, most of the acetone molecules desorb from the mixture as indicated by the

IR measurement. The RHEED pattern indicates that the water film is ordered; that is, this is a crystalline ice film which is cubic, as the observed diffraction patterns match with the earlier diffraction studies<sup>66,67</sup> of ice I<sub>c</sub>. Time-dependent RHEED experiments were carried out at 130 and 120 K as well. We observed in Figure 2d that after 12 h at 130 K, the ice became cubic. However, at 120 K, the ice I<sub>c</sub> diffraction patterns were not observed, even after conducting the study for 24 h (Figure 2e,f). These observations are in accordance with the RAIR spectra presented in Figure 1. From an analysis of the diffraction patterns in Figure 2, it is evident that ice I<sub>c</sub> was formed only through the dissociation of acetone hydrate.

Figure 3 shows the TPD-MS spectra of 300 MLs of acetone:H<sub>2</sub>O (1:1). Here, the ice film was heated at 30 K·

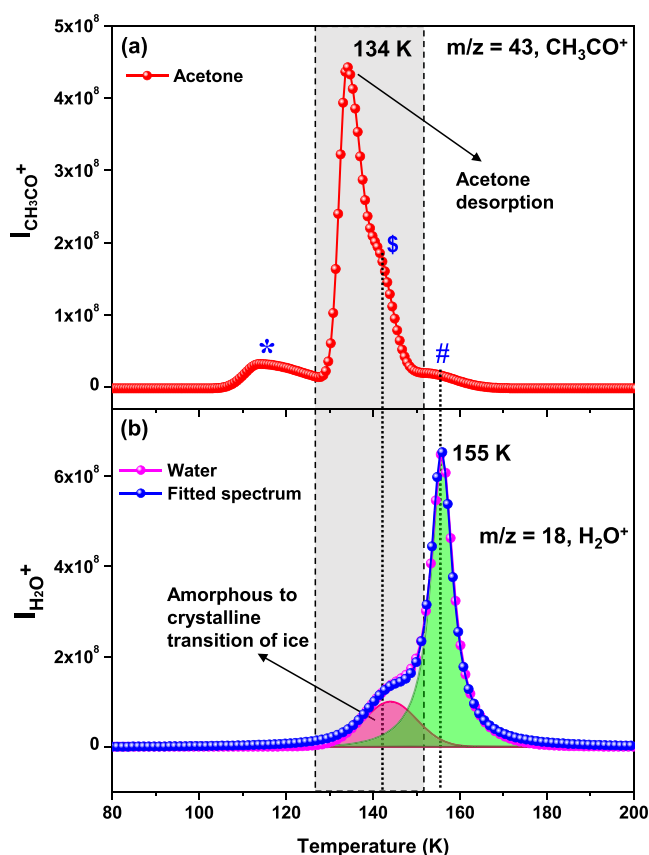


**Figure 3.** TPD-MS spectra of 300 MLs of acetone:H<sub>2</sub>O (1:1). The ramping rate was 30 K·min<sup>-1</sup>. Here, the intensities of CH<sub>3</sub>CO<sup>+</sup> ( $m/z = 43$ ) and H<sub>2</sub>O<sup>+</sup> ( $m/z = 18$ ) are plotted. (a) Desorption trace of acetone ( $m/z = 43$ ) shows a sharp peak at 134 K, which is attributed to the untrapped acetone desorption. The shoulder labeled \$ is due to acetone hydrate desorption. The peak labeled \* is attributed to acetone desorption due to premelting of ice upon annealing, and that labeled # is due to desorption of acetone along with the processes in ice. (b) The desorption trace of water ( $m/z = 18$ ) shows a sideband, which is due to the amorphous-to-crystalline ice transition. It coincides with the shoulder labeled \$. The peak at 155 K is due to the complete desorption of ice.

min<sup>-1</sup> to obtain the TPD spectra. In Figure 3a, for the desorption trace of acetone, the intensity of CH<sub>3</sub>CO<sup>+</sup> ( $m/z = 43$ ) is shown as a function of temperature. It shows a sharp desorption feature at 134 K due to the dissociation of untrapped acetone which exists outside the hydrate cage. It was further confirmed by the TPD of pure acetone, which shows a

desorption peak at 132 K (Figure S9). It is to be noted that acetone starts to form a hydrate just by annealing to 130 K, as shown in Figure S2. In TPD, the shoulder marked with \$ is due to acetone hydrate dissociation. This feature of acetone (Figure 3a) may have a contribution from the molecular volcano (MV) of acetone as it coincides with the transition of ASW to crystalline ice (Figure 3b). Upon deconvoluting the desorption trace of acetone (Figure S10), the amount of desorption due to acetone hydrate is estimated to be 24.26% of the total acetone at this condition, and it is correlated to the amount of acetone in hydrate form calculated from the IR data (Figure 1). Note that the shoulder peak is indeed narrow, much like the feature at 134 K (Figure S10). The feature marked with \* is due to the premelting of ice, which releases some amount of trapped acetone, whereas the # feature is due to release of still smaller amounts of acetone, which desorb along with ice at 155 K. This smaller amount of acetone is also observed in the RAIRS study as shown in Figure 1 where a weak feature at  $\sim 1702$  cm<sup>-1</sup> was observed even after hydrate dissociation, which was further confirmed in a separate experiment shown in Figure S3. The desorption trace of H<sub>2</sub>O<sup>+</sup> ( $m/z = 18$ ) consists of two features as shown by spectral deconvolution. The vapor pressure (desorption rate) of ASW is higher than that of crystalline ice, which resulted in a bump indicated by pink shading.<sup>68</sup> Interestingly, this bump occurs right at the same temperature when acetone hydrate dissociated. Therefore, this is additional evidence to suggest that dissociation of acetone hydrate resulted in the crystallization of ice.

Kinetic parameters of ice I<sub>c</sub> crystallization were evaluated by conducting time-dependent RAIRS studies at different temperatures. Previous reports<sup>61,68,69</sup> suggest that the crystallization kinetics of ASW can be evaluated by monitoring the change in O–H stretching band during crystallization. The decoupled O–D stretch in HDO was also found to be effective in predicting the crystallization kinetics.<sup>70,71</sup> Here, both these methods were adopted for a conclusive evaluation of the kinetics.

The time-dependent RAIR spectra of acetone:HDO (5% D<sub>2</sub>O in H<sub>2</sub>O) at different temperatures (130, 132, 135, and 137 K) are shown in Figures S11–S14. In Figure S13a, the bottom most spectrum (0 h trace) indicates a pure ASW film which was crystallized with time. We have evaluated the crystallization fraction,  $x(t)$ , from changes in the absorbance ( $\Delta A$ ) at a fixed wavenumber (3307 cm<sup>-1</sup> in Figure S13a, indicated by the vertical line) for each temperature. A similar approach was adopted in several previous reports.<sup>61,68,69</sup> Also in Figure S13b, the initially broad amorphous spectrum (0 min trace) eventually was transformed into a relatively sharp crystalline spectrum with a peak at  $\sim 2427$  cm<sup>-1</sup>. Here, differences in the integrated peak area between the completely ASW and (partly) crystalline films at each time interval were considered. However, changes in the absorbance ( $\Delta A$ ) at a fixed wavenumber ( $\sim 2427$  cm<sup>-1</sup> in Figure S13b, indicated by a vertical line) produced almost the same result for  $x(t)$  as that obtained from the integrated peak area. The crystallization fraction was calculated by eq 1

$$x(t) = \frac{\Delta A(1)}{\Delta A(2)} \quad (1)$$

where  $\Delta A(1)$  is the difference in the absorbance at a particular time “ $t$ ” and that at time zero;  $\Delta A(2)$  is the difference in



absorbance of a completely crystallized film and that at time zero.

Panels a and b of Figure S15 illustrate the changes in the crystallization fractions as measured from the O–H and decoupled O–D stretching bands, conducted at different temperatures as shown. It was evident that the rate of crystallization was increased with rise in temperature. This change was reflected in the change of the curve shape from sigmoidal to exponential with temperature.<sup>69</sup> Next, the crystallization fraction at different temperatures was fitted to the Avrami equation<sup>72,73</sup>

$$x(t) = 1 - \exp[-k(T) \cdot t^n] \quad (2)$$

where  $t$  is time,  $k(T)$  the rate constant, and  $n$  the Avrami exponent. For all temperatures,  $n$  is a parameter whose value indicates the geometry of the growing particles and the type of nucleation, whether it is diffusion- or interface-controlled.<sup>2,74</sup> Thus, the nature of the crystallization process can be predicted from the knowledge of Avrami exponent,  $n$ . After rearranging, this equation becomes

$$\ln(-\ln[1 - x(t)]) = n \ln(t) + n \ln k(T) \quad (3)$$

Panels a and b of Figures S16 show linearly fitted straight lines using eq 3, for different temperatures as shown. The values of  $n$  are determined from the slopes. Using the values of  $n$  and intercept of the straight lines for each temperature, the rate constants,  $k(T)$ , are estimated. Values of  $n$  and  $k(T)$  obtained from the analysis of O–H and O–D stretching bands at different temperatures are summarized in Table S1.

The obtained values of  $n$  (2.59–1.62, in Table S1) suggest that the crystallization kinetics is diffusion-controlled with particles growing into a predominantly spherical geometry.<sup>74–76</sup> Previous studies also suggest that the crystallization kinetics of water to ice  $I_c$  at  $T < 150$  K is diffusion-controlled with predominantly spherical growth.<sup>74</sup> Here, we suggest that dissociation of acetone hydrate can promote the diffusion or mobility of  $H_2O$  molecules which essentially trigger the formation of crystalline ice. Panels c and d of Figure S16 show the Arrhenius plot obtained from the analysis of the O–H and the O–D stretching regions, respectively. The slope of these linearly fitted lines gave the values of the activation energy ( $E_a$ ), which were estimated to be  $\sim 57.92$  and  $\sim 57.58$  kJ mol<sup>−1</sup>, respectively. This is comparable to the previously reported activation energy values ( $E_a = 60–77$  kJ mol<sup>−1</sup>) for the crystallization of pure ASW obtained by different experimental techniques.<sup>69,70,77–79</sup> Here, the high mobility of the water molecules during hydrate dissociation can overcome the kinetic barrier to form crystals even at a lower than usual ice-crystallization temperature.

In conclusion, we found that dissociation of acetone hydrate leads to the formation of ice  $I_c$  under UHV. CHs are known to dissociate under prolonged exposure to vacuum and result in an entirely different crystalline structure of ice.<sup>51</sup> The nucleation of ice  $I_c$  occurs below the crystallization temperature, and molecular rearrangement during hydrate dissociation favors it. It is known that water-ice exists in comets, and acetone has also been found there recently.<sup>45</sup> This study shows that acetone hydrate can exist in the extreme low-pressure conditions present in comets. Here, we believe that we present a missing piece of the puzzle linking the existence of ice  $I_c$  and CH in comets. We suggest that this may be the mechanistic route for the formation of ice  $I_c$  in such environments. This study may hint at the ice composition of a comet (amorphous

or crystalline), which have implications from the cometary science perspective.

## ■ ASSOCIATED CONTENT

### Supporting Information

The Supporting Information is available free of charge at <https://pubs.acs.org/doi/10.1021/acs.jpclett.9b03063>.

Experimental methods; crystallization kinetics; isothermal time-dependent RAIR spectra of pure acetone, acetone:H<sub>2</sub>O, and acetone:HDO at different temperatures; TPD-MS spectra of pure acetone; crystallization fractions and different crystallization parameters of acetone:HDO at different temperatures (PDF)

## ■ AUTHOR INFORMATION

### Corresponding Author

\*E-mail: [pradeep@iitm.ac.in](mailto:pradeep@iitm.ac.in).

### ORCID

Thalappil Pradeep: 0000-0003-3174-534X

### Present Address

<sup>‡</sup>R.G.B.: Lehrstuhl für Physikalische Chemie II, Friedrich-Alexander-Universität Erlangen-Nürnberg, Egerlandstr. 3, 91058 Erlangen, Germany.

### Notes

The authors declare no competing financial interest.

## ■ ACKNOWLEDGMENTS

J.G. thanks the University Grants Commission (UGC) for his research fellowship. We thank the Department of Science and Technology (DST), Government of India, for supporting our research. We thank Dr. Ryutaro Souda for helping us with the RHEED studies.

## ■ REFERENCES

- (1) Jenniskens, P.; Blake, D. F. Structural Transitions in Amorphous Water Ice and Astrophysical Implications. *Science* **1994**, *265*, 753–756.
- (2) Jenniskens, P.; Blake, D. F. Crystallization of Amorphous Water Ice in the Solar System. *Astrophys. J.* **1996**, *473*, 1104–1113.
- (3) Petrenko, V. F.; Whitworth, R. W. *Physics of Ice*; OUP: Oxford, 2002.
- (4) Chou, I. M.; Blank, J. G.; Goncharov, A. F.; Mao, H.-k.; Hemley, R. J. In Situ Observations of a High-Pressure Phase of H<sub>2</sub>O Ice. *Science* **1998**, *281*, 809–812.
- (5) Kohl, I.; Mayer, E.; Hallbrucker, A. The Glassy Water–Cubic Ice System: A Comparative Study by X-Ray Diffraction and Differential Scanning Calorimetry. *Phys. Chem. Chem. Phys.* **2000**, *2*, 1579–1586.
- (6) Lobban, C.; Finney, J. L.; Kuhs, W. F. The Structure of a New Phase of Ice. *Nature* **1998**, *391*, 268–270.
- (7) Millot, M.; Coppari, F.; Rygg, J. R.; Correa Barrios, A.; Hamel, S.; Swift, D. C.; Eggert, J. H. Nanosecond X-ray diffraction of Shock-Compressed Superionic Water Ice. *Nature* **2019**, *569*, 251–255.
- (8) König, H. A Cubic Modification of Ice. *Z. Kristallogr. - Cryst. Mater.* **1943**, *105*, 279–286.
- (9) Kuhs, W. F.; Sippel, C.; Falenty, A.; Hansen, T. C. Extent and Relevance of Stacking Disorder in “ice  $I_c$ ”. *Proc. Natl. Acad. Sci. U. S. A.* **2012**, *109*, 21259–21264.
- (10) Thürmer, K.; Nie, S. Formation of Hexagonal and Cubic Ice during Low-Temperature Growth. *Proc. Natl. Acad. Sci. U. S. A.* **2013**, *110*, 11757–11762.
- (11) Honjo, G.; Kitamura, N.; Shimaoka, K.; Mihama, K. Low Temperature Specimen Method for Electron Diffraction and Electron Microscopy. *J. Phys. Soc. Jpn.* **1956**, *11*, 527–536.

- (12) Blackman, M.; Lisgarten, N. D. The Cubic and Other Structural Forms of Ice at Low Temperature and Pressure. *Proc. R. Soc. London A* **1957**, 239, 93–107.
- (13) Shallcross, F. V.; Carpenter, G. B. X-Ray Diffraction Study of the Cubic Phase of Ice. *J. Chem. Phys.* **1957**, 26, 782–784.
- (14) Steytler, D. C.; Dore, J. C.; Wright, C. J. Neutron Diffraction Study of Cubic Ice Nucleation in a Porous Silica Network. *J. Phys. Chem.* **1983**, 87, 2458–2459.
- (15) Dore, J. C.; Dunn, M.; Chieux, P. Neutron Diffraction Studies of Ice Nucleation in Porous Silica. *J. Phys. Colloques* **1987**, 48, C1–457.
- (16) Baker, J. M.; Dore, J. C.; Behrens, P. Nucleation of Ice in Confined Geometry. *J. Phys. Chem. B* **1997**, 101, 6226–6229.
- (17) Malkin, T. L.; Murray, B. J.; Brukhno, A. V.; Anwar, J.; Salzmann, C. G. Structure of Ice Crystallized from Supercooled Water. *Proc. Natl. Acad. Sci. U. S. A.* **2012**, 109, 1041–1045.
- (18) Mayer, E.; Hallbrucker, A. Cubic Ice from Liquid Water. *Nature* **1987**, 325, 601–602.
- (19) Murray, B. J.; Knopf, D. A.; Bertram, A. K. The Formation of Cubic Ice under Conditions Relevant to Earth's Atmosphere. *Nature* **2005**, 434, 202–205.
- (20) Murray, B. J.; Bertram, A. K. Formation and Stability of Cubic Ice in Water Droplets. *Phys. Chem. Chem. Phys.* **2006**, 8, 186–192.
- (21) Bertie, J. E.; Calvert, L. D.; Whalley, E. Transformations of Ice II, ice III, and Ice V at Atmospheric Pressure. *J. Chem. Phys.* **1963**, 38, 840–846.
- (22) Handa, Y. P.; Klug, D. D.; Whalley, E. Energies of the Phases of Ice at Low Temperature and Pressure Relative to Ice I<sub>h</sub>. *Can. J. Chem.* **1988**, 66, 919–924.
- (23) McMillan, J. A.; Los, S. C. Vitreous ice: Irreversible transformations during warm-up. *Nature* **1965**, 206, 806–807.
- (24) Yamamuro, O.; Oguni, M.; Matsuo, T.; Suga, H. Heat Capacity and Glass Transition of Pure and Doped Cubic Ices. *J. Phys. Chem. Solids* **1987**, 48, 935–942.
- (25) Dowell, L. G.; Rinfret, A. P. Low-Temperature Forms of Ice as Studied by X-Ray Diffraction. *Nature* **1960**, 188, 1144–1148.
- (26) McMillan, J. A.; Los, S. C. Vitreous Ice: Irreversible Transformations During Warm-Up. *Nature* **1965**, 206, 806–807.
- (27) Falenty, A.; Hansen, T. C.; Kuhs, W. F. Cubic Ice Formation and Annealing During CO<sub>2</sub> Clathrate Hydrate Decomposition at Low Temperatures. *Physics and Chemistry of Ice* **2010**, 2010, 411.
- (28) Falenty, A.; Kuhs, W. F. Self-Preservation of CO<sub>2</sub> Gas Hydrates-Surface Microstructure and Ice Perfection. *J. Phys. Chem. B* **2009**, 113, 15975–15988.
- (29) Kuhs, W. F.; Genov, G.; Staykova, D. K.; Hansen, T. Ice Perfection and Onset of Anomalous Preservation of Gas Hydrates. *Phys. Chem. Chem. Phys.* **2004**, 6, 4917–4920.
- (30) Takeya, S.; Uchida, T.; Nagao, J.; Ohmura, R.; Shimada, W.; Kamata, Y.; Ebinuma, T.; Narita, H. Particle Size Effect of CH<sub>4</sub> Hydrate for Self-Preservation. *Chem. Eng. Sci.* **2005**, 60, 1383–1387.
- (31) Gronkowski, P. The Search for a Cometary Outbursts Mechanism: A Comparison of Various Theories. *Astron. Nachr.* **2007**, 328, 126–136.
- (32) Prialnik, D.; Bar-Nun, A. Crystallization of Amorphous Ice as the Cause of Comet P/Halley's outburst at 14 AU. *Astron. Astrophys.* **1992**, 258, L9–L12.
- (33) Blake, D.; Allamandola, L.; Sandford, S.; Hudgins, D.; Freund, F. Clathrate Hydrate Formation in Amorphous Cometary Ice Analogs in Vacuo. *Science* **1991**, 254, 548–551.
- (34) Riikonen, M.; Sillanpää, M.; Virta, L.; Sullivan, D.; Moilanen, J.; Luukkonen, I. Halo Observations Provide Evidence of Airborne Cubic Ice in the Earth's Atmosphere. *Appl. Opt.* **2000**, 39, 6080–6085.
- (35) Whalley, E. Scheiner's Halo: Evidence for Ice I<sub>c</sub> in the Atmosphere. *Science* **1981**, 211, 389–390.
- (36) Whalley, E. Cubic Ice in Nature. *J. Phys. Chem.* **1983**, 87, 4174–4179.
- (37) Miller, S. L. The occurrence of gas hydrates in the solar system. *Proc. Natl. Acad. Sci. U. S. A.* **1961**, 47, 1798–1808.
- (38) Ghosh, J.; Methikkalam, R. R. J.; Bhuin, R. G.; Ragupathy, G.; Choudhary, N.; Kumar, R.; Pradeep, T. Clathrate Hydrates in Interstellar Environment. *Proc. Natl. Acad. Sci. U. S. A.* **2019**, 116, 1526–1531.
- (39) Klinger, J. Extraterrestrial ice. A review. *J. Phys. Chem.* **1983**, 87, 4209–4214.
- (40) Patashnick, H.; Rupprecht, G.; Schuerman, D. W. Energy Source for Comet Outbursts. *Nature* **1974**, 250, 313–314.
- (41) Klinger, J. Influence of a Phase Transition of Ice on the Heat and Mass Balance of Comets. *Science* **1980**, 209, 271–272.
- (42) Smoluchowski, R. Amorphous Ice and the behavior of Cometary Nuclei. *Astrophys. J.* **1981**, 244, L31–L34.
- (43) Klinger, J. Some Consequences of a Phase Transition of Water Ice on the Heat Balance of Comet Nuclei. *Icarus* **1981**, 47, 320–324.
- (44) Almeida, G. C.; Pilling, S.; Andrade, D. P. P.; Castro, N. L. S.; Mendoza, E.; Bochat-Roberty, H. M.; Rocco, M. L. M. Photo-desorption and Photostability of Acetone Ices: Relevance to Solid Phase Astrochemistry. *J. Phys. Chem. C* **2014**, 118, 6193–6200.
- (45) Goesmann, F.; Rosenbauer, H.; Bredehöft, J. H.; Cabane, M.; Ehrenfreund, P.; Gautier, T.; Giri, C.; Krüger, H.; Le Roy, L.; MacDermott, A. J.; McKenna-Lawlor, S.; Meierhenrich, U. J.; Caro, G. M. M.; Raulin, F.; Roll, R.; Steele, A.; Steininger, H.; Sternberg, R.; Szopa, C.; Thiemann, W.; Ulamec, S. Organic Compounds on Comet 67P/Churyumov-Gerasimenko Revealed by COSAC Mass Spectrometry. *Science* **2015**, 349, aab0689.
- (46) Luspai-Kuti, A.; Mousis, O.; Hässig, M.; Fuselier, S. A.; Lunine, J. I.; Marty, B.; Mandt, K. E.; Wurz, P.; Rubin, M. The Presence of Clathrates in Comet 67P/Churyumov-Gerasimenko. *Sci. Adv.* **2016**, 2, No. e1501781.
- (47) Schaff, J. E.; Roberts, J. T. Structure Sensitivity in the Surface Chemistry of Ice: Acetone Adsorption on Amorphous and Crystalline Ice Films. *J. Phys. Chem.* **1994**, 98, 6900–6902.
- (48) Schaff, J. E.; Roberts, J. T. Toward an Understanding of the Surface Chemical Properties of Ice: Differences between the Amorphous and Crystalline Surfaces. *J. Phys. Chem.* **1996**, 100, 14151–14160.
- (49) Schaff, J. E.; Roberts, J. T. The Adsorption of Acetone on Thin Films of Amorphous and Crystalline Ice. *Langmuir* **1998**, 14, 1478–1486.
- (50) Souda, R. Adsorption, Diffusion, Dewetting, and Entrapment of Acetone on Ni(111), Surface-Modified Silicon, and Amorphous Solid Water studied by Time-of-Flight Secondary Ion Mass Spectrometry and Temperature Programmed Desorption. *J. Chem. Phys.* **2011**, 135, 164703.
- (51) Falenty, A.; Hansen, T. C.; Kuhs, W. F. Formation and Properties of Ice XVI Obtained by Emptying a type sII Clathrate Hydrate. *Nature* **2014**, 516, 231–233.
- (52) Monreal, I. A.; Devlin, J. P.; Maşlakçı, Z.; Çiçek, M. B.; Uras-Aytemiz, N. Controlling Nonclassical Content of Clathrate Hydrates Through the Choice of Molecular Guests and Temperature. *J. Phys. Chem. A* **2011**, 115, 5822–5832.
- (53) Consani, K. Infrared Bands of Acetone in Solid Argon and the Structure II Clathrate 2-Acetylene/Acetone/17-Water. *J. Phys. Chem.* **1987**, 91, 5586–5588.
- (54) Mitlin, S.; Leung, K. T. Surface Chemistry of OH Dangling Bonds in Vapour-Deposited Ice Films at 128–185 K: Hydrogen-Bonding Interactions with Acetone. *Surf. Sci.* **2002**, 505, L227–L236.
- (55) Shin, S.; Kang, H.; Kim, J. S.; Kang, H. Phase Transitions of Amorphous Solid Acetone in Confined Geometry Investigated by Reflection Absorption Infrared Spectroscopy. *J. Phys. Chem. B* **2014**, 118, 13349–13356.
- (56) Hudson, R. L.; Gerakines, P. A.; Ferrante, R. F. IR Spectra and Properties of Solid Acetone, An Interstellar and Cometary Molecule. *Spectrochim. Acta, Part A* **2018**, 193, 33–39.
- (57) Backus, E. H. G.; Grecea, M. L.; Kleyn, A. W.; Bonn, M. Surface Crystallization of Amorphous Solid Water. *Phys. Rev. Lett.* **2004**, 92, 236101.

- (58) Buch, V.; Devlin, J. P.; Monreal, I. A.; Jagoda-Cwiklik, B.; Uras-Aytemiz, N.; Cwiklik, L. Clathrate Hydrates with Hydrogen-Bonding Guests. *Phys. Chem. Chem. Phys.* **2009**, *11*, 10245–10265.
- (59) Whalley, E. A Detailed Assignment of the O–H Stretching Bands of Ice I. *Can. J. Chem.* **1977**, *55*, 3429–3441.
- (60) Hagen, W.; Tielens, A. G. G. M.; Greenberg, J. M. The Infrared Spectra of Amorphous Solid Water and Ice I<sub>c</sub> between 10 and 140 K. *Chem. Phys.* **1981**, *56*, 367–379.
- (61) Smith, R. S.; Matthiesen, J.; Knox, J.; Kay, B. D. Crystallization Kinetics and Excess Free Energy of H<sub>2</sub>O and D<sub>2</sub>O Nanoscale Films of Amorphous Solid Water. *J. Phys. Chem. A* **2011**, *115*, 5908–5917.
- (62) Su, X.; Lianos, L.; Shen, Y. R.; Somorjai, G. A. Surface-Induced Ferroelectric Ice on Pt(111). *Phys. Rev. Lett.* **1998**, *80*, 1533–1536.
- (63) Bu, C.; Shi, J.; Raut, U.; Mitchell, E. H.; Baragiola, R. A. Effect of Microstructure on Spontaneous Polarization in Amorphous Solid Water Films. *J. Chem. Phys.* **2015**, *142*, 134702.
- (64) Ghosh, J.; Bhuin, R. G.; Ragupathy, G.; Pradeep, T. Spontaneous Formation of Tetrahydrofuran Hydrate in Ultrahigh Vacuum. *J. Phys. Chem. C* **2019**, *123*, 16300–16307.
- (65) Ghosh, J.; Hariharan, A. K.; Bhuin, R. G.; Methikkalam, R. R. J.; Pradeep, T. Propane and Propane-Water Interactions: A Study at Cryogenic Temperatures. *Phys. Chem. Chem. Phys.* **2018**, *20*, 1838–1847.
- (66) Lisgarten, N. D.; Blackman, M. The Cubic Form of Ice. *Nature* **1956**, *178*, 39–40.
- (67) Kouchi, A.; Kuroda, T. Amorphization of Cubic Ice by Ultraviolet Irradiation. *Nature* **1990**, *344*, 134–135.
- (68) Smith, R. S.; Petrik, N. G.; Kimmel, G. A.; Kay, B. D. Thermal and Nonthermal Physiochemical Processes in Nanoscale Films of Amorphous Solid Water. *Acc. Chem. Res.* **2012**, *45*, 33–42.
- (69) Lee, D. H.; Kang, H. Acid-Promoted Crystallization of Amorphous Solid Water. *J. Phys. Chem. C* **2018**, *122*, 24164–24170.
- (70) Yuan, C.; Smith, R. S.; Kay, B. D. Communication: Distinguishing between Bulk and Interface-Enhanced Crystallization in Nanoscale Films of Amorphous Solid Water. *J. Chem. Phys.* **2017**, *146*, No. 031102.
- (71) Xu, Y.; Petrik, N. G.; Smith, R. S.; Kay, B. D.; Kimmel, G. A. Growth Rate of Crystalline Ice and the Diffusivity of Supercooled Water from 126 to 262 K. *Proc. Natl. Acad. Sci. U. S. A.* **2016**, *113*, 14921.
- (72) Avrami, M. Kinetics of Phase Change. I General Theory. *J. Chem. Phys.* **1939**, *7*, 1103–1112.
- (73) Avrami, M. Kinetics of Phase Change. II Transformation-Time Relations for Random Distribution of Nuclei. *J. Chem. Phys.* **1940**, *8*, 212–224.
- (74) Hage, W.; Hallbrucker, A.; Mayer, E.; Johari, G. P. Crystallization Kinetics of Water below 150 K. *J. Chem. Phys.* **1994**, *100*, 2743–2747.
- (75) Rao, C. N. R.; Rao, K. J. In *Phase Transitions in Solids: An Approach to the Study of the Chemistry and Physics of Solids*; McGraw-Hill: New York, 1978; pp 81–173.
- (76) Doremus, R. H. *Rates of Phase Transformations*; Academic Press, Inc.: Orlando, FL, 1985.
- (77) Kondo, T.; Kato, H. S.; Bonn, M.; Kawai, M. Deposition and crystallization studies of thin amorphous solid water films on Ru(0001) and on CO-precovered Ru(0001). *J. Chem. Phys.* **2007**, *127*, No. 094703.
- (78) Safarik, D. J.; Mullins, C. B. The nucleation rate of crystalline ice in amorphous solid water. *J. Chem. Phys.* **2004**, *121*, 6003–6010.
- (79) Smith, R. S.; Matthiesen, J.; Knox, J.; Kay, B. D. Crystallization Kinetics and Excess Free Energy of H<sub>2</sub>O and D<sub>2</sub>O Nanoscale Films of Amorphous Solid Water. *J. Phys. Chem. A* **2011**, *115*, 5908–5917.

# Formation of Cubic Ice via Clathrate Hydrate, Prepared in Ultrahigh Vacuum under Cryogenic Conditions

*Jyotirmoy Ghosh,<sup>†</sup> Radha Gobinda Bhuin,<sup>†,‡</sup> Gaurav Vishwakarma,<sup>†</sup> and Thalappil*

*Pradeep<sup>†, \*</sup>*

<sup>†</sup>DST Unit of Nanoscience (DST UNS) and Thematic Unit of Excellence (TUE), Department of Chemistry, Indian Institute of Technology Madras, Chennai 600036, India

<sup>‡</sup>Present Address: Lehrstuhl für Physikalische Chemie II, Friedrich-Alexander-Universität Erlangen-Nürnberg, Egerlandstr. 3, 91058 Erlangen, Germany

Corresponding Author

\*To whom correspondence should be addressed, E-mail: [pradeep@iitm.ac.in](mailto:pradeep@iitm.ac.in)

## Table of contents

Name	Description	Page number
	Experimental section	S3-S5
Figure S1	Isothermal time-dependent RAIR spectra of 150 MLs of pure acetone film at 115, 120, and 125 K.	S6
Figure S2	Temperature-dependent RAIR spectra of 300 MLs acetone:H <sub>2</sub> O (1:1).	S7
Figure S3	Temperature-dependent RAIR spectra of 300 MLs acetone:H <sub>2</sub> O (1:20).	S8

Figure S4	Time-dependent RAIR spectra of 300 MLs of acetone:H <sub>2</sub> O for two different ratios; (1:10) and (1:20)	S9
Figure S5	Time-dependent RAIR spectra of 300 MLs of acetone:H <sub>2</sub> O (1:1) at 130 K.	S10
Figure S6	Time-dependent RAIR spectra of 300 MLs of acetone:H <sub>2</sub> O (1:1) at 120 K.	S11
Figure S7	Time-dependent RAIR spectra of 300 MLs of acetone:D <sub>2</sub> O (1:1) at 140 K.	S12
Figure S8	Time-dependent RAIR spectra of 150 MLs of solid H <sub>2</sub> O film at 120 K, and 130 K.	S13
Figure S9	TPD-MS spectra of 150 MLs of pure acetone.	S14
Figure S10	Deconvoluted desorption trace of acetone, taken from the TPD spectra shown in Figure 3a of the main manuscript.	S15
Figure S11	Time-dependent RAIR spectra of 300 MLs of acetone:HDO (5% D <sub>2</sub> O in H <sub>2</sub> O) at 130 K.	S16
Figure S12	Time-dependent RAIR spectra of 300 MLs of acetone:HDO (5% D <sub>2</sub> O in H <sub>2</sub> O) at 132 K.	S17
Figure S13	Time-dependent RAIR spectra of 300 MLs of acetone:HDO (5% D <sub>2</sub> O in H <sub>2</sub> O) at 135 K.	S18
Figure S14	Time-dependent RAIR spectra of 300 MLs of acetone:HDO (5% D <sub>2</sub> O in H <sub>2</sub> O) at 137 K.	S19
Figure S15	Crystallization fractions of 300 MLs of acetone:HDO (5% D <sub>2</sub> O in H <sub>2</sub> O) at 130, 132, 135, and 137 K.	S20
Table S1	Different crystallization parameters of Ice I <sub>c</sub> at 130, 132, 135, and 137 K.	S21
Figure S16	Plot of $\ln(-\ln[1-x(t)])$ vs. $\ln(t)$ at 130, 132, 135, and 137 K.	S22



## Experimental Section:

Experiments were carried in an ultrahigh vacuum (UHV) chamber (base pressure  $\sim 5 \times 10^{-10}$  mbar). Details of the instrument are described elsewhere.<sup>1</sup> This kind of low pressure is an essential condition for simulating the ISM or cometary environments. The vacuum was maintained by several oil-free turbomolecular pumps backed by diaphragm pumps (Pfeiffer Vacuum). In brief, the chamber was equipped with reflection absorption infrared (RAIR) spectroscopy and temperature-programmed desorption (TPD) mass spectrometry. Here, a Ru(0001) single crystal was used as the substrate. A thin film of ice was grown on top of this substrate, mounted on a copper holder, which in turn, was attached at the tip of a closed cycle helium cryostat (ColdEdge Technologies). The temperature was measured by using a K-type thermocouple connected to it. Repeated heating at 400 K before vapor deposition ensured surface cleanliness. The temperature ramping was controlled and monitored by a temperature controller (Lakeshore 336).

Acetone hydrate was formed by using  $\sim 99.99\%$  pure acetone, purchased from Sigma-Aldrich and Millipore water ( $\text{H}_2\text{O}$  of  $18.2 \text{ M}\Omega$  resistivity), taken in separate test tubes, connected to the sample line through a glass-to-metal seal. Here, both acetone and water were additionally purified through several freeze-pump-thaw cycles before introduction into the experimental chamber. The sample lines were connected to the experimental chamber through a high precision all-metal leak valve. These leak valves were used to control the flow or inlet pressure of different samples. Out of the two sample inlet lines, one was exclusively used for acetone while the other line was used for water deposition. During the exposure of different samples into the UHV chamber, their purities were checked using a quadrupole mass spectrometer (Extrel) installed in the chamber. Recorded mass spectra were used to monitor purity as well as to measure the ratio of the mixtures. The ratio of the mixed ice was determined by controlling the flow or inlet pressure of the sample. Here, we express the film thickness in terms of the monolayer (ML), assuming that  $1.33 \times 10^{-6} \text{ mbar.s} = 1 \text{ ML}$  which has been estimated to contain  $\sim 1.1 \times 10^{15} \text{ molecules.cm}^{-2}$ . A number of reports<sup>2-4</sup> adopted this calculation for the estimation of surface coverages. The inlet pressure during sample deposition was decided based on the coverage desired at the time of the experiment. The substrate was kept in a fixed perpendicular position for uniform growth of ice. For accurate estimations, the relative sensitivities of ion gauge response (ion gauge coefficient) towards different molecules have to be accounted.<sup>5</sup> Other ways of estimating coverage include determination of molecular flux by Hertz-Knudsen equation, numerical integration of thermal desorption spectra.<sup>6</sup> Despite this limitation, the

present method was chosen for its simplicity. A 1:1 monolayer mixture of acetone:H<sub>2</sub>O will be 3.22:1 in molar ratio. However, it is difficult to estimate the actual ratio (acetone:H<sub>2</sub>O) during the nucleation of acetone hydrate at higher temperature, due to the desorption of acetone. The nucleation is primarily governed by the annealing temperature and residence time. Therefore, the accurate measurement of the ratio of the mixture is insignificant for this study.

Here, to prepare 300 MLs of acetone:H<sub>2</sub>O (1:1), the UHV chamber was backfilled at a total pressure of  $\sim 5 \times 10^{-7}$  mbar (where, acetone inlet pressure =  $2.5 \times 10^{-7}$  mbar, and water inlet pressure =  $2.5 \times 10^{-7}$  mbar) and deposition was continued for 10 minutes. Now, this mixed ice was slowly (heating rate = 2 K.min<sup>-1</sup>) heated to the required experimental temperatures (120, 130, and 135 K). At these temperatures, the mixed ice was monitored constantly by RAIRS with time. For decoupled O-D stretching analysis, the samples were prepared using D<sub>2</sub>O (~5%) in H<sub>2</sub>O.<sup>7</sup> In this solution, D<sub>2</sub>O undergoes H/D exchange to form HDO. The use of HDO facilitates the observation of ASW crystallization because the O-D stretching vibration is decoupled from intramolecular and intermolecular O-H stretching vibrations.<sup>7-9</sup>

RAIR spectra were recorded using a Bruker FT-IR spectrometer, Vertex 70. The external IR beam was focused onto the substrate using gold plated mirrors through ZnSe flanges (transparent to IR beam), attached to the vacuum chamber. The reflected IR beam from the substrate was re-focused using another gold-plated mirror to a liquid N<sub>2</sub> cooled external MCT IR detector. The spectra were collected in the 4000-550 cm<sup>-1</sup> range with 2 cm<sup>-1</sup> resolution. Each spectrum was averaged for 512 scans to get a better signal to noise ratio.

The CHs produced in the UHV condition were further characterized by temperature programmed desorption-mass spectrometry (TPD-MS) analysis. For TPD-MS, after ice deposition or clathrate hydrate formation, the substrate was moved to a fixed position by using a sample manipulator to ensure that the surface is very close to the mass spectrometer inlet and the substrate was ramped at a constant heating rate (30 K.min<sup>-1</sup>). Suitable masses of the desorbed species ( $m/z = 43$  for acetone,  $m/z = 18$  for H<sub>2</sub>O) were selected by a linear quadrupole mass spectrometer analyzer, and the intensity of the desorbed species was plotted as a function of substrate temperature. Extrel CMS, USA supplied the mass spectrometers.

Reflection high-energy electron diffraction (RHEED) study was carried out in a different UHV chamber of base pressure  $\sim 1.33 \times 10^{-10}$  mbar, which was described in detail elsewhere.<sup>10</sup> To obtain RHEED patterns, we used a focused high-energy electron beam (30 keV) that was generated by an electron gun (Eiko Co. Ltd., MB-1000). The diffraction pattern projected onto a phosphor screen was recorded using a high-sensitivity CCD camera intermittently (pulse duration of  $\sim 0.5$  s), only at specific temperatures and coverages of interest to reduce sample

damage. The typical electron beam current during the RHEED measurement was 5-7 nA, as determined using a Faraday cup. The spot size and glancing angle of the beam were 0.1 mm and 2-3°, respectively.

## Supporting Information 1:

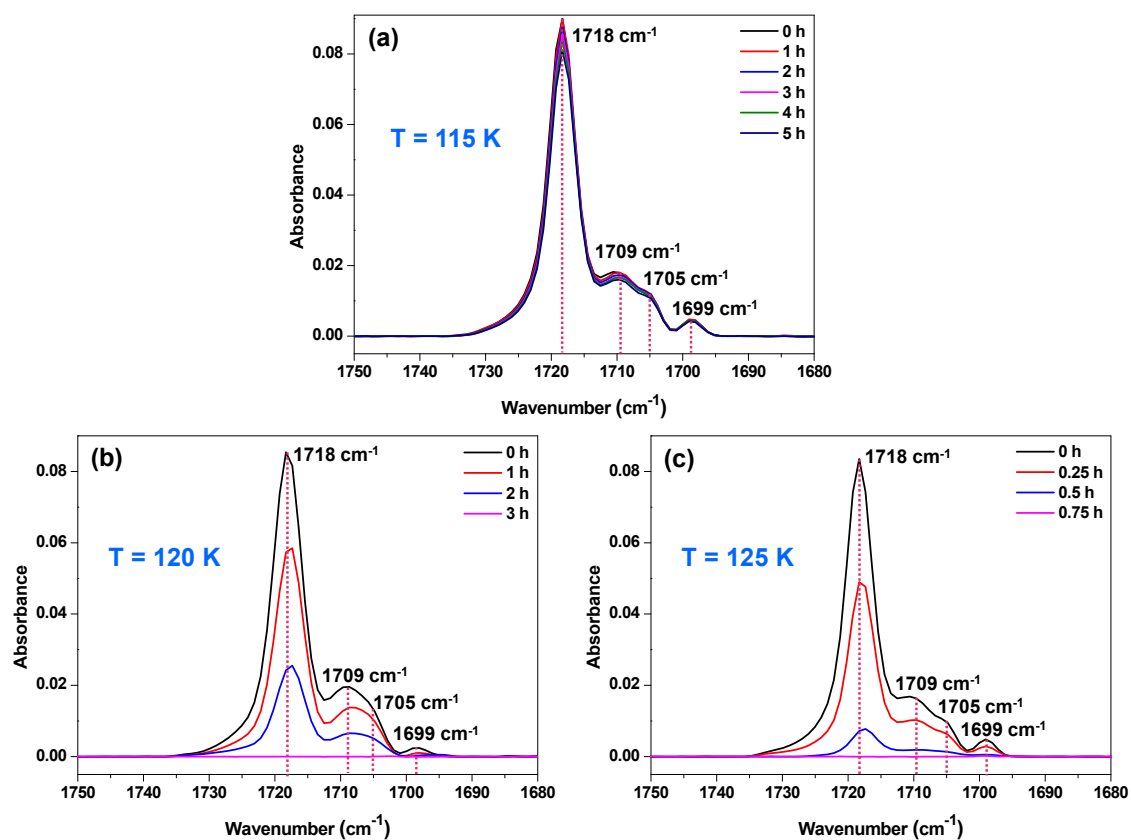


**Figure S1.** Isothermal time-dependent RAIR spectra of 150 MLs of pure acetone film at (a) 115, (b) 120, and (c) 125 K in the C=O stretching region. Time-dependent studies at relatively higher temperatures (130 or 135 K) could not be performed, since pure acetone desorbs within a few minutes at these temperatures.

## Supporting Information 2:

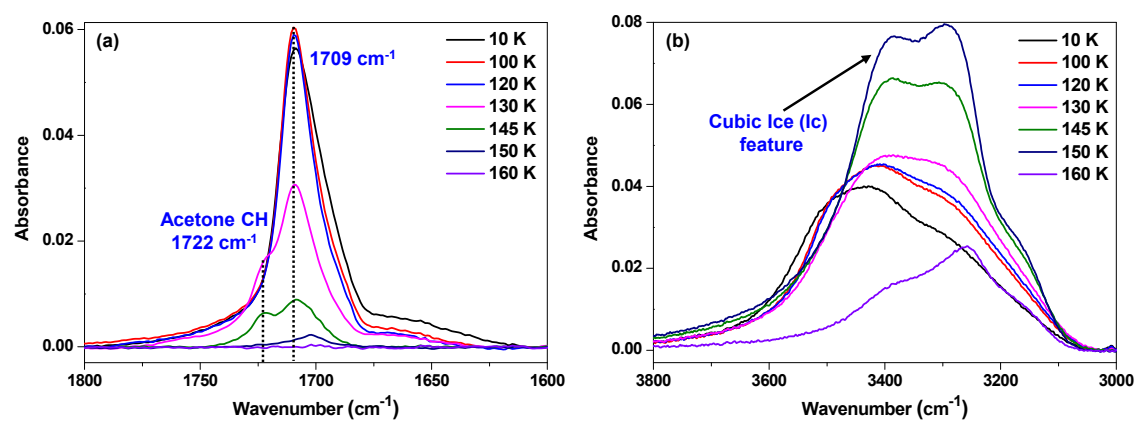


**Figure S2.** Temperature-dependent RAIR spectra of 300 MLs acetone:H<sub>2</sub>O (1:1) in the (a) C=O stretching region, and (b) O-H stretching region. The mixture was co-deposited on Ru(0001) substrate at 10 K, and annealed at a rate of 2 K.min<sup>-1</sup>.

### Supporting Information 3:

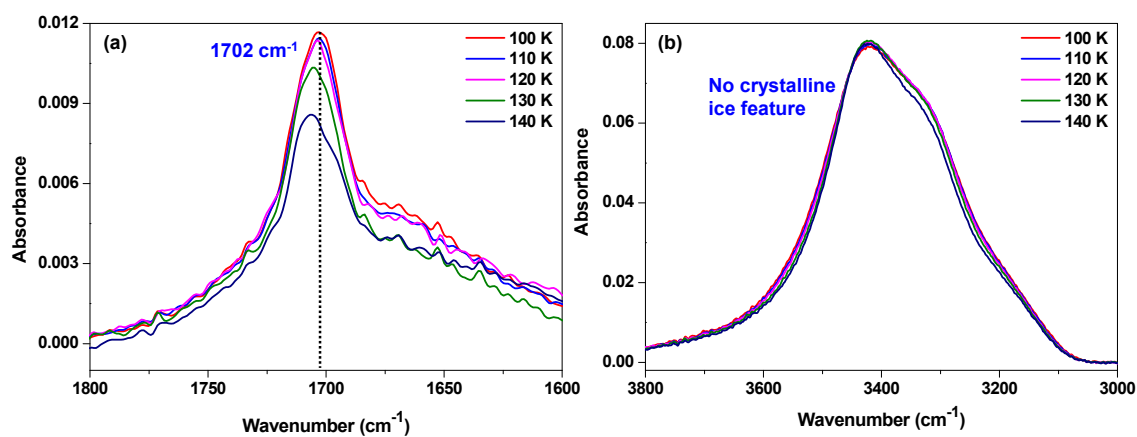


**Figure S3.** Temperature-dependent RAIR spectra of 300 MLs acetone:H<sub>2</sub>O (1:20) in the (a) C=O stretching region, and (b) O-H stretching region. The mixture was co-deposited on Ru(0001) substrate at 10 K, and annealed at a rate of 2 K.min<sup>-1</sup> to 140 K. The C=O stretching region partly overlaps with the O-H bending feature. Noise in the spectra is due to the reduced concentration of acetone.

## Supporting Information 4:

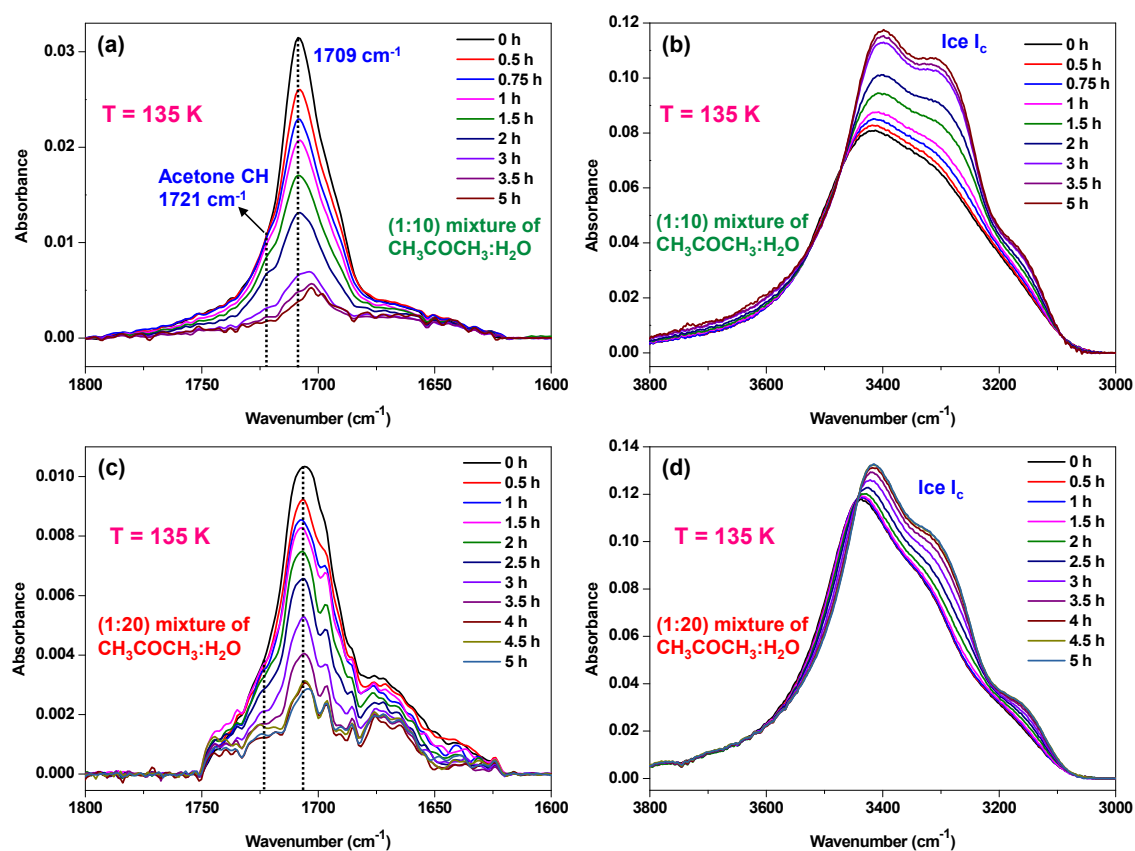


**Figure S4.** Time-dependent RAIR spectra of 300 MLs of acetone:H<sub>2</sub>O for two different ratios; (1:10) and (1:20) as shown in the top and bottom panels, respectively.

## Supporting Information 5:

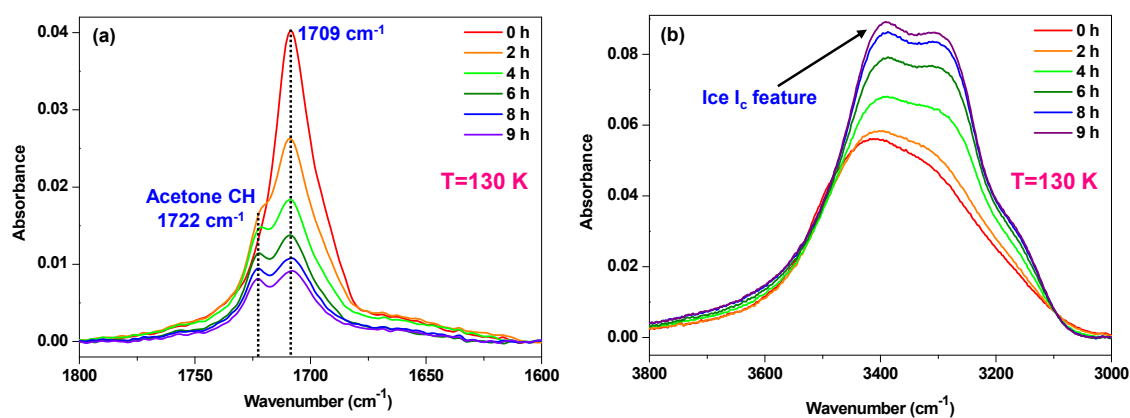


**Figure S5.** Time-dependent RAIR spectra of 300 MLs of acetone:H<sub>2</sub>O (1:1) at 130 K in the (a) C=O stretching region, and (b) O-H stretching region. The mixture was co-deposited on Ru(0001) substrate at 10 K, and annealed at a rate of 2 K.min<sup>-1</sup> to 130 K.



## Supporting Information 6:

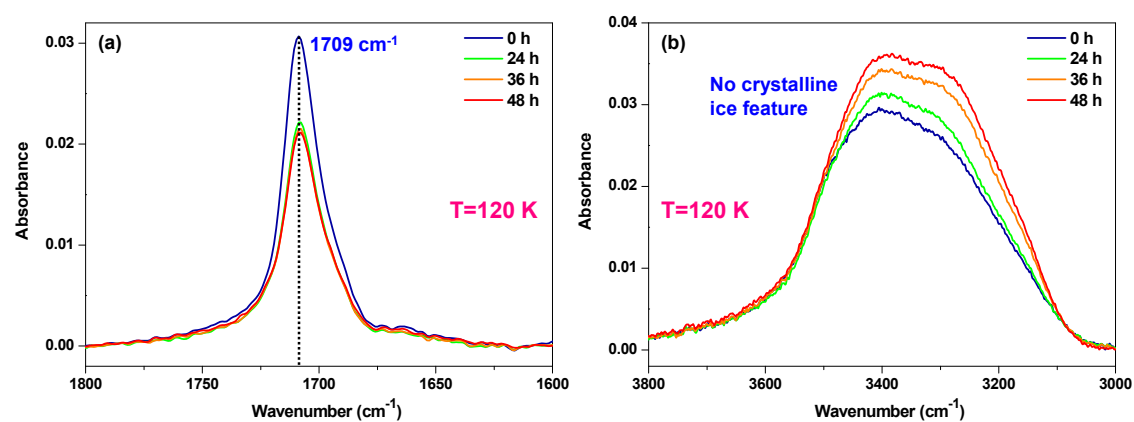


**Figure S6.** Time-dependent RAIR spectra of 300 MLs of acetone:H<sub>2</sub>O (1:1) at 120 K in the (a) C=O stretching region, and (b) O-H stretching region. The mixture was co-deposited on Ru(0001) substrate at 10 K, and annealed at a rate of 2 K.min<sup>-1</sup> to 120 K.

## Supporting Information 7:

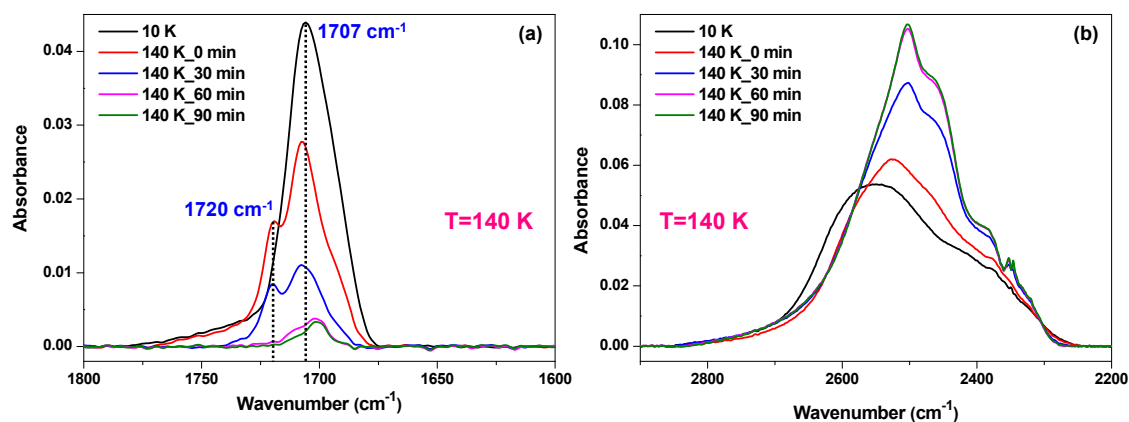


**Figure S7.** Time-dependent RAIR spectra of 300 MLs of acetone:D<sub>2</sub>O (1:1) at 140 K in the (a) C=O stretching region, and (b) O-D stretching region. The mixture was co-deposited on Ru(0001) substrate at 10 K, and annealed at a rate of 2 K.min<sup>-1</sup> to 140 K. The small peak at ~2349  $\text{cm}^{-1}$  is due to the uncompensated gas phase CO<sub>2</sub> from the background.

## Supporting Information 8:

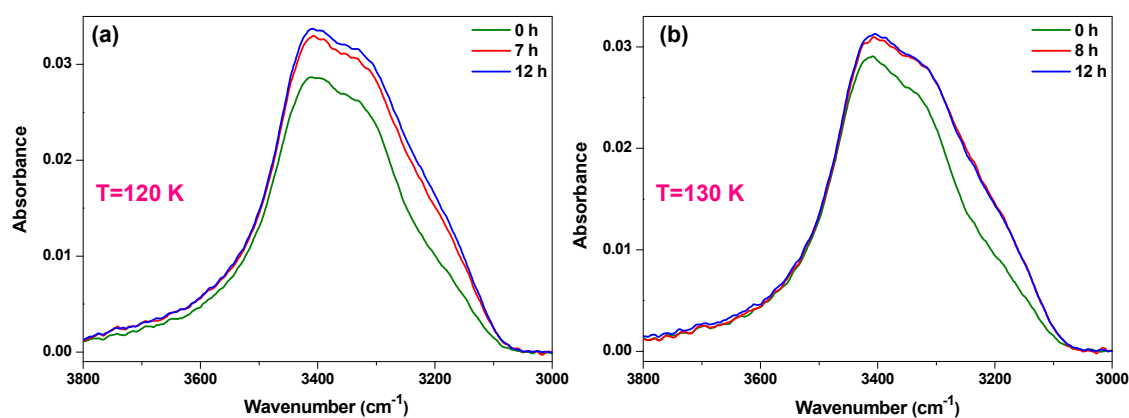


**Figure S8.** Time-dependent RAIR spectra of 150 MLs of solid H<sub>2</sub>O film at (a) 120 K, and (b) at 130 K in the O-H stretching region. The water vapour was deposited at 10 K on Ru(0001) substrate. The ice films were annealed at 2 K.min<sup>-1</sup> rate to the respective temperatures.

Supporting Information 9:

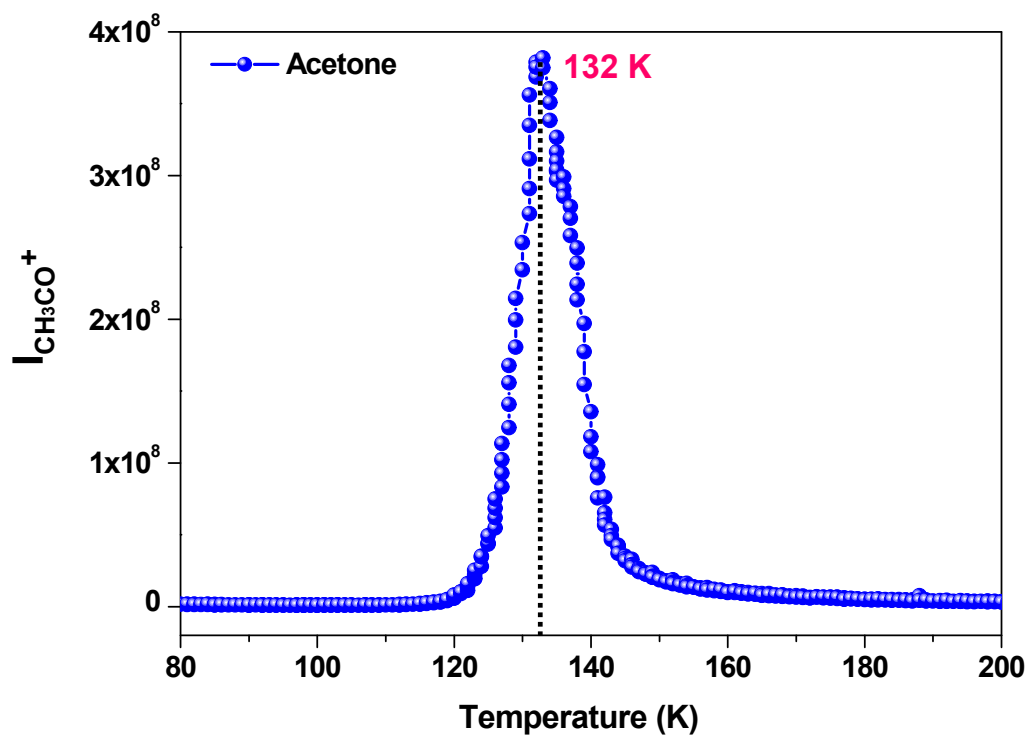


**Figure S9.** TPD-MS spectra of 150 MLs of pure acetone. Ramping rate = 30 K.min<sup>-1</sup>.

### Supporting Information 10:

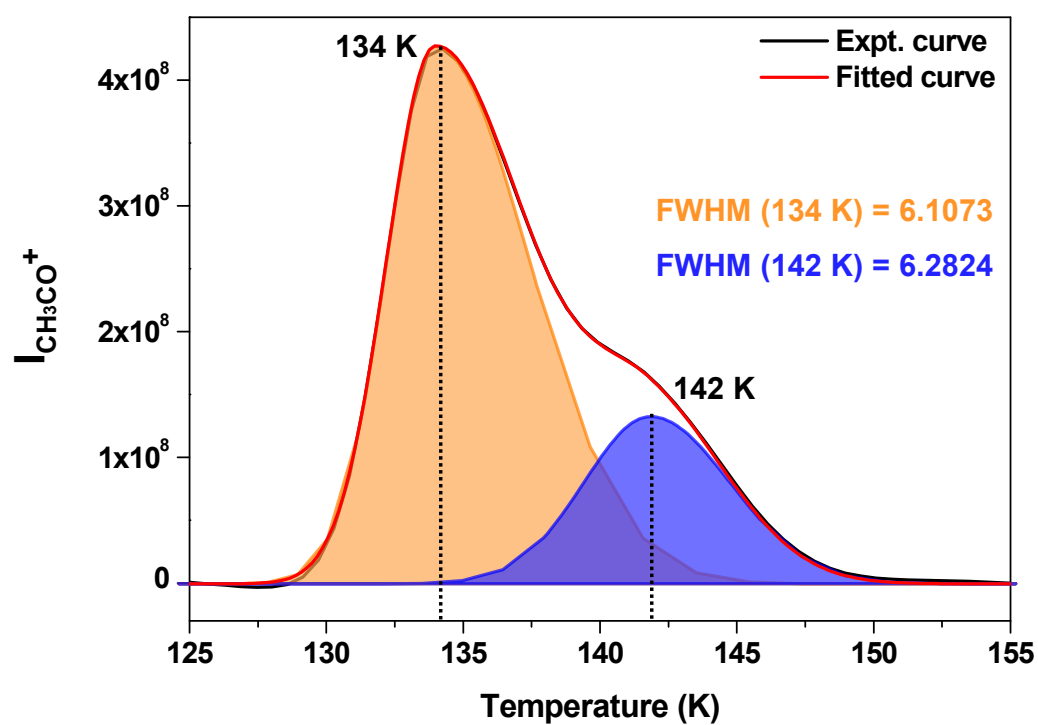


**Figure S10.** Deconvoluted desorption trace of acetone, taken from the TPD spectra shown in Figure 3a of the main manuscript. Here, two components are fitted to show their spectral widths are almost the same.

## Supporting Information 11:

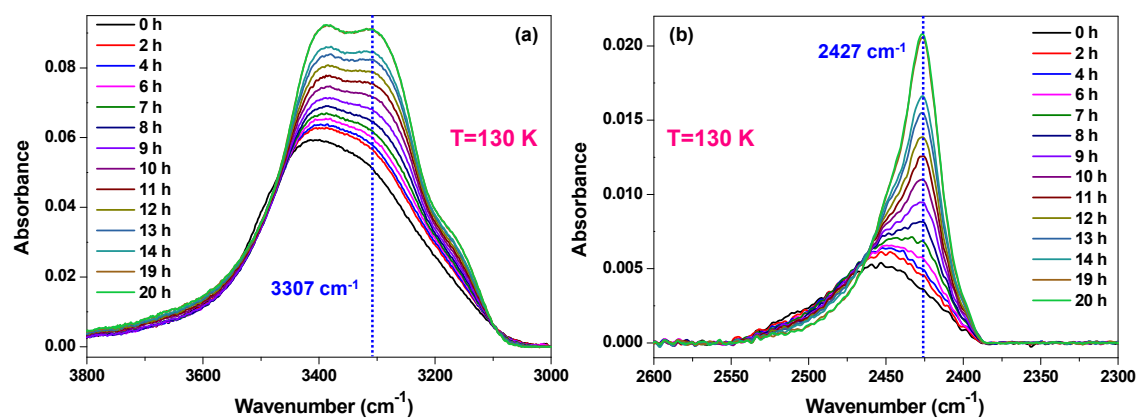


**Figure S11.** Time-dependent RAIR spectra of 300 MLs of acetone:HDO (5%  $\text{D}_2\text{O}$  in  $\text{H}_2\text{O}$ ) at 130 K in the (a) O-H stretching region, and (b) O-D stretching region.

## Supporting Information 12:

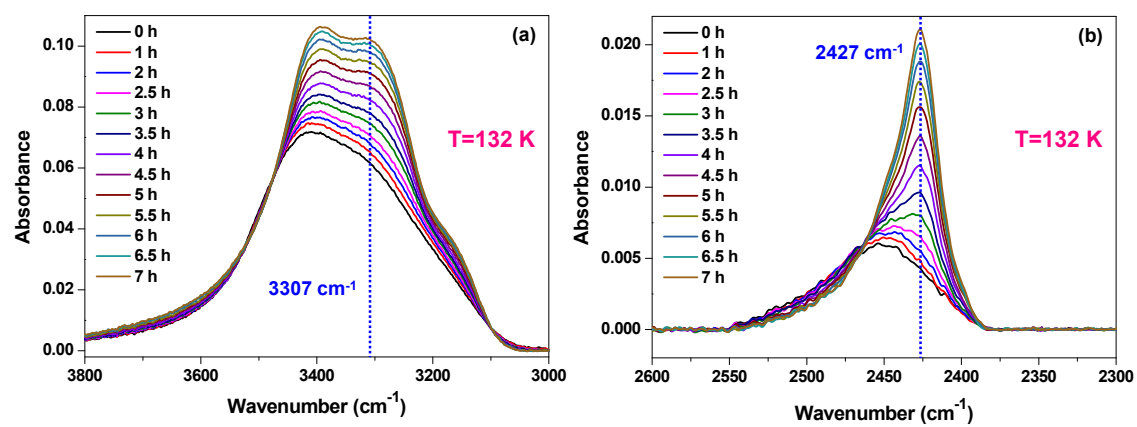


**Figure S12.** Time-dependent RAIR spectra of 300 MLs of acetone:HDO (5% D<sub>2</sub>O in H<sub>2</sub>O) at 132 K in the (a) O-H stretching region, and (b) O-D stretching region.

### Supporting Information 13:

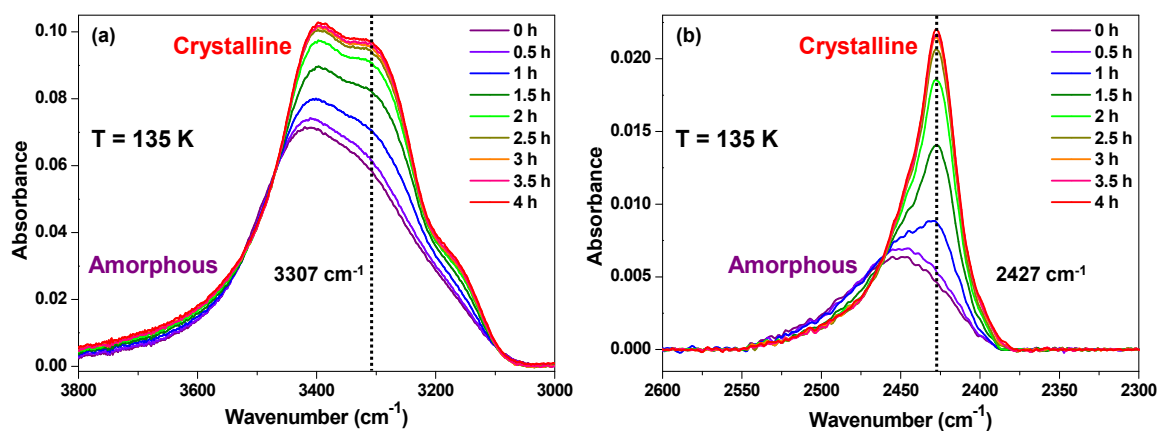


**Figure S13.** Time-dependent RAIR spectra of 300 MLs of acetone:HDO (5% D<sub>2</sub>O in H<sub>2</sub>O) at 135 K in the (a) O-H stretching region, and (b) O-D stretching region. The mixture was co-deposited on Ru(0001) substrate at 10 K, and annealed at a rate of 2 K.min<sup>-1</sup> to 135 K. The vertical lines at a fixed wavenumber are used to measure the absorbance changes with time, which was further utilized for calculation of crystallization fraction.



## Supporting Information 14:

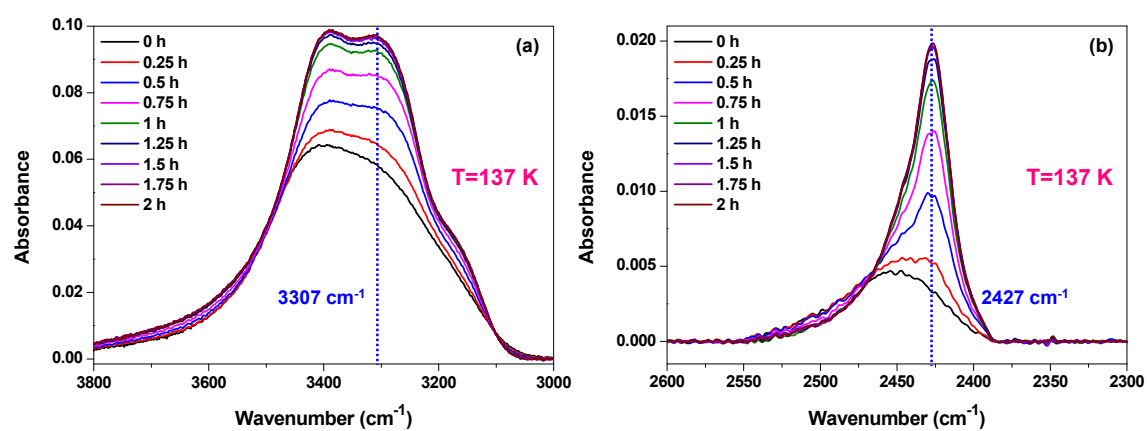


**Figure S14.** Time-dependent RAIR spectra of 300 MLs of acetone:HDO (5%  $\text{D}_2\text{O}$  in  $\text{H}_2\text{O}$ ) at 137 K in the (a) O-H stretching region, and (b) O-D stretching region.

## Supporting Information 15:

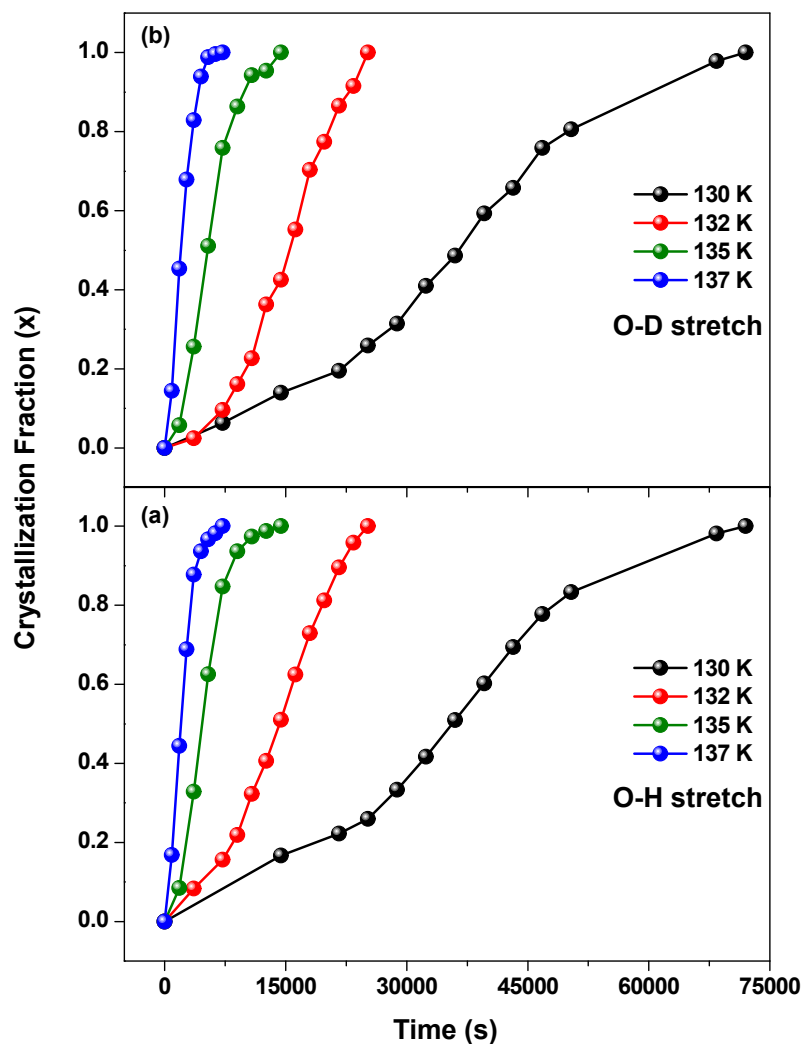


**Figure S15.** Crystallization fraction of 300 MLs of acetone:HDO (5% D<sub>2</sub>O in H<sub>2</sub>O) obtained from isothermal RAIRS measurements at 130, 132, 135, and 137 K. The extent of crystallization were estimated from, (a) the 3307 cm<sup>-1</sup> peak in the O-H stretching region, and (b) the 2427 cm<sup>-1</sup> peak in the decoupled O-D stretching region.

**Table S1:** The parameters for crystallization of ice Ic during the dissociation of acetone hydrate at different temperatures.

	Temperature (K)	$n$	Rate constant; $k$ (s <sup>-1</sup> )
O-H stretching	130	2.49	$2.47 \times 10^{-5}$
	132	2.45	$6.37 \times 10^{-5}$
	135	2.05	$1.80 \times 10^{-4}$
	137	1.62	$4.04 \times 10^{-4}$
O-D stretching	130	2.59	$2.36 \times 10^{-5}$
	132	2.51	$5.76 \times 10^{-5}$
	135	2.08	$1.50 \times 10^{-4}$
	137	1.81	$3.94 \times 10^{-4}$

## Supporting Information 16:

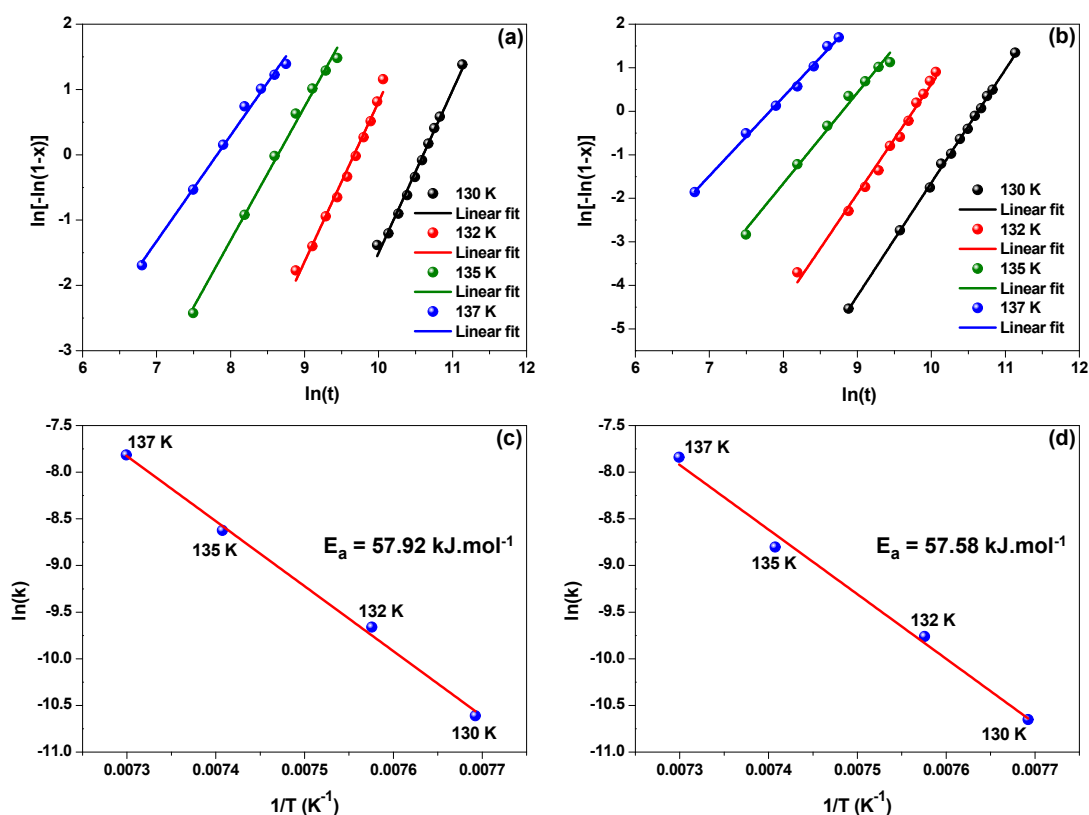


**Figure S16.** Plot of  $\ln(-\ln[1-x(t)])$  vs.  $\ln(t)$  at different temperatures of 130, 132, 135, and 137 K. These data points are obtained from the analysis of (a) the O-H, and (b) the O-D stretching regions and fitted using Avrami equation (eqn. 3). Plot of  $\ln k(T)$  vs. inverse temperature ( $1/T$ ), obtained from the analysis of (c) the O-H, and (d) the O-D stretching regions, respectively. The data points were fitted to obtain a straight line. Activation energy ( $E_a$ ) can be calculated from the slope of the straight line.

## References:

- (1) Bag, S.; Bhuin, R. G.; Methikkalam, R. R. J.; Pradeep, T.; Kephart, L.; Walker, J.; Kuchta, K.; Martin, D.; Wei, J.: Development of Ultralow Energy (1 - 10 eV) Ion Scattering Spectrometry Coupled with Reflection Absorption Infrared Spectroscopy and Temperature Programmed Desorption for the Investigation of Molecular Solids. *Rev. Sci. Instrum.* **2014**, *85*, 014103/1-014103/7.
- (2) Kim, Y.; Moon, E.-s.; Shin, S.; Kang, H.: Acidic Water Monolayer on Ruthenium(0001). *Angew. Chem., Int. Ed.* **2012**, *51*, 12806-12809.
- (3) Ghosh, J.; Hariharan, A. K.; Bhuin, R. G.; Methikkalam, R. R. J.; Pradeep, T.: Propane and propane-water interactions: a study at cryogenic temperatures. *Phys. Chem. Chem. Phys.* **2018**, *20*, 1838-1847.
- (4) Kang, H.; Shin, T. H.; Park, S. C.; Kim, I. K.; Han, S. J.: Acidity of Hydrogen Chloride on Ice. *J. Am. Chem. Soc.* **2000**, *122*, 9842-9843.
- (5) Bartmess, J. E.; Georgiadis, R. M.: Empirical methods for determination of ionization gauge relative sensitivities for different gases. *Vacuum* **1983**, *33*, 149-153.
- (6) Gottfried, J. M.; Schmidt, K. J.; Schroeder, S. L. M.; Christmann, K.: Oxygen chemisorption on Au(110)-(1×2) II. Spectroscopic and reactive thermal desorption measurements. *Surf. Sci.* **2003**, *525*, 197-206.
- (7) Yuan, C.; Smith, R. S.; Kay, B. D.: Communication: Distinguishing between bulk and interface-enhanced crystallization in nanoscale films of amorphous solid water. *J. Chem. Phys.* **2017**, *146*, 031102.
- (8) Li, F.; Skinner, J. L.: Infrared and Raman line shapes for ice Ih. II. H<sub>2</sub>O and D<sub>2</sub>O. *J. Chem. Phys.* **2010**, *133*, 244504.
- (9) Li, F.; Skinner, J. L.: Infrared and Raman line shapes for ice Ih. I. Dilute HOD in H<sub>2</sub>O and D<sub>2</sub>O. *J. Chem. Phys.* **2010**, *132*, 204505.
- (10) Souda, R.; Aizawa, T.: Crystallization kinetics of water on graphite. *Phys. Chem. Chem. Phys.* **2018**, *20*, 21856-21863.

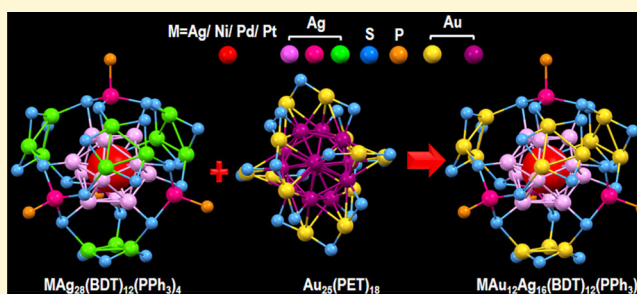
# Intercluster Reactions Resulting in Silver-Rich Trimetallic Nanoclusters

Esma Khatun, Papri Chakraborty, Betsy Rachel Jacob, Ganesan Paramasivam, Mohammad Bodiuzzaman, Wakeel Ahmed Dar, and Thalappil Pradeep\*

Department of Chemistry, DST Unit of Nanoscience (DST UNS) and Thematic Unit of Excellence (TUE), Indian Institute of Technology Madras, Chennai 600036, India

## Supporting Information

**ABSTRACT:** Herein, we present an intercluster reaction leading to new trimetallic nanoclusters (NCs) using bimetallic and monometallic NCs as reactants. Dithiol protected bimetallic  $\text{MAg}_{28}(\text{BDT})_{12}(\text{PPh}_3)_4$  (BDT = 1,3-benzenedithiol and  $\text{M} = \text{Ni}, \text{Pd}, \text{or Pt}$ ) and monothiol protected  $\text{Au}_{25}(\text{PET})_{18}$  (PET = 2-phenylethanethiol) were used as model NCs. A mixture of trimetallic  $\text{MAu}_x\text{Ag}_{28-x}(\text{BDT})_{12}(\text{PPh}_3)_4$  ( $x = 1-12$ ) and bimetallic  $\text{Ag}_x\text{Au}_{25-x}(\text{PET})_{18}$  ( $x = 1-7$ ) NCs were formed during the reaction as understood from time-dependent electrospray ionization mass spectrometry (ESI MS). Detailed studies of intercluster reaction between  $\text{Ag}_{29}(\text{BDT})_{12}(\text{PPh}_3)_4$  and  $\text{Au}_{25}(\text{PET})_{18}$  were also performed. Although both  $\text{MAg}_{28}(\text{BDT})_{12}(\text{PPh}_3)_4$  ( $\text{M} = \text{Ag}, \text{Ni}, \text{Pd}, \text{or Pt}$ ) and  $\text{Au}_{25}(\text{PET})_{18}$  contain 13 atoms icosahedral core, only a maximum of 12 Au doped NCs were formed for the former as a major product and not the 13 Au doped one, unlike the previous reports of intercluster reaction. The transfer of Ni, Pd, or Pt atom from the center of icosahedron of  $\text{MAg}_{28}(\text{BDT})_{12}(\text{PPh}_3)_4$  to  $\text{Au}_{25}(\text{PET})_{18}$  was not observed, which suggests that the central atom is not involved in the reaction. Density functional theory (DFT) calculations were performed to know structures and properties of the formed NCs. This study demonstrates the use of intercluster reaction as an effective synthetic protocol to make multimetallic alloy NCs.



## INTRODUCTION

Atomically precise nanoclusters (NCs) composed of an interior metal-core and exterior metal–ligand shell have gained significant attention due to their precise compositions and well-defined structures.<sup>1–4</sup> Robust stability of some NCs allows the growth of single crystals enabling structure determination by single-crystal X-ray diffraction leading to a detailed understanding of cluster-based materials.<sup>5–8</sup> They exhibit fascinating optical, catalytic, magnetic, and electrochemical properties which make them suitable for various applications.<sup>9–14</sup> The unique properties of NCs can be tuned by changing their structure, atomicity, protecting ligands, etc.<sup>4,15–18</sup> Among different NCs, alloy NCs composed of two or more metals are of great interest nowadays.<sup>19–24</sup> Alloying in Au and Ag NCs usually shows significant effects on catalysis, optics, etc., and therefore, it is of high importance in broadening their applications.<sup>25–27</sup> The very first example of an atomically precise bimetallic cluster synthesized was  $\text{PdAu}_{24}(\text{SR})_{18}$ .<sup>28,29</sup> After that, many alloy NCs were synthesized which exhibited drastic change in structure and properties from their monometallic analogues. For example, 26-fold enhancement in photoluminescence (PL) was observed by the doping of 5 Au atoms in  $\text{Ag}_{29}(\text{BDT})_{12}(\text{PPh}_3)_4$  (BDT = 1,3-benzenedithiol and in short  $\text{Ag}_{29}$ ).<sup>30</sup> Also, doping of Au increases the stability of NCs as observed in

$\text{Ag}_{17}(\text{TBBT})_{12}$  (*tert*-butylbenzenethiol).<sup>31</sup> Although poor stability of  $\text{Ag}_{17}(\text{TBBT})_{12}$  did not allow the formation of its single crystals, doping of one Au atom improved its stability and  $\text{AuAg}_{16}(\text{TBBT})_{12}$  was crystallized.<sup>32</sup> The effect of heteroatom doping in catalysis is well-studied.<sup>12,33</sup> Alloy NCs displayed higher catalytic activity than the monometallic analogues as observed in the oxidation of benzyl alcohol using Pd doped  $\text{Au}_{25}(\text{PET})_{18}$  (PET = 2-phenylethanethiol and in short  $\text{Au}_{25}$ ).<sup>34</sup>

A wide variety of combinations and compositions are possible for alloy NCs.<sup>35</sup> Their structures depend on synthetic methods and conditions applied.<sup>25</sup> Among different synthetic procedures of alloy NCs, the most common procedures are coreduction, galvanic reduction, antigalvanic reduction, and intercluster reaction.<sup>36–38</sup> Depending on the metal atom and synthetic procedures, the doping position in alloy NCs can be defined which has significant effect on their properties.<sup>22</sup> A large number of alloy NCs have been synthesized by the coreduction method. However, it is hard to control the structures of the obtained alloy NCs. In the case of galvanic and antigalvanic reduction methods, structures and morphol-

Received: November 3, 2019

Revised: December 3, 2019

Published: December 4, 2019

ogy of the formed NCs depend on the metal precursor used in the reaction.<sup>39</sup> Properties of NCs depend on the morphology as in the case of sphere and rodlike Au<sub>25</sub> NCs which showed different catalytic activity toward electro-reduction of CO<sub>2</sub>.<sup>40</sup>

Intercluster reaction is a new and effective method for the synthesis of alloy NCs.<sup>41</sup> Krishnadas et al. introduced intercluster reactions between Au<sub>25</sub> and Ag<sub>44</sub>(FTP)<sub>30</sub> (FTP = 4-fluorothiophenol and in short Ag<sub>44</sub>), which resulted in a mixture of bimetallic NCs.<sup>42</sup> Further, they studied the intercluster reaction between structurally similar Au and Ag NCs, Au<sub>25</sub> and Ag<sub>25</sub>(DMBT)<sub>18</sub> (DMBT = 2,4-dimethylbenzenethiol and in short Ag<sub>25</sub>).<sup>43</sup> These intercluster reactions manifested the molecule-like reactions possible between atomically precise NCs. The bimetallic NCs formed during these reactions showed the conservation of structures. Other than these conventional methods, a new synthetic protocol was reported by Bürgi et al. where metal foils were used as doping reagents.<sup>44</sup> Their study revealed the importance of ligands and the metal-core during intercluster reactions. Though the reaction between monometallic NCs has been studied for the past several years, intercluster reaction using multimetallic NCs is still unexplored.

In this report, we have presented the formation of trimetallic NCs by intercluster reaction between dithiol protected bimetallic NCs, MAg<sub>28</sub>(BDT)<sub>12</sub>(PPh<sub>3</sub>)<sub>4</sub> (M = Ni/Pd/Pt) (in short MAg<sub>28</sub>) and a monothiol protected NC, Au<sub>25</sub>. At first, we synthesized new bimetallic NCs, PdAg<sub>28</sub> and NiAg<sub>28</sub> along with the synthesis of known PtAg<sub>28</sub> by ligand exchange-induced structural transformation (LEIST) method starting from MAg<sub>24</sub> NCs (M = Ni/Pd/Pt). The synthesized bimetallic NCs were used as precursors for the reaction with Au<sub>25</sub> leading to the formation of trimetallic alloy NCs, MAu<sub>x</sub>Ag<sub>28-x</sub>(BDT)<sub>12</sub>(PPh<sub>3</sub>)<sub>4</sub> (in short MAu<sub>x</sub>Ag<sub>28-x</sub> where M is Ni/Pd/Pt and  $x = 1-12$ ). Also, a detailed understanding of the intercluster reaction between Ag<sub>29</sub> and Au<sub>25</sub> has been presented which was not been addressed in our previous work.<sup>45</sup> The intercluster reaction between Ag<sub>29</sub> and Au<sub>25</sub> led to the formation of a mixture of bimetallic NCs, Au<sub>x</sub>Ag<sub>29-x</sub>(BDT)<sub>12</sub>(PPh<sub>3</sub>)<sub>4</sub> (in short Au<sub>x</sub>Ag<sub>29-x</sub> where  $x = 1-12$ ) and Ag<sub>x</sub>Au<sub>25-x</sub>(PET)<sub>18</sub> (in short Ag<sub>x</sub>Au<sub>25-x</sub> where  $x = 1-7$ ). Unlike the previous intercluster reactions where the metal-core was fully replaced by Au atoms, in this case, we found the formation of Au<sub>12</sub>Ag<sub>17</sub> as the major product rather than Au<sub>13</sub>Ag<sub>16</sub> upon completion of the reaction. The reaction between MAg<sub>28</sub> and Au<sub>25</sub> also resulted in the formation of MAu<sub>12</sub>Ag<sub>16</sub> as the major product, which is understood as due to the reaction occurring at the surface of the NCs. The inner icosahedral core is seemingly protected by the metal-dithiol linkages in such a way that direct interaction with the metal-cores is not possible during the reaction. This was further confirmed from the fact that the central Ni, Pd, or Pt of MAg<sub>28</sub> was not being transferred to Au<sub>25</sub>. Further, theoretical calculations were carried out to understand structures and properties of the formed NCs.

## RESULTS AND DISCUSSION

We synthesized bimetallic MAg<sub>24</sub> (M = Ni/Pd/Pt) NCs following a reported protocol as mentioned in the Experimental Section. NiAg<sub>24</sub>, synthesized for the first time, exhibited prominent absorption features at 483 and 665 nm (panel b in Figure S1A). The absorption maximum of NiAg<sub>24</sub> was 7 nm blue-shifted from that of Ag<sub>25</sub> (panel a in Figure S1A). Panel b' in Figure S1B presents ESI MS of NiAg<sub>24</sub> which

exhibits a sharp peak at  $m/z$  2558 with 2<sup>−</sup> charge state corresponding to [NiAg<sub>24</sub>(DMBT)<sub>18</sub>]<sup>2−</sup>. The formed NiAg<sub>24</sub> is stable at low temperature for a few months. However, at room temperature, it is less stable than Ag<sub>25</sub>. Their absorption spectra at room temperature are presented in Figure S1C. Panels c/c' and d/d' in Figure S1 show UV-vis absorption spectra and ESI MS of PdAg<sub>24</sub> and PtAg<sub>24</sub>, respectively, which are in accordance with the previous reports.<sup>46</sup>

The LEIST method was followed for the synthesis of unknown Ni/PdAg<sub>28</sub> and previously known PtAg<sub>28</sub> (details are given in the Experimental Section). Optical absorption spectrum of Ni-doped Ag<sub>29</sub> shown in Figure 1A manifests a

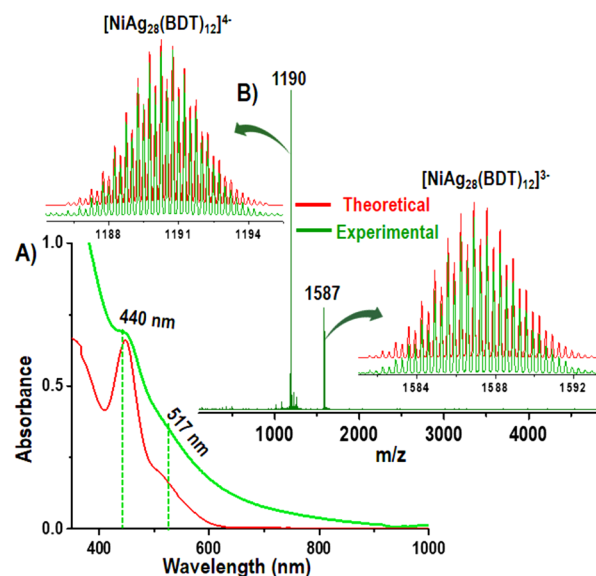


**Figure 1.** (A) UV-vis absorption spectrum of NiAg<sub>28</sub> (green trace), compared to Ag<sub>29</sub> (red trace). (B) ESI MS of NiAg<sub>28</sub> which shows two peaks at  $m/z$  1190 and 1587, corresponding to [NiAg<sub>28</sub>(BDT)<sub>12</sub>]<sup>4−</sup> and [NiAg<sub>28</sub>(BDT)<sub>12</sub>]<sup>3−</sup>, respectively. Theoretical and experimental isotopic distributions of [NiAg<sub>28</sub>(BDT)<sub>12</sub>]<sup>4−</sup> and [NiAg<sub>28</sub>(BDT)<sub>12</sub>]<sup>3−</sup> are shown in the inset of (B) which match perfectly.

well-defined absorption peak at 440 nm along with a shoulder peak at 517 nm (green trace). The absorption maximum is 7 nm blue-shifted, while the shoulder peak is 4 nm red-shifted from that of Ag<sub>29</sub> (red trace in Figure 1A).<sup>47</sup> An intense peak at  $m/z$  1190 was observed along with a less intense peak at  $m/z$  1587 in ESI MS which corresponded to [NiAg<sub>28</sub>(BDT)<sub>12</sub>]<sup>4−</sup> and [NiAg<sub>28</sub>(BDT)<sub>12</sub>]<sup>3−</sup>, respectively (Figure 1B). Theoretical and experimental isotopic patterns of [NiAg<sub>28</sub>(BDT)<sub>12</sub>]<sup>4−/3−</sup> matched exactly with each other as shown in the inset of Figure 1B. The NiAg<sub>28</sub> got ionized at high pressure and high voltage conditions in which detachment of all PPh<sub>3</sub> ligands took place. On the other hand, the species did not get ionized at low voltage and low gas pressure conditions, and hence, we were unable to get PPh<sub>3</sub> attached peaks in ESI MS. X-ray photoelectron spectrum (XPS) of NiAg<sub>28</sub> given in Figure S2 shows the presence of Ag 3d<sub>5/2</sub>, Ni 2p<sub>3/2</sub>, P 2p<sub>3/2</sub>, and S 2p<sub>3/2</sub> at 368.6, 853.9, 132.0, 163.0 eV, respectively. The NiAg<sub>28</sub> is more stable than the NiAg<sub>24</sub> which is revealed from their time-dependent absorption spectra presented in Figure S2B. It also shows good stability at high temperature (60 °C), although it is less stable than that of Ag<sub>29</sub> as shown in Figure S2C.



Pd doped  $\text{Ag}_{29}$  cluster was synthesized by the LEIST method which manifested distinct absorption features at 444 and 518 nm (Figure 2A). The absorption maximum (444 nm)

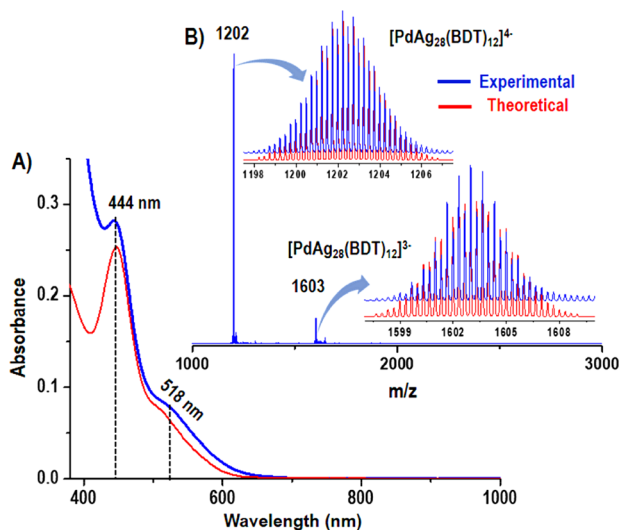


**Figure 2.** (A) UV-vis absorption spectrum of  $\text{PdAg}_{28}$  having a maximum at  $\sim 444$  nm (blue trace) is compared with that of  $\text{Ag}_{29}$  (red trace). (B) ESI MS of  $\text{PdAg}_{28}$  which shows an intense peak at  $m/z$  1202 corresponding to  $[\text{PdAg}_{28}(\text{BDT})_{12}]^{4+}$  along with a less intense peak at  $m/z$  1603 corresponding to  $[\text{PdAg}_{28}(\text{BDT})_{12}]^{3-}$ . Insets show experimental and theoretical isotopic distributions of  $[\text{PdAg}_{28}(\text{BDT})_{12}]^{4+}$  and  $[\text{PdAg}_{28}(\text{BDT})_{12}]^{3-}$  which fitted well with each other.

was 3 nm blue-shifted than that of  $\text{Ag}_{29}$ , while the shoulder peak was  $\sim 5$  nm red-shifted. ESI MS shown in Figure 2B consists of an intense peak at  $m/z$  1202 along with a weak peak at  $m/z$  1603. These correspond to  $4^-$  and  $3^-$  charge states of  $[\text{PdAg}_{28}(\text{BDT})_{12}]$ . The presence of four  $\text{PPh}_3$  ligands was confirmed by ESI MS measurement under low voltage and low gas pressure conditions (see Figure S3).  $\text{PdAg}_{28}$  was also characterized with the help of other analytical tools such as XPS and secondary electron microscopy/energy dispersive X-ray spectroscopy (SEM/EDS) (Figure S4). XPS shows the presence of P, S, Pd, and Ag (Figure S4A). The Ag  $3d_{5/2}$  peak

appears at 368.5 eV which is at a higher value than that of Ag (0) (367.9 eV).

The Pd  $3d_{5/2}$  peak appears at 337.5 eV which is also at a higher value than that of Pd (0) (335.5 eV). SEM/EDS characterization of the cluster is shown in Figure S4B. The elemental mapping clearly shows the presence of C, P, S, Ag, and Pd. The inset of Figure S4B shows the SEM image of the solid cluster and EDS mapping of the elements. Following a similar procedure,  $\text{PtAg}_{28}$  was synthesized. Absorption spectrum presented in Figure S5A displays two prominent features at 425 and 491 nm which are in agreement with the previous report.<sup>48</sup> Two peaks at  $m/z$  1224 and 1632 were noticed in ESI MS which are due to  $[\text{PtAg}_{28}(\text{BDT})_{12}]^{4+}$  and  $[\text{PtAg}_{28}(\text{BDT})_{12}]^{3-}$ , respectively. Theoretical isotopic distribution of the peak at  $m/z$  1224 matched exactly with the experimental one confirming the assignment of  $[\text{PtAg}_{28}(\text{BDT})_{12}]^{4+}$  (inset of Figure S5B). Unlike  $\text{MAg}_{24}$ , the  $\text{MAg}_{28}$  ( $M = \text{Ni/Pd/Pt}$ ) clusters show both the  $4^-$  and  $3^-$  charge states which imply that Ni, Pd, or Pt act as both zerovalent and univalent dopants ( $d^{10}s^0$  and  $d^9s^1$ ), although the intensity of the zerovalent one is higher than the other.

For the sake of understanding the structure of the newly synthesized  $\text{NiAg}_{28}$  and  $\text{PdAg}_{28}$ , we measured ESI MS as a function of collision energy (CE), and the data are presented in Figure S6. We observed the loss of smaller fragments such as  $[\text{Ag}_5(\text{BDT})_3]^-$  and  $[\text{Ag}_3(\text{BDT})_2]^-$  at higher CE. Ni or Pd atoms were not found in smaller fragments which suggest that Ni or Pd atoms do not occupy the staple motifs, rather they occupy the icosahedral core, similar to the case of  $\text{PtAg}_{28}$ .<sup>48</sup> This is because of their higher electronegativity similar to the previous reports.<sup>26,46,49</sup> Absorption spectra of both  $\text{NiAg}_{28}$  and  $\text{PdAg}_{28}$  are similar to  $\text{Ag}_{29}$ , suggesting that they have the same structures. Hence, we calculated the structures of  $\text{NiAg}_{28}$  and  $\text{PdAg}_{28}$  using density functional theory (DFT) and the most stable structures are presented in the insets of Figure 3A,B. Detailed descriptions of DFT calculations are given in the Experimental Section. Their optical absorption spectra calculated using time-dependent DFT (TDDFT) method are given in Figure 3A,B. They are consistent with the experimental ones, although there are some red-shifts (14 and 5 nm for  $\text{NiAg}_{28}$  and  $\text{PdAg}_{28}$ , respectively) which are in accordance with the previous reports.<sup>47,50</sup> Other possible

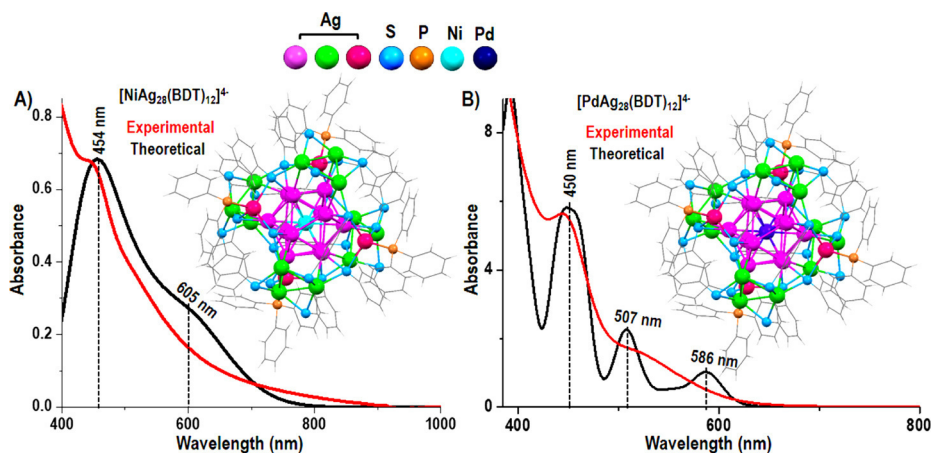


**Figure 3.** Theoretical (black) and experimental (red) UV-vis absorption spectra of (A)  $\text{NiAg}_{28}$  and (B)  $\text{PdAg}_{28}$ . Insets of (A) and (B) show the DFT-calculated most stable structures of  $\text{NiAg}_{28}$  and  $\text{PdAg}_{28}$ , respectively. Color code: light green, light pink, and pink denote Ag atoms, cyan denotes S atoms, orange denotes P atoms, sea blue denotes the Ni atom, and navy blue denotes the Pd atom.



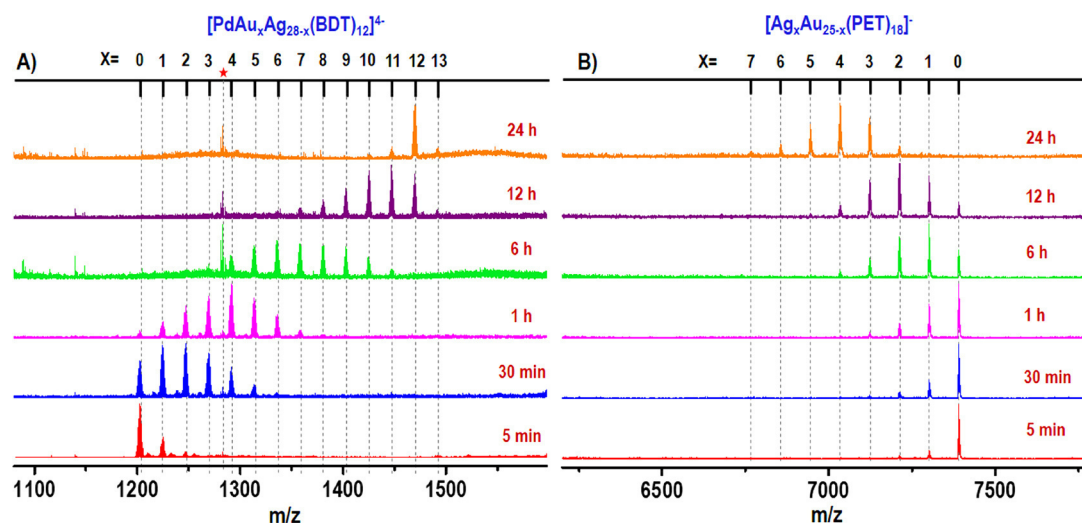


**Figure 4.** Time-dependent ESI MS of intercluster reaction between PdAg<sub>28</sub> and Au<sub>25</sub> (1:5 ratio) where panel (A) shows the reaction at the PdAg<sub>28</sub> side and panel (B) presents the reaction at the Au<sub>25</sub> side. The red asterisk corresponds to thiolates produced during the reaction. The species observed are [PdAu<sub>x</sub>Ag<sub>28-x</sub>(BDT)<sub>12</sub>]<sup>4+</sup> and [Ag<sub>x</sub>Au<sub>25-x</sub>(PET)<sub>18</sub>]<sup>-</sup> abbreviated as PdAu<sub>x</sub>Ag<sub>28-x</sub> and Ag<sub>x</sub>Au<sub>25-x</sub>, respectively, and the charged species are not mentioned in the text for simplicity.

structures of NiAg<sub>28</sub> and PdAg<sub>28</sub> but higher in energy available from computations are shown in Figure S7.

**Intercluster Reaction between PdAg<sub>28</sub> and Au<sub>25</sub>.** After the synthesis of bimetallic MAg<sub>28</sub> (M = Ni/Pd/Pt) NCs and their thorough characterization, they were used for intercluster reaction with Au<sub>25</sub>. At first, intercluster reactions between PdAg<sub>28</sub> and Au<sub>25</sub> were performed for the synthesis of trimetallic PdAu<sub>x</sub>Ag<sub>28-x</sub> NCs ( $x = 1-12$ ). From the time-dependent ESI MS of the reaction mixture of PdAg<sub>28</sub> and Au<sub>25</sub> presented in Figure 4, it is evident that the intercluster reaction ended up with the formation of a stable trimetallic alloy NC, PdAu<sub>12</sub>Ag<sub>16</sub> along with an unstable PdAu<sub>13</sub>Ag<sub>15</sub> which disappeared with time. Along with the trimetallic NCs, bimetallic Ag<sub>x</sub>Au<sub>25-x</sub> ( $x = 1-7$ ) NCs were also formed (Figure 4) as the final products. The rate of intercluster reaction between PdAg<sub>28</sub> and Au<sub>25</sub> was found to be highly dependent on their molar ratio. To study the concentration dependence, we carried out reactions using different molar ratios of PdAg<sub>28</sub> and Au<sub>25</sub> such as 4:1, 2:1, 1:1, 1:2, and 1:5, which are shown in Figure S8. The reaction rate was observed to be extremely slow when the amount of Au<sub>25</sub> used was less than that of PdAg<sub>28</sub> (for 4:1 and 2:1 ratios of PdAg<sub>28</sub>:Au<sub>25</sub>). Using a 1:1 ratio, we saw a satisfactory rate, although it took more than 1 day for the completion of the reaction. However, an increase in the amount of Au<sub>25</sub> (PdAg<sub>28</sub>:Au<sub>25</sub> = 1:5) led to the completion of the intercluster reaction within 24 h. Figure 4A shows that after 5 min, 2 Au atoms replace 2 Ag atoms to form PdAu<sub>x</sub>Ag<sub>28-x</sub> and consequently 2 Ag atoms replace 2 Au atoms, forming Ag<sub>x</sub>Au<sub>25-x</sub> where  $x$  is 0–2 (red traces in Figure 4A,B). But with increasing time, the number of doped Au atoms in PdAg<sub>28</sub> and doped Ag atoms in Au<sub>25</sub> were not the same. After 30 min of reaction, we noticed that 6 Au atoms were doped in PdAg<sub>28</sub> while only 3 Ag atoms were doped in Au<sub>25</sub> (blue traces in Figure 4A,B). At 1 h, 6 h, and 12 h, 8, 11, and 12 Au-doped PdAg<sub>28</sub>, respectively, were formed while only 3, 4, and 5 Ag atom doping in Au<sub>25</sub> were seen (pink, green, and violet traces, respectively, in Figure 4A,B). After 12 h, a small amount of 13 Au-doped product, PdAu<sub>13</sub>Ag<sub>15</sub>, was observed but when the reaction was continued up to 24 h, only 12 Au-doped product PdAu<sub>12</sub>Ag<sub>16</sub> was formed as the main product (orange trace in

Figure 4A). After 24 h, only up to 7 Ag-doped Au<sub>25</sub> NCs were formed (orange trace in Figure 4B). Theoretical and experimental isotopic distributions of PdAu<sub>12</sub>Ag<sub>16</sub> are presented in Figure S9 which fit well with each other, confirming the assigned composition. Time-dependent absorption spectra of the reaction mixture were measured, which are presented in Figure S10. The reaction mixture contains both trimetallic and bimetallic NCs as observed in ESI MS, but absorption spectra show the features of Ag<sub>x</sub>Au<sub>25-x</sub> (1–7). This is because of the higher Au<sub>25</sub> concentration used in the reaction than PdAg<sub>28</sub> which masks the absorbance of PdAg<sub>28</sub>. Interesting aspect in this intercluster reaction is that the Au atoms of Au<sub>25</sub> are getting doped in PdAg<sub>28</sub> to make trimetallic NCs, while no Pd atom is getting inserted in Au<sub>25</sub> to make the corresponding bi and trimetallic NC. To understand the mechanism, we studied other bimetallic NCs, PtAg<sub>28</sub> and NiAg<sub>28</sub> and performed their intercluster reactions with Au<sub>25</sub>, and the data are discussed in the subsequent section.

**Intercluster Reaction between PtAg<sub>28</sub> and Au<sub>25</sub>.** Time-dependent ESI MS of the intercluster reaction between PtAg<sub>28</sub> and Au<sub>25</sub> (PtAg<sub>28</sub>:Au<sub>25</sub> = 1:5) is presented in Figure 5. Similar to PdAg<sub>28</sub>, the intercluster reaction using PtAg<sub>28</sub> displayed systematic progress with time. The reaction was completed within 30 h which showed the formation of trimetallic PtAu<sub>12</sub>Ag<sub>16</sub> NC as the major product (orange trace in Figure 5). Theoretical and experimental isotopic distributions of PtAu<sub>12</sub>Ag<sub>16</sub> matched perfectly as shown in Figure S11. ESI MS of the reaction toward the Au<sub>25</sub> side presented in Figure S12 manifests only 7 Au doping similar to the reaction between PdAg<sub>28</sub> and Au<sub>25</sub>. Time-dependent absorption spectra are shown in Figure S13 which also reveal systematic change with time, and the final spectrum looks more like Ag<sub>7</sub>Au<sub>18</sub> NCs due to the use of higher concentration of Au<sub>25</sub> than that of PtAg<sub>28</sub>.

**Intercluster Reaction between NiAg<sub>28</sub> and Au<sub>25</sub>.** To demonstrate the intercluster reaction between NiAg<sub>28</sub> and Au<sub>25</sub>, we performed time-dependent ESI MS as shown in Figure S14. After 4 h of mixing, we found doping of 8 Au atoms in NiAg<sub>28</sub>. Further monitoring of ESI MS was not possible due to the lower intensity of the formed trimetallic NCs. Therefore, we assume that similar to Pd and Pt, in the

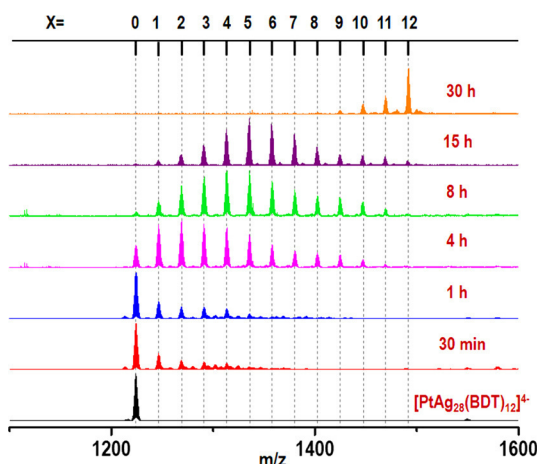


**Figure 5.** Time-dependent ESI MS of intercluster reaction between  $\text{PtAg}_{28}$  and  $\text{Au}_{25}$  (1:5 ratio) showing the reaction at the  $\text{PtAg}_{28}$  side. The reaction starts slowly and gets over within 30 h. The species formed are  $[\text{PtAu}_x\text{Ag}_{28-x}(\text{BDT})_{12}]^{4-}$  abbreviated as  $\text{PtAu}_x\text{Ag}_{28-x}$  and the charged species are not mentioned in the text for simplicity.

case of  $\text{NiAg}_{28}$ , doping of 12 Au atoms is feasible, although we were unable to detect  $\text{NiAu}_{12}\text{Ag}_{16}$  due to its lower ionization efficiency. Theoretical and experimental isotopic distributions of  $\text{NiAuAg}_{27}$  are shown in Figure S15 which fit well with each other.

**Intercluster Reaction between  $\text{Ag}_{29}$  and  $\text{Au}_{25}$ .** To get more insight into the reaction mechanism, intercluster reaction between  $\text{Ag}_{29}$  and  $\text{Au}_{25}$  was performed in detail which was not mentioned in our previous report.<sup>45</sup> Similar to  $\text{Mg}_{28}$  ( $\text{M} = \text{Ni/Pd/Pt}$ ), this reaction also required higher  $\text{Au}_{25}$  concentration in comparison to  $\text{Ag}_{29}$  (Figure S16). Time-dependent ESI MS corresponding to the reaction of 1:5 mixture of  $\text{Ag}_{29}$  and  $\text{Au}_{25}$  is presented in Figure S17. It exhibited a slower reaction rate than  $\text{Mg}_{28}$  ( $\text{M} = \text{Ni/Pd/Pt}$ ) and was not completed even after 36 h. This is because of the lower reactivity of undoped NCs than the doped ones as evident from the previous reports.<sup>51</sup> To increase the rate, the reaction was carried out at a higher temperature which is shown in Figure 6. At 60 °C, the reaction was completed within 4 h which led to the formation of highly intense  $\text{Au}_{12}\text{Ag}_{17}$  along with a small amount of  $\text{Au}_{11}\text{Ag}_{18}$  and  $\text{Au}_{13}\text{Ag}_{16}$  (see blue trace in Figure 6). Though  $\text{Ag}_{29}$  is having a similar  $\text{Ag}_{13}$  icosahedral core compared to  $\text{Ag}_{25}$ ,  $\text{Au}_{12}\text{Ag}_{17}$  was formed as a major product rather than  $\text{Au}_{13}\text{Ag}_{16}$ . The experimental isotopic distribution of  $\text{Au}_{12}\text{Ag}_{17}$  is shown in Figure S18, which is in good agreement with the theoretical one. The reaction at  $\text{Au}_{25}$  side shows the insertion of 7 Ag atoms similar to the  $\text{Mg}_{28}$  ( $\text{M} = \text{Ni/Pd/Pt}$ ), as shown in Figure S19. Time-dependent absorption spectra of the mixture shown in Figure S20 also display similar absorption features to that of the reaction product of  $\text{Mg}_{28}$  ( $\text{M} = \text{Ni/Pd/Pt}$ ).

**Mechanistic Details.** Understanding the mechanism of a chemical reaction is an important aspect. According to the early reports of intercluster reactions, the metal–ligand interface plays an important role.<sup>4,41</sup> Hence, dithiol protected NCs exhibit slow reaction rate than the monothiol protected ones due to the stronger metal–ligand binding as well as higher intracluster noncovalent interactions between the protective ligands. In the case of monothiol protected NCs, the exchange of both metals and ligands were observed. However, for dithiol protected NCs, only metal exchange but

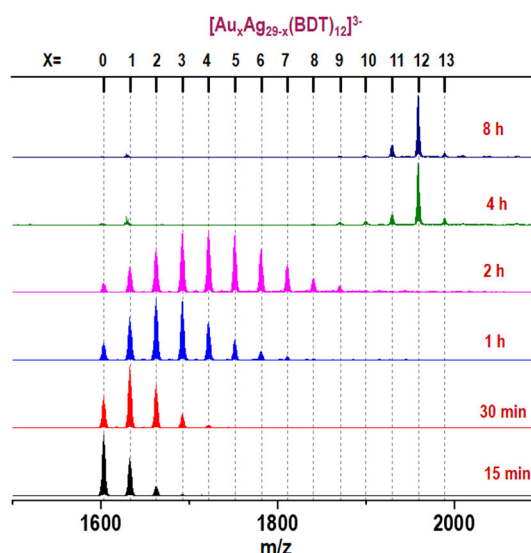


**Figure 6.** Time-dependent ESI MS of the reaction mixture of  $\text{Ag}_{29}$  and  $\text{Au}_{25}$  ( $\text{Ag}_{29}:\text{Au}_{25} = 1:5$ ) at a higher temperature (60 °C). The reaction at the  $\text{Ag}_{29}$  side is shown here. The species observed are  $[\text{Au}_x\text{Ag}_{29-x}(\text{BDT})_{12}]^{3-}$  abbreviated as  $\text{Au}_x\text{Ag}_{29-x}$  and the charged species are not mentioned in the text for simplicity.

no ligand exchange was feasible. It is also due to the strong binding of dithiol which cannot be replaced by a monothiol.<sup>45</sup>

In the previous example of intercluster reactions involving monothiol protected NCs such as  $\text{Ag}_{25}$  and  $\text{Au}_{25}$ , exchange of more than 12 atoms was observed during the reaction as they have more fluxional structures which were demonstrated by the Borromean ring model.<sup>43</sup> According to the Borromean ring model, NCs were viewed as a combination of three interlocked rings among which breakage of one ring can lead to the destruction of the whole structure during the reaction. Hence, the core atoms became easily accessible for interaction during the reaction which resulted in the doping of more than 12 atoms.<sup>41,52</sup> However, the structure of  $\text{Ag}_{29}$  (or  $\text{Mg}_{28}$ ) is different from that of  $\text{Ag}_{25}$ . It has the  $\text{Ag}_{13}$  icosahedron protected by four  $\text{Ag}_3\text{S}_6$  crown motifs and four  $\text{AgPPh}_3$  units.<sup>47</sup> Out of the two kinds of staples present in  $\text{Ag}_{29}$ , crown-like  $\text{Ag}_3\text{S}_6$  staples are easier to interact due to their less crowded surroundings as shown in Figure 7A. On the other hand,  $\text{Au}_{25}$  consists of  $\text{Au}_{13}$  icosahedron and six  $\text{Au}_2\text{S}_3$  staples (shown in Figure 7A). During the reaction, there may be weak van der Waals interactions of one  $\text{Ag}_{29}$  with four  $\text{Au}_{25}$  approaching from four tetrahedral directions at different times in the process of reaction which may lead to the formation of  $\text{Au}_{12}\text{Ag}_{17}$  at the end of the reaction. This kind of van der Waals interactions were feasible during the intercluster reaction between  $\text{Ag}_{25}$  and  $\text{Au}_{25}$ .<sup>43</sup> We suppose that 12 Au atoms occupy the crown motifs (see Figure 7B) of  $\text{Ag}_{29}$ . In an early report, 5 Au atoms were doped in  $\text{Ag}_{29}$  following the coreduction method. The crystal structure of  $\text{AuAg}_{28}$  was reported where the Au atom occupies the central position. Further, the use of a higher amount of  $\text{AuPPh}_3\text{Cl}$  led to the incorporation of more number of Au atoms which were incorporated at the terminal positions according to the NMR study. However, no crystal structure was reported for the higher number of Au doped NC.<sup>30</sup> In the case of intercluster reactions involving  $\text{Mg}_{28}$  ( $\text{M} = \text{Ag/Ni/Pd/Pt}$ ) and  $\text{Au}_{25}$ , Ag atoms of the crown motifs get exchanged due to the geometry of approach of the two NCs during their interaction. Further,

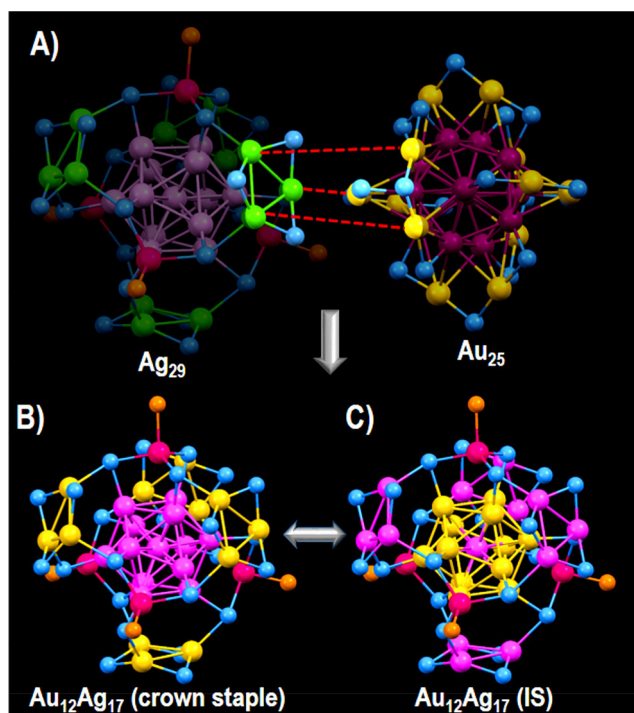


**Figure 7.** (A) The weak van der Waals interactions between staple metals of  $\text{Ag}_{29}$  and  $\text{Au}_{25}$  which results in (B) the formation of  $\text{Au}_{12}\text{Ag}_{17}$  where Au atoms are doped in the crown motifs of  $\text{Ag}_{29}$ . (C) The rapid interchange between Au atoms on staples and Ag atoms on the icosahedral surface leads to the formation of a thermodynamically stable isomer of  $\text{Au}_{12}\text{Ag}_{17}$ .

the Au atoms present in crown motifs can rapidly interchange their positions to form other isomers which are energetically more stable.<sup>53,54</sup> There are four doping positions in  $\text{MAG}_{28}$  ( $\text{M} = \text{Ag}/\text{Ni}/\text{Pd}/\text{Pt}$ ), among which the central atom is not getting replaced by Au atoms as we observed experimentally. Among the remaining three positions, icosahedral surface (IS) is energetically more stable (DFT calculated structure of  $\text{Au}_{12}\text{Ag}_{17}$  is given in Figure 7C) than the other isomers as per DFT calculations. However, other isomers of  $\text{Au}_{12}\text{Ag}_{17}$  also can exist in the solution, and their structures are shown in Figure S21. As  $\text{Ni}/\text{Pd}/\text{PtAg}_{28}$  NCs are having similar structures to that of  $\text{Ag}_{29}$ , they exhibit the same reaction mechanism and form similar products. Also,  $\text{Ni}/\text{Pd}/\text{PtAu}_{12}\text{Ag}_{16}$  possess similar structures to that of  $\text{Au}_{12}\text{Ag}_{17}$  containing Ni, Pd, or Pt at the center of the icosahedron.

We used higher concentration of  $\text{Au}_{25}$  than  $\text{Ag}_{29}$  or  $\text{MAG}_{28}$  to speed up the reaction as discussed above which resulted in the doping of less number of Ag atoms in  $\text{Au}_{25}$  than the number of exchanges in  $\text{Ag}_{29}$  (experimentally, incorporation of 7 Ag atoms were observed). Similar to  $\text{Ag}_{29}$ , Ag atoms are supposed to dope first in the staple of  $\text{Au}_{25}$  during the reaction and then undergo rapid atom exchange to attain the energetically favored structure of  $\text{Ag}_x\text{Au}_{25-x}$  ( $x = 1-7$ ) where Ag atoms are doped in the icosahedral surface positions.<sup>55,56</sup>

## CONCLUSION

In conclusion, we discussed the formation of trimetallic NCs by intercluster reaction of bimetallic and monometallic NCs. We used dithiol protected  $\text{MAG}_{28}$  ( $\text{M} = \text{Ni}, \text{Pd}, \text{or Pt}$ ) and monothiol protected  $\text{Au}_{25}$  for the reaction. The reaction was monitored by time-dependent ESI MS measurements. The

reactions revealed that the central doped metal atoms, Ni, Pd, or Pt of  $\text{MAG}_{28}$  were unavailable for exchange by Au atoms and hence only Ag-rich trimetallic NCs got formed. At the end of the reaction, 12 Ag atoms of  $\text{MAG}_{28}$  were replaced by 12 Au atoms to form  $\text{MAu}_{12}\text{Ag}_{16}$ . The intercluster reaction between  $\text{Ag}_{29}$  and  $\text{Au}_{25}$  also showed the formation of  $\text{Au}_{12}\text{Ag}_{17}$  as the major product. The study demonstrates that unlike the monothiol protected NCs, dithiol protected ones show strong metal–ligand binding due to the presence of strong non-covalent intracluster interactions between protective ligands. This led to the formation of  $\text{MAu}_{12}\text{Ag}_{16}$  ( $\text{M} = \text{Ag}/\text{Ni}/\text{Pd}/\text{Pt}$ ) by the outer metal–ligand shell interactions with  $\text{Au}_{25}$ . Therefore, inner cores were not involved in the reaction directly and remained unchanged. Intercluster reaction is thus found to be a useful tool to make multimetallic NCs that enrich the chemistry of atomically precise NCs.

## EXPERIMENTAL SECTION

**Materials and Chemicals.** Sodium borohydride ( $\text{NaBH}_4$ , 95%), 1,3-benzenedithiol (BDT) ( $\geq 99\%$ ), 2,4-dimethylbenzenethiol (DMBT), 2-phenylethanethiol (PET), chloroauric acid trihydrate ( $\text{HAuCl}_4 \cdot 3\text{H}_2\text{O}$ ), tetraoctylammonium bromide (TOAB), tetraphenylphosphonium bromide ( $\text{PPh}_4\text{Br}$ ), palladium acetate ( $\text{Pd}(\text{OAc})_2$ ), nickel acetate ( $\text{Ni}(\text{OAc})_2$ ), chloroplatinic acid ( $\text{K}_2\text{PtCl}_4$ ), and triethylamine were purchased from Sigma-Aldrich. Silver nitrate ( $\text{AgNO}_3$ ) was purchased from Rankem chemicals. Triphenylphosphine ( $\text{PPh}_3$ , 98%) was purchased from Spectrochem. Dichloromethane (DCM), dimethylformamide (DMF), acetone, tetrahydrofuran (THF), and methanol (MeOH) were purchased from Rankem and were of HPLC grade. All chemicals were used without further purification.

**Synthesis of  $\text{Au}_{25}(\text{PET})_{18}$  ( $\text{Au}_{25}$ ).** For the synthesis of  $\text{Au}_{25}$ , we followed a reported synthetic procedure.<sup>57</sup> About 40 mg of  $\text{HAuCl}_4 \cdot 3\text{H}_2\text{O}$  was taken in 7.5 mL of THF and  $\sim 65$  mg of TOAB was added and stirred for 15 min to get a deep red solution. Next,  $\sim 68$   $\mu\text{L}$  of PET was added, and the solution was stirred for 2 h to get a colorless solution indicating the formation of Au-SR. Then, the formed thiolate was reduced by adding  $\sim 39$  mg of  $\text{NaBH}_4$  (in 2.5 mL of ice-cold water), and the stirring was continued for another 6–7 h to get a reddish-brown colored solution. After that, the reaction mixture was completely dried in rotavapor, and the cluster was precipitated by the addition of MeOH. The precipitate was washed thoroughly by MeOH to remove excess thiol and other impurities that were discarded with the supernatant solution. This washing was repeated for 2–3 times followed by the extraction of the  $\text{Au}_{25}$  cluster in acetone which helps to remove bigger particles and then the pure cluster was extracted in DCM.

**Synthesis of  $\text{Ag}_{25}(\text{DMBT})_{18}$  ( $\text{Ag}_{25}$ ).** The cluster was synthesized following a reported method after a few modifications.<sup>58</sup> About 38 mg of  $\text{AgNO}_3$  was dissolved in 5 mL of MeOH and then  $\sim 9$  mL of DCM was added to it. To this solution,  $\sim 90$   $\mu\text{L}$  of DMBT was added which resulted in a thick yellow mixture. After 5 min,  $\sim 6$  mg of  $\text{PPh}_4\text{Br}$  (in 0.5 mL of MeOH) was added followed by the addition of 0.5 mL of an ice-cold aqueous solution of  $\text{NaBH}_4$  ( $\sim 23$  mg) after 20 min. The reaction mixture was stirred for  $\sim 8$  h and aged for 24 h. The dark brown solution was centrifuged, and then the supernatant was concentrated to  $\sim 5$  mL using a rotary evaporator. The cluster was precipitated by the addition of excess MeOH and washed several times with MeOH. Then the precipitate was dissolved in DCM and the cluster was extracted.

**Synthesis of  $\text{MAG}_{24}(\text{DMBT})_{18}$  ( $\text{MAG}_{24}$  where  $\text{M} = \text{Ni}, \text{Pd}, \text{or Pt}$ ).** For the synthesis of  $\text{NiAg}_{24}$ , we followed a reported method after some modifications.<sup>46</sup> At first,  $\sim 10$  mg of  $\text{AgNO}_3$  was dissolved in MeOH (5 mL) along with  $\sim 10$  mg of  $\text{Ni}(\text{OAc})_2$  (9 mL of DCM). Then,  $\sim 10$   $\mu\text{L}$  of DMBT in 0.5 mL of DCM was added to the mixture followed by the addition of  $\sim 10$  mg of  $\text{PPh}_4\text{Br}$  (in 0.5 mL of DCM). After  $\sim 20$  min,  $\text{NaBH}_4$  (40 mg in 0.5 mL of ice-cold water) was added, resulting in the reduction of Ag-Ni-phosphine-thiolate to form



NCs, and 50  $\mu\text{L}$  of triethylamine was added after 5 min. The solution was kept stirring overnight. The formed cluster solution was evaporated and then washed with MeOH. The clusters were extracted in DCM. Following the similar synthetic route,  $\text{PtAg}_{24}$  and  $\text{PdAg}_{24}$  were synthesized using  $\text{K}_2\text{PtCl}_4$  and  $\text{Pd}(\text{OAc})_2$ , respectively, instead of  $\text{Ni}(\text{OAc})_2$ .

**Synthesis of  $\text{Ag}_{29}(\text{BDT})_{12}(\text{PPh}_3)_4$  ( $\text{Ag}_{29}$ ).** The cluster was synthesized adopting an already reported method.<sup>47</sup> First,  $\sim 20$  mg of  $\text{AgNO}_3$  was dissolved in 5 mL of MeOH, and then 9 mL of DCM was added. After a few mins,  $\sim 13.5$   $\mu\text{L}$  of BDT (0.5 mL of DCM) was added to the solution. Then, after 5 min of stirring in the dark,  $\sim 200$  mg of  $\text{PPh}_3$  (in 0.5 mL of DCM) was added to the mixture, and next, 0.5 mL of an ice-cold aqueous solution containing  $\sim 11$  mg of  $\text{NaBH}_4$  was added, which immediately changed the color of the solution to dark brown. The reaction was kept for 3 h under dark conditions. Then, the precipitate (red color) was collected by centrifugation and the concentrated solution was collected by rotary evaporation. The cluster was washed several times with MeOH and then dissolved in DCM. The reddish-orange colored cluster was collected after the removal of unwanted byproducts.

**Synthesis of  $\text{MAG}_{28}(\text{BDT})_{12}(\text{PPh}_3)_4$  ( $\text{MAG}_{28}$  where  $\text{M} = \text{Ni, Pd, or Pt}$ ).** The ligand exchange induced structural/size transformation (LEIST)<sup>8</sup> method was used for the synthesis of  $\text{MAG}_{28}$ .  $\text{MAG}_{24}$  was taken in DCM as precursors, and then BDT and  $\text{PPh}_3$  were added to the solution which was kept for 1 h. After that, DCM was evaporated and the formed cluster was washed with MeOH several times. Then, the cluster was extracted in DMF and used for further characterizations.

**Synthesis of  $\text{MAu}_x\text{Ag}_{28-x}(\text{BDT})_{12}(\text{PPh}_3)_4$  ( $\text{MAu}_x\text{Ag}_{28-x}$  where  $\text{M} = \text{Ni, Pd, or Pt}$ ;  $x = 1-13$ ).** The trimetallic clusters were prepared through the intercluster reaction between  $\text{MAG}_{28}$  and  $\text{Au}_{25}$ .  $\text{MAG}_{28}$  was taken in DMF and mixed with DCM solution of  $\text{Au}_{25}$ . Excess DMF was added to the mixture and then characterized using absorption spectroscopy and high-resolution electrospray ionization mass spectrometry (ESI MS).

**Characterizations.** Optical absorption spectra of samples were obtained using a PerkinElmer Lambda 25 spectrometer. Electrospray ionization (ESI) mass spectra (MS) of samples were measured using a Waters Synapt G2-Si high-resolution mass spectrometer. X-ray photoelectron spectra of samples were obtained using an Omicron ESCA Probe spectrometer with polychromatic Al  $K\alpha$  X-rays ( $h\nu = 1486.7$  eV). The pass energy for survey scans was kept at 50 eV during the measurements and changed to 20 eV for specific regions. Calibration of binding energies (BE) of the core levels was done with C 1s BE set at 285 eV. Secondary electron microscopic (SEM) measurements were done using FEI Quanta 200 operating at 30 kV equipped with energy-dispersive X-ray spectroscopy (EDS).

**Computational Details.** The structure and optical properties of  $\text{NiAg}_{28}$ ,  $\text{PdAg}_{28}$ , and  $\text{Au}_{12}\text{Ag}_{17}$  were calculated using density functional theory (DFT) and time-dependent DFT (TDDFT) which were implemented in Grid-Based Projector Augmented Wave method (GPAW).<sup>59,60</sup> In order to include only the interactions of the valence electrons, the PAW setup was considered as  $\text{Ag}(4d^{10}5s^15p^6)$ ,  $\text{S}(3s^23p^4)$ ,  $\text{P}(3s^23p^3)$ ,  $\text{C}(2s^22p^2)$ , and  $\text{H}(1s^1)$  with scalar relativistic effects which were included for Ag. Initially, the reported crystal structure of  $\text{Ag}_{29}$  was taken and the other structures were built up by replacing Ag atoms with Ni, Pd, and Au atoms. The geometry of all clusters was optimized using the PBE exchange function<sup>61</sup> in real-space finite difference (FD) mode in GPAW.51 having a grid spacing of 0.2 Å, and the convergence criterion for the forces on each atom was set to 0.05 eV/Å. Further, the optical absorption spectra were calculated by time-dependent DFT (TDDFT) using the optimized structures.<sup>62</sup>

## ■ ASSOCIATED CONTENT

### ● Supporting Information

The Supporting Information is available free of charge at <https://pubs.acs.org/doi/10.1021/acs.chemmater.9b04530>.

UV–vis spectra, ESI MS, XPS, SEM/EDS, and theoretical analysis (PDF)

## ■ AUTHOR INFORMATION

### Corresponding Author

E-mail: [pradeep@iitm.ac.in](mailto:pradeep@iitm.ac.in)

### ORCID

Thalappil Pradeep: 0000-0003-3174-534X

### Notes

The authors declare no competing financial interest.

## ■ ACKNOWLEDGMENTS

We thank the Department of Science and Technology (DST) for supporting our research program. E.K. thanks IIT Madras for an institute doctoral fellowship. P.C. thanks the Council of Scientific and Industrial Research (CSIR) for a research fellowship. M.B. thanks U.G.C. for a research fellowship. G.P. thanks IITM for an Institute Postdoctoral Fellowship. W.A.D. thanks SERB-DST for the award of a National Postdoctoral fellowship. E.K. thanks Mr. Jyotirmoy Ghosh and Mr. M. P. Kannan for their help during XPS measurements.

## ■ REFERENCES

- (1) Chakraborty, I.; Pradeep, T. Atomically Precise Clusters of Noble Metals: Emerging Link between Atoms and Nanoparticles. *Chem. Rev. (Washington, DC, U. S.)* **2017**, *117* (12), 8208–8271.
- (2) Jin, R.; Zeng, C.; Zhou, M.; Chen, Y. Atomically Precise Colloidal Metal Nanoclusters and Nanoparticles: Fundamentals and Opportunities. *Chem. Rev. (Washington, DC, U. S.)* **2016**, *116* (18), 10346–10413.
- (3) Xavier, P. L.; Chaudhari, K.; Bakshi, A.; Pradeep, T. Protein-Protected Luminescent Noble Metal Quantum Clusters: An Emerging Trend in Atomic Cluster Nanoscience. *Nano Rev.* **2012**, *3* (1), 14767.
- (4) Krishnadas, K. R.; Natarajan, G.; Bakshi, A.; Ghosh, A.; Khatun, E.; Pradeep, T. Metal–Ligand Interface in the Chemical Reactions of Ligand-Protected Noble Metal Clusters. *Langmuir* **2019**, *35* (35), 11243–11254.
- (5) Higaki, T.; Li, Q.; Zhou, M.; Zhao, S.; Li, Y.; Li, S.; Jin, R. Toward the Tailoring Chemistry of Metal Nanoclusters for Enhancing Functionalities. *Acc. Chem. Res.* **2018**, *51* (11), 2764–2773.
- (6) Sakthivel, N. A.; Theivendran, S.; Ganeshranj, V.; Oliver, A. G.; Dass, A. Crystal Structure of Faradaurate-279:  $\text{Au}_{279}(\text{SPh-TBu})_{84}$  Plasmonic Nanocrystal Molecules. *J. Am. Chem. Soc.* **2017**, *139* (43), 15450–15459.
- (7) Jensen, K. M. Ø.; Juhas, P.; Tofanelli, M. A.; Heinecke, C. L.; Vaughan, G.; Ackerson, C. J.; Billinge, S. J. L. Polymorphism in Magic-Sized  $\text{Au}_{144}(\text{SR})_{60}$  Clusters. *Nat. Commun.* **2016**, *7*, 11859.
- (8) Zeng, C. Precision at the Nanoscale: On the Structure and Property Evolution of Gold Nanoclusters. *Pure Appl. Chem.* **2018**, *90* (9), 1409–1427.
- (9) Tang, Q.; Hu, G.; Fung, V.; Jiang, D. E. Insights into Interfaces, Stability, Electronic Properties, and Catalytic Activities of Atomically Precise Metal Nanoclusters from First Principles. *Acc. Chem. Res.* **2018**, *51* (11), 2793–2802.
- (10) Mathew, A.; Pradeep, T. Noble Metal Clusters: Applications in Energy, Environment, and Biology. *Part. Part. Syst. Charact.* **2014**, *31* (10), 1017–1053.
- (11) Higaki, T.; Li, Y.; Zhao, S.; Li, Q.; Li, S.; Du, X.-S.; Yang, S.; Chai, J.; Jin, R. Atomically Tailored Gold Nanoclusters for Catalytic Application. *Angew. Chem., Int. Ed.* **2019**, *58* (25), 8291–8302.
- (12) Tyo, E. C.; Vajda, S. Catalysis by Clusters with Precise Numbers of Atoms. *Nat. Nanotechnol.* **2015**, *10*, 577–588.
- (13) Li, G.; Jin, R. Atomically Precise Gold Nanoclusters as New Model Catalysts. *Acc. Chem. Res.* **2013**, *46* (8), 1749–1758.

- (14) Halawa, M. I.; Lai, J.; Xu, G. Gold Nanoclusters: Synthetic Strategies and Recent Advances in Fluorescent Sensing. *Mater. Today Nano* **2018**, *3*, 9–27.
- (15) Joshi, C. P.; Bootharaju, M. S.; Bakr, O. M. Tuning Properties in Silver Clusters. *J. Phys. Chem. Lett.* **2015**, *6* (15), 3023–3035.
- (16) Kang, X.; Zhu, M. Tailoring the Photoluminescence of Atomically Precise Nanoclusters. *Chem. Soc. Rev.* **2019**, *48* (8), 2422–2457.
- (17) Li, G.; Abroshan, H.; Liu, C.; Zhuo, S.; Li, Z.; Xie, Y.; Kim, H. J.; Rosi, N. L.; Jin, R. Tailoring the Electronic and Catalytic Properties of Au<sub>25</sub> Nanoclusters via Ligand Engineering. *ACS Nano* **2016**, *10* (8), 7998–8005.
- (18) Du, Y.; Guan, Z.-J.; Wen, Z.-R.; Lin, Y.-M.; Wang, Q.-M. Ligand-Controlled Doping Effects in Alloy Nanoclusters Au<sub>4</sub>Ag<sub>23</sub> and Au<sub>5</sub>Ag<sub>24</sub>. *Chem. - Eur. J.* **2018**, *24* (60), 16029–16035.
- (19) Kumar, B.; Niihori, Y.; Kurashige, W.; Negishi, Y. Controlled Thiolate-Protected Gold and Alloy Clusters. In *Descriptive Inorganic Chemistry Researches of Metal Compounds*; InTech, 2017; p 13.
- (20) Mohanty, J. S.; Xavier, P. L.; Chaudhari, K.; Bootharaju, M. S.; Goswami, N.; Pal, S. K.; Pradeep, T. Luminescent, Bimetallic AuAg Alloy Quantum Clusters in Protein Templates. *Nanoscale* **2012**, *4* (14), 4255–4262.
- (21) Ferrando, R.; Jellinek, J.; Johnston, R. L. Nanoalloys: From Theory to Applications of Alloy Clusters and Nanoparticles. *Chem. Rev.* **2008**, *108* (3), 845–910.
- (22) Jin, R.; Zhao, S.; Xing, Y.; Jin, R. All-Thiolate-Protected Silver and Silver-Rich Alloy Nanoclusters with Atomic Precision: Stable Sizes, Structural Characterization and Optical Properties. *CrystEngComm* **2016**, *18* (22), 3996–4005.
- (23) Kang, X.; Abroshan, H.; Wang, S.; Zhu, M. Free Valence Electron Centralization Strategy for Preparing Ultrastable Nanoclusters and Their Catalytic Application. *Inorg. Chem.* **2019**, *58* (16), 11000–11009.
- (24) Kang, X.; Wei, X.; Jin, S.; Yuan, Q.; Luan, X.; Pei, Y.; Wang, S.; Zhu, M.; Jin, R. Rational Construction of a Library of M<sub>29</sub> Nanoclusters from Monometallic to Tetrametallic. *Proc. Natl. Acad. Sci. U. S. A.* **2019**, *116* (38), 18834–18840.
- (25) Wang, S.; Li, Q.; Kang, X.; Zhu, M. Customizing the Structure, Composition, and Properties of Alloy Nanoclusters by Metal Exchange. *Acc. Chem. Res.* **2018**, *51* (11), 2784–2792.
- (26) Liu, X.; Yuan, J.; Yao, C.; Chen, J.; Li, L.; Bao, X.; Yang, J.; Wu, Z. Crystal and Solution Photoluminescence of MAg<sub>24</sub>(SR)<sub>18</sub> (M = Ag/Pd/Pt/Au) Nanoclusters and Some Implications for the Photoluminescence Mechanisms. *J. Phys. Chem. C* **2017**, *121* (25), 13848–13853.
- (27) Yan, J.; Su, H.; Yang, H.; Hu, C.; Malola, S.; Lin, S.; Teo, B. K.; Häkkinen, H.; Zheng, N. Asymmetric Synthesis of Chiral Bimetallic [Ag<sub>28</sub>Cu<sub>12</sub>(SR)<sub>24</sub>]<sup>4+</sup> Nanoclusters via Ion Pairing. *J. Am. Chem. Soc.* **2016**, *138* (39), 12751–12754.
- (28) Fields-Zinna, C. A.; Crowe, M. C.; Dass, A.; Weaver, J. E. F.; Murray, R. W. Mass Spectrometry of Small Bimetal Monolayer-Protected Clusters. *Langmuir* **2009**, *25* (13), 7704–7710.
- (29) Tofanelli, M. A.; Ni, T. W.; Phillips, B. D.; Ackerson, C. J. Crystal Structure of the PdAu<sub>24</sub>(SR)<sub>18</sub><sup>0</sup> Superatom. *Inorg. Chem.* **2016**, *55* (3), 999–1001.
- (30) Soldan, G.; Aljuhani, M. A.; Bootharaju, M. S.; AbdulHalim, L. G.; Parida, M. R.; Emwas, A.-H.; Mohammed, O. F.; Bakr, O. M. Gold Doping of Silver Nanoclusters: A 26-Fold Enhancement in the Luminescence Quantum Yield. *Angew. Chem., Int. Ed.* **2016**, *55* (19), 5749–5753.
- (31) Wickramasinghe, S.; Atnagulov, A.; Yoon, B.; Barnett, R. N.; Griffith, W. P.; Landman, U.; Bigioni, T. P. M<sub>3</sub>Ag<sub>17</sub>(SPh)<sub>12</sub> Nanoparticles and Their Structure Prediction. *J. Am. Chem. Soc.* **2015**, *137* (36), 11550–11553.
- (32) Conn, B. E.; Atnagulov, A.; Yoon, B.; Barnett, R. N.; Landman, U.; Bigioni, T. P. Confirmation of a de Novo Structure Prediction for an Atomically Precise Monolayer-Coated Silver Nanoparticle. *Sci. Adv.* **2016**, *2* (11), No. e1601609.
- (33) Kwak, K.; Lee, D. Electrochemistry of Atomically Precise Metal Nanoclusters. *Acc. Chem. Res.* **2019**, *52* (1), 12–22.
- (34) Xie, S.; Tsunoyama, H.; Kurashige, W.; Negishi, Y.; Tsukuda, T. Enhancement in Aerobic Alcohol Oxidation Catalysis of Au<sub>25</sub> Clusters by Single Pd Atom Doping. *ACS Catal.* **2012**, *2* (7), 1519–1523.
- (35) Hossain, S.; Niihori, Y.; Nair, L. V.; Kumar, B.; Kurashige, W.; Negishi, Y. Alloy Clusters: Precise Synthesis and Mixing Effects. *Acc. Chem. Res.* **2018**, *51* (12), 3114–3124.
- (36) Ghosh, A.; Mohammed, O. F.; Bakr, O. M. Atomic-Level Doping of Metal Clusters. *Acc. Chem. Res.* **2018**, *51* (12), 3094–3103.
- (37) Gan, Z.; Xia, N.; Wu, Z. Discovery, Mechanism, and Application of Antigalvanic Reaction. *Acc. Chem. Res.* **2018**, *51* (11), 2774–2783.
- (38) Yang, S.; Chai, J.; Song, Y.; Fan, J.; Chen, T.; Wang, S.; Yu, H.; Li, X.; Zhu, M. In Situ Two-Phase Ligand Exchange: A New Method for the Synthesis of Alloy Nanoclusters with Precise Atomic Structures. *J. Am. Chem. Soc.* **2017**, *139* (16), 5668–5671.
- (39) Wiley, B.; Sun, Y.; Chen, J.; Cang, H.; Li, Z.-Y.; Li, X.; Xia, Y. Shape-Controlled Synthesis of Silver and Gold Nanostructures. *MRS Bull.* **2005**, *30* (5), 356–361.
- (40) Zhao, S.; Austin, N.; Li, M.; Song, Y.; House, S. D.; Bernhard, S.; Yang, J. C.; Mpourmpakis, G.; Jin, R. Influence of Atomic-Level Morphology on Catalysis: The Case of Sphere and Rod-Like Gold Nanoclusters for CO<sub>2</sub> Electroreduction. *ACS Catal.* **2018**, *8* (6), 4996–5001.
- (41) Krishnadas, K. R.; Baksi, A.; Ghosh, A.; Natarajan, G.; Som, A.; Pradeep, T. Interparticle Reactions: An Emerging Direction in Nanomaterials Chemistry. *Acc. Chem. Res.* **2017**, *50* (8), 1988–1996.
- (42) Krishnadas, K. R.; Ghosh, A.; Baksi, A.; Chakraborty, I.; Natarajan, G.; Pradeep, T. Intercluster Reactions between Au<sub>25</sub>(SR)<sub>18</sub> and Ag<sub>44</sub>(SR)<sub>30</sub>. *J. Am. Chem. Soc.* **2016**, *138* (1), 140–148.
- (43) Krishnadas, K. R.; Baksi, A.; Ghosh, A.; Natarajan, G.; Pradeep, T. Structure-Conserving Spontaneous Transformations between Nanoparticles. *Nat. Commun.* **2016**, *7* (1), 13447.
- (44) Kazan, R.; Müller, U.; Bürgi, T. Doping of Thiolate Protected Gold Clusters through Reaction with Metal Surfaces. *Nanoscale* **2019**, *11* (6), 2938–2945.
- (45) Ghosh, A.; Ghosh, D.; Khatun, E.; Chakraborty, P.; Pradeep, T. Unusual Reactivity of Dithiol Protected Clusters in Comparison to Monothiol Protected Clusters: Studies Using Ag<sub>51</sub>(BDT)<sub>19</sub>(TPP)<sub>3</sub> and Ag<sub>29</sub>(BDT)<sub>12</sub>(TPP)<sub>4</sub>. *Nanoscale* **2017**, *9* (3), 1068–1077.
- (46) Yan, J.; Su, H.; Yang, H.; Malola, S.; Lin, S.; Häkkinen, H.; Zheng, N. Total Structure and Electronic Structure Analysis of Doped Thiolated Silver [MAg<sub>24</sub>(SR)<sub>18</sub>]<sup>2-</sup> (M = Pd, Pt) Clusters. *J. Am. Chem. Soc.* **2015**, *137* (37), 11880–11883.
- (47) AbdulHalim, L. G.; Bootharaju, M. S.; Tang, Q.; Del Gobbo, S.; AbdulHalim, R. G.; Eddaoudi, M.; Jiang, D.; Bakr, O. M. Ag<sub>29</sub>(BDT)<sub>12</sub>(TPP)<sub>4</sub>: A Tetravalent Nanocluster. *J. Am. Chem. Soc.* **2015**, *137* (37), 11970–11975.
- (48) Bootharaju, M. S.; Kozlov, S. M.; Cao, Z.; Shkurenko, A.; El-Zohry, A. M.; Mohammed, O. F.; Eddaoudi, M.; Bakr, O. M.; Cavallo, L.; Basset, J.-M. Tailoring the Crystal Structure of Nanoclusters Unveiled High Photoluminescence via Ion Pairing. *Chem. Mater.* **2018**, *30* (8), 2719–2725.
- (49) Alkan, F.; Pandeya, P.; Aikens, C. M. Understanding the Effect of Doping on Energetics and Electronic Structure for Au<sub>25</sub>, Ag<sub>25</sub>, and Au<sub>38</sub> Clusters. *J. Phys. Chem. C* **2019**, *123* (14), 9516–9527.
- (50) Chen, T.; Yang, S.; Chai, J.; Song, Y.; Fan, J.; Rao, B.; Sheng, H.; Yu, H.; Zhu, M.; et al. Crystallization-Induced Emission Enhancement: A Novel Fluorescent Au-Ag Bimetallic Nanocluster with Precise Atomic Structure. *Sci. Adv.* **2017**, *3* (8), No. e1700956.
- (51) Liu, Y.; Chai, X.; Cai, X.; Chen, M.; Jin, R.; Ding, W.; Zhu, Y. Central Doping of a Foreign Atom into the Silver Cluster for Catalytic Conversion of CO<sub>2</sub> toward C–C Bond Formation. *Angew. Chem., Int. Ed.* **2018**, *57* (31), 9775–9779.
- (52) Natarajan, G.; Mathew, A.; Negishi, Y.; Whetten, R. L.; Pradeep, T. A Unified Framework for Understanding the Structure

and Modifications of Atomically Precise Monolayer Protected Gold Clusters. *J. Phys. Chem. C* **2015**, *119* (49), 27768–27785.

(53) Zheng, K.; Fung, V.; Yuan, X.; Jiang, D.-E.; Xie, J. Real-Time Monitoring of the Dynamic Intra-Cluster Diffusion of Single Gold Atoms into Silver Nanoclusters. *J. Am. Chem. Soc.* **2019**, *141*, 18977.

(54) Chakraborty, P.; Nag, A.; Natarajan, G.; Bandyopadhyay, N.; Paramasivam, G.; Panwar, M. K.; Chakrabarti, J.; Pradeep, T. Rapid Isotopic Exchange in Nanoparticles. *Sci. Adv.* **2019**, *5* (1), eaau7555.

(55) Kauffman, D. R.; Alfonso, D.; Matranga, C.; Qian, H.; Jin, R. A Quantum Alloy: The Ligand-Protected  $\text{Au}_{25-x}\text{Ag}_x(\text{SR})_{18}$  Cluster. *J. Phys. Chem. C* **2013**, *117* (15), 7914–7923.

(56) Kumara, C.; Aikens, C. M.; Dass, A. X-Ray Crystal Structure and Theoretical Analysis of  $\text{Au}_{25-x}\text{Ag}_x(\text{SCH}_2\text{CH}_2\text{Ph})_{18}^-$  Alloy. *J. Phys. Chem. Lett.* **2014**, *5* (3), 461–466.

(57) Bhat, S.; Baksi, A.; Mudedla, S. K.; Natarajan, G.; Subramanian, V.; Pradeep, T.  $\text{Au}_{22}\text{Ir}_3(\text{PET})_{18}$ : An Unusual Alloy Cluster through Intercluster Reaction. *J. Phys. Chem. Lett.* **2017**, *8* (13), 2787–2793.

(58) Joshi, C. P.; Bootharaju, M. S.; Alhilaly, M. J.; Bakr, O. M.  $[\text{Ag}_{25}(\text{SR})_{18}]^-$ : The “Golden” Silver Nanoparticle Silver Nanoparticle. *J. Am. Chem. Soc.* **2015**, *137* (36), 11578–11581.

(59) Enkovaara, J.; Rostgaard, C.; Mortensen, J. J.; Chen, J.; Dulak, M.; Ferrighi, L.; Gavnholt, J.; Glinesvad, C.; Haikola, V.; Hansen, H. A.; et al. Electronic Structure Calculations with GPAW: A Real-Space Implementation of the Projector Augmented-Wave Method. *J. Phys.: Condens. Matter* **2010**, *22* (25), 253202.

(60) Mortensen, J. J.; Hansen, L. B.; Jacobsen, K. W. Real-Space Grid Implementation of the Projector Augmented Wave Method. *Phys. Rev. B: Condens. Matter Mater. Phys.* **2005**, *71* (3), 035109.

(61) Perdew, J. P.; Burke, K.; Ernzerhof, M. Generalized Gradient Approximation Made Simple. *Phys. Rev. Lett.* **1996**, *77* (18), 3865–3868.

(62) Frisch, M. J.; Trucks, G. W.; Schlegel, H. B.; Scuseria, G. E.; Robb, M. A.; Cheeseman, J. R.; Scalmani, G.; Barone, V.; Mennucci, B.; Petersson, G. A.; et al. *Gaussian 09, revision B.01*; Gaussian, Inc.: Wallingford, CT, 2009.

**Supporting information for:**

**Intercluster Reactions Resulting in Silver-Rich Trimetallic  
Nanoclusters**

Esma Khatun, Papri Chakraborty, Betsy Rachel Jacob, Ganesan Paramasivam, Mohammad  
Bodiuzzaman, Wakeel Ahmed Dar and Thalappil Pradeep\*

*Department of Chemistry, DST Unit of Nanoscience (DST UNS) and Thematic Unit of  
Excellence (TUE)*

*Indian Institute of Technology Madras*

*Chennai, 600 036, India*

E-mail: [pradeep@iitm.ac.in](mailto:pradeep@iitm.ac.in)

**Table of Contents**

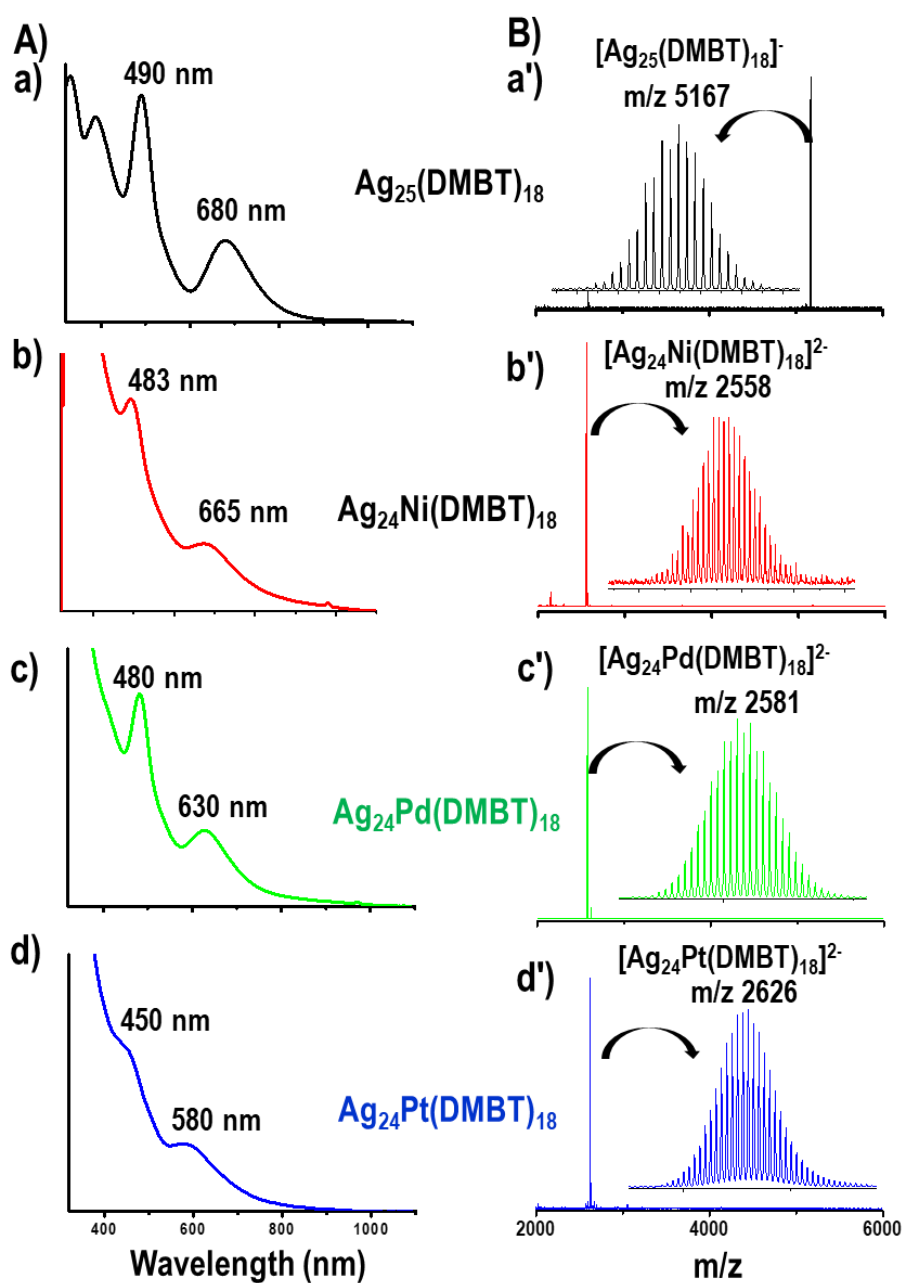
List of figures	Description	Page number
S1	UV-vis absorption spectra and ESI MS of Ag <sub>25</sub> and MAg <sub>24</sub> where 'M' is Ni, Pd or Pt	3-4
S2	XPS spectrum of NiAg <sub>28</sub> and time-dependent absorption spectra of NiAg <sub>24</sub> , NiAg <sub>28</sub> and Ag <sub>29</sub>	4-5
S3	ESI MS of PdAg <sub>28</sub> measured under low voltage and low gas pressure conditions	5
S4	XPS and SEM/EDS spectra of PdAg <sub>28</sub>	6
S5	UV-vis absorption spectrum and ESI MS of PtAg <sub>28</sub>	7

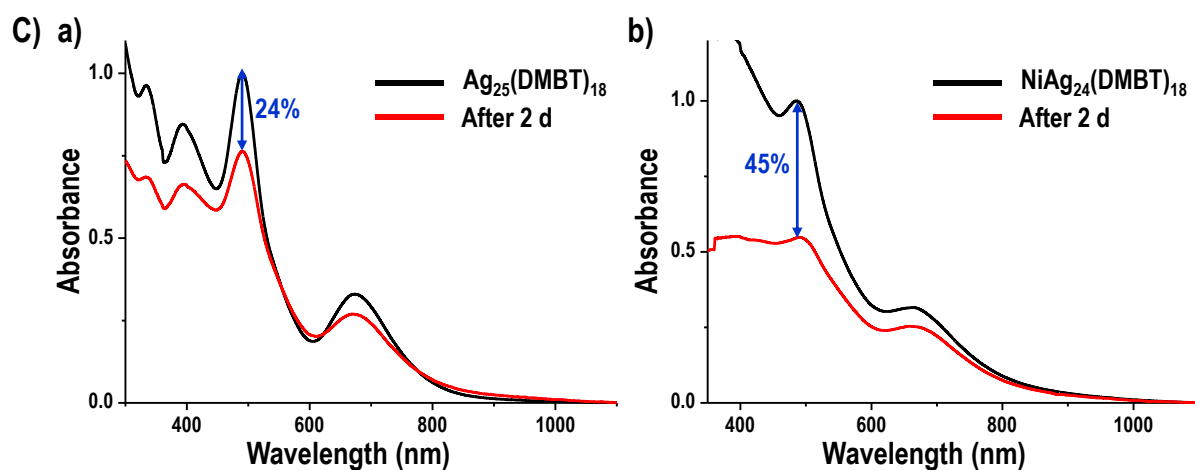
S6	The collision-induced dissociation mass spectra of $[\text{NiAg}_{28}(\text{BDT})_{12}]^{4+}$ and $[\text{PdAg}_{28}(\text{BDT})_{12}]^{4+}$	8
S7	Theoretical structures of various isomers of $\text{NiAg}_{28}$ and $\text{PdAg}_{28}$	9-10
S8	Concentration-dependent ESI MS of the reaction between $\text{PdAg}_{28}$ and $\text{Au}_{25}$	11
S9	Theoretical and experimental isotopic distributions of $\text{PdAu}_{12}\text{Ag}_{16}$	11
S10	Time-dependent UV-vis absorption spectra of intercluster reaction between $\text{PdAg}_{28}$ and $\text{Au}_{25}$	12
S11	Theoretical and experimental isotopic distributions of $\text{PtAu}_{12}\text{Ag}_{16}$	12
S12	Time-dependent ESI MS of intercluster reaction between $\text{PtAg}_{28}$ and $\text{Au}_{25}$ showing the reaction at $\text{Au}_{25}$	13
S13	Time-dependent UV-vis absorption spectra of intercluster reaction between $\text{PtAg}_{28}$ and $\text{Au}_{25}$	13
S14	Time-dependent ESI MS of $\text{NiAg}_{28}$ which show the formation of trimetallic $\text{NiAu}_x\text{Ag}_{28-x}$	14
S15	Experimental and theoretical isotopic patterns of $\text{NiAu}_{12}\text{Ag}_{16}$	14
S16	Concentration-dependent ESI MS of the reaction between $\text{Ag}_{29}$ and $\text{Au}_{25}$	15
S17	Time-dependent absorption spectra of the reaction between $\text{Ag}_{29}$ and $\text{Au}_{25}$ at room temperature	15
S18	Experimental and theoretical isotopic patterns of $\text{Au}_{12}\text{Ag}_{17}$	16
S19	Time-dependent ESI MS of the reaction between $\text{Ag}_{29}$ and $\text{Au}_{25}$ at $\text{Au}_{25}$ side (higher temperature)	16
S20	Time-dependent UV-vis absorption spectra of the intercluster reaction between $\text{Ag}_{29}$ and $\text{Au}_{25}$	17



S21	Three different DFT optimized geometric isomers of $\text{Au}_{12}\text{Ag}_{17}$ and their energies	17-18
-----	--	-------

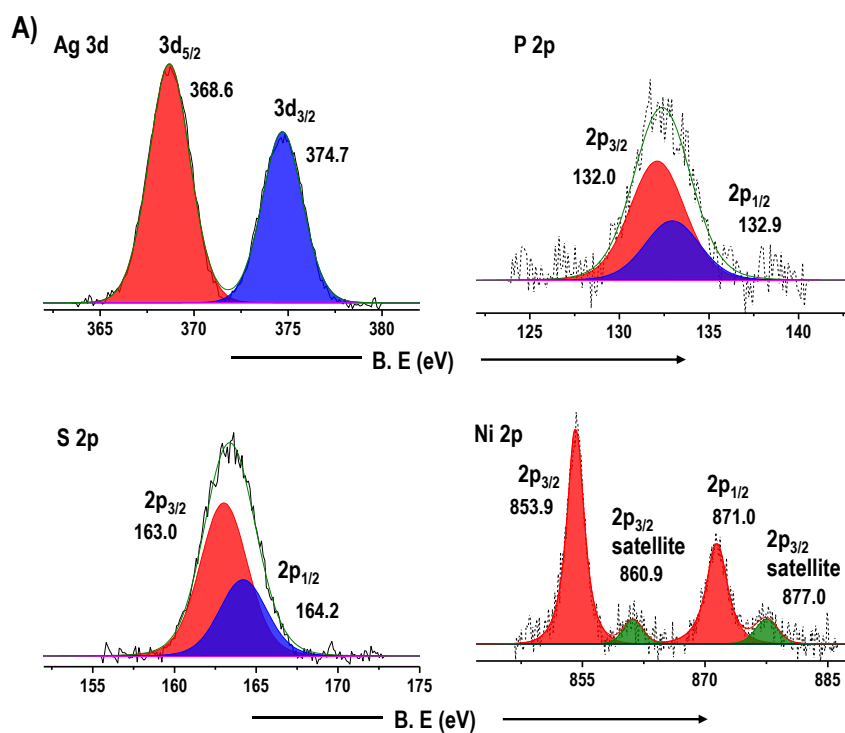
### Supporting information 1:

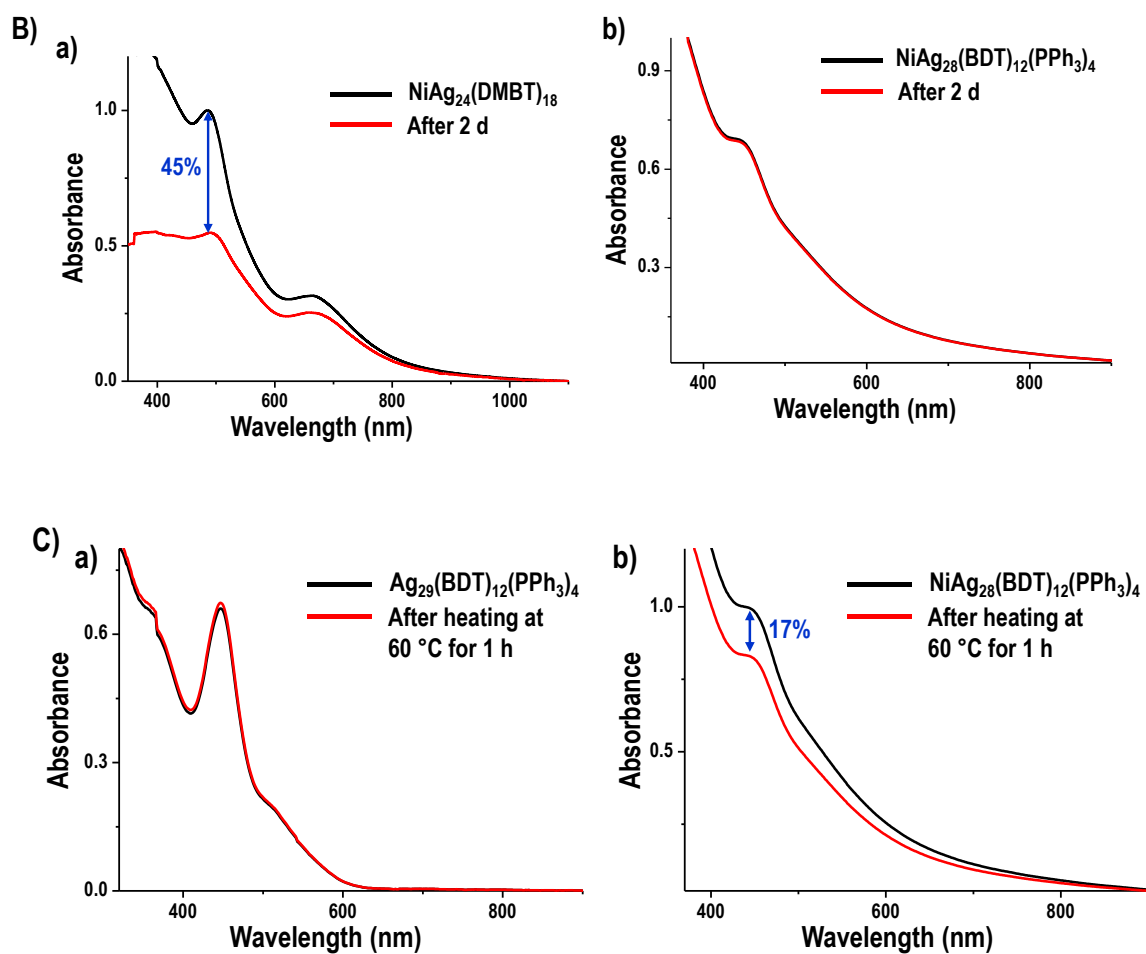




**Figure S1.** (A) UV-vis absorption spectra and (B) ESI MS of  $\text{Ag}_{25}$  (panel a/a') and  $\text{MAg}_{24}$  where 'M' is Ni, Pd and Pt (panel b/b', c/c' and d/d'). Upon doping of Ni, Pd and Pt in  $\text{Ag}_{25}$ , absorption features show gradual blue-shifts. (C) Time-dependent absorption spectra of (a)  $\text{Ag}_{25}$  and (b)  $\text{NiAg}_{24}$  which were kept at room temperature.

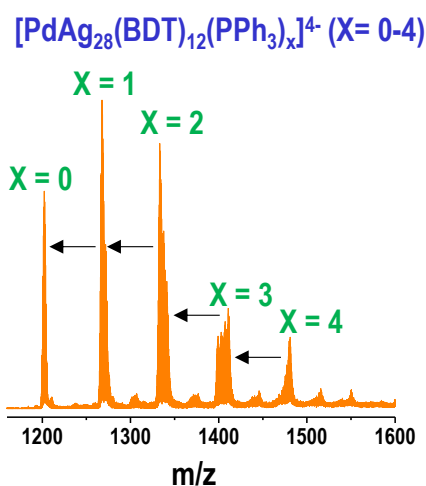
## Supporting information 2:





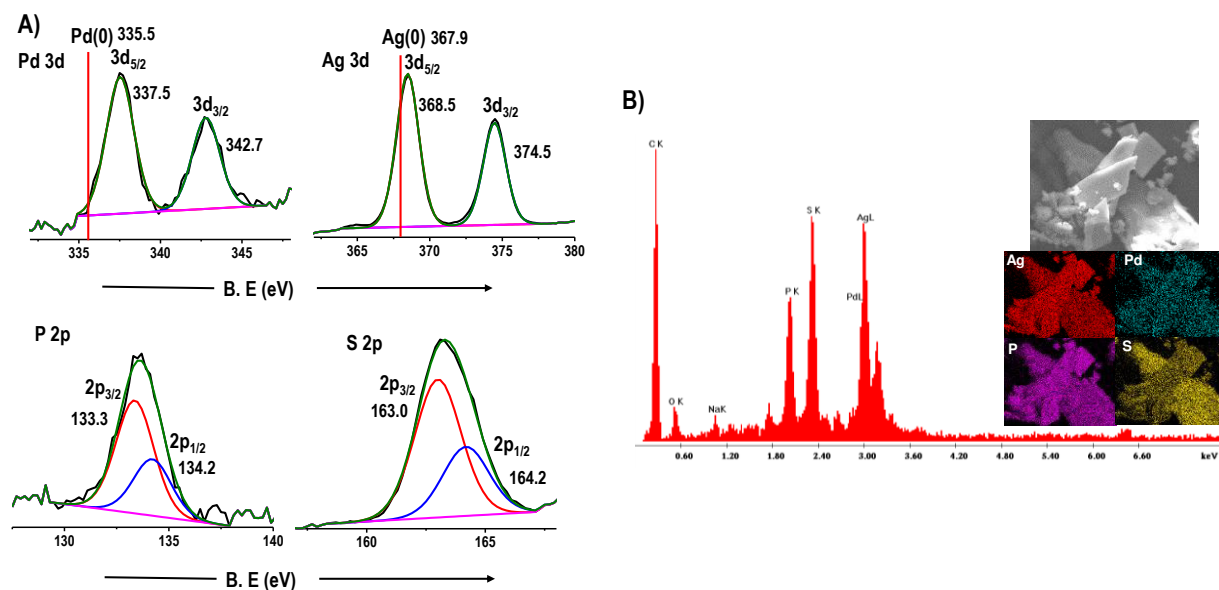
**Figure S2.** (A) XPS spectrum of NiAg<sub>28</sub> shows the presence of Ni 2p, Ag 3d, P 2p and S 2p. (B) Time-dependent absorption spectra of (a) NiAg<sub>24</sub> and (b) NiAg<sub>28</sub> at room temperature. (C) Time-dependent absorption spectra of (a) Ag<sub>29</sub> and (b) NiAg<sub>28</sub> at 60°C temperature.

### Supporting information 3:



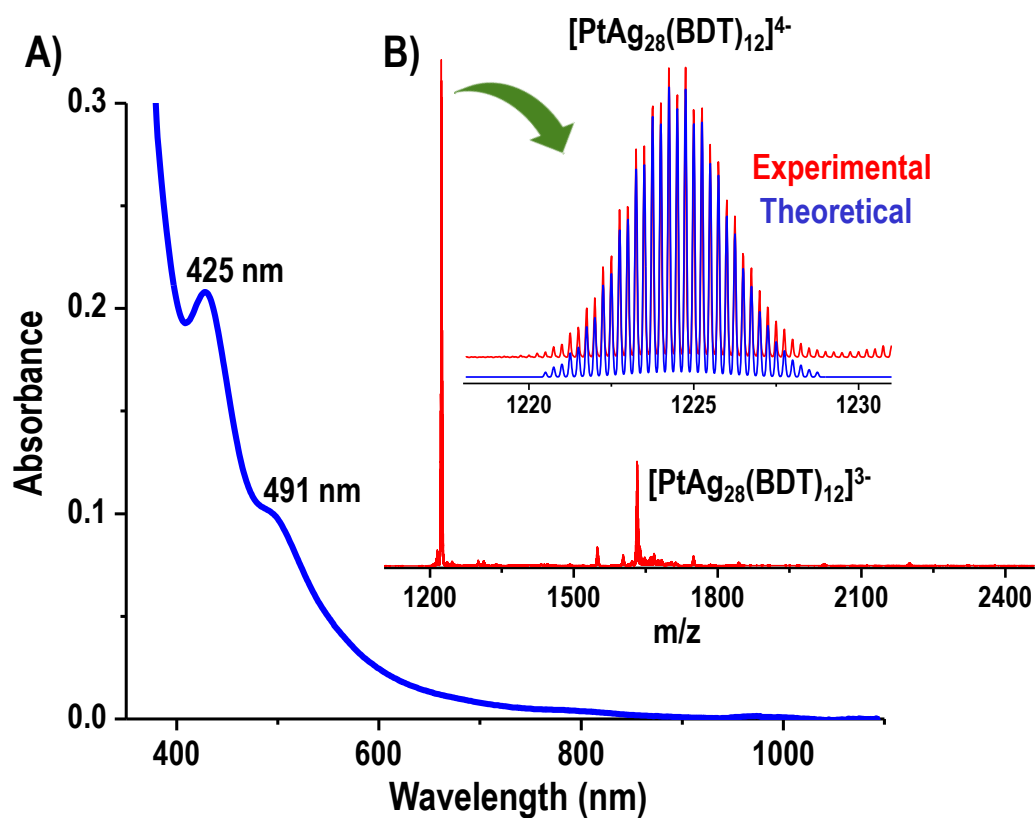
**Figure S3.** ESI MS of PdAg<sub>28</sub> measured under low voltage and low gas pressure conditions shows the presence of four PPh<sub>3</sub> ligands.

#### Supporting information 4:



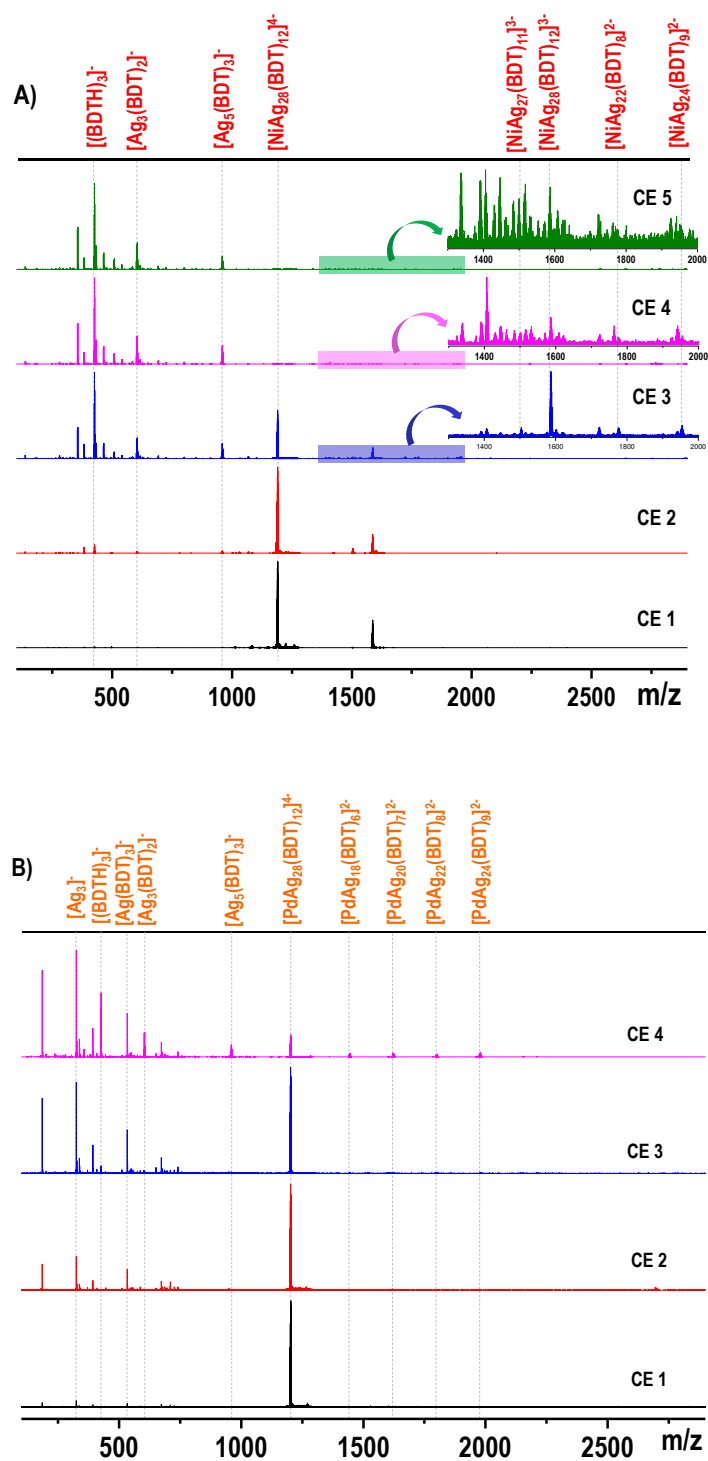
**Figure S4.** (A) XPS spectrum of PdAg<sub>28</sub> shows the presence of Pd, Ag, P and S. Pd 3d<sub>5/2</sub> peak arises at 337.5 eV which is higher than that of Pd (0) (335.5 eV) and Ag 3d<sub>5/2</sub> peak arises at 368.5 eV which is also at a higher value than that of Ag (0) (367.9 eV) which manifest a partial charge transfer from Pd to Ag. (B) SEM image of PdAg<sub>28</sub> and EDS mapping of C, P, S, Ag and Pd.

Supporting information 5:



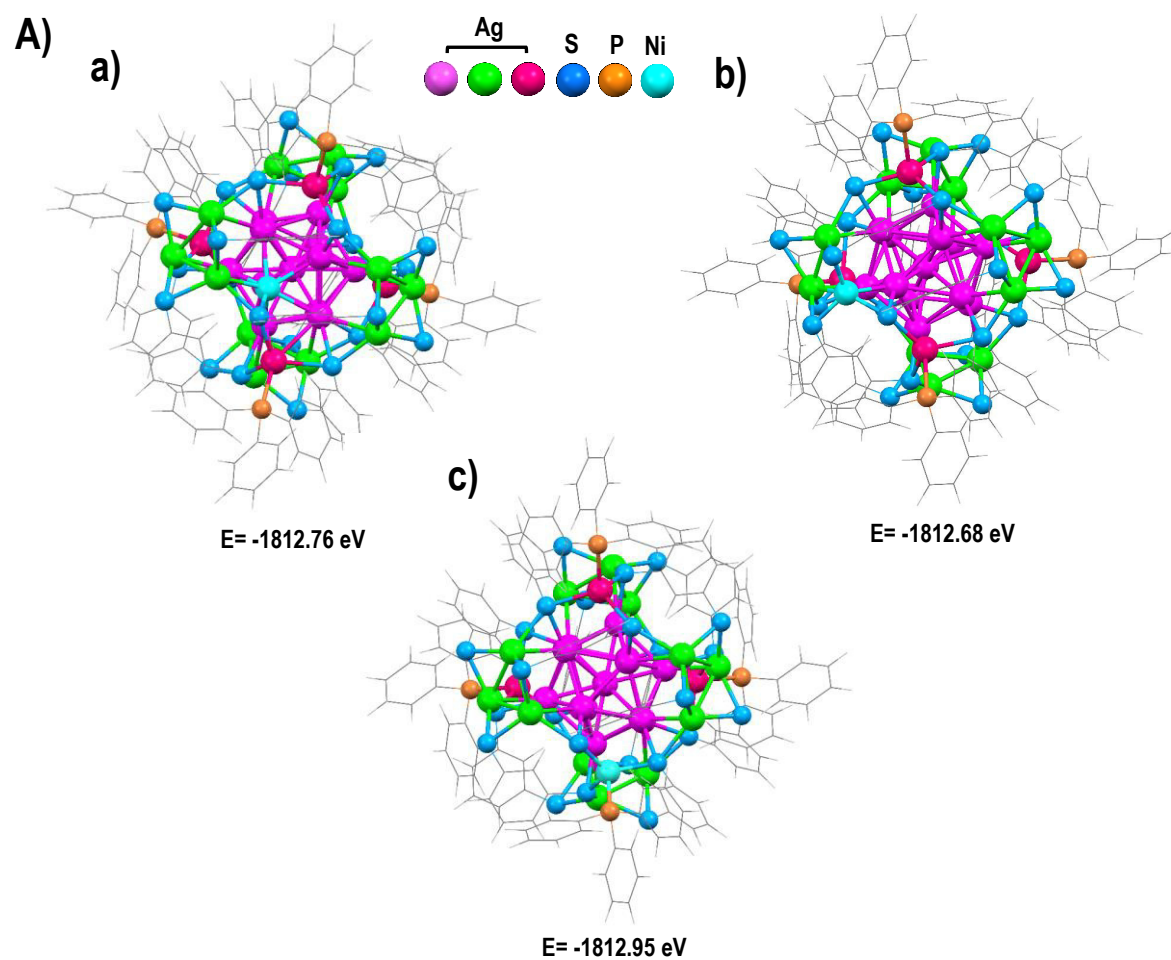
**Figure S5.** (A) UV-vis absorption spectrum of  $\text{PtAg}_{28}$  which possesses two prominent features at 425 and 491 nm. The absorption peaks are 22 nm blue-shifted from that of  $\text{Ag}_{29}$ . (B) ESI MS of  $\text{PtAg}_{28}$  exhibits two intense peaks at m/z 1224 and 1632 which correspond to  $[\text{PtAg}_{28}(\text{BDT})_{12}]^{4-}$  and  $[\text{PtAg}_{28}(\text{BDT})_{12}]^{3-}$ , respectively. Theoretical and experimental isotopic distributions of  $[\text{PtAg}_{28}(\text{BDT})_{12}]^{4-}$  are shown in the inset of (B) which are well fitted.

## Supporting information 6:



**Figure S6.** The collision-induced dissociation mass spectra of (A)  $[\text{NiAg}_{28}(\text{BDT})_{12}]^{4-}$  (m/z 1190) and (B)  $[\text{PdAg}_{28}(\text{BDT})_{12}]^{4-}$  (m/z 1202).

Supporting information 7:



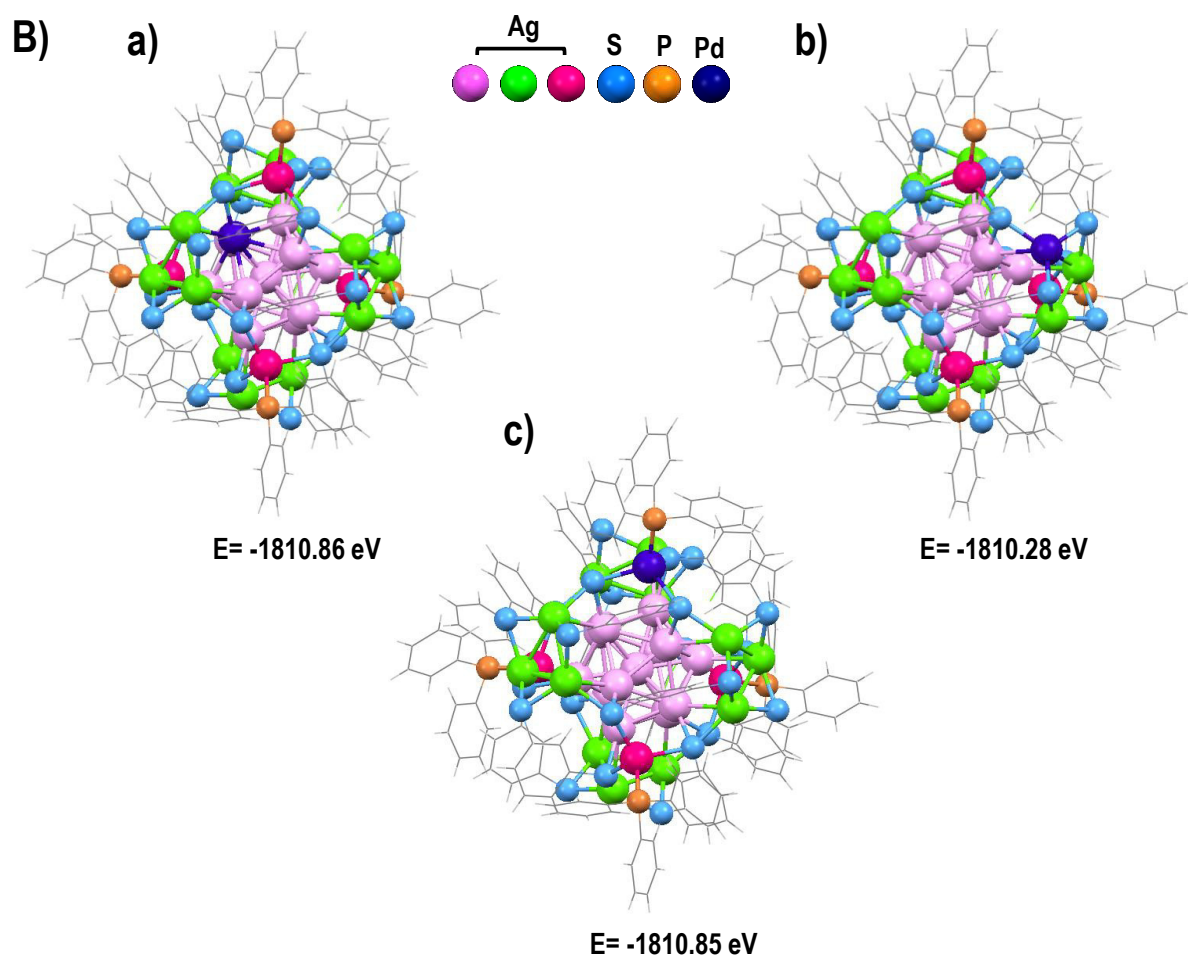


**Figure S7.** Theoretical structures of different isomers of (A) NiAg<sub>28</sub> and (B) PdAg<sub>28</sub>. Mainly four isomers of NiAg<sub>28</sub> and PdAg<sub>28</sub> were observed and three of them are shown here; (a) Ni/Pd atom is doped in the icosahedral surface, (b) Ni/Pd atom is doped in crown staples and (c) Ni/Pd atom replaces Ag atom which is bonded to PPh<sub>3</sub>.



## Supporting information 8:

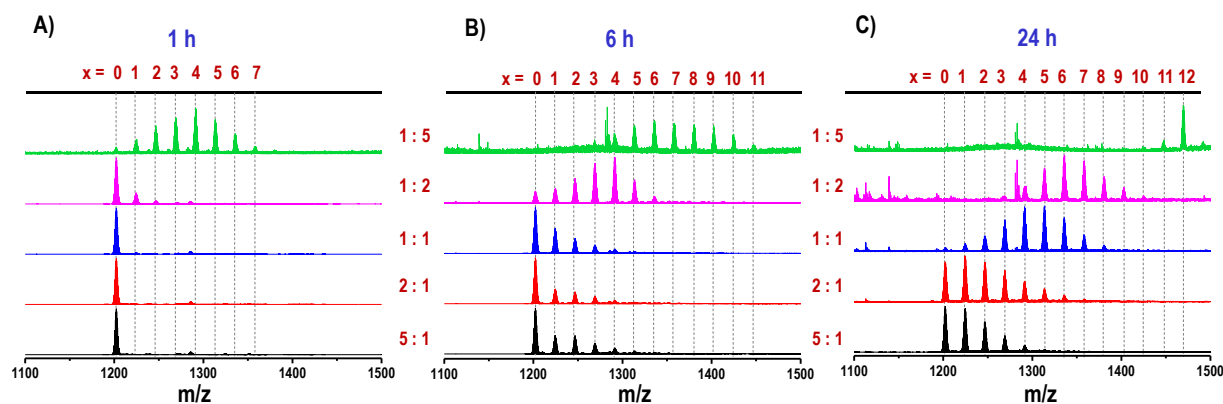


**Figure S8.** Concentration-dependent ESI MS of the reaction between  $\text{PdAg}_{28}$  and  $\text{Au}_{25}$  using 4:1, 2:1, 1:1, 1:2 and 1:5 molar ratios at three different time intervals, (A) 1 h, (B) 6 h and (C) 24 h.

## Supporting information 9:

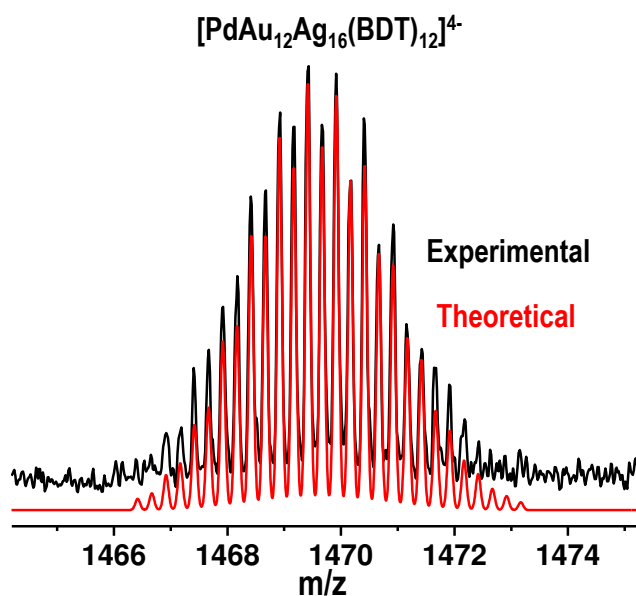


**Figure S9.** The experimental isotopic distribution (black trace) of  $\text{PdAu}_{12}\text{Ag}_{16}$  which matches exactly with the theoretical one (red trace).

**Supporting information 10:**

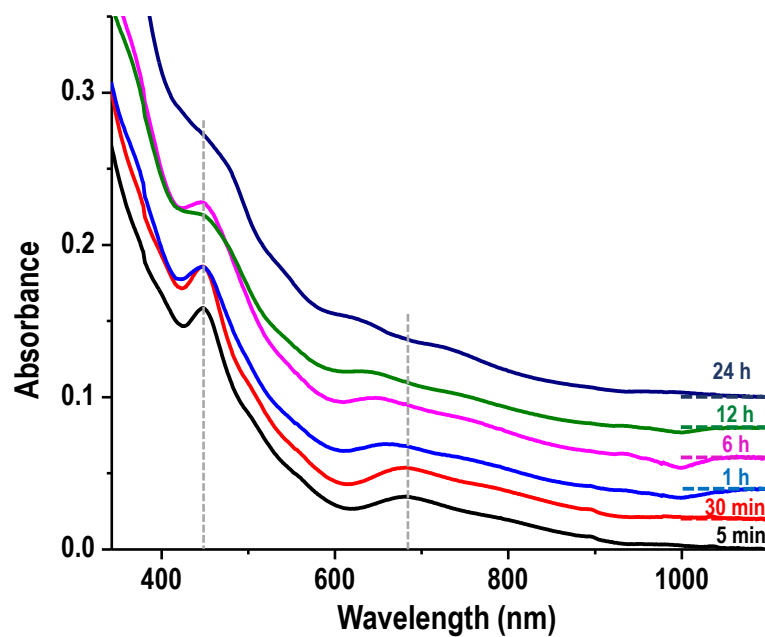


**Figure S10.** Time-dependent UV-vis absorption spectra of intercluster reaction between PdAg<sub>28</sub> and Au<sub>25</sub> using a 1:5 molar ratio.

**Supporting information 11:**

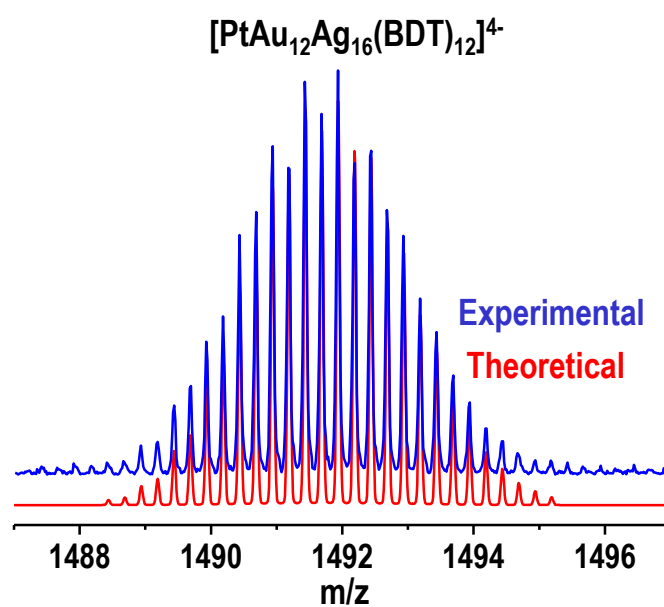


**Figure S11.** The experimental isotopic distribution (blue trace) of PtAu<sub>12</sub>Ag<sub>16</sub> which matches exactly with the theoretical one (red trace).

### Supporting information 12:

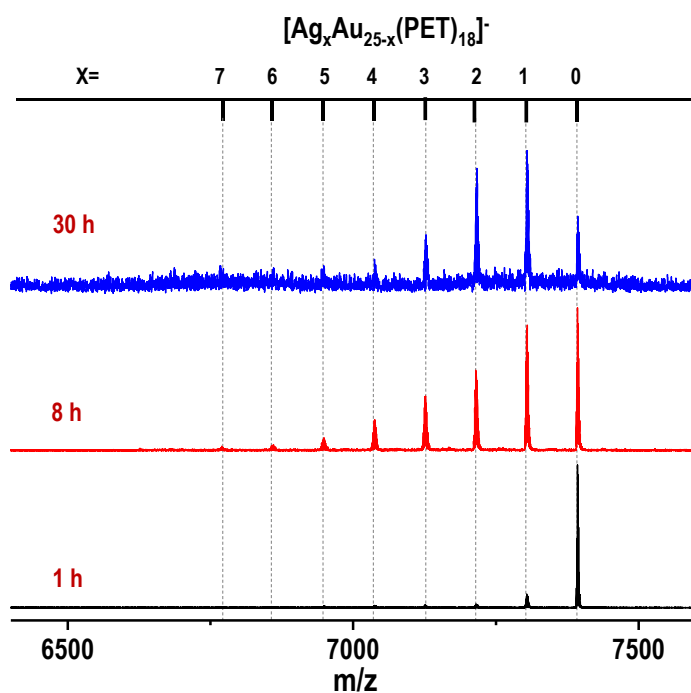


**Figure 12.** Time-dependent ESI MS of intercluster reaction between PtAg<sub>28</sub> and Au<sub>25</sub> (1:5 molar ratio) showing the reaction at Au<sub>25</sub> side which show formation of Ag<sub>x</sub>Au<sub>25-x</sub> (x= 0-7).

### Supporting information 13:

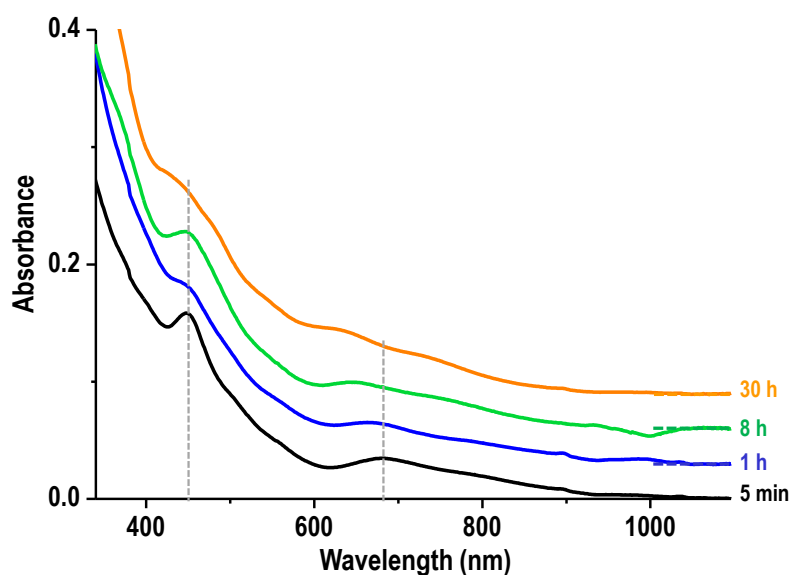


**Figure S13.** Time-dependent UV-vis absorption spectra of intercluster reaction between PtAg<sub>28</sub> and Au<sub>25</sub> using a 1:5 molar ratio.

#### Supporting information 14:

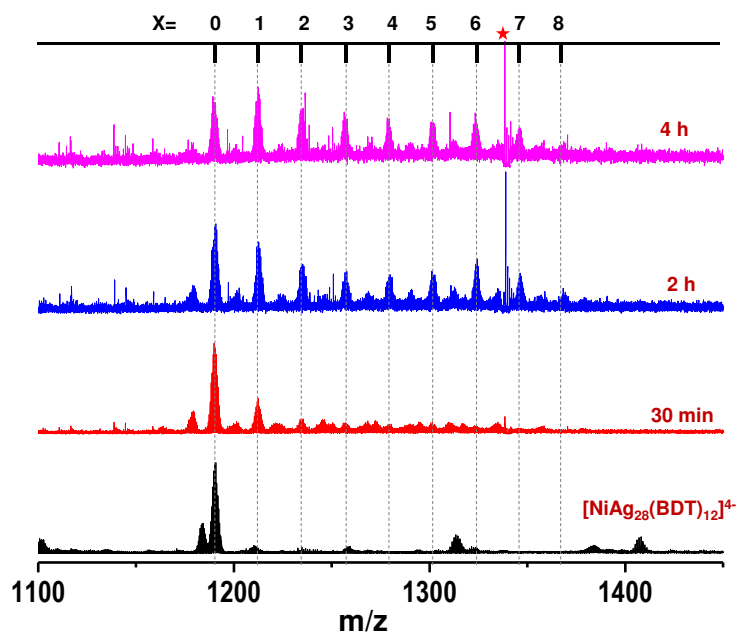


**Figure S14.** Time-dependent ESI MS of intercluster reaction between  $\text{NiAg}_{28}$  and  $\text{Au}_{25}$  using a 1:5 molar ratio which show the formation of trimetallic  $\text{NiAu}_x\text{Ag}_{28-x}$ .

#### Supporting information 15:

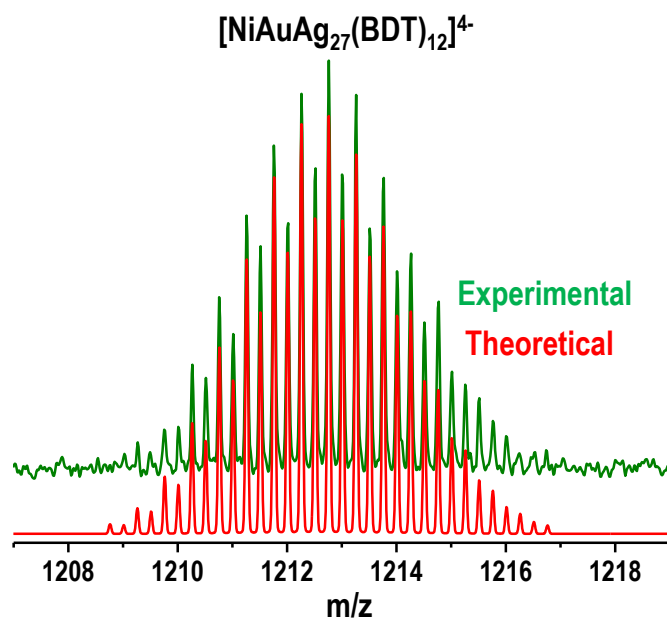


**Figure S15.** Experimental and theoretical isotopic patterns (green trace) of  $\text{NiAuAg}_{27}$  (red trace) fit well with each other.

### Supporting information 16:

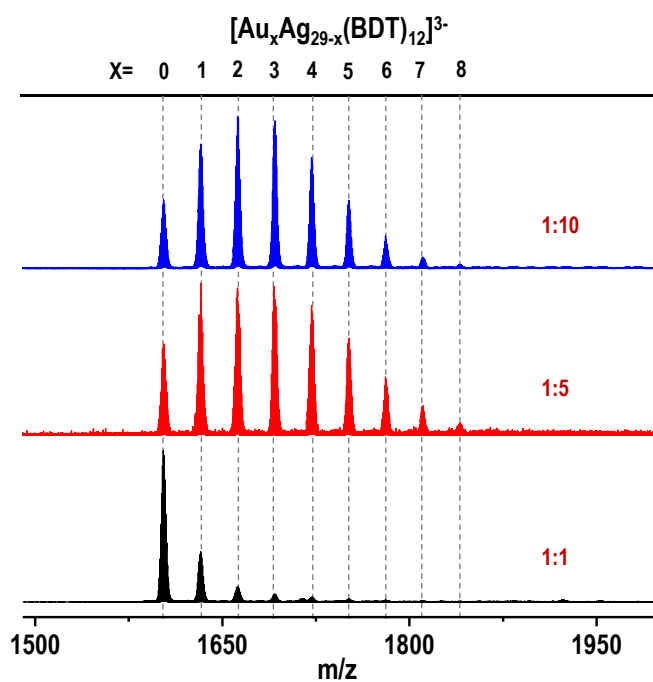


**Figure S16.** Concentration-dependent ESI MS of the reaction between  $\text{Ag}_{29}$  and  $\text{Au}_{25}$  using 1:1, 1:5 and 1:10 molar ratios at 6h which lead to the formation of  $\text{Au}_x\text{Ag}_{29-x}$  ( $x = 1-8$ ).

### Supporting information 17:

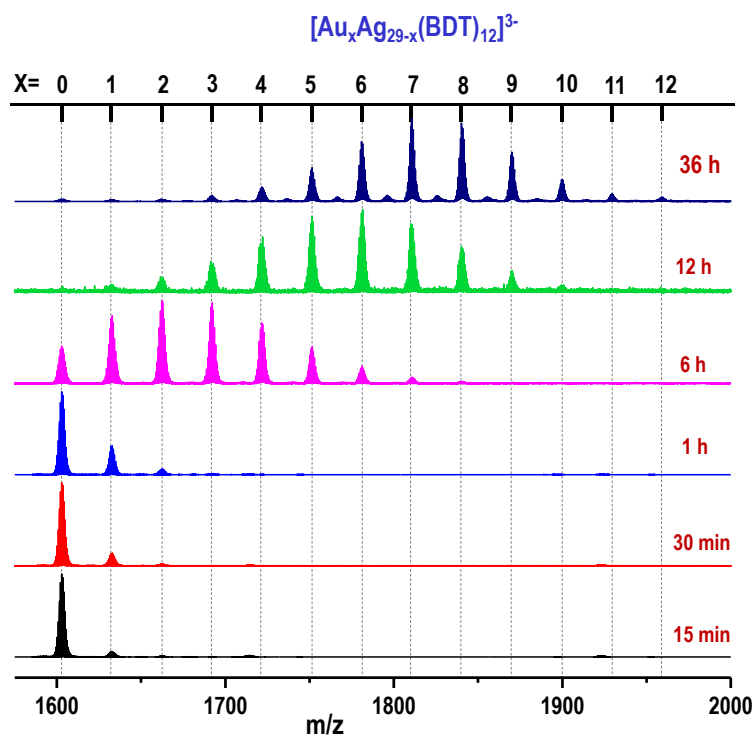


**Figure S17.** Time-dependent absorption spectra of the reaction between Ag<sub>29</sub> and Au<sub>25</sub> (1:5 ratio) at room temperature resulting in the formation of Au<sub>x</sub>Ag<sub>29-x</sub> (x = 1-12).

**Supporting information 18:**

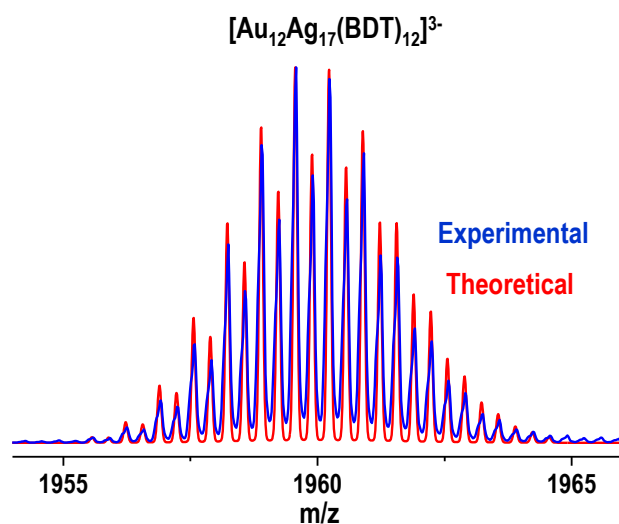


**Figure S18.** Experimental and theoretical isotopic patterns of Au<sub>12</sub>Ag<sub>17</sub> which shows good agreement with each other.

**Supporting information 19:**

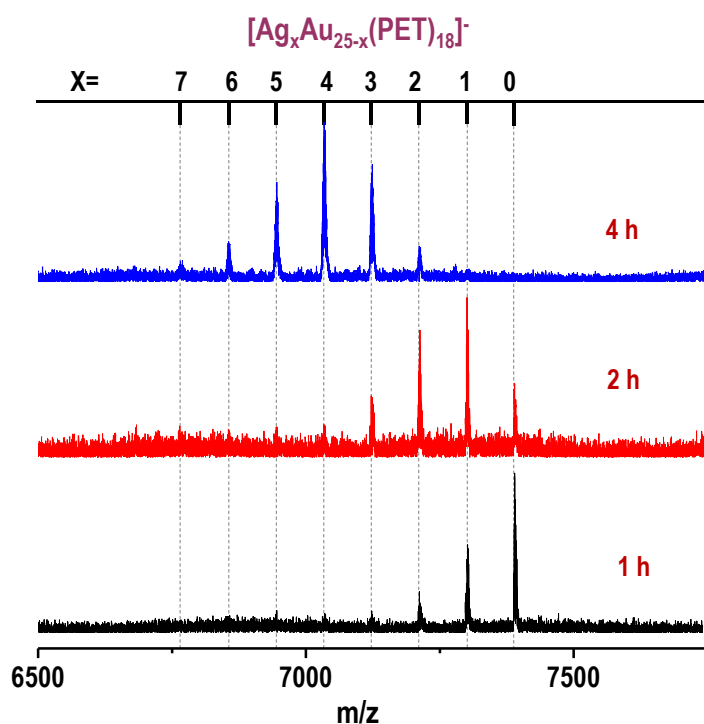


**Figure S19.** Time-dependent ESI MS of the reaction between Ag<sub>29</sub> and Au<sub>25</sub> (1:5 ratio) at the Au<sub>25</sub> side (higher temperature).

**Supporting information 20:**

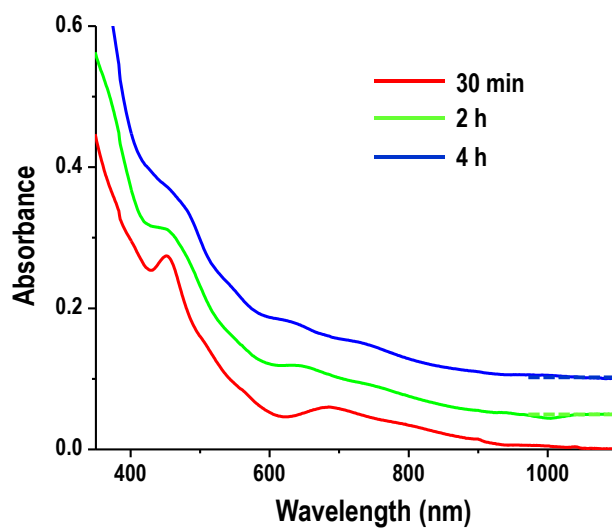


**Figure S20.** Time-dependent UV-vis absorption spectra of the intercluster reaction between Ag<sub>29</sub> and Au<sub>25</sub> using a 1:5 molar ratio.

**Supporting information 21:**

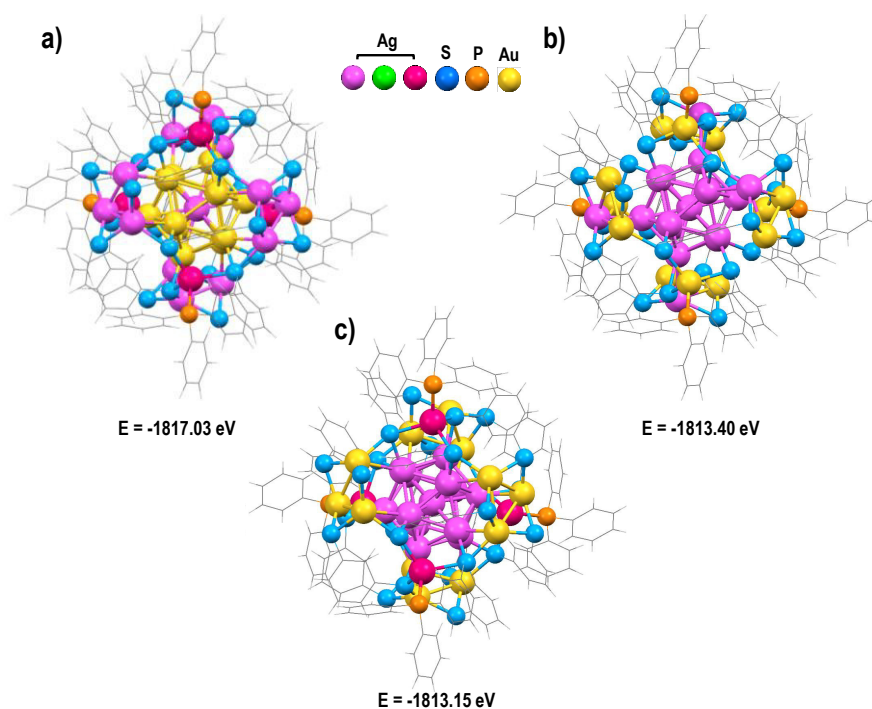


**Figure S21.** Three different geometric isomers of  $\text{Au}_{12}\text{Ag}_{17}$ ; (a) 12 Au atoms are doped in the icosahedral surface, (b) among 12 Au atoms, 8 Au atoms are doped in the crown staples and remaining 4 Au atoms are doped in Ag-PPh<sub>3</sub> motifs and (c) 12 Au atoms are doped in the crown motifs.



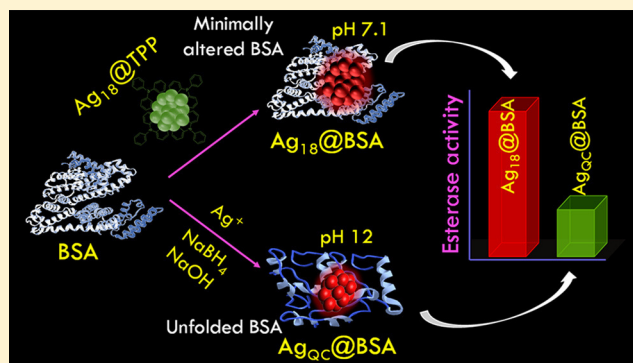
# Internalization of a Preformed Atomically Precise Silver Cluster in Proteins by Multistep Events and Emergence of Luminescent Counterparts Retaining Bioactivity

Debasmita Ghosh,<sup>†</sup> Mohammad Bodiuzzaman,<sup>†</sup> Anirban Som,<sup>†</sup> Sebastian Raja,<sup>‡</sup> Ananya Baksi,<sup>†</sup> Atanu Ghosh,<sup>†</sup> Jyotirmoy Ghosh,<sup>†</sup> Akshayaa Ganesh,<sup>‡</sup> Priyanka Samji,<sup>‡</sup> Sundarasamy Mahalingam,<sup>‡</sup> Devarajan Karunakaran,<sup>‡</sup> and Thalappil Pradeep<sup>\*,†</sup>

<sup>†</sup>DST Unit of Nanoscience (DST UNS) and Thematic Unit of Excellence, Department of Chemistry and <sup>‡</sup>Department of Biotechnology, Indian Institute of Technology Madras, Chennai 600036, India

## Supporting Information

**ABSTRACT:** A new synthetic protocol is introduced which preserves the secondary structure of protecting proteins encapsulating a luminescent atomically-precise silver cluster. This was achieved by using a preformed triphenylphosphine (TPP)-protected silver cluster as the precursor forming bovine serum albumin (BSA)- and human serum albumin (HSA)-protected Ag<sub>18</sub> clusters. This is the first example of the formation of luminescent protein-protected clusters in a neutral medium, without using any reducing agent, which results in minimal alteration of the protein structure during cluster growth. The cluster formed showed exceptional stability, unlike other silver clusters of this class. The formation of these red luminescent clusters was visualized by UV–vis and photoluminescence spectroscopy. The identification of Ag<sub>18</sub> core was made through matrix-assisted laser desorption/ionization mass spectrometry (MALDI MS), and a plausible mechanism of the formation was identified by monitoring the systematic growth of the cluster core by time-dependent MALDI MS experiments and electrospray ionization mass spectrometry (ESI MS) of the reaction mixture. The cluster was successfully employed as a luminescent probe for cancer cell imaging. Retention of protein conformation in the clusters was confirmed through circular dichroism (CD) spectroscopy, and the same was reflected in the retention of 89% of the esterase activity of BSA in the Ag<sub>18</sub>@BSA clusters synthesized by this method, compared to only 28.7% for Ag<sub>QC</sub>@BSA clusters synthesized using previous protocols, conducted in basic medium.



## INTRODUCTION

Protein-protected noble metal nanoclusters (NCs),<sup>1–3</sup> a subclass of atomically-precise protected noble metal clusters,<sup>4,5</sup> are the most studied ones among this class of materials. Due to their intense luminescence with high quantum yield, stability in ambient condition for months, and biocompatibility, these materials are considered as a new class of biohybrid materials with potential applications in diverse areas,<sup>6,7</sup> especially in sensing<sup>8–10</sup> and biology.<sup>11–14</sup> Development of such stable, sensitive, and reliable platforms are highly desirable for specific binding and targeted drug delivery,<sup>15,16</sup> multimodal imaging,<sup>17–19</sup> therapeutic applications,<sup>20</sup> targeted biolabeling,<sup>2,21,22</sup> and so on. Bovine serum albumin (BSA) is the most commonly used protein to synthesize Au and Ag clusters like Au<sub>9</sub>@BSA,<sup>23</sup> Au<sub>16</sub>@BSA,<sup>24</sup> Au<sub>25</sub>@BSA,<sup>1</sup> Au<sub>30</sub>@BSA,<sup>25</sup> Au<sub>38</sub>@BSA,<sup>21</sup> Ag<sub>8</sub>@BSA,<sup>26</sup> Ag<sub>15</sub>@BSA,<sup>27</sup> and Ag<sub>31</sub>@BSA.<sup>28</sup> Other than BSA, large proteins with high molecular weight such as human serum albumin (HSA) (Au@HSA),<sup>29</sup> lactotransferrin (Au<sub>25,34,40</sub>),<sup>30,31</sup> human serum transferrin (Au),<sup>32</sup> pepsin (Au<sub>8,13,25</sub>),<sup>33</sup> horseradish peroxidase (Au),<sup>34</sup> egg white (Au,

Pt),<sup>35</sup> and ovalalbumin (Au)<sup>36</sup> have been employed to synthesize Au, Pt, and Ag clusters. Small proteins with low molecular weight such as insulin (Au),<sup>37</sup> lysozyme (Au<sub>8,10–12</sub>),<sup>10,38</sup> and trypsin (Au)<sup>39</sup> have also been used to synthesize protein-protected clusters. In all of these cases, gold is preferred to make such clusters due to the ease of synthesis and greater stability of the resultant clusters, and the number of silver clusters reported is substantially less.

In a typical protein-directed cluster synthesis, the metal ion is complexed with the protein and subsequently reduced either by a strong reducing agent, like NaBH<sub>4</sub>, or by increasing the pH (11–12) of the solution.<sup>1,27,28</sup> However, in the presence of a strong reducing agent (NaBH<sub>4</sub>) or alkaline pH of the reaction mixture, proteins undergo irreversible conformational changes, and this results in the partial or complete loss of their inherent bioactivity.<sup>40,41</sup> Sometimes it leads to the formation of

Received: August 14, 2019

Revised: November 4, 2019

Published: November 11, 2019



protein oligomerization.<sup>42,43</sup> Reduced bioactivity is one of the factors limiting the widespread use of such materials in biomedical research. Therefore, a milder synthetic method retaining the bioactivity of the as-synthesized NCs is needed. With these objectives, we explored the possibility of using preformed clusters as precursors to synthesize luminescent clusters, retaining the bioactivity of the protein.

Phosphine-protected clusters of gold have been known and studied for some time.<sup>4,44</sup> A new class of atomically precise NCs of silver coprotected by hydride and phosphines as ligands was reported recently.<sup>45,46</sup> Such clusters are expected to be more reactive, having accessible metal sites compared to the thiol-protected clusters due to the presence of labile phosphines. Here we report that such a cluster,  $[\text{Ag}_{18}\text{H}_{16}(\text{TPP})_{10}]^{2+}$  (to be abbreviated as I subsequently), where TPP is triphenylphosphine, can be systematically transformed into highly stable and luminescent silver clusters protected by proteins under neutral pH conditions, preserving the bioactivity of the encapsulating proteins. The precursor I acts as a source of atomic Ag species toward the formation of the red luminescent  $\text{Ag}_{18}@\text{BSA}$  at neutral pH. The retention of the protein's bioactivity and secondary structure in the course of cluster formation has been confirmed experimentally. Such transformations were not observed with more stable nanoparticles and thiol-protected cluster systems, implying the sensitivity of the method to the specificity and chemical stability of the starting materials.

## METHODS

**Materials.**  $\text{AgNO}_3$  was purchased from Rankem Chemicals. Sodium borohydride ( $\text{NaBH}_4$ , 98%) was purchased from Sigma-Aldrich. Triphenylphosphine (TPP) was purchased from Spectrochem. BSA was purchased from the Sisco Research Laboratory. All of the chemicals were used as received without further purification. All solvents (dichloromethane (DCM), methanol (MeOH)) were purchased from Rankem and were of analytical grade. Milli-Q water with a resistivity of 18.2  $\text{M}\Omega\cdot\text{cm}$  was used for synthesis. The protein, BSA, contained  $\text{Na}^+$  in the as-received form.

**Instrumentation.** UV-vis spectra were recorded using a PerkinElmer Lambda 25 UV-vis spectrometer. Absorption spectra were typically measured in the range of 200–1100 nm with a band-pass filter of 1 nm.

MALDI MS of  $\text{Ag}_{18}@\text{BSA}$  cluster was measured using a Voyager-DE PRO Biospectrometry Workstation from Applied Biosystems. A pulsed nitrogen laser of 337 nm was used for ionizing the sample, and sinapic acid was used as the matrix. Spectra were collected in the positive mode, and an average of 250 shots was used for each spectrum. The matrix solution was prepared by dissolving 10 mg of sinapic acid in a 1:3 mixture of acetonitrile and 0.1% trifluoroacetic acid (TFA) in Milli-Q water (overall volume of 1 mL). A 5  $\mu\text{L}$  amount of the cluster solution, without dilution, was mixed thoroughly with 50  $\mu\text{L}$  of the matrix mixture. A 2.5  $\mu\text{L}$  amount of the resulting mixture was used for spotted by dried droplet method.

ESI MS experiments were done using a Waters Synapt G2Si HDMS instrument. The instrument consists of an electrospray source, quadrupole ion guide/trap, ion mobility cell, and TOF detector. All of the experiments were done in positive ion mode.

Photoluminescence measurement was carried out in a HORIBA, Jobin Yvon NanoLog Fluorescence spectrometer

with a band pass of 3 nm for both emission and excitation spectra.

Circular dichroism (CD) spectra were measured in a Jasco 815 spectropolarimeter with Peltier setup for the temperature-dependent measurements. CD studies were done with a 10 mm path length cell. The concentration of the sample in the cuvette used for CD measurement was  $2 \times 10^{-7} \text{ g mL}^{-1}$ .

Scanning electron microscopy (SEM) and energy-dispersive analysis (EDS) images were conducted using an FEI QUANTA-200 SEM. For the measurements (SEM and EDS), samples were spotted on an indium tin oxide (ITO) conducting glass substrate and dried in ambient conditions.

High-resolution transmission electron microscopy (HRTEM) was performed with a JEOL 3010, 300 kV instrument equipped with an ultrahigh-resolution (UHR) pole piece. Samples were prepared by dropping the dispersion on carbon-coated copper grids for HRTEM.

The cells were imaged using a LSM880 laser scanning confocal microscope (Carl Zeiss, Germany), and image acquisition was performed using a high-NA oil immersion objective (Plan-Apochromat 63 $\times$ /1.4) using Zen 2009 software (Carl Zeiss, Germany). Laser lines at 405 and 488 nm were used for excitation. For 405 nm excitation, emission was collected from 410 to 550 nm, and for 488 nm excitation, emission was collected from 491 to 550 nm. Each image was acquired with an exposure time of 80 and 100 ms. The total thickness of the sample was about 4–5  $\mu\text{m}$ , leading to the acquisition of 25–30 optical sections. Images were processed through Zen BLACK software (Carl Zeiss) and exported into TIF format. Selected cellular regions were cropped and analyzed further in ZEN Blue software for 3D reconstruction with a 180-frame rotation series along the Y axis. The orthogonal view and 3-D images reconstruction were made using ZEN Blue software. The intracellular distribution was projected using Imaris 3D rendering software.

**Synthesis of  $[\text{Ag}_{18}\text{H}_{16}(\text{TPP})_{10}]^{2+}$  (Cluster I).** Initially, 20 mg of  $\text{AgNO}_3$  was dissolved in 5 mL of methanol. To the above solution TPP (70 mg in 10 mL of chloroform) was added under stirring conditions. After 20 min, 6 mg of  $\text{NaBH}_4$  dissolved in 0.5 mL of ice-cold Milli-Q water was added to the above reaction mixture. After addition of aqueous  $\text{NaBH}_4$  solution, the colorless solution immediately turned light yellow. The stirring was continued for 3 h. The final color of the solution was deep green, which confirmed the formation of cluster. The solvent was removed from the reaction mixture by rotary evaporation. The cluster was then washed 6–7 times with Milli-Q water to remove the unreacted silver ions and  $\text{NaBH}_4$ . After being washed, the green-colored precipitate was dissolved in 1 mL of methanol. The final concentration of I is 15 mM.

**Synthesis of  $[\text{Ag}_{18}@\text{BSA}]$ .** A 25 mg amount BSA was dissolved in 1.6 mL of Milli-Q water. Then the solution was stirred for 1 min. Under stirring condition 400  $\mu\text{L}$  of I was added from the 1 mL of methanol solution. The addition of I into the BSA solution made the reaction mixture turbid. Stirring was continued for 12 h. The turbid solution was centrifuged, and from the supernatant the brown-colored cluster solution was collected. This solution was used for characterization.

**Synthesis of  $[\text{Ag}_{\text{QC}}@\text{BSA}]$ .** A 5 mL amount of 10 mM silver nitrate solution was added to a solution of 250 mg of BSA dissolved in 5 mL of Milli Q water with vigorous stirring at room temperature. About 0.3 mL of 1 M NaOH solution

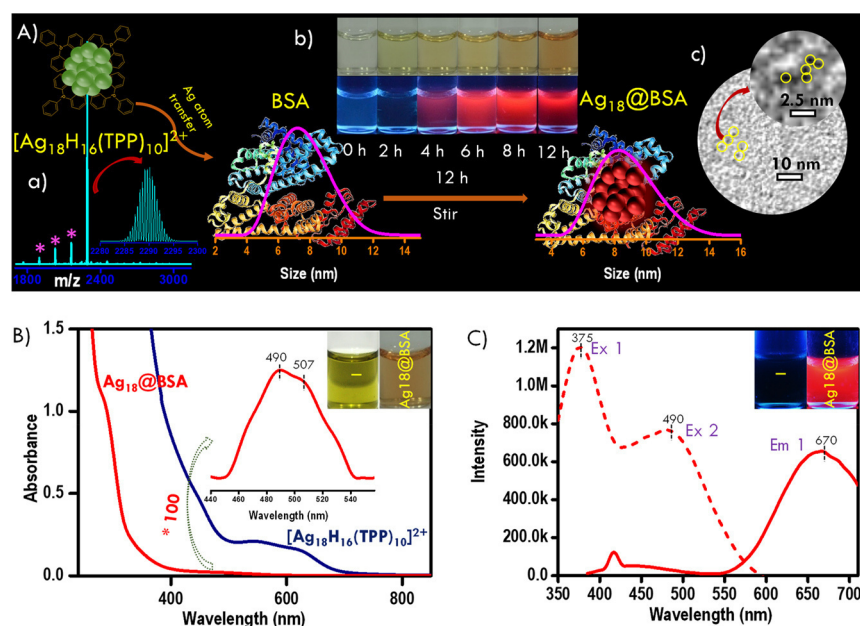


**Figure 1.** (A) Schematic of the formation of  $\text{Ag}_{18}\text{@BSA}$  from I. Hydrodynamic diameters of BSA and  $\text{Ag}_{18}\text{@BSA}$  are shown in the schematic. ESI MS of I is shown in inset a, where peaks marked with asterisks (\*) are due to the phosphine losses from I. Expanded view of the molecular ion peak is also shown. Pictorial representation of the time-dependent change in color of the solution under visible and UV light is shown as inset b. TEM image of  $\text{Ag}_{18}\text{@BSA}$  is shown as inset c. Cluster cores are marked. (B) UV-vis spectra of  $\text{Ag}_{18}\text{@BSA}$  and I. Inset shows the solutions of I and  $\text{Ag}_{18}\text{@BSA}$  under visible light. (C) Luminescence profile of  $\text{Ag}_{18}\text{@BSA}$ . Inset shows the solutions of I and  $\text{Ag}_{18}\text{@BSA}$  under UV light. Absorption and emission maxima are marked on the traces. Concentration of  $\text{Ag}_{18}\text{@BSA}$  cluster solution is  $7.5 \times 10^{-4}$  mol/L.

was added followed by 10 mM  $\text{NaBH}_4$  solution dropwise until the solution turns from colorless to reddish brown, indicating formation of the  $\text{Ag}_{\text{QC}}\text{@BSA}$  cluster.

**Cell Viability.** The cellular toxicity of  $\text{Ag}_{18}\text{@BSA}$  was determined by resazurin reduction, a colorimetric assay. HeLa cells were seeded in a 96-well plate at a density of 5000 per well and grown overnight. They were treated with different concentrations of the clusters. After 24 h of incubation, each well was washed with phosphate-buffered saline. Resazurin dye was added and incubated for the 3 h for the reduction. The blue dye resazurin became to pink resorufin, and the absorbance was measured at 570 and 595 nm. Three replicates were performed.

**Cellular Uptake Studies by Confocal Fluorescence Microscopy.** HeLa cells were cultured on chamber slides (BD Biosciences, USA) and incubated with  $\text{Ag}_{18}\text{@BSA}$  (5  $\mu\text{M}$  concentration) NCs for 5 and 24 h. After incubation, the cells were fixed with 4% (w/v) paraformaldehyde followed by permeabilization using 0.1% Triton X-100 and washed with PBS buffer. The cells were mounted in the mounting medium (Vector Laboratories, USA) containing Hoechst 33342 to stain the nuclei. These cells were covered with a coverslip, sealed with nail polish, and kept for imaging.

**Evaluation of Esterase Activity.** The bioactivity of BSA and the  $\text{Ag}_{18}\text{@BSA}$  was determined by monitoring the appearance of the hydrolysis product of *p*-nitro-phenyl acetate (PNA) in a manner similar to a previously reported method.<sup>47</sup> The concentration of PNA was 100  $\mu\text{M}$ , and the concentrations of BSA and  $\text{Ag}_{18}\text{@BSA}$  were 1 mg/mL.

## RESULTS AND DISCUSSION

**Luminescent Cluster from a Nonluminescent one.** Synthesis of  $\text{Ag}_{18}\text{@BSA}$  was initiated by mixing I with a solution of BSA at pH 7.1 under continuous magnetic stirring.

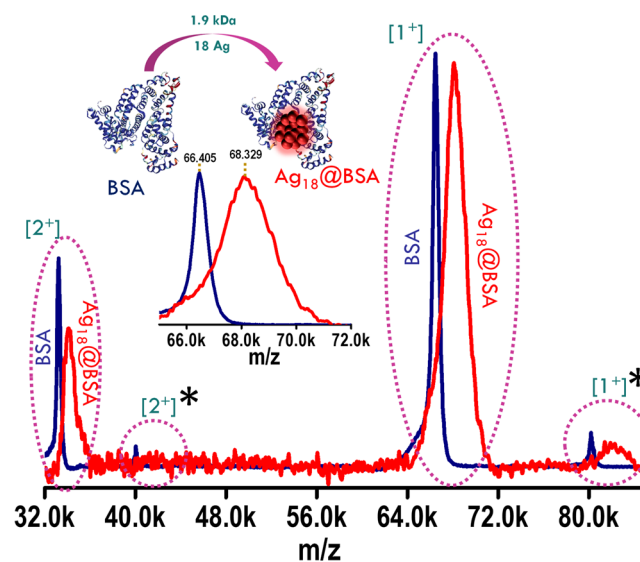


**Figure 2.** MALDI MS of pure BSA (blue trace) collected in the linear positive ion mode using sinapic acid as the matrix and that of as-prepared, red-emitting  $\text{Ag}_{18}\text{@BSA}$  (red trace). Peaks due to singly charged ions of  $\text{Ag}_{18}\text{@BSA}$  are expanded in the inset along with those of BSA. Presence of conalbumin in the BSA is indicated with an asterisk (\*).

A schematic of the formation of  $\text{Ag}_{18}\text{@BSA}$  from I (ESI MS shown in inset a) is represented in Figure 1A. A gradual color change of the mixture during the course of the reaction was observed, accompanied by the evolution of red luminescence, generally associated with the formation of metal clusters. The time evolution of cluster growth observed under visible and UV illumination is shown in the inset b of Figure 1A. Such a gradual change in color and luminescence of the protein



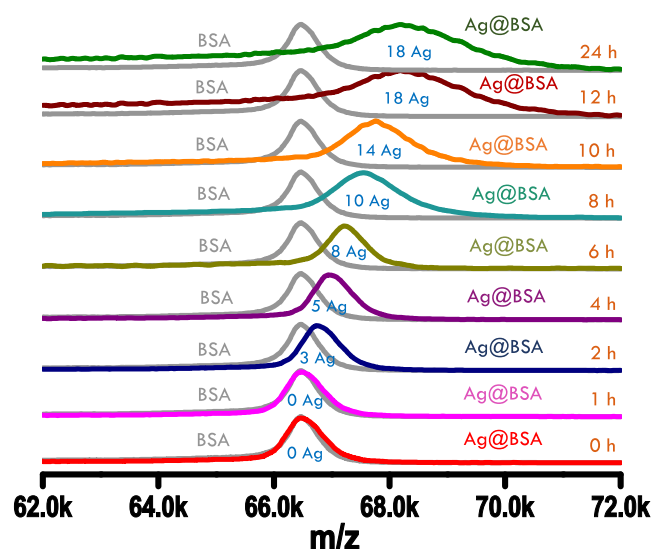


**Figure 3.** Time-dependent MALDI MS showing the evolution of  $\text{Ag}_{18}\text{@BSA}$  cluster. MALDI MS of parent BSA is shown for comparison.

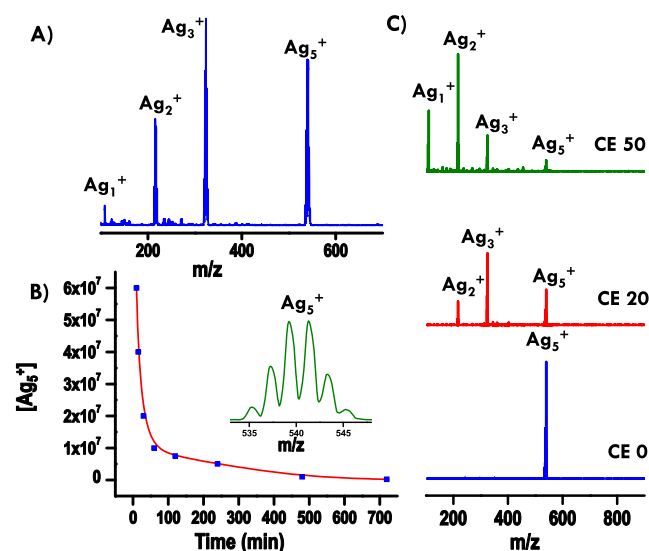


**Figure 4.** (A) ESI MS of the reaction mixture after 10 min, showing the presence of small Ag clusters. (B) Decay in the ion intensity of  $\text{Ag}_5^+$  with the progress of the reaction. Isotopic distribution of  $\text{Ag}_5^+$  is shown in the inset. (C) MS/MS study of  $\text{Ag}_5^+$ , showing the formation of other small Ag clusters can arise from the fragmentation of  $\text{Ag}_5^+$ . Collision energy (CE) is in instrumental limit.

solution indicated slow nucleation of the cluster core within the protein template. After 12 h of reaction, a colorless BSA solution turned into a brown-colored, intense red luminescent solution. No perceptible change in the color of the solution was observed when incubation was continued beyond 12 h. Monolayer-protected NCs generally exhibit well-defined molecular transitions in the absorption profile.<sup>4</sup> The blue trace in Figure 1B shows the UV–vis spectrum of precursor I with maxima at 550 and 620 nm.<sup>45,46</sup> The UV–vis spectrum of  $\text{Ag}_{18}\text{@BSA}$  (red trace, Figure 1B) predominantly exhibits the characteristic absorption of BSA at 280 nm along with a broad absorption in the 440–540 nm region. Expansion of this region (inset of the Figure 1B) clearly shows two absorption maxima around 490 and 507 nm, further indicating the formation of a

protein-protected silver cluster. The change in the color of the cluster solution from green (parent I) to brown (formed  $\text{Ag}_{18}\text{@BSA}$  NCs) under visible light is shown in the inset of Figure 1B. The photoluminescence profile of the cluster (Figure 1C) shows two excitation peaks around 375 and 490 nm along with a bright red emission centered around 670 nm. The excitation maximum at 375 nm is due to the presence of the protein shell, and the other excitation maximum at 490 nm is because of the presence of the cluster core. Both excitations give the same emission but with different intensities. Photographs under UV illumination showing the transformation of I into a red luminescent cluster are presented in the inset of Figure 1C. The quantum yield of the cluster was 25.1% using fluorescein as reference (in water). It is also worth mentioning that in the course of formation of the protein-protected NCs in solution an insoluble product was also formed, which was removed through centrifugal precipitation, and the centrifugate containing the NCs was characterized in detail. EDS analysis of the precipitate formed after 12 h showed the presence of water-insoluble phosphines along with Ag and proteins (Figure S1).

Formation of the cluster core in the protein template results in swelling of the protein.<sup>48</sup> The hydrodynamic diameter of the parent BSA was 7.2 nm. At the end of the reaction, the average size of the proteins was increased by about 1 nm, as shown in Figure 1A. It is very difficult to determine the exact core size for clusters from HRTEM analysis as the high-energy electron beam is known to induce cluster coalescence. Low-dose microscopy was performed to confirm the formation as well as to have a definite idea about the size of the cluster core. The cluster core appears as tiny black dots in the HRTEM image (inset c, Figure 1A) having a size of  $\sim 1$  nm. This also confirmed the absence of bigger plasmonic nanoparticles in solution.

**Identification of the Atomicity.** Mass spectrometry has emerged as an essential tool in understanding the atomicity of the clusters. We measured the MALDI MS of the as-prepared NCs to assign the nuclearity of the cluster core. The spectra of the cluster (red trace) and of BSA (blue trace) are shown in Figure 2. BSA showed its molecular ion peak at  $m/z$  66.4 kDa and a peak at  $m/z$  33.2 kDa, corresponding to the +2 charge state in the MS. In the case of the cluster, both peaks were seen, albeit they appear at higher masses from that of BSA. The mass shift to a higher mass region in the NCs from the parent protein in both +1 and +2 states clearly indicate the growth of a cluster core in the protein cavity. An expanded view of the +1 region of the MS (inset, Figure 2) shows a 1.9 kDa shift, corresponding to the incorporation of 18 Ag atoms into the protein core, forming  $\text{Ag}_{18}\text{@BSA}$ . The dication shows one-half the shift, as expected. This confirms that the cluster core is incorporated in a single protein moiety. It is to be noted that the peaks around  $m/z$  80 kDa (+1 charge) and  $m/z$  40 kDa (+2 charge) present in the MALDI MS are associated with the presence of the protein conalbumin, an internal standard used in BSA.<sup>27,49</sup> These peaks were shifted to higher mass in the case of the cluster. This increased shift is attributed to the formation of  $\text{Ag}_{18}$  core in this protein also.

The EDS spectrum collected from the NCs showed the presence of Ag and S in the formed cluster (Figure S2). Quantitative analysis of the EDS spectrum gives an S:Ag ratio of 2.2, expected for the  $\text{Ag}_{18}\text{@BSA}$  composition (2.22). Note that BSA has 35 S atoms due to cysteine and 5 S atoms due to methionine. XPS spectra in the Ag 3d region (Figure S3)

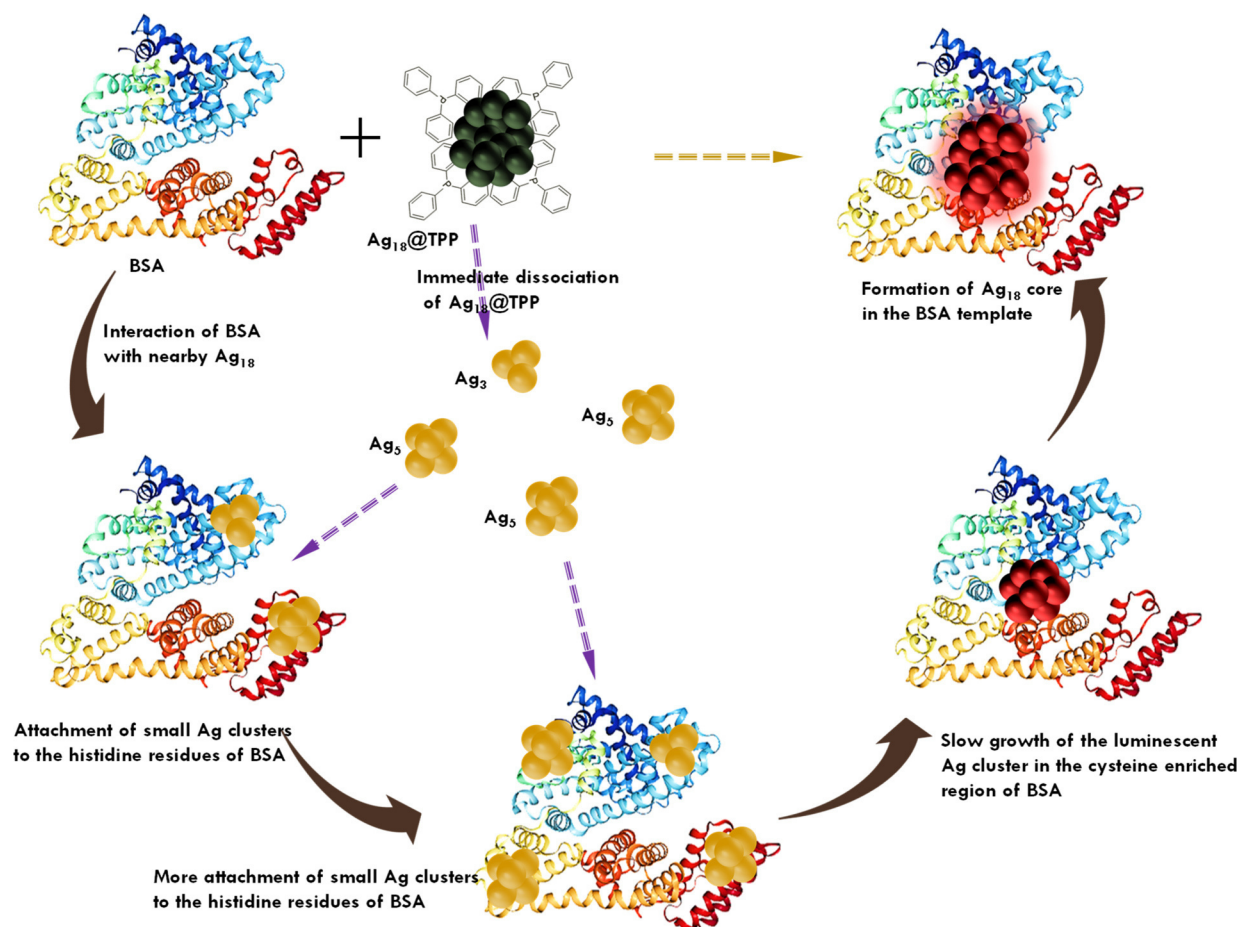


**Figure 5.** Probable mechanism of the formation of  $\text{Ag}_{18}@\text{BSA}$  from **I**.

shows Ag in zero (0) oxidation state ( $\text{Ag } 3d_{5/2}$  at 368 eV), and the S 2p region shows S to be thiolate kind ( $\text{S } 2p_{3/2}$  at 161.5 eV) in  $\text{Ag}_{18}@\text{BSA}$  NCs.<sup>27</sup> It further confirmed the chemical composition of the cluster.

Cysteine as well as methionine residues in the proteins are perceived to be responsible for protecting the metal core through the formation of metal–sulfur (M–S) bonds in the protein-protected NCs.<sup>38,50,51</sup> Nuclearity of the cluster cores formed in the proteins, for this reason, depends on the number of cysteine residues present in a particular protein. We chose human serum albumin (HSA), a protein with the same number of cysteine residues as that of BSA to form the cluster through the addition of **I**. This was also seen to uptake Ag atoms from the precursor cluster, forming  $\text{Ag}_{18}@\text{HSA}$  after 12 h. The UV–vis spectra, luminescence profile, and MALDI MS corresponding to this transformation are shown in Figures S4 and S5.

Lactoferrin (Lf), an 83 kDa protein with different number and position of cysteine and methionine groups, was also used to synthesize Ag NCs following our new method. UV–vis and luminescence spectra of the new system are shown in Figures S6A and S6B, respectively. The MALDI MS shown in Figure S6C confirmed the formation of  $\text{Ag}_{13}@\text{Lf}$  cluster. The difference in atomicity is attributed to the structural differences, stabilizing a smaller cluster. Though the molecular weight of Lf is higher than BSA and HSA, the number of histidine (His) residues present in Lf is less. Thus, the ability of Lf to stabilize the small clusters formed at the initial stage is expected to be lower than both BSA and HSA. This probably

results in the formation of a smaller 13-atom Ag cluster in this case. Relevant data are summarized in Table S1.

**Mechanism of Multistep Evolution of the Cluster.** Formation of  $\text{Ag}_{18}@\text{BSA}$  through the reaction between **I** and BSA was accompanied by a gradual change in the luminescence of the solution (inset b, Figure 1A and Figure S7). This indicated a gradual evolution of the  $\text{Ag}_{18}$  cluster during the course of the reaction. To shed light into the time evolution, time-dependent MALDI MS was recorded from aliquots collected at different intervals, as shown in Figure 3. At the initial stages of the reaction (0–1 h), no mass shift from the parent BSA peak was seen. This indicated a different pathway of cluster formation in the current method than the traditional method, in which attachment of metal ions to the protein at the beginning of the reaction is manifested by an abrupt mass shift just after addition of the metal salt.<sup>31</sup> Such a shift is not noticed here as shown by the 0 and 1 h spectra. With further progression of the reaction, a gradual shift to higher mass was seen in the MS up to 12 h, indicating growth of the cluster core inside the protein template over time. The nuclearity reaches  $\text{Ag}_{18}$  after 12 h, and neither the continuation of the reaction beyond this point nor further addition of fresh **I** to the reaction mixture changes the final  $\text{Ag}_{18}@\text{BSA}$ . Once formed, the cluster was stable for months, even when stored at room temperature, an attribute generally seen only in gold clusters.

Time-dependent MALDI MS suggests that the formation of  $\text{Ag}_{18}@\text{BSA}$  from **I** happens slowly, in steps, rather than through transfer of the Ag core from the monolayer protected cluster

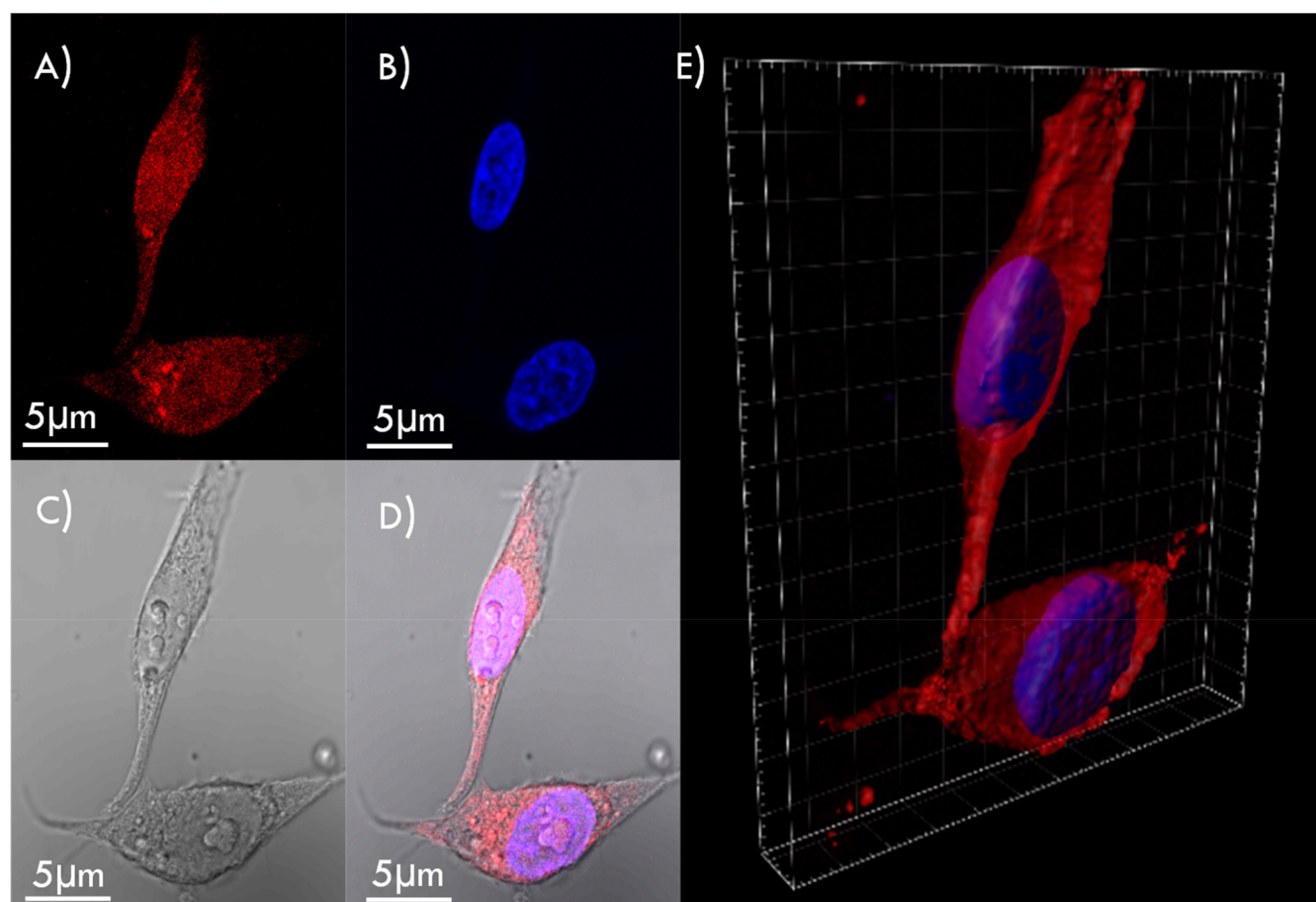


**Figure 6.** Confocal microscopic images of internalization of  $\text{Ag}_{18}\text{@BSA}$  cluster in HeLa cells after 24 h incubation. (A) Fluorescence image of NCs exhibiting red luminescence inside the cell. (B) Cell nucleus stained with DAPI. (C) Bright-field image of the corresponding cells. (D) Overlay of these three images. (E) 3D reconstruction of the cells confirming internalization of the cluster.

into the protein in a single step. To gain further insight into the mechanism of formation of  $\text{Ag}_{18}\text{@BSA}$ , ESI MS of the reaction mixture was collected at various stages of the reaction. ESI MS of the reaction surprisingly showed the presence of small naked Ag clusters (Figure 4A). The few atom naked Ag clusters were observed at maximum intensities in ESI MS at the early stages of reaction, and their concentration (ion intensity) diminishes as the reaction progresses (Figure 4B).  $\text{Ag}_5^+$  appeared as one of the major peaks in the ESI MS, and MS/MS of the same showed that other clusters seen could very well be its fragmentation products (Figure 4C).  $\text{Ag}_4^+$  was not seen in ESI MS and is due to lower stability of the three-electron system ( $\text{Ag}_4^+$ ). For this reason  $\text{Ag}_5^+$  directly fragmented to  $\text{Ag}_3^+$  during MS/MS study. It could also be due to the stability of the neutral fragment,  $\text{Ag}_2$ . While ESI MS of the reaction mixture at the early stages of the reaction showed the clear presence of naked clusters, MALDI MS at these stages did not indicate formation of any protein-protected cluster species. This led us to infer that the  $\text{Ag}_{18}$  cluster with labile phosphine protection slowly disintegrates under the reaction conditions, releasing the few atom Ag clusters into the protein molecules present in solution, which immediately captures these small clusters. It is important to note that the proximity of the protein molecules to the released few atom silver clusters play an important role in the stabilization of such clusters. Formation of larger silver nanoparticles was observed when the protein concentration in the reaction mixture was

decreased by 1 order of magnitude (Figure S8). The protein molecules remain further apart in solution at this lower concentration, so they cannot capture and protect the small Ag clusters efficiently enough, and they grow into larger nanoparticles.

The initial attachment between the few atom Ag clusters and BSA, however, happens through weak interactions and results in their detachment during mass spectrometric ionization processes (ESI and MALDI). This leads to the observation of naked Ag cluster in ESI MS, while only free protein is observed in the MALDI MS. Stabilization of small Au clusters at the His residues of crystalline protein cage (apoferritin) has been reported recently.<sup>52</sup> We believe that similar attachment of the Ag clusters at the His residues of BSA is responsible for their initial stabilization. These clusters attached to His are then slowly transferred to cysteine (Cys) residues of the protein through the formation of M–S bonds with better thermodynamic stability. This initiates the formation of protein-protected cluster species. The cluster core protected by Cys continues to grow in size with time through the sequential transfer of His-bound Ag cluster followed by their coalescence. These stable cluster species, although unfortunately did not ionize in ESI MS, are seen in MALDI MS as intermediates. Growth of the protein-protected cluster core with time also results in the reduction of the concentration of His-bound Ag cluster. This was reflected in the decrease in the ion intensity of the naked clusters with reaction time (Figure 4B). The



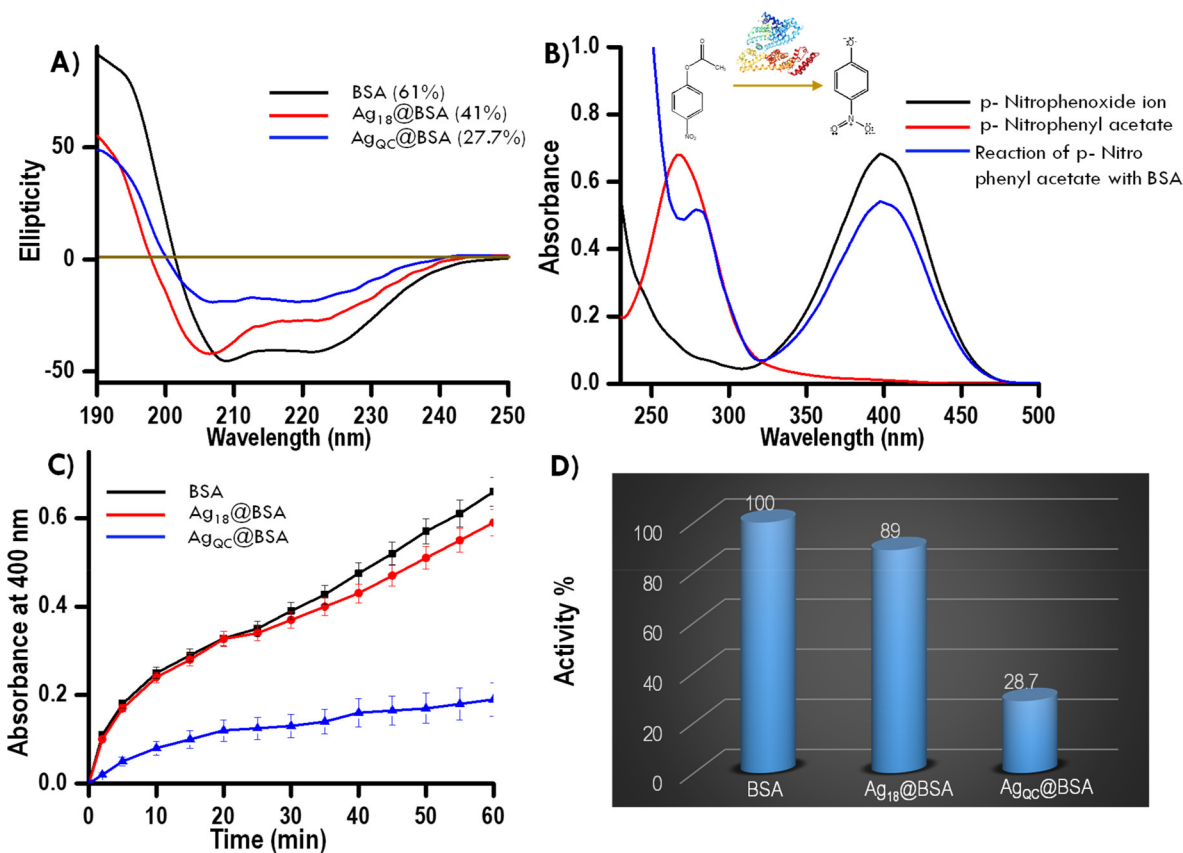


**Figure 7.** (A) CD spectra of the pure BSA an Ag<sub>18</sub>@BSA and Ag<sub>QC</sub>@BSA clusters. (B) UV-vis profile of esterase activity of BSA. (C) Ester hydrolysis reaction of pure protein and Ag<sub>18</sub>@BSA and Ag<sub>QC</sub>@BSA clusters as a function of time. (D) Percentage activity of pure protein and clusters.

reaction stops when the largest stable cluster that can be accommodated by these cysteine residues without significant alteration of the protein structure is formed, which turned out to be 18 for both BSA and HSA, probably due to their structural similarity. A schematic representation of this probable reaction mechanism is shown in Figure 5. Since preformed Ag(0) species are involved in the cluster formation, the process did not require the addition of a reducing agent. Formation of Ag<sub>18</sub>@BSA cluster was not observed through the reaction of BSA with citrate-capped silver nanoparticles as well as with thiol (glutathione)-protected Ag clusters (Figure S9), presumably due to their enhanced stability, restricting them from producing the Ag(0) or Ag<sub>n</sub> species needed in the process.

**Cluster as Potential Bioimaging Probe.** Entrapment of the metal core inside the biomolecular template through a formation of a strong M–S bond is expected to make the Ag<sub>18</sub>@BSA clusters biocompatible. Their potential cytotoxicity was evaluated by incubating HeLa cells with the NCs and accessing the viability of these cells after 24 h through resazurin assay (results are shown in Figure S10). This confirmed the biocompatibility of the as-synthesized Ag<sub>18</sub>@BSA NCs.

Their bright red luminescence can potentially be exploited for bioimaging applications given their ultrahigh stability in the biologically relevant conditions. Furthermore, the cluster being made at neutral pH eliminates the possibility of pH-induced changes in luminescence in physiological conditions. HeLa cells were used to study the cellular uptake without any special purification or conjugation of as-synthesized clusters. Attach-

ment of the clusters along the cell membrane was observed after 5 h of incubation (Figure S11). The cluster gradually diffused into the cytosol and was observed to be completely internalized after 24 h (Figure 6). Three-dimensional reconstruction of the corresponding cells (Figure 6E and video V1) from the *z* stack images (shown in Figure S12) confirmed the localization of the clusters in the cytoplasm, demonstrating the cluster to be an excellent bioimaging probe. The cell nucleus was stained with DAPI in these experiments.

#### Retention of Protein Structure and Bioactivity.

Reactions performed at solutions of high pH or use of strong reducing agents are thought to be the reasons for large changes in the secondary structure of the protein during cluster formation. Since the aforementioned process using a preformed cluster as precursor involves neither, retention of the protein structure to a greater degree is expected in the Ag<sub>18</sub>@BSA. Conformational change in the protein structure can be measured by the change in the CD (circular dichroism) spectrum, which is shown in Figure 7A. The fraction of  $\alpha$ -helix, a measure of the conformational change, was calculated for both Ag<sub>18</sub>@BSA and Ag<sub>QC</sub>@BSA clusters (synthesized through conventional route) from CD spectra. A higher degree of retention of  $\alpha$ -helicity was indeed observed in Ag<sub>18</sub>@BSA (41%) over Ag<sub>QC</sub>@BSA (27.7%), confirming lesser alteration of the protein structure in the new synthetic methodology.

Function or bioactivity of a protein is also closely related to its structural integrity. BSA is known to possess esterase activity,<sup>47,53–55</sup> the ability to catalyze the hydrolysis of esters into component acids and alcohols. The retention of this

biological function in  $\text{Ag}_{18}\text{@BSA}$  was tested using PNA as a model compound and was compared with that of  $\text{Ag}_{\text{QC}}\text{@BSA}$ . PNA shows a peak around 270 nm in its UV–vis spectrum (red trace, Figure 7B). This characteristic feature of PNA changes in the presence of BSA (blue trace, Figure 7B) to give a peak around 400 nm, indicating the formation of the phenolate ion (black trace, Figure 7B) in the solution through hydrolysis. Kinetics of the catalyzed hydrolysis of PNA was monitored by following the concentration of the phenolate ions through UV–vis spectroscopy (Figure 7c). After 1 h of reaction,  $\text{Ag}_{18}\text{@BSA}$  was found to be 89% as active as parent BSA, compared to only 28.7% in the case of  $\text{Ag}_{\text{QC}}\text{@BSA}$  (Figure 7D). This can be related to the changes in the primary and secondary structures of the protein during the synthesis of  $\text{Ag}_{\text{QC}}\text{@BSA}$ . Basic medium used in this conventional protocol can modify the tyrosine and arginine residues, thought to be responsible for the esterase activity of BSA,<sup>56,57</sup> causing disruption of H bonds and electrostatic interactions, leading to the loss in helicity. On the other hand, synthesis of  $\text{Ag}_{18}\text{@BSA}$  involves only the capture and encapsulation of Ag clusters from solution and retains the structural integrity as well the bioactivity of the protein. This improved bioactivity is supported by studies using  $\text{Ag}_{13}\text{@Lf}$  as well. Lf possesses several enzymatic activities; among them, phosphatase activity was monitored in a similar way for native Lf and the  $\text{Ag}_{13}\text{@Lf}$ . The cluster showed 90% catalytic activity (Figure S13).

## CONCLUSIONS

We introduced a new protocol to synthesize red luminescent protein-protected clusters using preformed clusters as the metal source. Internalization of the silver clusters released in solution from nonluminescent phosphine-protected precursor cluster by the protein was manifested in the change of the luminescence of the solution. The presence of an 18 Ag atom core associated with each protein molecule in the final cluster was identified through MALDI MS, and the mechanism of formation was elucidated from time-dependent mass spectra. A higher degree of structural intactness of the protein in the formed cluster could be achieved by this protocol. This resulted in the addition of extra functionality to the proteins while the inherent bioactivity is retained, addressing a major problem associated with the conventional method of synthesis. The clusters were found to be excellent luminescent probes for cancer cell imaging. The combination of stable yet sensitive luminescence of the clusters formed inside minimal structurally altered and functionally active proteins is expected to aid in the further development of biomedical applications of such clusters.

## ASSOCIATED CONTENT

### Supporting Information

The Supporting Information is available free of charge at <https://pubs.acs.org/doi/10.1021/acs.jpcc.9b07765>.

Protocols for the synthesis of  $[\text{Ag}_{18}\text{HSA}]$  and  $[\text{Ag}_{13}\text{Lf}]$ , EDS spectrum of the precipitate, SEM EDS and XPS of the  $\text{Ag}_{18}\text{@BSA}$ , characterization of  $\text{Ag}_{18}\text{@HSA}$  and  $\text{Ag}_{13}\text{@Lf}$ , time-dependent luminescence profile of  $\text{Ag}_{18}\text{@BSA}$  and reaction of  $[\text{Ag}_{18}\text{H}_{16}(\text{TPP})_{10}]^{2+}$  with Ag nanoparticles, cell viability test, confocal fluorescence image of NCs incubated HeLa cells (PDF)

Three-dimensional reconstruction of the corresponding cells (AVI)

## AUTHOR INFORMATION

### Corresponding Author

\*E-mail: [pradeep@iitm.ac.in](mailto:pradeep@iitm.ac.in).

### ORCID

Anirban Som: 0000-0002-6646-679X

Thalappil Pradeep: 0000-0003-3174-534X

### Notes

The authors declare no competing financial interest.

## ACKNOWLEDGMENTS

We thank the Department of Science and Technology, Government of India, for continuous support of our research program on nanomaterials. D.G. thanks IIT Madras for student fellowships.

## REFERENCES

- (1) Xie, J.; Zheng, Y.; Ying, J. Y. Protein-Directed Synthesis of Highly Fluorescent Gold Nanoclusters. *J. Am. Chem. Soc.* **2009**, *131*, 888–889.
- (2) Xavier, P. L.; Chaudhari, K.; Bakshi, A.; Pradeep, T. Protein-Protected Luminescent Noble Metal Quantum Clusters: An Emerging Trend in Atomic Cluster Nanoscience. *Nano Rev.* **2012**, *3*, 14767.
- (3) Chevrier, D. M.; Thanthirige, V. D.; Luo, Z.; Driscoll, S.; Cho, P.; MacDonald, M. A.; Yao, Q.; Guda, R.; Xie, J.; Johnson, E. R.; Chatt, A.; Zheng, N.; Zhang, P. Structure and Formation of Highly Luminescent Protein-Stabilized Gold Clusters. *Chem. Sci.* **2018**, *9*, 2782–2790.
- (4) Chakraborty, I.; Pradeep, T. Atomically Precise Clusters of Noble Metals: Emerging Link between Atoms and Nanoparticles. *Chem. Rev. (Washington, DC, U. S.)* **2017**, *117*, 8208–8271.
- (5) Diez, I.; Ras, R. H. A. Fluorescent Silver Nanoclusters. *Nanoscale* **2011**, *3*, 1963–1970.
- (6) Goswami, N.; Zheng, K.; Xie, J. Bio-Ncs - the Marriage of Ultrasmall Metal Nanoclusters with Biomolecules. *Nanoscale* **2014**, *6*, 13328–13347.
- (7) Sun, C.; Yang, H.; Yuan, Y.; Tian, X.; Wang, L.; Guo, Y.; Xu, L.; Lei, J.; Gao, N.; Anderson, G. J.; Liang, X.-J.; Chen, C.; Zhao, Y.; Nie, G. Controlling Assembly of Paired Gold Clusters within Apoferritin Nanoreactor for in Vivo Kidney Targeting and Biomedical Imaging. *J. Am. Chem. Soc.* **2011**, *133*, 8617–8624.
- (8) Mathew, A.; Sajanlal, P. R.; Pradeep, T. Selective Visual Detection of TNT at the Sub-zeptomole Level. *Angew. Chem., Int. Ed.* **2012**, *51*, 9596–9600.
- (9) Hu, D.; Sheng, Z.; Gong, P.; Zhang, P.; Cai, L. Highly Selective Fluorescent Sensors for  $\text{Hg}^{2+}$  Based on Bovine Serum Albumin-Capped Gold Nanoclusters. *Analyst (Cambridge, U. K.)* **2010**, *135*, 1411–1416.
- (10) Chen, T.-H.; Tseng, W.-L. (Lysozyme Type Vi)-Stabilized  $\text{Au}_8$  Clusters: Synthesis Mechanism and Application for Sensing of Glutathione in a Single Drop of Blood. *Small* **2012**, *8*, 1912–1919.
- (11) Song, X.-R.; Goswami, N.; Yang, H.-H.; Xie, J. Functionalization of Metal Nanoclusters for Biomedical Applications. *Analyst (Cambridge, U. K.)* **2016**, *141*, 3126–3140.
- (12) Wang, Y.; Chen, J.-T.; Yan, X.-P. Fabrication of Transferrin Functionalized Gold Nanoclusters/Graphene Oxide Nanocomposite for Turn-on near-Infrared Fluorescent Bioimaging of Cancer Cells and Small Animals. *Anal. Chem. (Washington, DC, U. S.)* **2013**, *85*, 2529–2535.
- (13) Mathew, M. S.; Davis, J.; Joseph, K. Green Synthesis of a Plant-Derived Protein Protected Copper Quantum Cluster for Intrauterine Device Application. *Analyst (Cambridge, U. K.)* **2018**, *143*, 3841–3849.
- (14) Basu, K.; Gayen, K.; Mitra, T.; Baral, A.; Roy, S. S.; Banerjee, A. Different Color Emissive Copper Nanoclusters for Cancer Cell Imaging. *ChemNanoMat* **2017**, *3*, 808–814.



- (15) Wang, Y.; Chen, J.; Irudayaraj, J. Nuclear Targeting Dynamics of Gold Nanoclusters for Enhanced Therapy of Her2+ Breast Cancer. *ACS Nano* **2011**, *5*, 9718–9725.
- (16) Yu, Y.; New, S. Y.; Xie, J.; Su, X.; Tan, Y. N. Protein-Based Fluorescent Metal Nanoclusters for Small Molecular Drug Screening. *Chem. Commun. (Cambridge, U. K.)* **2014**, *50*, 13805–13808.
- (17) Zhang, A.; Tu, Y.; Qin, S.; Li, Y.; Zhou, J.; Chen, N.; Lu, Q.; Zhang, B. Gold Nanoclusters as Contrast Agents for Fluorescent and X-Ray Dual-Modality Imaging. *J. Colloid Interface Sci.* **2012**, *372*, 239–244.
- (18) Zhou, W.; Cao, Y.; Sui, D.; Guan, W.; Lu, C.; Xie, J. Ultrastable BSA-Capped Gold Nanoclusters with a Polymer-Like Shielding Layer against Reactive Oxygen Species in Living Cells. *Nanoscale* **2016**, *8*, 9614–9620.
- (19) Wu, X.; He, X.; Wang, K.; Xie, C.; Zhou, B.; Qing, Z. Ultrasmall near-Infrared Gold Nanoclusters for Tumor Fluorescence Imaging in Vivo. *Nanoscale* **2010**, *2*, 2244–2249.
- (20) Zhang, X.-D.; Chen, J.; Luo, Z.; Wu, D.; Shen, X.; Song, S.-S.; Sun, Y.-M.; Liu, P.-X.; Zhao, J.; Huo, S.; Fan, S.; Fan, F.; Liang, X.-J.; Xie, J. Enhanced Tumor Accumulation of Sub-2 Nm Gold Nanoclusters for Cancer Radiation Therapy. *Adv. Healthcare Mater.* **2014**, *3*, 133–141.
- (21) Habeeb Muhammed, M. A.; Verma, P. K.; Pal, S. K.; Retnakumari, A.; Koyakutty, M.; Nair, S.; Pradeep, T. Luminescent Quantum Clusters of Gold in Bulk by Albumin-Induced Core Etching of Nanoparticles: Metal Ion Sensing, Metal-Enhanced Luminescence, and Biolabeling. *Chem. - Eur. J.* **2010**, *16*, 10103–10112.
- (22) Lin, C.-A. J.; Yang, T.-Y.; Lee, C.-H.; Huang, S. H.; Sperling, R. A.; Zanella, M.; Li, J. K.; Shen, J.-L.; Wang, H.-H.; Yeh, H.-I.; Parak, W. J.; Chang, W. H. Synthesis, Characterization, and Bioconjugation of Fluorescent Gold Nanoclusters toward Biological Labeling Applications. *ACS Nano* **2009**, *3*, 395–401.
- (23) Fernandez-Iglesias, N.; Bettmer, J. Synthesis, Purification and Mass Spectrometric Characterisation of a Fluorescent Au<sub>9</sub>@BSA Nanocluster and Its Enzymatic Digestion by Trypsin. *Nanoscale* **2014**, *6*, 716–721.
- (24) Yue, Y.; Liu, T.-Y.; Li, H.-W.; Liu, Z.; Wu, Y. Microwave-Assisted Synthesis of BSA-Protected Small Gold Nanoclusters and Their Fluorescence-Enhanced Sensing of Silver(I) Ions. *Nanoscale* **2012**, *4*, 2251–2254.
- (25) Mohanty, J. S.; Baksi, A.; Lee, H.; Pradeep, T. Noble Metal Clusters Protected with Mixed Proteins Exhibit Intense Photoluminescence. *RSC Adv.* **2015**, *5*, 48039–48045.
- (26) Le Guevel, X.; Hotzer, B.; Jung, G.; Hollemeyer, K.; Trouillet, V.; Schneider, M. Formation of Fluorescent Metal (Au, Ag) Nanoclusters Capped in Bovine Serum Albumin Followed by Fluorescence and Spectroscopy. *J. Phys. Chem. C* **2011**, *115*, 10955–10963.
- (27) Mathew, A.; Sajanlal, P. R.; Pradeep, T. A Fifteen Atom Silver Cluster Confined in Bovine Serum Albumin. *J. Mater. Chem.* **2011**, *21*, 11205–11212.
- (28) Mohanty, J. S.; Xavier, P. L.; Chaudhari, K.; Bootharaju, M. S.; Goswami, N.; Pal, S. K.; Pradeep, T. Luminescent, Bimetallic AuAg Alloy Quantum Clusters in Protein Templates. *Nanoscale* **2012**, *4*, 4255–4262.
- (29) Chan, P.-H.; Chen, Y.-C. Human Serum Albumin Stabilized Gold Nanoclusters as Selective Luminescent Probes for Staphylococcus Aureus and Methicillin-Resistant Staphylococcus Aureus. *Anal. Chem. (Washington, DC, U. S.)* **2012**, *84*, 8952–8956.
- (30) Xavier, P. L.; Chaudhari, K.; Verma, P. K.; Pal, S. K.; Pradeep, T. Luminescent Quantum Clusters of Gold in Transferrin Family Protein, Lactoferrin Exhibiting FRET. *Nanoscale* **2010**, *2*, 2769–2776.
- (31) Chaudhari, K.; Xavier, P. L.; Pradeep, T. Understanding the Evolution of Luminescent Gold Quantum Clusters in Protein Templates. *ACS Nano* **2011**, *5*, 8816–8827.
- (32) Le Guevel, X.; Daum, N.; Schneider, M. Synthesis and Characterization of Human Transferrin-Stabilized Gold Nanoclusters. *Nanotechnology* **2011**, *22*, 275103.
- (33) Kawasaki, H.; Hamaguchi, K.; Osaka, I.; Arakawa, R. pH-Dependent Synthesis of Pepsin-Mediated Gold Nanoclusters with Blue-, Green-, and Red-Fluorescent Emission. *Adv. Funct. Mater.* **2011**, *21*, 3508–3515.
- (34) Wen, F.; Dong, Y.; Feng, L.; Wang, S.; Zhang, S.; Zhang, X. Horseradish Peroxidase Functionalized Fluorescent Gold Nanoclusters for Hydrogen Peroxide Sensing. *Anal. Chem. (Washington, DC, U. S.)* **2011**, *83*, 1193–1196.
- (35) Li, M.; Yang, D.-P.; Wang, X.; Lu, J.; Cui, D. Mixed Protein-Templated Luminescent Metal Clusters (Au and Pt) for H<sub>2</sub>O<sub>2</sub> Sensing. *Nanoscale Res. Lett.* **2013**, *8*, 182.
- (36) Shi, H.; Ou, M. Y.; Cao, J. P.; Chen, G. F. Synthesis of Ovalbumin-Stabilized Highly Fluorescent Gold Nanoclusters and Their Application as an Hg<sup>2+</sup> Sensor. *RSC Adv.* **2015**, *5*, 86740–86745.
- (37) Liu, C.-L.; Wu, H.-T.; Hsiao, Y.-H.; Lai, C.-W.; Shih, C.-W.; Peng, Y.-K.; Tang, K.-C.; Chang, H.-W.; Chien, Y.-C.; Hsiao, J.-K.; Cheng, J.-T.; Chou, P.-T. Insulin-Directed Synthesis of Fluorescent Gold Nanoclusters: Preservation of Insulin Bioactivity and Versatility in Cell Imaging. *Angew. Chem., Int. Ed.* **2011**, *50*, 7056–7060.
- (38) Baksi, A.; Xavier, P. L.; Chaudhari, K.; Goswami, N.; Pal, S. K.; Pradeep, T. Protein-Encapsulated Gold Cluster Aggregates: The Case of Lysozyme. *Nanoscale* **2013**, *5*, 2009–2016.
- (39) Kawasaki, H.; Yoshimura, K.; Hamaguchi, K.; Arakawa, R. Trypsin-Stabilized Fluorescent Gold Nanocluster for Sensitive and Selective Hg<sup>2+</sup> Detection. *Anal. Sci.* **2011**, *27*, S91–S96.
- (40) Yu, Y.; Luo, Z.; Teo, C. S.; Tan, Y. N.; Xie, J. Tailoring the Protein Conformation to Synthesize Different-Sized Gold Nanoclusters. *Chem. Commun. (Cambridge, U. K.)* **2013**, *49*, 9740–9742.
- (41) Gao, X.; Chan, W. C. W.; Nie, S. Quantum-Dot Nanocrystals for Ultrasensitive Biological Labeling and Multicolor Optical Encoding. *J. Biomed. Opt.* **2002**, *7*, S32–S37.
- (42) Russell, B. A.; Jachimska, B.; Komorek, P.; Mulheran, P. A.; Chen, Y. Lysozyme Encapsulated Gold Nanoclusters: Effects of Cluster Synthesis on Natural Protein Characteristics. *Phys. Chem. Chem. Phys.* **2017**, *19*, 7228–7235.
- (43) Soleilhac, A.; Bertorelle, F.; Antoine, R. Sizing Protein-Templated Gold Nanoclusters by Time Resolved Fluorescence Anisotropy Decay Measurements. *Spectrochim. Acta, Part A* **2018**, *193*, 283–288.
- (44) Jin, R.; Zeng, C.; Zhou, M.; Chen, Y. Atomically Precise Colloidal Metal Nanoclusters and Nanoparticles: Fundamentals and Opportunities. *Chem. Rev. (Washington, DC, U. S.)* **2016**, *116*, 10346–10413.
- (45) Bootharaju, M. S.; Dey, R.; Gevers, L. E.; Hedhili, M. N.; Basset, J.-M.; Bakr, O. M. A New Class of Atomically Precise, Hydride-Rich Silver Nanoclusters Co-Protected by Phosphines. *J. Am. Chem. Soc.* **2016**, *138*, 13770–13773.
- (46) Ghosh, A.; Bodiuzzaman, M.; Nag, A.; Jash, M.; Baksi, A.; Pradeep, T. Sequential Dihydrogen Desorption from Hydride-Protected Atomically Precise Silver Clusters and the Formation of Naked Clusters in the Gas Phase. *ACS Nano* **2017**, *11*, 11145–11151.
- (47) De, P.; Li, M.; Gondi, S. R.; Sumerlin, B. S. Temperature-Regulated Activity of Responsive Polymer-Protein Conjugates Prepared by Grafting-from Via Raft Polymerization. *J. Am. Chem. Soc.* **2008**, *130*, 11288–11289.
- (48) Goswami, N.; Giri, A.; Bootharaju, M. S.; Xavier, P. L.; Pradeep, T.; Pal, S. K. Copper Quantum Clusters in Protein Matrix: Potential Sensor of Pb<sup>2+</sup> Ion. *Anal. Chem. (Washington, DC, U. S.)* **2011**, *83*, 9676–9680.
- (49) Chan, R.; Chen, V.; Bucknall, M. P. Quantitative Analysis of Membrane Fouling by Protein Mixtures Using MALDI-MS. *Biotechnol. Bioeng.* **2004**, *85*, 190–201.
- (50) Ghosh, D.; Baksi, A.; Mudella, S. K.; Nag, A.; Ganayee, M. A.; Subramanian, V.; Pradeep, T. Gold-Induced Unfolding of Lysozyme: Toward the Formation of Luminescent Clusters. *J. Phys. Chem. C* **2017**, *121*, 13335–13344.
- (51) Ghosh, D.; Mudella, S. K.; Islam, M. R.; Subramanian, V.; Pradeep, T. Conformational Changes of Protein Upon Encapsulation

of Noble Metal Clusters: An Investigation by Hydrogen/Deuterium Exchange Mass Spectrometry. *J. Phys. Chem. C* **2019**, *123*, 17598–17605.

(52) Maity, B.; Abe, S.; Ueno, T. Observation of Gold Sub-Nanocluster Nucleation within a Crystalline Protein Cage. *Nat. Commun.* **2017**, *8*, 14820.

(53) Chakraborty, S.; Joshi, P.; Shanker, V.; Ansari, Z. A.; Singh, S. P.; Chakrabarti, P. Contrasting Effect of Gold Nanoparticles and Nanorods with Different Surface Modifications on the Structure and Activity of Bovine Serum Albumin. *Langmuir* **2011**, *27*, 7722–7731.

(54) Cordova, J.; Ryan, J. D.; Boonyaratanakornkit, B. B.; Clark, D. S. Esterase Activity of Bovine Serum Albumin up to 160°C: A New Benchmark for Biocatalysis. *Enzyme Microb. Technol.* **2008**, *42*, 278–283.

(55) Sakurai, Y.; Ma, S.-F.; Watanabe, H.; Yamaotsu, N.; Hirono, S.; Kurono, Y.; Kragh-Hansen, U.; Otagiri, M. Esterase-Like Activity of Serum Albumin: Characterization of Its Structural Chemistry Using P-Nitrophenyl Esters as Substrates. *Pharm. Res.* **2004**, *21*, 285–292.

(56) Ahmad, B.; Kamal, M. Z.; Khan, R. H. Alkali-Induced Conformational Transition in Different Domains of Bovine Serum Albumin. *Protein Pept. Lett.* **2004**, *11*, 307–315.

(57) Hart, B. J.; Wilting, J.; de Gier, J. J. Evidence for Distinct Consecutive Steps in the Neutral to Base Transition of Human Serum Albumin. *Biochem. Pharmacol.* **1986**, *35*, 1005–1009.

## Supporting Information

### Internalization of a Preformed Atomically Precise Silver Cluster in Proteins by Multistep Events and Emergence of Luminescent Counterparts Retaining Bioactivity

*Debasmita Ghosh,<sup>1</sup> Mohammad Bodiuzzaman,<sup>1</sup> Anirban Som,<sup>1</sup> Sebastian Raja,<sup>2</sup> Ananya Baksi,<sup>1</sup> Atanu Ghosh,<sup>1</sup> Jyotirmoy Ghosh,<sup>1</sup> Akshayaa Ganesh,<sup>2</sup> Priyanka Samji,<sup>2</sup> Sundarasamy Mahalingam,<sup>2</sup> Devarajan Karunagaran,<sup>2</sup> and Thalappil Pradeep<sup>1\*</sup>*

<sup>1</sup>DST Unit of Nanoscience (DST UNS) and Thematic Unit of Excellence, Department of Chemistry, Indian Institute of Technology Madras, Chennai 600036, India

<sup>2</sup>Department of Biotechnology, Indian Institute of Technology Madras, Chennai 600036, India

#### Table of Contents

Number	Description	Page Number
SI	Protocols for the synthesis of [Ag <sub>18</sub> HSA] and [Ag <sub>13</sub> Lf]	S2
Figure S1	The EDS spectrum of the precipitate	S3
Figure S2	The EDS spectrum of the cluster	S4
Figure S3	Total XPS survey spectrum of Ag <sub>18</sub> @BSA	S5
Figure S4	Characterization of the Ag <sub>18</sub> @HSA cluster	S6
Figure S5	MALDI MS of the Ag <sub>18</sub> @HSA cluster	S7
Figure S6	Characterization of Ag <sub>13</sub> @Lf cluster	S8

<b>Table S1</b>	Number of cysteine/methionine, Trp/Tyr/His, and disulfide bridges present in BSA, HSA, and Lf	S9
<b>Figure S7</b>	Time dependent luminescence profile of the Ag <sub>18</sub> @BSA cluster	S10
<b>Figure S8</b>	Reaction of [Ag <sub>18</sub> H <sub>16</sub> (TPP) <sub>10</sub> ] <sup>2+</sup> with less amount of BSA	S11
<b>Figure S9</b>	Reaction of BSA with Ag NP	S12
<b>Figure S10</b>	Cell viability with Ag <sub>18</sub> @BSA	S13
<b>Figure S11</b>	Confocal fluorescence imaging of HeLa cells with NCs after 5 h incubation	S14
<b>Figure S12</b>	Z stacking of all images	S15
<b>Figure S13</b>	Phosphatase activity of pure Lf and Ag <sub>13</sub> @Lf	S16

#### **Protocol for the synthesis of [Ag<sub>18</sub>HSA]:**

25 mg HSA was dissolved in 1.6 mL Milli-Q water. Then stirred the solution for 1 min. Under stirring condition, 400 µL of I was added. The addition of I into the HSA solution made the reaction mixture turbid. The turbid solution was centrifuged after 12 h and from the supernatant the brown colored cluster solution was collected. This solution was used for characterization.

#### **Protocol for the synthesis of [Ag<sub>13</sub>Lf]:**

25 mg Lf was dissolved in 1.6 mL Milli-Q water. Then stirred the solution for 1 min. Under stirring condition, 400 µL of I was added. The addition of I into the Lf solution made the reaction mixture turbid. The turbid solution was centrifuged after 12 h and from the supernatant the brown colored cluster solution was collected. This solution was used for characterization.

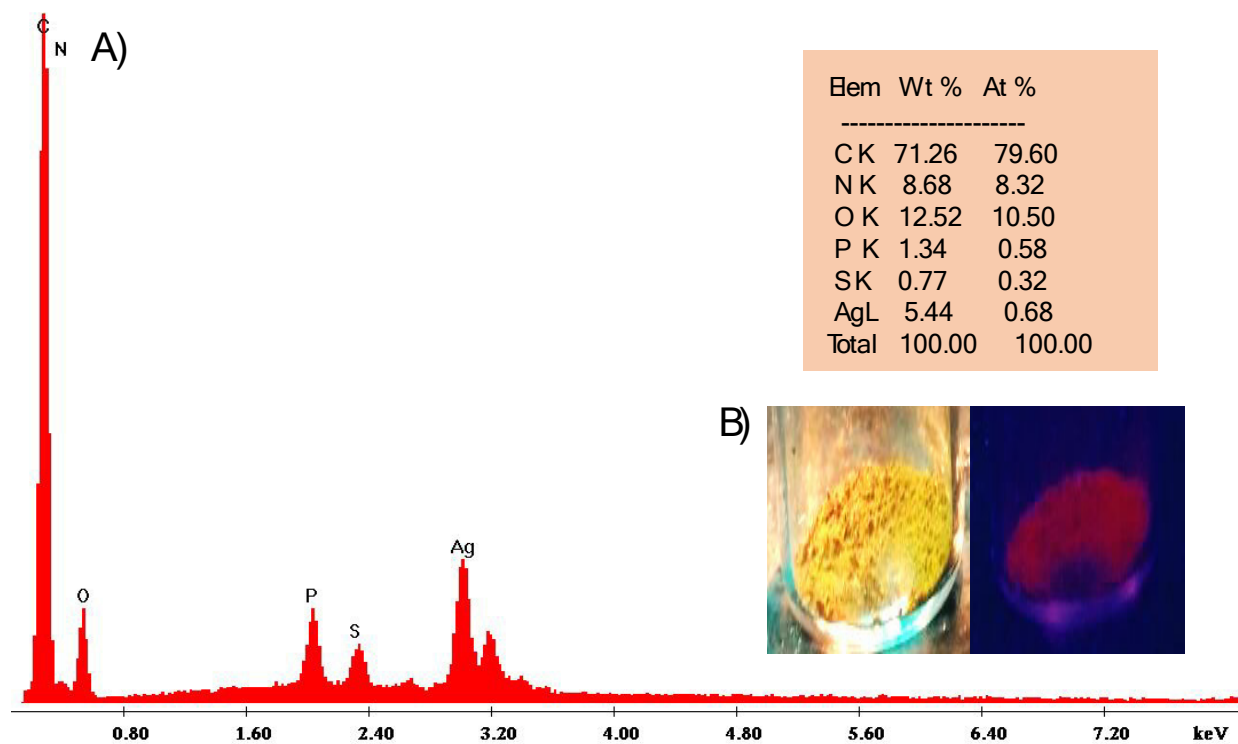


**Figure S1:** The EDS spectrum of the precipitate along with the quantification data (A). (B) is the image of the precipitate under visible light (left) and under UV light (right).

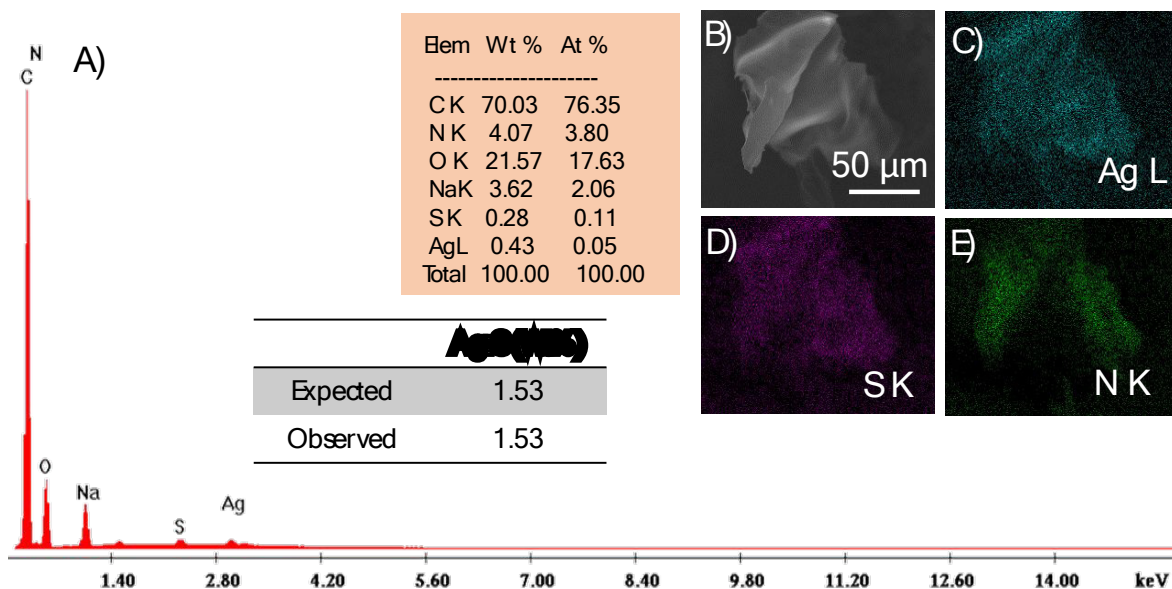


**Figure S2:** The EDS spectrum of the Ag<sub>18</sub>@BSA cluster along with the quantification data (A). (C–E) are the EDS images of the cluster collected using Ag Lα, S Kα, and N Kα emissions. Corresponding SEM image of the Ag<sub>18</sub>@BSA is shown in B. The quantification data suggest that the Ag:S ratio is in good agreement with the theoretical value for Ag<sub>18</sub>@BSA.

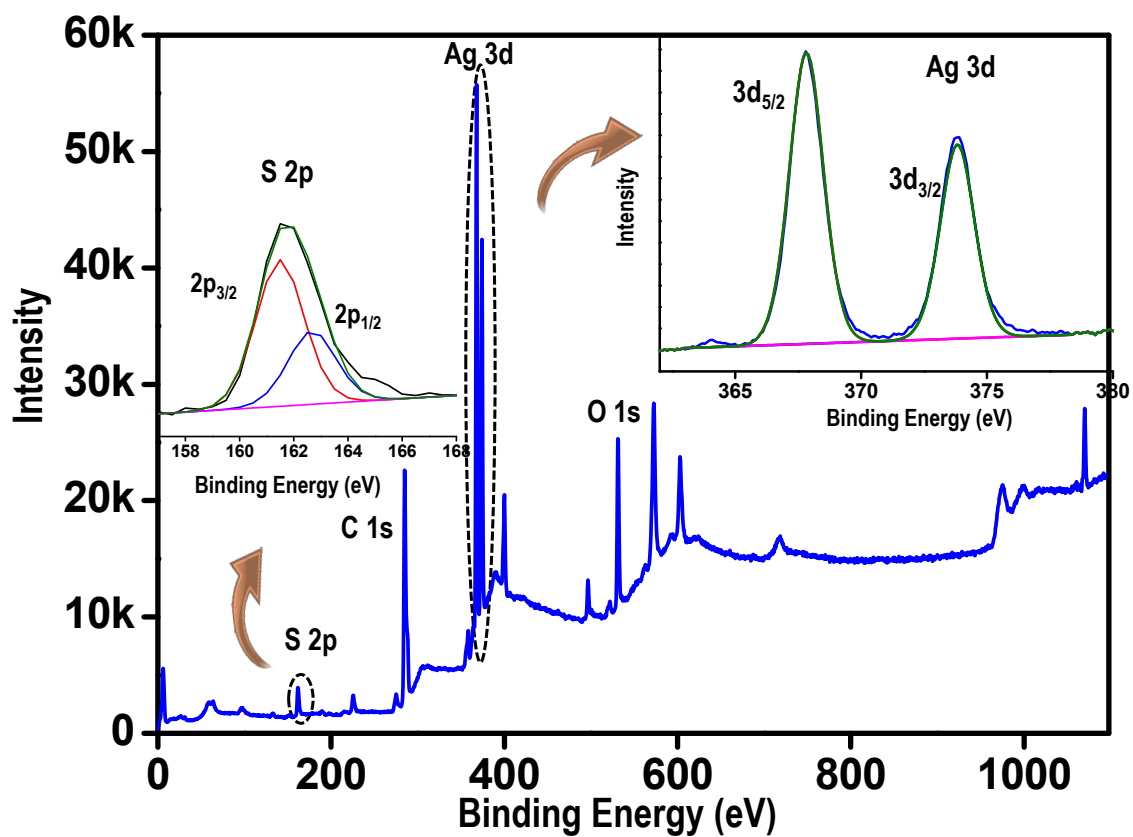


**Figure S3:** Total XPS survey spectrum of  $\text{Ag}_{18}\text{@BSA}$ . The insets show the spectra of the cluster in the Ag 3d region and S 2p regions.

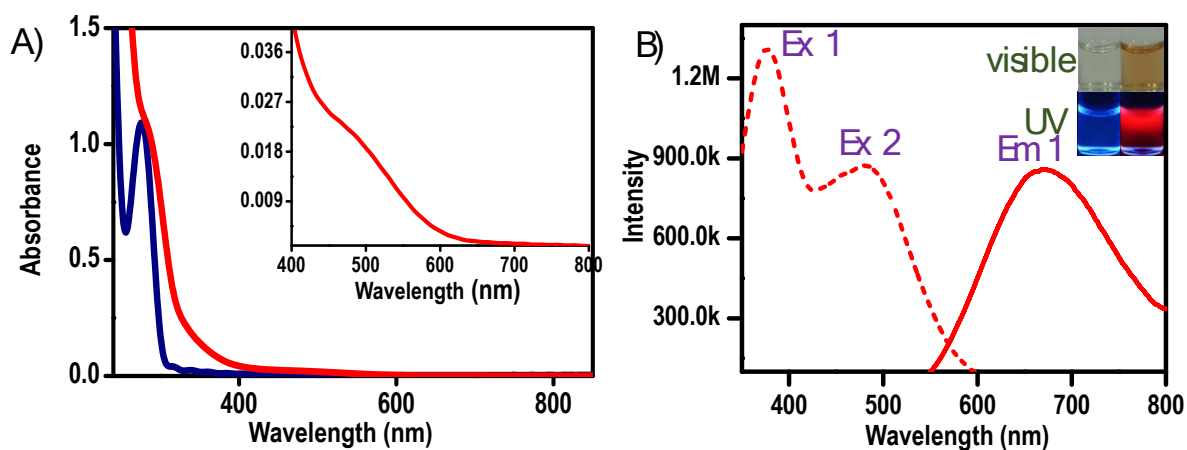


**Figure S4:** Characterization of the  $\text{Ag}_{18}\text{@HSA}$  cluster. (A) UV-vis profile of HSA (blue trace) and  $\text{Ag}_{18}\text{@HSA}$  cluster (red trace). (B) Luminescence profile of the  $\text{Ag}_{18}\text{@HSA}$  cluster. Inset shows the color of HSA and the cluster under visible light (top) and under UV light (bottom).



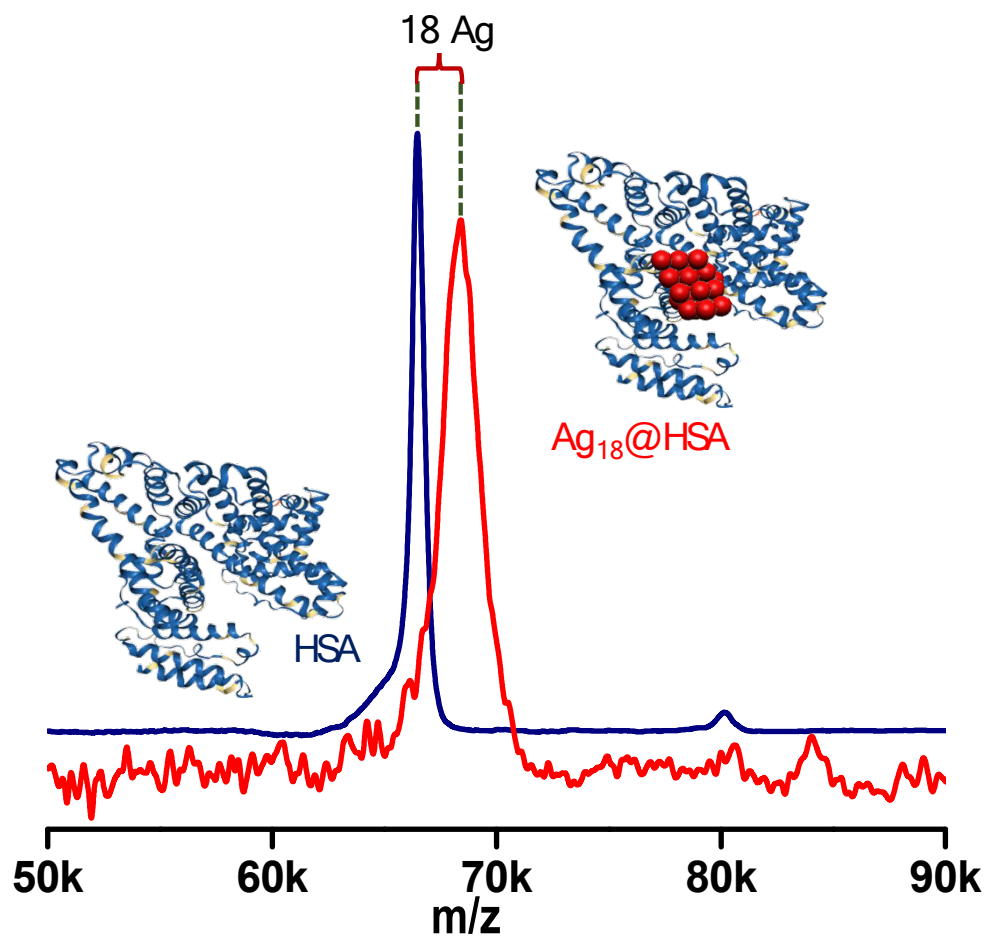


**Figure S5:** MALDI MS of pure HSA (blue trace) collected in linear positive ion mode using sinapic acid as matrix and that of the as-prepared red emitting  $Ag_{18}@HSA$  (red trace).

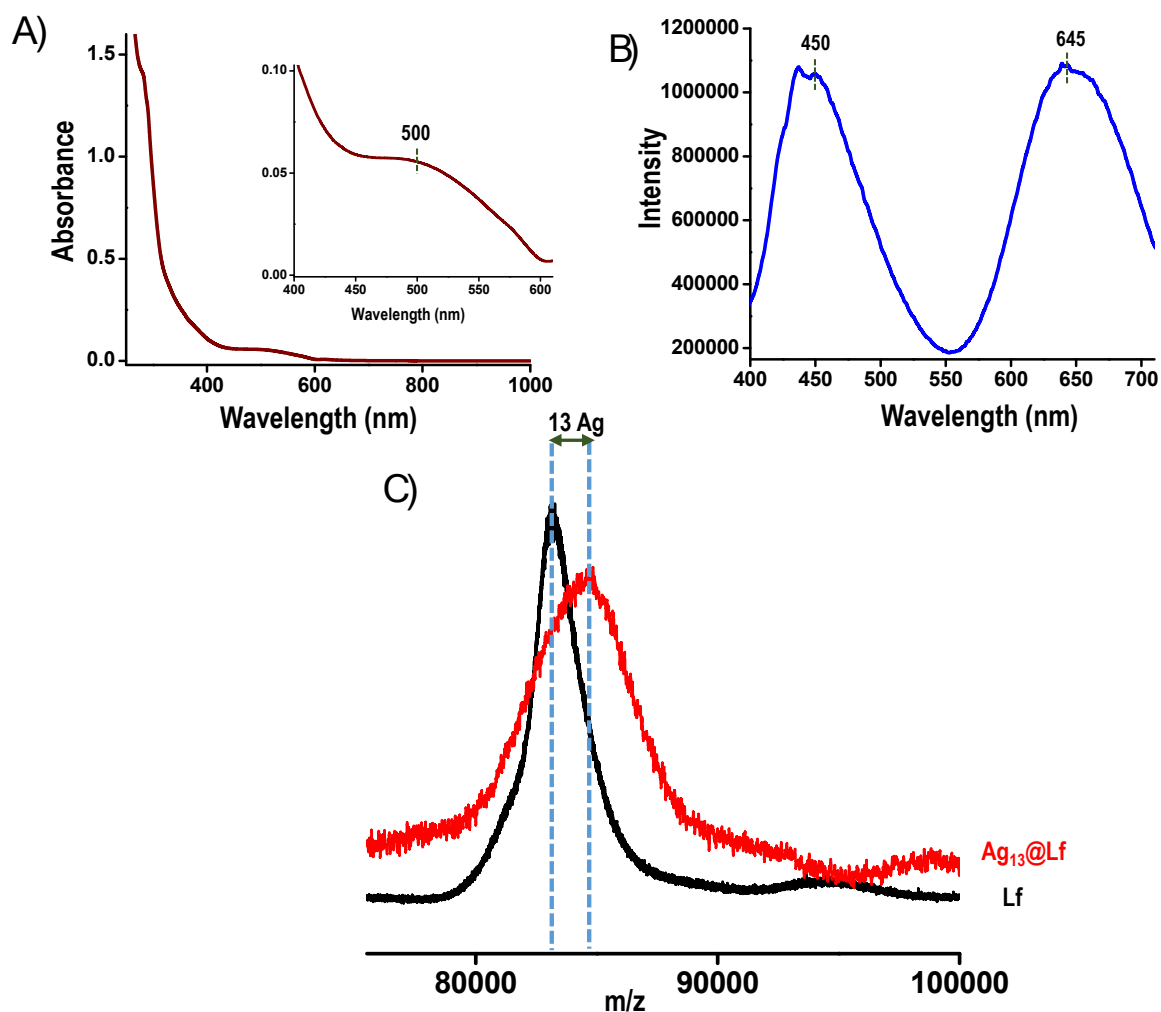


**Figure S6:** Characterization of  $\text{Ag}_{13}@\text{Lf}$  cluster. (A,B) UV-vis and luminescence spectra (excitation at 365 nm) of  $\text{Ag}_{13}@\text{Lf}$  cluster. C) MALDI MS spectra of the parent protein and the cluster showing the formation of the  $\text{Ag}_{13}@\text{Lf}$  cluster.

**Table S1:** Number of cysteine/methionine, Trp/Tyr/His, and disulfide bridges present in BSA, HSA, and Lf.

	Cys (C)	Met (M)	Trp (W)	Tyr (Y)	His (H)	Disulfide bond
BSA	35	5	2	19	17	17
HSA	35	5	1	16	17	17
Lf	33	3	13	19	10	16

Note: Though the molecular weight of Lf is high than BSA and HSA, the number of His residue present in Lf is less. Thus the ability of Lf to stabilize the small clusters formed at initial stage is expected to be lower than both BSA and HSA. This probably result in the formation of a smaller 13-atom Ag cluster in this case.

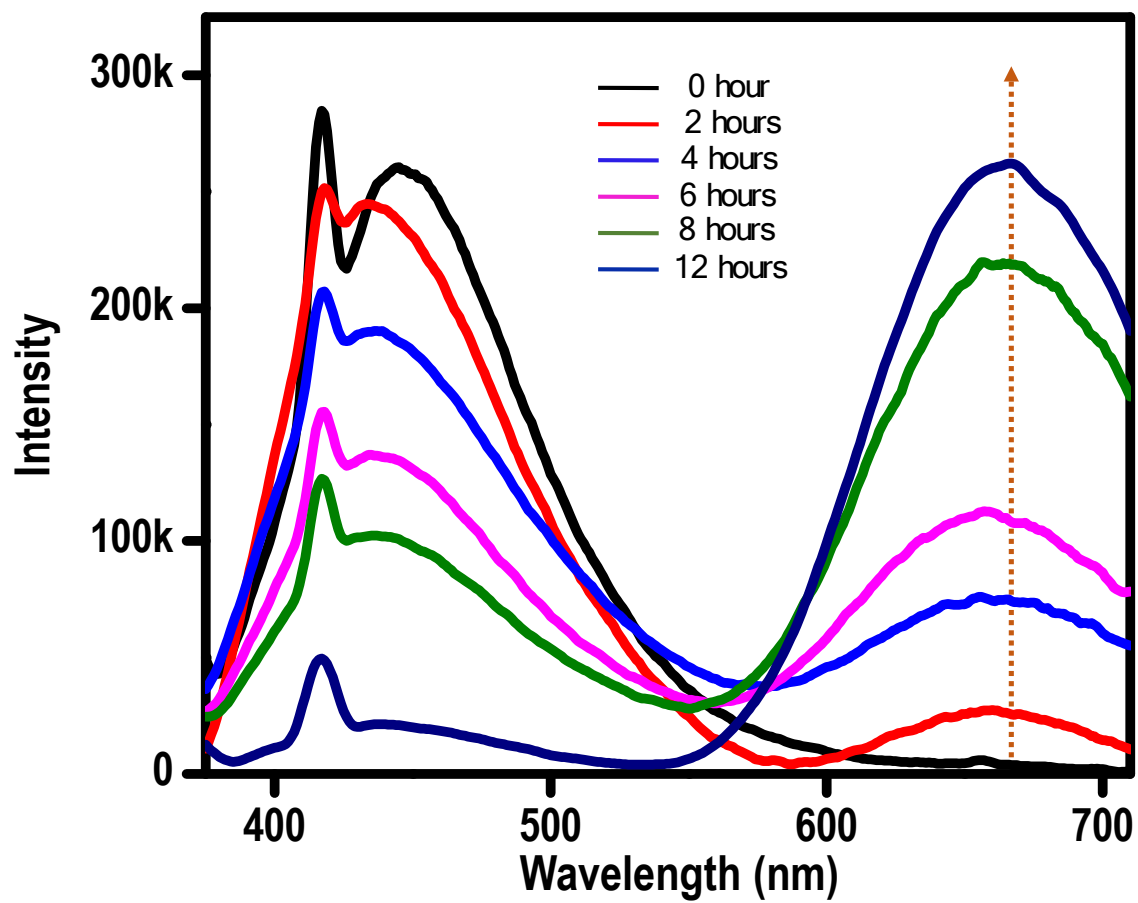


**Figure S7:** Time dependent luminescence profile of the Ag<sub>18</sub>@BSA cluster during synthesis.

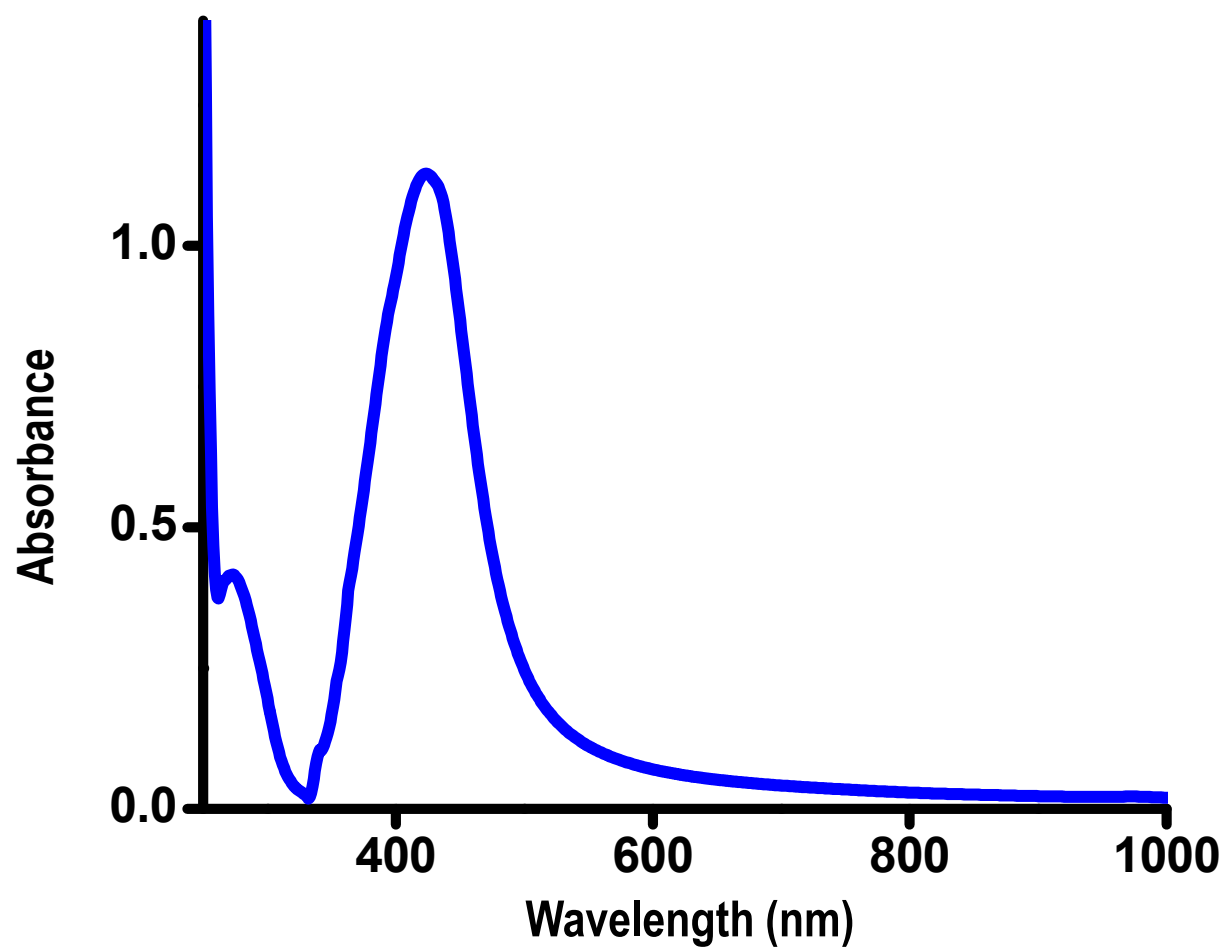


**Figure S8:** UV-vis profile of Ag nanoparticle formed in a reaction of  $[\text{Ag}_{18}\text{H}_{16}(\text{TPP})_{10}]^{2+}$  cluster with reduced concentration of protein.

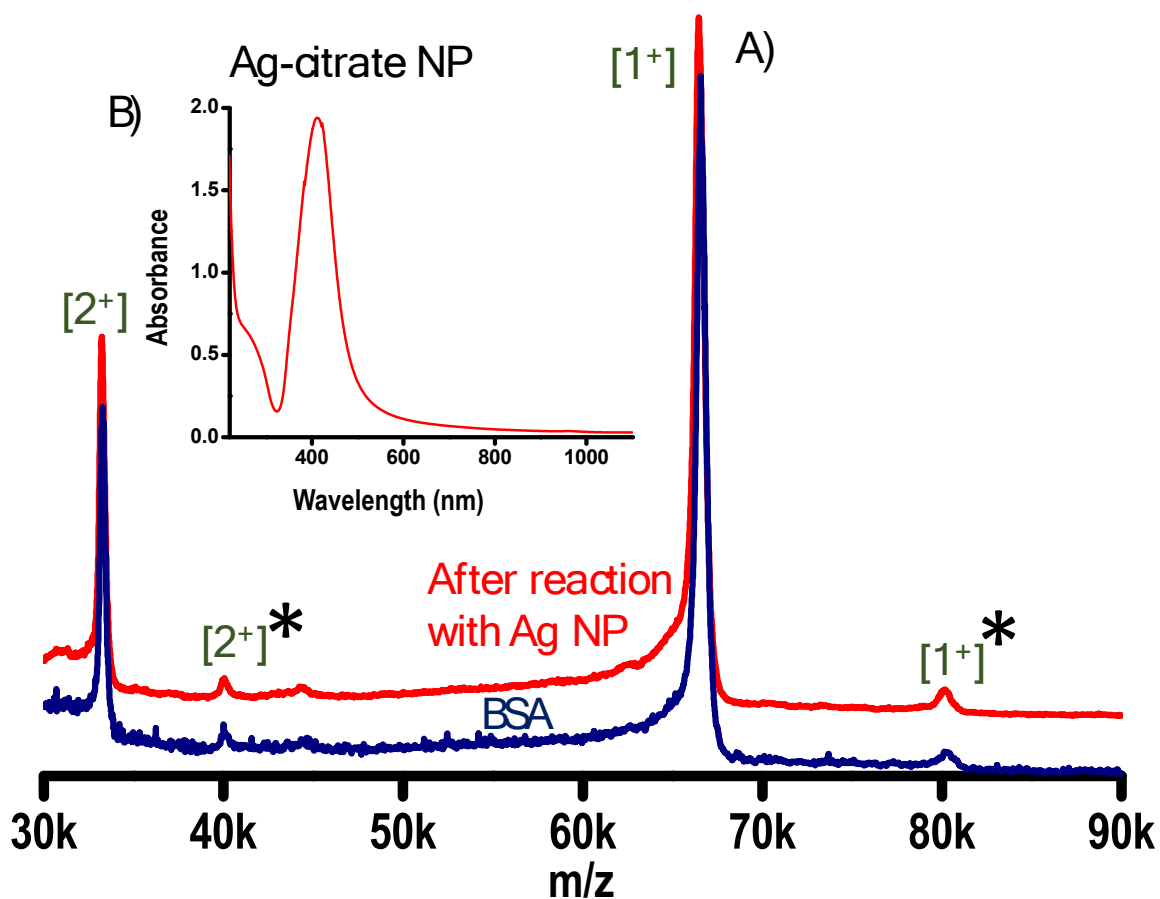


**Figure S9:** (A) MALDI MS of BSA before (blue) and after (red) reaction with Ag Nps. The presence of conalbumin in the BSA solution is indicated with an asterisk (\*). (B) UV-vis spectrum of Ag Nps.

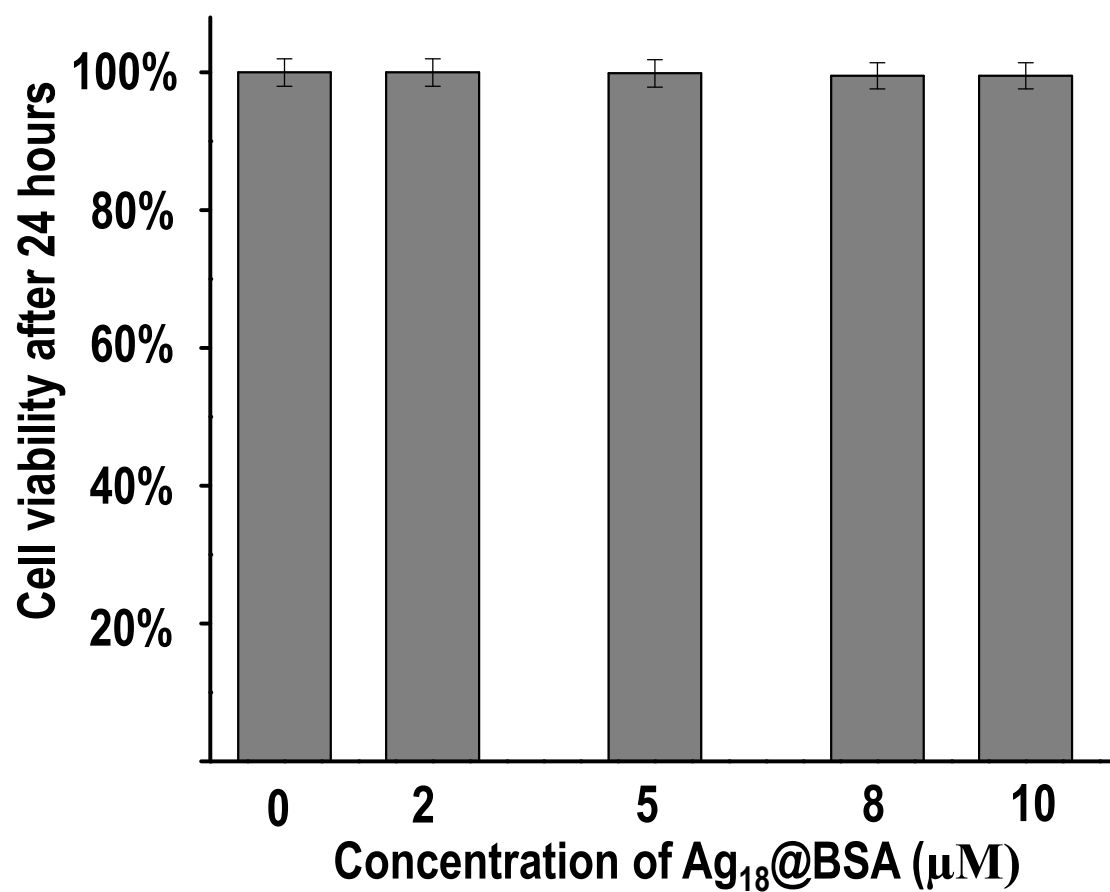


**Figure S10:** The viability of HeLa cells after treating with different concentrations of Ag<sub>18</sub>@BSA NCs for 24 hours. The viability was obtained by resazurin assay. The error bar represents standard error of 3 trials.

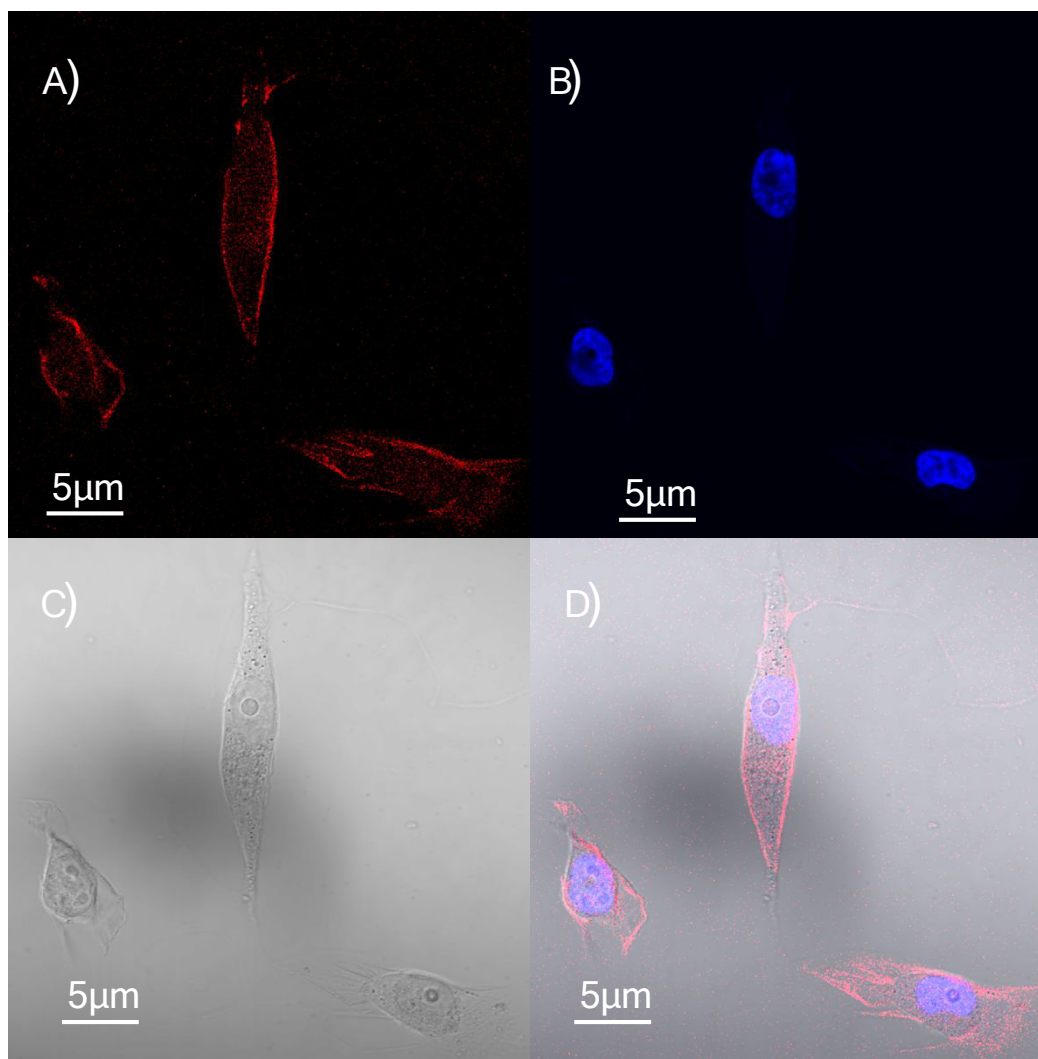


**Figure S11:** Microscopic images of the HeLa cells after 5 h incubation with NCs. (A) Fluorescence image of NCs in cells (B) Cell nucleus stained with DAPI. (C) Bright-field image of the corresponding fluorescence images. (D) An overlay of these three images.



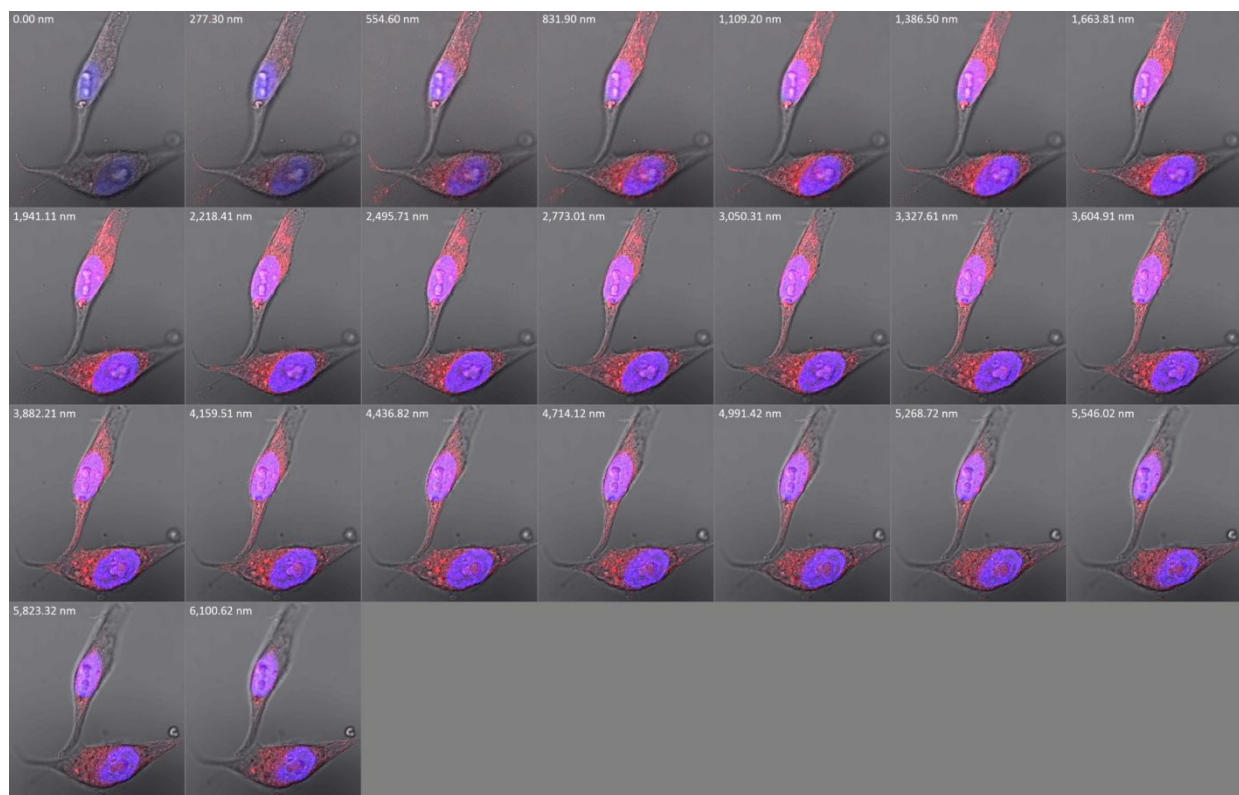


**Figure S12:** Z stacking images of cells shows the internalization of NCs in the HeLa cells.

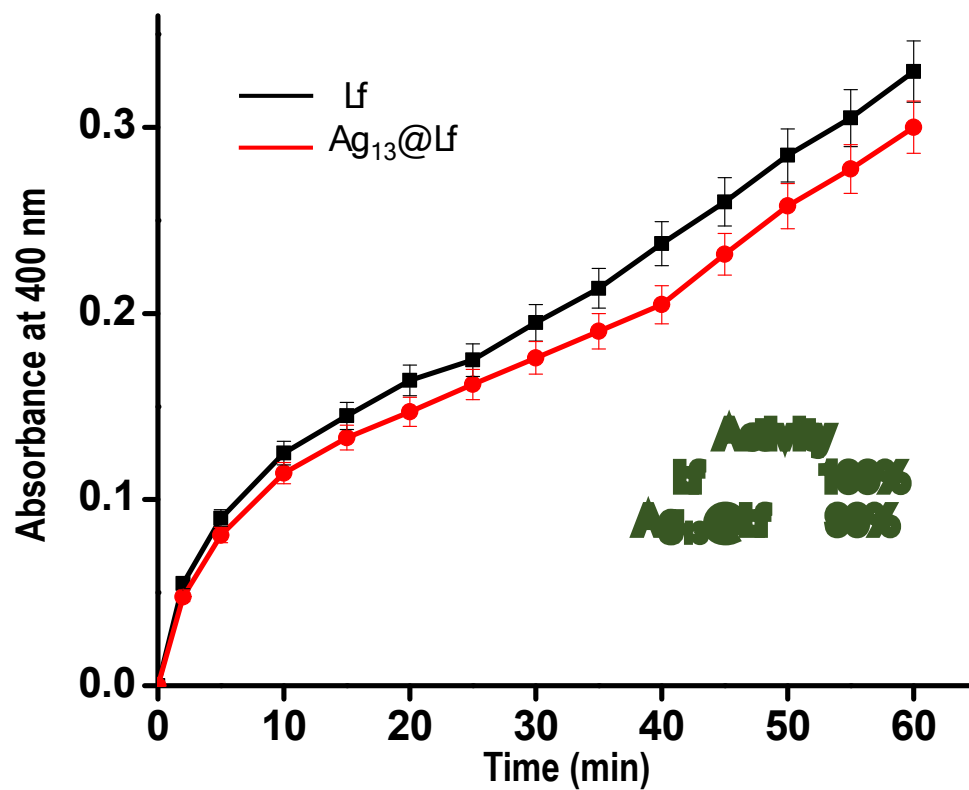


**Figure S13:** Phosphatase activity of pure Lf and Ag<sub>13</sub>@Lf clusters as a function of time. Cluster showed 90% catalytic activity.

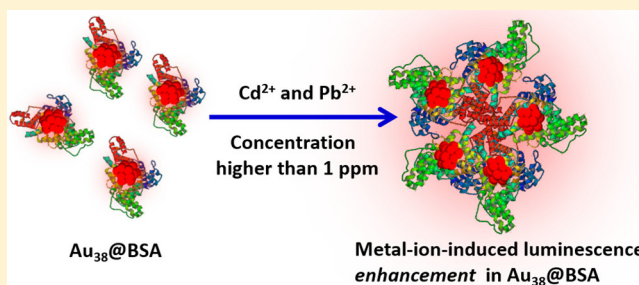
# Metal-Ion-Induced Luminescence Enhancement in Protein Protected Gold Clusters

Jyoti Sarita Mohanty, Kamalesh Chaudhari, Chennu Sudhakar, and Thalappil Pradeep\*

DST Unit of Nanoscience (DST UNS) and Thematic Unit of Excellence (TUE), Department of Chemistry, Indian Institute of Technology Madras, Chennai 600 036, India

## Supporting Information

**ABSTRACT:** We probed the interaction between  $\text{Au}_{38}@\text{BSA}$  and various heavy metal ions using luminescence spectroscopy. Interestingly,  $\text{Au}_{38}@\text{BSA}$  showed luminescence enhancement upon interaction with  $\text{Cd}^{2+}$  and  $\text{Pb}^{2+}$  at concentrations higher than 1 ppm, due to the formation of cluster aggregates. Such aggregates were detected by dynamic light scattering (DLS) and high resolution electron microscopy (HRTEM) studies. Luminescence enhancement of  $\text{Au}_{38}@\text{BSA}$  in the presence of  $\text{Cd}^{2+}$  was due to the interaction of  $\text{Cd}^{2+}$  with the cluster core, while  $\text{Pb}^{2+}$ -induced luminescence enhancement was due to BSA- $\text{Pb}^{2+}$  interaction. Observations were further supported by X-ray photoelectron spectroscopy (XPS) studies. This kind of phenomenon has been observed in protein protected clusters for the first time. We believe that such metal-ion-induced luminescence enhancement can be used to synthesize cluster systems with enhanced optical properties and different ion–cluster interactions can be used to develop metal ion sensors using  $\text{Au}_{38}@\text{BSA}$ .



## INTRODUCTION

The study of noble metal nanoclusters consisting of a few to hundred metal atoms has become fascinating due to their unique optical and electronic properties.<sup>1–4</sup> Especially, Au and Ag metal nanoclusters have been studied extensively due to their attractive optical properties. Such nanoclusters typically use thiols as protecting ligands, and various protocols in the solution phase<sup>1</sup> as well as solid state<sup>5</sup> have been developed for their synthesis. Macromolecular templates such as DNA,<sup>6</sup> dendrimers,<sup>7</sup> and most recently proteins,<sup>3,8,9</sup> have also been used for the synthesis of such nanoclusters. The most commonly used proteins are bovine serum albumin (BSA),<sup>8,10–13</sup> lysozyme (Lyz),<sup>14–16</sup> lactoferrin (Lf),<sup>17,18</sup> human serum albumin (HSA),<sup>19,20</sup> and a few others.<sup>3,21</sup> Protein protected noble metal clusters (PPCs) have been synthesized under basic pH and are stable over a wide pH range.<sup>8,10,18</sup> Typically the core of such nanoclusters is less than 2 nm in diameter. PPCs exhibit attractive optical, electronic, catalytic, and magnetic properties.<sup>22</sup> Luminescence of PPCs is stable under different pH conditions, and their quantum yield is high as compared to their monolayer protected counterparts. Due to the simple synthetic procedure and ease of modification with various functional groups, PPCs have been considered as major candidates for biolabeling, *in vivo* and *in vitro* imaging<sup>13,23</sup> and various sensing applications.<sup>3,22</sup> They are biocompatible due to lower metallic content and use of bulky proteins as ligands. High quantum yield and presence of various functionalities of PPCs can be used for highly selective and sensitive detection of analytes in various applications.

Owing to their small size, biocompatibility, luminescence, and low toxicity, PPCs are good candidates for sensing of metal ions<sup>24–26</sup> and small molecules.<sup>20,27–30</sup>

Intense photoluminescence (PL) is one of the most interesting properties of PPCs. According to the previous reports, the reason for the high quantum yield of such clusters is FRET between the protein shell and the core of the cluster.<sup>3,17</sup> Recently, Chevrier et al. have studied the structural and intense luminescence properties of the BSA-stabilized gold cluster in detail.<sup>31</sup> It is also possible to tune the luminescence property of nanoclusters by changing the composition through alloying,<sup>12</sup> doping,<sup>32</sup> etc. Enhancement of luminescence through different routes has been studied by several groups. In our previous report, we have shown that an Au cluster protected by mixed proteins shows 3-fold enhancement in luminescence due to FRET.<sup>33</sup> Luo et al. have reported aggregation-induced luminescence enhancement of Au(I) thiolate where they have shown that the Au(I) thiolate shell surrounding the Au(0) core plays a role in enhancing the luminescence.<sup>34</sup> Metal-induced luminescence enhancement has been reported by Muhammed et al.,<sup>13</sup> where they found that the enhancement of luminescence in  $\text{Au}_{\text{QC}}@\text{BSA}$  was due to Ag nanoparticles where protein acts as a spacer between the gold cluster and the nanoparticles. A similar study has been demonstrated for glutathione-capped Au clusters by Ji et al.,

Received: August 2, 2019

Revised: October 29, 2019

Published: November 4, 2019



where they have found that the enhancement was due to the formation of aggregates through GSH–Pb<sup>2+</sup> interaction.<sup>35</sup> Exchanging the core with other metals can significantly change the luminescence property of a cluster as shown by Wang et al., where they observed drastic fluorescence enhancement in an Au cluster when it was doped with Ag atoms.<sup>32</sup>

It can be concluded from the above discussion that reactivity of clusters with metal ions can change their properties drastically. In particular, heavy metal ions can react with clusters in different ways, either with the core or with the protecting shell. Heavy metal ion contamination is one of the serious threats to human health and environment due to their toxic effects. Some of the heavy metals are biologically essential such as copper (Cu),<sup>36</sup> zinc (Zn),<sup>37</sup> and iron (Fe)<sup>38</sup> but at higher concentrations they can lead to toxicity while other heavy metals, namely, mercury (Hg),<sup>39</sup> cadmium (Cd),<sup>40</sup> and lead (Pb),<sup>41</sup> are not biologically essential, and their presence even at lower concentrations can cause harm to the organism.<sup>42</sup> Although various conventional analytical techniques have been used for analyzing metal ions,<sup>43,44</sup> PL spectroscopy is one of the simplest tools for such analysis.<sup>13,24,25,45</sup>

Due to strong surface plasmon resonance and its dependence on the surface protection, gold nanoparticles have been employed to detect heavy metal ions.<sup>46,47</sup> DNzyme biosensors also showed good selectivity and sensitivity for detecting heavy metal ions.<sup>48</sup> PPCs are highly sensitive to the presence of specific metal ions and due to their high quantum yield, change in luminescence can be visualized with naked eyes and thus it can be an ideal candidate for sensing metal ions. Xie et al. have shown for the first time that BSA-stabilized Au clusters can be used for sensing Hg<sup>2+</sup>, which quenches the luminescence of the former completely.<sup>24</sup> Sensing of Cu<sup>2+</sup> ions in live cells using Au<sub>QC</sub>@BSA has been reported by Durgadas et al.<sup>49</sup> Zeptomolar detection of explosives such as TNT and Hg<sup>2+</sup> by using a hybrid material of Ag<sub>QC</sub>@BSA and Au mesoflower has been shown by Mathew et al.<sup>27</sup> Goswami et al. have reported quenching of Pb<sup>2+</sup> using Cu<sub>QC</sub>@BSA.<sup>45</sup> Several other groups have also demonstrated sensing of various metal ions through luminescence quenching.<sup>3,22</sup>

Here in this paper, we report the luminescence enhancement in Au<sub>38</sub>@BSA through metal-ion-induced aggregation. This phenomenon has been observed for the first time. It was found that Au<sub>38</sub>@BSA forms aggregates when treated with higher concentrations of Cd<sup>2+</sup> and Pb<sup>2+</sup> which leads to a significant change in their luminescence property. The resulting aggregates were thoroughly characterized using various spectroscopic and microscopic techniques. The effect of Cd<sup>2+</sup> and Pb<sup>2+</sup> on Au<sub>38</sub>@BSA has been studied in detail.

## EXPERIMENTAL METHODS

**Reagents and Materials.** All the chemicals were commercially available and used without further purification. Bovine serum albumin (pH 6–7, SRL Chemical Co. Ltd., India), sodium hydroxide (RANKEM, India), tetrachloroauric acid trihydrate (CDH, India), PbCl<sub>2</sub> (CDH, India), CdCl<sub>2</sub> (CDH, India), FeCl<sub>2</sub> (CDH, India), HgCl<sub>2</sub> (Merck, India), CuCl<sub>2</sub> (Merck, India), and Sinapinic acid (Sigma-Aldrich) were used for the experiments. Triply distilled water was used for all the experiments.

**Instrumentation.** UV–vis spectra were collected using a PerkinElmer Lambda 25 spectrometer in the range of 200–1100 nm with a scan rate of 480 nm per minute. Luminescence

measurements were carried out using a Jobin Yvon NanoLog spectrometer. For both excitation and emission, spectra were collected with a band-pass of 3 nm and the samples were excited at 365 nm. High resolution transmission electron microscopy (HRTEM) was performed with a JEOL 3010 instrument working at 300 kV, equipped with an ultra high resolution (UHR) polepiece. Energy dispersive X-ray analysis (EDS) was carried out with an Oxford EDAX housed in the TEM. Sample for HRTEM was prepared by dropping the dispersion on a carbon coated copper grid and drying under ambient conditions. MALDI MS study was conducted using an Applied Biosystems Voyager DE PRO Biospectrometry Workstation. A pulsed nitrogen laser of 337 nm was used for the studies and an average of 250 shots was used for each spectrum measurement. Sinapinic acid was used as the matrix for MALDI MS measurement. Dynamic light scattering (DLS) measurements were performed using a Malvern Zetasizer ZSP instrument. X-ray photoelectron spectroscopy (XPS) studies were carried out with an Omicron ESCA probe spectrometer with polychromatic Mg K $\alpha$  X-rays ( $h\nu = 1253.6$  eV). The samples were spotted as drop cast films on a sample stub.

**Synthesis.** *Synthesis of Au<sub>QC</sub>@BSA.* Au<sub>QC</sub>@BSA was synthesized as reported previously.<sup>8</sup> In a typical synthesis, 1 mL of 6 mM tetrachloroauric acid trihydrate (HAuCl<sub>4</sub>·3H<sub>2</sub>O) solution was added to 25 mg of BSA powder in 1 mL of distilled water, under vigorous stirring. The mixture was allowed to stir for 5 min. Then 100  $\mu$ L of 1 M NaOH was added to the above mixture and stirred for 12 h until the solution turned golden brown in color. The reaction was carried out at room temperature. The solution of Au<sub>QC</sub>@BSA was stored at 4 °C for further use.

*Study of Interaction of Au<sub>38</sub>@BSA with Different Metal Ions.* For performing metal ion interaction studies with Au<sub>QC</sub>@BSA, various metal ions such as Cd<sup>2+</sup>, Pb<sup>2+</sup>, Hg<sup>2+</sup>, Fe<sup>2+</sup>, and Cu<sup>2+</sup> were chosen. Metal ion solutions of various concentrations were obtained by serial dilution of the stock solution. Typically, 5  $\mu$ L of the cluster solution was diluted 400 times with distilled water. To study the interaction, different concentrations of metal ions were added to the above-mentioned cluster solution. After addition, the solution was mixed well and incubated for 2 min before recording the luminescence spectrum. It is well-known that Cu<sup>2+</sup> and Hg<sup>2+</sup> ions can quench the luminescence of Au<sub>QC</sub>@BSA but the interaction of Au<sub>QC</sub>@BSA with other metal ions has not been studied in detail. Therefore, from the perspective of toxic heavy metal ions, interactions of Cd<sup>2+</sup> and Pb<sup>2+</sup> were studied in detail.

## RESULTS AND DISCUSSION

**Spectroscopic and Microscopic Characterizations of Au<sub>QC</sub>@BSA.** Synthesis and characterization of gold cluster within BSA template was reported by Xie et al.<sup>8</sup> Briefly, the addition of HAuCl<sub>4</sub>·3H<sub>2</sub>O to BSA forms Au<sup>+</sup>–BSA complex. BSA contains 21 tyrosine residues which can reduce Au<sup>3+</sup> to Au<sup>+</sup>. Further reduction of Au<sup>+</sup> to Au<sup>0</sup> occurs by adding NaOH into the mixture. At alkaline pH, BSA acts both as a reducing and as a capping agent for Au cluster synthesis.<sup>18</sup> Due to the bulkiness of BSA, it provides steric protection to the cluster. Au<sub>QC</sub>@BSA has been characterized using different spectroscopic and microscopic techniques (Figure 1), and the core of the cluster has been assigned using MALDI MS study (Figure S1).



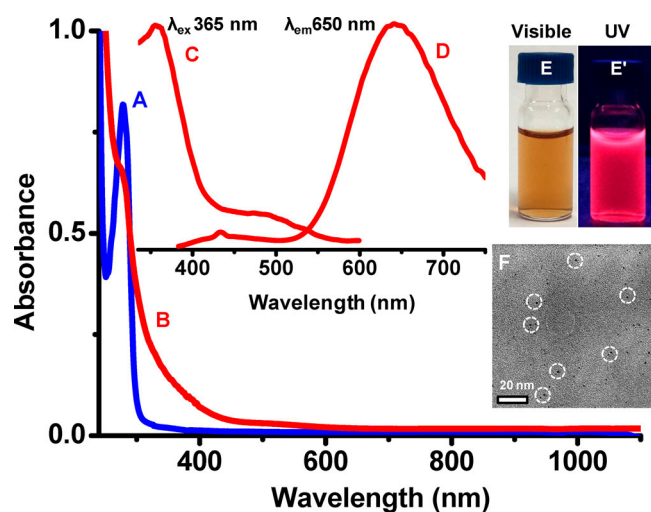


**Figure 1.** Comparison of UV-vis spectra for (A) pure BSA and (B)  $\text{Au}_{38}\text{@BSA}$ . PL (C) excitation and (D) emission spectra of the cluster. The cluster shows an emission maximum at 645 nm and an excitation maximum at 365 nm. Inset shows the photograph of cluster solution under (E) visible and (E') UV light. (F) HRTEM image of the sample shows a core size of around 1.8 nm. The clusters are shown with dotted circles. Scale bar in the HRTEM image is 20 nm.

A comparison between UV-vis absorption spectra for pure BSA and  $\text{Au}_{38}\text{@BSA}$  is depicted in parts A and B of Figure 1, respectively. BSA shows an absorption feature at 280 nm due to the presence of aromatic amino acids such as tyrosine and tryptophan residues. In the case of  $\text{Au}_{38}\text{@BSA}$ , a decrease in the absorption intensity at 280 nm was observed along with a shoulder at 375 nm as compared to that of pure BSA. The absence of a well-defined absorption feature in the case of clusters has been attributed to the encapsulation of the cluster by bulky BSA.<sup>13</sup> The PL excitation and emission spectra of the cluster are presented in parts C and D of Figure 1, respectively. Two excitation maxima around 365 and 500 nm were observed for the cluster as previously reported.<sup>12</sup> When the cluster was excited at 365 nm, two emission maxima, one around 450 nm which is due to weak luminescence from the protein and the other at 645 nm because of emission from the cluster, were found. The cluster showed bright red luminescence and photographs of the cluster under visible light and UV light are shown in Figure 1, parts E and E', respectively. To study the size of clusters, HRTEM analysis was performed (Figure 1F). The core of the cluster was found to be below 2 nm, and no particles of bigger size were found. MALDI MS study was performed to assign the core of the cluster. The calculated mass difference between the parent protein and the cluster formed provides the number gold atoms present in the core of the cluster.  $\text{Au}_{38}\text{@BSA}$  has a peak at  $m/z \sim 74\,210$  and the mass difference between  $\text{Au}_{38}\text{@BSA}$  and BSA ( $m/z \sim 66\,700$ ) was  $\sim 7.5$  kDa, suggesting the formation of  $\text{Au}_{38}\text{@BSA}$ . So, henceforth  $\text{Au}_{38}\text{@BSA}$  will be referred as  $\text{Au}_{38}\text{@BSA}$ .

With this background, our studies on the interaction of different metal ions with the cluster are discussed in the next section.

**Metal-Induced Enhancement of Photoluminescence in  $\text{Au}_{38}\text{@BSA}$ .** Clusters can interact with various metal ions through chemical functionalities of the protein or through the metal core. Interaction between different metal ions and clusters can bring changes in the PL as well as other properties of the cluster. Here, we have studied the effect of various metal

ions such as  $\text{Cd}^{2+}$  and  $\text{Pb}^{2+}$  on the PL of  $\text{Au}_{38}\text{@BSA}$ . The emission spectra for  $\text{Au}_{38}\text{@BSA}$  and BSA in the presence of  $\text{Cd}^{2+}$  and  $\text{Pb}^{2+}$  ions at different concentrations are shown in Figure 2.

As shown in Figure 2A, different concentrations of  $\text{Cd}^{2+}$  were added to  $\text{Au}_{38}\text{@BSA}$  to monitor its effect on the luminescence profile. A decrease in the PL intensity was observed upon addition of 100 ppb  $\text{Cd}^{2+}$ . However, at 500 ppb, instead of further decrease, it leads to an increase in the PL intensity. Moreover, the addition of 1 ppm of  $\text{Cd}^{2+}$  resulted in higher emission intensity as compared to the parent cluster. With further increase in the concentration of  $\text{Cd}^{2+}$  from 1 to 10 ppm, luminescence intensity increased systematically. A gradual blue shift in the emission peaks from 650 to 630 nm was also noticed in the process, and when the concentration of  $\text{Cd}^{2+}$  reached at 10 ppm, it resulted in a  $\sim 2.7$  fold enhancement of emission intensity. To find out the role of BSA on  $\text{Cd}^{2+}$  and  $\text{Au}_{38}\text{@BSA}$  interaction, similar concentrations of  $\text{Cd}^{2+}$  were added to BSA, and emission spectra were collected (Figure 2B). BSA showed an emission maximum  $\sim 335$  nm when excited at 280 nm. At lower concentrations of  $\text{Cd}^{2+}$ , no change in the protein emission was noticed. Upon addition of increasing concentrations of  $\text{Cd}^{2+}$ , changes in the luminescence of BSA were less marked and were opposite to that of  $\text{Au}_{38}\text{@BSA}$ . Thus, it is suggested that PL enhancement in  $\text{Au}_{38}\text{@BSA}$  is due to the interaction of  $\text{Cd}^{2+}$  with the cluster core and not with the protein shell. Further studies with DLS and HRTEM were performed to understand the effect of  $\text{Cd}^{2+}$  on  $\text{Au}_{38}\text{@BSA}$ . These results are discussed in the next section of the paper.

Similar measurements were conducted to know the effect of  $\text{Pb}^{2+}$  on the PL properties of  $\text{Au}_{38}\text{@BSA}$ . Upon addition of 100 ppb of  $\text{Pb}^{2+}$ , a decrease in the PL intensity of  $\text{Au}_{38}\text{@BSA}$  was observed (Figure 2C) which was similar to that of  $\text{Cd}^{2+}$ . Further addition of  $\text{Pb}^{2+}$  (500 ppb to 10 ppm) resulted in a gradual increase in the luminescence intensity. Addition of 10 ppm  $\text{Pb}^{2+}$  caused a  $\sim 1.6$  fold enhancement of the cluster. To understand the role of protein in this interaction, similar concentrations of  $\text{Pb}^{2+}$  were added to BSA. A systematic decrease in the protein emission was observed with increase in concentration of  $\text{Pb}^{2+}$  from 100 ppb to 10 ppm without any change in the position of emission.  $\text{Pb}^{2+}$  has a tendency to bind to proteins which could induce the aggregation of clusters through protein-protein interaction.<sup>35</sup> Such aggregation can result in aggregation-induced enhancement in luminescence. Although enhancement was observed in the presence of both the metal ions,  $\text{Cd}^{2+}$  showed a higher enhancement than  $\text{Pb}^{2+}$  at similar concentration, although reasons for enhancement could be different in both the cases. In the case of  $\text{Cd}^{2+}$ , major interaction was with the core and in the case of  $\text{Pb}^{2+}$ , major interaction was with the protein shell of the cluster. A shift in the cluster emission toward the blue region upon interaction with  $\text{Cd}^{2+}$  also suggests that the core itself is changing after interaction with  $\text{Cd}^{2+}$ . The calculated quantum yields for  $\text{Au}_{38}\text{@BSA}$  and  $\text{Au}_{38}\text{@BSA}$  in the presence of  $\text{Pb}^{2+}$  and  $\text{Cd}^{2+}$  were found to be 8.0%, 13.0% and 15.0%, respectively.

Control PL study was performed to check the sensitiveness of the incubation time (Figure S2A). Same parameters were maintained during each measurement. No enhancement in the emission intensity was observed in the parent cluster over time. During the course of time, no precipitates were seen either in the solution of parent cluster or in the presence of  $\text{Pb}^{2+}$  and  $\text{Cd}^{2+}$ . Time-dependent changes in  $I_{650}$  of  $\text{Au}_{38}\text{@BSA}$  upon

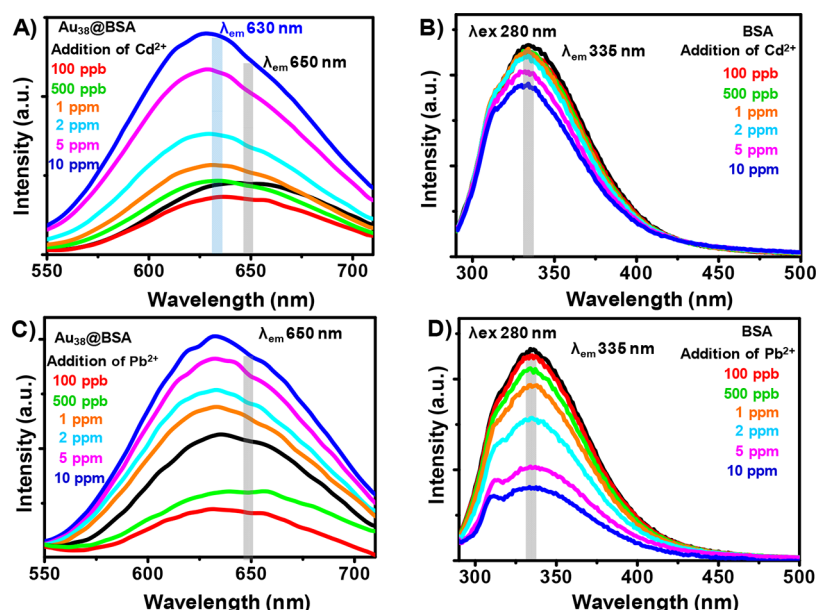


**Figure 2.** PL emission spectra of Au<sub>38</sub>@BSA after treatment with (A) Cd<sup>2+</sup> and (C) Pb<sup>2+</sup>. The PL emission spectra of BSA after treatment with (B) Cd<sup>2+</sup> and (D) Pb<sup>2+</sup>. Excitation wavelengths for Au<sub>38</sub>@BSA and BSA are 365 and 280 nm, respectively.

addition of 1 ppm concentration of Pb<sup>2+</sup> and Cd<sup>2+</sup> were measured to check the stability of the cluster. When Pb<sup>2+</sup> (Figure S2B) and Cd<sup>2+</sup> (Figure S2C) were added to the cluster solution, a large increase in *I*<sub>650</sub> counts was observed, which was stable over long time. This suggested that the *enhancement* in emission intensity was due to the presence of Pb<sup>2+</sup> and Cd<sup>2+</sup>.

UV–vis absorption spectra of Au<sub>38</sub>@BSA in the absence and presence of metal ions have been measured (Figure S3). As mentioned earlier, prominent absorption features were absent in protein protected gold clusters due to encapsulation by the bulky protein. The absorption peak at 280 nm is the characteristic feature of aromatic amino acids of the protein. No prominent change in the absorption features was seen upon adding Cd<sup>2+</sup> to the cluster solution while a significant change was found upon Pb<sup>2+</sup> addition. This change indicated that there is an interaction of Pb<sup>2+</sup> with the protein shell of the cluster which also supports the PL studies.

**Metal-Ion-Induced Aggregation Studies of Au<sub>38</sub>@BSA by DLS and HRTEM.** To investigate the effect of metal ions on the size of Au<sub>38</sub>@BSA, DLS measurements were performed (Figure 3, parts A and B). From the DLS study, the size of BSA was found to be ~ 7.6 nm and parent Au<sub>38</sub>@BSA has a size of ~ 9.7 nm, which are closely matching with the values reported (Figure S4).<sup>50</sup> This suggested that the cluster core to be of ~ 2.1 nm and this value is slightly more than the size observed in HRTEM analysis (Figure 1F). The larger size observed in DLS measurement than by HRTEM is due to the presence of a solvation shell around the cluster in water. The volume fraction-dependent DLS measurement was carried out for the parent cluster. But no change in the size was observed with increase in concentration of the cluster (Figure S5). Figure 3A shows the changes in the size distributions of Au<sub>38</sub>@BSA when different concentrations of Cd<sup>2+</sup> were added to the former. Size of the cluster (9.7 nm) increased gradually upon interaction with increasing concentrations of Cd<sup>2+</sup>, and finally, it reached ~40 nm at 10 ppm of Cd<sup>2+</sup>. Similar results were also obtained in the case of Pb<sup>2+</sup> (Figure 3B) but at 10 ppm, it led to bigger aggregates of the clusters. Changes in the size of the parent cluster in the presence of Cd<sup>2+</sup> and Pb<sup>2+</sup> implied that the

interaction of both the metal ions with the cluster induced their aggregation.

To further confirm the aggregation of the cluster, HRTEM analysis was performed at a higher concentration of metal ions (Figure 3, parts C, C', D, and D'). TEM images of the clusters with Cd<sup>2+</sup> are shown in Figure 3, parts C and C'. It clearly shows aggregation of the clusters. Similar aggregates were also found in the case of Pb<sup>2+</sup> (Figure 3, parts D and D'). Compact aggregation of clusters was seen in this case (Figure 3D). These aggregates are mostly spherical in shape. Magnified image of one such spherical aggregate is shown in Figure 3D'. In both the cases, sizes of the clusters are much larger than the parent one (Figure 1F). This result confirms the metal-ion-induced aggregation of the cluster. The presence of Cd<sup>2+</sup> and Pb<sup>2+</sup> has been confirmed by EDS analyses (Figures S6 and S7).

**XPS Studies of Au<sub>38</sub>@BSA in the Presence of Cd<sup>2+</sup> and Pb<sup>2+</sup>.** X-ray photoelectron spectroscopy (XPS) is an important tool to reveal the oxidation states of elements in the sample. XPS analysis of parent Au<sub>38</sub>@BSA has shown that Au 4f<sub>7/2</sub> appears at 84.1 eV, confirming the presence of a stable metallic core (Au<sup>0</sup> state) in the cluster (Figure S8A).<sup>17</sup> The binding energy of S 2p<sub>3/2</sub> at 162.1 eV suggested Au–S bonding which stabilizes the core through cysteine residues of the protein (Figure S8B). The PL data shown in Figure 2 proposed that the major interaction of Cd<sup>2+</sup> is with the core of the cluster whereas Pb<sup>2+</sup> interacts with the BSA shell of the cluster. To further investigate metal-ion-induced changes in the oxidation states of cluster core and interacting elements, we carried out XPS analysis of Au<sub>38</sub>@BSA upon interaction with Cd<sup>2+</sup> and Pb<sup>2+</sup> (Figure 4).

Due to the interaction of Cd<sup>2+</sup>, Au 4f<sub>7/2</sub> at 84.1 eV got shifted to 85.3 eV suggesting the oxidation of the core to Au<sup>1+</sup>. However, two peaks at 406.4 and 404.6 eV binding energy were seen in the Cd 3d region and assigned as Cd<sup>2+</sup> and Cd<sup>0</sup>, respectively. After interaction with Pb<sup>2+</sup>, only a change of 0.4 eV in the binding energy of Au 4f<sub>7/2</sub> was observed (from 84.1 to 84.5 eV), indicating the core to be closer to its metallic state, and the binding energy at 138.9 eV was the characteristic feature of Pb<sup>2+</sup>. The XPS data have shown that Cd<sup>2+</sup> induced a

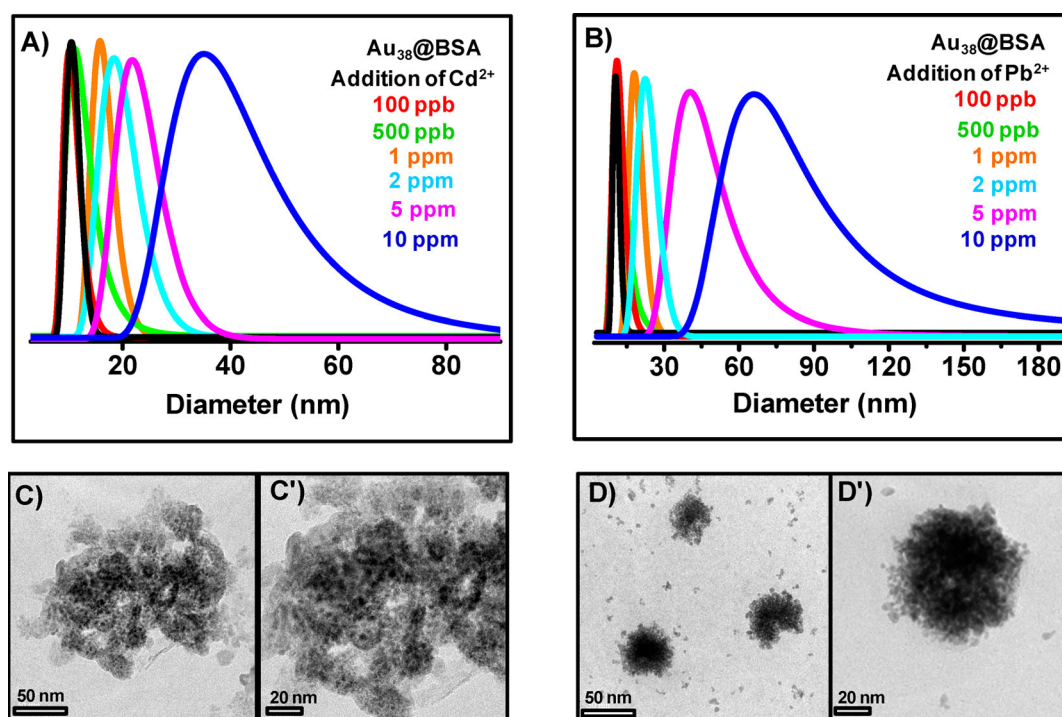


**Figure 3.** DLS spectra of  $\text{Au}_{38}\text{@BSA}$  at various concentrations of (A)  $\text{Cd}^{2+}$  and (B)  $\text{Pb}^{2+}$ . Data for parent  $\text{Au}_{38}\text{@BSA}$  are also shown. TEM images showing the aggregation of clusters upon adding (C)  $\text{Cd}^{2+}$  and (D)  $\text{Pb}^{2+}$ . The corresponding higher magnification TEM images are shown in parts C' and D', respectively.

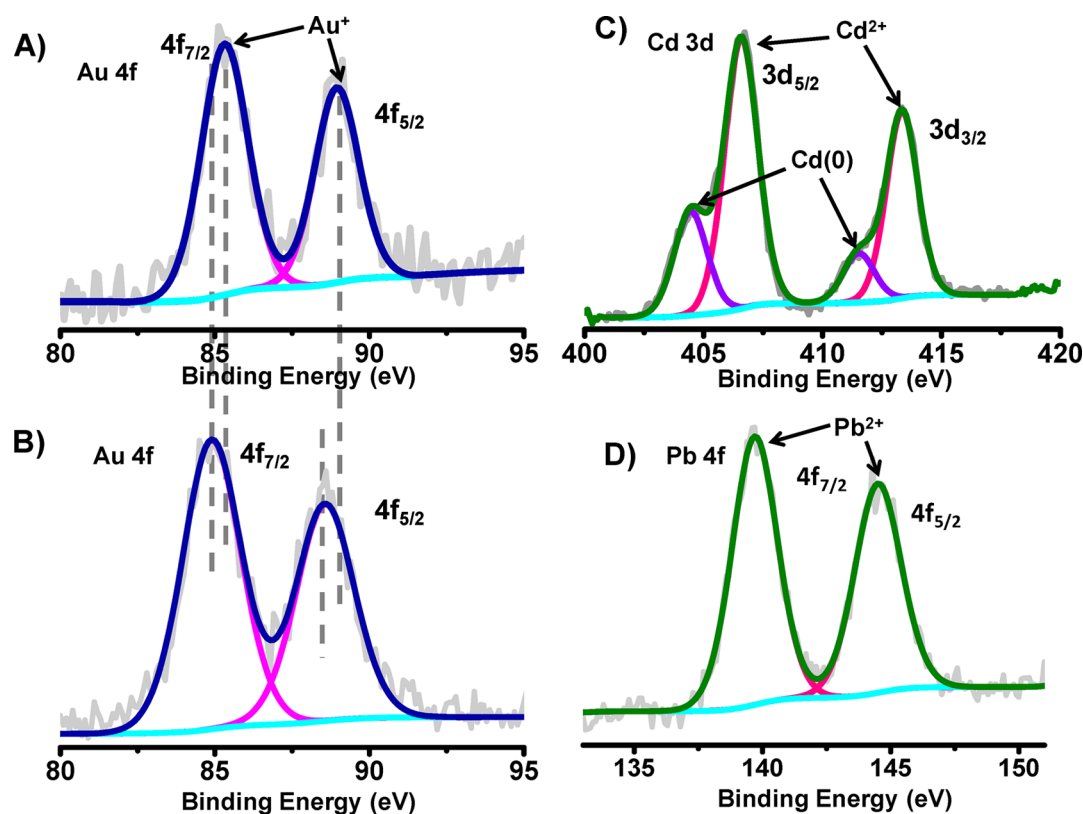


**Figure 4.** (A and B) Au 4f region of  $\text{Au}_{38}\text{@BSA}$  upon interaction with  $\text{Cd}^{2+}$  and  $\text{Pb}^{2+}$ , respectively. (C and D) Corresponding Cd 3d and Pb 4f regions, respectively.

change in the oxidation state of the cluster core, i.e. from  $\text{Au}^0$  to  $\text{Au}^+$  whereas  $\text{Pb}^{2+}$  did not bring a significant change in the

core of the cluster. This also supported the results obtained from PL studies discussed earlier.



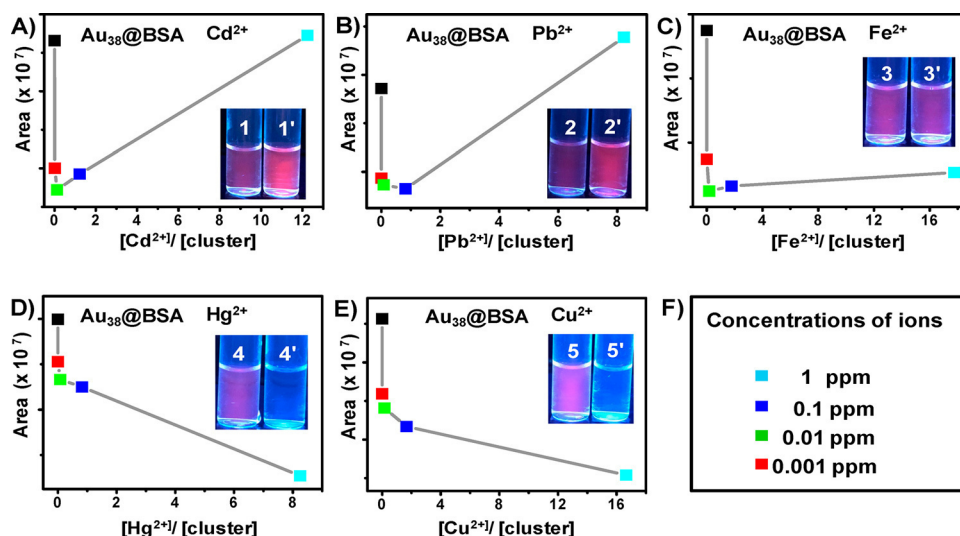


**Figure 5.** Area under the emission spectra at different molar ratios of metal ions to cluster concentrations. (A) Cd<sup>2+</sup>, (B) Pb<sup>2+</sup>, (C) Fe<sup>2+</sup>, (D) Hg<sup>2+</sup>, and (E) Cu<sup>2+</sup>. (F) Color coding for the concentrations of metal ions used. Inset shows the photographs of Au<sub>38</sub>@BSA before (1, 2, 3, 4, 5) and after interaction with 1 ppm of Cd<sup>2+</sup>, Pb<sup>2+</sup>, Fe<sup>2+</sup>, Hg<sup>2+</sup>, and Cu<sup>2+</sup> (1', 2', 3', 4', 5'), respectively.

**Selective Luminescence Enhancement of Au<sub>38</sub>@BSA Due to Metal Ions.** The interactions of Au<sub>38</sub>@BSA with Cd<sup>2+</sup> and Pb<sup>2+</sup> were discussed in the earlier sections and enhancement of luminescence was observed at higher concentrations of Cd<sup>2+</sup> and Pb<sup>2+</sup> while luminescence was quenched at lower concentration. The luminescence response of Au<sub>38</sub>@BSA was studied with other divalent metal ions such as Fe<sup>2+</sup>, Hg<sup>2+</sup>, and Cu<sup>2+</sup>, and the changes were compared with Cd<sup>2+</sup> and Pb<sup>2+</sup> ions. Figure 5 shows the change in the luminescence of the cluster after treatment with metal ion concentrations starting from 1 ppb to 1 ppm. Area under the emission spectrum of Au<sub>38</sub>@BSA (550–710 nm wavelength range) is plotted against the molar ratio of metal ion to Au<sub>38</sub>@BSA, for different analyte ions.

After addition of each concentration of metal ion to cluster, the cluster solution was incubated for 2 min before collecting the emission spectra. Only in the presence of Cd<sup>2+</sup> and Pb<sup>2+</sup>, luminescence enhancement was seen but not in the case of Fe<sup>2+</sup>. Whereas at lower concentrations of Cd<sup>2+</sup>, Pb<sup>2+</sup>, and Fe<sup>2+</sup>, a decrease in the emission intensity was noticed. Enhancement in emission started from 0.1 ppm of Cd<sup>2+</sup> and Pb<sup>2+</sup> onward. In the earliest sections, we have already discussed the effect of increase in the concentration of Cd<sup>2+</sup> and Pb<sup>2+</sup> (Figure 2, parts A and C). Unlike Hg<sup>2+</sup>, Cu<sup>2+</sup> also is known to quench the luminescence of Au<sub>38</sub>@BSA.<sup>13,24</sup> In both cases, at lower concentrations (up to 100 ppb), a decrease in the luminescence intensity was observed, but complete quenching occurred only at 1 ppm of ions. The interaction of Cu<sup>2+</sup> with BSA shell of the cluster has been proposed as a possible reason for this luminescence quenching, whereas a similar quenching effect in the case of Hg<sup>2+</sup> is due to the interaction between the metal ion and the core of the cluster.<sup>13,24</sup>

## CONCLUSIONS

The interaction of Au<sub>38</sub>@BSA with Cd<sup>2+</sup> and Pb<sup>2+</sup> has been investigated in great detail. Au<sub>38</sub>@BSA was found to have aggregation-induced emission enhancement in the presence of Cd<sup>2+</sup> and Pb<sup>2+</sup>, for concentrations higher than 1 ppm. This phenomenon has been studied for the first time in the case of PPCs. The enhancement of luminescence is due to aggregation

of clusters, and such aggregates were detected by DLS and HRTEM analyses. PL studies have shown that, in the case of Cd<sup>2+</sup>, enhancement in the luminescence is due to interaction between Cd<sup>2+</sup> and cluster core whereas PL enhancement in Au<sub>38</sub>@BSA upon Pb<sup>2+</sup> is due to Pb<sup>2+</sup>–protein shell interaction. These observations were further supported by XPS data, where it was shown that interaction with Cd<sup>2+</sup> resulted in the oxidation of the cluster core from Au<sup>0</sup> to Au<sup>+</sup> along with changes in binding energy of Cd<sup>2+</sup>, but interaction of Pb<sup>2+</sup> did not affect the core of the cluster. Interactions of other metal ions such as Fe<sup>2+</sup>, Hg<sup>2+</sup>, and Cu<sup>2+</sup> with Au<sub>38</sub>@BSA were also studied and it showed that such interaction is selective to Cd<sup>2+</sup> and Pb<sup>2+</sup>. Difference in the nature of interactions between heavy metal ions and Au<sub>38</sub>@BSA may be used to develop a sensor with a logical readout for identifying different metal ions. Also, such metal-ion-induced aggregation of clusters leading to emission enhancement will open up the possibility of developing clusters with enhanced optical properties and associated applications.

## ASSOCIATED CONTENT

### Supporting Information

The Supporting Information is available free of charge on the ACS Publications website at DOI: 10.1021/acs.jpcc.9b07370.

Comparative MALDI MS of BSA and ~Au<sub>38</sub>@BSA, control PL study and time dependent change in I<sub>650</sub> of Au<sub>38</sub>@BSA, UV–vis absorption spectra of Au<sub>38</sub>@BSA in the presence of Cd<sup>2+</sup> and Pb<sup>2+</sup>, DLS data, HRTEM EDS spectra, and XPS data of Au<sub>38</sub>@BSA (PDF)

## AUTHOR INFORMATION

### Corresponding Author

\*(T.P.) E-mail: [pradeep@iitm.ac.in](mailto:pradeep@iitm.ac.in). Fax: +91-44-2257-0545.

### ORCID

Thalappil Pradeep: 0000-0003-3174-534X

### Notes

The authors declare no competing financial interest.



## ACKNOWLEDGMENTS

We thank the Department of Science and Technology, Government of India for their continuous support on our research program on nanomaterials. J.S.M. thanks Council of Scientific and Industrial Research (CSIR) for her research fellowship. C.S. thanks IIT Madras for his research fellowship.

## REFERENCES

- (1) Jin, R. Quantum Sized, Thiolate-Protected Gold Nanoclusters. *Nanoscale* **2010**, *2*, 343–362.
- (2) Mathew, A.; Pradeep, T. Noble Metal Clusters: Applications in Energy, Environment, and Biology. *Part. Part. Syst. Charact.* **2014**, *31*, 1017–1053.
- (3) Xavier, P. L.; Chaudhari, K.; Baksi, A.; Pradeep, T. Protein-Protected Luminescent Noble Metal Quantum Clusters: An Emerging Trend in Atomic Cluster Nanoscience. *Nano Rev.* **2012**, *3*, 14767–14782.
- (4) Chevrier, D. M.; Chatt, A.; Zhang, P. Properties and Applications of Protein-Stabilized Fluorescent Gold Nanoclusters: Short Review. *J. Nanophotonics* **2012**, *6*, 064504.
- (5) Rao, T. U. B.; Nataraju, B.; Pradeep, T. Ag<sub>9</sub> Quantum Cluster through a Solid-State Route. *J. Am. Chem. Soc.* **2010**, *132*, 16304–16307.
- (6) Sharma, J.; Rocha, R. C.; Phipps, M. L.; Yeh, H.-C.; Balatsky, K. A.; Vu, D. M.; Shreve, A. P.; Werner, J. H.; Martinez, J. S. A DNA-Templated Fluorescent Silver Nanocluster with Enhanced Stability. *Nanoscale* **2012**, *4*, 4107–4110.
- (7) Zheng, J.; Zhang, C.; Dickson, R. M. Highly Fluorescent, Water-Soluble, Size-Tunable Gold Quantum Dots. *Phys. Rev. Lett.* **2004**, *93*, 077402.
- (8) Xie, J.; Zheng, Y.; Ying, J. Y. Protein-Directed Synthesis of Highly Fluorescent Gold Nanoclusters. *J. Am. Chem. Soc.* **2009**, *131*, 888–889.
- (9) Goswami, N.; Zheng, K.; Xie, J. Bio-NCs - the Marriage of Ultrasmall Metal Nanoclusters with Biomolecules. *Nanoscale* **2014**, *6*, 13328–13347.
- (10) Mathew, A.; Sajanlal, P. R.; Pradeep, T. A Fifteen Atom Silver Cluster Confined in Bovine Serum Albumin. *J. Mater. Chem.* **2011**, *21*, 11205–11212.
- (11) Li, H.-W.; Ai, K.; Wu, Y. Fluorescence Visual Gel-Separation of Dansylated BSA-Protected Gold-Nanoclusters. *Chem. Commun. (Cambridge, U. K.)* **2011**, *47*, 9852–9854.
- (12) Mohanty, J. S.; Xavier, P. L.; Chaudhari, K.; Bootharaju, M. S.; Goswami, N.; Pal, S. K.; Pradeep, T. Luminescent, Bimetallic AuAg Alloy Quantum Clusters in Protein Templates. *Nanoscale* **2012**, *4*, 4255–4262.
- (13) Habeeb Muhammed, M. A.; Verma, P. K.; Pal, S. K.; Retnakumari, A.; Koyakutty, M.; Nair, S.; Pradeep, T. Luminescent Quantum Clusters of Gold in Bulk by Albumin-Induced Core Etching of Nanoparticles: Metal Ion Sensing, Metal-Enhanced Luminescence, and Biolabeling. *Chem. - Eur. J.* **2010**, *16*, 10103–10112.
- (14) Baksi, A.; Pradeep, T. Noble Metal Alloy Clusters in the Gas Phase Derived from Protein Templates: Unusual Recognition of Palladium by Gold. *Nanoscale* **2013**, *5*, 12245–12254.
- (15) Baksi, A.; Pradeep, T.; Yoon, B.; Yannouleas, C.; Landman, U. Bare Clusters Derived from Protein Templates: Au<sub>25</sub><sup>+</sup>, Au<sub>38</sub><sup>+</sup> and Au<sub>102</sub><sup>+</sup>. *ChemPhysChem* **2013**, *14*, 1272–1282.
- (16) Baksi, A.; Xavier, P. L.; Chaudhari, K.; Goswami, N.; Pal, S. K.; Pradeep, T. Protein-Encapsulated Gold Cluster Aggregates: The Case of Lysozyme. *Nanoscale* **2013**, *5*, 2009–2016.
- (17) Xavier, P. L.; Chaudhari, K.; Verma, P. K.; Pal, S. K.; Pradeep, T. Luminescent Quantum Clusters of Gold in Transferrin Family Protein, Lactoferrin Exhibiting FRET. *Nanoscale* **2010**, *2*, 2769–2776.
- (18) Chaudhari, K.; Xavier, P. L.; Pradeep, T. Understanding the Evolution of Luminescent Gold Quantum Clusters in Protein Templates. *ACS Nano* **2011**, *5*, 8816–8827.
- (19) Anand, U.; Ghosh, S.; Mukherjee, S. Toggling between Blue- and Red-Emitting Fluorescent Silver Nanoclusters. *J. Phys. Chem. Lett.* **2012**, *3*, 3605–3609.
- (20) Chan, P.-H.; Chen, Y.-C. Human Serum Albumin Stabilized Gold Nanoclusters as Selective Luminescent Probes for Staphylococcus Aureus and Methicillin-Resistant Staphylococcus Aureus. *Anal. Chem. (Washington, DC, U. S.)* **2012**, *84*, 8952–8956.
- (21) Liu, C.-L.; et al. Insulin-Directed Synthesis of Fluorescent Gold Nanoclusters: Preservation of Insulin Bioactivity and Versatility in Cell Imaging. *Angew. Chem., Int. Ed.* **2011**, *50*, 7056–7060.
- (22) Li, H.; Zhu, W.; Wan, A.; Liu, L. The Mechanism and Application of the Protein-Stabilized Gold Nanocluster Sensing System. *Analyst (Cambridge, U. K.)* **2017**, *142*, 567–581.
- (23) Habeeb Muhammed, M. A.; Ramesh, S.; Sinha, S. S.; Pal, S. K.; Pradeep, T. Two Distinct Fluorescent Quantum Clusters of Gold Starting from Metallic Nanoparticles by pH-Dependent Ligand Etching. *Nano Res.* **2008**, *1*, 333–340.
- (24) Xie, J.; Zheng, Y.; Ying, J. Y. Highly Selective and Ultrasensitive Detection of Hg<sup>2+</sup> Based on Fluorescence Quenching of Au Nanoclusters by Hg<sup>2+</sup>-Au<sup>+</sup> Interactions. *Chem. Commun. (Cambridge, U. K.)* **2010**, *46*, 961–963.
- (25) Liu, Y.; Ai, K.; Cheng, X.; Huo, L.; Lu, L. Gold-Nanocluster-Based Fluorescent Sensors for Highly Sensitive and Selective Detection of Cyanide in Water. *Adv. Funct. Mater.* **2010**, *20*, 951–956.
- (26) Wei, H.; Wang, Z.; Yang, L.; Tian, S.; Hou, C.; Lu, Y. Lysozyme-Stabilized Gold Fluorescent Cluster: Synthesis and Application as Hg<sup>2+</sup> Sensor. *Analyst (Cambridge, U. K.)* **2010**, *135*, 1406–1410.
- (27) Mathew, A.; Sajanlal, P. R.; Pradeep, T. Selective Visual Detection of TNT at the Sub-Zeptomole Level. *Angew. Chem., Int. Ed.* **2012**, *51*, 9596–9600.
- (28) Chen, T.-H.; Tseng, W.-L. (Lysozyme Type VI)-Stabilized Au<sub>8</sub> Clusters: Synthesis Mechanism and Application for Sensing of Glutathione in a Single Drop of Blood. *Small* **2012**, *8*, 1912–1919.
- (29) Shao, C.; Yuan, B.; Wang, H.; Zhou, Q.; Li, Y.; Guan, Y.; Deng, Z. Eggshell Membrane as a Multimodal Solid State Platform for Generating Fluorescent Metal Nanoclusters. *J. Mater. Chem.* **2011**, *21*, 2863–2866.
- (30) Li, M.; Yang, D.-P.; Wang, X.; Lu, J.; Cui, D. Mixed Protein-Templated Luminescent Metal Clusters (Au and Pt) for H<sub>2</sub>O<sub>2</sub> Sensing. *Nanoscale Res. Lett.* **2013**, *8*, 182.
- (31) Chevrier, D. M.; et al. Structure and Formation of Highly Luminescent Protein-Stabilized Gold Clusters. *Chem. Sci.* **2018**, *9*, 2782–2790.
- (32) Wang, S.; Meng, X.; Das, A.; Li, T.; Song, Y.; Cao, T.; Zhu, X.; Zhu, M.; Jin, R. A 200-Fold Quantum Yield Boost in the Photoluminescence of Silver-Doped AgAu<sub>25-x</sub> Nanoclusters: The 13th Silver Atom Matters. *Angew. Chem., Int. Ed.* **2014**, *53*, 2376–2380.
- (33) Mohanty, J. S.; Baksi, A.; Lee, H.; Pradeep, T. Noble Metal Clusters Protected with Mixed Proteins Exhibit Intense Photoluminescence. *RSC Adv.* **2015**, *5*, 48039–48045.
- (34) Luo, Z.; Yuan, X.; Yu, Y.; Zhang, Q.; Leong, D. T.; Lee, J. Y.; Xie, J. From Aggregation-Induced Emission of Au(I)-Thiolate Complexes to Ultrabright Au(0)@Au(I)-Thiolate Core-Shell Nanoclusters. *J. Am. Chem. Soc.* **2012**, *134*, 16662–16670.
- (35) Ji, L.; Guo, Y.; Hong, S.; Wang, Z.; Wang, K.; Chen, X.; Zhang, J.; Hu, J.; Pei, R. Label-Free Detection of Pb<sup>2+</sup> Based on Aggregation-Induced Emission Enhancement of Au-Nanoclusters. *RSC Adv.* **2015**, *5*, 36582–36586.
- (36) Wu, C.-S.; Cupps, J. M.; Fan, X. Compact Quantum Dot Probes for Rapid and Sensitive DNA Detection Using Highly Efficient Fluorescence Resonant Energy Transfer. *Nanotechnology* **2009**, *20*, 305502.
- (37) Todd, M. D.; Lee, M. J.; Williams, J. L.; Nalezny, J. M.; Gee, P.; Benjamin, M. B.; Farr, S. B. The Cat-Tox (L) Assay: A Sensitive and Specific Measure of Stress-Induced Transcription in Transformed Human Liver Cells. *Fundam. Appl. Toxicol.* **1995**, *28*, 118–128.

- (38) Brewer, G. J. Risks of Copper and Iron Toxicity During Aging in Humans. *Chem. Res. Toxicol.* **2010**, *23*, 319–326.
- (39) Miyake, Y.; et al. MercuryII-Mediated Formation of Thymine-HgII-Thymine Base Pairs in DNA Duplexes. *J. Am. Chem. Soc.* **2006**, *128*, 2172–2173.
- (40) Kim, H.-K.; Rasnik, I.; Liu, J.; Ha, T.; Lu, Y. Dissecting Metal Ion-Dependent Folding and Catalysis of a Single DNzyme. *Nat. Chem. Biol.* **2007**, *3*, 763–768.
- (41) Needleman, H. Lead Poisoning. *Annu. Rev. Med.* **2004**, *55*, 209–222.
- (42) Hussein, H.; Farag, S.; Kandil, K.; Moawad, H. Tolerance and Uptake of Heavy Metals by Pseudomonads. *Process Biochem. (Oxford, U. K.)* **2005**, *40*, 955–961.
- (43) Kunkel, R.; Manahan, S. E. Atomic Absorption Analysis of Strong Heavy Metal Chelating Agents in Water and Waste Water. *Anal. Chem.* **1973**, *45*, 1465–1468.
- (44) Ochsenkuhn-Petropoulou, M.; Ochsenkuhn, K. M. Comparison of Inductively Coupled Plasma-Atomic Emission Spectrometry, Anodic Stripping Voltammetry and Instrumental Neutron-Activation Analysis for the Determination of Heavy Metals in Airborne Particulate Matter. *Fresenius' J. Anal. Chem.* **2001**, *369*, 629–632.
- (45) Goswami, N.; Giri, A.; Bootharaju, M. S.; Xavier, P. L.; Pradeep, T.; Pal, S. K. Copper Quantum Clusters in Protein Matrix: Potential Sensor of Pb<sup>2+</sup> Ion. *Anal. Chem. (Washington, DC, U. S.)* **2011**, *83*, 9676–9680.
- (46) Saha, K.; Agasti, S. S.; Kim, C.; Li, X.; Rotello, V. M. Gold Nanoparticles in Chemical and Biological Sensing. *Chem. Rev. (Washington, DC, U. S.)* **2012**, *112*, 2739–2779.
- (47) Liu, J.; Lu, Y. Preparation of Aptamer-Linked Gold Nanoparticle Purple Aggregates for Colorimetric Sensing of Analytes. *Nat. Protoc.* **2006**, *1*, 246–252.
- (48) Liu, J.; Lu, Y. Improving Fluorescent Dnzyme Biosensors by Combining Inter- and Intramolecular Quenchers. *Anal. Chem.* **2003**, *75*, 6666–6672.
- (49) Durgadas, C. V.; Sharma, C. P.; Sreenivasan, K. Fluorescent Gold Clusters as Nanosensors for Copper Ions in Live Cells. *Analyst (Cambridge, U. K.)* **2011**, *136*, 933–940.
- (50) Baksi, A.; Mitra, A.; Mohanty, J. S.; Lee, H.; De, G.; Pradeep, T. Size Evolution of Protein-Protected Gold Clusters in Solution: A Combined SAXS-MS Investigation. *J. Phys. Chem. C* **2015**, *119*, 2148–2157.

## Supporting Information

# Metal-Ion-Induced Luminescence *Enhancement* in Protein Protected Gold Clusters

Jyoti Sarita Mohanty,<sup>†</sup> Kamalesh Chaudhari,<sup>‡</sup> Chennu Sudhakar<sup>‡</sup> and Thalappil Pradeep\*

<sup>†</sup>DST Unit of Nanoscience (DST UNS), and Thematic Unit of Excellence (TUE),

Department of Chemistry, Indian Institute of Technology Madras, Chennai - 600 036, India

\*E-mail: [pradeep@iitm.ac.in](mailto:pradeep@iitm.ac.in)

## Table of Contents

Sl. No	Description	Page No.
Figure S1	Comparative MALDI MS of BSA and Au <sub>38</sub> @BSA	S2
Figure S2	Control PL study and time dependent change in I <sub>650</sub> of Au <sub>38</sub> @BSA	S3
Figure S3	UV-vis absorption spectra of Au <sub>38</sub> @BSA without and with presence of Pb <sup>2+</sup> and Cd <sup>2+</sup>	S4
Figure S4	DLS data of BSA and Au <sub>38</sub> @BSA showing the size of cluster core	S5
Figure S5	Volume fraction-dependent DLS spectra of Au <sub>38</sub> @BSA	S6
Figure S6	HRTEM EDS spectrum showing the presence of Cd <sup>2+</sup>	S7
Figure S7	HRTEM EDS spectrum showing the presence of Pb <sup>2+</sup>	S7
Figure S8	XPS data of Au <sub>38</sub> @BSA	S8

Supporting Figure 1

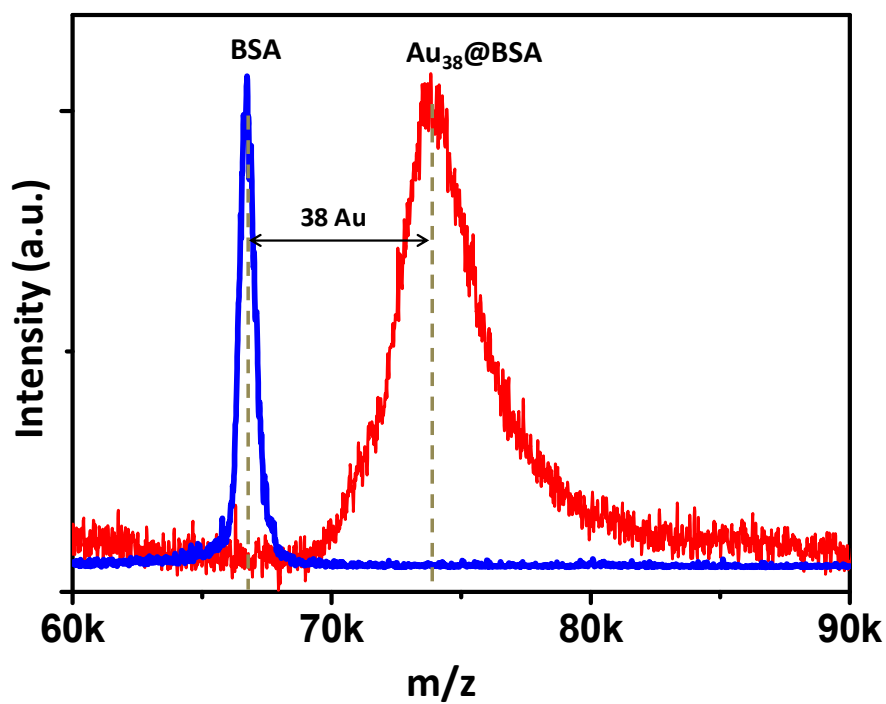


**Figure S1:** Comparison between MALDI MS of BSA and Au<sub>QC</sub>@BSA showing mass shift of 7.5 kDa from parent protein after cluster formation. The cluster is assigned as ~Au<sub>38</sub>@BSA.

## Supporting Figure 2

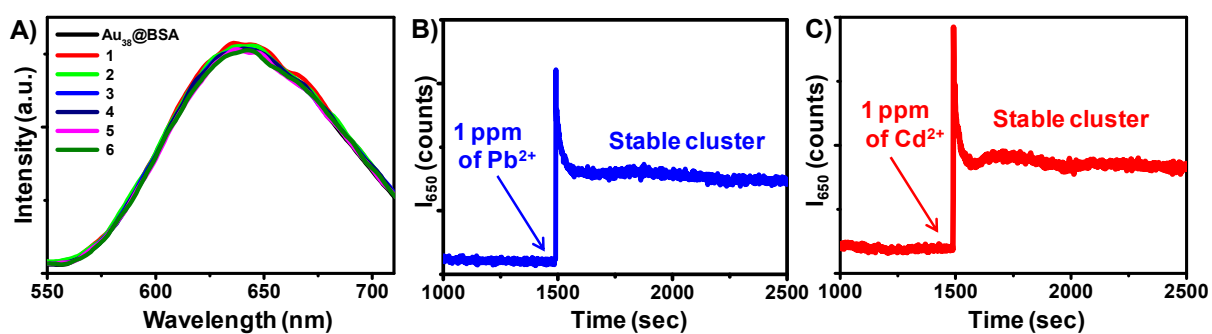


**Figure S2:** (A) The PL emission spectra of Au<sub>38</sub>@BSA. Spectra from 1 to 6 were measured at a time interval of 2 min to check the stability of the parent cluster (all the parameters were kept same during the measurement). Excitation wavelength for Au<sub>38</sub>@BSA was 365 nm. Time-dependent changes in I<sub>650</sub> of Au<sub>38</sub>@BSA upon addition of 1 ppm (B) Pb<sup>2+</sup> and (C) Cd<sup>2+</sup>.

Supporting Figure 3

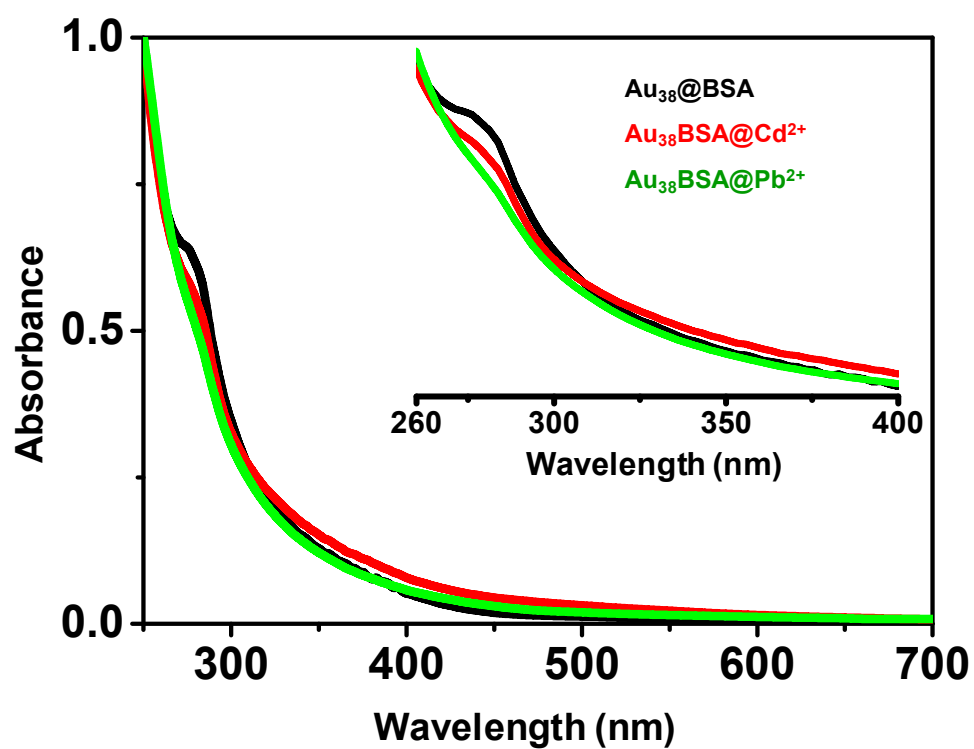


**Figure S3:** UV-vis absorption spectra of parent  $\text{Au}_{38}\text{@BSA}$  (black trace) and after treatment with  $\text{Cd}^{2+}$  (red trace) and  $\text{Pb}^{2+}$  (green trace). Inset shows the expanded view of the absorption feature.

**Supporting Figure 4**

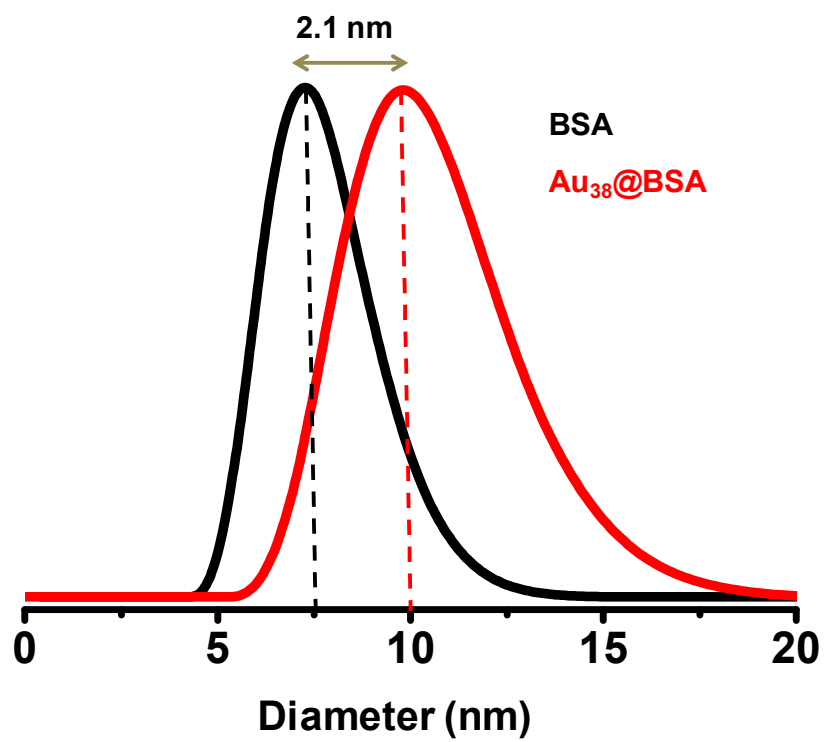


**Figure S4:** DLS data of BSA and Au<sub>38</sub>@BSA showing the presence of ~2.1 nm cluster core.



## Supporting Figure 5

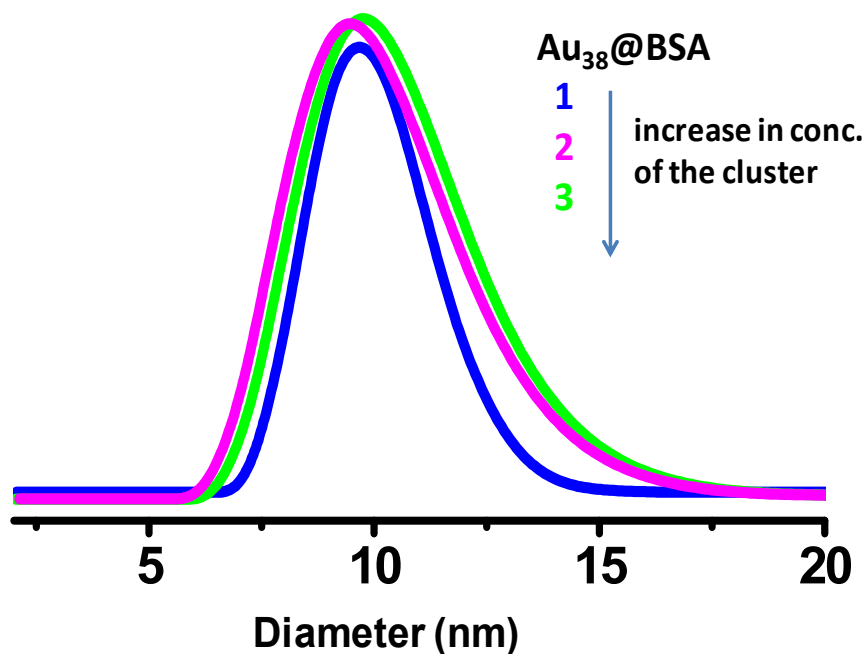


**Figure S5:** Volume fraction-dependent DLS spectra of Au<sub>38</sub>@BSA showing the size of the cluster remained same with increase in concentration of the cluster. Concentrations 1, 2, and 3 correspond to 5, 20 and 50  $\mu\text{L}$  of cluster solution in 2 mL of DI H<sub>2</sub>O, respectively. Therefore, the last two correspond to 4 and 10 times enhanced concentration than the first.

### Supporting Figure 6

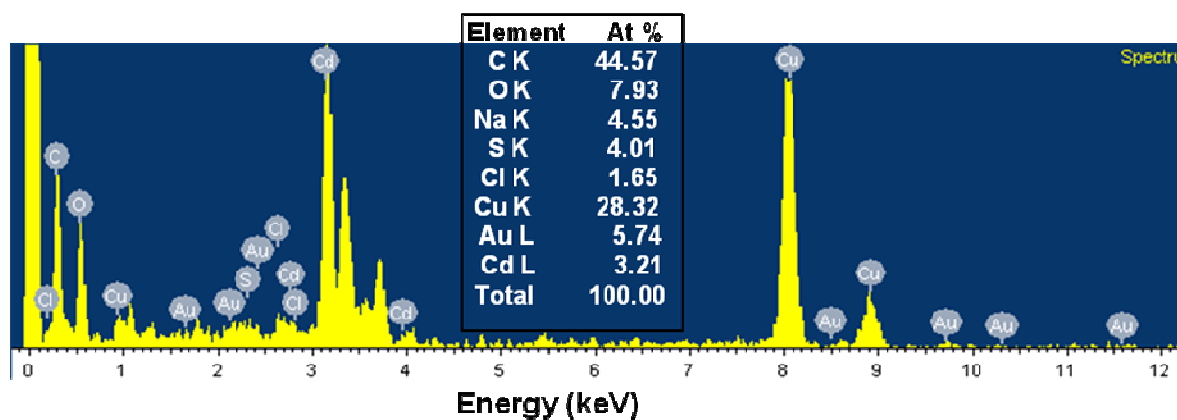


**Figure S6:** HRTEM EDS spectrum with quantification data showing the presence of  $\text{Cd}^{2+}$  and other expected elements in  $\text{Au}_{38}@\text{BSA}$ .

### Supporting Figure 7

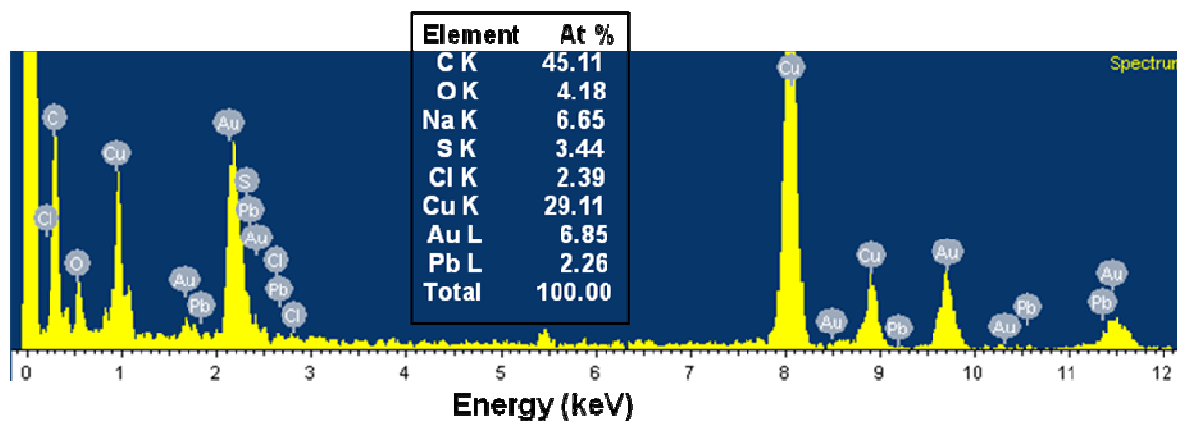


**Figure S7:** HRTEM EDS spectrum with quantification data showing the presence of  $\text{Pb}^{2+}$  and other expected elements in  $\text{Au}_{38}@\text{BSA}$ .

## Supporting Figure 8

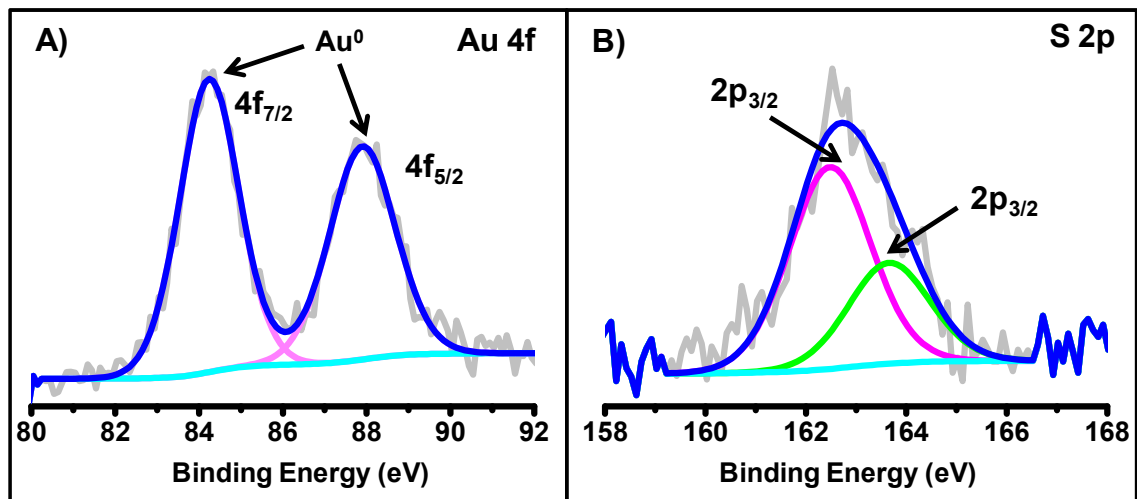


**Figure S8:** XPS spectra of  $Au_{38}@BSA$  showing the metallic (A) Au 4f and thiolate (B) S 2p regions.

# Interparticle Reactions between Silver Nanoclusters Leading to Product Cocrystals by Selective Cocrystallization

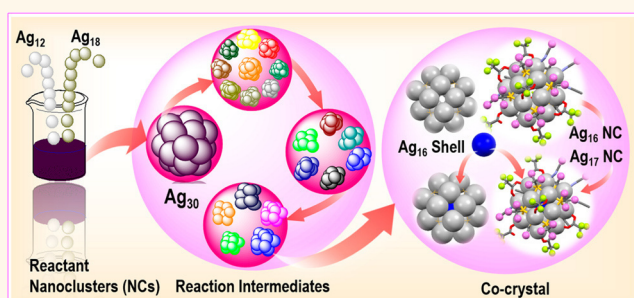
Wakeel Ahmed Dar,<sup>†</sup> Mohammad Bodiuzzaman,<sup>†</sup> Debasmita Ghosh, Ganesan Paramasivam, Esma Khatun, Korath Shivan Sugi, and Thalappil Pradeep\*<sup>✉</sup>

Department of Chemistry, DST Unit of Nanoscience and Thematic Unit of Excellence, Indian Institute of Technology Madras, Chennai 600036, India

## S Supporting Information

**ABSTRACT:** We present an example of an interparticle reaction between atomically precise nanoclusters (NCs) of the same metal, resulting in entirely different clusters. In detail, the clusters  $[\text{Ag}_{12}(\text{TBT})_8(\text{TFA})_5(\text{CH}_3\text{CN})]^+$  (TBT = *tert*-butylthiolate, TFA = trifluoroacetate,  $\text{CH}_3\text{CN}$  = acetonitrile) and  $[\text{Ag}_{18}(\text{TPP})_{10}\text{H}_{16}]^{2+}$  (TPP = triphenylphosphine) abbreviated as  $\text{Ag}_{12}$  and  $\text{Ag}_{18}$ , respectively, react leading to  $[\text{Ag}_{16}(\text{TBT})_8(\text{TFA})_7(\text{CH}_3\text{CN})_3\text{Cl}]^+$  and  $[\text{Ag}_{17}(\text{TBT})_8(\text{TFA})_7(\text{CH}_3\text{CN})_3\text{Cl}]^+$ , abbreviated as  $\text{Ag}_{16}$  and  $\text{Ag}_{17}$ , respectively. The two product NCs crystallize together as both possess the same metal chalcogenolate shell, composed of  $\text{Ag}_{16}\text{S}_8$ , making them indistinguishable. The occupancies of  $\text{Ag}_{16}$  and  $\text{Ag}_{17}$  are 66.66 and 33.33%, respectively, in a single crystal. Electrospray ionization mass spectrometry (ESI MS) of the reaction product and a dissolved crystal show the population of  $\text{Ag}_{16}$  and  $\text{Ag}_{17}$  NCs to be in a 1:1 and 2:1 ratio, respectively. This suggests selective crystallization in the cocrystal. Time-dependent ESI MS was employed to understand the formation of product clusters by monitoring the reaction intermediates formed in the course of the reaction. We present an unprecedented growth mechanism for the formation of silver NCs mediated by silver thiolate intermediates.

**KEYWORDS:** nanoclusters, intercluster reactions, homometallic clusters, cocrystals,  $\text{Ag}_{16}$  and  $\text{Ag}_{17}$



Atomically precise noble metal nanoclusters (NCs) are an emerging class of materials. Studies on them are motivated by their unusual structures and associated properties.<sup>1–6</sup> NCs possess exceptional geometric and electronic structures, having a core size below 3 nm, exhibiting intriguing properties due to molecule-like energy levels, strong photoluminescence, color tunability, high catalytic activity, facile surface tailorability, and good photostability, which are different from bulk nanoparticles, with diameters >3 nm.<sup>3–7</sup> Scalable fabrication of the NCs results in new materials with distinctly different applications.<sup>8,9</sup> Attempts to design novel NCs have been there using diverse methodologies. Clusters with varying cores can be obtained by different synthetic procedures such as size focusing methodology,<sup>10,11</sup> interparticle reactions,<sup>12</sup> and many others.<sup>2–6</sup> To understand the distinct properties of NCs, detailed knowledge of their structures is important. In the recent past, atomically precise silver (Ag) nanoclusters with a wide range of nuclearity have been characterized, including  $\text{Ag}_{14}$ ,<sup>13</sup>  $\text{Ag}_{16}$ ,<sup>14</sup>  $\text{Ag}_{17}$ ,<sup>15</sup>  $\text{Ag}_{33}$ ,<sup>16</sup>  $\text{Ag}_{20}$ ,<sup>17</sup>  $\text{Ag}_{21}$ ,<sup>18</sup>  $\text{Ag}_{25}$ ,<sup>19</sup>  $\text{Ag}_{22}$ ,<sup>20</sup>  $\text{Ag}_{29}$ ,<sup>21</sup>  $\text{Ag}_{40}$ ,<sup>22</sup>  $\text{Ag}_{44}$ ,<sup>23</sup>  $\text{Ag}_{46}$ ,<sup>22</sup>  $\text{Ag}_{123}$ ,<sup>24</sup>  $\text{Ag}_{320}$ ,<sup>25</sup>  $\text{Ag}_{344}$ ,<sup>24</sup>  $\text{Ag}_{352}$ ,<sup>25</sup>  $\text{Ag}_{490}$ ,<sup>25</sup> etc., with varying

thiols, as well as with secondary ligands, mostly phosphines. Charge is an integral part of the cluster system, with many existing in multianionic forms. Structural studies of nanoclusters revealed that the metal core is protected by an outer layer, composed of the metal and ligands. A closed-shell electronic structure makes these clusters stable, which often results in an overall charge for the system. In a few cases, an unusual possibility of two NCs of similar outer structure covering varied inner cores exist during the nucleation of a crystal, leading to the formation of multicomponent molecular solids or cocrystals.<sup>22</sup> They have properties of both the clusters. The study of cocrystals is a well-known aspect of modern crystal engineering.<sup>26</sup> They may have several applications in pharmaceutical sciences.<sup>27</sup> Many cocrystals of noble metal NCs are known now.<sup>22,28–30</sup> These have been synthesized either by reducing thiolate or phosphine complexes or by ligand-exchange-induced size transformation

**Received:** August 25, 2019

**Accepted:** November 1, 2019

**Published:** November 1, 2019

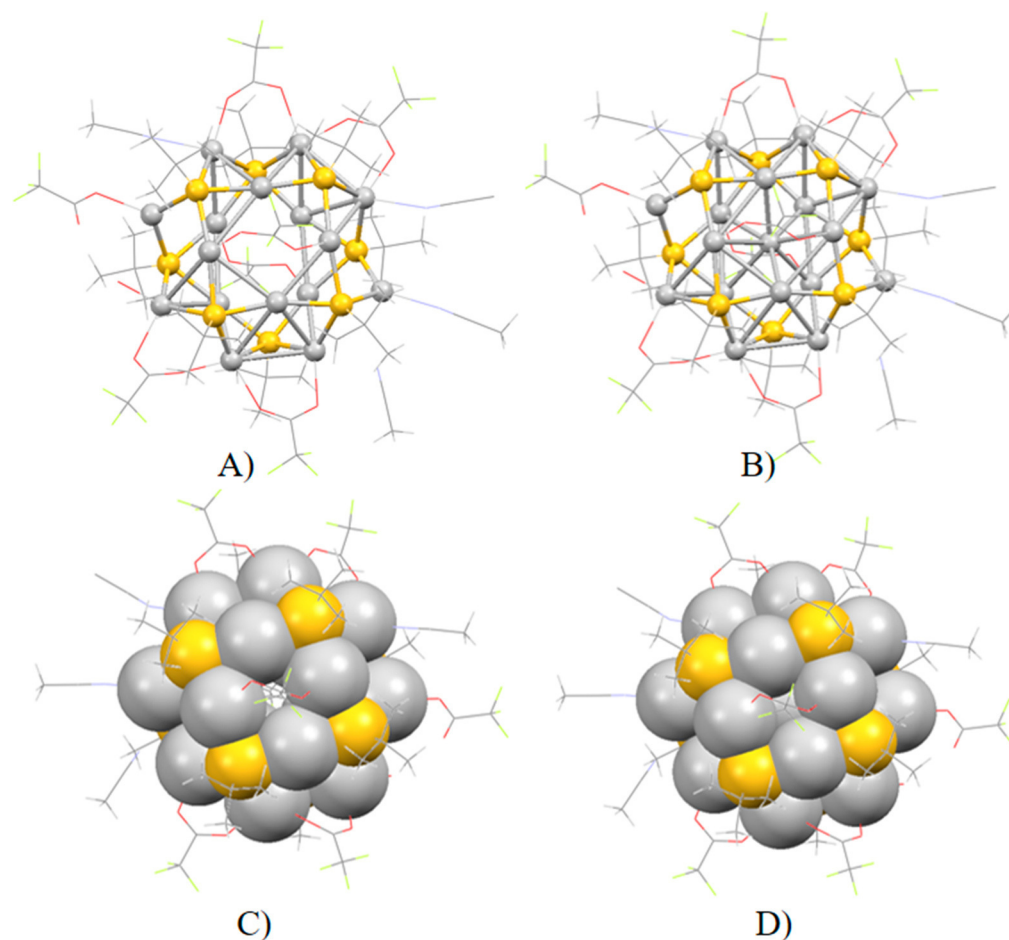


**Figure 1.** Total structures of (A)  $[\text{Ag}_{16}(\text{TBT})_8(\text{TFA})_7(\text{CH}_3\text{CN})_3(\text{Cl})]^+$  and (B)  $[\text{Ag}_{17}(\text{TBT})_8(\text{TFA})_7(\text{CH}_3\text{CN})_3(\text{Cl})]^+$ . The  $\text{Ag}_{16}$  NC is hollow inside, and  $\text{Ag}_{17}$  contains one additional Ag atom inside. Light gray and yellow spheres in the ball-and-stick model represent Ag and S atoms, respectively, and other nonmetals are represented by a wire frame model. Space-filling models of (C)  $\text{Ag}_{16}$  and (D)  $\text{Ag}_{17}$ . Color code: Ag, light gray; S, yellow; F, light green; C, gray; N, light blue; Cl, black.

reactions (LEIST).<sup>31</sup> NCs are considered as stable entities and are expected to retain their identity in solution. Chemical reactions between NCs or interparticle reactions belong to a special class of reactions introduced by our group, which typically involve the exchange of metals and ligands between different clusters, leading to product clusters.<sup>32–34</sup> These reactions were performed by reacting monolayer-protected clusters composed of different metals, for example, Ag and Au NCs. Reaction between  $\text{Au}_{25}$  and  $\text{Ag}_{44}$  were reported initially followed by the reaction of  $\text{Ag}_{25}$  and  $\text{Au}_{25}$ .<sup>32,33</sup> Many others were also studied subsequently.<sup>34–37</sup> Here, we explored an interparticle reaction methodology between homometallic clusters to make new clusters. To understand the growth of NCs, time-dependent electrospray ionization mass spectrometry (ESI MS) studies were performed. We note that the size evolution mechanism for the formation of Ag and Au NCs via homoleptic thiolate-stabilized precursors has been reported recently.<sup>28,38,39</sup>

We present the synthesis, optical properties, ESI MS analysis, and structures of atomically precise NCs, costabilized by TBT (*tert*-butylthiolate) and TFA (trifluoroacetate) ligands. The synthesis involves a homometallic interparticle reaction of silver NCs using  $[\text{Ag}_{12}(\text{TBT})_8(\text{TFA})_5(\text{CH}_3\text{CN})]^+$  and a hydride and phosphine coprotected cluster,  $[\text{Ag}_{18}(\text{TPP})_{10}\text{H}_{16}]^{2+}$ , abbreviated as  $\text{Ag}_{12}$  and  $\text{Ag}_{18}$ , respectively, as reactants, which are known previously.<sup>40,41</sup> The

reaction mixture formed cocrystals of product NCs viz.  $[\text{Ag}_{16}(\text{TBT})_8(\text{TFA})_7(\text{CH}_3\text{CN})_3\text{Cl}]^+$  denoted as  $\text{Ag}_{16}$  and  $[\text{Ag}_{17}(\text{TBT})_8(\text{TFA})_7(\text{CH}_3\text{CN})_3\text{Cl}]^+$  denoted as  $\text{Ag}_{17}$ . The two NCs are structurally similar and are indistinguishable in the lattice. We probed the mechanism of interparticle reaction using time-dependent ESI MS and UV–vis spectroscopy, which gave deep insights into the formation of the NCs mediated by silver thiolate intermediates. Our approach represents a different method of synthesizing atomically precise NC cocrystals, which could result in unusual properties and applications.

## RESULTS AND DISCUSSION

The  $\text{Ag}_{12}$  NC was synthesized by dissolving silver thiolate,  $\text{Ag}(\text{TBT})_n$ , and  $\text{CF}_3\text{COOAg}$  in a mixture of acetonitrile and methanol. To this was added a methanolic solution of  $\text{Ag}_{18}$  (synthesized by a reported method).<sup>41,42</sup> A dark brown solution along with a black precipitate was formed; the mixture was kept stirring for 1 h, and the solution was centrifuged at 8000 rpm (5868g). The black precipitate was discarded as it did not dissolve in various organic solvents. The resultant supernatant dark brown solution was initially analyzed by UV–vis absorption spectroscopy for its optical properties that displayed the characteristic molecular transitions at 439 and 611 nm. The solution obtained after

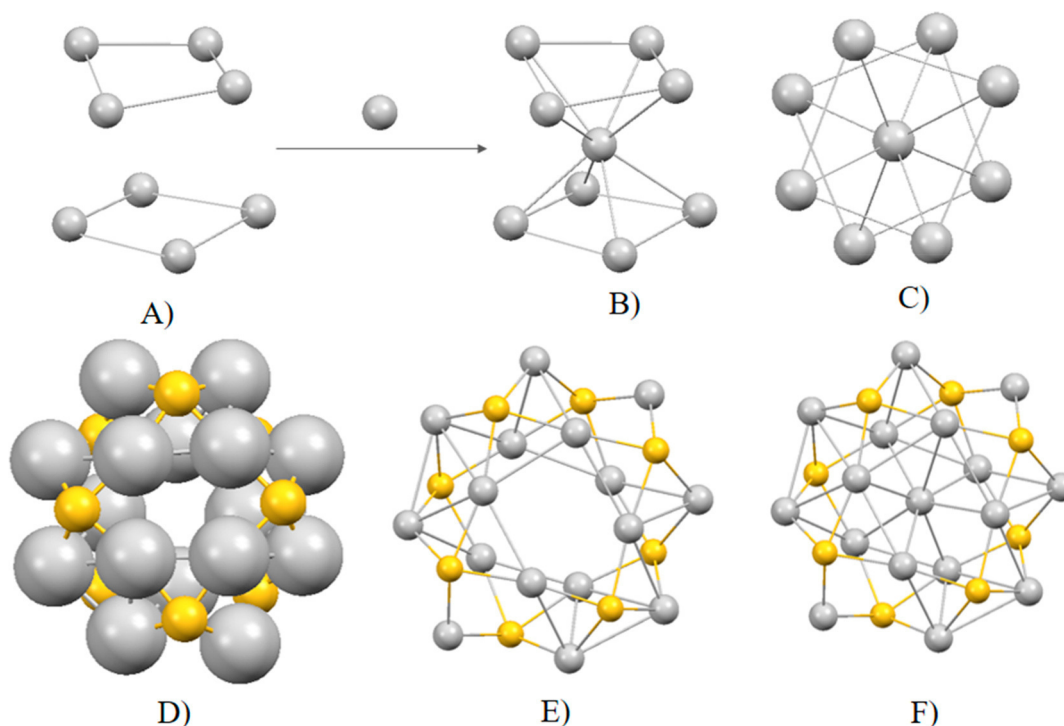


**Figure 2.** (A) Construction of Ag<sub>17</sub> by the addition of one silver atom between the Ag atoms, (B) showing distorted square anti-biprismatic geometry in which the central Ag atom is bonded to eight Ag atoms. (C) Top view of the Ag<sub>9</sub> metallic framework. (D) View of Ag<sub>16</sub>S<sub>8</sub> shell showing Ag<sub>4</sub>S capping around the periphery of the shell. (E) Top view of Ag<sub>16</sub> and (F) Ag<sub>17</sub> NC shells: Ag (gray) and S (yellow).

centrifugation was left for slow evaporation at  $5 \pm 5$  °C for crystallization, and after 1 week, light brown crystals suitable for single-crystal X-ray diffraction (SCXRD) were obtained. SCXRD, ESI MS, and UV–vis spectroscopic techniques were employed to characterize the product formed.

A block-shaped single crystal was evaluated by SCXRD. Analysis of the crystallographic data showed that there exist two types of NC entities *viz.*  $[\text{Ag}_{16}(\text{TBT})_8(\text{TFA})_7(\text{CH}_3\text{CN})_3\text{Cl}]^+$  and  $[\text{Ag}_{17}(\text{TBT})_8(\text{TFA})_7(\text{CH}_3\text{CN})_3\text{Cl}]^+$ , acronymed as Ag<sub>16</sub> and Ag<sub>17</sub>, respectively, in a single crystal, as shown in Figure 1. Each NC exhibits a sandwich-like molecular structure, assembled in a monoclinic  $P2_1/n$  space group (Table S1). These NCs have identical outer structures, and they can easily exchange positions in a lattice. They are, therefore, not able to distinguish each other and crystallize together. The geometrical framework of the Ag<sub>16</sub> NC can be represented by surface-connected 16 Ag and 8 S atoms, thereby forming an Ag<sub>16</sub>S<sub>8</sub> hollow shell, arranged in a layered fashion: Ag<sub>4</sub>S<sub>4</sub>–Ag<sub>8</sub>–Ag<sub>4</sub>S<sub>4</sub>, forming a sandwich-like structure (Figure S1). For the Ag<sub>17</sub> NC, a single Ag atom is encapsulated in the Ag<sub>16</sub> shell and has an occupancy of 1/3. Thus, in the cocrystal, 2/3 NCs have 16 Ag atoms and 1/3 NCs have 17 Ag atoms. In Ag<sub>16</sub>S<sub>8</sub> shell, each S atom is coordinated to four Ag atoms, forming Ag<sub>4</sub>S capping around the periphery of the shell (Figure 2D). The Ag<sub>16</sub> and Ag<sub>17</sub> NCs in a cocrystal are primarily protected by the TBT ligand. In addition, seven units of TFA, three molecules of acetonitrile and one chlorine atom are coordinated to the Ag<sub>16</sub>S<sub>8</sub> shell. One molecule of acetonitrile per unit cell is also located in the lattice. The Ag<sub>16</sub> NC structure is almost similar to the shell of a recently reported  $[\text{Ag}_{16}\text{Cl}(\text{S}^t\text{Bu})_8(\text{CF}_3\text{COO})_7(\text{DMF})_4(\text{H}_2\text{O})] \cdot 1.5(\text{DMF})$  NC, although it encapsulates Cl<sup>−</sup> within the cluster core.<sup>43</sup> Recently, a  $[\text{Ag}_{17}\text{I}_3\text{S}(\text{C}_2\text{B}_{10}\text{H}_{10}\text{S}_2)_6(\text{CH}_3\text{CN})_{11}]$  NC was reported, but it

has a different geometry.<sup>15</sup> The construction of Ag<sub>17</sub> is shown in Figure 2A–C, in which the central Ag atom is coordinated to eight Ag atoms of the shell, resulting in a distorted square anti-biprismatic geometry. We have not seen any counterion upon solving the structure of these NCs. To identify the counterion, we have performed the IR (infrared) spectroscopy of a cocrystal. The IR spectrum exhibits a characteristic band at 1365 cm<sup>−1</sup> (Figure S2), which can be assigned to N–O stretching of the NO<sub>3</sub><sup>−</sup> ion.<sup>44</sup> It indicates that the NO<sub>3</sub><sup>−</sup> ion is the counterion existing in a cocrystal. The NO<sub>3</sub><sup>−</sup> has its origin from AgNO<sub>3</sub> used in the synthesis of Ag<sub>18</sub> NCs.<sup>41,42</sup>

ESI MS was performed to probe the existence of NCs in the solution. A single crystal was dissolved in acetonitrile for carrying out mass spectral measurements. Other details of the sample preparation and instrumental conditions are described in the instrumentation section of the Supporting Information (SI). The mass spectrum (MS) exhibits three major peaks at  $m/z$  3055, 3277, and 3499 in the positive ion mode (Figure 3Ai). Expanded peaks show a characteristic peak separation of  $m/z$  1.00, which confirms the +1 charge state. Therefore, the peaks at  $m/z$  3499, 3277, and 3055 are assigned to  $[\text{Ag}_{17}(\text{TBT})_8(\text{TFA})_7(\text{CH}_3\text{CN})_3\text{Cl}]^+$ ,  $[\text{Ag}_{16}(\text{TBT})_8(\text{TFA})_7(\text{CH}_3\text{CN})_3\text{Cl}]^+$ , and  $[\text{Ag}_{15}(\text{TBT})_8(\text{TFA})_5(\text{CH}_3\text{CN})_3\text{Cl}]^+$ , respectively. This was further confirmed by matching the experimental (violet trace) and simulated (red trace) isotopic distributions of the peaks (Figure 3Aii). The presence of Ag<sub>15</sub> and Ag<sub>16</sub> peaks in the mass spectrum may be a result of fragmentation. To probe this, we performed collision-induced dissociation (CID) experiments of the peaks due to Ag<sub>16</sub> and Ag<sub>17</sub> by varying the laboratory collision energy. For the Ag<sub>16</sub> peak, CID results in the Ag<sub>15</sub> moiety, as a result of the loss of CF<sub>3</sub>COOAg. Other fragmented species were also formed upon increasing the collision energy (Figure S3). CID studies of the Ag<sub>17</sub> peak



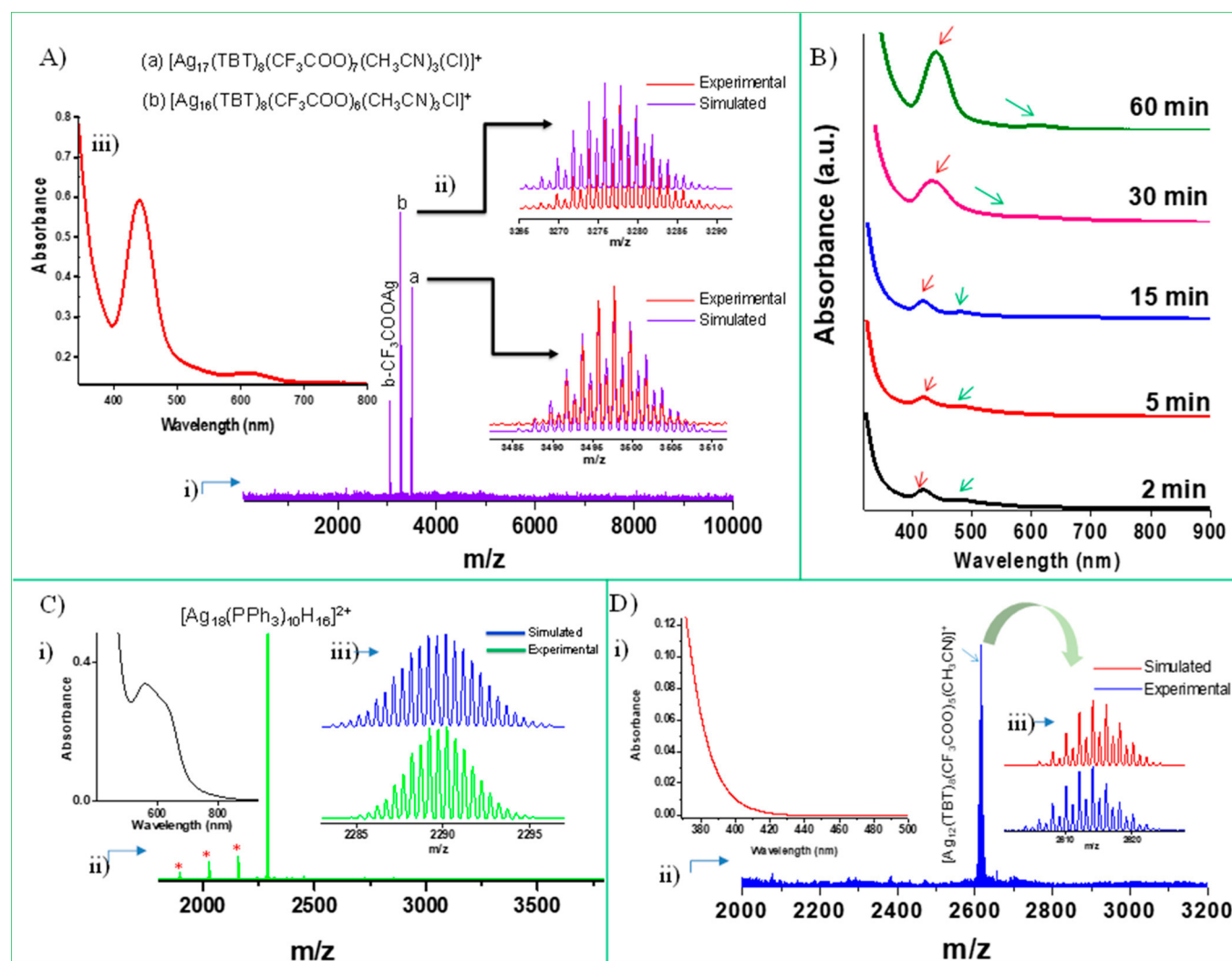


**Figure 3.** (A) (i) ESI MS in positive ion mode of crystals dissolved in acetonitrile solution. Peak (a) corresponds to  $[\text{Ag}_{17}(\text{TBT})_8(\text{TFA})_7(\text{CH}_3\text{CN})_3(\text{Cl})]^+$ . Peak (b) corresponds to  $[\text{Ag}_{16}(\text{TBT})_8(\text{TFA})_6(\text{CH}_3\text{CN})_3(\text{Cl})]^+$ , and another peak corresponds to  $\text{b-CF}_3\text{COOAg}$ . (ii) Isotopic distribution of (a) experimental spectrum (violet trace) is compared with simulated spectrum (red trace). (iii) UV-vis absorption spectrum of a crystal dissolved in acetonitrile solution. (B) UV-vis spectra of a reaction mixture in acetonitrile during  $t = 2\text{--}60$  min. Arrows mark the position of absorption bands. (C) UV-vis and ESI MS of the methanolic solution of  $[\text{Ag}_{18}(\text{PPh}_3)_{10}\text{H}_{16}]^{2+}$ . (D) UV-vis and ESI MS of  $[\text{Ag}_{12}(\text{TBT})_8(\text{TFA})_5(\text{CH}_3\text{CN})]^+$  in acetonitrile. Experimental and simulated mass spectra are compared in the insets of (Ciii) and (Diii).

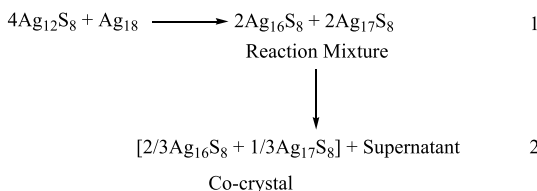
shows the systematic loss of TBT and TFA moieties, with an increase in collision energy, but no signature of the conversion to  $\text{Ag}_{16}$  NC was observed, as shown in Figure S4. We conclude that the peak corresponding to  $\text{Ag}_{16}$  is due to a separate entity and not arising from a fragment of  $\text{Ag}_{17}$ . The above observation proves the presence of two kinds of NCs in solution. Populations of  $\text{Ag}_{16}$  and  $\text{Ag}_{17}$  are not equal in the ESI MS (Figure 3Ai), assuming that both the species have similar ionization efficiencies. The  $\text{Ag}_{16}$  peak, whose population is more than  $\text{Ag}_{17}$  in the crystal, supports its appearance as the major NC species. Although there are additional factors such as ionization efficiency and ion transmission, which determine mass spectral intensities, the intensity ratio supports excess concentration of  $\text{Ag}_{16}$ . MS of the solution obtained after 1 h of the reaction shows the population of  $\text{Ag}_{16}$  and  $\text{Ag}_{17}$  to be almost equal (Figure S5). In order to correlate the findings of the single crystal and the reaction mixture, we carried out the MS of the supernatant left behind after crystallization. It was observed that the supernatant also contains peaks correspond-

ing to  $\text{Ag}_{16}$  and  $\text{Ag}_{17}$  (Figure S6). These findings suggest that the single crystal stabilizes with a population of 66.66 and 33.33% of  $\text{Ag}_{16}$  and  $\text{Ag}_{17}$  NCs, respectively, rather than the 1:1 ratio noted in another set of clusters,<sup>22</sup> despite the presence of extra  $\text{Ag}_{17}$  species in the supernatant. This could be due to the minimum energy considerations.<sup>22</sup> These results allow us to write a balanced chemical equation given below (considering the mass balance of silver and sulfur atoms only). To the best of our knowledge, this is the early observation of a homometallic interparticle reaction of silver NCs yielding cocrystals. We believe that the hydride-rich  $\text{Ag}_{18}$  is important for inducing the reaction. We suggest the following processes (Scheme 1).

The mass spectral intensities in the reaction mixture and supernatant support this conclusion. Equal intensities of  $\text{Ag}_{16}$  and  $\text{Ag}_{17}$  in the reaction mixture were changed to 2:1 for a solution prepared from the crystal. In the supernatant, the amount of  $\text{Ag}_{17}$  increased, although the ratio in the supernatant is not 1:2, which is understandable as some of the  $\text{Ag}_{16}$  and



### Scheme 1



Ag<sub>17</sub> may have only crystallized. To further explore the individual properties of Ag<sub>16</sub> and Ag<sub>17</sub> NCs, attempts were made to synthesize these separately by changing the reaction conditions, but we could not succeed in this process.

ESI MS of the reaction mixture measured at various time intervals ( $t = 2, 5, 15, 30, 60$  min and 7 days) after the addition

of a methanolic solution of  $\text{Ag}_{18}$  into a solution of  $\text{Ag}_{12}$  are shown in Figure 4. These measurements show that the characteristic peaks of individual  $\text{Ag}_{18}$  and  $\text{Ag}_{12}$  NCs disappeared completely after mixing them. At  $t = 2$  min (right after the reaction), a characteristic peak at  $m/z$  4928, which could be assigned to  $[\text{Ag}_{30}(\text{TBT})_9(\text{TFA})_6(\text{CH}_3\text{CN})_5]^+$ , denoted as  $\text{Ag}_{30}$ , was observed. The appearance of this peak suggests that an addition reaction had taken place between  $\text{Ag}_{12}$  and  $\text{Ag}_{18}$  NCs. Many peaks were observed in the range between  $m/z$  100 and 1000. All of these low molecular weight species ( $m/z < 1000$ ) were assigned to thiolates and phosphines formed during the reaction, shown in Figure S7. MS recorded after 5 min of reaction show many peaks in the region between  $m/z$  1000 and 3000, which were assigned to the heteroleptic reaction intermediates. No such peak was

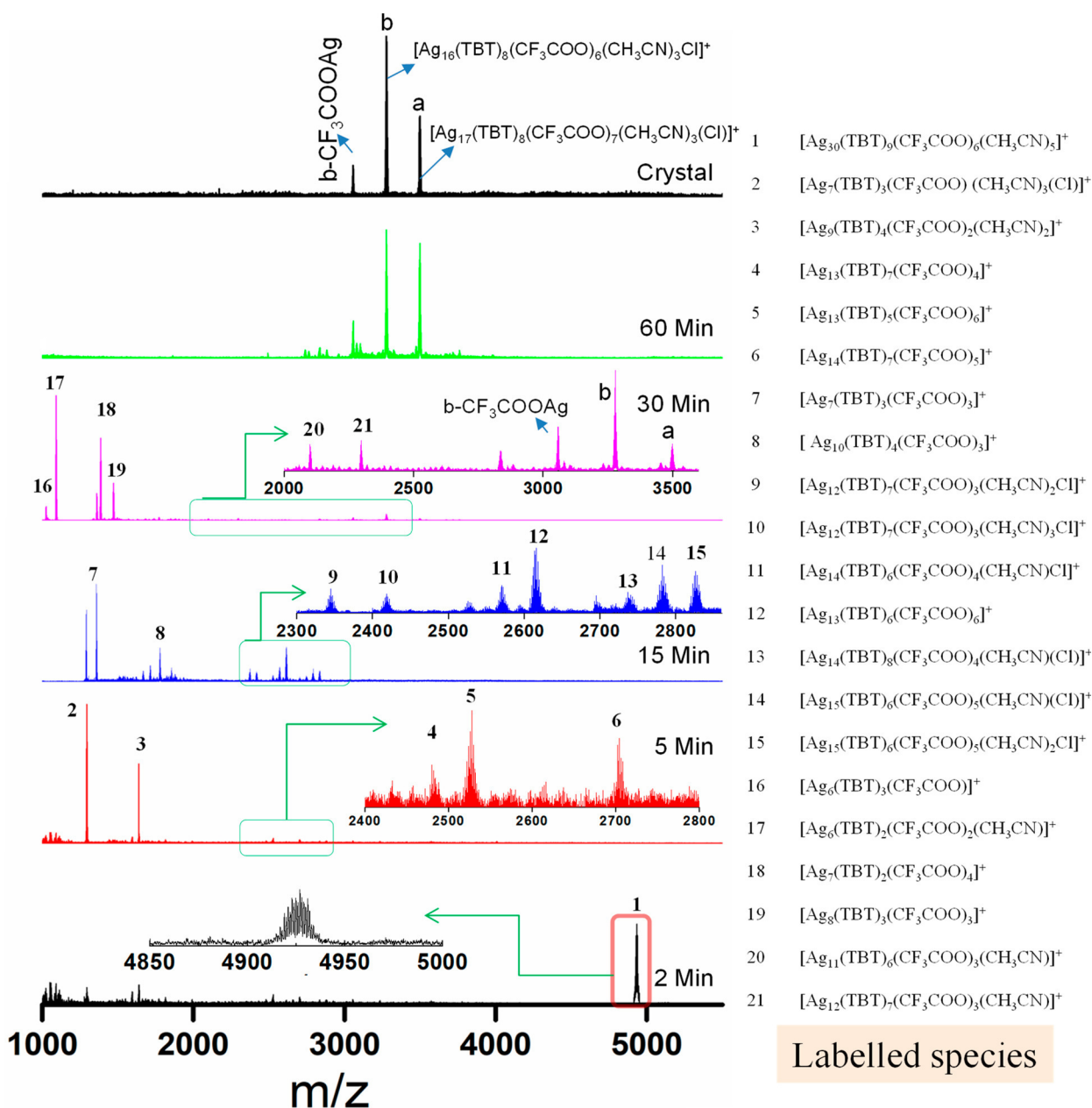


Figure 4. Time-dependent ESI MS spectra of the reaction mixture during the synthesis of  $[\text{Ag}_{16}(\text{TBT})_8(\text{TFA})_6(\text{CH}_3\text{CN})_3(\text{Cl})]^+$  and  $[\text{Ag}_{17}(\text{TBT})_8(\text{TFA})_7(\text{CH}_3\text{CN})_3(\text{Cl})]^+$  via silver-thiolate-based reaction intermediates (assigned from 1 to 21). Insets shows the magnified regions of ESI MS containing intermediates. Assignments of the peaks are on the right.

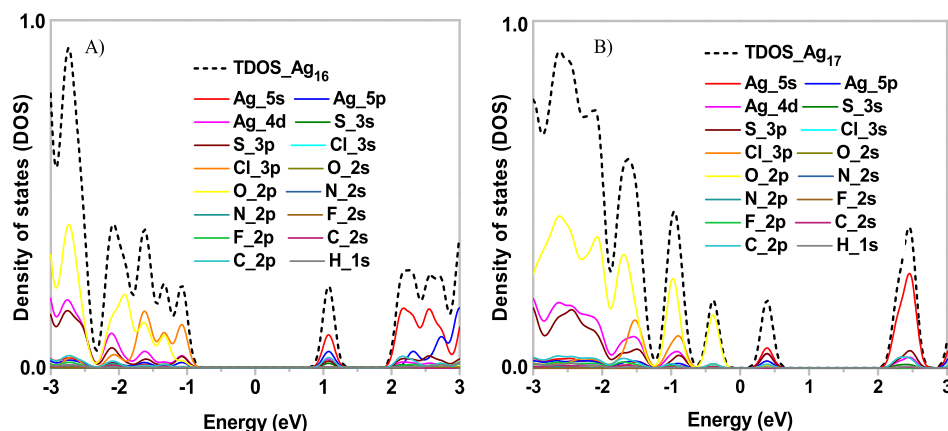


Figure 5. DOS analysis of molecular orbitals of the model cluster, (A)  $[\text{Ag}_{16}(\text{TBT})_8(\text{TFA})_7(\text{CH}_3\text{CN})_3\text{Cl}]^+$  and (B)  $[\text{Ag}_{17}(\text{TBT})_8(\text{TFA})_7(\text{CH}_3\text{CN})_3\text{Cl}]^+$ .

observed at  $m/z$  4928. This suggests that the adduct  $\text{Ag}_{30}$  is fragmented into smaller intermediates. Therefore, it appears to be a top-down approach and is different from the reported one.<sup>28,38</sup> MS monitored from time  $t = 15$ –30 min shows that significant changes occur. Color of the reaction mixture changes from dark to light brown. An important aspect noticed after 30 min is the emergence of different peaks whose  $m/z$  match with the molecular mass of  $[\text{Ag}_{15}(\text{TBT})_8(\text{TFA})_5(\text{CH}_3\text{CN})_3\text{Cl}]^+$ ,  $[\text{Ag}_{16}(\text{TBT})_8(\text{TFA})_6(\text{CH}_3\text{CN})_3\text{Cl}]^+$ , and  $[\text{Ag}_{17}(\text{TBT})_8(\text{TFA})_7(\text{CH}_3\text{CN})_3\text{Cl}]^+$ . After 1 h, MS does not show the appearance of any kind of intermediate(s). Intensities of the peaks corresponding to  $\text{Ag}_{16}$  and  $\text{Ag}_{17}$  were stabilized. MS of the crystal dissolved in acetonitrile also show signatures corresponding to  $\text{Ag}_{15}$ ,  $\text{Ag}_{16}$ , and  $\text{Ag}_{17}$  similar to that obtained after 1 h of the reaction, however, with different intensities. It suggests that stable NCs are formed after 1 h of the reaction. We were able to identify as many as 21 intermediates in the entire path of the reaction, which undergo dissociation and rearrangement via a “growth mechanism” which leads to the formation of  $\text{Ag}_{16}$  and  $\text{Ag}_{17}$  NCs. These intermediates can be represented by a general formula,  $[\text{Ag}_p(\text{TBT})_q(\text{TFA})_r(\text{CH}_3\text{CN})_s\text{Cl}]^+$ , where  $p = 6$ –15 and 30,  $q = 2$ –9,  $r = 1$ –6,  $s = 0$ –5, and  $t = 0$ –1 (Table S3). We, therefore, conclude that all of the silver thiolate intermediates formed during the reaction will size-focus to stable NCs, viz.  $[\text{Ag}_{16}(\text{TBT})_8(\text{TFA})_6(\text{CH}_3\text{CN})_3\text{Cl}]^+$  and  $[\text{Ag}_{17}(\text{TBT})_8(\text{TFA})_7(\text{CH}_3\text{CN})_3\text{Cl}]^+$ . Both the NCs have zero valence electron count. A flowchart of the reaction is shown in Scheme S1.

UV–vis absorption spectra of the reaction mixture were studied at different time intervals ( $t = 2, 5, 15, 30, 60$  min and 7 days) after the addition of a methanolic solution of  $\text{Ag}_{18}$  into a solution of  $\text{Ag}_{12}$ , as shown in Figure 3B. The UV–vis measurements during time  $t = 2$ –15 min show a broad absorption band with  $\lambda_{\text{max}}$  at 419 nm, followed by a shoulder at 483 nm. The absorption features of  $\text{Ag}_{12}$  and  $\text{Ag}_{18}$  NCs disappeared completely upon mixing them (Figure 3Ci, Di). This suggests the possibility that a reaction had taken place between  $\text{Ag}_{18}$  and  $\text{Ag}_{12}$  NCs. During  $t = 30$ –60 min, a notable red shift was observed, and the absorption peaks were shifted to  $\lambda_{\text{max}}$  438 and 611 nm (Figure 3B). The color of the reaction mixture changed from dark to light brown. After 1 week, the UV–vis absorption features of the crystal dissolved in acetonitrile were similar to that observed after 60 min of the

reaction (Figure 3Aiii). This implies that a stable composition had formed, and the reaction products did not transform subsequently.

Time-dependent density functional theory calculations were performed on the optimized structures of  $\text{Ag}_{16}$  and  $\text{Ag}_{17}$  NCs to understand their optical transitions (Figure S8). In the optimized structures, F, C, and H atoms were relaxed, and all other atoms were kept fixed. This setup was established using the hybrid Perdew, Burke, and Ernzerhof (PBE) model without any symmetry constraints. The following PAW setups,  $\text{Ag}(4d^{10}5s^1)$ ,  $\text{Cl}(3s^23p^5)$ ,  $\text{S}(3s^23p^4)$ ,  $\text{F}(2s^22p^5)$ ,  $\text{O}(2s^22p^4)$ ,  $\text{N}(2s^22p^3)$ ,  $\text{C}(2s^22p^2)$ , and  $\text{H}(1s^1)$ , were used including the scalar-relativistic effects for silver. The optical absorption spectra of optimized clusters having the simplified model ligand ( $\text{CH}_3$ ) were calculated using linear response time-dependent density functional theory.<sup>45</sup> The oscillator strengths of both  $\text{Ag}_{16}$  and  $\text{Ag}_{17}$  NCs were added in a 2:1 ratio in order to obtain the absorption spectrum of the cocrystal. The absorption spectrum was plotted with a Gaussian broadening of 0.085 eV in the energy range of 400–900 nm, and it is compared with the experimental spectrum (red trace), as shown in Figure S9. The calculated spectrum displays the molecular transitions at 356 and 742 nm. The absorption peaks were observed at 439 and 611 nm in the experiment which are blue-shifted by 43 nm and red-shifted by 103 nm, respectively, from the calculated spectrum. This difference could be due to the reduced structure utilized for theoretical calculations.<sup>45,46</sup> The molecular orbitals (MOs) involved for the transitions at 356 and 742 nm are shown in Figures S10 and S11, respectively. These transitions have mainly ligand to metal character. From the density of states (DOS) analysis, it is seen that significant difference in the spectra between  $\text{Ag}_{16}$  and  $\text{Ag}_{17}$  clusters lies only in the frontier orbitals (Figure 5). HOMO of the clusters is dominated by 2p and 3p atomic orbitals (AOs) of ligands, whereas LUMO is composed of 5s of Ag. The HOMO–LUMO gap is larger for  $\text{Ag}_{16}$  than for the  $\text{Ag}_{17}$  cluster and may be due to the presence of a central Ag atom, which significantly alters its electronic structure. Therefore, to understand the role of the central Ag atom in the  $\text{Ag}_{17}$  cluster, the partial DOS spectrum was separately plotted for the central Ag atom and of the  $\text{Ag}_{16}$  shell (Figure 6). From this, it is clearly noted that the AOs of the central Ag atom were extensively populated only in the frontier orbitals, and the rest of the MOs were dominated by the AOs of the  $\text{Ag}_{16}$  shell. However, the HOMO is comparably contributed by the 4d AOs of  $\text{Ag}_{16}$  shell

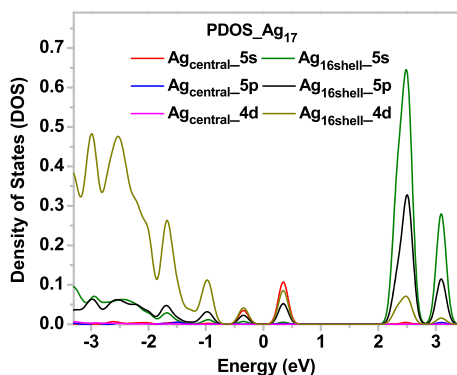


**Figure 6.** Partial DOS analysis of molecular orbitals of the model cluster,  $[\text{Ag}_{17}(\text{TBT})_8(\text{TFA})_7(\text{CH}_3\text{CN})_3\text{Cl}]^+$ .

and 5s AOs of the central Ag atom, whereas the near LUMOs are predominantly due to 5s AOs of the central Ag atom. Furthermore, the optical absorption transitions of both  $\text{Ag}_{17}$  and the cocrystal at a wavelength of  $\sim 742$  nm might be significantly influenced by the high spherical symmetry of 5s AOs of the central Ag atom of  $\text{Ag}_{17}$  rather than the 4d AOs of the  $\text{Ag}_{16}$  shell. Therefore, the peaks at 742 and 356 nm are attributed to sp–sp intraband transition and pd–sp transition, respectively. Contributions of AOs to the MOs were analyzed using the Kohn–Sham MOs and DOS.

## CONCLUSIONS

To summarize, we report an interparticle reaction between two atomically precise NCs  $[\text{Ag}_{12}(\text{TBT})_8(\text{TFA})_5(\text{CH}_3\text{CN})]^+$  and  $[\text{Ag}_{18}(\text{TPP})_{10}\text{H}_{16}]^{2+}$  abbreviated as  $\text{Ag}_{12}$  and  $\text{Ag}_{18}$ , respectively, resulting in products  $[\text{Ag}_{16}(\text{TBT})_8(\text{TFA})_7(\text{CH}_3\text{CN})_3\text{Cl}]^+$  and  $[\text{Ag}_{17}(\text{TBT})_8(\text{TFA})_7(\text{CH}_3\text{CN})_3\text{Cl}]^+$  which cocrystallize together. The reaction proceeds *via* a growth mechanism utilizing silver thiolate intermediates. Both the NCs have an identical  $\text{Ag}_{16}\text{S}_8$  shell, arranged in a layered fashion of  $\text{Ag}_4\text{S}_4$ – $\text{Ag}_8$ – $\text{Ag}_4\text{S}_4$ , forming a sandwich. This makes the NCs indistinguishable, and they cocrystallize. In a single crystal, the occupancies of  $\text{Ag}_{16}$  and  $\text{Ag}_{17}$  NCs are 66.66 and 33.33%, respectively. MS of the reaction product shows the population of  $\text{Ag}_{16}$  and  $\text{Ag}_{17}$  to be almost equal, whereas that of a crystal dissolved in acetonitrile shows a 2:1 ratio of their intensities. This may possibly suggest that the concentrations of  $\text{Ag}_{16}$  and  $\text{Ag}_{17}$  are almost equal in the product, but selective incorporation occurs in the crystal. For further validation, MS of the supernatant after crystallization was measured which showed peaks corresponding to  $\text{Ag}_{16}$  and  $\text{Ag}_{17}$  NCs, but with an excess of the latter. These findings support that the single crystal stabilizes with 2:1 ratio of  $\text{Ag}_{16}$  and  $\text{Ag}_{17}$  NCs, despite the presence of extra  $\text{Ag}_{17}$  species in the supernatant. Our results allowed us to write a balanced chemical equation for the reaction. We believe that our results will initiate more activities in the area of atomically precise clusters.

## EXPERIMENTAL SECTION

**Chemicals and Materials.** *tert*-Butylthiol (TBT), silver trifluoroacetate ( $\text{CF}_3\text{COOAg}$ ), triphenylphosphine (TPP), and sodium borohydride ( $\text{NaBH}_4$ , 98%) were purchased from Aldrich. Silver nitrate ( $\text{AgNO}_3$ ) was purchased from Rankem Chemicals. All chemicals were used as received without further purification. All of the solvents, such as dichloromethane (DCM), methanol (MeOH), acetonitrile ( $\text{CH}_3\text{CN}$ ), and chloroform ( $\text{CHCl}_3$ ), were purchased

from Rankem Chemicals and were of analytical grade. Milli-Q water was used for the synthesis.

**Synthesis of a Mixture of  $[\text{Ag}_{16}(\text{TBT})_8(\text{CF}_3\text{COO})_7(\text{CH}_3\text{CN})_2\text{Cl}]^+$  and  $[\text{Ag}_{17}(\text{TBT})_8(\text{CF}_3\text{COO})_7(\text{CH}_3\text{CN})_2\text{Cl}]^+$ .** Synthesis of  $[\text{Ag}_{12}(\text{TBT})_8(\text{TFA})_5(\text{CH}_3\text{CN})]^+$ : 200 mg of silver thiolate,  $\text{Ag}(\text{TBT})_m$ , was added to a solution of acetonitrile and methanol (3 mL each). To this was added 200 mg of  $\text{CF}_3\text{COOAg}$  upon stirring, and after some time, a clear transparent solution appeared, which resulted in the formation of  $[\text{Ag}_{12}(\text{TBT})_8(\text{TFA})_5(\text{CH}_3\text{CN})]^+$  denoted as  $\text{Ag}_{12}$ . About 1 mL of methanolic solution of  $[\text{Ag}_{18}(\text{TPP})_{10}\text{H}_{16}]^{2+}$  denoted as  $\text{Ag}_{18}$  ( $\sim 5$  mg/mL) was added to the above reaction mixture.  $\text{Ag}_{18}$  was synthesized by a reported procedure (see the [Supporting Information](#) for a detailed synthesis).<sup>41,42</sup> A dark brown solution along with a black precipitate was formed; the mixture was kept stirring for 1 h, and the solution was centrifuged at 8000 rpm (5868g). The black precipitate was discarded. The solution obtained after centrifugation was left for slow evaporation at  $5 \pm 5$  °C for crystallization, and after 1 week, light brown crystals were obtained. Crystals were soluble in acetonitrile, methanol, ethanol, and DCM. Yield of the synthesis was 25% in terms of silver.

## ASSOCIATED CONTENT

### Supporting Information

The Supporting Information is available free of charge on the ACS Publications website at DOI: 10.1021/acsnano.9b06740.

Experimental section, instrumentation, X-ray crystallographic parameters, additional experimental data (PDF)  
X-ray data for compound 1 (CIF)

## AUTHOR INFORMATION

### Corresponding Author

\*E-mail: [pradeep@iitm.ac.in](mailto:pradeep@iitm.ac.in).

### ORCID

Thalappil Pradeep: 0000-0003-3174-534X

### Author Contributions

<sup>†</sup>W.A.D. and M.B. contributed equally.

### Notes

The authors declare no competing financial interest.

## ACKNOWLEDGMENTS

We thank the Department of Science and Technology (DST) for supporting our research program. We thank the Sophisticated Analytical Instruments Facility, Indian Institute of Technology Madras for SCXRD data collection. W.A.D. thanks SERB-DST for the award of a National Postdoctoral Fellowship (NPDF). M.B. and K.S.S. thank U.G.C. for their research fellowships. G.P. thanks IITM for an Institute Postdoctoral Fellowship. D.G. and E.K. thank IIT Madras for Institute Doctoral Fellowships.

## REFERENCES

- (1) Schmid, G. *Nanoparticles: From Theory to Application*, 2nd ed.; Wiley-VCH: Weinheim, Germany, 2010; pp 1–533.
- (2) Jin, R.; Zeng, C.; Zhou, M.; Chen, Y. Atomically Precise Colloidal Metal Nanoclusters and Nanoparticles: Fundamentals and Opportunities. *Chem. Rev.* **2016**, *116*, 10346–10413.
- (3) Chakraborty, I.; Pradeep, T. Atomically Precise Clusters of Noble Metals: Emerging Link between Atoms and Nanoparticles. *Chem. Rev.* **2017**, *117*, 8208–8271.
- (4) Su, Y. M.; Wang, Z.; Zhuang, G. L.; Zhao, Q. Q.; Wang, X. P.; Tung, C. H.; Sun, D. Unusual fcc-Structured  $\text{Ag}_{10}$  Kernels Trapped in  $\text{Ag}_{70}$  Nanoclusters. *Chem. Sci.* **2019**, *10*, 564–568.
- (5) Liu, J. W.; Wang, Z.; Chai, Y. M.; Kurmoo, M.; Zhao, Q. Q.; Wang, X. P.; Tung, C. H.; Sun, D. Core Modulation of 70-Nuclei



Core-Shell Silver Nanoclusters. *Angew. Chem., Int. Ed.* **2019**, *58*, 6276–6279.

(6) Niihori, Y.; Hashimoto, S.; Koyama, Y.; Hossain, S.; Kurashige, W.; Negishi, Y. Dynamic Behavior of Thiolate-Protected Gold-Silver 38-Atom Alloy Clusters in Solution. *J. Phys. Chem. C* **2019**, *123*, 13324–13329.

(7) Du, Y.; Sheng, H.; Astruc, D.; Zhu, M. Atomically Precise Noble Metal Nanoclusters as Efficient Catalysts: A Bridge between Structure and Properties. *Chem. Rev.* **2019**, DOI: 10.1021/acs.chemrev.8b00726.

(8) Chakraborty, P.; Nag, A.; Chakraborty, A.; Pradeep, T. Approaching Materials with Atomic Precision Using Supramolecular Cluster Assemblies. *Acc. Chem. Res.* **2019**, *52*, 2–11.

(9) Lin, C. A. J.; Yang, T. Y.; Lee, C. H.; Huang, S. H.; Sperling, R. A.; Zanella, M.; Li, J. K.; Shen, J. L.; Wang, H. H.; Yeh, H. I.; et al. Synthesis, Characterization, and Bioconjugation of Fluorescent Gold Nanoclusters toward Biological Labeling Applications. *ACS Nano* **2009**, *3*, 395–401.

(10) Jin, R. Atomically Precise Metal Nanoclusters: Stable Sizes and Optical Properties. *Nanoscale* **2015**, *7*, 1549–1565.

(11) Jin, R.; Qian, H.; Wu, Z.; Zhu, Y.; Zhu, M.; Mohanty, A.; Garg, N. Size Focusing: A Methodology for Synthesizing Atomically Precise Gold Nanoclusters. *J. Phys. Chem. Lett.* **2010**, *1*, 2903–2910.

(12) Krishnadas, K. R.; Baksi, A.; Ghosh, A.; Natarajan, G.; Som, A.; Pradeep, T. Interparticle Reactions: An Emerging Direction in Nanomaterials Chemistry. *Acc. Chem. Res.* **2017**, *50*, 1988–1996.

(13) Wang, Z. Y.; Wang, M. Q.; Li, Y. L.; Luo, P.; Jia, T. T.; Huang, R. W.; Zang, S. Q.; Mak, T. C. W. Atomically Precise Site-Specific Tailoring and Directional Assembly of Supratomic Silver Nanoclusters. *J. Am. Chem. Soc.* **2018**, *140*, 1069–1076.

(14) Yang, H.; Wang, Y.; Zheng, N. Stabilizing Subnanometer Ag(0) Nanoclusters by Thiolate and Diphosphine Ligands and Their Crystal Structures. *Nanoscale* **2013**, *5*, 2674–2677.

(15) Li, Y.-L.; Wang, Z.-Y.; Ma, X.-H.; Luo, P.; Du, C.-X.; Zang, S.-Q. Distinct Photophysical Properties in Atom-Precise Silver and Copper Nanocluster Analogues. *Nanoscale* **2019**, *11*, 5151–5157.

(16) Li, B.; Huang, R. W.; Qin, J. H.; Zang, S. Q.; Gao, G. G.; Hou, H. W.; Mak, T. C. W. Thermochromic Luminescent Nest-Like Silver Thiolate Cluster. *Chem. - Eur. J.* **2014**, *20*, 12416–12420.

(17) Dhayal, R. S.; Lin, Y. R.; Liao, J. H.; Chen, Y. J.; Liu, Y. C.; Chiang, M. H.; Kahlal, S.; Saillard, J. Y.; Liu, C. W. A Superatom Complex with a Chiral Metallic Core and High Potential for Isomerism. *Chem. - Eur. J.* **2016**, *22*, 9943–9947.

(18) Dhayal, R. S.; Liao, J. H.; Liu, Y. C.; Chiang, M. H.; Kahlal, S.; Saillard, J. Y.; Liu, C. W.  $[\text{Ag}_{21}\{\text{S}_2\text{P}(\text{O}^i\text{Pr})_2\}_{12}]^+$ : An Eight-Electron Superatom. *Angew. Chem., Int. Ed.* **2015**, *54*, 3702–3706.

(19) Joshi, C. P.; Bootharaju, M. S.; Alhilaly, M. J.; Bakr, O. M.  $[\text{Ag}_{25}(\text{SR})_{18}]^-$ : The “Golden” Silver Nanoparticle. *J. Am. Chem. Soc.* **2015**, *137*, 11578–11581.

(20) Khatun, E.; Bodiuzzaman, M.; Sugi, K. S.; Chakraborty, P.; Paramasivam, G.; Dar, W. A.; Ahuja, T.; Antharjanam, S.; Pradeep, T. Confining an  $\text{Ag}_{10}$  Core in an  $\text{Ag}_{12}$  Shell: A Four-Electron Superatom with Enhanced Photoluminescence upon Crystallization. *ACS Nano* **2019**, *13*, 5753–5759.

(21) AbdulHalim, L. G.; Bootharaju, M. S.; Tang, Q.; Del Gobbo, S.; AbdulHalim, R. G.; Eddaoudi, M.; Jiang, D.-E.; Bakr, O. M.  $[\text{Ag}_{29}(\text{BDT})_{12}(\text{TPP})_4]$ : A Tetravalent Nanocluster. *J. Am. Chem. Soc.* **2015**, *137*, 11970–11976.

(22) Bodiuzzaman, M.; Ghosh, A.; Sugi, K. S.; Nag, A.; Khatun, E.; Varghese, B.; Paramasivam, G.; Antharjanam, S.; Natarajan, G.; Pradeep, T. Camouflaging Structural Diversity: Co-Crystallization of Two Different Nanoparticles Having Different Cores but the Same Shell. *Angew. Chem., Int. Ed.* **2019**, *58*, 189–194.

(23) Yang, H.; Wang, Y.; Huang, H.; Gell, L.; Lehtovaara, L.; Malola, S.; Häkkinen, H.; Zheng, N. All-Thiol-Stabilized  $\text{Ag}_{44}$  and  $\text{Au}_{12}\text{Ag}_{32}$  Nanoparticles with Single-Crystal Structures. *Nat. Commun.* **2013**, *4*, 2422.

(24) Fenske, D.; Anson, C. E.; Eichhöfer, A.; Fuhr, O.; Ingendoh, A.; Persau, C.; Richert, C. Syntheses and Crystal Structures of

$[\text{Ag}_{123}\text{S}_{35}(\text{S}^t\text{Bu})_{50}]$  and  $[\text{Ag}_{344}\text{S}_{124}(\text{S}^t\text{Bu})_{96}]$ . *Angew. Chem., Int. Ed.* **2005**, *44*, 5242–5246.

(25) Anson, C. E.; Eichhöfer, A.; Issac, I.; Fenske, D.; Fuhr, O.; Sevilano, P.; Persau, C.; Stalke, D.; Zhang, J. Synthesis and Crystal Structures of the Ligand-Stabilized Silver Chalcogenide Clusters  $[\text{Ag}_{154}\text{Se}_{77}(\text{Dppxy})_{18}]$ ,  $[\text{Ag}_{320}(\text{S}^t\text{Bu})_{60}\text{S}_{130}(\text{Dppp})_{12}]$ ,  $[\text{Ag}_{352}\text{S}_{128}(\text{S}^t\text{C}_5\text{H}_{11})_{96}]$  and  $[\text{Ag}_{490}\text{S}_{188}(\text{S}^t\text{C}_5\text{H}_{11})_{114}]$ . *Angew. Chem., Int. Ed.* **2008**, *47*, 1326–31.

(26) Braga, D.; Maini, L.; Grepioni, F. Mechanochemical Preparation of Co-Crystals. *Chem. Soc. Rev.* **2013**, *42*, 7638–7648.

(27) Vishweshwar, P.; McMahon, J. A.; Bis, J. A.; Zaworotko, M. J. Pharmaceutical Co-Crystals. *J. Pharm. Sci.* **2006**, *95*, 499–516.

(28) Cao, Y.; Guo, J.; Shi, R.; Waterhouse, G. I. N.; Pan, J.; Du, Z.; Yao, Q.; Wu, L. Z.; Tung, C. H.; Xie, J.; et al. Evolution of Thiolate-Stabilized Ag Nanoclusters from Ag-Thiolate Cluster Intermediates. *Nat. Commun.* **2018**, *9*, 2379.

(29) Yan, J.; Malola, S.; Hu, C.; Peng, J.; Dittrich, B.; Teo, B. K.; Häkkinen, H.; Zheng, L.; Zheng, N. Co-Crystallization of Atomically Precise Metal Nanoparticles Driven by Magic Atomic and Electronic Shells. *Nat. Commun.* **2018**, *9*, 3357.

(30) Wu, Z.; He, L.; Gan, Z.; Xia, N.; Liao, L. Alternative Array Stacking of  $\text{Ag}_{26}\text{Au}$  and  $\text{Ag}_{24}\text{Au}$  Nanoclusters. *Angew. Chem., Int. Ed.* **2019**, *58*, 9897–9901.

(31) Zeng, C.; Chen, Y.; Das, A.; Jin, R. Transformation Chemistry of Gold Nanoclusters: From One Stable Size to Another. *J. Phys. Chem. Lett.* **2015**, *6*, 2976–2986.

(32) Krishnadas, K. R.; Ghosh, A.; Baksi, A.; Chakraborty, I.; Natarajan, G.; Pradeep, T. Intercluster Reactions between  $\text{Au}_{25}(\text{SR})_{18}$  and  $\text{Ag}_{44}(\text{SR})_{30}$ . *J. Am. Chem. Soc.* **2016**, *138*, 140–148.

(33) Krishnadas, K. R.; Baksi, A.; Ghosh, A.; Natarajan, G.; Pradeep, T. Structure-Conserving Spontaneous Transformations between Nanoparticles. *Nat. Commun.* **2016**, *7*, 13447.

(34) Bhat, S.; Baksi, A.; Mudedla, S. K.; Natarajan, G.; Subramanian, V.; Pradeep, T.  $\text{Au}_{22}\text{Ir}_3(\text{PET})_{18}$ : An Unusual Alloy Cluster through Intercluster Reaction. *J. Phys. Chem. Lett.* **2017**, *8*, 2787–2793.

(35) Krishnadas, K. R.; Ghosh, D.; Ghosh, A.; Natarajan, G.; Pradeep, T. Structure-Reactivity Correlations in Metal Atom Substitutions of Monolayer-Protected Noble Metal Alloy Clusters. *J. Phys. Chem. C* **2017**, *121*, 23224–23232.

(36) Krishnadas, K. R.; Baksi, A.; Ghosh, A.; Natarajan, G.; Pradeep, T. Manifestation of Geometric and Electronic Shell Structures of Metal Clusters in Intercluster Reactions. *ACS Nano* **2017**, *11*, 6015–6023.

(37) Ghosh, A.; Ghosh, D.; Khatun, E.; Chakraborty, P.; Pradeep, T. Unusual Reactivity of Dithiol Protected Clusters in Comparison to Monothiol Protected Clusters: Studies Using  $\text{Ag}_{51}(\text{BDT})_{19}(\text{TPP})_3$  and  $\text{Ag}_{29}(\text{BDT})_{12}(\text{TPP})_4$ . *Nanoscale* **2017**, *9*, 1068–1077.

(38) Luo, Z.; Nachammai, V.; Zhang, B.; Yan, N.; Leong, D. T.; Jiang, D. E.; Xie, J. Toward Understanding the Growth Mechanism: Tracing All Stable Intermediate Species from Reduction of  $\text{Au}(\text{I})$ -Thiolate Complexes to Evolution of  $\text{Au}_{25}$  nanoclusters. *J. Am. Chem. Soc.* **2014**, *136*, 10577–10580.

(39) Yao, Q.; Yuan, X.; Fung, V.; Yu, Y.; Leong, D. T.; Jiang, D. E.; Xie, J. Understanding Seed-Mediated Growth of Gold Nanoclusters at Molecular Level. *Nat. Commun.* **2017**, *8*, 927.

(40) Huang, R. W.; Wei, Y. S.; Dong, X. Y.; Wu, X. H.; Du, C. X.; Zang, S. Q.; Mak, T. C. W. Hypersensitive Dual-Function Luminescence Switching of a Silver-Chalcogenolate Cluster-Based Metal-Organic Framework. *Nat. Chem.* **2017**, *9*, 689–697.

(41) Ghosh, A.; Bodiuzzaman, M.; Nag, A.; Jash, M.; Baksi, A.; Pradeep, T. Sequential Dihydrogen Desorption from Hydride-Protected Atomically Precise Silver Clusters and the Formation of Naked Clusters in the Gas Phase. *ACS Nano* **2017**, *11*, 11145–11151.

(42) Bootharaju, M. S.; Dey, R.; Gevers, L. E.; Hedhili, M. N.; Basset, J. M.; Bakr, O. M. A New Class of Atomically Precise, Hydride-Rich Silver Nanoclusters Co-Protected by Phosphines. *J. Am. Chem. Soc.* **2016**, *138*, 13770–13773.

(43) Alhilaly, M. J.; Huang, R.-W.; Naphade, R.; Alamer, B.; Hedhili, M. N.; Emwas, A.-H.; Maity, P.; Yin, J.; Shkurenko, A.; Mohammed,

O. F.; et al. Shkurenko, Assembly of Atomically Precise Silver Nanoclusters into Nanocluster-Based Frameworks. *J. Am. Chem. Soc.* **2019**, *141*, 9585–9592.

(44) Qu, M.; Li, H.; Xie, L. H.; Yan, S. T.; Li, J. R.; Wang, J. H.; Wei, C. Y.; Wu, Y. W.; Zhang, X. M. Bidentate Phosphine-Assisted Synthesis of an All-Alkynyl-Protected Ag<sub>74</sub> Nanocluster. *J. Am. Chem. Soc.* **2017**, *139*, 12346–12349.

(45) Walter, M.; Häkkinen, H.; Lehtovaara, L.; Puska, M.; Enkovaara, J.; Rostgaard, C.; Mortensen, J. J. Time-Dependent Density-Functional Theory in the Projector Augmented-Wave Method. *J. Chem. Phys.* **2008**, *128*, 244101–244110.

(46) Alhilaly, M. J.; Bootharaju, M. S.; Joshi, C. P.; Besong, T. M.; Emwas, A. H.; Juarez-Mosqueda, R.; Kaappa, S.; Malola, S.; Adil, K.; Shkurenko, A.; et al. [Ag<sub>67</sub>(SPhMe<sub>2</sub>)<sub>32</sub>(PPh<sub>3</sub>)<sub>8</sub>]<sup>3+</sup>: Synthesis, Total Structure, and Optical Properties of a Large Box-Shaped Silver Nanocluster. *J. Am. Chem. Soc.* **2016**, *138*, 14727–14732.

# Supporting Information

## Interparticle Reactions between Silver Nanoclusters Leading to Product Cocrystals by Selective Cocrystallization

*Wakeel Ahmed Dar,<sup>†</sup> Mohammad Bodiuzzaman,<sup>†</sup> Debasmita Ghosh, Ganesan Paramasivam, Esma Khatun, Korath Shivan Sugi and Thalappil Pradeep\**

Department of Chemistry, DST Unit of Nanoscience and Thematic Unit of Excellence, Indian Institute of Technology Madras, Chennai 600036, India

Name	Description	Page no.
	Experimental section	3
	Instrumentation	4
	UV/Vis spectroscopy	4
	General instrumental parameters used for ESI measurements	4
	X-ray crystallography	5

	Single crystal X-ray diffraction analysis	5
	Electron Count formula of intermediates	6
Figure S1	Space-filling model of Ag <sub>16</sub> S <sub>8</sub> shell in NCs	6
Figure S2	IR spectrum of Ag <sub>16</sub> :Ag <sub>17</sub> co-crystal	7
Figure S3	MSMS spectra of [Ag <sub>16</sub> (TBT) <sub>8</sub> (CF <sub>3</sub> COO) <sub>6</sub> (CH <sub>3</sub> CN) <sub>3</sub> (Cl)] <sup>+</sup>	8
Figure S4	MSMS spectra of [Ag <sub>17</sub> (TBT) <sub>8</sub> (CF <sub>3</sub> COO) <sub>7</sub> (CH <sub>3</sub> CN) <sub>3</sub> (Cl)] <sup>+</sup>	9
Figure S5	ESI MS of a reaction product in acetonitrile	10
Figure S6	ESI MS of a supernatant obtained after crystallization	11
Figure S7	ESI MS spectra from m/z 100-1000	12
Scheme 1	Flow chart of reaction process	13
Figure S8	Optimized geometry of Ag <sub>16</sub> and Ag <sub>17</sub>	14
Figure S9	Experimental and calculated absorption spectra	15
Figure S10	Molecular orbitals observed at 356 nm	16
Figure S11	Molecular orbitals observed at 742 nm	17
Table S1	Crystal Structure data	18
Table S2	Silver complexes, silver thiolates and phosphine intermediates	19
Table S3	Reaction intermediates	20
	References	22



## Experimental Section

### Synthesis of $[\text{Ag}_{18}(\text{TPP})_{10}\text{H}_{16}]^{2+}$ nanocluster

Phosphine and hydride co-protected  $[\text{Ag}_{18}(\text{TPP})_{10}\text{H}_{16}]^{2+}$  nanocluster (TPP – triphenylphosphine) assigned as  $\text{Ag}_{18}$  was synthesized by a reported method.<sup>1-2</sup> 20 mg of  $\text{AgNO}_3$  was dissolved in the mixed solvents of 5 mL methanol and 9 mL of chloroform. After that 70 mg of TPP, dissolved in 1 mL of  $\text{CH}_3\text{Cl}$ , was added to the above reaction mixture under stirring condition. After 20 min of stirring, 6 mg of  $\text{NaBH}_4$  in 0.5 mL of ice cold water was added. Upon addition of the reducing agent, colourless solution changes to yellow. The reaction mixture was kept for continuous stirring for 3 h under dark condition. After 3 h the yellow colour solution changes to dark green which indicated the formation of the  $\text{Ag}_{18}$  cluster. The reaction mixture was allowed for solvent evaporation under reduced pressure. The green solid product collected was washed several times with water to remove excess silver precursor and the reducing agent. After washing, the pure material was extracted using methanol. The green colour solution of NC was characterized using UV-vis and ESI MS and was used for further reaction.

## **Instrumentation**

### **(a) UV/Vis spectroscopy**

UV-vis spectra were recorded using a Perkin Elmer Lambda 25 instrument in the range 200 – 1100 nm.

### **(b) General instrumental parameters used for ESI measurements**

Cluster sample was analysed by Waters Synapt G2Si High Definition Mass Spectrometer equipped with electrospray ionization (ESI) and ion mobility (IM) separation. The sample was analysed in positive ESI mode. The optimized conditions for the sample analysed is given below:

Sample concentration: 10 µg/mL

Solvent: CH<sub>3</sub>CN

Flow rate: 30 uL/min

Capillary voltage: 2- 3 kV

Cone voltage: 30 V

Source offset: 20 V

Trap collision Energy: 0 V

Transfer collision Energy: 0 V

Source temperature: 100°C

Desolvation temperature: 200°C

Desolvation gas Flow: 400 L/h

Trap gas flow: 10 L/h

### **(c) X-ray crystallography**

Single crystal data were measured using a Bruker Kappa APEX III CMOS diffractometer using CuK $\alpha$  ( $\lambda = 1.54178 \text{ \AA}$ ) radiation. Indexing was performed using APEX III. Data integration and reduction were performed using SAINT V8.37A. Absorption correction was performed by multi-scan method implemented in SADABS (Bruker, 2016). Space group was determined using XPREP implemented in APEX III.

### **Single crystal X-ray diffraction (SCXRD) analysis**

Structure was solved using SHELXT-2017 and least-squares refined using SHELXL-2017. Crystal data and refinement conditions are shown in Table S1. Suitable restraints were applied during the least-squares (LS) refinement. Upon refinement, it was observed that Ag<sub>16</sub> and Ag<sub>17</sub> were not disordered. The existence of two types of molecules in the same site results in the additional symmetry related disorders in both the molecules. Three of the CF<sub>3</sub> moieties are doubly disordered and one acetonitrile was also disordered. Their disorders have been resolved. The molecule has a crystallographic P2<sub>1</sub>/n space group. A more detailed explanation of Ag<sub>16</sub> and Ag<sub>17</sub> structure reveals the atom Ag in the shell centre of Ag<sub>17</sub> which has occupancy of 1/3 (33.33%). This depicts that in the co-crystal structure 2/3 (66.66%) NC molecules have 16 Ag atoms and 1/3 molecules have 17 Ag atoms. The difference Fourier map towards the end showed the presence of acetonitrile molecule in the lattice.

### Electron count formula

The total valence electron count (M) for each intermediates,  $[\text{Ag}_p(\text{TBT})_q(\text{TFA})_r(\text{CH}_3\text{CN})_s\text{Cl}_t]^+$  is counted by the formula,  $M = p - q - r - t - c$ , where p, q, r, t and c are the number of silver atoms, thiolate, trifluoroacetates, chloride and net positive charge on the molecule, respectively (Table S3-S5).<sup>3</sup>

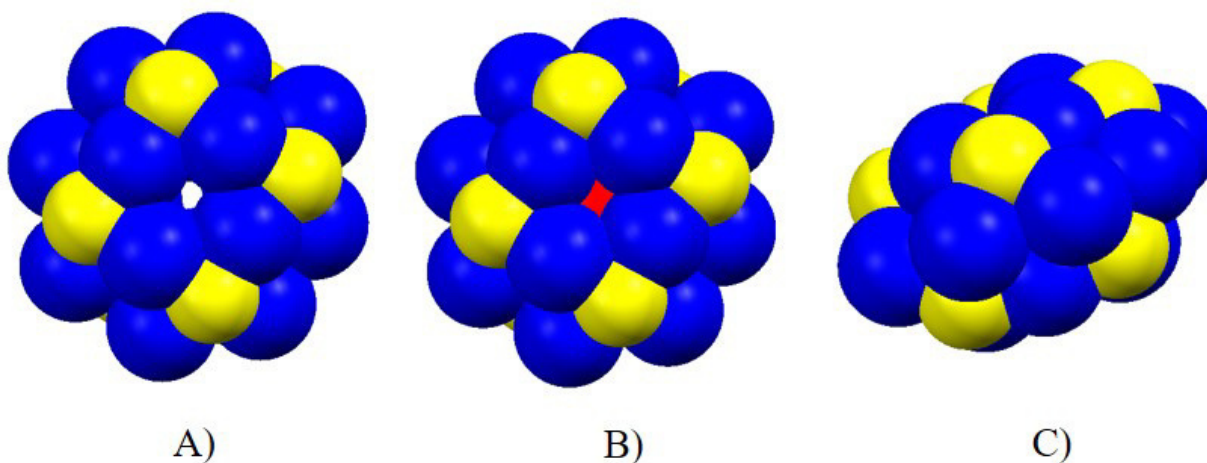


**Figure S1.** Space-filling model of  $\text{Ag}_{16}\text{S}_8$  shell in (A)  $\text{Ag}_{16}$  and (B)  $\text{Ag}_{17}$  NCs. (C) Lateral view of the  $\text{Ag}_{16}\text{S}_8$  shell.

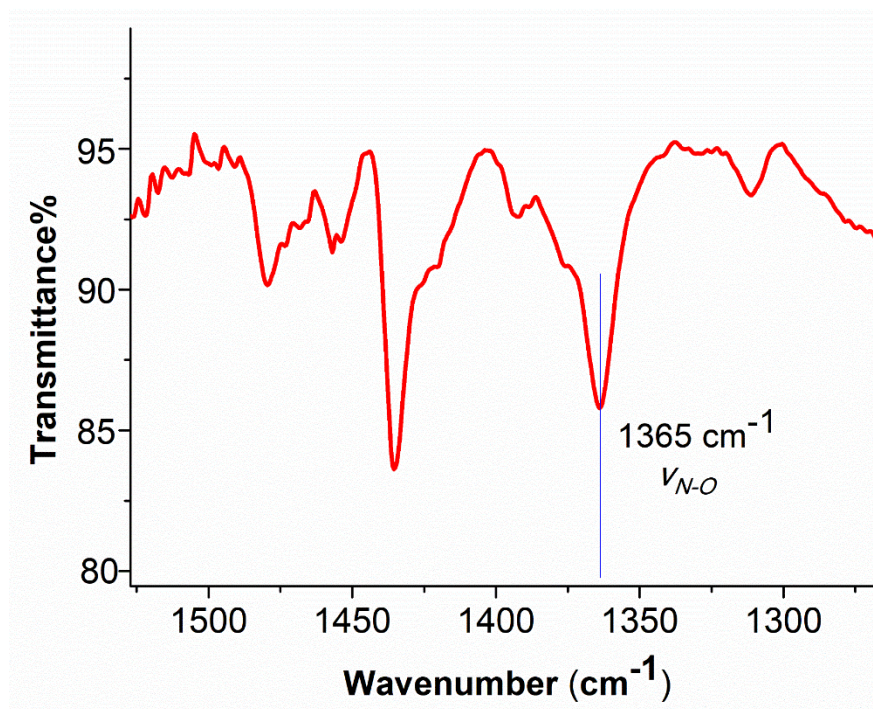


**Figure S2.** FTIR spectrum of Ag<sub>16</sub>:Ag<sub>17</sub> co-crystal. The absorption band at 1365 cm<sup>-1</sup> is assigned to N–O stretching in NO<sub>3</sub><sup>-</sup>.

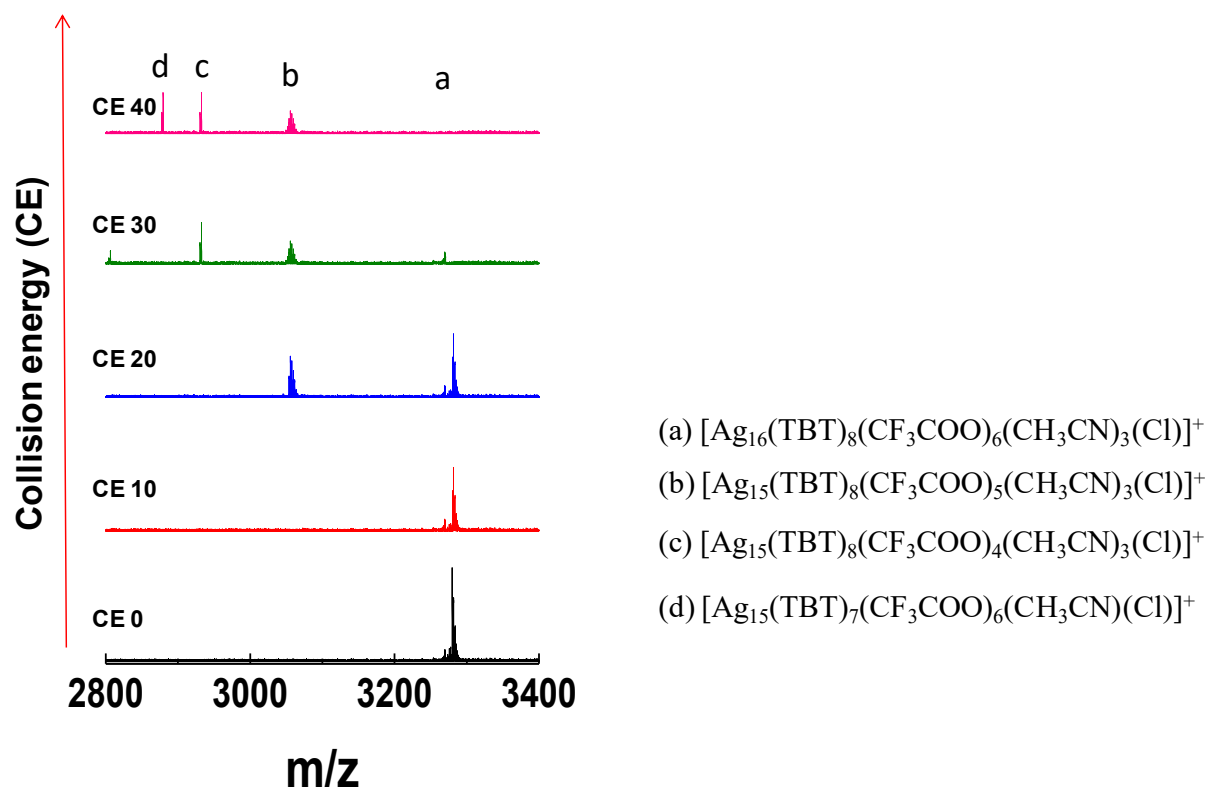


**Figure S3.** MSMS spectra of  $[Ag_{16}(TBT)_8(CF_3COO)_6(CH_3CN)_3(Cl)]^+$  for different collision energies (I : 0 eV, II : 10 eV, III : 20 eV, IV : 30 eV, IV : 40 eV). With the increase in collision energy the fragmentation occurs in  $Ag_{16}$  NC and gives rise to the formation of  $Ag_{15}$  species.

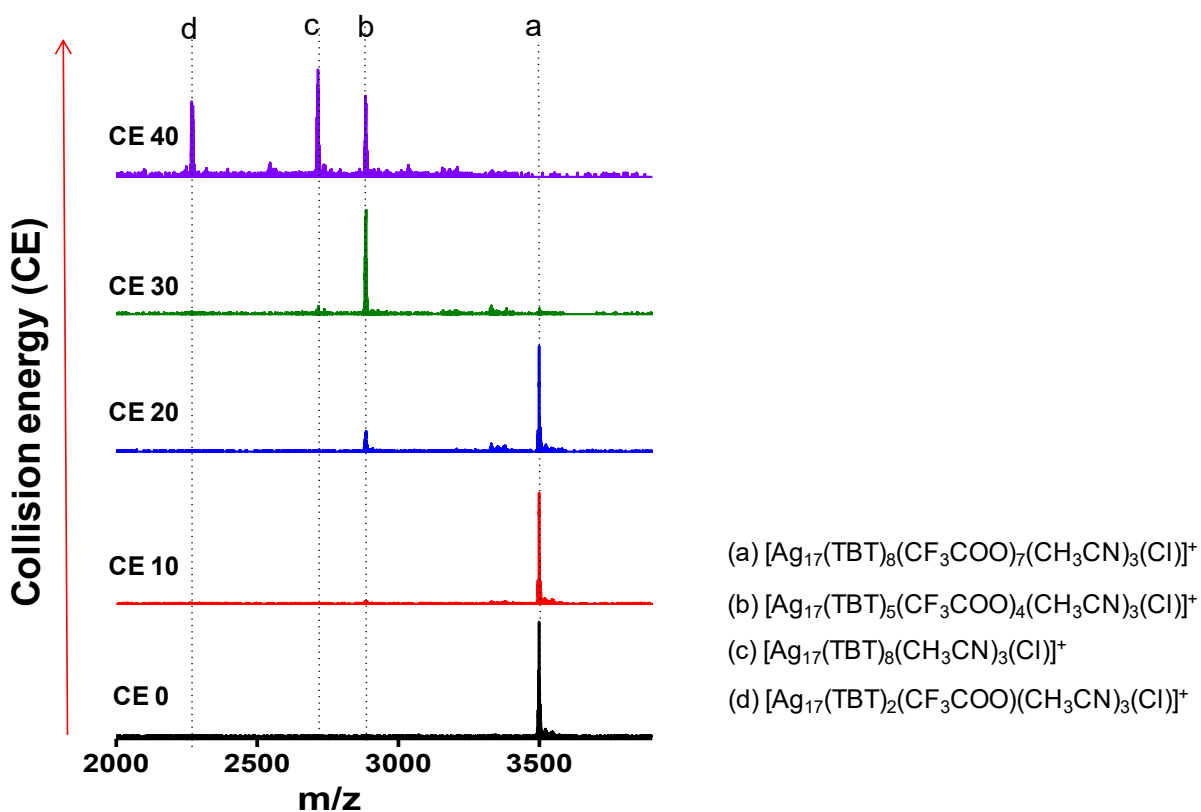


**Figure S4.** MSMS spectra of  $[\text{Ag}_{17}(\text{TBT})_8(\text{CF}_3\text{COO})_7(\text{CH}_3\text{CN})_3(\text{Cl})]^+$  for different collision energies (I : 0 eV, II : 10 eV, III : 20 eV, IV : 30 eV, IV : 40 eV). With increase in the collision energy the ligands are removed and the number of Ag-atoms remains intact indicates  $\text{Ag}_{17}$  moiety is stable and does not give any  $\text{Ag}_{16}$  species.



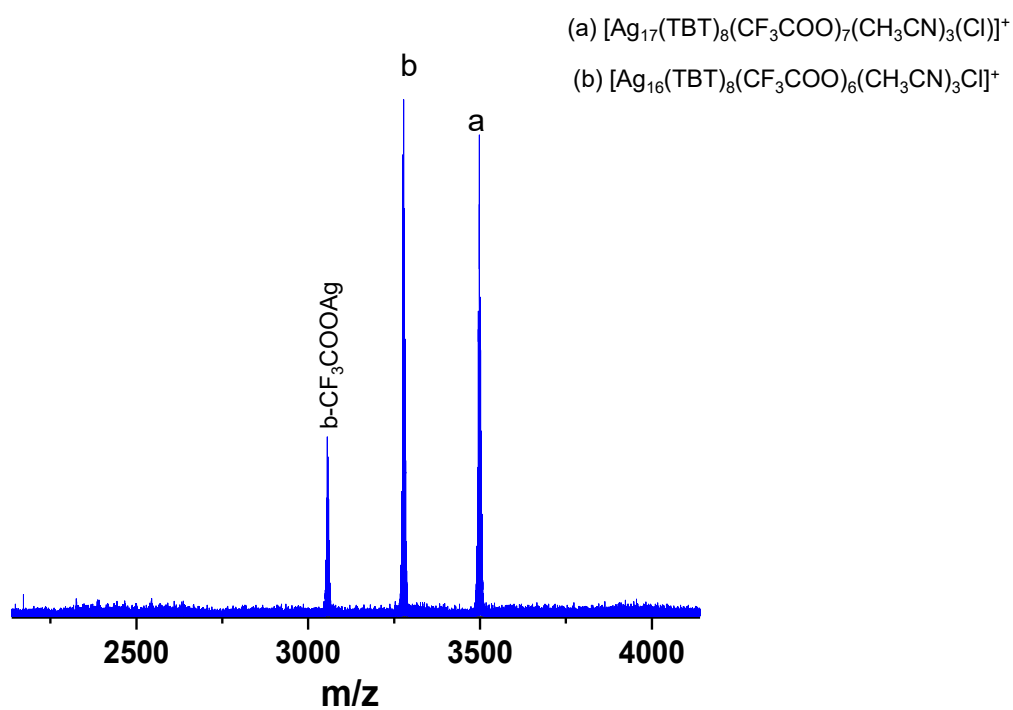


**Figure S5.** ESI MS of a reaction product in acetonitrile. ESI MS of the reaction mixture shows the population of Ag<sub>16</sub> and Ag<sub>17</sub> clusters to be almost equal.

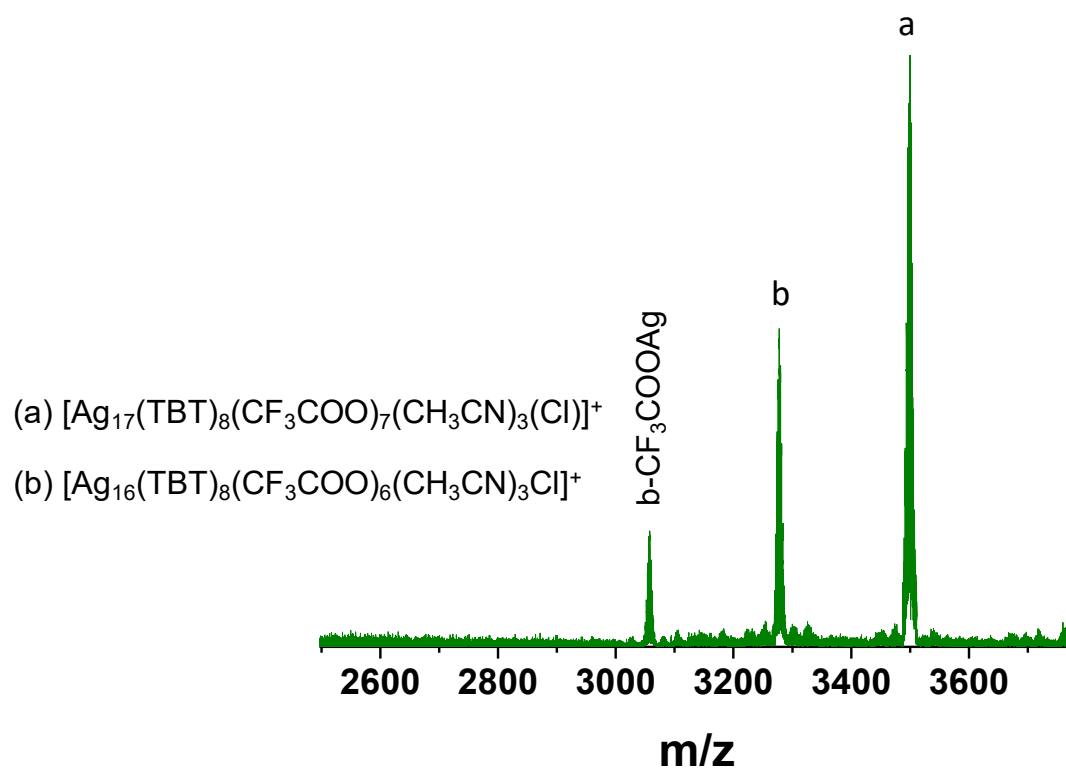


**Figure S6.** ESI MS of supernatant obtained after crystallization. The intensities of the peaks imply that the population of  $\text{Ag}_{17}$  is more than  $\text{Ag}_{16}$  which supports our assumption that selective crystallization occurred.

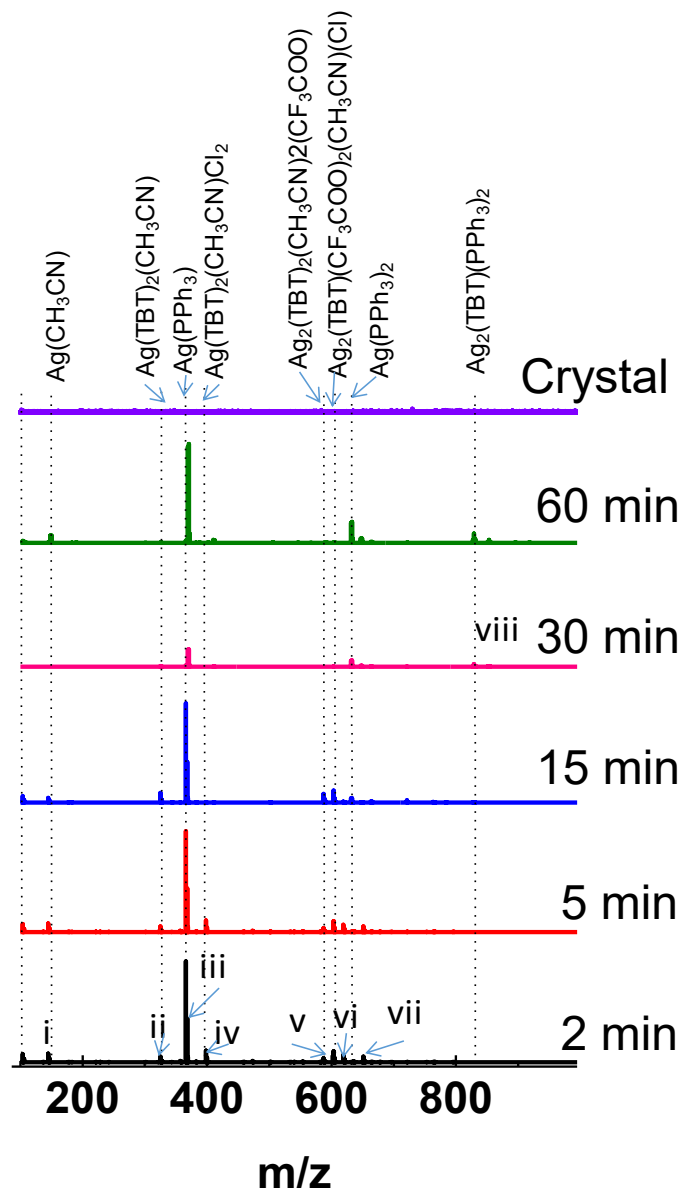
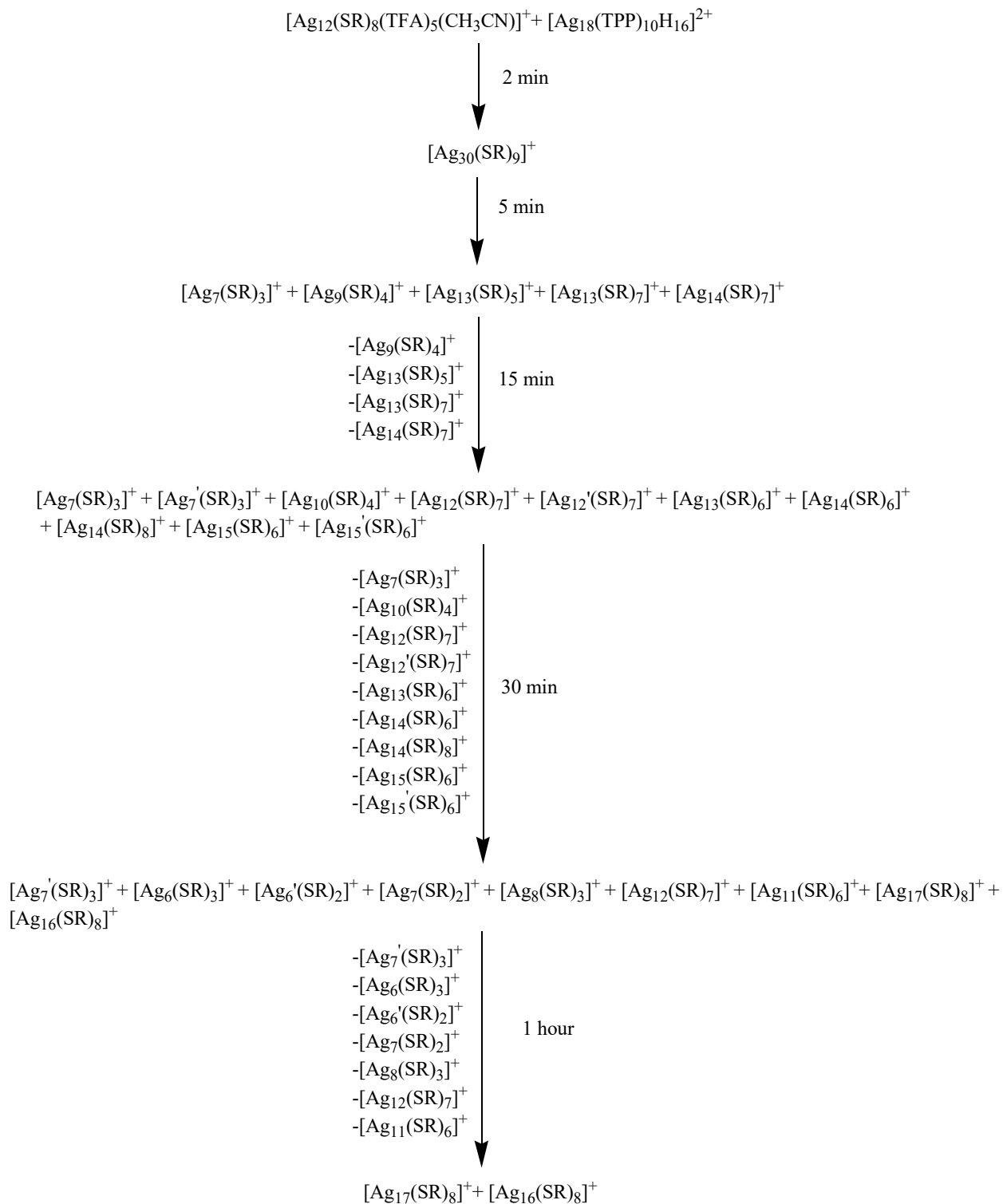


**Figure S7.** Time-dependent ESI MS spectra from  $m/z$  100-1000. The peaks are assigned and marked by arrow. The species formed in this region are mainly silver-thiolate-phosphine complexes.

**Scheme 1:** Flow chart of the reaction process



Where SR is tertiary-butylthiolate (TBT). The other ligands (TFA, CH<sub>3</sub>CN and Cl) have not been included.

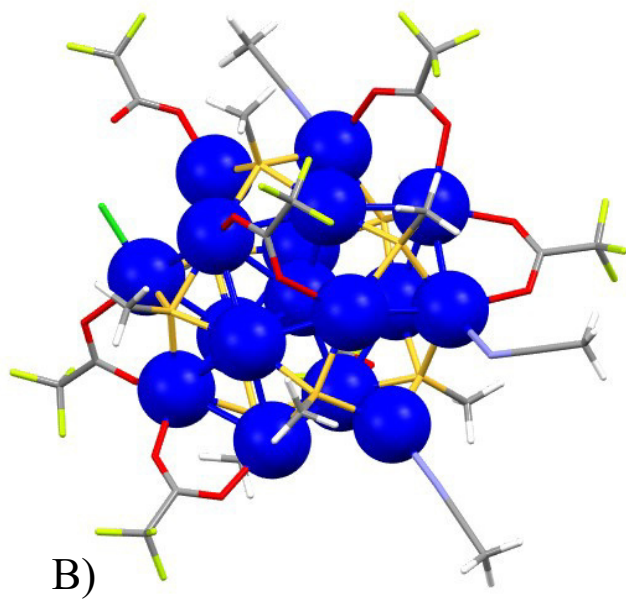
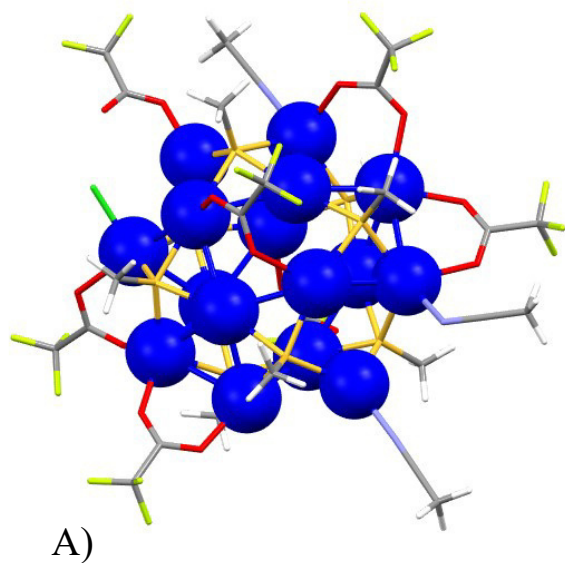


**Figure S8.** Optimized geometry of (A) Ag<sub>16</sub> and (B) Ag<sub>17</sub>.

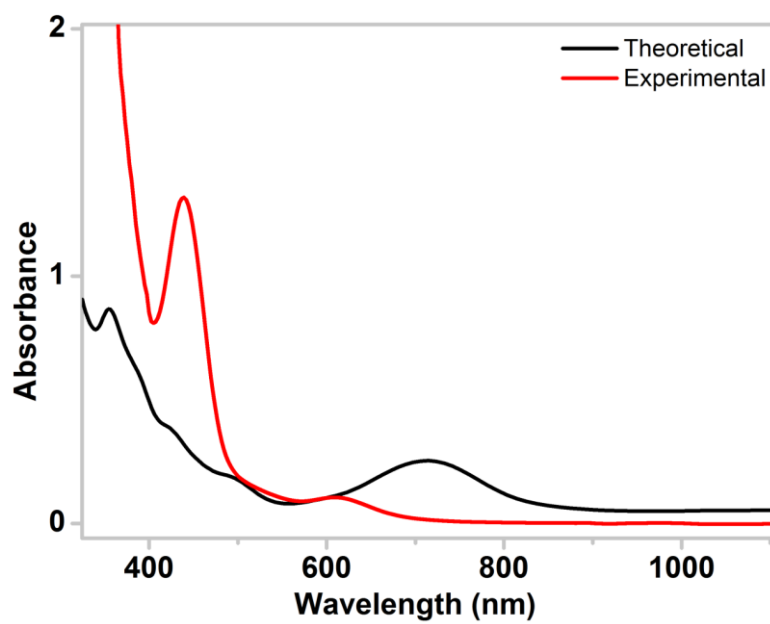


**Figure S9.** Experimental (red) and theoretical (black) optical absorption spectra of a crystal.

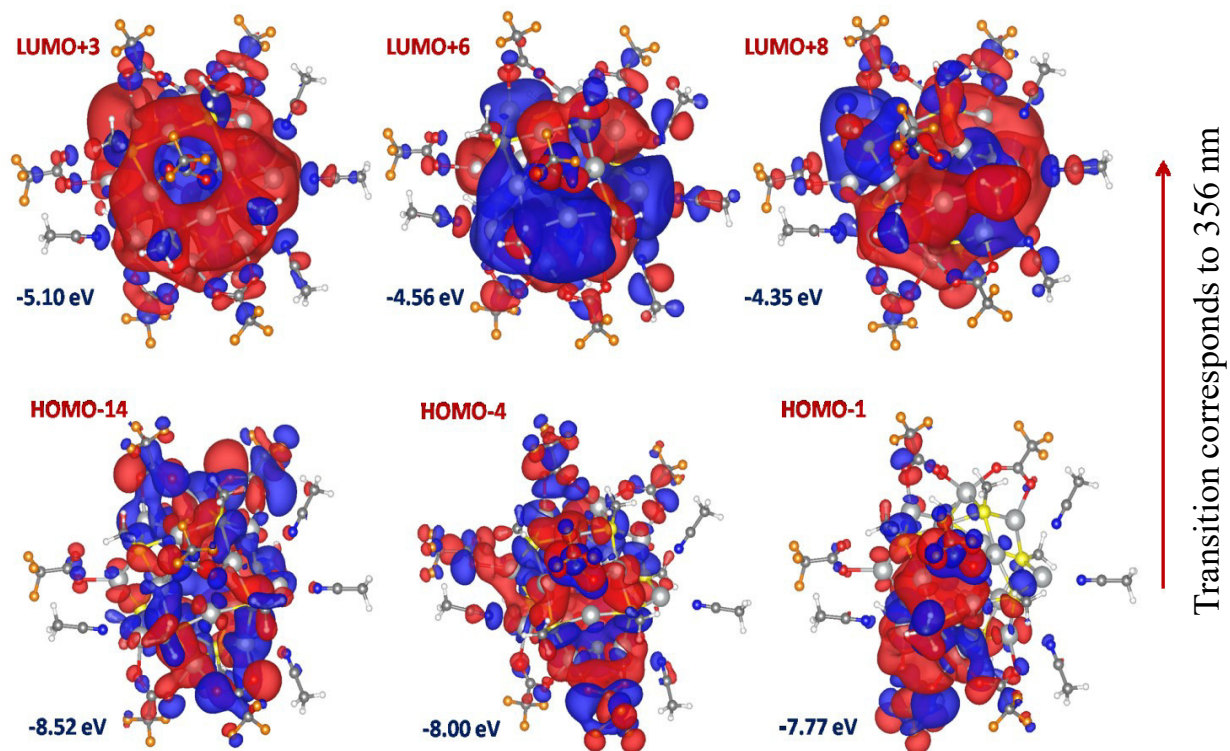


**Figure S10.** Molecular orbitals responsible for the optical transition of the peak at 356 nm.



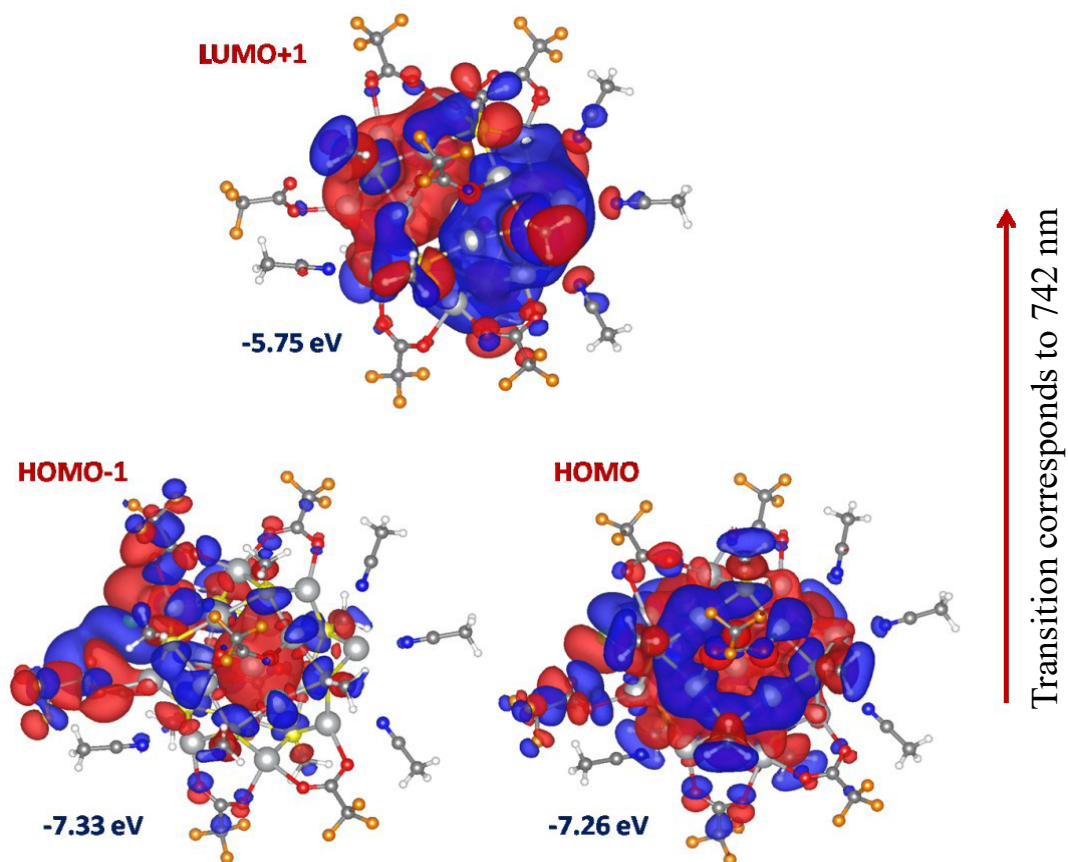


**Figure S11.** Molecular orbitals responsible for the optical transition of the peak at 742 nm.

**Table S1.** Crystal data and structure refinement for co-crystal

Identification code	new1	
Empirical formula	C <sub>54</sub> H <sub>81</sub> Ag <sub>16.33</sub> F <sub>21</sub> N <sub>4</sub> O <sub>14</sub> S <sub>8</sub> Cl	
Formula weight	3462.94	
Temperature	293(2) K	
Wavelength	0.71073 Å	
Crystal system	Monoclinic	
Space group	P2 <sub>1</sub> /n	
Unit cell dimensions	a = 19.802(9) Å	α = 90°
	b = 22.502(10) Å	β = 98.198(14)°
	c = 22.792(11) Å	γ = 90°
Volume	10052(8) Å <sup>3</sup>	
Z	4	
Density (calculated)	2.288 Mg/m <sup>3</sup>	
Absorption coefficient	3.381 mm <sup>-1</sup>	
F(000)	6587	
Crystal size	0.200 x 0.150 x 0.100 mm <sup>3</sup>	
Theta range for data collection	2.856 to 25.000°	
Index ranges	-22 ≤ h ≤ 23, -26 ≤ k ≤ 26, -27 ≤ l ≤ 27	
Reflections collected	137308	
Independent reflections	17664 [R(int) = 0.1507]	
Completeness to theta = 25.000°	99.8 %	
Absorption correction	Semi-empirical from equivalents	
Max. and min. transmission	0.7453 and 0.5466	
Refinement method	Full-matrix least-squares on F <sup>2</sup>	
Data / restraints / parameters	17664 / 904 / 1192	
Goodness-of-fit on F <sup>2</sup>	1.050	
Final R indices [I > 2σ(I)]	R1 = 0.0812, wR2 = 0.2079	
R indices (all data)	R1 = 0.1811, wR2 = 0.3073	
Extinction coefficient	n/a	
Largest diff. peak and hole	1.946 and -1.274 e.Å <sup>-3</sup>	

**Table S2.** Silver complexes, silver thiolates and phosphines observed m/z below 1000

S. No.	[Intermediate] <sup>+</sup>	code	m/z
<b>1</b>	[Ag(CH <sub>3</sub> CN)] <sup>+</sup>	I	150.01
<b>2</b>	[Ag(TBT) <sub>2</sub> (CH <sub>3</sub> CN)] <sup>+</sup>	ii	326.11
<b>3</b>	[Ag(PPh <sub>3</sub> )] <sup>+</sup>	iii	368.14
<b>4</b>	[Ag(TBT) <sub>2</sub> (CH <sub>3</sub> CN)(Cl) <sub>2</sub> ] <sup>+</sup>	iv	398.11
<b>5</b>	[Ag <sub>2</sub> (TBT) <sub>2</sub> (CH <sub>3</sub> CN) <sub>2</sub> (CF <sub>3</sub> COO)] <sup>+</sup>	v	587.21
<b>6</b>	[Ag <sub>2</sub> (TBT)(CF <sub>3</sub> COO) <sub>2</sub> (CH <sub>3</sub> CN)(Cl)] <sup>+</sup>	vi	606.20
<b>7</b>	[Ag(PPh <sub>3</sub> ) <sub>2</sub> ] <sup>+</sup>	vii	631.18
<b>8</b>	[Ag <sub>2</sub> (TBT)(PPh <sub>3</sub> ) <sub>2</sub> ] <sup>+</sup>	viii	828.89

**Table S3.** Reaction intermediates formed during the reaction

[Intermediate] <sup>+</sup>	code	m/z	Electron count (M)
[Ag <sub>30</sub> (TBT) <sub>9</sub> (CF <sub>3</sub> COO) <sub>6</sub> (CH <sub>3</sub> CN) <sub>5</sub> ] <sup>+</sup>	1	4928.08	14
[Ag <sub>7</sub> (TBT) <sub>3</sub> (CF <sub>3</sub> COO) (CH <sub>3</sub> CN) <sub>3</sub> (Cl)] <sup>+</sup>	2	1294.97	1
[Ag <sub>9</sub> (TBT) <sub>4</sub> (CF <sub>3</sub> COO) <sub>2</sub> (CH <sub>3</sub> CN) <sub>2</sub> ] <sup>+</sup>	3	1635.29	2
[Ag <sub>13</sub> (TBT) <sub>7</sub> (CF <sub>3</sub> COO) <sub>4</sub> ] <sup>+</sup>	4	2479.99	1
[Ag <sub>13</sub> (TBT) <sub>5</sub> (CF <sub>3</sub> COO) <sub>6</sub> ] <sup>+</sup>	5	2526.24	1
[Ag <sub>14</sub> (TBT) <sub>7</sub> (CF <sub>3</sub> COO) <sub>5</sub> ] <sup>+</sup>	6	2703.01	1
[Ag <sub>7</sub> (TBT) <sub>3</sub> (CF <sub>3</sub> COO) <sub>3</sub> ] <sup>+</sup>	7	1361.51	0
[Ag <sub>10</sub> (TBT) <sub>4</sub> (CF <sub>3</sub> COO) <sub>3</sub> ] <sup>+</sup>	8	1774.09	2
[Ag <sub>12</sub> (TBT) <sub>7</sub> (CF <sub>3</sub> COO) <sub>3</sub> (CH <sub>3</sub> CN) <sub>2</sub> Cl] <sup>+</sup>	9	2377.02	0
[Ag <sub>12</sub> (TBT) <sub>7</sub> (CF <sub>3</sub> COO) <sub>3</sub> (CH <sub>3</sub> CN) <sub>3</sub> Cl] <sup>+</sup>	10	2418.34	0
[Ag <sub>14</sub> (TBT) <sub>6</sub> (CF <sub>3</sub> COO) <sub>4</sub> (CH <sub>3</sub> CN)Cl] <sup>+</sup>	11	2573.86	2
[Ag <sub>13</sub> (TBT) <sub>6</sub> (CF <sub>3</sub> COO) <sub>6</sub> ] <sup>+</sup>	12	2615.38	0
[Ag <sub>14</sub> (TBT) <sub>8</sub> (CF <sub>3</sub> COO) <sub>4</sub> (CH <sub>3</sub> CN)(Cl)] <sup>+</sup>	13	2751.97	0
[Ag <sub>15</sub> (TBT) <sub>6</sub> (CF <sub>3</sub> COO) <sub>5</sub> (CH <sub>3</sub> CN)(Cl)] <sup>+</sup>	14	2795.23	2
[Ag <sub>15</sub> (TBT) <sub>6</sub> (CF <sub>3</sub> COO) <sub>5</sub> (CH <sub>3</sub> CN) <sub>2</sub> Cl] <sup>+</sup>	15	2836.20	2
[Ag <sub>6</sub> (TBT) <sub>3</sub> (CF <sub>3</sub> COO)] <sup>+</sup>	16	1028.86	1

$[\text{Ag}_6(\text{TBT})_2(\text{CF}_3\text{COO})_2(\text{CH}_3\text{CN})]^+$	17	1092.62	1
$[\text{Ag}_7(\text{TBT})_2(\text{CF}_3\text{COO})_4]^+$	18	1385.95	0
$[\text{Ag}_8(\text{TBT})_3(\text{CF}_3\text{COO})_3]^+$	19	1469.89	1
$[\text{Ag}_{11}(\text{TBT})_6(\text{CF}_3\text{COO})_3(\text{CH}_3\text{CN})]^+$	20	2102.34	1
$[\text{Ag}_{12}(\text{TBT})_7(\text{CF}_3\text{COO})_3(\text{CH}_3\text{CN})]^+$	21	2298.93	1

## References

- (1) Ghosh, A.; Bodiuzzaman, M.; Nag, A.; Jash, M.; Baksi, A.; Pradeep, T. Sequential Dihydrogen Desorption from Hydride-Protected Atomically Precise Silver Clusters and the Formation of Naked Clusters in the Gas Phase. *ACS Nano* **2017**, *11*, 11145-11151.
- (2) Bootharaju, M. S.; Dey, R.; Gevers, L. E.; Hedhili, M. N.; Basset, J. M.; Bakr, O. M. A New Class of Atomically Precise, Hydride-Rich Silver Nanoclusters Co-Protected by Phosphines. *J. Am. Chem. Soc.* **2016**, *138*, 13770-13773.
- (3) Stellacci, F.; Tang, Y.; Pan, J.; Dass, A.; McLean, J. A.; Clifffel, D. E.; Kothalawala, N.; Harkness, K. M.; Demeler, B.; Bakr, O. M.  $[\text{Ag}_{44}(\text{SR})_{304}]^-$ : A Silver–Thiolate Superatom Complex. *Nanoscale* **2012**, *4*, 4269-4274.

# Mechanistic Elucidation of the Structure and Reactivity of Bare and Hydride-Protected $\text{Ag}_{17}^+$ Clusters

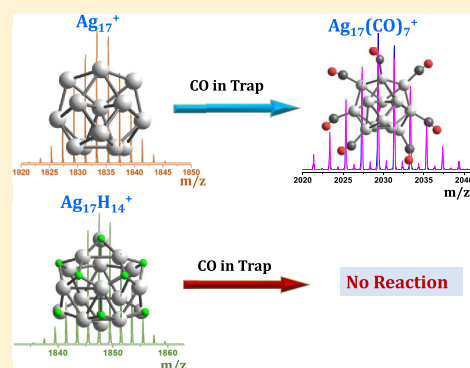
Ananya Bakshi,<sup>†,§</sup> Madhuri Jash,<sup>†,§</sup> Soumabha Bag,<sup>†,§</sup> Sathish Kumar Mudedla,<sup>†,§</sup> Mohammad Bodiuzzaman,<sup>†</sup> Debasmitta Ghosh,<sup>†</sup> Ganesan Paramasivam,<sup>†</sup> Venkatesan Subramanian,<sup>‡</sup> and Thalappil Pradeep<sup>\*,†,§</sup>

<sup>†</sup>DST Unit of Nanoscience and Thematic Unit of Excellence, Indian Institute of Technology Madras, Chennai 600036, India

<sup>‡</sup>Chemical Laboratory, CSIR-Central Leather Research Institute, Adyar, Chennai 600020, India

## Supporting Information

**ABSTRACT:** We report an approach to create bare silver cluster  $\text{Ag}_{17}^+$  and hydride-rich  $\text{Ag}_{17}\text{H}_{14}^+$  separately, as pure species uncontaminated with other entities, in the gas phase starting from a solution-phase monolayer-protected cluster,  $\text{Ag}_{18}\text{H}_{16}(\text{PPh}_3)_{10}^{2+}$ . These clusters can be synthesized just by applying a small potential on the cone of the mass spectrometer, during electrospray mass spectral analysis. Both the clusters were trapped and reacted with reactive gases like carbon monoxide and acetylene. Unusual products like  $\text{Ag}_{17}(\text{CO})_7^+$  were observed when  $\text{Ag}_{17}^+$  was reacted with CO in the trap. No intermediate species were found. Transfer of H from acetylene to the cluster during reaction was observed, which later reduced acetylene. All of the structures formed were calculated using density functional theory and show interesting facts about the composition of the products and the mechanism of their formation. Most of the structures were observed for the first time.



## 1. INTRODUCTION

Atomically precise monolayer-protected clusters is a rapidly growing area of research in the recent past.<sup>1</sup> Mass spectrometry has been used extensively as a characterization tool for the understanding of these types of clusters, which mostly show a single peak in their soft ionization mass spectra. Unprotected gas-phase clusters<sup>2</sup> produced in situ belong to a thoroughly researched subject area, and many such species were identified decades ago.<sup>3,4</sup> In most of the cases, clusters were produced by magnetron sputtering,<sup>5</sup> fast atom bombardment,<sup>6</sup> laser ablation,<sup>7</sup> etc., from metal salts in vacuum<sup>8</sup> or under ambient conditions<sup>9</sup> and were identified by mass spectrometry. Theoretical calculations on the structure and reactivity of such clusters have been important to understand their science in greater detail.<sup>10</sup> Numerous metallic,<sup>10,11</sup> semiconducting,<sup>12</sup> and other<sup>13</sup> clusters were created so far using these methods, and their unique and interesting properties and structural studies have expanded the field further as the scientific quest evolved. With the advancement in synthetic methods and mass spectrometric techniques, almost any metal or semiconductor cluster could be synthesized in the gas phase. The main drawback of such clusters lies in their broad size distribution and postsynthesis mass selection.<sup>3,14</sup> Although numerous attempts were made to create single-cluster ions in the gas phase, successes have been limited. Maximum number of studies were focused on catalytic activity of size-selected clusters.<sup>14</sup> Increased number of surface atoms may help in their high catalytic activity.<sup>15,16</sup>

In contrast, atomically precise monolayer-protected clusters are prepared in solution and their ions are detected in gas phase by mass spectrometry. Gas-phase reactivity study of this class of clusters is still limited as their surface is protected. One way to remove part of the protection is by partial fragmentation of such cluster ions. Collision-induced dissociation (CID) of such clusters results in smaller thiolate fragments, but they never result in intact bare clusters.<sup>17</sup>

Gas-phase silver clusters have been reported to show high reactivity and catalytic activity toward carbon monoxide oxidation where silver clusters with different atomicities have been used.<sup>18–20</sup> Other reactions include  $\text{O}_2$  adsorption,<sup>18</sup> propene oxidation,<sup>16</sup> acetylene and ethylene hydrogenation,<sup>21</sup> reactivity with chlorine,<sup>22</sup> reactivity with ethanethiol,<sup>23</sup> NO activation,<sup>24</sup> C–H and C–I activation,<sup>25</sup> oxygen reduction reaction,<sup>26</sup> reactivity toward ammonia,<sup>27</sup> selective activation<sup>28</sup> etc., to name a few. Supported silver clusters were used for photocatalysis,<sup>29</sup> selective hydrogenation,<sup>21</sup> hydrogen evolution,<sup>30</sup> dye degradation,<sup>30</sup> catalytic reduction,<sup>31</sup> dissociation of  $\text{N}_2\text{O}$ ,<sup>32</sup> etc. The surface oxidation tendency of such gas-phase clusters is very high,<sup>33</sup> and hence they have limited applications under ambient conditions.

A recent report on hydride-rich phosphine-protected silver clusters<sup>34</sup> shows a new possibility of creating bare cluster ions

Received: October 8, 2019

Revised: October 25, 2019

Published: October 25, 2019





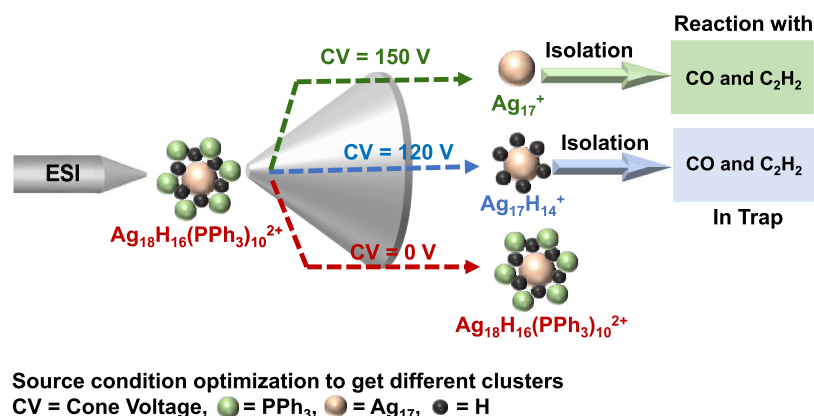


**Figure 1.** Schematic representation of the experimental process. Ions are generated by modifying parameters of the source. The desired ions are then mass-selected and allowed to react with reactive gases, and the products were analyzed. A generalized mass spectrometer setup is shown for clarity. Schematic of the complete instrument is shown in Figure S1.

in the gas phase as hydride ligands can be stripped off by collision-induced dissociation (CID). We had demonstrated a method of synthesis of a single gas-phase species  $\text{Ag}_{17}^+$  starting from a precursor  $[\text{Ag}_{18}\text{H}_{16}(\text{PPh}_3)_{10}]^{2+}$  in recent reports.<sup>35,36</sup> The precursor cluster  $[\text{Ag}_{18}\text{H}_{16}(\text{PPh}_3)_{10}]^{2+}$  was synthesized using an established procedure reported elsewhere.<sup>34</sup> Phosphine ligands were removed following in-source fragmentation by applying a higher cone (extraction) voltage, which resulted in  $\text{Ag}_{17}\text{H}_{14}^+$  clusters. Hydride protection was further removed by applying higher potential, and a pure  $\text{Ag}_{17}^+$  cluster was produced. This cluster  $\text{Ag}_{17}^+$  is an example of a single gas-phase cluster species produced in one step, synthesized from a different solution-phase precursor.

In the present report,  $\text{Ag}_{17}^+$  has been trapped and allowed to react with carbon monoxide and acetylene. Surprisingly,  $\text{Ag}_{17}\text{H}_{14}^+$  did not show any reactivity with CO, implying that the smallest possible ligand, namely, hydride was enough to passivate the reactive cluster surface toward reaction with CO. On the other hand, H exchange occurs when the cluster was reacted with acetylene. Unusual reactivity of the ions with these gas molecules was further studied using density functional theory (DFT) calculations. Theoretical studies show that specific structural sites are responsible for such an activity. All of the geometries discussed in this report were studied theoretically, and the results are in agreement with experiment.

## 2. EXPERIMENTAL SECTION

**2.1. Synthesis of  $[\text{Ag}_{18}\text{H}_{16}(\text{PPh}_3)_{10}]^{2+}$ .** The cluster was synthesized following a recently reported method by Boot-haraju et al.<sup>34</sup> In a typical synthesis, 20 mg of  $\text{AgNO}_3$  in 5 mL of MeOH was mixed with 100 mg of TPP in 7 mL of DCM and stirred for 20 min. To the colorless mixture, 1 mL of ice-cold  $\text{NaBH}_4$  (35 mg) was added and the color of the solution turned yellow immediately. The stirring was continued for another 10 h in the dark to get a green solution indicating the successful transformation of the reactant to cluster. The as-synthesized cluster was rotavapored to remove the solvents and washed repeatedly with Milli-Q water to remove excess reactant. Finally, the clusters were extracted in MeOH for further characterization. During the synthesis of  $[\text{Ag}_{18}\text{D}_{16}(\text{PPh}_3)_{10}]^{2+}$  cluster,  $\text{NaBH}_4$  was replaced with  $\text{NaBD}_4$  and a similar process was followed.

**2.2. Mass Spectrometric Details.** All mass spectral analyses were performed in a Waters Synapt G2Si instrument with electrospray ionization source (ESI) and ion mobility (IM) cell. This instrument is also capable of analyzing samples in matrix-assisted laser desorption ionization and atmospheric pressure chemical ionization mode. The data were analyzed using MassLynx 4.1 software. All of the species were identified in the positive-ion mode. To obtain intact cluster ion, about 100  $\mu\text{g/mL}$  sample solution was prepared in MeOH and diluted to 10 times before injecting into a mass spectrometer. The capillary voltage was set at 2 kV, and cone voltage and source offset were set to 0 V. For  $\text{Ag}_{17}\text{H}_{14}^+$  ion, the cone voltage and source offset were increased to 120 and 100 V, respectively. The cone voltage was further increased to 150 V to remove all of the H from  $\text{Ag}_{17}\text{H}_{14}^+$  to get bare  $\text{Ag}_{17}^+$  cluster ion. A constant 400 L/h desolvation gas flow rate was maintained throughout the experiment without any additional cone gas flow. The capillary temperature was fixed at 100  $^\circ\text{C}$ , and the desolvation temperature was set at 150  $^\circ\text{C}$ . For MS/MS analysis, the species were trapped and variable collision energy was supplied through high-purity Ar as collision gas (5 mL/min). Ultra-high-purity He was used as curtain gas in IM cell at a flow rate of 100 mL/min. High-purity  $\text{N}_2$  was used in the IM cell with a flow rate of 50 mL/min. A bias voltage of 45 V was applied, while the wave velocity and wave height were maintained at 400 m/s and 40 V, respectively. For reactions in trap, Ar gas was replaced with CO and  $\text{C}_2\text{H}_2$ . The Ar line was removed and attached to the respective gas cylinder, and the flow rates were controlled using the MassLynx software. Typical trap pressures for 2, 5, and 10 mL/min flow rates were  $1.3 \times 10^{-2}$ ,  $1.84 \times 10^{-2}$ , and  $3.4 \times 10^{-2}$  mbar, respectively. All of the reactions were performed at room temperature.

**2.3. Computational Details.** The structures of the complexes of  $\text{Ag}_{17}$  with hydrogen and CO were optimized using density functional theory with meta-generalized gradient approximation of Tao, Perdew, Staroverov, and Scuseria exchange-correlation functional. All of the structures were calculated as monocations. Silver atoms were treated with LANL2DZ basis set, and 6-31G\* was used for the remaining atoms. The geometry optimization was carried out with no geometric constraints. To ensure that the optimized structures correspond to true minimum, vibrational frequencies were calculated for all of the complexes. Imaginary frequencies were not observed for any structure. All of the calculations were

performed using Gaussian 09 software. The binding energies were calculated using the following equation

$$\text{binding energy} = E_{\text{complex}} - [E_{\text{monomer1}} + E_{\text{monomer2}}]$$

where  $E_{\text{complex}}$  is the energy of  $\text{Ag}_{17}(\text{CO})_n^+$ ,  $E_{\text{monomer1}}$  is the energy of  $\text{Ag}_{17}^+$ , and  $E_{\text{monomer2}}$  is the energy of  $n\text{CO}$ ,  $n = 1-7$ . In a similar way, thermal free-energy differences were calculated using the following equation

free energy difference

$$= \text{FE}_{\text{complex}} - [\text{FE}_{\text{monomer1}} + \text{FE}_{\text{monomer2}}]$$

where  $\text{FE}_{\text{complex}}$  is the free energy of  $\text{Ag}_{17}(\text{CO})_n^+$ ,  $\text{FE}_{\text{monomer1}}$  is the free energy of  $\text{Ag}_{17}^+$ , and  $\text{FE}_{\text{monomer2}}$  is the free energy of  $n\text{CO}$  ( $n = 1-7$ ).

### 3. RESULTS AND DISCUSSION

**3.1. Formation of  $\text{Ag}_{17}^+$  and  $\text{Ag}_{17}\text{H}_{14}^+$ .** Hydride-rich  $[\text{Ag}_{18}\text{H}_{16}(\text{PPh}_3)_{10}]^{2+}$  was synthesized following a recent report.<sup>34</sup> Cluster synthesis is sensitive to conditions, and it is important to follow these closely. The cluster was purified and dissolved in MeOH and analyzed by electrospray ionization mass spectrometry (ESI MS) in a Waters Synapt G2Si instrument, which is also equipped with ion mobility separation. At a lower spray voltage, an intact cluster was observed with the molecular ion peak at  $m/z$  2290, which is in agreement with the reported one. With increase in cone voltage and tuning of a few other experimental parameters, it was possible to remove all of the phosphine ligands as well as all of the hydrides from the cluster. In this process, one Ag atom was also lost from the parent cluster and it resulted in a bare  $\text{Ag}_{17}^+$  cluster in the gas phase. A schematic of the synthesis process is shown in Figure 1. In the experiments, source parameters were optimized such that only cone voltage and source offset voltages were changed maintaining all other parameters the same throughout the experiments. At lowest voltages (cone voltage and source offset at 0 V), the intact cluster in its 2+ charge state was observed at  $m/z$  2290. A few other smaller peaks were observed at lower  $m/z$ , which are due to  $\text{PPh}_3$  losses. When the cone voltage and source offset were set at 120 V, all of the  $\text{PPh}_3$  ligands were lost along with an Ag from the core. The peak maxima matched with  $\text{Ag}_{17}\text{H}_{14}^+$ . Some tailing was observed at lower mass, due to a few  $\text{H}_2$  losses during in-source fragmentation.<sup>35</sup> The peak was compared to  $\text{Ag}_{17}\text{H}_{14}^+$  and  $\text{Ag}_{17}\text{H}_8^+$  to show the  $\text{H}_2$  losses. Better optimization of the species to get fewer  $\text{H}_2$  losses is possible with fine tuning of the parameters. When the cone voltage was increased to 150 V, all of the H were lost and the peak due to  $\text{Ag}_{17}^+$  appeared, and the isotope distribution fitted exactly with the calculated one. Similar sequential ligand and  $\text{H}_2$  losses were observed during multistage tandem mass spectrometry of  $[\text{Ag}_x\text{H}_{x-2}\text{L}_6]^{2+}$  (where  $x = 9-15$ ).<sup>37</sup> Corresponding mass spectra at different cone voltages are shown in Figure 2. Isotope envelope for each peak is expanded and compared to the calculated pattern shown as insets (i)–(iii). Note that this type of bare cluster synthesis is not instrument-specific. A similar observation was made with another mass spectrometer (in ESI or NESI mode) by tuning the source parameters for effective in-source fragmentation.

Collision-induced dissociation of the parent cluster resulted in a similar type of fragmentation and  $\text{Ag}_{17}^+$  was formed.<sup>35</sup> Further CID on bare  $\text{Ag}_{17}^+$  cluster resulted in smaller silver

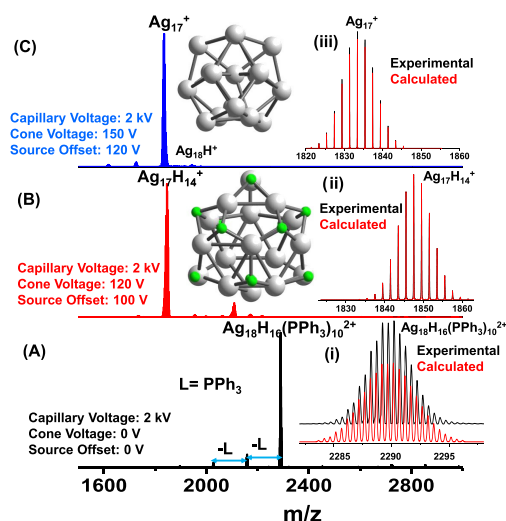


**Figure 2.** (A) ESI MS of  $[\text{Ag}_{18}\text{H}_{16}(\text{PPh}_3)_{10}]^{2+}$  in positive-ion mode showing a strong signal for 2+ charged species with a few additional  $\text{PPh}_3$  losses. Enlarged view of the molecular ion is shown in (i), which matches perfectly with its calculated isotope pattern. (B) With increasing cone voltage, all  $\text{PPh}_3$  ligands were lost from the cluster and a strong peak appeared at  $m/z$  1847, which was assigned as  $\text{Ag}_{17}\text{H}_{14}^+$ . (C) At the highest cone voltage, all H atoms were also lost and the bare  $\text{Ag}_{17}^+$  cluster peak was observed at  $m/z$  1833. Isotope patterns of each peak are shown in insets (ii) and (iii). DFT optimized structures of the clusters,  $\text{Ag}_{17}\text{H}_{14}^+$  and  $\text{Ag}_{17}^+$  are shown alongside the peaks. Parameters of the spectrometer are also given.

clusters, as shown in Figure S2A–E. A series of bare Ag clusters were seen with odd-numbered clusters being higher in intensity compared to the even-numbered ones. Although  $\text{Ag}_8^+$  was found at a reasonable intensity,  $\text{Ag}_{10}^+$  was completely absent in the current experimental condition. All of the clusters obtained in this process possess only one major peak in their respective ion mobility mass spectra, confirming the presence of only one type of structural isomer in the gas phase (see Figure S2F). Width of the drift time distribution decreased with the core size. Typically gas-phase clusters show different types of isomeric structures. The absence of multiple isomeric species may be due to enhanced stability of one isomer or very fast interconversion among isomers, faster than the mass spectrometric time scale. The resolution of the instrument might also not be enough to separate such isomers. Experimental  $^{\text{TWIMS}}\text{CCS}_{\text{N}_2}$  is shown in Table S1.

The structure of  $\text{Ag}_{17}$  was determined based on the previous report.<sup>38</sup> One Ag atom is in the core, while other 16 Ag atoms form the shell. Distribution of these 16 silver atoms is such that four Ag atoms form a parallelogram with the Ag–Ag–Ag bond angle ranging between  $58^\circ$  and  $62^\circ$  and Ag–Ag bond lengths ranging between 2.80 and 2.83 Å. The highest occupied molecular orbital–lowest unoccupied molecular orbital (HOMO–LUMO) gap ( $\Delta\text{HL}$ ) was found to be 0.205 eV for neutral  $\text{Ag}_{17}$  and 0.260 eV for  $\text{Ag}_{17}^+$ . The optimized structure was used for further calculations. Calculations indicate that 16 silver atoms available on the surface of  $\text{Ag}_{17}$  can bind with equal number of hydrogen (H), which is one hydrogen to each surface Ag atom. When the same structure was optimized to a local minimum on the potential energy surface, the terminal H ligands change their bonding pattern to bridge between Ag atoms. During the reorganization process, two vicinal H atoms are bonded to each other and evolved as hydrogen molecule. This may be because of crowding of

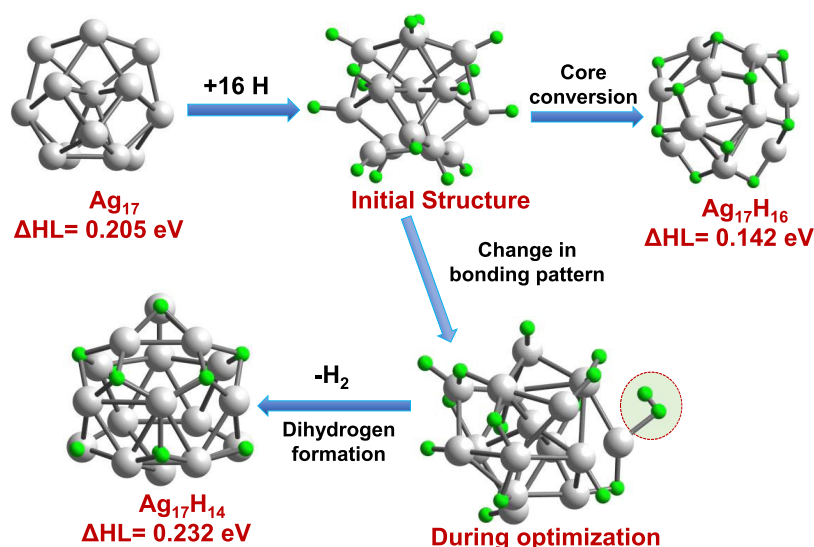


**Figure 3.** Formation of  $\text{Ag}_{17}\text{H}_{14}$  from  $\text{Ag}_{17}$  was calculated by DFT. During calculation, 16 H atoms were added initially to the DFT optimized structure of  $\text{Ag}_{17}$ . A complete core conversion was observed with 16 H attachment. During optimization, the bonding pattern of H with Ag changes and two of them were released as  $\text{H}_2$  to get the final optimized structure of  $\text{Ag}_{17}\text{H}_{14}$ . Silver atoms are gray, and hydrogen atoms are green in color.

hydrogens on the surface of  $\text{Ag}_{17}$  during reorganization. Now, the cluster has only 14 H on its surface, and the optimized geometry is shown in Figure 3. In the structure of  $\text{Ag}_{17}\text{H}_{14}$ , some hydrogens bind through two and three coordinations while one hydrogen is bonded to a single silver atom. We have also found that there are two vacant sites above the plane formed by three silver atoms. Bridging H is known for silver clusters. Zhao et al. calculated structures of small neutral and cationic  $\text{Ag}_n\text{H}$  ( $n = 1-7$ ) clusters by DFT<sup>39</sup> and found that bridged sites are preferred energetically for cationic and neutral silver clusters. The isomeric structures were constructed by changing the position of the hydrogen, which bind via three coordination as mentioned above. Three isomers were optimized for  $\text{Ag}_{17}\text{H}_{14}$ , and they are shown in Figure S3. The structure of  $\text{Ag}_{17}$  is slightly distorted after hydrogenation. The bond lengths between silver atoms increase due to the presence of H. Further, two more H were added to the  $\text{Ag}_{17}\text{H}_{14}$  cluster and optimized to local minimum on the potential energy surface. The structure of  $\text{Ag}_{17}\text{H}_{16}$  is also stable. Note that with more than 14 H on the surface, the overall structure of the cluster core also changes (see Figure 3). These data indicate that with more H loading, isomeric cores can be created. A similar core conversion was observed with  $\text{Ru}_{19}$  cluster anion upon H loading.<sup>40</sup>

**3.2. Reactivity of  $\text{Ag}_{17}^+$  with CO.** To understand the reactivity of the bare clusters, the instrumental setup was modified. Through the modified channels, reactive gases were leaked in at desired flow rates and allowed to react with the species of interest. We have made arrangements to inlet gases in the trap by replacing argon lines with a gas of our choice. For the first set of experiments, we have checked with the standard calibrant whether there is any mass shift or additional fragmentation when different gases were leaked into trap instead of Ar at the experimental conditions. Even at maximum flow rates used in our experiments, we have not seen any such anomalies. For the first set of experiments, carbon monoxide (CO) was introduced in the trap (see Figures 1 and S1) and the trapped  $\text{Ag}_{17}^+$  ions were allowed to react with it and the product was identified by a time-of-flight mass analyzer. All of the experiments were performed in the resolution mode to get

a perfect isotope resolution, and the data are shown in Figure 4. At lower CO gas flow (2 mL/min), no CO added product

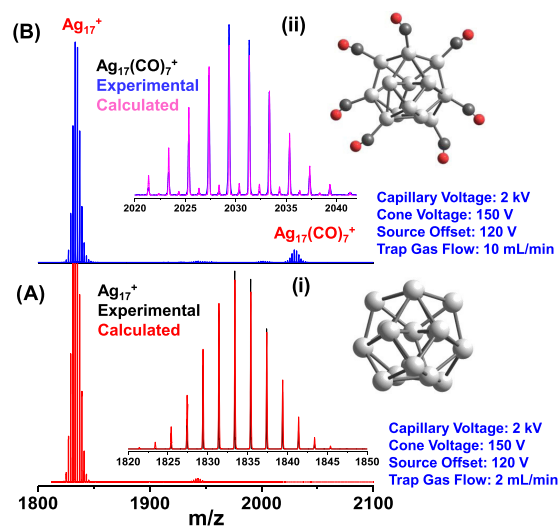


**Figure 4.** Reaction of  $\text{Ag}_{17}^+$  with (A) 2 mL/min and (B) 10 mL/min of CO in the trap showing a peak for 7 CO attachment with the cluster. Isotope patterns of both  $\text{Ag}_{17}^+$  and  $\text{Ag}_{17}(\text{CO})_7^+$  match with their calculated isotope patterns. The insets show DFT optimized structures of (i)  $\text{Ag}_{17}^+$  and (ii)  $\text{Ag}_{17}(\text{CO})_7^+$ . Parameters of the spectrometer are also given.

was seen. When the gas flow was gradually increased to 5 mL/min, a new peak appeared at  $m/z$  2030, which is assigned as  $\text{Ag}_{17}(\text{CO})_7^+$ . Dependence of the peak on CO flow is shown in Figure S4A. The peak was enhanced in intensity when 10 mL/min CO flow was maintained. A weak  $\text{Ag}_{17}(\text{CO})_6^+$  was also observed. Surprisingly, lesser number of CO added peaks were not observed in the lower region of the mass spectrum. When the species was allowed to fragment by CID, bare  $\text{Ag}_{17}^+$  was regenerated (see Figure S4B).

To get a clear picture of the fragmentation pattern, the ions were allowed to pass through the ion mobility cell before the TOF analysis. In this condition, we could find fragments of



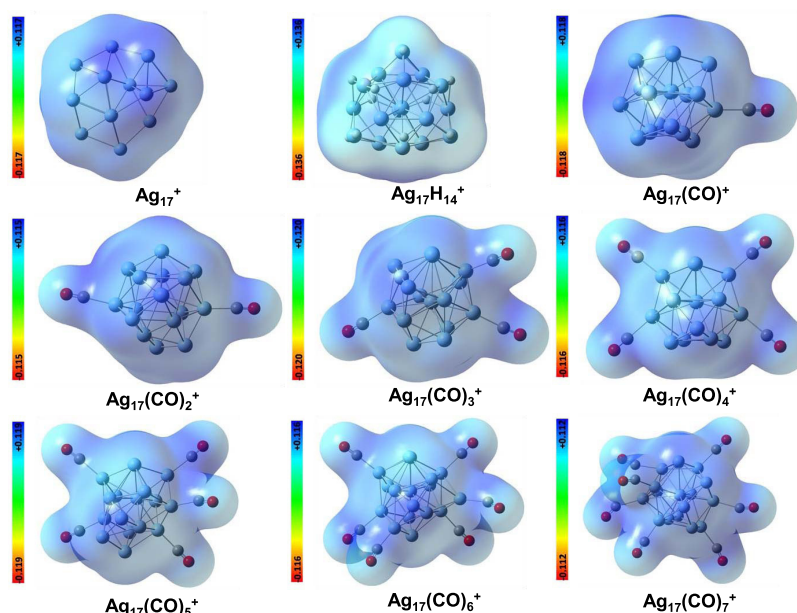


**Figure 5.** DFT optimized structure and electrostatic potential surface of  $\text{Ag}_{17}^+$ ,  $\text{Ag}_{17}\text{H}_{14}^+$ , and  $\text{Ag}_{17}(\text{CO})_1^+$ – $7$  showing electron density on atoms. The blue color represents positive potential, and the red color indicates negative potential.

$\text{Ag}_{17}(\text{CO})_6^+$ ,  $\text{Ag}_{17}(\text{CO})_5^+$ ,  $\text{Ag}_{17}(\text{CO})_4^+$ , etc., confirming stepwise fragmentation; however, all of these species were not seen when normal CID was performed confirming lower stability of such species in the experimental conditions (see Figure S4C). We could not increase the trap gas flow beyond 10 mL/min in the current setup; however, we believe that more CO attachment could be possible if the ions are allowed to react at higher partial pressures of the reacting gas. The hydride-protected  $\text{Ag}_{17}\text{H}_{14}^+$  did not show any CO uptake in similar experimental conditions.

**3.3. DFT Calculations.** The reactivity of a cluster depends on its HOMO–LUMO gap. The calculated HOMO–LUMO gaps for the bare and hydrogenated silver clusters ( $\text{Ag}_{17}$  and  $\text{Ag}_{17}\text{H}_{14}$ ) are 0.205 and 0.232 eV, respectively, implying that the reactivity of hydrogenated clusters is less compared to that of the bare one. Calculated electrostatic potential surfaces (based on the partial charge distribution) of the cluster ions are presented in Figure 5. The blue color represents positive potential, and the red color corresponds to negative potential. The electrostatic potential around  $\text{Ag}_{17}^+$  is different from that of  $\text{Ag}_{17}\text{H}_{14}^+$ . Most of the atoms are in highly positive potential in  $\text{Ag}_{17}^+$ , whereas the number of such atoms decreased in the case of  $\text{Ag}_{17}\text{H}_{14}^+$ . The decreased positive potential represents increased electron density on  $\text{Ag}_{17}\text{H}_{14}^+$  compared to  $\text{Ag}_{17}^+$ . Mulliken charges on each atom for both the structures ( $\text{Ag}_{17}^+$  and  $\text{Ag}_{17}\text{H}_{14}^+$ ) are tabled in the Supporting Information (see Tables S2 and S3). These charges also show that most of the atoms in  $\text{Ag}_{17}\text{H}_{14}^+$  are with partial negative charge. The negative charge distribution around  $\text{Ag}_{17}\text{H}_{14}^+$  may be the reason for its reduced reactivity toward CO. For structural optimization, a neutral CO molecule was added sequentially. Carbon monoxide can anchor on the silver cluster through terminal and bridge bonding. The CO molecule binds to the silver atoms of  $\text{Ag}_{17}$  in two bonding patterns. The terminal bonding of CO is more stable than the bridging one. Hence, CO is made to bind with  $\text{Ag}_{17}$  in terminal positions. There are six possible binding sites on  $\text{Ag}_{17}$  for one CO molecule. The possible isomeric structures were optimized (see Figure S5) for

neutral  $\text{Ag}_{17}$ . The most stable isomer with one CO has been used to bind with the second CO molecule. In the case of the second CO also, nine possible isomers were predicted, and the most stable isomer was used for further addition of a third CO (see Figures S6 and S7). Similarly, four CO attachments led to five isomers (see Figure S8). Like that, we have added five, six, and seven CO similarly (Figures S9–S11). It can be observed that the even-numbered CO molecules were added in a symmetric fashion. Among the most stable isomers in all of the cases presented in Figures S5–S11, the lowest-energy structures with CO (1–7) were further optimized with a positive charge (Figure S12). The binding of CO does not bring significant changes in the structure of  $\text{Ag}_{17}^+$ . The electrostatic potential surface of each  $\text{Ag}_{17}(\text{CO})_0^+$ – $7$  is shown in Figure 5, and the Mulliken charges for each atom are given in the Supporting Information (Tables S2 and S4–S10). The positive potential decreases in the core of cluster with the increase in CO concentration, which implies that electron density increases with the addition of CO. The free-energy change and binding energy of CO and  $\text{Ag}_{17}^+$  were calculated and are listed in Table 1. The negative sign of the binding energy values shows stability of these compounds. The binding energy increases with the addition of new CO molecule, and it is higher for  $\text{Ag}_{17}(\text{CO})_7^+$ . The CO uptake capacity of silver cluster increased with the increase in the number of CO molecules. Further, the free-energy changes and the binding

**Table 1.** Calculated Free-Energy Change and Binding Energy with Sequential Addition of CO for  $\text{Ag}_{17}^+$

cluster + CO	$\Delta G$ (kcal/mol)	binding energy (kcal/mol)
$\text{Ag}_{17}(\text{CO})^+$	3.61	−4.83
$\text{Ag}_{17}(\text{CO})_2^+$	−0.69	−19.17
$\text{Ag}_{17}(\text{CO})_3^+$	−3.84	−30.73
$\text{Ag}_{17}(\text{CO})_4^+$	−4.95	−41.46
$\text{Ag}_{17}(\text{CO})_5^+$	−15.85	−63.41
$\text{Ag}_{17}(\text{CO})_6^+$	−23.95	−78.51
$\text{Ag}_{17}(\text{CO})_7^+$	−17.89	−81.16

energies for the formation of complexes between CO and both the neutral and positively charged  $\text{Ag}_{17}$  were calculated and are given in Tables S11 and S12. The negative sign shows the feasibility of formation of those adducts, similar to the trends in binding energies.

**3.4. Reaction with Acetylene Molecules.** Both  $\text{Ag}_{17}^+$  and  $\text{Ag}_{17}\text{H}_{14}^+$  were separately allowed to react with acetylene in the trap. With increasing acetylene flow rate (from 2 mL/min in Figure 6A to 10 mL/min in Figure 6B),  $\text{Ag}_{17}^+$  showed a peak at

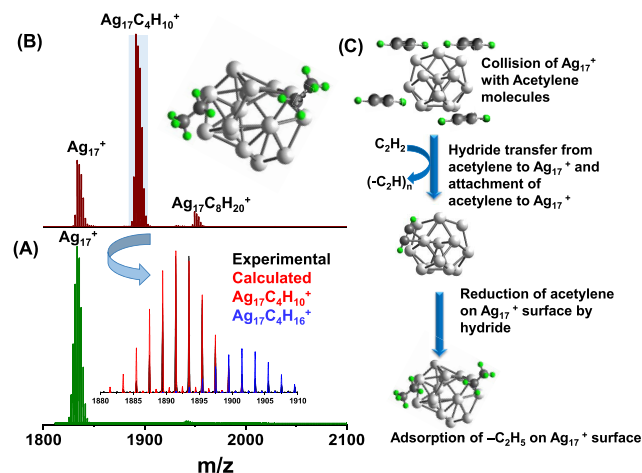
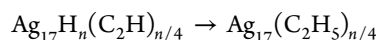
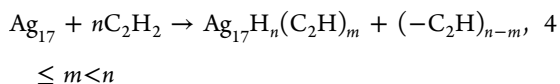


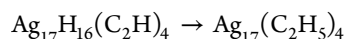
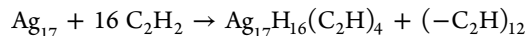
**Figure 6.** (A) Reaction of  $\text{Ag}_{17}^+$  with 2 mL/min and (B) 10 mL/min of  $\text{C}_2\text{H}_2$  in trap. At 10 mL/min  $\text{C}_2\text{H}_2$  flow rate, a strong peak was observed, which is assigned as  $\text{Ag}_{17}\text{C}_4\text{H}_{10}^+$ . During reaction, H transfer occurs between the cluster and acetylene molecules, and subsequently, acetylene is reduced. (C) Explanation of the mechanism. The structures were optimized with DFT.

$m/z$  1892 corresponding to  $\text{C}_4\text{H}_{10}$  addition. The peak also show tailing toward higher mass range depicting more H addition. The peak was compared to the calculated mass spectra of  $\text{Ag}_{17}\text{C}_4\text{H}_{10}^+$  and  $\text{Ag}_{17}\text{C}_4\text{H}_{16}^+$ , confirming that there is more H attachment possible to the cluster. Addition of two molecules of acetylene should increase the mass by  $m/z$  52. However, additional increase in mass was observed ( $m/z$  58), which could be due to the reduction of adsorbed acetylide ( $-\text{C}_2\text{H}$ ) to  $-\text{C}_2\text{H}_5$  on the surface of the  $\text{Ag}_{17}^+$  cluster. The other possibility could be that during collision with acetylene, the cluster uptakes a few H from acetylene molecules and reduces acetylene on the cluster surface. The H-deficient acetylene may react with each other and polymerize to oligoacetylene, which was not detected in the positive-ion mode. The next peak appears at another  $m/z$  58 difference ( $2 \times \text{C}_2\text{H}_5 = 58$ , the reaction discussed above), suggesting that initial H transfer may occur on the cluster surface and acetylene binds to it in the  $\text{Ag}-\text{C}\equiv\text{C}-\text{H}$  fashion. Assuming that no reduction of acetylene occurs on the surface, there were initially 16 active sites. Two acetylene molecules and 6 H occupy eight sites, and the remaining eight sites are occupied in the consecutive step, in a similar fashion. This could be the reason why more than four acetylene additions were not observed.

The mechanism of acetylene adsorption and subsequent reduction can be explained by the following equations



For the reaction shown in Figure 6,  $n = 16$ ,  $m = 4$ , the equation may be written as follows



Similar selective catalytic activation of acetylene and its chemisorption on the cluster surface were observed for anionic  $\text{Au}_n^{41}$  and cationic  $\text{Co}_n$  clusters.<sup>42</sup> Although studies of catalytic effect on acetylene hydrogenation are limited for silver clusters, selective hydrogenation occurs on the active sites of Ag-doped Pd nanoparticles.<sup>22</sup> But such type of intracuster H transfer to reduce adsorbed acetylene to ethane was not observed before. The structures of the reaction products were calculated by DFT, and a plausible reaction pathway is shown in Figure 6C. Isomeric structures arise due to one and two ethane adsorption on  $\text{Ag}_{17}^+$  surface, shown in Figures S13 and S14. The mechanism of H exchange was further confirmed when  $\text{Ag}_{17}\text{H}_{14}^+$  was used as the precursor for the reaction. The product peak was observed at  $m/z$  1897 and assigned as  $\text{Ag}_{17}\text{C}_4\text{H}_{15}^+$  (see Figure S15). The experimental isotope distribution matches exactly with the calculated spectrum. Here also, two molecules of acetylenes were attached at a time and H exchange occurs between  $\text{Ag}_{17}\text{H}_{14}^+$  and  $\text{C}_2\text{H}_2$ . Due to H exchange with the colliding  $\text{C}_2\text{H}_2$ , initial width of the parent peak changed, and finally, it got returned almost to its original width when the final product was formed. To support the mechanism,  $\text{Ag}_{17}\text{H}_{14}^+$  was replaced with  $\text{Ag}_{17}\text{D}_{14}^+$  ( $\text{NaBD}_4$  was used instead of  $\text{NaBH}_4$  during initial synthesis in solution). The product intensity was lower in the case of D. The peak was assigned as  $\text{Ag}_{17}\text{C}_4\text{H}_4\text{D}_{11}^+$ . This implies that at least three H/D should be removed from the surface to accommodate two  $\text{C}_2\text{H}_2$  molecules (see Figure S16). This study also proves the H/D-capturing capacity of bare  $\text{Ag}_{17}^+$  cluster, which may be used as a hydrogen storage material for controlled release of  $\text{H}_2$  in the gas phase.

## 4. CONCLUSIONS

The current work demonstrates a strategic method to create atomically precise gas-phase clusters from a different solution-phase entity. Completely bare and hydride-protected silver clusters show very different reactivities toward different reactive gases. While  $\text{Ag}_{17}^+$  shows seven CO attachments, no CO was attached to  $\text{Ag}_{17}\text{H}_{14}^+$ . The smallest possible ligand like H can also passivate the cluster surface toward CO and make it catalytically inert. This finding is very important in terms of choosing any such cluster system for catalytic studies. Bare cluster was very reactive toward acetylene and showed H exchange with  $\text{C}_2\text{H}_2$  during reaction. Hydride-protected cluster also showed similar reactions where the number of H exchange was proved by replacing H with D on the cluster surface. All structures were calculated by DFT, which shed light on the stability and reactivity of such clusters. Unusual product composition was also explained by calculations. We believe that this study will help create reactive clusters, which would enhance our understanding of selective catalysis.

## ■ ASSOCIATED CONTENT

### Supporting Information

The Supporting Information is available free of charge on the ACS Publications website at DOI: 10.1021/acs.jpcc.9b09465.

Instrumental details; control experiments; DFT optimized isomeric structures; Mulliken charge distributions (PDF)

## AUTHOR INFORMATION

### Corresponding Author

\*E-mail: [pradeep@iitm.ac.in](mailto:pradeep@iitm.ac.in).

### ORCID

Soumabha Bag: 0000-0002-0932-105X

Sathish Kumar Mudedla: 0000-0003-3173-5993

Thalappil Pradeep: 0000-0003-3174-534X

### Author Contributions

<sup>§</sup>A.B., M.J., S.B., and S.K.M. contributed equally.

### Notes

The authors declare no competing financial interest.

## ACKNOWLEDGMENTS

The authors acknowledge the Department of Science and Technology for constantly supporting their research program. M.J. and M.B. acknowledge UGC, India, for their fellowships. S.K.M. acknowledges DST for Inspire fellowship. D.G. acknowledges IIT Madras for her fellowship. G.P. acknowledges IITM for an Institute Postdoctoral Fellowship.

## REFERENCES

- Chakraborty, I.; Pradeep, T. Atomically Precise Clusters of Noble Metals: Emerging Link between Atoms and Nanoparticles. *Chem. Rev.* **2017**, *117*, 8208–8271.
- Morse, M. D. Clusters of Transition-Metal Atoms. *Chem. Rev.* **1986**, *86*, 1049–1109.
- van Bokhoven, J. A.; Vajda, S. Size Selected Clusters and Particles: From Physical Chemistry and Chemical Physics to Catalysis. *Phys. Chem. Chem. Phys.* **2014**, *16*, 26418–26420.
- Castleman, A. W., Jr. Cluster Structure and Reactions: Gaining Insights into Catalytic Processes. *Catal. Lett.* **2011**, *141*, 1243–1253.
- Luo, Z.; Gamboa, G. U.; Smith, J. C.; Reber, A. C.; Reveles, J. U.; Khanna, S. N.; Castleman, A. W. Spin Accommodation and Reactivity of Silver Clusters with Oxygen: The Enhanced Stability of  $\text{Ag}_{13}^-$ . *J. Am. Chem. Soc.* **2012**, *134*, 18973–18978.
- Cassady, C. J.; Sharpe, P. Gas-Phase Reactions of Silver Cluster Ions Produced by Fast Atom Bombardment. *Chem. Phys. Lett.* **1992**, *197*, 111–116.
- Dietz, T. G.; Duncan, M. A.; Powers, D. E.; Smalley, R. E. Laser Production of Supersonic Metal Cluster Beams. *J. Chem. Phys.* **1981**, *74*, 6511–6512.
- Rashidzadeh, H.; Guo, B. Generation of Large Gas-Phase Silver Cluster Ions by Laser Desorption/Ionization of Silver-Containing Salts. *Chem. Phys. Lett.* **1999**, *310*, 466–470.
- Wlekinski, M.; Sarkar, D.; Hollerbach, A.; Pradeep, T.; Cooks, R. G. Ambient Preparation and Reactions of Gas Phase Silver Cluster Cations and Anions. *Phys. Chem. Chem. Phys.* **2015**, *17*, 18364–18373.
- Cleveland, C. L.; Landman, U. The Energetics and Structure of Nickel Clusters - Size Dependence. *J. Chem. Phys.* **1991**, *94*, 7376–7396.
- Saito, Y.; Watanabe, M.; Hagiwara, T.; Nishigaki, S.; Noda, T. Magic Numbers in a Mass Spectrum of Lithium Clusters Emitted from a Liquid Metal Ion Source. *Jpn. J. Appl. Phys.* **1988**, *27*, 424.
- Alivisatos, A. P. Semiconductor Clusters, Nanocrystals, and Quantum Dots. *Science* **1996**, *271*, 933–937.
- Kroto, H. W.; Heath, J. R.; O'Brien, S. C.; Curl, R. F.; Smalley, R. E.  $\text{C}_{60}$ : Buckminsterfullerene. *Nature* **1985**, *318*, 162–163.
- Luo, Z.; Castleman, A. W.; Khanna, S. N. Reactivity of Metal Clusters. *Chem. Rev.* **2016**, *116*, 14456–14492.
- Liao, M.-S.; Watts, J. D.; Huang, M.-J. Theoretical Comparative Study of Oxygen Adsorption on Neutral and Anionic  $\text{Ag}_n$  and  $\text{Au}_n$  Clusters ( $N = 2-25$ ). *J. Phys. Chem. C* **2014**, *118*, 21911–21927.
- Molina, L. M.; Lopez, M. J.; Alonso, J. A. Ab Initio Studies of Propene Epoxidation on Oxidized Silver Surfaces. *Phys. Chem. Chem. Phys.* **2014**, *16*, 26546–26552.
- Chakraborty, P.; Bakshi, A.; Khatun, E.; Nag, A.; Ghosh, A.; Pradeep, T. Dissociation of Gas Phase Ions of Atomically Precise Silver Clusters Reflects Their Solution Phase Stability. *J. Phys. Chem. C* **2017**, *121*, 10971–10981.
- Socaciu, L. D.; Hagen, J.; Le Roux, J.; Popolan, D.; Bernhardt, T. M.; Woste, L.; Vajda, S. Strongly Cluster Size Dependent Reaction Behavior of CO with  $\text{O}_2$  on Free Silver Cluster Anions. *J. Chem. Phys.* **2004**, *120*, 2078–2081.
- De Haeck, J.; Veldeman, N.; Claes, P.; Janssens, E.; Andersson, M.; Lievens, P. Carbon Monoxide Adsorption on Silver Doped Gold Clusters. *J. Phys. Chem. A* **2011**, *115*, 2103–2109.
- Cao, X.; Chen, M.; Ma, J.; Yin, B.; Xing, X. CO Oxidation by the Atomic Oxygen on Silver Clusters: Structurally Dependent Mechanisms Generating Free or Chemically Bonded  $\text{CO}_2$ . *Phys. Chem. Chem. Phys.* **2017**, *19*, 196–203.
- Liu, J.-H.; Meng, L.-D.; Lv, C.-Q.; Wang, G.-C. Selective Hydrogenation of Acetylene over  $\text{TiO}_2$ -Supported PdAg Cluster: Carbon Species Effect. *RSC Adv.* **2016**, *6*, 14593–14601.
- Pei, G. X.; et al. Ag Alloyed Pd Single-Atom Catalysts for Efficient Selective Hydrogenation of Acetylene to Ethylene in Excess Ethylene. *ACS Catal.* **2015**, *5*, 3717–3725.
- Luo, Z.; Gamboa, G. U.; Jia, M.; Reber, A. C.; Khanna, S. N.; Castleman, A. W. Reactivity of Silver Clusters Anions with Ethanethiol. *J. Phys. Chem. A* **2014**, *118*, 8345–8350.
- Ma, J.; Cao, X.; Liu, H.; Yin, B.; Xing, X. The Adsorption and Activation of NO on Silver Clusters with Sizes up to One Nanometer: Interactions Dominated by Electron Transfer from Silver to NO. *Phys. Chem. Chem. Phys.* **2016**, *18*, 12819–12827.
- Khairallah, G. N.; O'Hair, R. A. J. Activation of the C-I and C-OH Bonds of 2-Iodoethanol by Gas Phase Silver Cluster Cations Yields Subvalent Silver-Iodide and -Hydroxide Cluster Cations. *Dalton Trans.* **2007**, *0*, 3149–3157.
- Jalili, S.; Goliaei, E. M.; Schofield, J. Silver Cluster Supported on Nitrogen-Doped Graphene as an Electrocatalyst with High Activity and Stability for Oxygen Reduction Reaction. *Int. J. Hydrogen Energy* **2017**, *42*, 14522–14533.
- Lian, L.; Mitchell, S. A.; Hackett, P. A.; Rayner, D. M. Size Dependence of Mobility on the Surface of Metal Clusters: Ammonia on  $\text{Ag}_{10}$  and  $\text{Ag}_{16}$ . *J. Chem. Phys.* **1996**, *104*, 5338–5344.
- Yang, T.; Dai, S.; Qin, C.; Huang, K.; Chen, Y.; Pan, H.; Zhang, S.; Zhang, K.; Xu, J. Selective Detection of Homocysteine by Using Poly Methyl Vinyl Ether-Alt-Maleic Silver Clusters. *Chin. J. Org. Chem.* **2016**, *36*, 867–871.
- Hayashido, Y.; Naya, S.-i.; Tada, H. Local Electric Field-Enhanced Plasmonic Photocatalyst: Formation of Ag Cluster-Incorporated AgBr Nanoparticles on  $\text{TiO}_2$ . *J. Phys. Chem. C* **2016**, *120*, 19663–19669.
- Sridharan, K.; Jang, E.; Park, J. H.; Kim, J.-H.; Lee, J.-H.; Park, T. J. Silver Quantum Cluster ( $\text{Ag}_9$ )-Grafted Graphitic Carbon Nitride Nanosheets for Photocatalytic Hydrogen Generation and Dye Degradation. *Chem. - Eur. J.* **2015**, *21*, 9126–9132.
- Wang, X.; Zhao, Z.; Ou, D.; Tu, B.; Cui, D.; Wei, X.; Cheng, M. Highly Active Ag Clusters Stabilized on  $\text{TiO}_2$  Nanocrystals for Catalytic Reduction of p-Nitrophenol. *Appl. Surf. Sci.* **2016**, *385*, 445–452.
- Sowmiya, M.; Senthilkumar, K. Dissociation of  $\text{N}_2\text{O}$  on Anatase  $\text{TiO}_2$  (001) Surface - the Effect of Oxygen Vacancy and Presence of Ag Cluster. *Appl. Surf. Sci.* **2016**, *389*, 1220–1232.
- Lünsken, T.; Walenta, C. A.; Heister, P.; Kartouzian, A.; Heiz, U. Surface Oxidation of Supported, Size-Selected Silver Clusters. *J. Cluster Sci.* **2017**, *28*, 2401–2408.
- Bootharaju, M. S.; Dey, R.; Gevers, L. E.; Hedhili, M. N.; Basset, J.-M.; Bakr, O. M. A New Class of Atomically Precise,



Hydride-Rich Silver Nanoclusters Co-Protected by Phosphines. *J. Am. Chem. Soc.* **2016**, *138*, 13770–13773.

(35) Ghosh, A.; Bodiuzzaman, M.; Nag, A.; Jash, M.; Baksi, A.; Pradeep, T. Sequential Dihydrogen Desorption from Hydride-Protected Atomically Precise Silver Clusters and Formation of Naked Clusters in Gas Phase. *ACS Nano* **2017**, *11*, 11145–11151.

(36) Jash, M.; Reber, A. C.; Ghosh, A.; Sarkar, D.; Bodiuzzaman, M.; Basuri, P.; Baksi, A.; Khanna, S. N.; Pradeep, T. Preparation of Gas Phase Naked Silver Cluster Cations Outside a Mass Spectrometer from Ligand Protected Clusters in Solution. *Nanoscale* **2018**, *10*, 15714–15722.

(37) Krstić, M.; Zavras, A.; Khairallah, G. N.; Dugourd, P.; Bonacic-Koutecky, V.; O'Hair, R. A. J. ESI/MS Investigation of Routes to the Formation of Silver Hydride Nanocluster Dications  $[\text{Ag}_x\text{H}_{x-2}\text{Ly}]^{2+}$  and Gas-Phase Unimolecular Chemistry of  $[\text{Ag}_{10}\text{H}_8\text{L}_6]^{2+}$ . *Int. J. Mass Spectrom.* **2017**, *413*, 97–105.

(38) Chen, M.; Dyer, J. E.; Li, K.; Dixon, D. A. Prediction of Structures and Atomization Energies of Small Silver Clusters,  $(\text{Ag})_N$ ,  $N < 100$ . *J. Phys. Chem. A* **2013**, *117*, 8298–8313.

(39) Zhao, S.; Liu, Z.-P.; Li, Z.-H.; Wang, W.-N.; Fan, K.-N. Density Functional Study of Small Neutral and Charged Silver Cluster Hydrides. *J. Phys. Chem. A* **2006**, *110*, 11537–11542.

(40) Bumüller, D.; Hehn, A.-S.; Waldt, E.; Ahlrichs, R.; Kappes, M. M.; Schooss, D. Ruthenium Cluster Structure Change Induced by Hydrogen Adsorption:  $\text{Ru}_{19}$ . *J. Phys. Chem. C* **2017**, *121*, 10645–10652.

(41) Ferraro, F.; Perez-Torres, J. F.; Hadad, C. Z. Selective Catalytic Activation of Acetylene by a Neutral Gold Cluster of Experimentally Known Gas-Phase Geometry. *J. Phys. Chem. C* **2015**, *119*, 7755–7764.

(42) Nakajima, A.; Kishi, T.; Sone, Y.; Nonose, S.; Kaya, K. Reactivity of Positively Charged Cobalt Cluster Ions with Methane, Nitrogen, Hydrogen, Ethylene, and Acetylene. *Z. Phys. D: At., Mol. Clusters* **1991**, *19*, 385–387.

## Supporting Information

### Mechanistic Elucidation of the Structure and Reactivity of Bare and Hydride-Protected Ag<sub>17</sub><sup>+</sup> Clusters

Ananya Bakshi,<sup>†,§</sup> Madhuri Jash,<sup>†,§</sup> Soumabha Bag,<sup>†,§</sup> Sathish Kumar Mudedla,<sup>‡§</sup> Mohammad Bodiuzzaman,<sup>†</sup> Debasmitta Ghosh,<sup>†</sup> Ganesan Paramasivam,<sup>†</sup> Venkatesan Subramanian,<sup>‡</sup> and Thalappil Pradeep<sup>\*,†</sup>

<sup>†</sup>DST Unit of Nanoscience and Thematic Unit of Excellence, Indian Institute of Technology Madras, India

<sup>‡</sup>Chemical Laboratory, CSIR-Central Leather Research Institute, Adyar, Chennai 600020, India

\*Email: [pradeep@iitm.ac.in](mailto:pradeep@iitm.ac.in)

§ Contributed equally

#### Content:

Serial Number	Description	Page Number
<b>Figure S1</b>	Schematic of the instrument	<b>S3</b>
<b>Figure S2</b>	CID of Ag <sub>17</sub> <sup>+</sup>	<b>S3</b>
<b>Table S1</b>	CCS of bare Ag cluster cations with varying nuclearity	<b>S4</b>
<b>Figure S3</b>	DFT optimized isomeric structures of Ag <sub>17</sub> H <sub>14</sub>	<b>S5</b>
<b>Figure S4</b>	Reaction of Ag <sub>17</sub> <sup>+</sup> with different flow of CO and CID of Ag <sub>17</sub> (CO) <sub>7</sub> <sup>+</sup>	<b>S6</b>
<b>Table S2</b>	Atomic coordinates and Mulliken charge distribution of Ag <sub>17</sub> <sup>+</sup>	<b>S7</b>
<b>Table S3</b>	Atomic coordinates and Mulliken charge distribution of Ag <sub>17</sub> H <sub>14</sub> <sup>+</sup>	<b>S8</b>
<b>Table S4</b>	Atomic coordinates and Mulliken charge distribution of Ag <sub>17</sub> (CO) <sub>1</sub> <sup>+</sup>	<b>S9</b>
<b>Table S5</b>	Atomic coordinates and Mulliken charge distribution of Ag <sub>17</sub> (CO) <sub>2</sub> <sup>+</sup>	<b>S9</b>
<b>Table S6</b>	Atomic coordinates and Mulliken charge distribution of Ag <sub>17</sub> (CO) <sub>3</sub> <sup>+</sup>	<b>S10</b>
<b>Table S7</b>	Atomic coordinates and Mulliken charge distribution of Ag <sub>17</sub> (CO) <sub>4</sub> <sup>+</sup>	<b>S11</b>
<b>Table S8</b>	Atomic coordinates and Mulliken charge distribution of Ag <sub>17</sub> (CO) <sub>5</sub> <sup>+</sup>	<b>S12</b>
<b>Table S9</b>	Atomic coordinates and Mulliken charge distribution of Ag <sub>17</sub> (CO) <sub>6</sub> <sup>+</sup>	<b>S13</b>
<b>Table S10</b>	Atomic coordinates and Mulliken charge distribution of Ag <sub>17</sub> (CO) <sub>7</sub> <sup>+</sup>	<b>S14</b>
<b>Figure S5</b>	Different isomeric structures of Ag <sub>17</sub> (CO) <sub>1</sub>	<b>S15</b>
<b>Figure S6</b>	Different isomeric structures of Ag <sub>17</sub> (CO) <sub>2</sub>	<b>S16</b>
<b>Figure S7</b>	Different isomeric structures of Ag <sub>17</sub> (CO) <sub>3</sub>	<b>S17</b>
<b>Figure S8</b>	Different isomeric structures of Ag <sub>17</sub> (CO) <sub>4</sub>	<b>S18</b>
<b>Figure S9</b>	Different isomeric structures of Ag <sub>17</sub> (CO) <sub>5</sub>	<b>S18</b>
<b>Figure S10</b>	Different isomeric structures of Ag <sub>17</sub> (CO) <sub>6</sub>	<b>S19</b>
<b>Figure S11</b>	Different isomeric structures of Ag <sub>17</sub> (CO) <sub>7</sub>	<b>S19</b>
<b>Figure S12</b>	DFT optimized structures of Ag <sub>17</sub> (CO) <sub>n</sub> <sup>+</sup> (n = 1-6)	<b>S20</b>
<b>Table S11</b>	Calculated free energy change with sequential CO addition for Ag <sub>17</sub> and Ag <sub>17</sub> <sup>+</sup>	<b>S21</b>
<b>Table S12</b>	Calculated binding energy change with sequential CO addition for Ag <sub>17</sub> and Ag <sub>17</sub> <sup>+</sup>	<b>S21</b>



<b>Figure S13</b>	Different isomeric structures of $\text{Ag}_{17}(\text{C}_2\text{H}_5)_1$	<b>S22</b>
<b>Figure S14</b>	Different isomeric structures of $\text{Ag}_{17}(\text{C}_2\text{H}_5)_2$	<b>S23</b>
<b>Figure S15</b>	Reaction of $\text{Ag}_{17}\text{H}_{14}^+$ with different flow of $\text{C}_2\text{H}_2$	<b>S24</b>
<b>Figure S16</b>	Comparison between reaction of $\text{C}_2\text{H}_2$ with A) $\text{Ag}_{17}\text{H}_{14}^+$ and B) $\text{Ag}_{17}\text{D}_{14}^+$	<b>S25</b>

## Supporting Information 1:

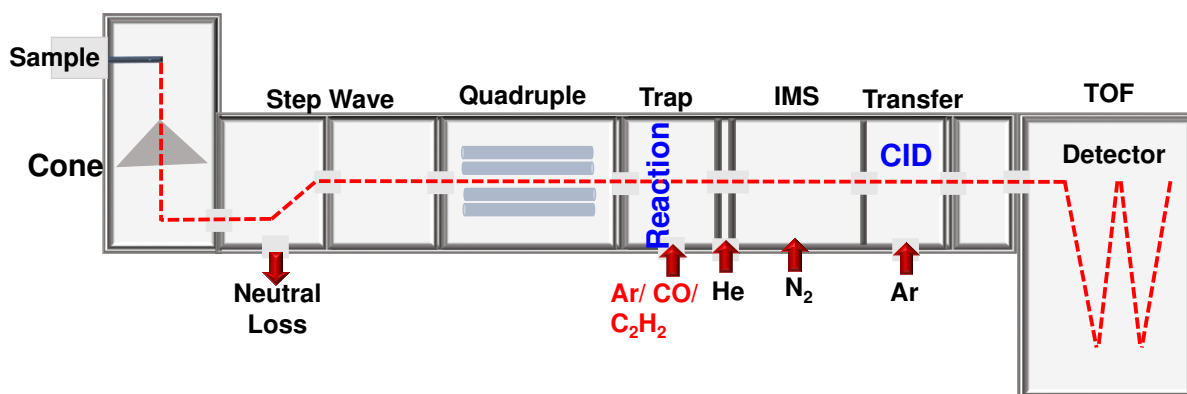


**Figure S1.** Schematic representation of the instrument. All the reactions were carried out in the trap region where Ar is used as collision gas. The Ar gas line was modified and reactive gases like CO and C<sub>2</sub>H<sub>2</sub> were incorporated.

## Supporting Information 2:

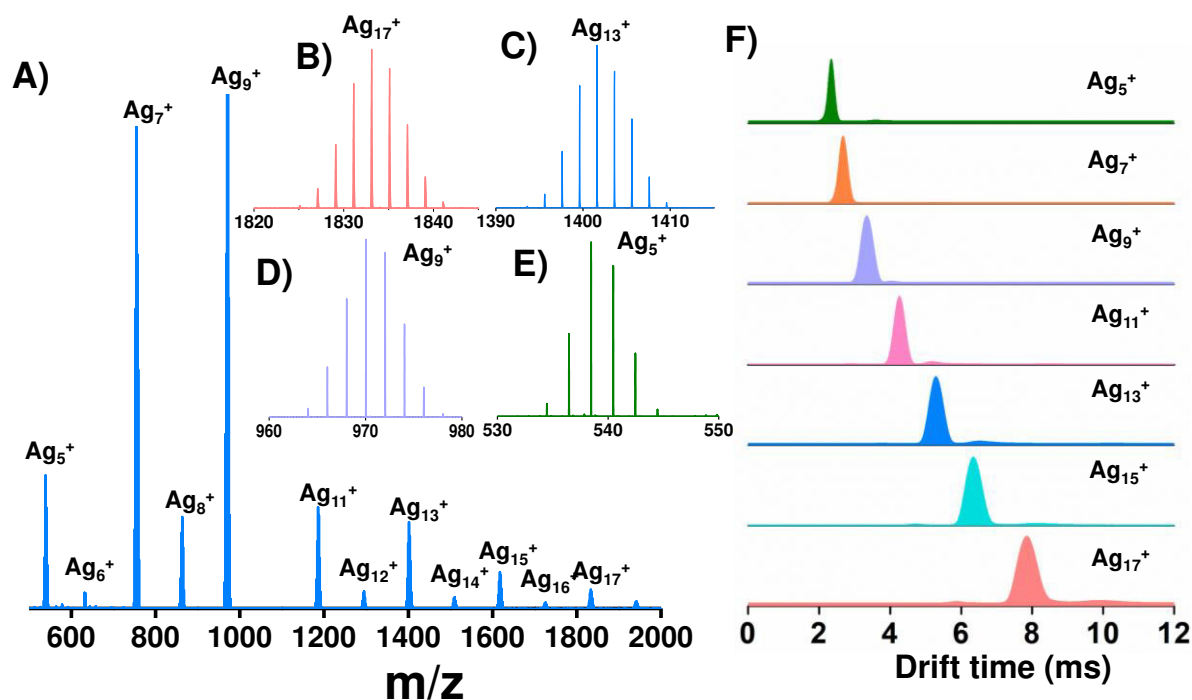


**Figure S2.** A) CID of Ag<sub>17</sub><sup>+</sup> shows different bare clusters. Odd numbered clusters are more stable than the even ones. Complete absence of Ag<sub>10</sub><sup>+</sup> confirms lesser stability of the clusters in the experimental condition. On the contrary higher intensity of Ag<sub>7</sub><sup>+</sup> and Ag<sub>9</sub><sup>+</sup> cluster confirms very high stability of these clusters in the experimental condition. Expanded m/z region for Ag<sub>17</sub><sup>+</sup>, Ag<sub>13</sub><sup>+</sup>, Ag<sub>9</sub><sup>+</sup> and Ag<sub>5</sub><sup>+</sup> are shown in B) to E). Extracted ion mobility data of

each of the odd numbered clusters are shown in F). Despite of the possibility of having multiple structural isomers of such gas phase clusters, only one isomer appeared at maximum abundance.

**Table S1.** CCS of bare Ag cluster cations with varying nuclearity.

Cluster	Arrival Time (ms)	<sup>TWIMS</sup> CCS <sub>N<sub>2</sub></sub> (Å <sup>2</sup> )
Ag <sub>17</sub> <sup>+</sup>	7.86	174
Ag <sub>15</sub> <sup>+</sup>	6.37	157
Ag <sub>13</sub> <sup>+</sup>	5.29	143
Ag <sub>11</sub> <sup>+</sup>	4.26	128
Ag <sub>9</sub> <sup>+</sup>	3.36	114
Ag <sub>7</sub> <sup>+</sup>	2.64	101
Ag <sub>5</sub> <sup>+</sup>	2.32	95

### Supporting Information 3:

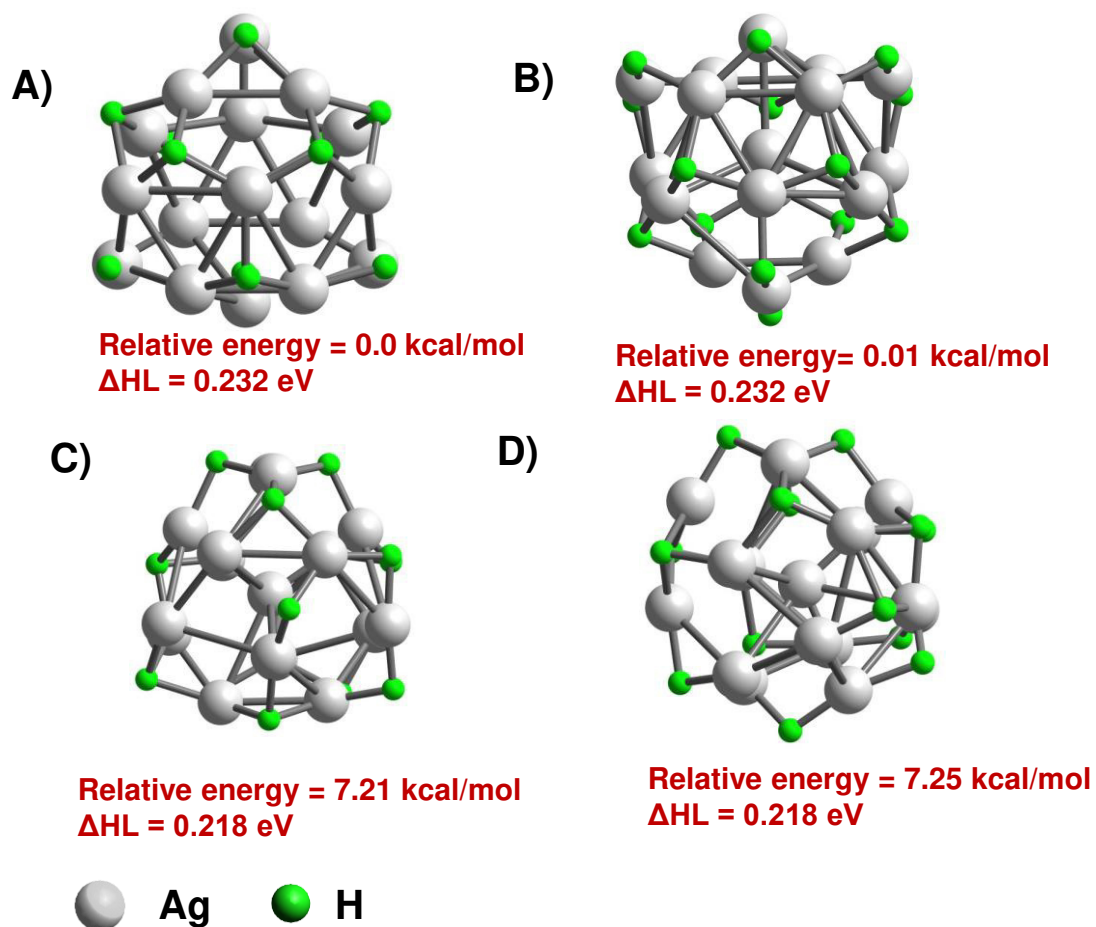


**Figure S3.** Four different isomeric structures of  $\text{Ag}_{17}\text{H}_{14}$ . The most stable geometry is shown in A. Other structures are arranged in their decreasing stability order.

## Supporting Information 4:

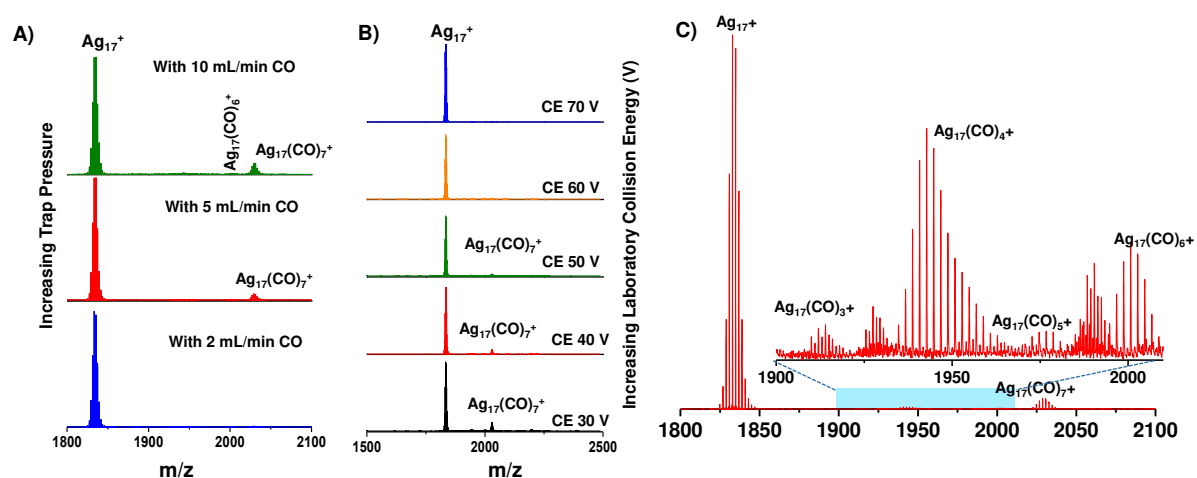


**Figure S4.** A) Reaction of  $\text{Ag}_{17}^+$  with different flow of CO showing  $\text{Ag}_{17}(\text{CO})_7^+$  formation. B) CID of  $\text{Ag}_{17}(\text{CO})_7^+$  with increasing collision energy lead to bare  $\text{Ag}_{17}^+$  cluster. C) CID of  $\text{Ag}_{17}(\text{CO})_7^+$  in IMS mode showing stepwise fragmentation. Mass range of  $m/z$  1900-2010 is expanded in the inset and the peaks are labelled.

**Table S2.** Atomic coordinates and the Mulliken charges of all the atoms of Ag<sub>17</sub><sup>+</sup>.

Atom	X (Å)	Y (Å)	Z (Å)	Charge (e)
Ag	-0.422181	1.119245	-2.065327	-0.433489
Ag	0.904745	-0.363006	0.289899	3.807301
Ag	1.481851	1.162071	2.671400	-0.162205
Ag	2.217860	-1.732583	2.545697	-0.175852
Ag	-1.064040	1.919193	0.938372	-0.433275
Ag	0.070397	-3.284642	0.889789	-0.225769
Ag	3.796133	0.309430	0.729353	-0.190571
Ag	2.836309	-2.500819	-0.332910	-0.175120
Ag	-3.045344	2.361957	-1.281071	0.110276
Ag	-1.218084	-0.730765	2.276860	-0.384785
Ag	-3.580418	0.262739	0.804231	0.005461
Ag	1.926890	2.484994	-0.249938	-0.321240
Ag	-0.458616	4.004579	-1.163998	0.177069
Ag	2.501173	-0.112171	-2.100598	-0.161443
Ag	-2.670202	-2.532826	0.101708	-0.057895
Ag	-2.953935	-0.519175	-2.135160	0.005956
Ag	-0.322537	-1.848222	-1.918304	-0.384422

**Table S3.** Atomic coordinates and Mulliken charges of all the atoms of Ag<sub>17</sub>H<sub>14</sub><sup>+</sup>.

Atom	X (Å)	Y (Å)	Z (Å)	Charge (e)
Ag	-2.479023	1.249976	-1.155632	0.002647
Ag	0.001521	-0.017348	-0.019685	2.289170
Ag	-1.358441	-2.011040	1.876284	-0.029752
Ag	1.367113	-2.031403	1.860834	-0.033481
Ag	-0.009942	-2.697551	-0.712330	-0.064818
Ag	3.027114	0.173746	1.536286	-0.107033
Ag	0.025561	0.294630	2.947703	-0.181389
Ag	1.414600	2.356064	1.385474	-0.040407
Ag	-1.465850	-1.116059	-2.547743	-0.064548
Ag	3.088052	-1.894396	-0.411921	-0.047127
Ag	1.438257	-1.121575	-2.560186	-0.065203
Ag	-3.027125	0.187463	1.554364	-0.112696
Ag	-3.096791	-1.888877	-0.385404	-0.048021
Ag	-1.386158	2.349688	1.401058	-0.034828
Ag	2.471274	1.240128	-1.177955	0.000428
Ag	-0.011379	1.391885	-2.709750	-0.021194
Ag	0.001081	3.486149	-0.846334	-0.089703
H	-0.016786	-2.346686	-2.799532	-0.009143
H	3.156187	1.833362	0.405569	-0.035586
H	3.312273	-1.731771	1.466822	-0.023872
H	-0.007941	3.298960	-2.598925	-0.007038
H	1.852161	0.755666	-2.859995	-0.034733
H	3.014384	-2.105384	-2.166916	-0.002376
H	1.780342	0.977247	2.855188	-0.051908
H	-3.306520	-1.719491	1.495331	-0.024255
H	0.013985	-1.825987	3.241125	-0.007378
H	-3.038416	-2.100553	-2.140916	-0.002192
H	-3.147381	1.847584	0.434769	-0.035114
H	0.009287	3.675321	1.005386	-0.031324
H	-1.878198	0.762037	-2.843923	-0.034475
H	-1.736908	0.960212	2.858079	-0.052651



**Table S4.** Atomic coordinates and Mulliken charges of all the atoms of Ag<sub>17</sub>CO<sup>+</sup>.

Atom	X (Å)	Y (Å)	Z (Å)	Charge (e)
Ag	-0.152740	-0.500183	-2.814555	-0.358639
Ag	0.016431	0.498993	-0.101547	4.248543
Ag	1.915894	-2.327944	1.772689	-0.090673
Ag	0.215125	-0.395975	2.929026	-0.135699
Ag	2.450072	0.449498	1.200759	-0.204132
Ag	-2.200389	0.519183	1.724306	-0.296592
Ag	-0.918054	-2.023904	1.105803	-0.065900
Ag	-3.622692	-1.708569	0.579099	-0.229536
Ag	2.325148	0.492051	-1.739962	-0.303678
Ag	0.114637	2.264144	2.089015	-0.283129
Ag	1.703455	2.832196	-0.140776	-0.312597
Ag	1.138859	-1.980251	-0.904499	-0.114686
Ag	3.807412	-1.485343	-0.242043	-0.244531
Ag	-1.685695	-2.474936	-1.495468	-0.059903
Ag	-1.640564	2.746040	-0.122042	-0.290208
Ag	0.054305	2.255208	-2.345054	-0.212777
Ag	-2.545217	0.242918	-1.088555	-0.197366
C	-0.805967	-0.441984	-4.883512	0.304239
O	-1.075726	-0.459408	-5.997726	-0.152738

**Table S5.** Atomic coordinates and Mulliken charges of all the atoms of Ag<sub>17</sub>(CO)<sub>2</sub><sup>+</sup>.

Atom	X (Å)	Y (Å)	Z (Å)	Charge (e)
Ag	0.697529	-2.769410	-0.283397	-0.343317
Ag	-0.011385	0.119446	0.348692	4.427883
Ag	-2.216992	1.108913	-2.444557	-0.038707
Ag	-0.784577	2.835312	-0.780180	-0.343296
Ag	-2.708319	0.841597	0.342705	-0.225303
Ag	1.867895	2.252202	0.126717	-0.310825
Ag	0.713868	1.084873	-2.228090	-0.183476
Ag	3.495723	0.993279	-1.842896	-0.242624
Ag	-1.886662	-2.002342	0.681838	-0.310813
Ag	-0.475947	2.403456	1.957476	-0.228255
Ag	-1.603030	-0.052212	2.744464	-0.295113
Ag	-0.913914	-1.323290	-1.932005	-0.183492
Ag	-3.661291	-1.138804	-1.372205	-0.242633
Ag	1.993781	-1.409743	-2.350629	-0.038700
Ag	1.747713	0.742342	2.544117	-0.295112
Ag	0.584193	-1.811420	2.333078	-0.228245
Ag	2.683156	-0.609122	0.288573	-0.225317
C	1.571351	-4.705508	0.181543	0.306693
O	1.989165	-5.757502	0.363132	-0.153022
C	-1.636326	4.830978	-0.638560	0.306694
O	-2.047446	5.901120	-0.635195	-0.153022

**Table S6.** Atomic coordinates and Mulliken charges of all the atoms of  $\text{Ag}_{17}(\text{CO})_3^+$ .

Atom	X (Å)	Y (Å)	Z (Å)	Charge (e)
Ag	2.073421	-1.856447	-0.240905	-0.457123
Ag	0.014384	-0.008445	0.424871	4.338729
Ag	-2.373356	-0.009712	-2.687379	-0.053522
Ag	-2.112236	1.965991	-0.642065	-0.318334
Ag	-2.662695	-0.720065	0.149719	-0.224654
Ag	0.424905	2.789402	0.322033	-0.296522
Ag	0.030733	1.502430	-2.244675	-0.030647
Ag	2.367497	2.927843	-1.759476	-0.247100
Ag	-0.596065	-2.828610	0.409528	-0.318347
Ag	-1.593555	1.524077	2.065906	-0.340130
Ag	-1.525585	-1.232281	2.630336	-0.273557
Ag	-0.066094	-1.384489	-1.979222	-0.139929
Ag	-2.531253	-2.740890	-1.713860	-0.277391
Ag	2.435214	0.073405	-2.268820	-0.053295
Ag	1.254262	1.022915	2.691318	-0.223261
Ag	1.168526	-1.802865	2.438562	-0.288702
Ag	2.669650	1.039254	0.302314	-0.260382
C	3.869733	-3.029590	0.195866	0.312390
O	4.813426	-3.659870	0.357882	-0.155385
C	-4.025279	2.991385	-0.744380	0.306019
O	-5.019021	3.558909	-0.821681	-0.156288
C	-2.375485	2.670492	3.764035	0.308493
O	-2.932579	3.252207	4.578761	-0.151062

**Table S7.** Atomic coordinates and Mulliken charges of all the atoms of  $\text{Ag}_{17}(\text{CO})_4^+$ .

Atom	X (Å)	Y (Å)	Z (Å)	Charge (e)
Ag	-2.876297	0.316087	0.631337	-0.387951
Ag	-0.003281	-0.356177	-0.149902	5.036299
Ag	2.027715	1.574328	2.201072	-0.034081
Ag	2.876913	0.639211	-0.297400	-0.385682
Ag	1.878347	-1.224010	1.728909	-0.413041
Ag	1.075403	0.451156	-2.604003	-0.341202
Ag	0.695727	2.392347	-0.454380	-0.223466
Ag	-0.627908	2.639475	-3.023203	-0.189002
Ag	-1.083199	-1.369807	2.225401	-0.341015
Ag	2.146289	-1.865249	-1.087965	-0.477254
Ag	0.260152	-3.250178	0.377936	-0.263599
Ag	-0.679169	1.507277	1.904206	-0.216795
Ag	0.634449	-0.025683	3.986586	-0.187281
Ag	-2.007882	2.663906	-0.618013	-0.028895
Ag	-0.289485	-2.169840	-2.462235	-0.266955
Ag	-2.168377	-2.090205	-0.441224	-0.482644
Ag	-1.887355	0.255159	-2.124530	-0.418073
C	-4.513388	1.482321	1.580087	0.327809
O	-5.366384	2.091307	2.044538	-0.152506
C	4.500915	2.154583	-0.205941	0.328340
O	5.341732	2.929692	-0.123491	-0.152735
C	3.663475	-2.920065	-2.146084	0.290269
O	4.508678	-3.488750	-2.674313	-0.155501
C	-3.689247	-3.574192	-0.297161	0.290383
O	-4.533563	-4.348922	-0.236562	-0.155422

**Table S8.** Atomic coordinates and Mulliken charges of all the atoms of  $\text{Ag}_{17}(\text{CO})_5^+$ .

Atom	X (Å)	Y (Å)	Z (Å)	Charge (e)
Ag	2.576615	0.601299	1.332050	-0.370551
Ag	0.144972	0.383839	-0.289139	4.494785
Ag	-1.700948	-2.733521	2.160618	-0.168713
Ag	-1.724181	-1.660058	-0.503622	-0.409807
Ag	-1.875282	0.069068	1.767872	-0.092390
Ag	-1.205090	-0.085288	-2.862200	-0.376148
Ag	0.271550	-3.545136	0.190560	-0.045716
Ag	0.413823	-2.337349	-2.397542	-0.034533
Ag	0.338176	1.286612	2.935412	-0.178923
Ag	-2.594012	1.088815	-0.719655	-0.385007
Ag	-0.714128	2.778189	0.778755	-0.299342
Ag	0.705978	-1.362657	1.950637	0.026075
Ag	-0.862041	-0.915131	4.214668	-0.221115
Ag	2.197424	-1.488067	-0.446062	-0.464810
Ag	-0.547301	2.519964	-2.121373	-0.321695
Ag	1.879456	2.503425	-0.730216	-0.457041
Ag	1.655409	0.317938	-2.587137	-0.467918
C	4.342199	1.567571	2.221995	0.300159
O	5.295811	1.796673	2.816728	-0.153147
C	-3.185658	-3.054397	-1.335641	0.346521
O	-3.986831	-3.771742	-1.738096	-0.167946
C	-4.552838	2.031719	-0.913719	0.304403
O	-5.606456	2.446451	-1.094654	-0.158070
C	3.250730	4.243792	-0.932958	0.309784
O	3.858800	5.136014	-1.314481	-0.148041
C	4.018763	-2.583322	-0.737535	0.304222
O	4.988703	-3.179231	-0.888608	-0.165035

**Table S9.** Atomic coordinates and Mulliken charges of all the atoms of  $\text{Ag}_{17}(\text{CO})_6^+$ .

Atom	X (Å)	Y (Å)	Z (Å)	Charge (e)
Ag	-2.976161	-1.016472	-1.728311	-0.293969
Ag	0.035193	0.493358	0.829594	4.697460
Ag	2.342580	-2.261354	-1.213469	-0.261852
Ag	2.419791	-0.566938	1.358948	-0.478297
Ag	1.755838	0.492423	-1.378643	-0.178389
Ag	1.081410	1.405862	3.254348	-0.403868
Ag	0.597782	-2.816834	0.988047	-0.018511
Ag	-0.013720	-1.197958	3.152971	-0.361085
Ag	-0.871196	0.732489	-2.716627	-0.127955
Ag	2.140262	2.279881	0.801783	-0.462497
Ag	-0.014074	2.790833	-1.078540	-0.214532
Ag	-0.320857	-1.555304	-1.285048	0.244664
Ag	1.153981	-1.100599	-3.586197	-0.189954
Ag	-2.000001	-1.375325	0.984539	-0.494681
Ag	-0.577402	3.135926	1.644695	-0.380328
Ag	-2.330687	1.299265	-0.152565	-0.463265
Ag	-1.973108	0.872238	2.708072	-0.517160
C	-4.760212	-1.753630	-2.885572	0.299206
O	-5.370659	-2.434977	-3.574917	-0.141476
C	4.198512	-1.580913	2.060994	0.314680
O	5.166155	-2.067569	2.439349	-0.165486
C	3.616309	3.858018	0.597702	0.303189
O	4.440774	4.653630	0.555274	-0.159030
C	-4.031776	2.417355	-0.878447	0.321667
O	-4.937046	3.011344	-1.259339	-0.166780
C	-3.232286	-3.029425	1.633299	0.313358
O	-3.925460	-3.882383	1.966280	-0.167176
C	4.069433	-3.617798	-1.512833	0.301076
O	4.776269	-4.469164	-1.810094	-0.149008

**Table S10.** Atomic coordinates and Mulliken charges of all the atoms of  $\text{Ag}_{17}(\text{CO})_7^+$ .

Atom	X (Å)	Y (Å)	Z (Å)	Charge (e)
Ag	-1.777119	-2.098640	-0.750455	-0.340047
Ag	-0.486815	0.469798	0.472462	4.031895
Ag	3.264833	-0.965593	1.142947	-0.220736
Ag	1.996354	1.726158	1.108778	-0.453451
Ag	2.001002	0.069326	-1.117654	0.174550
Ag	-0.428460	3.144670	1.352029	-0.393860
Ag	0.913589	-0.452412	2.743868	-0.323198
Ag	-1.694297	1.062457	2.882072	-0.405597
Ag	0.505095	-1.898356	-2.437015	-0.127586
Ag	0.476223	2.397418	-1.311271	-0.283872
Ag	0.940922	0.693563	-3.630534	-0.214385
Ag	0.815632	-2.100697	0.382095	-0.002107
Ag	3.075575	-2.466573	-1.277925	-0.186068
Ag	-1.556185	-1.610957	2.013415	-0.399965
Ag	-2.280087	2.555560	-0.735842	-0.273250
Ag	-1.369994	0.354782	-2.165050	-0.159403
Ag	-3.225933	0.136290	0.502871	-0.472134
C	-3.017956	-4.021252	-0.983809	0.315655
O	-3.178874	-5.124977	-0.710711	-0.150463
C	3.515651	2.879886	2.229671	0.308272
O	4.308777	3.663341	2.503008	-0.159696
C	1.165158	4.264886	-2.117403	0.303635
O	1.569171	5.255987	-2.534772	-0.168095
C	-2.803296	-0.993393	-3.157460	0.329908
O	-3.554418	-1.474873	-3.888344	-0.172061
C	-2.173786	-3.278195	3.244541	0.299562
O	-2.498248	-4.138389	3.931030	-0.160567
C	5.002751	-1.325545	2.475532	0.301337
O	5.788076	-1.726224	3.207733	-0.151265
C	-5.464250	-0.035281	0.519477	0.306300
O	-6.478401	-0.546861	0.682247	-0.153308

## Supporting Information 5:

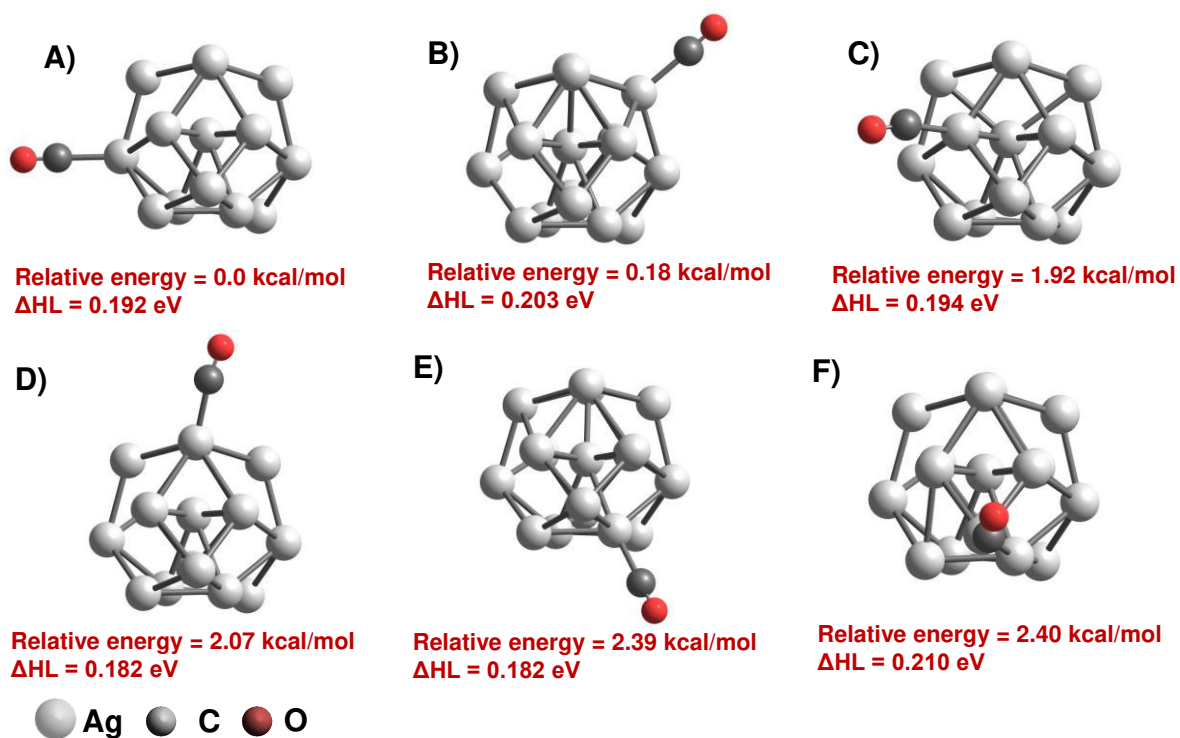


**Figure S5.** Six different isomeric structures of  $\text{Ag}_{17}(\text{CO})_1$ . The most stable geometry is shown in A. Other structures are arranged in their decreasing stability order.



## Supporting Information 6:

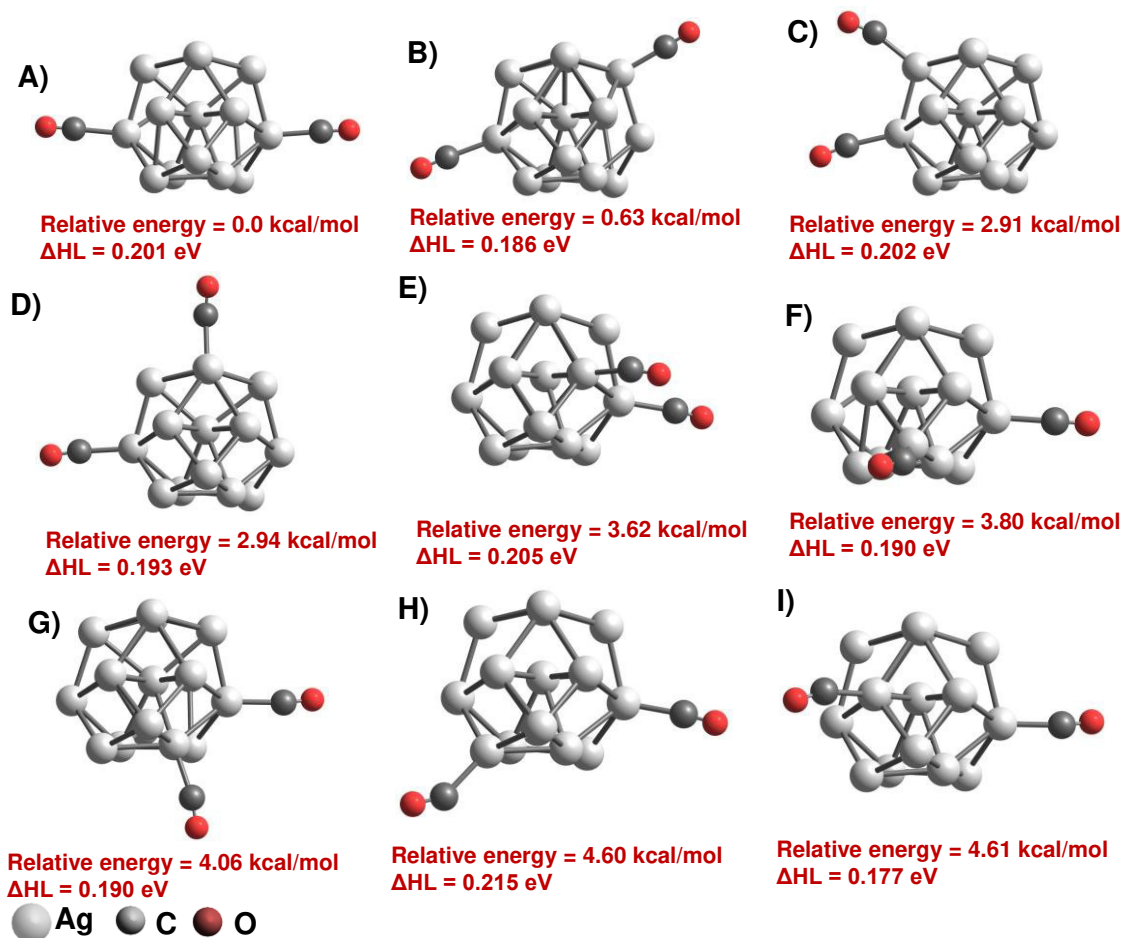


**Figure S6.** Nine different isomeric structures of  $\text{Ag}_{17}(\text{CO})_2$ . The most stable geometry is shown in A. Other structures are arranged in their decreasing stability order.

## Supporting Information 7:

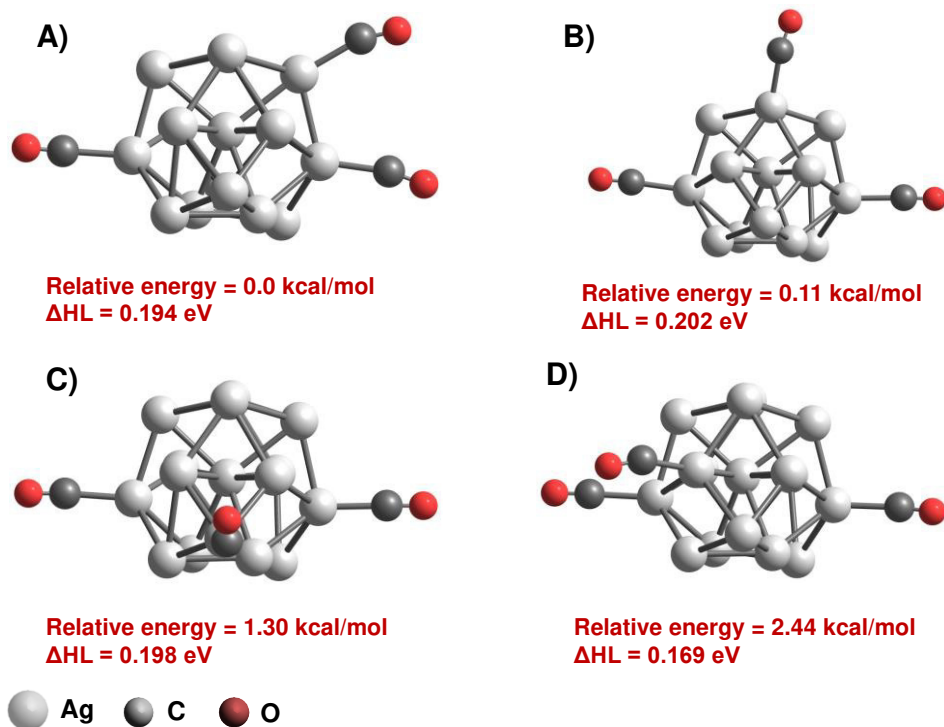


**Figure S7.** Four different isomeric structures of  $\text{Ag}_{17}(\text{CO})_3$ . The most stable geometry is shown in A. Other structures are arranged in their decreasing stability order.

### Supporting Information 8:

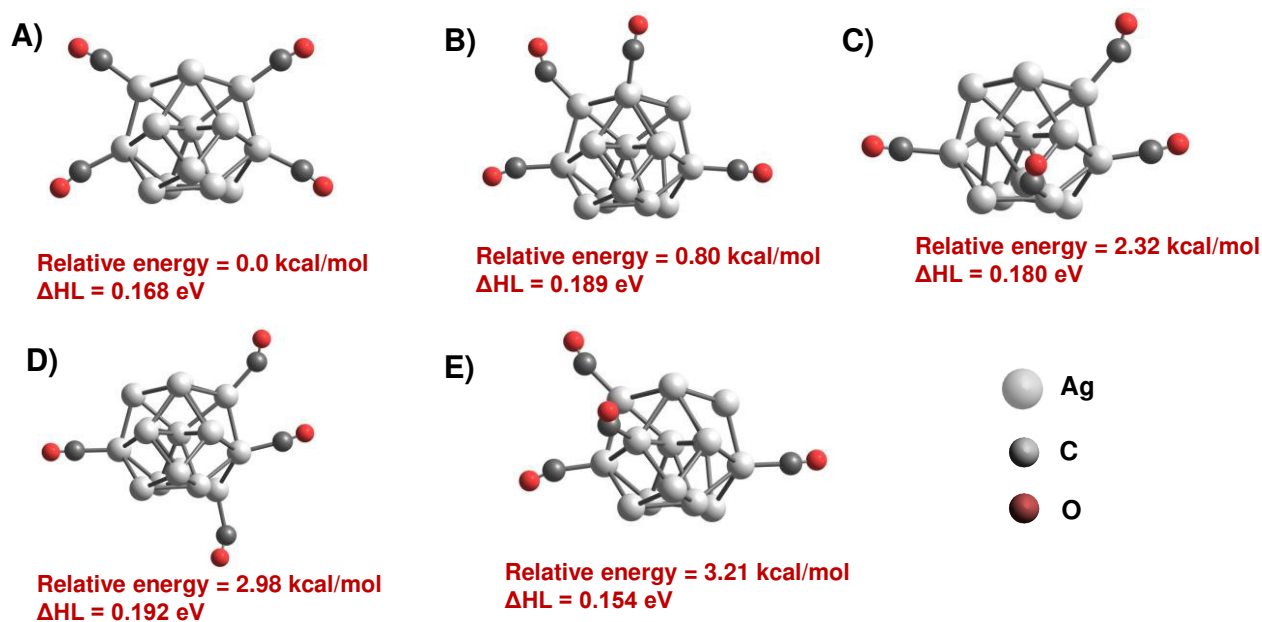


**Figure S8.** Five different isomeric structures of  $\text{Ag}_{17}(\text{CO})_4$ . The most stable geometry is shown in A. Other structures are arranged in their decreasing stability order.

### Supporting Information 9:

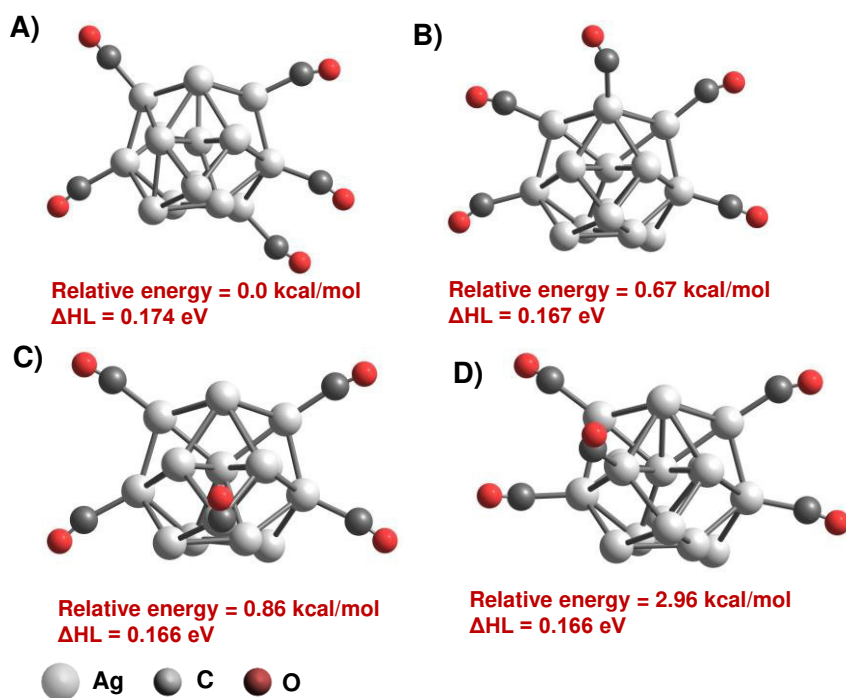


**Figure S9.** Four different isomeric structures of  $\text{Ag}_{17}(\text{CO})_5$ . The most stable geometry is shown in A. Other structures are arranged in their decreasing stability order.

## Supporting Information 10:

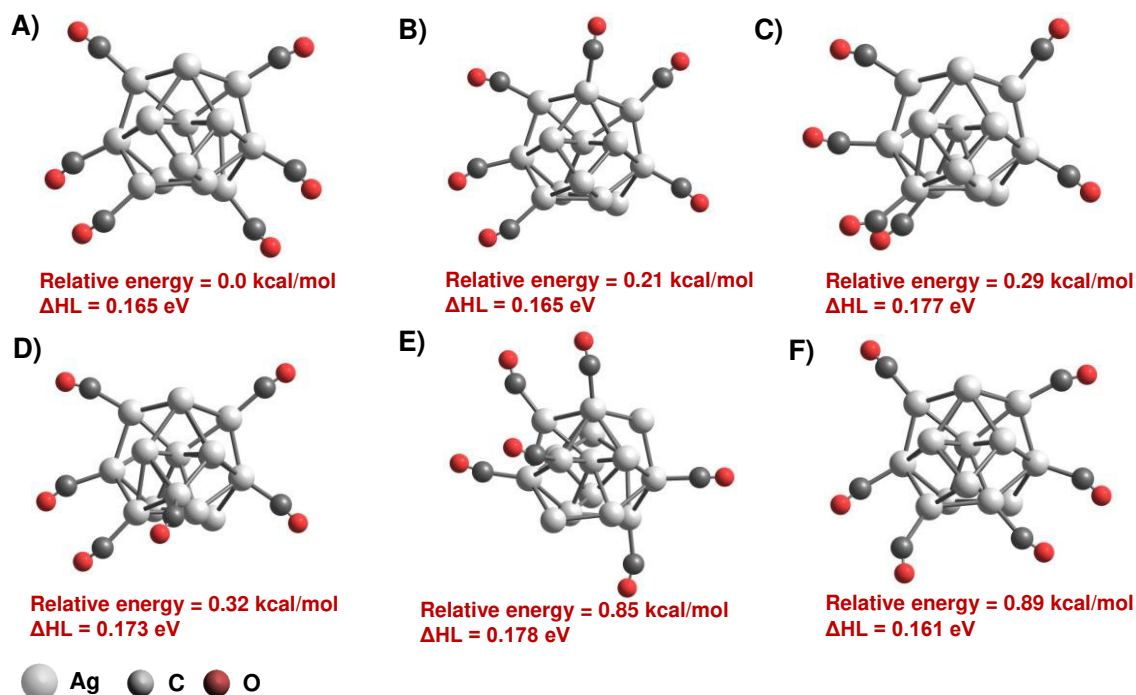


**Figure S10.** Six different isomeric structures of  $\text{Ag}_{17}(\text{CO})_6$ . The most stable geometry is shown in A. Other structures are arranged in their decreasing stability order.

## Supporting Information 11:

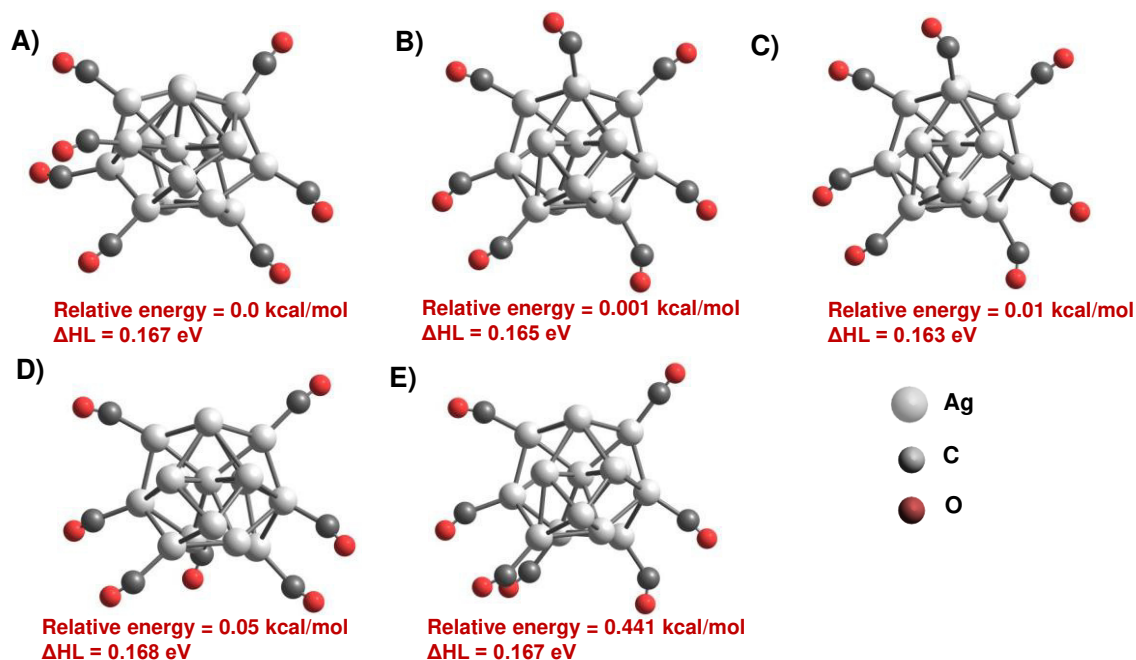


**Figure S11.** Six different isomeric structures of  $\text{Ag}_{17}(\text{CO})_7$ . The most stable geometry is shown in A. Other structures are arranged in their decreasing stability order.

**Supporting Information 12:**

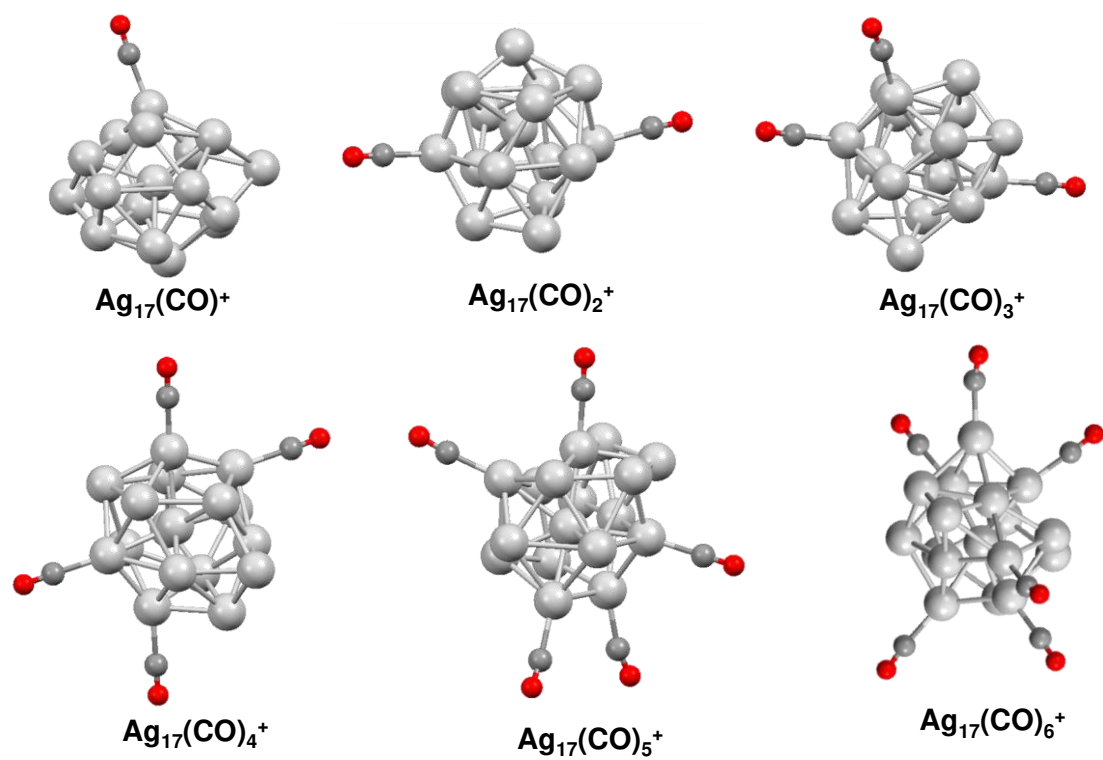


**Figure S12.** DFT optimized structures of  $\text{Ag}_{17}(\text{CO})_n^+$  ( $n = 1-6$ ). For  $\text{Ag}_{17}(\text{CO})_7^+$ , the DFT optimized structure is given in Figure 4.

**Table S11.** Calculated free energy change with sequential CO addition for Ag<sub>17</sub> and Ag<sub>17</sub><sup>+</sup>.

Cluster + CO	$\Delta G$ (kcal/mol)	Cluster + CO	$\Delta G$ (kcal/mol)
Ag <sub>17</sub> (CO) <sup>+</sup>	3.61	Ag <sub>17</sub> (CO)	-1.39
Ag <sub>17</sub> (CO) <sub>2</sub> <sup>+</sup>	-0.69	Ag <sub>17</sub> (CO) <sub>2</sub>	-4.89
Ag <sub>17</sub> (CO) <sub>3</sub> <sup>+</sup>	-3.84	Ag <sub>17</sub> (CO) <sub>3</sub>	-5.54
Ag <sub>17</sub> (CO) <sub>4</sub> <sup>+</sup>	-4.95	Ag <sub>17</sub> (CO) <sub>4</sub>	-7.28
Ag <sub>17</sub> (CO) <sub>5</sub> <sup>+</sup>	-15.85	Ag <sub>17</sub> (CO) <sub>5</sub>	-6.64
Ag <sub>17</sub> (CO) <sub>6</sub> <sup>+</sup>	-23.95	Ag <sub>17</sub> (CO) <sub>6</sub>	-6.18
Ag <sub>17</sub> (CO) <sub>7</sub> <sup>+</sup>	-17.89	Ag <sub>17</sub> (CO) <sub>7</sub>	-6.65

**Table S12.** Calculated binding energy change with sequential CO addition for Ag<sub>17</sub> and Ag<sub>17</sub><sup>+</sup>.

Cluster + CO	Binding Energy (kcal/mol)	Cluster + CO	Binding Energy (kcal/mol)
Ag <sub>17</sub> (CO) <sup>+</sup>	-4.83	Ag <sub>17</sub> (CO)	-14.18
Ag <sub>17</sub> (CO) <sub>2</sub> <sup>+</sup>	-19.17	Ag <sub>17</sub> (CO) <sub>2</sub>	-12.23
Ag <sub>17</sub> (CO) <sub>3</sub> <sup>+</sup>	-30.73	Ag <sub>17</sub> (CO) <sub>3</sub>	-9.18
Ag <sub>17</sub> (CO) <sub>4</sub> <sup>+</sup>	-41.46	Ag <sub>17</sub> (CO) <sub>4</sub>	-10.21
Ag <sub>17</sub> (CO) <sub>5</sub> <sup>+</sup>	-63.41	Ag <sub>17</sub> (CO) <sub>5</sub>	-8.75
Ag <sub>17</sub> (CO) <sub>6</sub> <sup>+</sup>	-78.51	Ag <sub>17</sub> (CO) <sub>6</sub>	-7.88
Ag <sub>17</sub> (CO) <sub>7</sub> <sup>+</sup>	-81.16	Ag <sub>17</sub> (CO) <sub>7</sub>	-7.82

### Supporting Information 13:

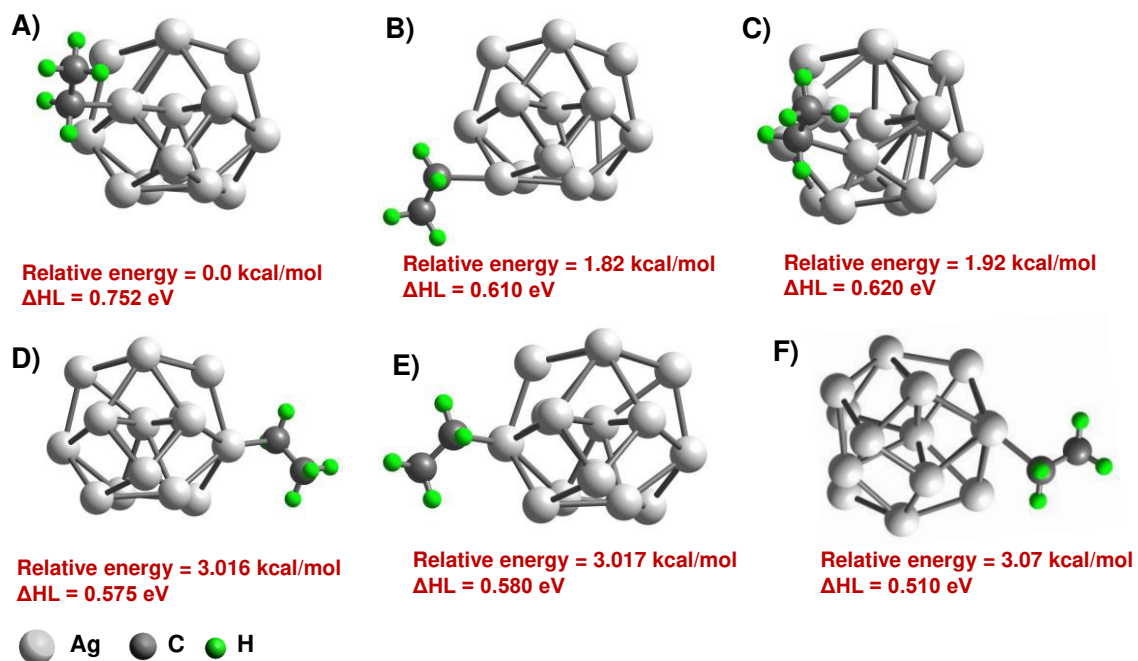


**Figure S13.** Six different isomeric structures of  $\text{Ag}_{17}(\text{C}_2\text{H}_5)_1$ . The most stable geometry is shown in A. Other structures are arranged in their decreasing stability order.



Supporting Information 14:

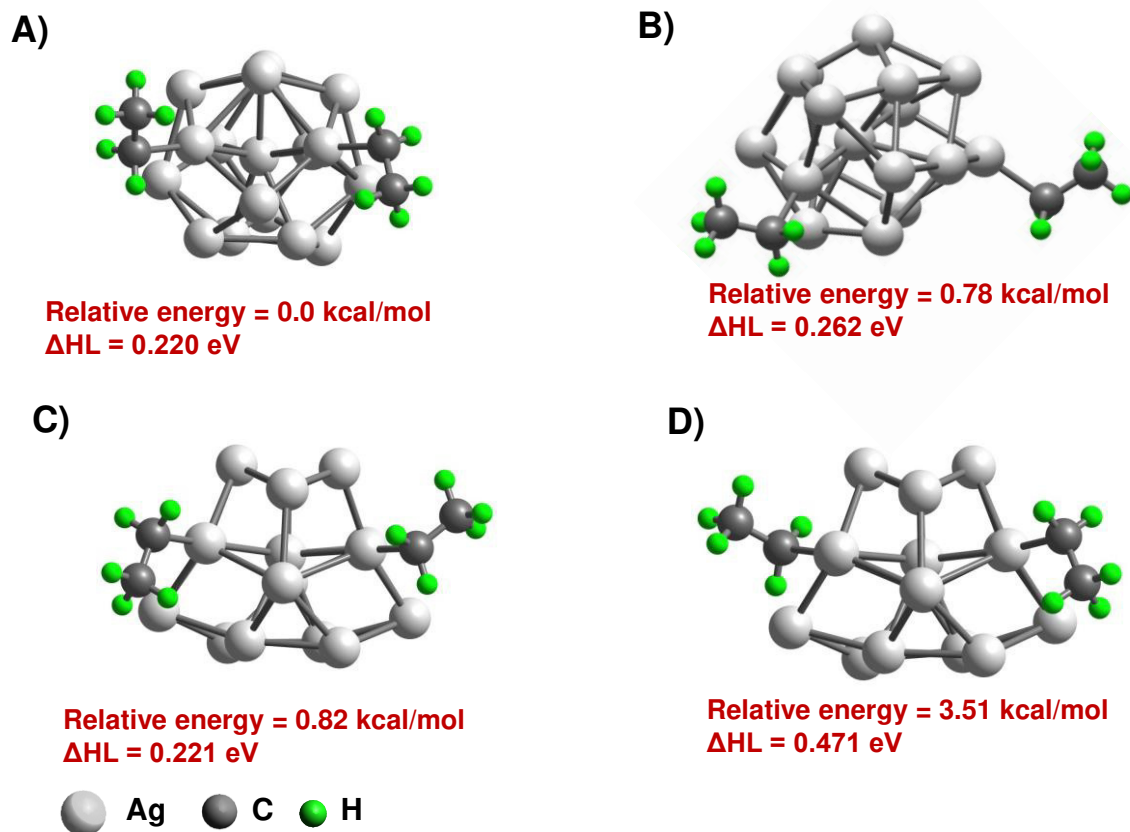


**Figure S14.** Four different isomeric structures of  $\text{Ag}_{17}(\text{C}_2\text{H}_5)_2$ . The most stable geometry is shown in A. Other structures are arranged in their decreasing stability order.

## Supporting Information 15:

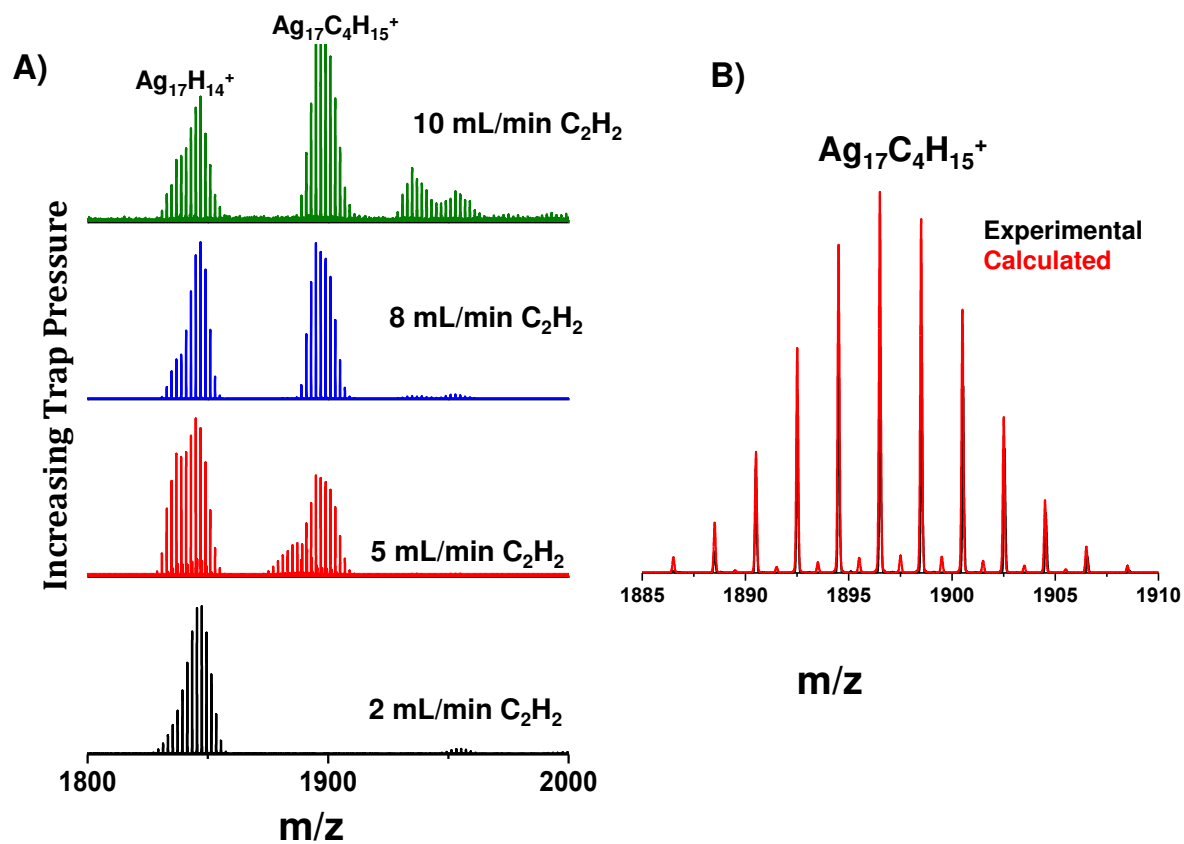


**Figure S15.** A) Reaction of  $\text{Ag}_{17}\text{H}_{14}^+$  with different flow of  $\text{C}_2\text{H}_2$  showing  $\text{Ag}_{17}\text{C}_4\text{H}_{15}^+$  formation. B) Experimental isotope distribution of  $\text{Ag}_{17}\text{C}_4\text{H}_{15}^+$  matches exactly with the calculated one.

Supporting Information 16:

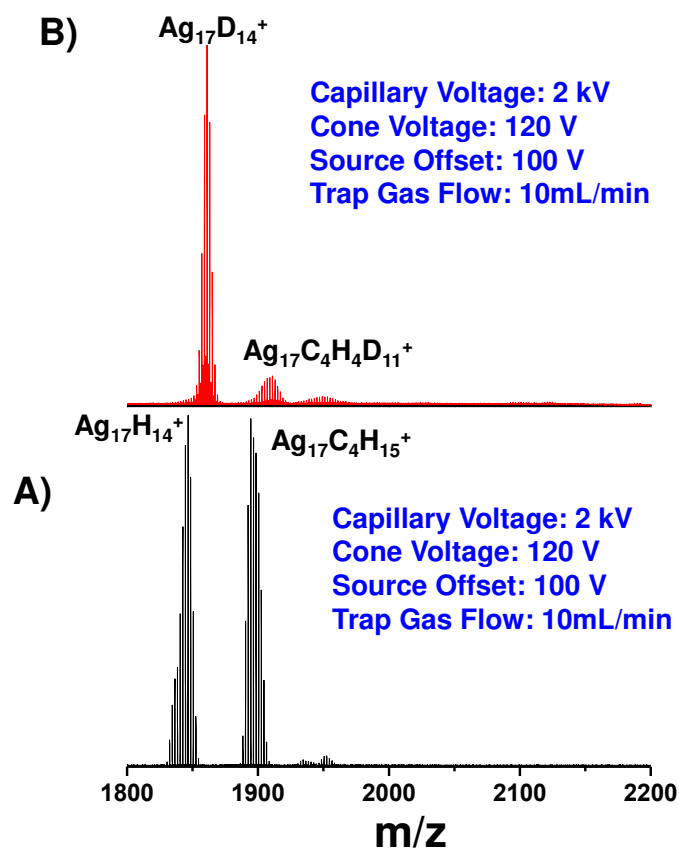


**Figure S16.** Comparison between reaction of  $C_2H_2$  with A)  $Ag_{17}H_{14}^+$  and B)  $Ag_{17}D_{14}^+$  showing H exchange and formation of  $Ag_{17}C_4H_{15}^+$  and  $Ag_{17}C_4H_4D_{11}^+$ . Three H sites are now replaced with two acetylene.



# Enhancing the sensitivity of point-of-use electrochemical microfluidic sensors by ion concentration polarisation – A case study on arsenic

Vidhya Subramanian<sup>a,b</sup>, Sangjun Lee<sup>c</sup>, Sanjoy Jena<sup>d</sup>, Sourav Kanti Jana<sup>a</sup>, Debdutta Ray<sup>d</sup>, Sung Jae Kim<sup>c,e,f</sup>, Pradeep Thalappil<sup>a,\*</sup>

<sup>a</sup> DST Unit on Nanoscience and Thematic Unit of Excellence (TUE), Department of Chemistry, Indian Institute of Technology, Madras, Chennai 600 036, India

<sup>b</sup> Department of Biotechnology, Indian Institute of Technology, Madras, Chennai 600 036, India

<sup>c</sup> Department of Electrical and Computer Engineering, Seoul National University, Seoul 08826, Republic of Korea

<sup>d</sup> Department of Electrical Engineering, Indian Institute of Technology, Madras, Chennai 600 036, India

<sup>e</sup> Inter-University Semiconductor Research Center, Seoul National University, Seoul, South Korea

<sup>f</sup> Nano Systems Institute, Seoul National University, Seoul, South Korea

## ARTICLE INFO

### Keywords:

Point of use sensor  
Electrochemical microfluidic sensor  
Ion concentration polarisation  
Arsenic  
Heavy metal ions

## ABSTRACT

Point of use (POU) sensors are extremely relevant, being capable of providing fast and reliable analysis in remote and resource-limited settings. Of all the diverse techniques utilised for POU sensors, a combination of electrochemistry and microfluidics may have the greatest potential towards quantitative assessment of heavy metal ions. The major challenge in combining these for sensing applications lies in the complexity of fabricating integrated devices and the insufficient quantity of analytes in the sample volume. To address these issues, we have developed a radial microfluidic device capable of electrokinetic preconcentration by ion concentration polarization (ICP) and integrated it with electroactive surfaces. The proposed sensor is the first demonstration of concentration of heavy metal ions by ICP and its quantitative assessment by voltammetry. Utilising the integrated sensor, we have shown the sensing of  $\text{As}^{3+}$  down to 1 ppb by linear sweep voltammetry with  $\sim 40 \mu\text{L}$  of sample. The sensor was also tested successfully for sensing  $\text{As}^{3+}$  in a field sample from an arsenic affected region of India. The sensor was also tested for the detection of other metal ions too. This work would facilitate the development of highly sensitive POU hand-held sensors for water quality monitoring in resource-limited areas.

## 1. Introduction

Presence of naturally occurring arsenic in water is of particular concern and has received considerable attention owing to its high toxicity. Specifically, trivalent form of arsenic ( $\text{As}^{3+}$ ) has been noted to cause various adverse health effects ranging from vomiting, abdominal pain, etc., in case of acute poisoning while chronic exposure can lead to skin, lungs and bladder cancer [1]. Arsenic compromises the body's immune functions, damages lung cells and causes inflammation of heart cells. Presence of 19 ppb of arsenic in human body reduces lung functions considerably and when it is above 120 ppb, the lung's ability is affected to the same extent as that of long term smokers [2]. Being tasteless and odorless in water, the presence of arsenic cannot be detected easily. For accurate detection of arsenic, various lab - based instrumentation [3] such as atomic absorption spectroscopy (AAS) [4] and inductively coupled plasma mass spectrometry (ICP-MS) [5] exist. Though these instruments provide accurate measurements, their

shortcoming lies in their size and requirement of trained personnel which limit their portability. One of the techniques that can be used to address these issues is electrochemistry [2]. Electrochemical sensors are based on the transfer of electrons on the surface of the electrodes and their advantages lie in low cost with ease of miniaturization, minimal sample pre-treatment and portability [6]. The advantage of portability in utilising electrochemical sensors arise from the fabrication and development of portable potentiostats that can perform most of the electrochemical measurements. Portable electrochemical detectors are currently being extensively researched upon because of their potential value in point-of-use applications [7–9]. Added advantage of such a system lies in its use as peripheral devices which can be integrated with mobile phones through bluetooth and the data can be uploaded to a data storage system anywhere in the world using the current mobile technology making it useful in resource limited settings [8] for remote monitoring of remediation solutions. These parameters of the electrochemical sensors make it suitable for developing point of use sensors for

\* Corresponding author.

E-mail address: [pradeep@iitm.ac.in](mailto:pradeep@iitm.ac.in) (P. Thalappil).

<https://doi.org/10.1016/j.snb.2019.127340>

Received 17 September 2019; Received in revised form 23 October 2019; Accepted 24 October 2019

Available online 30 October 2019

0925-4005/ © 2019 Elsevier B.V. All rights reserved.

arsenic and other metallic elements [10].

Integrating electrochemistry to microfluidics has given rise to the development of electrochemical microfluidic devices leading to micro total analysis systems ( $\mu$ TAS). The advent of  $\mu$ TAS changed the outlook for various applications [11,12]. Microfluidics form the core technology in  $\mu$ TAS owing to its versatility and requirement of smaller volumes for analysis. The major constraint one encounters while using microfluidics for sensors is the insufficient amount of analytes in the volume utilised. To rectify this, various preconcentration techniques such as isoelectric focusing [13], electric field gradient focusing [14], electrokinetic trapping [15], immunocapture based trapping [16], etc. [17], are being looked at. Of particular interest is electrokinetic trapping where in the presence of micro-nano junctions in a microchannel, different phenomena like ion exclusion enrichment effect, ion depletion enrichment effect, and amplified electrokinetic effect are exhibited [18,19] near the micro-nano interface. During electrokinetic trapping, the application of an external electric field results in an ion imbalance between the microchannel and nanochannel due to electro-migration flux, inducing the formation of a concentration gradient near the micro/nanochannel interface. This causes a diffusion flux which works to balance the ion flux of the system. The micro-nano junction is usually created by placing a membrane in the microchannel, where the nanopores of the membrane in contact with the microchannel form the micro-nano junction. These membranes are preferably electronegative with preferential cation permeability, where the charge selectivity is caused by the acidic impurities present on the pores of the membrane [20]. This technique has been termed as ion concentration polarization (ICP). Although the abbreviation ICP is commonly used for inductively coupled plasma, we propose to use the same as the literature has accepted it. ICP has been extensively used for the concentration of dyes, biomolecules, etc. [21–23]. Multiple theoretical studies have been performed to understand the mechanism of concentration and the scaling laws involved [24].

Here in this paper, we have integrated a radial channel ICP device directly to electrodes to perform electrochemistry. Even though ICP is capable of concentrating ions in microchannel, its major limitation lies in the incapability to quantitatively analyse the concentrated analyte, hence limiting most of the ICP devices to qualitative analysis. We have rectified this issue by combining our microfluidic devices to electrodes. Radial microchannels were utilized to increase the analyte volume used for preconcentration. The device design was kept simple to enable ease of fabrication and analysis. Multiple ions were analysed in the device to study their concentration mechanism and detection by voltammetry, with particular interest to arsenic.

## 2. Experimental

### 2.1. Materials

Gold wire, chrome pellets, silver wire, platinum wire, copper (II) acetate, lead (II) acetate, iron (II) acetate and manganese (II) acetate were purchased from Sigma – Aldrich. Sodium arsenite was purchased from SD Fine Chem Ltd. Potassium hydroxide, sulphuric acid ( $\text{H}_2\text{SO}_4$ ), acetone and iso-propyl alcohol were sourced from Rankem. Sylgard kit was purchased from Dow-Corning. Nafion perfluorinated resin solution was purchased from Aldrich. All chemicals were of analytical grade and were used without further purification. Distilled water was used throughout the experiments unless mentioned otherwise.

### 2.2. Instrumentation

For the electrode fabrication, spin coating was performed using Spin Coaters Spin 150 followed by UV beam exposure in mask aligner using OAI model 5000. For chrome and gold deposition, electron beam lithography was performed using BOC Edwards Auto 306. Scanning electron microscope (SEM) images were taken using FEI QUANTA-200

SEM. Spin coating of PDMS was performed using Spin NXG – P1a. Plasma bonding was done using Harrick Plasma Plasma Cleaner PDC-002-HP. The electrochemical measurements were performed using CHI 600A (CH Instruments, USA). External voltage was applied using Keithley 2611 B sourcemeter. Optical Imaging was done using Leica DMI 3000 B inverted microscope.

### 2.3. Electrode fabrication

The gold electrodes on glass were patterned using photolithography. The process included the heating of glass slides in an oven at 120 °C followed by spin coating of SU-8 photoresist on the substrate and further baking at 60 °C. The photoresist coated slide was then exposed to UV beam for 20 s through the mask. The exposed substrate was developed by placing in KOH solution for 20 s. The patterned slide was then washed in distilled water and blow dried. Gold was deposited on these substrates by electron beam deposition and subsequently washed in IPA to remove the excess followed by washing in distilled water and blow dried by  $\text{N}_2$  gas. Thickness of the electrode was maintained at 80 nm with 5 nm chrome layer and 75 nm gold layer. The fabrication process is demonstrated in SI Figure S1.

### 2.4. Microchannel fabrication

We designed an 8-way radial channels with 100  $\mu\text{m}$  height, 100  $\mu\text{m}$  width and 1 cm length. The master wafer was fabricated using standard photolithography process [25]. The radial devices were then fabricated by using standard soft lithography technology from literature [26]. The inlet and outlet for the channels were made using a 2 mm punch.

### 2.5. Patterning of perm-selective membrane

We patterned a circular nafion film on a 250  $\mu\text{m}$  thick PDMS layer with a 2 mm central hole by stamping method. The radius of the stamp was 2.5 mm. The PDMS film was then heated on a hotplate at 75 °C for 5 min to remove the solvent.

### 2.6. Chip fabrication

The fabricated device was composed of four layers: radial microchannels (top layer), nafion patterned PDMS layer with 2 mm hole (second layer from top), PDMS layer with 3 mm hole interconnecting the sensing layer and the concentration layer (third layer from top) and electrochemical sensor (bottom layer). Two layers from the top acted as the working layer. Nafion in the second layer was patterned in a circular manner of diameter 2.5 mm to enable the concentration in all the 8 microchannels. This design caused the ions to concentrate at the centre of the 8 channels. The 2 mm hole at the centre of the second layer acted as the pathway for the concentrated ions to move towards the electrodes. The diameter of the hole was optimised at 2 mm to minimise the trapping of bubbles in the bottom two layers. The third layer was composed of a PDMS layer with a 3 mm window. The thickness for the second and third layer were maintained as 250  $\mu\text{m}$  each. The bottom layer consisted of 3 electrodes patterned in a circular manner with a total diameter of 2.5 mm.

### 2.7. Electrochemical measurements and data analysis

The electrochemical measurements were performed by an electrochemical workstation at room temperature. Electrochemical measurements were carried out using a three electrode system consisting of bare gold as working and counter electrodes. Silver wire was used as the reference electrode. To monitor the stability of the electrodes, the device was continuously observed using an inverted microscope during the experiment.

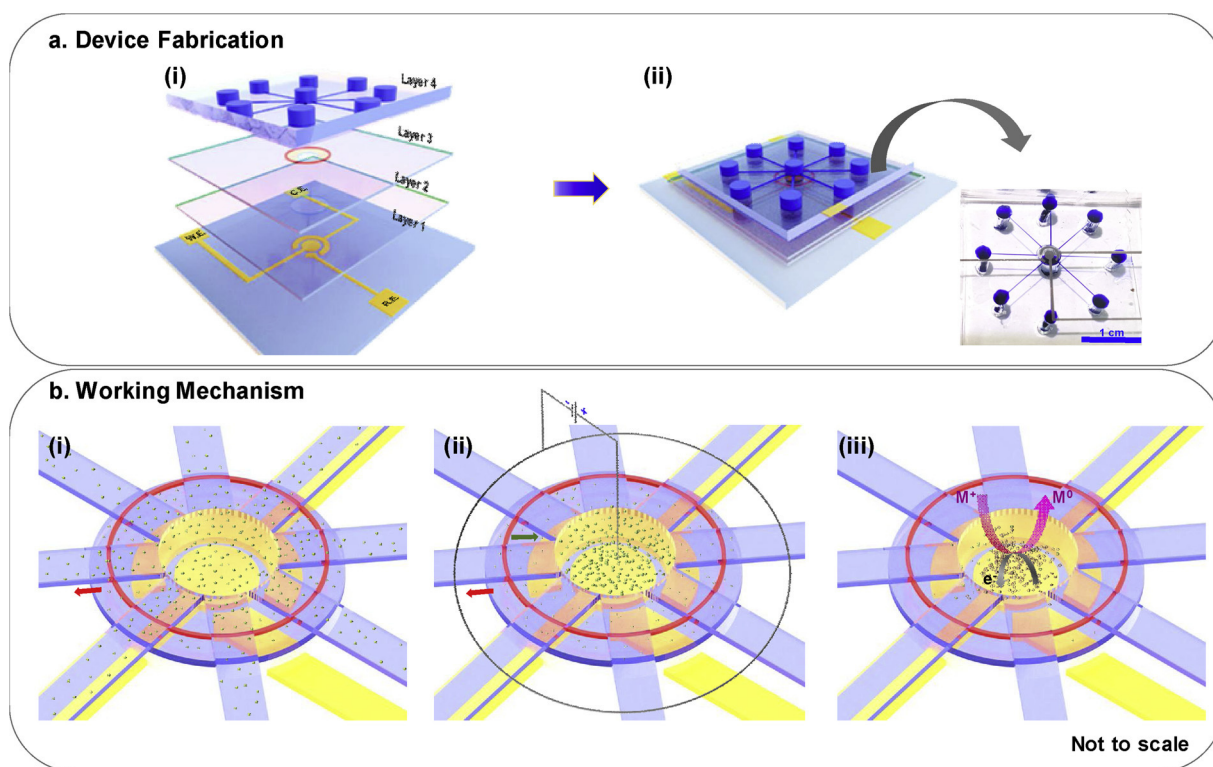


**Fig. 1.** A schematic of the device fabrication protocol and its working mechanism. Panel a shows the device fabrication, (i) representation of the various layers of the device, Layer 1 contains the electrodes, Layer 2 consists of a 3 mm window at the center, Layer 3 contains a 2 mm window at the center along with circularly patterned nafion of 2.5 mm radius and Layer 4 contains the microchannels, (ii) shows the fully fabricated device, inset shows an optical image of the fabricated device (bottom view). Panel b shows the working mechanism of the device. (i) schematic showing the top view of the device, the device is filled with the analyte, outward (red) arrow depicts the direction of flow (ii) represents application of external voltage (anode is placed at the central well and ring electrode at the outer wells) to induce ion concentration, inward (green) arrow shows the direction of ion movement and (iii) upward (magenta) arrow at the center of the radial device depicts the reduction of concentrated ions after ICP.

### 3. Results and discussion

#### 3.1. Characterization of the electrodes and microfluidic device

The optical image of the electrode is given in the inset of SI Figure S2a. The surface morphology of the electrodes was analysed using SEM as represented in SI Figure S2a. SEM images showed that the electrodes have a homogeneous surface. The dimensions of the electrode are given in SI Figure S2b. For the electrochemical characterization of the fabricated electrodes, cyclic voltammetry (CV) of ferro/ferricyanide complex was performed, given in SI Figure S3. We observed reversible redox peaks at the electrolyte - electrode interface confirming that the electrode surface was electroactive. Ion concentration polarization in a radial microfluidic device has already been established [27,28].

#### 3.2. Working mechanism

The experimental steps involved in the fabrication and sensing is depicted in Fig. 1. After fabricating the device, the sample is injected by utilising a commercial pipette tip. The pipette tip was placed at the centre of the radial device and the sample was injected into the microchannels by applying pressure. Volume of the sample present in the microchannels at any given time during the analysis was calculated to be 8  $\mu\text{L}$  while the total volume in the device was  $\sim 40 \mu\text{L}$ . Detailed calculations for analyte volume in the microchannels and the device are given in SI S4. Following this, the measurements were carried out in two steps. The first step involved the application of an external DC voltage to the platinum wire placed in the micropipette tip containing the analyte to induce ICP. This voltage is applied for a stipulated time to induce ion concentration. The next step was to do the voltammetry

measurements. These measurements were initiated 3 s after the externally applied voltage is switched off. The intermediate 3 s acted as the buffer time to minimise the noise due to external applied voltage on the working electrode.

#### 3.3. Working principle

ICP is an electrokinetic phenomenon consisting of dynamic ion concentration changes with ion depletion and ion enrichment across nanochannels/nanopores [19]. Cation exchange membranes such as nafion use sulfone anion ( $\text{R-SO}_3^-$ ) as a fixed charge making it cation selective by nature [20]. When an analyte is flowed in a microchannel connected to a cation selective membrane and a DC electric field is applied, only cations will pass through the micro-nano junction while anions will concentrate on the other side of the membrane. To satisfy the laws of electro-neutrality, an extended space charge (ESC) layer forms adjacent to the electrical double layer [28,29]. By varying the applied voltage, both anions and cations can be pushed towards the anode leading to an ion enriched zone at the cathodic side of the nanochannel and ion depletion zone on the other side [30]. In contrast to the conventional ICP devices, which utilise a buffer channel along with the analyte channel, our devices work on the concept of “a buffer-channel-less radially structured preconcentrator” [28]. The use of a radial configuration enhances throughput, electrokinetic stability and causes local increase in concentration at the centre of the device during ICP. In our device, the anode was placed perpendicular to the electrodes meant for voltammetry. After the ions were concentrated at the anode by ICP, the concentration of the ions was analysed by linear sweep voltammetry.



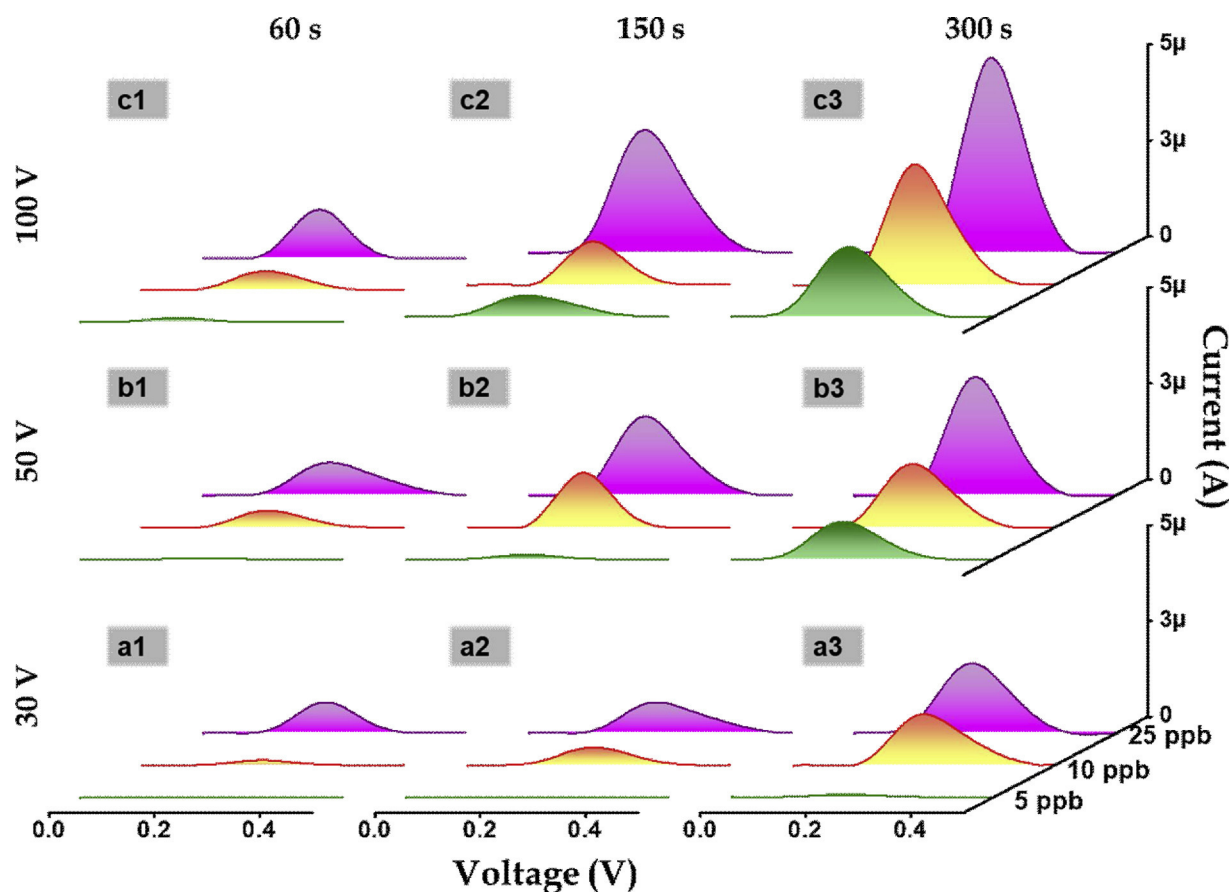


Fig. 2. Electrochemical characterization of  $\text{As}^{3+}$  after ICP. The x-axis represents the voltage applied during voltammetry and the current is plotted in y-axis. Green trace represents 5 ppb of  $\text{As}^{3+}$  in 0.1 M  $\text{H}_2\text{SO}_4$ , while orange and magenta traces are for 10 and 25 ppb, respectively. Voltage applied during ICP is given as a, b and c which stand for 30, 50 and 100 V respectively. Labels 1, 2 and 3 depict the durations for which the voltages were applied, which were 60, 150 and 300 s respectively. For example, a1 represents LSV obtained after applying 30 V for 60 s during ICP.

### 3.4. Ion pre-concentration and detection

The fabricated chip was utilised to concentrate the ions in the sample. To study the concentration effects with varying time and voltage, the pre-concentration was carried out by applying 30, 50 and 100 V in varying durations of 60, 150 and 300 s for 5, 10 and 25 ppb of  $\text{As}^{3+}$  in 0.1 M  $\text{H}_2\text{SO}_4$ . After concentrating, linear sweep voltammetry was utilised for quantitative assessment of analyte concentration. For linear sweep voltammetry, potential for the measurements were optimised from 0 to 5 V, since the oxidation peak of  $\text{As}^{3+}$  in acidic medium is known to be at 0.21 V.

Fig. 2 shows the voltammogram of the concentrated ions. For clearer understanding, the values are tabulated in SI Table 1. It is known that at acidic pH,  $\text{As}^{3+}$  exists as  $\text{H}_3\text{AsO}_3$  which is neutral in charge [31].

The experiment was expected to proceed in two steps, the first step involved a local increase in the concentration of ions in the vicinity of the working electrode caused by ICP. This was followed by the oxidation and reduction of metal ions on the working electrode during LSV as given in eqn. 1 and eqn. 2.

As such, it was expected that the combination of ICP with LSV acts similar to Anodic Stripping Voltammetry (ASV). In ASV, the first step is to apply a controlled potential to deposit the metal ions on the working electrode. This causes the local increase in concentration of analyte by depositing the ions from the larger volume of solution to the electrode. This is then followed by stripping of the electrode for measurements. Major limitation in ASV arises due to the incomplete stripping of the working electrode after deposition, effectively reducing the surface active sites available in the electrode for subsequent measurements

[32]. This limitation was rectified in our device, as during ICP the local increase in concentration of the ions is caused by transferring the ions from the microchannels to the 3 mm well where the electrodes are located without affecting the working electrode during the concentration process and reducing the ion residence time on the electrodes. This results in no or reduced effect on the active sites of the working electrode. For our experiments, the peak value of  $\text{As}^{3+}$  was noted to be  $0.21 \pm 0.02$  V. The shift can be attributed to the deviation in ionic current of the electrolyte as a result of applying potential to the microchannels during ICP. The buffer time between the application of ICP voltage and voltammetry measurements was optimised to 3 s. If the buffer time is lesser, the background current is too high, resulting in increase in noise in the voltammogram. In case its more than 3 s, there is a loss in the ions concentrated by ICP.

There was no peak seen in the absence of ICP. The minimum current obtained for 5 ppb at 30 V was  $3.49 \times 10^{-3} \mu\text{A}$  after concentrating for 60 s. No voltammetric peaks were seen at reduced potential or time. From this it can be understood that 30 V was the voltage required for a stable junction formation at the micro-nano interface. Upper threshold voltage was determined by doing ICP at 100 V up to which we obtained linear increase in voltammetric current. ICP performed with applied voltage of 150 V did not show linearity in concentration which is due to the instability of the junction. Maximum current for 5 ppb was observed during the application of 100 V for 300 s and it was  $1.82 \mu\text{A}$  while the application of 30 V to a 5 ppb solution for the same duration exhibited a current of  $6.02 \times 10^{-2} \mu\text{A}$  showing a 30-fold increase in the current intensity. Measurements for the concentration of 10 ppb and 25 ppb when concentrated for 300 s, at 30 and 100 V, showed a 3-fold enhancement in the current. Except for the minimum concentration of



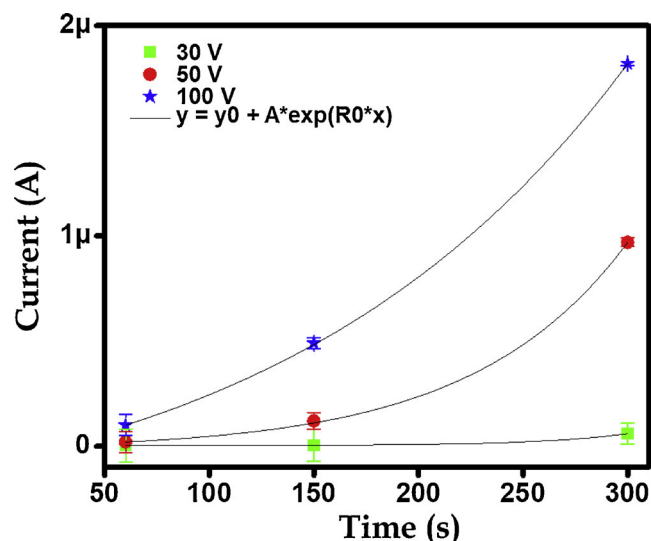


Fig. 3. Variation of the voltammetric signal at the peak voltage (0.21 V) for 5 ppb  $\text{As}^{3+}$  with time at different ICP voltages. The data are fitted with straight lines.

5 ppb, ICP of 10 and 25 ppb showed similar concentration enhancement factors. Applying voltage for a longer time will result in higher concentration of ions at the anode. The maximum time for ICP was kept at 300 s taking into account its possible use as a point of use sensor where shorter analysis time is a major requirement. WHO's provisional guideline for arsenic in drinking water is 0.01 mg/l i.e. 10 ppb, hence, all the experiments were conducted with 5 ppb as lower limit.

From the literature [22,33], it is known that ICP is an ion transport phenomenon caused by the selective passage of ions through ion exchange membranes. Nafion being a cation permeable membrane allows the selective passage of cations restricting the movement of anions. In the presence of an external voltage, the anions are attracted to the anode while to maintain electroneutrality, the cations also move to the anodic side. This leads to the increase in the concentration of ions at the anode which in turn results in the increase in the local ion concentration around the electrodes meant for voltammetry as these electrodes are placed directly below the anode. This results in the better detection, although the samples have lower bulk concentration. Fig. 3 shows the voltammetric signal of  $\text{As}^{3+}$  at the peak voltage (0.21 V) for the input concentration of 5 ppb. A linear increase in the peak current of the voltammetric signal was observed with varying ICP factors of time and voltage. Similar phenomenon was observed for 10 and 25 ppb solutions as given in SI Figure S5. This confirms the usefulness of the approach for quantitative analysis.

The efficiency of the device in sensing other metal ions was also studied. For this, 10 ppb of  $\text{Fe}^{2+}$ ,  $\text{Mn}^{2+}$ ,  $\text{Cu}^{2+}$  and  $\text{Pb}^{2+}$  were added

separately to 0.1 M  $\text{H}_2\text{SO}_4$  and subjected to ICP at 30 V for 60 and 150 s and LSV studies were performed. Fig. 4a depicts the voltammetric peak of  $\text{Fe}^{2+}$  at 0.44 V. The current intensity was 20  $\mu\text{A}$  after concentration for 150 s which was very high as compared to the other ions. The voltammetric peak for oxidation of  $\text{Cu}^{2+}$  was seen at 0.49 V with an intensity of 2  $\mu\text{A}$ , as shown in Fig. 4b. Fig. 4c represents the LSV of  $\text{Mn}^{2+}$ . ICP performed at 30 V for 60 and 150 s both showed a peak at 0.1 V during LSV which corresponds to the oxidation of  $\text{Mn}^{2+}$  on the electrode, while another peak was noted at 0.26 V only in case of 150 s. We speculate that increase in ICP duration increases the local concentration of  $\text{Mn}^{2+}$  leading to the formation of  $\text{MnO}_2$  on the gold electrodes during oxidation following either ECE or disproportionation mechanism [34]. This results in the formation of anisotropic structures on the working electrode and the peak at 0.26 V. The peak at 0.26 V can be attributed to  $\text{Mn}^{4+}$  which forms during the oxidation of  $\text{Mn}^{2+}$  following the disproportionation mechanism. The structures deposited on gold working electrodes are shown in SI Figure S6. The LSV of  $\text{Pb}^{2+}$  is shown in Fig. 4d. The ion  $\text{Pb}^{2+}$  showed an oxidation peak at 0.16 V with an intensity of 0.05  $\mu\text{A}$  which was the least in the cations analysed. The obtained peak positions were confirmed from literature [35,36], to correspond to the respective ions. It was seen that the concentration of these ions were much higher than  $\text{As}^{3+}$ .

This can be attributed to the charge of ions in the electrolyte. At acidic pH, arsenic exists as a neutral species while the other ions measured stay as cations. ICP as an electrokinetic technique is highly influenced by ionic size and charge. Cations with larger charge to size ratios tend to migrate faster than those with smaller ratios, which was seen by the reduced concentration of  $\text{Pb}^{2+}$  as compared to the other cations. The ionic radius of  $\text{Pb}^{2+}$  is 119 pm, larger compared to  $\text{Fe}^{2+}$  (77 pm),  $\text{Cu}^{2+}$  (73 pm) and  $\text{Mn}^{2+}$  (80 pm). The mobility of cations during ICP is much higher compared to that of anions and neutral species and was attributed to a combination of electrophoretic and electroosmotic phenomena. Arsenic being a neutral species, does not exhibit any electrophoretic mobility and hence the concentration of arsenic by ICP was expected to be caused by only electroosmotic mobility [37,38].

To analyse the capability of our device for field applications, 5 ppb of arsenic was spiked in tap water and tested. Fig. 5a shows the LSV of tap water after ICP. ICP was performed by applying 30 V for 60 s, 150 s and 300 s. It was seen that there were no peaks present in the region of interest which depicted the absence of certain ions. In case of synthetic water sample as given in Fig. 5b, a peak was noted at 0.1 V which increased with increase in the duration for which ICP was performed. The shift in the peak position was due to the change in pH of the electrolyte. Subsequent measurements of tap water and synthetic sample by ICP-MS also showed the same results. The ability of the device to perform in field water was confirmed by analysing water sample from arsenic affected region of West Bengal (India) given in Fig. 5c. The sensor depicted a peak at 0.1 V which can be attributed to arsenic at neutral pH [39,40]. ICP-MS analysis of the field sample showed the arsenic

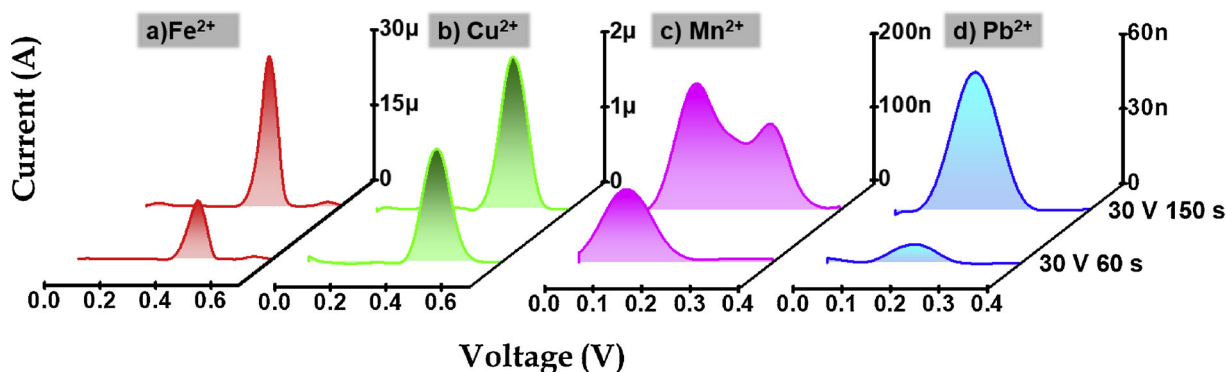


Fig. 4. Electrochemical characterization of 10 ppb of heavy metal ions concentrated at 30 V for 60 and 150 s: a)  $\text{Fe}^{2+}$ , b)  $\text{Cu}^{2+}$ , c)  $\text{Mn}^{2+}$  and d)  $\text{Pb}^{2+}$ .

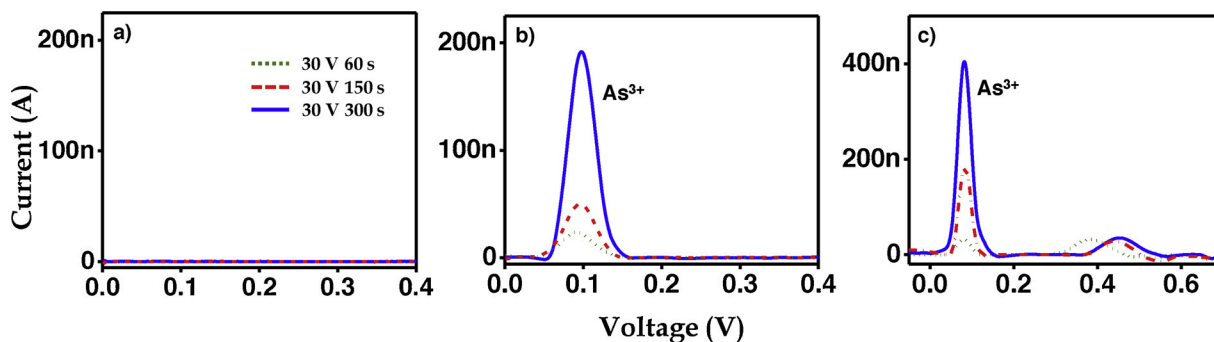


Fig. 5. Electrochemical characterization of a) tap water, b) tap water + 5 ppb  $\text{As}^{3+}$  and c) field water concentrated at 30 V for 60, 150 and 300 s.

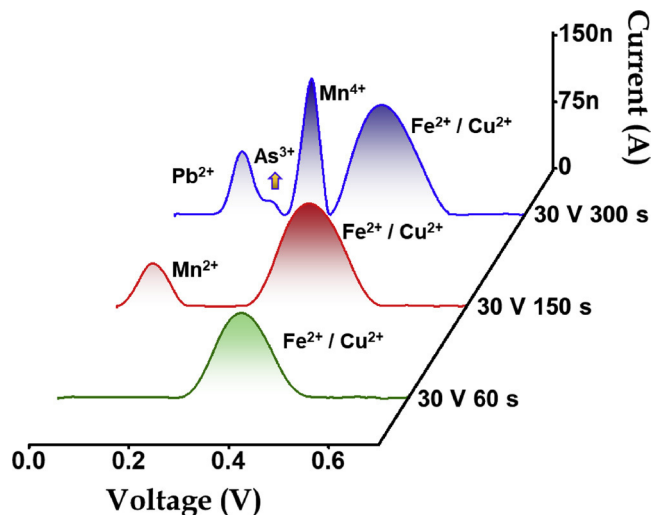


Fig. 6. Electrochemical characterization of 5 ppb of  $\text{Pb}^{2+}$ ,  $\text{As}^{3+}$ ,  $\text{Fe}^{2+}$ ,  $\text{Mn}^{2+}$  and  $\text{Cu}^{2+}$  in 0.1 M  $\text{H}_2\text{SO}_4$ , concentrated at 30 V for 60, 150 and 300 s.

concentration to be about 7 ppb which related to the data previously obtained. Another peak was obtained varying between 0.3 – 0.5 V which was noted to be from  $\text{Fe}^{2+}$ . The working electrode of our sensor was plain gold electrode with no functionalisation to induce specificity. Fig. 6 shows the performance of our sensor when subjected to multiple ions.

Experiment was conducted on a synthetic multi ion solution created by spiking 5 ppb of  $\text{Pb}^{2+}$ ,  $\text{As}^{3+}$ ,  $\text{Fe}^{2+}$ ,  $\text{Mn}^{2+}$  and  $\text{Cu}^{2+}$  in 0.1 M  $\text{H}_2\text{SO}_4$ . Fig. 6 LSV showed the generation of more peaks as the duration of ICP was increased. When 30 V was applied for 60 s (green trace), a single peak was seen at 0.4 V which was expected to be of  $\text{Fe}^{2+}$  or  $\text{Cu}^{2+}$  or a combination of both as both  $\text{Fe}^{2+}$  and  $\text{Cu}^{2+}$  were expected to give

peaks in that range. When continued for another 90 s (red trace), another peak at 0.1 V attributed to  $\text{Mn}^{2+}$  was noted along with the previously observed peak. Increasing the duration to 300 s gave multiple peaks at 0.15, 0.19, 0.26 and 0.45 V which were assigned to  $\text{Pb}^{2+}$ ,  $\text{As}^{3+}$ ,  $\text{Mn}^{4+}$  and  $\text{Fe}^{2+}/\text{Cu}^{2+}$ , respectively based on the results obtained previously. During sensing, it was noted that the ions didn't exhibit similar peak intensity during voltammetry even though the initial concentrations of the ions in the electrolyte were maintained the same. The concentration of the ions was seen to follow the conventions of electrophoretic and electroosmotic mobility. The ion,  $\text{As}^{3+}$  which happens to be neutral at pH 2 exhibits the minimum concentration while the other cations exhibit varying concentrations depending on their ionic radii. This data showed the sensors ability to be used in samples with a combination of ions. To develop a highly specific sensor, the working electrode can be functionalised.

A point of use sensor places high importance on sensitivity and reproducibility. The sensitivity of the sensor for  $\text{As}^{3+}$  was tested by analysing 1 ppb of  $\text{As}^{3+}$  in 0.1 M  $\text{H}_2\text{SO}_4$  as represented in Fig. 7a. Oxidation peak of  $\text{As}^{3+}$  was obtained at 0.23 V with intensity current of 0.05  $\mu\text{A}$  demonstrating good sensitivity. The time taken for sensing 1 ppb of  $\text{As}^{3+}$  was noted to be 600 s with no current being observed at lesser time durations. This reemphasises the conjecture that as the duration for ICP was increased, the number of ions concentrated will increase if there is a continuous flow from the inlet. Continuous injection of the sample in the device along with an increased duration for ICP would probably allow us to extend the LOD further.

The reproducibility of the device was confirmed by utilising three different devices and studying their performance under the same applied conditions of 25 ppb of  $\text{As}^{3+}$  in 0.1 M  $\text{H}_2\text{SO}_4$ , concentrated at 30 V for 300 s. The devices exhibited very high repeatability with oxidation peak at 0.23 V and a slight variation in current intensity ranging from 2.32 to 2.39  $\mu\text{A}$  as shown in Fig. 7b. the reproducibility of the data was within  $\pm 0.08 \mu\text{A}$ . The present technique was also compared to other recently reported studies as given in SI Table 2.

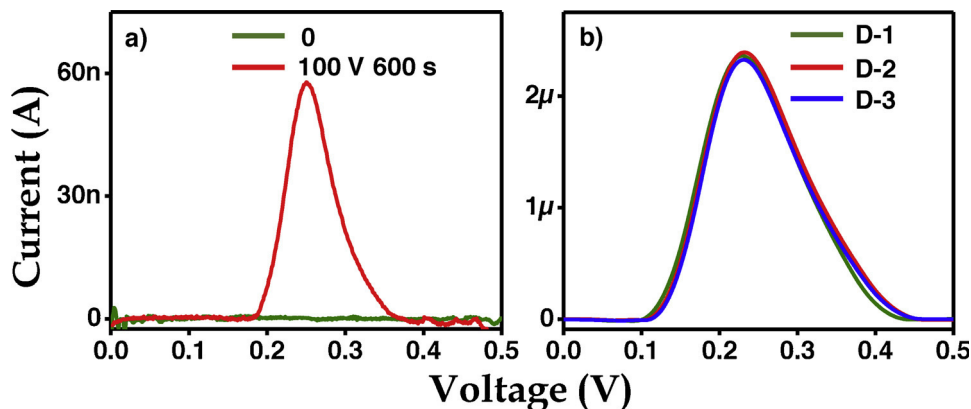


Fig. 7. Electrochemical characterization of a) 1 ppb  $\text{As}^{3+}$  in 0.1 M  $\text{H}_2\text{SO}_4$  b) 25 ppb  $\text{As}^{3+}$  in 0.1 M  $\text{H}_2\text{SO}_4$  concentrated at 30 V for 300 s for three devices.

The fabricated sensor was single use and non-specific in nature owing to the working electrode being only gold. Specificity in a sensor refers to being completely specific to one analyte in its ideal form. Non-specificity in a sensor leads to decrease in the detection sensitivity of the target as there are at times high similarity between analytes [41]. Also, other ions will interact with the surface of the working electrode, reducing the number of sites for the target to react on. Thus, non-specificity of our device presents a serious limitation for it to be applied in the field conditions. This issue can be rectified by the surface functionalisation of the working electrode with materials exhibiting specificity to arsenic such as nanoparticles [42],  $\text{MnO}_2$  [43], enzymes [44], amino acids [45], etc.

#### 4. Conclusion

In this research, we have developed an electrochemical microfluidic sensor with radial microchannels for sensing of arsenite in field water samples. Nanoelectrokinetic pre-concentration by ICP was combined with an electrochemical microfluidic sensor to enable the pre-concentration and detection of the analyte to attain high sensitivity with limited volume of the sample, down to 40  $\mu\text{L}$ . The sensor fabrication was simplified without the use of valves to ensure portability. The sensor showed the capability to detect  $\text{As}^{3+}$  down to 1 ppb. The sensor was also tested for the detection of other metal ions such as  $\text{Cu}^{2+}$ ,  $\text{Fe}^{2+}$ ,  $\text{Mn}^{2+}$  and  $\text{Pb}^{2+}$ . LSV based response of a mixture of the above mentioned ions was also investigated. The voltammogram showed the presence of peaks specific to each ion of the mixture. The performance of the sensor was stable and repeatable. Surface functionalisation of the working electrode of these sensors can make them extremely analyte specific. The device showed promising capability to be developed as a point of use sensor for resource-limited areas by combining it with a portable electrochemical analyser.

#### Declaration of Competing Interest

There are no conflicts of interest to declare.

#### Acknowledgements

We are thankful to the Department of Science and Technology, India, for constantly supporting our research on nanomaterials. The authors are thankful to the Centre for NEMS and Nanophotonics (CNNP), IIT Madras, India for facilitating device fabrication. V.S. is thankful to IIT Madras, India for student fellowship. SJ Kim acknowledged the financial supports from BK21 Plus program of the Creative Engineer Development IT, Seoul National University.

#### Appendix A. Supplementary data

Supplementary material related to this article can be found, in the online version, at doi:<https://doi.org/10.1016/j.snb.2019.127340>.

#### References

- [1] Y.-S. Hong, K.-H. Song, J.-Y. Chung, Health effects of chronic arsenic exposure, *J. Prev. Med. Public Health* 47 (2014) 245–252.
- [2] J.H.T. Luong, E. Lam, K.B. Male, Recent advances in electrochemical detection of arsenic in drinking and ground waters, *Anal. Methods* 6 (2014) 6157–6169.
- [3] D.Q. Hung, O. Nekrasova, R.G. Compton, Analytical methods for inorganic arsenic in water: a review, *Talanta* (2004) 269–277.
- [4] J.R. Behari, R. Prakash, Determination of total arsenic content in water by atomic absorption spectroscopy (AAS) using vapour generation assembly (VGA), *Chemosphere* 63 (2006) 17–21.
- [5] I. Komorowicz, D. Baralkiewicz, Determination of total arsenic and arsenic species in drinking water, surface water, wastewater, and snow from Wielkopolska, Kujawy-Pomerania, and Lower Silesia provinces, Poland, *Environ. Monit. Assess.* 188 (2016) 504.
- [6] D.G. Rackus, M.H. Shamsi, A.R. Wheeler, Electrochemistry, biosensors and microfluidics: a convergence of fields, *Chem. Soc. Rev.* 44 (2015) 5320–5340.
- [7] A. Ainla, M.P.S. Mousavi, M.-N. Tsaloglou, J. Redston, J.G. Bell, M.T. Fernández-Abedul, et al., Open-source potentiostat for wireless electrochemical detection with smartphones, *Anal. Chem.* 90 (2018) 6240–6246.
- [8] A. Nemiroski, D.C. Christodouleas, J.W. Hennek, A.A. Kumar, E.J. Maxwell, M.T. Fernández-Abedul, et al., Universal mobile electrochemical detector designed for use in resource-limited applications, *Proc. Natl. Acad. Sci. U. S. A.* 111 (2014) 11984.
- [9] A.C. Sun, C. Yao, A.G. Venkatesh, D.A. Hall, An efficient power harvesting mobile phone-based electrochemical biosensor for point-of-care health monitoring, *Sens. Actuators B, Chem.* 235 (2016) 126–135.
- [10] S. Li, C. Zhang, S. Wang, Q. Liu, H. Feng, X. Ma, et al., Electrochemical microfluidics techniques for heavy metal ion detection, *Analyst* 143 (2018) 4230–4246.
- [11] D.R. Reyes, D. Iossifidis, P.-A. Auroux, A. Manz, Micro total analysis systems. 1. Introduction, theory, and technology, *Anal. Chem.* 74 (2002) 2623–2636.
- [12] C.T. Culbertson, T.G. Mickleburgh, S.A. Stewart-James, K.A. Sellens, M. Pressnall, Micro total analysis systems: fundamental advances and biological applications, *Anal. Chem.* 86 (2014) 95–118.
- [13] W.-L. Hsu, D.W. Inglis, M.A. Startsev, E.M. Goldys, M.R. Davidson, D.J.E. Harvie, Isoelectric focusing in a silica nanofluidic channel: effects of electromigration and electroosmosis, *Anal. Chem.* 86 (2014) 8711–8718.
- [14] M. Solsona, E.Y. Westerbeek, J.G. Bomer, W. Olthuis, A. van den Berg, Gradient in the electric field for particle position detection in microfluidic channels, *Lab Chip* 19 (2019) 1054–1059.
- [15] J. Dai, T. Ito, L. Sun, R.M. Crooks, Electrokinetic trapping and concentration enrichment of DNA in a microfluidic channel, *J. Am. Chem. Soc.* 125 (2003) 13026–13027.
- [16] T. Salafi, K.K. Zeming, Y. Zhang, Advancements in microfluidics for nanoparticle separation, *Lab Chip* 17 (2017) 11–33.
- [17] C. Zhao, Z. Ge, C. Yang, Microfluidic techniques for analytes concentration, *Micromachines* 8 (2017) 28.
- [18] Y. Kang, D. Li, Electrokinetic motion of particles and cells in microchannels, *Microfluid. Nanofluidics* 6 (2009) 431–460.
- [19] Q. Pu, J. Yun, H. Temkin, S. Liu, Ion-enrichment and ion-depletion effect of nanochannel structures, *Nano Lett.* 4 (2004) 1099–1103.
- [20] Z. Slouka, S. Senapati, H.-C. Chang, Microfluidic systems with ion-selective membranes, *Annu. Rev. Anal. Chem.* 7 (2014) 317–335.
- [21] S.J. Kim, Y.-A. Song, J. Han, Nanofluidic concentration devices for biomolecules utilizing ion concentration polarization: theory, fabrication, and applications, *Chem. Soc. Rev.* 39 (2010) 912–922.
- [22] S.Y. Son, S. Lee, H. Lee, S.J. Kim, Engineered nanofluidic preconcentration devices by ion concentration polarization, *Biochip J.* 10 (2016) 251–261.
- [23] H. Lee, J. Choi, E. Jeong, S. Baek, H.C. Kim, J.-H. Chae, et al., dCas9-mediated nanoelectrokinetic direct detection of target gene for liquid biopsy, *Nano Lett.* 18 (2018) 7642–7650.
- [24] W. Ouyang, X. Ye, Z. Li, J. Han, Deciphering ion concentration polarization-based electrokinetic molecular concentration at the micro-nanofluidic interface: theoretical limits and scaling laws, *Nanoscale* 10 (2018) 15187–15194.
- [25] M. Kim, M. Jia, T. Kim, Ion concentration polarization in a single and open microchannel induced by a surface-patterned perm-selective film, *Analyst* 138 (2013) 1370–1378.
- [26] Y. Xia, G.M. Whitesides, Soft lithography, *Ann. Rev. Mater. Sci.* 28 (1998) 153–184.
- [27] S. Lee, S. Park, N.L. Jeon, S.J. Kim, Nanoelectrokinetic radial preconcentrator/extractor based on ion concentration polarization, 2017 IEEE 30th International Conference on Micro Electro Mechanical Systems (MEMS), IEEE (2017) 1285–1288.
- [28] S. Lee, S. Park, W. Kim, S. Moon, H.-Y. Kim, H. Lee, et al., Nanoelectrokinetic bufferchannel-less radial preconcentrator and online extractor by tunable ion depletion layer, *Biomicrofluidics* 13 (2019) 034113.
- [29] C.L. Druzgalski, M.B. Andersen, A. Mani, Direct numerical simulation of electro-convective instability and hydrodynamic chaos near an ion-selective surface, *Phys. Fluids* 25 (2013) 110804.
- [30] S.A. Hong, Y.-J. Kim, S.J. Kim, S. Yang, Electrochemical detection of methylated DNA on a microfluidic chip with nanoelectrokinetic pre-concentration, *Biosens. Bioelectron.* 107 (2018) 103–110.
- [31] W.R. Cullen, K.J. Reimer, Arsenic speciation in the environment, *Chem. Rev.* 89 (1989) 713–764.
- [32] M.E. Hyde, C.E. Banks, R.G. Compton, Anodic stripping voltammetry: an AFM study of some problems and limitations, *Electroanalysis* 16 (2004) 345–354.
- [33] H. Jeon, H. Lee, K.H. Kang, G. Lim, Ion concentration polarization-based continuous separation device using electrical repulsion in the depletion region, *Sci. Rep.* 3 (2013) 3483.
- [34] A. Manivel, N. Ilayaraja, D. Velayutham, M. Noel, Medium effects on the electro-deposition of  $\text{MnO}_2$  on glassy carbon electrode: a comparative study in alkane, perfluoro alkane carboxylic acids and methanesulphonic acid, *Electrochim. Acta* 52 (2007) 7841–7848.
- [35] G.W. Tindall, S. Bruckenstein, A ring-disk electrode study of the electrochemical reduction of copper(II) in 0.2M sulfuric acid on platinum, *Anal. Chem.* 40 (1968) 1051–1054.
- [36] P. Vanýsek, CRC Handbook of Chemistry and Physics, 91 edition, CRC Press, 2010.
- [37] D. Yan, C. Yang, N.-T. Nguyen, X. Huang, Electrokinetic flow in Microchannels with finite reservoir size effects, *J. Phys. Conf. Ser.* 34 (2006) 385–392.
- [38] J.G. Santiago, Electroosmotic flows in Microchannels with finite inertial and pressure forces, *Anal. Chem.* 73 (2001) 2353–2365.
- [39] D. Yamada, T.A. Ivandini, M. Komatsu, A. Fujishima, Y. Einaga, Anodic stripping voltammetry of inorganic species of  $\text{As}^{3+}$  and  $\text{As}^{5+}$  at gold-modified boron doped diamond electrodes, *J. Electroanal. Chem.* 615 (2008) 145–153.
- [40] A.D. Robles, S.N. Vettorelo, M. Gerpe, F. Garay, The electrochemical reaction

- mechanism of arsenic on gold analyzed by anodic stripping Square-wave voltammetry, *Electrochim. Acta* 227 (2017) 447–454.
- [41] W.J. Peveler, M. Yazdani, V.M. Rotello, Selectivity and specificity: pros and cons in sensing, *ACS Sens.* 1 (2016) 1282–1285.
- [42] N. Moghimi, M. Mohapatra, K.T. Leung, Bimetallic nanoparticles for arsenic detection, *Anal. Chem.* 87 (2015) 5546–5552.
- [43] S. Zhou, X. Han, H. Fan, Y. Liu, Electrochemical sensing toward trace As(III) based on mesoporous  $\text{MnFe}_2\text{O}_4/\text{Au}$  hybrid nanospheres modified glass carbon electrode, *Sens. Basel (Basel)* 16 (2016) 935.
- [44] M. Park, S.-L. Tsai, W. Chen, Microbial biosensors: engineered microorganisms as the sensing machinery, *Sens. Basel (Basel)* 13 (2013) 5777–5795.
- [45] T. Yang, X.-X. Zhang, J.-Y. Yang, Y.-T. Wang, M.-L. Chen, Screening arsenic(III)-binding peptide for colorimetric detection of arsenic(III) based on the peptide induced aggregation of gold nanoparticles, *Talanta* 177 (2018) 212–216.

# SUPPLEMENTARY INFORMATION

## Enhancing the Sensitivity of Point-of-Use Electrochemical Microfluidic Sensors by Ion Concentration Polarisation - A Case Study on Arsenic

Vidhya Subramanian<sup>a,b</sup>, Lee Sangjun<sup>c</sup>, Sanjoy Jena<sup>d</sup>, Sourav Kanti Jana<sup>a</sup>, Debdutta  
Ray<sup>d</sup>, Sung Jae Kim<sup>c</sup> and Thalappil Pradeep<sup>\*a</sup>

<sup>a</sup>DST Unit on Nanoscience and Thematic Unit of Excellence (TUE), Department of Chemistry, Indian Institute of Technology, Madras, Chennai 600 036, India

<sup>b</sup>Department of Biotechnology, Indian Institute of Technology, Madras, Chennai 600 036, India

<sup>c</sup>Department of Electrical and Computer Engineering, Seoul National University, Seoul 08826, Korea

<sup>d</sup>Department of Electrical Engineering, Indian Institute of Technology, Madras, Chennai 600 036, India

E-mail: [pradeep@iitm.ac.in](mailto:pradeep@iitm.ac.in)

### Contents

Schematic for the fabrication of electrodes and microfluidic device	S1
SEM image of the electrodes and its optical image	S2
Electrochemical characterization of the gold electrode	S3
Calculations for volume in microchannel and microfluidic device	S4
Table for electrochemical characterization of As <sup>3+</sup>	Table 1
Variation of the voltammetric signal at the peak voltage (0.21 V) for a) 10 ppb and b) 25 ppb of As <sup>3+</sup> with time at different ICP voltages.	S5
SEM image of Mn <sup>2+</sup> deposition on gold electrode	S6
Table comparing parameters between different studies for As <sup>3+</sup> detection	Table 2

## S-1. Supplementary Information 1

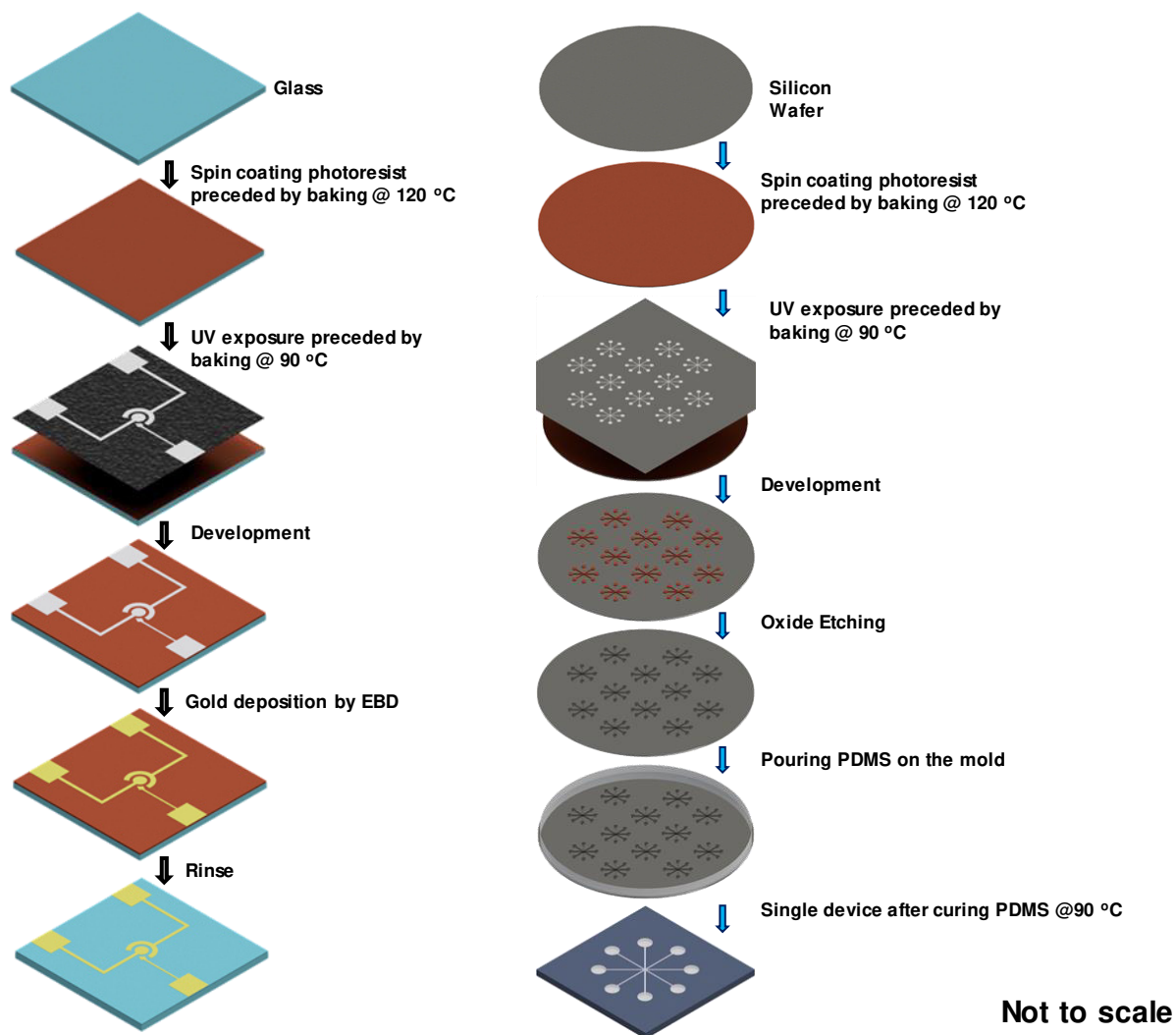


**Figure S1.** Schematic for the fabrication of electrodes (left) and microfluidic device (right).



## S-2. Supplementary Information 2

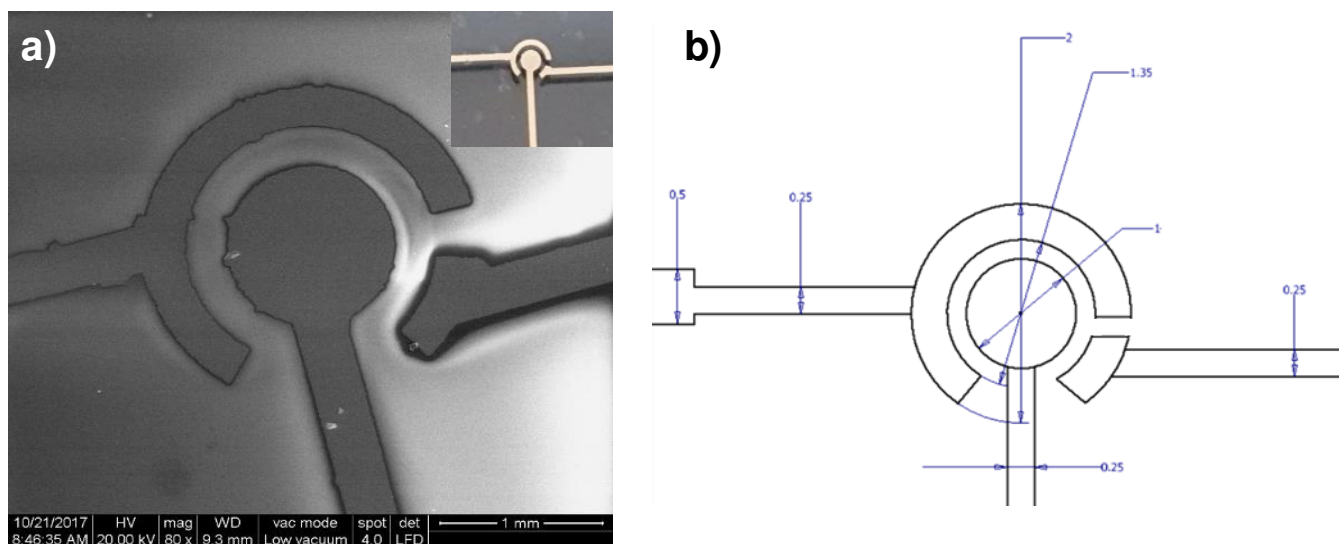


**Figure S2.** a) SEM image of the electrodes and inset shows its optical image and

b) Schematic of the electrode with dimensions. All dimensions are in mm.



### S-3. Supplementary Information 3

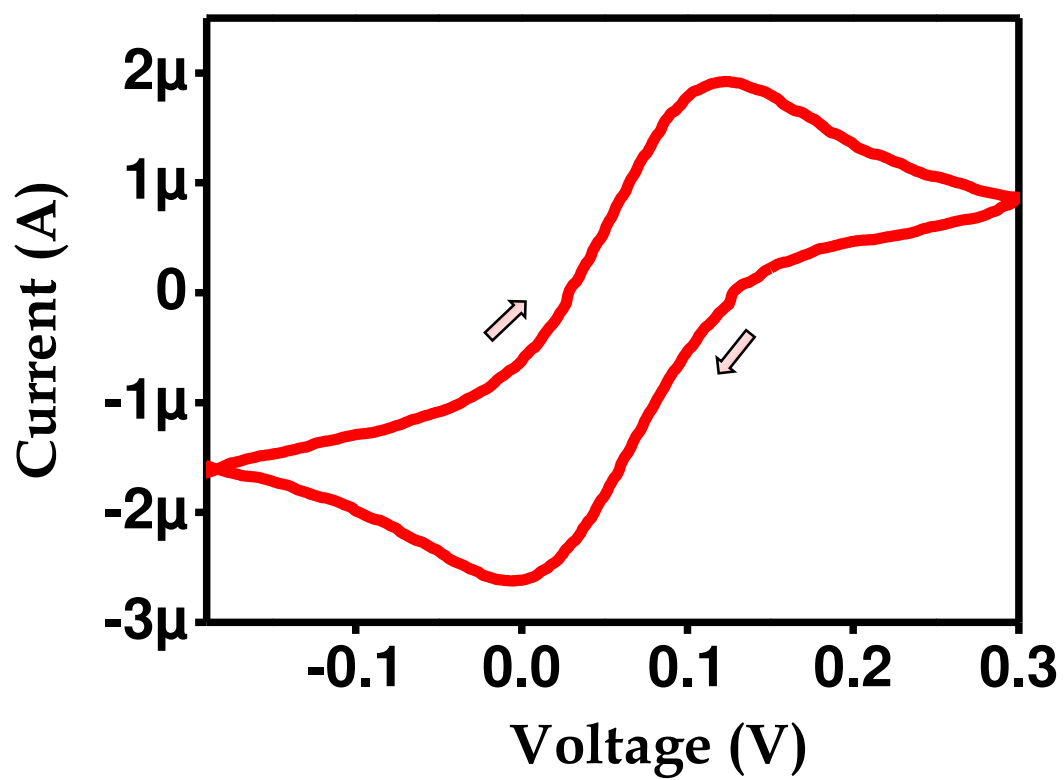


**Figure S3.** Cyclic voltammetry of 2 mM ferro/ferricyanide complex using the fabricated Au electrode.

#### Supplementary Information – S -4

Calculations for volume in microchannel and microfluidic device

Microchannel height, width and length are 100  $\mu\text{m}$ , 100  $\mu\text{m}$  and 1 cm respectively.

Volume of a cuboid / 1 microchannel = (l x b x h)

Volume of radial (8) microchannels =  $8(0.1 \times 0.1 \times 10) \text{ mm}^3$

$$= 0.8 \text{ mm}^3 = 8 \mu\text{L}$$

The outlet of each channel has a radius of 1 mm and height 1 mm. Considering it as a cylinder,

Volume of a cylinder / 1 outlet =  $\pi r^2 h$

Volume of 8 outlets =  $8 (3.14 \times 1 \times 1) \text{ mm}^3$

$$= 25.12 \text{ mm}^3 = 25.12 \mu\text{L}$$

The inlet has a radius of 1 mm and is connected to a 10  $\mu\text{L}$  pipette containing ~5  $\mu\text{L}$  solution to provide electrical connection.

The electrodes are placed inside 2 layers of PDMS, one with radius of 1.5 mm and the other with radius of 1 mm, both are of 250  $\mu\text{m}$  height.

Volume of solution above the electrode =  $(3.14 \times 1.5^2 \times 0.25) + (3.14 \times 1^2 \times 0.25)$

$$= 2.6 \text{ mm}^3 = 2.6 \mu\text{L}$$

Total volume of sample in radial microchannels = 8  $\mu\text{L}$

Total volume of sample in device =  $8 + 25.12 + 5 + 2.6 \mu\text{L}$

$$= 40.72 \mu\text{L}$$

## Supplementary Information

Concentration (ppb)	Current (μA)			
	Voltage (V) Time (s)	30	50	100
5	60	$3.49 \times 10^{-3}$	0.02	0.10
	150	$5.18 \times 10^{-3}$	0.12	0.49
	300	$6.02 \times 10^{-2}$	0.97	1.82
10	60	0.12	0.43	0.55
	150	0.45	1.41	1.11
	300	1.33	1.63	3.11
25	60	0.79	0.86	1.25
	150	0.81	2.05	3.18
	300	1.81	3.09	5.08

**Table 1.** Tabular column representing the data of electrochemical characterization of  $\text{As}^{3+}$  for different concentrations, potentials and durations.

## S-5 Supplementary Information 5

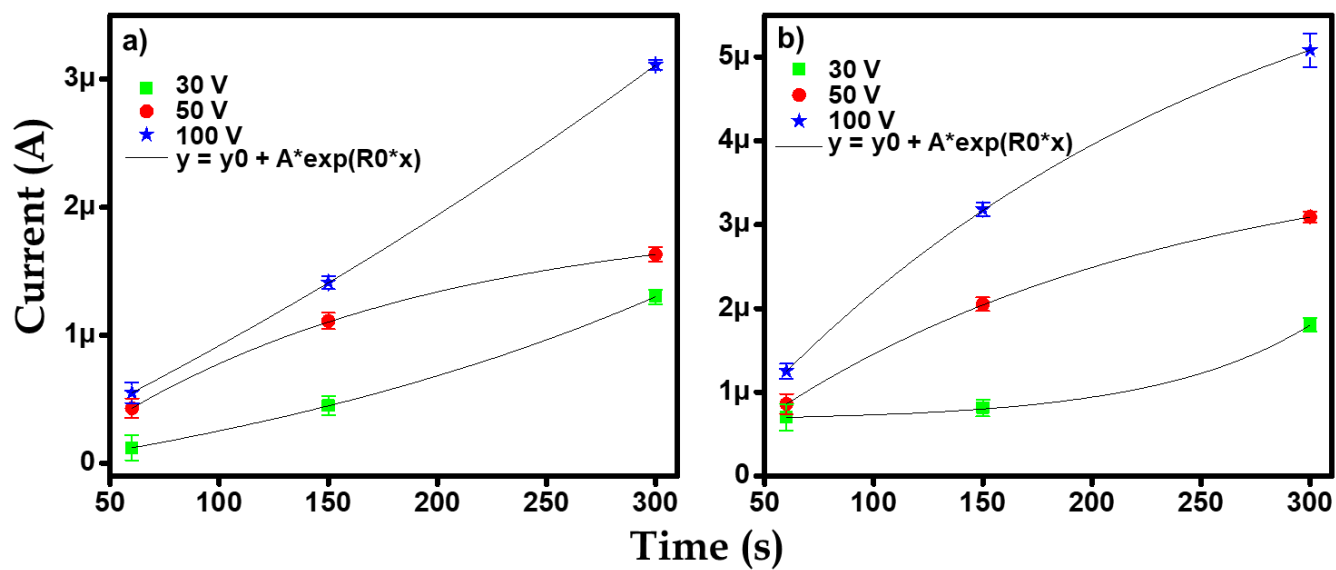


**Figure S5.** Variation of the voltammetric signal at the peak voltage (0.21 V) for a) 10 ppb and b) 25 ppb of  $\text{As}^{3+}$  with time at different ICP voltages. The data are fitted with straight lines.

**S-6 Supplementary Information 6**

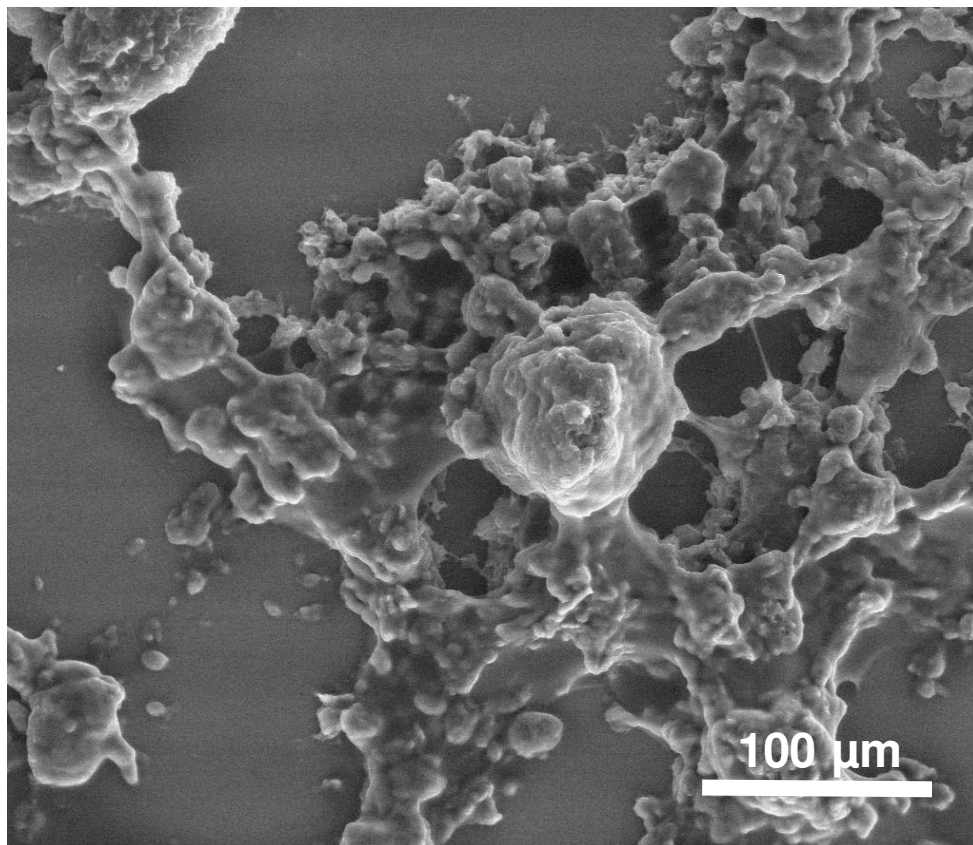


**Figure S6.** SEM image of Mn<sup>2+</sup> deposition on gold electrode after ICP at 30 V for 150 s.

## Supplementary Information

Electrode	Electrolyte	Technique/ Deposition time (s)	Experimental LOD (ppb)	Ref
ZrO <sub>2</sub> /Nafion/Au electrode	PBS	CV	5	1
Au/Fe <sub>3</sub> O <sub>4</sub> modified screen printed carbon electrode	0.1 M HAc- NaAc	SWASV/120 s	0.1	2
NH <sub>2</sub> -GO modified Au μelectrode	PBS	SWASV/ 150 s	4.113	3
AuNPs/CeO <sub>2</sub> -ZrO <sub>2</sub> /GCE	0.1 M HAc- NaAc	SWASV/ 150 s	0.5	4
FePt NP coated Si (100) substrate	PBS	SWASV/ 60 s	0.8	5
Au NPs on Boron Doped Diamond electrode	Phosphate buffer	ASV/ 300 s	1	6
Glutathione, dithiothreitol and <i>N</i> -acetyl-L-cysteine on gold electrode	HCl	LSV /150 s	0.5	7
Tin oxide nano needles on graphite pencil electrode	Water	CV	10	8
Fe-Chitosan coated Carbon electrode	Mining wastewater	SWASV/ 180 s	1.12	9
Au electrode	H <sub>2</sub> SO <sub>4</sub> / Water	Microfluidics + LSV	1 / 7	This work

**Table 2.** Comparison of performance parameters between different studies for the detection of As<sup>3+</sup>


## REFERENCES

1. G. Bhanjana, N. Dilbaghi, S. Chaudhary, K.-H. Kim and S. Kumar, *Analyst*, 2016, **141**, 4211-4218.
2. S.-S. Li, W.-Y. Zhou, M. Jiang, Z. Guo, J.-H. Liu, L. Zhang and X.-J. Huang, *Analytical Chemistry*, 2018, **90**, 4569-4577.
3. M. Yang, T.-J. Jiang, Y. Wang, J.-H. Liu, L.-N. Li, X. Chen and X.-J. Huang, *Sensors and Actuators B: Chemical*, 2017, **245**, 230-237.
4. M. Yang, P.-H. Li, W.-H. Xu, Y. Wei, L.-N. Li, Y.-Y. Huang, Y.-F. Sun, X. Chen, J.-H. Liu and X.-J. Huang, *Sensors and Actuators B: Chemical*, 2018, **255**, 226-234.
5. N. Moghimi, M. Mohapatra and K. T. Leung, *Analytical Chemistry*, 2015, **87**, 5546-5552.
6. L. Rassaei, M. Sillanpää, R. W. French, R. G. Compton and F. Marken, *Electroanalysis*, 2008, **20**, 1286-1292.
7. L. Chen, N. Zhou, J. Li, Z. Chen, C. Liao and J. Chen, *Analyst*, 2011, **136**, 4526-4532.
8. G. Bhanjana, N. Mehta, G. R. Chaudhary, N. Dilbaghi, K.-H. Kim and S. Kumar, *Journal of Molecular Liquids*, 2018, **264**, 198-204.
9. J.-H. Hwang, P. Pathak, X. Wang, K. L. Rodriguez, J. Park, H. J. Cho and W. H. Lee, *Sensors and Actuators B: Chemical*, 2019, **294**, 89-97.



Cite this: *Analyst*, 2019, **144**, 7412

# Ambient electrospray deposition Raman spectroscopy (AESD RS) using soft landed preformed silver nanoparticles for rapid and sensitive analysis†

Tripti Ahuja,‡ Atanu Ghosh,‡ Sandip Mondal, Pallab Basuri, Shantha Kumar Jenifer, Pillalamarri Srikrishnarka, Jyoti Sarita Mohanty, Sandeep Bose and Thalappil Pradeep  \*

We introduce a technique called ambient electrospray deposition Raman spectroscopy (AESD RS) for rapid and sensitive surface-enhanced Raman scattering (SERS) based detection of analytes using a miniature Raman spectrometer. Using electrospray, soft landing of preformed silver nanoparticles (AgNPs) was performed for 30–40 seconds for different concentrations of analytes deposited on conducting glass slides. Using AESD RS, SERS signals were collected within 4–6 minutes, including sample preparation. Transmission electron microscopy (TEM) and dark-field microscopy (DFM) were used to characterize the preformed AgNPs before and after electrospray. We achieved the nanomolar and micromolar detection of *p*-mercaptobenzoic acid (*p*-MBA) and 2,4-dinitrotoluene (2,4-DNT), respectively. In this work, 0.3 µL of preformed AgNPs were used, which is ~33 times less in volume than the quantity needed for conventional SERS. Quantitation of unknown concentration of analytes was also possible. A similar amount of electrosprayed AgNPs was utilized to characterize *Escherichia coli* (*E. coli*) bacteria of different concentrations. Viability of bacteria was tested using fluorescence microscopic imaging. Besides reduced analysis time and improved reproducibility of the data in every analysis, which is generally difficult in SERS, the amount of AgNPs required is an order of magnitude lower in this method. This method could also be used to probe the real-time changes in molecular and biological species under ambient conditions.

Received 2nd September 2019,

Accepted 14th October 2019

DOI: 10.1039/c9an01700c

rsc.li/analyst

## Introduction

Surface-enhanced Raman spectroscopy (SERS) is used widely as a powerful tool for sensitive detection of surface adsorbed species.<sup>1–5</sup> It has also been used to probe molecular orientations over nanoparticle surfaces.<sup>6–8</sup> Numerous analytical applications in different fields including electrochemistry, catalysis, biology, medicine, art conservation and materials science have been reported using SERS because of the rich

vibrational spectroscopic information it provides.<sup>9–11</sup> It has also extended applications in the field of sensors such as chemosensors, biosensors, *etc.*<sup>12–14</sup> Silver nanoparticles (AgNPs) are well known SERS substrates used for analyzing chemical and biological systems. They are easy to synthesize, have a high surface area to volume ratio, and possess excellent plasmonic properties. Raman scattering using AgNPs is useful in chemical sensing and catalysis, as in the catalytic reduction of *p*-nitro thiophenol (*p*-NTP) to *p*-amino thiophenol (*p*-ATP).<sup>15,16</sup> However, the toxicity of AgNPs has been a hindrance for their efficient use in biological studies. They affect bacterial cells by disrupting the cell membrane and consequently, the cellular functions by causing oxidative damage.<sup>17,18</sup> Limiting the exposure time of AgNPs can reduce their toxic effects and minimizing their amount used for analysis is a small step toward lessening the impact of AgNPs on the environment.<sup>19</sup> This is particularly important as AgNPs are one of the most marketed nanoparticles (NPs) worldwide.<sup>20</sup>

Conventional SERS substrates are fabricated by three usual methods: (i) mixing plasmonic NPs with a dilute solution of analytes, (ii) spin/drop-casting of analyte solution on a solid/

DST Unit of NanoScience (DST UNS) and Thematic Unit of Excellence (TUE), Department of Chemistry, Indian Institute of Technology Madras, Chennai 600 036, India. E-mail: pradeep@iitm.ac.in; Tel: +91044-2257-4208

†Electronic supplementary information (ESI) available: Optical photograph of the actual AESD RS set-up, characterization of the as-synthesized AgNPs by UV-Vis and DFM, comparative plot between conventional SERS and AESD RS signals, tables showing error bar calculations of calibration curves of *p*-MBA and 2,4-DNT, band assignment tables of SERS features of *p*-MBA and *E. coli*, 'replica plating' of ITO slide dropcast with *E. coli*, viability test of bacteria using fluorescence microscopic imaging and enhancement factor calculations. See DOI: 10.1039/c9an01700c

‡These authors contributed equally to this work.

dried film of NPs, and (iii) incubating particles with a dilute solution of analytes for a period of time for better adsorption.<sup>21,22</sup> In these approaches, the preferred adsorption of NPs at specific sites do not happen efficiently within a short period. However, there are other ways of preparing SERS substrates using templated nanostructures on surfaces which are stable, reproducible and convenient to handle.<sup>23,24</sup> These substrates have mastered the technology of engineering hotspots that result in high SERS enhancement factors and extraordinary signal uniformities over large sampling areas.<sup>25–27</sup> But their fabrication procedures have rendered them considerably more expensive and uncommon. An alternative approach for the preparation of SERS substrates is possible by ambient electrospray deposition (AESD).<sup>28–30</sup> Ambient electrospray is a process of producing charged micro or nano-droplets by applying direct current (DC) voltages of the order of a few kilovolts (kV) on liquids confined in a micro-capillary, while soft landing is a process where polyatomic ions are deposited directly onto a specified location of the surface at near-zero kinetic energy.<sup>29,30</sup> Previously reported results have shown the synthesis of plasmonic NPs using AESD.<sup>31–33</sup> A combination of ambient electrospray and soft landing can produce a uniform distribution of localized NPs on conducting surfaces.<sup>30</sup> Localization of NPs can limit the effective area for SERS examination, but better enhancement of signals can be achieved. Tremendous efforts have been made to obtain efficient SERS substrates by modifying the nanoparticle surfaces. This has enhanced their utility in various analytical applications.<sup>33,34</sup> In this regard, AESD of preformed AgNPs can be used as a promising technique to prepare SERS substrates for the rapid detection of analytes with a good enhancement factor. In this approach, a stream of electrosprayed droplets composed of AgNPs was sprayed on the dropcast film of an analyte and SERS spectra were recorded from the opposite side of the support.

Here, we report the rapid SERS detection of *p*-mercaptobenzoic acid (*p*-MBA – a Raman tag), 2,4-dinitrotoluene (2,4-DNT – an explosive organic compound) and *Escherichia coli* (*E. coli* – a biological analyte) by AESD of preformed citrate-capped AgNPs. For this, we introduce the AESD RS technique where ambient electrospray deposition was coupled with a miniature Raman spectrometer. This technique helped us in reducing the exposure time and the amount of AgNPs used for SERS analysis. Nanomolar and micromolar concentrations of *p*-MBA and 2,4-DNT, respectively, were detected with a small volume of sprayed AgNPs (0.3  $\mu$ L) in shorter durations (30–40 s). Complete SERS measurements were performed within 4–6 minutes, starting from the sample preparation to data acquisition. Calibration curves were plotted for *p*-MBA as well as for 2,4-DNT. A linear correlation between SERS signals versus the logarithm of concentration was observed which could be used for the quantitation of unknown analytes, within the uncertainties in intensity measurements. We have also shown the capability of the AESD RS technique to detect *E. coli* at its lowest concentration limit of  $10^2$  CFU  $\text{mL}^{-1}$  and performed live dead imaging of bacteria to show their viability after electrospray deposition (ESD).

## Experimental methods and materials

### Materials

Trisodium citrate (>99%) was purchased from Merck Life Science Private Limited. Silver nitrate (99.9%) from RANKEM, India. *p*-MBA and 2,4-DNT were purchased from Sigma Aldrich. Luria Bertani (LB) broth and growth media were obtained from HiMedia. *E. coli* (MTCC 443) was obtained from Microbial Type Culture Collection and Gene Bank. A LIVE/DEAD BacLight™ bacterial viability kit was purchased from Molecular Probes, Eugene, OR. Other reagents were of analytical grade and used without any further purification or treatment. Deionized water (DI) ( $\sim 18.2$  M $\Omega$ ) obtained from Milli-Q® was used throughout the experiments.

### Synthesis of AgNPs

Citrate-capped silver sols were prepared using the modified Turkevich method,<sup>35</sup> wherein 17 mg of AgNO<sub>3</sub> was dissolved in 100 mL of DI H<sub>2</sub>O, and the solution was heated to 100 °C. A solution of 1% sodium citrate (4 mL) was added dropwise to the boiling solution. The solution was kept boiling for 10–15 min until it became pale yellow. This colored solution was allowed to cool to room temperature and was finally stored in the dark at 4 °C. The prepared sols were diluted with DI water (1 : 1) for electrospray SERS measurements.

### Sample preparation and SERS measurements

SERS sample preparation was done by drop-casting analyte solution (40  $\mu$ L) on the conductive surface of a clean indium tin oxide (ITO), in a controlled manner (2  $\mu$ L solution spotted every 2 s, 20 times at the same spot) such that the analyte solution spreads equally in all directions. However, after drying, it forms a ring. Four spots near the periphery of the ring (Fig. S2†) were selected and used for AESD. Spots more than 4 were not used to prevent interference between AgNPs electrosprayed at these spots. Diluted concentrations of analyte were made from a stock concentration by dissolving 5 mg of a compound (*p*-MBA and 2,4-DNT) in 1 mL of ethanol. Signals were collected instantly after electrospraying preformed AgNPs for 30–40 s based on the analyte concentration. We have monitored 2 samples of each concentration, with 3 spectra each from 4 different locations of the sample. A total of 24 spectra (2 samples  $\times$  4 locations  $\times$  3 spectra) was averaged, plotted and used for statistical variance calculations. Note that no Raman signals were obtained from the analytes at such concentrations dropcast onto ITO glass slides, without AgNPs.

### Preparation of bacterial samples

For this study, *E. coli* cells were grown overnight in LB broth at 37 °C and 220 rpm in an orbital shaker. The cells were then diluted to a concentration of  $8 \times 10^8$  CFU  $\text{mL}^{-1}$  in LB ( $\text{OD}_{600} = 0.1$ ). The cells were separated from the media by centrifugation at 3000 rpm for 5 min. The pellet was washed twice with DI water by centrifugation. Other dilutions ( $10^2$ – $10^5$  CFU  $\text{mL}^{-1}$ ) of bacteria samples were prepared similarly to  $\sim 10^8$  CFU  $\text{mL}^{-1}$  concentration. For fluorescence microscopic analysis, 40  $\mu$ L of

the bacterial sample was dropcast onto cleaned ITO glass slides and 20  $\mu\text{L}$  of propidium iodide-SYTO 9 mix (1 : 1) was loaded on top of the sample. The mixture was sealed with a 0.145 mm thick cleaned coverslip (Schott) and incubated in the dark for 5 min.

### Instrumentation

UV-Visible spectroscopic measurements were performed using a PerkinElmer Lambda 25 spectrophotometer in the range of 200–1100 nm. Transmission electron microscopic (TEM) measurements were performed using a JEOL 3010, 300 kV instrument. As-synthesized AgNPs were spotted on a carbon-coated copper grid by drop-casting followed by air drying. For an electrosprayed sample, the copper grid was placed near the silica capillary tip and preformed AgNPs were sprayed for 40 s on a grid followed by air drying. Confocal Raman imaging experiments were performed using WITec alpha300 S equipment. Frequency-doubled Nd:YAG laser (532 nm) with a maximum output power of 20 mW was used for the excitation of the sample. For dark-field imaging, an attachment was designed to use a CytoViva<sup>TM</sup> high-resolution dark-field condenser (oil immersion) and 100X oil immersion objective (UPLFLN, Olympus) in the above-mentioned confocal Raman set-up. For white light illumination (400 to 1000 nm), an L1090-Halogen lamp from International Light Technologies Inc. was used. The laser was focused onto the sample using a

100X oil immersion objective (UPLFLN, Olympus). Signals after passing through a 532 nm bandpass filter were dispersed using a grating spectrometer (600 grooves per mm) onto a charge-coupled detector (CCD). Spectral images were scanned using the sample mounted on a piezo stage. Fluorescence staining experiments were performed using a CytoViva<sup>TM</sup> microscopy system.

### AESD RS set-up

A custom-built AESD RS set-up (schematic in Fig. 1A) incorporates a nanoESI emitter with a high voltage DC power supply of  $\sim 2.5$ –3 kV and a Raman spectrometer (Research India Co.) with a 532 nm excitation laser of 20 mW power on the sample. A grating of 1800 grooves per mm and an accumulation time of 0.3 s were used. The home-made electrospray source was made by continuously infusing a dilute solution of preformed AgNPs (1 : 1 AgNPs : water, 0.284 nM) through a fused silica capillary using a 500  $\mu\text{L}$  Hamilton syringe and a syringe pump. The inner and outer diameters of the fused capillary were 150 and 300  $\mu\text{m}$ , respectively. The flow rate was set to 0.5  $\mu\text{L min}^{-1}$  that generated a gentle electrospray plume. The positive polarity of a high voltage DC power supply was connected to the needle of the syringe to apply the required potential. A fused silica capillary was connected to the syringe through a finger tight union connector. 100–120 nA current was observed for the electrosprayed AgNPs at  $\sim 3$  kV, using a picoammeter.

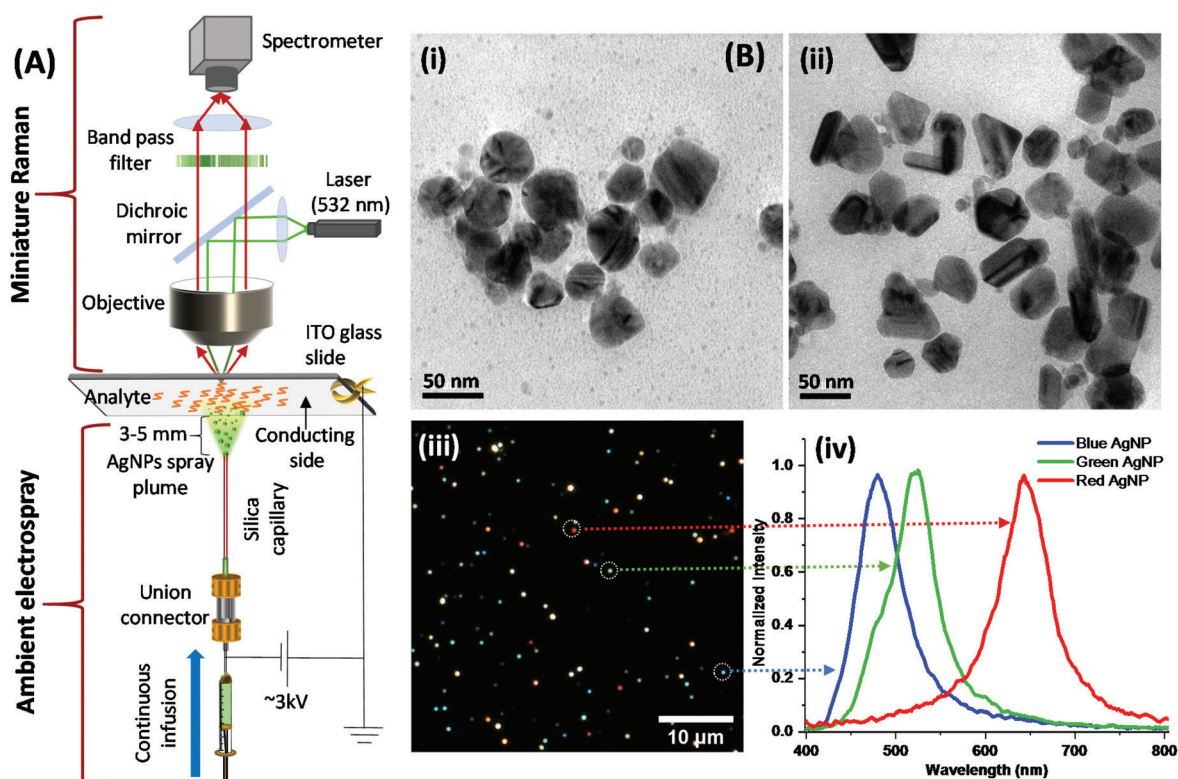


Fig. 1 (A) Schematic representation of the AESD RS set-up, (B) characterization of the soft landed AgNPs before and after electrospray, (i and ii) TEM images of the preformed AgNPs before and after electrospray, respectively, (iii) DFM image of the soft landed AgNPs, and (iv) plasmonic scattering spectra corresponding to each of the AgNPs encircled in (iii).



The tip of the capillary was placed in such a way that the soft landing of nanoparticles can be done over one side of the ITO plate containing the analyte of interest. The ITO plate was then connected to the ground to dissipate the charge of the droplets.

### Data processing by the clustering algorithm

Cluster analysis for confocal Raman spectral image was performed using an in-built clustering algorithm of the WITec software.

## Results and discussion

### Ambient electrospray deposition Raman spectroscopy (AESD RS)

The set-up incorporates a nanoESI emitter (a fused silica capillary) with a high voltage module and a miniature Raman spectrometer with a green laser as the excitation source. Details of the set-up are discussed in the Experimental section. The charged AgNPs generated by the ion source were soft landed on the analyte film which was dropcast onto an ITO glass plate placed at a distance of 3–5 mm from the tip of the silica capillary. Instead of placing the analyte coated glass slide facing the Raman objective, it was placed in an inverted position such that it faces the tip of the silica capillary. A schematic illustration of the set-up is shown in Fig. 1A and an optical photograph of the actual set-up with a zoomed-in image of the sample region is shown in Fig. S1.†

Experiments involved the recording of SERS spectra from dropcast analyte on ITO after spraying AgNPs for 30–40 s until enhanced SERS signals appeared. Signals were recorded from four locations of the sample (see Fig. S2† for details). In this work, we have probed *p*-MBA, 2,4-DNT, and *E. coli* for analysis. Characterization of the as-synthesized AgNPs was performed by UV-Vis absorption spectroscopy and DFM, as shown in Fig. S3.† The absorption peak of AgNPs appeared at 420 nm in solution (see Fig. S3†), which confirmed the formation of plasmonic nanoparticles. Subsequent studies were performed on the electrosprayed AgNPs by TEM and DFM. TEM images of the preformed AgNPs before and after electrospray are shown in Fig. 1B(i and ii), showing that applying such high voltage brings about some changes in the morphology of the NPs, although this aspect has not been investigated here. These modified AgNPs served as better SERS substrates having more hotspots due to the increase in polydispersity and sharper edges of the particles. Increased polydispersity after electrospray is influenced by the parent sample, surfactants in the medium, and electrospray parameters. These need to be optimized, and we are currently pursuing this study to obtain ideal conditions. Increased polydispersity of AgNPs leads to SERS enhancement, but it causes spatial variations in intensity. Post-characterization of the sprayed AgNPs was performed by DFM and plasmonic scattering spectroscopy, as shown in Fig. 1B(iii & iv). Multiple colors of AgNPs in the corresponding DF image indicate the polydispersity of the sample, which has been supported by the TEM image (ii). The particle size distribution

of the AgNPs before and after electrospray is shown in Fig. S4.† Size distribution calculations were performed using DF images and the ImageJ software. These plots suggested that before and after electrospray, the average size of AgNPs remained approximately the same. However, some aggregates were formed by electrospray as evidenced by the DFM image and the scattering spectra. With better understanding and characterization of the SERS substrates, the detection of analytes was pursued, and the corresponding data are presented in the next section.

### Rapid and sensitive detection of *p*-MBA and 2,4-DNT using AESD RS

For SERS detection, 40  $\mu\text{L}$  of an ethanolic solution of analytes were dropcast onto ITO glass slides and air-dried. We achieved detection in the range of 100  $\mu\text{M}$  to 1 nM (15  $\mu\text{g mL}^{-1}$  to 0.15  $\text{ng mL}^{-1}$ ) for *p*-MBA and 3 to 0.5  $\mu\text{M}$  (0.45  $\mu\text{g mL}^{-1}$  to 0.075  $\mu\text{g mL}^{-1}$ ) for 2,4-DNT, respectively. The compound *p*-MBA, being a good Raman probe, has been used widely for SERS detection and also for pH sensing which is nowadays used for cellular imaging.<sup>36</sup> Hence, it was used as a model analyte for AESD RS but to prove the ability of our technique over a wide range of analytes, 2,4-DNT (an explosive surrogate) and *E. coli* (a biological species) were also tested. A waterfall plot of SERS spectra of *p*-MBA at different concentrations is shown in Fig. 2A. The spectra are dominated by two features at 1586 and 1080  $\text{cm}^{-1}$ , which are assigned to  $\nu_{8a}$  and  $\nu_{12}$  aromatic ring vibrations, respectively.<sup>37</sup> A second sharp peak appears at 1377  $\text{cm}^{-1}$  due to the symmetric stretching of the carboxylate. Also, the bending mode of carboxylate appears at 844  $\text{cm}^{-1}$ , which was broad and weak at lower concentrations. In our experiments, the absence of 910 and 2580  $\text{cm}^{-1}$  peaks, which correspond to  $\delta(\text{CSH})$  and  $\nu(\text{SH})$  bonds, respectively, indicates that the analyte was bound with the electrosprayed AgNPs. Major peak assignments are shown in Fig. 2A and complete assignments of the vibrational bands are listed in Table S1.† A pictorial representation of *p*-MBA molecules bound to the Ag surface is shown in the inset of Fig. 2A. The signal intensity of the molecule increases gradually with an increase in the concentration from 1 nM to 100  $\mu\text{M}$ . A calibration curve was plotted between SERS intensity (counts) of the 1377  $\text{cm}^{-1}$  peak versus the logarithm of concentration, as shown in Fig. 2B. Intensities used in the calibration plot were taken after averaging 24 spectra at each concentration. The linear correlation ( $R$  square value is 0.9895) observed could be helpful in the quantification of unknown analytes.<sup>38</sup> Mean and standard deviation values of the calibration curve calculated from the weighted intensities of the sample (*p*-MBA) are shown in Table S2.† Variance observed in the calibration plot is due to the morphological changes occurred in AgNPs as a result of ESD. Such morphological changes will alter the number and position of hotspots on the nanoparticles. As the variance is large, the quantitation of analytes using AESD RS is semi-quantitative. We also calculated the enhancement factor<sup>30,39</sup> (EF) for the SERS system probed by AESD RS. An EF of  $2 \times 10^8$  was observed for 1  $\mu\text{M}$  concentration. EF calculations were per-

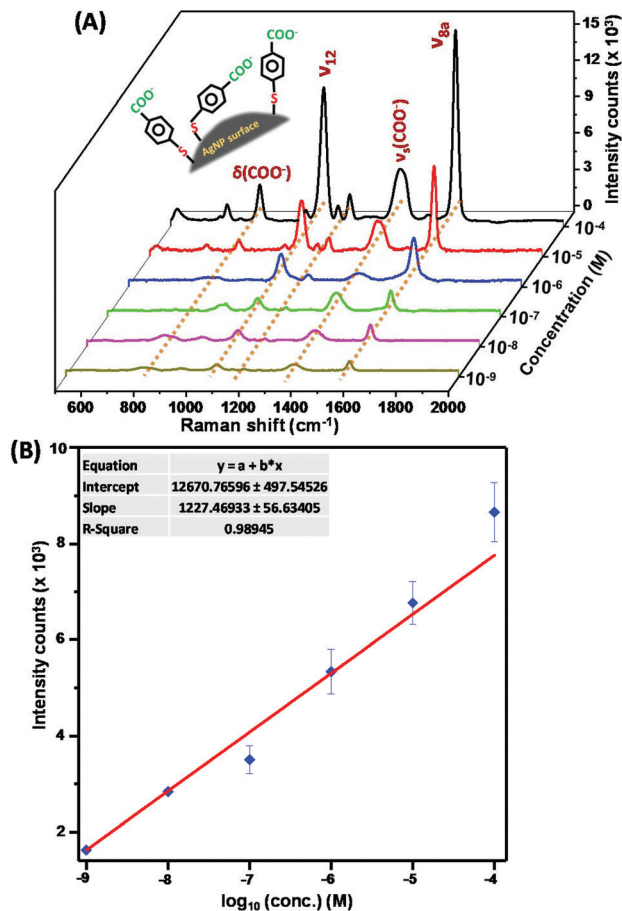


Fig. 2 (A) SERS spectra of *p*-MBA of various concentrations ranging from 100  $\mu\text{M}$  to 1 nM, the inset shows the pictorial representation of *p*-MBA molecules adsorbed on the AgNP surface and (B) calibration curve of SERS intensity of the 1377  $\text{cm}^{-1}$  peak vs. logarithm of the concentration of *p*-MBA. Data are fitted with a straight line.

formed using the weighted intensity counts of the 1586  $\text{cm}^{-1}$  peak, and the details are discussed in the ESI.<sup>†</sup>

Control experiments of blank ITO and citrate-capped AgNPs were also performed to show that *p*-MBA signals were significantly different from those of citrate-capped particles and ITO. The spectra of ITO and citrate are shown in Fig. S5.<sup>†</sup> ITO signals appeared as two broad bands in the region of 500–700 and 900–1200  $\text{cm}^{-1}$ , respectively, which are in good agreement with the values reported in the literature.<sup>40</sup> Since citrate has very weak Raman scattering cross-section, sharp and well-resolved SERS features were not observed in the preformed AgNPs before and after spray. Symmetric and asymmetric  $\text{COO}^-$  stretching features of citrate in the 1370–1385 and 1580–1590  $\text{cm}^{-1}$  window were detectable with reduced intensity.<sup>41</sup> In addition to the control experiments, a comparative study was performed between dropcast and electrospayed SERS signals, as shown in Fig. S5.<sup>†</sup> We observed that in the case of dropcast colloidal AgNPs (10  $\mu\text{L}$ ) solution on dried *p*-MBA (40  $\mu\text{L}$ ), SERS was observed, but intensity and sharpness of the signals were much lower than that obtained from

the electrospayed AgNPs. Signal intensities for the dropcast AgNPs were in the range of 1500–2000 counts (for 1586  $\text{cm}^{-1}$ ), whereas, in the electro spray method, intensities enhanced to 10 000 counts which were  $\sim 5$  times that obtained for the same analyte concentration (see Fig. S5.<sup>†</sup>). In the AESD method, a colloidal solution of preformed AgNPs was sprayed for 40 s at a flow rate of 0.5  $\mu\text{L min}^{-1}$  to obtain the signals of the analyte. It was observed that the utilized volume of the colloidal solution is  $\sim 33$  times lesser than the volume used in the conventional dropcasting methods for SERS analysis. We also compared the EF between dropcast and electrospayed SERS signals using 10  $\mu\text{M}$  concentration of *p*-MBA with 0.3  $\mu\text{L}$  of AgNPs. Calculations showed that the EF of electrospayed SERS is 5.2 times higher than that of the dropcast SERS (shown in the ESI.<sup>†</sup>). Similar concentration-based experiments were performed on 2,4-DNT, an organic compound used as a surrogate for trinitrotoluene (TNT). Its detection was performed sequentially from 3  $\mu\text{M}$  to its toxicity threshold limit (0.5  $\mu\text{M}$ ), and the corresponding data are listed in Fig. S6.<sup>†</sup> A stacked plot of different concentrations of DNT is shown in Fig. S6A.<sup>†</sup> and a calibration curve was also plotted (Fig. S6B.<sup>†</sup>). Error calculations of the calibration curve are shown in Table S3.<sup>†</sup> With the help of this curve, spiked DNT concentrations can also be quantified approximately. Assignments of the vibrational bands are shown in Fig. S6A.<sup>†</sup><sup>42</sup> Hence, soft landing of preformed AgNPs using AESD RS serves as a robust method for making useful SERS substrates for the rapid detection and semi-quantitation of analytes.

#### Post-characterization of electrospayed AgNPs by DFM and confocal Raman imaging

The SERS experiments presented in the previous section showed that electro spray facilitates the rapid and efficient detection of analytes. However, it is equally essential to ensure that SERS signals appeared only from the locations where the spray has happened and are absent otherwise. To do this, we performed confocal Raman imaging aided with dark-field microscopy on the sprayed samples separately, as our AESD RS system was not integrated with the imaging technique.

However, the intensity of SERS signals collected in AESD RS will be different from those measured in the confocal system as the sample was dried before performing dark-field assisted confocal Raman measurements. At first, the optical image stitching of the sprayed sample was performed, shown in the inset of Fig. 3A, then the boundary of the electrospayed AgNPs was focused with a dark-field objective followed by confocal Raman imaging of an area of  $20 \times 20 \mu\text{m}^2$ . The observed boundary in the inset (Fig. 3A) is due to the size distribution of droplets in electro spray, which suggests that some droplets are deposited on the substrate in the wet form, while many nanoparticles are deposited directly. However, the fraction of charged droplets vs. NPs is not clear from the AESD RS data. As micro and nano-droplets travel more distance, the solvent keeps evaporating and thus increasing the distance would increase the soft landing of dry and charged NPs and concomitantly it will decrease the number of droplets from being de-

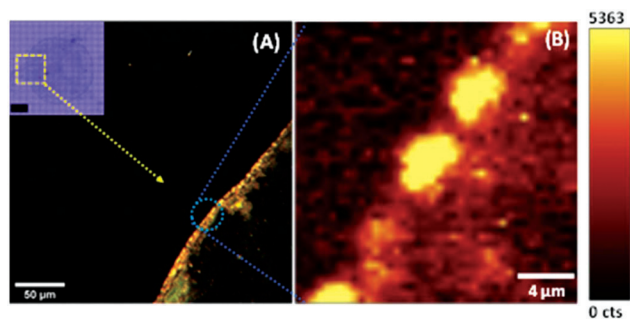


**Fig. 3** Image mapping of the electro sprayed AgNPs. (A) Dark-field image of one of the portions of the boundary of electro sprayed AgNPs, and (B) confocal Raman imaging of the region encircled in (A) with a heat map shown next to it, where 0 and 5363 indicate the CCD counts in the SERS spectra. An image in (B) corresponds to the total SERS intensity of the spectrum. An optical image of the sprayed region shown in the inset of (A), scale bar in the optical image is 500 µm. The dotted region is expanded in (A).

posited. To ensure that the formation of charged droplets is minimum during AESD, we have increased the tip to collector distance from ~4 mm (original distance) to ~8 mm and ~12 mm, respectively. At larger distances, SERS signals (Fig. S7†) were still observed (for 10 µM *p*-MBA) but with the reduced intensity as compared to ~4 mm distance. Thus, we conclude that at a distance of ~4 mm, the relative contribution of charged droplets on SERS signals will be more compared to that of the dry NPs. It will be difficult to distinguish quantitatively the fraction of charged droplets vs. dry NPs on the observed signals when AESD and SERS are happening simultaneously. The optical image, DFM image of the boundary with sprayed AgNPs and the corresponding confocal Raman imaging of one of those regions are shown in Fig. 3. It is evident from the confocal Raman map that only at the electro-sprayed AgNP locations, SERS signals were observed, while no signal was detected where AgNPs were absent. Raman imaging was performed for 10 µM concentration of *p*-MBA.

### Confocal Raman map analysis by the clustering algorithm

A clustering algorithm is one of the simplest algorithms for spectral image analysis. It groups the spectra according to their similarity in peak positions, widths and signal intensities, forming clusters which represent the regions of the image with identical molecular properties.<sup>43</sup> Confocal Raman image of the electro sprayed AgNPs shown in Fig. 3 has been subjected to cluster analysis to obtain the SERS spectra of *p*-MBA at different regions of the map. Cluster analysis gives the average spectra of various regions. The cluster analyzed spectra are shown in Fig. 4, which resulted in two sets of groups as (i–iv) and (v). The first group (i–iv) corresponds to those regions of the map where SERS signals were observed due to the presence of sprayed AgNPs on the dropcast analyte. However, the other group (v) corresponds to that region of the map where no SERS was observed. Insignificant intensity for the whole region in this spectrum (component v) shows that *p*-MBA at

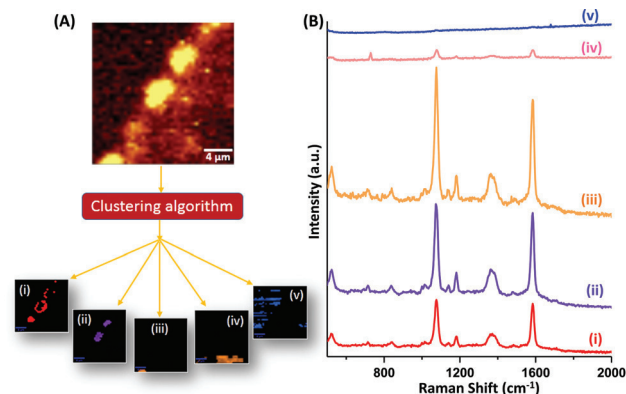


**Fig. 4** Cluster analysis of the electro sprayed region, (A) confocal Raman map of the region as shown in Fig. 3, (i)–(iv) indicate the respective regions of map A, where SERS signals of *p*-MBA were observed in the presence of AgNPs, and (v) shows the region of map A, where no SERS was observed in the absence of AgNP spray, and the spectra corresponding to regions (i–v) are shown in (B), scale bar in all images is 4 µm.

this concentration (10 µM) could not be detected without AgNPs being present. Along with the cluster spectra (Fig. 3B), the corresponding Raman images (Fig. 3A) are also shown (i–v). The SERS spectra obtained for different regions of the Raman map were similar with spatial variations in the intensity which could be due to nanoparticle reshaping caused by laser irradiation as reported recently.<sup>35</sup> Thus, the clustering of the Raman map ensured that the SERS signals of *p*-MBA were observed only in the regions of spray and were absent otherwise.

### AESD RS as a tool for biological applications

The bio-molecules of bacteria interacting with AgNPs show distinct SERS spectra.<sup>17,44–46</sup> Contact between bacteria and AgNPs is necessary for obtaining reliable SERS signals. Although AgNPs perform well as SERS substrates, they are known to possess antimicrobial properties.<sup>47</sup> AgNPs induced apoptosis influences the spectra to a large extent.<sup>47,48</sup> Overcoming this toxicity of AgNPs while utilizing them as SERS substrates have been a challenge.

We present a technique, wherein the volume of AgNPs sprayed on bacterial cells is similar to the amount used for the detection and quantification of previous analytes. In this case, the time for exposure to AgNPs was 40–50 s, which was slightly more as compared to *p*-MBA and 2,4-DNT. During this short time, the signals can be obtained without much effect on the bacterial cells. As the time of exposure to AgNPs is shortened, the uptake of AgNPs by the bacterial cells will be reduced. The cells are not suspended in colloidal AgNPs solutions,<sup>49</sup> as done in conventional techniques. Thus, we can use the AESD RS method without much sample preparation for analyzing bacteria in water, food, clinical, and environmental samples. DFM images of the untreated bacteria and the bacteria treated with sprayed AgNPs are shown in Fig. 5A and B, respectively. Expanded DFM images of the individual bacterium are shown



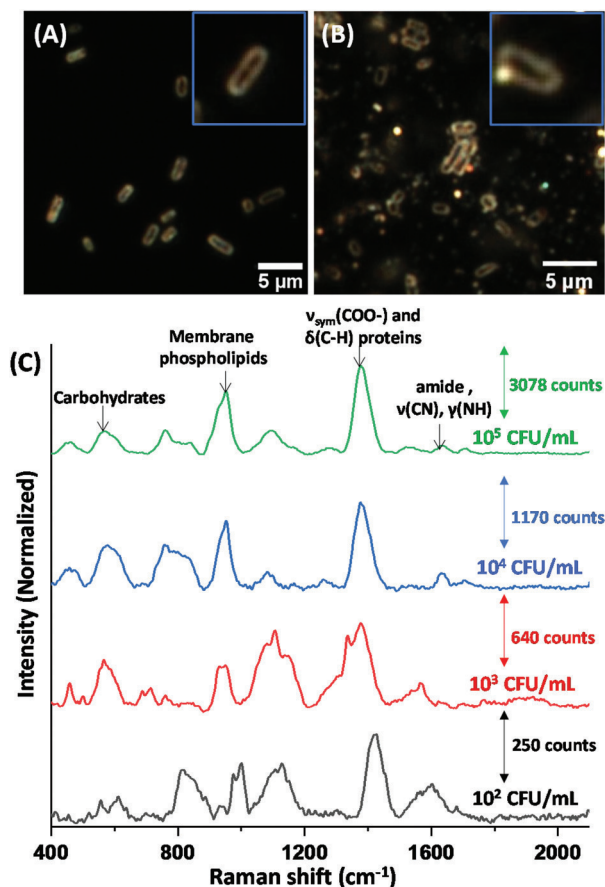


Fig. 5 (A and B) DFM images of the bacteria before and after electrospray. An individual bacterium is expanded in the inset of (A) and (B), and (C) SERS spectra of *E. coli* (MTCC 443) at different concentrations (10<sup>5</sup>–10<sup>2</sup> CFU mL<sup>-1</sup>) with their vibrational band assignments.

in the insets of Fig. 5A and B. Average spectra of different concentrations of *E. coli* are shown in Fig. 5C. The resultant SERS spectra are dominated by peaks at 1370–1420, 950–1000 and 560–640 cm<sup>-1</sup> which were attributed to symmetric COO<sup>-</sup> stretching, membrane phospholipids and carbohydrates, respectively.<sup>17</sup> Complete band assignments are listed in Table S4.† Although AESD RS can analyse bacteria, we wanted to know whether these organisms are indeed alive during analysis. Therefore, we have performed ‘replica plating’ of the ITO glass slide, dropcast with *E. coli*, on two types of agar-based growth media. Nutrient agar (general nutrient media for algae, bacteria, etc.) and MacConkey agar (media specific to Gram-negative bacteria) were used for the replica plating. The first replica was made with the glass slide dropcast with *E. coli* on the agar plate. Then, the same slide was removed from the agar plate and used for electrospray deposition. This AgNP deposited plate was used for the second replica on a fresh agar plate. These plates were incubated at 37 degrees for 24 hours. Results for these four plates are shown in Fig. S8.† The growth of the bacteria after the electrospray showed that they were not killed during deposition.

Our claim that *E. coli* have survived after electrospray deposition is to show that the conditions at which the electrospray was performed enable analysis on live bacteria as well. The exposure time of AgNPs to bacterial cells was just 60 s. The volume and concentration of AgNPs used for the sample are 0.5 μL and 0.284 nM, respectively. The effect of AgNPs at this condition cannot be ascertained quantitatively as the current AESD RS set-up is not integrated with an imaging system. Thus, we have shown the effect qualitatively. We have also performed fluorescence microscopic imaging (see Fig. S9†) to show the viability of bacteria and a statistical count of live and dead bacteria.<sup>50</sup> For *E. coli* after electrospray deposition, the death rate of bacteria was somewhat higher than that of *E. coli* before electrospray. However, it is evident from images (Ai, Aii, Bi, and Bii, Fig. S9†) that a large number of bacteria survived even after ESD. Statistical calculations were performed using ImageJ analysis and it was seen that 94.2% bacteria were alive after ESD, while 96.7% bacteria were alive prior to ESD. The location of nanoparticles can be ascertained using correlated optical DFM and fluorescence images (Ci, Cii, Di, and Dii, Fig. S9†), but the understanding of the effect of nanoparticles on bacteria cannot be quantified as the exposure time is very short and the number of NPs interacting with each bacteria is different. Inferences from replica plating and fluorescence imaging experiments support that AESD RS can help in the analysis of live bacterial cells.

## Conclusions

In conclusion, the technique of AESD RS was introduced, which is capable of rapid and sensitive SERS detection of molecules in diverse systems. Nanomolar and micromolar concentrations of *p*-MBA and 2,4-DNT were detected within 4–6 minutes, including sample preparation. A linear plot of SERS signal intensity versus logarithm of concentration was observed, which can be used for the semi-quantitative analysis of spiked analytes. AESD RS provides an enhanced signal intensity of the order of 10<sup>8</sup> for 1 μM concentration, which is 5.2 times higher than that of the drop-casting SERS method. As the AESD RS set-up was not integrated with an imaging technique, post-characterization of the electrosprayed AgNPs was performed using confocal Raman imaging aided with DFM. Post-characterization helped us to ensure that the SERS signals appeared only from the sprayed locations. Cluster analysis of the Raman image of *p*-MBA resulted in two groups, where one showed SERS signals in the sprayed region, and another group where no SERS was observed. Furthermore, our technique proved to be an important tool for detecting and characterizing *E. coli* at its lowest concentration of 10<sup>2</sup> CFU mL<sup>-1</sup>. Qualitative experiments of replica plating showed that bacteria survived after ESD. Live and dead fluorescence imaging of *E. coli* provided a statistical count of live and dead bacteria after ESD. The AESD RS technique can also serve the purpose of single bacterium detection if an imaging system is coupled with it. We believe that the real-time changes in

molecular and biological species can also be performed efficiently using the presented technique to get better insights into the orientations and intermediates of the analyte in a similar time scale.

## Conflicts of interest

There are no conflicts to declare.

## Acknowledgements

We thank the Department of Science and Technology, Government of India, for constantly supporting our research program on nanomaterials. T. A., P. B., S. P., J. S. K., and S. B. acknowledge institute graduate fellowships. J. S. M. thanks the University Grants Commission for a research fellowship.

## References

- 1 A. Haddad, M. A. Comanescu, O. Green, T. A. Kubie and J. R. Lombardi, *Anal. Chem.*, 2018, **90**, 12678–12685.
- 2 K. Kneipp, H. Kneipp, I. Itzkan, R. R. Dasari and M. S. Feld, *Chem. Rev.*, 1999, **99**, 2957–2976.
- 3 Z. Q. Tian, *J. Raman Spectrosc.*, 2005, **36**, 466–470.
- 4 S. E. J. Bell, J. N. Mackle and N. M. S. Sirimuthu, *Analyst*, 2005, **130**, 545–549.
- 5 S. Dick, M. P. Konrad, W. W. Y. Lee, H. McCabe, J. N. McCracken, T. M. D. Rahman, A. Stewart, Y. Xu and S. E. J. Bell, *Adv. Mater.*, 2016, 5705–5711.
- 6 S. J. Sang and K. Jurae, *J. Raman Spectrosc.*, 1998, **29**, 143–148.
- 7 A. G. Brolo, Z. Jiang and D. E. Irish, *J. Electroanal. Chem.*, 2003, **547**, 163–172.
- 8 M. J. Trujillo, S. L. Strausser, J. C. Becca, J. F. DeJesus, L. Jensen, D. M. Jenkins and J. P. Camden, *J. Phys. Chem. Lett.*, 2018, **9**, 6779–6785.
- 9 M. R. K. Ali, Y. Wu, T. Han, X. Zang, H. Xiao, Y. Tang, R. Wu, F. M. Fernández and M. A. El-Sayed, *J. Am. Chem. Soc.*, 2016, **138**, 15434–15442.
- 10 E. A. Sprague-Klein, B. Negru, L. R. Madison, S. C. Coste, B. K. Rugg, A. M. Felts, M. O. McAnally, M. Banik, V. A. Apkarian, M. R. Wasielewski, M. A. Ratner, T. Seideman, G. C. Schatz and R. P. Van Duyne, *J. Am. Chem. Soc.*, 2018, **140**, 10583–10592.
- 11 E. A. Sprague-Klein, M. O. McAnally, D. V. Zhdanov, A. B. Zrimsek, V. A. Apkarian, T. Seideman, G. C. Schatz and R. P. Van Duyne, *J. Am. Chem. Soc.*, 2017, **139**, 15212–15221.
- 12 W. H. Kim, J. U. Lee, S. Song, S. Kim, Y. J. Choi and S. J. Sim, *Analyst*, 2019, **144**, 1768–1776.
- 13 V. Dugandžić, S. Kupfer, M. Jahn, T. Henkel, K. Weber, D. Cialla-May and J. Popp, *Sens. Actuators, B*, 2019, **279**, 230–237.
- 14 N. Feliu, M. Hassan, E. Garcia Rico, D. Cui, W. Parak and R. Alvarez-Puebla, *Langmuir*, 2017, **33**, 9711–9730.
- 15 W. Xie and S. Schlücker, *Chem. Commun.*, 2018, **54**, 2326–2336.
- 16 E. M. van Schrojenstein Lantman, P. De Peinder, A. J. G. Mank and B. M. Weckhuysen, *ChemPhysChem*, 2015, **16**, 547–554.
- 17 S. Vishnupriya, K. Chaudhari, R. Jagannathan and T. Pradeep, *Part. Part. Syst. Charact.*, 2013, **30**, 1056–1062.
- 18 E. T. Hwang, J. H. Lee, Y. J. Chae, Y. S. Kim, B. C. Kim, B. I. Sang and M. B. Gu, *Small*, 2008, **4**, 746–750.
- 19 S. Juan Yu, Y. Guang Yin and J. Fu Liu, *Environ. Sci.: Processes Impacts*, 2013, **15**, 78–92.
- 20 S. León-Silva, F. Fernández-Luqueño and F. López-Valdez, *Water, Air, Soil Pollut.*, 2016, **9**, 227–306.
- 21 P. Z. El-Khoury, G. E. Johnson, I. V. Novikova, Y. Gong, A. G. Joly, J. E. Evans, M. Zamkov, J. Laskin and W. P. Hess, *Faraday Discuss.*, 2015, **184**, 339–357.
- 22 D. Wang, F. Liang, P. Ma, Q. Yang, D. Gao, D. Song and X. Wang, *Food Anal. Methods*, 2016, **9**, 934–941.
- 23 C. Hanske, G. González-Rubio, C. Hamon, P. Formentín, E. Modin, A. Chuvilin, A. Guerrero-Martínez, L. F. Marsal and L. M. Liz-Marzán, *J. Phys. Chem. C*, 2017, **121**, 10899–10906.
- 24 X. Zhang, Y. Zheng, X. Liu, L. Wei, J. Dai, D. Y. Lei and D. R. MacFarlane, *Adv. Mater.*, 2015, **27**, 1090–1096.
- 25 R. A. Alvarez-Puebla, A. Agarwal, P. Manna, B. P. Khanal, P. Aldeanueva-Potel, E. Carbó-Argibay, N. Pazos-Pérez, L. Vigderman, E. R. Zubarev, N. A. Kotov and L. M. Liz-Marzán, *Proc. Natl. Acad. Sci. U. S. A.*, 2011, **108**, 8157–8161.
- 26 C. Hamon, S. Novikov, L. Scarabelli, L. Basabe-Desmonts and L. M. Liz-Marzán, *ACS Nano*, 2014, **8**, 10694–10703.
- 27 T. Li, K. Wu, T. Rindzevicius, Z. Wang, L. Schulte, M. S. Schmidt, A. Boisen and S. Ndoni, *ACS Appl. Mater. Interfaces*, 2016, **8**, 15668–15675.
- 28 A. Jaworek, *J. Mater. Sci.*, 2007, **42**, 266–297.
- 29 A. K. Badu-Tawiah, C. Wu and R. G. Cooks, *Anal. Chem.*, 2011, **83**, 2648–2654.
- 30 A. Li, Z. Baird, S. Bag, D. Sarkar, A. Prabhath, T. Pradeep and R. G. Cooks, *Angew. Chem., Int. Ed.*, 2014, **53**, 12528–12531.
- 31 A. Li, Q. Luo, S. J. Park and R. G. Cooks, *Angew. Chem., Int. Ed.*, 2014, **53**, 3147–3150.
- 32 J. K. Lee, D. Samanta, H. G. Nam and R. N. Zare, *Nat. Commun.*, 2018, **9**, 1–9.
- 33 J. Wang, L. Yang, B. Liu, H. Jiang, R. Liu, J. Yang, G. Han, Q. Mei and Z. Zhang, *Anal. Chem.*, 2014, **86**, 3338–3345.
- 34 J. F. Li, Y. F. Huang, Y. Ding, Z. L. Yang, S. B. Li, X. S. Zhou, F. R. Fan, W. Zhang, Z. Y. Zhou, D. Y. Wu, B. Ren, Z. L. Wang and Z. Q. Tian, *Nature*, 2010, **464**, 392–395.
- 35 K. Chaudhari, T. Ahuja, V. Murugesan, V. Subramanian, A. G. Mohd, T. Thundat and T. Pradeep, *Nanoscale*, 2018, **11**, 321–330.



- 36 Z. Zhang, K. Bando, K. Mochizuki, A. Taguchi, K. Fujita and S. Kawata, *Anal. Chem.*, 2019, **91**, 3254–3262.
- 37 A. Michota and J. Bukowska, *J. Raman Spectrosc.*, 2003, **34**, 21–25.
- 38 Y. Zhang, Y. Zou, F. Liu, Y. Xu, X. Wang, Y. Li, H. Liang, L. Chen, Z. Chen and W. Tan, *Anal. Chem.*, 2016, **88**, 10611–10616.
- 39 P. L. Stiles, J. A. Dieringer, N. C. Shah and R. P. Van Duyne, *Annu. Rev. Anal. Chem.*, 2008, **1**, 601–626.
- 40 R. K. Pandey, C. Upadhyay and R. Prakash, *RSC Adv.*, 2013, **3**, 15712–15718.
- 41 C. H. Munro, W. E. Smith, M. Garner, J. Clarkson and P. C. White, *Langmuir*, 1995, **11**, 3712–3720.
- 42 J. M. Sylvia, J. A. Janni, J. D. Klein and K. M. Spencer, *Anal. Chem.*, 2000, **72**, 5834–5840.
- 43 F. Bonnier and H. J. Byrne, *Analyst*, 2012, **137**, 322–332.
- 44 P. A. Mosier-Boss, *Biosensors*, 2017, **7**, 51.
- 45 R. M. Jarvis and R. Goodacre, *Anal. Chem.*, 2004, **76**, 40–47.
- 46 H. Zhou, D. Yang, N. P. Ivleva, N. E. Mircescu, R. Niessner and C. Haisch, *Anal. Chem.*, 2014, **86**, 1525–1533.
- 47 K. Chaudhari and T. Pradeep, *J. Biomed. Opt.*, 2015, **20**, 046011.
- 48 X. Meng, H. Wang, N. Chen, P. Ding, H. Shi, X. Zhai, Y. Su and Y. He, *Anal. Chem.*, 2018, **90**, 5646–5653.
- 49 A. P. Olson, K. B. Spies, A. C. Browning, P. A. G. Soneral and N. C. Lindquist, *Sci. Rep.*, 2017, **7**, 1–9.
- 50 J. R. Swathy, M. U. Sankar, A. Chaudhary, S. Aigal, S. Anshup and T. Pradeep, *Sci. Rep.*, 2014, **4**, 7161.

## Electronic Supplementary Information

### Ambient Electrospray Deposition Raman Spectroscopy (AEDS RS) using Soft Landed Preformed Silver Nanoparticles for Rapid and Sensitive Analysis

Tripti Ahuja,<sup>a#</sup> Atanu Ghosh,<sup>a#</sup> Sandip Mondal,<sup>a</sup> Pallab Basuri,<sup>a</sup> Jenifer Shantha Kumar,<sup>a</sup> Pillalamarri Srikrishnarka,<sup>a</sup> Jyoti Sarita Mohanty,<sup>a</sup> Sandeep Bose,<sup>a</sup> and Thalappil Pradeep<sup>a\*</sup>

<sup>a</sup>DST Unit of NanoScience (DST UNS) and Thematic Unit of Excellence (TUE), Department of Chemistry, Indian Institute of Technology Madras, Chennai 600 036, India, Tel: +91044-2257-4208, E-mail: [pradeep@iitm.ac.in](mailto:pradeep@iitm.ac.in)

#Equal contribution

\*Corresponding author

#### Table of Contents:

Number	Title	Page No.
Fig. S1	Optical photograph of the set-up	2
Fig. S2	Schematic representation of selecting locations for electrospray deposition	2
Fig. S3	Characterization of as-synthesized AgNPs by UV-Vis absorption spectroscopy and dark-field microscopy	3
Fig. S4	Analysis of the particle size distribution of AgNPs before and after electrospray	3
Fig. S5	A comparative plot between conventional SERS and AEDS RS signals	4
Table S1	Band assignments of SERS features of p-MBA	5
Table S2	Calculation of mean and standard deviation for calibration curve of p-MBA	5
Fig. S6	SERS waterfall plot of 2,4-DNT of different concentrations and calibrations curve between SERS intensity and concentration	6
Table S3	Calculation of mean and standard deviation for calibration curve of 2,4-DNT	6
Fig S7	Distance (tip to collector) dependent SERS measurements using electrosprayed AgNPs	7
Table S4	Band assignments of SERS features of <i>E. coli</i>	7
Fig. S8	Replica culture of ITO glass slides drop casted with <i>E.coli</i> on agar plates	8
Fig. S9	Live/dead fluorescent microscopic imaging of <i>E. coli</i> before and after electrospray	8
Equations S1	Enhancement factor calculations	9-10
List of	References	10

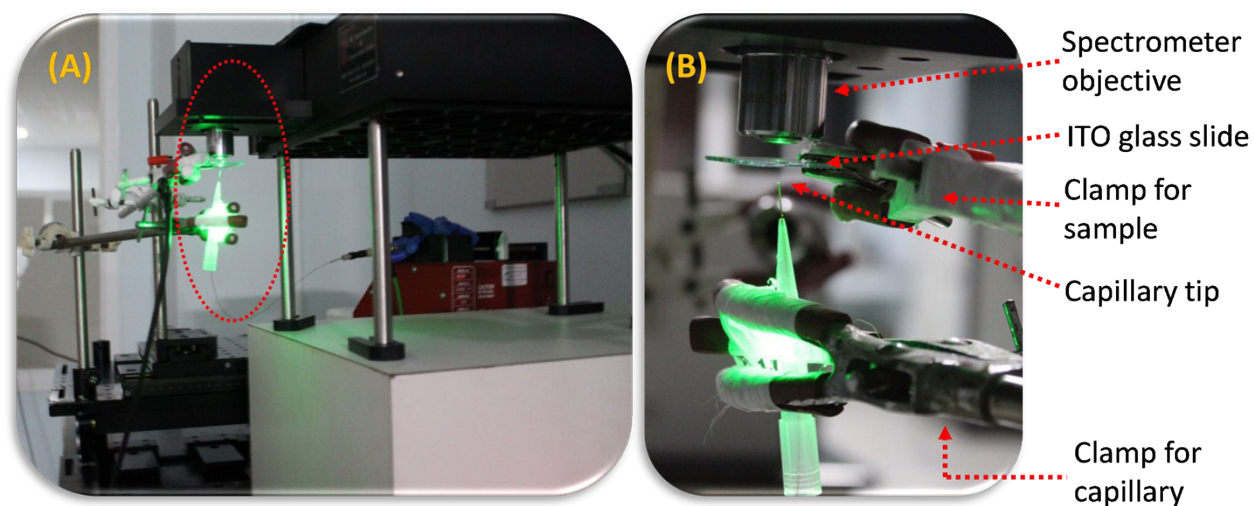


**Fig. S1** (A) Optical photograph of the AESD RS set-up and (B) zoomed-in region of A, highlighted in a red-colored ellipse.

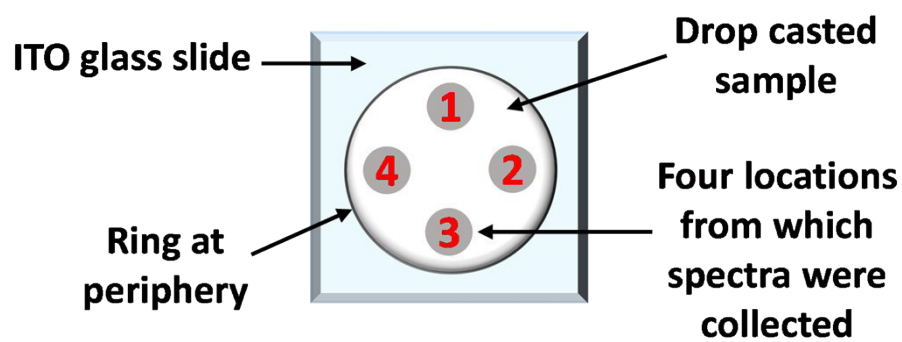


**Fig. S2** A schematic representation of selecting four locations from the drop casted analyte for AESD.

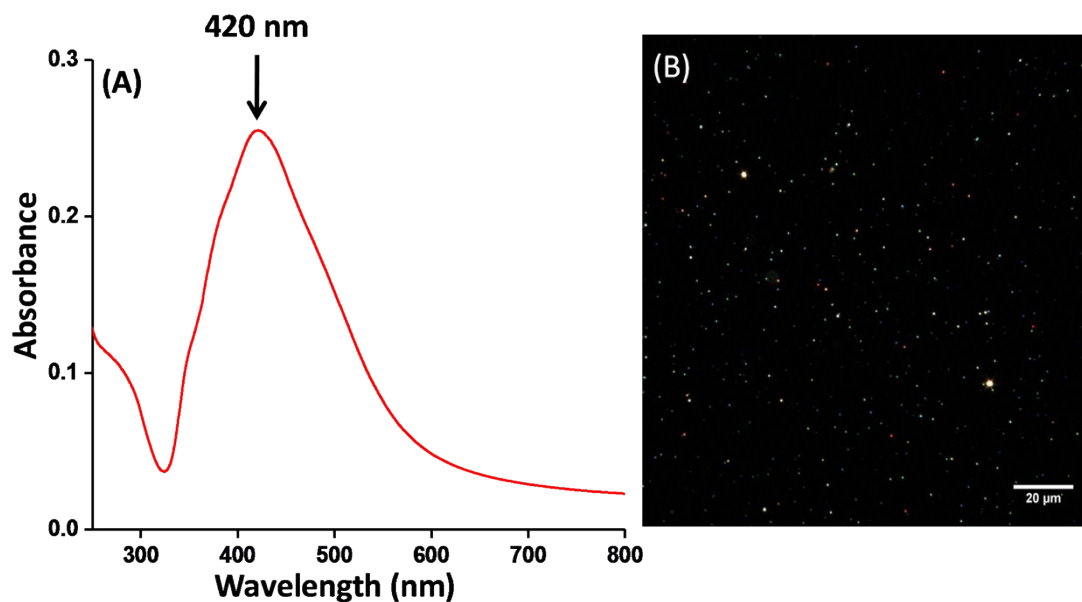


**Fig. S3** (A) UV-Vis absorption spectrum of the as-prepared AgNPs, and (B) DFM image of the preformed AgNPs immobilized on an ultra-clean glass slide.

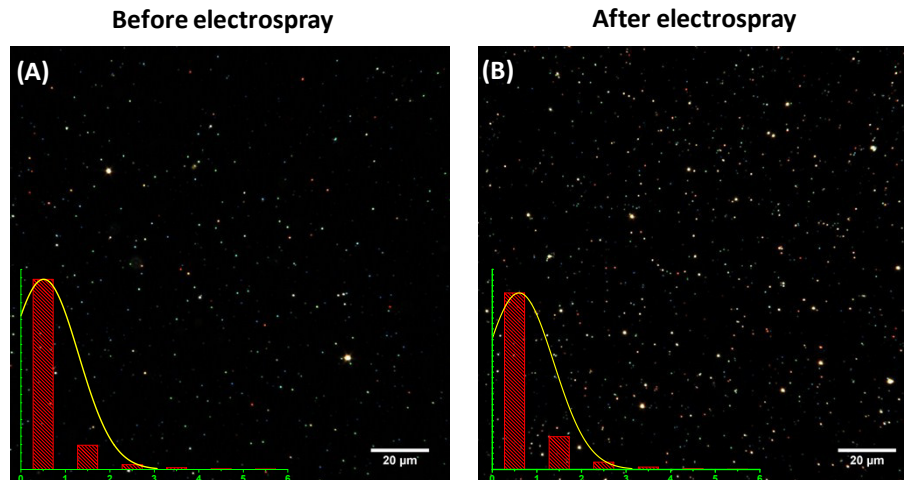


**Fig. S4** DFM images and their corresponding histograms of the particle size distribution of AgNPs, (A) before and (B) after electrospray.

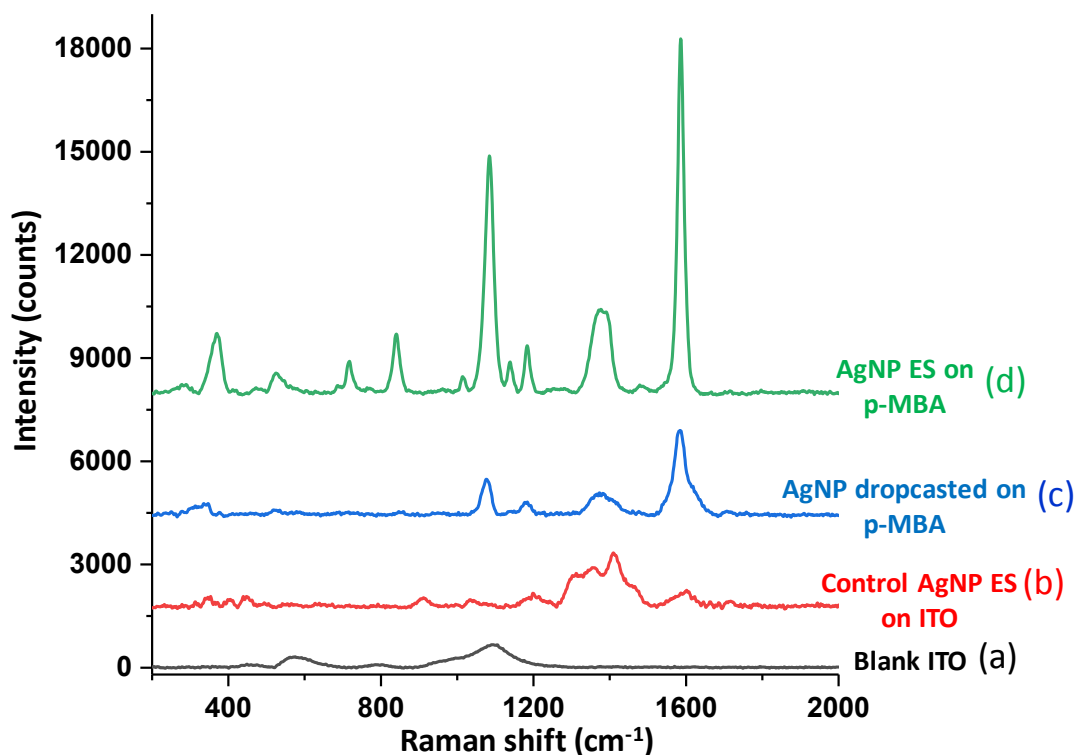


**Fig. S5** A comparative plot between conventional SERS and AESD SERS signals. (a) Blank ITO, (b) control SERS of only AgNPs electro spray without p-MBA, (c) SERS of p-MBA when AgNPs were drop casted, and (d) SERS of p-MBA when AgNPs were electro sprayed. Spectra were background corrected and vertically shifted for clarity, but no other manipulation was performed.

**Table S1** Band assignments of SERS features of p-MBA

Peak position (cm <sup>-1</sup> )	Assignments <sup>[1-2]</sup>
717	$\gamma$ (CCC) (aromatic)
842	$\delta$ (COO <sup>-</sup> )
absent	$\delta$ (CSH)
1013	Ring deformation
1136	$13\beta$ (CCC) + $\nu$ (C-S) + $\nu$ (C-COOH)
1186	$\delta$ (C-H)
1078-1086	$\nu_{12}$ (ring)
1375-1380	$\nu_s$ (COO <sup>-</sup> )
1585-1588	$\nu_{8a}$ (ring)

**Table S2** Calculation of mean and standard deviation for calibration curve of p-MBA

Concentration (M)	Mean of intensity counts	Standard deviation of intensity counts
$10^{-9}$	1628.277	26.106
$10^{-8}$	2839.332	53.173
$10^{-7}$	3504.938	294.986
$10^{-6}$	5344.406	467.998
$10^{-5}$	6769.224	441.697
$10^{-4}$	8661.805	613.920

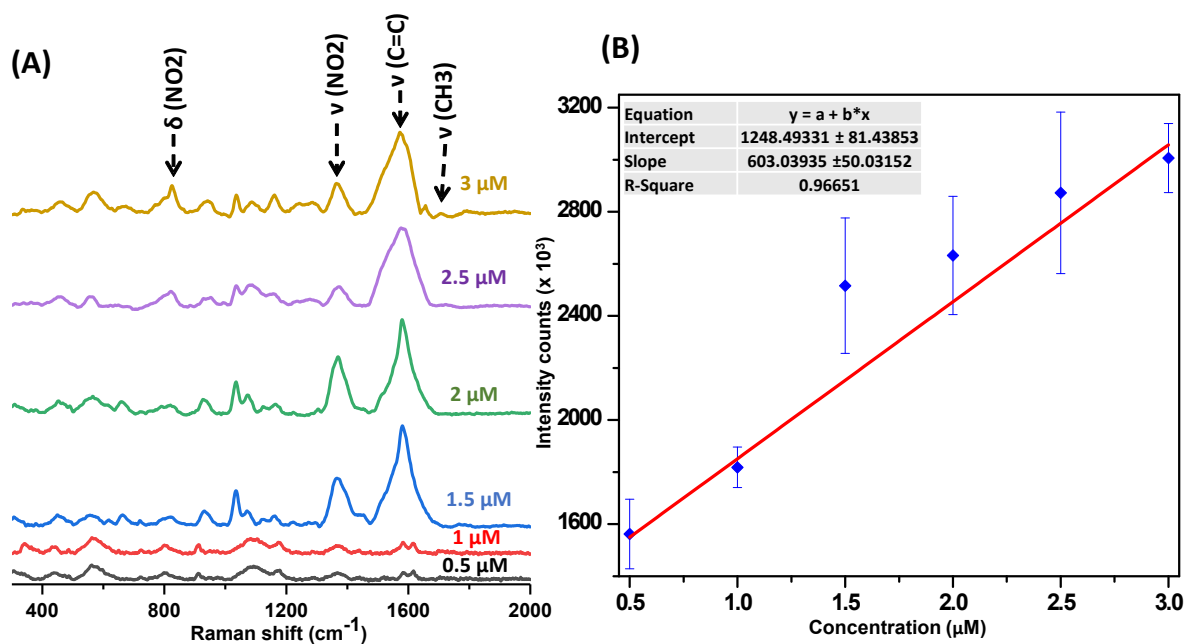


**Fig. S6** (A) Stacked SERS plot of 2,4-DNT at different concentrations ranging from 3 to 0.5  $\mu\text{M}$  and (B) calibration curve between SERS intensity ( $1589\text{ cm}^{-1}$  counts) and concentrations of 2,4-DNT.

**Table S3** Calculation of mean and standard deviation for calibration curve of 2,4-DNT

Concentration ( $\mu\text{M}$ )	Mean of intensity counts	Standard deviation of intensity counts
0.5	1562.224	133.654
1	1818.565	78.055
1.5	2516.361	260.221
2	2632.293	227.489
2.5	2872.928	310.216
3	3006.579	132.228



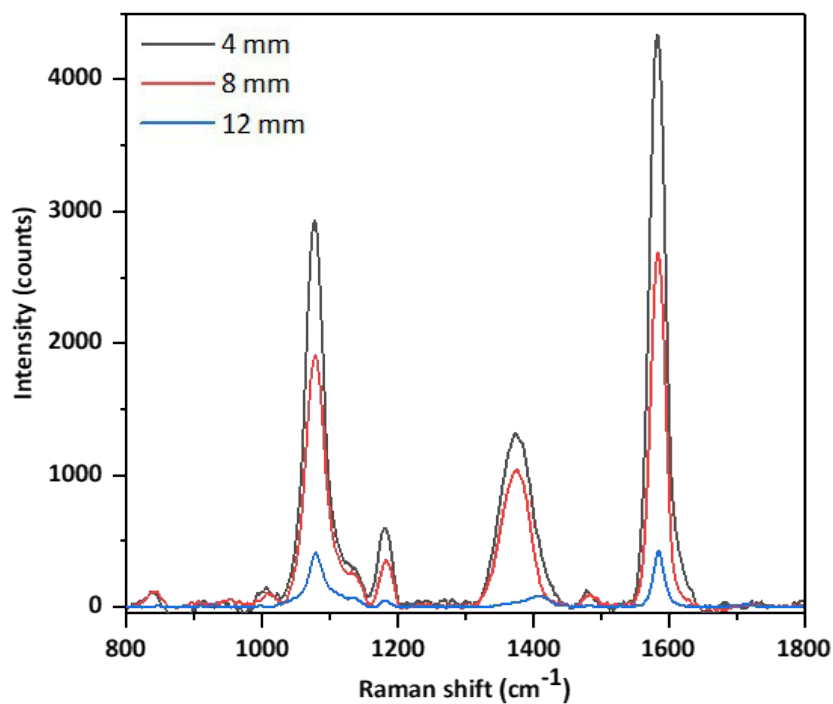


**Fig. S7** SERS spectra of 10  $\mu$ M p-MBA with electro sprayed AgNPs at different tip to collector distances.

**Table S4.** Band assignments of SERS features of *E. coli*.

Peak position ( $\text{cm}^{-1}$ )	Assignments <sup>[3-4]</sup>
560-640	$\delta(\text{COO})$ + carbohydrates
760-815	Tryptophan
950-1000	Membrane phospholipids
1080-1130	Proteins + lipids + carbohydrates
1370-1420	$\nu_{\text{sym}}(\text{COO}^-)$ and $\delta(\text{C-H})$ proteins
1530-1630	amide , $\nu(\text{CN})$ , $\gamma(\text{NH})$

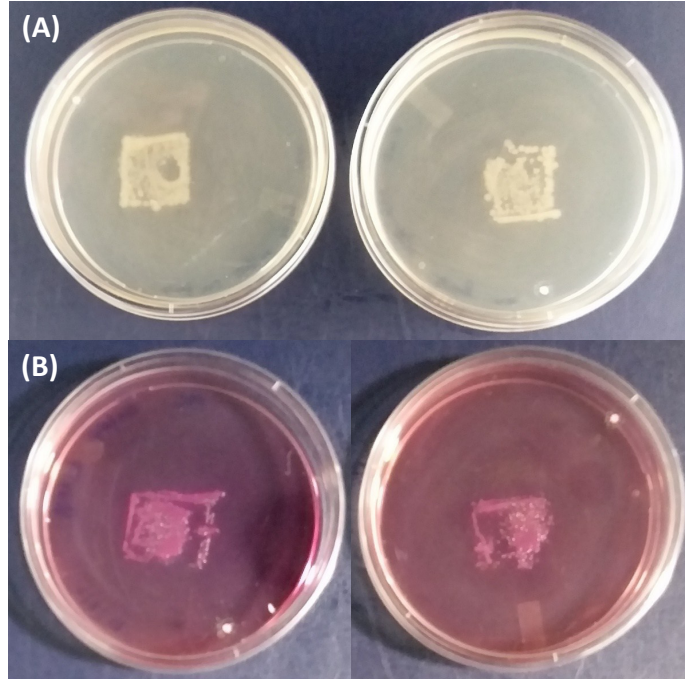
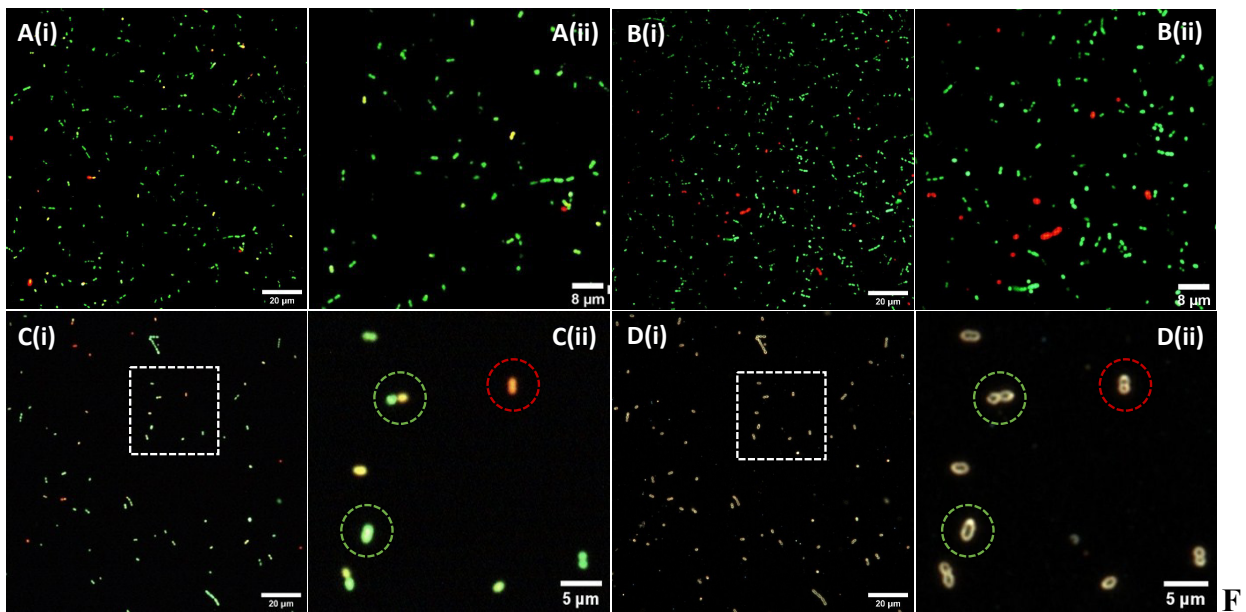


**Fig. S8** Replica culture of ITO glass slides drop casted with *E.coli* on A) Nutrient agar before (left) and after electrospray (right), and B) MacConkey agar before (left) and after electrospray (right).



**ig. S9** Fluorescence microscopic imaging of bacteria, (Ai) *E. coli* before electrospray, (Aii) zoomed-in view of (Ai), (Bi) *E. coli* after electrospray deposition, (Bii) zoomed-in view of (Bi), (Ci) fluorescence image of region of *E. coli* interacted with AgNPs, (Cii) zoomed-in view of (Ci)

shown in dotted square, (Di) optical DFM image corresponding to (Ci) to show AgNPs, and (Dii) zoomed-in view of (Di) shown in dotted square. Green and red dotted circles in (Cii) and (Dii) represent live and dead bacteria after their interaction with AgNPs.

### Enhancement factor calculations:

Enhancement factor (EF) for SERS system can be described by the equation<sup>5,6</sup> given below:

$$EF = (I_{\text{SERS}}/N_{\text{surface}})/(I_{\text{NRS}}/N_{\text{bulk}}) \quad (1)$$

$I_{\text{SERS}}$  and  $I_{\text{NRS}}$  are the observed intensities arising from the interaction of drop casted analyte (here p-MBA) with the electrosprayed AgNPs and the normal Raman scattering intensity of analyte molecule in the absence of electrosprayed AgNPs (normal Raman signal). Parameters  $N_{\text{surface}}$  and  $N_{\text{bulk}}$  are the number of analyte molecules excited under the laser spot interacted with sprayed AgNPs and the number of analyte molecules under the laser spot for the bulk specimen.

From experimental data,  $I_{\text{SERS}} = 8068$  counts (obtained after the average of 24 spectra of 1  $\mu\text{M}$  concentration for 1586  $\text{cm}^{-1}$ ) and  $I_{\text{RS}} = 298$  counts (52 mM).

$$N_{\text{surface}} = 4\pi r^2 \cdot C \cdot A \cdot N \quad (2)$$

where  $r$ ,  $C$ ,  $A$ ,  $N$  are average particle radius of the Ag nanoparticles in the spot, surface density of the analyte drop casted, area of the laser spot and the average number of particles per square micrometer area, respectively. The average particle radius  $r$  was taken (from ImageJ analysis of TEM images) as 20 nm, the density of analyte molecules ( $C$ ) drop casted (1  $\mu\text{M}$  concentration for 40  $\mu\text{L}$  volume) was calculated as  $10^6/\mu\text{m}^2$ , the area of the laser spot (10 $\times$  objective, Numerical Aperture = 0.25) diameter was 7.6  $\mu\text{m}$  ( $A = \sim 45 \mu\text{m}^2$ ), and the number of particles per square micrometer ( $N$ ) from DFM measurement was 12.

$N_{\text{bulk}}$  was calculated using the formula:

$$N_{\text{bulk}} = N_A \cdot A \cdot h \cdot \rho / M \quad (3)$$

where  $A$  is the area of the laser spot,  $h$  is the penetration depth of the laser,  $\rho$  is the density of the solid analyte (1.3  $\text{g}/\text{cm}^3$  in case of p-MBA) and  $M$  is the molecular weight of the analyte (in

this work, 154.19 g/mol for p-MBA). The laser spot diameter was 7.6  $\mu\text{m}$ ; penetration depth of laser  $h$  was calculated as  $\sim 1244.3 \mu\text{m}$  [ $h = (2 \times 3.14 \times \omega^2) / \lambda \times n$ , where  $\omega$  is laser spot size,  $\lambda$  is laser wavelength, i.e. 532 nm and  $n$  is the refractive index of Nd-YAG laser, i.e., 1.825].

Using these parameters and the previously quoted equations (1-3), the EF for the SERS system (p-MBA and electrosprayed AgNPs) was calculated to be  $2 \times 10^8$ .

#### **Comparison of enhancement factor values between electrospray versus drop casted SERS:**

10  $\mu\text{M}$  p-MBA sample was treated with 0.3  $\mu\text{L}$  of electrosprayed and drop casted AgNPs, respectively.

In electrospray, the SERS intensity of  $1586 \text{ cm}^{-1}$  peak was 11191 counts.

In drop cast method, the SERS intensity for the corresponding peak was 1084 counts.

Using EF equation described above, values for electrospray and drop casted SERS were  $2.78 \times 10^8$  and  $5.37 \times 10^7$ , respectively.

Quantification of EF = EF of electrospray/EF of dropcast =  $2.78 \times 10^8 / 5.37 \times 10^7 = 5.2$

#### **References:**

- 1 A. Michota and J. Bukowska, *J. Raman Spectrosc.*, 2003, **34**, 21–25.
- 2 Y. Zong, Q. Guo, M. Xu, Y. Yuan, R. Gao and J. Yao, *RSC Adv.*, 2014, **4** (60), 31810–31816.
- 3 S. Vishnupriya, K. Chaudhari, R. Jagannathan and T. Pradeep, *Part. Part. Syst. Charact.*, 2013, **30**, 1056–1062.
- 4 K. Chaudhari and T. Pradeep, *J. Biomed. Opt.*, 2015, **20**, 046011.
- 5 P. L. Stiles, J. A. Dieringer, N. C. Shah and R. P. Van Duyne, *Annu. Rev. Anal. Chem.*, 2008, **1**, 601–26.
- 6 A. Li, Z. Baird, S. Bag, D. Sarkar, A. Prabhath, T. Pradeep and Cooks, *Angew. Chemie - Int. Ed.*, 2014, **53**, 12528–12531.

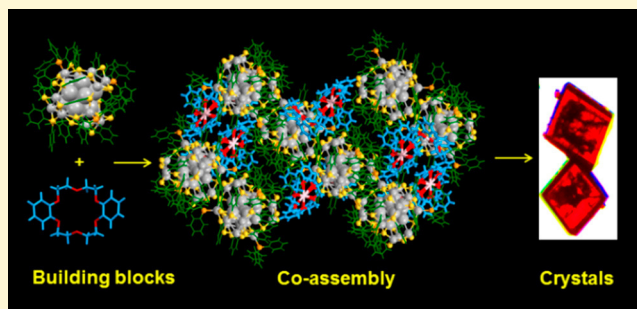
# Crystallization of a Supramolecular Coassembly of an Atomically Precise Nanoparticle with a Crown Ether

Papri Chakraborty, Abhijit Nag, Korath Shivan Sugi, Tripti Ahuja, Babu Varghese, and Thalappil Pradeep\*<sup>✉</sup>

Department of Chemistry, DST Unit of Nanoscience and Thematic Unit of Excellence, Indian Institute of Technology Madras, Chennai 600 036, India

## S Supporting Information

**ABSTRACT:** We report the crystal structure of a supramolecular coassembly of a red luminescent silver cluster,  $[\text{Ag}_{29}(\text{BDT})_{12}(\text{TPP})_4]^{3-}$  (referred to as  $\text{Ag}_{29}$ ) (BDT, 1,3-benzene dithiol; TPP, triphenyl phosphine), with dibenzo-18-crown-6 (DB18C6). The structure may be viewed as crystallization-induced self-organization of DB18C6 molecules into cage-like hexamers in the interstitial spaces of the lattice of trigonal  $\text{Ag}_{29}$  ( $\text{Ag}_{29}\text{T}$ ) clusters, which resulted in an anisotropic expansion of the  $\text{Ag}_{29}\text{T}$  lattice along its  $z$ -axis. This structure corresponds to a new family of “lattice inclusion” compounds in nanoclusters. Supramolecular forces guide the assembly of the clusters and the crown ethers, which pack into complex hierarchical patterns in their crystal lattice. We identified the effect of such a coassembly on the solid-state luminescence of the cluster. The crystals containing the coassembly were  $\sim 3.5$ -fold more luminescent than the parent  $\text{Ag}_{29}\text{T}$  crystals. We also used high-resolution electrospray ionization mass spectrometry to get further insights into the nature of the complexation between  $\text{Ag}_{29}$  cluster and DB18C6. This study provides a new strategy for designing cluster-assembled functional materials with enhanced properties.



Atomically precise noble metal nanoclusters exhibit a rich diversity in their core and ligand structures.<sup>1–6</sup> Precision in their structure, optical absorption features, and chemical reactivity confirm the molecular nature of such particles.<sup>7,8</sup> Because of their unique physical and chemical properties, they also find applications in sensing, catalysis,<sup>9</sup> and optoelectronics.<sup>10</sup> Noncovalent interactions of the ligands, such as  $\text{C}-\text{H}\cdots\pi$ ,  $\pi-\pi$ , H-bonding, van der Waals, electrostatic interactions, etc., can induce different forms of assemblies in them.<sup>11</sup> Such interactions also play an important role in organizing the clusters in their crystal lattice.<sup>12–14</sup> Self-organization of the ligands into various patterns was observed in the lattice of  $[\text{Au}_{246}(\text{p-MBT})_{80}]$ ,<sup>15</sup> and the packing was similar to that observed in biomolecules. Noncovalent interactions also controlled polymorphism in  $[\text{Ag}_{29}(\text{BDT})_{12}(\text{TPP})_4]^{3-}$  (BDT, 1,3-benzene dithiol; TPP, triphenyl phosphine) clusters.<sup>16</sup> Extensive H-bonding was observed in the lattice of the cluster,  $[\text{Ag}_{44}(\text{p-MBA})_{30}]^{4-}$  (p-MBA, para mercapto benzoic acid).<sup>12</sup> Self-organization of  $[\text{Au}_{102}(\text{p-MBA})_{44}]$  clusters into colloidal sheets and capsids were also driven by weak supramolecular forces.<sup>17</sup> Moreover, noncovalent interactions were decisive in determining the assemblies formed by clusters with cyclodextrins (CDs)<sup>18,19</sup>

and fullerenes.<sup>20,21</sup> Mathew et al. showed that supramolecular functionalization of  $[\text{Au}_{25}(\text{SBB})_{18}]^-$  (SBB is 4-(*t*-butyl)benzyl mercaptan) clusters with CDs increased the stability of the cluster core and enhanced the luminescence of the cluster.<sup>18</sup> Nag et al. demonstrated that supramolecular complexation can lead to the emergence of interesting properties like isomerism in nanoclusters.<sup>19</sup> Such reports reveal the growing interest in supramolecular chemistry of atomically precise clusters.<sup>11,22</sup> Though supramolecular assemblies of clusters have been studied using different techniques, such as mass spectrometry, spectroscopy, transmission electron microscopy, theoretical calculations, etc.,<sup>11</sup> the complete structures of the supramolecular adducts of clusters have not yet been solved with atomic precision.

Crown ethers are an interesting class of heterocyclic compounds, which are well-known to form a wide variety of supramolecular host-guest complexes.<sup>23–26</sup> They possess a hydrophilic cavity of ether oxygen atoms which is capable of

Received: August 27, 2019

Accepted: October 8, 2019

Published: October 8, 2019

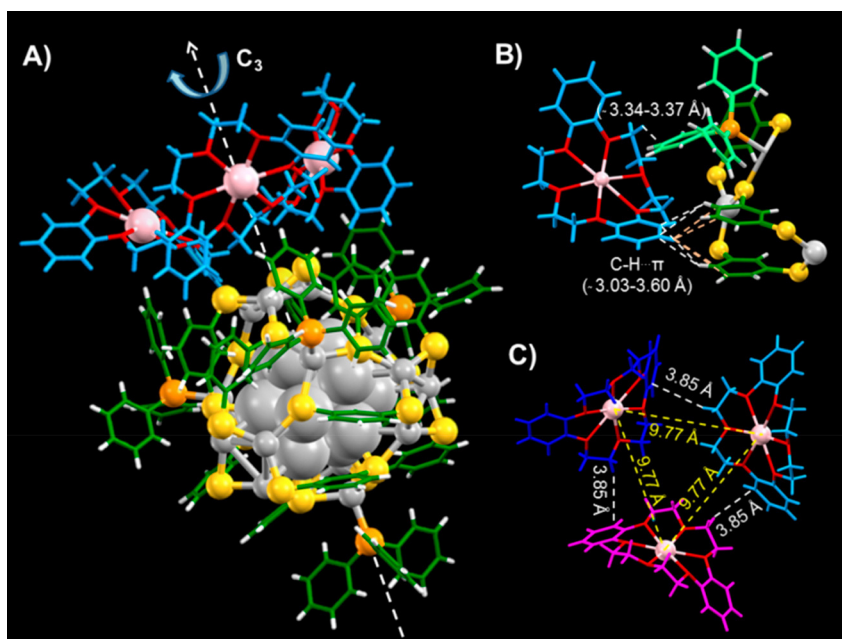


**Figure 1.** (A) Structure of I, (B) expanded view showing the interaction between one of the DB18C6Na<sup>+</sup> molecules and BDT and TPP ligands of the cluster, and (C) expanded view of the three DB18C6Na<sup>+</sup> molecules attached on the cluster surface. Color codes: gray, Ag; yellow, S; orange, P; red, O; green, C of BDT and TPP; white, H of BDT and TPP; light blue, C and H of DB18C6; pink, Na. In panel C, C and H of the three DB18C6Na<sup>+</sup> molecules are colored differently in light blue, dark blue, and purple, respectively.

capturing alkali and alkaline earth metal ions, and surrounding this cavity there are hydrophobic ethylenic groups. Functionalized crown ethers have also been designed due to the possibilities of new properties that can be generated in them.<sup>27</sup> Due to such properties, crown ethers find numerous applications in phase-transfer catalysis,<sup>26</sup> ion transport mechanism,<sup>28</sup> and as building blocks for supramolecular assemblies.<sup>25</sup> Supramolecular architectures resulting from the interaction of functionalized crown ethers with polyoxometallates have been examined.<sup>29,30</sup> Recently, Guy et al. reported that molybdenum cluster salts, such as A<sub>2</sub>MoX<sub>14</sub> (A = Cs/K and X = Cl/Br), can interact with functionalized 15-crown-5 and assemble into liquid crystalline phases with strong NIR emission.<sup>31</sup> Such studies suggest the potential of using crown ethers as building blocks for designing advanced functional materials.

Herein, we resolved the crystal structure of a supramolecular coassembly of an atomically precise red luminescent cluster, [Ag<sub>29</sub>(BDT)<sub>12</sub>(TPP)<sub>4</sub>]<sup>3-</sup> (referred to as Ag<sub>29</sub>)<sup>32</sup> with dibenzo-18-crown-6 (DB18C6). By using single-crystal X-ray diffraction (SCXRD), we show that the crown ethers self-organized into cage-like hexamers in the void spaces of the lattice of Ag<sub>29</sub> clusters. This resulted in an anisotropic expansion of the lattice of the parent cluster. We also investigated the effect of such a coassembly on the solid-state luminescence of the cluster and investigated the mechanism of assembly formation by using high-resolution electrospray ionization mass spectrometry (ESI MS).

Ag<sub>29</sub> cluster was chosen as the model cluster system for this study due to its high stability and luminescence properties. The cluster was synthesized following a reported protocol<sup>32</sup> and characterized using optical absorption and ESI MS (Figure S1). Vapor diffusion of methanol into a dimethylformamide solution of Ag<sub>29</sub> and DB18C6 resulted in the formation of dark red crystals (Figure S2) containing the coassembly of the two entities. Details of synthesis and crystallization are presented in

**Supporting Information.** SCXRD revealed the existence of two molecules, [Ag<sub>29</sub>(BDT)<sub>12</sub>(TPP)<sub>4</sub>][(DB18C6Na)<sub>3</sub>] (I) and [Ag<sub>29</sub>(BDT)<sub>12</sub>(TPP)][(DB18C6Na)<sub>3</sub>] (II), with a relative occupancy of 0.765:0.235 in the crystal lattice. The crystal structure of I is shown in Figure 1A. Three DB18C6Na<sup>+</sup> molecules were assembled over one of the Ag<sub>3</sub>S<sub>3</sub> faces of the cluster and oriented symmetrically around the C<sub>3</sub> axis of I, which passed through the center of the icosahedron of the cluster and the Ag–P bond opposite to the Ag<sub>3</sub>S<sub>3</sub> face. As crown ethers bind to alkali metal ions, Na<sup>+</sup> was trapped in the cavity of DB18C6.<sup>33</sup> Though Na<sup>+</sup> was not added externally during the crystallization process, the source of Na<sup>+</sup> was probably NaBH<sub>4</sub> used for cluster synthesis. Intermolecular C–H...π interactions between DB18C6Na<sup>+</sup> and the BDT and TPP ligands of the cluster existed in the crystal structure. Moreover, electrostatic interactions between the anionic Ag<sub>29</sub> cluster and the three cationic units, DB18C6Na<sup>+</sup>, favored the crystallization. An expanded view showing the interactions between one DB18C6Na<sup>+</sup> molecule and the neighboring BDT and TPP ligands of the cluster is presented in Figure 1B. One of the benzene rings of DB18C6Na<sup>+</sup> comes in close proximity to a pair of BDT ligands of the cluster, and interacted by intense C–H...π contacts at distances of ~3.03–3.60 Å, which is comparable to the interaction distances observed in other supramolecular adducts of clusters.<sup>11</sup> The C–H of the –CH<sub>2</sub> group of DB18C6Na<sup>+</sup> also interacted with the aromatic ring of a TPP ligand at a distance of ~3.34–3.37 Å. The three DB18C6Na<sup>+</sup> molecules, attached on the cluster surface, also interacted between themselves through intermolecular C–H...π contacts at interaction distances of ~3.85 Å (Figure 1C). The Na<sup>+</sup> at the center of three crown ethers were oriented in a triangular fashion with a distance of 9.77 Å between them, as shown in Figure 1C, and the 3-fold symmetry axis of I passed through the center of this triangle. In addition, H<sub>2</sub>O was also coordinated to Na<sup>+</sup> with a Na–O distance of ~2.33 Å (Figure S3). II also showed similar geometry but it contained only one



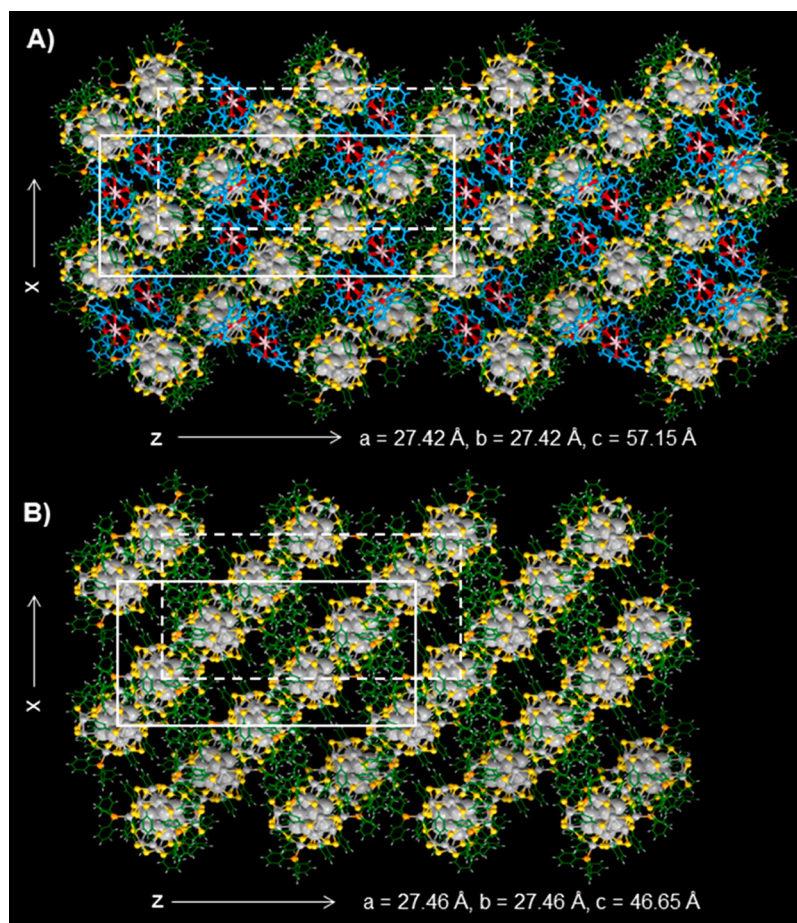


Figure 2. Crystallographic packing of (A) I and (B)  $\text{Ag}_{29}\text{T}$ , viewed from  $y$ -axis.

TPP ligand, which is opposite to the site of attachment of the crown ethers (Figure S4). Due to the labile binding of the TPP ligands of  $\text{Ag}_{29}$  cluster, some of them were lost during crystallization to form II, which constituted a minor component in the crystal lattice. The structure was also carefully explored to find whether any meaningful disorder or inexplicable connectivity existed at any other part of the structure. But none could be found, indicating that no other molecule/fragment existed in the lattice. Further details on solving the crystal structure is presented in the supporting information (Table S1).

A mixture of I and II crystallized into a single crystal in the trigonal crystal system and  $R\bar{3}$  space group. I and II share the same site in X-ray structure of which 76.5% of the sites in the crystal are occupied by I and 23.5% are occupied by II. The crystal containing the mixture of I and II is referred to as  $\text{Ag}_{29}\text{-DB18C6}$  in the following discussion. The packing of  $\text{Ag}_{29}\text{-DB18C6}$  was comparable to the packing of the trigonal polymorph of  $\text{Ag}_{29}$  clusters ( $\text{Ag}_{29}\text{T}$ ).<sup>16</sup> Along the  $z$ -axis, the unit cell was elongated to 57.15 Å in case of  $\text{Ag}_{29}\text{-DB18C6}$ , compared to 46.65 Å in case of  $\text{Ag}_{29}\text{T}$ , whereas the dimensions along the  $x$ - and  $y$ -axis were similar in both cases. This expansion of the lattice along one direction expanded the volume of the unit cell to 37,225 Å<sup>3</sup>, from the unit cell volume of 30,474 Å<sup>3</sup> of  $\text{Ag}_{29}\text{T}$ .<sup>16</sup> Anisotropic expansion of the crystal lattice by the inclusion of guest molecules was also observed in the case of inclusion of gases in the lattice of clathrate hydrates.<sup>34</sup> A view of the packing of I and  $\text{Ag}_{29}\text{T}$  from the  $y$ -axis, presented in Figure 2A and B, revealed that the interstitial

spaces in the lattice of  $\text{Ag}_{29}\text{T}$  were occupied by DB18C6. The crown ethers were packed in between the clusters by  $\text{C-H}\cdots\pi$  contacts, which increased the inter-cluster distances by  $\sim 0.53$  nm along  $z$ -axis, compared to that of  $\text{Ag}_{29}\text{T}$ . The nature of packing was similar when viewed from the  $x$ -axis (Figure S5). A view from the  $z$ -axis showed that the void spaces along the  $z$ -axis of  $\text{Ag}_{29}\text{T}$  were occupied by the crown ethers in the case of I (Figure S6). The packing of II was also similar. The extensive interlocking of ligands in the lattice of  $\text{Ag}_{29}\text{-DB18C6}$  resulted in a densely packed structure. Moreover, the crown ethers were assembled into discrete hexameric units throughout the crystal lattice, view from the  $y$ -axis is presented in Figure 3A. The formation of these hexamers of crown ethers was favored by local intermolecular  $\text{C-H}\cdots\pi$  contacts and the symmetry of the crystal packing. An expanded view of one such unit,  $(\text{DB18C6Na})_6^{6+}$ , presented in Figure 3B, reveals that each hexamer formed a hollow cage-like structure, where the pairs of opposite crown ethers on the surface of the cage were related by a centre of inversion. The six Na atoms of the cage were oriented in rectangular bipyramidal geometry (Figure 3C). Six water molecules were trapped inside the cavity of these supramolecular cages (Figure S7). Similar molecular cages were also observed in the case of hexameric assemblies of resorcarenes,<sup>35</sup> calixarenes,<sup>36</sup> insulin,<sup>37</sup> etc., and such cages usually act as hosts for trapping guest molecules,<sup>38</sup> and also as molecular capsules for catalyzing certain reactions.<sup>39</sup> Thus, crystal structure of  $\text{Ag}_{29}\text{-DB18C6}$  may be described as a “lattice inclusion compound” or “lattice clathrate”,<sup>40</sup> where guest molecules (crown ether hexamers) get crystallized in the



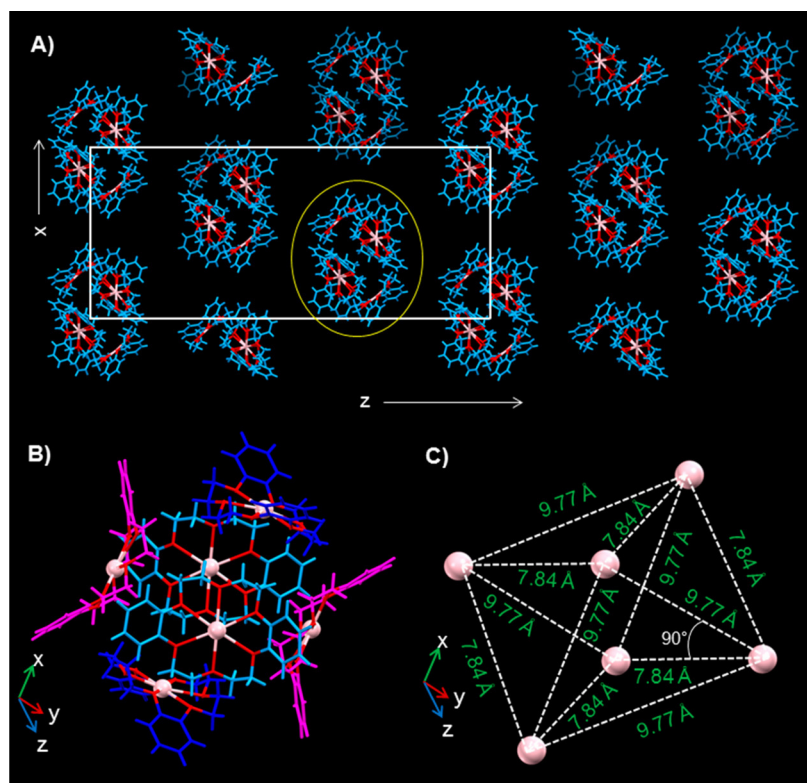


**Figure 3.** (A) Packing of DB18C6Na<sup>+</sup> molecules into hexameric units throughout the crystal lattice, view from the y-axis. (B) Expanded view of one of the hexameric units (circled in yellow in A) showing the formation of cage-like structures. Opposite crown ethers, shown in similar colors, are related by a center of inversion. (C) The orientation of the Na<sup>+</sup> of the crown ether hexamer in a rectangular bipyramidal geometry.

interstitial spaces of the host lattice (Ag<sub>29</sub>T) and depending on the size of the guest molecules, expansion of the crystal lattice occurs. Such a phenomenon was not observed earlier in the case of nanoclusters.

In the structure of I/II, two types of host-guest interactions may be visualized: first, at the molecular level where crown ethers trap Na<sup>+</sup> and secondly, complexation of these crown ethers with the cluster, where the cluster can be considered as a colloidal-level molecule. Moreover, from the packing of Ag<sub>29</sub>-DB18C6, it is evident that Ag<sub>29</sub> clusters and DB18C6 molecules show hierarchical assembly in their crystal lattice. While the lattice of the cluster acts as a host for trapping the crown ether cages, these cages further act as a host for trapping water as the guest molecules. Further, the cages themselves are formed by self-organization of six DB18C6Na<sup>+</sup> units and each DB18C6Na<sup>+</sup> unit is formed by the capture of Na<sup>+</sup> in the cavity of DB18C6. In the crystal lattice, there are cluster–cluster, crown ether–crown ether, and cluster–crown ether interactions. Supramolecular forces guide the assembly behavior at each level. The packing patterns represent an emerging phenomenon in nanoscience where simple building blocks evolve into complex architectures with new features that are not manifested in individual entities.

We compared the emission from both Ag<sub>29</sub>-DB18C6 and Ag<sub>29</sub>T to understand the effect of the noncovalent interactions on their solid-state luminescence. Though the density of the particles in Ag<sub>29</sub>-DB18C6 (~1.85 g cm<sup>-3</sup>), was slightly less compared to the density in the lattice of Ag<sub>29</sub>T (~2.041 g cm<sup>-3</sup>), there was ~3.5 fold enhancement in the luminescence of the former (excitation at 532 nm). Details of the luminescence measurements and calculation of enhancement

factors are discussed under the experimental section in the [Supporting Information](#). Dense packing of the ligands in the case of Ag<sub>29</sub>-DB18C6 resulted in greater rigidity and restriction of the intramolecular rotations of the TPP ligands which caused an enhancement of the radiative transitions,<sup>16,41,42</sup> compared to the lattice of Ag<sub>29</sub>T. Ion pairing effects of the negatively charged clusters with the positively charged DB18C6Na<sup>+</sup> in their crystal may have also contributed to the enhancement of the luminescence.<sup>43</sup> The slight red shift and broadening in the emission spectrum of Ag<sub>29</sub>-DB18C6 may be attributed to changes in electronic coupling and electron-phonon interactions<sup>32</sup> in the two crystals. Despite the structural complexity of the inclusion compound (Ag<sub>29</sub>-DB18C6), the uniformity in the properties of the single crystal makes the luminescence comparison possible. Similar phenomenon was also observed in the case of the polymorphic crystals of the cluster where the cubic polymorph (Ag<sub>29</sub>C) exhibited a more rigid packing and higher luminescence compared to Ag<sub>29</sub>T.<sup>16</sup> The Ag<sub>29</sub>-DB18C6 crystals were more luminescent compared to Ag<sub>29</sub>C (density ~2.11 g cm<sup>-3</sup>) too ([Figure S8](#)). However, when Ag<sub>29</sub>-DB18C6 crystals were dissolved in DMF, there was no change in the emission compared to the solution-phase emission of the parent Ag<sub>29</sub> clusters ([Figure S9A](#)), which further supported that the enhancement was due to the strong intermolecular interactions in the crystalline state and in solution-phase such intermolecular interactions were lost due to random arrangement of the molecules. The optical absorption features were also unchanged compared to that of the parent cluster ([Figure S9B](#)), which suggested weak interaction between the molecules in solution.

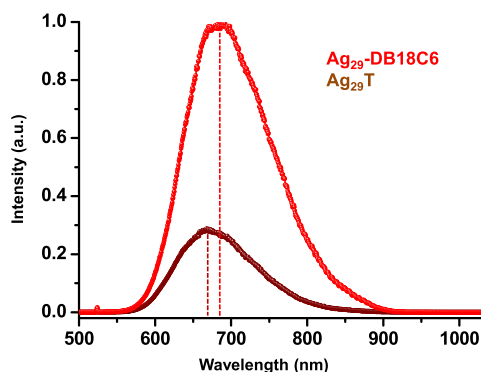


Figure 4. Emission from  $\text{Ag}_{29}$ -DB18C6 and  $\text{Ag}_{29}\text{T}$  crystals, excited at 532 nm.

To understand the nature of solution-phase complexation, we dissolved the  $\text{Ag}_{29}$ -DB18C6 crystals in DMF and analysed these by ESI MS. In the negative ion mode, the adducts,  $[\text{Ag}_{29}(\text{BDT})_{12}(\text{TPP})_n(\text{DB18C6})_m]^{3-}$  ( $n = 0-4$ ,  $m = 0-3$ ) were detected (Figure 5). The peaks are labelled with  $(n, m)$

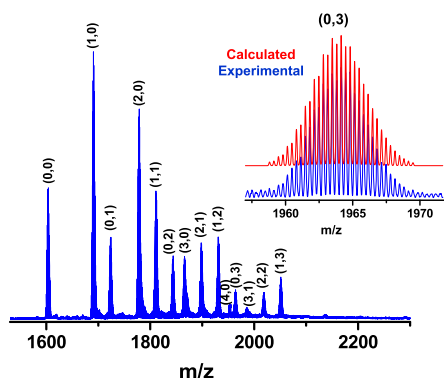


Figure 5. ESI MS from the crystals of coassemblies of  $\text{Ag}_{29}$  cluster and DB18C6, dissolved in DMF, in negative mode showing the detection of the adducts,  $[\text{Ag}_{29}(\text{BDT})_{12}(\text{TPP})_n(\text{DB18C6})_m]^{3-}$  ( $n = 0-4$ ,  $m = 0-3$ ). The comparison of the theoretical and experimental isotopic distribution patterns of  $[\text{Ag}_{29}(\text{BDT})_{12}(\text{DB18C6})_3]^{3-}$  is shown in the inset. The labels  $(x, y)$  means  $x$  = number of TPP ( $n$ ) and  $y$  = number of DB18C6 molecules ( $m$ ) attached to the cluster.

indices. As the TPP ligands were labile and DB18C6 molecules were noncovalently bound, they were detached from the cluster during ionization. This complicated the exact quantification of the adducts and the abundances of the species could not be compared with their occupancy in the crystal structure. However, a maximum of three DB18C6 molecules was found to be attached to the cluster with varying number of TPP ligands. Moreover, in the positive ion mode, the species,  $\text{DB18C6Na}^+$  was detected (Figure S10). This suggested the existence of two types of equilibria in solution: (i) attachment of neutral DB18C6 to the cluster and (ii) capture of  $\text{Na}^+$  by DB18C6. Both these processes contributed to the crystallization of  $\text{Ag}_{29}$ -DB18C6.

In summary, we crystallized a supramolecular coassembly of  $\text{Ag}_{29}$  and DB18C6 molecules. The structure showed an anisotropic expansion of the parent  $\text{Ag}_{29}\text{T}$  lattice due to the incorporation of DB18C6 hexamers in the interstitial spaces of its lattice. The crystals of the coassembly of  $\text{Ag}_{29}$  with DB18C6 exhibited greater luminescence compared to the crystals of the

parent  $\text{Ag}_{29}\text{T}$ . This supramolecule may find application as a luminescent probe for selective cation sensing. The hexameric cages of crown ethers in the crystal lattice may also be utilized for trapping gases or other suitable guest molecules. Similar interactions may also be explored for a range of different clusters and crown ethers. The crystallization of such supramolecular assemblies of clusters unfolds a new direction in nanoparticle engineering and such functional materials may show enhanced optical and mechanical properties. By choosing the appropriate crown ether, cluster assembled liquid crystalline phases may be created, which may find applications in optoelectronic devices. As crown ethers are sensitive to all alkali metal ions, others, such as  $\text{Li}^+$ , may be incorporated in the nanoparticle assemblies and these modified materials may find applications in electrochemical devices. Noble metal cluster assemblies assisted by crown ethers are expected to enhance the area.

## ■ ASSOCIATED CONTENT

### Supporting Information

The Supporting Information is available free of charge on the ACS Publications website at DOI: 10.1021/acsmaterialslett.9b00352.

Materials and methods, crystal structure data, optical absorption and emission, and ESI MS (PDF)

Crystallographic information file for  $\text{Ag}_{29}$ -DB18C6 (CIF)

## ■ AUTHOR INFORMATION

### Corresponding Author

\*E-mail: pradeep@iitm.ac.in.

### ORCID

Thalappil Pradeep: 0000-0003-3174-534X

### Notes

The authors declare no competing financial interest.

CCDC 1888965 contains the crystallographic data for this paper. These data are provided free of charge by The Cambridge Crystallographic Data Centre.

## ■ ACKNOWLEDGMENTS

P.C. thanks the Council of Scientific and Industrial Research (CSIR) for a research fellowship. A.N. and T.A. thank IITM for their fellowship. K.S.S. thanks the University Grants Commission (UGC) for her fellowship. We thank the Department of Science and Technology, Government of India, for continuously supporting our research programme. We thank the Sophisticated Analytical Instruments Facility, IITM, for SCXRD data collection. Authors thank Dr. Sudhadevi Antharjanam for useful discussions on the SCXRD data.

## ■ REFERENCES

- (1) Chakraborty, I.; Pradeep, T. Atomically Precise Clusters of Noble Metals: Emerging Link between Atoms and Nanoparticles. *Chem. Rev.* **2017**, *117*, 8208–8271.
- (2) Jin, R.; Zeng, C.; Zhou, M.; Chen, Y. Atomically Precise Colloidal Metal Nanoclusters and Nanoparticles: Fundamentals and Opportunities. *Chem. Rev.* **2016**, *116*, 10346–10413.
- (3) Yao, Q.; Chen, T.; Yuan, X.; Xie, J. Toward Total Synthesis of Thiolate-Protected Metal Nanoclusters. *Acc. Chem. Res.* **2018**, *51*, 1338–1348.

- (4) Maity, P.; Xie, S.; Yamauchi, M.; Tsukuda, T. Stabilized Gold Clusters: From Isolation toward Controlled Synthesis. *Nanoscale* **2012**, *4*, 4027–4037.
- (5) Ghosh, A.; Mohammed, O. F.; Bakr, O. M. Atomic-Level Doping of Metal Clusters. *Acc. Chem. Res.* **2018**, *51*, 3094–3103.
- (6) Krishnadas, K. R.; Natarajan, G.; Baksi, A.; Ghosh, A.; Khatun, E.; Pradeep, T. Metal–Ligand Interface in the Chemical Reactions of Ligand-Protected Noble Metal Clusters. *Langmuir* **2019**, *35*, 11243–11254.
- (7) Krishnadas, K. R.; Baksi, A.; Ghosh, A.; Natarajan, G.; Som, A.; Pradeep, T. Interparticle reactions: An Emerging Direction in Nanomaterials Chemistry. *Acc. Chem. Res.* **2017**, *50*, 1988–1996.
- (8) Natarajan, G.; Mathew, A.; Negishi, Y.; Whetten, R. L.; Pradeep, T. A Unified Framework for Understanding the Structure and Modifications of Atomically Precise Monolayer Protected Gold Clusters. *J. Phys. Chem. C* **2015**, *119*, 27768–27785.
- (9) Higaki, T.; Li, Y.; Zhao, S.; Li, Q.; Li, S.; Du, X.-S.; Yang, S.; Chai, J.; Jin, R. Atomically Tailored Gold Nanoclusters for Catalytic Application. *Angew. Chem.* **2019**, *131*, 8377–8388.
- (10) Mathew, A.; Pradeep, T. Noble Metal Clusters: Applications in Energy, Environment, and Biology. *Part. Part. Syst. Char.* **2014**, *31*, 1017–1053.
- (11) Chakraborty, P.; Nag, A.; Chakraborty, A.; Pradeep, T. Approaching Materials with Atomic Precision using Supramolecular Cluster Assemblies. *Acc. Chem. Res.* **2019**, *52*, 2–11.
- (12) Yoon, B.; Luedtke, W. D.; Barnett, R. N.; Gao, J.; Desiredy, A.; Conn, B. E.; Bigioni, T.; Landman, U. Hydrogen-Bonded Structure and Mechanical Chiral Response of a Silver Nanoparticle Superlattice. *Nat. Mater.* **2014**, *13*, 807.
- (13) Yao, Q.; Yu, Y.; Yuan, X.; Yu, Y.; Zhao, D.; Xie, J.; Lee, J. Y. Counterion-Assisted Shaping of Nanocluster Supracrystals. *Angew. Chem., Int. Ed.* **2015**, *54*, 184–189.
- (14) Li, Q.; Russell, J. C.; Luo, T.-Y.; Roy, X.; Rosi, N. L.; Zhu, Y.; Jin, R. Modulating the Hierarchical Fibrous Assembly of Au Nanoparticles with Atomic Precision. *Nat. Commun.* **2018**, *9*, 3871.
- (15) Zeng, C.; Chen, Y.; Kirschbaum, K.; Lambright, K. J.; Jin, R. Emergence of Hierarchical Structural Complexities in Nanoparticles and their Assembly. *Science* **2016**, *354*, 1580–1584.
- (16) Nag, A.; Chakraborty, P.; Bodiuzzaman, M.; Ahuja, T.; Antharjanam, S.; Pradeep, T. Polymorphism of  $\text{Ag}_{29}(\text{BDT})_{12}(\text{TPP})_4^{3-}$  Cluster: Interactions of Secondary Ligands and their Effect on Solid State Luminescence. *Nanoscale* **2018**, *10*, 9851–9855.
- (17) Nonappa; Lahtinen, T.; Haataja, J. S.; Tero, T.-R.; Häkkinen, H.; Ikkala, O. Template-Free Supracolloidal Self-Assembly of Atomically Precise Gold Nanoclusters: From 2D Colloidal Crystals to Spherical Capsids. *Angew. Chem., Int. Ed.* **2016**, *55*, 16035–16038.
- (18) Mathew, A.; Natarajan, G.; Lehtovaara, L.; Häkkinen, H.; Kumar, R. M.; Subramanian, V.; Jaleel, A.; Pradeep, T. Supramolecular Functionalization and Concomitant Enhancement in Properties of  $\text{Au}_{25}$  Clusters. *ACS Nano* **2014**, *8*, 139–152.
- (19) Nag, A.; Chakraborty, P.; Paramasivam, G.; Bodiuzzaman, M.; Natarajan, G.; Pradeep, T. Isomerism in Supramolecular Adducts of Atomically Precise Nanoparticles. *J. Am. Chem. Soc.* **2018**, *140*, 13590–13593.
- (20) Chakraborty, P.; Nag, A.; Paramasivam, G.; Natarajan, G.; Pradeep, T. Fullerene-Functionalized Monolayer-Protected Silver Clusters:  $[\text{Ag}_{29}(\text{BDT})_{12}(\text{C}_{60})_n]^{3-}$  ( $n = 1-9$ ). *ACS Nano* **2018**, *12*, 2415–2425.
- (21) Ahmed, G. H.; Parida, M. R.; Tosato, A.; AbdulHalim, L. G.; Usman, A.; Alsulami, Q. A.; Murali, B.; Alarousu, E.; Bakr, O. M.; Mohammed, O. F. The Impact of Electrostatic Interactions on Ultrafast Charge Transfer at  $\text{Ag}_{29}$  Nanoclusters–Fullerene and CdTe Quantum Dots–Fullerene Interfaces. *J. Mater. Chem. C* **2016**, *4*, 2894–2900.
- (22) Nonappa; Ikkala, O. Hydrogen Bonding Directed Colloidal Self-Assembly of Nanoparticles into 2D Crystals, Capsids, and Supracolloidal Assemblies. *Adv. Funct. Mater.* **2018**, *28*, 1704328.
- (23) Gokel, G. W.; Leevy, W. M.; Weber, M. E. Crown Ethers: Sensors for Ions and Molecular Scaffolds for Materials and Biological Models. *Chem. Rev.* **2004**, *104*, 2723–2750.
- (24) Elbasyouny, A.; Bruegge, H. J.; Von Deuten, K.; Dickel, M.; Knochel, A.; Koch, K. U.; Kopf, J.; Melzer, D.; Rudolph, G. Host-Guest Complexes of 18-Crown-6 with Neutral Molecules Possessing the Structure Element  $\text{XH}_2$  ( $\text{X} = \text{Oxygen, Nitrogen, or Carbon}$ ). *J. Am. Chem. Soc.* **1983**, *105*, 6568–6577.
- (25) Liu, Z.; Nalluri, S. K. M.; Stoddart, J. F. Surveying Macrocyclic Chemistry: From Flexible Crown Ethers to Rigid Cyclophanes. *Chem. Soc. Rev.* **2017**, *46*, 2459–2478.
- (26) Hiraoka, M. *Crown Ethers and Analogous Compounds*; Elsevier Science & Technology Books, 1992.
- (27) Shinkai, S. *Functionalization of Crown Ethers and Calixarenes: New Applications as Ligands, Carriers, and Host Molecules*; Springer: Berlin, 1990; pp 161–195.
- (28) He, G.-X.; Kurita, M.; Ishii, I.; Wada, F.; Matsuda, T. New Applications of Crown Ethers. 11. Structural Effect of the Counter Anion on Crown-Ether Mediated Cation Extraction and Transport. A Direct Examination of the Crown Ether-Cation Complex in the Organic Phase of Extraction and Transport. *J. Membr. Sci.* **1992**, *69*, 61–73.
- (29) You, W.; Wang, E.; Xu, Y.; Li, Y.; Xu, L.; Hu, C. An Alkali Metal–Crown Ether Complex Supported by a Keggin Anion through the Three Terminal Oxygen Atoms in a Single  $\text{M}_3\text{O}_{13}$  Triplet: Synthesis and Characterization of  $[\{\text{Na}(\text{Dibenzo-18-Crown-6})-(\text{MeCN})\}_3\{\text{PMo}_{12}\text{O}_{40}\}]$ . *Inorg. Chem.* **2001**, *40*, 5468–5471.
- (30) Akutagawa, T.; Endo, D.; Noro, S.-I.; Cronin, L.; Nakamura, T. Directing Organic–Inorganic Hybrid Molecular-Assemblies of Polyoxometalate Crown-Ether Complexes with Supramolecular Cations. *Coord. Chem. Rev.* **2007**, *251*, 2547–2561.
- (31) Guy, K.; Ehni, P.; Paofai, S.; Forschner, R.; Roiland, C.; Amela-Cortes, M.; Cordier, S.; Laschat, S.; Molard, Y. Lord of the Crowns: A New Precious in the Kingdom of Clustomesogens. *Angew. Chem., Int. Ed.* **2018**, *57*, 11692–11696.
- (32) AbdulHalim, L. G.; Bootharaju, M. S.; Tang, Q.; Del Gobbo, S.; AbdulHalim, R. G.; Eddaoudi, M.; Jiang, D.-e.; Bakr, O. M.  $\text{Ag}_{29}(\text{BDT})_{12}(\text{TPP})_4$ : A Tetravalent Nanocluster. *J. Am. Chem. Soc.* **2015**, *137*, 11970–11975.
- (33) Li, Y.; Wang, E.; Wang, S.; Lu, Y.; Hu, C.; Hu, N.; Jia, H. Synthesis, Characterization and Crystal Structures of Dibenzo-18-Crown-6 Sodium Isopolytungstates. *J. Mol. Struct.* **2002**, *607*, 133–141.
- (34) Murayama, K.; Takeya, S.; Alavi, S.; Ohmura, R. Anisotropic Lattice Expansion of Structure of Clathrate Hydrates Induced by Help Guest: Experiments and Molecular Dynamics Simulations. *J. Phys. Chem. C* **2014**, *118*, 21323–21330.
- (35) Wierzbicki, M.; Glowacka, A. A.; Szymański, M. P.; Szumna, A. A Chiral Member of the Family of Organic Hexameric Cages. *Chem. Commun.* **2017**, *53*, S200–S203.
- (36) Pasquale, S.; Sattin, S.; Escudero-Adán, E. C.; Martínez-Belmonte, M.; de Mendoza, J. Giant Regular Polyhedra from Calixarene Carboxylates and Uranyl. *Nat. Commun.* **2012**, *3*, 785.
- (37) Smith, G. D.; Swenson, D. C.; Dodson, E. J.; Dodson, G. G.; Reynolds, C. D. Structural Stability in the 4-Zinc Human Insulin Hexamer. *Proc. Natl. Acad. Sci. U. S. A.* **1984**, *81*, 7093–7097.
- (38) Liu, L.; Zhang, Y.; Wang, X.-L.; Luo, G.-G.; Xiao, Z.-J.; Cheng, L.; Dai, J.-C. Supramolecular Network of Triaminotriptycene and its Water Cluster Guest: Synthesis, Structure, and Characterization of  $[(\text{tatr})_4 \cdot 17\text{H}_2\text{O}]_n$ . *Cryst. Growth Des.* **2018**, *18*, 1629–1635.
- (39) Bolliger, J. L. Self-Assembled Coordination Cages and Organic Capsules as Catalytic Supramolecular Reaction Vessels. *Effects of Nanoconfinement on Catalysis*; Poli, R., Ed.; Springer International Publishing: Cham, 2017; pp 17–48.
- (40) Bishop, R. Designing New Lattice Inclusion Hosts. *Chem. Soc. Rev.* **1996**, *25*, 311–319.
- (41) Khatun, E.; Ghosh, A.; Chakraborty, P.; Singh, P.; Bodiuzzaman, M.; Ganesan, P.; Natarajan, G.; Ghosh, J.; Pal, S. K.; Pradeep, T. A Thirty-fold Photoluminescence Enhancement

Induced by Secondary Ligands in Monolayer Protected Silver Clusters. *Nanoscale* **2018**, *10*, 20033–20042.

(42) Chandra, S.; Nonappa, G.; Beaune, G.; Som, A.; Zhou, S.; Lahtinen, J.; Jiang, H.; Timonen, J. V. I.; Ikkala, O.; Ras, R. H. A. Highly Luminescent Gold Nanocluster Frameworks. *Adv. Opt. Mater.* **2019**, 1900620.

(43) Bootharaju, M. S.; Kozlov, S. M.; Cao, Z.; Shkurenko, A.; El-Zohry, A. M.; Mohammed, O. F.; Eddaoudi, M.; Bakr, O. M.; Cavallo, L.; Basset, J.-M. Tailoring the Crystal Structure of Nanoclusters Unveiled High Photoluminescence *via* Ion Pairing. *Chem. Mater.* **2018**, *30*, 2719–2725.



## Supporting Information

### Crystallization of a Supramolecular Coassembly of an Atomically Precise Nanoparticle with a Crown Ether

Papri Chakraborty, Abhijit Nag, Korath Shivan Sugi, Tripti Ahuja, Babu Varghese and Thalappil Pradeep\*

*DST Unit of Nanoscience and Thematic Unit of Excellence, Department of Chemistry, Indian Institute of Technology Madras, Chennai 600036, India*

\*Email: [pradeep@iitm.ac.in](mailto:pradeep@iitm.ac.in)

#### Table of contents

Name	Description	Page no
	Experimental section	S2
Figure S1	UV-vis and ESI MS of $[\text{Ag}_{29}(\text{BDT})_{12}(\text{TPP})_4]^{3-}$ cluster	S3
Figure S2	Optical images of $\text{Ag}_{29}$ -DB18C6 crystals	S4
Figure S3	Expanded view of three DB18C6Na <sup>+</sup> molecules, attached on cluster surface, showing the coordination of H <sub>2</sub> O to Na <sup>+</sup>	S4
Figure S4	Crystal structure of $[\text{Ag}_{29}(\text{BDT})_{12}(\text{TPP})(\text{DB18C6Na})_3]$	S5
Figure S5	Crystallographic packing of A) <b>I</b> and B) $\text{Ag}_{29}\text{T}$ , viewed from x-axis	S6
Figure S6	Crystallographic packing of A) <b>I</b> and B) $\text{Ag}_{29}\text{T}$ , viewed from z-axis	S6
Figure S7	Trapping of water molecules inside the crown ether cages	S7
Figure S8	Emission from $\text{Ag}_{29}$ -DB18C6, $\text{Ag}_{29}\text{T}$ and $\text{Ag}_{29}\text{C}$ crystals, excited at 532 nm	S7
Figure S9	Solution-phase emission and absorption spectra of $\text{Ag}_{29}$ clusters and $\text{Ag}_{29}$ -DB18C6 crystals dissolved in DMF	S8
Figure S10	Positive mode ESI MS showing the detection of DB18C6Na <sup>+</sup> . The comparison of the theoretical and experimental isotope distribution patterns of DB18C6Na <sup>+</sup> is shown in the inset.	S8
Table S1	Crystal structure data	S9

## EXPERIMENTAL SECTION

**Materials.** All the reagents were commercially available and used without further purification. Silver nitrate ( $\text{AgNO}_3$ , 99.9%) was purchased from Rankem, India. 1,3-Benzene dithiol (BDT), dibenzo-18-crown-6 (DB18C6) and  $\text{NaBH}_4$  were purchased from Sigma Aldrich and triphenyl phosphine (TPP) was purchased from Spectrochem, India. The solvents used, MeOH, DCM, DMF, were of the HPLC grade.

**Synthesis of  $[\text{Ag}_{29}(\text{BDT})_{12}(\text{TPP})_4]^{3-}$  cluster.**  $[\text{Ag}_{29}(\text{BDT})_{12}(\text{TPP})_4]^{3-}$  cluster was synthesized following a reported protocol.<sup>1</sup> About 20 mg of  $\text{AgNO}_3$  was dissolved in a mixture of 5 mL methanol and 10 mL DCM. Then, 13.5  $\mu\text{L}$  of BDT ligand was added to this mixture. The color of the solution turned turbid yellow. The mixture was kept under the stirring condition and shortly after this; 200 mg of  $\text{PPh}_3$  dissolved in 1 mL of DCM was added. The solution turned colorless indicating the formation of Ag-S-P complex. After about 15 min, 10.5 mg of  $\text{NaBH}_4$  in 500  $\mu\text{L}$  of water was added. The color of the solution turned to dark brown. Gradually the color changed to orange, indicating the formation of the nanoclusters. After 3 h of continuous reaction under dark conditions, the reaction mixture was centrifuged, and the supernatant was discarded. The precipitate was washed repeatedly with methanol to remove all the unreacted compounds and the purified cluster was extracted in DMF.

**Crystallization of coassemblies of  $[\text{Ag}_{29}(\text{BDT})_{12}(\text{TPP})_4]^{3-}$  clusters with DB18C6.** About 10 mg of  $[\text{Ag}_{29}(\text{BDT})_{12}(\text{TPP})_4]^{3-}$  cluster and 3 mg of DB18C6 was dissolved in 1 mL of DMF and ~ 2.5 mL of MeOH was allowed to vapor diffuse into the solution. Dark red crystals, suitable for SCXRD, were obtained after a week.

## INSTRUMENTATION

Optical absorption measurements were performed in a PerkinElmer Lambda 25 UV-vis spectrophotometer.

A Horiba Jobin Yvon Nanolog spectrometer was used for the photoluminescence measurements in solution. The samples were excited at 450 nm. The excitation and the emission band pass was set at 3 nm.

Emission spectra of crystals were collected in a Witec GmbH, Alpha-SNOM alpha300 S confocal Raman instrument using 532 nm laser as the excitation source. For comparing the luminescence from different crystals, all the parameters like laser power, beam spot size, accumulation time and integration time were kept constant in all cases. The maximum emission intensities were considered to compare the enhancement in luminescence of one crystal with respect to the other. By keeping all the parameters same, number of clusters in the illumination volume will be nearly the same in both (parent and crown ether-included crystals) the cases. Inhomogeneity of the crystal surfaces, if any, are averaged out by multiple measurements.

Mass spectrometric measurements were done with a Waters Synapt G2 Si high resolution mass spectrometer. Measurements were done using the following conditions:

Capillary voltage: 3 kV, Cone voltage: 0 V

Source temperature: 50 °C, Desolvation temperature: 80 °C, Desolvation gas flow: 300 L/h

Single crystal X-ray diffraction data were collected using a Bruker D8 VENTURE APEX3 CMOS. Crystal data and refinement conditions are presented in Table S1. The crystal data has been deposited to The Cambridge Structural Database and the CCDC number: 1888965.

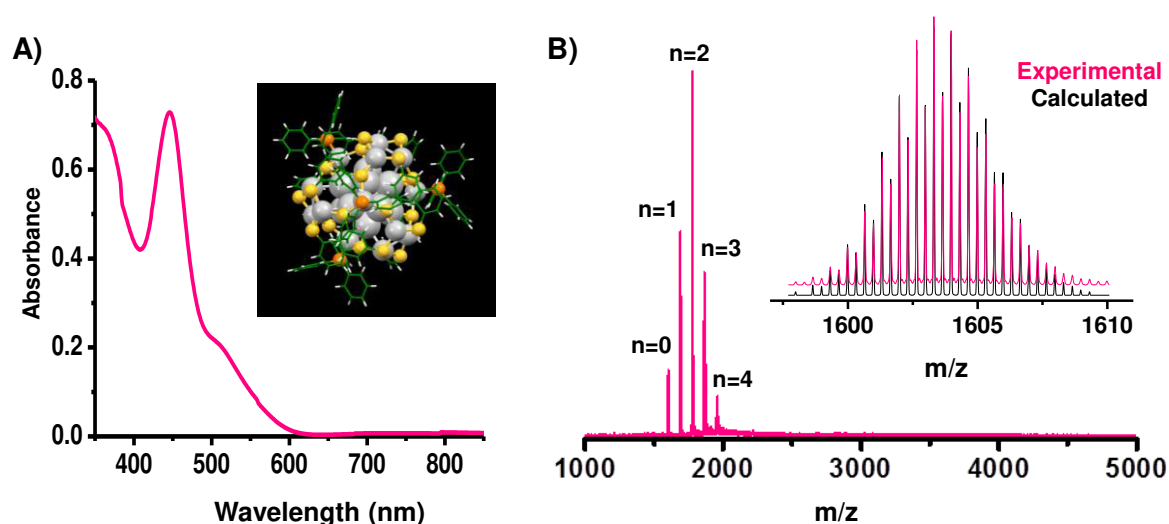


**Figure S1.** A) UV-vis spectrum of  $[\text{Ag}_{29}(\text{BDT})_{12}(\text{TPP})_4]^{3-}$  cluster. Inset shows the structure of the cluster, B) ESI MS of  $[\text{Ag}_{29}(\text{BDT})_{12}(\text{TPP})_n]^{3-}$  ( $n=0-4$ ). Inset shows the comparison of the experimental and theoretical isotopic patterns of  $[\text{Ag}_{29}(\text{BDT})_{12}]^{3-}$ .



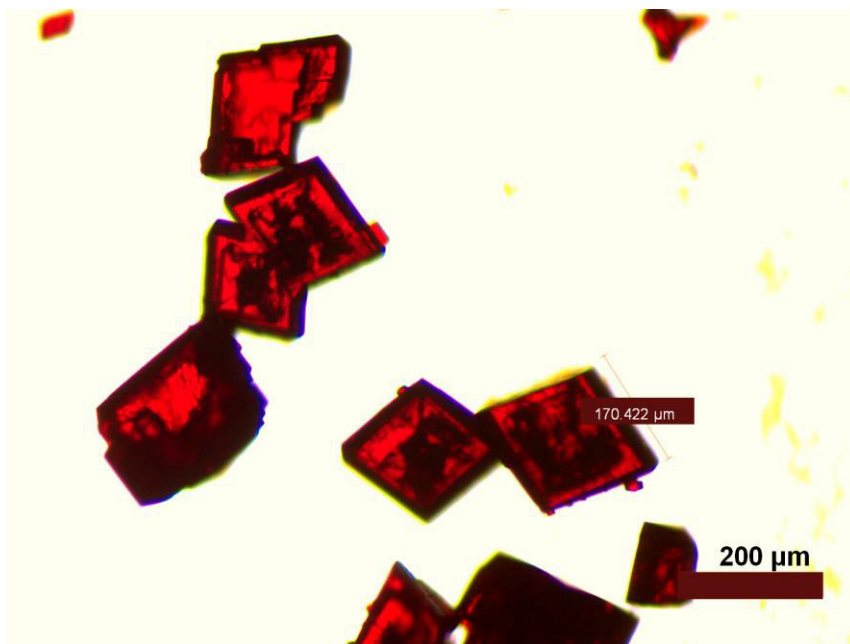


**Figure S2.** Optical images of the crystals of the coassemblies of  $[\text{Ag}_{29}(\text{BDT})_{12}(\text{TPP})_4]^{3-}$  cluster with DB18C6 molecules.

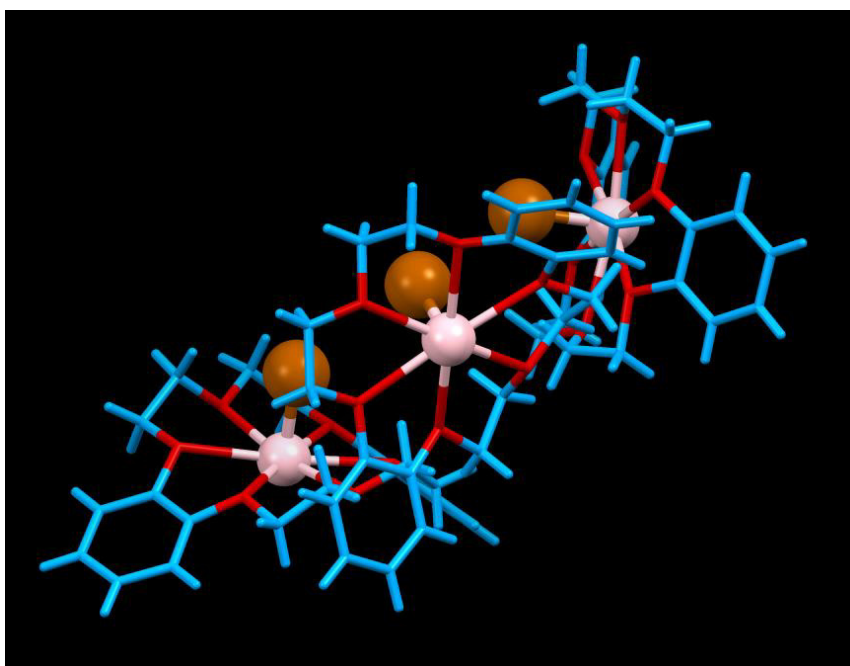


**Figure S3.** Expanded view of the three DB18C6Na<sup>+</sup> molecules attached on the cluster surface, showing the coordination of H<sub>2</sub>O to Na<sup>+</sup>. The O atoms of H<sub>2</sub>O are shown in brown color. The H atoms of H<sub>2</sub>O were not resolved from the crystal structure.

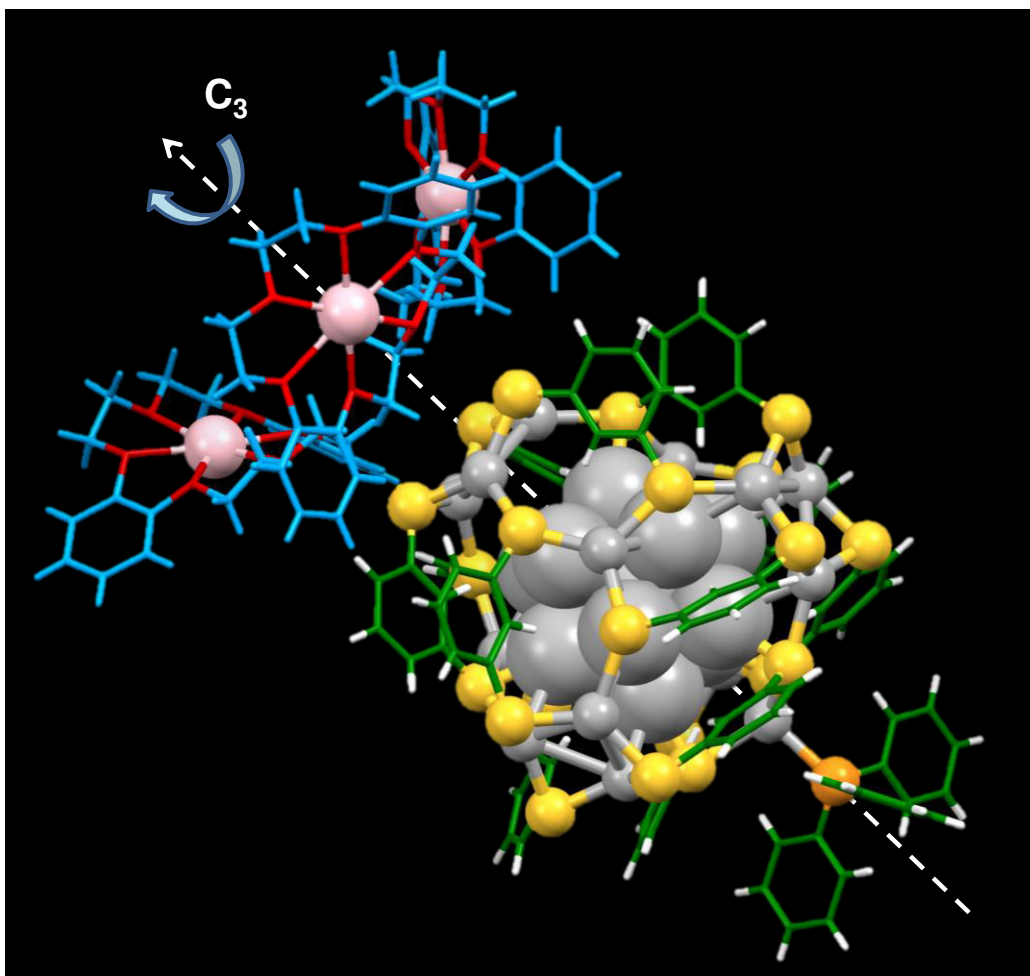


**Figure S4.** Structure of **II**.

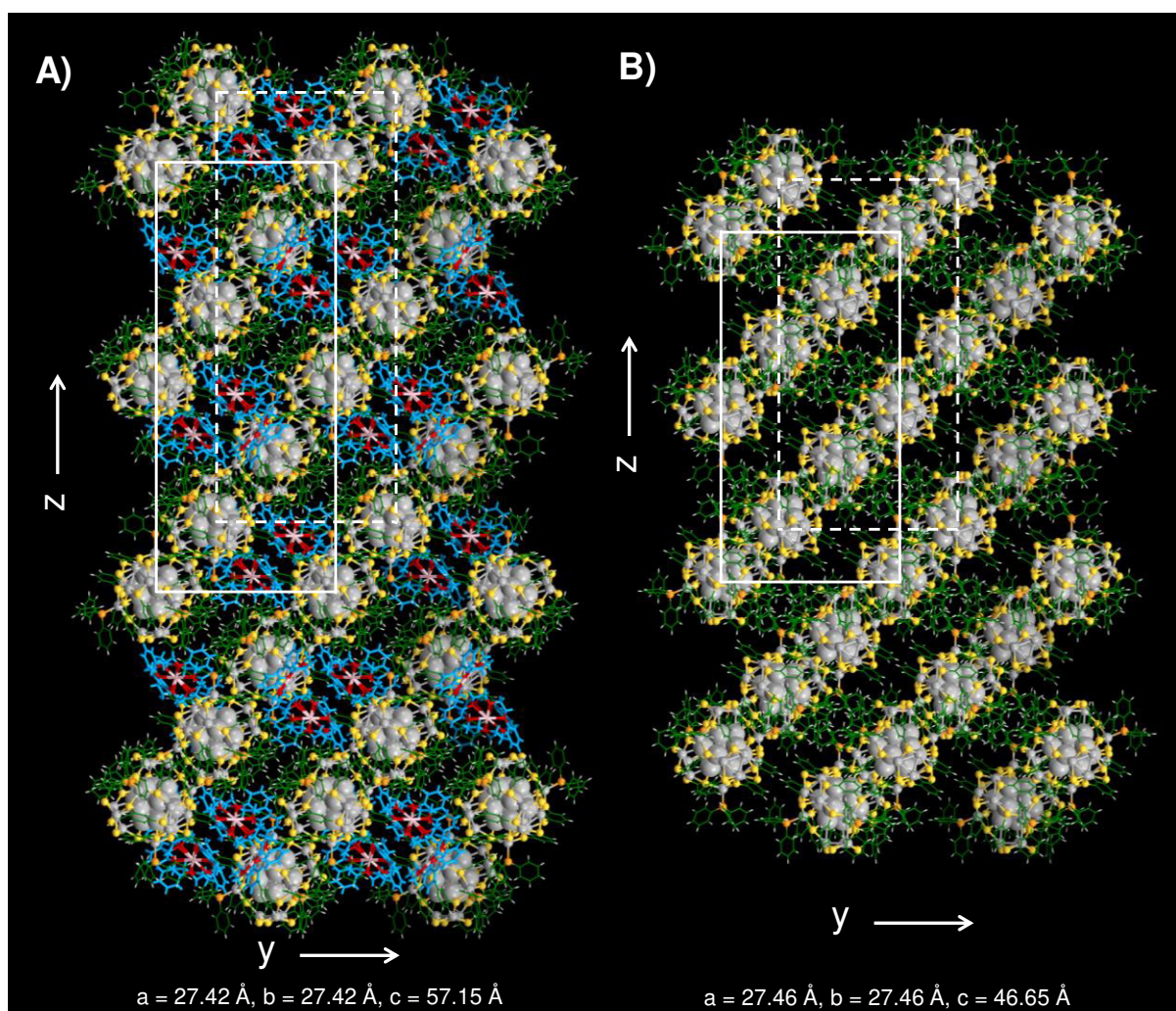


**Figure S5.** Crystallographic packing of A) **I** and B)  $\text{Ag}_{29}\text{T}$ , viewed from x-axis.

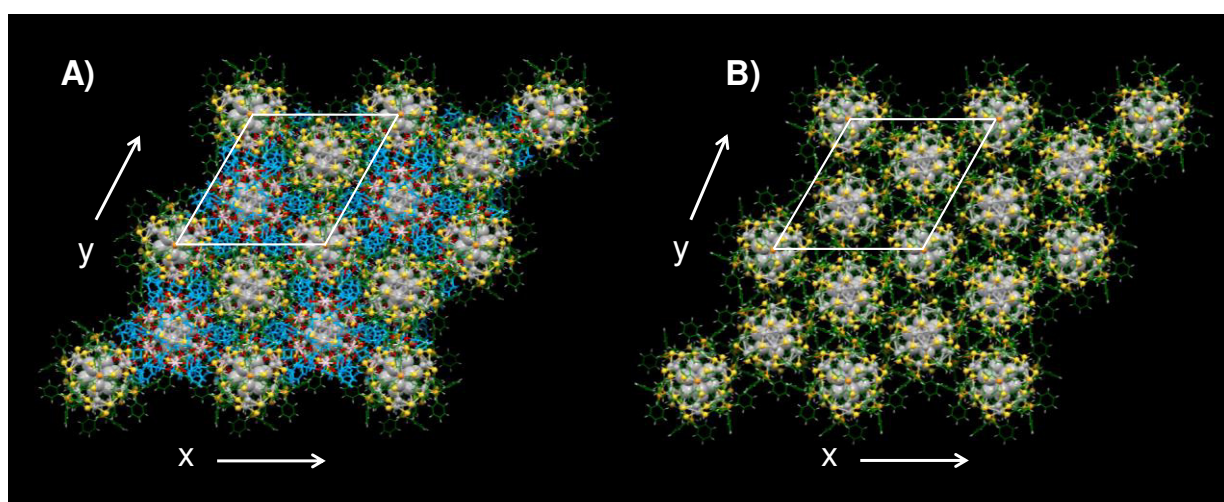


**Figure S6.** Crystallographic packing of A) **I** and B)  $\text{Ag}_{29}\text{T}$ , viewed from z-axis.

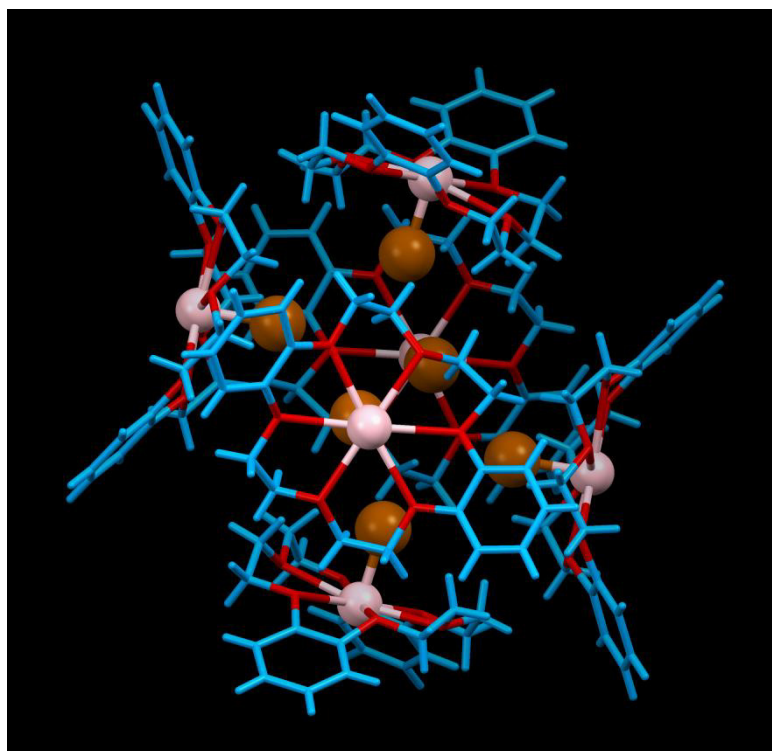


**Figure S7.** Trapping of water molecules inside the crown ether cages. The H<sub>2</sub>O molecules are coordinated to Na<sup>+</sup>. The O atoms of H<sub>2</sub>O are shown in brown color. The H atoms of H<sub>2</sub>O were not resolved from the crystal structure.

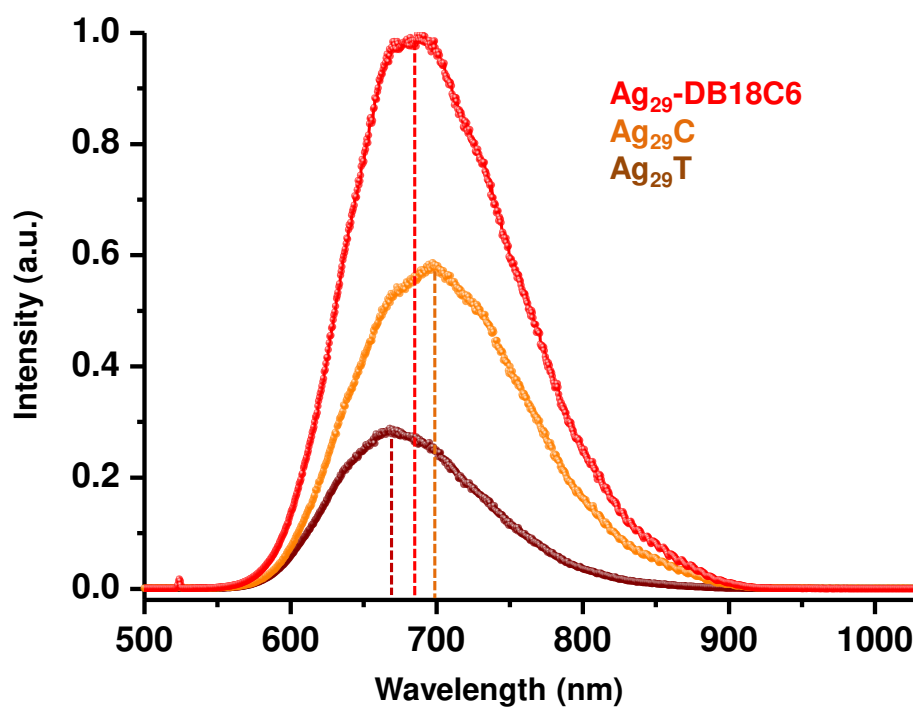


**Figure S8.** Emission from Ag<sub>29</sub>-DB18C6, Ag<sub>29</sub>T and Ag<sub>29</sub>C crystals, excited at 532 nm.



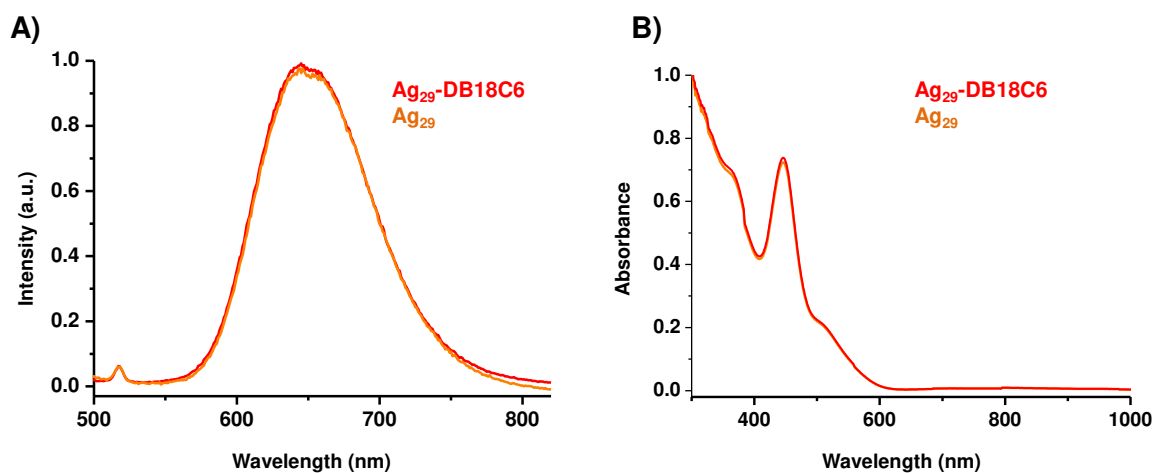


**Figure S9.** A) Solution-phase emission spectra of  $\text{Ag}_{29}$  clusters and  $\text{Ag}_{29}$ -DB18C6 crystals dissolved in DMF, excited at 450 nm. B) Optical absorption spectra of  $\text{Ag}_{29}$  clusters and  $\text{Ag}_{29}$ -DB18C6 crystals dissolved in DMF.

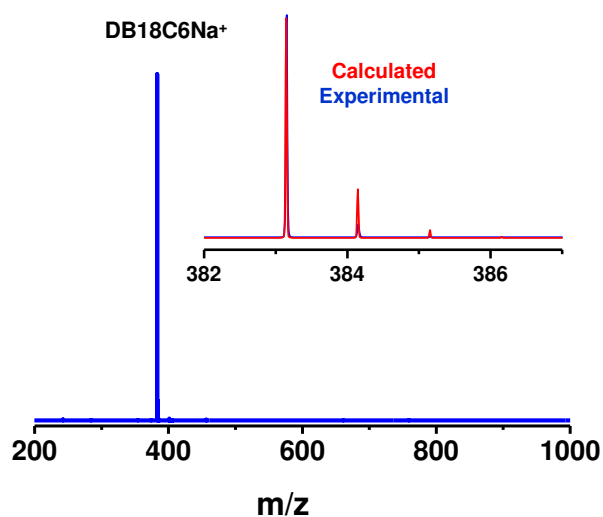


**Figure S10.** Positive mode ESI MS showing the detection of  $\text{DB18C6Na}^+$ . The comparison of the theoretical and experimental isotopic distribution patterns of  $\text{DB18C6Na}^+$  is shown in the inset.

**Table S1. Crystal structure data**

Identification code	Ag29DB18C6
Empirical formula	C192.63 H181.27 Ag29 Na3 O22.50 P3.29 S24
Formula weight	6924.53
Temperature	296(2) K
Wavelength	0.71073 Å
Crystal system	Trigonal
Space group	R-3
Unit cell dimensions	a = 27.424(5) Å      a = 90° b = 27.424(5) Å      b = 90° c = 57.155(10) Å      g = 120°
Volume	37225(14) Å <sup>3</sup>
Z	6
Density (calculated)	1.853 Mg/m <sup>3</sup>
Absorption coefficient	2.507 mm <sup>-1</sup>
F(000)	20078
Crystal size	0.150 x 0.100 x 0.050 mm <sup>3</sup>
Theta range for data collection	2.971 to 26.061°
Index ranges	-33 ≤ h ≤ 33, -33 ≤ k ≤ 33, -70 ≤ l ≤ 66
Reflections collected	139409
Independent reflections	16328 [R(int) = 0.0891]
Completeness to theta = 25.242°	99.8 %
Absorption correction	Semi-empirical from equivalents
Max. and min. transmission	0.78 and 0.55
Refinement method	Full-matrix least-squares on F <sup>2</sup>
Data / restraints / parameters	16328 / 1264 / 893
Goodness-of-fit on F <sup>2</sup>	1.412
Final R indices [I > 2sigma(I)]	R1 = 0.1136, wR2 = 0.3261
R indices (all data)	R1 = 0.1834, wR2 = 0.3989
Extinction coefficient	n/a
Largest diff. peak and hole	6.738 and -1.806 e.Å <sup>-3</sup>

**Details on refinement of crystal structure.** From X-ray diffraction two molecules were found in the crystal lattice: [Ag<sub>29</sub>(BDT)<sub>12</sub>(TPP)<sub>4</sub>][(DB18C6Na)<sub>3</sub>] (**I**) and [Ag<sub>29</sub>(BDT)<sub>12</sub>(TPP)][(DB18C6Na)<sub>3</sub>] (**II**). During the initial stages of structure determination itself, when atom Ag1 was omitted from structure, the Fourier map clearly showed two peak positions which could not be refined as a single atom. The refinement results showed two disordered positions for the Ag atom, each showing different connectivity. The structure was carefully explored to find out whether any meaningful disorder or inexplicable connectivity

existed at any other part of the structure. But none could be found, indicating that no other molecule/fragment existed in the lattice.

The quality of diffraction was not sufficient to justify refinement of hydrogen atoms of H<sub>2</sub>O molecules. Minor absorption errors coupled with Fourier series termination effects could have resulted in the positive electron densities near the heavy atom positions. Since all the heavy atoms are assigned full occupancy of the site, any minor Fourier electron density at heavy atom sites may be thought as due to small errors in the data.

## References

1. AbdulHalim, L. G.; Bootharaju, M. S.; Tang, Q.; Del Gobbo, S.; AbdulHalim, R. G.; Eddaoudi, M.; Jiang, D.-e.; Bakr, O. M., Ag<sub>29</sub>(BDT)<sub>12</sub>(TPP)<sub>4</sub>: A Tetravalent Nanocluster. *J. Am. Chem. Soc.* **2015**, 137, 11970-11975.



# Tribochemical Degradation of Polytetrafluoroethylene in Water and Generation of Nanoplastics

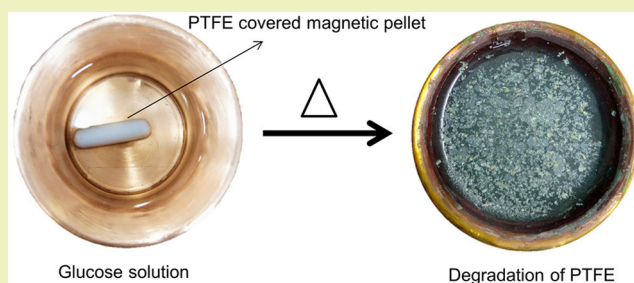
Abhijit Nag, Ananya Bakshi, Jyotirmoy Ghosh, Vishal Kumar, Soumabha Bag,<sup>1b</sup> Biswajit Mondal, Tripti Ahuja, and Thalappil Pradeep\*<sup>1b</sup>

DST Unit of Nanoscience and Thematic Unit of Excellence, Department of Chemistry, Indian Institute of Technology Madras, Chennai-600036, India

## S Supporting Information

**ABSTRACT:** Polytetrafluoroethylene (PTFE) is probably the most extensively used chemically inert and thermally stable polymer. We report the degradation of PTFE in water in the presence of common metals and carbohydrates resulting in polymeric fragments. About 53 mg of solid materials consisting of polymeric fragments and copper was separated from a copper vessel in 15 days when a PTFE pellet of about 920 mg was stirred with 1000 ppm glucose in 70 mL of water at 70 °C. Degradation produced fluorocarbon species in water were detected by high-resolution electrospray ionization mass spectrometry. Triboelectric charging of the PTFE surface during stirring and consequent interaction of the charged surface with the metal ions, brought to solution by carbohydrate-induced corrosion, is attributed to this phenomenon. We show that such a process can be extended to other polymers such as polypropylene. The study suggests important consequences of nanoplastics to environment and health, including impact of such chemistry to cooking.

**KEYWORDS:** Tribochemical degradation, Polytetrafluoroethylene, Nanoplastics, Dissolution, Polymer degradation



## INTRODUCTION

Polytetrafluoroethylene (PTFE), commonly called Teflon, is regarded as the most common chemically inert synthetic polymer known to mankind.<sup>1</sup> Its stability in acids, bases, and at high temperatures has made it one of the most popular materials used to enhance durability of common appliances such as in kitchenware. There are very few reports on the degradation of PTFE due to its high chemical inertness. Kavan et al. degraded PTFE in the presence of highly reactive alkali metals (Li and Na).<sup>2</sup> In this Letter, we present experimental proof of significant degradation of PTFE in water in the presence of common metals and carbohydrates producing nanoplastics in solution. The onset of chemical reactions has also been observed through the detection of short fragments of PTFE in solution.

## RESULTS AND DISCUSSION

The experiments performed (as described in the methods section) in which a PTFE covered pellet was stirred in glucose solution (1 mg/mL) of water in the presence of a gold foil, gave a red luminescent polymeric film (Figure 1 and Figure S1A) on the liquid surface after 30 days of reaction. We know that PTFE is not a luminescent material (Figure S2). Chemical analysis of the film by scanning electron microscopy/energy dispersive analysis of X-rays (SEM/EDS) confirmed that it is composed of PTFE with 0.04% Au (Figure S3C). Additional experiments were discussed below to prove that the film was

composed of PTFE and gold. Bright red luminescence of the film implied the presence of Au–C bonding as several Au–C compounds exhibit such emission.<sup>3,4</sup> Gradual evolution of Au concentration in the solution (Figure S3B) from 1 ppb on day 3 to 15 ppb on day 30, confirms the glucose-induced dissolution of gold.

Similar degradation of PTFE occurred also with other metals (Cu, Zn, Ag, and Fe) in which a PTFE covered magnetic pellet was stirred in a vessel of metal, containing glucose solution. In every case, these polymeric films were separated and characterized using SEM/EDS, Raman spectroscopy, and X-ray photoelectron spectroscopy (XPS). Compositions of the floating films were similar to varying amounts of metals. Fluorine (39.95%) and copper (2.36%) were quantified by EDS mapping of the solid material separated from the copper vessel (Figure S4B). Microscopic localization of copper (1.17%) was observed in the cracks of the materials (Figure S5C). The existence of fluorine (43.09%) and zinc (1.27%) was confirmed by EDS of the zinc vessel-derived material (Figure S6B).

Similar results were obtained for other metal vessels, too (Figure S7). However, the films were non-luminescent unlike in the case of gold, as expected. Materials with the M–C bond

Received: June 24, 2019

Revised: August 14, 2019

Published: September 3, 2019

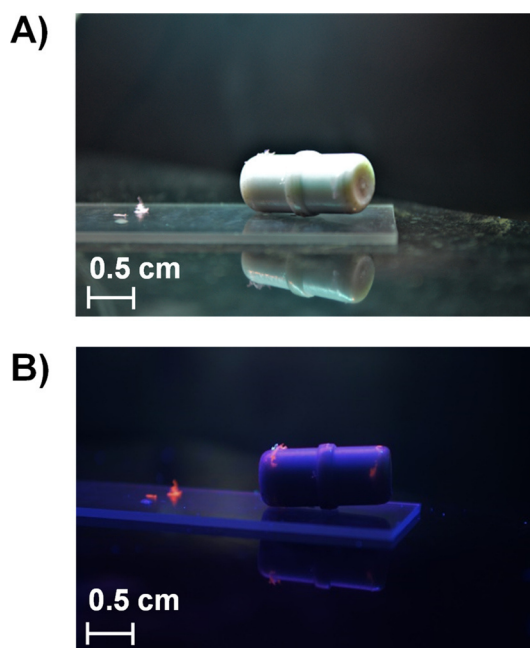


**Figure 1.** Photographs of the reaction product of PTFE and gold in the presence of glucose under (A) visible light and (B) UV light (mercury vapor lamp). The magnetic pellet pictured here has the reaction product attached on it. The reaction product found floating on the water was kept on the glass slide. The material was red luminescent under UV light.

(Cu–C, Zn–C) are not known to be luminescent under UV light. The thin films from the copper vessel were greenish-blue (Figure S1B) in color suggesting a high amount of Cu

incorporation into PTFE and probably Cu remains in its +2 oxidation state. The dissolution of metals and emergence of the polymeric film are related. The process occurred even at room temperature but upon longer time of reaction. As higher temperature also caused evaporation of water, we conducted the experiment at 60–70 °C as the process was monitored for weeks. Experiments were performed with PTFE samples of different sources (local and Sigma-Aldrich) and shapes (pellet, granules, and sheet) to ensure that these variations did not affect the results.

To get further information on bonding, Raman spectroscopy was performed for the material collected from copper and stainless steel vessels and the spectra were compared with that of pure PTFE. Peaks from the material obtained from copper and stainless steel vessels and pure PTFE are shown in Figure 2Aa,b,c, respectively. Peaks labeled as 1, 2, 3, 4, 5, 6, and 7 represent CF<sub>2</sub> wagging (1), CF<sub>2</sub> twisting (2), CF<sub>3</sub> symmetric deformation (3), CF<sub>2</sub> symmetric stretching (4), CF<sub>2</sub> asymmetric stretching (5), C–C stretching (6), and C–F stretching (7), respectively.<sup>5</sup> A new peak was seen at 472 and 473 cm<sup>−1</sup> for copper and iron-containing samples, respectively which is absent in pure PTFE. About 1 cm<sup>−1</sup> Raman shift was observed, which suggested the presence of different metals and chemical environments (Figure S8A). Independent Raman measurements were performed on the separated polymer from copper and stainless steel vessels to check the reproducibility (Figure S9). In a previous report, the Pt–C stretching mode was found in-between 470 and 500 cm<sup>−1</sup>, depending on the ligand environment<sup>6</sup> which is in agreement with M–C bond formation in the examined materials. Shifts of 2 and 4 cm<sup>−1</sup> were observed for C–C stretching (peak 6) for copper and

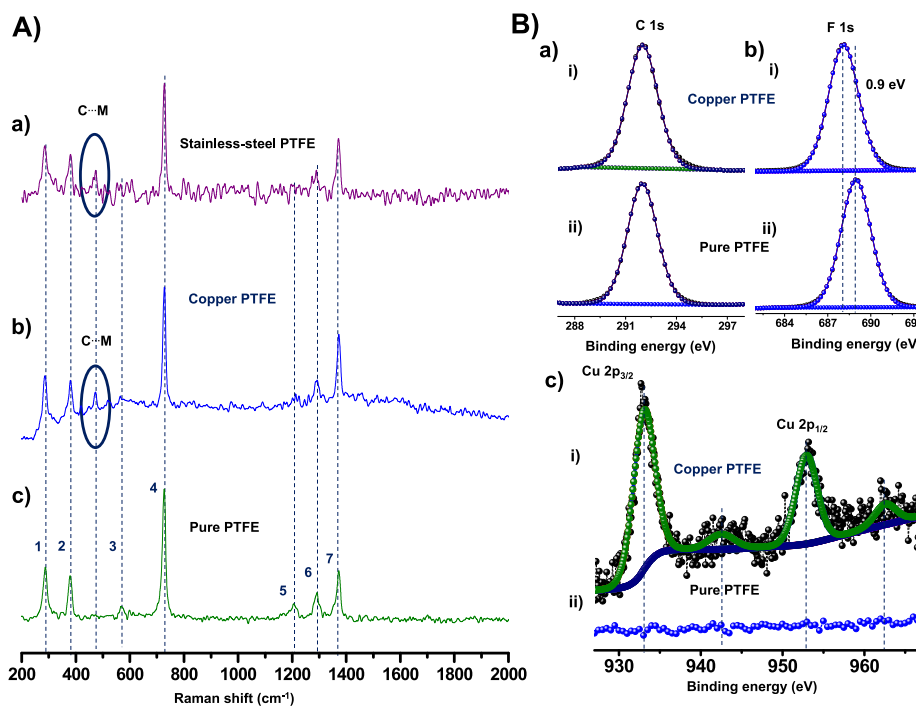


**Figure 2.** (A) Raman spectra of the polymeric materials derived from stainless steel (a) and copper (b) vessels compared with pure PTFE (c). Appearance of a new peak at 473 and 472 cm<sup>−1</sup> were seen for stainless steel and copper-derived materials, respectively in addition to the PTFE features. Peaks 1, 2, 3, 4, 5, 6, and 7 are CF<sub>2</sub> wagging, CF<sub>2</sub> twisting, CF<sub>3</sub> symmetric deformation, CF<sub>2</sub> symmetric stretching, C–C stretching, CF<sub>2</sub> asymmetric stretching, and C–F stretching of PTFE, respectively. (B) XPS data to confirm the presence of carbon (a), fluorine (b), and copper (c) in the copper-derived material. Data for pure PTFE are also shown.

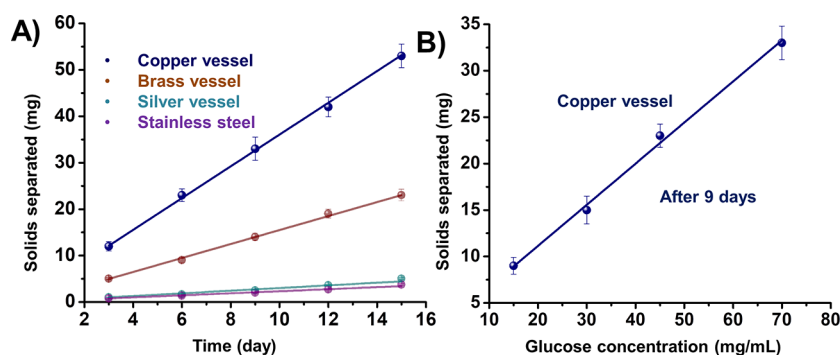


**Figure 3.** Mass of the solid material separated from different vessels plotted as a function of time (A). Mass of the material separated from the copper vessel as a function of glucose concentration (B).

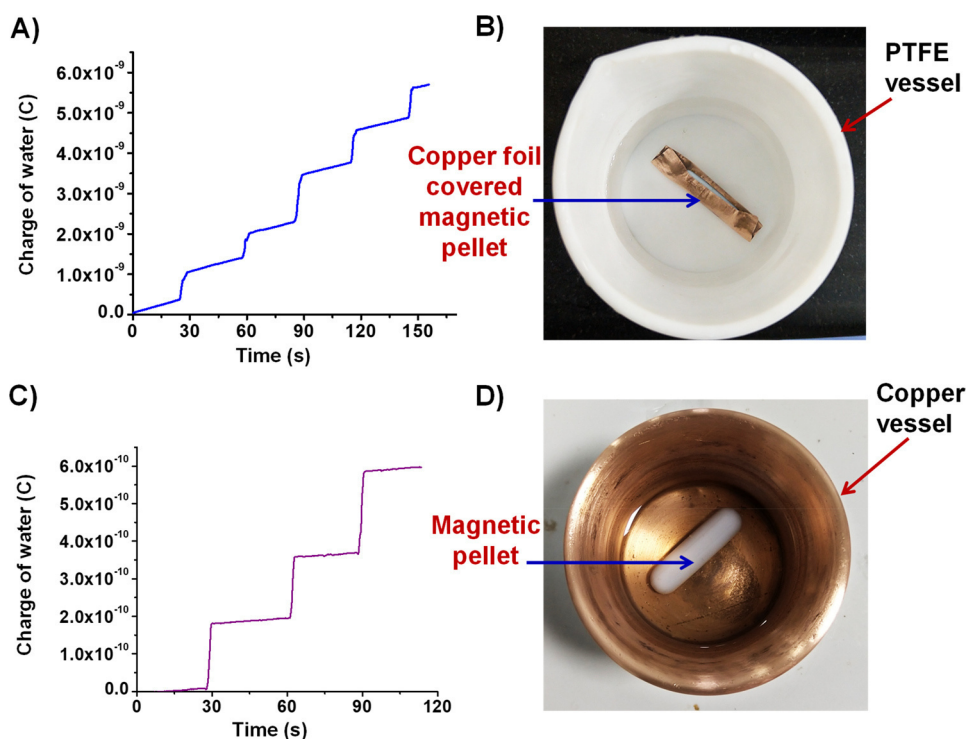


**Figure 4.** (A) Plot showing the positive charge acquired by the water in a PTFE beaker. (B) Photograph of the PTFE beaker containing 100 mL water with a magnetic pellet covered by a copper foil. (C) Plot showing the positive charge acquired by the water in the copper vessel. (D) Photograph of the copper vessel containing 50 mL water with a magnetic PTFE pellet. Charge was measured by dropping 1 mL of the water into a Faraday cup connected to an electrometer.

iron-containing samples, respectively compared to pure PTFE, as shown in Figure S10A.

XPS was performed as an alternate analytical technique to obtain elemental information. Peaks at 933.0 and 953.0 eV are attributed to Cu 2p<sub>3/2</sub> and Cu 2p<sub>1/2</sub>, respectively (Figure 2Bci). Presence of the satellite peaks due to configurational interaction at 943.0 and 963.0 eV confirmed the oxidation state of copper (+2). All the spectra were calibrated with C 1s and there was no significant change in the C 1s peak position for copper-derived PTFE compared to pure PTFE (Figure 2Bb). Both of them showed a strong signal for F 1s, further confirming the material to be composed of fragmented PTFE. While F 1s peak appeared at 689.0 eV for pure PTFE, the peak position got shifted to 688.1 eV in copper–PTFE which can be due to the M–C bond formation (Figure 2Bbi). Both Raman spectroscopy and XPS are in good agreement with M–C bond formation in metal-derived PTFE compounds.

Several control experiments were performed to understand the mechanism of such unusual reactivity of PTFE. A linear relation was found between the amounts of solid collected from each vessel with the reaction time (Figure 3A). About 53 mg of solid materials was isolated from the copper vessel after 15 days of reaction. The amount of separated solid materials decreased gradually from copper to stainless steel. A very similar trend was observed for the extracted metal ion concentration in the solution, which is highest for Cu and lowest for Fe (Table S1). A brief summary of the degradation of PTFE with metal ion concentration is provided in Table S1. At higher glucose and hence higher metal ion concentration in solution, the amount of solid precipitate also increased significantly (Figure 3B). Bakshi et al. have shown the mechanism of the extraction of silver by glucose.<sup>7</sup> A similar type of degradation was observed when metal ions (Cu<sup>2+</sup>) were added to the water in the absence of glucose (Figure S11). No



considerable degradation was found in the absence of glucose. The separated materials were colored in nature. These observations confirmed that metal ions play an important role in degrading PTFE and this phenomenon is not because of mechanical abrasions.

The reaction between the PTFE surface and metal ions may be responsible for the generation of M-PTFE products as suggested by the above-mentioned results. We propose that triboelectric charges generated<sup>8</sup> on the rotating PTFE-coated magnetic pellet may lead to reaction with metal ions on its surface to initiate the degradation. The triboelectric phenomenon was proven by measuring the charge accumulated in water as a result of the process of stirring the pellet. The experiment was conducted in two ways: (a) stirring a copper foil-covered magnetic pellet in a PTFE beaker (Figure 4A,B) and (b) stirring a PTFE pellet in a copper vessel (Figure 4C,D), in water. The extent of charge accumulated in water was larger in panel a as the area of the PTFE exposed was larger in it. An increasing positive charge in water was noticed in the course of stirring (Figure 4). From earlier studies, it was proven that when water was passed over a PTFE surface, the former acquires a positive charge and the latter acquires a negative charge.<sup>9–11</sup> The method used is outlined in Supporting Information. The acquired negative charge on the PTFE surface makes the metal ions to interact with it, resulting in degradation. Triboelectric degradation was further supported by the linear dependence of the amount of product on the glucose concentration in solution (Figure 3B), which in turn increased the metal ion concentration. Degradation of PTFE was not noticed without stirring, which also suggested that it is likely to be due to triboelectric phenomenon.

This reaction between the charged surface of PTFE and metal ions, termed as tribochemical reaction, results in metal–(CF<sub>2</sub>)<sub>n</sub> bonding, which could destabilize certain C–C bonds, leading to their breakage. It is known that triboelectric charges accumulated at dielectric materials may cause reduction<sup>12</sup> or transfer<sup>13</sup> of palladium(II) and copper(II).

To understand the degradation products of PTFE in this process, we performed high-resolution electrospray ionization mass spectrometry (HRESI MS) of the solution derived from a copper vessel, after 15 days of reaction. While scanning the *m/z* range from 30 to 70, the presence of CF<sub>3</sub><sup>+</sup>, C<sub>3</sub>F<sup>+</sup>, C<sub>2</sub>F<sup>+</sup>, and CF<sup>+</sup> were detected as shown in Figure 5 along with the isotopic peak of CF<sub>3</sub><sup>+</sup>. Calculated and experimental mass spectra for CF<sub>3</sub><sup>+</sup> are given in the inset of Figure 5. These fragments confirm the chemical degradation of PTFE.

Similar results have been observed for a brass vessel (Figure S12). Fluorocarbon species were also obtained from a copper vessel in the presence of dissolved Cu<sup>2+</sup> from CuCl<sub>2</sub> without glucose (Figure S13), confirming the need for metal ions and not sugar for the reaction.

As the concentration of these soluble fluorocarbon fragments were very less in the solution, other spectroscopic studies in solution such as nuclear magnetic resonance (NMR) were impossible. Similar results were obtained for other types of carbohydrates like cyclodextrins (Figure S14 and Figure S15).

Degradation of PTFE in the presence of metals generated nanoplastics in water. We observed 4–10 μm and 200–400 nm pieces of polymer particles in the solution. Transmission electron microscopy (TEM) images of the nanoplastics are shown in Figure S16. We have analyzed the TEM grid by SEM also. SEM image and EDS mapping information is provided in

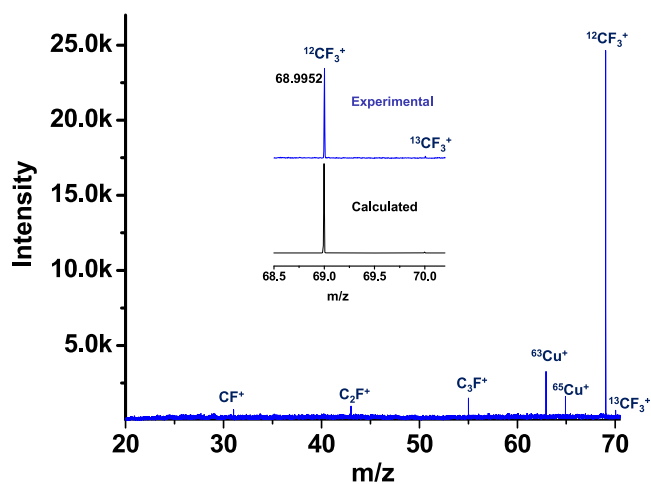


**Figure 5.** HRESI MS of the solution derived from a copper vessel. Presence of various fluorocarbon species in solution was identified by mass spectrometry. Inset of Figure 5 shows the calculated and experimental mass spectra of CF<sub>3</sub><sup>+</sup>.

**Figure S17.** Presence of fluorine and copper were confirmed by EDS mapping.

Degradation of polypropylene was also noticed after reaction with glucose solution in a copper vessel (Figure S18). Raman (Figures S19 and S20) and SEM (Figure S21) studies confirmed the formation of plastic particles of polypropylene in solution.

Nowadays, PTFE is utilized as a coating for different cooking appliances. Presence of different metal ions in foodstuff and carbohydrates-induced dissolution of metals from the container could lead to fluorocarbon fragmentation, which may bring plastics into the solution.

As the process requires no high temperature, hard chemicals or additional activation, we believe that this method offers a new and greener strategy for polymer degradation.

## CONCLUSION

In summary, we have investigated an unusual reaction between PTFE and various metal ions derived from bulk such as gold, copper, zinc, silver, and iron (stainless steel) in an aqueous solution of carbohydrates like glucose and cyclodextrins, leading to the degradation of the polymer. A red luminescent product was obtained by the reaction between gold and PTFE, and non-luminescent products were obtained for other metals. Presence of the M–C bond in such products was confirmed by Raman spectroscopy and XPS. Tribochemical reactions and interaction of metal ions with charged PTFE surfaces are proposed to be the possible pathways for the degradation of PTFE. HRESI MS confirmed the presence of small fragmented fluorocarbon species in water. We have detected nanoplastics in water that may lead to toxicity. The method presented was extended to polypropylene. We postulate that the method opens up greener strategies for polymer degradation. The impact of such chemistry on food through cooking practices points to the need for additional studies. We note that many of the non-stick cookware is coated with PTFE these days. High-temperature processing of foodstuffs containing metal ions could initiate such degradation.

## ■ ASSOCIATED CONTENT

### Supporting Information

The Supporting Information is available free of charge on the ACS Publications website at DOI: 10.1021/acssuschemeng.9b03573.

Materials and methods section, instrumentation employed, photograph of PTFE degradation, SEM/EDS of the PTFE–metal polymeric film, reactions of PTFE with metal ions, HRESI MS of the solution, TEM images of the nanoplastics after reaction, SEM/EDS of the plastics particles after reaction, reaction of polypropylene, Raman spectra of polypropylene, SEM/EDS of the copper-derived polypropylene polymeric film (PDF)

## ■ AUTHOR INFORMATION

### Corresponding Author

\*T.P. (pradeep@iitm.ac.in).

### ORCID

Soumabha Bag: 0000-0002-0932-105X

Thalappil Pradeep: 0000-0003-3174-534X

### Author Contributions

A.N. designed and conducted all experiments. A.B. supervised some of the experiments. J.G. carried out the XPS measurements. A.N. and V.K. carried out the charge measurements. S.B. carried out Raman measurements. B.M. carried out the TEM measurements. T.P. proposed and supervised the whole project.

### Notes

The authors declare no competing financial interest.

## ■ ACKNOWLEDGMENTS

Equipment support was provided by the Department of Science and Technology, Government of India through the Nano Mission. A.N. thanks IIT Madras for a doctoral fellowship. A.B. thanks IIT Madras for a postdoctoral fellowship. J.G. thanks the University Grants Commission (UGC) for his research fellowship. A.N. thanks Papri Chakraborty, Srikrishnarka Pillalamarri, Sundar Raj, and M. P. Kannan for helpful discussions.

## ■ REFERENCES

- (1) Puts, G. J.; Crouse, P.; Ameduri, B. M. Polytetrafluoroethylene: synthesis and characterization of the original extreme polymer. *Chem. Rev.* **2019**, *119* (3), 1763–1805.
- (2) Kavan, L.; Dousek, F. P.; Janda, P.; Weber, J. Carbonization of highly oriented poly(tetrafluoroethylene). *Chem. Mater.* **1999**, *11* (2), 329–335.
- (3) Feuerstein, T. J.; Poß, M.; Seifert, T. P.; Bestgen, S.; Feldmann, C.; Roesky, P. W. A highly luminescent octanuclear gold(I) carbide cluster. *Chem. Commun.* **2017**, *53* (64), 9012–9015.
- (4) Carlos Lima, J.; Rodríguez, L. Applications of gold(I) alkynyl systems: a growing field to explore. *Chem. Soc. Rev.* **2011**, *40* (11), 5442–5456.
- (5) Mihály, J.; Sterkel, S.; Ortner, H. M.; Kocsis, L.; Hajba, L.; Furdyga, É.; Minka, J. FTIR and FT-Raman spectroscopic study on polymer based high pressure digestion vessels. *Croatica Chemica Acta* **2006**, *79* (3), 497–501.
- (6) Memering, M. N.; Jones, L. H.; Bailar, J. C. Vibrational spectra and bonding in pentacyanohaloplatinate(IV) complexes. *Inorg. Chem.* **1973**, *12* (12), 2793–2801.
- (7) Bakshi, A.; Gandhi, M.; Chaudhari, S.; Bag, S.; Gupta, S. S.; Pradeep, T. Extraction of silver by glucose. *Angew. Chem., Int. Ed.* **2016**, *55* (27), 7777–7781.

(8) Tasker, S.; Chambers, R. D.; Badyal, J. P. S. Surface defluorination of PTFE by sodium atoms. *J. Phys. Chem.* **1994**, *98* (47), 12442–12446.

(9) Yatsuzuka, K.; Mizuno, Y.; Asano, K. Electrification phenomena of pure water droplets dripping and sliding on a polymer surface. *J. Electrostat.* **1994**, *32* (2), 157–171.

(10) Kwak, S. S.; Lin, S.; Lee, J. H.; Ryu, H.; Kim, T. Y.; Zhong, H.; Chen, H.; Kim, S.-W. Triboelectrification-induced large electric power generation from a single moving droplet on graphene/polytetrafluoroethylene. *ACS Nano* **2016**, *10* (8), 7297–7302.

(11) Burgo, T. A. L.; Galembeck, F.; Pollack, G. H. Where is water in the triboelectric series? *J. Electrostat.* **2016**, *80*, 30–33.

(12) Liu, C.-y.; Bard, A. J. Chemical redox reactions induced by cryptoelectrons on a PMMA surface. *J. Am. Chem. Soc.* **2009**, *131* (18), 6397–6401.

(13) Piperno, S.; Cohen, H.; Bendikov, T.; Lahav, M.; Lubomirsky, I. The absence of redox reactions for palladium(II) and copper(II) on electrostatically charged Teflon: relevance to the concept of “cryptoelectrons”. *Angew. Chem., Int. Ed.* **2011**, *50* (25), 5654–5657.

## Supporting Information

### **Tribochemical Degradation of Polytetrafluoroethylene in Water and Generation of Nanoplastics**

Abhijit Nag<sup>†</sup>, Ananya Bakshi<sup>†</sup>, Jyotirmoy Ghosh<sup>†</sup>, Vishal Kumar<sup>†</sup>, Soumabha Bag<sup>†</sup>, Biswajit Mondal<sup>†</sup>,  
Tripti Ahuja<sup>†</sup> and Thalappil Pradeep<sup>†\*</sup>

<sup>†</sup>DST Unit of Nanoscience and Thematic Unit of Excellence, Department of Chemistry  
Indian Institute of Technology Madras, Chennai-600036, India

Email: [pradeep@iitm.ac.in](mailto:pradeep@iitm.ac.in)

Totals – 23 pages, 21 figures, 1 table

Name	Table of contents	Page No.
	Materials and Methods	S2-S3
Table S1	A brief summary of the degradation of PTFE with metal concentration in solution	S4
Figure S1	Photograph of PTFE degradation by different metals	S5
Figure S2	Photograph of PTFE magnetic pellet	S5
Figure S3	SEM/EDS of the PTFE-gold polymeric film	S6
Figure S4	SEM/EDS of the copper derived PTFE polymeric film	S7
Figure S5	SEM/EDS of the copper derived PTFE polymeric film in the cracks	S8
Figure S6	SEM/EDS of the brass derived PTFE polymeric film	S9
Figure S7	SEM/EDS of the silver-derived PTFE polymeric film	S10
Figure S8	Expanded view of the peaks for stainless steel and copper PTFE materials	S10
Figure S9	Independent Raman measurements	S11
Figure S10	Expanded view of the peaks for stainless steel and copper PTFE materials	S12
Figure S11	Reactions of PTFE with metal ions	S13
Figure S12	HRESI MS of the solution from brass vessel	S14

Figure S13	HRESI MS of the solution derived from a copper vessel in presence of CuCl <sub>2</sub> without glucose	S15
Figure S14	SEM/EDS of the copper derived PTFE polymeric film, after reaction with $\gamma$ -cyclodextrin solution	S16
Figure S15	Plot of amounts of solid material separated from a copper vessel vs time, after reaction with $\gamma$ -cyclodextrin solution	S17
Figure S16	TEM images of the nanoplastics after reaction	S18
Figure S17	SEM/EDS of the plastics particles after reaction	S19
Figure S18	Reaction of polypropylene with glucose solution in copper vessel	S20
Figure S19	Raman spectra of polypropylene from a copper vessel	S21
Figure S20	Expanded view of the Raman spectra	S22
Figure S21	SEM/EDS of the copper-derived polypropylene polymeric film	S23

## Materials and Methods

### Methods

**Chemicals and Materials:** Vessels of copper, silver (with 90.50% purity), brass (60.66% copper, 36.58% zinc), stainless steel and polypropylene were purchased from the local market. (D+)-glucose (G),  $\gamma$ -CD (cyclodextrin), magnetic pellet and gold foil were purchased from Sigma-Aldrich. Milli-Q water was used throughout the experiment. Experiments were performed with various types of PTFE samples (from local and Sigma Aldrich) to ensure that source of the samples did not affect the results. Experiments were repeated with magnetic pellets (coated with PTFE) as well as different forms of PTFE (tape, granules and sheet).

### Experimental methods:

For the reaction between gold surface and PTFE, a 2 cm  $\times$  2 cm gold foil was inserted into a 250 mL PTFE beaker containing 100 mL aqueous solution of glucose (~1 mg/mL) having a PTFE coated magnetic pellet at 60-70°C. Samples were collected at regular intervals for inductively coupled plasma mass spectrometry (ICP MS) and other analyses.

We measured the weight of the PTFE pellet after taking out the magnet from it.

$\gamma$ -CD/glucose (~70 mg) was placed in silver, copper, brass and stainless steel vessels in milli-Q water (70 mL). The reaction mixtures were kept stirring at 60-70 °C for 15 days. Samples were collected at regular intervals for ICP MS and other analyses.



For the reaction of polypropylene, a magnetic pellet was inserted into the polypropylene vial (Figure S16). Reaction conditions were same as of PTFE.

#### **Instrumentation:**

**ICP MS:** ICP MS was performed using Perkin Elmer NexION 300X instrument equipped with Ar plasma. Before analysing any sample, the instrument was first calibrated with Au standard of four different concentrations (0, 10, 100, and 1000 ppb) to get a calibration curve with  $R^2=0.9999$ . Calibration was done with other elemental standards also.

#### **ESI MS:**

The fluorocarbon species were studied by Waters Synapt G2Si HDMS instrument. Optimized conditions for these measurements were as follows: Flow rate: 30-50  $\mu\text{L}/\text{min}$ , capillary voltage: 3 kV, cone voltage: 80-120 V, source offset: 100-130 V, desolvation gas flow: 400 L/h.

#### **Spectroscopy:**

Raman spectroscopic measurements were performed in a Witec GmbH, Alpha-SNOM alpha300 S confocal Raman instrument equipped with a 532 nm laser as the excitation source.

#### **Microscopy:**

SEM (scanning electron microscopy) and energy dispersive analysis of X-rays (EDS) were performed using an FEI QUANTA-200 SEM.

HRTEM (high resolution transmission electron microscopy) was performed with a JEOL 3010, 300 kV instrument equipped with a UHR polepiece.

#### **XPS:**

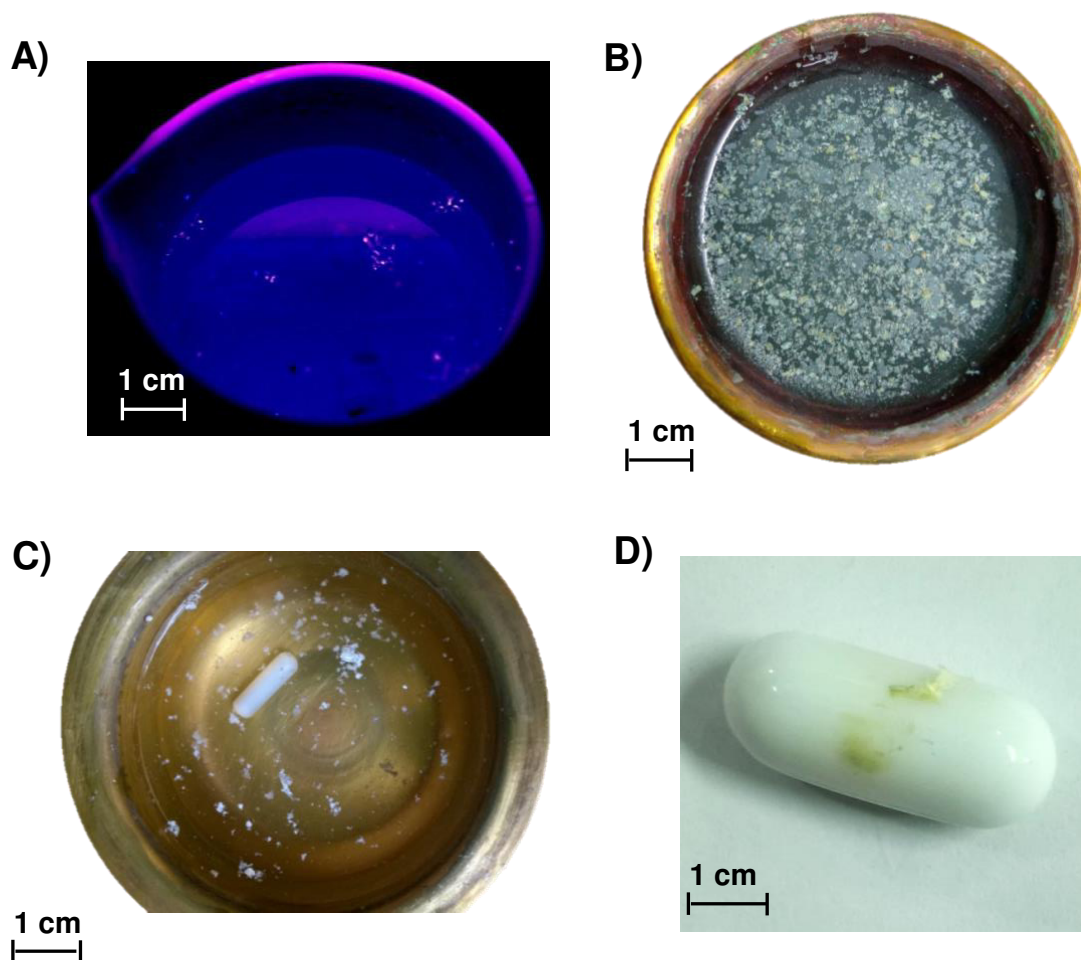
XPS measurements were carried out with an Omicron ESCA Probe Spectrometer. It consists of EA 125 energy analyzer, XM 1000 MkII X-ray source and monochromator, DAR 400 X-ray source (Al/Mg), VUV source HIS 13, CN 10 and CN 10+ charge neutralizer system, ISE 10 sputter ion source and MKS residual gas analyzer for TPD. Polychromatic Al  $K\alpha$  X-rays ( $h\nu = 1486.6\text{ eV}$ ) were used for analysis. 300 W X-ray power was applied.

#### **Charge measurement:**

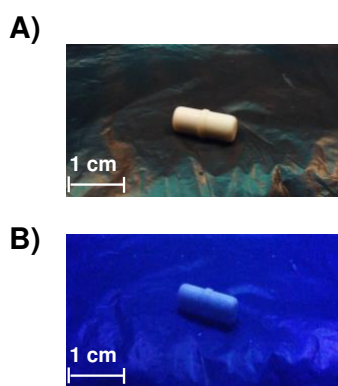
We took a PTFE beaker containing 100 mL milli-Q water. A magnetic pellet covered with copper foil was immersed in the beaker (Figure 4). Magnetic pellet was rotated at 60-70  $^\circ\text{C}$ . We took 1 mL water from the beaker at  $\sim 30$  seconds interval and measured the charge of this water using a home-built Faraday cup and an electrometer.

**Table S1.** Concentration of metals from the solution of their corresponding vessels, analyzed by ICP MS. Amount of solid material separated from each vessel is also given.

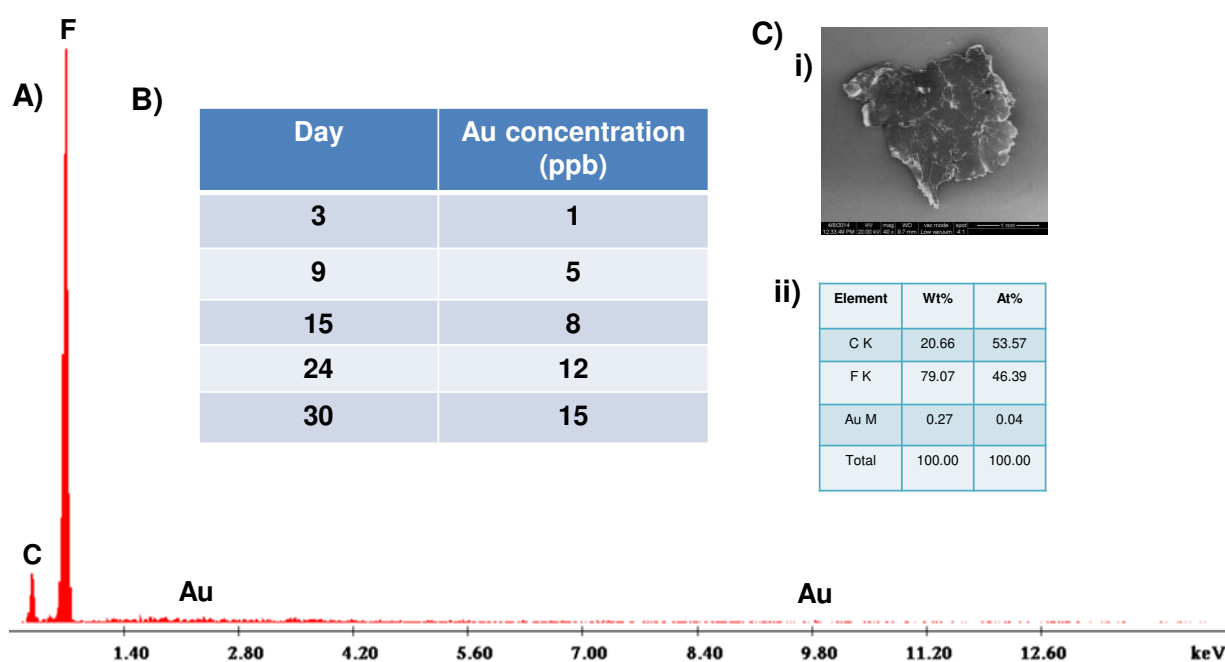
Metal vessel	Metal	Time	Metal ion concentration (ppm)	Amount of metal-PTFE (mg)
Copper	Cu	Day 03	153.2	12.00
		Day 06	223.0	23.00
		Day 09	291.1	33.00
		Day 12	347.8	42.00
		Day 15	419.3	53.00
Brass	Zn	Day 03	78.5	05.00
		Day 06	109.5	09.00
		Day 09	132.8	14.00
		Day 12	167.3	19.00
		Day 15	195.8	23.00
Silver	Ag	Day 03	0.4	01.00
		Day 06	0.7	01.75
		Day 09	0.9	02.50
		Day 12	1.3	03.50
		Day 15	1.9	05.00
Stainless steel	Fe	Day 03	0.3	00.75
		Day 06	0.5	01.40
		Day 09	0.7	02.00
		Day 12	1.1	02.70
		Day 15	1.3	03.50



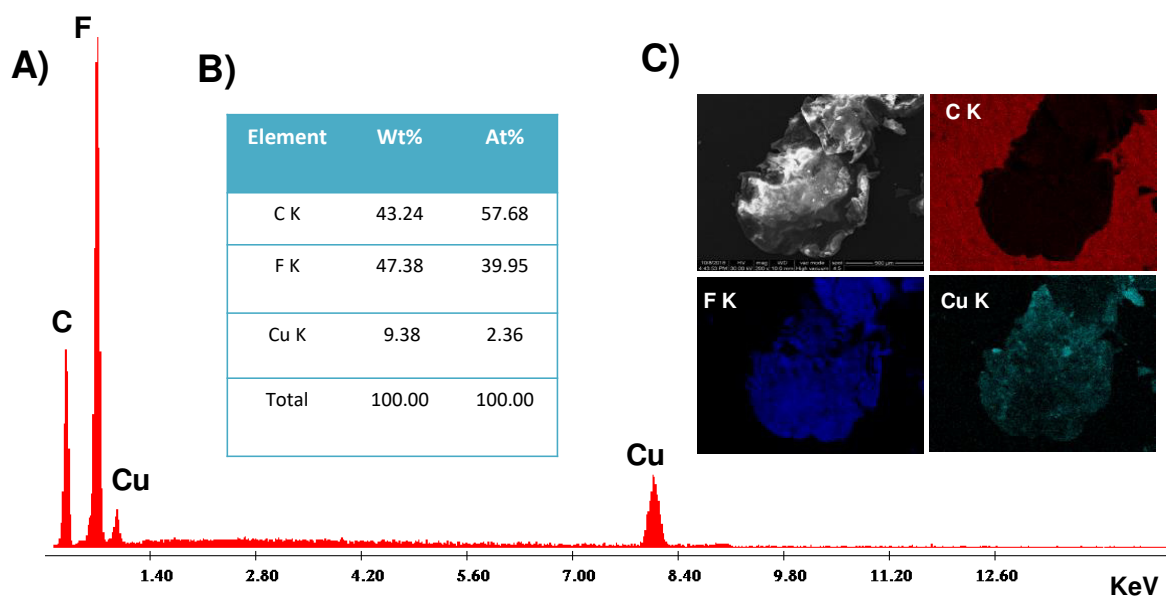
**Figure S1.** Photograph of PTFE degradation by different metals. A), B) and C) correspond to gold foil, copper and brass vessel, respectively. A) Red luminescent polymeric films appearing on the liquid surface after reaction with gold foil. D) Color of the PTFE-metal polymeric films after reaction in copper vessels.



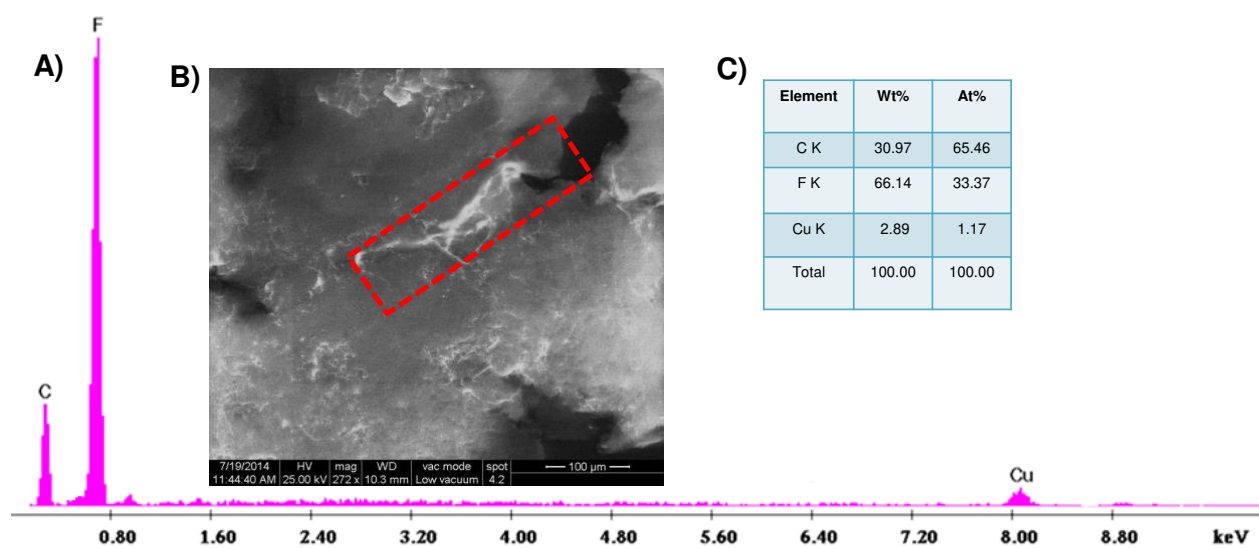
**Figure S2.** Photographs of the PTFE covered magnetic pellet A) under visible light and B) UV light (mercury vapor lamp).



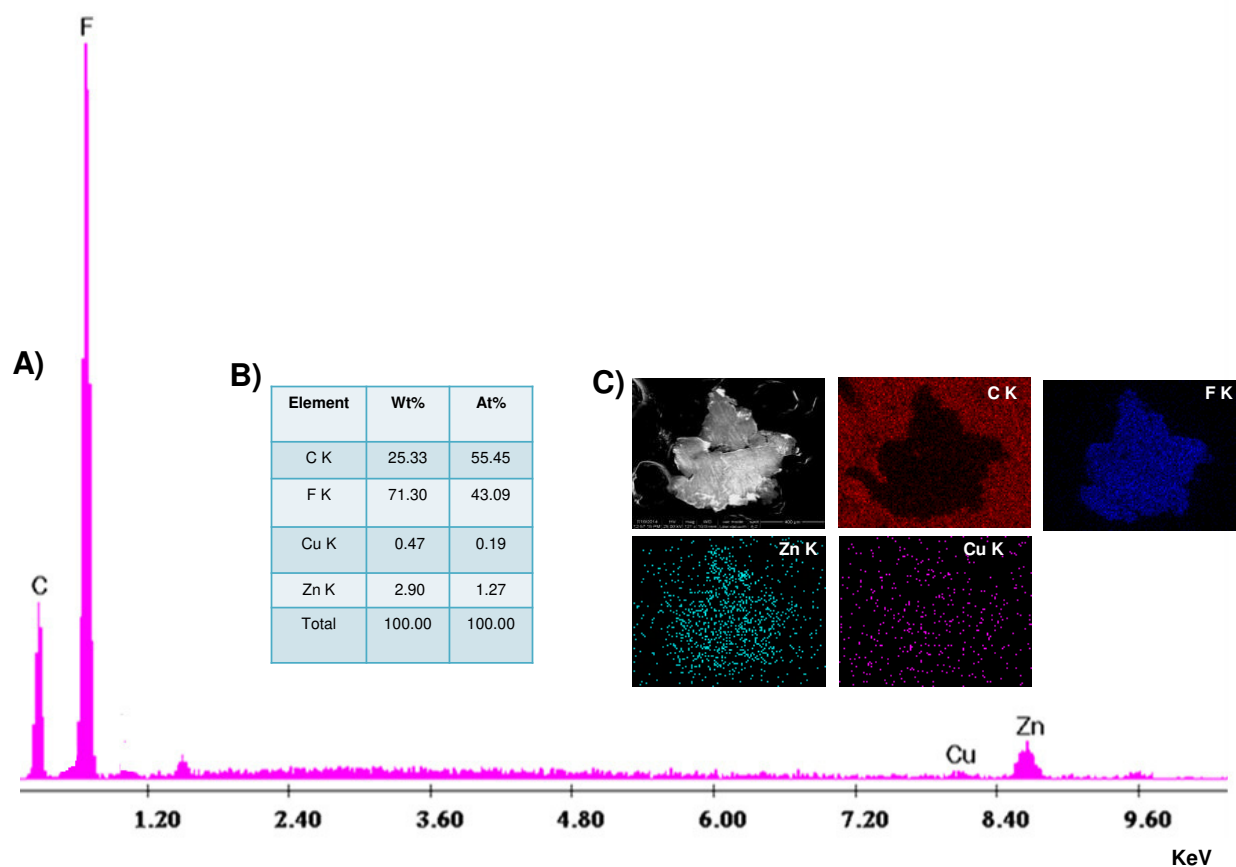
**Figure S3.** SEM/EDS of the PTFE-gold polymeric film. A) EDS of the PTFE-gold polymeric film. B) Extraction of gold by glucose in the course of 30 days. SEM image and elemental analysis data are presented in C) i) and ii), respectively. As we have performed the SEM/EDS on a carbon tape, the % of carbon will be different from the expected value.



**Figure S4.** SEM/EDS of the copper derived PTFE polymeric film. A) EDS of the copper derived PTFE polymeric film. B) Elemental analysis, showing the presence of copper and fluorine. C) Elemental mapping of the material. Scale bar is the same for all images in C).

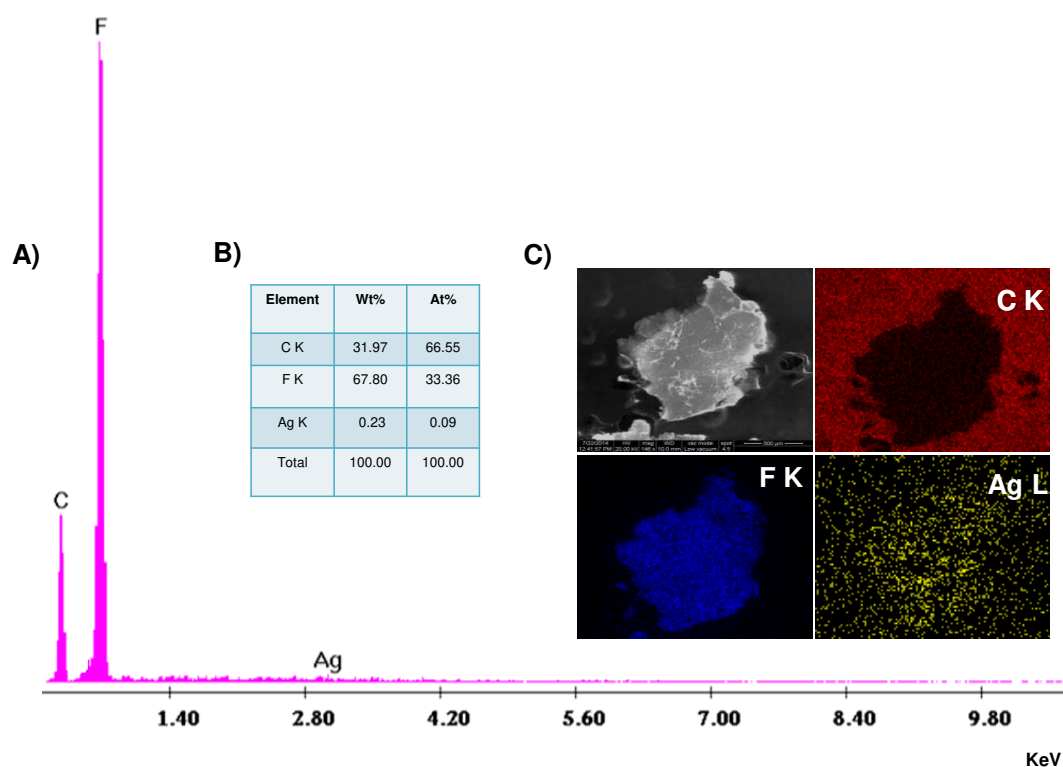


**Figure S5.** SEM/EDS of the copper derived PTFE polymeric film. A) SEM EDS, B) SEM image and C) elemental analysis of the polymeric film at the cracks. Presence of copper was detected from these cracks.

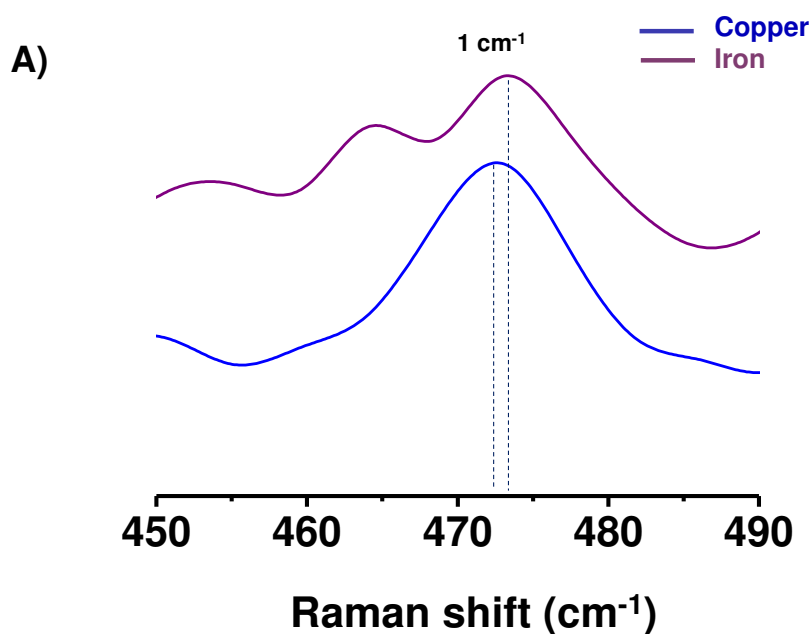


**Figure S6.** SEM/EDS of the brass derived PTFE polymeric film. A) EDS of the brass derived PTFE polymeric film. B) Elemental analysis, showing the presence of copper, zinc and fluorine. C) Elemental mapping of the material. Scale bar is the same for all images in C).

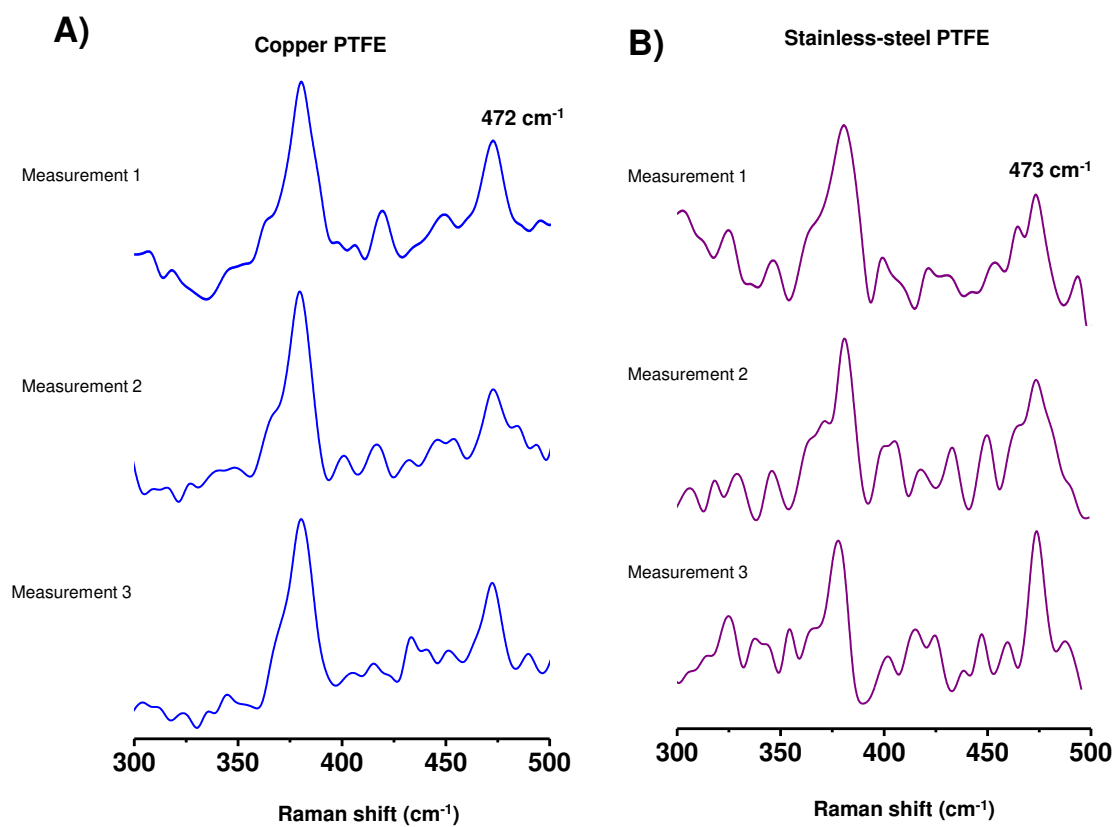




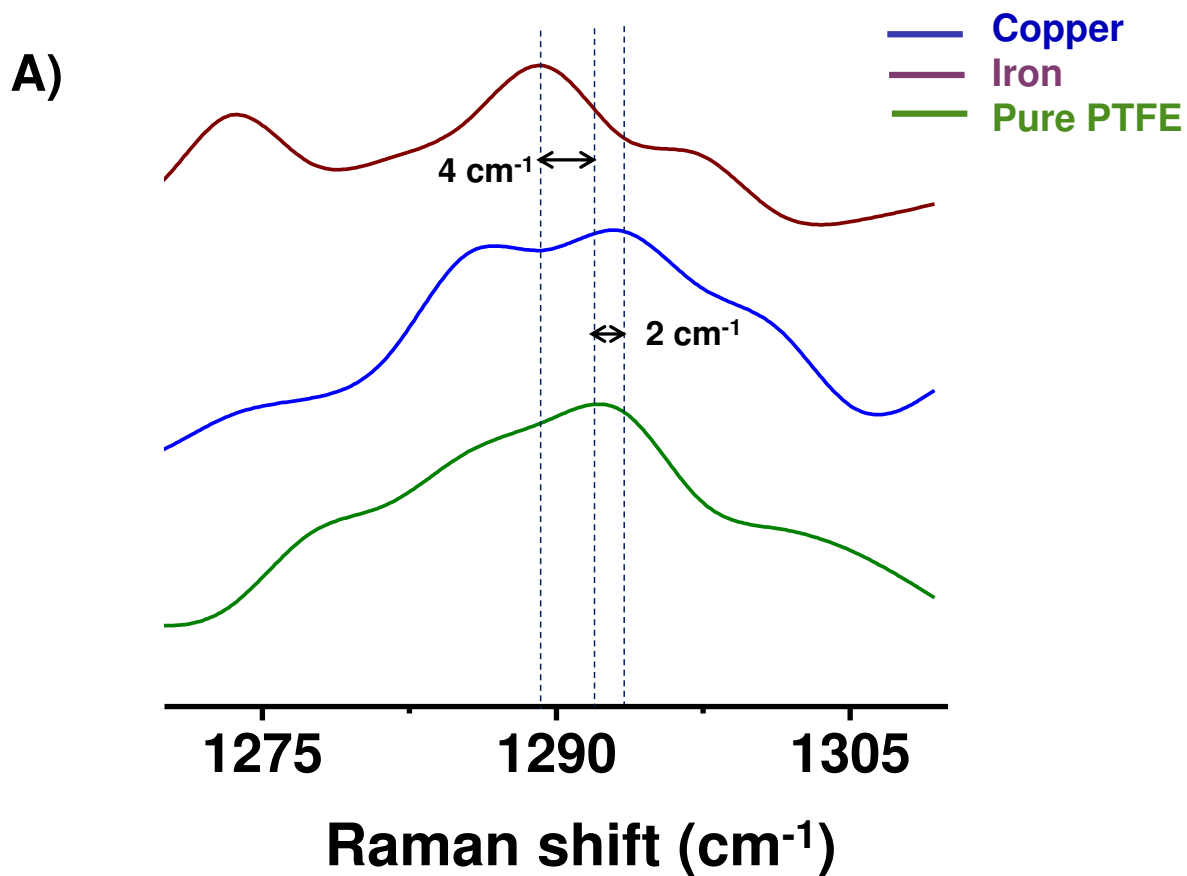
**Figure S7.** SEM/EDS of the silver derived PTFE polymeric film. A) SEM EDS of the silver derived PTFE polymeric film. B) Elemental analysis, showing the presence of silver and fluorine. C) Elemental mapping of the material. Scale bar is the same for all images in C).



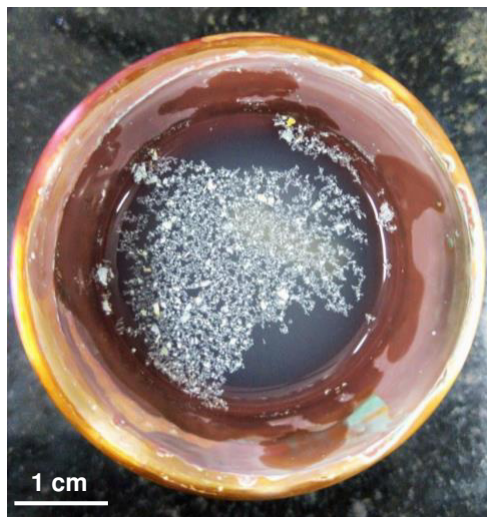
**Figure S8.** Raman Spectra of the PTFE-metal composite. A) Expanded view of the peaks at 473 and 472  $\text{cm}^{-1}$  for stainless steel (purple) and copper (blue) PTFE material, respectively from Figure 2. A shift of 1  $\text{cm}^{-1}$  was observed for copper and iron-containing samples, respectively.



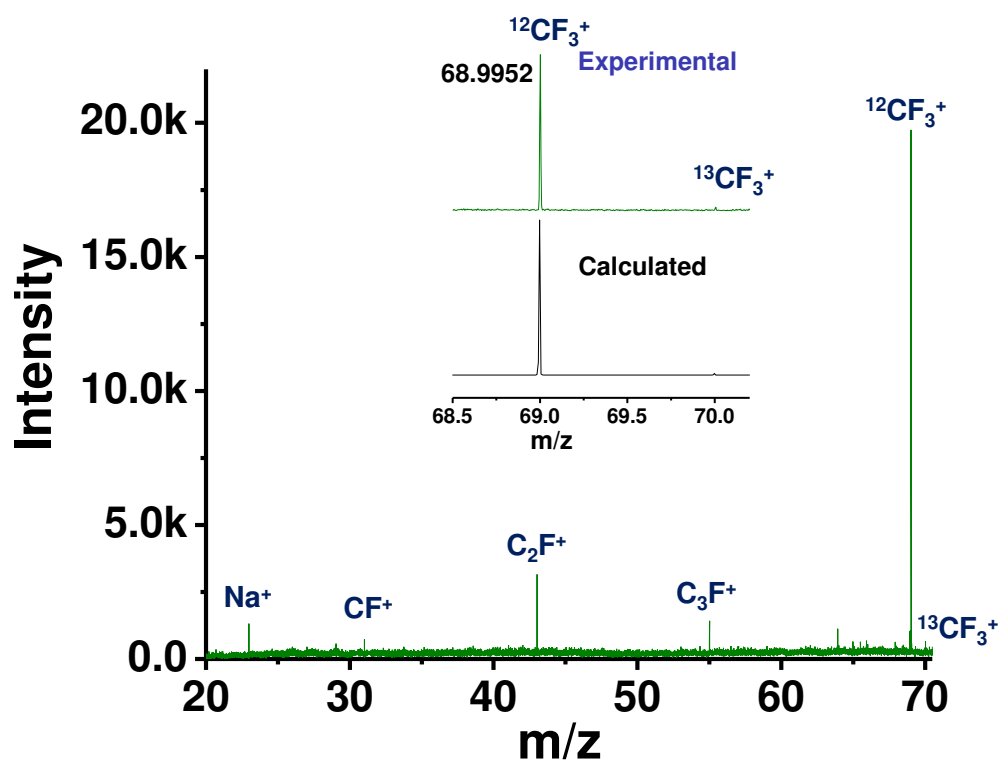
**Figure S9.** Independent Raman measurements from the polymer separated from A) copper PTFE and B) stainless-steel PTFE experiments. Peaks due to the polymer are reproduced in all measurements.



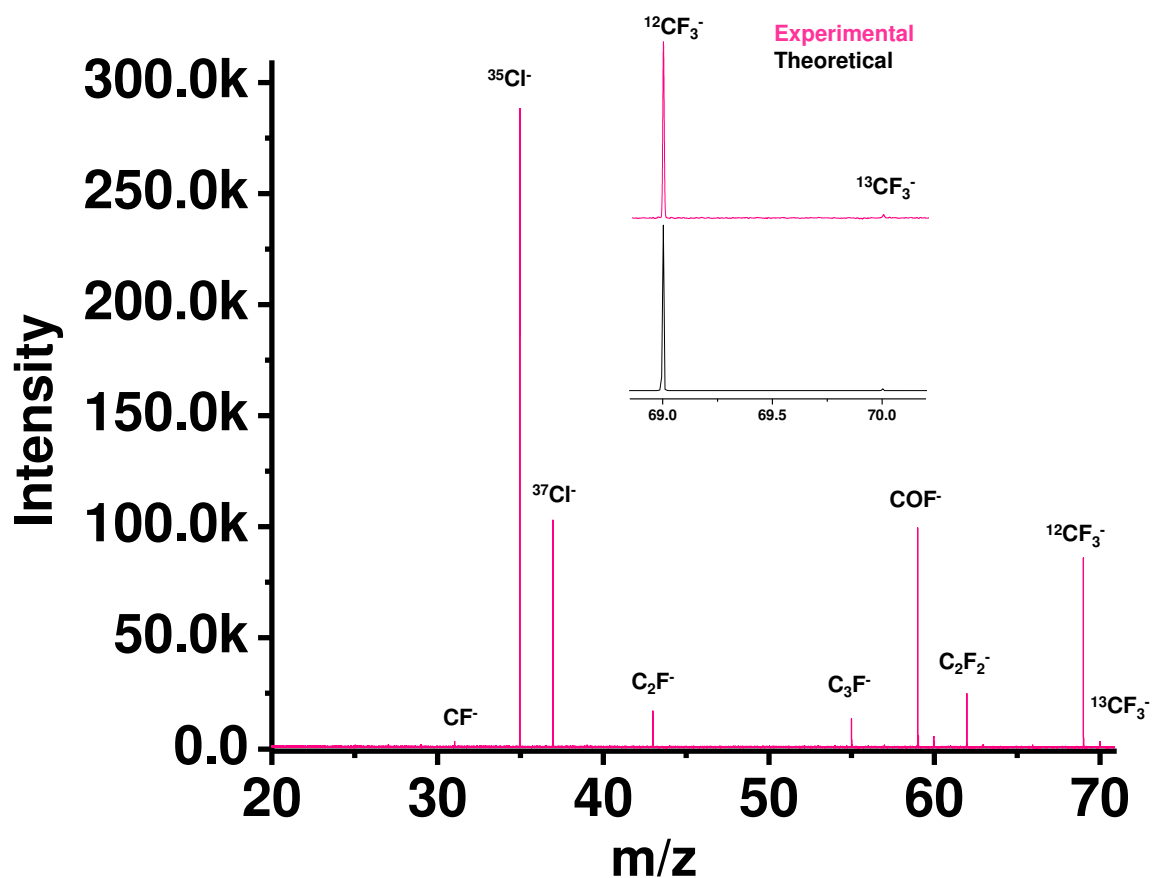
**Figure S10.** Raman Spectra of the PTFE-metal composite. A) Expanded view of peak 6 of Figure 2. Shifts of 2 and 4 cm<sup>-1</sup> were observed for the C-C stretching (peak 6) for copper and iron-containing samples, respectively compared to pure PTFE.

**A)****B)**

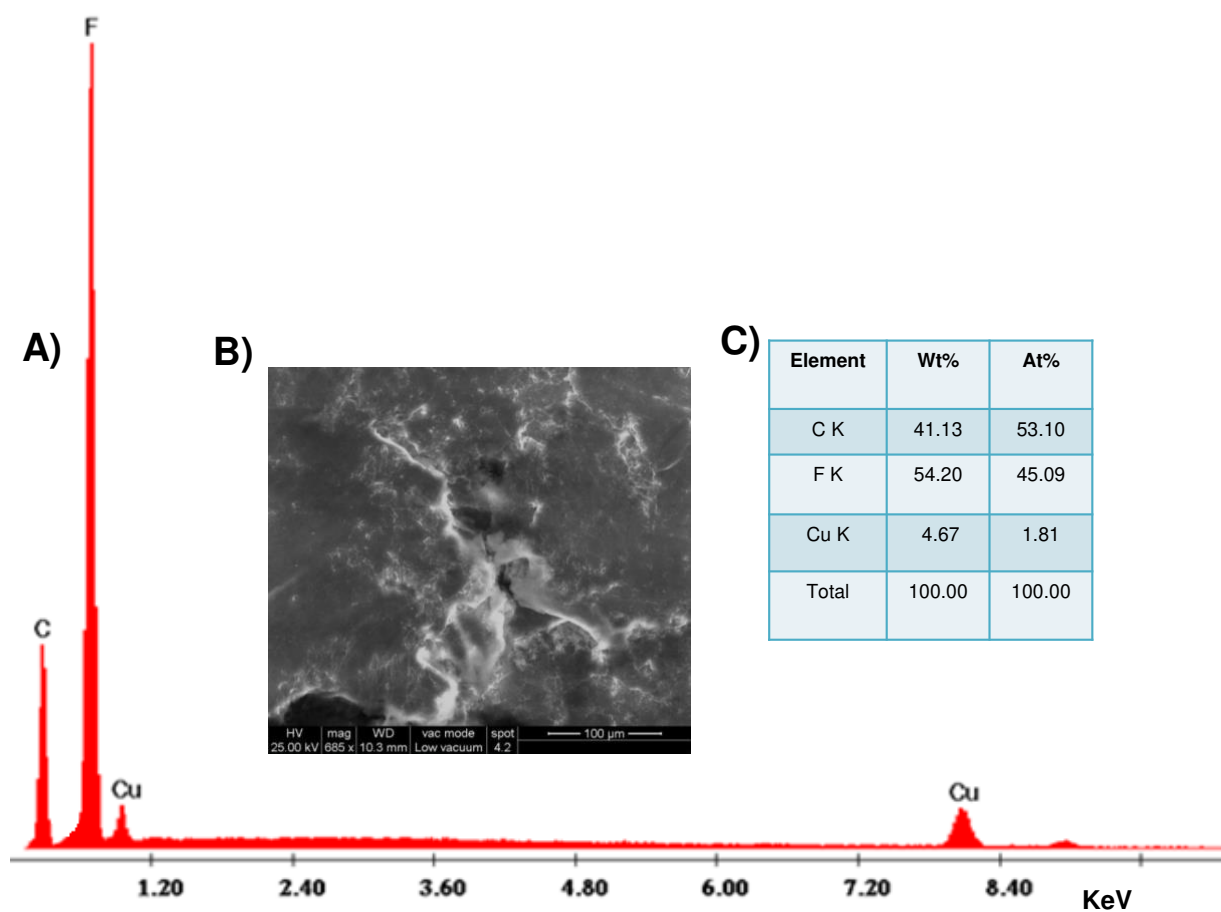
**Figure S11.** Reaction of PTFE pellet with copper chloride. Reaction of copper chloride solution (20 mg  $\text{CuCl}_2$  in 50 mL water) with PTFE magnetic pellet in copper vessel A) and PTFE beaker B). Similar kind of degradation has been observed for copper (II) ions. Greenish blue color PTFE-metal composite has been observed. This reaction was performed without glucose.



**Figure S12.** HRESI MS of the solution from brass vessel. Presence of the fluorocarbon species has been confirmed. Inset of Figure S12 shows the calculated and experimental mass spectra of  $\text{CF}_3^+$ .

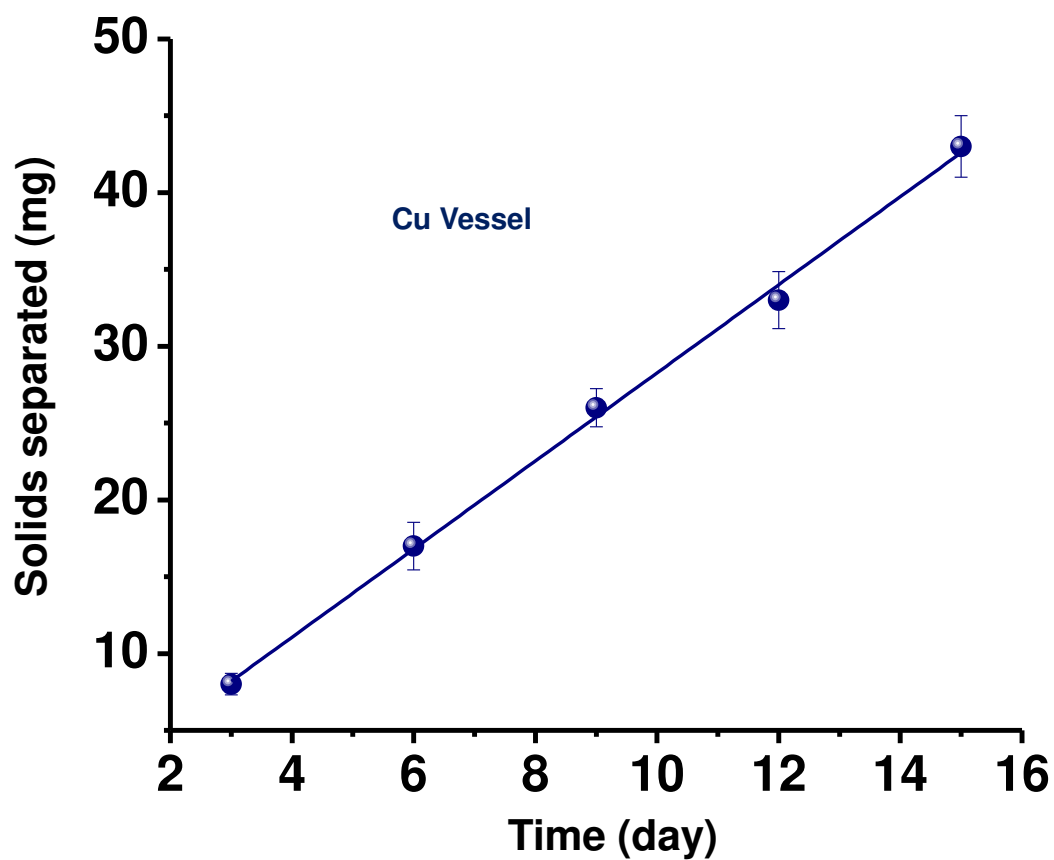


**Figure S13.** HRESI MS of the solution derived from a copper vessel in presence of CuCl<sub>2</sub> without glucose. Presence of various fluorocarbon species in solution was identified by mass spectrometry. Inset of Figure S13 shows the calculated and experimental mass spectra of CF<sub>3</sub><sup>-</sup>.

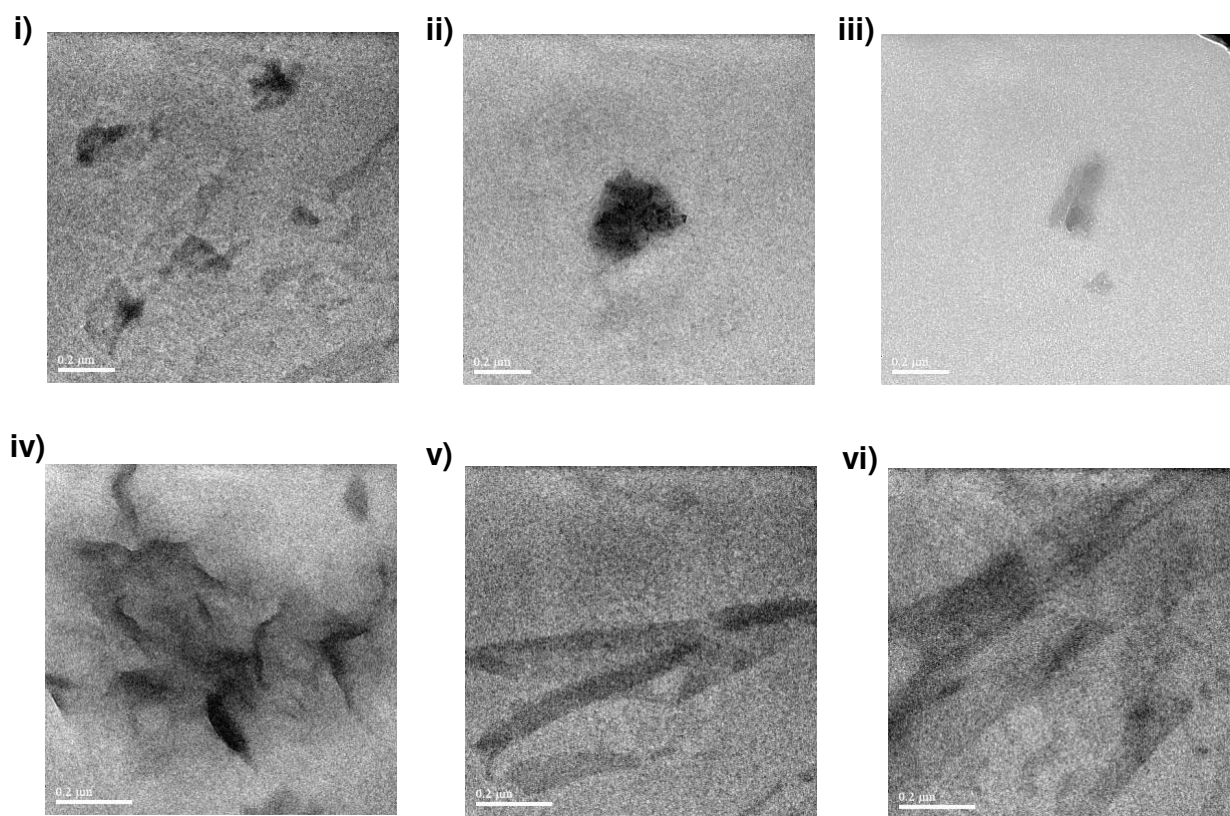


**Figure S14.** SEM/EDS of the copper derived PTFE polymeric film. A) SEM/EDS B) SEM image and C) elemental EDS of the material from copper derived PTFE, after reaction using  $\gamma$ -cyclodextrin. Presence of copper and fluorine was noticed.

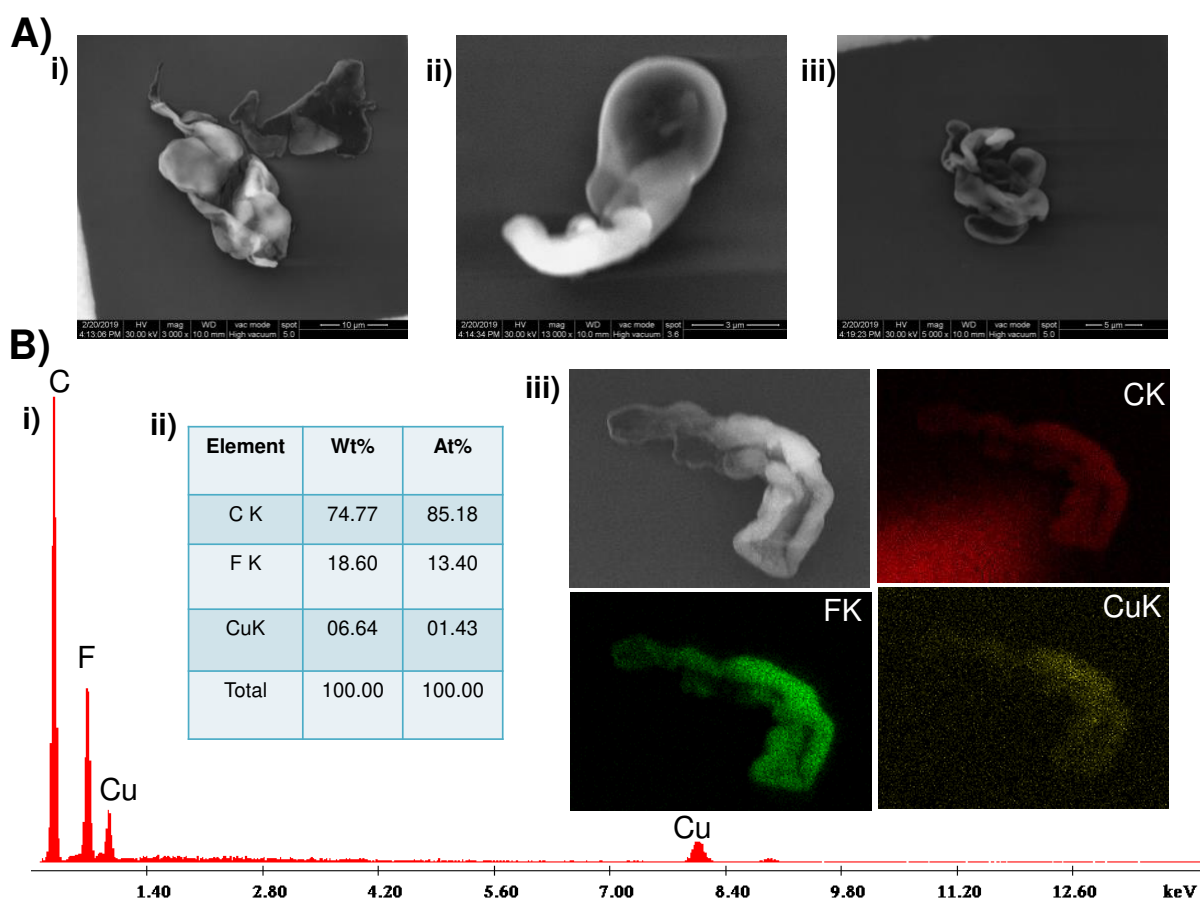




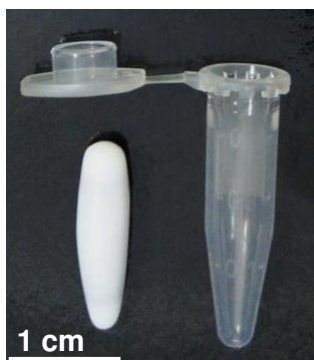
**Figure S15.** Amount of solid material separated from a copper vessel plotted as a function of time, after reaction with  $\gamma$ -cyclodextrin.



**Figure S16.** i-vi TEM images of the nanoplastics with different sizes, varying from 200-400 nm. Images from different regions of the grid are presented.



**Figure S17.** A) i-iii) SEM images of the plastic particles of different sizes varying from 4-10  $\mu\text{m}$ . B) i)-ii) Elemental analyses, showing the presence of copper and fluorine. iii) Elemental mapping of the plastic particles. Scale bars in iii) are the same as in the SEM images. The percentage of carbon will be different from the expected value because we have performed the analysis on a carbon coated copper grid. By the interaction of copper ions with charged PTFE surface, the fluorocarbon species could come into the solution.

**A)****i)****ii)****B)**

**Figure S18.** A) i) Photograph of the polypropylene vial. ii) A magnetic pellet was inserted into this vial. B) Reaction of polypropylene with glucose solution in copper vessel which was stirred to cause degradation. Degradation of polypropylene was noticed after 10 days of reaction. Spectroscopic and elemental analysis of the floating materials are presented in Figure S19–S20 and Figure S21, respectively.

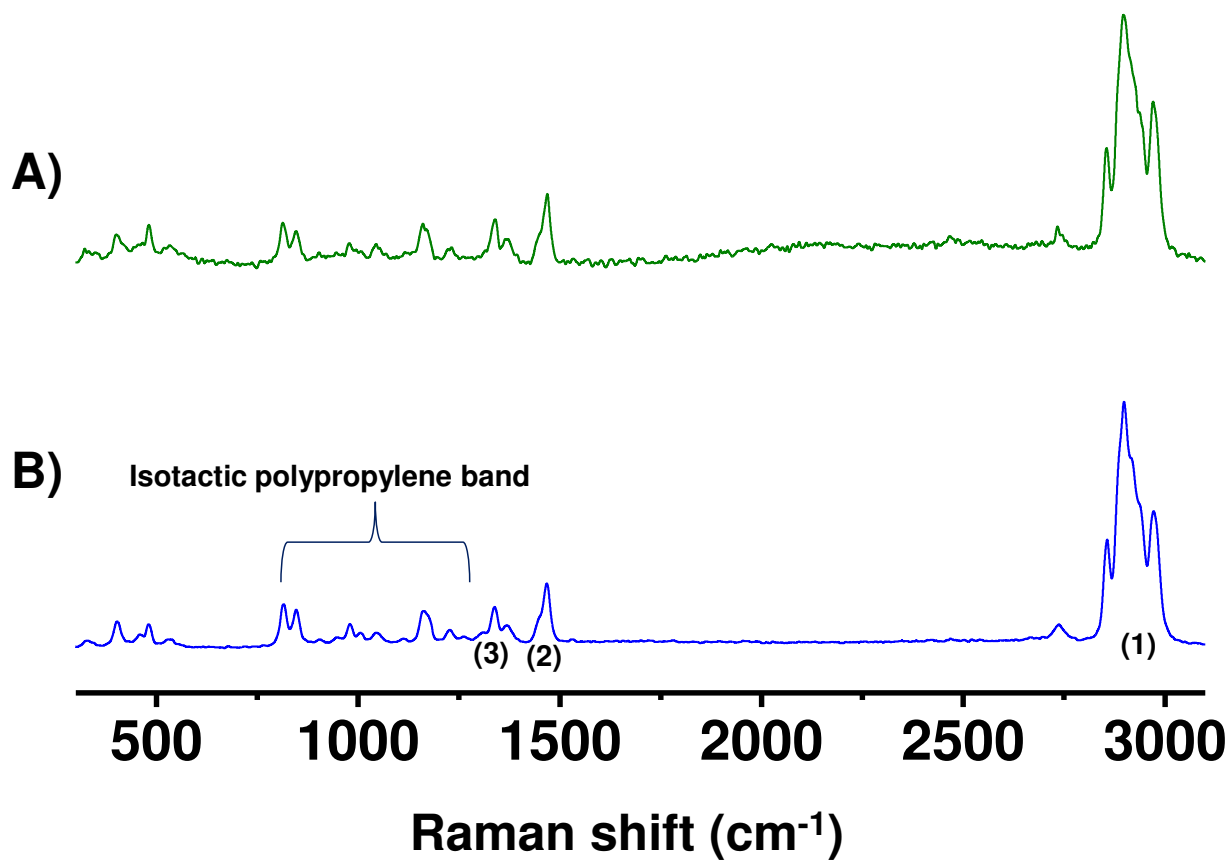


**Figure S19.** Raman spectra of the polypropylene-copper composite (A) and that of pure polypropylene (B). Peaks 1, 2, and 3 represent C-H stretching, CH<sub>2</sub> deformation, and symmetric CH<sub>3</sub> deformation.

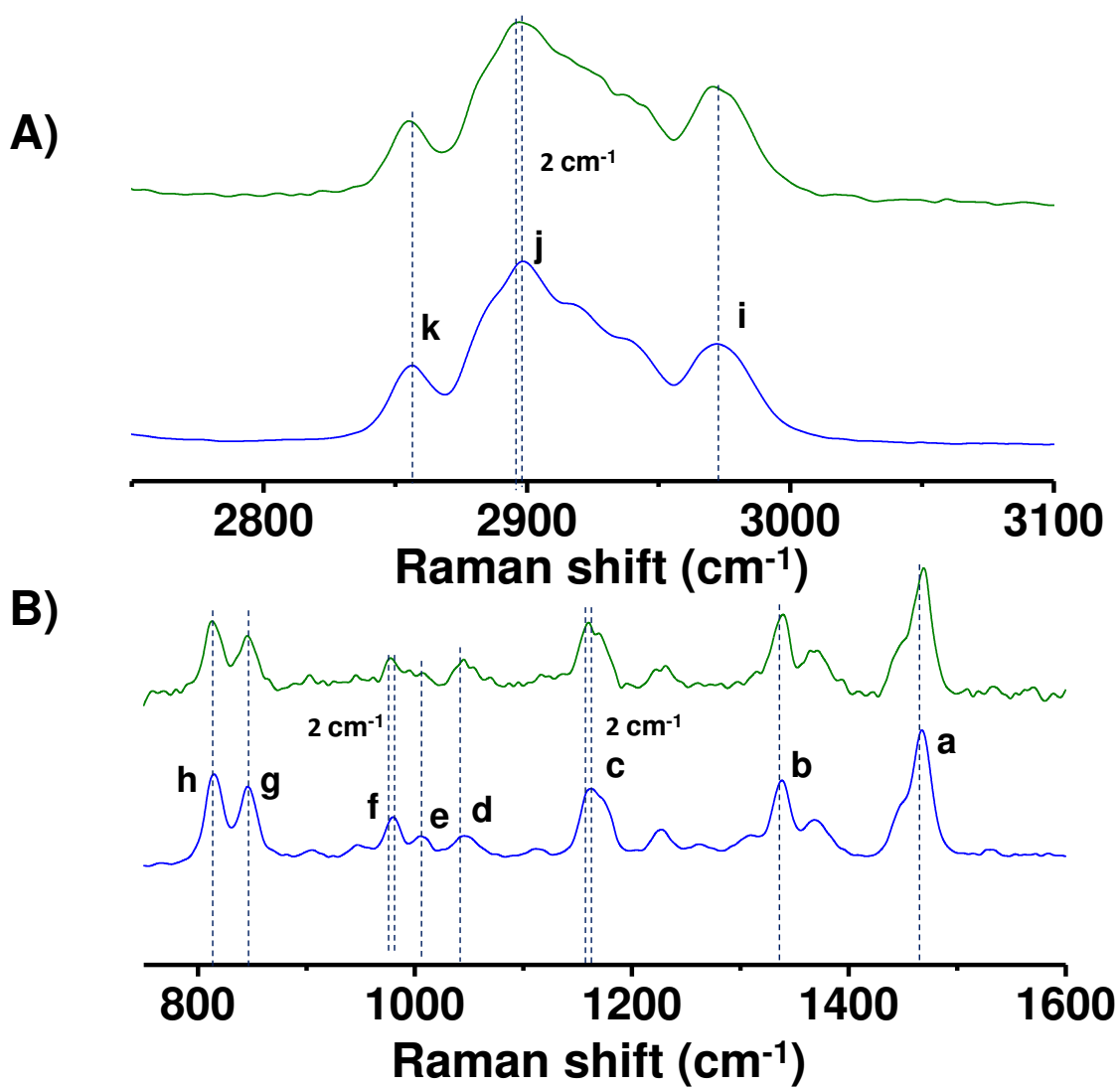


**Figure S20.** Expanded views of the Raman spectra of the same samples as in Figure 19. Spectral colors correspond to the same as in Figure 19. Peaks c, f, and j show  $2\text{ cm}^{-1}$  shift. Peak splitting was observed in the case of c.

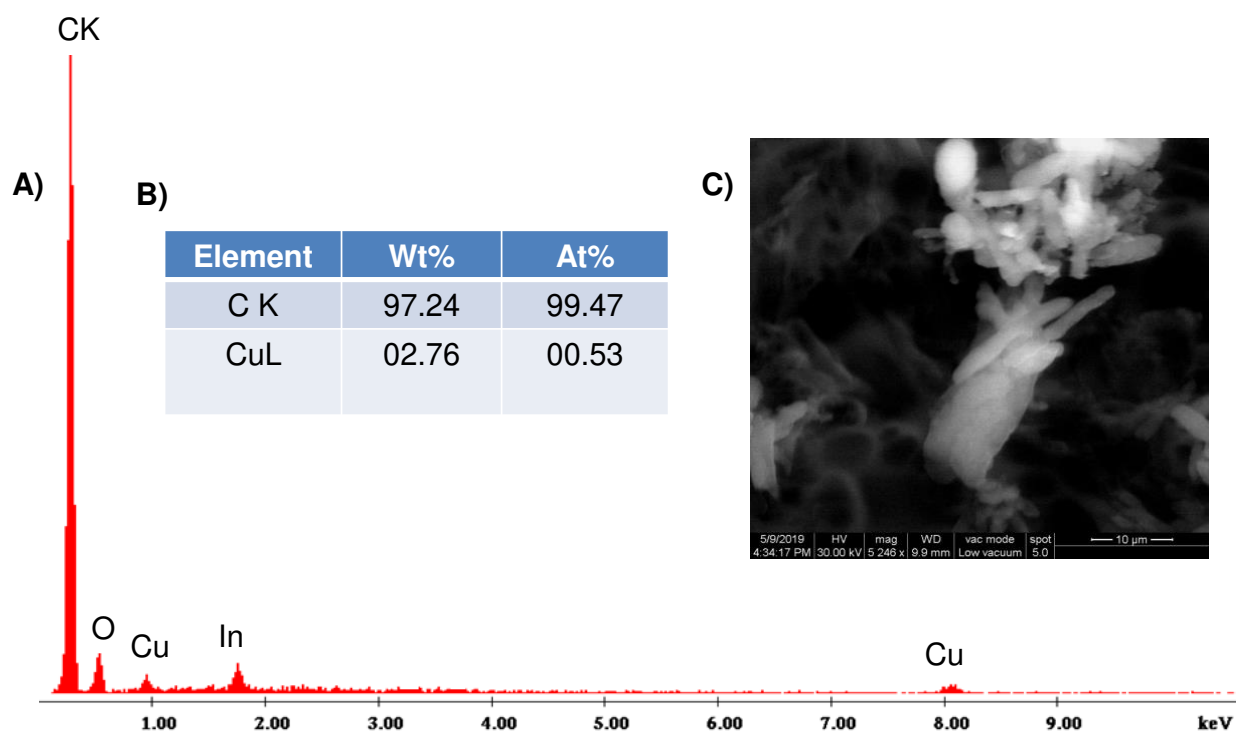


**Figure S21.** A) SEM/EDS of the copper-derived polypropylene polymeric film. B) Elemental analysis, showing the presence of copper and carbon. Other peaks are because of the ITO plate used as the substrate. C) Image of plastic particles of polypropylene found in the solution.



# Waterborne Fluorine-Free Superhydrophobic Surfaces Exhibiting Simultaneous CO<sub>2</sub> and Humidity Sorption

Avijit Baidya, Anagha Yatheendran, Tripti Ahuja, Chennu Sudhakar, Sarit Kumar Das, Robin H. A. Ras, and Thalappil Pradeep\*

Recent progress in the field of superhydrophobic materials has proven their potential to solve many problems of the contemporary society. However, the use of such materials to capture moisture and CO<sub>2</sub> from air, to help reduce the impact of global climate change is not explored. In addition, most of the time, fabrication of these materials needs organic solvents and fluorinated molecules involving multiple steps that hinder the use of nonwetable materials in everyday life. Herein, a waterborne, fluorine-free, robust superhydrophobic material synthesized at room temperature through a one-step chemical-modification process is reported, which exhibits moisture and CO<sub>2</sub> capturing capability. While covalently grafted low surface energy hydrocarbon molecules control the bulk superhydrophobicity, the incorporated amine functionalities facilitate moisture and CO<sub>2</sub> adsorption as these molecules (H<sub>2</sub>O and CO<sub>2</sub>) can easily diffuse through hydrocarbon assemblies. Being polar, H<sub>2</sub>O molecules are observed to readily interact with amine groups and favor the adsorption process. Synthesized material shows an approximate CO<sub>2</sub> adsorption of 480 ppm (10.90 mmol L<sup>-1</sup>) in ambient conditions having 75% humidity. Multifunctionality along with durability of this material will help expand the applications of superhydrophobic materials.

## 1. Introduction

Mimicking natural phenomena is probably the best way to explore smartness. Over the years this has made Mother Nature an idol of architecture. Among many others, surfaces of various biological species having interesting nonwetting characteristics have attracted both industry and academia and have become some of the intensely pursued research areas because of their enormous potential in various domains.<sup>[1]</sup> Although several methodologies have been introduced to fabricate these surfaces, complicated multistep processes, limitation in large area production, durability, etc., have restricted their use in everyday life.<sup>[2]</sup> Recently, a few such robust liquid repelling surfaces have been reported.<sup>[2c,3]</sup> However, in most of the cases, achieving such a property involves the use of 1) fluorine-containing chemicals (offering low surface energy) and 2) hazardous organic solvents.<sup>[3a,4]</sup> While fluorinated hydrocarbons can lead to bioaccumulation and toxicity, the use of organic solvents increases environmental

concerns.<sup>[5]</sup> Recently, a few superhydrophobic materials have also been designed with reduced environmental impact.<sup>[6]</sup> For example, Chen and co-workers have demonstrated the fabrication of a fluorine-free robust superhydrophobic surface, but organic solvents were used in the process.<sup>[7]</sup> We have shown the fabrication of organic-solvent-free superhydrophobic materials that contain fluorinated molecules.<sup>[8]</sup> Therefore, designing a water-based fluorine-free robust low energy materials at ambient conditions is important from the perspective of reduced environmental impact and industrial significance.

Imparting new properties such as conductivity, chemical sensitivity, etc., especially to nonwetable materials is important.<sup>[9]</sup> For example, introduction of carbon-based materials such as graphite, reduced-graphene, and carbon nanotubes to enhance the mechanical, thermal, and electrical conductivity,<sup>[10]</sup> incorporation of inorganic nanoparticles such as TiO<sub>2</sub>, and ZnO to impart biodegradation, etc.,<sup>[2a,11]</sup> to superhydrophobic surfaces are well known. However, in most of the cases, these modified surfaces were developed through the incorporation of different micro/nanomaterials. In contrast, fabrication of superhydrophobic materials having molecularly grafted functionalities

Dr. A. Baidya, A. Yatheendran, T. Ahuja, C. Sudhakar, Prof. T. Pradeep  
DST Unit of Nanoscience  
Thematic Unit of Excellence  
Department of Chemistry  
Indian Institute of Technology Madras  
Chennai 600036, India  
E-mail: pradeep@iitm.ac.in

Dr. A. Baidya, Prof. R. H. A. Ras  
Department of Applied Physics  
Aalto University School of Science  
Puumiehenkuja 2, 02150 Espoo, Finland

Dr. A. Baidya, Prof. S. K. Das  
Department of Mechanical Engineering  
Indian Institute of Technology Madras  
Chennai 600036, India

Prof. R. H. A. Ras  
Department of Bioproducts and Biosystems  
Aalto University School of Chemical Engineering  
Kemistintie 1, 02150 Espoo, Finland



The ORCID identification number(s) for the author(s) of this article can be found under <https://doi.org/10.1002/admi.201901013>.

DOI: 10.1002/admi.201901013

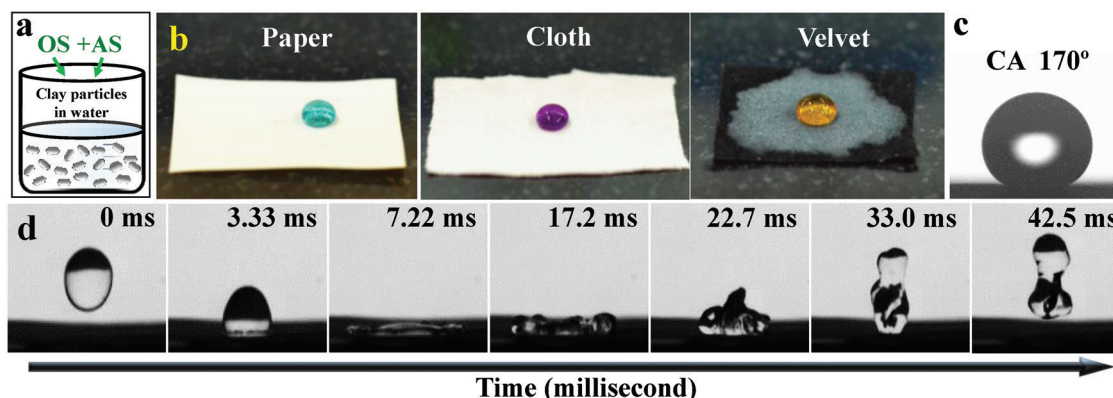


**Figure 1.** a) Schematic representation of the synthesis of a waterborne superhydrophobic material. b) Photograph of colored water droplets over various coated substrates. Aqueous solutions of  $\text{CuCl}_2$ ,  $\text{KMnO}_4$ , and  $\text{K}_2\text{Cr}_2\text{O}_7$  were used instead of pure water to add color contrast. c) Static water contact angle over a superhydrophobic paper. d) Time resolved bouncing of water droplet over a coated filter paper (soft surface).

to address various environmentally relevant problems has not been explored. In the context of recent concerns about the climate change, both moisture and  $\text{CO}_2$  have great influence on the rise of atmospheric temperature. Although some superhydrophobic/omniophobic membranes<sup>[12]</sup> and MOFs (metal organic frameworks)<sup>[13]</sup> are known to capture  $\text{CO}_2$ , their fabrication processes involve multiple steps, hazardous organic solvents, and fluorine-containing molecules. In the case of membranes, liquid repelling property enhances gas diffusion through them as the pores are not blocked by water molecules.  $\text{CO}_2$  diffusion through the membranes is typically dissolved and separated by alkaline amine solutions.<sup>[12a]</sup> For MOFs, even though it shows an uptake of  $\approx 11.0 \text{ mol L}^{-1}$  at 298 K and 55 bar with 100 mg of the material, stability, complex fabrication protocols, bio and environmental-compatibility as well as industrial scale production require additional efforts. These limit the usability of these materials in everyday life even though they may possess good  $\text{CO}_2$  adsorption capability.

Herein, we have designed an environment-friendly waterborne clay-based material at ambient conditions that provides a robust large-area superhydrophobic coating at room temperature and adsorbs moisture (water vapor) and  $\text{CO}_2$  from air at the same time without affecting its nonwetting property. These multifunctional properties of the material arise from the covalently grafted chemical-functionalities having different molecular dimensions. While the incorporated hydrocarbon chain decreases the surface free energy of the material, amino functionalities (wrapped with clay sheets) facilitate adsorption of moisture and  $\text{CO}_2$  through electronegative nitrogen atoms. Being synthesized and dispersed in water at neutral pH, it also minimizes the safety concerns, environmental pollution, and operational cost, enhancing industrial viability. Applicability of this material to develop a robust and flexible waterproof paper is also demonstrated and tested with various external perturbations. In short, herein a waterborne green superhydrophobic material is developed through a one-step wet-chemical process that possesses environmentally relevant multifunctional properties and shows potential applicability in various industries such as paints, packaging, clothing, and paper.

## 2. Results and Discussion

**Figure 1a** schematically represents one-pot chemical modification of native clay (NC) particles with two different types of silanes, octadecyltriethoxysilane (OS) and 3-(2-aminoethyl-amino)propyltrimethoxysilane (AS), at room temperature, in water. This results in excellent water-repelling thin films upon spray coating the suspension over various soft and hard substrates (Figure 1b). OS molecules, that possess low surface energy because of the hydrocarbon chain, get slowly adsorbed over clay sheets through hydroxyl groups and finally form covalent bonds through hydrolysis.<sup>[8a]</sup> These hydrocarbon chains introduce nonwetting characteristics to the hydrophilic clay material that forced water droplet to sit as a sphere having a static contact angle (CA) of  $170^\circ$  (Figure 1c). Thermodynamically, it also minimizes the air–water–solid interfacial energy of water droplet and facilitates its rolling-off. Water-repelling property of the material was evaluated with advancing and receding contact angle (AC and RC) and contact angle hysteresis (CAH) measurements, which are more sensitive to the droplet dynamics on the surface (Figure S1, Supporting Information). This was further extended to droplet drag test (DDT) and vertical droplet adhesion test (VDAT)<sup>[8a]</sup> (Figure S2 and Videos S1 and S2, Supporting Information). Bouncing of a water droplet even over a soft surface (coated filter paper) is pictorially presented in Figure 1d and Video S3 in the Supporting Information.

Modified clay (MC) induces nanoscale surface roughness, one of the prerequisites for superhydrophobicity, which was revealed through atomic force microscopy (AFM) (Figure 2a). While average surface roughness of the coated glass surface was  $\approx 180 \text{ nm}$ , NC coated glass surface showed an average roughness of 30 nm (Figure S3, Supporting Information). Such enhancement in roughness is known to be controlled by the hydrophobic effect,<sup>[8a]</sup> namely an interaction between water and low surface energy molecules. Surface morphology of MC coated filter paper was imaged by scanning electron microscopy with a tilt angle of  $45^\circ$  (Figure S4, Supporting Information). Uniformly distributed nanoscale features over micrometer sized fibrous matrices facilitate the trapping of air, leading to an excellent water-repelling property. Inset demonstrates the

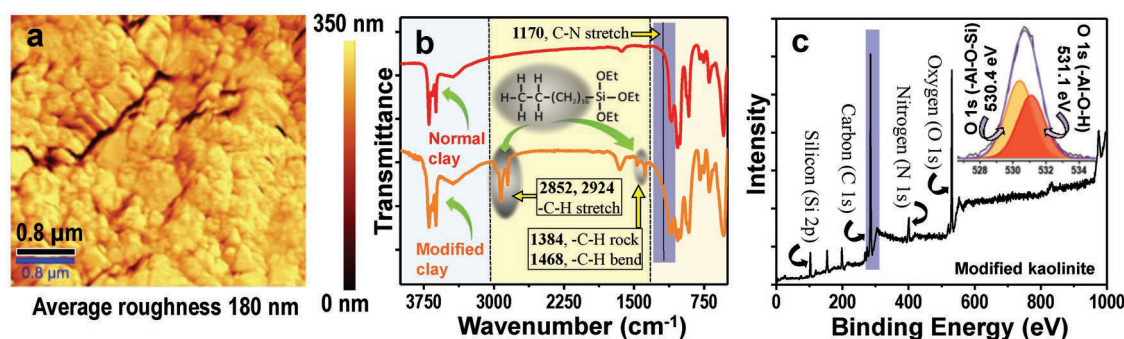


**Figure 2.** a) AFM image of the coated glass substrate reveals the roughness of the coating (average roughness 180 nm). b) IR spectra of the superhydrophobic material (normal and modified clay). Peaks at 2852, 2924, 1384, and 1468  $\text{cm}^{-1}$  (marked area) correspond to various vibrational modes of the C–H bond. Shoulder at 1170  $\text{cm}^{-1}$  (for expanded view, see Figure S6, Supporting Information), which broadened the spectrum, corresponds to C–N stretching. c) Survey and deconvoluted XPS spectra in the O1s region showing the relative concentrations of Al–O–H and Al–O–Si linkages, over chemically functionalized clay-coated surface.

top/perpendicular view ( $0^\circ$ ) of the surface. Figure S5 in the Supporting Information demonstrates the cross-sectional view of the layered superhydrophobic thin film, coated over a glass substrate. Average thickness of the coating was 8–10  $\mu\text{m}$ .

Mode of attachment of the incorporated chemical-functionalities with NC particles, being the underlying reason to provide durable superhydrophobicity, was studied with IR spectroscopy and X-ray photoelectron spectroscopy (XPS). Additional peaks at 2852, 2924, 1384, and 1468  $\text{cm}^{-1}$  (marked) in the IR spectrum of MC particles are related to the stretching, rocking and bending vibrational modes of the C–H bond (Figure 2b). This confirmed the chemical attachment of AS and OS with NC particles which is solely inorganic in nature (being an aluminosilicate). Apart from this, a shoulder at 1170  $\text{cm}^{-1}$  (marked, expanded view Figure S6, Supporting Information), which is associated with the broadening of IR spectrum of MC in the region of 1100–1200  $\text{cm}^{-1}$ , is related to the C–N stretching. NC particles (kaolinite) mostly consist of Al–O–H and Al–O–Si groups where the upper-most layer of the surface contains relatively higher concentration of Al–O–H (than Al–O–Si) groups (Figure S7, Supporting Information). These active O–H groups readily react with silane molecules resulting in an increase of Al–O–Si network over the surface. Figure 2c shows the relative concentrations of Al–O–H and Al–O–Si for the MC coated surface. Incorporation of hydrocarbon functionalities over the clay surfaces also reflects the presence of substantial amount of carbon (Figure 2c) compared to the unmodified one (Figure S8, Supporting Information). Small peak in the region of 285 eV in the spectrum of the NC corresponds to carbon, which mostly comes from the organic species (Figure S8, Supporting Information). Eventually, the covalent attachment between Si (from OS or AS) and OH (from NC) leads to the long-standing stability of the material. This was also tested by keeping both the as-synthesized MC dispersion and the coated substrates for 3 months at normal atmospheric condition and room temperature (30–38  $^\circ\text{C}$ ) (Experimental Section) in the laboratory condition.

Mechanical durability being an essential parameter toward various industrial applications, MC coated superhydrophobic surfaces were tested with several hard and soft abrasion tests. Static and dynamic contact angles of water droplets over abraded surfaces are graphically presented in Figure 3a. After

every ten completed abrasion cycles, water CA were measured and continued for 100 cycles. For instance, in the hard abrasion tests, the coated surface was subjected to sand paper abrasion test with a load of 50 g and mechanical-pressing test with a pressure of 264.4 atm (equivalent to a weight of 5 ton) (Figure S9i,ii, Supporting Information). In the first case, even though 100 abrasion cycles result in the removal of a few layers of the coating, the underlying layers helped to retain their water-repelling property intact<sup>[8a,14]</sup> and made water droplets to roll-off through the abraded surface areas (Figure 3a). Similar water-repellent property was observed after mechanical-pressing test where the coated surface was subjected to a pressure of 264.4 atm (equivalent to a weight of 5 ton) (Figure S9ii, Supporting Information). For soft abrasions, the coated surface was tested with tissue paper abrasion and finger wiping test in a cyclic fashion (Figure S9iii,iv, Supporting Information). Here also, nonwettability was unchanged with spontaneous rolling-off of the water droplets through the abraded areas (Figure 3a). Unaltered superhydrophobicity of the abraded surface was further examined with DDT and VDAT. DDT over finger-wiped surface and VDAT over sand paper abraded surface are presented in Figure S10a,b and Videos S4 and S5 in the Supporting Information. To demonstrate the applicability of the material for various paper-based technologies, the coated superhydrophobic paper was subjected to various manual-bending-movements (Figure 3b,1–4) that are comparable to everyday applications. These were performed 100 times and the treated-surfaces were evaluated with CA and CAH measurements (Figure 3c). Durability of the coated surface was further tested with the oil-wash experiment (Figure S11, Supporting Information) where the superhydrophobic surface (filter paper) was artificially wetted with silicone oil and washed manually with ethanol and hexane. Retention of water-repelling characteristic upon the abovementioned experiments not only proves the durability of the material, it also showed the effective binding of the material with the substrate without any adhesive. This binding is due to the self-polymerization of secondary amine groups during the spontaneous drying process<sup>[8a]</sup> that assists the binding between the clay particles as well as between the material and the substrate. These bending experiments also demonstrate the flexibility of the coated paper.



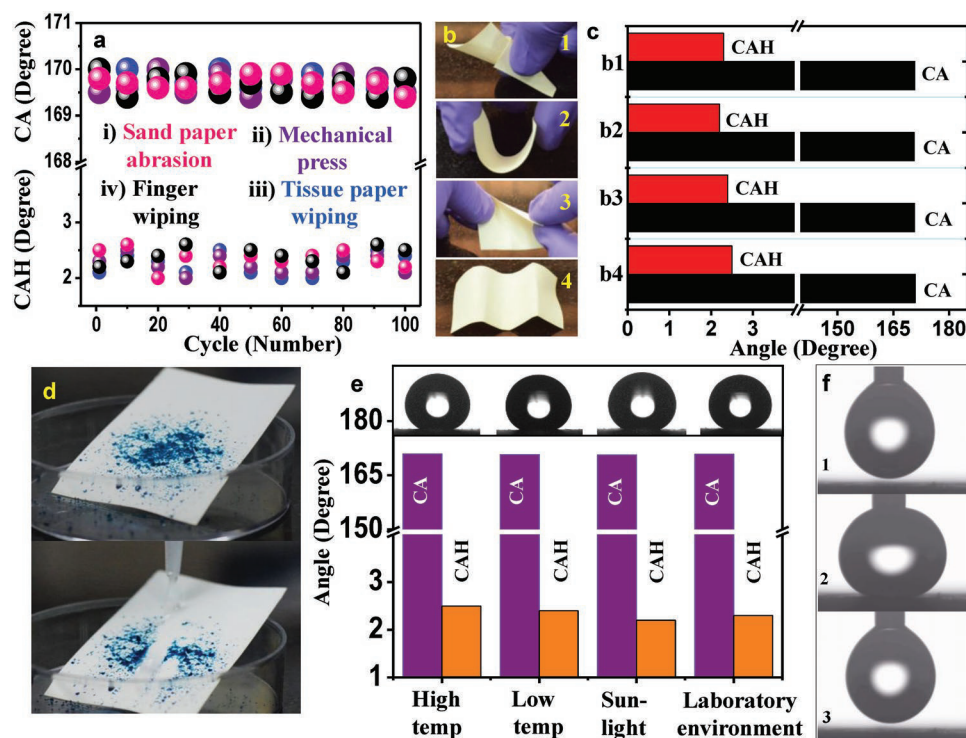


**Figure 3.** a) Durability of the water-repelling surface in terms of the change in CA and CAH of water droplet during multiple abrasion cycles. i) Sand paper abrasion with 50 g of load (abrasion distance of 5 cm), ii) mechanical pressing with a pressure of 264.4 atm (equivalent to the weight of 5 ton), iii) tissue paper abrasion, and iv) finger wiping test. b) Possible bending movements of the superhydrophobic paper (1)–(4). c) Change of nonwetting property of the superhydrophobic paper (presented through static CA and CAH) upon manual bending cycles illustrated in (b), for 100 times. d) Water-repelling and self-cleaning property of the coated paper after treating with an organic solvent (THF treated surface is demonstrated here). Water droplets carry the dust and roll off. e) Durability of the coated paper upon various environmental perturbations such as temperature treatments for 2 h (150 and  $-80^{\circ}\text{C}$ ), exposure to direct sunlight and normal laboratory environment for 3 months. Inset: Static contact angles of water droplet after corresponding experiments. f) Vertical droplet adhesion test over high-temp-treated superhydrophobic surface (1)–(3). Detachment of the water droplet without leaving any trace of water over the treated surface proves the retained nonwetting property of the coated substrate.

Similar to the mechanical durability, stability of the material toward low-surface-tension liquids that stick and penetrate the surface easily, was tested with multiple organic solvents having a range of polarity (Experimental Section). In the first case, surfaces were washed with different organic solvents and tested with the movement of water droplets after proper drying. In all the cases, surfaces were observed to maintain their superhydrophobicity and self-cleaning property. This is presented for tetrahydrofuran (THF)-treated surface in Figure 3d (pictorially) and Video S6 in the Supporting Information. In the second case, surfaces were immersed in selected solvents and kept for a long time (50 h) at room temperature in a closed container (to avoid the evaporation of the solvents). Water-repelling property of these surfaces was evaluated through CA and CAH measurements after every 5 h interval (Figure S12, Supporting Information). Behavior of acidic and basic ( $\text{pH} = 1$  and  $\text{pH} = 14$ ) water droplets over the coated surface was tested with CA measurements and VDAs (Figures S13 and S14, Supporting Information). Effect of various extreme environmental conditions such as high-temp ( $150^{\circ}\text{C}$ ), low-temp ( $-80^{\circ}\text{C}$ ), exposure to direct sunlight and normal laboratory conditions for long time were also tested in order to test the industrial relevance of this material (Figure 3e). Details are given in the Experimental Section. Inset shows the CA of the water droplet

after corresponding experiment. Treated surfaces were further tested with VDAT. Figure 3f and Video S7 in the Supporting Information correspond to VDAT over high-temp-treated surfaces. Temperature stability of the material was further investigated in detail till  $250^{\circ}\text{C}$  and the exposed surfaces were studied with CA and VDAT measurements (Figure S15a,b, Supporting Information). VDAT with  $250^{\circ}\text{C}$  temperature treated surface was presented in Figure S15b in the Supporting Information.

Apart from superhydrophobicity, the synthesized material showed interesting and environmentally relevant properties, such as adsorption of moisture and  $\text{CO}_2$ . To demonstrate the moisture capturing ability of the material, coated filter papers were subjected to humid air (85% relative humidity, RH) in a closed container and change of RH with time was studied at constant temperature ( $25^{\circ}\text{C}$ ). Surprisingly, within 2 min, RH of the enclosure was seen to decrease to less than 20% (marked, Figure 4a) and finally reached a constant value of  $(10 \pm 2)\%$  RH with time. This change in RH was not seen for filter paper and NC (Figure S16, Supporting Information). Amino-functionalities being the active sites to facilitate moisture-adsorption, along with the superhydrophobic material (AS + OS@clay) that contain AS, a control study was performed with only-amine functionalized clay (AS@clay) (Figure 4a, inset).

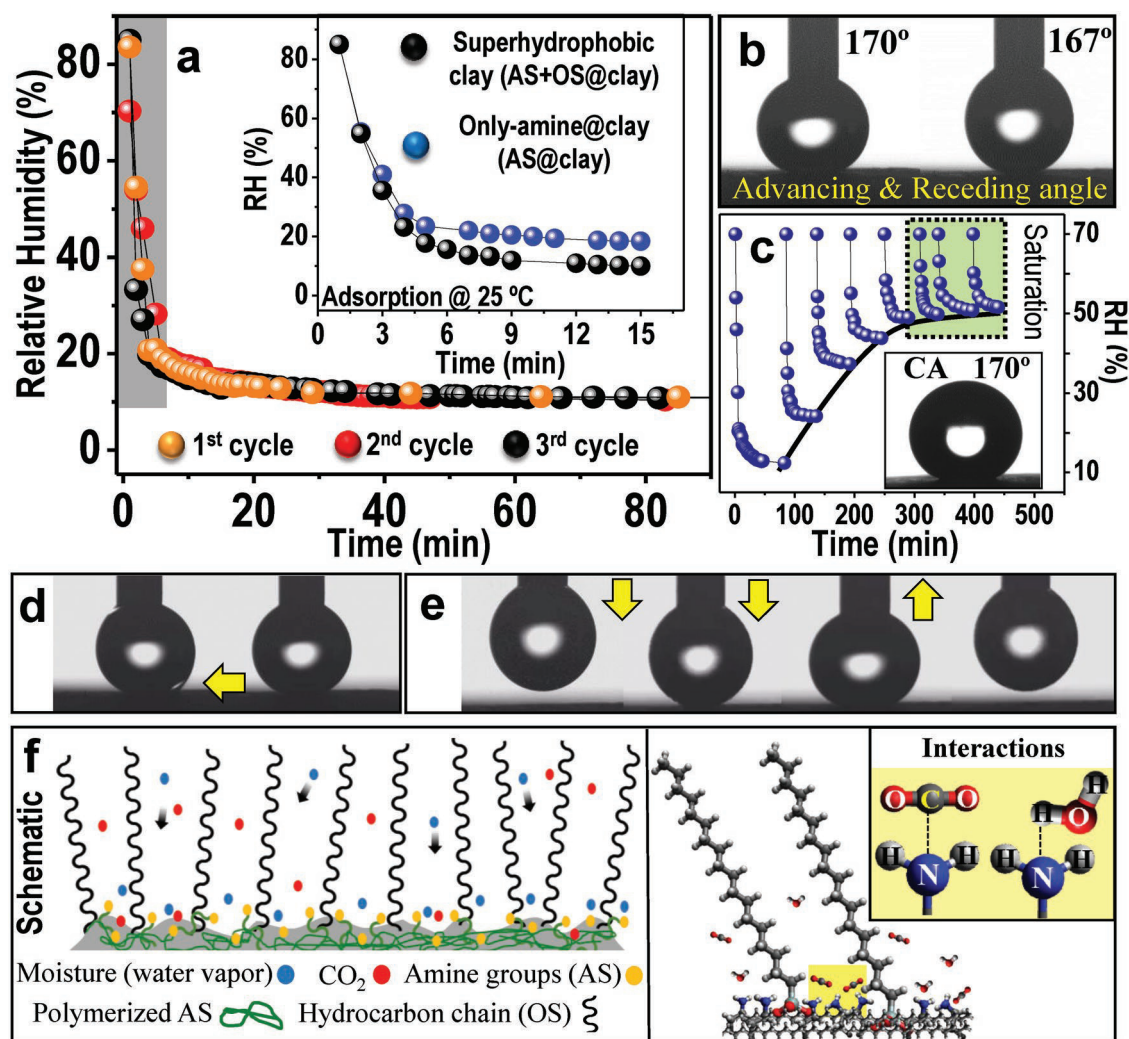


**Figure 4.** a) Rapid adsorption of moisture by superhydrophobic material at constant temperature. (Inset) Experiments with amine functionalized (AS@clay) and superhydrophobic (AS + OS@clay) surfaces prove that the amine functionalities are the underlying reason for moisture adsorption. Control experiment with NC is shown in Figure S16 in the Supporting Information. Both amine-functionalized clay and superhydrophobic clay contain the same amount of amine functionality. b) Advancing and receding water contact angles over superhydrophobic surface after the moisture-adsorption experiment (a). c) Consecutive cycles to achieve moisture saturation of the coated surface at constant temperature. Black curve represents the sigmoidal nature of moisture adsorption toward saturation. (Inset) Static CA of water droplet over saturated superhydrophobic surface derived from the experiment (c). d) Droplet drag test and e) vertical droplet adhesion test over moisture saturated superhydrophobic surface. f) A molecular-surface-functionality model to illustrate the moisture adsorption phenomenon over functional superhydrophobic material. Assembled hydrocarbon chains that control the bulk nonwettability (by decreasing surface energy and trapped air) but allow air molecules (moisture and CO<sub>2</sub>) to diffuse into the assemblies. Inset: Interactions between electronegative nitrogen atom of amine group with water and CO<sub>2</sub>.

Similar decrease of RH for both the cases revealed the moisture-adsorption mechanism as well as the importance of amino-functionalities to impart such a property to the coating material. Being an electronegative element, nitrogen atoms easily interact with water molecules through hydrogen bonds and facilitate adsorption of water. It is also possible through the electrostatic interaction between amine and water molecules, as secondary amine groups sometimes possess distinct positive charges. This reflects the fast adsorption kinetics of water molecules. Comparatively less adsorption of moisture for AS@clay compared to the AS + OS@clay, although concentration of amine-functionality was equal in both the materials, suggests that along with the presence

of active-chemical-functionalities, hydrophobic effect-induced enhancement of surface roughness (Figure 2a) results in higher surface exposure for the AS + OS@clay. However, the kinetics of this moisture adsorption was seen to be identical for both the materials, at constant temperature (25 °C). As surrounding temperature having a great influence on both RH and adsorption kinetics, temperature-dependent studies were performed with constant initial RH of 85% (Figure S17, Supporting Information) where negligible difference in the moisture adsorption was observed. Temperatures were chosen near indoor values. Although all these experiments were performed between 20 and 30 °C, rapid moisture adsorbing capability of the material is expected to be enhanced at lower surrounding temperatures.

Surprisingly, the water-repellent property of the material remained intact even after adsorption of moisture from air. Corresponding AC, RC, and CA over moisture adsorbed surfaces are presented in Figure 4b and Figure S18 in the Supporting Information. This was further studied in detail with a moisture-saturated superhydrophobic surface where the saturation-adsorption of the coated surface was carried out through multiple adsorption cycles at 25 °C, presented in Figure 4c. CA over this moisture-saturated sample was 170° (Figure 4c, inset), similar to the untreated surface (Figure 1c). Nonwettability of the moisture-saturated surface was also studied in detail with DDT and VDAT (Figure 4d,e and Video S8, Supporting Information). This can be correlated with the previously discussed experiments in Figure 3e where even after long exposure to sunlight and normal laboratory conditions (it results in the moisture-saturated surface), surfaces retain their water-repelling characteristics. For better understanding of such moisture adsorption phenomenon over a functional superhydrophobic material, a molecular-surface-functionality model is presented in Figure 4f. While small AS molecules get wrapped over the clay particles through a spontaneous self-polymerization of secondary amines, OS molecules with hydrocarbon chain mostly stay perpendicular to the surface<sup>[15]</sup> and control the bulk nonwetting property of the surface by reducing the surface energy and by trapping air inside the assemblies. Although these assemblies restrict the penetration of water droplets, water vapor or moisture (blue dots) can easily diffuse between these giant molecular walls and get adsorbed with amine functionalities. Nitrogen

atom-induced interaction between amine functionalities and water molecules is shown in Figure 4f, inset. In short, the local molecular structure (and dimension) with proper chemical functionalities impart this property to the new superhydrophobic material.

For CO<sub>2</sub> capturing experiments, the coated surface was subjected to an artificially injected closed CO<sub>2</sub> environment. Figure 5a shows different cycles of CO<sub>2</sub> adsorption at 25 °C and a RH of 20%. Chemically, in this case also, molecular functionalities such as primary and secondary amines facilitate the adsorption of CO<sub>2</sub>. This is schematically presented in Figure 4f where red color dots represent CO<sub>2</sub> molecules. Material shows an approximate CO<sub>2</sub> uptake of 480 ppm (10.90 mmol L<sup>-1</sup>) under ambient conditions having 75% humidity. However, in this case, the adsorption kinetics was observed to be slower than the previous one (humidity adsorption). Unchanged wettability of the CO<sub>2</sub>-adsorbed material was measured with CA (Figure 5a, inset). To identify the nature of chemical-bonding between CO<sub>2</sub> molecules and amine groups, CO<sub>2</sub>-adsorbed material was characterized with IR spectroscopy (Figure 5b–d). As percentage of clay content is very high in the material and clay has various IR active modes in the lower region, only-amine (AS) which plays the key role to adsorb CO<sub>2</sub> was used to locate the chemical signatures related to the adsorption and interaction of CO<sub>2</sub> with amine groups (Figure 5b,c). Generally, CO<sub>2</sub> molecules bind with amine functionalities and form amide groups. Observed peak at 1650 cm<sup>-1</sup> relates to this C=O stretching of amides. Peaks at 1310 and 1412 cm<sup>-1</sup> correspond to the NCOO stretching

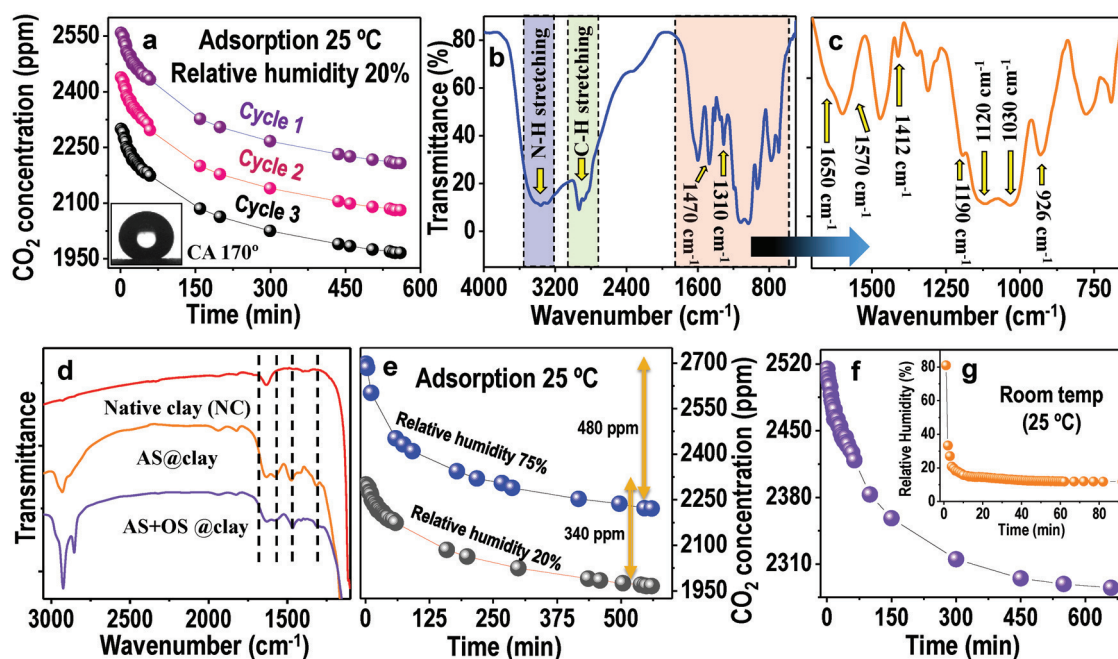


**Figure 5.** a) CO<sub>2</sub> capturing phenomenon over superhydrophobic surface at constant temperature. Inset: Static water contact angle over CO<sub>2</sub> adsorbed surface showing the retained superhydrophobicity of the coated substrates. b) IR spectrum of only-amine (AS) after CO<sub>2</sub> adsorption. As clay has different IR active sites (in lower region), to locate the chemical changes properly upon CO<sub>2</sub> adsorption, only-amine was used here. Signatures correspond to the uptake of CO<sub>2</sub> are marked. c) Enlarged view of the area of interest in the spectrum (b). d) IR spectra of CO<sub>2</sub>-adsorbed native clay, amine-clay, and superhydrophobic clay. Characteristic features upon CO<sub>2</sub> adsorption are marked by dotted lines. These are present in both amine-clay and superhydrophobic clay but not observed in the IR spectrum of native clay. e) Influence of relative humidity on CO<sub>2</sub> adsorption process at constant temperature. f,g) Moisture and CO<sub>2</sub> adsorption performance (together) of the material at ambient conditions.



which also confirms the binding of CO<sub>2</sub> with amine functionalities. While peaks at 1030, 1120, and 1570 cm<sup>-1</sup> (shoulder) are associated with ammonium carbamate, peak at 1470 cm<sup>-1</sup> comes from NH<sub>3</sub><sup>+</sup>/NH<sub>2</sub><sup>+</sup>. Distinct peak at 926 cm<sup>-1</sup> relates to the N–H wagging of primary amine. However, these peaks are not present in pure amine.<sup>[16]</sup> Figure 5d represents the IR spectra of CO<sub>2</sub>-adsorbed NC, AS@clay, and AS + OS@clay, where none of the characteristic features of CO<sub>2</sub> adsorption were seen for NC (features due to CO<sub>2</sub> adsorption in AS@clay and AS + OS@clay are marked). Humidity being an influential parameter for chemical adsorption of CO<sub>2</sub>, humidity dependent experiments were also performed at a constant temperature of 25 °C (Figure 5e). Adsorption of larger amount of CO<sub>2</sub> in higher RH (75%) compared to the low humid condition (20% RH) again validated the CO<sub>2</sub> capture mechanism of the material.<sup>[17]</sup> While at low RH (25%), surface was observed to show adsorption of 350 ± 15 ppm CO<sub>2</sub>, at RH 75% it was in the range of 480 ± 15 ppm CO<sub>2</sub> on an average. To demonstrate the real-life usability of the material, moisture and CO<sub>2</sub> capture experiments were performed together at constant temperature (Figure 5f,g). As seen before, in this case also, rapid adsorption of water vapor/moisture was observed and it decreased below 20% RH within a few minutes. At the same time, CO<sub>2</sub> capturing ability of the material remained unaltered. Having such important properties toward environmental issues along with its durable nonwettability, we believe that this multifunctional superhydrophobic material will enhance its usability in different technologies including paints, flexible electronics, and microfluidic devices.

### 3. Conclusion

In conclusion, we demonstrate the development of a green and multifunctional waterborne superhydrophobic material having an enhanced environmental relevance. Ability to adsorb moisture and CO<sub>2</sub> at the same time without affecting the water-repelling characteristics makes this material novel and industrially valuable. Being synthesized in water and ambient conditions, it promotes bulk production and minimizes additional environmental concerns and safety related issues. Durability of the coated surfaces against various external perturbations revealed the applicability of the material in day-to-day life. This includes various paper-based technologies, clothing, packaging, and many others. Molecular functionality-driven rapid adsorption of moisture at different temperatures promotes the versatile use of the material for different purposes. CO<sub>2</sub> adsorption capability even in dry condition highlights the potential of the material as well. Finally, the ease of synthesis and ecofriendly nature of the material not only broadens its industrial adoptability, it also addresses the urgent environmental need toward reducing the impact of air pollution and climate change.

### 4. Experimental Section

**Materials:** All the chemicals were purchased from commercial sources and used without further purification. Kaolinite clay was purchased from Alpha minerals and chemicals (India). OS (95%) was

purchased from Gelest (USA). AS (commercial grade) was purchased from Rishichem Distributors (India). Ethanol, hexane, heptane, dimethyl sulfoxide (DMSO), and THF were procured from RANKEM, India. All the chemicals were used without further purification. Sandpaper (P320) was purchased from a local hardware shop.

**Synthesis:** Chemical modification of the hydrophilic clay particles was performed solely in water through a wet chemical process (Figure 1a and Figure S19, Supporting Information). One pot synthesis of the material includes the mixing of two differently functionalized silane molecules, AS (1 mL) and OS (0.7 mL), with well-dispersed aqueous clay solution (2.75 wt%) at room temperature and was kept under vigorous stirring condition for 10–12 h. Although the silanes are generally very reactive in water, chemical attachment of OS with clay particles was controlled, as the solubility of OS in water is very low because of the long hydrophobic tail. Having silane functionality in another end, this low surface energy molecule initially gets adsorbed on the hydroxylated surfaces of clay particles and slowly underwent hydrolysis forming chemical bond with the clay sheet. As-synthesized dispersed material was then spray coated over various substrates and kept for drying. Although the coated surfaces were dried at room temperature (32 °C) and showed excellent water-repelling characteristic, to enhance the evaporation rate of water, coated substrates were also allowed to dry in warm condition (50 °C) that does not change the chemical and physical properties of the material (Figure S20, Supporting Information). Therefore, to prepare the bulk samples for multiple experiments, this condition (drying at 50 °C) was followed all the time.

**Long Term Stability of the Material:** Long-term stability of the material was tested through two different ways. In the first case, as synthesized material was immediately coated over the surfaces and kept for 3 months. In the second case, the synthesized material was stored for 3 months and then coated over the surfaces. In both the cases, surfaces showed similar water-repelling property compared to the freshly prepared samples (as-synthesized material immediately coated and dried). In addition, the stability of the chemical attachments of these molecules (AS and OS) with clay particles was also studied through IR spectroscopy. Here, the dried material was sonicated in water for 30 min and the supernatant was studied by IR spectroscopy (Figure S21, Supporting Information). In the Figure, spectrum of the supernatant (blue) does not contain any characteristic peak of either AS (black) and OS (red). Whereas the spectrum was similar to pure water (orange).

**DDT and VDAT:** For the drag test, a water droplet (≈5 µL) attached with a needle was dragged back and forth by 5 cm over a coated surface and the change was observed in the shape of droplet during the movement. Whereas in the second experiment, vertical droplet adhesion test, water droplet (≈5 µL) attached with a needle was moved up and down and pushed vertically over the surface to deform the shape of the droplet. Detachment of the water droplet from the superhydrophobic surface without leaving any traces showed the extent of the water-repelling nature of the material. These were performed in different locations of the surface as well.

**Sand Paper Abrasion and Mechanical Pressing Test:** For sand paper abrasion test, sand paper was placed between the surface and a load of 50 g and moved for 5 cm back and forth. After each ten consecutive cycles CA, AC, and RC of water droplet over abraded surface were measured and presented in Figure 3a. This was continued for 100 cycles. For mechanical pressing test, coated superhydrophobic paper was subjected to a pressure of 264.4 atm (equivalent to the weight of 5 ton). In this case, after every 1 h, CA, AC, and RC of water droplet was measured. This pressure treatment of 1 h corresponds to ten complete cycles.

**Oil-Wash Experiment:** For the oil-wash experiment, a coated filter paper was artificially wetted with viscous silicone oil. Being oleophilic in nature, oil adsorbs on the surface nicely and goes inside the rough surface structure. Adsorbed oil was then manually washed with ethanol and hexane. Washed filter paper was further kept inside hexane for 12 h and was tested with water after complete drying.

**Chemical Durability Against Organic Solvents:** Durability of the coated surface against organic solvent was performed in two ways with THF, DMSO, ethanol, and heptane. Solvents were chosen having different



polarity. In the first case, coated surfaces were washed with these solvents and tested with the movement of water droplets and self-cleaning property. For the second one, coated surfaces were immersed inside the organic solvents for 50 h in a closed container and tested with CA, AC, RC, and CAH measurements every 5 h intervals.

**Durability against Environmental Stresses:** Durability of the coated surface against various environmental stresses were evaluated by treating the surface with extreme temperature, direct sunlight, and normal laboratory atmosphere for long times. For temperature treatment, surfaces were kept at 150 °C and −80 °C for 2 h. Treated surfaces were tested with static and dynamic water contact angle measurements once they reached to ambient temperature. Change in wetting property of the surface upon exposure to sunlight and normal laboratory atmosphere for long time was tested by keeping the surfaces outside (under direct sunlight and laboratory environment) for 3 months. However, even after a year the surfaces were observed to retain their superhydrophobicity.

**Temperature Stability Experiment:** For studying the stability of the material at higher temperature (>150 °C), the coated surfaces were tested at 200, 225, and 250 °C. In all the cases, to eliminate the aerial oxidation, surfaces were heated in vacuum condition for 30 min. Nonwettability of the treated surfaces was examined with CA and VDAT. While till 250 °C, water droplets were observed to roll off nicely, above this, pinning of the droplets was seen.

**Moisture and CO<sub>2</sub> Adsorption Experiments:** Both moisture and CO<sub>2</sub> adsorption experiments were carried out with coated filter paper in a closed container at constant temperature (25 °C). On an average ≈1 g material was used to coat the filter papers. Reproducibility of such rapid moisture adsorption and CO<sub>2</sub> adsorption were studied with same coated filter paper for multiple time in a cyclic way. These are presented in Figures 4a and 5a. In between the experiments, coated surfaces were reactivated by desorbing the adsorbed water and CO<sub>2</sub> molecules at a relatively warm condition (50–60 °C) for 10 min.

## Supporting Information

Supporting Information is available from the Wiley Online Library or from the author.

## Acknowledgements

The authors thank the Department of Science and Technology, Government of India for constantly supporting this research program on nanomaterials. A.B. acknowledges support of INSPIRE Fellowship, Department of Science and Technology, Govt. of India. R.H.A.R. acknowledges support by European Research Council (ERC-2016-CoG No. 725513 “SuperRepel”) and the Academy of Finland Centres of Excellence Programme (2014–2019). This work was supported by Finnish National Agency for Education. The authors thank Prof. Mahesh V. Panchagnula for helping in bouncing of water droplets experiments.

## Conflict of Interest

The authors declare no conflict of interest.

## Keywords

environment-friendly, moisture sorption and CO<sub>2</sub> capture, robust, superhydrophobicity, waterborne

Received: June 10, 2019

Revised: July 22, 2019

Published online:

- [1] a) T. Sun, L. Feng, X. Gao, L. Jiang, *Acc. Chem. Res.* **2005**, *38*, 644; b) G. Kwon, E. Post, A. Tuteja, *MRS Commun.* **2015**, *5*, 475; c) Y. Zheng, H. Bai, Z. Huang, X. Tian, F.-Q. Nie, Y. Zhao, J. Zhai, L. Jiang, *Nature* **2010**, *463*, 640; d) M. P. Sousa, J. F. Mano, *ACS Appl. Mater. Interfaces* **2013**, *5*, 3731.
- [2] a) K. Liu, M. Cao, A. Fujishima, L. Jiang, *Chem. Rev.* **2014**, *114*, 10044; b) H. Teisala, M. Tuominen, J. Kuusipalo, *Adv. Mater. Interfaces* **2014**, *1*, 1300026; c) S. Wang, K. Liu, X. Yao, L. Jiang, *Chem. Rev.* **2015**, *115*, 8230; d) G. B. Hwang, K. Page, A. Patir, S. P. Nair, E. Allan, I. P. Parkin, *ACS Nano* **2018**, *12*, 6050.
- [3] a) C. Peng, Z. Chen, M. K. Tiwari, *Nat. Mater.* **2018**, *17*, 355; b) J. E. Mates, T. M. Schutzius, I. S. Bayer, J. Qin, D. E. Walldrop, C. M. Megaridis, *Ind. Eng. Chem. Res.* **2014**, *53*, 222; c) D. Soto, A. Ugur, T. A. Farnham, K. K. Gleason, K. K. Varanasi, *Adv. Funct. Mater.* **2018**, *28*, 1707355.
- [4] a) Y. Lu, S. Sathasivam, J. Song, C. R. Crick, C. J. Carmalt, I. P. Parkin, *Science* **2015**, *347*, 1132; b) L. Li, B. Li, J. Dong, J. Zhang, *J. Mater. Chem. A* **2016**, *4*, 13677; c) X. Deng, L. Mammen, H.-J. Butt, D. Vollmer, *Science* **2012**, *335*, 67; d) X. Du, M. Wang, A. Welle, F. Behboodi-Sadabad, Y. Wang, P. A. Levkin, Z. Gu, *Adv. Funct. Mater.* **2018**, *28*, 1803765; e) D. Yoo, Y. Kim, M. Min, G. H. Ahn, D.-H. Lien, J. Jang, H. Jeong, Y. Song, S. Chung, A. Javey, T. Lee, *ACS Nano* **2018**, *12*, 11062; f) S. Pan, R. Guo, M. Björnalm, J. J. Richardson, L. Li, C. Peng, N. Bertleff-Zieschang, W. Xu, J. Jiang, F. Caruso, *Nat. Mater.* **2018**, *17*, 1040.
- [5] a) K. Chen, S. Zhou, S. Yang, L. Wu, *Adv. Funct. Mater.* **2015**, *25*, 1035; b) T. Darmanin, F. Guittard, *Soft Matter* **2013**, *9*, 5982.
- [6] a) A. M. Rather, U. Manna, *ACS Appl. Mater. Interfaces* **2018**, *10*, 23451; b) Z.-h. Zhang, H.-j. Wang, Y.-h. Liang, X.-j. Li, L.-q. Ren, Z.-q. Cui, C. Luo, *Sci. Rep.* **2018**, *8*, 3869.
- [7] H. Ye, L. Zhu, W. Li, H. Liu, H. Chen, *ACS Appl. Mater. Interfaces* **2017**, *9*, 858.
- [8] a) A. Baidya, M. A. Ganayee, S. Jakka Ravindran, K. C. Tam, S. K. Das, R. H. A. Ras, T. Pradeep, *ACS Nano* **2017**, *11*, 11091; b) A. Baidya, S. K. Das, R. H. A. Ras, T. Pradeep, *Adv. Mater. Interfaces* **2018**, *5*, 1701523.
- [9] a) Y. Ren, Z. Lin, X. Mao, W. Tian, T. Voorhis, T. A. Hatton, *Adv. Funct. Mater.* **2018**, *28*, 1801466; b) R. Wang, J. Zhu, K. Meng, H. Wang, T. Deng, X. Gao, L. Jiang, *Adv. Funct. Mater.* **2018**, *28*, 1800634; c) V. Jokinen, E. Kankuri, S. Hoshian, S. Franssila, R. H. A. Ras, *Adv. Mater.* **2018**, *30*, 1705104.
- [10] a) Y. C. Jung, B. Bhushan, *ACS Nano* **2009**, *3*, 4155; b) L. Ye, J. Guan, Z. Li, J. Zhao, C. Ye, J. You, Y. Li, *Langmuir* **2017**, *33*, 1368; c) A. Das, J. Deka, A. M. Rather, B. K. Bhunia, P. P. Saikia, B. B. Mandal, K. Raidongia, U. Manna, *ACS Appl. Mater. Interfaces* **2017**, *9*, 42354; d) K. K. Jung, Y. Jung, C. J. Choi, J. S. Ko, *ACS Omega* **2018**, *3*, 12956.
- [11] L. Chen, X. Sheng, D. Wang, J. Liu, R. Sun, L. Jiang, X. Feng, *Adv. Funct. Mater.* **2018**, *28*, 1801483.
- [12] a) F. Geyer, C. Schönecker, H.-J. Butt, D. Vollmer, *Adv. Mater.* **2017**, *29*, 1603524; b) Y.-F. Lin, W.-W. Wang, C.-Y. Chang, *J. Mater. Chem. A* **2018**, *6*, 9489.
- [13] a) C. Serre, *Angew. Chem., Int. Ed.* **2012**, *51*, 6048; b) P. Z. Moghadam, J. F. Ivy, R. K. Arvapally, A. M. dos Santos, J. C. Pearson, L. Zhang, E. Tylianakis, P. Ghosh, I. W. H. Oswald, U. Kaipa, X. Wang, A. K. Wilson, R. Q. Snurr, M. A. Omary, *Chem. Sci.* **2017**, *8*, 3989.
- [14] T. Verho, C. Bower, P. Andrew, S. Franssila, O. Ikkala, R. H. A. Ras, *Adv. Mater.* **2011**, *23*, 673.
- [15] C. Nicosia, J. Huskens, *Mater. Horiz.* **2014**, *1*, 32.
- [16] S. Ek, E. I. Iiskola, L. Niinistö, *J. Phys. Chem. B* **2004**, *108*, 9650.
- [17] a) J. J. Lee, C.-H. Chen, D. Shimon, S. E. Hayes, C. Sievers, C. W. Jones, *J. Phys. Chem. C* **2017**, *121*, 23480; b) A. Gholidoust, J. D. Atkinson, Z. Hashisho, *Energy Fuels* **2017**, *31*, 1756.



## Supporting Information

for *Adv. Mater. Interfaces*, DOI: 10.1002/admi.201901013

**Waterborne Fluorine-Free Superhydrophobic Surfaces  
Exhibiting Simultaneous CO<sub>2</sub> and Humidity Sorption**

*Avijit Baidya, Anagha Yatheendran, Tripti Ahuja, Chennu  
Sudhakar, Sarit Kumar Das, Robin H. A. Ras, and Thalappil  
Pradeep\**

## Supporting Information

**Waterborne Fluorine-Free Superhydrophobic Surfaces Exhibiting Simultaneous CO<sub>2</sub> and Humidity Sorption**

*Avijit Baidya<sup>a,b,c</sup>, Anagha Yatheendran<sup>a</sup>, Tripti Ahuja<sup>a</sup>, Chennu Sudhakar<sup>a</sup>, Sarit Kumar Das<sup>c</sup>, Robin H.A. Ras<sup>b,d</sup>, Thalappil Pradeep<sup>a,\*</sup>*

<sup>a</sup>DST Unit of Nanoscience, Thematic Unit of Excellence, Department of Chemistry, Indian Institute of Technology Madras, Chennai, India, E-mail: [pradeep@iitm.ac.in](mailto:pradeep@iitm.ac.in)

<sup>b</sup>Department of Applied Physics, Aalto University School of Science, Puumiehenkuja 2, 02150 Espoo, Finland

<sup>c</sup>Department of Mechanical Engineering, Indian Institute of Technology Madras, Chennai 600036, India

<sup>d</sup>Department of Bioproducts and Biosystems, Aalto University School of Chemical Engineering, Kemistintie 1, 02150 Espoo, Finland

**Table of contents**

Figure No.	Description	Page No.
S1	Advancing angle, receding angle and CAH of water droplet over a coated surface	3
S2	Drag test and vertical drop adhesion test over superhydrophobic surface	3
S3	AFM image of unmodified clay coated glass surface	4
S4	SEM image of modified clay coated filter paper (tilt angle 45°). (Inset) Perpendicular view	4
S5	Cross-sectional SEM image, thickness of the coating	5
S6	Expanded IR spectrum of superhydrophobic and native clay (from figure 2b)	5
S7	Deconvoluted XPS spectrum in the O1s region showing the relative concentration of Al-O-H and Al-O-Si linkage over native clay coated surface	6
S8	XPS Survey spectrum of native clay (peak at 285eV corresponds to carbon of organic species)	6
S9	Images of various mechanical abrasion test	7
S10	Image of (a) droplet drag test over finger wiped surface and (b) vertical droplet	7

	adhesion test over sand paper abraded surface	
S11	Oil-wash experiment	8
S12	Change in wetting property of the coated surfaces upon immersion inside various organic solvents for 50 h. Static CA and CAH of water droplet was measured after taking the surface out from the solvent in a regular time interval of 5 h	8
S13	CA measurements with acidic (pH=1) and basic (pH=14) water droplet	9
S14	VADTs with acidic (pH=1) and basic (pH=14) water droplet	9
S15	(a) CA measurements over 200, 225, 250 °C temperature treated surface. (b) VADTs over 250 °C temperature treated surface	10
S16	Moisture adsorption studies with filter paper and native clay (NC)	10
S17	Effect of temperature on moisture adsorption	11
S18	Static water contact angle over humidity adsorbed superhydrophobic surface.	11
S19	Schematic presentation of fabrication process	12
S20	Effect of drying temperature on non-wetting property of the material	12
S21	Stability of the chemical attachments between AS and OS with clay particles	12

Video No.	Description
V1	Droplet drag test (DDT) over superhydrophobic surface
V2	Verticle droplet adhesion test (VDAT) over superhydrophobic surface
V3	Bouncing of water droplet over coated filter paper
V4	Droplet drag test (DDT) over finger-wiped superhydrophobic surface
V5	Vertical droplet adhesion test (VDAT) over sand paper abraded superhydrophobic surface
V6	Self-cleaning property and movement of water droplets over THF-washed superhydrophobic surface
V7	Vertical droplet test (VDAT) over high temp treated superhydrophobic surface
V8	Droplet drag test (DDT) and vertical droplet adhesion test (VDAT) over moisture saturated superhydrophobic surface

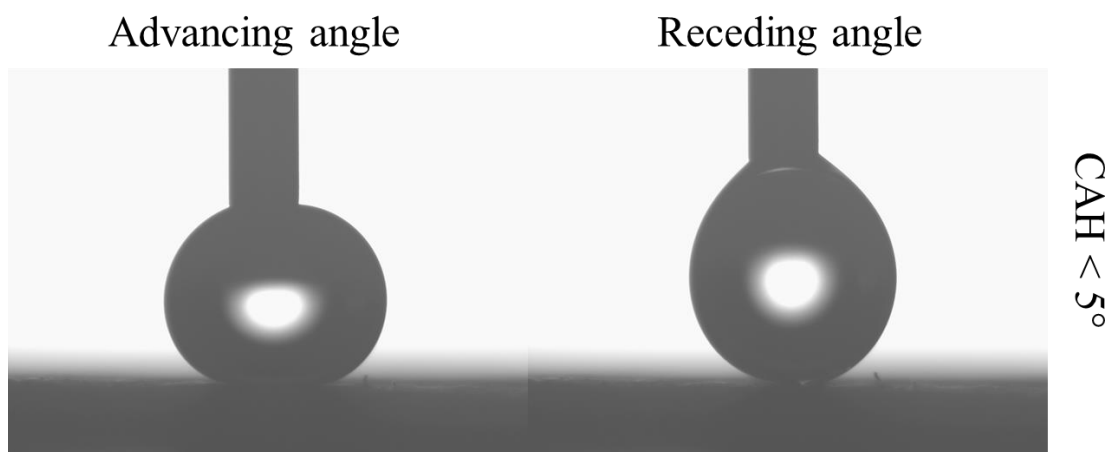


**Figure S1.** Advancing angle (170°), receding angle (167°) and the difference of these two, contact angle hysteresis (CAH) over coated surface.

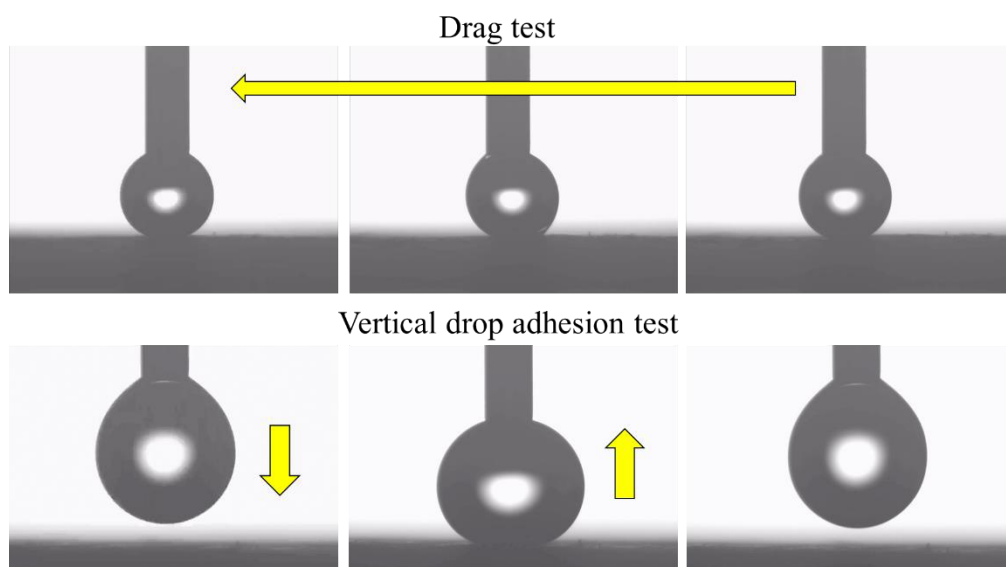


**Figure S2.** Drag test and vertical drop adhesion test over superhydrophobic surface. Arrows represent the directions of droplet movement.

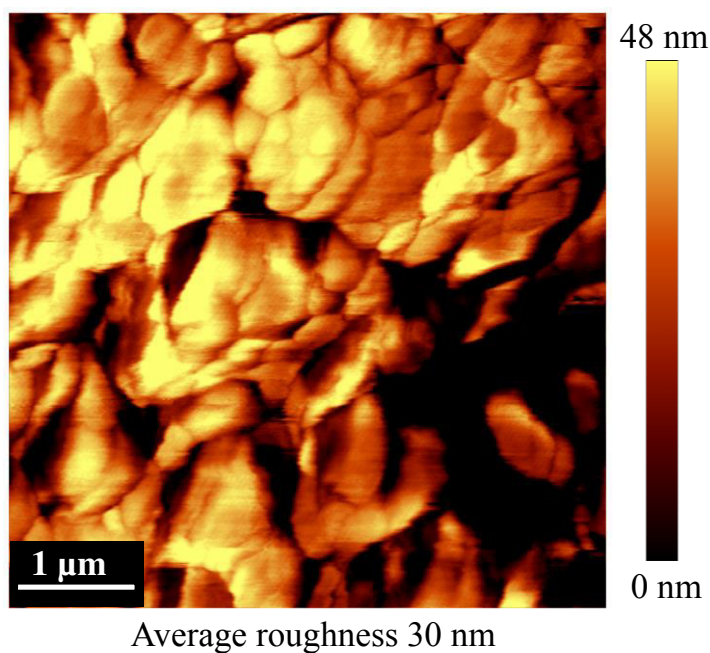


**Figure S3.** AFM image of unmodified clay coated glass surface.

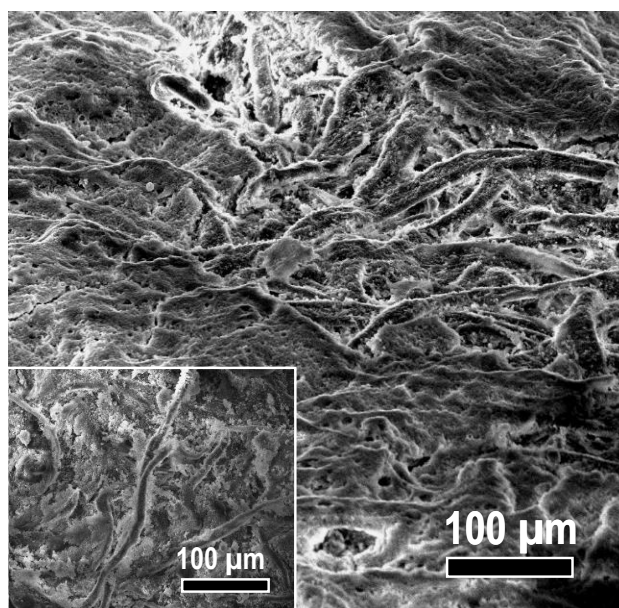


**Figure S4.** SEM image of modified clay coated filter paper (tilt angle 45°). (Inset) Perpendicular view.

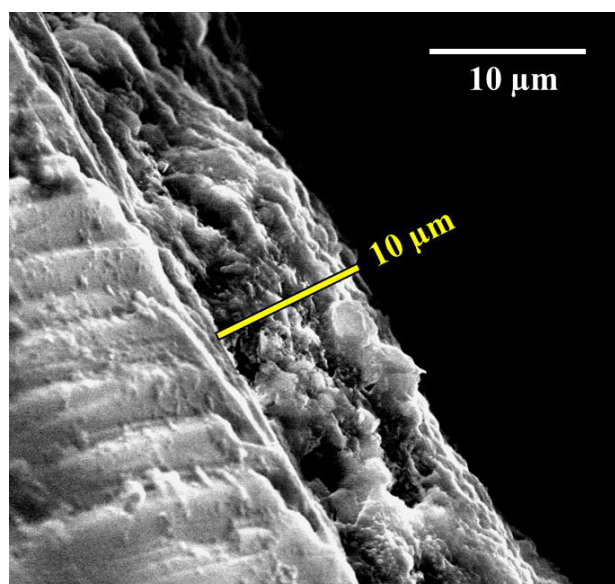


**Figure S5.** Cross-sectional SEM image shows the thickness of the coating.

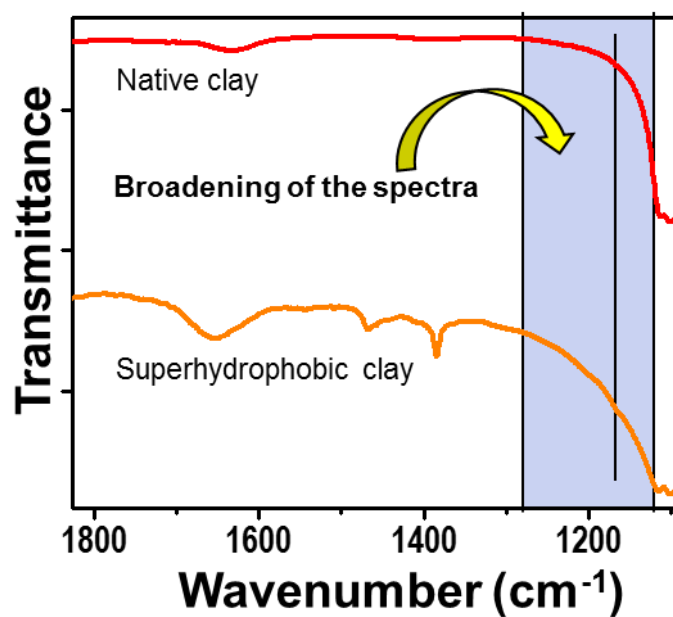


**Figure S6.** Expanded IR spectra of superhydrophobic clay and native clay. Hump at 1170 cm<sup>-1</sup> and broadening of the spectrum for superhydrophobic clay (marked in black line and blue shade) corresponds to the C-N stretching, coming from the incorporated amine functionality.



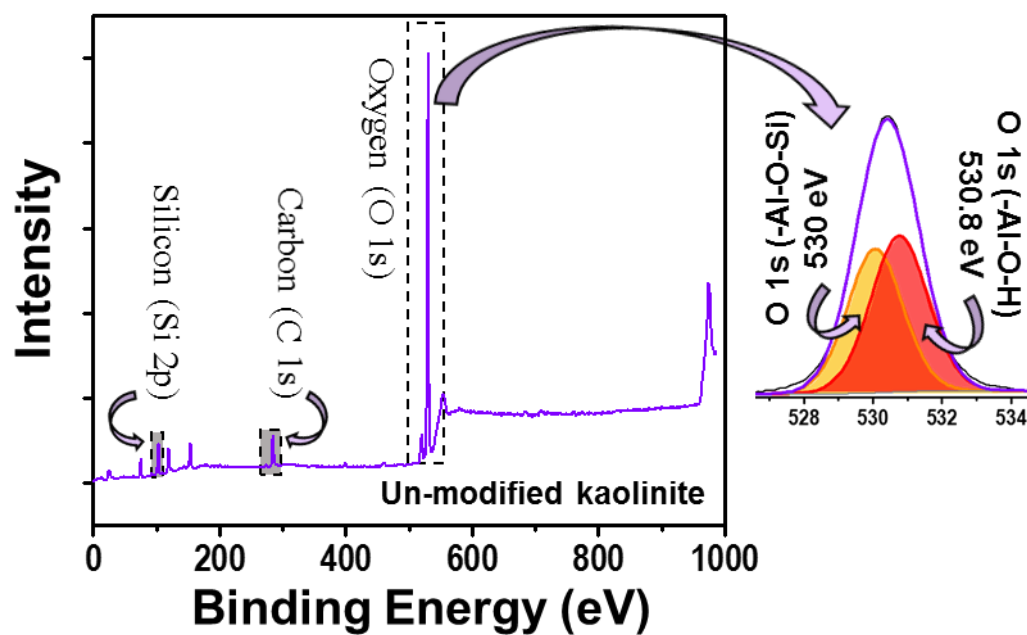


**Figure S7.** Survey spectrum and deconvoluted XPS spectrum in the O1s region showing the relative concentration of Al-O-H and Al-O-Si linkage over native clay coated surface.

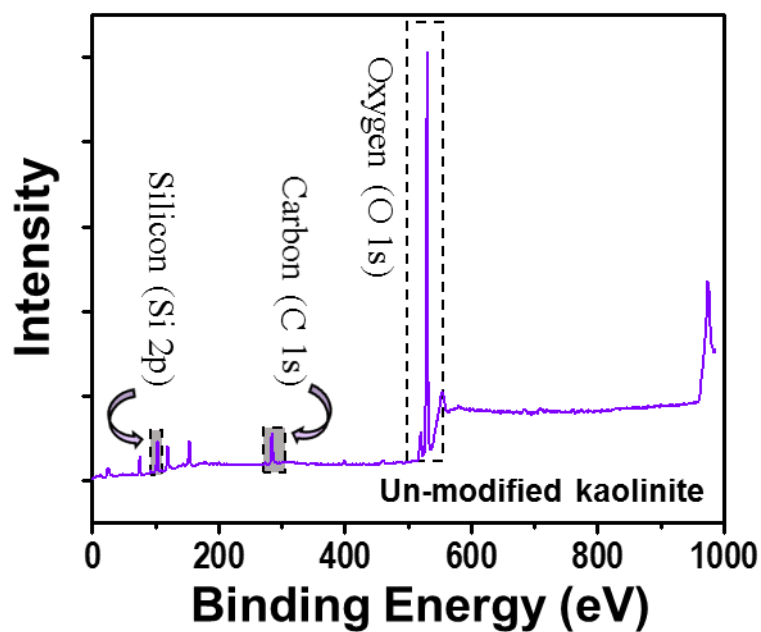


**Figure S8.** XPS survey spectrum of native clay. Peak at 285 eV corresponds to carbon, mostly comes from the organic species.

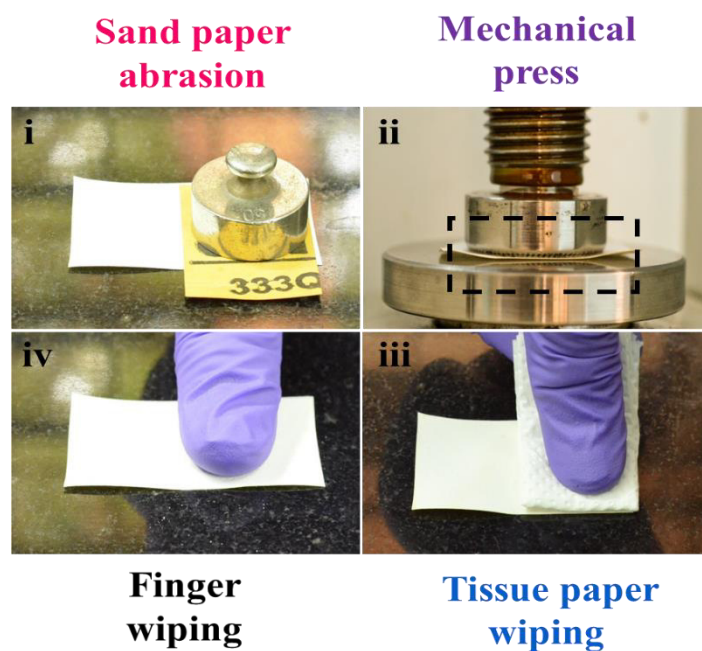


**Figure S9.** Image of various mechanical test. i) Sand paper abrasion, ii) mechanical pressing, iii) tissue paper wiping and iv) finger wiping.

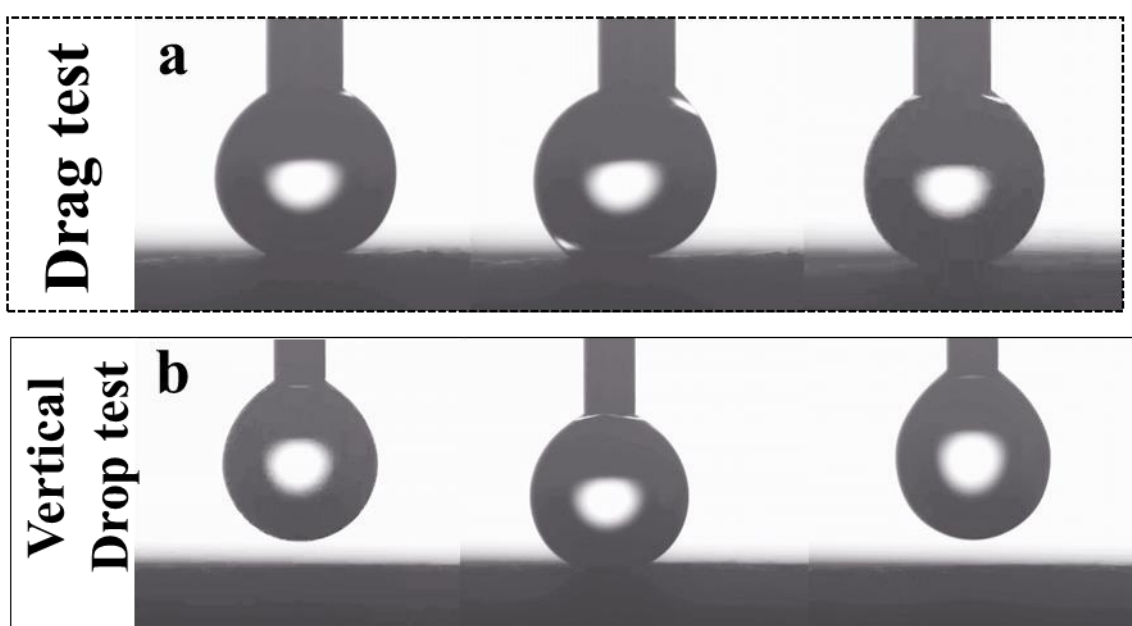


**Figure S10.** Image of (a) droplet drag test over finger wiped surface and (b) vertical droplet adhesion test over sand paper abraded surface.

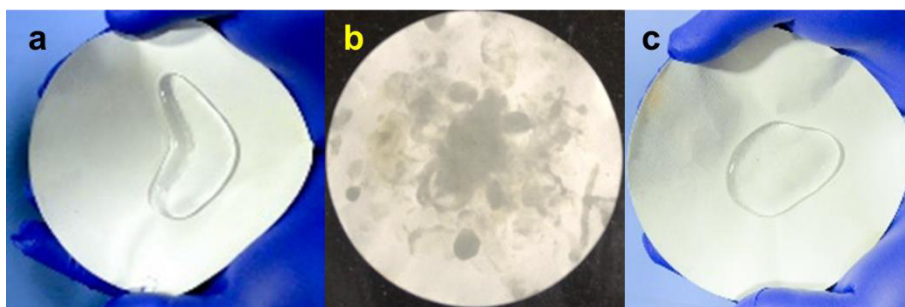


**Figure S11.** Oil-wash experiment. Image of (a) water over untreated superhydrophobic surface, (b) adsorbed oil over the superhydrophobic surface and (c) water over oil-washed superhydrophobic surface.

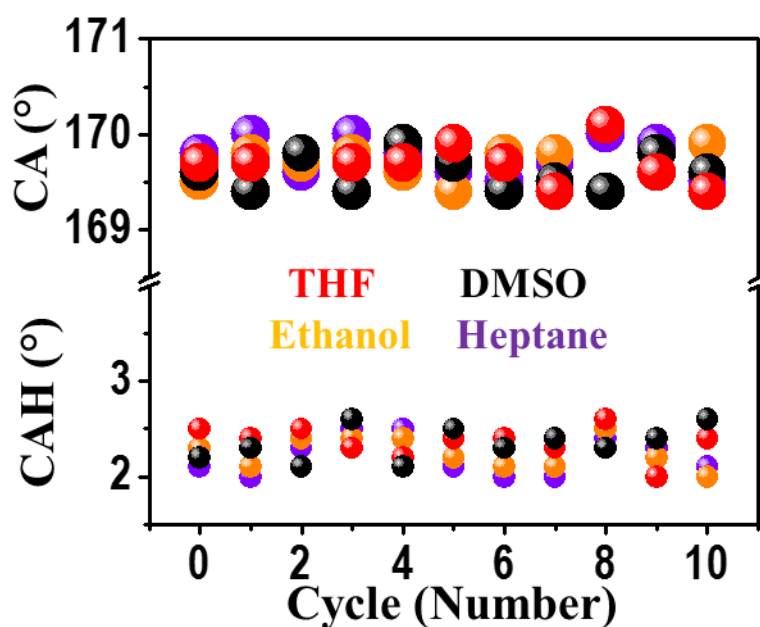


**Figure S12.** Change in wetting property of the coated surfaces upon immersion inside various organic solvents for 50 h. Static CA and CAH of water droplet was measured after taking the surface out from the solvent in a regular time interval of 5 h.

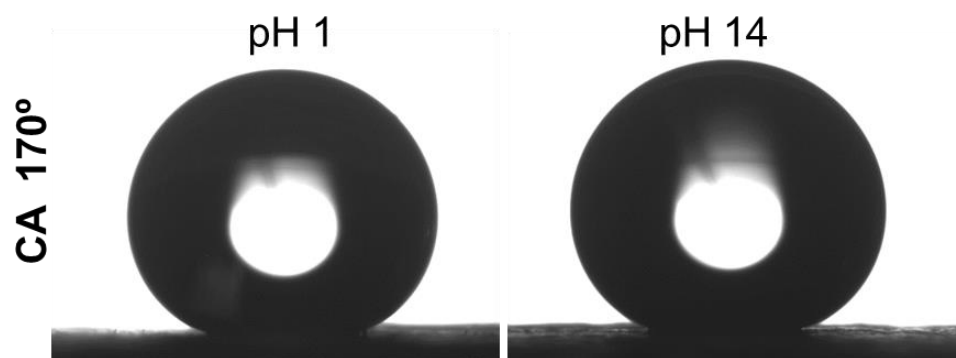


**Figure S13.** CA measurements with acidic (pH=1) and basic (pH=14) water droplets.

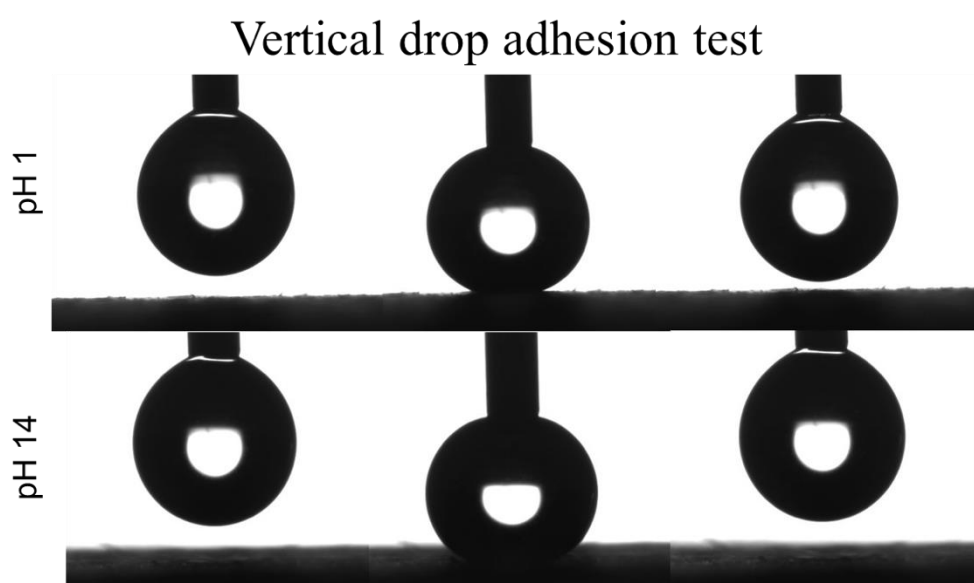


**Figure S14.** VDATs measurements with acidic (pH=1) and basic (pH=14) water droplets.

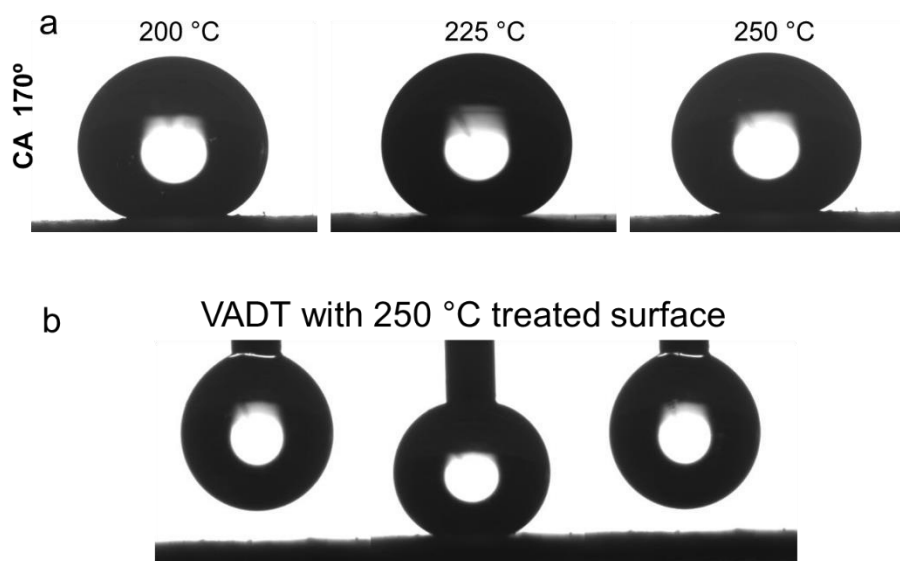


**Figure S15.** (a) CA measurements over 200, 225, 250 °C temperature treated surface. (b) VADTs over 250 °C temperature treated surface

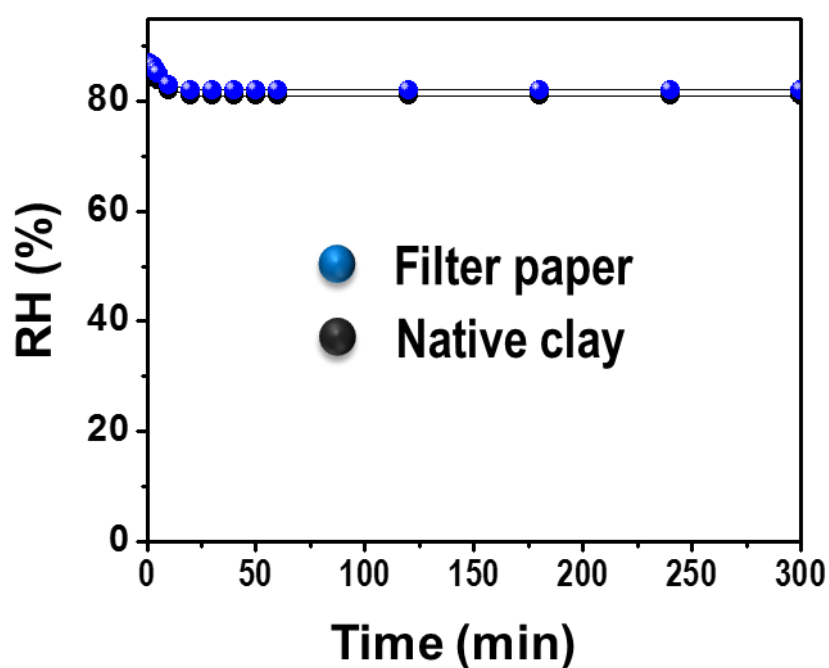


**Figure S16.** Moisture adsorption control study with filter paper and native clay.

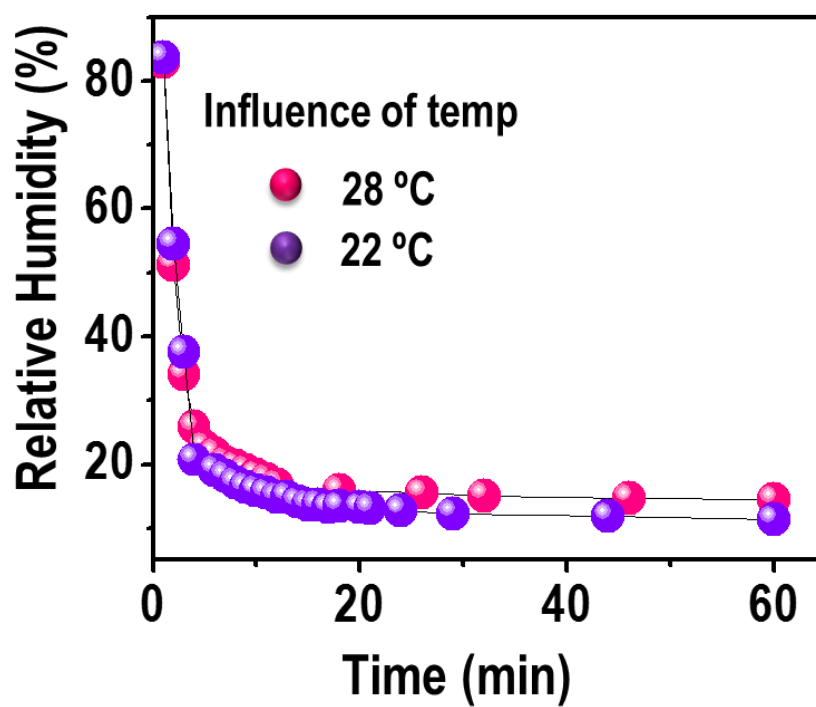


**Figure S17.** Effect of temperature on moisture adsorption

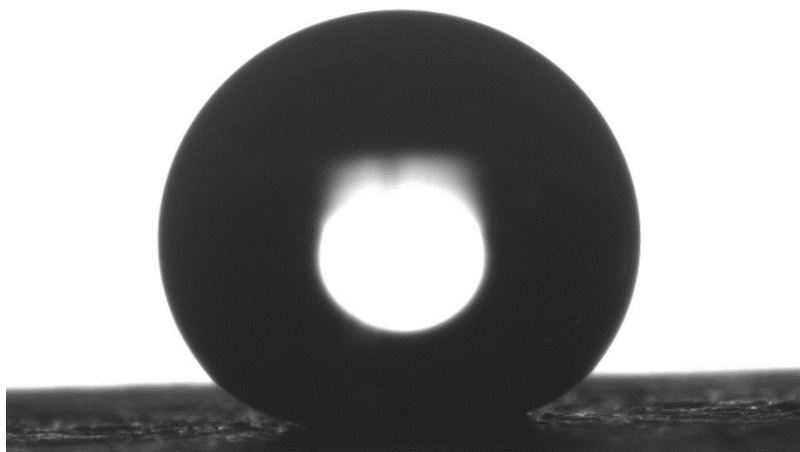


**Figure S18.** Static water contact angle (170°) over moisture adsorbed superhydrophobic surface.

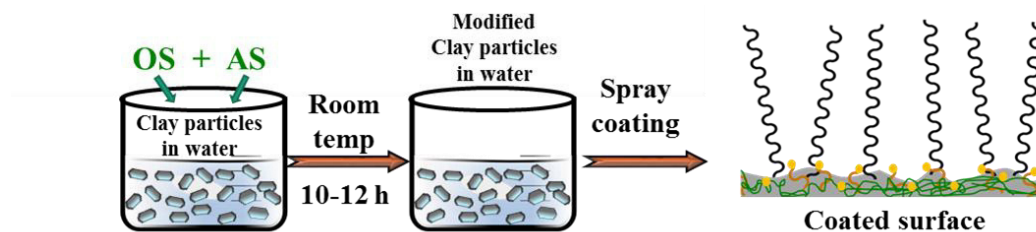


**Figure S19.** Schematic presentation of fabrication process.

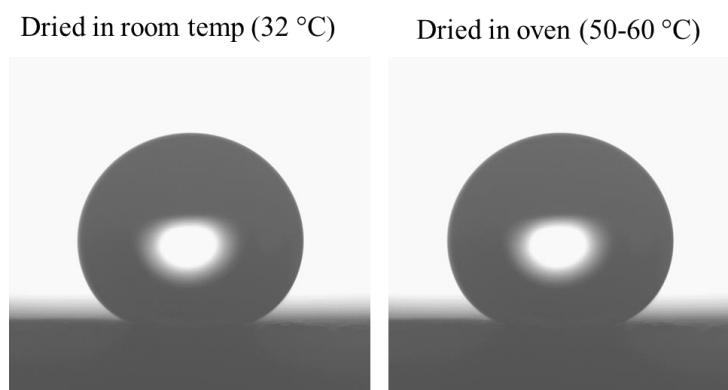


**Figure S20.** Effect of drying temperature on non-wetting property of the material. In both the cases static contact angle of water droplet was 170°.

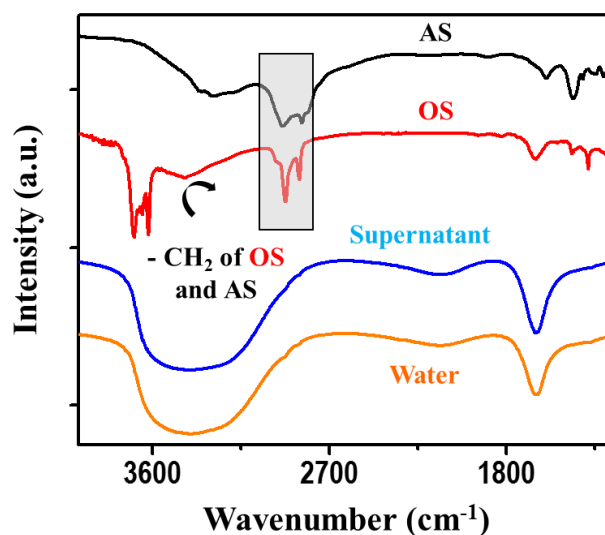
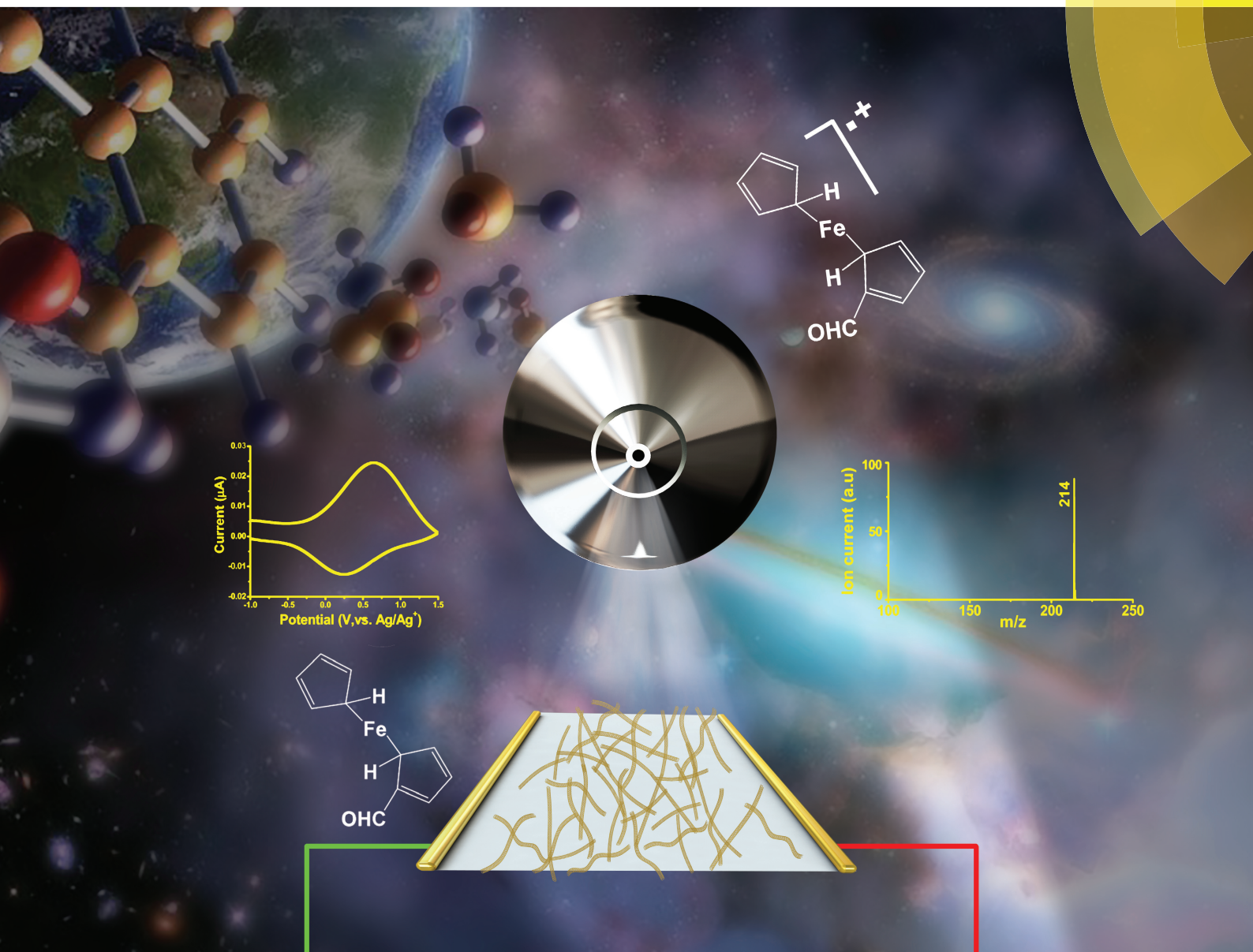


**Figure S21.** Stability of the chemical attachments between AS and OS with clay particles. IR spectra of supernatant, AS, OS, and water. IR spectrum of supernatant (blue) does not contain any characteristic peak of AS (black) and OS (red). It is similar to pure water (orange).



# Analyst

rsc.li/analyst



ISSN 0003-2654



ROYAL SOCIETY  
OF CHEMISTRY

Celebrating  
IYPT 2019

## PAPER

Thalappil Pradeep *et al.*

*In situ* monitoring of electrochemical reactions through  
CNT-assisted paper cell mass spectrometry

Cite this: *Analyst*, 2019, **144**, 5404

## *In situ* monitoring of electrochemical reactions through CNT-assisted paper cell mass spectrometry†

Rahul Narayanan,<sup>‡a</sup> Pallab Basuri,<sup>‡a</sup> Sourav Kanti Jana,<sup>a</sup> Ananthu Mahendranath,<sup>a,b</sup> Sandeep Bose<sup>a</sup> and Thalappil Pradeep<sup>ib</sup> \*<sup>a</sup>

A novel method of coupling electrochemistry (EC) with mass spectrometry (MS) is illustrated with a paper-based electrochemical cell supported by carbon nanotubes (CNTs). The electrochemically formed ions, created at appropriate electrochemical potentials, are ejected into the gas phase from the modified paper, without the application of additional potential. The electrochemical cell was fabricated by using a rectangular CNT-coated Whatman 42 filter paper with printed electrodes, using silver paste. This was used for studying the electrochemical conversion of thiols to disulfides, and the functionalization of polycyclic aromatic hydrocarbons (PAHs), which involve S–S and C–C bond formations, respectively. We also demonstrate the versatility of the set-up by utilizing it for the detection of radical cations of metallocenes, monitoring the oxidation of sulfides through the detection of reactive intermediates, and the detection of radical cations of PAHs, all of which occur at specific applied potentials. Finally, the applicability of this technique for qualitative and quantitative analyses of environmentally relevant molecules has been demonstrated by studying the electrochemical oxidation of glucose (Glu) to gluconic acid (GlcA) and saccharic acid (SacA).

Received 2nd May 2019,  
Accepted 15th July 2019  
DOI: 10.1039/c9an00791a  
rsc.li/analyst

## Introduction

It has been more than four decades since researchers have been engaged in coupling electrochemistry with mass spectrometry (MS).<sup>1–5</sup> Being a sensitive analytical tool, mass spectrometry can be utilized for the identification of many molecular species revealing compositional and structural information. The importance of electrochemistry-mass spectrometry (EC-MS) resulted from two important facts. First, MS can act as an analytical tool to reveal structural and compositional information. Second, the coupling of EC with MS may enhance the ionization efficiency of many analytes which are difficult to be detected with mass spectrometry.<sup>5,6</sup> The coupling of EC with MS can lead to the identification of many

electrochemical products<sup>7</sup> or reactants which are useful in bio-analytical applications.<sup>8–18</sup>

The first attempt to couple EC with MS was made in 1971 by Bruckenstein and Gadde.<sup>1</sup> They carried out an *in situ* mass spectrometric determination of volatile electrochemical reaction products. After that many developments have occurred in this field and several ionization methods have coupled EC with MS.<sup>19–23</sup> Thermospray (TS),<sup>24</sup> fast atom bombardment (FAB),<sup>25</sup> inductively coupled plasma (ICP),<sup>26</sup> chemical ionization (CI),<sup>27</sup> atmospheric pressure chemical ionization (APCI),<sup>28</sup> atmospheric pressure photoionization (APPI),<sup>29</sup> and electrospray ionization<sup>30</sup> are some of the techniques. Paper-based electrochemical cells offer many advantages over other types of cells because they are cheap, foldable, disposable, easy to use and simple.<sup>31,32</sup> The coupling of paper-based electrochemical cells with MS was first attempted recently by Liu *et al.*<sup>33</sup> They had employed the technique for studying various electrochemical cell reactions.

Paper spray, an ambient ionization technique, has been in use since 2010 and it has undergone tremendous changes over the past few years.<sup>34</sup> Normal paper spray ionization works in the high voltage range, but the incorporation of carbon nanotubes (CNTs) on the paper substrate made the analysis possible at 1 V.<sup>35</sup> This technique has been extended to other nanostructures.<sup>36,37</sup> In the present work, we have coupled a

<sup>a</sup>DST Unit of Nanoscience and Thematic Unit of Excellence, Department of Chemistry, Indian Institute of Technology Madras, Chennai 600036, India.  
E-mail: pradeep@iitm.ac.in

<sup>b</sup>Department of Metallurgical and Materials Engineering, Indian Institute of Technology Madras, Chennai 600036, India

†Electronic supplementary information (ESI) available. See DOI: 10.1039/c9an00791a

‡These authors contributed equally. The manuscript was written through contributions of all authors.

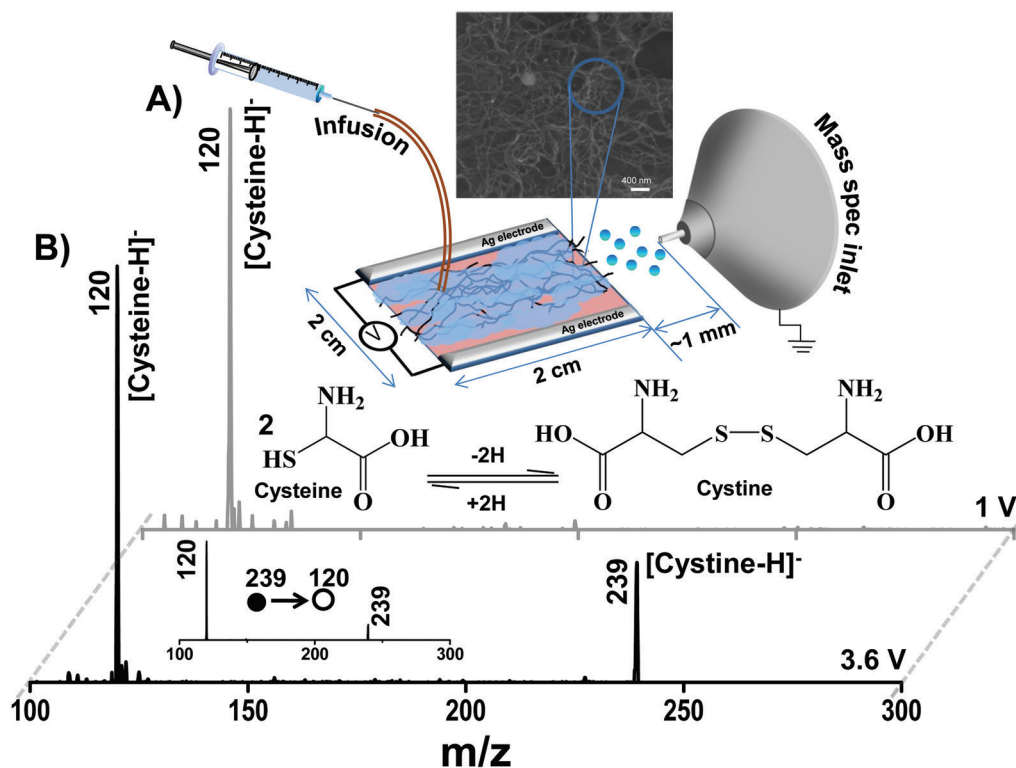


**Fig. 1** (A) Normal low voltage (1 V) mass spectrum of cysteine collected from the CNT-coated paper. Schematic representations of the experimental set-up, along with an FESEM image of the CNT-coated paper, and the electrochemical oxidation of cysteine are shown in the inset. (B) Mass spectrum of cysteine collected from a paper-based electrochemical cell at a cell potential ( $\Delta V$ ) of 3.6 V.  $MS^2$  data of the product ion peak is shown in the inset.

carbon nanotube coated paper-based electrochemical cell with MS and it has been utilized for the study of various electrochemical cell reactions; some applications have also been demonstrated. Compared to other reported EC-MS techniques, this technique allows the detection of electrochemically generated species at low voltages. Here the nanostructures have been used to achieve low voltage ionization and have helped in transporting electrochemically generated species from a paper-based cell to the mass spectrometer inlet. The present technique has been demonstrated for studying *in situ* S-S and C-C bond formation reactions as well as the electrochemical oxidation of analytes. We have understood the electrochemical oxidation of diphenyl sulfide through the detection of reactive intermediates. We have further demonstrated the generation of ions through an electrochemical oxidation event by coupling a CH electrochemical analyser with a mass spectrometer using a three electrode paper cell set-up.

## Experimental

The paper-based electrochemical cells (both two and three electrode configurations) were fabricated from a modified carbon nanotube infused paper. A Whatman 42 filter paper in the required geometry was taken and metallic electrodes were patterned with silver paste for designing an electrochemical

cell. CNTs were obtained from Nanocyl SA, USA. The sample was composed of 1  $\mu\text{m}$  long multiwalled CNTs of mixed diameters. A CNT suspension was prepared in water and was coated in the space between the two electrodes, leaving a gap of nearly 2 mm near the electrodes in order to avoid the possibility of short circuit (Fig. 1A). This set-up was used in most of the studies. More detailed studies were performed with the three electrode set-up.

The two electrode cell was connected with an external voltage supply and was held in front of the mass spectrometer inlet. All mass spectrometric measurements were done using a linear ion trap LTQ XL of Thermo Scientific, San Jose, California. Mass spectrometric conditions used are presented in the ESI.† All analytes used were at ppm concentrations and they were infused using a syringe pump for each measurement. The following conditions were the experimental conditions for mass spectrometry: source voltage: 0 V and above, capillary temperature: 150  $^{\circ}\text{C}$ ; capillary voltage: 0 V; and tube lens voltage: 0 V. The collision-induced dissociation technique was used for  $MS^2$  analysis. A field emission scanning electron microscope (FESEM) was used for imaging the modified paper. Methanol, dichloromethane (DCM), acetonitrile (ACN) and sulphuric acid were purchased from Rankem. Trifluoroacetic acid, KCl, ferrocene, ferrocenecarboxaldehyde, nickelocene, glucose, diphenyl sulfide (PhSPh), 1,2-benzanthracene, and naphthalene were bought from Sigma Aldrich,



India. Sodium acetate and acetic acid were purchased from Merck Ltd, Mumbai, India. Cysteine (Cys) was bought from Fisher Scientific Pvt. Ltd, Mumbai, India, and glutathione was from Sisco Research Laboratories Pvt. Ltd, Mumbai, India. Benzene was bought from S D Fine Chem Ltd, Chennai, India. Mesitylene was bought from Spectrochem Pvt. Ltd, Mumbai, India. The blood serum sample used in this work was obtained from the collection that was part of a recent study.<sup>38</sup> The sample belonged to a non-diabetic control participant. Ethical clearance was obtained from Kovai Medical Centre and Hospital, Coimbatore, India (Ref. EC/AP/356/02/2015 dated 16/02/2015), with informed consent from the participant.

In a similar way, the three electrode set-up was prepared in which the length of the middle electrode was made smaller than the other two to avoid hindrance during paper spray ionization. Detailed *in situ* electrochemical analysis and mass spectrometry were carried out by placing this three electrode paper cell in front of a mass spectrometer inlet and the three electrodes of the paper cell were connected to a CH 600A electrochemical analyser. Cyclic voltammetry was performed to obtain the oxidation potential of the analytes. The electrodes were connected in such a manner that the middle electrode was the reference and the other two were the working and counter electrodes, respectively. To demonstrate the methodology of ion generation through the electrochemical event, ferrocenecarboxaldehyde was chosen as a potent candidate. Paper used for the construction of the cell was the same as that used before.

## Results and discussion

A paper-based two electrode electrochemical cell (Fig. 1A) was placed in front of the MS inlet at a distance of 1 mm from it and was connected to an external voltage supply. A DC voltage was applied across the cell through the Ag electrodes. Analytes, along with the solvent and the electrolyte, were introduced on the cell with the help of a continuous sampling system (syringe injection pump). Data from the three electrode set-up will be presented at a later part of the paper.

### Monitoring electrochemical reactions

One of the major advantages that comes with coupling electrochemistry with low voltage paper spray ionization mass spectrometry is the capability to *in situ* monitor the electrochemical reactions. Here we have demonstrated reactions that involve S–S and C–C bond formations. In addition to this we have also demonstrated the oxidation of analytes such as metallocenes, PAHs, and glucose.

### Electrochemical S–S bond formation reaction

**Oxidation of cysteine to cystine.** Initial measurements were carried out with a well-known electrochemical reaction which is the conversion of thiols to disulfides *via* electrochemical oxidation. For this, cysteine was chosen and its solution was prepared in a methanol:water (1:1 by volume) mixture at 100 ppm concentration. About 100 ppm of KCl (in water) was

used as the electrolyte. Following the introduction of the sample solution on the cell, the potential was varied across the cell with the help of an external power supply. The results are shown in Fig. 1.

Fig. 1A shows a typical low voltage mass spectrum of cysteine at 1 V showing a deprotonated molecular ion peak at  $m/z$  120. This was collected from the CNT-coated paper containing cysteine in methanol:water (1:1 by volume), by the application of 1 V on it. Other mass spectrometric conditions are presented in the ESI† A solution of KCl at 100 ppm concentration (electrolyte) was applied on the paper-based cell followed by the introduction of cysteine in methanol:water (1:1 by volume), with an injection syringe. A cell potential ( $\Delta V$ ) of 3.6 V was applied across the electrodes and the resulting mass spectrum is shown in Fig. 1B. Here a deprotonated peak of cysteine disulfide appears at  $m/z$  239 along with the peak at  $m/z$  120. MS<sup>2</sup> analysis confirmed the identity of the product ion (inset of Fig. 1B). Here a typical electrochemical strategy is followed for the formation of disulfide from cysteine; the reaction scheme is shown in the inset of Fig. 1A. It occurs through an electrochemical oxidation, involving the removal of two hydrogens from two molecules of cysteine, leading to the formation of cysteine disulfide by S–S linkage. It is clear from the control experiment that the reaction requires an electrochemical environment. The expected product (cystine disulfide), was not observed neither during the typical low voltage paper spray ionization experiment nor from a paper cell, at cell potential of 0 and 1 V (Fig. S2A, ESI†). The mechanism of formation of the electrochemical products from the current experiment involves two important events. First is the electrochemical oxidation of the analyte species on the paper by the application of voltage and second is the low voltage ionization of the formed species from the paper with the aid of CNTs protruding from the paper.<sup>35</sup> These two events together make the reaction possible at 3.6 V.

The electrochemical mechanism was tested by a voltage variation study, in which the same experiment was carried out by sweeping the voltage from 0 V to 6 V. It was observed that the electrochemically formed cysteine disulfide peak appeared at 3.6 V and reached a saturation value at 4 V. Fig. S1A (ESI†) shows the product ion intensity (cysteine disulfide) as a function of applied voltage, suggesting the involvement of electrochemical event in the reaction pathway. The mass spectra collected at different voltages in the voltage variation experiment are shown in Fig. S2A (ESI†).

**Oxidation of glutathione.** A replication of the same experiment with glutathione resulted in glutathione disulfide in a similar manner (Fig. 2). A solution of glutathione was prepared in a methanol:water solvent system (1:1 by volume). The experiment was performed in a way similar to cysteine. The cell potential was varied from 0 to 6 V. The electrochemically formed glutathione disulfide was detected at 3.6 V. A further increase in the voltage resulted in the saturation of the product ion intensity at 4 V (Fig. S1B, ESI†). Fig. 2A shows the 1 V mass spectrum and Fig. 2B shows the spectrum at a cell potential of 3.6 V. The latter shows the presence of an electro-

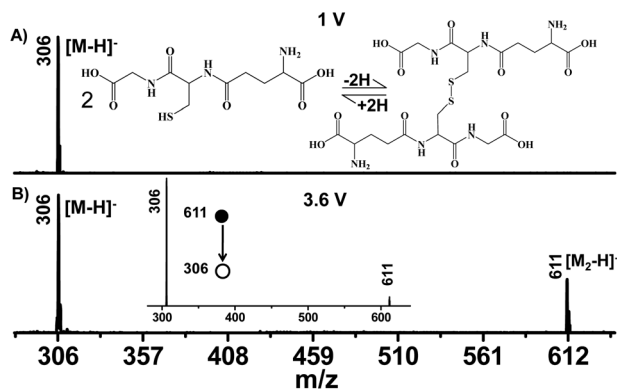


Fig. 2 (A) Normal low voltage (1 V) mass spectrum of glutathione collected from the CNT-coated paper, and (B) mass spectrum of glutathione at a cell potential ( $\Delta V$ ) of 3.6 V.  $MS^2$  spectrum of glutathione disulfide is shown in the inset of B. Schematic representation of the electrochemical oxidation of glutathione is shown in the inset of A.

chemically formed glutathione disulfide. The  $MS^2$  spectrum shown in the inset of Fig. 2B confirms the product.

The results obtained during a voltage variation experiment are shown in Fig. S2B (ESI†). Fig. S2B (ESI†) shows the mass spectra collected for the voltage variation study. These two results support an electrodic event involved in the observed species.

**Electrochemical C–C bond formation reactions.** To demonstrate the monitoring of electrochemical C–C bond formation reactions, three hydrocarbons, *viz* benzene, mesitylene, and naphthalene, were selected as reagents. This also indicates the additional advantage that comes by coupling EC with low voltage MS wherein such undetectable species (typically, molecular species without any functional groups) are detected *via* electrochemical functionalization. The solutions of these analytes were prepared in a 1:1 acetic acid:sodium acetate mixture at 100 ppm concentration. Here acetic acid acted as a solvent and sodium acetate as an electrolyte as well as a reagent. The mixture was continuously injected into the electrochemical cell and the potential was swept from 0 to 5 V. The results are shown in Fig. 3

Fig. 3A shows a control experiment carried out with benzene in acetic acid and sodium acetate. This mass spectrum was collected using the normal low voltage paper spray ionization technique. The spectrum shows the presence of an acetate ion, a proton bound dimer of the acetate ion and a sodium bound dimer of the acetate ion at  $m/z$  59, 119 and 141, respectively. No benzene was detected. The same set of analytes were introduced on the paper-based electrochemical cell and the DC voltage was changed from 0 V to higher positive voltages. As a result, a new product peak appeared at  $m/z$  135 at a cell potential of 1.8 V (Fig. 3B) and it has been assigned as benzene acetic acid as confirmed from  $MS^2$  data shown in Fig. S3A (ESI†). Similar experiments were performed with mesitylene and naphthalene as well (Fig. 3C–F). Note that parent hydrocarbons were not detected. Two new peaks appeared at  $m/z$  177 and 185 (Fig. 3D and F) corresponding to the carboxy-

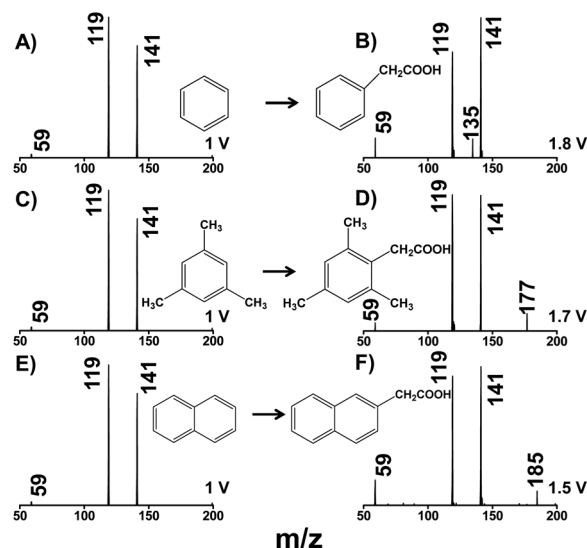


Fig. 3 Electrochemical functionalization of different hydrocarbons. Low voltage mass spectra of (A) benzene, (C) mesitylene, and (E) naphthalene, respectively, in acetic acid containing sodium acetate, at 1 V (blank experiments). Mass spectrum showing the electrochemical functionalization of (B) benzene to benzene acetic acid at a cell potential ( $\Delta V$ ) of 1.8 V, (D) mesitylene to mesitylene acetic acid at a cell potential ( $\Delta V$ ) of 1.7 V, and (F) naphthalene to naphthalene acetic acid at 1.5 V across the electrode. The spectra were collected in negative ion mode. Schematic representations of these three reactions are also shown.

lated products of mesitylene and naphthalene, respectively (mesitylene acetic acid and naphthalene acetic acid). The corresponding  $MS^2$  data are shown in Fig. S3B and S3C (ESI†). A voltage variation study was performed with these analytes in order to prove the event as an electrodic event. For this, each of these analytes were introduced on the electrochemical cell and the external power supply was swept from 0 V to higher voltages. The results are shown in Fig. S4 (ESI†). In the case of benzene, a new peak corresponding to benzene acetic acid started to appear at 1.8 V and got saturated at 2 V.

For mesitylene, the carboxylated peak appeared at 1.7 V and got saturated at 1.9 V. Similarly for naphthalene, the peak appeared at 1.5 V and got saturated at 1.7 V. These experiments proved that the above events occurred as a result of an electrochemical pathway occurring at the electrode. The mass spectra collected in a voltage variation study are shown in Fig. S5 (ESI†). We did not see the presence of multiply carboxylated hydrocarbons as a result of electrochemical functionalization, the reason for which is unclear at present.

**Electrochemical oxidation of metallocenes.** Metallocenes are another class of compounds which can be oxidized electrochemically. Here we have used the paper-based electrochemical cell in order to ionize selected metallocenes *via* electrochemical oxidation. For this, three metallocenes were chosen and solutions were prepared in a ACN/ $CH_2Cl_2$  solvent mixture (1:1 by volume) at 100 ppm concentration. The cell was saturated with trifluoroacetic acid as an electrolyte and the analytes were applied with the help of an injection syringe.

Subsequently the potential was applied through an external power supply. The results are shown in Fig. 4.

The results show the presence of metallocenes as radical ions generated *via* electrochemical oxidation. The insets of Fig. 4A–C show the mass spectra of metallocenes (in ACN/CH<sub>2</sub>Cl<sub>2</sub> with trifluoroacetic acid as an electrolyte), collected from the paper cell at a cell potential of 0 V. These blank spectra suggest the absence of an electrochemical event when the cell is in off condition. The electrochemically generated radical ions appeared at the corresponding cell potentials when the voltage was swept from 0 V to higher voltages. These results are shown in Fig. 4A–C for ferrocene, ferrocenecarboxaldehyde, and nickelocene, respectively. These results provide evidence for an electrochemical event.

**Monitoring oxidation reaction of diphenyl sulfide.** Anodic oxidation of diphenyl sulfide is a well-known electrochemical

reaction whose mechanism proceeds *via* an unstable radical cation.<sup>33</sup> This cation has been detected. For this, diphenyl sulfide was introduced on the cell in the ACN/CH<sub>2</sub>Cl<sub>2</sub> solvent system along with KCl as an electrolyte at 100 ppm concentration. The potential was applied with the help of an external power supply and the mass spectrum was recorded. The actual mechanism of diphenyl sulfide oxidation proceeds *via* the formation of an unstable radical cation, finally leading to the formation of a pseudo dimer sulfonium ion followed by hydration. Scheme 1 shows the mechanism involved in the oxidation of diphenyl sulfide.

The mass spectrum collected at a cell potential of 1.2 V in Fig. 5 shows the presence of the unstable radical cation at *m/z* 186.

This cation loses a proton and forms a deprotonated species of mass 185. The other species that were detected included a pseudodimersulfonium ion and its hydrated adduct, at *m/z* 371 and 387, respectively. A plot of the product ion intensity *vs.* voltage (Fig. S6, ESI†) shows the emergence of an electrochemically activated species (product ions and reaction intermediates) at a cell potential of 1.2 V followed by saturation at 1.8 V.

**Quantification of glucose in body fluid.** The cell has been used for the identification of some environmentally relevant species in both a quantitative and qualitative manner. Electrochemical oxidation of Glu to GlcA and SacA is a well-studied electrochemical event of biological relevance. As a trial method, Glu solution was prepared in Millipore water at a con-

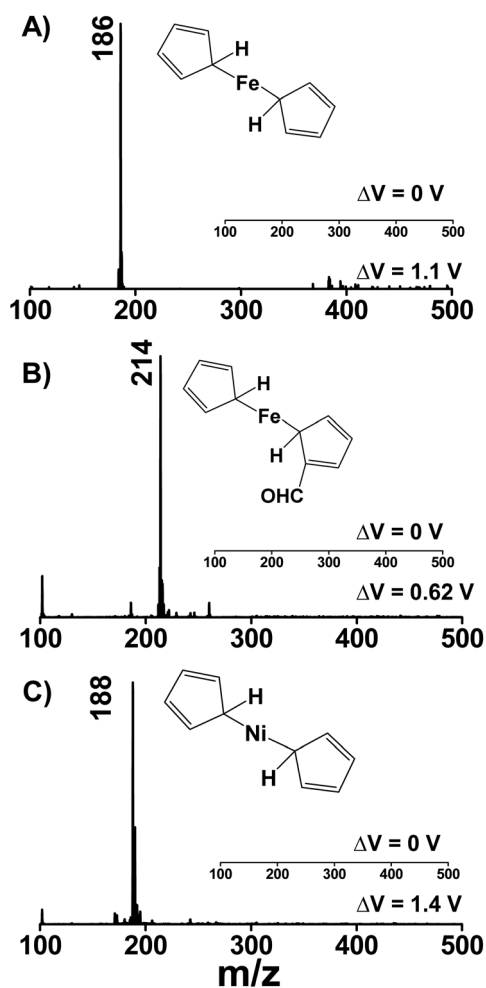
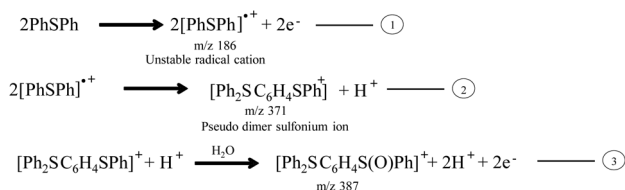


Fig. 4 Electrochemical oxidation of metallocenes. Mass spectra of (A) ferrocene, (B) ferrocenecarboxaldehyde, and (C) nickelocene at cell potentials ( $\Delta V$ ) as indicated in the inset in each case, collected in positive ion mode. For all cases, ACN/CH<sub>2</sub>Cl<sub>2</sub> was used as the solvent mixture with trifluoroacetic acid as an electrolyte. The corresponding mass spectra obtained at a cell potential ( $\Delta V$ ) of 0 V, is shown in the inset in each case. Peaks, other than those labelled, are due to the background.



Scheme 1 Schematic representation of the possible mechanism of diphenyl sulfide oxidation.<sup>33</sup>

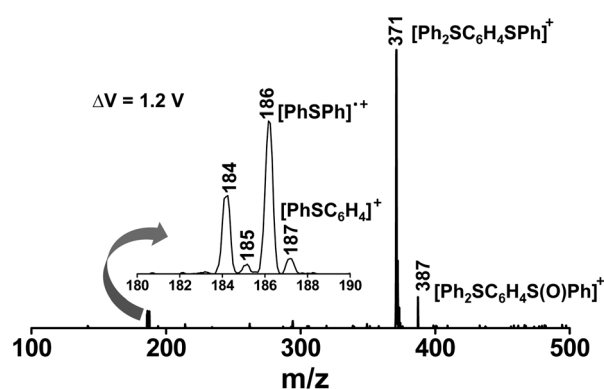


Fig. 5 Mass spectrum of diphenyl sulfide (in ACN/CH<sub>2</sub>Cl<sub>2</sub> solvent mixture with KCl as an electrolyte) collected from the paper cell at a cell potential ( $\Delta V$ ) of 1.2 V. The spectrum is in the positive ion mode.

centration of 100 ppm and it was applied on the cell along with a small amount of  $\text{H}_2\text{SO}_4$  (1%). The application of a DC voltage of 3.4 V across the cell resulted in the oxidation of Glu to both GlcA and SacA. The inset of Fig. 6A shows a normal low voltage (1 V) mass spectrum of Glu (in Millipore water containing 1%  $\text{H}_2\text{SO}_4$ ), which clearly shows the presence of a deprotonated peak of glucose at  $m/z$  179. The same set of reagents were applied to the paper cell and it showed the presence of both GlcA and SacA formed as a result of Glu oxidation at a cell potential of 3.4 V (Fig. 6A). A voltage variation study confirmed the oxidation as an electroodic event and the result is shown in Fig. 6C.

This experimental result prompted us to carry out qualitative and quantitative analyses of blood serum glucose. For this, the paper cell was saturated with blood serum along with a small amount of  $\text{H}_2\text{SO}_4$  and the cell potential was varied and it resulted in the formation of GlcA and SacA at 3.4 V (Fig. 6B). A quantitative analysis was carried out with a series of concentrations of glucose and the results are shown in Fig. 6D and S7 (ESI<sup>†</sup>). These results clearly show a glucose concentration of 0.45  $\mu\text{M}$  in the blood serum. The value is in good agreement

with the expected value of glucose in blood for a normal person.<sup>39</sup>

**Selective detection of polycyclic hydrocarbons.** We demonstrate the practicality of the paper-based electrochemical cell for a selective detection of hydrocarbons from a mixture (Fig. 7). For this, three hydrocarbons were chosen and their mixture (in  $\text{ACN}/\text{CH}_2\text{Cl}_2$ ) was saturated on the cell along with KCl as the electrolyte. The mixture was applied in two different ways on the cell, in equimolar and non-equimolar concentration ratios. A variation of voltage from 0 V to higher voltages resulted in the emergence of each hydrocarbon according to its oxidation potential. Fig. 7 presents the result which shows the presence of 1,2-benzanthracene, naphthalene, and benzene at cell potentials of 1.2 V, 1.5 V and 1.8 V, respectively. Variations in ion intensities for each of the ions depend on multiple factors such as ionization efficiency, stability of the ions in solution, efficiency of ion transport into the MS, *etc.* The capability of the cell to identify environmentally relevant species has been demonstrated through the detection of 1,2-benzanthracene and glucose. The detection limits of the species were 1 ppt and 10 ppm for glucose and 1,2-benzanthracene, respectively (see Fig. S8, ESI<sup>†</sup>).

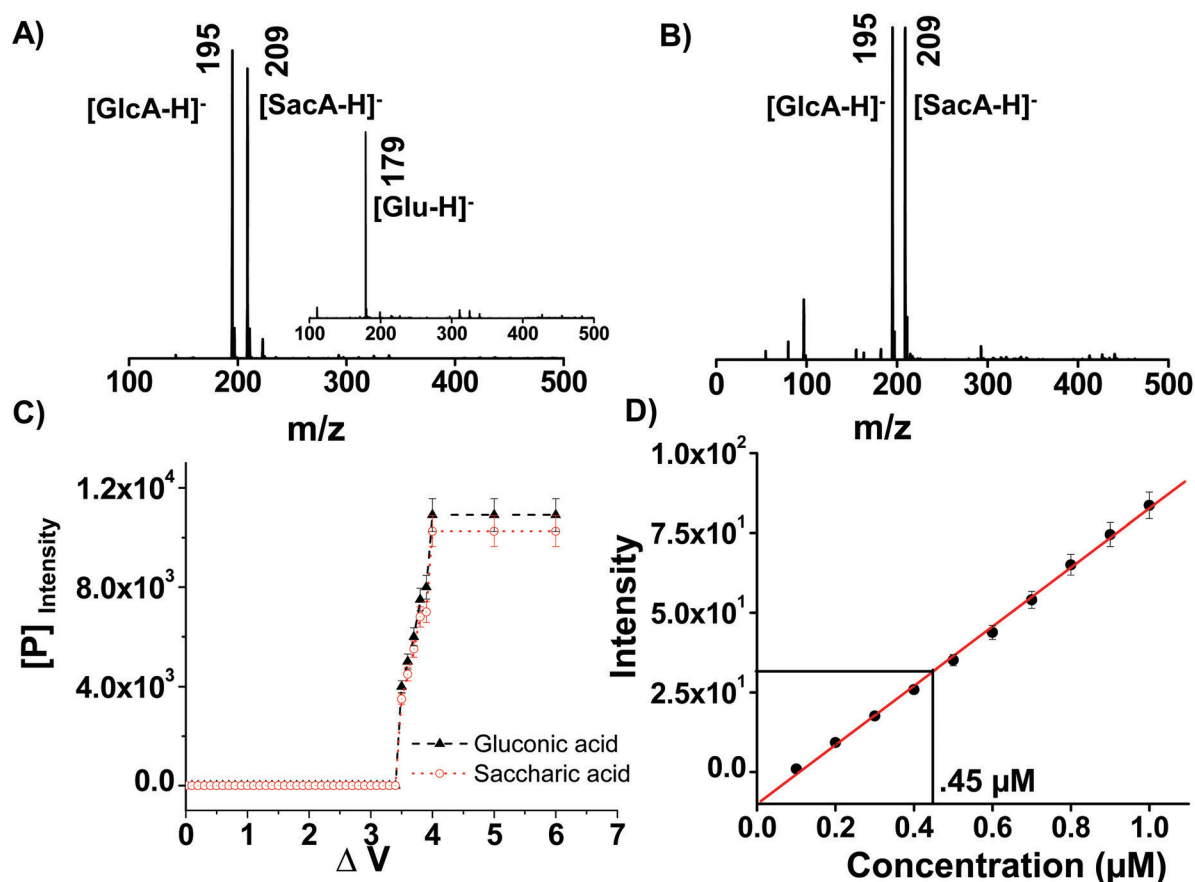


**Fig. 6** Electrochemical oxidation of Glu. (A) Mass spectrum of glucose collected from a paper-based electrochemical cell at a cell potential ( $\Delta V$ ) of 3.4 V. Normal low voltage (1 V) mass spectrum of glucose collected from the CNT-coated paper is shown in the inset. (B) Mass spectrum of the human blood serum collected from a paper-based electrochemical cell at a cell potential ( $\Delta V$ ) of 3.4 V, showing the presence of Glu in it. Peaks, other than those labelled, are due to the background. (C) A plot of product ion intensity (electrochemically generated species) as a function of applied voltage for glucose detection. (D) Intensity–concentration profile for Glu to GlcA oxidation.



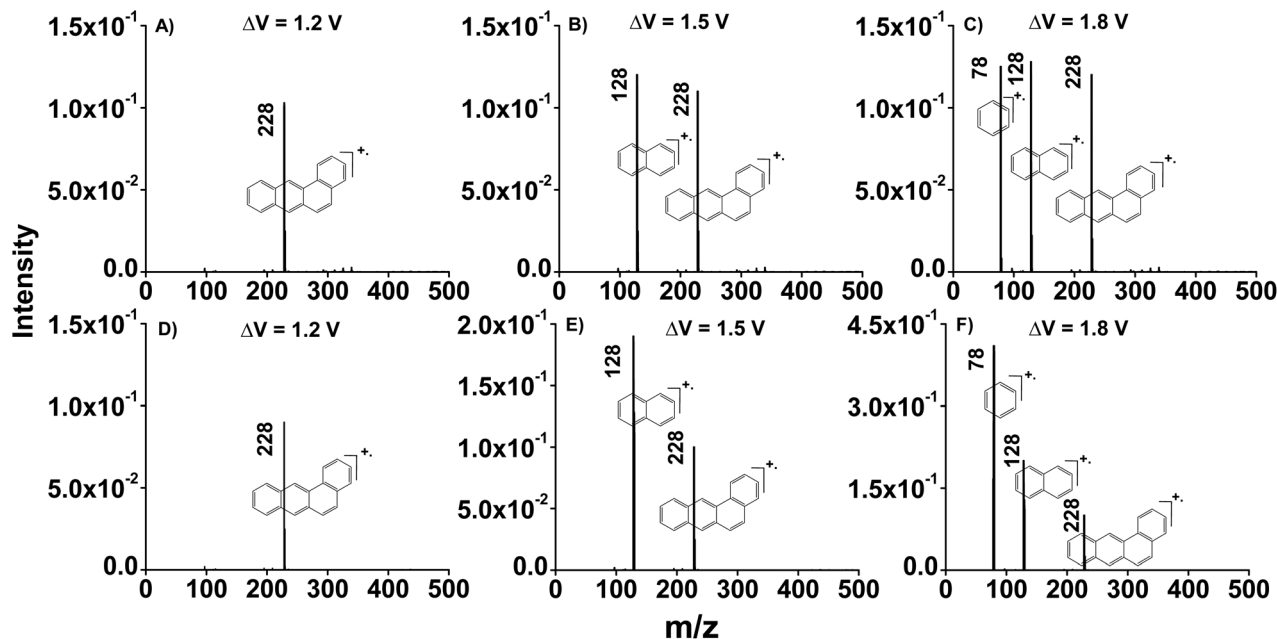


Fig. 7 Electrochemical oxidation of a mixture containing different hydrocarbons at different cell potentials. A, B, and C show mass spectra of an equimolar mixture of benzene, naphthalene and 1,2-benzanthracene, showing the presence of electrochemically oxidized hydrocarbons at their respective cell potentials with equal ion intensities. D, E, and F show mass spectra of a non-equimolar mixture of benzene, naphthalene and 1,2-benzanthracene showing the presence of electrochemically oxidized hydrocarbons at their respective cell potentials with different ion intensities.

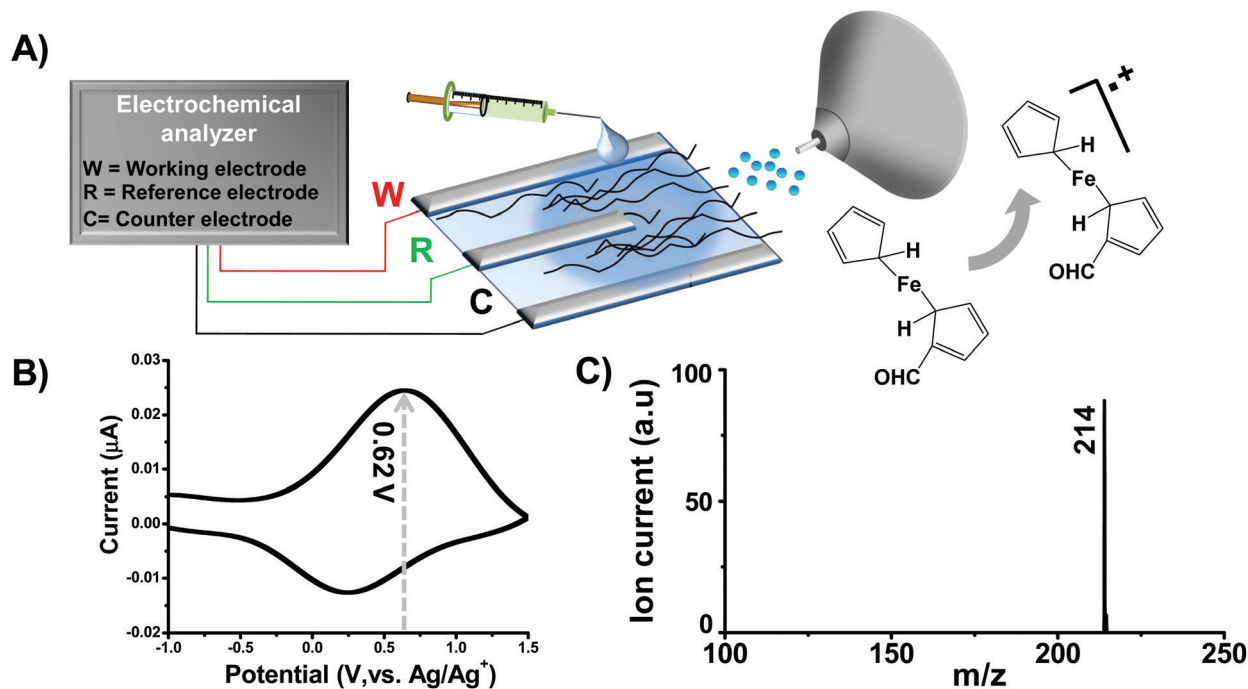


Fig. 8 *In situ* analysis of the electrochemical oxidation of ferrocenecarboxaldehyde with three electrode paper cell mass spectrometry coupled with an electrochemical analyzer. (A) Schematic representation of the coupled set-up. (B) Cyclic voltammogram and (c) *in situ* mass spectrum of the electrochemically oxidized species of ferrocenecarboxaldehyde.

***In situ* monitoring of ferrocenecarboxaldehyde and PAH oxidation reaction.** Fig. 8 shows a schematic representation of the experimental set-up, in which a three electrode based electro-

chemical cell was designed on a CNT coated Whatman 42 filter paper, coupled with a CH electrochemical analyser and a mass spectrometer. This experiment was performed to

confirm whether the phenomena outlined above occur under standard electrochemical conditions. Fig. 8B shows the cyclic voltammogram of the redox reaction. The characteristic oxidation peak of ferrocenecarboxaldehyde is seen at  $\sim 0.62$  V (vs. Ag/Ag<sup>+</sup> electrode). The data are in good agreement with the previous report in which CV was measured in the standard three electrode system where gold electrodes were used.<sup>40</sup> At the same time, we monitored the mass spectrum of the oxidised species of ferrocenecarboxaldehyde in positive ion mode, shown in Fig. 8C. The peak at  $m/z$  214 corresponds to the ferrocenecarboxaldehyde ion which supports the electrochemical oxidation phenomenon. For polycyclic aromatic hydrocarbons, the required potentials (threshold potentials) to eject the electrochemically oxidised species to the gas phase for mass spectrometric analysis are slightly different from the oxidation potentials in the solution phase. However, we observed that these threshold potentials follow a similar trend, similar to the oxidation potentials. In Table S1 (ESI<sup>†</sup>), the oxidation potentials and the potentials required for mass spectrometric detection in a three electrode paper cell of benzene, naphthalene, and 1,2-benzanthracene are listed. These oxidation potentials are in good agreement with the literature.<sup>41</sup> Fig. S9 (ESI<sup>†</sup>) presents the cyclic voltammogram of benzene, naphthalene, and 1,2-benzanthracene.

## Conclusions

In conclusion, we report a CNT incorporated paper-based electrochemical cell which utilizes the advantages of both low voltage ionization and electrochemistry. Integrating these two principles makes the *in situ* ionization and detection of analytes at low voltage possible, by electrochemically transforming them. Using this device, we have studied the electrochemical conversion of thiols to disulfides. The electrochemical functionalization of three different hydrocarbons has been performed with the paper-based electrochemical cell. Additionally, the detection of metallocenes as well as an unstable radical cation has been achieved with the cell. The study shows that a detection limit of 1 ppt can be reached for specific species. Quantitative analysis is also possible as demonstrated in the case of glucose. The cell has been used for the analysis of different environmentally relevant species. These results open up the possibility of developing such point-of-use devices for various applications by combining known techniques, using nanomaterials.

## Conflicts of interest

There are no conflicts to declare.

## Acknowledgements

We thank Dr Krishnan Swaminathan, MD, FRCP (Edin), Kovai Medical Centre and Hospital, Coimbatore, India, for providing

the blood serum sample for analysis. T. P. acknowledges financial support from the Department of Science and Technology, Government of India for his research program on nanomaterials. R. N. thanks the University Grants Commission for a research fellowship. A. M., P. B., and S. B. thank the IIT Madras for research fellowships.

## Notes and references

- 1 S. Bruckenstein and R. R. Gadde, *J. Am. Chem. Soc.*, 1971, **93**, 793–794.
- 2 F. Zhou and G. J. Van Berkel, *Anal. Chem.*, 1995, **67**, 3643–3649.
- 3 H. P. Permentier and A. P. Bruins, *J. Am. Soc. Mass Spectrom.*, 2004, **15**, 1707–1716.
- 4 H. Faber, M. Vogel and U. Karst, *Anal. Chim. Acta*, 2014, **834**, 9–21.
- 5 P. Liu, M. Lu, Q. Zheng, Y. Zhang, H. D. Dewald and H. Chen, *Analyst*, 2013, **138**, 5519–5539.
- 6 J. Gun, S. Bharathi, V. Gutkin, D. Rizkov, A. Voloshenko, R. Shelkov, S. Sladkevich, N. Kyi, M. Rona, Y. Wolanov, D. Rizkov, M. Koch, S. Mizrahi, P. V. Pridkhochenko, A. Modestov and O. Lev, *Isr. J. Chem.*, 2010, **50**, 360–373.
- 7 H. Deng and G. J. Van Berkel, *Anal. Chem.*, 1999, **71**, 4284–4293.
- 8 H. Deng and G. J. Van Berkel, *Electroanalysis*, 1999, **11**, 857–865.
- 9 H. P. Permentier, A. P. Bruins and R. Bischoff, *Mini-Rev. Med. Chem.*, 2008, **8**, 46–56.
- 10 J. Li, H. D. Dewald and H. Chen, *Anal. Chem.*, 2009, **81**, 9716–9722.
- 11 Y. Zhang, H. D. Dewald and H. Chen, *J. Proteome Res.*, 2011, **10**, 1293–1304.
- 12 C. McClintock, V. Kertesz and R. L. Hettich, *Anal. Chem.*, 2008, **80**, 3304–3317.
- 13 A. Baumann, W. Lohmann, S. Jahn and U. Karst, *Electroanalysis*, 2010, **22**, 286–292.
- 14 S. Jahn and U. Karst, *J. Chromatogr. A*, 2012, **1259**, 16–49.
- 15 K. Xu, Y. Zhang, B. Tang, J. Laskin, P. J. Roach and H. Chen, *Anal. Chem.*, 2010, **82**, 6926–6932.
- 16 Z. Wang, Y. Zhang, H. Zhang, P. B. Harrington and H. Chen, *J. Am. Soc. Mass Spectrom.*, 2012, **23**, 520–529.
- 17 A. D. Modestov, S. Srebnik, O. Lev and J. Gun, *Anal. Chem.*, 2001, **73**, 4229–4240.
- 18 D. Momotenko, L. Qiao, F. Cortés-Salazar, A. Lesch, G. Wittstock and H. H. Girault, *Anal. Chem.*, 2012, **84**, 6630–6637.
- 19 G. Hambitzer and J. Heitbaum, *Anal. Chem.*, 1986, **58**, 1067–1070.
- 20 J. E. Bartmess and L. R. Phillips, *Anal. Chem.*, 1987, **59**, 2012–2014.
- 21 J. R. Pretty, E. H. Evans, E. A. Blubaugh, W. L. Shen, J. A. Caruso and T. M. Davidson, *J. Anal. At. Spectrom.*, 1990, **5**, 437–443.
- 22 M. C. S. Regino and A. Brajter-Toth, *Anal. Chem.*, 1997, **69**, 5067–5072.

- 23 G. Diehl, A. Liesener and U. Karst, *Analyst*, 2001, **126**, 288–290.
- 24 C. R. Blakley, J. J. Carmody and M. L. Vestal, *J. Am. Chem. Soc.*, 1980, **102**, 5931–5933.
- 25 M. Barber, R. S. Bordoli, R. D. Sedgwick and A. N. Tyler, *J. Chem. Soc., Chem. Commun.*, 1981, 325–327, DOI: 10.1039/c39810000325.
- 26 R. S. Houk, V. A. Fassel, G. D. Flesch, H. J. Svec, A. L. Gray and C. E. Taylor, *Anal. Chem.*, 1980, **52**, 2283–2289.
- 27 M. S. B. Munson and F. H. Field, *J. Am. Chem. Soc.*, 1966, **88**, 2621–2630.
- 28 D. I. Carroll, I. Dzidic, R. N. Stillwell, K. D. Haegele and E. C. Horning, *Anal. Chem.*, 1975, **47**, 2369–2372.
- 29 D. B. Robb, T. R. Covey and A. P. Bruins, *Anal. Chem.*, 2000, **72**, 3653–3659.
- 30 M. Yamashita and J. B. Fenn, *J. Phys. Chem.*, 1984, **88**, 4451–4459.
- 31 D. M. Cate, J. A. Adkins, J. Mettakoonpitak and C. S. Henry, *Anal. Chem.*, 2015, **87**, 19–41.
- 32 W. Dungchai, O. Chailapakul and C. S. Henry, *Anal. Chem.*, 2009, **81**, 5821–5826.
- 33 Y.-M. Liu and R. H. Perry, *J. Am. Soc. Mass Spectrom.*, 2015, **26**, 1702–1712.
- 34 J. Liu, H. Wang, N. E. Manicke, J.-M. Lin, R. G. Cooks and Z. Ouyang, *Anal. Chem.*, 2010, **82**, 2463–2471.
- 35 R. Narayanan, D. Sarkar, R. G. Cooks and T. Pradeep, *Angew. Chem., Int. Ed.*, 2014, **53**, 5936–5940.
- 36 R. Narayanan, D. Sarkar, A. Som, M. S. Wlekinski, R. G. Cooks and T. Pradeep, *Anal. Chem.*, 2015, **87**, 10792–10798.
- 37 P. Basuri, D. Sarkar, G. Paramasivam and T. Pradeep, *Anal. Chem.*, 2018, **90**, 4663–4668.
- 38 G. Velmurugan, K. Swaminathan, G. Veerasekar, J. Q. Purnell, S. Mohanraj, M. Dhivakar, A. K. Avula, M. Cherian, N. G. Palaniswami, T. Alexander and T. Pradeep, *Occup. Environ. Med.*, 2018, **75**, 661–667.
- 39 F.-F. Li, L.-Y. Fu, W.-L. Zhang, X.-F. Su, J.-D. Wu, J. Sun, L. Ye and J.-H. Ma, *J. Diabetes Res.*, 2016, **2016**, 8.
- 40 C. Padeste, A. Grubelnik and L. Tiefenauer, *Biosens. Bioelectron.*, 2000, **15**, 431–438.
- 41 G. J. Hoijtink, *Recl. Trav. Chim. Pays-Bas Belg.*, 1958, **77**, 555–558.

## Supplementary Information

### In-situ Monitoring of Electrochemical Reactions Through CNTs-assisted Paper Cell Mass Spectrometry

Rahul Narayanan,<sup>†a</sup> Pallab Basuri,<sup>†a</sup> Sourav Kanti Jana,<sup>a</sup> Ananthu Mahendranath,<sup>a,b</sup> Sandeep Bose,<sup>a</sup> and Thalappil Pradeep<sup>\*a</sup>

<sup>a</sup> DST Unit of Nanoscience and Thematic Unit of Excellence, Department of Chemistry, Indian Institute of Technology Madras, Chennai 600036, India.

<sup>b</sup> Department of Metallurgical and Materials Engineering, Indian Institute of Technology Madras, Chennai 600036, India.

Number	Description	Page Number
SI-1	Mass spectrometry	2
SI-2	Product ion intensity - cell potential profile	2
SI-3	Mass spectra of cysteine and glutathione at different cell potentials	3
SI-4	MS <sup>2</sup> spectra of functionalized hydrocarbons	3
SI-5	Product ion intensity - cell potential profile	4
SI-6	Mass spectra of benzene, mesitylene and naphthalene at different cell potentials	4
SI-7	Product ion intensity - cell potential profile	5
SI-8	Quantitation of glucose	6
SI-9	Electrochemical analysis of glucose (1 ppt) and 1,2-benzanthracene (10 ppm)	7
SI-10	Table S1: Oxidation and threshold potentials of PAHs	7
SI-11	Cyclic voltammograms of PAHs during in-situ electrochemical mass spectrometry	8

## Supplementary Information 1

### Mass spectrometry:

All the experiments were performed using an ion trap LTQ XL with the following mass spectrometric conditions. Source voltage: 0-6 V. This was applied through an external power supply, and was connected to the silver electrodes. As it is a two electrode system, the positive 0-6 V was applied to anode and the opposite polarity was applied to the cathode, from the same power source. Capillary temperature: was set at 150 °C (the temperature was set in the low range in order to avoid heavy fragmentation). Capillary and tube lens voltages were set at 0 V to avoid further fragmentation inside mass spectrometer. The sheath gas flow rate was also set to zero. All mass spectra correspond to an average of 25 scans. The identity of each species was confirmed by collision-induced dissociation. Three electrode experiments were performed to confirm the electrochemical events.

## Supplementary Information 2

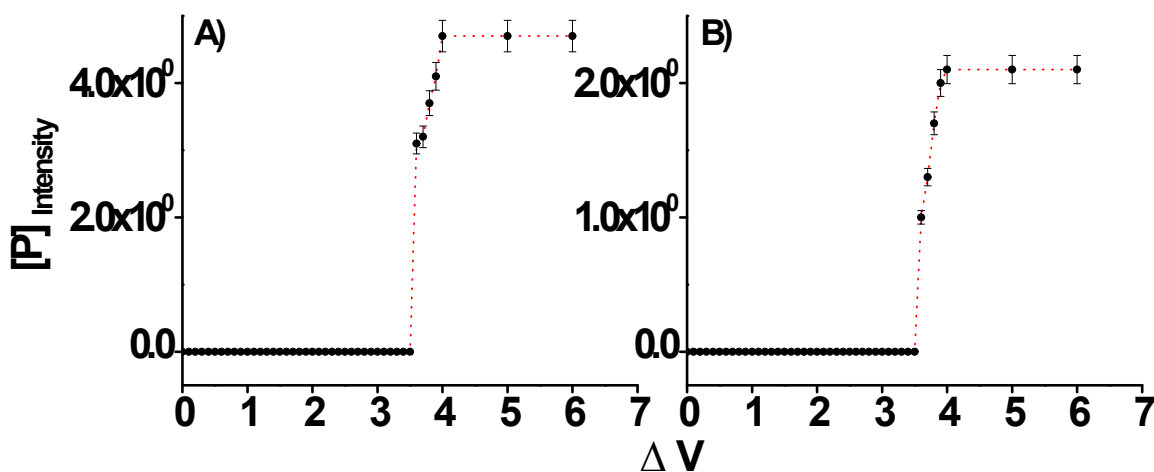


**Figure S1.** Product ion intensity - cell potential profile of A) cysteine and B) glutathione.

### Supplementary Information 3

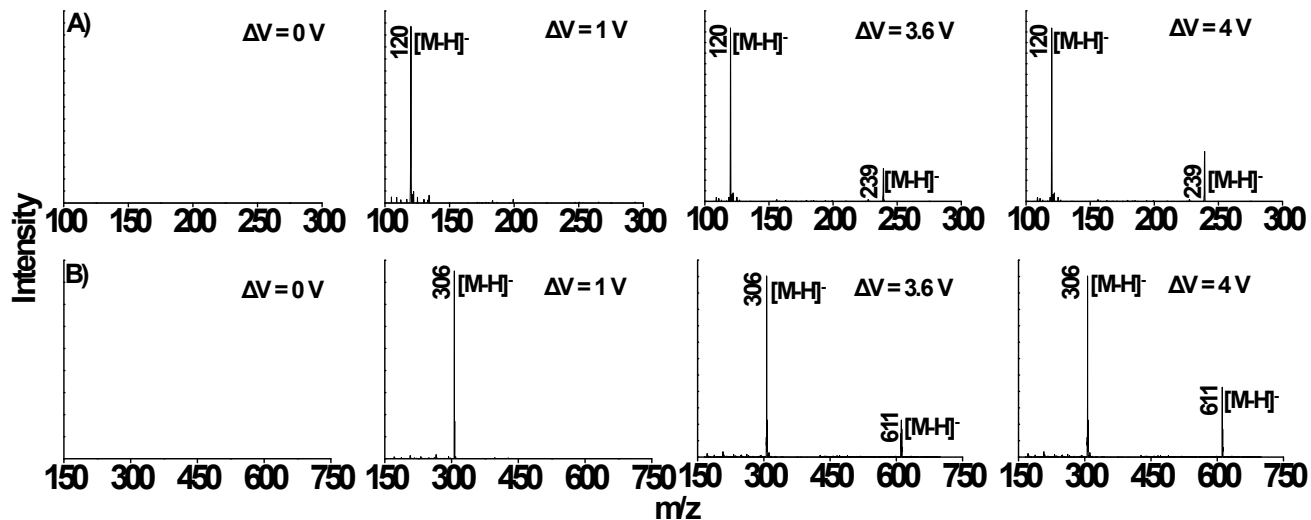


**Figure S2.** A) Mass spectra of cysteine (in methanol:water solvent mixture with KCl as an electrolyte) at different cell potentials, and B) Mass spectra of glutathione (in methanol: water solvent mixture with KCl as an electrolyte) at different cell potentials.

### Supplementary Information 4

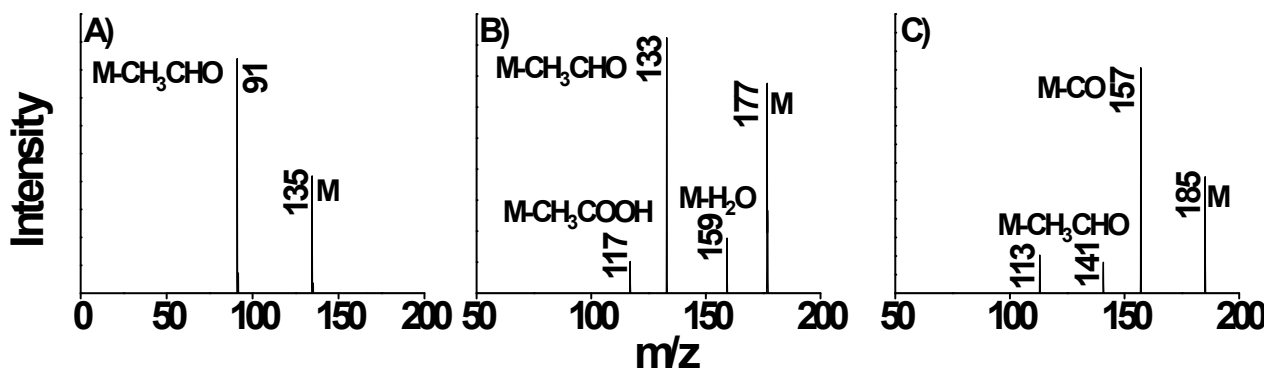


**Figure S3.** MS<sup>2</sup> spectra of A) benzene acetic acid, B) mesitylene acetic acid and C) naphthalene acetic acid.

## Supplementary Information 5

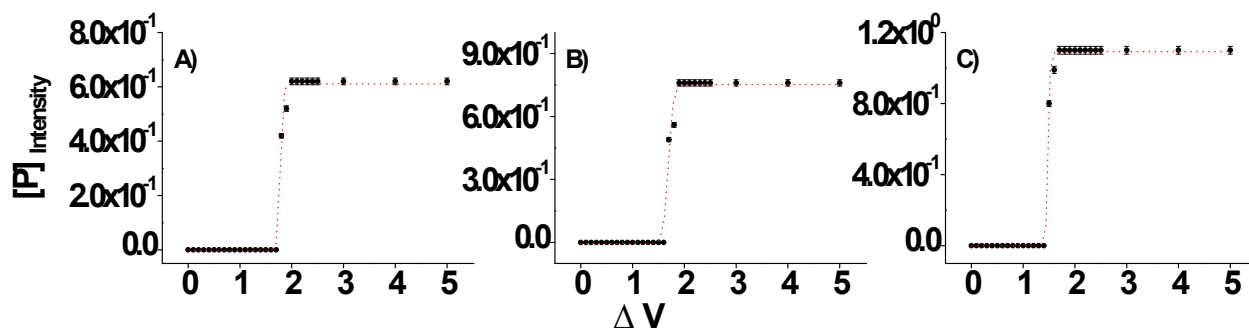


**Figure S4.** Product ion intensity - cell potential profile of A) benzene, B) mesitylene and C) naphthalene.

## Supplementary Information 6

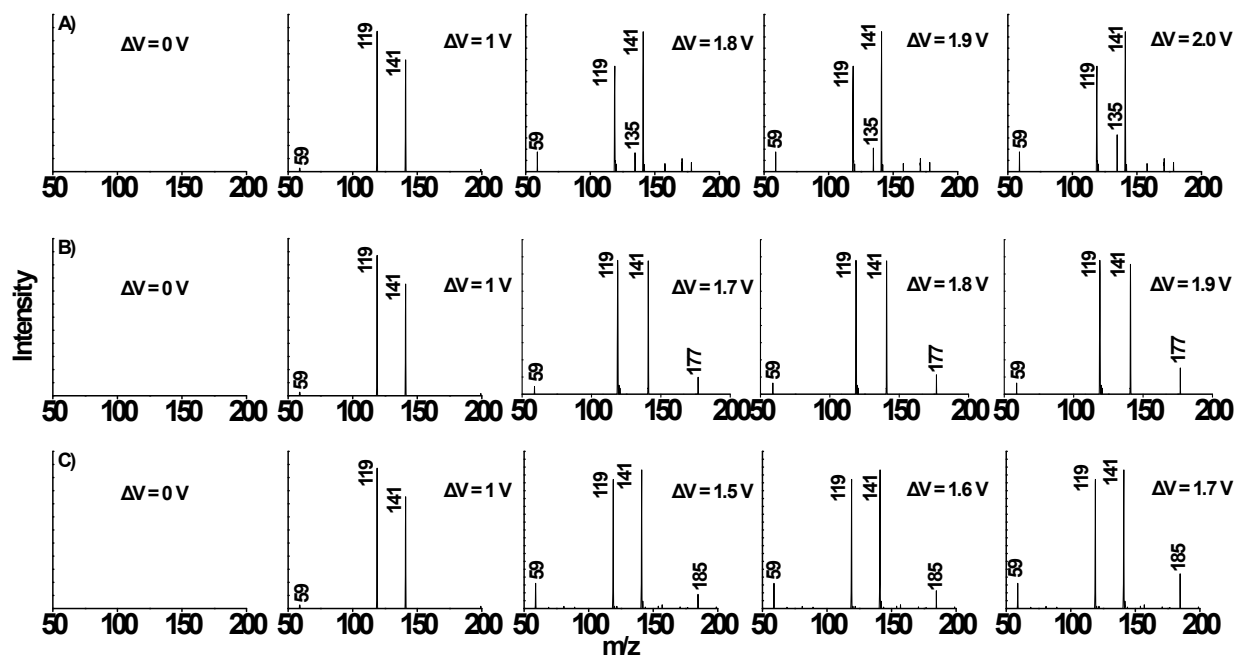


**Figure S5.** Mass spectra of A) benzene (in acetic acid solvent with sodium acetate as an electrolyte) at different cell potentials, B) mesitylene (in acetic acid solvent with sodium acetate as an electrolyte) at different cell potentials and C) naphthalene (in acetic acid solvent with sodium acetate as an electrolyte) at different cell potentials.



## Supplementary Information 7

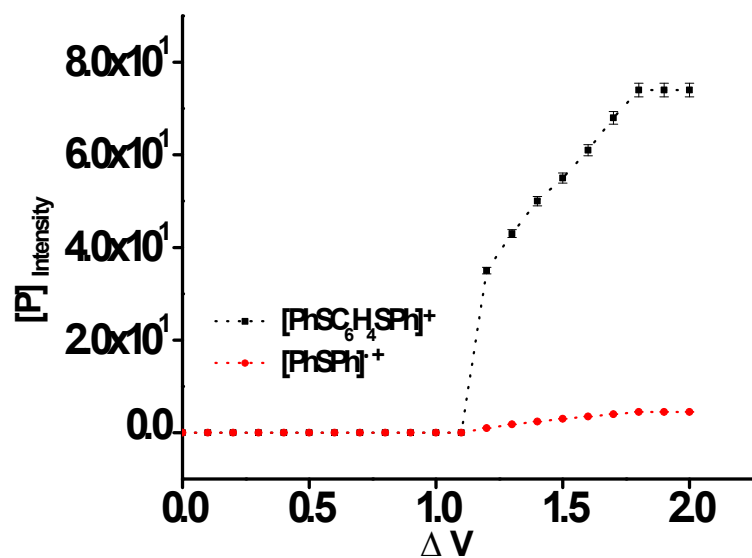


**Figure S6.** Product ion intensity-voltage profile for the electrochemical oxidation of diphenyl sulfide.

## Supplementary Information 8

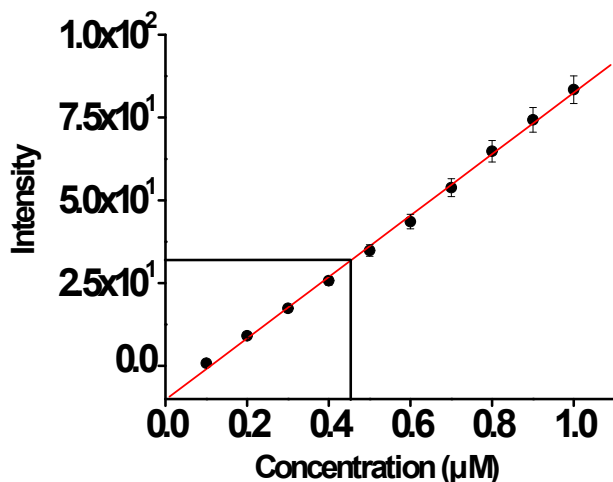
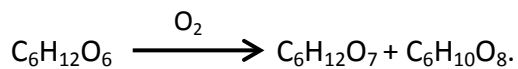


**Figure S7.** Intensity – concentration profile for glucose to saccharic acid oxidation.

### Quantitation of glucose in blood serum

Volume of blood serum used – 100 μL

Assuming that 1mole of glucose produces 1 mole of gluconic acid and 1 mole of saccharic acid according to the following equation,



Product ion intensity in the experimental result indirectly implies the amount of glucose in blood serum.

The experimental result indicates the presence of 0.45 μM of glucose in 100 μL volume of blood serum, which is in good agreement with the actual value.

## Supplementary Information 9

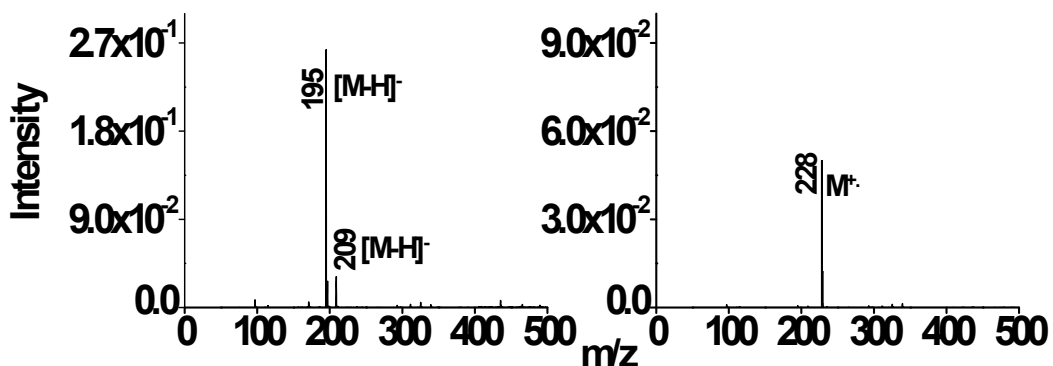


**Figure S8.** Electrochemical analysis of glucose (1 ppt) and 1, 2-benzanthracene (carcinogen) (10 ppm).

## Supplementary Information 10

**Table S1:** Observed and reported<sup>1</sup> oxidation and threshold potentials for in-situ electrochemical mass spectrometric measurement of polycyclic aromatic hydrocarbons.

No	Name of the chemical	Observed oxidation potential (V)	Threshold potential (V)	Observed mass speak (m/z)	Oxidation potential (V) from literature <sup>1</sup>
1	Benzene	1.57	1.80	78	1.80
2	Napthalene	1.26	1.50	128	1.31
3	Benzanthracene	0.99	1.20	228	0.92

## Supplementary Information 11

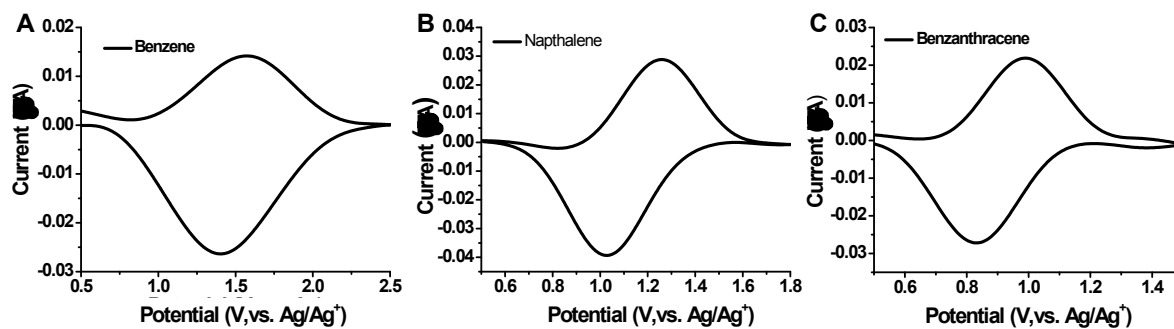


**Figure S9.** Cyclic voltammogram of A) benzene, B) naphthalene, and C) benzanthracene during in-situ electrochemical mass spectrometry measurements.

## References

1. Hoijtink, G. J., Oxidation potentials of conjugated hydrocarbons. *Recl. Trav. Chim. Pays-Bas Belg.* **1958**, 77, 555-8.

# Highly Sensitive As<sup>3+</sup> Detection Using Electrodeposited Nanostructured MnO<sub>x</sub> and Phase Evolution of the Active Material during Sensing

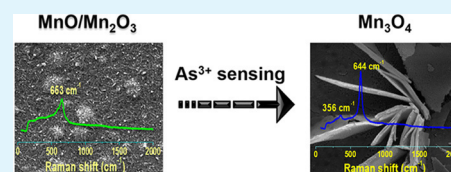
Tanvi Gupte,<sup>†,‡,§</sup> Sourav Kanti Jana,<sup>†,§</sup> Jyoti Sarita Mohanty,<sup>†</sup> Pillalamarri Srikrishnarka,<sup>†</sup> Sritama Mukherjee,<sup>†</sup> Tripti Ahuja,<sup>†</sup> Chennu Sudhakar,<sup>†</sup> Tiju Thomas,<sup>\*,‡</sup> and Thalappil Pradeep<sup>\*,†</sup>

<sup>†</sup>DST Unit of Nanoscience (DST UNS) and Thematic Unit of Excellence, Department of Chemistry and <sup>‡</sup>Department of Metallurgical and Materials Engineering, Indian Institute of Technology Madras, Chennai 600036, India

## Supporting Information

**ABSTRACT:** A simple, one-step electrodeposition approach has been used to fabricate MnO<sub>x</sub> on an indium-doped tin oxide substrate for highly sensitive As<sup>3+</sup> detection. We report an experimental limit of detection of 1 ppb through anodic stripping voltammetry with selectivity to As<sup>3+</sup> in the presence of 10 times higher concentrations of several metal ions. Additionally, we report the simultaneous phase evolution of active material occurring through multiple stripping cycles, wherein MnO/Mn<sub>2</sub>O<sub>3</sub> eventually converts to Mn<sub>3</sub>O<sub>4</sub> as a result of change in the oxidation states of manganese. This occurs with concomitant changes in morphology. Change in the electronic property (increased charge transfer resistance) of the material due to sensing results in an eventual decrease in sensitivity after multiple stripping cycles. In a nutshell, this paper reports stripping-voltammetry-induced change in morphology and phase of as-prepared Mn-based electrodes during As sensing.

**KEYWORDS:** arsenic, nanostructured electrode, manganese oxide, electrochemical sensor, stripping voltammetry



## 1. INTRODUCTION

Arsenic (As) contamination in water is a serious concern, affecting over 140 million people worldwide.<sup>1</sup> Arsenic mainly exists as arsenate [As(V)] and arsenite [As(III)] ions in water and soil.<sup>2</sup> Currently, the World Health Organization (WHO) and U.S. Environmental Protection Agency recommended that the limit of arsenic content in drinking water is 10 µg/L (or 10 parts per billion (ppb)).<sup>3,4</sup> Use of As-contaminated water for the preparation of food, irrigation of crops, and drinking has serious consequences on human health.<sup>3</sup> Most known As and inorganic As compounds are classified as Group 1 human carcinogens by International Agency for Research on Cancer.<sup>5</sup> Group 1 compounds are those for which there is sufficient evidence for concluding their carcinogenicity in humans. Prolonged exposure to high concentrations of arsenic may cause cancer of skin, lungs, kidney, uterus, and liver. It can also lead to disorders of cardiovascular, gastrointestinal, and central nervous systems.<sup>6</sup> The trivalent arsenic (As<sup>3+</sup>) has higher mobility in groundwater and is more toxic than the pentavalent (As<sup>5+</sup>) analogue.<sup>7</sup>

Therefore, accurate and selective detection of As<sup>3+</sup> in water is more important to identify the contaminated source, to help prevent its deleterious effects on health, and also to optimize arsenic remediation technologies. Various laboratory-based arsenic detection techniques have been used such as hydride generation/atomic absorption spectrometry, graphite furnace atomic absorption spectrometry, inductively coupled plasma-mass spectrometry (ICP-MS), atomic fluorescence spectrometry, etc.<sup>2,8,9</sup> However, such techniques are expensive,

unsuitable for on-field testing, and often require prior separation of arsenic species (speciation). Thus, there is a demand for an affordable arsenic sensor, especially because most of the arsenic-affected people are poor. Electrochemical sensors offer a low-cost, rapid, portable, reliable, and sensitive method. For the detection of arsenic, both enzymatic<sup>10–12</sup> and non-enzymatic<sup>13–16</sup> electrochemical sensors have been developed. Non-enzymatic sensors are important as they can offer stability and cost-effectiveness and support diverse operating conditions.

On the other hand, enzyme-based biosensors have an advantage due to their analyte specificity and lower limits of detection. However, they have certain intrinsic limitations such as complicated enzyme immobilization procedures, limited lifetime, instability at various pH and temperature conditions, and expensive preparation and storage conditions.<sup>17–20</sup> Therefore, tailoring of non-enzymatic electrode surfaces is desirable for As<sup>3+</sup> sensing with good sensitivity and stability.

Anodic stripping voltammetry (ASV) has been used widely for quantitative measurement of arsenic in water.<sup>13,14,21,15</sup> It is an ultrasensitive, two-step voltammetric technique for quantitative determination of specific ionic species. The first step is the deposition or preconcentration step in which the analyte of interest is usually electrodeposited on the working electrode at a constant potential for a certain time. This step

Received: April 6, 2019

Accepted: July 12, 2019

Published: July 12, 2019

involves reduction of the metal ions from the solution to the electrode surface (for example,  $\text{As}^{3+}$  to  $\text{As}^0$ ). In the second step, the potential of the working electrode is raised to a higher value by applying a voltage scan (termed as anodic stripping). At a definite potential, specific metal species which are deposited onto the electrode surface are stripped (oxidized) into the solution (for example,  $\text{As}^0$  to  $\text{As}^{3+}$ ). The oxidation of analyte (arsenic in this case) is recorded as a peak in terms of Faradaic oxidation current in the voltammogram at a particular potential called the oxidation potential of the arsenic species. The peak intensity is proportional to the  $\text{As}^{3+}$  concentration present in the electrolyte.<sup>17</sup> In our study, linear sweep stripping voltammetry (LSSV), a type of ASV technique, has been used for  $\text{As}^{3+}$  detection, wherein the potential is swept linearly with time.

In this work, a transition metal oxide (TMO) (manganese oxide ( $\text{MnO}_x$ ))-based working electrode was developed and used as an electrochemical sensor to detect  $\text{As}^{3+}$  present in water. TMO adsorbents are considered as some of the promising materials for removal of toxic heavy metal ions from high-total dissolved solid groundwater because of their abundant physicochemical properties such as large surface area, specific adsorption sites, and catalytic activity.<sup>4</sup> These properties are mainly affected by the electronic properties and surface morphology of the TMO. Manganese oxides exist as  $\text{MnO}_6$  octahedra that form tunnels and/or layered structures.<sup>22,23</sup> The tunnels and layers are connected by corner or edge sharing. Cations and water molecules can occupy these tunnels or interlayers.<sup>24</sup> The nanostructured  $\text{MnO}_x$  provides active sites for arsenic adsorption during sensing. Sorption of As on manganese oxide ( $\text{MnO}_x$ )-based materials due to their selective adsorption property is widely reported.<sup>25–27</sup> Mn oxides are known to be one of the strongest naturally occurring oxidizing agents.<sup>24</sup> Also, the surface areas of different oxides of manganese may vary from 3 to  $\sim 200 \text{ m}^2/\text{g}$ .<sup>28</sup> These properties of  $\text{MnO}_x$  influence the biogeochemical cycling of contaminants, such as chromium (Cr), uranium (U), selenium (Se), and arsenic.<sup>24</sup> Several electrochemical As sensors have been developed to utilize these properties of  $\text{MnO}_x$ . Many of them use working electrodes of  $\text{MnO}_x$  modified with gold nanoparticles,<sup>15,29</sup> reduced graphene oxide,<sup>13</sup> etc. for better sensitivity and selectivity. Here, we would like to mention that this study deals with two aspects: one is electrochemically developing a nanostructured  $\text{MnO}_x$ -based electrode for  $\text{As}^{3+}$  sensing. The second aspect is a detailed insight into the fundamental, yet unexplored, issue of phase evolution and morphological changes in the nanosystem during electrochemical sensing. Manganese oxides exist in several oxidation states. The stripping-voltammetry-induced changes in nanostructures and oxidation states are studied in this paper by performing several characterization studies before and after sensing. As of now, a few  $\text{MnO}_x$ -based composite nanostructures have been reported for  $\text{As}^{3+}$  sensing.<sup>13,29,30</sup> However, reports are scarce about the impact of voltammetric techniques on the active material and it is important to understand the phase and structural stability of the material during the process of sensing. This is a crucial contributing factor for limiting the performance of such sensors in the course of their operation.

Here, we have used a noble-metal-free working electrode, wherein  $\text{MnO}_x$  was electrodeposited on an indium-doped tin oxide (ITO)-coated glass substrate for As detection. Various working electrode substrates have been used for As detection, e.g., platinum,<sup>31</sup> gold,<sup>14,18,31</sup> glassy carbon,<sup>13,15,29</sup> boron-doped

diamond,<sup>16,32</sup> etc. Although these materials are promising, there are often disadvantages associated with their use such as high cost, need of strongly acidic media for operation (which can produce toxic arsine gas), chemical modification with an electron transfer mediator, etc. ITO as an electrode substrate is of great interest in electrochemical sensors because of low cost and good electrical conductivity ( $\sim 10^4 \text{ S/cm}$ ).<sup>33</sup> We have studied the electrochemistry-induced evolution of phase and morphology of  $\text{MnO}_x$  and its impact on the electronic conductivity and electrochemical property of the electrodeposited material.

The phase and morphology of  $\text{MnO}_x$  were controlled through electrodeposition by the cyclic voltammetry (CV) technique performed at three different potential windows. The electrodes were characterized by electron microscopy, spectroscopy, and electrochemical techniques. LSSV was performed using different concentrations of  $\text{As}^{3+}$ . Quantitative detection of  $\text{As}^{3+}$  with a linear response range from 1 to 150 ppb was observed using an optimized  $\text{MnO}_x/\text{ITO}$  electrode. The  $\text{As}^{3+}$  response was saturated at  $\sim 125$ – $150$  ppb after multiple stripping cycles. The phase evolution of active material wherein  $\text{MnO}/\text{Mn}_2\text{O}_3$  eventually got converted to  $\text{Mn}_3\text{O}_4$  resulted in an increase in the charge transfer resistance of the material, which was studied by impedance spectroscopy. This may be the reason for eventual decrease in sensitivity after multiple stripping cycles. Moreover, selectivity of the electrode for  $\text{As}^{3+}$  was successfully studied in the presence of 10 times higher concentrations of several metal ions.

## 2. EXPERIMENTAL SECTION

**2.1. Materials.** Anhydrous manganese acetate [ $\text{Mn}(\text{CH}_3\text{COO})_2$ ], sodium sulfate ( $\text{Na}_2\text{SO}_4$ ), sodium arsenite ( $\text{NaAsO}_2$ ), ITO-coated glass substrates, and Millipore-produced deionized (DI) water ( $\sim 18.2 \text{ M}\Omega$ ) were used throughout the experiments.

**2.2. Preparation of Working Electrode by Electrodeposition.** ITO-coated glass substrates were cleaned by ultrasonically cleaning them sequentially in acetone, ethanol, and distilled water for 5 min each, followed by drying in nitrogen. The working electrode was prepared by electrodeposition of manganese oxide on the cleaned ITO substrate ( $\sim 1 \text{ cm}^2$ ), and this as-prepared electrode is termed  $\text{MnO}_x/\text{ITO}$ . The geometric surface area of ITO was maintained by sticking a strip of scotch tape as a mask on the substrate. A three-electrode setup comprising ITO as the working electrode, platinum wire as a counter electrode, and Ag/AgCl as a reference electrode was used during electrochemical measurements. An aqueous solution of  $0.05 \text{ M Mn}(\text{CH}_3\text{COO})_2$  was used as a precursor, and  $0.1 \text{ M}$  sodium sulfate ( $\text{Na}_2\text{SO}_4$ ) was used as electrolyte during electrochemical deposition of  $\text{MnO}_x$ . Electrodeposition was carried out by CV at three different potential ranges:  $0.8$ – $1.3 \text{ V}$  (8 cycles),  $-0.2$ – $0.9 \text{ V}$  (15 cycles), and  $-1$ – $1.3 \text{ V}$  (4 cycles) at a scan rate of  $0.05 \text{ V/s}$  using a CHI 600A electrochemical workstation at room temperature. Subsequently, these samples were named **M1**, **M2**, and **M3**, respectively, and the same will be used further in this paper. The electrodeposition potential ranges were set based on the Pourbaix diagram of manganese (Figure S1).<sup>34</sup> After electrodeposition, the samples were washed in distilled water, dried in air, and finally stored at room temperature before using for further material characterization and electrochemical analysis.

**2.3. Electrochemical Analysis.** Arsenic sensing was carried out by the linear sweep stripping voltammetry (LSSV) technique using  $\text{NaAsO}_2$  dissolved in phosphate-buffered saline (PBS,  $\text{pH} \sim 7.4$ ) with the following optimized parameters: deposition potential (DP) of  $\text{As}^{3+}$  of  $-0.7 \text{ V}$ , deposition time (DT) of  $180 \text{ s}$ , stripping potential range of  $-0.40$ – $0.20 \text{ V}$ , and scan rate of  $0.05 \text{ V/s}$ . All of the electrochemical measurements were performed using  $\text{MnO}_x/\text{ITO}$ , Pt wire, and Ag/AgCl as working, counter, and reference electrodes,



respectively. For arsenite sensing, different concentrations of  $\text{As}^{3+}$  were prepared in PBS just before recording LSSV. The electrodes were washed with DI water between consecutive measurements. CV measurements for testing the performance of bare ITO at optimized parameters were performed using bare ITO as the working electrode. Counter and reference electrodes were the same as above. The redox molecule used was  $32.6 \mu\text{M}$  potassium ferricyanide ( $\text{K}_3\text{Fe}(\text{CN})_6$ ) in  $3.2 \text{ mM}$  potassium chloride (KCl) as the supporting electrolyte. The volume of electrolyte was maintained constant for all of the electrochemical measurements.

**2.4. Instrumentation.** All electrochemical measurements including electrodeposition and LSSV for  $\text{As}^{3+}$  detection were performed using a CH 600A (CH Instruments) electrochemical workstation. Surface morphology of  $\text{MnO}_x$  samples was obtained using a MIRA 3 (TESCAN) field emission scanning electron microscope (FESEM). All high-resolution transmission electron microscopy (HRTEM) images were obtained using JEOL JFD 3010 (JEOL Japan), a  $300 \text{ kV}$  transmission electron microscope, equipped with an ultra-high-resolution pole piece. X-ray diffraction (XRD) patterns of  $\text{MnO}_x$  were obtained with Bruker X8 KAPPA using  $\text{Cu K}\alpha$  radiation as the source. Electrochemical impedance spectroscopy (EIS) measurements were performed using a Biologic electrochemical analyser (SP200). Inductively coupled plasma-mass spectrometry (ICP-MS (NexION 300X; PerkinElmer)) analysis was performed before and after electrochemical sensing of  $\text{As}^{3+}$ . A Witec GmbH, Alpha-SNOM alpha300S confocal Raman instrument equipped with a  $532 \text{ nm}$  laser as the excitation source was used for Raman analysis. Measurements were carried out with a  $20\times$  objective (Plan-Apochromat, Zeiss),  $600 \text{ grooves/mm}$  grating, and at  $1 \text{ s}$  acquisition time. A laser power of  $\sim 10 \text{ mW}$  was maintained on the sample during measurement. X-ray photoelectron spectroscopy (XPS) measurements were conducted using an Omicron Nanotechnology ESCA probe TPD spectrometer with polychromatic  $\text{Al K}\alpha$  as the X-ray source ( $h\nu = 1486.6 \text{ eV}$ ).  $\text{MnO}_x/\text{ITO}$  samples were mounted on a carbon tape, supported on the sample stub. A constant analyzer energy of  $20 \text{ eV}$  was used for the measurements. Binding energy was calibrated with respect to  $\text{C } 1\text{s}$  at  $284.8 \text{ eV}$ . All of the XPS spectra were deconvoluted using CasaXPS software.

### 3. RESULTS AND DISCUSSION

**3.1. Characterization by SEM and HRTEM.** Surface morphologies of the as-prepared  $\text{MnO}_x/\text{ITO}$  electrodes were analyzed using FESEM micrographs. Gold was sputtered on all electrodes prior to FESEM analyses. Difference in surface morphologies was observed in the electrodes prepared at three different CV potential windows. Also, there is a characteristic change in the morphologies at the nanoscale after using the electrode for  $\text{As}^{3+}$  sensing (as seen in FESEM micrographs of Figure 1A,C).

Figure S2A,B in the Supporting Information (SI) shows the low- and high-magnification FESEM micrographs of as-prepared M1 illustrating their surface morphology. Porous, globular structures ( $\sim 800 \text{ nm}$  to  $1 \mu\text{m}$  diameter) with nanorod-like features diverging from the globular surface are observed on as-prepared electrode M1. This morphology is found to be similar to sea urchins. The entire electrode surface, including the surface of the spheres, is rough consisting of nanorods with uniform diameter and length. Song et al. have reported such sea urchin-shaped  $\text{MnO}_2$  nanostructures prepared by the sodium dodecyl sulfate-assisted hydrothermal method.<sup>35</sup> Figure S2C,D shows FESEM micrographs of M1 after  $\text{As}^{3+}$  sensing. The nanorods, which were observed on the as-prepared electrode, were flattened after multiple stripping cycles of arsenic sensing.

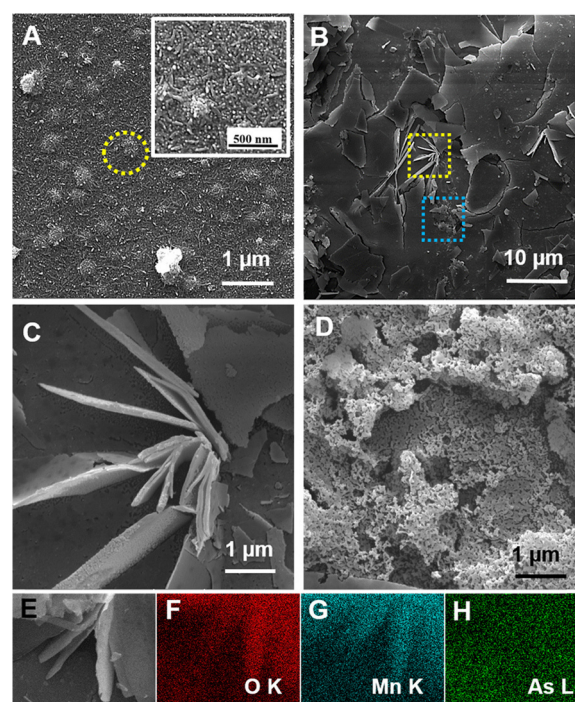


**Figure 1.** FESEM micrographs of (A) as-prepared M3 and (B–D) after  $\text{As}^{3+}$  sensing. The surface morphology before sensing (A) shows several globular structures (one such structure is marked by a yellow circle) embedded in a rough-surfaced mat of nanorods with the inset showing a high-magnification image. After  $\text{As}^{3+}$  sensing, platelike structures ( $\sim 5\text{--}10 \mu\text{m}$  diameter) as seen in (B) are observed all over the electrode surface. (C) and (D) are high-magnification micrographs. (C) Flower-shaped platelike structure (marked by the yellow square in (B)) and (D) porous surrounding morphology of the electrode (marked by blue square in (B)). (E) is the optical image, and (F)–(H) are the corresponding SEM–energy dispersive X-ray analysis maps for O, Mn, and As, respectively, after using M3 for  $\text{As}^{3+}$  sensing.

The M2 appeared as flakes before sensing (Figure S3A,B), while after  $\text{As}^{3+}$  sensing, dendritic structures (Figure S3C,D) were observed on the same electrode surface.

The FESEM micrograph of as-prepared electrode M3 shows that the surface is covered with nanosized globular structures having a diameter of about  $150\text{--}200 \text{ nm}$  (Figure 1A). These are embedded in a hierarchical porous, spongy mat composed of an assembly of disordered nanorods. These  $\text{MnO}_x$  nanorods can be seen clearly in the inset of Figure 1A, the diameter is approximately  $20\text{--}40 \text{ nm}$ , and the length of the nanorods is in the range of  $150\text{--}200 \text{ nm}$ . However, FESEM micrographs of the same electrode after  $\text{As}^{3+}$  sensing show platelike structures shaped as flowers of  $\sim 5\text{--}10 \mu\text{m}$  diameter spread all over the electrode (Figure 1B). Figure 1C,D shows high-magnification micrographs showing one such structure and the porous nature of the electrode surface, respectively, obtained after  $\text{As}^{3+}$  sensing. Figure 1E is the optical image, and Figure 1F–H shows the corresponding SEM–energy dispersive spectroscopy maps for O, Mn, and As elements after using electrode M3 for  $\text{As}^{3+}$  sensing. EDX analysis (shown in Figure S4) of the M3 before and after  $\text{As}^{3+}$  sensing shows the loss of manganese ions from the parent material, during stripping of  $\text{As}^{3+}$ .

Samples for HRTEM measurements were prepared by dispersing the electrodeposited  $\text{MnO}_x$  layer from the electrode into ethanol by ultrasonication for  $30 \text{ min}$ . The dispersion was



then spotted on a carbon-coated copper grid and dried under ambient conditions.

HRTEM analysis shows the polycrystalline nature of electrodeposited  $\text{MnO}_x$ . The morphology and lattice spacing of the electrode M3 before and after  $\text{As}^{3+}$  sensing are different, which is evident from the HRTEM micrographs shown in Figure 2. The HRTEM of as-prepared electrode (Figure 2A,B)

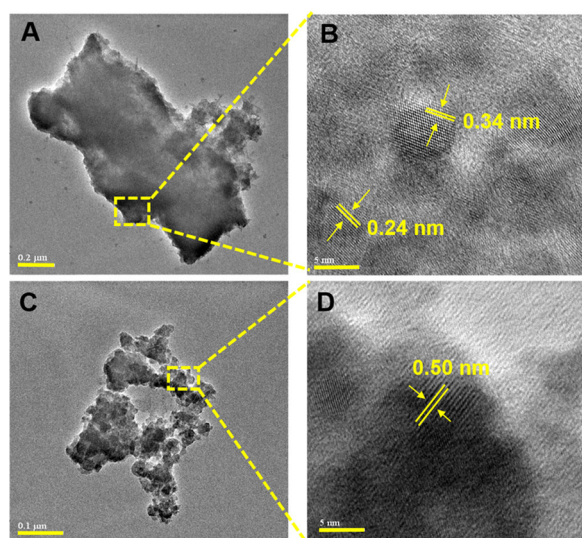


**Figure 2.** HRTEM micrographs of polycrystalline  $\text{MnO}_x$  from M3 (A, B) as-prepared electrode and (C, D) after  $\text{As}^{3+}$  sensing. (A) and (C) are low-magnification images where (A) shows a large particle ( $\sim 1.5 \mu\text{m}$  in length) and (C) shows a cluster of several nanosized particles of  $\text{MnO}_x$ . The high-magnification micrographs (B, D) show that the particles have definite lattice spacing before and after sensing. This signifies the phase transformation of as-prepared  $\text{MnO}_x$  after  $\text{As}^{3+}$  stripping. The scale bars are  $0.2 \mu\text{m}$ ,  $5 \text{ nm}$ ,  $0.1 \mu\text{m}$ , and  $5 \text{ nm}$  for (A), (B), (C), and (D), respectively.

shows that it is composed of larger particles with different lattice orientations. Moreover, there might be a possibility of nucleation of a mixed phase in the as-prepared samples. The lattice spacing of the sample after sensing ( $0.50 \text{ nm}$ ) changed drastically compared to that of the as-prepared sample ( $0.24$  and  $0.34 \text{ nm}$ ). This confirms the evolution of a new phase of the electrode material. The lattice spacing of the electrode after sensing corresponds to the  $\text{Mn}_3\text{O}_4$  phase.<sup>36</sup> The lattice orientation and arrangement of  $\text{Mn}_3\text{O}_4$  crystallites are almost unidirectional, which is observed in Figure 2D. The evolution of  $\text{Mn}_3\text{O}_4$  after  $\text{As}^{3+}$  sensing is presumably because of in situ growth of the material by successive deposition of  $\text{As}^{3+}$  on  $\text{MnO}/\text{Mn}_2\text{O}_3$  of the as-prepared electrode, followed by stripping of  $\text{As}^{3+}$  from the electrode surface. During the deposition step of stripping voltammetry, there may be a formation of  $\text{Mn-O-As}$  complex due to weak interactions between Mn ions of the electrode and  $\text{As}^{3+}$  ions from the electrolyte. Some of the Mn ions are released along with  $\text{As}^{3+}$  during the anodic stripping step. In the subsequent stripping cycle, some Mn ions (present in the electrolyte due to the previous stripping cycle) may redeposit on the parent surface and, finally, get stripped out further with  $\text{As}^{3+}$ . It should be noted that the rates of desorption and deposition of Mn in the stripping cycles are different. This is confirmed by Mn and As ion analysis by ICP-MS. This successive desorption and deposition of Mn ions during LSSV cycles may be the cause for phase evolution of the parent material.

For the ICP-MS experiment, samples were collected from the electrolyte for ICP-MS analysis before performing LSSV ( $\text{As}^{3+}$  sensing). The second-set samples for ICP-MS analysis were collected after the LSSV. This was repeated each time for different concentrations of  $\text{As}^{3+}$  ( $1\text{--}100 \text{ ppb}$ ). The Mn ion release and As ion uptake by the electrode are indicated by the difference in concentrations of Mn and As ions before and after LSSV. We have analyzed the concentrations for three different M3 electrodes. We observed that after each stripping step a minor change in the concentrations of manganese and arsenic ions is seen (Figure S5). The release of manganese ions from the electrode is more during the initial stripping cycles. The average concentration of manganese ions released into the electrolyte after each stripping cycle varies between  $60$  and  $90 \text{ ppb}$ . The uptake of arsenic by an electrode at each stripping cycle is less than  $\sim 2 \text{ ppb}$ . This is not a significant change in concentration. However, this result proves that the electrode retains very less amount of arsenic after completion of a stripping voltammetric cycle. The arsenic deposited during the deposition step ( $\text{As}^{3+}$  to  $\text{As}^0$ ) is effectively getting stripped off during the anodic stripping step ( $\text{As}^0$  to  $\text{As}^{3+}$ ). Low arsenic retention by an electrode is beneficial for accurate results.

HRTEM micrographs of electrodes M1 and M2 (as-prepared and after  $\text{As}^{3+}$  sensing) are given in Figures S6 and S7, respectively. Change in morphology and lattice spacing after  $\text{As}^{3+}$  sensing was also observed in both these electrodes. HRTEM images of as-prepared M1 and M2 demonstrate nanorod-like structures with a lattice spacing of  $\sim 0.24 \text{ nm}$  in Figures S6A,B and S7A,B. The morphology of electrode M2 was changed to a crumpled paperlike structure after using it for sensing. The lattice spacings of M1 (Figure S6C,D) and M2 (Figure S7C,D) changed to  $\sim 0.24$  and  $\sim 0.3 \text{ nm}$  after sensing.

**3.2. X-ray Diffraction (XRD) Patterns, X-ray Photoelectron Spectroscopy (XPS), and Raman Spectral Analysis of Electrode M3.** The electrodeposited  $\text{MnO}_x$  electrodes were air-dried and subsequently used directly for X-ray diffraction analysis. Figure 3A,B shows the XRD patterns obtained for M3. Crystallinity of the as-prepared  $\text{MnO}_x$  sample was poor except that a diffraction peak of the electrodeposited material was observed at  $\sim 33.8^\circ$  corresponding to either  $\text{MnO}$ ,  $\text{Mn}_2\text{O}_3$ , or both (JCPDS file nos. 751090 and 894836 for  $\text{MnO}$  and  $\text{Mn}_2\text{O}_3$ , respectively). Manganese oxide-based compounds have  $\text{MnO}_6$  octahedral units, which are connected by corner or edge sharing and form a structure with random intergrowth.<sup>22,23</sup> This is evident from the random lattice orientations in electron microscopy images (Figure 2B). There might also be a chance of coexistence of the mixed phase in the same sample, which has been discussed already in the HRTEM image analysis. The random arrangement of  $\text{MnO}/\text{Mn}_2\text{O}_3$  phase imparts different crystal orientations (Figure 2B) and demonstrate that they are not epitaxial in growth. The XRD patterns of the as-prepared  $\text{MnO}/\text{Mn}_2\text{O}_3$  sample showed small diffraction peaks because of disorientation of the crystal planes, which can lead to diffused X-ray scattering. The sharp peaks, which are observed in Figure 3A, are mainly crystalline planes of the underlying ITO substrate (JCPDS file no: 71-2194) as shown in Figure S8A. However, the XRD features of the same electrode after  $\text{As}^{3+}$  stripping (Figure 3B) differ distinctly from those of the as-prepared samples. There is an evolution of a new phase after  $\text{As}^{3+}$  stripping, which is confirmed by the sharp diffraction peaks ( $2\theta \sim 16, 32.3, \text{ and } 49^\circ$ ) in the XRD pattern shown in Figure 3B. The peaks correspond to  $\text{Mn}_3\text{O}_4$  (JCPDS file 894837). The

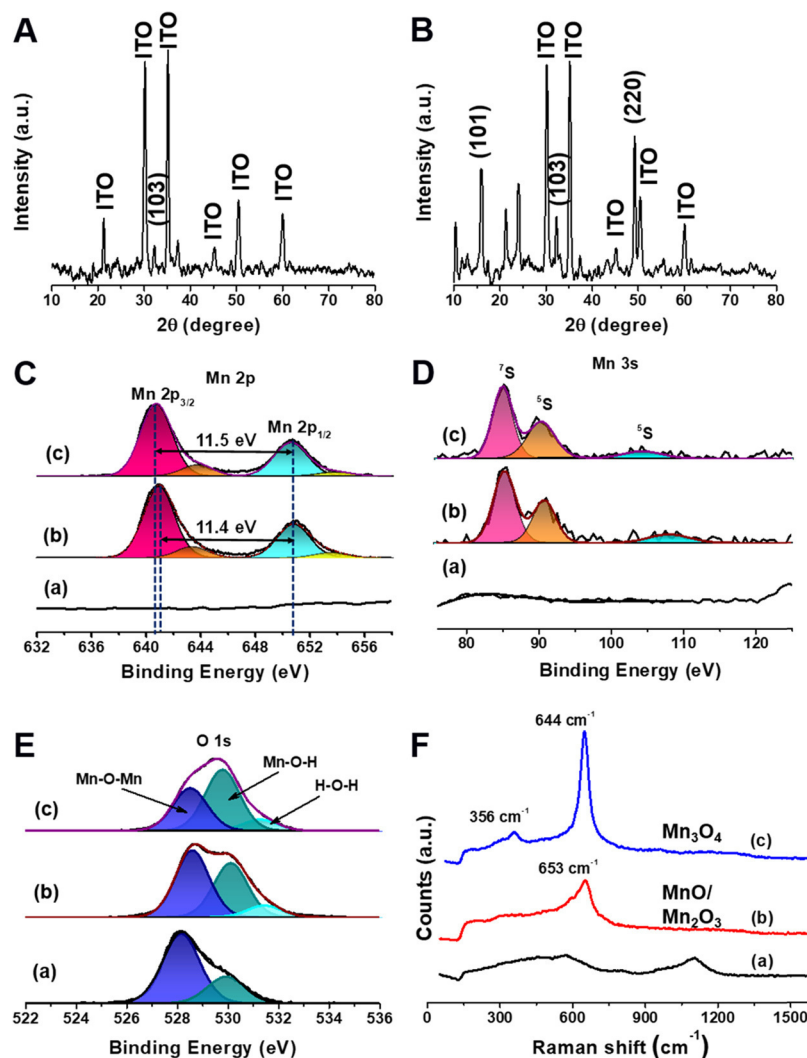


**Figure 3.** Characterization of electrode M3: (A) and (B) are XRD patterns of M3. The (*hkl*) planes are indicated. Planes for the as-prepared electrode correspond to the (A) MnO or Mn<sub>2</sub>O<sub>3</sub> phase and (B) Mn<sub>3</sub>O<sub>4</sub> after As<sup>3+</sup> sensing. The unassigned peaks correspond to the XRD pattern of the ITO glass substrate, which are mentioned in Figure S8A. The data were recorded using a Cu K $\alpha$  source. (C), (D), and (E) are XPS data of the Mn 2p, Mn 3s, and O 1s regions, respectively. (F) Raman spectra of electrode M3. (a), (b), and (c) in (C)–(F) correspond to bare ITO, as-prepared MnO<sub>x</sub> electrodes (before sensing), and MnO<sub>x</sub> electrodes after sensing, respectively.

evolution into Mn<sub>3</sub>O<sub>4</sub> is governed by the successive electrochemical adsorption and desorption of As<sup>3+</sup> during deposition and stripping events of the LSSV cycle, respectively. During the deposition step of As<sup>3+</sup> on manganese oxide, there may be a formation of Mn–O–As species on the electrode surface because of the scavenging effect of MnO<sub>x</sub> toward As<sup>3+</sup>. Subsequently, during the As<sup>3+</sup> stripping step, the release of manganese ions with As<sup>3+</sup> (dissolution–reprecipitation of manganese) may change the oxidation states or phase of parent MnO/Mn<sub>2</sub>O<sub>3</sub>. Initial degradation of the manganese oxide surface during stripping voltammetry leads to the formation of a new microstructure along with the phase evolution to Mn<sub>3</sub>O<sub>4</sub>. To verify the conjecture whether As<sup>3+</sup> has a role in the evolution of the new material or not, we have performed a control experiment. For that, LSSV was performed on M3 in two different electrolytes: distilled water and PBS. This was followed by washing the electrode with distilled water (without As<sup>3+</sup>) and, subsequently, XRD data were taken (Figure S8B). No additional XRD peak was observed after performing LSSV in the absence of As<sup>3+</sup> in both distilled water and PBS.

To get more insight into the oxidation states of Mn, we have performed XPS of the as-prepared electrodeposited electrodes. XPS data of the Mn 2p, O 1s, As 3d, and Mn 3s regions were measured before and after As sensing to understand the effect of LSSV on the oxidation state of electrodeposited MnO<sub>x</sub>. The Mn 2p spectra (Figure 3C) of both, before and after sensing, MnO<sub>x</sub> electrodes exhibit a spin–orbit doublet composed of Mn 2p<sub>3/2</sub> and Mn 2p<sub>1/2</sub> peaks. A slight change in the  $\Delta J$  values of 11.4 and 11.5 eV was observed for electrodes before and after sensing, respectively. Both Mn 2p<sub>3/2</sub> and Mn 2p<sub>1/2</sub> peaks were deconvoluted for both the samples. The Mn 2p<sub>3/2</sub> peak of the as-prepared MnO<sub>x</sub> electrode is observed at 640.4 eV, which is the main characteristic peak of Mn<sup>3+</sup>.<sup>37</sup> The Mn 2p<sub>3/2</sub> peak of the same electrode after electrochemical sensing exhibited a small shift in binding energy (640 eV). Mn 3s spectra (Figure 3D) of the electrode before and after sensing were also analyzed to get more information about the oxidation states of Mn. The splitting of Mn 3s spectra arises from exchange interaction between the unpaired electrons in the 3s orbital and the 3d valence band electrons.<sup>38</sup> Splitting energy of the Mn 3s spectrum (5.4 eV between 7s and 5s states) affirms the

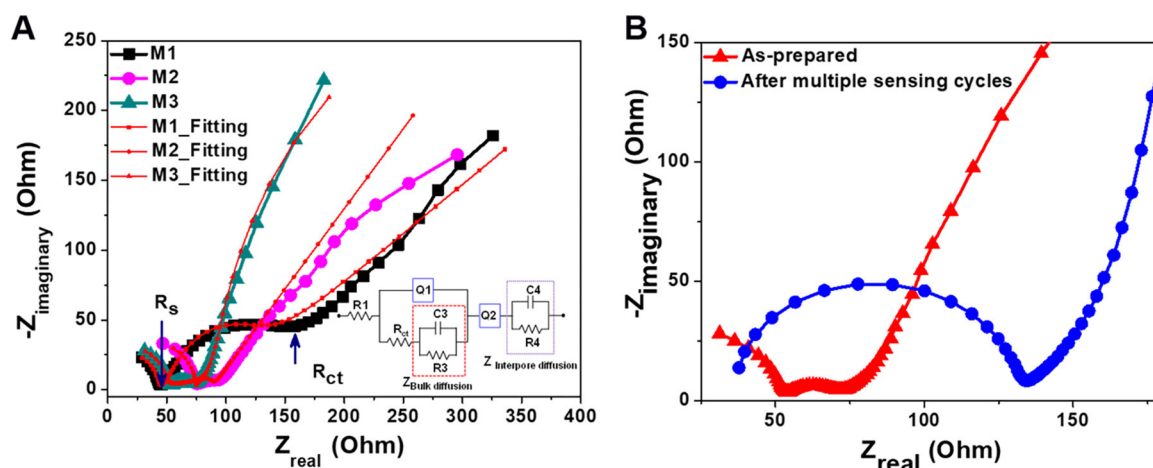


**Figure 4.** (A) Nyquist plots of electrochemical impedance spectra for MnO<sub>x</sub>/ITO electrodes (M1, M2, and M3) in PBS. Each Nyquist plot can be fitted with the same electronic circuit shown in the inset. The value of each component is different for each electrode and is shown in Table S1. The electronic components have their individual significance in the electrochemical process. (B) A comparative study of the Nyquist plot for as-prepared M3 and the same electrode after multiple stripping cycles for arsenic sensing.

Mn<sup>3+</sup> oxidation state of the electrode before electrochemical sensing.<sup>19,39</sup> The splitting energy of 5.5 eV of the same electrode after electrochemical sensing corresponds to the Mn<sub>3</sub>O<sub>4</sub> phase, which is consistent with previous reports.<sup>38,39</sup>

The O 1s spectra (Figure 3E) of the electrode, before and after sensing, showed a broad peak, which was deconvoluted into three peaks. The peak at 528 eV belongs to the Mn–O–Mn binding energy, the peak at 530 eV corresponds to hydroxyl groups attached to manganese (Mn–OH), and the 531 eV peak belongs to water or hydroxyl groups, which were physically adsorbed on the surface of the electrode. After sensing, there is a significant rise in the 530 eV peak compared to the 528 eV peak; this attributes to hydration of surface Mn–O–Mn groups. No peak was observed in the As 3d region of 44–46 eV (As(III)/As(V)) before and after sensing (Figure S9). Thus, there is no considerable amount of arsenic binding to the surface after multiple stripping cycles of As sensing.

To get more profound insights into the phase evolution of the initially deposited material, we have performed Raman spectroscopy measurements on electrode M3, before and after As<sup>3+</sup> sensing along with a bare ITO substrate as a control. The spectra are shown in Figure 3F. Raman spectrum of the as-prepared sample (spectrum b) shows the main characteristic peak at 653 cm<sup>−1</sup>, which corresponds to the symmetric stretching of the Mn–O–Mn bond of MnO<sub>6</sub> octahedron of MnO/Mn<sub>2</sub>O<sub>3</sub>. This is in good agreement with the previous reports.<sup>40</sup> However, after electrochemical arsenic sensing, the same sample exhibits a relatively higher-intensity Raman peak at 646 cm<sup>−1</sup> with a blue shift of the vibrational frequency of the symmetric stretching mode of MnO<sub>6</sub> octahedron. Distortion of the MnO<sub>6</sub> octahedron resulting from the formation of Mn–O–As species during deposition of As<sup>3+</sup> in LSSV cycles leads to a blue shift. Furthermore, the release of manganese along with As<sup>3+</sup> into the electrolyte leads to the appearance of a lower-frequency peak at 357 cm<sup>−1</sup> due to the deformation mode of the Mn–O chain in the MnO<sub>6</sub> octahedron. This results suggests the evolution of the material with a new oxidation state corresponding to Mn<sub>3</sub>O<sub>4</sub>. The release of manganese ions along with As<sup>3+</sup> during multiple stripping cycles is supported by SEM–EDX elemental analysis (Figure S4) and ICP–MS analysis (Figure S5) of the M3 before and after As<sup>3+</sup> stripping.

**3.3. Electrochemical Impedance Spectroscopy Studies on MnO<sub>x</sub> Electrodes.** Electrochemical properties including interfacial charge transport characteristics at the electrode–electrolyte interface largely depend upon the phase and electronic conductivity of the electrode material, while bulk diffusion and inter pore diffusion are influenced by the hierarchical surface morphology of each MnO<sub>x</sub>/ITO electrode. The electrochemical properties at the electrode surface can be viewed as a nonlinear phenomenon, and each phenomenon can be estimated in terms of electronic components (resistor, capacitor, and constant phase element) of a nonlinear electronic circuit. Thus, an impedance spectrum simulated from an alternating current (AC) perturbation applied to a nonlinear electronic circuit can be fitted with the experimental impedance spectrum obtained from EIS measurements of an individual electrode. Electronic properties of as-prepared MnO<sub>x</sub>/ITO electrodes electrodeposited at different potential windows and their influence on the electrochemical properties were analyzed by EIS. An AC signal of 10 mV was applied to the MnO<sub>x</sub>/ITO electrode with respect to the reference electrode, and subsequently, the current was measured between working and counter electrodes. EIS was carried out in PBS electrolyte, and impedance was recorded at each frequency of the AC signal, which was varied from 200 kHz to 100 mHz at 6 dB per decade.

In the complex impedance (Nyquist) plot shown in Figure 4A, the semicircle describes the interfacial electron transport property of the MnO<sub>x</sub>/ITO electrode, while the straight line after the semicircle is known as Warburg impedance. This corresponds to the diffusion of bulk ions to the electrode–electrolyte interface. Each semicircle of the electrode consists of two intercepts; the first intercept is related to the equivalent series resistance (R<sub>s</sub>) between MnO<sub>x</sub> and current collector (here ITO), while the second intercept is associated with the charge transfer resistance (R<sub>ct</sub>) from the electrolyte to the MnO<sub>x</sub> electrode through the Faradaic redox reaction. The R<sub>s</sub> and R<sub>ct</sub> for electrode M1 are indicated in Figure 4A. Summary of these two resistances of all of the samples and EIS spectra recorded for the bare ITO glass substrate are presented in Table 1 and Figure S10, respectively. The inset in Figure 4A is the corresponding electronic circuit for the Nyquist plot. Parallel combinations of both C3–R3 and C4–R4 are



**Table 1. Summary of Equivalent Series Resistance ( $R_s$ ) and Charge Transfer Resistance ( $R_{ct}$ ) of Different  $\text{MnO}_x/\text{ITO}$  Electrodes Obtained from EIS Measurements**

electrodeposition voltage window	equivalent series resistance ( $R_s$ ) ( $\text{MnO}_x$ to ITO) ( $\Omega$ )	charge transfer resistance ( $R_{ct}$ ) (electrolyte to $\text{MnO}_x$ ) ( $\Omega$ )
M1 (0.8–1.3 V)	44	115
M2 (−0.2–0.9 V)	74	23
M3 (−1–1.3 V)	53	23

impedances that are related to diffusion of ions from the bulk electrolyte into the hierarchical rough surface of the as-prepared electrode. Q1 and Q2 are called constant phase elements, which are associated with the double-layer capacitance formed in the inter-/intraparticle rough surface of the electrode. The values of these components for electrodes M1, M2, and M3 are given in Table S1. From the Nyquist plot (Figure 4A) and Table S1, we observe that both bulk diffusion and interparticle diffusion on the surface of M1, M2, and M3 are almost similar. Therefore, the differences in the surface morphologies of electrodes do not affect the ion diffusion toward the electrode surface. However, a significant change in  $R_{ct}$  ( $\sim 23 \Omega$ ) is observed at the electrode–electrolyte interface of M3 compared to M1 and M2. Electrode M1 exhibited the highest  $R_{ct}$  among all three electrodes and has poor response to arsenic sensing although it showed lowest  $R_s$ . Thus, redox reactions occur faster on the M3 electrode surface during stripping voltammetry (Figure 5B). On the other hand, electrode M2 showed almost the same  $R_{ct}$  as compared to electrode M3, but its high  $R_s$  hinders the arsenic sensing

response for higher arsenic concentrations. However, the  $R_s$  of M2 is highest compared to the other electrodes. Here, we would like to mention that  $R_s$  is the combination of both solution (or electrolyte) resistance and material's internal resistance. Since we have used the same electrolyte (PBS) during EIS measurements, any change in  $R_s$  is because of the change in electronic conductivity of the electrode material. For electrochemical sensor applications, the electrode must have low series and charge transfer resistances. Since electrode M3 has lower internal resistance and it promotes better charge transfer compared to the other electrodes, this electrode is the best choice for sensing applications. The interfacial charge transfer property is a crucial factor for an electrochemical sensor as it directly influences the arsenite sensing response by the electrodes. Electrode M3 is a better choice in terms of this property too.

EIS of M3 before and after  $\text{As}^{3+}$  sensing was also studied, and the corresponding results are shown in Figure 4B. After multiple stripping cycles for  $\text{As}^{3+}$  sensing, the internal resistance of M3 is lowered; however, there was an increase in the interfacial charge transfer resistance at the electrode–electrolyte interface. The decrease in the internal resistance of electrode may be attributed to the phase evolution of the crystalline  $\text{Mn}_3\text{O}_4$  phase with unidirectional lattice orientation (Figure 2D) after  $\text{As}^{3+}$  sensing. Since manganese is released into the electrolyte with  $\text{As}^{3+}$  stripping, the effective electrochemical surface area of M3 is reduced, and as a result, an increase in charge transfer resistance is observed.

### 3.4. Electrochemical Analysis for Arsenite ( $\text{As}^{3+}$ ) Sensing Using Optimized Electrode M3 and Determination of Detection Limit

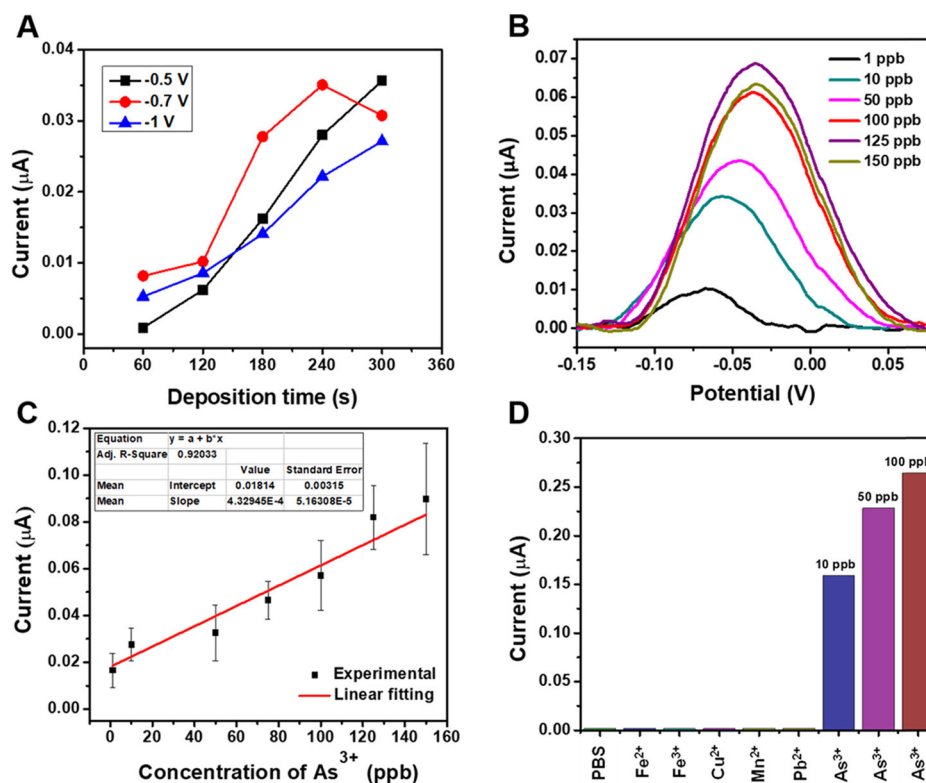


**Figure 5.** Electrochemical arsenite sensing by M3 in PBS: (A) optimization of deposition potential and time for  $\text{As}^{3+}$  sensing. (B) LSSV response for various concentrations (1–150 ppb) of  $\text{As}^{3+}$ . (C) Linearity analysis of chronoamperometric current for different concentrations of  $\text{As}^{3+}$ . Error bars represent interelectrode variability. (D) Interfering ions study with different metal ions (100 ppb  $\text{Fe}^{2+}$ ,  $\text{Fe}^{3+}$ ,  $\text{Cu}^{2+}$ ,  $\text{Mn}^{2+}$ , and  $\text{Pb}^{2+}$  added sequentially) and the response of arsenic in the presence of all of the metal ions using M3.

**nation of Limit of Detection (LOD) through Linear Response to  $\text{As}^{3+}$  by the Electrode.** To obtain the best performance for detection of trace amount of  $\text{As}^{3+}$  in water with our  $\text{MnO}_x/\text{ITO}$  electrode, crucial experimental parameters like deposition potential (DP) and deposition time (DT) were optimized. PBS was used as the electrolyte during all of the LSSV measurements. For optimization, we varied DT from 60 to 300 s at a constant DP and concentration of arsenic. Subsequently, the stripping current peak was monitored. This was repeated for three DPs of  $-0.5$ ,  $-0.7$ , and  $-1$  V at 10 ppb  $\text{As}^{3+}$ . Figure 5A shows the peak current as a function of DT. It is observed that the stripping current at each DT is higher for  $-0.7$  V compared to other DPs and that it reaches a maximum at 240 s. Thus, the parameters of  $-0.7$  V and 180 s were selected as DP and DT, respectively, for stripping voltammetry. For arsenite sensing, the stripping current was recorded at these optimized parameters during the anodic potential sweep with different concentrations of  $\text{As}^{3+}$ . Arsenite concentration as low as 1 ppb was experimentally detected by LSSV using electrodes prepared at all of the three voltage windows of deposition (M1, M2, and M3). However, the current intensity of the  $\text{As}^{3+}$  peak is different for each of the three electrodes. The electrode M3 exhibited the best  $\text{As}^{3+}$  sensing behavior with linear concentration-dependent response over the concentration range of 1–150 ppb. Figure 5B illustrates the LSSV signal of electrode M3 for various concentrations of  $\text{As}^{3+}$  in PBS. However, Figure S11A,B show the LSSV signal for  $\text{As}^{3+}$  by electrodes M1 and M2, respectively.

The electrochemical analysis revealed that the electrode M3 has a higher electrochemical activity toward  $\text{As}^{3+}$ . The limit of detection (LOD) obtained experimentally using our  $\text{MnO}_x$  electrode was 1 ppb. Researchers have reported theoretical LODs of 0.825 ppb using  $\text{CoO}_x$  on a glassy carbon electrode in PBS of pH 7,<sup>41</sup> 0.1 ppb using a rGO/ $\text{MnO}_2$  nanohybrid on glassy carbon electrodes in acetate buffer of pH 5,<sup>13</sup> etc. However, one interesting aspect of our experiment is that we have carried out electrochemical analysis through LSSV at slightly basic pH ( $\sim 7.4$ ), which leads to the practical viability in field water analysis. Furthermore, arsenic dissolution in a basic pH electrolyte does not generate toxic arsine gas, which is produced when arsenic is dissolved in an acidic medium.

The saturation concentration of  $\text{As}^{3+}$  is different for the three different electrodes (M1, M2, and M3). As shown in Figure 5B, the response of M3 was saturated at  $\sim 125$ –150 ppb, while M1 (Figure S10A) and M2 (Figure S10B) were saturated at  $\sim 100$ –110 and  $\sim 60$ –70 ppb  $\text{As}^{3+}$ , respectively. The linear response of M3 is shown in Figure 5C. The data is recorded with three different M3 electrodes. Error bars represent interelectrode variability. The stripping current varied linearly with the concentration of  $\text{As}^{3+}$  over the range of 1–150 ppb. The eventual decrease in sensitivity observed after multiple stripping cycles may be explained by the change in electronic properties (wherein the active material converts into  $\text{Mn}_3\text{O}_4$  from as-prepared  $\text{MnO}/\text{Mn}_2\text{O}_3$ ) as reported in EIS studies. The current response is fitted with the linear regression equation of  $y = 0.0004x + 0.018$  (where  $y$  is the sensor response current and  $x$  is the  $\text{As}^{3+}$  concentration), and the regression correlation coefficient was 0.92. The theoretical LOD was 0.012 ppb, and the calculation is given in formulas 1 and 2 of SI.

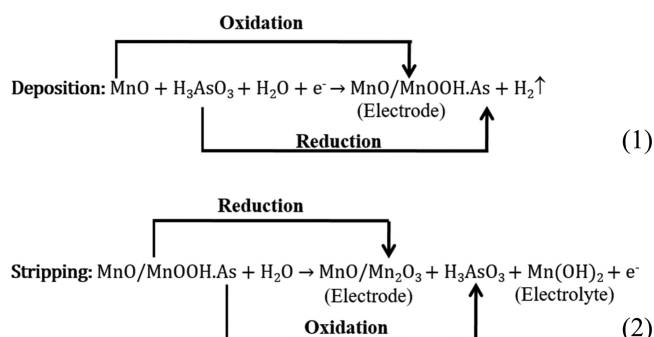
The electrodes M1, M2, and M3 showed different sensing behaviors for various  $\text{As}^{3+}$  concentrations (data for M1 and M2 are shown in Figure S11A,B, respectively). Different sensing

results by the three electrodes are influenced by their individual material properties such as morphology, phase, and interfacial charge transfer.

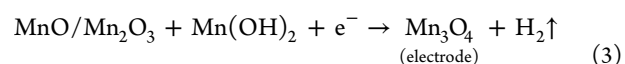
A control experiment was performed to check the impact of the optimized parameters on the electrochemical performance of the bare ITO electrode. For this, cyclic voltammetry was performed on the bare ITO electrode using a redox molecule before and after performing stripping voltammetry (at optimized parameters in PBS). CV measurements confirmed that there is no significant change in redox peaks even after application of  $-0.7$  V for 180 s for ten LSSV cycles. These experimental results support the electrochemical stability of ITO and absence of electrochemical hindrance at the electrode–electrolyte interface. The corresponding cyclic voltammogram is given in Figure S12.

Interference study with different metal ions (shown in Figure 5D) using electrode M3 was performed in PBS. The concentration of all of the metal ions ( $\text{Fe}^{2+}$ ,  $\text{Fe}^{3+}$ ,  $\text{Cu}^{2+}$ ,  $\text{Mn}^{2+}$ , and  $\text{Pb}^{2+}$ ) was maintained at 100 ppb during the study. Later, three arsenic concentrations (10, 50, and 100 ppb) were analyzed in the presence of these metals. The metal ions were added sequentially, as represented in Figure 5D. Stripping voltammetry was performed for all metal ions keeping the deposition potential constant at  $-0.7$  V, and stripping of the ions was performed within the fixed potential window ( $-0.40$ – $-0.20$  V). The peak potential and current were monitored for each ion. Electrode M3 was inert toward both  $\text{Fe}^{2+}$  and  $\text{Fe}^{3+}$  ions, and an absence of peak current was seen. A peak current was registered with  $\text{Cu}^{2+}$ ,  $\text{Mn}^{2+}$ , and  $\text{Pb}^{2+}$  at the oxidation potential value of  $-0.17$  V for  $\text{Cu}^{2+}$  and  $\text{Mn}^{2+}$  and  $-0.18$  V for  $\text{Pb}^{2+}$ . Moreover, the current intensity of the  $\text{Mn}^{2+}$  peak was higher as compared to that of  $\text{Cu}^{2+}$  at the same potential. There is no interference of metal ions at the oxidation potential of  $\text{As}^{3+}$  and hence electrode M3 is highly selective for  $\text{As}^{3+}$  detection. Enhancement of the oxidation current of  $\text{As}^{3+}$  was observed with a sequential increase of  $\text{As}^{3+}$  concentration in the presence of all metal ions.

The probable mechanism for phase evaluation of the active material during sensing may be explained by the following chemical reactions.



Phase evolution:



Electrochemical sensing of arsenic by the as-prepared electrode and subsequent phase evolution of the parent material after sensing involve various reaction steps. In the deposition step of LSSV (eq 1), electrodeposited  $\text{MnO}_x$  gets oxidized ( $\text{Mn}^{2+}$  to  $\text{Mn}^{3+}$ ) and  $\text{As}^{3+}$  from the electrolyte is reduced to  $\text{As}^0$  on the electrode. The Mn–O–As complex thus formed may exist as

MnOOH-As species on the parent MnO<sub>x</sub> electrode. During the subsequent stripping step, As<sup>0</sup> is stripped out from the electrode in an oxidized form (As<sup>3+</sup>) into the electrolyte. Concomitantly, some manganese ions are also released into the electrolyte (as proved from ICP-MS data, Figure S5B) in the form of Mn(OH)<sub>2</sub> along with As<sup>3+</sup>. This leads to the evolution of a new phase (Mn<sub>2</sub>O<sub>3</sub>) on the parent MnO<sub>x</sub> material. The phase evolution occurs gradually over successive LSSV cycles. Some of the manganese ions in the electrolyte (Mn(OH)<sub>2</sub>) get redeposited on the electrode surface during subsequent LSSV cycles, eventually leading to the formation of Mn<sub>3</sub>O<sub>4</sub>. This is supported by both XPS and Raman spectroscopy.

## 4. CONCLUSIONS

This study established a simple, fast, efficient, and non-enzymatic electrochemical technique for As<sup>3+</sup> detection. The cyclic-voltammetry-based electrodeposition method is demonstrated for MnO<sub>x</sub>/ITO electrode preparation and its application in the detection of trace amount of arsenite (~1 ppb) in an aqueous electrolyte via linear sweep stripping voltammetry. Detailed characterization of MnO<sub>x</sub> samples before and after LSSV confirmed the evolution of a new phase along with the appearance of new morphology of the active material. In situ growth of the new phase on the electrode was observed during stripping voltammetry. The experimental limit of detection (LOD) of 1 ppb obtained by the MnO<sub>x</sub>/ITO electrode is well below the guideline value for As(III) in drinking water (10 ppb) as specified by the World Health Organization (WHO). The advantages of this electrode are its suitability for As<sup>3+</sup> sensing with significant sensitivity, selectivity, low LOD, reproducibility, and importantly low cost. Moreover, the electrode is capable of interference-free As<sup>3+</sup> detection in alkaline medium.

## ■ ASSOCIATED CONTENT

### Supporting Information

The Supporting Information is available free of charge on the ACS Publications website at DOI: 10.1021/acsami.9b06023.

Values of each component of the electronic circuit used to fit Nyquist plots of EIS for M1, M2, and M3 electrodes; Pourbaix diagram (Eh–pH) of various forms of manganese oxide and hydroxide; characterization of electrodes M1 and M2 including FESEM, EDX, TEM, and XRD; ICP-MS data for change in As and Mn ion concentrations in the electrolyte for M3; Nyquist plot of bare ITO; response of As<sup>3+</sup> using electrodes M1 and M2; CV of bare ITO at optimized parameters; and calculation of LOD (PDF)

## ■ AUTHOR INFORMATION

### Corresponding Authors

\*E-mail: [tijuthomas@iitm.ac.in](mailto:tijuthomas@iitm.ac.in) (T.T.).

\*E-mail: [pradeep@iitm.ac.in](mailto:pradeep@iitm.ac.in) (T.P.).

### ORCID

Sourav Kanti Jana: 0000-0001-5772-7022

Pillalamarri Srikrishnarka: 0000-0001-5187-6879

Thalappil Pradeep: 0000-0003-3174-534X

### Author Contributions

<sup>§</sup>T.G. and S.K.J. contributed equally.

### Notes

The authors declare no competing financial interest.

## ■ ACKNOWLEDGMENTS

The authors thank the Department of Science and Technology, Government of India, for supporting our research program. T.G., S.K.J., P.S., S.M., T.A., and C.S. thank IIT Madras for their fellowships. J.S.M. thanks the CSIR for research fellowship. The authors thank the Centre for Nano and Soft Matter Sciences (CeNS) for their FESEM facility.

## ■ REFERENCES

- (1) Ravenscroft, P. *Predicting the Global Extent of Arsenic Pollution of Groundwater and Its Potential Impact on Human Health*; UNICEF: New York, 2007.
- (2) Gómez-Ariza, J. L.; Sánchez-Rodas, D.; Giraldez, I.; Morales, E. A Comparison between ICP-MS and AFS Detection for Arsenic Speciation in Environmental Samples. *Talanta* **2000**, *51*, 257–268.
- (3) WHO. *Guidelines for Drinking-Water Quality*; WHO, 2011; pp 315–318.
- (4) USEPA. *Technical Factsheet: Final Rule for Arsenic in Drinking Water*; USEPA, 2001; pp 1–6.
- (5) International Agency for Research on Cancer (IARC). Arsenic and Arsenic Compounds Monograph. *IARC Monogr. Eval. Carcinog. Risks Hum.* **2012**, *100C*, 41–93.
- (6) Bibi, S.; Kamran, M. A.; Sultana, J.; Farooqi, A. Occurrence and Methods to Remove Arsenic and Fluoride Contamination in Water. *Environ. Chem. Lett.* **2017**, *15*, 125–149.
- (7) Masscheleyn, P. H.; Delaune, R. D.; Patrick, W. H. Effect of Redox Potential and PH on Arsenic Speciation and Solubility in a Contaminated Soil. *Environ. Sci. Technol.* **1991**, *25*, 1414–1419.
- (8) Fish, R. H.; Brinckman, F. E.; Jewett, K. L. Fingerprinting Inorganic Arsenic and Organoarsenic Compounds in Situ Oil Shale Retort and Process Waters Using a Liquid Chromatograph Coupled with an Atomic Absorption Spectrometer as a Detector. *Environ. Sci. Technol.* **1982**, *16*, 174–179.
- (9) Luong, J. H. T.; Majid, E.; Male, K. B. Analytical Tools for Monitoring Arsenic in the Environment. *Open Anal. Chem. J.* **2007**, *1*, 7–14.
- (10) Male, K. B.; Hrapovic, S.; Santini, J. M.; Luong, J. H. T. Biosensor for Arsenite Using Arsenite Oxidase and Multiwalled Carbon Nanotube Modified Electrodes. *Anal. Chem.* **2007**, *79*, 7831–7837.
- (11) Fuku, X.; Iftikar, F.; Hess, E.; Iwuoha, E.; Baker, P. Cytochrome c Biosensor for Determination of Trace Levels of Cyanide and Arsenic Compounds. *Anal. Chim. Acta* **2012**, *730*, 49–59.
- (12) Merulla, D.; Buffi, N.; Beggah, S.; Truffer, F.; Geiser, M.; Renaud, P.; Van der Meer, J. R. Bioreporters and Biosensors for Arsenic Detection. *Biotechnological Solutions for a World-Wide Pollution Problem. Curr. Opin. Biotechnol.* **2013**, *24*, 534–541.
- (13) Devi, P.; Bansod, B.; Kaur, M.; Bagchi, S.; Nayak, M. K. Co-Electrodeposited RGO/MnO<sub>2</sub> Nanohybrid for Arsenite Detection in Water by Stripping Voltammetry. *Sens. Actuators B Chem* **2016**, *237*, 652–659.
- (14) Jiang, T. J.; Guo, Z.; Liu, J. H.; Huang, X. J. Gold Electrode Modified with Ultrathin SnO<sub>2</sub> Nanosheets with High Reactive Exposed Surface for Electrochemical Sensing of As(III). *Electrochim. Acta* **2016**, *191*, 142–148.
- (15) Yang, M.; Chen, X.; Jiang, T. J.; Guo, Z.; Liu, J. H.; Huang, X. J. Electrochemical Detection of Trace Arsenic(III) by Nanocomposite of Nanorod-Like α-MnO<sub>2</sub> Decorated with ~5 Nm Au Nanoparticles: Considering the Change of Arsenic Speciation. *Anal. Chem.* **2016**, *88*, 9720–9728.
- (16) Ivandini, T. A.; Sato, R.; Makide, Y.; Fujishima, A.; Einaga, Y. Electrochemical Detection of Arsenic(III) Using Iridium-Implanted Boron-Doped Diamond Electrodes. *Anal. Chem.* **2006**, *78*, 6291–6298.
- (17) March, G.; Nguyen, T. D.; Piro, B. Modified Electrodes Used for Electrochemical Detection of Metal Ions in Environmental Analysis. *Biosensors* **2015**, *5*, 241–275.



- (18) Bhanjana, G.; Dilbaghi, N.; Chaudhary, S.; Kim, K. H.; Kumar, S. Robust and Direct Electrochemical Sensing of Arsenic Using Zirconia Nanocubes. *Analyst* **2016**, *141*, 4211–4218.
- (19) Saha, B.; Jana, S. K.; Majumder, S.; Satpati, B.; Banerjee, S. Selective Growth of Co-Electrodeposited Mn<sub>2</sub>O<sub>3</sub>-Au Spherical Composite Network Towards Enhanced Non-Enzymatic Hydrogen Peroxide Sensing. *Electrochim. Acta* **2015**, *174*, 853–863.
- (20) Panagiotopoulos, A.; Gkouma, A.; Vassi, A.; Johnson, C. J.; Cass, A. E. G.; Topoglidis, E. Hemin Modified SnO<sub>2</sub> Films on ITO-PET with Enhanced Activity for Electrochemical Sensing. *Electroanalysis* **2018**, *30*, 1956–1964.
- (21) Xiao, L.; Wildgoose, G. G.; Compton, R. G. Sensitive Electrochemical Detection of Arsenic (III) Using Gold Nanoparticle Modified Carbon Nanotubes via Anodic Stripping Voltammetry. *Anal. Chim. Acta* **2008**, *620*, 44–49.
- (22) Aghazadeh, M.; Maragheh, M. G.; Ganjali, M. R.; Norouzi, P.; Faridbod, F. Electrochemical Preparation of MnO<sub>2</sub> Nanobelts through Pulse Base-Electrogeneration and Evaluation of Their Electrochemical Performance. *Appl. Surf. Sci.* **2016**, *364*, 141–147.
- (23) Zhang, K.; Han, X.; Hu, Z.; Zhang, X.; Tao, Z.; Chen, J. Nanostructured Mn-Based Oxides for Electrochemical Energy Storage and Conversion. *Chem. Soc. Rev.* **2015**, *44*, 699–728.
- (24) Schacht, L.; Ginder-Vogel, M. Arsenite Depletion by Manganese Oxides: A Case Study on the Limitations of Observed First Order Rate Constants. *Soil Syst.* **2018**, *2*, 39.
- (25) Zhang, G. S.; Qu, J. H.; Liu, H. J.; Liu, R. P.; Li, G. T. Removal Mechanism of As(III) by a Novel Fe-Mn Binary Oxide Adsorbent: Oxidation and Sorption. *Environ. Sci. Technol.* **2007**, *41*, 4613–4619.
- (26) Maliyekkal, S. M.; Philip, L.; Pradeep, T. As(III) Removal from Drinking Water Using Manganese Oxide-Coated-Alumina: Performance Evaluation and Mechanistic Details of Surface Binding. *Chem. Eng. J.* **2009**, *153*, 101–107.
- (27) Dalvi, A. A.; Ajith, N.; Swain, K. K.; Verma, R. Sorption of Arsenic on Manganese Dioxide Synthesized by Solid State Reaction. *J. Environ. Sci. Health, Part A: Toxic/Hazard. Subst. Environ. Eng.* **2015**, *50*, 866–873.
- (28) McKenzie, R. M. The Synthesis of Birnessite, Cryptomelane, and Some Other Oxides and Hydroxides of Manganese. *Mineral. Mag.* **1971**, *38*, 493–502.
- (29) Zhou, S.; Han, X.; Fan, H.; Liu, Y. Electrochemical Sensing toward Trace As(III) Based on Mesoporous MnFe<sub>2</sub>O<sub>4</sub>/Au Hybrid Nanospheres Modified Glass Carbon Electrode. *Sensors* **2016**, *16*, No. 935.
- (30) Wu, S.; Zhao, Q.; Zhou, L.; Zhang, Z. Stripping Analysis of Trace Arsenic Based on the MnOx/ AuNPs Composite Film Modified Electrode in Alkaline Media. *Electroanalysis* **2014**, *26*, 1840–1849.
- (31) Bu, L.; Gu, T.; Ma, Y.; Chen, C.; Tan, Y.; Xie, Q.; Yao, S. Enhanced Cathodic Preconcentration of As(0) at Au and Pt Electrodes for Anodic Stripping Voltammetry Analysis of As(III) and As(V). *J. Phys. Chem. C* **2015**, *119*, 11400–11409.
- (32) Salimi, A.; Hyde, M. E.; Banks, C. E.; Compton, R. G. Boron Doped Diamond Electrode Modified with Iridium Oxide for Amperometric Detection of Ultra Trace Amounts of Arsenic(III). *Analyst* **2004**, *129*, 9–14.
- (33) Granqvist, C. G.; Hult aker, A. Transparent and Conducting ITO Films: New Developments and Applications. *Thin Solid Films* **2002**, *411*, 1–5.
- (34) Freitas, R. M.; Perilli, T. A. G.; Ladeira, A. C. Q. Oxidative Precipitation of Manganese from Acid Mine Drainage by Potassium Permanganate. *J. Chem.* **2013**, *2013*, 1–8.
- (35) Song, X. C.; Zhao, Y.; Zheng, Y. F. Synthesis of MnO<sub>2</sub> Nanostructures with Sea Urchin Shapes by a Sodium Dodecyl Sulfate-Assisted Hydrothermal Process. *Cryst. Growth Des.* **2007**, *7*, 159–162.
- (36) Song, R.; Feng, S.; Wang, H.; Hou, C. Effect of Organic Solvents on Particle Size of Mn<sub>3</sub>O<sub>4</sub> Nanoparticles Synthesized by a Solvothermal Method. *J. Solid State Chem.* **2013**, *202*, 57–60.
- (37) Kar, P.; Sardar, S.; Ghosh, S.; Parida, M. R.; Liu, B.; Mohammed, O. F.; Lemmens, P.; Pal, S. K. Nano Surface Engineering of Mn<sub>2</sub>O<sub>3</sub> for Potential Light-Harvesting Application. *J. Mater. Chem. C* **2015**, *3*, 8200–8211.
- (38) Lee, J. W.; Hall, A. S.; Kim, J. D.; Mallouk, T. E. A Facile and Template-Free Hydrothermal Synthesis of Mn<sub>3</sub>O<sub>4</sub> Nanorods on Graphene Sheets for Supercapacitor Electrodes with Long Cycle Stability. *Chem. Mater.* **2012**, *24*, 1158–1164.
- (39) Wu, T. H.; Hesp, D.; Dhanak, V.; Collins, C.; Braga, F.; Hardwick, L. J.; Hu, C. C. Charge Storage Mechanism of Activated Manganese Oxide Composites for Pseudocapacitors. *J. Mater. Chem. A* **2015**, *3*, 12786–12795.
- (40) Julien, C. M.; Massot, M.; Poinson, C. Lattice Vibrations of Manganese Oxides: Part I. Periodic Structures. *Spectrochim. Acta, Part A* **2004**, *60*, 689–700.
- (41) Salimi, A.; Mamkhezri, H.; Hallaj, R.; Soltanian, S. Electrochemical Detection of Trace Amount of Arsenic(III) at Glassy Carbon Electrode Modified with Cobalt Oxide Nanoparticles. *Sens. Actuators B Chem* **2008**, *129*, 246–254.



## Supporting Information

# Highly-Sensitive As<sup>3+</sup> Detection Using Electrodeposited Nanostructured MnO<sub>x</sub> and Phase Evolution of the Active Material During Sensing

*Tanvi Gupte<sup>a,b,‡</sup>, Sourav Kanti Jana<sup>a,‡</sup>, Jyoti Sarita Mohanty<sup>a</sup>, Pillalamarri*

*Srikrishnarka<sup>a</sup>, Sritama Mukherjee<sup>a</sup>, Tripti Ahuja<sup>a</sup>, Chennu Sudhakar<sup>a</sup>, Tiju Thomas<sup>b,\*</sup>,*

*Thalappil Pradeep<sup>a,\*</sup>*

<sup>a</sup>DST Unit of Nanoscience (DST UNS) and Thematic Unit of Excellence, Department  
of Chemistry, Indian Institute of Technology Madras

<sup>b</sup>Department of Metallurgical and Materials Engineering, Indian Institute of  
Technology Madras

\* Corresponding authors: pradeep@iitm.ac.in (Prof. T. Pradeep),  
tijuthomas@iitm.ac.in (Dr. Tiju Thomas)

‡These authors contributed equally.

## TABLE OF CONTENTS

Figure/ Table No.	Title	Page No.
<b>Table S1</b>	Values of each component of the electronic circuit used to fit Nyquist plots of EIS for <b>M1</b> , <b>M2</b> , and <b>M3</b> electrodes	S3
<b>Figure S1</b>	Pourbaix (Eh-pH) diagram showing the predominant forms of manganese oxide and hydroxide	S4
<b>Figure S2</b>	FESEM micrographs of <b>M1</b> electrode	S5
<b>Figure S3</b>	FESEM micrographs of <b>M2</b> electrode	S6
<b>Figure S4:</b>	EDX spectra of <b>M3</b> electrode before (A) and after (B) $\text{As}^{3+}$ sensing	S7
<b>Figure S5</b>	ICP-MS data for change in the arsenic and manganese ion concentrations before and after $\text{As}^{3+}$ sensing of <b>M3</b> electrode	S8
<b>Figure S6</b>	TEM micrographs of <b>M1</b> electrode	S9
<b>Figure S7</b>	TEM micrographs of <b>M2</b> electrode	S10
<b>Figure S8</b>	XRD analysis of ITO glass substrate and control experiment on <b>M3</b> electrode	S11
<b>Figure S9</b>	XPS spectra of As 3d region	S12
<b>Figure S10</b>	Nyquist plot of bare ITO glass substrate	S13
<b>Figure S11</b>	Electrochemical arsenite sensing response by <b>M1</b> and <b>M2</b> electrodes	S14
<b>Figure S12</b>	CV of bare ITO at optimized parameters	S15
	Calculation of LOD	S16
<b>References</b>		S17



**Table S1.** Values of each component of the electronic circuit used to fit Nyquist plots of electrochemical impedance spectra (EIS) for **M1**, **M2**, and **M3** MnO<sub>x</sub>/ITO electrodes. R<sub>1</sub> is the internal resistance of the material, which directly influences the contact resistance between ITO and the electrodeposited material. R<sub>ct</sub> is the charge transfer resistance at the electrode-electrolyte interface. Parallel combinations of both, C3-R3 and C4-R4 are related to diffusion of ions from the bulk electrolyte into porous network of the as-prepared electrode. Q1 and Q2 are called constant phase elements which are associated with the double layer capacitance formed in inter/intra particular porous structure.

	<b>M1</b>	<b>M2</b>	<b>M3</b>
<b>R<sub>s</sub></b>	47.2 Ω	72.5 Ω	58.2 Ω
<b>Q1</b>	9*10 <sup>-3</sup> F.s <sup>(a-1)</sup>	0.2*10 <sup>-3</sup> F.s <sup>(a-1)</sup>	2*10 <sup>-3</sup> F.s <sup>(a-1)</sup>
<b>R<sub>ct</sub></b>	121	26.3 Ω	21.8
<b>C3</b>	31.7 *10 <sup>-6</sup> F	40.4 *10 <sup>-6</sup> F	6.57 *10 <sup>-6</sup> F
<b>R3</b>	1.12 KΩ	115.8 Ω	558.4 Ω
<b>C4</b>	1.9 *10 <sup>-9</sup> F	1.7 *10 <sup>-9</sup> F	2.5*10 <sup>-9</sup> F
<b>R4</b>	54.07 Ω	66.3 Ω	119 Ω
<b>Q2</b>	1.4*10 <sup>-2</sup> F.s <sup>(a-1)</sup>	0.2*10 <sup>-3</sup> F.s <sup>(a-1)</sup>	1.3 *10 <sup>-2</sup> F.s <sup>(a-1)</sup>

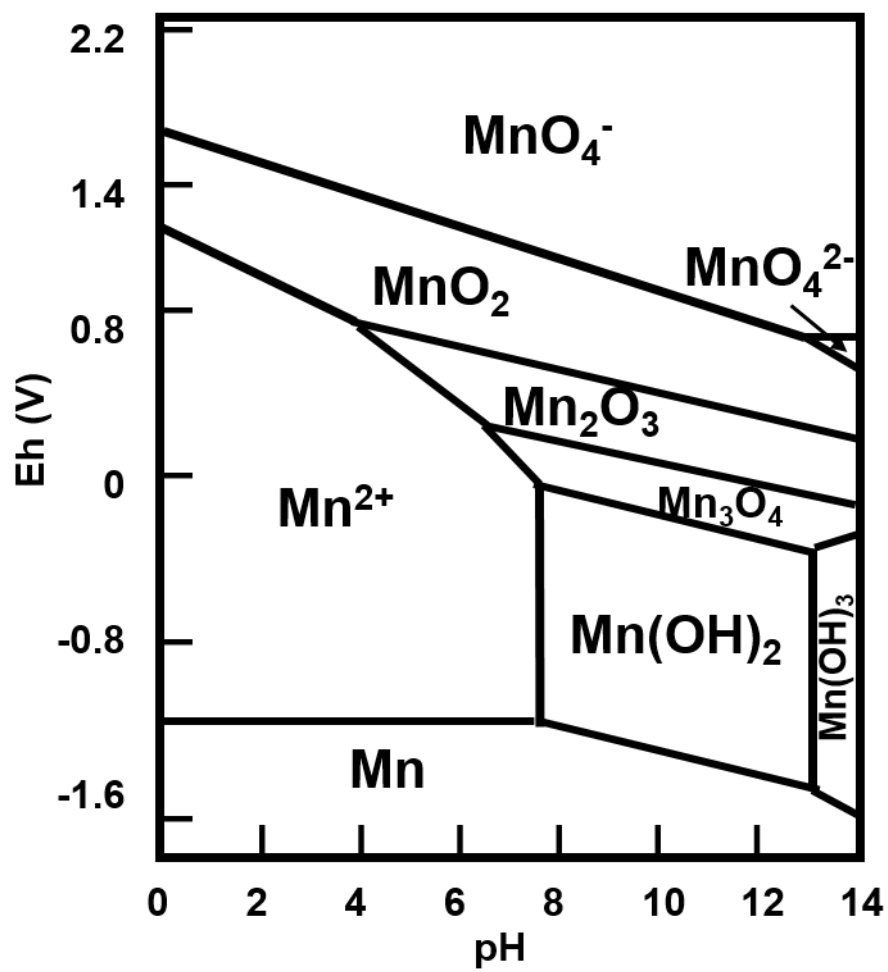


**Figure S1.** Pourbaix (Eh-pH) diagram showing the predominant forms of manganese oxide and hydroxide at  $25^\circ\text{C} \pm 0.5$ .<sup>1</sup>

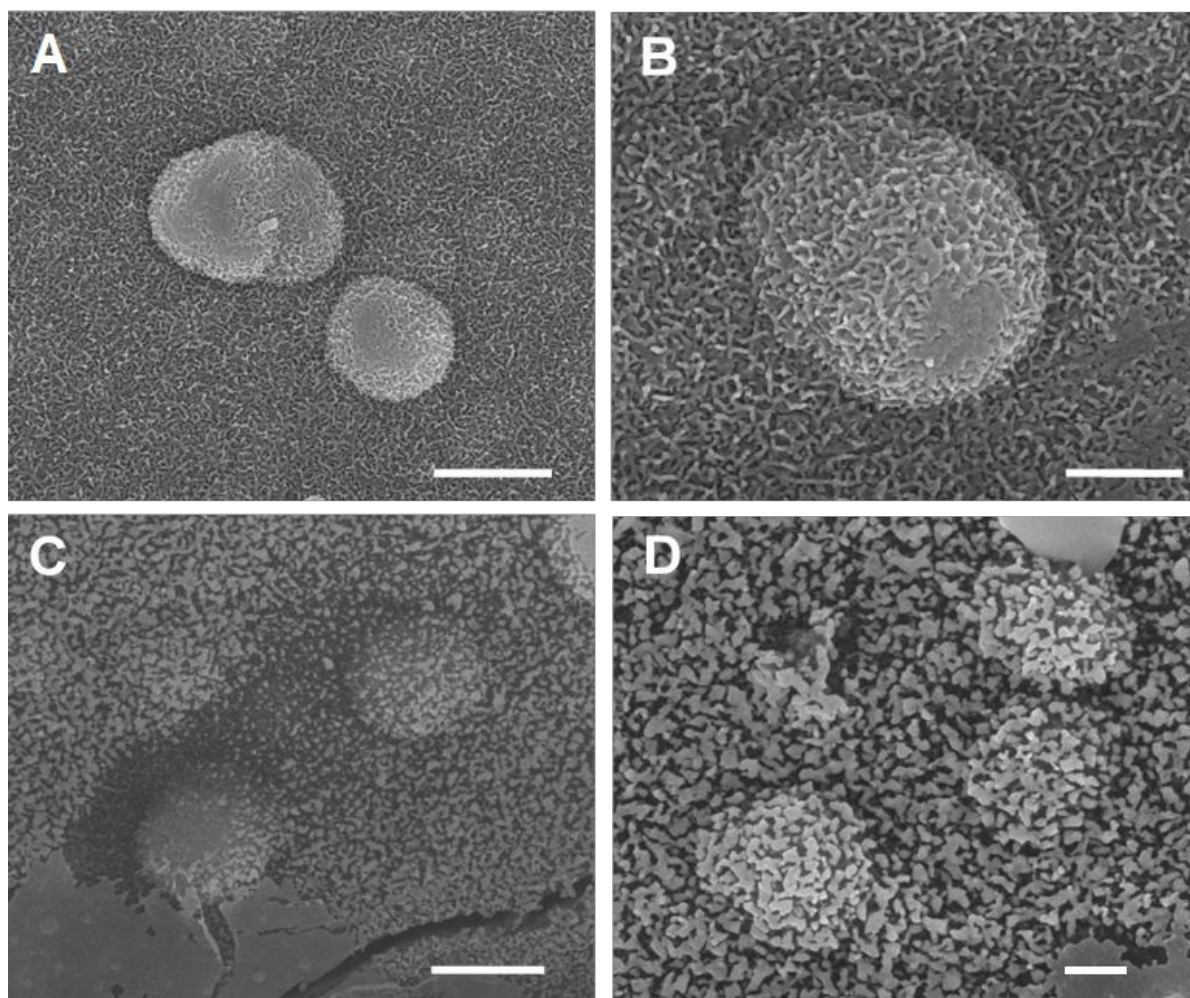


**Figure S2.** FESEM micrographs of (A and B) as-prepared **M1** MnO<sub>x</sub>/ITO electrode and (C and D) after As<sup>3+</sup> sensing. The scale bars are 1  $\mu$ m for A and C, and 500 nm for B and D.

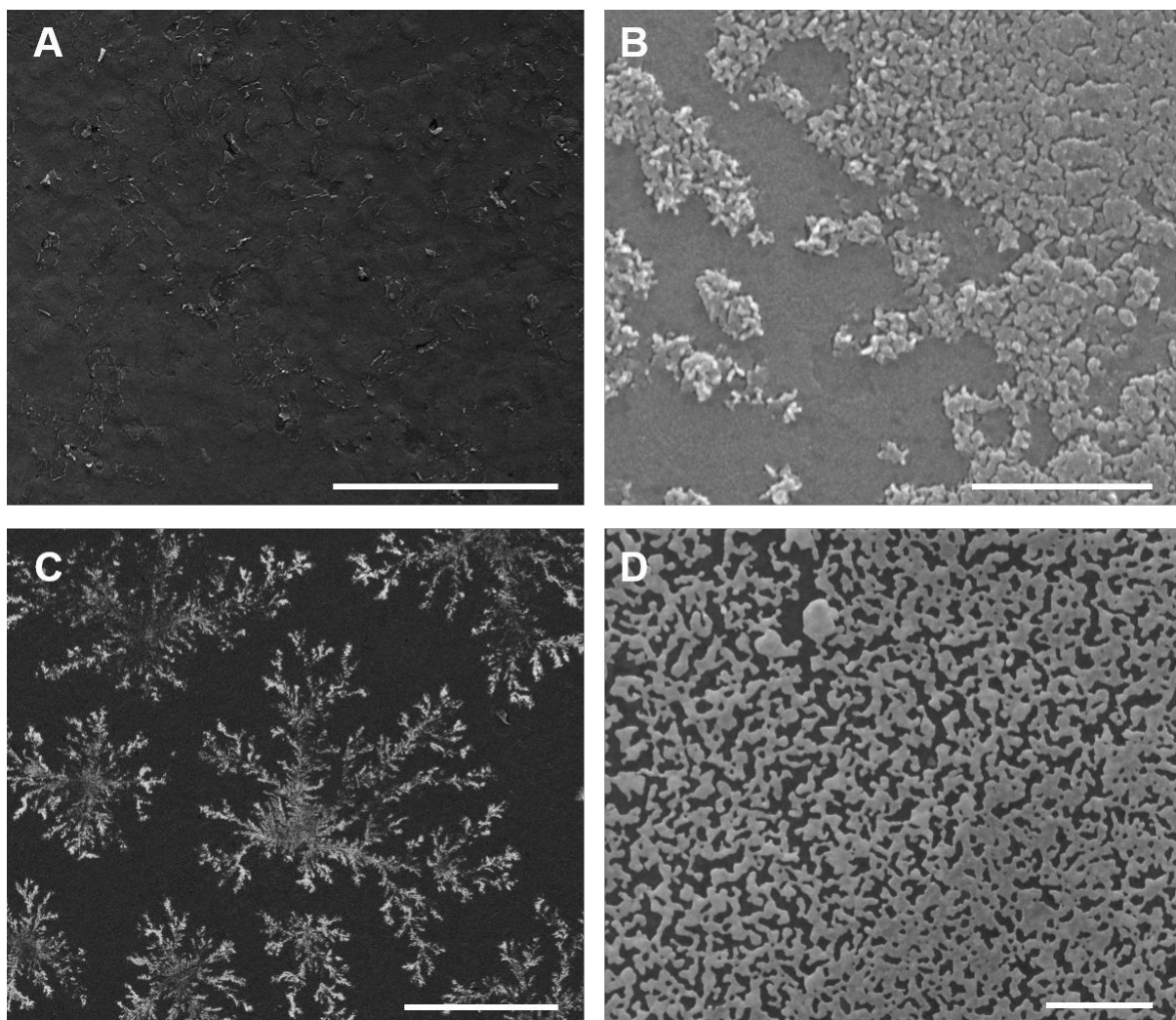


**Figure S3.** FESEM micrographs of (A and B) as-prepared **M2** MnO<sub>x</sub>/ITO electrode and (C and D) after As<sup>3+</sup> sensing. The scale bars are 100 μm for A and C, and 1 μm for B and D.



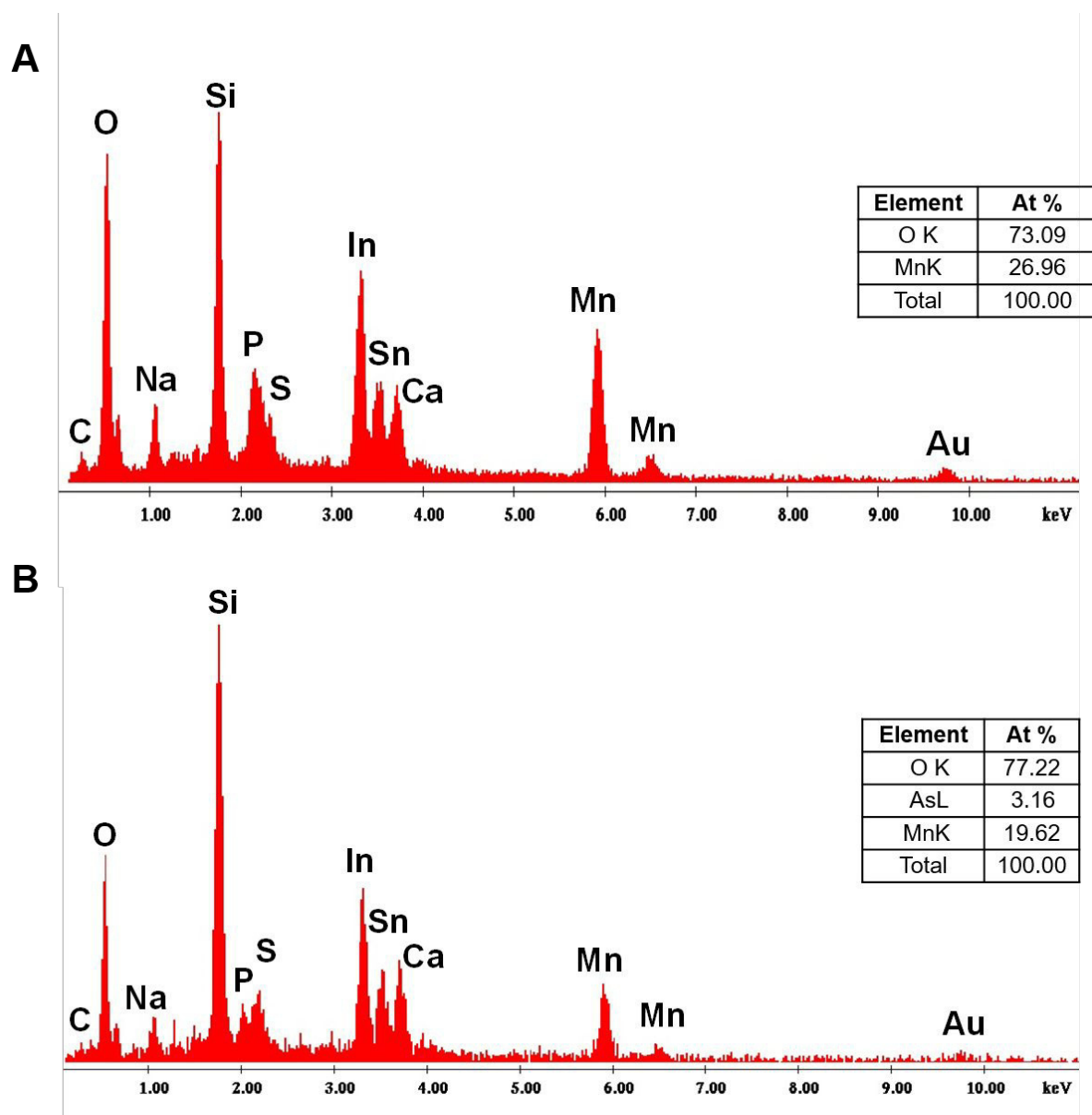


**Figure S4.** EDX spectra of **M3** electrode (A) before and (B) after  $\text{As}^{3+}$  sensing. Inset shows the element analysis. The change in Atomic % of Mn is attributed to the loss of Mn ions from the parent material by dissolution into the electrolyte during LSSV stripping of  $\text{As}^{3+}$ . Sn and In are from the substrate used.

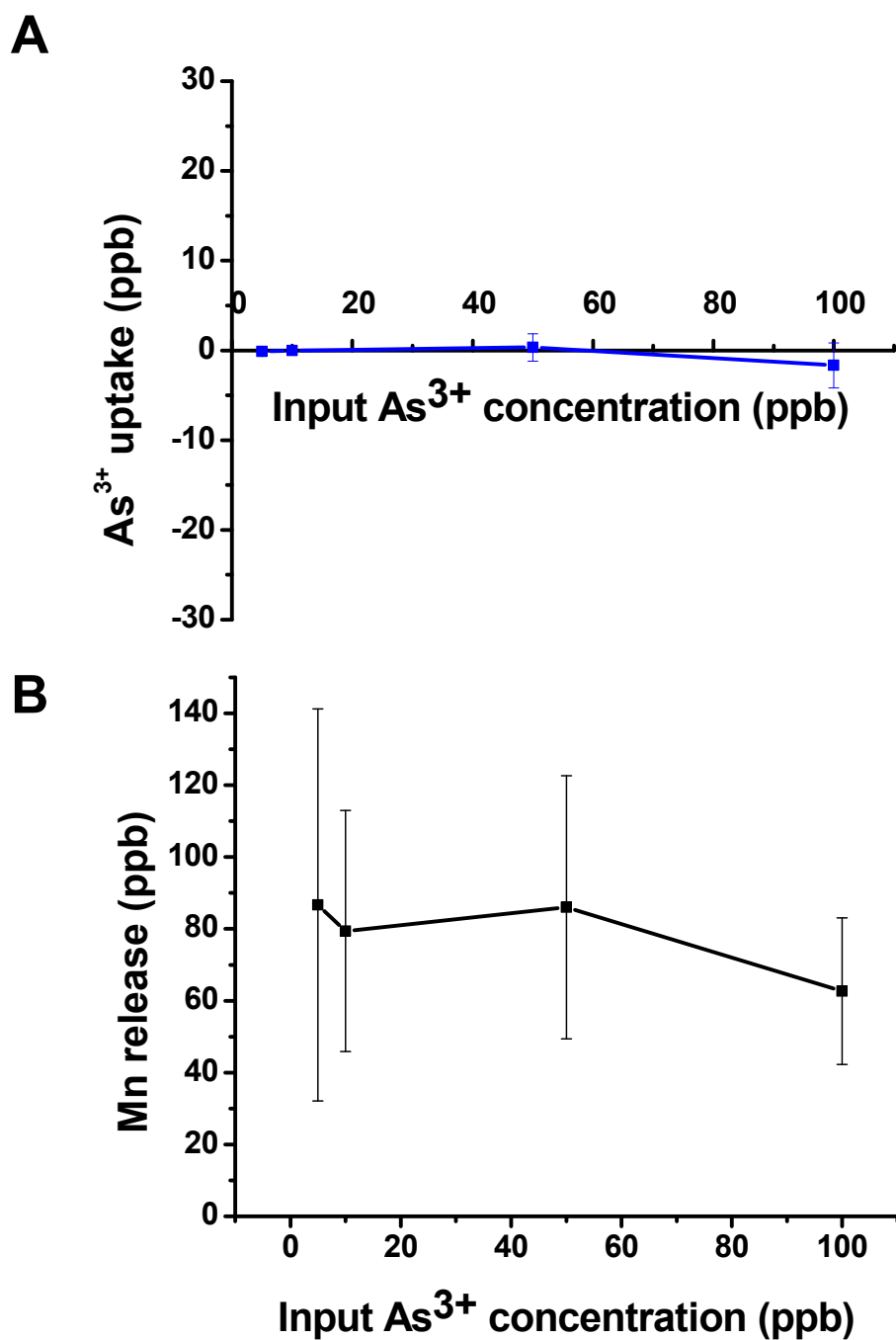


**Figure S5:** ICP-MS data of electrode **M3** for change in the (A) arsenic and (B) manganese ion concentrations in the electrolyte due to LSSV. The data is recorded with three different **M3** electrodes.

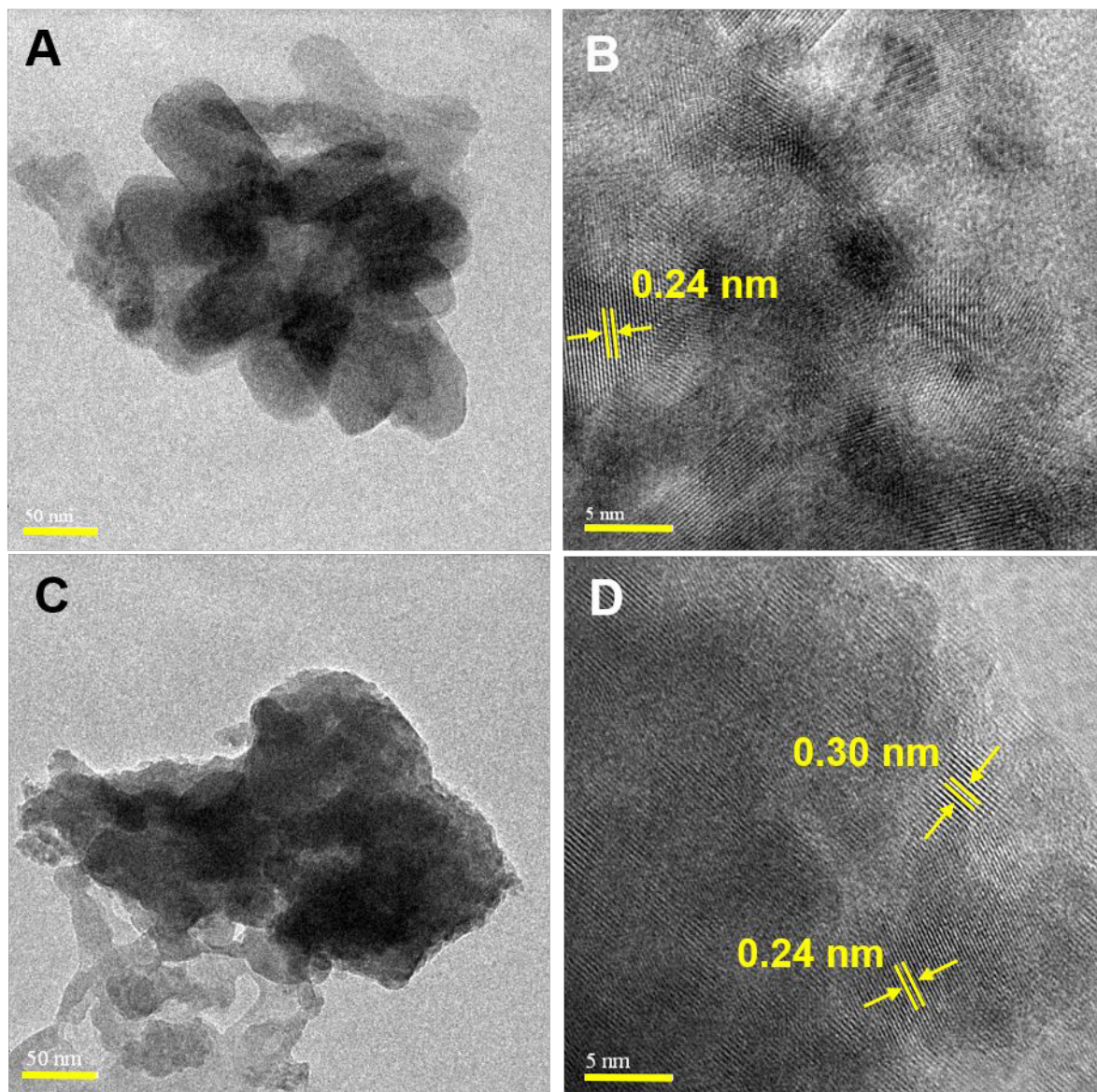


**Figure S6.** HRTEM micrographs of MnO<sub>x</sub> from electrode **M1** (A and B) as-prepared and (C and D) after As<sup>3+</sup> sensing. (A) Aggregated nanorod-like structures. (B) corresponding lattice spacing of ~0.24 nm. (C) Sheets of MnO<sub>x</sub>. (D) corresponding lattice spacing of 0.24 and 0.30 nm. The scale bars are 50 nm for A and C, and 5 nm for B and D.



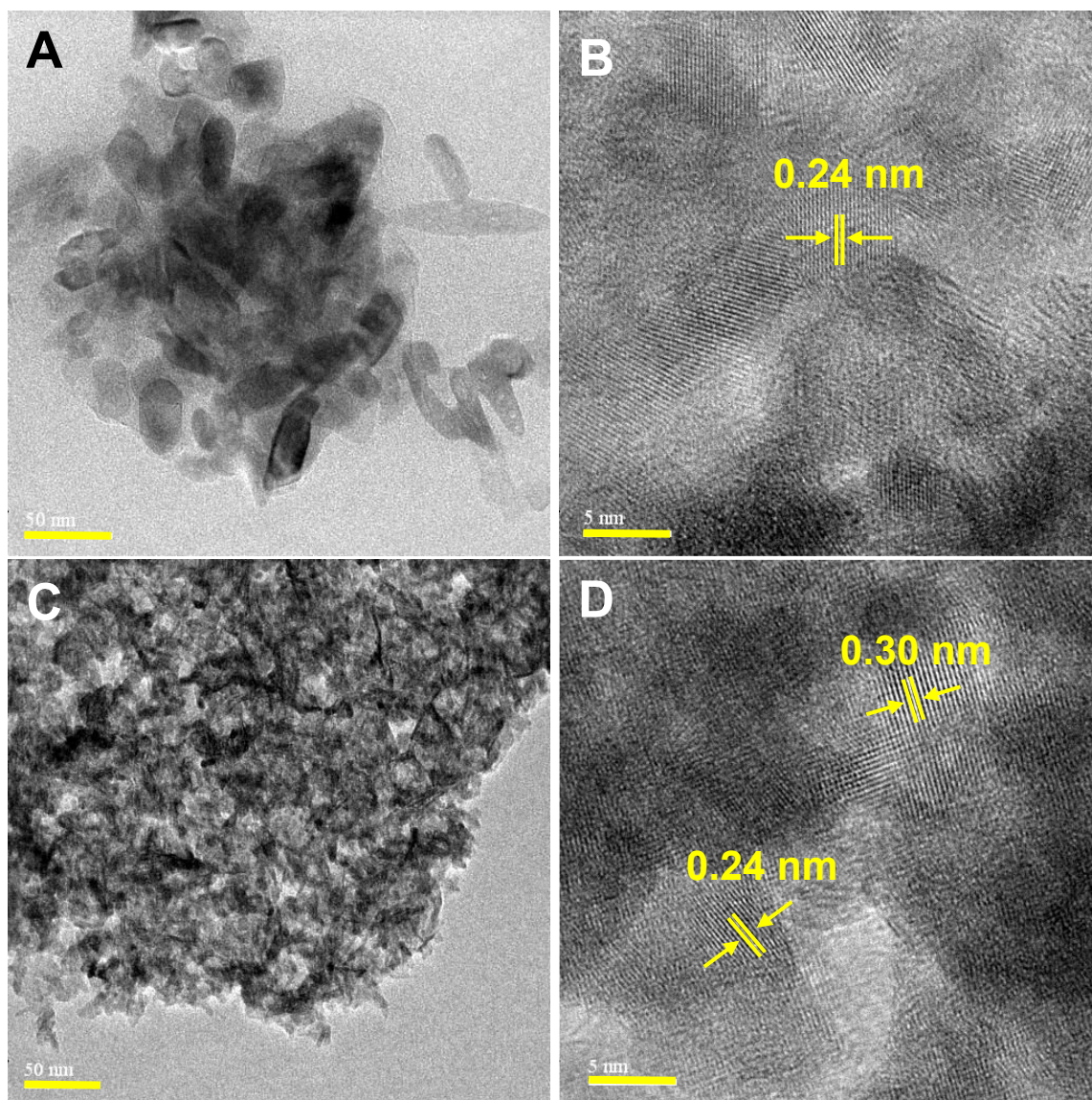


**Figure S7.** HRTEM micrographs of  $\text{MnO}_x$  from electrode **M2** (A and B) as-prepared and (C and D) after  $\text{As}^{3+}$  sensing. (A) Nanorod-like structures with their corresponding lattice spacing of  $\sim 0.24$  nm in (B). (C) Crumpled paper-like morphology of  $\text{MnO}_x$  with lattice spacing of 0.24 and 0.30 nm in (D). The scale bars are 50 nm for A and C, and 5 nm for B and D.

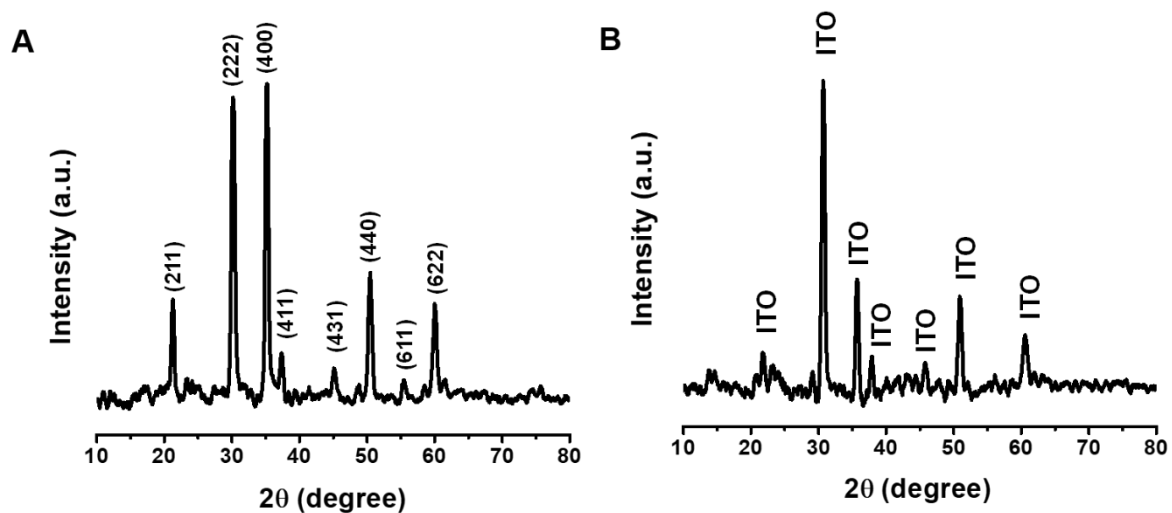


**Figure S8.** XRD patterns of (A) bare ITO glass substrate (JCPDS file no: 71-2194) and (B) control experiment on electrode **M3** involving LSSV in DI water and PBS electrolyte followed by washing with DI water. All peaks in B belong to ITO substrate, no additional peaks were observed.

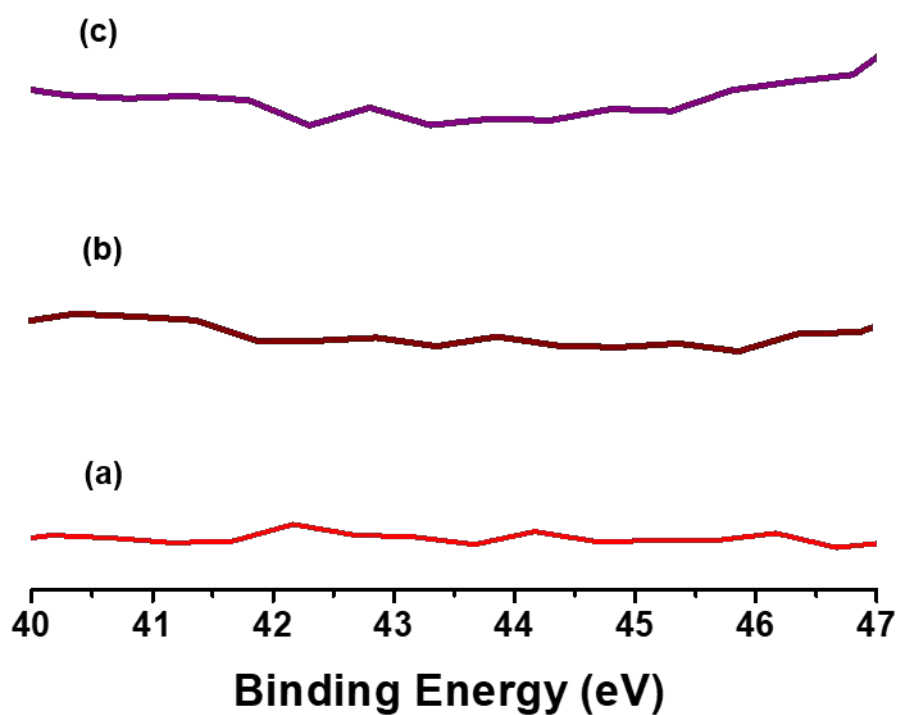


**Figure S9.** XPS spectra of As 3d region for electrode **M3**. (a), (b) and (c) correspond to bare ITO, before sensing and after sensing, respectively. Absence of As peak in (c) indicates that arsenic is not bound to the electrode surface after sensing.

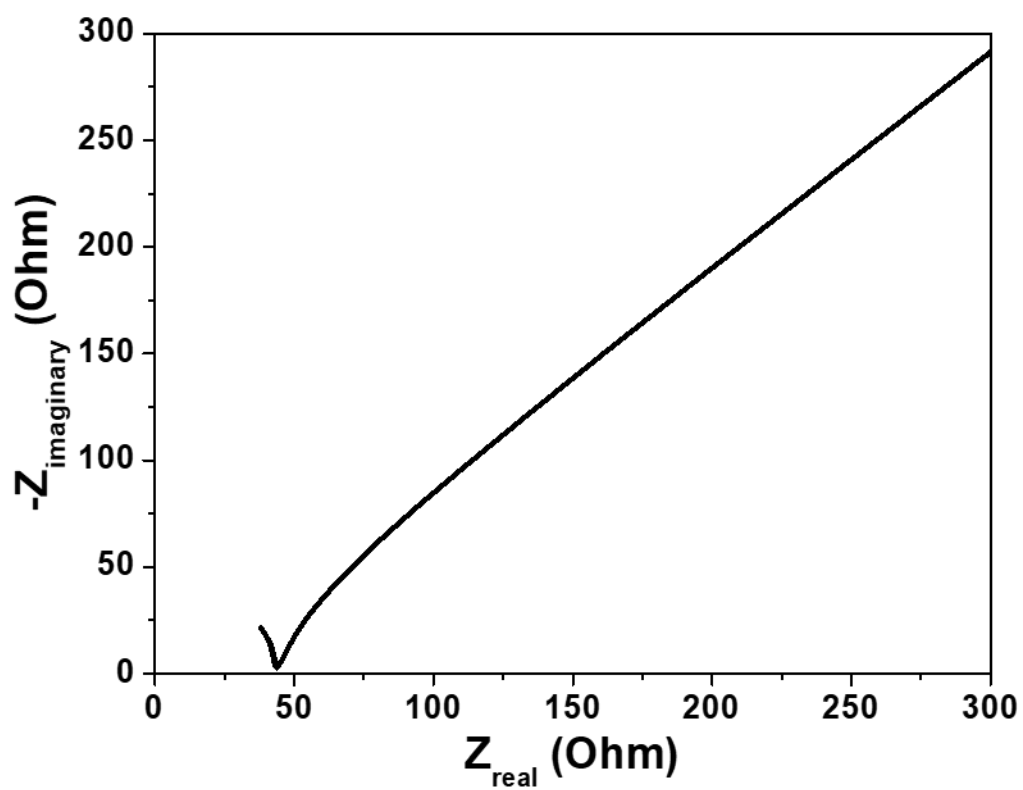


**Figure S10.** Nyquist plot of electrochemical impedance spectra for bare ITO glass substrate in PBS electrolyte (pH  $\sim$  7.4).



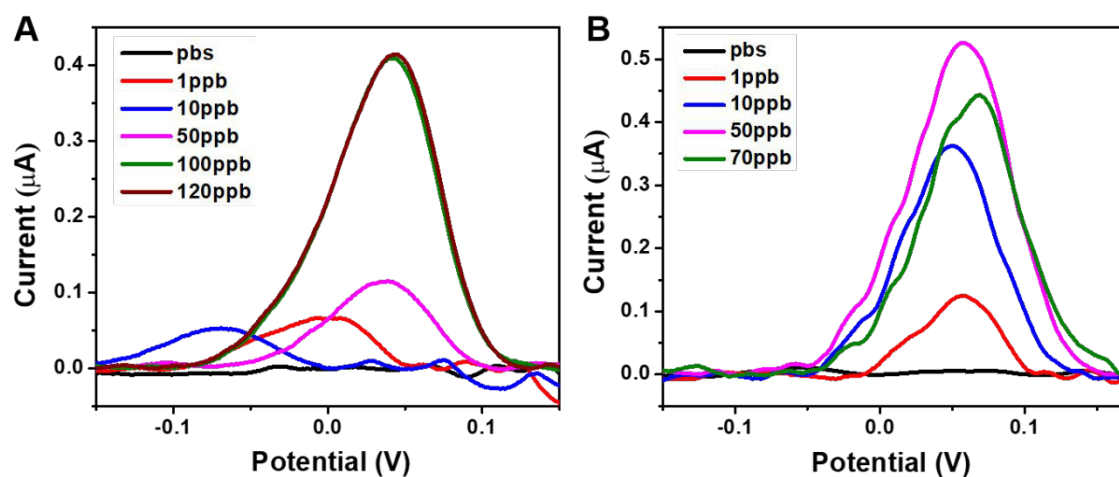


**Figure S11.** Electrochemical arsenite sensing response by MnO<sub>x</sub>/ITO electrodes prepared at different CV voltage-windows: (A) **M1** and (B) **M2**.

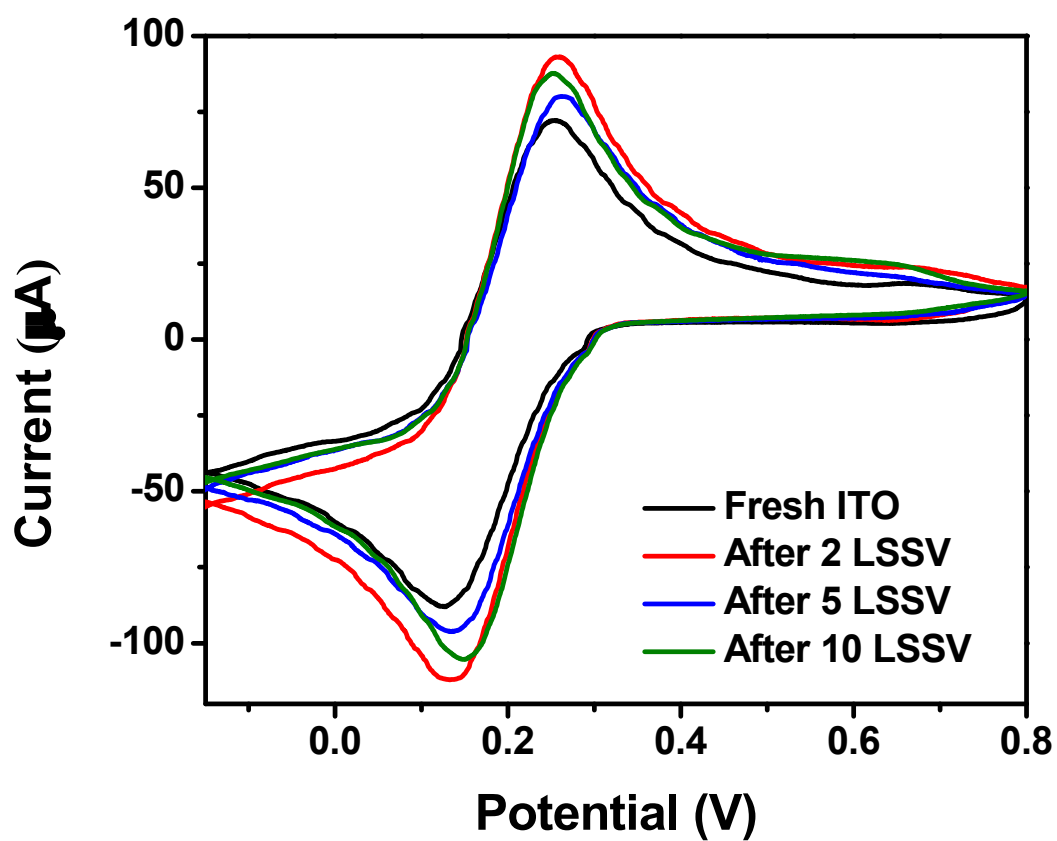


**Figure S12.** Cyclic voltammogram of bare ITO in 32.6  $\mu\text{M}$  of potassium ferricyanide ( $\text{K}_3\text{Fe}(\text{CN})_6$ ) and 3.2 mM potassium chloride (KCl) as supporting electrolyte after performing LSSV at optimized parameters.

### Calculation of LOD

The theoretical limit of detection (LOD) was calculated using the following formulae.<sup>2</sup>

LOB was estimated by measuring replicates of a blank sample and calculating both mean value and standard deviation (SD).

$$\begin{aligned}\text{Limit of blank (LOB)} &= \text{Mean blank} + z\text{-score} \times \text{standard deviation of blank sample} & [1] \\ &= 1.32 \times 10^{-8} + 1.645 \times 4.15 \times 10^{-8} \\ &= 8.146 \times 10^{-8}\end{aligned}$$

$$\begin{aligned}\text{Theoretical Limit of detection (LOD)} &= \text{LOB} + z\text{-score} \times (\text{standard deviation of measured lowest concentration of sample}) & [2] \\ &= 8.146 \times 10^{-8} + 1.645 \times 0.0072 \\ &= 0.01195 \text{ ppb} \\ &\approx 0.012 \text{ ppb}\end{aligned}$$

The z-score in Equations 1 and 2 is the number of standard deviations based on 90% confidence level. It is a statistical parameter.

## References

1. Freitas, R. M.; Perilli, T. A. G.; Ladeira, A. C. Q. Oxidative Precipitation of Manganese from Acid Mine Drainage by Potassium Permanganate. *J. Chem.* **2013**, 2013, 1–8.
2. Armbruster, D. A.; Pry, T. Limit of Blank, Limit of Detection and Limit of Quantitation. *Clin. Biochem. Rev.* **2008**, 29 (August), 49–52.

# Conformational Changes of Protein upon Encapsulation of Noble Metal Clusters: An Investigation by Hydrogen/Deuterium Exchange Mass Spectrometry

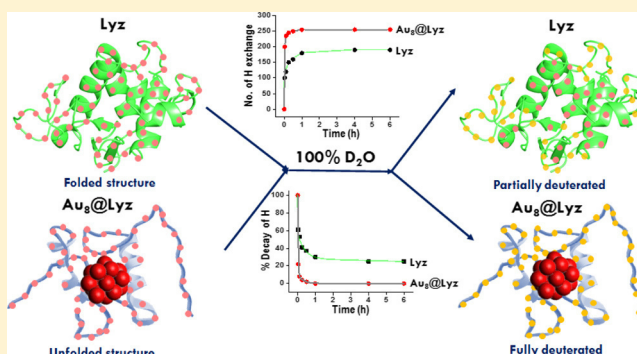
Debasmita Ghosh,<sup>†</sup> Sathish Kumar Mudedla,<sup>‡</sup> Md Rabiul Islam,<sup>†</sup> Venkatesan Subramanian,<sup>‡</sup> and Thalappil Pradeep<sup>\*,†</sup>

<sup>†</sup>DST Unit of Nanoscience (DST UNS) & Thematic Unit of Excellence (TUE), Department of Chemistry, Indian Institute of Technology Madras, Chennai 600036, India

<sup>‡</sup>Chemical Laboratory, CSIR-Central Leather Research Institute, Adyar, Chennai 600020, India

## Supporting Information

**ABSTRACT:** Hydrogen/deuterium exchange mass spectrometry was employed to probe the conformational changes in lysozyme (Lyz) during the course of formation of a protein-protected atomically precise Au<sub>8</sub> cluster. MALDI MS showed the protein, Lyz, to be present in a denatured state in the cluster. Detailed ESI MS analysis of the Au-attached Lyz adducts, an intermediate of cluster formation, confirmed that these conformational changes are brought about by Au–S bond formation and a similar conformation is retained in the final cluster. These results were supported by computational results, which showed an increase in solvent accessible surface area upon the formation of the adducts. Infrared spectroscopy established that change in the rate as well as the extent of the hydrogen/deuterium exchange observed in the cluster was due to the change in the amide II region of the encapsulating protein. Hydrogen/deuterium exchange ESI MS of Cu adducts of Lyz showed a lower degree of denaturation than their Au counterparts. XPS analysis revealed that Cu binds differently to Lyz than it does with Au, which is likely because of the stronger soft–soft Au–S interaction. Alkali metal ion binding, on the other hand, does not affect the protein conformation because such ions do not affect the disulfide bonds.



## INTRODUCTION

Protein-protected clusters<sup>1,2</sup> have been found to be useful as chemical sensors<sup>3–5</sup> due to their excellent inherent photoluminescence, which is easily affected by the presence of foreign bodies in the medium. Their ease of synthesis, exceptional stability, and biocompatibility have also resulted in applications in imaging,<sup>6</sup> drug delivery,<sup>7</sup> and other biomedical fields.<sup>8</sup> Despite their wide range of applications, very little is known about the structure of protein-protected clusters. This is in stark contrast to their monolayer-protected counterparts, the exact atomic structure for several of those have been derived successfully.<sup>9–11</sup> Understanding the structure of these clusters can not only help shed light on their unique reactivity<sup>12–14</sup> but also help tune their luminescence<sup>15</sup> and surface functionality.<sup>16</sup> A similar clear understanding of the structure of protein-protected clusters will help fine tune these clusters for specific problems, pushing the envelope of their applications to the next level.

Protein-protected clusters are biohybrid materials, in which an inorganic cluster composed of tens of atoms of noble metals is grown inside a protein template. The complete structural identification of a protein-protected cluster would thus require

characterization of both these components. Structure of the proteins is generally derived from X-ray crystallography<sup>17,18</sup> or single-particle cryoelectron microscopy.<sup>19,20</sup> X-ray crystallography is one of the main techniques used for the characterization of monolayer-protected clusters as well.<sup>21</sup> However, protein-protected clusters could not be crystallized till date, and thus X-ray structure could not be determined. MALDI MS has been used traditionally to characterize such clusters. Detailed understanding of the growth kinetics of gold clusters in proteins through comprehensive MALDI MS analysis of the intermediates was published in an earlier work.<sup>22</sup> However, such traditional mass spectrometric analysis could only reveal the atomicity of the clusters formed and not their structure. Synchrotron-based X-ray absorption fine structure spectroscopy was used more recently to identify the core structure, and interlocked gold–thiolate rings were identified, departure from the monolayer-protected ones which generally consist of a metal core protected by metal thiolate motifs.<sup>23</sup> However, the

Received: April 29, 2019

Revised: June 12, 2019

Published: June 25, 2019



aspicule structure of monolayer-protected clusters had suggested the existence of gold–thiolate rings in them.

Structural alteration of the protecting proteins in these clusters has not been examined well so far. This is an extremely important aspect to be addressed because the structure of a protein is closely related to its biological function. Any undesired alteration of the structure of its active site thus might lead to complete loss of such functions in the formed clusters. The cluster formation has been shown to increase the overall hydrodynamic diameter, indicating a departure from the native state of the corresponding protein.<sup>24</sup> It is known that Au–S bond formation is associated with breakage of the disulfide bonds in the protein and is likely to bring about structural changes. In our earlier work, by combining ion mobility with electrospray ionization (ESI) mass spectrometry, we showed that successive attachment of Au atoms to the protein backbone leads to gradual unfolding of the protein.<sup>25</sup> However, whether such unfolded conformers of the protein end up being retained in the final cluster or not was not addressed.

In the following, we present an investigation into the conformational change of lysozyme (Lyz) from its native state to the final cluster by hydrogen/deuterium exchange mass spectrometry and infrared spectroscopy. The extent of change in protein-protected clusters was found to be similar to that of the Au-attached protein adducts, implying that structural changes arise right from the initial stage of metal binding itself. Fast exchange of all labile hydrogens in the amide backbone of the adducts confirmed their greater solvent accessibility compared to the protein, courtesy of their unfolded nature. Similar unfolded structure of the protein leads to a rapid and complete exchange of all hydrogens in the cluster. This study has given a new insight into the changes in the protein structure upon cluster formation, which has been difficult to explore. The extent of structural change in Lyz was observed to be more for Au binding than for Cu and alkali-metal ions. Computations allowed us to understand the change in the solvent accessible area of protein and the specific regions in which such changes occurred. Collectively, data present new insights into an unknown area of structural changes in a protein in protein-protected clusters.

## METHODS

**Materials.** Tetrachloroauric acid trihydrate ( $\text{HAuCl}_4 \cdot 3\text{H}_2\text{O}$ ) was prepared in-house starting from elemental gold. Lyz (>90% purity) was purchased from Sigma-Aldrich. Sodium hydroxide pellets were purchased from a local supplier (Rankem, India). Milli-Q water and  $\text{D}_2\text{O}$  (Sigma-Aldrich) were used in all experiments. Sinapic acid (99% purity) used as a matrix for MALDI MS was purchased from Sigma-Aldrich. All chemicals in the experiment were used without further purification.

**Instrumentation.** Most of the experiments reported in this paper were carried out using a Waters Synapt G2Si HDMS instrument. This instrument consists of an electrospray source, quadrupole ion guide/trap, ion mobility cell, and TOF detector. Different gases were used in different parts of the instrument. All experiments were carried out in the positive ion mode. NaI was used for the calibration of the instrument. To get a well-resolved mass spectrum, the following optimized conditions were used.

Sample concentration: 1  $\mu\text{g}/\text{mL}$ .

Solvent: water and  $\text{D}_2\text{O}$ .

Flow rate: 10–20  $\mu\text{L}/\text{min}$ .

Capillary voltage: 2–3 kV.

Cone voltage: 20 V.

Source offset: 20 V.

Desolvation gas flow: 400 L/h.

Source temperature: 100  $^\circ\text{C}$ .

Desolvation temperature: 150  $^\circ\text{C}$ .

Fourier transform infrared (FTIR) spectra were measured with PerkinElmer Spectrum 2 with UATR attachment.

MALDI MS data of Lyz and  $\text{Au}_8\text{@Lyz}$  cluster were measured using a Voyager-DE PRO Biospectrometry Workstation of Applied Biosystems. A pulsed nitrogen laser of 337 nm was used for ionizing the protein and the cluster in the presence of the sinapic acid matrix. Spectra were collected in the positive mode and an average of 250 shots was used for each spectrum. The matrix solution was prepared using 1:3 mixture of acetonitrile and 0.1% trifluoroacetic acid (TFA) in Milli-Q water. For 100%  $\text{D}_2\text{O}$  experiment, acetonitrile- $\text{d}_3$ , deuterated TFA, and  $\text{D}_2\text{O}$  was used in the same ratio. The cluster solution (5  $\mu\text{L}$ ) was mixed thoroughly with 50  $\mu\text{L}$  of the matrix mixture. The resulting mixture (2.5  $\mu\text{L}$ ) was spotted, and the dried droplet was used for analysis.

**Synthesis of  $\text{Au}_8\text{@Lyz}$ .** Lyz (5 mg) was dissolved in 1 mL of Milli-Q water. 1.25 mM  $\text{Au}^{3+}$  aqueous solution was incubated with Lyz to make  $\text{Au}_n\text{–Lyz}$  adducts. NaOH (1 M) (100  $\mu\text{L}$ ) was added to the adduct to make  $\text{Au}_8\text{@Lyz}$  clusters. Before ESI MS, the adducts were diluted in Milli-Q water. For the hydrogen/deuterium exchange study, the samples were diluted in  $\text{H}_2\text{O}$  as well as  $\text{D}_2\text{O}$ . Finally, for a 100% hydrogen/deuterium MS experiment, the  $\text{Au}_n\text{–Lyz}$  adduct and the cluster was lyophilized and then dissolved in 100%  $\text{D}_2\text{O}$ .

**Computational Details.** In our previous study, gold-induced structural changes in Lyz were investigated using classical molecular dynamics simulations.<sup>25</sup> The simulated structures from our previous study have been taken further to understand the dynamics for 150 ns. In the simulations of Lyz and  $\text{Au}_8\text{–Lyz}$ , similar protocols were followed as in our previous study. The structure of Lyz was taken from the protein data bank (pdb id: 1AKI).<sup>17</sup> Details of the secondary structure have been calculated using dictionary of the secondary structure of the protein protocol.

## RESULTS AND DISCUSSION

Brown-colored  $\text{Au}_8\text{@Lyz}$  cluster solution exhibits intense red luminescence under UV light irradiation (inset, Figure 1a). The UV–vis spectrum of this cluster solution showed one broad peak around 280 nm and a broad hump from 320 to 380 nm, shown in Figure S1. This luminescent cluster showed two broad excitation peaks, one between 340 and 380 nm and another between 450 and 550 nm along with two emission peaks at 440 and 650 nm (Figure 1a). The first peak corresponds to the protein shell and the second one is due to the cluster core, respectively. Two-step formation of  $\text{Au}_8\text{@Lyz}$  involving the addition of  $\text{Au}^{3+}$  ions to form the  $\text{Au}_n\text{–Lyz}$  complex in the first step is followed by the addition of NaOH to complete the cluster formation inside the protein moiety in the second step, and it is shown schematically in Figure 1b.

The luminescent cluster along with its parent protein (Lyz) was subjected to MALDI MS to probe the atomicity of the gold core. Lyz showed its molecular ion peak at 14.3 kDa and a shift of 1576 Da from the parent protein confirmed the formation of the  $\text{Au}_8$  core inside the Lyz cavity (Figure 1c). Lyz consists of a total of 129 amino acids, 19 basic groups, and 255 labile hydrogens with 126 amide groups in the backbone.<sup>26</sup>

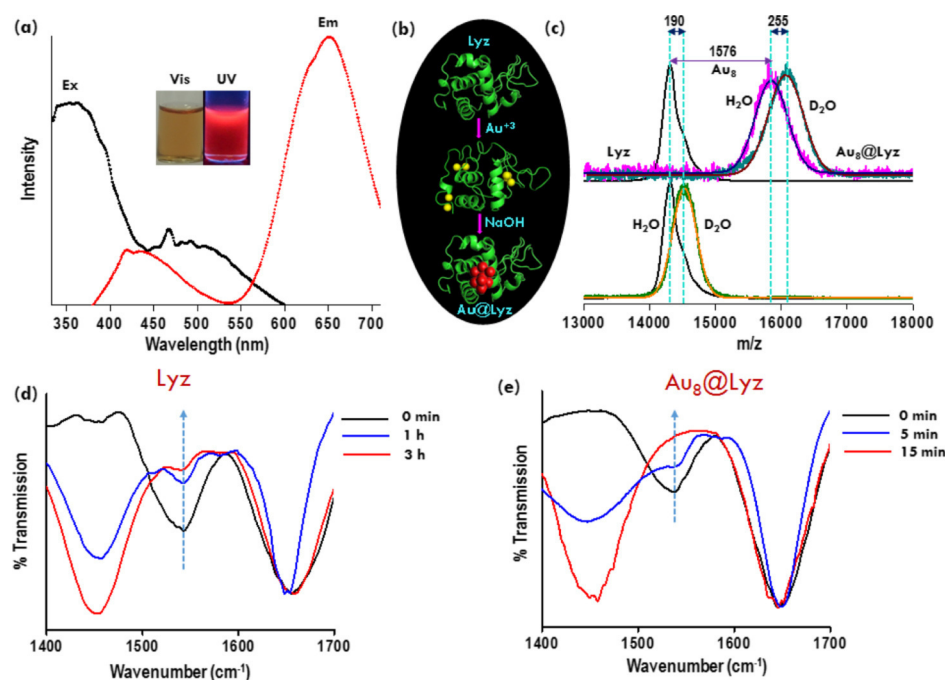


**Figure 1.** (a) Excitation and emission spectra of the  $\text{Au}_8\text{@Lyz}$  cluster. Photographs of the cluster solution taken under visible and UV light are shown in the inset. (b) Schematic representation of the one-pot formation of the luminescent cluster. (c) MALDI MS of Lyz (lower panel) and  $\text{Au}_8\text{@Lyz}$  (upper panel) showing their H/D exchange behavior. Time-dependent H/D exchange IR spectra for Lyz (d) and  $\text{Au}_8\text{@Lyz}$  (e). Time refers to the time of exchange reaction.

To access the change in the conformation of Lyz during the course of cluster formation, hydrogen/deuterium exchange mass spectrometry was employed. In these experiments, both Lyz and  $\text{Au}_8\text{@Lyz}$  were allowed to exchange for 24 h in 100%  $\text{D}_2\text{O}$ , followed by MALDI MS to quantify the number of exchanges in both the cases. The deuterated matrix was used in MALDI MS sample preparation to avoid the possibility of back exchanges. A shift of  $m/z$  255 was observed in the spectrum of  $\text{Au}_8\text{@Lyz}$ , corresponding to the exchange of all the labile hydrogens associated with the amide backbone but a shift of only  $m/z$  190 was observed for Lyz (Figure 1c). It indicates that all amide hydrogens were exchanged in the clusters, unlike in the case of the protein. It is to be noted that continuing the hydrogen/deuterium exchange reaction beyond 24 h for Lyz did not increase the extent of exchange, shown in Figure S2. The exchange behavior exhibited by  $\text{Au}_8\text{@Lyz}$  was very similar to that of denatured Lyz, reported earlier.<sup>26</sup> Denaturation of Lyz using dithiothreitol results in the breakage of the disulfide bonds, making all the amide hydrogens available for exchange; some of them are not available in the original globular form. Interaction of  $\text{Au}^{3+}$  with Lyz in the first step of cluster formation also results in the cleavage of disulfide bonds and formation of Au–S bonds.<sup>27</sup> Consequently, all amide hydrogens of  $\text{Au}_8\text{@Lyz}$  get exposed to the solvent, indicating structural alteration of Lyz upon cluster formation.

Monitoring the hydrogen/deuterium exchange with IR spectroscopy for both Lyz and  $\text{Au}_8\text{@Lyz}$  provided strong support to the mass spectrometric observations. The solutions of native Lyz and freeze-dried  $\text{Au}_8\text{@Lyz}$  in pure  $\text{D}_2\text{O}$  were subjected to time-dependent IR spectroscopy, and the intensity of the amide II band was closely monitored. In the deuterated medium, the band which originally appears around  $1550\text{ cm}^{-1}$  (band II) got shifted to around  $1450\text{ cm}^{-1}$ . The hydrogen/deuterium exchange (Figure 1d) resulted in a gradual decrease in the intensity of band II along with an increase in the

intensity of  $1450\text{ cm}^{-1}$ . However, it is important to note that complete disappearance of band II was never observed, even after prolonged (24 h) incubation. On the other hand, the complete disappearance of band II happened within 15 min in the case of  $\text{Au}_8\text{@Lyz}$  (Figure 1e). Note that spectra were collected with attenuated total reflection–FTIR and data collection typically took <1 min. This shows a clear difference in the secondary structure between Lyz and the protein shell in  $\text{Au}_8\text{@Lyz}$ . A similar observation of the hydrogen/deuterium exchange was reported for heated protein solutions where heat promotes the formation of random coils.<sup>28</sup> Hydrogen/deuterium exchange of heated Lyz is shown in Figure S3. The random coils formed were exposed more to the solvent compared to highly organized  $\alpha$ -helices and  $\beta$ -sheets. Therefore, complete hydrogen/deuterium exchange happened, at a faster rate. During cluster formation, the protein secondary structure gets similarly uncoiled; thus, complete exchange is observed in the case of  $\text{Au}_8\text{@Lyz}$ , unlike in the native protein.

Further insights into the rate of the hydrogen/deuterium exchange in connection with change in the protein conformation during cluster formation required a fast analysis method with minimal sample preparation to perform time-dependent analysis. Because MALDI MS requires extensive sample preparation, it is unsuitable for such a study. ESI, on the other hand, is a fast soft ionization method, which produces intact, multiple protonated ions from protein molecules in solution without the need of sample preparation.<sup>26</sup> Moreover, the well-defined charge state distribution of a protein in ESI MS is often used as a thumbprint and change in their charge state distribution is used to probe the changes in protein conformations, making it a suitable technique for our purpose. The conformational alteration of the protein due to the formation of  $\text{Au}_n\text{–Lyz}$  adducts in the first step of cluster formation was probed first to get an idea about the changes associated with the breakage of the disulfide bonds in this step.



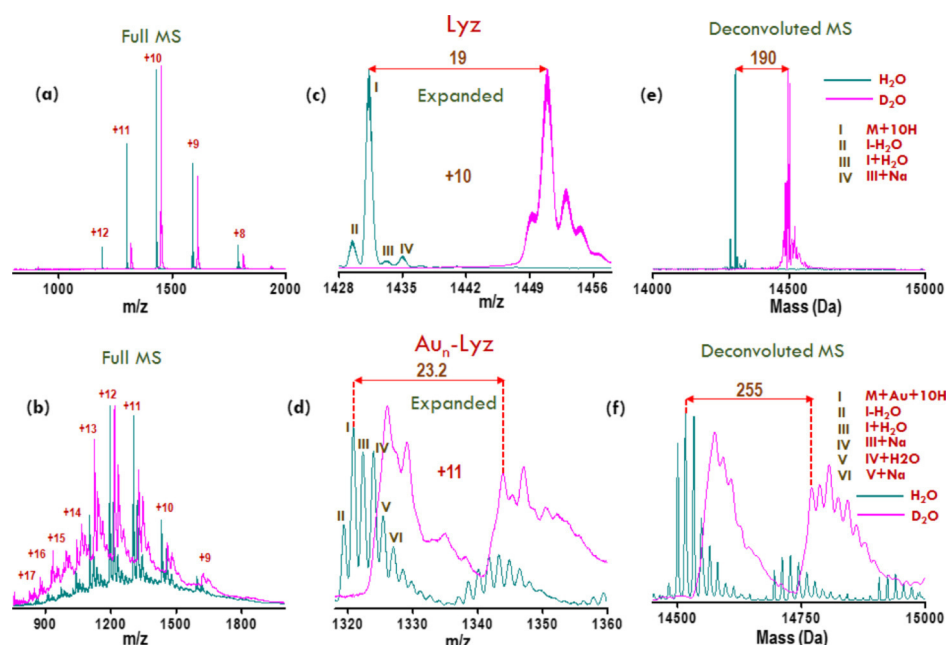


**Figure 2.** H/D exchange mass spectra of Lyz and  $\text{Au}_n\text{-Lyz}$ , respectively, in 100%  $\text{D}_2\text{O}$ , ESI MS (a,b); expanded ESI MS from a single-charge state (c,d); and deconvoluted MS (e,f).

The net positive charge on the native protein in solution is lower than the unfolded one. Protein molecules are tightly folded in their native state having some of their basic sites buried and involved in strong H-bonded interaction, and these do not protonate in solution.<sup>26</sup> This is observed in ESI MS of Lyz (Figure 2a), which consists of 129 amino acid residues having 19 basic sites, but all these charge states do not appear in the mass spectrum. Interaction of Lyz with  $\text{Au}^{3+}$  during cluster formation results in the breakage of all four disulfide bonds present in it. This in turn unfolds the protein, and all basic sites became exposed to the solvent, resulting in an increment in the intensity of the higher charge states (Figure 2b). The simulated structures of Lyz and  $\text{Au}_8\text{-Lyz}$  were shown in Figure S4. The loss of the helical content on binding with gold ions was noticed when compared to parent Lyz. Helical and beta conformations after binding of gold ions decreased by 15 and 3%, respectively. A decrease in the number of H-bonds between the backbones, which is responsible for the formation of different secondary structures, was calculated (Figure S5). The reduction of hydrogen bonds is more in the case of  $\text{Au}_8\text{-Lyz}$  than for Lyz. The average number of hydrogen bonds in Lyz and  $\text{Au}_8\text{-Lyz}$  are 88 and 76, respectively. The reduction of hydrogen bonds correlates with the loss of helical and beta sheet content due to adduct formation, in line with the denaturation of Lyz in the process. Spectra obtained after a complete exchange of replaceable hydrogens for both Lyz and  $\text{Au}_n\text{-Lyz}$  in 100%  $\text{D}_2\text{O}$  are overlaid in Figure 2a,b, respectively. Expansion of the +10 charge state for Lyz and +11 charge state for  $\text{Au}_n\text{-Lyz}$  (selected due to reduction in the intensity of the +10 state), respectively, is shown in Figure 2c,d, which showed clear differences in deuterium exchange that became apparent upon deconvolution. The deconvoluted spectrum for Lyz (Figure 2e) showed a mass shift of 190; same was observed in MALDI MS, while  $\text{Au}_n\text{-Lyz}$  (Figure 2f) showed a mass shift of 255. The mass shift for  $\text{Au}_n\text{-Lyz}$  adducts matched with the mass shift observed for the  $\text{Au}_8\text{@Lyz}$  clusters. This points to the fact that structural change in the amide region of the protein happens in the beginning stage of incubation with  $\text{Au}^{3+}$

ions, and the cluster acquires a similar protein shell structure, in terms of position and accessibility of the amide groups. Because the final cluster ( $\text{Au}_8\text{@Lyz}$ ) does not ionize under electrospray conditions, detailed experiments were carried out with the  $\text{Au}_n\text{-Lyz}$  adducts.

A basic idea about the extent of structural change in the proteins could be derived by exploring how fast and how many of the hydrogens can be exchanged.<sup>29</sup> This again would be dependent on both the exposure of exchangeable hydrogens toward the solvent molecules as well as the percentage of  $\text{D}_2\text{O}$  in the surrounding medium. To account for both these effects, we monitored the kinetics of exchange at different  $\text{D}_2\text{O}$  concentrations (20, 50, and 100%) through ESI MS. Surprisingly, at the lowest  $\text{D}_2\text{O}$  (20%) concentration, both Lyz and  $\text{Au}_n\text{-Lyz}$  exhibited similar behavior in terms of speed of exchange and the number of total hydrogens exchanged (Figure S6). This indicates that parts of the protein structure remained intact even after cluster formation. Because the structure is closely related to protein function, those functional parts are also likely to remain intact, which has been seen in the past.<sup>30</sup> We have not evaluated the functions of  $\text{Au}_8\text{@Lyz}$ . Increasing the  $\text{D}_2\text{O}$  concentration to 50% starts to show differences in the exchange behavior. Figure 3a shows the hydrogen/deuterium exchange of the native protein with time, and Figure 3b shows the same for the Au-added protein. Time-dependent exchange shows gradual change in the case of Lyz, which is distinct from the adduct behavior. Figure 3c,d shows the exchange behavior for the native protein and Au-added protein in 100%  $\text{D}_2\text{O}$ , respectively. In 50%  $\text{D}_2\text{O}$ , a shift in the  $m/z$  value is less for both of the species. This can be explained in two ways. One aspect is that as the samples are in equilibrium, the back exchange made a broad distribution. The other possibility is that reduced availability of deuterium in 50% than in 100% medium made the difference. In 100% medium, the environment is fully deuterated, and there was no back-exchange, thus the difference for both the species will increase. In the case of the adduct in 100%  $\text{D}_2\text{O}$ , within 15 min, all exchangeable hydrogens were exchanged with

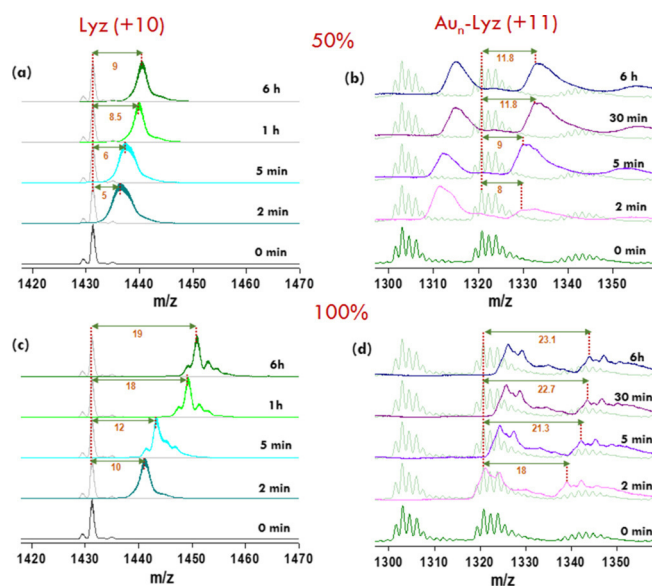


**Figure 3.** Time-dependent MS of Lyz and  $\text{Au}_8\text{-Lyz}$  in 50 and 100%  $\text{D}_2\text{O}$  in specific regions. (a,c) Change of the mass spectrum for Lyz with time in 50 and 100%  $\text{D}_2\text{O}$ , respectively, (b,d) same data for  $\text{Au}_8\text{-Lyz}$ . The MS of Lyz and  $\text{Au}_8\text{-Lyz}$  are in +10 and +11 charge states, respectively.

deuterium, whereas for the parent protein, 180 hydrogens were exchanged in 1 h. This large change in the number and the time of hydrogen exchange of the adduct points toward the structural change of the adduct. Addition of  $\text{Au}^{3+}$  to Lyz increased the availability of the amide hydrogens for exchange. The ESI MS of hydrogen/deuterium exchange (with all the charge states) in 50%  $\text{D}_2\text{O}$  (Figure S7) and in 100%  $\text{D}_2\text{O}$  (Figure S8) are presented separately.

A kinetic plot of the % decay of H, that is, reduction in number of hydrogen due to exchange with deuterium and total

number of H exchanged with time is presented in Figure 4a. When a protein is exposed to  $\text{D}_2\text{O}$  environment, the rate of hydrogen exchange will depend on the presence of the amide hydrogens whether they are H-bonded or accessible to the aqueous solvent. The kinetics of percentage decay of hydrogen with time is fitted for both the species. Because a mono- and biexponential fit was inadequate to cover all the data points, a triexponential fit was used. The three rate constants,  $k_1$ ,  $k_2$ , and  $k_3$  are  $0.7 \times 10^2 \text{ h}^{-1}$ ,  $0.2 \times 10 \text{ h}^{-1}$ , and  $0.2 \times 10^{-1} \text{ h}^{-1}$  for native protein and for the adduct, the values are, respectively,  $16 \times 10^2 \text{ h}^{-1}$ ,  $3.3 \times 10 \text{ h}^{-1}$ , and  $33 \times 10^{-1} \text{ h}^{-1}$ . Initially, the exchange rates were fast but with time, it decreased. The difference in the rate constants indicates the difference in the structure of the exchanging species. This difference indicates that the amide hydrogens in the adduct were more exposed to the solvent than the protein. Solvent accessible surface area (SASA) is the surface area of a biomolecule, which is accessible to smaller molecules.<sup>31</sup> The calculation of SASA is often used to determine the folding and stability of the protein in solution. The calculation of the SASA value at the atomic level is very difficult experimentally. The breakage of hydrogen bonds between amide bonds in the helical conformation made the hidden back bone expose to the environment. Figure 4b showed that the calculated SASA value was more for the adduct than for the native protein. The overlapped structure (amide region) of the adduct and Lyz (Figure 4c) and the same in mapped surface areas (Figure S9) showed the increased surface area in  $\text{Au}_8\text{-Lyz}$  compared to Lyz. The availability of amide bonds to the environment increased the hydrogen/deuterium exchange, which was observed in our experiments. The increased value in the adduct indicated the unfolded structure of the protein. During cluster formation, the folded structure of Lyz became relaxed and less ordered. This change in the protein structure enhanced the exchange rate than the tightly folded structure of native Lyz.

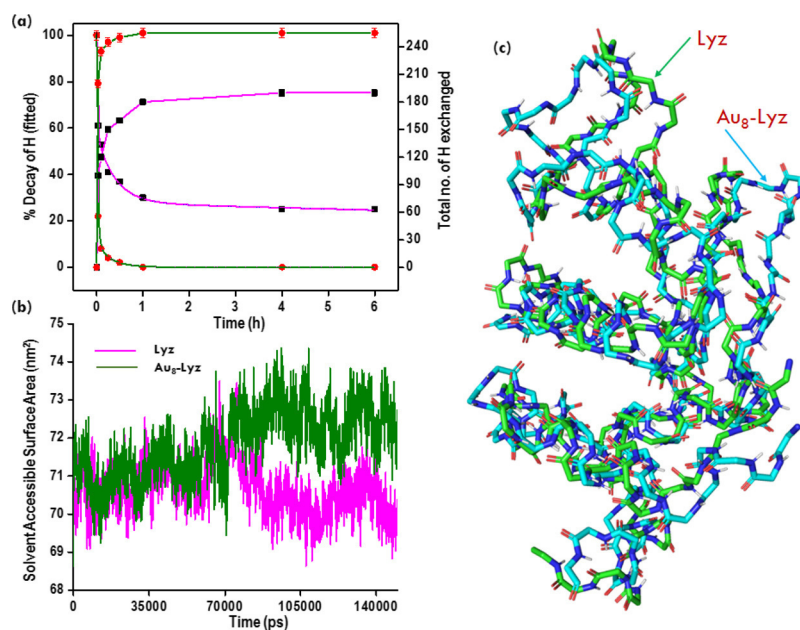


**Figure 4.** (a) Comparison of H/D exchange kinetics of Lyz and  $\text{Au}_8\text{-Lyz}$  in 100% of  $\text{D}_2\text{O}$ . The % decay in the number of H and total number of H exchanged is plotted against reaction time. The decay curve was fitted triexponentially. (b) Computationally obtained SASA for Lyz and  $\text{Au}_8\text{-Lyz}$ . (c) Overlapped structures of Lyz and the protein backbone (without the metal) of  $\text{Au}_8\text{-Lyz}$ , showing structural deviation from the native state.

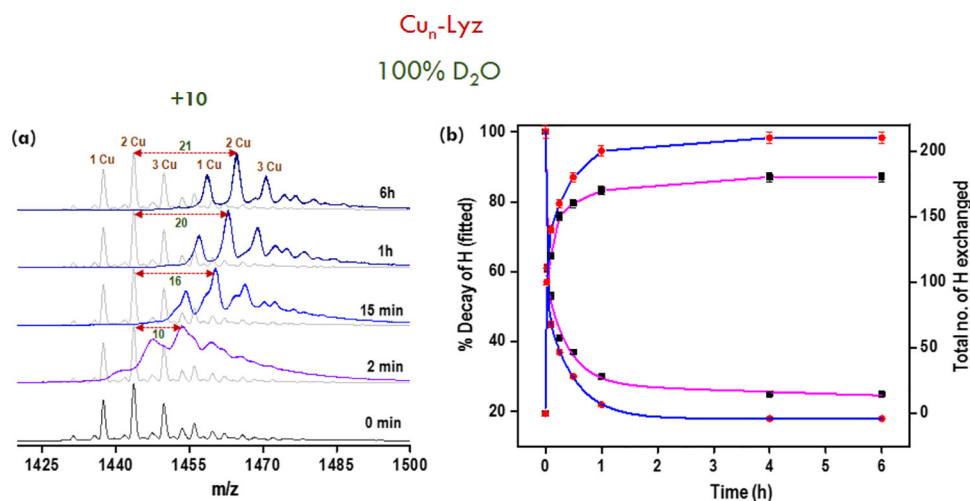


**Figure 5.** (a) Time-dependent MS of  $\text{Cu}_n\text{-Lyz}$  in 100%  $\text{D}_2\text{O}$ , showing the changes in the +10 charge state. (b) % decay of H and total number of H exchanged with time. The decay curve was fitted with a triexponential function.

Although not as diverse in their applications as the Au ones, protein-protected Cu clusters have also been synthesized. These clusters are generally blue luminescent,<sup>32,33</sup> though a few red luminescent ones have also been reported.<sup>34</sup>  $\text{Cu}^{2+}$  salts are generally used as the precursor to synthesize such clusters. To explore if metal to protein interaction follows a general trend leading to the formation of clusters, we prepared  $\text{Cu}_n\text{-Lyz}$  adducts and followed their hydrogen/deuterium exchange behavior. ESI MS of  $\text{Cu}_n\text{-Lyz}$  adducts showed that a maximum of eight Cu could bind with Lyz (Figure S10).<sup>35</sup> The time evolution of hydrogen/deuterium exchange, followed with ESI MS, for the +10 region (Figure 5a), in 100%  $\text{D}_2\text{O}$  medium showed a few key differences than in  $\text{Au}_n\text{-Lyz}$  adducts. While the total number of hydrogens exchanged were higher than that in Lyz (Figure 5b), the rate of exchange was much slower than in  $\text{Au}_n\text{-Lyz}$ . A similar observation was again made when the reaction was performed in 50%  $\text{D}_2\text{O}$  medium (Figure S11). Moreover, a complete exchange of all exchangeable hydrogens was never achieved in these cases, even with prolonged incubation of  $\text{Cu}_n\text{-Lyz}$  in 100%  $\text{D}_2\text{O}$  (data are presented in Figures S12 and 5a). To compare the kinetics, the rate constants of hydrogen/deuterium exchange were calculated in 100%  $\text{D}_2\text{O}$  environment (Figure 5b). Slightly higher values of the rate constant were observed for  $\text{Cu}_n\text{-Lyz}$  ( $k_1$ ,  $k_2$ , and  $k_3$  were  $0.7 \times 10^2 \text{ h}^{-1}$ ,  $0.4 \times 10 \text{ h}^{-1}$ , and  $0.5 \times 10^{-1} \text{ h}^{-1}$ , respectively), albeit of the same order as observed in Lyz. This indicates that while Cu-binding also alters the structure of a protein from its native state, the degree of alteration is less pronounced than brought about by Au binding. This could possibly stem from differences in the mode of binding of the metal ions.

XPS of both  $\text{Au}_n\text{-Lyz}$  and  $\text{Cu}_n\text{-Lyz}$  was performed to confirm whether different binding modes of metal ions are indeed responsible for the different degrees of alteration of the protein structure. The XPS spectrum in the Au 4f region (Figure 6a) showed that almost all gold is in the +1 charge state (Au  $4f_{7/2}$  and Au  $4f_{5/2}$  at 85.2 and 88.9 eV, respectively). This is in line with the notion that  $\text{Au}^{3+}$  oxidizes and breaks the disulfide bonds in protein and gets reduced to  $\text{Au}^{1+}$  in the process (during the first step of cluster synthesis). XPS of Au 4f for the cluster is shown in Figure S13. Cu  $2p_{3/2}$  in  $\text{Cu}_n\text{-Lyz}$  was observed at 940.4 eV (Figure 6b), revealing that copper

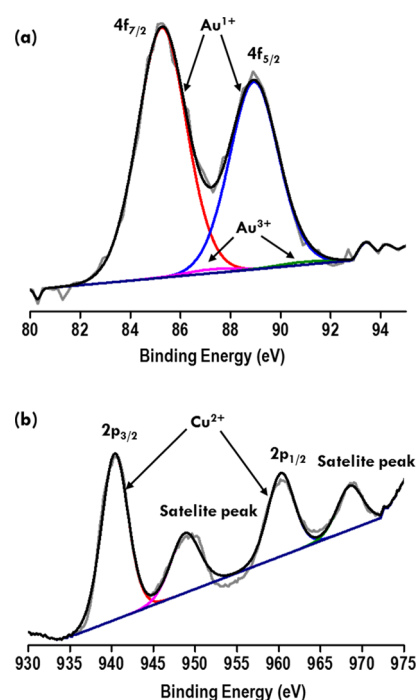


**Figure 6.** XPS spectra of  $\text{Au}_n\text{-Lyz}$  (a) and  $\text{Cu}_n\text{-Lyz}$  (b), in the Au 4f and Cu 2p regions, respectively, showing that  $\text{Au}^{1+}$  and  $\text{Cu}^{2+}$  are present in them. Peaks were fitted after background subtraction.

remained in the +2 oxidation state in the adduct. The configuration interaction satellite peaks for both Cu  $2p_{3/2}$  and  $2p_{1/2}$  were also present. The presence of  $\text{Cu}^{2+}$  in the  $\text{Cu}_n\text{-Lyz}$  adduct indicates that its binding to Lyz does not involve oxidation–reduction reaction unlike in the case of Au. It is likely that Cu binding does not result in complete disruption of the disulfide bonds, and hence, the protein structure was found to be less altered. A higher degree of affinity of S toward Au over Cu could very well be the reason for their different binding modes in proteins.

ESI MS examination of the alkali metal adducts of Lyz showed clear differences in their interaction in comparison to Au and Cu. Attachment of 8–10  $\text{Na}^+$  ions, 6–8  $\text{K}^+$  ions, and 2–3  $\text{Rb}^+$  ions is shown in Figure 7a. With increase in the ionic



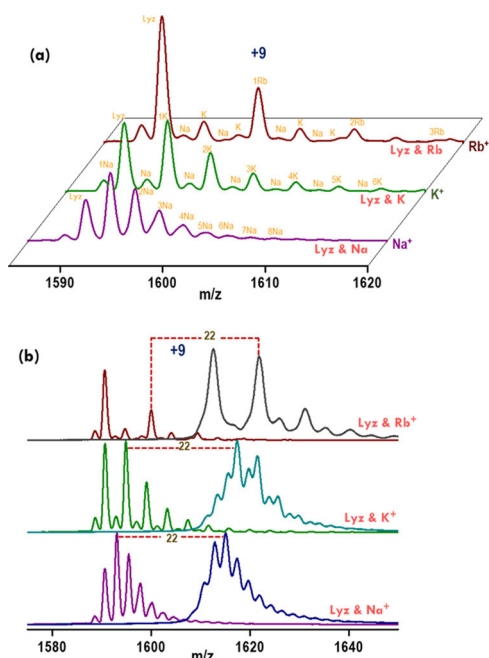


**Figure 7.** Interaction of Lyz with alkali metals; (a) ESI MS of alkali metal-attached Lyz adducts. (b) H/D exchange MS in the +9 charge state of alkali metal-Lyz adducts in 100% D<sub>2</sub>O showing similar exchange for all alkali metal ions.

radii down the group showed reduced number of attachments. However, a very similar distribution of the charge state to native Lyz for all alkali metal ions (Figure S14) confirms retention of the protein structure in these adducts. The interaction of alkali metals with protein is of great interest due to their physiological roles and has been studied extensively. They are known to coordinate with proteins through cation- $\pi$  interactions. Aromatic amino acids of proteins such as phenylalanine, tyrosine, and tryptophan are the binding sites for such interaction.<sup>36</sup> Na<sup>+</sup> has been known to bind with indole present in the side chain of tryptophan residues in the case of Lyz.<sup>37,38</sup> Hydrogen/deuterium exchange MS studies further prove the retention of protein conformation upon alkali metal ion binding (Figure 7b). The number of hydrogens exchanged was the same for all these ions and are also equal to that for Lyz. Because for the aromatic amino acids, which are the binding sites for alkali metal ions remaining exposed to the solvent in the native protein itself, the metal ion attachment does not affect the structure of the protein. On the other hand, both Au and Cu binding affect the disulfide bonds in Lyz, bringing about large structural changes in the process.

## CONCLUSIONS

Conformational changes in the protein structure in the Au<sub>8</sub>@Lyz cluster were manifested in more protons being exchanged in hydrogen/deuterium exchange mass spectrometry. The uncoiling of Lyz during the course of cluster synthesis exposes all 255 amide hydrogens to the solvent, making their exchange possible. A part of these amide groups remain buried deep inside, in the tightly folded native state of Lyz, resulting in only 190 exchanges. These changes in the amide region of the protein became further apparent from IR spectroscopy. Mass spectrometric examination of the intermediate Au-bound Lyz adducts revealed their uncoiled nature to be similar to Au<sub>8</sub>@Lyz and was supported by the computational results.

Attachment of Au<sup>3+</sup> ions to the cysteine residues through the cleavage of the disulfide bonds in the first step of cluster synthesis brings about structural changes in Lyz and those are retained in the final cluster. Structural deviation in the Cu<sub>n</sub>-Lyz complexes was much less prominent than the Au ones, while alkali metal ions did not alter the structure at all. This could be attributed to the lower binding affinity of Cu toward S than Au and therefore, the corresponding ions interact differently with Lyz. For alkali metal ions, binding occurs only on the exposed amino acids. This study presents a step toward understanding the structure of the protein shell in protein-protected clusters, without which a complete picture of these complex entities would remain elusive.

## ASSOCIATED CONTENT

### Supporting Information

The Supporting Information is available free of charge on the ACS Publications website at DOI: 10.1021/acs.jpcc.9b04009.

IR spectra of heat-treated Lyz in D<sub>2</sub>O, simulated structure of Lyz and Au<sub>8</sub>-Lyz, simulated data for breaking of H-bonds in Au<sub>8</sub>-Lyz, time-dependent H/D exchange in 20, 50, and 100% D<sub>2</sub>O for Lyz, Au<sub>n</sub>-Lyz, and Cu<sub>n</sub>-Lyz (50 and 100%), the mapped surface area of Lyz and Au<sub>8</sub>-Lyz, interaction of Lyz with Cu<sup>2+</sup> and alkali metals, and XPS study of Au<sub>8</sub>@Lyz clusters (PDF)

## AUTHOR INFORMATION

### Corresponding Author

\*E-mail: pradeep@iitm.ac.in.

### ORCID

Sathish Kumar Mudedla: 0000-0003-3173-5993

Venkatesan Subramanian: 0000-0003-2463-545X

Thalappil Pradeep: 0000-0003-3174-534X

### Notes

The authors declare no competing financial interest.

## ACKNOWLEDGMENTS

We thank the Department of Science and Technology, Government of India, for continuous support of our research program on nanomaterials. D.G. thanks IIT Madras for student fellowships.

## REFERENCES

- (1) Xie, J.; Zheng, Y.; Ying, J. Y. Protein-Directed Synthesis of Highly Fluorescent Gold Nanoclusters. *J. Am. Chem. Soc.* **2009**, *131*, 888–889.
- (2) Xavier, P. L.; Chaudhari, K.; Bakshi, A.; Pradeep, T. Protein-Protected Luminescent Noble Metal Quantum Clusters: An Emerging Trend in Atomic Cluster Nanoscience. *Nano Rev* **2012**, *3*, 14767.
- (3) Wei, H.; Wang, Z.; Yang, L.; Tian, S.; Hou, C.; Lu, Y. Lysozyme-Stabilized Gold Fluorescent Cluster: Synthesis and Application as Hg<sup>2+</sup> Sensor. *Analyst* **2010**, *135*, 1406–1410.
- (4) Hu, D.; Sheng, Z.; Gong, P.; Zhang, P.; Cai, L. Highly Selective Fluorescent Sensors for Hg<sup>2+</sup> Based on Bovine Serum Albumin-Capped Gold Nanoclusters. *Analyst* **2010**, *135*, 1411–1416.
- (5) Muhammed, M. A. H.; Verma, P. K.; Pal, S. K.; Retnakumari, A.; Koyakutty, M.; Nair, S.; Pradeep, T. Luminescent Quantum Clusters of Gold in Bulk by Albumin-Induced Core Etching of Nanoparticles: Metal Ion Sensing, Metal-Enhanced Luminescence, and Biolabeling. *Chem.—Eur. J.* **2010**, *16*, 10103–10112.
- (6) Wu, X.; He, X.; Wang, K.; Xie, C.; Zhou, B.; Qing, Z. Ultrasmall near-Infrared Gold Nanoclusters for Tumor Fluorescence Imaging in Vivo. *Nanoscale* **2010**, *2*, 2244–2249.

- (7) Wang, Y.; Chen, J.; Irudayaraj, J. Nuclear Targeting Dynamics of Gold Nanoclusters for Enhanced Therapy of Her2+ Breast Cancer. *ACS Nano* **2011**, *5*, 9718–9725.
- (8) Song, X.-R.; Goswami, N.; Yang, H.-H.; Xie, J. Functionalization of Metal Nanoclusters for Biomedical Applications. *Analyst* **2016**, *141*, 3126–3140.
- (9) Chakraborty, I.; Pradeep, T. Atomically Precise Clusters of Noble Metals: Emerging Link between Atoms and Nanoparticles. *Chem. Rev.* **2017**, *117*, 8208–8271.
- (10) Desiredy, A.; et al. Ultraprecise Silver Nanoparticles. *Nature* **2013**, *501*, 399–402.
- (11) Zhu, M.; Aikens, C. M.; Hollander, F. J.; Schatz, G. C.; Jin, R. Correlating the Crystal Structure of a Thiol-Protected Au<sub>25</sub> Cluster and Optical Properties. *J. Am. Chem. Soc.* **2008**, *130*, 5883–5885.
- (12) Krishnadas, K. R.; Ghosh, A.; Baksi, A.; Chakraborty, I.; Natarajan, G.; Pradeep, T. Intercluster Reactions between Au<sub>25</sub>(SR)<sub>18</sub> and Ag<sub>44</sub>(SR)<sub>30</sub>. *J. Am. Chem. Soc.* **2016**, *138*, 140–148.
- (13) Krishnadas, K. R.; Ghosh, D.; Ghosh, A.; Natarajan, G.; Pradeep, T. Structure-Reactivity Correlations in Metal Atom Substitutions of Monolayer-Protected Noble Metal Alloy Clusters. *J. Phys. Chem. C* **2017**, *121*, 23224–23232.
- (14) Krishnadas, K. R.; Baksi, A.; Ghosh, A.; Natarajan, G.; Pradeep, T. Structure-Conserving Spontaneous Transformations between Nanoparticles. *Nat. Commun.* **2016**, *7*, 13447.
- (15) AbdulHalim, L. G.; Bootharaju, M. S.; Tang, Q.; Del Gobbo, S.; AbdulHalim, R. G.; Eddaoudi, M.; Jiang, D.-e.; Bakr, O. M. Ag<sub>29</sub>(Bdt)<sub>12</sub>(Tpp)<sub>4</sub>: A Tetraivalent Nanocluster. *J. Am. Chem. Soc.* **2015**, *137*, 11970–11975.
- (16) Tian, S.; Li, Y.-Z.; Li, M.-B.; Yuan, J.; Yang, J.; Wu, Z.; Jin, R. Structural Isomerism in Gold Nanoparticles Revealed by X-Ray Crystallography. *Nat. Commun.* **2015**, *6*, 8667.
- (17) Artymiuk, P. J.; Blake, C. C. F.; Rice, D. W.; Wilson, K. S. The Structures of the Monoclinic and Orthorhombic Forms of Hen Egg-White Lysozyme at 6 Å Resolution. *Acta Crystallogr., Sect. B* **1982**, *38*, 778–783.
- (18) Curry, S.; Mandelkow, H.; Brick, P.; Franks, N. Crystal Structure of Human Serum Albumin Complexed with Fatty Acid Reveals an Asymmetric Distribution of Binding Sites. *Nat. Struct. Biol.* **1998**, *5*, 827–835.
- (19) Cheng, Y.; Grigorieff, N.; Penczek, P. A.; Walz, T. A Primer to Single-Particle Cryo-Electron Microscopy. *Cell* **2015**, *161*, 438–449.
- (20) Cheng, Y. Single-Particle Cryo-Em at Crystallographic Resolution. *Cell* **2015**, *161*, 450–457.
- (21) Jadzinsky, P. D.; Calero, G.; Ackerson, C. J.; Bushnell, D. A.; Kornberg, R. D. Structure of a Thiol Monolayer-Protected Gold Nanoparticle at 1.1 Å Resolution. *Science* **2007**, *318*, 430–433.
- (22) Chaudhari, K.; Xavier, P. L.; Pradeep, T. Understanding the Evolution of Luminescent Gold Quantum Clusters in Protein Templates. *ACS Nano* **2011**, *5*, 8816–8827.
- (23) Chevrier, D. M.; et al. Structure and Formation of Highly Luminescent Protein-Stabilized Gold Clusters. *Chem. Sci.* **2018**, *9*, 2782–2790.
- (24) Baksi, A.; Mitra, A.; Mohanty, J. S.; Lee, H.; De, G.; Pradeep, T. Size Evolution of Protein-Protected Gold Clusters in Solution: A Combined SxS-Ms Investigation. *J. Phys. Chem. C* **2015**, *119*, 2148–2157.
- (25) Ghosh, D.; Baksi, A.; Mudella, S. K.; Nag, A.; Ganayee, M. A.; Subramanian, V.; Pradeep, T. Gold-Induced Unfolding of Lysozyme: Toward the Formation of Luminescent Clusters. *J. Phys. Chem. C* **2017**, *121*, 13335–13344.
- (26) Katta, V.; Chait, B. T. Hydrogen/Deuterium Exchange Electrospray Ionization Mass Spectrometry: A Method for Probing Protein Conformational Changes in Solution. *J. Am. Chem. Soc.* **1993**, *115*, 6317–6321.
- (27) Baksi, A.; Xavier, P. L.; Chaudhari, K.; Goswami, N.; Pal, S. K.; Pradeep, T. Protein-Encapsulated Gold Cluster Aggregates: The Case of Lysozyme. *Nanoscale* **2013**, *5*, 2009–2016.
- (28) Blout, E. R.; De Loze, C.; Asadourian, A. Deuterium Exchange of Water-Soluble Polypeptides and Proteins as Measured by Infrared Spectroscopy. *J. Am. Chem. Soc.* **1961**, *83*, 1895–1900.
- (29) Konermann, L.; Pan, J.; Liu, Y.-H. Hydrogen Exchange Mass Spectrometry for Studying Protein Structure and Dynamics. *Chem. Soc. Rev.* **2011**, *40*, 1224–1234.
- (30) Liu, C.-L.; et al. Insulin-Directed Synthesis of Fluorescent Gold Nanoclusters: Preservation of Insulin Bioactivity and Versatility in Cell Imaging. *Angew. Chem., Int. Ed.* **2011**, *50*, 7056–7060.
- (31) Codreanu, S. G.; Thompson, L. C.; Hachey, D. L.; Dirr, H. W.; Armstrong, R. N. Influence of the Dimer Interface on Glutathione Transferase Structure and Dynamics Revealed by Amide H/D Exchange Mass Spectrometry. *Biochemistry* **2005**, *44*, 10605–10612.
- (32) Ghosh, R.; Sahoo, A. K.; Ghosh, S. S.; Paul, A.; Chattopadhyay, A. Blue-Emitting Copper Nanoclusters Synthesized in the Presence of Lysozyme as Candidates for Cell Labeling. *ACS Appl. Mater. Interfaces* **2014**, *6*, 3822–3828.
- (33) Goswami, N.; Giri, A.; Bootharaju, M. S.; Xavier, P. L.; Pradeep, T.; Pal, S. K. Copper Quantum Clusters in Protein Matrix: Potential Sensor of Pb<sup>2+</sup> Ion. *Anal. Chem.* **2011**, *83*, 9676–9680.
- (34) Wang, C.; Wang, C.; Xu, L.; Cheng, H.; Lin, Q.; Zhang, C. Protein-Directed Synthesis of Ph-Responsive Red Fluorescent Copper Nanoclusters and Their Applications in Cellular Imaging and Catalysis. *Nanoscale* **2014**, *6*, 1775–1781.
- (35) Moreau, S.; Awade, A. C.; Molle, D.; Le Graet, Y. e.; Brule, G. Hen Egg White Lysozyme-Metal Ion Interactions: Investigation by Electrospray Ionization Mass Spectrometry. *J. Agric. Food Chem.* **1995**, *43*, 883–889.
- (36) Gokel, G. W.; Barbour, L. J.; Ferdani, R.; Hu, J. Lariat Ether Receptor Systems Show Experimental Evidence for Alkali Metal Cation-Π Interactions. *Acc. Chem. Res.* **2002**, *35*, 878–886.
- (37) Gokel, G. W.; De Wall, S. L.; Meadows, E. S. Experimental Evidence for Alkali Metal Cation-Π Interactions. *Eur. J. Org. Chem.* **2000**, 2967–2978.
- (38) Wouters, J. Cation-Π (Na<sup>+</sup>-Trp) Interactions in the Crystal Structure of Tetragonal Lysozyme. *Protein Sci* **1998**, *7*, 2472–2475.

## Supporting Information

### Conformational Changes of Protein upon Encapsulation of Noble Metal Clusters: An Investigation by Hydrogen/Deuterium Exchange Mass Spectrometry

*Debasmita Ghosh,<sup>1</sup> Sathish Kumar Mudedla,<sup>2</sup> Md Rabiul Islam,<sup>1</sup> Venkatesan Subramanian,<sup>2</sup> and Thalappil Pradeep<sup>1\*</sup>*

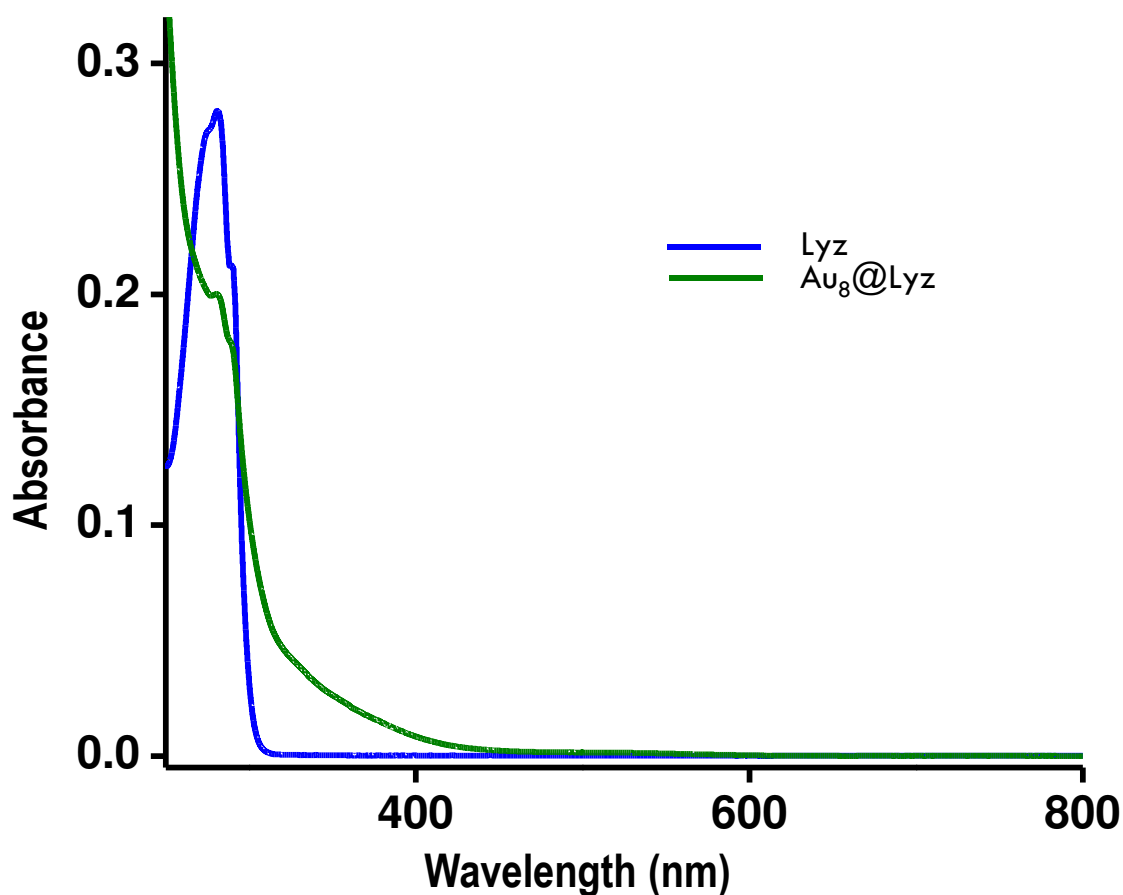
<sup>1</sup>DST Unit of Nanoscience (DST UNS) & Thematic Unit of Excellence (TUE), Department of Chemistry, Indian Institute of Technology Madras, Chennai-600036, India

<sup>2</sup>Chemical Laboratory, CSIR-Central Leather Research Institute, Adyar, Chennai- 600020

#### Table of Contents

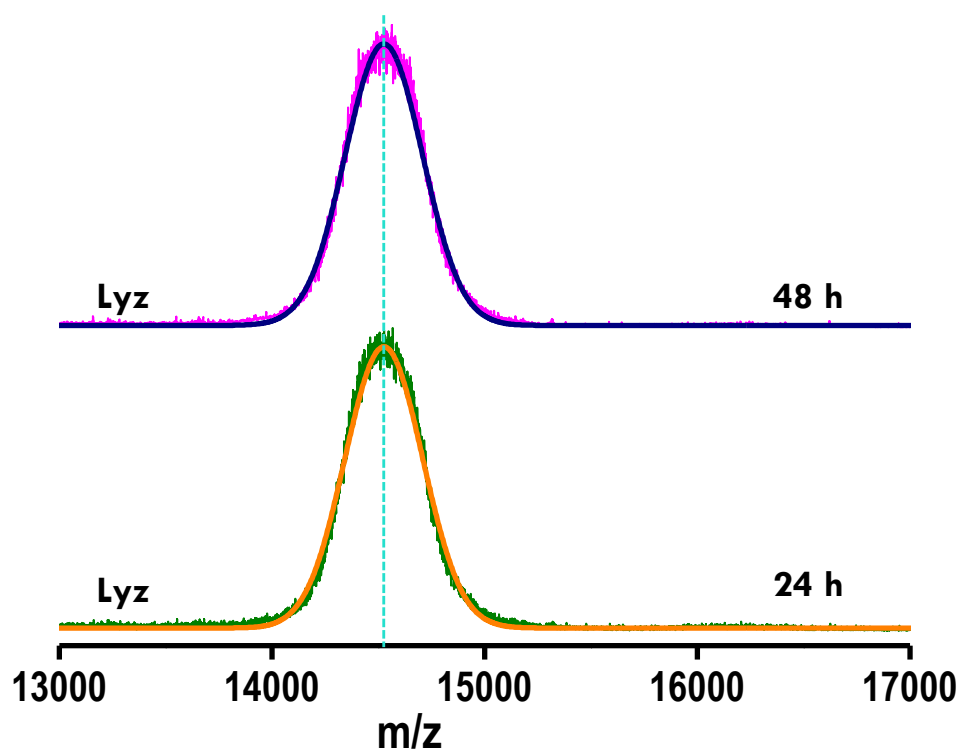
Number	Description	Page Number
Figure S1	UV-vis spectra of Lyz and Au <sub>8</sub> @Lyz.	S2
Figure S2	MALDI MS spectra of Lyz after 24 h and 48 h of H/D exchange	S3
Figure S3	IR spectra of heat-treated Lyz in D <sub>2</sub> O	S4
Figure S4	Simulated structure of Lyz and Au <sub>8</sub> -Lyz	S5
Figure S5	Simulated data of breaking of H-bonds in Au <sub>8</sub> -Lyz	S6
Figure S6	Time dependent H/D exchange in 20% D <sub>2</sub> O	S7
Figure S7	Time dependent H/D exchange in 50% D <sub>2</sub> O	S8
Figure S8	Time dependent H/D exchange in 100% D <sub>2</sub> O	S9

Figure S9	The mapped surface area of Lyz and Au <sub>8</sub> -Lyz	S10
Figure S10	Interaction of Cu <sup>2+</sup> with Lyz	S11
Figure S11	Time dependent H/D exchange in 50% D <sub>2</sub> O (Cu <sub>n</sub> -Lyz)	S12
Figure S12	Time dependent H/D exchange in 100% D <sub>2</sub> O(Cu <sub>n</sub> -Lyz)	S13
Figure S13	XPS study of the Au <sub>8</sub> @Lyz	S14
Figure S14	Interaction of Lyz with alkali metals	S15



**Figure S1:** UV-vis spectra of Lyz and Au<sub>8</sub>@Lyz. Protein protected clusters showed almost featureless absorption spectrum unlike monolayer protected clusters; the later exhibit distinct features that can give information about the core formed. In the case of protein protected clusters, mostly ill-defined spectra have been reported with a peak near 280 nm corresponding to absorption of the protein.





**Figure S2:** MALDI MS spectra of Lyz after 24 h and 48 h of hydrogen/deuterium exchange. The spectra have been fitted.

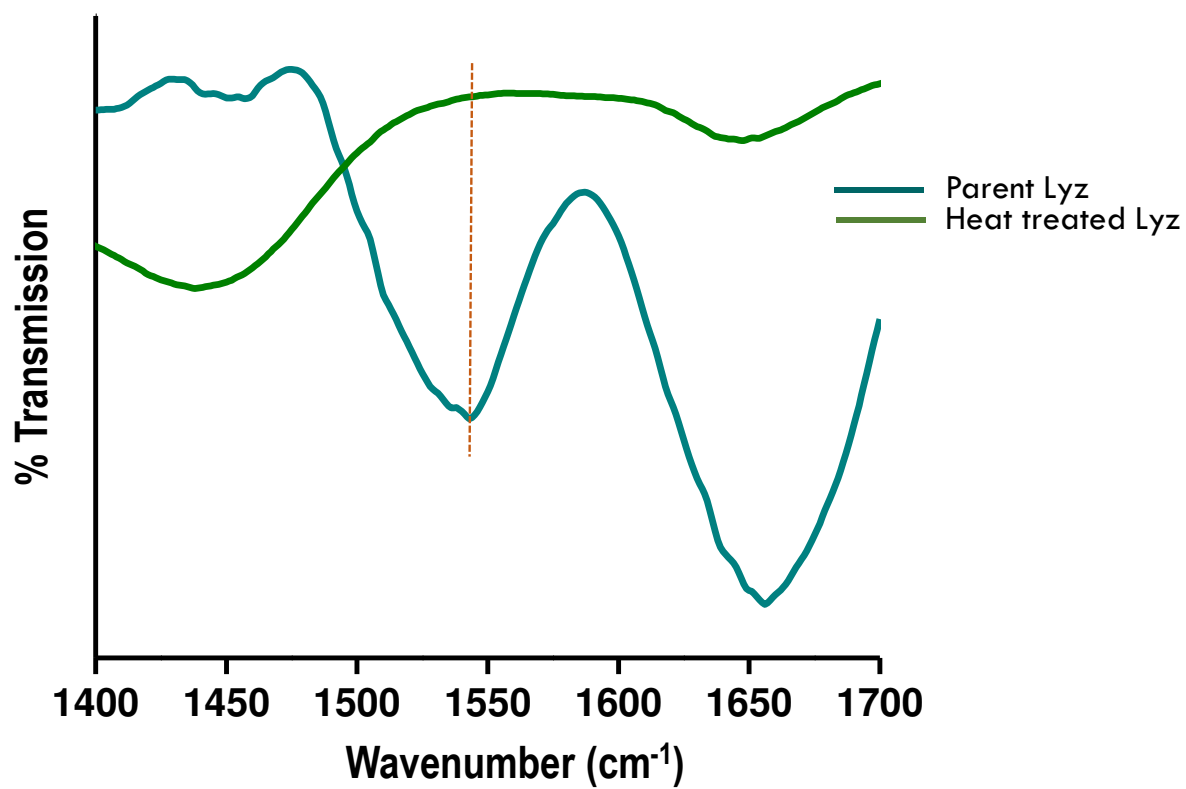


**Figure S3:** IR spectrum (in the amide region) of Lyz in D<sub>2</sub>O, after heating for 2 hours at 65°C. This shows the disappearance of the band near 1550 cm<sup>-1</sup>.

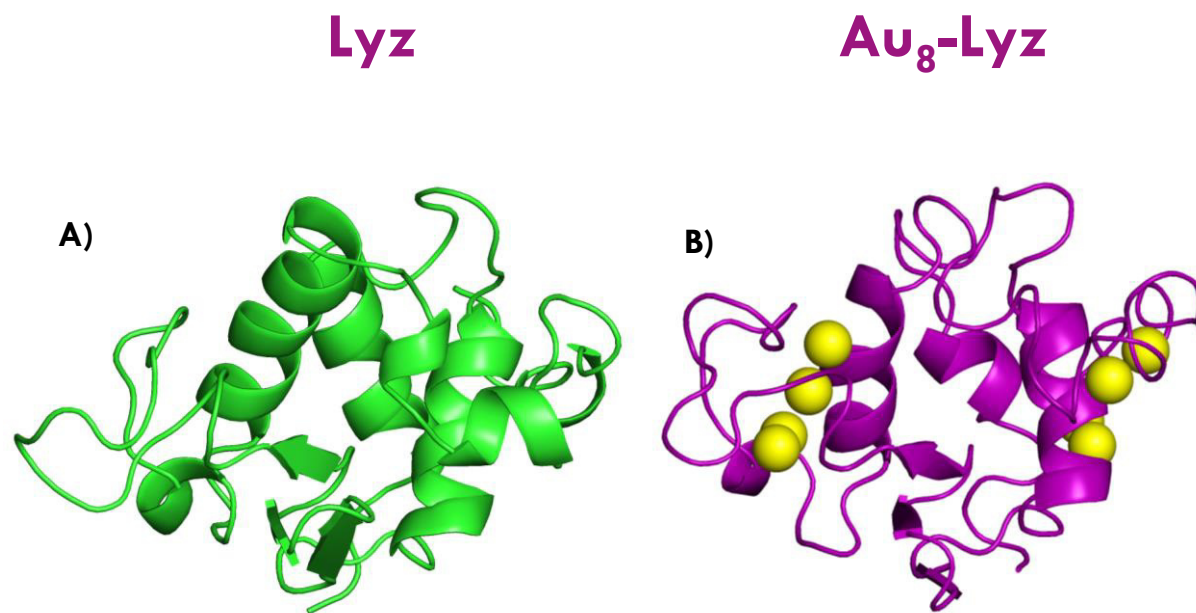
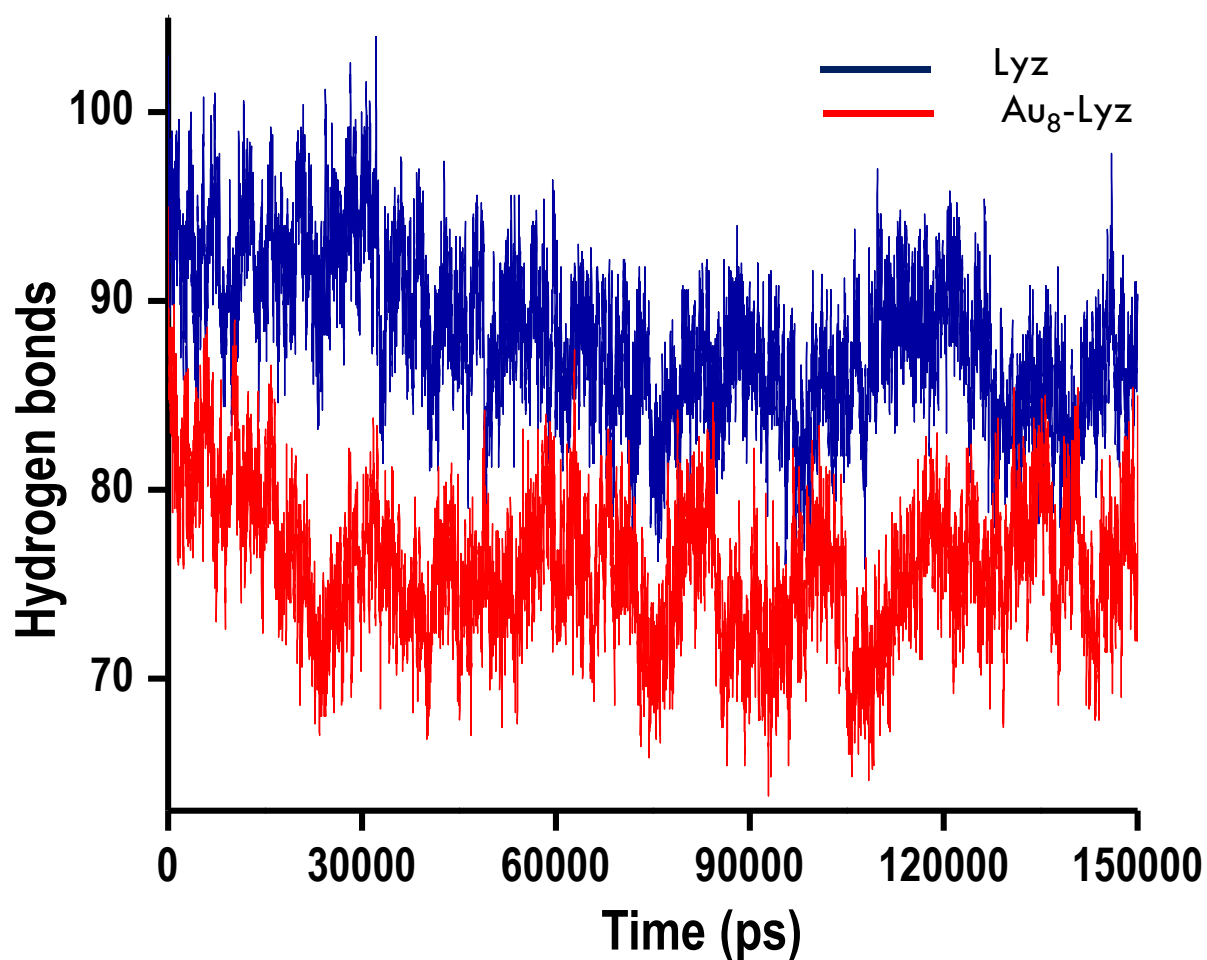


**Figure S4:** Simulated structure (simulation for 150 ns) of Lyz (A) and Au<sub>8</sub>-Lyz (B). (B) Covalent binding of Au<sup>1+</sup> ions to cysteine of Lyz.



	Coil (%)	Beta sheet (%)	Beta bridge (%)	Bend (%)	Turn (%)	Helix (%)
Lyz	16	7	2	16	21	38
Au <sub>8</sub> -Lyz	17	4	1	21	34	23

**Figure S5:** Breaking of H-bonds with time for Lyz and Au<sub>8</sub>-Lyz. This simulated data show the decrease in H-bonds in Au<sub>8</sub>-Lyz adducts than in native Lyz, with time. Table represents the calculated secondary structure of each of the components in the case of Lyz and Au<sub>8</sub>-Lyz.

20%

Lyz

Au<sub>n</sub>-Lyz

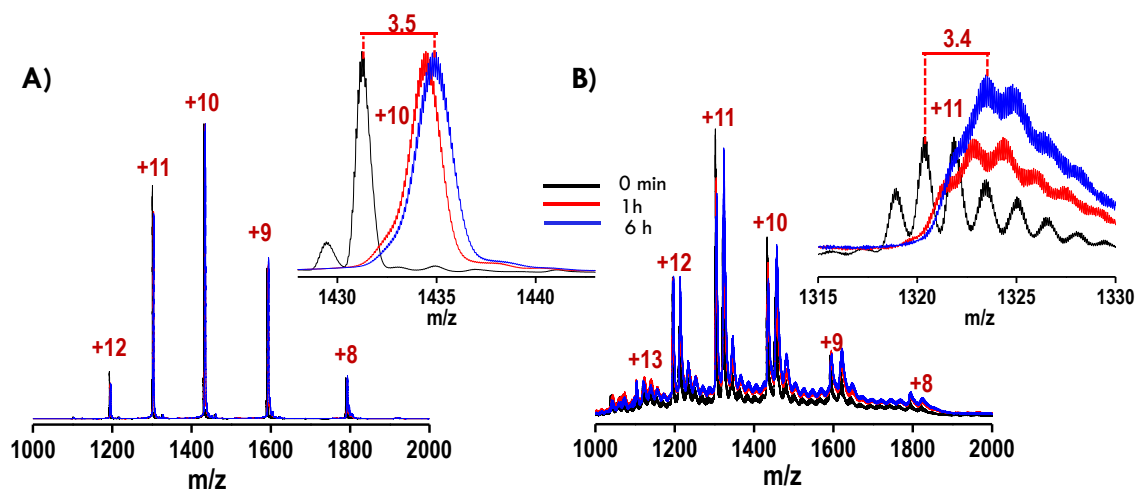


**Figure S6:** Time-dependent H/D exchange MS of Lyz (A), and Au<sub>n</sub>-Lyz (B) in 20% D<sub>2</sub>O. Inset of (A) shows the expanded view of Lyz in +10 charge state and inset of (B) shows the expanded view of in +11 charge state of Au<sub>n</sub>-Lyz. Comparison of both spectra revealed that in 20% D<sub>2</sub>O, the mass shift is the same for Lyz and Au<sub>n</sub>-Lyz.

50%

Lyz

Au<sub>n</sub>-Lyz

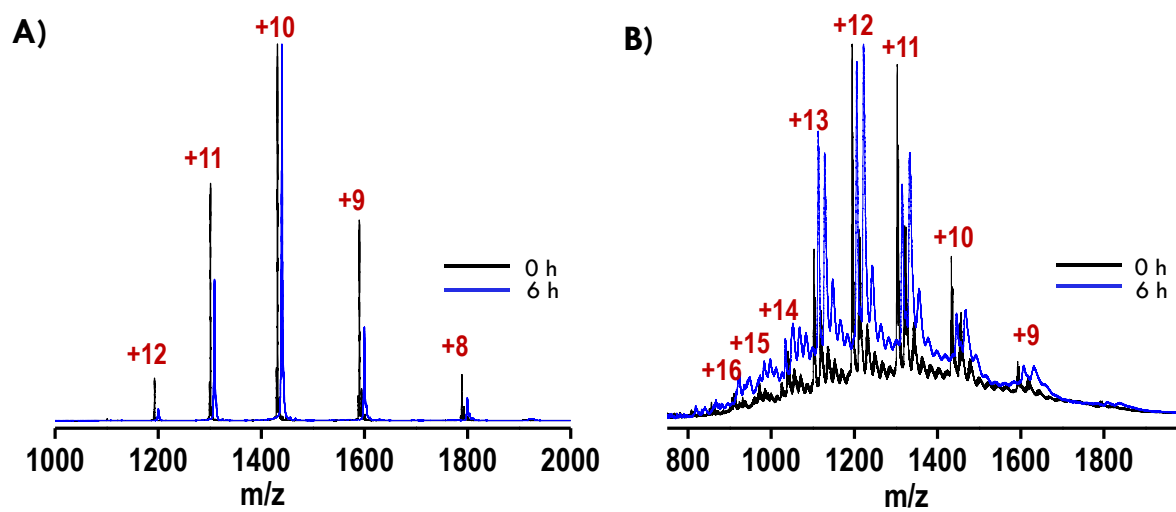


**Figure S7:** Time-dependent H/D exchange ESI MS of Lyz (A), and Au<sub>n</sub>-Lyz (B) in 50% D<sub>2</sub>O.

100%

Lyz

Au<sub>n</sub>-Lyz

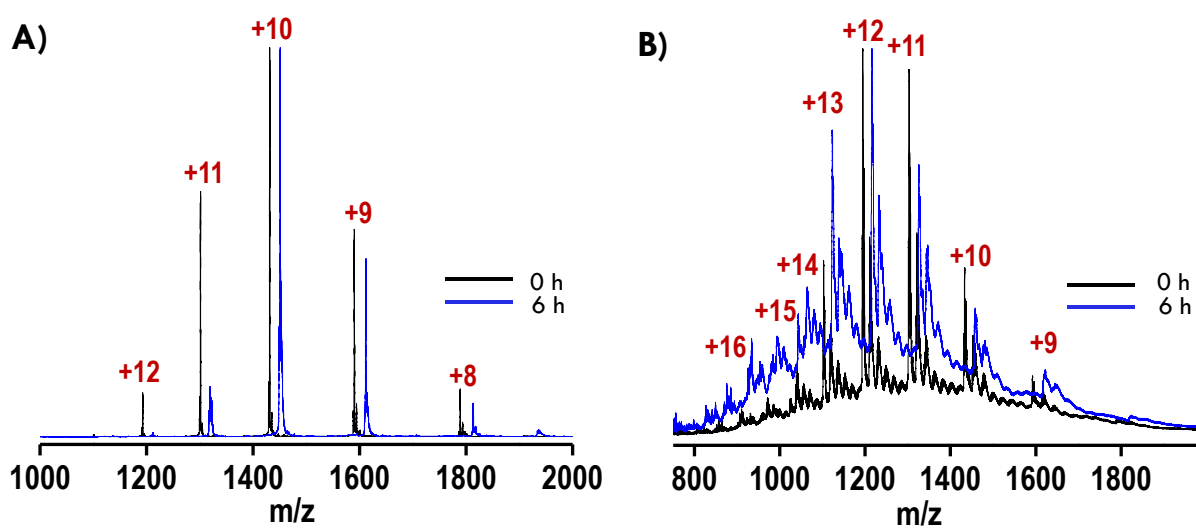


**Figure S8:** Time-dependent H/D exchange ESI MS of Lyz (A), and Au<sub>n</sub>-Lyz (B) in 100% D<sub>2</sub>O.



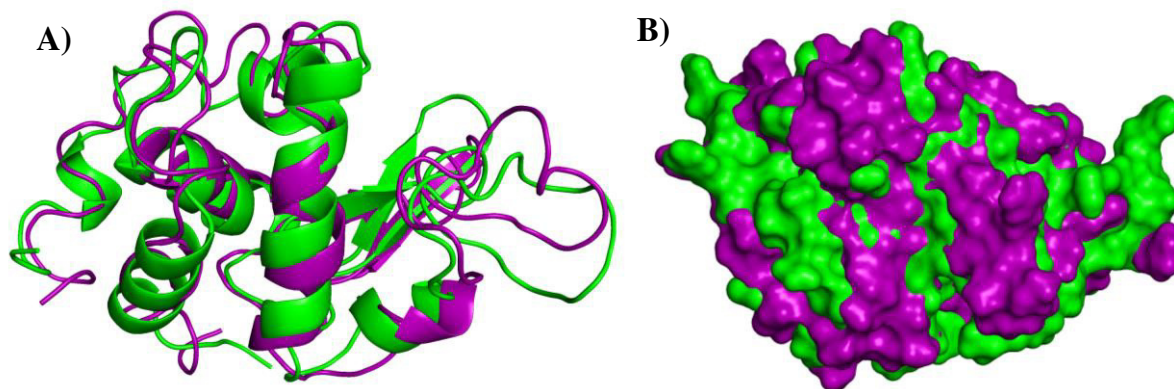


**Figure S9:** (A) Overlapped image of Lyz (green) and Au<sub>8</sub>-Lyz (purple). (B) The mapped surface area of Lyz and Au<sub>8</sub>-Lyz.

## Cu attachment

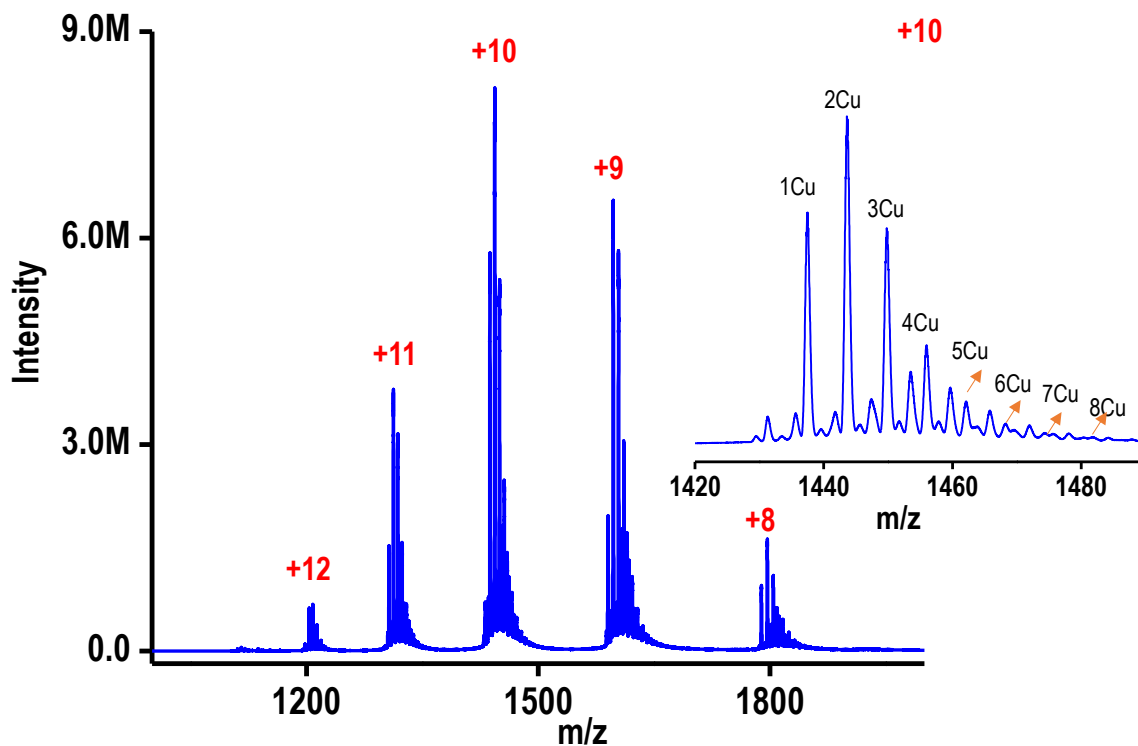


**Figure S10:** ESI MS of  $\text{Cu}_n\text{-Lyz}$  adduct; inset shows the expansion of +10 charge state. Interaction of  $\text{Cu}^{2+}$  with Lyz shows that a maximum of 8 Cu can attach with Lyz. Almost similar distribution of charges like in native Lyz suggests the difference in reactivity of Au and Cu with Lyz.

50%

$\text{Cu}_n\text{-Lyz}$

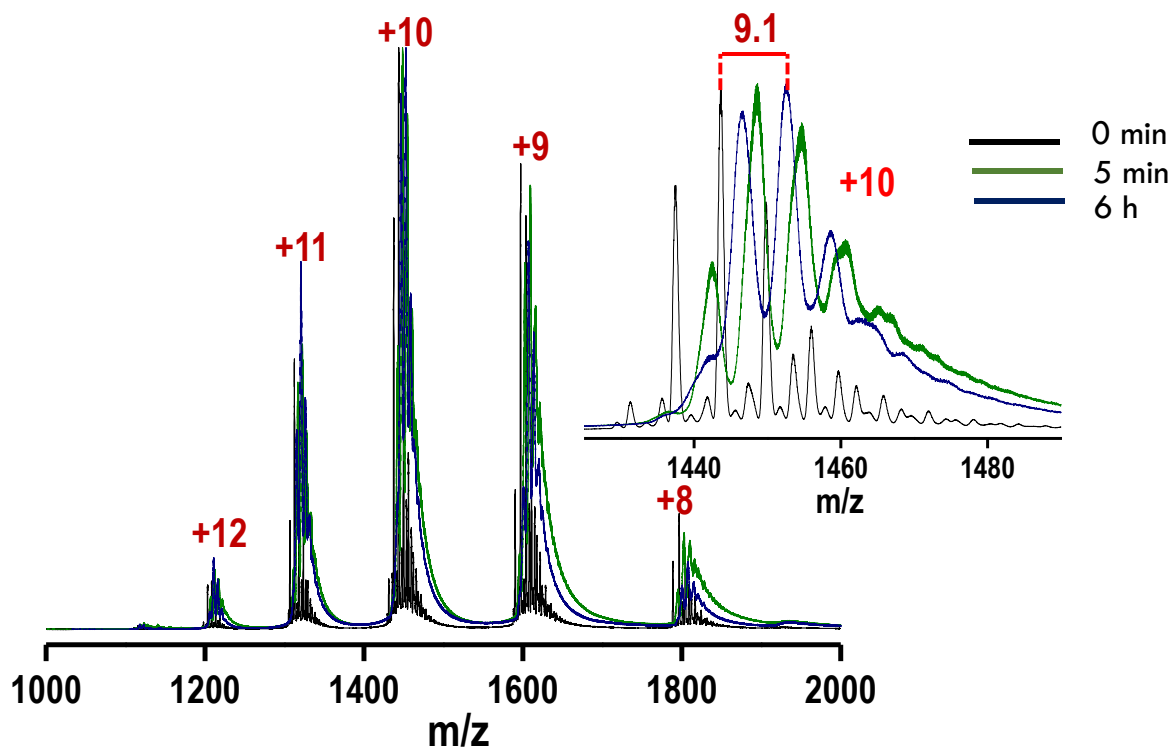


**Figure S11:** Time-dependent H/D exchange MS of  $\text{Cu}_n\text{-Lyz}$  in 50%  $\text{D}_2\text{O}$ . The inset shows the expanded view of  $\text{Cu}_n\text{-Lyz}$  in +10 charge state. A slow exchange like in native Lyz was observed in this case.

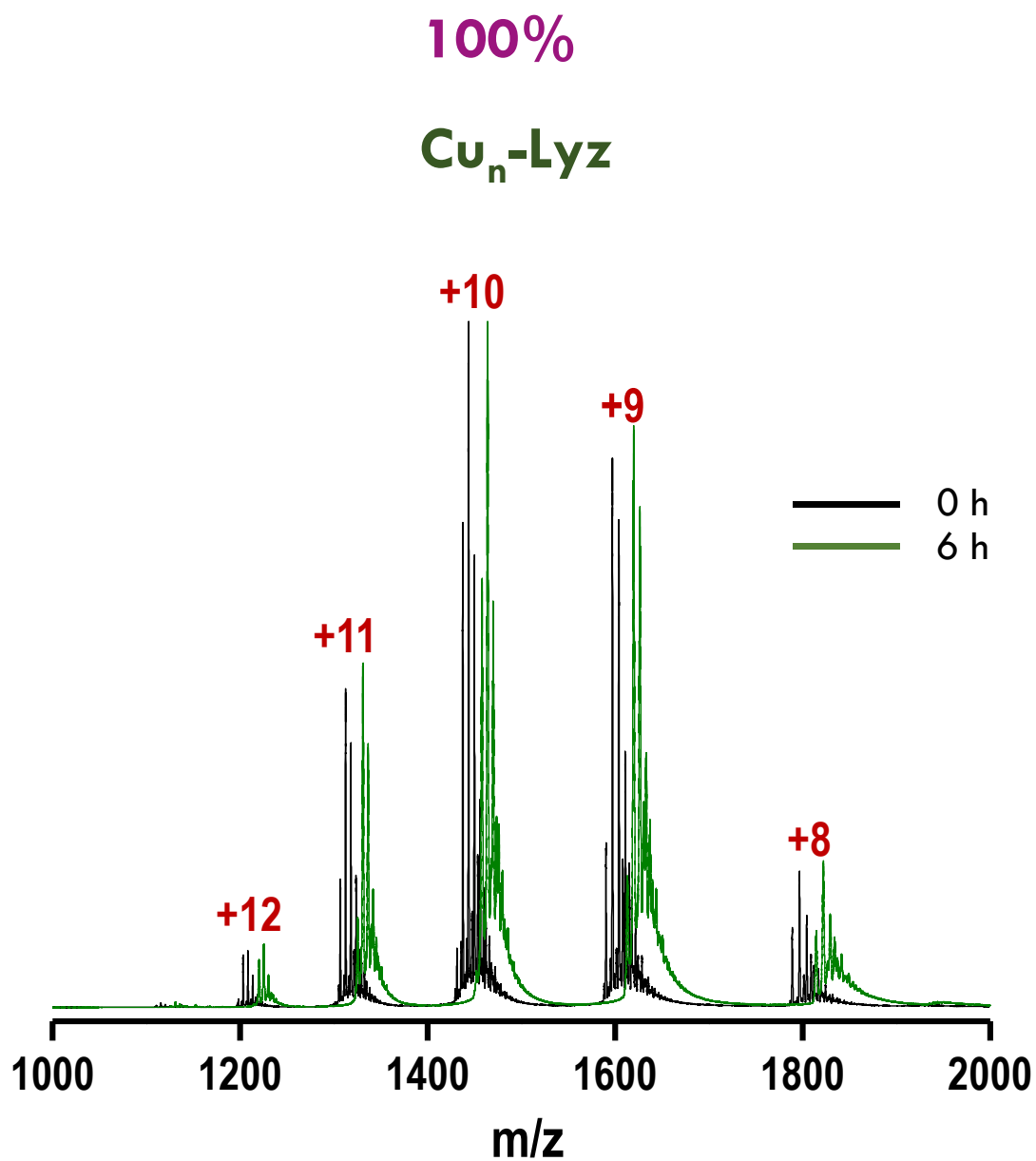


**Figure S12:** Time-dependent H/D exchange ESI MS of  $\text{Cu}_n\text{-Lyz}$  in 100%  $\text{D}_2\text{O}$ . ESI MS shows that the mass shift will be different for different charge states.

## XPS of the cluster

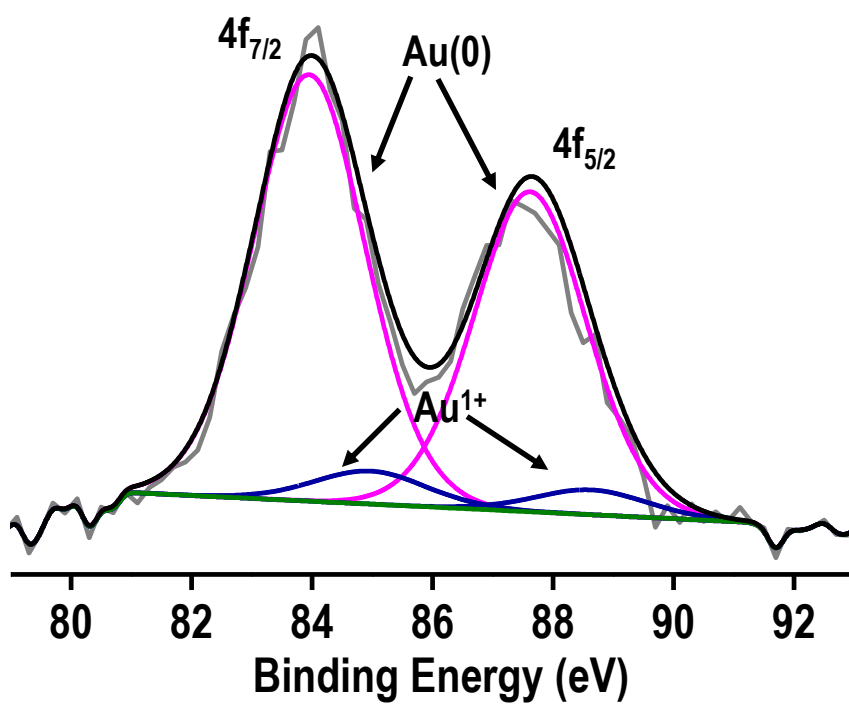


**Figure S13:** XPS data of Au<sub>8</sub>@Lyz cluster shows the presence of Au (0) and Au (I) in the 4f region.

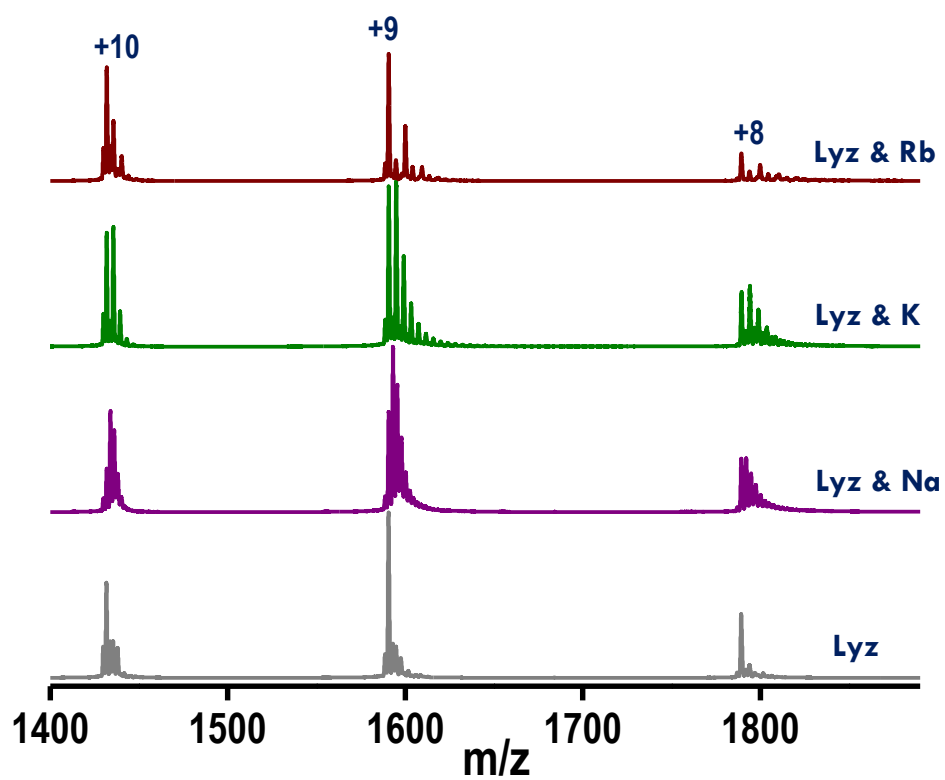


**Figure S14:** ESI MS of alkali metal attached Lyz adducts showing similar charge state distribution to the native protein in 100% D<sub>2</sub>O.

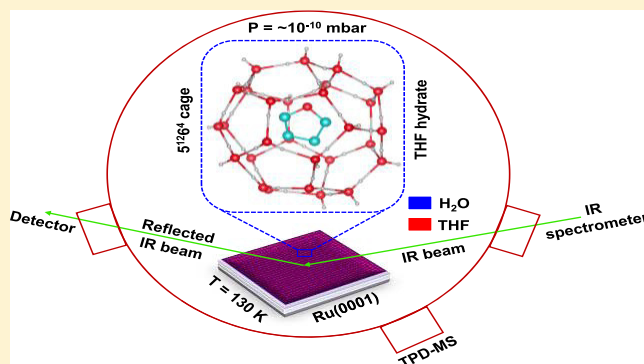
# Spontaneous Formation of Tetrahydrofuran Hydrate in Ultrahigh Vacuum

Jyotirmoy Ghosh, Radha Gobinda Bhui,† Gopi Ragupathy,‡ and Thalappil Pradeep\*<sup>§</sup>

DST Unit of Nanoscience (DST UNS) and Thematic Unit of Excellence (TUE), Department of Chemistry, Indian Institute of Technology Madras, Chennai 600036, India

## Supporting Information

**ABSTRACT:** Clathrate hydrates (CHs) typically nucleate under high-pressure conditions, but their existence in ultrahigh vacuum (UHV) is an open question. Here, we report the formation of tetrahydrofuran (THF) hydrate in UHV, using reflection absorption infrared spectroscopy (RAIRS). Annealing both sequentially and co-deposited mixtures of THF and H<sub>2</sub>O to 130 K for adequate time, originally prepared at 10 K, led to the formation of THF hydrate, at 10<sup>−10</sup> mbar. Nucleation of THF hydrate was associated with the crystallization of amorphous solid water. Crystallization kinetics was examined through isothermal kinetic measurements using RAIRS in the temperature range of 120–130 K. The kinetic measurements revealed that the THF hydrate formation was a diffusion-controlled process and the overall activation energy for the process was found to be ~23.12 kJ mol<sup>−1</sup>. This considerably lower activation energy as compared to that for the crystallization of pure ice established the spontaneity of the process. The results provide valuable insights into the low-pressure characteristics of CHs and associated thermodynamics.



## INTRODUCTION

Clathrate hydrates (CHs) are solid inclusion compounds, which are crystalline and contain guest molecules in the hydrogen-bonded water cages.<sup>1–3</sup> There are several guest molecules such as CH<sub>4</sub>, CO<sub>2</sub>, tetrahydrofuran (THF), etc., which could potentially form CHs at different conditions. These hydrates are found in ocean floor and permafrost regions of the earth.<sup>1</sup> CHs are important materials in terms of their wide applications in the areas of H<sub>2</sub> storage,<sup>4–7</sup> renewable energy,<sup>8</sup> CO<sub>2</sub> sequestrations,<sup>9</sup> and desalination.<sup>10</sup> High pressure and ambient<sup>11</sup> or low temperature<sup>12</sup> are the essential conditions for the formation of CHs. However, the requirement of high pressures for the nucleation of CHs is disadvantageous from an application point of view. Our present study reveals that such compounds are indeed feasible to form at extreme conditions. We have recently shown that methane and CO<sub>2</sub> can form hydrates at 10<sup>−10</sup> mbar and 10–30 K, conditions analogous to space.<sup>13</sup> The presence of CHs in space was speculated for long.<sup>3,14</sup> Interaction of the trapped species with vapor-deposited amorphous solid water (ASW) plays important roles in the formation of CHs. This implies the feasibility of CH formation over a wide temperature and pressure window.

ASW has significant relevance to chemical,<sup>15,16</sup> biological,<sup>17</sup> physical,<sup>18</sup> astrophysical,<sup>19,20</sup> and materials sciences.<sup>21,22</sup> It is highly porous and formed by vapor deposition at temperatures below 120 K. Its porous morphology facilitates the entrapment

of different species within the ASW network.<sup>20,23</sup> Interaction of the entrapped species with ASW can lead to different phenomena like phase segregation,<sup>24</sup> homogeneous mixing,<sup>25</sup> diffusion,<sup>26</sup> H-bonding,<sup>27</sup> chemical reaction,<sup>28</sup> CH formation,<sup>13,29–31</sup> etc. Among different known CHs, THF hydrate has drawn special interest as it can recover CO<sub>2</sub> from flue gas<sup>32</sup> as well as store hydrogen.<sup>5,6,33</sup> In general, THF forms the s-II hydrate structure below  $T = 277.6$  K and at 5 kPa (50 mbar).<sup>34,35</sup> According to the calculation of dissociation pressures of different hydrates,<sup>3</sup> it should be stable at low pressures and low temperatures. In view of the possible formation of CHs under vacuum or low pressure, various methods were developed to observe this process, such as direct vapor deposition,<sup>12</sup> annealing an appropriate solid mixture to the required temperature,<sup>31</sup> and interaction of the guest molecule in the vapor phase with ice nanocrystals.<sup>36,37</sup> Richardson et al. showed that THF hydrate can be formed under vacuum ( $\sim 1 \mu$  or  $\sim 1.33 \times 10^{-3}$  mbar) by vapor deposition.<sup>31</sup> Hallbrucker and co-workers have shown the formation of CHs of NO,<sup>38</sup> N<sub>2</sub>,<sup>39–41</sup> O<sub>2</sub>,<sup>39–43</sup> CO,<sup>40</sup> and Ar<sup>40</sup> from vapor-deposited ASW in a high vacuum ( $\sim 10^{-6}$  mbar) experimental chamber, which was subsequently pressurized with 1 bar “external” pressure of the guest molecule. Here, we

Received: May 8, 2019

Revised: June 12, 2019

Published: June 13, 2019



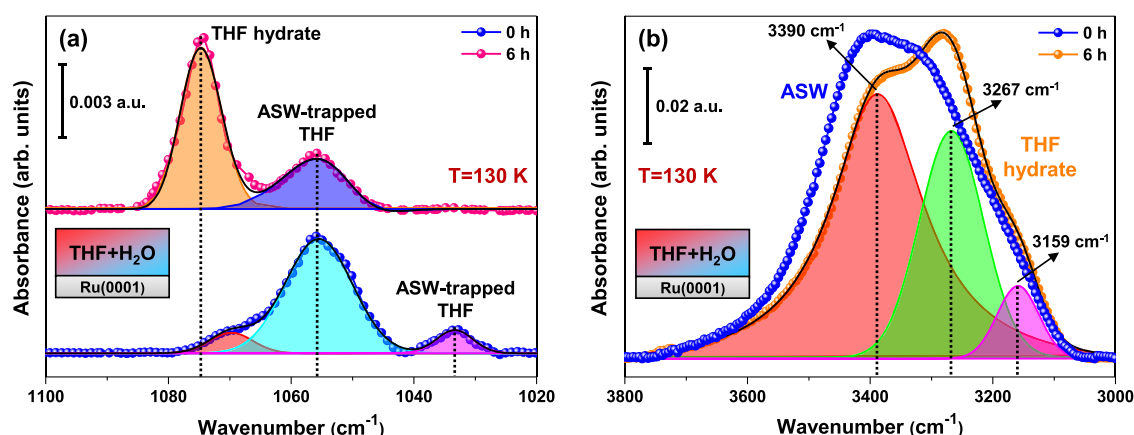


**Figure 1.** Isothermal time-dependent RAIR spectra of 300 MLs of a THF/H<sub>2</sub>O (1:5) mixture (a) in the asymmetric C–O stretching region and (b) in the O–H stretching region, at 130 K. Prior to data collection, the mixture was co-deposited on the Ru(0001) substrate at 10 K and annealed at a rate of 2 K min<sup>−1</sup> to 130 K. In (b), the spectrum labeled 6 h was deconvoluted to show its components and the spectrum of ASW was multiplied by 1.5 to match the intensity with the former.

have studied the formation of THF hydrate at  $\sim 10^{-10}$  mbar and 120–130 K by surface-sensitive reflection absorption infrared spectroscopy (RAIRS). We have also studied the associated kinetics and explored the thermodynamic parameters. THF is known to be a stabilizing guest or promoter for the formation of binary CHs.<sup>33,44</sup> So far, there are no experimental studies to the best of our knowledge on the formation of THF hydrate at extremely low pressures like  $\sim 10^{-10}$  mbar. This study can help in further exploring the formation and stabilization of binary CHs in ultrahigh vacuum (UHV).

In the experiments, we co-deposited a 1:5 mixture of THF and water from their vapor phase to a precooled Ru(0001) substrate at 10 K inside a UHV chamber.<sup>45</sup> Annealing the mixture to 130 K and keeping it for 6 h led to the formation of THF hydrate. RAIRS was used to monitor hydrate formation. Evolution of THF hydrate showed temperature-dependent kinetics, which was established by carrying out a time-dependent RAIRS study of similar systems at different temperatures. The time-dependent RAIRS study at 130 K also showed the formation of THF hydrate in the case of sequential deposition (THF@H<sub>2</sub>O).

## EXPERIMENTAL SECTION

The experiments were conducted in a UHV chamber with a base pressure of  $\sim 5 \times 10^{-10}$  mbar. The UHV chamber has been described in detail elsewhere.<sup>45</sup> Briefly, the chamber was equipped with RAIRS and temperature-programmed desorption mass spectrometry facilities. The substrate, a Ru(0001) single crystal, was cooled by a closed-cycle helium cryostat to 10 K. The substrate temperature was measured using a K-type thermocouple wire connected to it. The substrate was cleaned by heating to 400 K multiple times prior to vapor deposition. Desired molecular solid films were grown on Ru(0001) by vapor deposition at 10 K. The surface coverage of molecular solids was represented in terms of monolayers (MLs)<sup>46</sup> assuming that  $1.33 \times 10^{-6}$  mbar s = 1 ML, which was estimated to contain  $\sim 1.1 \times 10^{15}$  molecules cm<sup>−2</sup>. In a number of earlier reports,<sup>47,48</sup> such calculation was used for the estimation of surface coverages. One point to be noted is that all of the experiments were performed under multilayer deposition conditions; therefore, the substrate does not play any role in the processes mentioned here.

THF (Sigma-Aldrich, 99%) and H<sub>2</sub>O (Milli-Q, 18.2 MΩ resistivity) were purified by multiple freeze–pump–thaw cycles. The molecular solids of water and THF were prepared on a Ru(0001) substrate by sequential and co-deposition methods as per the need of the experiment. The vapors of THF and water were backfilled into the UHV chamber through variable all-metal leak valves. For the deposition of 300 MLs of (1:5) mixed THF and water, the chamber was backfilled at a total pressure of  $\sim 5 \times 10^{-7}$  mbar (where THF and water partial pressures were  $1 \times 10^{-7}$  and  $4 \times 10^{-7}$  mbar, respectively, monitored by the mass spectrometer during deposition) and the mixture was exposed to the substrate for 10 min. To prepare other mixtures, the partial pressures of the individual components were set as per their requirement. The deposited mixed ice was slowly annealed (heating rate = 2 K min<sup>−1</sup>) to 130 K, and time-dependent RAIR spectra were recorded. RAIRS measurements were performed using a Bruker FT-IR spectrometer, Vertex 70 with a liquid-nitrogen-cooled mercury cadmium telluride detector. The IR beam path outside the UHV chamber was purged with dry nitrogen gas. All RAIR spectra were collected in the 4000–550 cm<sup>−1</sup> range with 2 cm<sup>−1</sup> spectral resolution, averaged over 512 scans.

**Computational Details.** The three most common cages of CHs were considered for calculations. Geometry optimizations for the water cages and the host–guest complexes were performed using the B3LYP method in conjunction with the 6-311++G(d,p) basis set. All of the optimized geometries in this work were confirmed to be minima in the potential energy surface by the absence of imaginary frequencies in vibrational frequency analysis. It was shown that this basis set produced quite well all of the geometries, frequencies, and electric properties of THF hydrate.<sup>49</sup> The electronic structure calculations were performed using the GAUSSIAN 09 program.<sup>50</sup> The input configurations of the water cages were taken from our previous work and were subsequently optimized.<sup>13</sup> The optimized structures corresponding to the 5<sup>12</sup>, 5<sup>12</sup>6<sup>2</sup>, and 5<sup>12</sup>6<sup>4</sup> cages are shown later. It was observed that the 5<sup>12</sup>6<sup>4</sup> THF hydrate cage was quite stable; stability also depends on the size of the guest molecule.

## RESULTS AND DISCUSSION

Figure 1a shows the RAIR spectra of 300 MLs of a THF/H<sub>2</sub>O mixture (1:5), which was co-deposited at 10 K on the

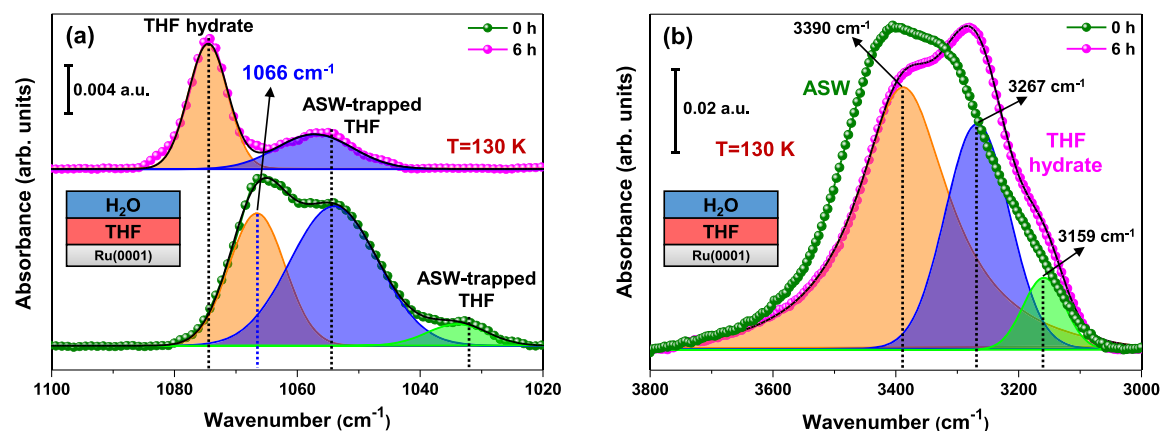


**Figure 2.** Time-dependent RAIR spectra of 300 MLs of a THF@H<sub>2</sub>O mixture (1:1) in the (a) asymmetric C–O stretching region and (b) O–H stretching region, which was sequentially deposited at 10 K on the Ru(0001) substrate. This mixture was annealed at a rate of 2 K min<sup>−1</sup> to 130 K. In (b), the spectrum labeled 6 h was deconvoluted to show its components and the spectrum of ASW was multiplied by 1.5 to match the intensity with the former.

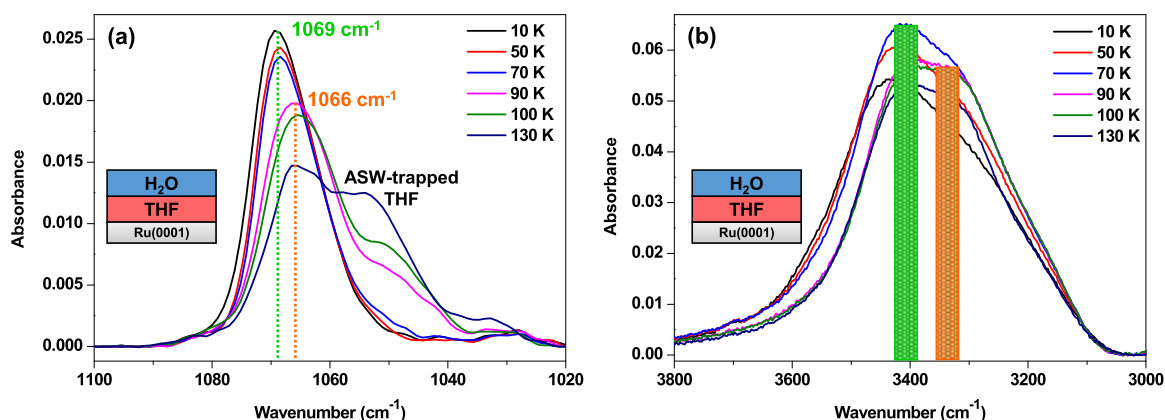


**Figure 3.** Temperature-dependent RAIR spectra of 300 MLs of a THF@H<sub>2</sub>O mixture (1:1) in the (a) asymmetric C–O stretching region and (b) O–H stretching region, which was sequentially deposited at 10 K on the Ru(0001) substrate. The sequential deposition was carried by condensing 150 MLs of H<sub>2</sub>O film over the same coverage of THF film, thus making it a (1:1) mixture. This mixture was annealed at 2 K min<sup>−1</sup> heating rate, and the spectra were collected.

Ru(0001) substrate. After deposition, it was slowly heated at 2 K min<sup>−1</sup> to 130 K and kept at this temperature for 6 h. Water is known to have orientational freedom at this temperature.<sup>51</sup> Due to such motions, molecular organization can occur in the process of annealing. We note that isothermal annealing for extended periods on the order of the tens of hours was essential to form hydrates of methane at cryogenic conditions.<sup>13</sup> The RAIR spectrum was measured immediately after heating to 130 K, which represents the 0 h spectrum. Here, the asymmetric C–O stretching band of THF showed two peaks at ~1034 and ~1053 cm<sup>−1</sup>, which were due to THF trapped in different sites of ASW.<sup>31</sup> The shoulder at 1070 cm<sup>−1</sup> converted gradually to a new peak at ~1074 cm<sup>−1</sup> after 6 h at 130 K (time-dependent spectra for each time interval are presented in Figure S1). This new peak is the characteristic feature of the asymmetric C–O stretching of THF hydrate.<sup>27,30,49,52</sup> It serves as a convenient indicator of THF hydrate since it lies well above the IR peak positions of other likely condensed phases of THF.<sup>30,31,36</sup> The intensity of this new peak continued to increase over time, while the intensity of other two peaks reduced gradually. After 6 h, the intensity of this new peak reached a maximum, whereas that of the 1034 cm<sup>−1</sup> peak was reduced almost to zero. This suggests the conversion of THF hydrate from the ASW-trapped THF.

Figure 1b depicts the corresponding data in the O–H stretching region. The broad peak present originally got ordered and red-shifted with time, which is an indication of crystallization.<sup>53–55</sup> Therefore, it can be concluded that THF gradually transformed into its hydrate structure at 130 K over 6 h; consequently, the morphology of the ice film turns to crystalline from its amorphous phase. The O–H stretching band for the THF hydrate was deconvoluted to show its components. To eliminate the possibility of self-crystallization of ice, we have shown in Figure S2a,b that ice by itself is not capable of forming its crystalline analogue over time at 120 and 130 K. It needs a higher temperature (~145 K; crystallization temperature of ice) in the absence of a guest molecule.<sup>51</sup>

We further investigated whether co-deposition was a prerequisite for hydrate formation. To check this, 150 MLs of THF were first deposited on Ru(0001) at 10 K, and subsequently, the film was covered with 150 MLs of H<sub>2</sub>O. This sequential deposition is represented as THF@H<sub>2</sub>O. It was annealed at 2 K min<sup>−1</sup> to 130 K, and time-dependent spectra were collected as shown in Figure 2. The asymmetric C–O stretching region in Figure 2a shows IR features at 1066, 1053, and 1034 cm<sup>−1</sup> at 0 h at 130 K. These two peaks at ~1034 and ~1053 cm<sup>−1</sup> are due to THF trapped in different sites of ASW, as explained earlier. The origin of the ~1066 cm<sup>−1</sup> peak can be

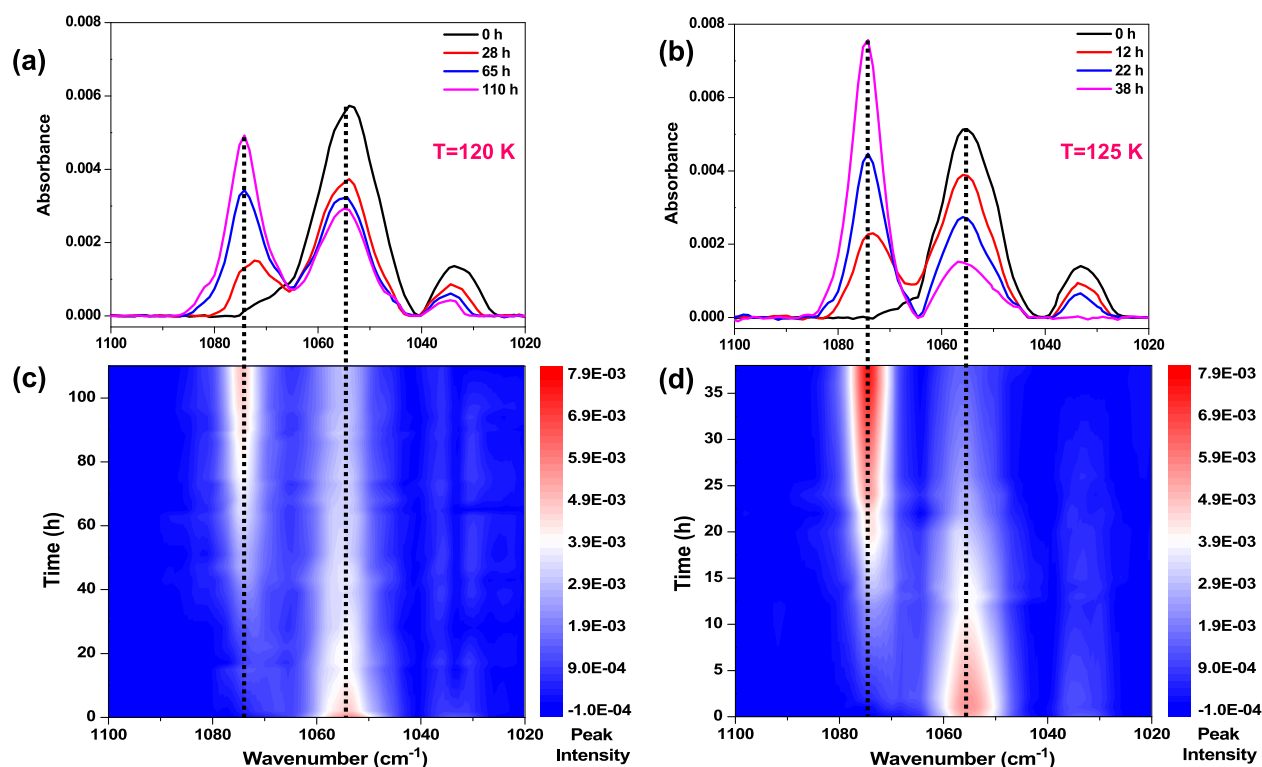


**Figure 4.** Time-dependent RAIR spectra of 300 MLs of a THF/H<sub>2</sub>O mixture (1:5) at (a) 120 K and (b) 125 K, in the asymmetric C–O stretching region; the mixture was co-deposited at 10 K on the Ru(0001) substrate. This mixture was annealed at 2 K min<sup>−1</sup> to the respective temperatures. Variation of the IR peak intensities of 1053 and 1074 cm<sup>−1</sup>, plotted as a contour plot as a function of time at (c) 120 K and (d) 125 K. Intensity values are on the right.

explained from temperature-dependent RAIR spectra of a THF@H<sub>2</sub>O mixture (Figure 3a), where the same peak was observed at 90 K and beyond. The peak at  $\sim 1066 \text{ cm}^{-1}$  is due to the formation of irregular THF crystallites. These crystallites form due to the diffusion of THF into the over layers of the ASW network, at  $\geq 90 \text{ K}$ . Pure THF undergoes crystallization at  $>90 \text{ K}$ , as observed from an independent study composed of 150 MLs (Figure S3). As shown in Figure 3b, at 90 K, the O–H stretching band shifts to a lower wavenumber, as indicated by the vertical bars of two different colors (green and orange). This again supports the formation of irregular THF crystallites within the ASW pores, which influences the ASW network. This type of diffusion of dichloromethane followed by crystallization has been reported previously.<sup>56</sup>

Interestingly, the sequential deposition does not lead to the formation of THF hydrate just by annealing, as the characteristic peak ( $\sim 1074 \text{ cm}^{-1}$ ) of the same was not observed in Figure 3a. However, the formation of THF hydrate was observed only when this THF@H<sub>2</sub>O film was kept at 130 K for a few hours (time-dependent spectra for each time interval are presented in Figure S4). The characteristic THF hydrate peak at  $\sim 1074 \text{ cm}^{-1}$  started appearing with time and becomes more prominent after 6 h as shown in Figure S4. Alongside, the broad O–H stretching band also attained crystalline features with time. Diffusion of THF into the overlayer ice network took place by annealing as explained before. After diffusion, a fraction of THF molecules got trapped as the ASW pores collapsed by annealing. Several studies suggest that ASW possesses a porous structure and the porosity disappears upon annealing.<sup>57–59</sup> After the diffusion and the collapse of ASW pores by annealing, THF molecules got sufficient time to interact with the water molecules, which

resulted in the THF hydrate. It can be concluded from here that both sequential and co-deposition methods can result in THF hydrate provided sufficient time for intermolecular interaction between THF and water. Diffusion plays a significant role in facilitating the interaction.

We examined the effect of temperature on the formation of THF hydrate. Figure 4a,b shows the time-dependent RAIR spectra of a 1:5 THF/H<sub>2</sub>O mixture in the asymmetric C–O stretching region of THF at 120 and 125 K, respectively. In contour plots (Figure 4c,d), the intensities of peaks at 1053 and 1074  $\text{cm}^{-1}$  are plotted to follow the hydrate formation. At 120 K, the rate of conversion of THF hydrate is so slow that even after 110 h it is incomplete (Figure 4a).

However, at 125 K, the rate of conversion is relatively faster as the 1074  $\text{cm}^{-1}$  peak showed substantial intensity within 38 h. Earlier, we observed that it required not less than 6 h at 130 K for substantial nucleation of THF hydrate. This demonstrates that the formation of THF hydrate is a temperature- and time-dependent process, and it follows certain kinetics.

It was observed that the formation of THF hydrate was associated with the crystallization of ASW (Figures 1b and 2b) and that the crystallization process showed both time- and temperature-dependent kinetics. The progress of crystallization was followed monitoring the evolution of the 1074  $\text{cm}^{-1}$  peak. Here, the intensity of the 1074  $\text{cm}^{-1}$  peak is proportional to the extent of clathrate formation, which in turn is a measure of crystallization of the ice. We have observed that with the enhancement of this peak intensity, the O–H stretching became more ordered, indicating crystallinity of the ice as shown in Figure S1. We have followed the crystallization kinetics by isothermal annealing experiments conducted at different temperatures. Here, we used the Avrami equation that

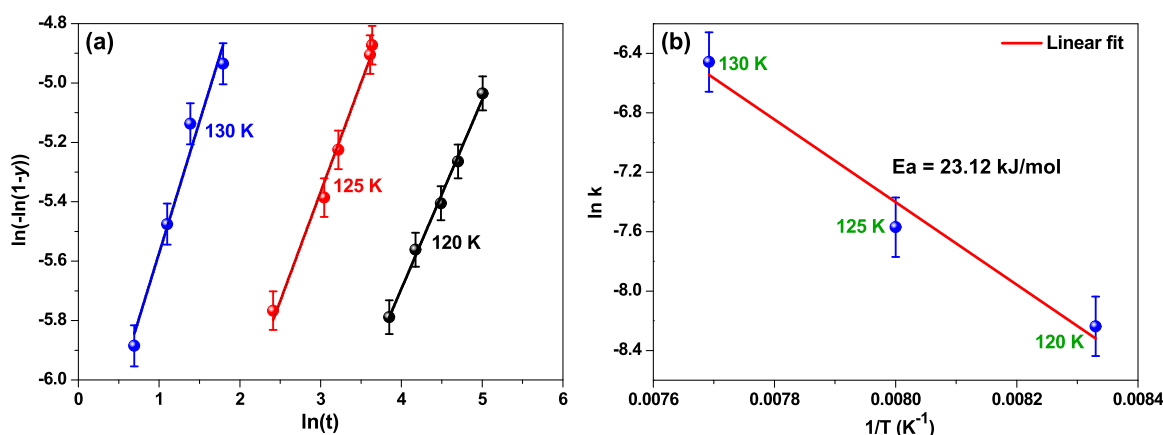


**Figure 5.** (a) Plot of  $\ln(-\ln[1 - y(T)])$  vs  $\ln(t)$  at different temperatures of 130, 125, and 120 K. The data points were fitted using the Avrami equation (eq 2). These data correspond to a straight line. (b) Plot of  $\ln k(T)$  vs inverse temperature ( $1/T$ ). The data points were fitted to obtain a straight line. Activation energy ( $E_a$ ) can be calculated from the slope of the straight line.

describes the extent of crystallization ( $y$ ) as a function of time ( $t$ ) during isothermal annealing at temperature  $T$ .<sup>60–62</sup> The equation is as follows

$$y(T) = 1 - \exp[-k(T) \cdot t^n] \quad (1)$$

where  $t$  is the time,  $k(T)$  is the rate constant, and  $n$  is related to the crystallization mechanism. For all temperatures,  $n$  is a parameter whose magnitude is determined by the geometry of the growing particles and whether the transformation is diffusion- or interface-controlled.<sup>60,62</sup> For an interface-controlled transformation,  $n$  is an integer from 1 to 4, depending upon the shape of the particle, whereas in a diffusion-controlled transformation,  $n$  is usually a fraction except for the cylindrical geometry of the particle when it is equal to 1.<sup>62,63</sup> Thus, the nature of crystallization process can be predicted from the knowledge of the parameter  $n$ . To find out the values of  $n$  and  $k(T)$  at different temperatures, eq 1 can be rewritten as

$$\ln(-\ln[1 - y(T)]) = n \ln(t) + \ln k(T) \quad (2)$$

Figure 5a shows three linearly fitted straight lines corresponding to three different temperatures. These data points were obtained using eq 2, where the extent of crystallization ( $y$ ) was assumed to be directly proportional to the intensity of the 1074 cm<sup>-1</sup> peak (THF hydrate), as explained before. The slope of each straight line corresponds to the value of  $n$  at different temperatures. The rate constants of the crystallization process, which in turn is the formation of hydrate at different temperatures, can be evaluated from the intercept values (from eq 2) of each straight line (Figure 5a). Once the rate constant is known at different temperatures, it is possible to calculate the activation energy involved in the process. The values of  $n$  and the rate constants at different temperatures are given in Table 1. Here, the fractional values of  $n$  indicate that the crystallization process or the formation of CH is diffusion-

controlled, as mentioned earlier. It is already known, according to the criteria for the values of  $n$ , that the crystallization kinetics of water at  $T < 150$  K is diffusion-controlled.<sup>62</sup>

The experimental data as shown in Figure 5b were fitted to the Arrhenius equation. The slope of this line gives the activation energy ( $E_a$ ), which was estimated to be  $\sim 23.12$  kJ mol<sup>-1</sup>. This is lesser than the previously reported activation energy ( $E_a$ ) values (60–77 kJ mol<sup>-1</sup>) for crystallization of pure ASW obtained by different experimental techniques.<sup>64–68</sup> This considerably lower activation energy suggests the feasibility of the process; however, the process is kinetically hindered at such low temperature due to limited diffusion. At elevated temperature, due to thermal motion of the molecules, the entropy of the system is increased, which in turn enhances the diffusion process and results in hydrate formation. At a temperature of 120 K or above, H<sub>2</sub>O ice undergoes a structural change,<sup>51</sup> and this temperature is very close to the desorption temperature of THF; therefore, these molecules also possess sufficient thermal motion. A combination of these two effects may be responsible for the formation of the hydrate. Due to hydrate formation, the system reaches a thermodynamically stable crystalline structure.

It would be interesting to know about the structures of THF hydrates that are formed at such low pressures. One would expect that the low-pressure hydrate can be structurally different from the conventional high-pressure hydrates. Unfortunately, our experimental setup is not equipped with in situ diffraction tools, neither it has a setup to transfer the sample for diffraction studies to get insight into the structural details. We have compared the O–H stretching of THF hydrate, cubic ice ( $I_c$ ), and hexagonal ice ( $I_h$ ) as shown in Figure S5. The crystalline forms (hexagonal and cubic) of ice were prepared separately by annealing 150 MLs of ASW to respective crystallization temperatures. It was observed that the O–H stretching of THF hydrate is similar in shape to hexagonal ice than that of cubic ice (Figure S5). We may conclude that during the formation of THF hydrate the overall ice is attaining a structure comparable to the hexagonal ice. We note that THF hydrate is known to form s-II hydrate, which is cubic in nature. Computationally, optimized structures of THF entrapped in different CH cages ( $5^{12}$ ,  $5^{12}6^2$ , and  $5^{12}6^4$ ) are shown in Figure 6. These calculated structures revealed that a large cage ( $5^{12}6^4$ ) is favored for the entrapment of THF, whereas the other two cages are unstable. Formation of THF

**Table 1.** Parameters for Crystallization of Water During the Formation of THF Hydrate at Different Temperatures

temperature (K)	$n$	rate constant; $k$ (s <sup>-1</sup> )
120	0.64	$2.64 \times 10^{-4}$
125	0.73	$5.16 \times 10^{-4}$
130	0.88	$1.57 \times 10^{-3}$



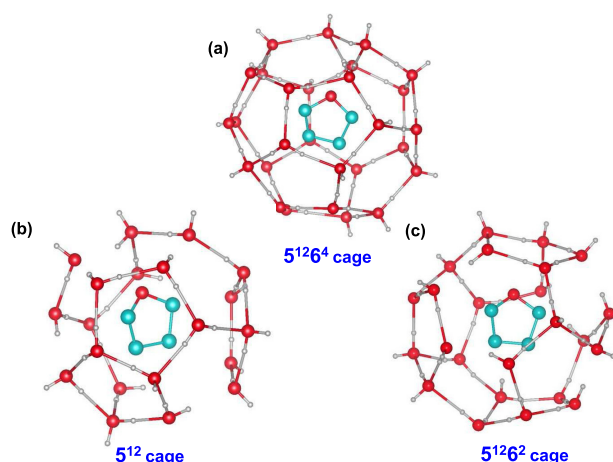


**Figure 6.** DFT-optimized structures of THF trapped within different CH cages, such as (a)  $5^{12}6^4$  cage, (b)  $5^{12}$  cage, and (c)  $5^{12}6^2$  cage. Here, water cage and the guest molecule (THF) are shown. H atoms of THF molecules in all of the structures are omitted for clarity. Color code used: cyan, C; red, O; and gray, H.

hydrate around atmospheric pressure reveals that due to the large size of the THF molecule, it forms an s-II hydrate structure and occupies the large cage ( $5^{12}6^4$ ).<sup>34</sup> Here, the computed shift in the C–O asymmetric mode of the  $5^{12}6^4$  cage closely matches the experimental shift of the same (Table S1). Other possible cages computed ( $5^{12}6$  and  $5^{12}6^2$ ) have a reduced or an opposite shift, respectively (Table S1). In Table S2, we have presented the coordinates of the optimized geometries of THF in  $5^{12}$ ,  $5^{12}6^2$ , and  $5^{12}6^4$  CH cages.

In this paper, we have discussed a suitable method to form spontaneous and stable THF hydrate at cryogenic conditions under UHV. The hydrate formation is found to be diffusion-controlled and is associated with the formation of the thermodynamically stable crystalline structure at a lower than usual crystallization temperature of ice. Kinetic measurements reveal that the crystallization process at <120 K is kinetically hindered due to limited motion of the guest and host molecules. However, upon achieving significant molecular motion or mobility at a warmer temperature (near 130 K or above), both THF and water molecules rearrange themselves to form the more stable hydrate structure.

## CONCLUSIONS

In conclusion, we have studied the formation of THF hydrate at cryogenic temperatures in UHV using surface-sensitive RAIRS. THF hydrate forms in the temperature range of 120–130 K and at  $10^{-10}$  mbar. We find that co-deposition as well as sequential deposition of THF and  $H_2O$  results in the formation of THF hydrate. IR spectral analysis of the O–H stretching region suggests that the hydrate formation is associated with the conversion of ASW to its crystalline analogue. This conversion follows both time- and temperature-dependent kinetics, and we calculated the activation energy ( $E_a$ ) for this process. Kinetic studies showed reduced overall activation energy, which makes the formation of THF hydrate spontaneous even in UHV. This approach provides an opportunity to explore the formation of CHs in extreme or ultralow ( $P$ ,  $T$ ) regions of the phase diagram that were previously inaccessible due to experimental limitations. In addition, there is a future scope to study certain binary CHs in

UHV, since THF hydrate acts as a stabilizer or promoter for their formation.

## ASSOCIATED CONTENT

### Supporting Information

The Supporting Information is available free of charge on the ACS Publications website at DOI: 10.1021/acs.jpcc.9b04370.

Time- and temperature-dependent IR spectra; comparison of the experimental and computational vibrational shifts; Cartesian coordinates of the hydrates; and comparison of IR spectra of THF hydrate, cubic ice, and hexagonal ice (PDF)

## AUTHOR INFORMATION

### Corresponding Author

\*E-mail: pradeep@iitm.ac.in.

### ORCID

Thalappil Pradeep: 0000-0003-3174-534X

### Present Addresses

<sup>†</sup>Lehrstuhl für Physikalische Chemie II, Friedrich-Alexander-Universität Erlangen-Nürnberg, Egerlandstr. 3, 91058 Erlangen, Germany (R.G.B.).

<sup>‡</sup>The Institute of Chemistry and The Farkas Center for Light-Induced Processes, The Hebrew University of Jerusalem, Givat Ram, Jerusalem 91904, Israel (G.R.).

### Author Contributions

J.G. designed and performed the experiments. J.G., R.G.B., and G.R. analyzed the results. G.R. carried out the calculations. T.P. proposed the project and supervised the progress. The manuscript was written through contributions of all authors.

### Notes

The authors declare no competing financial interest.

## ACKNOWLEDGMENTS

J.G. thanks the University Grants Commission (UGC) for his research fellowship. We thank the Department of Science and Technology (DST), Government of India, for supporting our research.

## REFERENCES

- (1) Sloan, E. D., Jr. Fundamental principles and applications of natural gas hydrates. *Nature* **2003**, 426, 353–363.
- (2) Ripmeester, J. A.; Tse, J. S.; Ratcliffe, C. I.; Powell, B. M. A new clathrate hydrate structure. *Nature* **1987**, 325, 135–136.
- (3) Miller, S. L. The occurrence of gas hydrates in the solar system. *Proc. Natl. Acad. Sci. U.S.A.* **1961**, 47, 1798–1808.
- (4) Mao, W. L.; Mao, H.-k.; Goncharov, A. F.; Struzhkin, V. V.; Guo, Q.; Hu, J.; Shu, J.; Hemley, R. J.; Somayazulu, M.; Zhao, Y. Hydrogen Clusters in Clathrate Hydrate. *Science* **2002**, 297, 2247–2249.
- (5) Sugahara, T.; Haag, J. C.; Prasad, P. S. R.; Warntjes, A. A.; Sloan, E. D.; Sum, A. K.; Koh, C. A. Increasing Hydrogen Storage Capacity Using Tetrahydrofuran. *J. Am. Chem. Soc.* **2009**, 131, 14616–14617.
- (6) Lee, H.; Lee, J.-w.; Kim, D. Y.; Park, J.; Seo, Y.-T.; Zeng, H.; Moudrakovski, I. L.; Ratcliffe, C. I.; Ripmeester, J. A. Tuning clathrate hydrates for hydrogen storage. *Nature* **2005**, 434, 743–746.
- (7) Mao, W. L.; Mao, H.-k. Hydrogen storage in molecular compounds. *Proc. Natl. Acad. Sci. U.S.A.* **2004**, 101, 708–710.
- (8) Khurana, M.; Yin, Z.; Linga, P. A Review of Clathrate Hydrate Nucleation. *ACS Sustainable Chem. Eng.* **2017**, 5, 11176–11203.
- (9) Park, Y.; Kim, D.-Y.; Lee, J.-W.; Huh, D.-G.; Park, K.-P.; Lee, J.; Lee, H. Sequestering carbon dioxide into complex structures of naturally occurring gas hydrates. *Proc. Natl. Acad. Sci. U.S.A.* **2006**, 103, 12690–12694.

- (10) Kang, K. C.; Linga, P.; Park, K.-n.; Choi, S.-J.; Lee, J. D. Seawater desalination by gas hydrate process and removal characteristics of dissolved ions ( $\text{Na}^+$ ,  $\text{K}^+$ ,  $\text{Mg}^{2+}$ ,  $\text{Ca}^{2+}$ ,  $\text{B}^{3+}$ ,  $\text{Cl}^-$ ,  $\text{SO}_4^{2-}$ ). *Desalination* **2014**, *353*, 84–90.
- (11) Veluswamy, H. P.; Kumar, S.; Kumar, R.; Rangsunvigit, P.; Linga, P. Enhanced clathrate hydrate formation kinetics at near ambient temperatures and moderate pressures: Application to natural gas storage. *Fuel* **2016**, *182*, 907–919.
- (12) Fleyfel, F.; Devlin, J. P. FT-IR spectra of 90 K films of simple, mixed, and double clathrate hydrates of trimethylene oxide, methyl chloride, carbon dioxide, tetrahydrofuran, and ethylene oxide containing decoupled  $\text{D}_2\text{O}$ . *J. Phys. Chem. B* **1988**, *92*, 631–635.
- (13) Ghosh, J.; Methikkalam, R. R. J.; Bhuin, R. G.; Ragupathy, G.; Choudhary, N.; Kumar, R.; Pradeep, T. Clathrate hydrates in interstellar environment. *Proc. Natl. Acad. Sci. U.S.A.* **2019**, *116*, 1526–1531.
- (14) Kargel, J. S.; Lunine, J. I. *Solar System Ices*, Based on Reviews Presented at the International Symposium “Solar System Ices” held in Toulouse, France, on March 27–30, 1995; Schmitt, B.; De Bergh, C.; Festou, M., Eds.; Springer: Netherlands: Dordrecht, 1998; pp 97–117.
- (15) Fecht, H. J. Defect-induced melting and solid-state amorphization. *Nature* **1992**, *356*, 133–135.
- (16) Badan, C.; Heyrich, Y.; Koper, M. T. M.; Juurlink, L. B. F. Surface Structure Dependence in Desorption and Crystallization of Thin Interfacial Water Films on Platinum. *J. Phys. Chem. Lett.* **2016**, *7*, 1682–1685.
- (17) Levinger, N. E. Water in Confinement. *Science* **2002**, *298*, 1722–1723.
- (18) Ghormley, J. A.; Hochanadel, C. J. Amorphous Ice: Density and Reflectivity. *Science* **1971**, *171*, 62–64.
- (19) Stevenson, K. P.; Kimmel, G. A.; Dohnálek, Z.; Smith, R. S.; Kay, B. D. Controlling the Morphology of Amorphous Solid Water. *Science* **1999**, *283*, 1505–1507.
- (20) Bar-nun, A.; Herman, G.; Laufer, D.; Rappaport, M. L. Trapping and release of gases by water ice and implications for icy bodies. *Icarus* **1985**, *63*, 317–332.
- (21) Thürmer, K.; Nie, S. Formation of hexagonal and cubic ice during low-temperature growth. *Proc. Natl. Acad. Sci. U.S.A.* **2013**, *110*, 11757–11762.
- (22) Svishchev, I. M.; Kusalik, P. G. Electrofreezing of Liquid Water: A Microscopic Perspective. *J. Am. Chem. Soc.* **1996**, *118*, 649–654.
- (23) Bar-Nun, A.; Dror, J.; Kochavi, E.; Laufer, D. Amorphous water ice and its ability to trap gases. *Phys. Rev. B* **1987**, *35*, 2427–2435.
- (24) Bhuin, R. G.; Methikkalam, R. R. J.; Sivaraman, B.; Pradeep, T. Interaction of Acetonitrile with Water-Ice: An Infrared Spectroscopic Study. *J. Phys. Chem. C* **2015**, *119*, 11524–11532.
- (25) Herrero, V. J.; Gálvez, Ó.; Maté, B.; Escibano, R. Interaction of  $\text{CH}_4$  and  $\text{H}_2\text{O}$  in ice mixtures. *Phys. Chem. Chem. Phys.* **2010**, *12*, 3164–3170.
- (26) Ghosh, J.; Hariharan, A. K.; Bhuin, R. G.; Methikkalam, R. R. J.; Pradeep, T. Propane and propane-water interactions: a study at cryogenic temperatures. *Phys. Chem. Chem. Phys.* **2018**, *20*, 1838–1847.
- (27) Buch, V.; Devlin, J. P.; Monreal, I. A.; Jagoda-Cwiklik, B.; Uras-Aytemiz, N.; Cwiklik, L. Clathrate hydrates with hydrogen-bonding guests. *Phys. Chem. Chem. Phys.* **2009**, *11*, 10245–10265.
- (28) Park, Y.; Shin, S.; Kang, H. Entropy-Driven Spontaneous Reaction in Cryogenic Ice: Dissociation of Fluoroacetic Acids. *J. Phys. Chem. Lett.* **2018**, *9*, 4282–4286.
- (29) Blake, D.; Allamandola, L.; Sandford, S.; Hudgins, D.; Freund, F. Clathrate hydrate formation in amorphous cometary ice analogs in vacuo. *Science* **1991**, *254*, 548–551.
- (30) Fleyfel, F.; Devlin, J. P. Carbon dioxide clathrate hydrate epitaxial growth: spectroscopic evidence for formation of the simple type-II carbon dioxide hydrate. *J. Phys. Chem. B* **1991**, *95*, 3811–3815.
- (31) Richardson, H. H.; Wooldridge, P. J.; Devlin, J. P. FT-IR spectra of vacuum deposited clathrate hydrates of oxirane  $\text{H}_2\text{S}$ , THF, and ethane. *J. Chem. Phys.* **1985**, *83*, 4387–4394.
- (32) Kang, S.-P.; Lee, H. Recovery of  $\text{CO}_2$  from Flue Gas Using Gas Hydrate: Thermodynamic Verification through Phase Equilibrium Measurements. *Environ. Sci. Technol.* **2000**, *34*, 4397–4400.
- (33) Florusse, L. J.; Peters, C. J.; Schoonman, J.; Hester, K. C.; Koh, C. A.; Dec, S. F.; Marsh, K. N.; Sloan, E. D. Stable Low-Pressure Hydrogen Clusters Stored in a Binary Clathrate Hydrate. *Science* **2004**, *306*, 469–471.
- (34) Makino, T.; Sugahara, T.; Ohgaki, K. Stability Boundaries of Tetrahydrofuran+Water System. *J. Chem. Eng. Data* **2005**, *50*, 2058–2060.
- (35) Lehmkuhler, F.; Sakko, A.; Sternemann, C.; Hakala, M.; Nygård, K.; Sahle, C. J.; Galambosi, S.; Steinke, I.; Tiemeyer, S.; Nyrow, A.; et al. Anomalous Energetics in Tetrahydrofuran Clathrate Hydrate Revealed by X-ray Compton Scattering. *J. Phys. Chem. Lett.* **2010**, *1*, 2832–2836.
- (36) Hernandez, J.; Uras, N.; Devlin, J. P. Coated Ice Nanocrystals from Water-Adsorbate Vapor Mixtures: Formation of Ether- $\text{CO}_2$  Clathrate Hydrate Nanocrystals at 120 K. *J. Phys. Chem. B* **1998**, *102*, 4526–4535.
- (37) Gulluru, D. B.; Devlin, J. P. Rates and Mechanisms of Conversion of Ice Nanocrystals to Ether Clathrate Hydrates: Guest-Molecule Catalytic Effects at  $\sim 120$  K. *J. Phys. Chem. A* **2006**, *110*, 1901–1906.
- (38) Hallbrucker, A. A clathrate hydrate of nitric oxide. *Angew. Chem., Int. Ed.* **1994**, *33*, 691–693.
- (39) Hallbrucker, A.; Mayer, E. Unexpectedly stable clathrate hydrates formed from microporous vapor-deposited amorphous solid water at low “external” guest pressures and their astrophysical implications. *Icarus* **1991**, *90*, 176–180.
- (40) Hallbrucker, A.; Mayer, E. Unexpectedly stable nitrogen, oxygen, carbon monoxide and argon clathrate hydrates from vapour-deposited amorphous solid water: an X-ray and two-step differential scanning calorimetry study. *J. Chem. Soc., Faraday Trans.* **1990**, *86*, 3785–3792.
- (41) Mayer, E.; Hallbrucker, A. Unexpectedly stable nitrogen and oxygen clathrate hydrates from vapour deposited amorphous solid water. *J. Chem. Soc., Chem. Commun.* **1989**, 749–751.
- (42) Hallbrucker, A. Raman spectroscopic monitoring of oxygen clathrate hydrate formation from microporous amorphous solid water. *J. Chem. Soc., Faraday Trans.* **1994**, *90*, 293–295.
- (43) Hallbrucker, A.; Mayer, E. Formation and decomposition of oxygen clathrate hydrate as seen by two-step differential scanning calorimetry; novel method for investigating reactions accompanied by gas release. *J. Chem. Soc., Chem. Commun.* **1990**, 873–874.
- (44) Duarte, A. R. C.; Shariati, A.; Rovetto, L. J.; Peters, C. J. Water Cavities of sH Clathrate Hydrate Stabilized by Molecular Hydrogen: Phase Equilibrium Measurements. *J. Phys. Chem. B* **2008**, *112*, 1888–1889.
- (45) Bag, S.; Bhuin, R. G.; Methikkalam, R. R. J.; Pradeep, T.; Kephart, L.; Walker, J.; Kuchta, K.; Martin, D.; Wei, J. Development of Ultralow Energy (1–10 eV) Ion Scattering Spectrometry Coupled with Reflection Absorption Infrared Spectroscopy and Temperature Programmed Desorption for the Investigation of Molecular Solids. *Rev. Sci. Instrum.* **2014**, *85*, No. 014103.
- (46) Moon, E.-S.; Heon, K.; Yasuhiro, O.; Naoki, W.; Akira, K. Direct Evidence for Ammonium Ion Formation in Ice through Ultraviolet-induced Acid-Base Reaction of  $\text{NH}_3$  with  $\text{H}_3\text{O}^+$ . *Astrophys. J.* **2010**, *713*, 906–911.
- (47) Kim, Y.; Moon, E.-s.; Shin, S.; Kang, H. Acidic Water Monolayer on Ruthenium(0001). *Angew. Chem., Int. Ed.* **2012**, *51*, 12806–12809.
- (48) Kang, H.; Shin, T. H.; Park, S. C.; Kim, I. K.; Han, S. J. Acidity of Hydrogen Chloride on Ice. *J. Am. Chem. Soc.* **2000**, *122*, 9842–9843.
- (49) Monreal, I. A.; Devlin, J. P.; Maşlakçı, Z.; Çiçek, M. B.; Uras-Aytemiz, N. Controlling Nonclassical Content of Clathrate Hydrates

Through the Choice of Molecular Guests and Temperature. *J. Phys. Chem. A* **2011**, *115*, 5822–5832.

(50) Frisch, M. J.; Trucks, G. W.; Schlegel, H. B.; Scuseria, G. E.; Robb, M. A.; Cheeseman, J. R.; Scalmani, G.; Barone, V.; Petersson, G. A.; Nakatsuji, H.; et al. *Gaussian 09*, revision B.01; Gaussian Inc.: Wallingford, CT, 2009.

(51) Jenniskens, P.; Blake, D. F. Structural transitions in amorphous water ice and astrophysical implications. *Science* **1994**, *265*, 753–756.

(52) Monreal, I. A.; Cwiklik, L.; Jagoda-Cwiklik, B.; Devlin, J. P. Classical to Nonclassical Transition of Ether-HCN Clathrate Hydrates at Low Temperature. *J. Phys. Chem. Lett.* **2010**, *1*, 290–294.

(53) Backus, E. H. G.; Grecea, M. L.; Kleyn, A. W.; Bonn, M. Surface Crystallization of Amorphous Solid Water. *Phys. Rev. Lett.* **2004**, *92*, No. 236101.

(54) Wong, A.; Shi, L.; Auchettl, R.; McNaughton, D.; Appadoo, D. R. T.; Robertson, E. G. Heavy snow: IR spectroscopy of isotope mixed crystalline water ice. *Phys. Chem. Chem. Phys.* **2016**, *18*, 4978–4993.

(55) Berggren, M. S.; Schuh, D.; Sceats, M. G.; Rice, S. A. The OH stretching region infrared spectra of low density amorphous solid water and polycrystalline ice Ih. *J. Chem. Phys.* **1978**, *69*, 3477–3482.

(56) Bhuin, R. G.; Methikkalam, R. R. J.; Bag, S.; Pradeep, T. Diffusion and Crystallization of Dichloromethane within the Pores of Amorphous Solid Water. *J. Phys. Chem. C* **2016**, *120*, 13474–13484.

(57) Hill, C. R.; Mitterdorfer, C.; Youngs, T. G. A.; Bowron, D. T.; Fraser, H. J.; Loerting, T. Neutron Scattering Analysis of Water's Glass Transition and Micropore Collapse in Amorphous Solid Water. *Phys. Rev. Lett.* **2016**, *116*, No. 215501.

(58) Mitterdorfer, C.; Bauer, M.; Youngs, T. G. A.; Bowron, D. T.; Hill, C. R.; Fraser, H. J.; Finney, J. L.; Loerting, T. Small-angle neutron scattering study of micropore collapse in amorphous solid water. *Phys. Chem. Chem. Phys.* **2014**, *16*, 16013–16020.

(59) Mitterdorfer, C.; Bauer, M.; Loerting, T. Clathrate hydrate formation after CO<sub>2</sub>-H<sub>2</sub>O vapour deposition. *Phys. Chem. Chem. Phys.* **2011**, *13*, 19765–19772.

(60) Jenniskens, P.; Blake, D. F. Crystallization of Amorphous Water Ice in the Solar System. *Astrophys. J.* **1996**, *473*, 1104–1113.

(61) Smith, R. S.; Petrik, N. G.; Kimmel, G. A.; Kay, B. D. Thermal and Nonthermal Physiochemical Processes in Nanoscale Films of Amorphous Solid Water. *Acc. Chem. Res.* **2012**, *45*, 33–42.

(62) Hage, W.; Hallbrucker, A.; Mayer, E.; Johari, G. P. Crystallization kinetics of water below 150 K. *J. Chem. Phys.* **1994**, *100*, 2743–2747.

(63) Rao, C. N. R.; Rao, K. J. *Phase Transitions in Solids: An Approach to the Study of the Chemistry and Physics of Solids*; McGraw-Hill: New York, 1978; pp 81–173.

(64) Yuan, C.; Smith, R. S.; Kay, B. D. Communication: Distinguishing between bulk and interface-enhanced crystallization in nanoscale films of amorphous solid water. *J. Chem. Phys.* **2017**, *146*, No. 031102.

(65) Kondo, T.; Kato, H. S.; Bonn, M.; Kawai, M. Deposition and crystallization studies of thin amorphous solid water films on Ru(0001) and on CO-precovered Ru(0001). *J. Chem. Phys.* **2007**, *127*, No. 094703.

(66) Safarik, D. J.; Mullins, C. B. The nucleation rate of crystalline ice in amorphous solid water. *J. Chem. Phys.* **2004**, *121*, 6003–6010.

(67) Smith, R. S.; Matthiesen, J.; Knox, J.; Kay, B. D. Crystallization Kinetics and Excess Free Energy of H<sub>2</sub>O and D<sub>2</sub>O Nanoscale Films of Amorphous Solid Water. *J. Phys. Chem. A* **2011**, *115*, 5908–5917.

(68) Lee, D. H.; Kang, H. Acid-Promoted Crystallization of Amorphous Solid Water. *J. Phys. Chem. C* **2018**, *122*, 24164–24170.



# Spontaneous Formation of Tetrahydrofuran Hydrate in Ultrahigh Vacuum

*Jyotirmoy Ghosh, Radha Gobinda Bhui,† Gopi Ragupathy,‡ and Thalappil Pradeep\**

DST Unit of Nanoscience (DST UNS) and Thematic Unit of Excellence (TUE), Department of Chemistry, Indian Institute of Technology Madras, Chennai 600036, India

<sup>†</sup>Present Address: Lehrstuhl für Physikalische Chemie II, Friedrich-Alexander-Universität Erlangen-Nürnberg, Egerlandstr. 3, 91058 Erlangen, Germany

<sup>‡</sup>Present Address: The Institute of Chemistry and The Farkas Center for Light-Induced Processes, The Hebrew University of Jerusalem, Givat Ram, Jerusalem, 91904, Israel

Corresponding Author

\*To whom correspondence should be addressed, E-mail: [pradeep@iitm.ac.in](mailto:pradeep@iitm.ac.in)

## Table of contents

List of Figures	Description	Page number
Figure S1	Time-dependent RAIR spectra of 300 MLs of a THF+H <sub>2</sub> O (1:5) mixture at 130 K.	S3
Figure S2	Time-dependent RAIR spectra of 150 MLs of solid H <sub>2</sub> O film at 120 K, and at 130 K at O-H stretching region.	S4
Figure S3	Temperature-dependent RAIR spectra of 150 MLs THF at C-O antisymmetric stretching region.	S5
Figure S4	Time-dependent RAIR spectra of 300 MLs of a THF@H <sub>2</sub> O (1:1) mixture at 130 K.	S6

Figure S5	Comparison of O-H stretching region of THF hydrate, cubic ice and hexagonal ice.	S7
Table S1	Experimental and computational vibrational shift of THF hydrate.	S8
Table S2	Cartesian coordinate values for the different optimized cages of THF hydrate.	S9-S15

## Supporting Information 1:

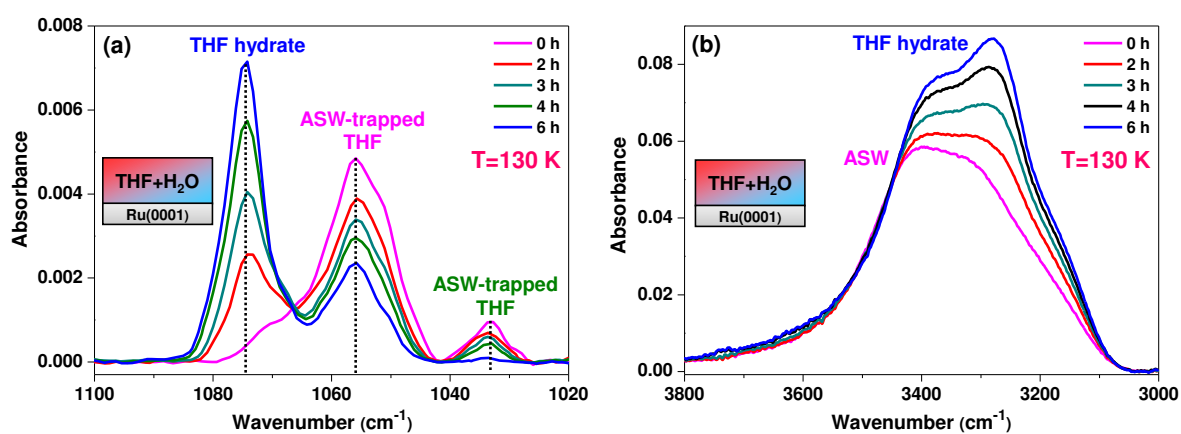


**Figure S1.** Time-dependent RAIR spectra of 300 MLs of a THF+H<sub>2</sub>O (1:5) mixture, (a) in the asymmetric C-O stretching region, and (b) O-H stretching region at 130 K, which was co-deposited on Ru(0001) substrate. This mixture was annealed at 2 K.min<sup>-1</sup> rate after co-deposition at 10 K.

## Supporting Information 2:

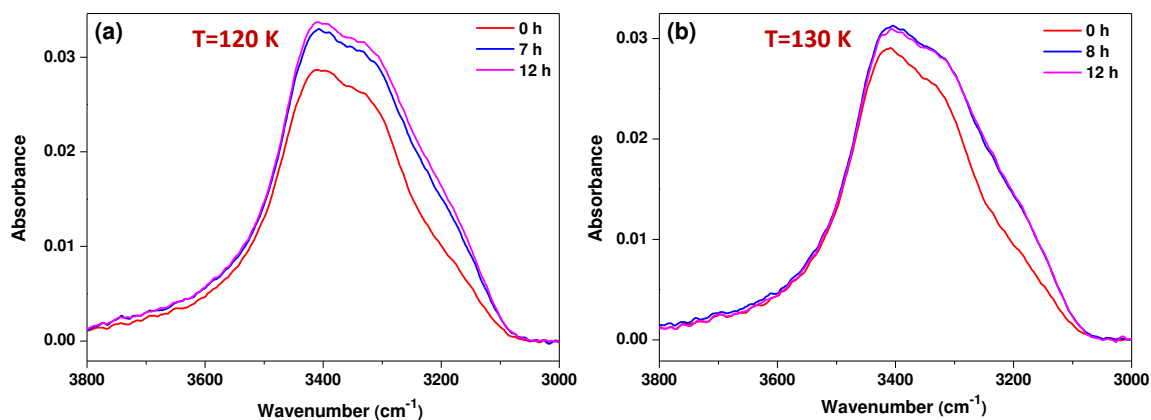


**Figure S2.** Time-dependent RAIR spectra of 150 MLs of solid H<sub>2</sub>O film at (a) 120 K, and (b) at 130 K in the O-H stretching region. Water vapor was deposited at 10 K on Ru(0001) substrate. The ice films were annealed at 2 K.min<sup>-1</sup> to the respective temperatures.

### Supporting Information 3:

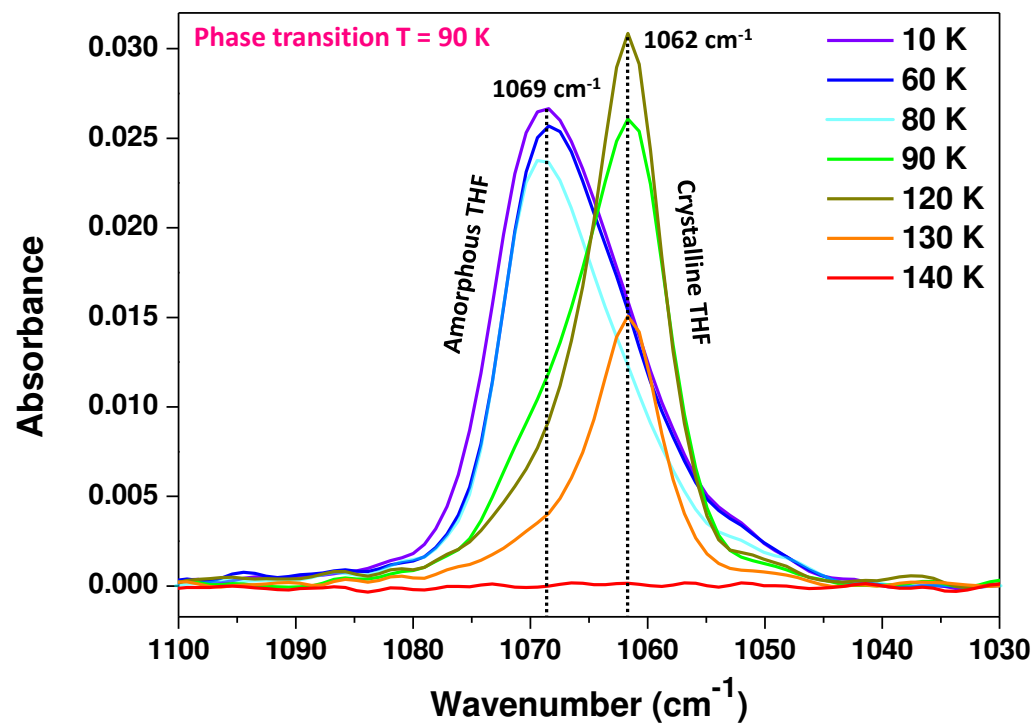


**Figure S3.** Temperature-dependent RAIR spectra of 150 MLs THF in the C-O antisymmetric stretching region.

## Supporting Information 4:

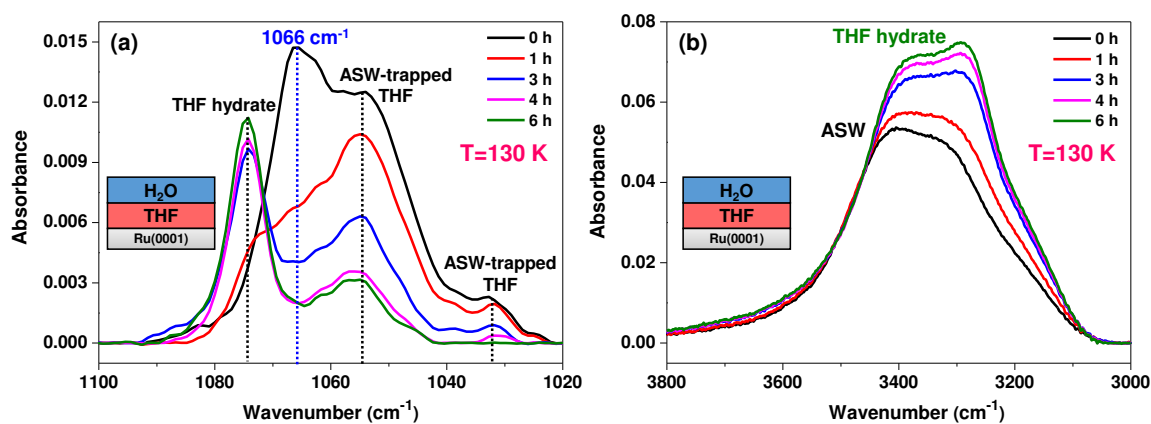


**Figure S4.** Time-dependent RAIR spectra of 300 MLs of a THF@H<sub>2</sub>O mixture (1:1) in the (a) asymmetric C-O stretching region, and (b) O-H stretching region, at 130 K, which was sequentially deposited at 10 K on the Ru(0001) substrate. The sequential deposition was carried out by condensing 150 MLs of H<sub>2</sub>O film over the same coverage of THF film, thus making it a (1:1) mixture.

## Supporting Information 5:

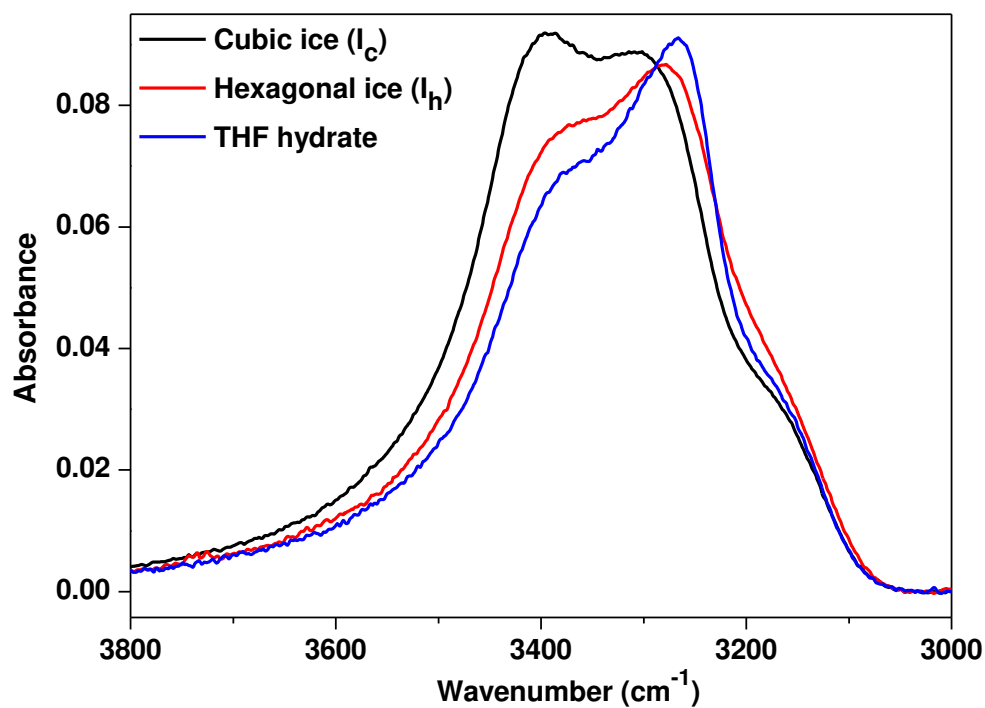


**Figure S5.** Comparison of the O-H stretching region of THF clathrate hydrate, hexagonal ice (I<sub>h</sub>), and cubic ice (I<sub>c</sub>), respectively. The cubic and hexagonal ices were formed by annealing at 145 K and 150 K, in separate sets of experiments.



**Table S1:**

Comparison of the computational and experimental vibrational shifts of THF clathrate hydrate. Computations were performed using B3LYP level of theory with 6-311++G (d, p) basis set.

<b>THF clathrate hydrate</b>	<b>5<sup>12</sup> cage</b>	<b>5<sup>12</sup> 6<sup>2</sup> cage</b>	<b>5<sup>12</sup> 6<sup>4</sup> cage</b>
<b>Experimental shift</b>	-	-	19.0 cm <sup>-1</sup>
<b>Computational shift</b>	3.2 cm <sup>-1</sup>	-10.3 cm <sup>-1</sup>	27.4 cm <sup>-1</sup>

**Table S2:**

Cartesian coordinates of THF clathrate hydrate in  $5^{12}$ ,  $5^{12}6^2$ , and  $5^{12}6^4$  cages. The structure is optimized by using B3LYP level of theory and 6-311G (d, p) basis set.

**1. Cartesian coordinates of THF hydrate,  $5^{12}$  cage:**

O	-3.682521000	-0.998104000	1.763573000
H	-3.035226000	-0.866700000	2.493269000
H	-3.787980000	-0.125330000	1.357865000
O	1.092542000	0.493839000	-3.575893000
H	1.897690000	0.640201000	-3.054436000
H	0.474915000	1.208872000	-3.339951000
O	-1.753901000	-0.564608000	3.717801000
H	-0.973431000	-1.139036000	3.608164000
H	-1.426274000	0.350172000	3.754553000
O	3.583155000	0.832824000	-2.011474000
H	3.477089000	1.618489000	-1.433649000
H	4.267523000	1.064619000	-2.648603000
O	-2.832497000	-1.723020000	-2.736829000
H	-2.921351000	-2.207747000	-1.901940000
H	-1.914391000	-1.904385000	-3.025289000
O	4.036332000	-0.971622000	1.988747000
H	4.064214000	-1.289603000	1.048157000
H	4.785790000	-1.390619000	2.424046000
O	-3.114222000	1.074563000	-2.444422000
H	-3.077202000	0.098716000	-2.573281000
H	-3.462663000	1.225904000	-1.551249000
O	3.713657000	1.780980000	2.123808000
H	3.846474000	0.805937000	2.093262000
H	4.278076000	2.106624000	2.829439000
O	-0.212405000	-4.020313000	0.848483000
H	-0.955025000	-3.459804000	0.549144000
H	-0.592718000	-4.887638000	1.020599000
O	-1.875847000	3.790030000	1.234954000
H	-1.167130000	3.906182000	0.555602000
H	-2.172461000	4.679308000	1.454394000
O	1.743833000	-3.501371000	-1.221326000
H	1.099801000	-3.667754000	-0.502284000
H	1.953027000	-4.367289000	-1.585556000
O	0.065712000	4.035256000	-0.728876000
H	-0.231608000	3.556994000	-1.529874000
H	0.975581000	3.746184000	-0.568324000
O	-2.980279000	-3.041229000	0.086454000

H	-3.253841000	-2.322069000	0.710272000
H	-3.674674000	-3.704312000	0.149076000
O	-0.905037000	2.502464000	-2.929182000
H	-1.125770000	2.994788000	-3.727157000
H	-1.715669000	1.949055000	-2.737951000
O	-0.824732000	2.274383000	3.571853000
H	-1.226351000	2.783847000	2.845832000
H	0.123157000	2.336428000	3.412413000
O	4.046819000	-1.743644000	-0.613860000
H	3.902412000	-0.944146000	-1.148277000
H	3.318659000	-2.352082000	-0.837987000
O	3.146063000	3.034295000	-0.264299000
H	3.725911000	3.799127000	-0.337928000
H	3.338697000	2.642617000	0.620929000
O	0.453212000	-2.442898000	3.283852000
H	1.363023000	-2.148701000	3.165436000
H	0.247925000	-2.965510000	2.487698000
O	-0.067074000	-2.095789000	-3.355735000
H	0.356275000	-1.224553000	-3.489714000
H	0.468764000	-2.534740000	-2.678443000
O	-3.872901000	1.773582000	0.366165000
H	-3.232419000	2.446605000	0.668611000
H	-4.743357000	2.162701000	0.503637000
O	-0.229599000	-1.387018000	0.174729000
C	1.049016000	-0.762497000	0.285623000
C	-1.091334000	-0.390740000	-0.379463000
C	0.788151000	0.725497000	0.600987000
C	-0.729759000	0.878050000	0.375433000
H	-0.894706000	-0.294494000	-1.450036000
H	1.573350000	-0.862942000	-0.668174000
H	1.358063000	1.359681000	-0.073686000
H	1.613562000	-1.283815000	1.054053000
H	1.081783000	0.980812000	1.619193000
H	-0.979368000	1.775688000	-0.181565000
H	-1.252852000	0.894968000	1.329844000
H	-2.114216000	-0.713939000	-0.233812000

## 2. Cartesian coordinates of THF hydrate, 5<sup>12</sup>6<sup>2</sup> cage:

O	1.929592000	4.354383000	-0.376871000
H	2.583637000	3.709538000	-0.075880000
H	3.244250000	1.643202000	2.222184000
O	-3.738463000	-2.747541000	0.743398000
H	1.630871000	4.036352000	-1.247940000

H	3.019328000	1.696461000	3.760801000
O	3.963034000	2.444642000	0.765006000
H	-3.161875000	-3.190937000	0.090795000
H	5.444451000	0.481098000	-1.502423000
O	-1.945693000	-3.933105000	-1.123039000
H	-4.461991000	-3.356545000	0.918765000
H	4.436923000	-0.345387000	-0.641034000
O	-3.996757000	1.808552000	1.410355000
H	4.721514000	3.025979000	0.895256000
H	0.761431000	-5.374600000	0.267486000
O	4.212199000	-1.823495000	0.135620000
H	4.232479000	1.795743000	0.071592000
H	1.208654000	-4.063308000	-0.445225000
O	-2.610990000	3.918551000	-0.340372000
H	-1.083769000	-4.042440000	-0.653159000
H	-1.686389000	-2.662606000	-2.552414000
O	2.470481000	-3.374829000	-1.470234000
H	-2.166310000	-4.809228000	-1.453735000
H	-1.840312000	-2.376571000	-4.070420000
O	3.107315000	-1.627117000	2.844445000
H	-3.453350000	1.443799000	2.139872000
H	1.793880000	-0.919340000	-3.366039000
O	-2.117427000	-1.974056000	3.104682000
H	-4.717208000	2.288008000	1.830360000
H	0.451490000	-1.756662000	-3.277248000
O	-4.642170000	-0.138271000	-0.628747000
H	3.621648000	-2.409938000	-0.375879000
H	-2.318832000	2.304183000	-3.091174000
O	-2.364303000	0.663374000	3.449744000
H	3.890928000	-1.834442000	1.053587000
H	-2.137006000	3.467567000	-2.077696000
O	2.824358000	1.170290000	2.975197000
H	-3.092423000	3.244319000	0.160178000
H	-0.239546000	3.788749000	1.987660000
O	4.569420000	0.528558000	-1.098690000
H	-1.850078000	4.156615000	0.231134000
H	0.426663000	4.480452000	0.764564000
O	0.495045000	-4.463526000	0.107556000
H	2.048936000	-2.743001000	-2.140060000
H	0.694175000	2.173912000	-1.879927000
O	-1.469618000	-2.020244000	-3.255586000
H	2.965741000	-4.006611000	-2.003690000
H	-0.055942000	3.013721000	-2.892717000
O	1.422969000	-1.825412000	-3.266166000

H	3.018922000	-0.657413000	2.966084000
H	1.255650000	-2.681441000	2.868155000
O	-1.798929000	3.111630000	-2.928088000
H	3.672408000	-1.930030000	3.561744000
H	0.433335000	-3.517125000	1.869680000
O	-0.396208000	4.447130000	1.289874000
H	-1.233926000	-2.393023000	3.040154000
H	2.060859000	1.470962000	-3.339107000
O	0.868978000	2.791245000	-2.603149000
H	-2.635825000	-2.295862000	2.347107000
H	3.250652000	0.740192000	-2.649311000
O	0.439462000	-3.200912000	2.787689000
H	-4.434551000	-0.980871000	-0.197710000
H	-3.766835000	0.350188000	-2.285992000
O	2.603542000	0.660732000	-3.367075000
H	-4.479140000	0.537124000	0.052888000
H	-2.617276000	-0.213365000	-3.144778000
O	-3.200721000	0.551175000	-3.058259000
H	-2.250086000	-0.318521000	3.325262000
H	-0.740722000	1.696467000	3.285104000
O	0.024802000	2.295073000	3.228665000
H	-2.669944000	0.770551000	4.357250000
H	0.795421000	1.741727000	3.041060000
O	-0.389915000	-1.440042000	0.123165000
C	-1.442628000	-0.491306000	-0.125858000
C	0.687268000	-0.716911000	0.711511000
C	-0.783677000	0.896898000	-0.248461000
C	0.717231000	0.610694000	-0.039290000
H	0.501091000	-0.558483000	1.781734000
H	-2.155863000	-0.527934000	0.700448000
H	-1.150387000	1.577443000	0.518784000
H	-1.944714000	-0.800599000	-1.036871000
H	-1.007852000	1.355940000	-1.209640000
H	1.220294000	1.401126000	0.518531000
H	1.228354000	0.478653000	-0.995576000
H	1.588989000	-1.314320000	0.597059000

### 3. Cartesian coordinates of THF hydrate, 5<sup>12</sup>6<sup>4</sup> cage:

O	-0.103165000	4.250630000	2.013985000
H	-1.010632000	3.897222000	2.103611000
H	-3.954335000	-1.899726000	1.007892000
O	-2.760565000	3.159732000	2.108663000
H	0.438447000	3.795651000	2.683189000

H	-3.764804000	-2.746669000	-0.289587000
O	0.482979000	4.758000000	-0.692579000
H	-2.784980000	2.281026000	2.526130000
H	4.612246000	1.184297000	-0.631358000
O	-4.026818000	2.809424000	-0.549887000
H	-3.109698000	3.046544000	1.206684000
H	5.197015000	2.444382000	0.097129000
O	1.443374000	2.740930000	4.013149000
H	-0.328884000	4.412200000	-1.099753000
H	0.753897000	1.813369000	-3.762424000
O	-2.799460000	0.750351000	3.729814000
H	0.369520000	4.619567000	0.273151000
H	2.083033000	2.431063000	-3.086984000
O	-1.981510000	3.963680000	-2.126636000
H	-4.241885000	1.873278000	-0.764557000
H	-3.360689000	0.133004000	-2.803356000
O	-0.078709000	0.481846000	4.680014000
H	-4.880825000	3.262203000	-0.473880000
H	-2.573297000	-0.827507000	-3.744297000
O	2.692620000	3.563741000	-1.914580000
H	2.198498000	2.332995000	3.501986000
H	2.762516000	-1.484156000	3.224998000
O	-4.690968000	0.198416000	-1.302924000
H	1.836316000	3.313739000	4.681926000
H	3.755960000	-1.698073000	2.023859000
O	-3.353984000	-1.849788000	2.808972000
H	-3.085535000	-0.152188000	3.477171000
H	-0.782613000	-3.658785000	1.823182000
O	3.351729000	1.578834000	2.590257000
H	-3.321722000	1.014632000	4.497448000
H	-0.956868000	-4.101956000	3.310763000
O	-0.919333000	2.021878000	-3.965619000
H	-2.746105000	3.623931000	-1.614240000
H	3.864583000	-0.480651000	-2.241145000
O	1.204545000	-1.839353000	3.990945000
H	-2.255400000	4.800034000	-2.522747000
H	5.402290000	-0.541916000	-2.177851000
O	-4.319070000	-2.050858000	0.115163000
H	-0.968847000	0.624573000	4.313072000
H	-1.824975000	-4.343466000	-0.643528000
O	4.376910000	1.982627000	-0.113822000
H	0.427219000	1.304956000	4.514007000
H	-3.028847000	-4.840579000	-1.512415000
O	1.736954000	1.720850000	-3.686565000

H	1.957507000	4.068505000	-1.498653000
H	2.376242000	0.421508000	-3.681967000
O	-2.898702000	0.090845000	-3.658276000
H	3.176902000	3.133504000	-1.190161000
H	3.310956000	-0.658521000	-4.439057000
O	3.618626000	-1.185115000	2.836948000
H	-4.565352000	-0.630736000	-0.764180000
H	-1.991414000	-2.944921000	-2.675597000
O	-1.054898000	-3.348319000	2.717394000
H	-5.473727000	0.050597000	-1.852647000
H	-0.744626000	-2.533536000	-3.500637000
O	4.629299000	-0.494334000	-1.595288000
H	-2.540631000	-2.409799000	2.842727000
H	4.459282000	-1.842821000	-0.435709000
O	-2.625995000	-4.048086000	-1.116566000
H	-4.058427000	-2.351644000	3.245330000
H	5.138244000	-2.907215000	0.493621000
O	2.849681000	-0.507449000	-3.605429000
H	3.561427000	0.633073000	2.772308000
H	0.570459000	-4.433154000	-0.049018000
O	-1.722843000	-2.511598000	-3.503519000
H	3.368164000	1.668790000	1.624868000
H	-0.073776000	-5.633630000	0.698402000
O	4.279237000	-2.586415000	0.190868000
H	-1.571220000	1.288816000	-3.923808000
H	1.298706000	-2.925655000	-2.366232000
O	-0.267554000	-4.745821000	0.369450000
H	-1.302563000	2.740599000	-3.429950000
H	1.624538000	-1.897512000	-3.464965000
O	1.119589000	-2.721537000	-3.295528000
H	0.534098000	-2.324305000	3.485480000
H	2.958020000	-3.680318000	-0.417450000
O	2.192532000	-4.179664000	-0.780671000
H	0.761410000	-0.999255000	4.266811000
H	2.531880000	-4.734138000	-1.495062000
O	-0.181008000	-1.564217000	0.009575000
C	-1.263763000	-0.674542000	-0.327519000
C	0.909735000	-0.771949000	0.504473000
C	-0.671964000	0.743275000	-0.505184000
C	0.838565000	0.565692000	-0.233486000
H	0.814390000	-0.625885000	1.588327000
H	-2.011141000	-0.710016000	0.474675000
H	-1.122841000	1.413821000	0.231271000
H	-1.721628000	-1.059897000	-1.240640000



H	-0.871096000	1.149366000	-1.498680000
H	1.227037000	1.377745000	0.386830000
H	1.407912000	0.570729000	-1.168216000
H	1.827279000	-1.335770000	0.315711000

# Geologically Inspired Monoliths for Sustainable Release of Essential Minerals into Drinking Water

Swathy Jakka Ravindran,<sup>†,‡,✉</sup> Ananthu Mahendranath,<sup>†</sup> Pillalamarri Srikrishnarka,<sup>†</sup> Avula Anil Kumar,<sup>†,✉</sup> Md Rabiul Islam,<sup>†</sup> Sritama Mukherjee,<sup>†</sup> Ligy Philip,<sup>‡,✉</sup> and Thalappil Pradeep<sup>\*,†,✉</sup>

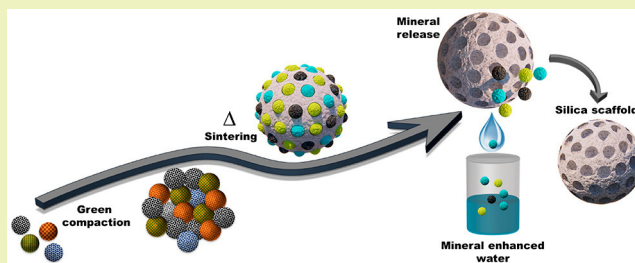
<sup>†</sup>DST Unit of Nanoscience (DST UNS) and Thematic Unit of Excellence (TUE), Department of Chemistry, Indian Institute of Technology Madras, Adyar, Chennai, Tamil Nadu 600 036, India

<sup>‡</sup>Environmental and Water Resources Engineering (EWRE) Division, Department of Civil Engineering, Indian Institute of Technology Madras, Adyar, Chennai, Tamil Nadu 600 036, India

## S Supporting Information

**ABSTRACT:** Decreasing mineral content in drinking water is a serious concern especially due to the proliferation of desalination technologies. We present an approach to remineralize water with essential minerals such that their concentrations are at the recommended daily dose. We accomplished this using composite materials whose composition and surface area were tuned to achieve constant release of minerals into water over a prolonged period of time. We developed a nature-mimicking tectosilicate porous composite matrix and used it as a structural framework to incorporate leachable minerals to the extent of 40% of the whole mass, which were released into the water during its functional working life. Release of not only the common macro minerals but also the vital trace minerals was possible in this work. Compacted composites of this kind have been used to create mineralization cartridges. The greenness of these composites evaluated from several sustainability metrics shows that the manufacturing process has minimum or negligible carbon emission, E-factor, and energy consumption. This methodology may be extended to encompass all the essential minerals expected to be present in water.

**KEYWORDS:** Essential minerals, Remineralization, Drinking water purification, Reverse osmosis, Tectosilicate monoliths



## INTRODUCTION

Minerals play a pivotal role in the smooth functioning of metabolism in life forms including humans and thus directly or indirectly affect their well-being. Human nutritional requirements demand at least 23 mineral elements which are spread across nutrient classes like macronutrients and micronutrients. The macronutrients are carbohydrates, fats, fibers, proteins, and water. Almost 99% of the mass of the human body is made up of elements of macronutrients, namely, oxygen, carbon, hydrogen, and nitrogen. The micronutrients are vitamins and minerals, and the latter are the chemical elements required by life forms.<sup>1</sup> They are further classified into macro and trace minerals. Macro minerals, namely, potassium, chloride, sodium, calcium, magnesium, and phosphorus, the abundant constituents of tissues, are involved in central functions such as the maintenance of osmotic pressure and membrane potential. They play dynamic roles in electrolytic balance, acid–base balance, protein synthesis, control of cellular growth/differentiation, immune system function, composition of bones and teeth, etc.<sup>2</sup> The other elements present in the human body are referred to as the trace or oligo elements, namely, iron, zinc, fluoride, manganese, boron, copper, iodine, selenium, molybdenum, vanadium, chromium, tin, and cobalt, which

are crucial and promote a healthy life style.<sup>3</sup> Trace minerals in general play an important role as cellular antioxidants, and each of them possess special contributions of their own. Selenium regulates thyroid hormone action and the oxidation/reduction status of vitamin C and other molecules. Metabolic function of copper includes collagen and elastin synthesis and formation of hemoglobin, red cells, and enzymes. Manganese is involved in the formation of bone. Of the trace elements, molybdenum acts as a cofactor for enzymes involved in catabolism of sulfur containing amino acids, purines, and pyrimidines. Cobalt is a part of the vitamin cyanocobalamin. Vanadium contributes to the regulation of Na<sup>+</sup>/K<sup>+</sup>-ATPase, phosphoryl transfer enzymes, adenylate cyclase, and protein kinases.<sup>4</sup>

A deficiency in the above-mentioned dietary minerals by definition must adversely affect the optimal biological function, and this change should be preventable or reversible by providing physiological amounts of the specific mineral. For example, magnesium (Mg<sup>2+</sup>) is an element of critical nutritional importance and is a cofactor in over 600 enzymatic

Received: April 4, 2019

Revised: June 3, 2019

Published: June 7, 2019

reactions vital for metabolic pathways like DNA/RNA/protein/ATP synthesis, cellular energy production, energy storage, glycolysis, and cellular secondary messenger systems.  $\text{Mg}^{2+}$  regulates the cellular ion channels, transporters, and signaling, which govern calcium, potassium, and sodium movement in and out of the cell. Therefore, deficiency of magnesium alone can lead to a cascade of malfunctions in the human metabolism.<sup>5</sup>

The chief source of mineral intake for human beings is through food and water. Essential inorganic minerals like calcium, magnesium, sodium, potassium, iron, and zinc which occur at milligram per kilogram (mg/kg) quantities in the body are crucial for the human system.<sup>6</sup> But the enteral suction of them is influenced by the source of intake as well. Since cooking processes can produce chemical transformations, they change the major nutrient composition and consequently affect the metal bioaccessibility and bioavailability.<sup>4</sup> Food processing and preservation techniques like freezing, canning, refining, and dehydrating contribute to the loss of various essential and trace minerals.<sup>7</sup> Usage of herbicides like glyphosates have been reported to reduce the physiological levels of essential mineral uptake by plants.<sup>8</sup> So, the mineral intake through the fluid pathway plays a key role in maintaining their balance within the body. Physiologically, waterborne minerals are in ionic form which tend to be bioavailable and are easily absorbed by the human gastrointestinal tract.<sup>9</sup> Although most of the surface waters and ground waters contain varying concentrations of minerals ( $\geq 250$  ppm), the hardness is removed which removes the essential minerals too. As divided doses throughout the day can promote mineral absorption efficiently in comparison to bolus consumption, it can be said that the best source to compensate these deficiencies is through mineral enriched waters.<sup>10</sup>

With shrinking freshwater reserves and rising water demands, water-stressed countries have begun to augment available water resources by utilizing oceans and inland seas as alternative water sources.<sup>11</sup> In a typical desalination unit, pressurized input water with high TDS (total dissolved solids) is fed to a membrane module, where a pure water permeate and a concentrate containing the retained salts are produced. This pure water is blended with 20% of the source water, a process called split treatment. In most cases, lime softening or ion exchange is performed to balance the demineralized water.<sup>12,13</sup> Nevertheless, both these approaches do not solve the problem completely, namely, the loss of essential and trace minerals. Numerous facilities have been developed without compliance with uniform guidelines, and they lack regulatory monitoring of essential mineral content. Most of the local bottled waters are low in all minerals<sup>14</sup> as they are usually obtained by membrane treatment, reverse osmosis, deionization, or distillation without any post-treatment.<sup>15</sup> Loss of essential minerals due to desalination especially by reverse osmosis has been a concern in the recent past.<sup>16</sup> A larger loss of magnesium has been detected in Israel in the recent studies as a result of desalination.<sup>17</sup> Based on existing knowledge and the fact that desalinated technologies constitute an increasing market in the world and may affect health, we can see an urgent need for more appropriate solutions for their mineral enhancement.

Controlled release of ions into water represent a promising technology for enriching the mineral content of potable water. As mentioned above, drinking water needs to have a certain minimum amount of macro- and trace minerals for it to

provide health benefits.<sup>2,7</sup> Geological studies on some prominent water basins across the world have shown the presence of various essential minerals. This is attributed to the silicate weathering that happened over a period of time.<sup>18,19</sup> Dissolution of sparingly soluble salts has been of partial interest in the context of pH control and water stabilization,<sup>20</sup> but these reports are not concerned with the release of essential and trace mineral ions for enriching the water quality. In order to mimic the geological conditions, we attempted to create stable structures of three-dimensional framework silicates called tectosilicates by embedding the desired mineral of interest in a leachable form. If each tetrahedron in the framework contains silicon as its central atom, the overall structure becomes electrically neutral (as in quartz). Whereas in tectosilicate structures, some of the tetravalent silicon are replaced by trivalent aluminum, giving rise to a deficiency of positive charge. The so-developed charge is balanced by the presence of cations elsewhere in the structure,<sup>21</sup> thereby trapping minerals within the porous three-dimensional framework cages. Many of the counter-cations in the network (i.e., exchangeable cations) are weakly held and thus are free to exchange with others in solution.<sup>22</sup> Since the Si–O are strong covalent bonds and the structure is interlocking, the tectosilicate minerals tend to have high hardness.

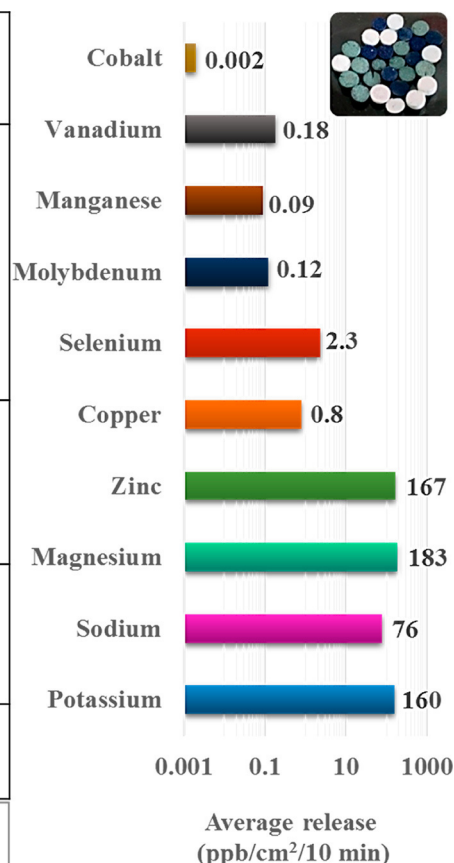
In our past work, we had shown sustainable release of carbonates into water from a composite matrix composed of porous inorganic networks.<sup>23</sup> In this work, we extend the science of constant release from such stable composites to a range of materials so that ionic release is controlled to the required level. A stable and robust composite of silica was achieved at a temperature below the melting point of the chosen mineral using carbonates as fluxes and by optimizing several combinations of the raw materials. The prepared monolith works as a controlled mineral releasing system maintaining an equilibrium concentration above which further release does not occur. The pores are small enough allowing the minerals to be preserved within, yet allowing sufficient interaction with water. By tuning the composition as well as the particle size, we demonstrate constant release of ten different ions such that their concentrations in water match with the recommended daily allowance (RDA) or dietary reference intake (DRI).<sup>24</sup> These ten minerals chosen for targeted release into water are categorized as four major and six trace minerals based on their quantity of recommended intake per day. The four major minerals shown here are magnesium, sodium, potassium, and zinc with RDAs of 320, 1500, 4700, and 8 mg/day, respectively. The six trace minerals shown here include manganese, copper, selenium, molybdenum, vanadium, and cobalt and with RDAs of 1800, 900, 55, 45, 25, and 0.06  $\mu\text{g}/\text{day}$ , respectively. Such materials have been compacted to produce mineral release pellets to be put as components of in-line filters to create affordable, optimally mineralized water. The concentrations of mineral intake from food and water are classified in Table 1 (see later in the text) with reference to the National Diet and Nutrition Survey (NDNS) and World health organization (WHO) report on trace minerals. We propose that all the essential minerals in water could be provided with such a strategy, yet delivering 100% safe potable water solving one of the important problems of the current water purification strategy.

These nature-inspired monoliths prepared in this work are in consonance with sustainability and greenness. A sustainable development is defined as the advancement that meets the

**Table 1.** Daily Recommended Intake of Essential Minerals for Human Metabolism (macro and trace), Recommended by NDNS and WHO, Their Tolerable Limit (left),<sup>4,9,24</sup> and Mineral Concentrations Supplemented through Designed Monoliths Given as ppb/cm<sup>2</sup> (right)

s.n	Type	Element	RDI (mg/day)	Tolerable limit (mg/day)	Total intake (food**) (mg/day)	Total intake (water***) (mg/day)	Reference for intake values
1	Macro	Calcium	1000	4500	830	600	1990 NDNS
2	Macro	Magnesium	320/420*	1400	280	100	NDNS 1986/7
3	Macro	Zinc	08/11*	40	9.8	10	1986/87 NDNS
4	Macro	Potassium	4700	4900	2800	24	NDNS, 1986/7
5	Macro	Sodium	1500	2300	7200	20–250	1986/1987 NDNS
6	Trace	Selenium	0.055	0.4	0.039	NA	1994 TDS
7	Trace	Chromium	.025/.035*	0.05	0.1	0.002	1997 TDS
8	Trace	Copper	0.9	10	1.4	.6	1986/87 NDNS
9	Trace	Manganese	1.8/2.3*	11	4.9	0.1	TDS, 1994
10	Trace	Molybdenum	0.045	2	0.11	0.02	1994 TDS
11	Trace	Cobalt	0.00006	1	0.012	0.02	1994 TDS
12	Trace	Vanadium	0.025	10	0.013	0.01	1980 UK TDS
13	Macro	Phosphorus	700	4000	1260	4.4	NDNS 1986/7
14	Macro	Chloride	2300	3600	-	-	-
15	Trace	Fluoride	3/4*	10	NA	NA	-
16	Trace	Iodine	0.15	1.1	0.22	-	1986/87 NDNS
17	Trace	Sulphur	NA	-	NA	NA	-
18	Trace	Boron	1	13	1.5	0.2–0.6	1994 TDS
19	Trace	Iron	18/8*	45	12	0.4	1986/87 NDNS
20	Trace	Nickel	NA	1	0.13	0.04	1997 TDS
21	Trace	Tin	0.01	2	1.8	NA	TDS, 1994
22	Trace	Silicon	NA	560	50	10	Bowen and Peggs 1984
23	Trace	Aluminium	NA	0.2	14	.2 to 2	WHO trace
24	Trace	Germanium	NA	0.007	0.004	NA	1994 TDS
25	Essential	Oxygen	No limits	No limits	No limits	NA	nil
26	Essential	Hydrogen	No limits	No limits	No limits	NA	nil
27	Essential	Nitrogen	No limits	No limits	No limits	NA	nil
28	Essential	Carbon	No limits	No limits	No limits	NA	nil

\* - Recommended intake for Female/Male  
 \*\* - Mean value  
 \*\*\* - Assuming drinking water intake of 2 L/day  
 NA - No data available



needs of the present without depletion of natural resources for the future generations to meet their own needs. Sustainability metrics and indices are measures of sustainability, which allows a clear assessment of a product and its manufacturing process. The essence of greenness can be defined as the efficient utilization of raw materials and elimination of waste in the production and application of a material. This also includes the efficiency in energy consumption, preferably the renewable resources. The use of toxic and/or hazardous solvents and reagents in the manufacture and application of a material should be minimized as much as possible.

## EXPERIMENTAL SECTION

Natural minerals of the tectosilicate group have three-dimensional arrays of interconnected silica and alumina tetrahedra linked to each other through shared oxygen atoms. If all of the corner oxygens are shared with another SiO<sub>4</sub> tetrahedra, then a framework structure develops. As a result, a crystal structure consisting of interconnected cavities and channels are formed. Our objective was to create such a nature-mimicking template of tectosilicate loaded with minerals of interest, held strongly along with controlled release. The mineral releasing monolith was synthesized using a solid state route. It was made by melting silica and alumina at the lowest possible temperature such that the incorporated mineral ions do not decompose. Various optimization studies were undertaken with respect to the Si–Al ratio, which ensures that the stability of the scaffold is maintained while the chosen cations are incorporated into its structure.

All the chemicals used were purchased from Sigma-Aldrich and used as such. Unless otherwise specified, all the chemicals used were of analytical grade.

**Synthesis of Sustained Mineral Releasing Materials.** Due to the requirement of the three-dimensional network that has chemical inertness and structural integrity, silica and alumina were our choices in mimicking mineral resources present in nature. The metal salt containing silica monoliths were, in general, comprised of a porous Si–O–Al scaffold loaded with the source of the chosen mineral, namely, magnesium carbonate (MgCO<sub>3</sub>), sodium carbonate (Na<sub>2</sub>CO<sub>3</sub>), potassium carbonate (K<sub>2</sub>CO<sub>3</sub>), copper carbonate (CuCO<sub>3</sub>), zinc oxide (ZnO), selenium trioxide (SeO<sub>3</sub>), cobalt oxide (CoO), manganese dioxide (MnO), vanadium pentoxide (V<sub>2</sub>O<sub>5</sub>), or molybdenum(VI) oxide (MoO<sub>3</sub>). The preference of carbonate or oxide forms of the mineral source was made based on the need for providing controlled bioavailability. For example, molybdenum(VI) oxide and calcium molybdate are absorbed well from the gastrointestinal tract. Zinc is an exception where zinc oxide and zinc carbonate possess a similar bioavailability. The minerals recommended in trace concentrations were chosen as oxide forms with ~20% bioavailability, whereas the macro minerals were in the carbonate forms with ~80% bioavailability. Figure 1 describes a schematic outline of the synthesis of the designed monolith and a water purification method based on the same.

Compositions of the raw materials were optimized in such a fashion that they form tectosilicate frameworks mimicking those present in nature. The framework structure and properties of the scaffold can be correlated with the molar ratio of Si/Al and was thus maintained in the window of 10–20. This provided us with the required properties of sustainable release, formation temperature < 850 °C, and robustness of the product. The composite consisted of 10 wt % of



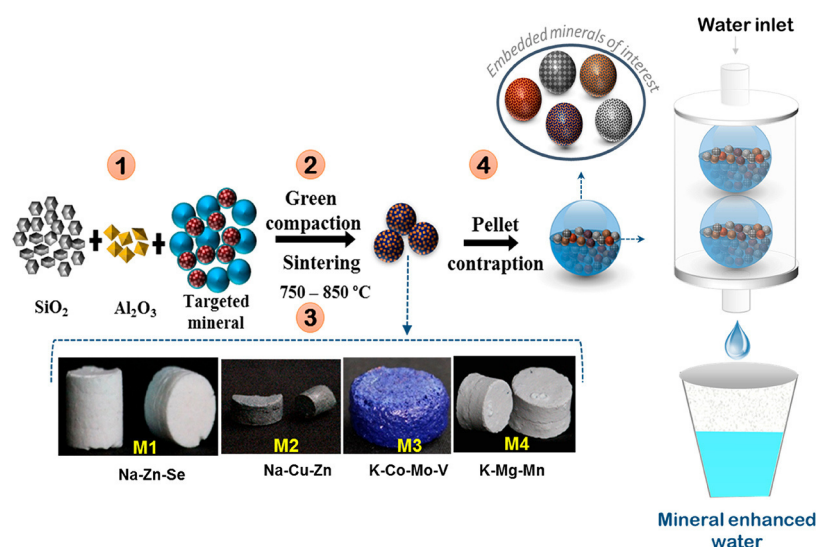


**Figure 1.** Schematic representation of the synthesis of mineral ion releasing monoliths (steps 1–4) and a water purification system based on the same. The monoliths are stable solids (in the shape of the mold) which may be combined as a contraption as per the need.

$\text{Na}_2\text{CO}_3$  which served as a flux to maintain the formation temperature as well as a source of sodium. The targeted mineral ions of interest were taken at a concentration of 15–25 wt % each, as per the recommended release in water. Four such monoliths, M1<sub>(Na-Zn-Se)</sub>, M2<sub>(Na-Cu-Zn)</sub>, M3<sub>(K-Co-Mo-V)</sub>, and M4<sub>(K-Mg-Mn)</sub> with 2–4 targeted minerals in each were synthesized in this work, thus demonstrating the release of a total of ten different mineral elements in water. Images of these ion-containing monoliths are presented in Figure 1.

The mixture of raw materials were homogenized and packed in molds and sintered at  $750\text{--}850\text{ }^\circ\text{C}$  for 1 h. The metal loading was performed homogeneously such that there were no specific regions of aggregation. This was important in achieving constant release of mineral ions in water. Decomposition temperatures of most of the chosen minerals were above  $850\text{ }^\circ\text{C}$  at atmospheric pressure.<sup>25</sup> The sintered monolith was cooled to room temperature followed by washing with water at ambient conditions up to 12 h and was used as such for further experiments. A contraption of such monoliths was made such that they can be used in an in-line water purification system.

**Characterization Techniques.** Metal-loaded monoliths were dried for 24 h at  $60\text{ }^\circ\text{C}$  in air and examined in detail for their morphological characteristics and elemental composition and were mapped for the elemental distribution using scanning electron microscopy (SEM) and transmission electron microscopy (TEM) equipped with energy dispersive spectroscopy (EDS). HRTEM images of the sample were obtained with JEM 3010 (JEOL, Japan) microscope operating at 300 kV with an ultrahigh resolution polepiece. Elemental mapping using TEM was done on an Oxford Semistem EDS system. The samples for HRTEM were prepared by dropping the dispersion on amorphous carbon films supported on a copper grid and subsequent drying. FEI Quanta 200/EDS was used for SEM. Identification of the tectosilicate and mineral phase(s) of all the samples was carried out by X-ray diffraction (XRD) using Cu  $K\alpha$  radiation at  $\lambda = 1.5418\text{ \AA}$  (Bruker AXS, D8 Discover, U.S.A.). Fourier transform infrared (FTIR) spectra of the samples were collected using a PerkinElmer FTIR spectrometer. The spectra were collected in the range of  $450\text{--}4000\text{ cm}^{-1}$ . X-ray photoelectron spectroscopy (XPS) measurements were performed using an ESCA Probe TPD of Omicron Nanotechnology with polychromatic Mg  $K\alpha$  as the X-ray source ( $h\nu = 1253.6\text{ eV}$ ), and the binding energy was calibrated with respect to C 1s at  $284.5\text{ eV}$ . The concentrations of mineral ions released in water were measured using inductively coupled plasma mass spectrometry (ICPMS) (PerkinElmer NexION 300X ICPMS).

**Kinetics of Ion Release.** Sustained release of minerals from the synthesized monoliths and their kinetics of release were studied using the following experimental procedure. About 500 mg of the as

prepared monolith pellets were rinsed thoroughly with distilled water before the experiments. Later, they were shaken briefly in 500 mL of deionized water. Concentrations of minerals released in the test water at different contact times (with 10 min interval) were measured based on the measurements at each step using ICPMS. The instrument was calibrated using commercial standards of selected ions. The measurements were performed using deionized water, and the initial concentration of any ion present was monitored for every individual experiment and was considered as blank.

**Sustained Release of Minerals in Water.** The performance of the material under continuous flow of water was tested in the cartridge mode. A cartridge containing 1 L of deionized water was treated with 1 g of the monolith material. After 15 min of standing time, the concentration of the released mineral was tested in the treated water. The cartridge was drained and filled with a fresh batch of deionized water (1 L), and the above procedure was repeated to monitor the release. This test was repeated up to 50 cycles. After every ten cycles of the above procedure, the material was dried for 18–20 h at room temperature and was tested for further mineral release.

**Prototype.** After evaluating the release performance of the material in batch and cartridge experiments, a mineral releasing prototype was developed. About 10 g of the synthesized composite pellets (each pellet of  $\sim 1\text{ g}$ ) was packed in a contraption that was assembled in-line along with a deionized water reservoir. The inlet and outlet flow rates of water were controlled such that there was sufficient contact time for the mineral to be released into it. The output water was analyzed after acidification (5%  $\text{HNO}_3$ ) and digestion, to ensure that all particulate matter that leached out, if at all, was also evaluated.

## RESULTS AND DISCUSSION

Tectosilicates have been commonly found in nature as well as synthesized artificially. Depending upon the type of raw materials used and the methods of synthesis adopted, properties of these tectosilicates would vary and, hence, their application can be modified. These tectosilicates in nature are often formed as a volcanic glass in various geological environments, under variable geochemical and physical conditions. Keeping this in view, a nature-mimicking scaffold loaded with mineral ions of interest were synthesized, and their properties are presented in the following.

**Characterization of Sustained Mineral Releasing Monoliths.** The SEM and TEM images of the granular particles of the monolith and their chemical compositions are

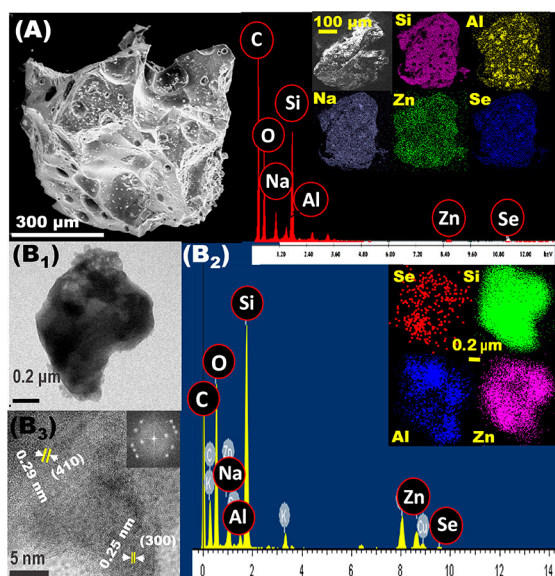


**Figure 2.** (A) SEM image of the material and the corresponding EDS spectra along with the elemental maps (right). (B<sub>1</sub>) TEM image of a grain of the material and (B<sub>2</sub>) the corresponding EDS spectra along with the elemental maps of the same grain (right). (B<sub>3</sub>) Lattice resolved image and its FFT pattern (inset).

shown in Figure 2. A granule of  $\sim 500\ \mu\text{m}$  of M<sub>1</sub> (see the Experimental Section) confirms the porous but crystalline morphology. Porosity is evident in the SEM image shown in Figure 2A, and the corresponding EDS confirms the presence of silicon, aluminum, sodium, zinc, and selenium. Elemental mapping of the metal ion-containing single grain of the monolith is presented in the inset. We can clearly see that the ions of interest are uniformly dispersed within the silica template and no specific aggregation of metals is found. This provides a uniform dissolution of the minerals when in contact with water. TEM image of a grain of material is shown in Figure 2B<sub>1</sub>. No metal particles can be detected, which means that the metal ions are located regularly along or in the pore walls of the silica network. The corresponding EDS spectra along with the elemental maps are shown. Also the lattice resolved image in Figure 2B<sub>3</sub> shows the lattice planes of crystallites at 0.29 nm indexed to 410 (*hkl*) corresponding to JCPDS PDF no. 88-2371 and at 0.25 nm indexed to 300 (*hkl*) corresponding to JCPDS PDF no. 22-0014. The fast Fourier transform (FFT) pattern in the inset of Figure 2B<sub>3</sub> shows crystalline nature of the monolith. SEM and TEM images of the granular particles of the monoliths, M<sub>2</sub>, M<sub>3</sub>, and M<sub>4</sub>, and their chemical compositions are shown in Figures S1–S3, respectively. Thus, SEM, TEM, EDS, and elemental mapping establish the formation of crystalline silicate monoliths with mineral ions evenly distributed in the network.

The X-ray diffraction patterns of the precursor composition and the amended granular composite are shown in Figure 3A,B. The pattern was analyzed using X'pert HighScore Plus Rietveld analysis software loaded with ICDD database, PDF-2 and JCPDS. Initially, the tetragonal phase of SiO<sub>2</sub> [00-001-0438] and Al<sub>2</sub>O<sub>3</sub> [00-037-1462] and monoclinic phases of SeO<sub>2</sub> [00-004-0429], ZnO [01-079-0207], and Na<sub>2</sub>CO<sub>3</sub> [01-071-1833] were the principal components of the precursor of composite M<sub>1</sub> (Figure 3A). Upon heating, the pattern shows peaks at  $2\theta$  (degree) at 22.00, 28.47, 31.49, 36.13, 36.41, 47.10, and 48.65 which correspond to (101), (111), (102), (200),

(112), (113), and (212) planes of cristobalite (39-1425), a framework silicate mineral having a tetragonal crystal structure along with Al<sub>2</sub>O<sub>3</sub> (hexagonal) and Na<sub>2</sub>O (cubic) (Figure 3B). Cristobalite present in nature is a high temperature SiO<sub>2</sub> polymorph and occurs in thermally metamorphosed sandstones. Despite the dominating cristobalite phase, the matrix also contains Al<sub>2</sub>(SeO<sub>4</sub>)<sub>3</sub> and Zn<sub>6</sub>Al<sub>12</sub>Si<sub>12</sub>O<sub>48</sub> which are embedded within the tectosilicate network. It should be noted that the decomposition temperatures of Na<sub>2</sub>CO<sub>3</sub> and K<sub>2</sub>CO<sub>3</sub> are 858 and 898 °C, respectively, at atmospheric pressure.<sup>25</sup>

Similarly, the XRD pattern of M<sub>2</sub> was matched with gehlenite and leucite (Figure S1A), M<sub>3</sub> was matched with cristobalite and feldspar (Figure S2A), and M<sub>4</sub> was matched with sanidine and orthoclase (Figure S3A).<sup>26</sup> These tectosilicates are composed of silica and alumina tetrahedra linked to each other through shared oxygen atoms. Because of the extended isomorphic substitution of Si<sup>4+</sup> by Al<sup>3+</sup> in the tetrahedra, a large unsatisfied negative charge is produced in the lattice. This negative charge is balanced by cations, which are retained by electrostatic bonds and move onto the surface or into the crystal structure of the tectosilicate network. The FTIR spectra in Figure 3C and Figures S1C, S2C, and S3C show metal-coordinated unidentate, bidentate, and bridged carbonate species along with Si–O–Si bending and Si–O stretching frequencies.<sup>27</sup> Figure 3D depicts the XPS analysis of the material. Deconvoluted spectra shown in Figure 3D (i) confirm the presence of oxygen, where O 1s peaks appear in the range of 531.5–532.0 eV for metal carbonates and 532.0–533.0 eV for SiO<sub>2</sub>. The C 1s appears at 284.8 eV due to C–C and at 288.5 eV due to O–C=O. Se 3d and Zn 2p are shown in Figure 3D (ii–iv). Two peaks located at 1043.1 and 1020.0 eV correspond to Zn 2p<sub>1/2</sub> and Zn 2p<sub>3/2</sub>, respectively, due to Zn<sup>2+</sup>, and the 3d peaks of selenium split into two well-defined peaks as 3d<sub>3/2</sub> and 3d<sub>5/2</sub>, which appeared at binding energies of 56.5 and 55.7 eV.<sup>28,29</sup> These indicate that the chosen mineral ions of interest are embedded in the SiO<sub>2</sub> matrix.

**Kinetics of Mineral Release from the Material.** From the release data presented in Figures 4 and 5, we understand that the targeted mineral ions are continuously leached into the water retaining the framework which is represented by negligible loss of the weight of the pellet (Figure S4A). Since the loss of weight is negligible after each release, all the mineral release experiments were done considering the same surface area calculated in the beginning. As the Al<sup>3+</sup> gets into the crystal lattice of the tectosilicate, it is not released into the water (Figure S4B). The structural integrity of the monolith is evident from the SEM image, and the corresponding EDS spectra along with the elemental maps and the powder XRD pattern of the material after 120 min of leaching are presented in Figure S5.

The concentration of mineral ions released into the water from the prepared monolith is highly tunable at relevant temperatures (5–35 °C) and varying TDS (100–1000 ppm). The release does not alter the pH of the water beyond the permissible limit of 6.5–8.5.<sup>30</sup> The release occurs within 5–15 min of contact time, and concentration of the release does not exceed their RDAs even when there is a prolonged contact time, tested up to 160 min in batch mode shown in Figure 4 for both major and trace minerals. The concentration of minerals released in deionized water is represented as ppb/cm<sup>2</sup> and reaches equilibrium. Average releases of 183 ppb of Mg<sup>2+</sup>/cm<sup>2</sup>, 76 ppb of Na<sup>+</sup>/cm<sup>2</sup>, 160 ppb of K<sup>+</sup>/cm<sup>2</sup>, 167 ppb of Zn<sup>2+</sup>/

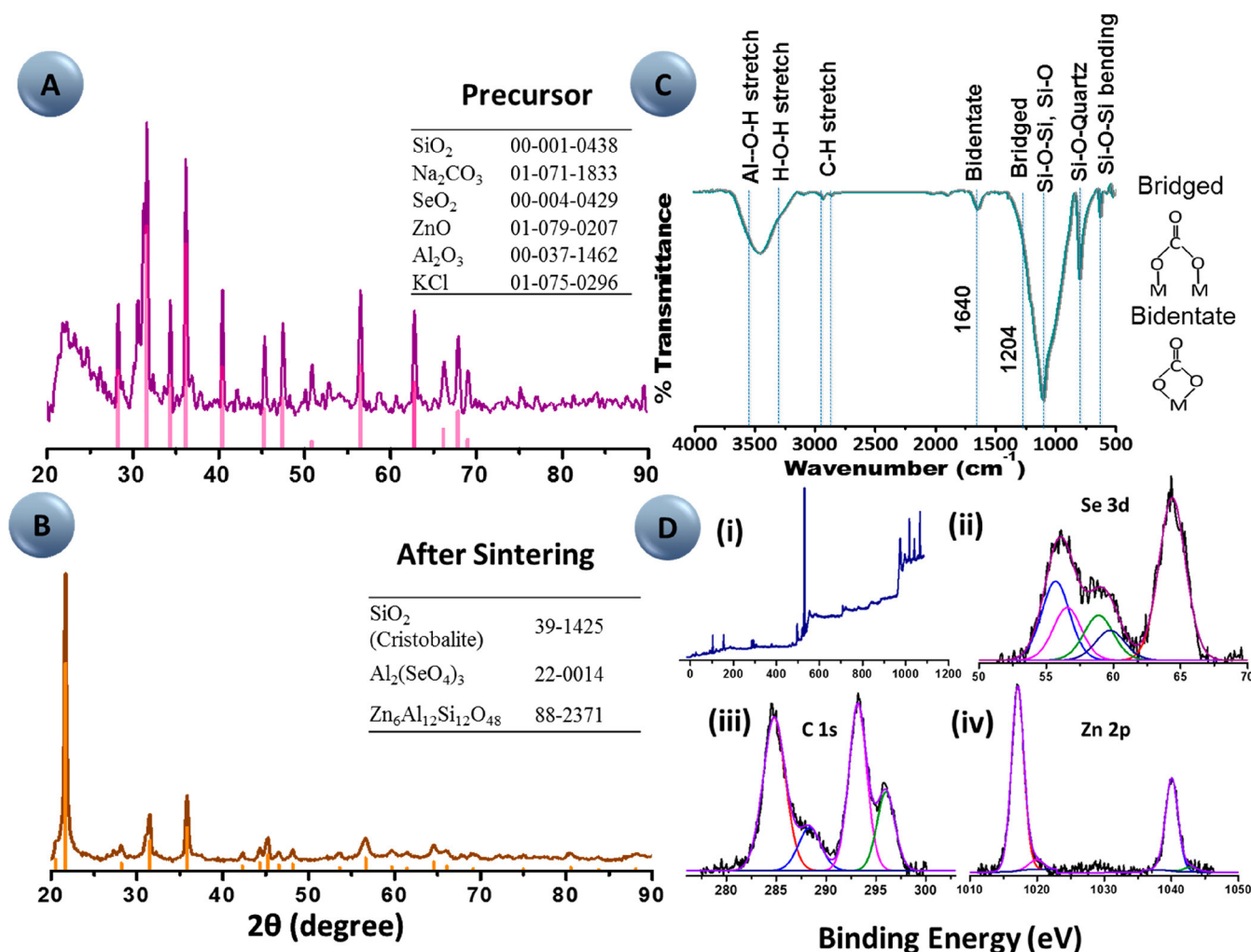


**Figure 3.** Powder XRD pattern of the precursor material (A) and the as prepared sintered pellet (B). The sintered pellet is compared with the low temperature form of SiO<sub>2</sub> cristobalite (JCPDS 39-1425). Specific features matching Al<sub>2</sub>(SeO<sub>4</sub>)<sub>3</sub> (JCPDS 22-0014) and Zn<sub>6</sub>Al<sub>12</sub>Si<sub>12</sub>O<sub>48</sub> (JCPDS 88-2371) are also observed. (C) Infrared spectrum of the mineral composite. (D) (i) XPS of the mineral ion releasing monolith. (ii–iv) Deconvoluted XPS spectra of corresponding Se 3d, C 1s, and Zn 2p regions, respectively.

cm<sup>2</sup>, 5 ppb of Se<sup>6+</sup>/cm<sup>2</sup>, and 0.9 ppb of Cu<sup>2+</sup>/cm<sup>2</sup> were observed. The possible release mechanism of the mineral ions is due to the intricate scaffold architecture of the calcined silica that allows only limited contact of water through its channel to dissolve it.

The performance of the material was studied under cartridge mode with continuous flow of water and sustained release data of mineral ions from the four major silica scaffolds, namely, M1<sub>(Na–Zn–Se)</sub>, M2<sub>(Na–Cu–Zn)</sub>, M3<sub>(K–Co–Mo–V)</sub>, and M4<sub>(K–Mg–Mn)</sub>, are shown in Figure 5. This was tested up to 50 cycles which demonstrates a constant and sustained release of the selected essential and trace minerals in drinking water, namely, Na<sup>+</sup>, K<sup>+</sup>, Mg<sup>2+</sup>, Zn<sup>2+</sup>, Se<sup>6+</sup>, Cu<sup>2+</sup>, Mn<sup>2+</sup>, V<sup>5+</sup>, Co<sup>2+</sup>, and Mo<sup>6+</sup>, in a strictly controlled fashion such that their concentrations match the RDA levels. Each data point is an average of triplicate experiments. After every ten cycles of exposure to water, the material was drained and dried for 18–20 h at room temperature and was tested for further release. After every step of drying of the sample, an increased release of sodium, potassium, and magnesium in the first round of exposure was observed (shown as a spike in the graph). The structural cavities and entry channels leading into the scaffold are large enough to retain water molecules within them, resulting in

prolonged soaking of the material by the stagnant water during the slower rate of drying at room temperature.<sup>23</sup> The dissolved cations inside the pore are released faster when the material is soaked in a fresh batch of water. This is not of consequence to the water purification device as the initial water collected is often discarded in typical reuse of the mineralization cartridge.

After evaluating the release performance of the material in batch and cartridge experiments, a mineral releasing prototype was developed as shown in Figure S6A. The efficiency of release from the contraption that was assembled in-line along with the deionized water reservoir is shown in Figure S6B–D. The inlet and outlet flow rates of water were controlled such that there is sufficient contact time for the mineral to be released into it.

Once released into water, understanding the speciation of ions is essential in order to confirm their bioavailability during consumption. Thus, a speciation diagram was prepared by including all the ions released into the system at pH = 7.5 and *T* = 25 °C. Figure S7 shows the number of complexes formed due to speciation of mineral ions at their specific release concentrations. The speciation diagram was prepared using simulations run on Visual MINTEQ software version 3.1 (freeware, available at <http://vminteq.lwr.kth.se>).



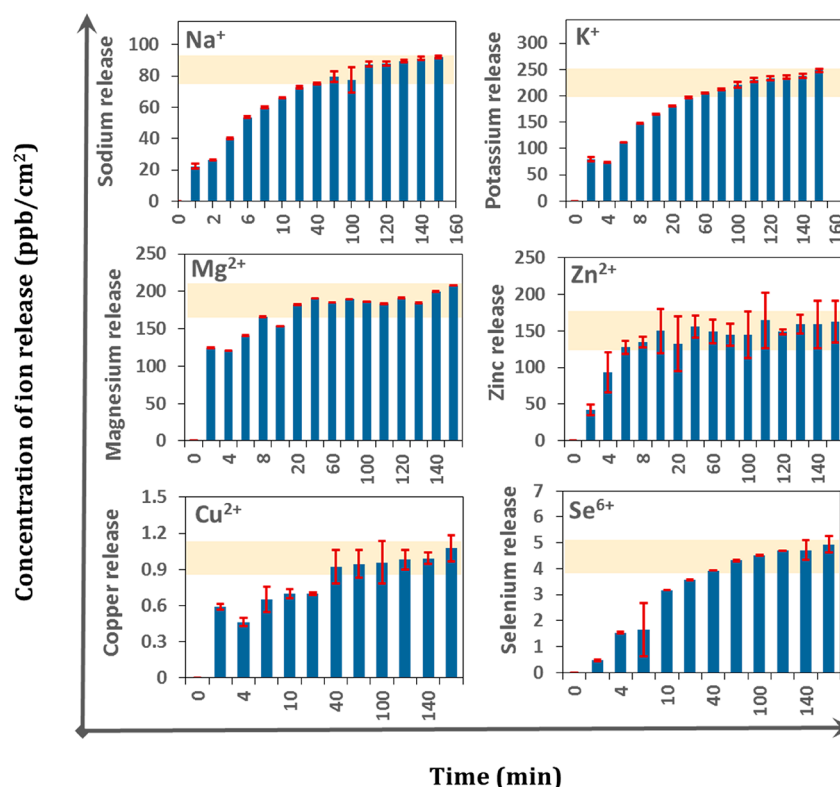


**Figure 4.** Kinetics of targeted mineral release from the monolith upon prolonged period of exposure to water. Equilibrium was attained typically beyond 100 min. The units are expressed in ppb/cm<sup>2</sup>, and the error bars are standard deviations from triplicate experiments.

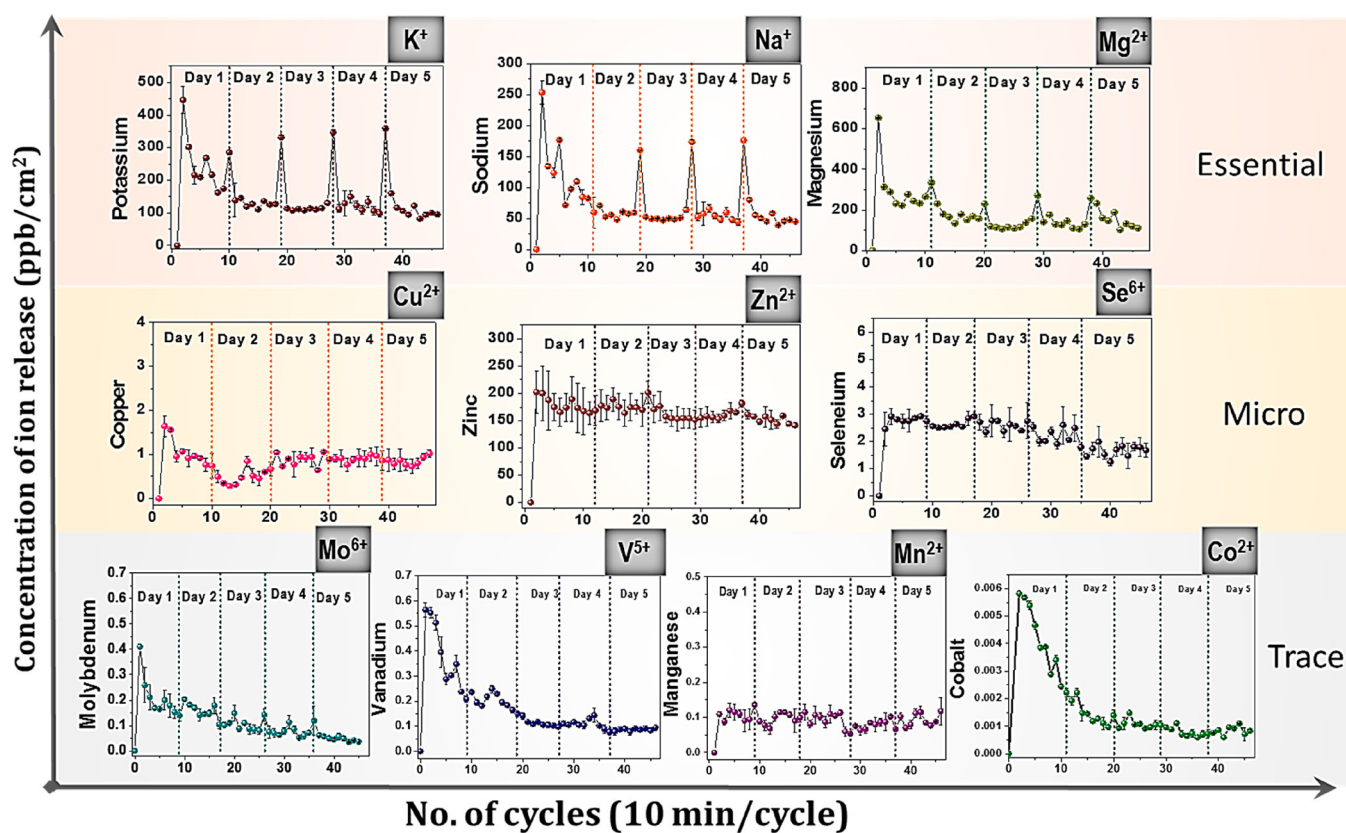


**Figure 5.** Sustained release of desired ions from the synthesized pellets, for up to 50 cycles. Ten cycles per day were conducted. Units are in ppb/cm<sup>2</sup>. A blank water was tested at the beginning of every 10 cycles designated as 0 ppb/cm<sup>2</sup> concentration. Error bars are standard deviations from triplicate experiments.

Table 2. Preliminary Sustainability Metrics Evaluated for the Synthesized Monoliths

materials	Sustainability Metrics Parameters					
	mass intensity (kg/kg)	solvent intensity (kg/kg)	reaction mass efficiency (%)	energy consumption (kWh)	E-factor (kg/kg)	CO <sub>2</sub> emission (mg/kg)
M1 <sub>(Na-Zn-Se)</sub>	1.204	4.75	83	3.2	0.025	40
M2 <sub>(Na-Cu-Zn)</sub>	1.388	5.47	72	4.0	0.060	80
M3 <sub>(K-Co-Mo-V)</sub>	1.408	5.55	71	3.2	0.046	80
M4 <sub>(K-Mg-Mn)</sub>	1.428	5.63	70	4.0	0.040	70

Therefore, by designing a mineral ion loaded silica monolith of tectosilicate structure, release of essential major minerals and trace minerals was achieved for remineralization of drinking water. An average concentration of the selected ten minerals released by the designed monolith is shown in Table 1. The table highlights the essential elements for human metabolism (macro and trace) recommended by National Diet and Nutrition Survey (NDNS)<sup>24</sup> and World health organization (WHO) report on trace elements,<sup>4</sup> their tolerable upper limit, total intake from food and water, and mineral concentrations supplemented via the designed monoliths.

**Sustainability Metrics Evaluation.** The “greenness” of all the four materials and their synthesis procedures were determined in terms of relevant sustainability parameters, as shown in Table 2.

**Raw Materials.** The major raw materials used for the scaffolds were silica/alumina which are sustainable in nature as they are known to be nonecotoxic and nonhazardous.<sup>31</sup> Crystalline silica (quartz) is not known to be ecotoxic; i.e., there are no data that suggest that crystalline silica (quartz) is toxic to birds, fish, invertebrates, microorganisms, or plants. The mass-based sustainability metrics were assessed where the mass intensities for M1<sub>(Na-Zn-Se)</sub>, M2<sub>(Na-Cu-Zn)</sub>, M3<sub>(K-Co-Mo-V)</sub>, and M4<sub>(K-Mg-Mn)</sub> were close to 1, indicating maximum conversion of raw materials into useful products with very high reaction mass efficiencies. As far as usage of solvents is concerned, the solid state synthesis route involves solvents in meager amounts, thus giving negligible water intensity numbers.

**Energy Consumption.** For getting the desired framework of Si/Al, the monolith materials had to be sintered at high temperatures in the furnace, which mainly contributes to the electrical energy consumption. A maximum energy usage of 4 kWh per kg of material was observed in this case which includes homogenization, compaction, and sintering. However, release of minerals from the composite occurs by diffusion/dissolution, and no energy is consumed during the process of mineralization of water. The energy used for production is comparatively less significant than the reported energy consumption required for the operation of reverse osmosis for per cubic meter of purified water<sup>32</sup> (2.2–6.7 kWh/m<sup>3</sup>). The cumulative energies consumed for the production of polymers<sup>33,34</sup> vary between 23–40 kWh/L.

**Resulting Emissions.** The synthesis, washing, and application of these monoliths generate a minimal amount of waste which can be seen by the calculated E-factors, one of the most important parameters used to evaluate sustainability. Finally, as a result of sintering of carbonate salts at high temperatures, there is evolution of some amount of carbon dioxide, shown as CO<sub>2</sub> emission values (<80 mg/kg). However, we can work toward minimizing the gas evolution by further optimizing the sintering temperature by addition of green fluxes. Though the total carbon footprint of a product is made up of emissions

produced at every stage of the life cycle, this value depicts only the gate-to-gate approach and focuses on only the synthesis procedure and ignores all steps before and after. A cradle-to-gate assessment of the material's CO<sub>2</sub> emission including the manufacture of raw materials and production of the designed monolith is presented in Table S1. The CO<sub>2</sub> emission due to the transport and disposal of finished goods is not included, and therefore it is not a cradle-to-grave assessment.

**Toxicity potential.** Ions like Se<sup>6+</sup>, Cu<sup>2+</sup>, Mn<sup>2+</sup>, V<sup>5+</sup>, Co<sup>2+</sup>, and Mo<sup>6+</sup> are trace minerals in the human body. Therefore, they are required in meager amounts, and concentrations beyond a particular limit show acute oral toxicity. Therefore, the manufacturing process should undertake precautionary measures. The LD 50 values of all the raw materials used for the composite preparation are shown in Table S2.

**Disposal of Waste.** Once the material is exhausted after complete leaching of minerals, the expected leftover material is the silica scaffold, which is again environment friendly. So, the issue of waste disposal is inherently solved in this case.

The equations used to for the evaluations of the sustainability metrics are listed in the Supporting Information (eqs 1–5).

## CONCLUSION

We report a composite material, forming a structurally stable monolith, releasing selective essential mineral ions in water at a fixed concentration for a prolonged period to enhance the quality of drinking water. Characterization studies indicate that the synthesized materials match tectosilicates present in nature. We have achieved the formation of robust three-dimensional tectosilicate matrices at temperatures below their standard formation temperatures, which entrap the cations of interest. The monoliths have been prepared with inert template-forming materials mimicking nature, which releases mineral ions at precise concentrations for each mineral, as described earlier. The matrices do not change even upon longer periods of exposure to water at room temperature. Such concentrations of minerals can reduce the occurrences of conditions such as osteoporosis, ulceration of epithelial lines, and other mineral deficiencies, observed in several parts of the world due to the consumption of demineralized water. This material can be used along with several water purification technologies to develop a synergetic enhancement system, delivering mineral-balanced potable water.

Although research shows that other trace elements like nickel, chromium, etc. are reported to be essential in human metabolism, there is no clear evidence on the RDA for these minerals. If known, several of these ions can also be released controllably in a similar fashion so that “enhanced” water may be supplied. By modifying the surface charge and surface properties using organic molecules or surfactants, a similar monolith with anion releasing property can be designed. Such modifications of the designed monolith with different

compositions can be developed for additional release of both anions and cations, with comparable performances.

## ■ ASSOCIATED CONTENT

### ■ Supporting Information

The Supporting Information is available free of charge on the ACS Publications website at DOI: 10.1021/acssuschemeng.9b01902.

Scanning and transmission electron microscopic images, energy dispersive X-ray spectra with elemental mapping from both SEM and TEM, XRD and XPS of the composites  $M2_{(Na-Cu-Zn)}$ ,  $M3_{(K-Co-Mo-V)}$ , and  $M4_{(K-Mg-Mn)}$ , and schematic of a prototype setup and kinetics of release of ten minerals during exposure to continuous flow of water and their speciation data (PDF)

## ■ AUTHOR INFORMATION

### Corresponding Author

\*(T.P.) E-mail: [pradeep@iitm.ac.in](mailto:pradeep@iitm.ac.in). Fax: +91-44-2257-0545.

### ORCID

Swathy Jakka Ravindran: 0000-0002-7882-7871

Avula Anil Kumar: 0000-0001-6878-8736

Ligy Philip: 0000-0001-8838-2135

Thalappil Pradeep: 0000-0003-3174-534X

### Author Contributions

T.P. and S.J.R. designed the experiments. S.J.R., A.M., P.S., A.A.K., Md.R.I., and S.M. performed the experiments. T.P., L.P., and J.R.S. analyzed the data and wrote the paper, with input from all authors.

### Notes

The authors declare no competing financial interest.

## ■ ACKNOWLEDGMENTS

We thank Mr. Sundar Raj for the technical support in SEM analysis. We thank Mr. Biswajit Mondal for the technical support in TEM analysis. We thank the Department of Science and Technology (Government of India) through Grants SR/NM/TP-92/2016(G) and DST/TM/WTI/WIC/2k17/82(G), which made this research possible.

## ■ REFERENCES

- (1) De la Guardia, M.; Garrigues, S. *Handbook of Mineral Elements in Food*; John Wiley & Sons: 2015.
- (2) World Health Organization. *Calcium and Magnesium in Drinking Water: Public Health Significance*; World Health Organization: 2009.
- (3) O'Dell, B. L.; Sunde, R. A. *Handbook of Nutritionally Essential Mineral Elements*; CRC Press: 1997.
- (4) Krishnamachari, K. A. *Trace Elements in Human Nutrition and Health*; World Health Organization: 1996.
- (5) Nielsen, F. H. Dietary Magnesium and Chronic Disease. *Adv. Chronic Kidney Dis.* **2018**, 25 (3), 230–235.
- (6) Zand, N.; Christides, T. L. E. *Dietary Intake of Minerals, Handbook of Mineral Elements in Food*; John Wiley & Sons, Ltd.: 2015.
- (7) Schroeder, H. A. Losses of Vitamins and Trace Minerals Resulting from Processing and Preservation of Foods. *Am. J. Clin. Nutr.* **1971**, 24 (5), 562–573.
- (8) Cakmak, I.; Yazici, A.; Tutus, Y.; Ozturk, L. Glyphosate Reduced Seed and Leaf Concentrations of Calcium, Manganese, Magnesium, and Iron in Non-Glyphosate Resistant Soybean. *Eur. J. Agron.* **2009**, 31 (3), 114–119.
- (9) World Health Organization. Nutrients in drinking water [https://www.who.int/water\\_sanitation\\_health/publications/nutrients-in-dw/en/](https://www.who.int/water_sanitation_health/publications/nutrients-in-dw/en/) (accessed Dec. 12, 2018).
- (10) Heaney, R. P.; Dowell, M. S. Absorbability of the Calcium in a High-Calcium Mineral Water. *Osteoporosis Int.* **1994**, 4 (6), 323–324.
- (11) Hoek, E. M. V. Turning on the Taps. *Npj Clean Water* **2018**, 1 (1), 4.
- (12) Glucina, K.; Alvarez, A.; Lainé, J. M. Assessment of an Integrated Membrane System for Surface Water Treatment. *Desalination* **2000**, 132 (1–3), 73–82.
- (13) Kim, Y. M.; Kim, S. J.; Kim, Y. S.; Lee, S.; Kim, I. S.; Kim, J. H. Overview of Systems Engineering Approaches for a Large-Scale Seawater Desalination Plant with a Reverse Osmosis Network. *Desalination* **2009**, 238 (1–3), 312–332.
- (14) Garzon, P.; Eisenberg, M. J. Variation in the Mineral Content of Commercially Available Bottled Waters: Implications for Health and Disease. *Am. J. Med.* **1998**, 105 (2), 125–130.
- (15) Kozisek, F. Health Risks from Drinking Demineralised Water. *Nutrients in Drinking Water*; World Health Organization: 2005; pp 148–163.
- (16) Safe Drinking Water Committee, National Research Council. *Drinking Water and Health*; National Academies Press: 1977.
- (17) Rosen, V. V.; Garber, O. G.; Chen, Y. Magnesium Deficiency in Tap Water in Israel: The Desalination Era. *Desalination* **2018**, 426, 88–96.
- (18) Singh, S. K.; France-Lanord, C. Tracing the Distribution of Erosion in the Brahmaputra Watershed from Isotopic Compositions of Stream Sediments. *Earth Planet. Sci. Lett.* **2002**, 202 (3–4), 645–662.
- (19) Rengarajan, R.; Singh, S. K.; Sarin, M. M.; Krishnaswami, S. Strontium Isotopes and Major Ion Chemistry in the Chambal River System, India: Implications to Silicate Erosion Rates of the Ganga. *Chem. Geol.* **2009**, 260 (1–2), 87–101.
- (20) World Health Organization. *Guidelines for Drinking-Water Quality*. Geneva, 2012.
- (21) Ma, W.; Brown, P. W.; Komarneni, S. Characterization and Cation Exchange Properties of Zeolite Synthesized from Fly Ashes. *J. Mater. Res.* **1998**, 13 (1), 3–7.
- (22) Widiastuti, N.; Wu, H.; Ang, M.; Zhang, D. The Potential Application of Natural Zeolite for Greywater Treatment. *Desalination* **2008**, 218 (1–3), 271–280.
- (23) Swathy, J. R.; Pugazhenthiran, N.; Sudhakar, C.; Anil Kumar, A.; Pradeep, T. Sparingly Soluble Constant Carbonate Releasing Inert Monolith for Enhancement of Antimicrobial Silver Action and Sustainable Utilization. *ACS Sustainable Chem. Eng.* **2016**, 4 (7), 4043–4049.
- (24) Copper, I. O. M. *Dietary Reference Intakes for Vitamin A Vitamin K, Arsenic, Boron, Chromium, Copper, Iodine, Iron, Manganese, Molybdenum, Nickel, Silicon, Vanadium, and Zinc*; The National Academies Press: Washington, DC, 2001.
- (25) Lide, D. R. E. *CRC Handbook of Chemistry and Physics*, 90th ed.; CRC Press: Boca Raton, FL, 2009.
- (26) Barthelmy, D. Mineralogy Database. <http://www.webmineral.com> (accessed Sep. 4, 2018).
- (27) Du, H.; Williams, C. T.; Ebner, A. D.; Ritter, J. A. In Situ FTIR Spectroscopic Analysis of Carbonate Transformations during Adsorption and Desorption of CO<sub>2</sub> in K-Promoted HTlc. *Chem. Mater.* **2010**, 22 (11), 3519–3526.
- (28) Wagner, C. D.; Riggs, W. M.; Davis, L. E.; Moulder, J. F.; Muilenberg, G. E. *Handbook of X-Ray Photoelectron Spectroscopy: A Reference Book of Standard Data for Use in X-Ray Photoelectron Spectroscopy*; Perkin-Elmer Corp.: Eden Prairie, MN, 1979.
- (29) Shchukarev, A.; Korolkov, D. XPS Study of Group IA Carbonates. *Open Chem.* **2004**, 2 (2), 347–362.
- (30) US EPA. National primary drinking water regulations. <https://www.epa.gov/ground-water-and-drinking-water/national-primary-drinking-water-regulations> (accessed Dec. 12, 2018).
- (31) Environmental protection agency. *Resource Conservation and Recovery Act*; EPA: 1976.

- (32) Buonomenna, M. G. Membrane Processes for a Sustainable Industrial Growth. *RSC Adv.* **2013**, 3 (17), 5694–5740.
- (33) Tabone, M. D.; Cregg, J. J.; Beckman, E. J.; Landis, A. E. Sustainability Metrics: Life Cycle Assessment and Green Design in Polymers. *Environ. Sci. Technol.* **2010**, 44 (21), 8264–8269.
- (34) Cornejo, P. K.; Santana, M. V. E.; Hokanson, D. R.; Mihelcic, J. R.; Zhang, Q. Carbon Footprint of Water Reuse and Desalination: A Review of Greenhouse Gas Emissions and Estimation Tools. *J. Water Reuse Desalin.* **2014**, 4 (4), 238–252.

# Geologically-inspired monoliths for sustainable release of essential minerals into drinking water

*Swathy Jakka Ravindran<sup>†‡</sup>, Ananthu Mahendranath<sup>†</sup>, Srikrishnarka Pillalamarri<sup>†</sup>, Avula Anil Kumar<sup>†</sup>, Md Rabiul Islam<sup>†</sup>, Sritama Mukherjee<sup>†</sup>, Ligy Philip<sup>‡</sup>, Thalappil Pradeep<sup>†\*</sup>*

<sup>†</sup>DST Unit of Nanoscience (DST UNS) and Thematic Unit of Excellence (TUE), Department of Chemistry, Indian Institute of Technology Madras, Adyar, Chennai 600 036, India.

<sup>‡</sup>Environmental and Water Resources Engineering (EWRE) Division, Department of Civil Engineering, Indian Institute of Technology Madras, Adyar, Chennai 600 036, India.

\*Corresponding Author: (T.P.) E-mail: [pradeep@iitm.ac.in](mailto:pradeep@iitm.ac.in). Fax: +91-44-2257-0545.

## SUPPORTING INFORMATION CONTENT

Total number of pages	:	11
Total number of figures	:	7
Total number of tables	:	2
Total number of equations	:	5

## TABLE OF CONTENTS

Supporting Figure	Title	Page No.
Figure S1	Characterization of microstructure and chemical composition of the sustained copper and zinc releasing monolith, M2 <sub>(Na-Cu-Zn)</sub>	3
Figure S2	Characterization of microstructure and chemical composition of monolith, M3 <sub>(K-Co-Mo-V)</sub> releasing oligo/trace elements namely cobalt, molybdenum and vanadium	4
Figure S3	Characterization of microstructure and chemical composition of monolith - M4 <sub>(K-Mg-Mn)</sub> releasing magnesium / manganese	5
Figure S4	Stability of scaffold material in the test water	6
Figure S5	Characterization and chemical composition of monolith – M1 <sub>(Na-Zn-Se)</sub> after 120 cycles of leaching (a) SEM image and the corresponding EDS spectra along with the elemental maps (b) Powder XRD pattern.	6
Figure S6	Mineral release trend from the designed prototype	7
Figure S7	Speciation of mineral ions formed in water after the release	8
Equation 1 – 5	Equations used for evaluation of sustainability metrics	9
Table S1	CO <sub>2</sub> emission (including raw material manufacture and monolith production)	10
Table S2	LD-50 of the raw materials used for the synthesis of material	11



## Supporting information 1

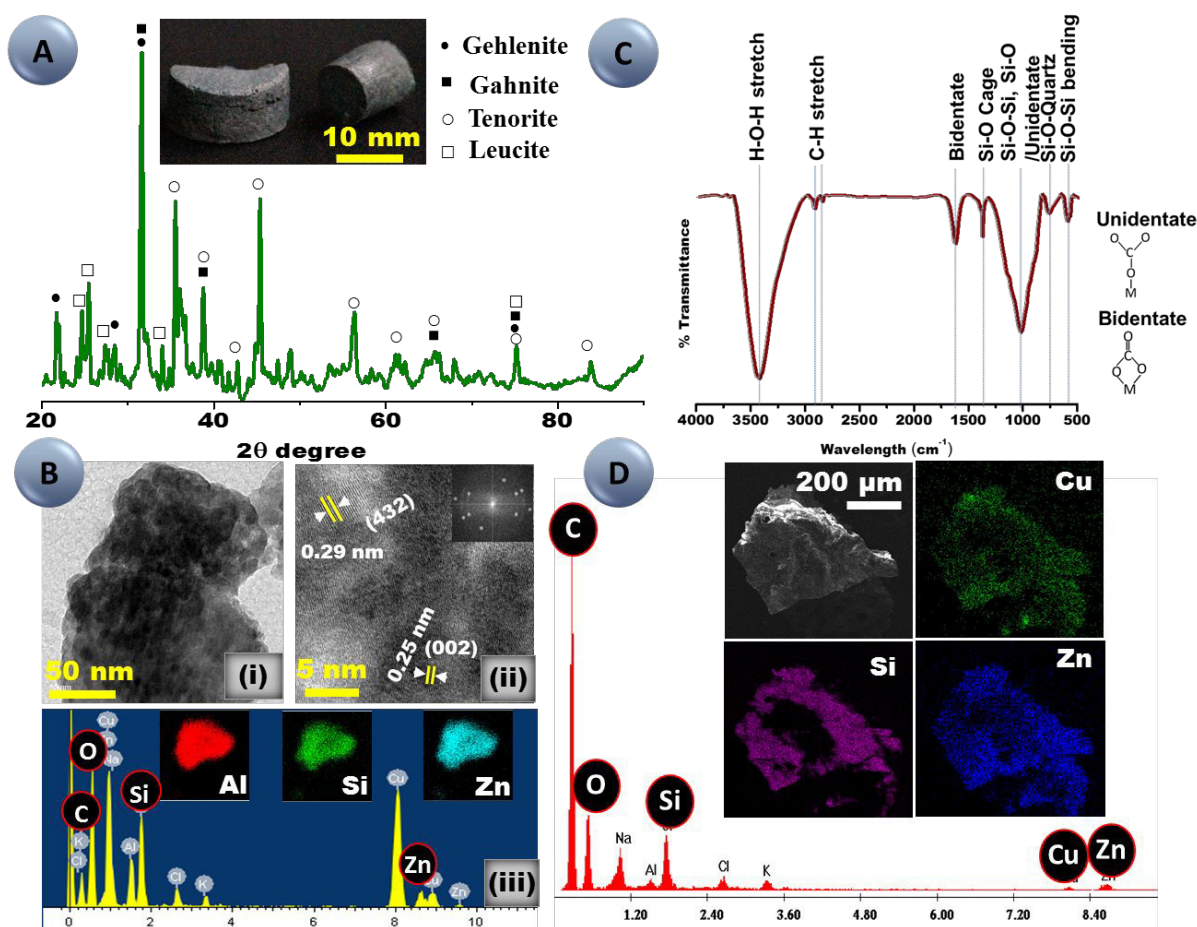


**Figure S1.** Characterization of microstructure and chemical composition of the sustained copper and zinc releasing monolith,  $M2_{(Na-Cu-Zn)}$ . (A) Powder XRD pattern of the sintered monolith compared with Gehlenite (Ca<sub>2</sub>Al(AlSi)O<sub>7</sub>), Gahnite (ZnAl<sub>2</sub>O<sub>4</sub>), Tenorite (CuO) and Leucite (KAl(Si<sub>2</sub>O<sub>6</sub>)). Inset shows the photograph of the monolith. (B) (i) TEM image of a grain of the material, (ii) the lattice resolved image of the same grain and its FFT pattern (inset) and (iii) the corresponding EDS spectra along with the elemental maps. As the TEM grid is made of copper, its mapping is not shown. (C) Infrared spectrum of the mineral composite. (D) SEM image of the material and the corresponding EDS spectrum along with elemental maps.



## Supporting information 2

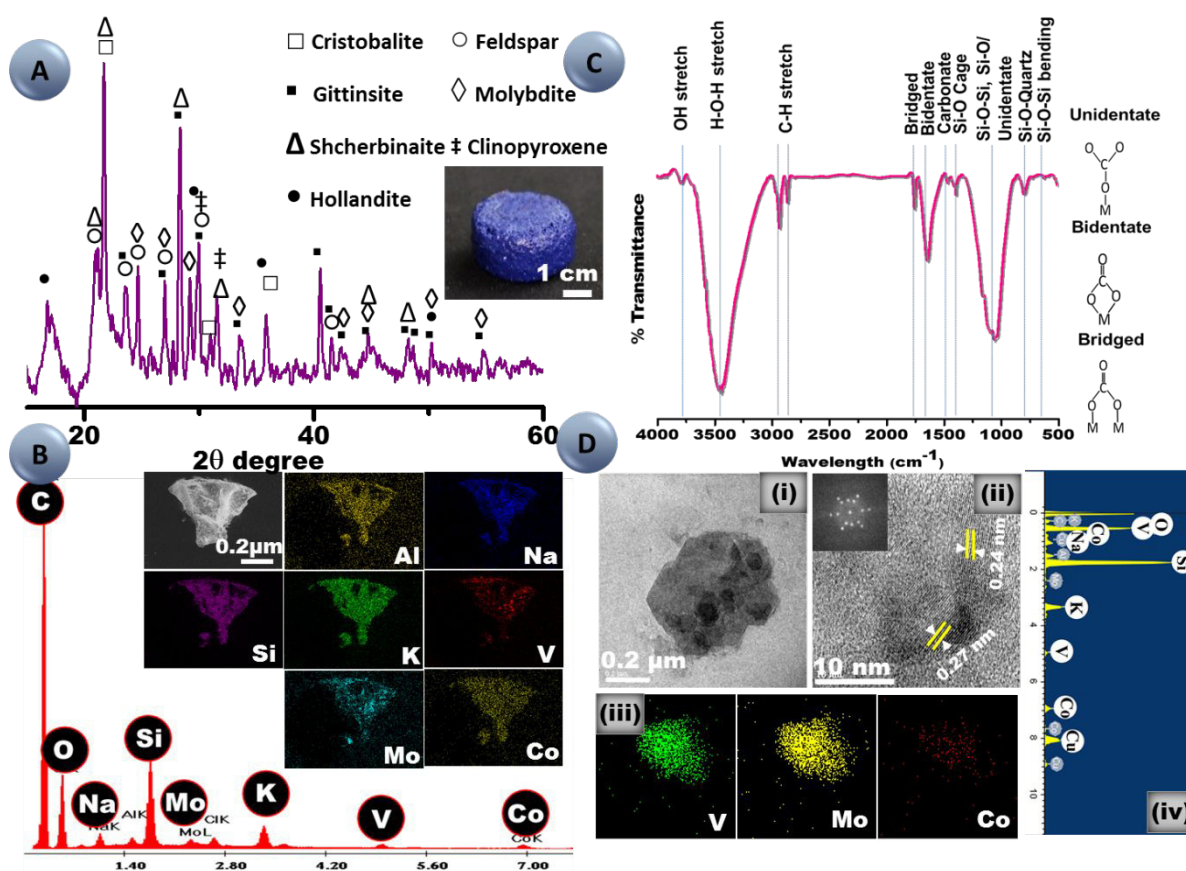


**Figure S2.** Characterization of microstructure and chemical composition of monolith,  $M3_{(K-C0-M0-V)}$  releasing oligo/trace elements namely cobalt, molybdenum and vanadium. (A) Powder XRD pattern of the sintered monolith and the photograph of the pellet (Inset). The material  $M3_{(K-C0-M0-V)}$  is matched with Cristobalite ( $SiO_2$ ), Feldspar sanidine ( $KAlSi_3O_8$ ) and other silicate phases like Clinopyroxene ( $Na_1O_6Si_2V$ ), Hollandite ( $K_{0.8}O_{17}V_{10}$ ) and Molybdate ( $MoO_3$ ), Shcherbinaite ( $V_2O_5$ ). (B) SEM image of the material and the corresponding EDS spectrum along with the elemental maps. (C) Infrared spectrum of the mineral composite (D) (i) TEM image of a grain of material and (ii) the lattice resolved image of the same grain with the FFT pattern (inset). The corresponding elemental maps (iii) and the EDS spectrum (iv).

### Supporting information 3

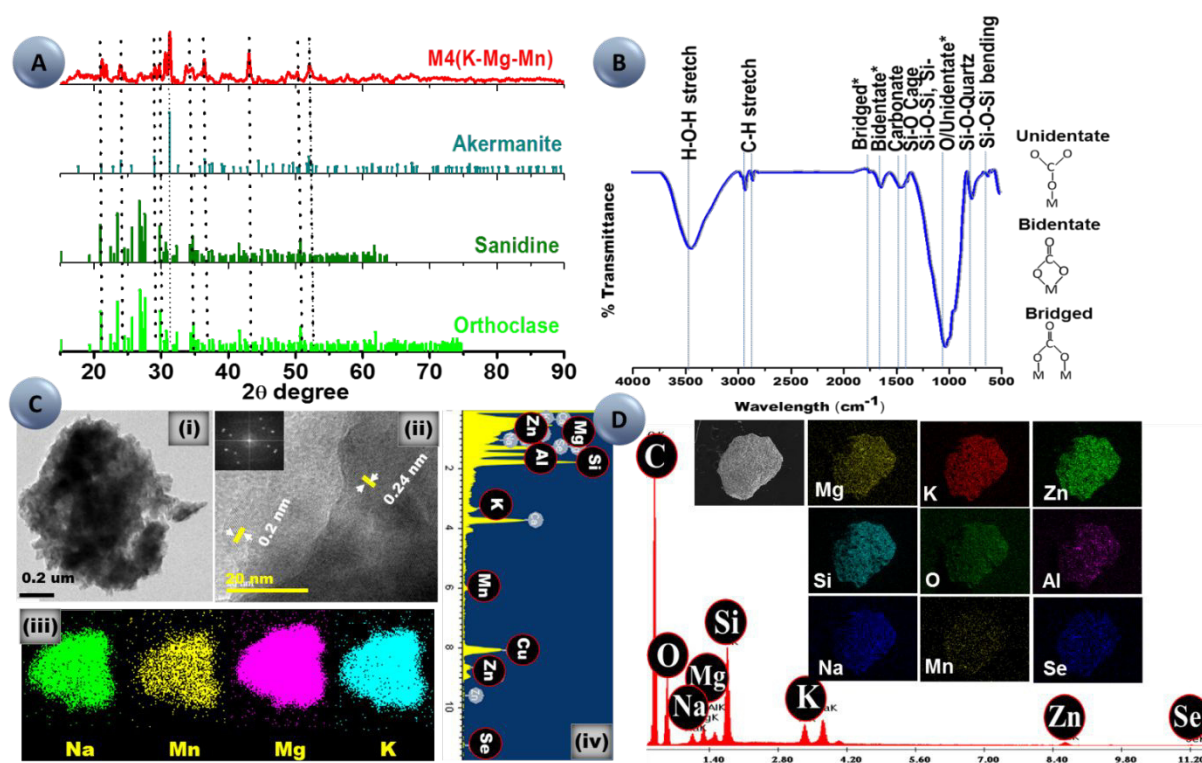


**Figure S3.** Characterization of microstructure and chemical composition of monolith - M4(K-Mg-Mn) releasing magnesium / manganese. The material was incorporated with 6 elements to show a simultaneous release from the single system. (A) Powder XRD pattern of the material, compared with Akermanite ( $\text{Ca}_2\text{Mg}[\text{Si}_2\text{O}_7]$ ), Sanidine ( $\text{K}(\text{AlSi}_3\text{O}_8)$ ) and Orthoclase ( $\text{KAlSi}_3\text{O}_8$ ). (B) Infrared spectrum of the mineral composite. (C) (i) TEM image of a grain of the material and (ii) the lattice resolved image of the same grain with the FFT pattern (Inset). The corresponding elemental maps (iii) and the EDS spectrum (iv). (D) SEM image of the material and corresponding EDS spectrum with elemental maps.

## Supporting information 4

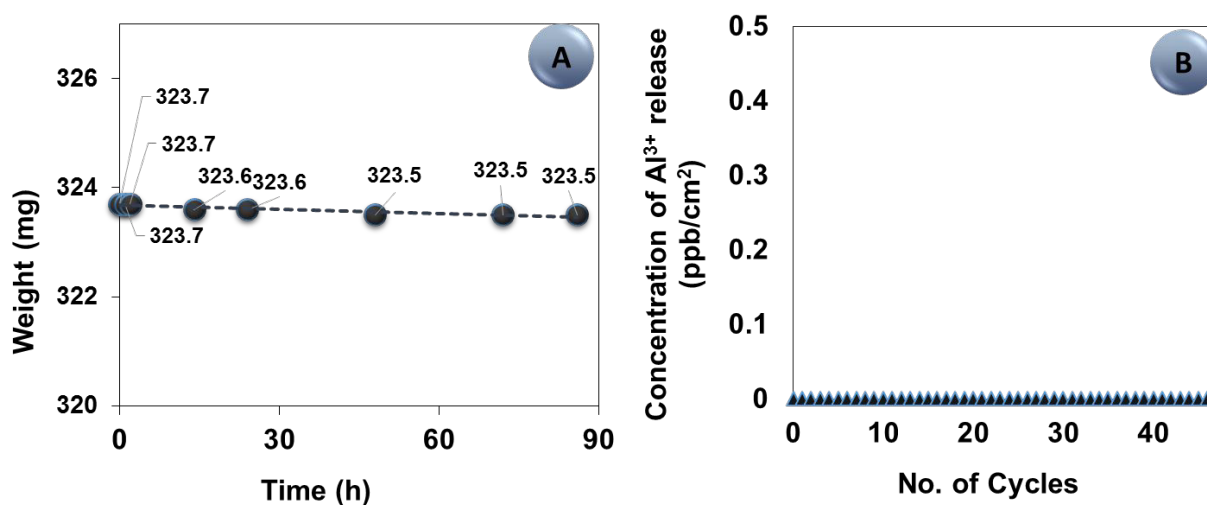


**Figure S4.** Stability of scaffold material in test water (A) Weight loss per cm<sup>2</sup> of the monoliths immersed in water as a function of time. (B) Concentration of Al<sup>3+</sup> release in water.

## Supporting information 5

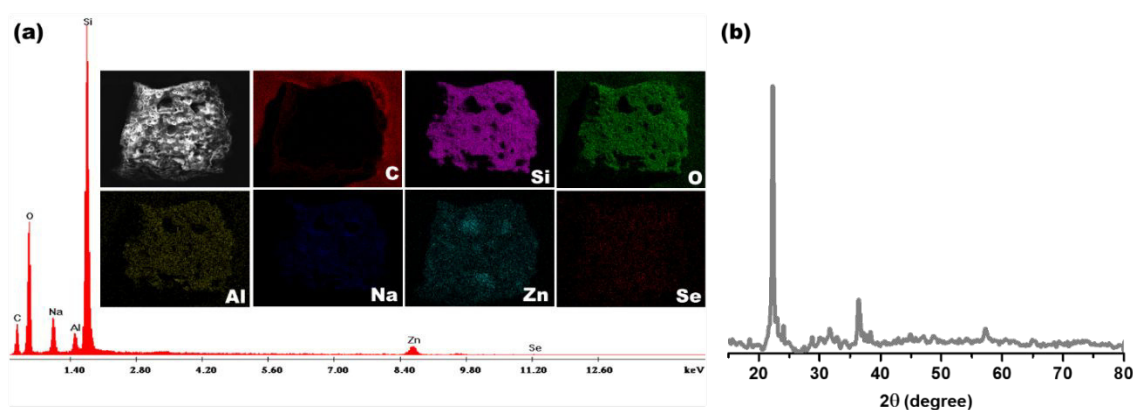


**Figure S5.** Characterization and chemical composition of monolith – M1<sub>(Na-Zn-Se)</sub> after 120 cycles of leaching (a) SEM image and the corresponding EDS spectra along with the elemental maps (b) Powder XRD pattern.

## Supporting information 6

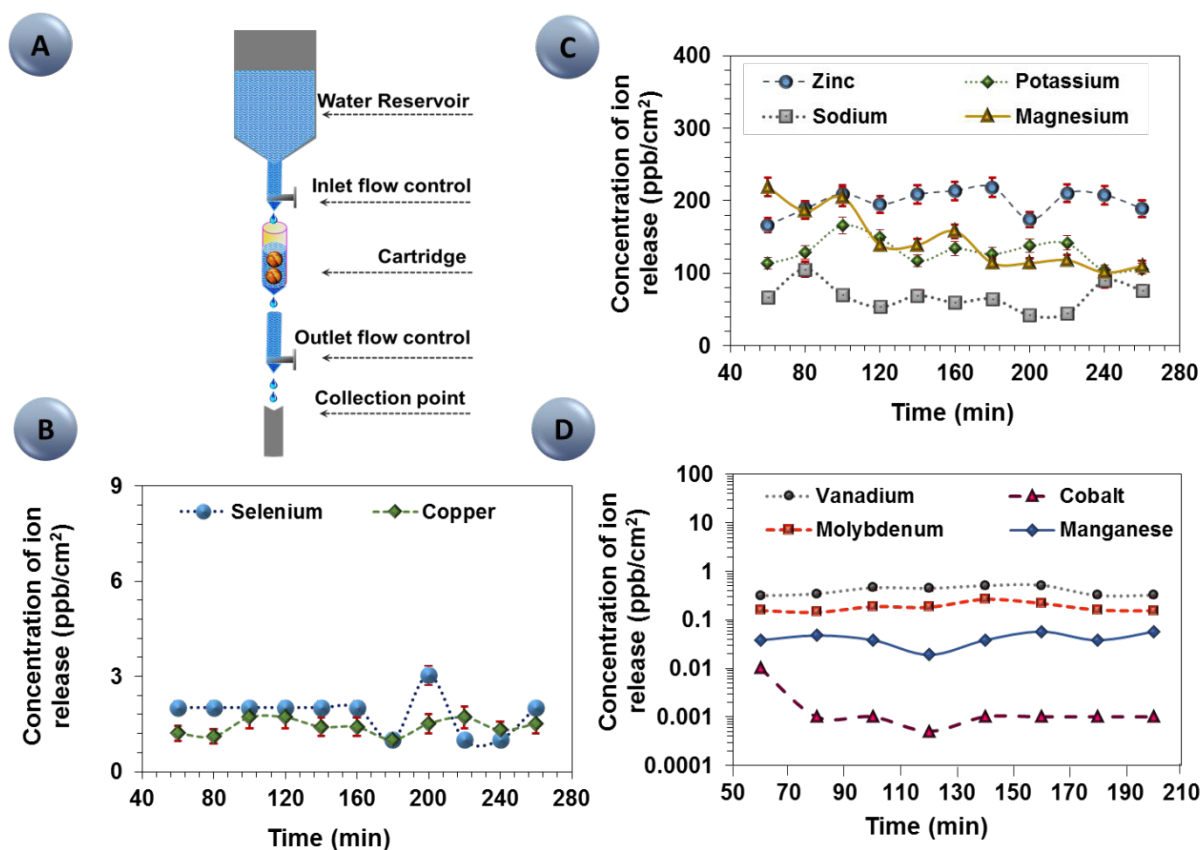


**Figure S6.** Mineral release trend from the designed prototype. The release of selected metal ions in a sustained fashion under continuous flow of water at a pilot scale at a flow rate of 2 mL per minute. (a) Schematic representation of the prototype design. (b-d) Release of select mineral ions as a function of time.

## Supporting information 7

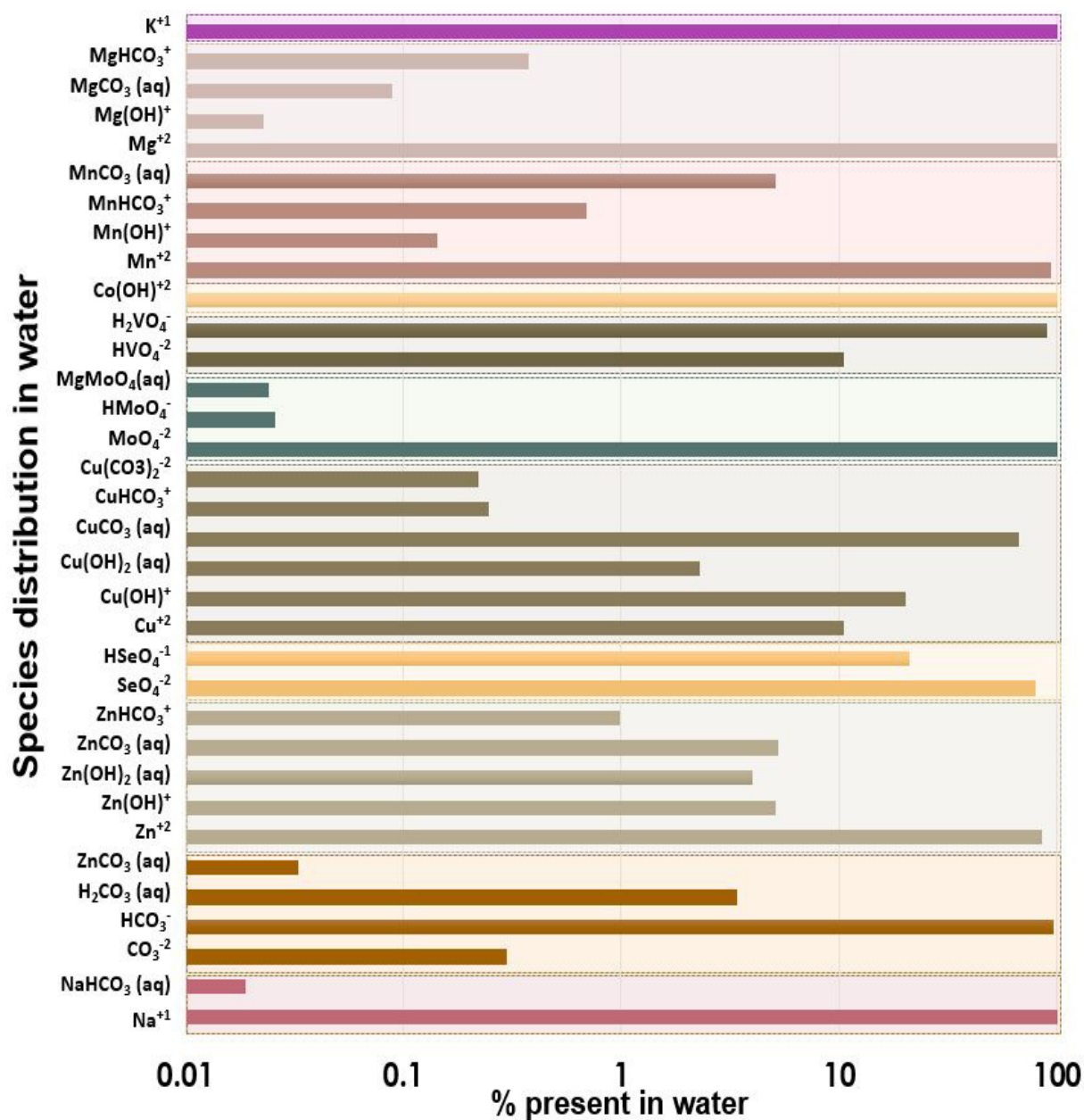


**Figure S7.** Speciation of mineral ions formed in water after the release. The speciation diagram was prepared using simulations run on Visual MINTEQ software version 3.1 (freeware, available at, <http://vminteq.lwr.kth.se>).

### Equations used for the evaluation of sustainability metrics

Equation (1) :      Mass intensity =  $\frac{\text{mass of all products used excluding water}}{\text{mass of product}}$  kg/kg product

Equation (2) :      Water intensity ( $W_P$ ) =  $\frac{\text{mass of all water used}}{\text{mass of product}}$  kg/kg product

Equation (3) :      Reaction mass efficiency (RME) =  $\frac{\text{mass of product}}{\text{mass of all reactants}} \times 100\%$

Equation (4) :      Energy Intensity =  $\frac{\text{amount of non renewable energy used}}{\text{mass of product}}$  kW.h/kg

Equation (5) :      E factor =  $\frac{[\text{kg}(\text{raw materials}) - \text{kg}(\text{desired product})]}{\text{kg}(\text{total product including water})}$

**Table S1:** CO<sub>2</sub> emission (including raw material manufacture and monolith production).

A cradle-to-gate assessment of the [M2<sub>(Na-Cu-Zn)</sub>] material's CO<sub>2</sub> emission including the manufacture of raw materials and production of designed monolith is presented below. The CO<sub>2</sub> emission due to transportation and disposal finished goods are not included and therefore it is not a cradle-to-grave assessment.

<b>List of raw materials used in M2<sub>(Na-Cu-Zn)</sub></b>	<b>CO<sub>2</sub> emission by manufacture of raw materials (kg/kg)</b>	<b>CO<sub>2</sub> emission by production of designed monolith (kg/kg)</b>	<b>Total (kg/kg)</b>
SiO <sub>2</sub>	0.373	-	0.373
Al <sub>2</sub> O <sub>3</sub>	0.492	-	0.492
Na <sub>2</sub> CO <sub>3</sub>	0.059	4x10 <sup>-5</sup>	0.05904
CuCO <sub>3</sub>	0.200	4x10 <sup>-5</sup>	0.20004
ZnO	0.582	-	0.582
KCl	0.0138	-	0.0138



**Table S2:** LD-50 of the raw materials used for the synthesis of material

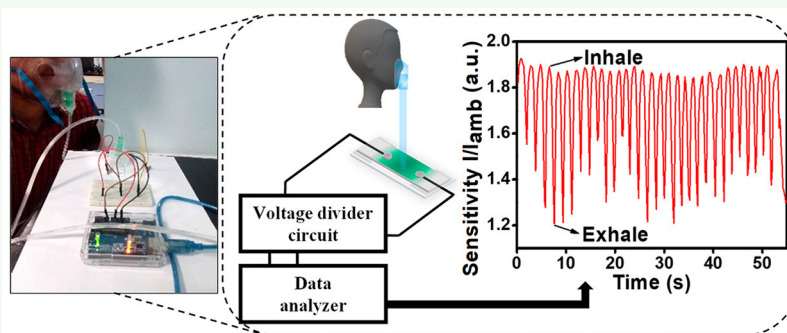
Elements used	LD-50 (mg/kg)
$\text{SiO}_2$	500
$\text{Al}_2\text{O}_3$	5000
$\text{Na}_2\text{CO}_3$	2800
$\text{K}_2\text{CO}_3$	2000
ZnO	7950
$\text{SeO}_3$	1.6
$\text{MgCO}_3$	NA
$\text{CuCO}_3$	1350
CoO	202
MnO	2000
$\text{V}_2\text{O}_5$	474
MoO	2689
KCl	2600

# Surface-Treated Nanofibers as High Current Yielding Breath Humidity Sensors for Wearable Electronics

Sathvik Ajay Iyengar,<sup>†</sup> Pillalamarri Srikrishnarka,<sup>†,‡</sup> Sourav Kanti Jana,<sup>†</sup> Md Rabiul Islam,<sup>†</sup> Tripti Ahuja,<sup>†</sup> Jyoti Sarita Mohanty,<sup>†</sup> and Thalappil Pradeep<sup>\*,†</sup>

<sup>†</sup>DST Unit of Nanoscience, Thematic Unit of Excellence, Department of Chemistry, and <sup>‡</sup>Department of Chemical Engineering, Indian Institute of Technology Madras, Chennai 600036, India

## Supporting Information



**ABSTRACT:** As wearable electronics have gained momentum in the past few years, there is a dire need for smart, responsive, and, most importantly, affordable sensors for biological monitoring. One such noninvasive method to gauge body metabolism is via breath analysis. In a successful attempt to sense and record relative humidity levels (%RH) in nasal and oral breath, this work presents an economical route to fabricate a wearable humidity sensor with high sensitivity and a response time of  $\sim 1$  s. The sensor consists of a flexible backbone of electrospun poly(vinylidene fluoride)/reduced graphene oxide (PVDF/rGO) nanofibers which have been selectively sensitized to humidity via surface polymerization of aniline using the inexpensive successive ionic layer adsorption and reaction (SILAR) technique. We report a high sensitivity and a full response range (0–95% RH) supported by a low working voltage and minimalistic circuitry as an attractive feature for integration into wearable electronics. Moreover, as the device sensitivity is adequate even up to 95% RH, it is conducive to detect nasal breath and saturated humidity conditions accurately. As the method utilizes electrospinning, this work involves the preparation of such humidity sensors on a large scale (up to 400 units using 8 mg of rGO) with the benefit of having affordable and cost-effective devices.

**KEYWORDS:** humidity sensing, reduced graphene oxide, nanofibers, polyaniline, SILAR

## ■ INTRODUCTION

Measurement of humidity is important from several perspectives. Industries such as that of electronics, food, medicine, materials, and metallurgy are concerned about varying humidity levels.<sup>1–4</sup> Relative humidity levels also have a significant impact on the survival rates of airborne infectious agents<sup>5–7</sup> and hence need to be monitored and controlled accordingly. On the other end of the spectrum, humidity levels in exhaled breath is a reliable marker of the quality of body metabolism and health.<sup>8,9</sup> Although it can be controlled, breath rate is almost always synchronous with heart rate. Hence, a subject's breath rate, tidal volumes, and exhaled air quality can be tied to various parameters such as their age, quality of living, and even heart rate and its condition.<sup>10</sup> This rich collection of data obtained in a noninvasive manner paves the way to monitor various hidden symptoms and diagnose conditions much before they manifest physically. For a technology of this kind to be available across the world, it must be sensitive and

selective with fast response time while, most importantly, being affordable. We demonstrate a methodology for making this possible.

Electrospinning is a simple, yet powerful tool for obtaining nanofibers which are used in many applications, varying from water purification and air filtration to production of anodic materials in solar cells and in batteries and capacitors.<sup>11–14</sup> Briefly, it is a technique wherein a high electrical potential is applied between a droplet and a collector plate, and as a result, the voltage overcomes the surface tension at the solution–air interface and causes the liquid droplet to change its shape to form a cone. The droplet then elongates, followed by continuous “drawing”, leading to the formation of nanofibers. Electrospun fibers with hierarchical structures of one or many

**Received:** February 26, 2019

**Accepted:** June 4, 2019

**Published:** June 4, 2019

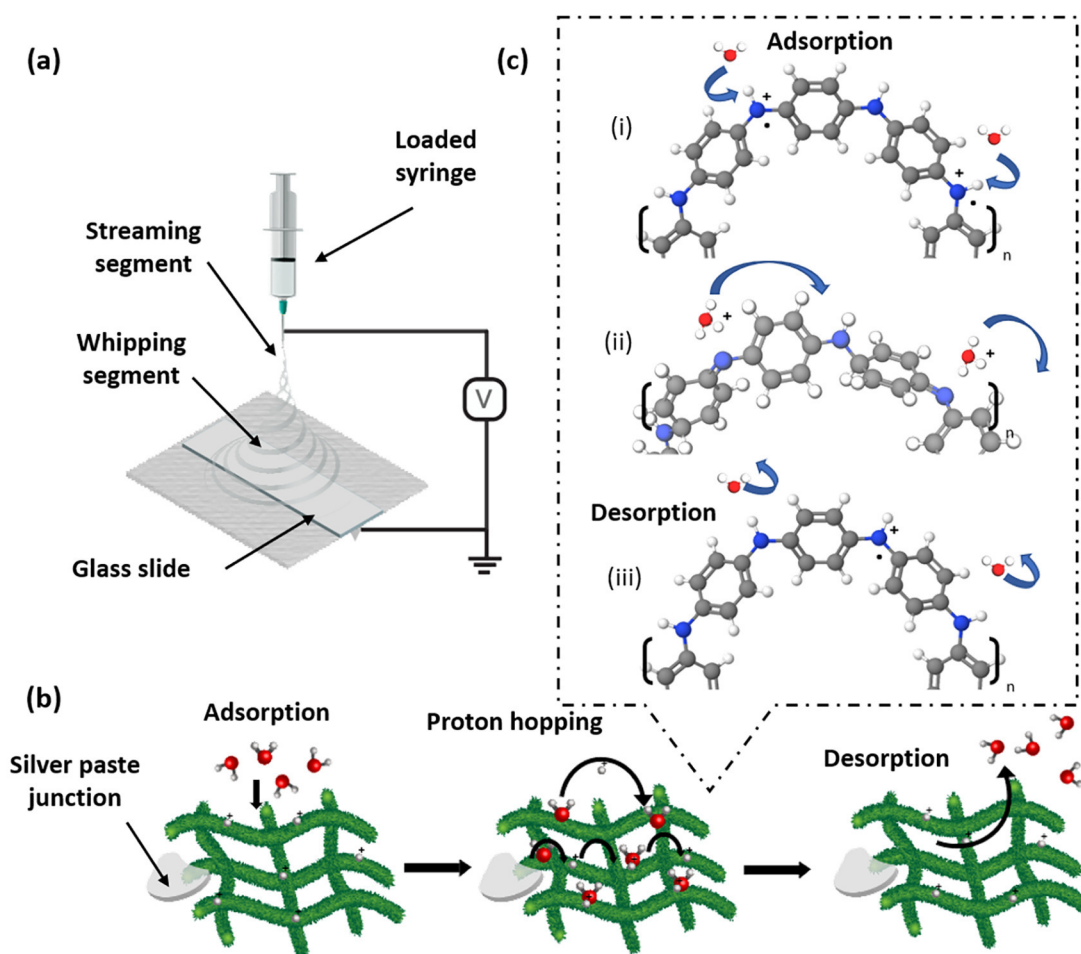


**Figure 1.** (a) Schematic showing electrospinning setup. (b) Zoomed-in schematic, elaborating the sensing process at the electrode junction. (c) Grotthuss mechanism of proton hopping: (i) adsorption of H<sub>2</sub>O onto PANi ES backbone; (ii) proton transfer from partly protonated PANi backbone to H<sub>2</sub>O, where (iii) proton hops from H<sub>3</sub>O<sup>+</sup> species to PANi ES.

constituents can be obtained by this technique. This process yields robust fibers, which can be replicated easily in large-scale once parameters such as flow rate, working voltage, sample distance, and number of revolutions of the collecting surface are optimized. In this work, we have prepared a poly(vinylidene difluoride) (PVDF) nanofiber backbone via electrospinning as it has been proven to be a durable and flexible substrate material for wearable electronics.<sup>15</sup> We have used the successive ionic layer adsorption reaction (SILAR) or the successive ionic layer deposition (SILD) as a cost-effective, simple, and versatile technique for obtaining thin film coating on PVDF fibers. This method was first introduced by Nicolau in the mid-1980s and has been used for the growth of quantum dots (QDs) such as CdSe, ZnS, and CdTe<sup>16</sup> for the fabrication of nanocrystal films<sup>17</sup> and gas sensors.<sup>18,19</sup> It is a highly versatile procedure involving the immersion of a substrate separately in two different precursor solutions and washing in water after each immersion to remove weakly bound species. Thus, one SILAR cycle consists of adsorption of the cation precursor, rinsing with water, and adsorption of the anion precursor, followed by a chemical reaction and another rinsing, in the process of synthesizing the above quantum dots. This self-limiting procedure gives good control of the layer growth. When these cycles are performed in succession, we observe the growth of a thin layer of the desired material.

Polyaniline (PANi) has been used for decades due to its versatility as a conducting polymer. Although other conducting polymers such as polypyrrole and porphyrin complexes have been used as sensors,<sup>20–25</sup> the reliability, stability, and hydrophilicity of PANi<sup>26,27</sup> combined with the sturdy backbone<sup>28–30</sup> and biocompatibility of PVDF<sup>31–33</sup> makes it conducive to prepare a sensing element tailored toward atmospheric and breath moisture. Previous reports of metal oxide nanostructures, graphene, and other active materials in humidity sensors indicate a response in the nanoamperes range, warranting expensive device fabrication, rectification, and amplification circuitry and energy-intensive methodologies.<sup>34–39</sup> Primary assembly of the sensor requires multiple steps starting from the preparation of metal oxide nanostructures, heat treatment to obtain the required phase, and finally the assembly of the electrode.<sup>40</sup>

Many reports on breath humidity sensors present faster response and good sensitivity, but these methods face economic challenges due to their complexity in the process of upscaling for mass production.<sup>41–43</sup> The use of common materials and room temperature operation conditions with fast response time of  $\sim 1$  s makes our material ideal for breath monitoring.<sup>44,45</sup> We further enhanced the performance by incorporating rGO in the electrospun fibers. There have been reports of improved conductance when rGO is introduced into a polymer matrix.<sup>46,47</sup> Also, in contrast to recent reports,<sup>48</sup> our

sensor uses minimal circuitry, and the material is optimized to be cost-effective. We have demonstrated a stark and previously unreported difference in nasal and oral breath humidity and breath patterns and established the advantage of increased sensitivity at higher RH levels.

## EXPERIMENTAL SECTION

Detailed experimental conditions for synthesizing rGO can be found elsewhere (see the [Supporting Information](#)).

**Preparation of Nanofiber Backbone.** PVDF (3.29 g) was dissolved in DMF (13 mL) and stirred for 3 h until homogeneity was obtained. Simultaneously, rGO (8 mg) was ultrasonicated in DMF (2 mL) for 30 min to obtain a uniform dispersion. This dispersion of rGO was subsequently added to the stirring solution of DMF to result in an 18 wt % PVDF solution in DMF. The final electrospinning solution was left to stir further for 6 h under ambient temperature. Nanofibers were prepared by using the ESPIN-NANO electrospinning machine by loading the e-spin solution into a 2 mL capacity syringe. Spinning parameters were set to a flow rate of  $2 \text{ mL h}^{-1}$ , a working distance of 13 cm, and a voltage of 13 kV for a period of 1 h. These PVDF/rGO nanofibers were thus spun onto a series of glass slides as shown in [Figure 1a](#).

**Surface Polymerization of Aniline on the Nanofibers.** Aniline (1 mL) [A] and APS (1.45 g) [B] were added separately to two beakers, each containing preprepared 1 M aqueous HCl (40 mL) solution. The electrospun fiber mat was then taped to the supporting glass slide to fix it in position. SILAR was then performed by alternately dipping and withdrawing the glass slides between solutions A and B. The dwell period was 3 min in solution A and 2 min in solution B. After each cycle, the slides were washed in deionized water to remove excess reactants. This was performed for 10 cycles, and the color change of the slides indicated the polymerization of aniline to PANi-emeraldine base (EB) and its phase change to the more conducting emeraldine salt (ES) form by the acid doping process. Finally, the chemically treated fibers were left to dry under ambient conditions for 2 h.

Other experimental details and characterization techniques are presented in the [Supporting Information](#).

## RESULTS AND DISCUSSION

**Synthesis of Nanofibers and Imaging by Scanning Electron Microscopy (SEM).** Electrospinning was used to fabricate the humidity sensor, wherein PVDF/rGO in DMF was electrospun under a voltage of 13 kV and a flow rate of  $2 \text{ mL h}^{-1}$  as previously discussed in the [Experimental Section](#). A schematic representation of the SILAR protocol for deposition of PANi on the PVDF fibers is shown in [Figure 2a](#). The initial diameter distribution of the fibers and their surface morphology are shown in the SEM micrograph shown in [Figure 2b](#). The fibers had a smooth surface, without any discontinuities. [Figure 2c](#) presents an even deposition of PANi on the fiber surface after SILAR, which explains the lateral widening of the fibers. The surface morphology has now been altered to attain a rough exterior, which is believed to aid in the adsorption–desorption process. The fiber diameters of the bare electrospun fibers were in the range 200–380 nm before and 525–550 nm after SILAR, with an average fiber diameter of 255 and 528 nm, respectively, as given in [Figure 2d](#). Conventionally, the width of the fibers has been represented as the diameter of the fibers.

**Raman Spectral Analysis of Nanofibers.** To confirm the presence of PVDF and rGO, Raman spectra were collected as shown in [Figure S1a](#). Solutions of PVDF and PVDF-rGO were drop-casted separately onto microscope slides and were left to dry. Once dried, the spots were viewed under a Raman microscope. The peaks present at 790 and  $886 \text{ cm}^{-1}$  confirm

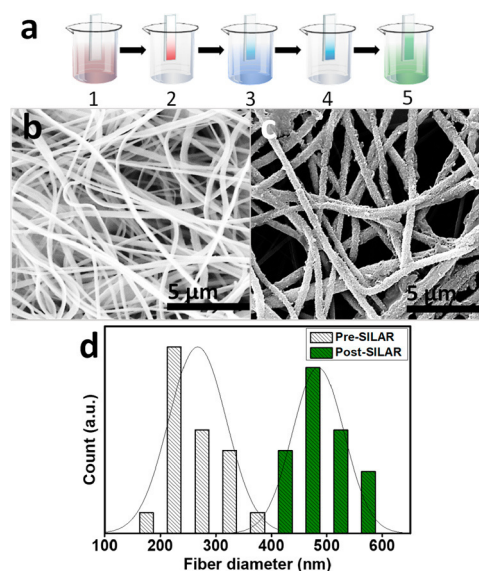


**Figure 2.** (a) Steps performed to surface polymerize aniline via SILAR: (1) PVDF/rGO fibers immersed in 0.28 mM aqueous solution of A, (2) fibers immersed in water to remove excess A, (3) fibers immersed in 0.15 mM aqueous solution of APS to initiate the polymerization, (4) fibers in water to remove the unreacted APS, and (5) PANi EB doped to ES. SEM of PVDF/rGO nanofibers (b) before SILAR treatment, (c) after SILAR treatment, and (d) diameter distribution extracted from the images.

the presence of  $\alpha$  and  $\beta$  phases of PVDF, respectively. The ratio of their intensities indicates the predominance of the  $\alpha$  phase, which was observed in commercial grade PVDF.<sup>53</sup> The peaks at  $1345$  and  $1595 \text{ cm}^{-1}$  in PVDF-rGO blend indicate the D and G bands of rGO. To confirm the formation of rGO, the prepared sample was drop-casted onto microscopic glass slides, and Raman spectra were collected as shown in [Figure S1a](#). The corresponding D, G 2D, and D+G bands of rGO have been indicated. The PANi-treated electrospun fiber mat was placed under a  $20\times$  objective of the Raman microscope for collecting the time lapse spectra. Initially, the sensor was saturated with humidity by continuous oral exhalation before placing it under the microscope. The Raman spectra with saturated humidity are shown in [Figure S1b](#). Also, the peak at  $831 \text{ cm}^{-1}$  corresponds to the  $\beta$  phase of PVDF, and the absence of a peak at  $790 \text{ cm}^{-1}$  suggests the complete conversion of the  $\alpha$  phase to  $\beta$  phase of PVDF, which possibly occurs during electrospinning.<sup>54</sup> A high voltage of  $20 \text{ MV/m}$  is usually applied for the phase transformation of  $\alpha$  to  $\beta$  due to the dipolar arrangement.<sup>55</sup> The peaks at  $1174$  and  $1344 \text{ cm}^{-1}$  are assigned to the  $\delta(\text{CH})$  in-plane bending and  $\nu(\text{C-N}^+)$  stretching, respectively. The peak at  $1507 \text{ cm}^{-1}$  corresponds to the  $\delta(\text{NH})$  bending, and the peaks in the  $1660$ – $1645 \text{ cm}^{-1}$  have been attributed to substituted phenazine<sup>56</sup> structures. This is understood to be crucial in the formation of the 2D polymer framework. The broad peak at  $3000 \text{ cm}^{-1}$  is attributed to the grouped stretching frequencies of C–H and N–H stretching at  $3300 \text{ cm}^{-1}$ .<sup>57</sup> The hydrogen bond present in water holds a key role in many biological and chemical processes. This can be studied by monitoring the OH stretching frequencies.<sup>58</sup> As water molecules have a tendency to form water clusters, the hydrogen bonding in water cluster could be classified into proton donor (PD) or proton acceptor (PA). A strong peak around  $3002 \text{ cm}^{-1}$  corresponds to the strongest hydrogen-bound OH for a single donor–double



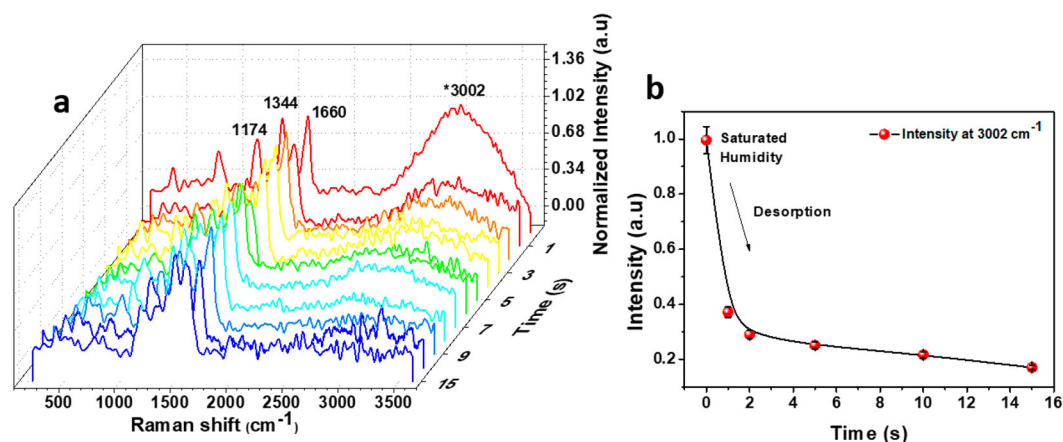


Figure 3. (a) Real-time Raman spectroscopy indicating desorption of water. (b) Variation of the 3002  $\text{cm}^{-1}$  peaks with time.

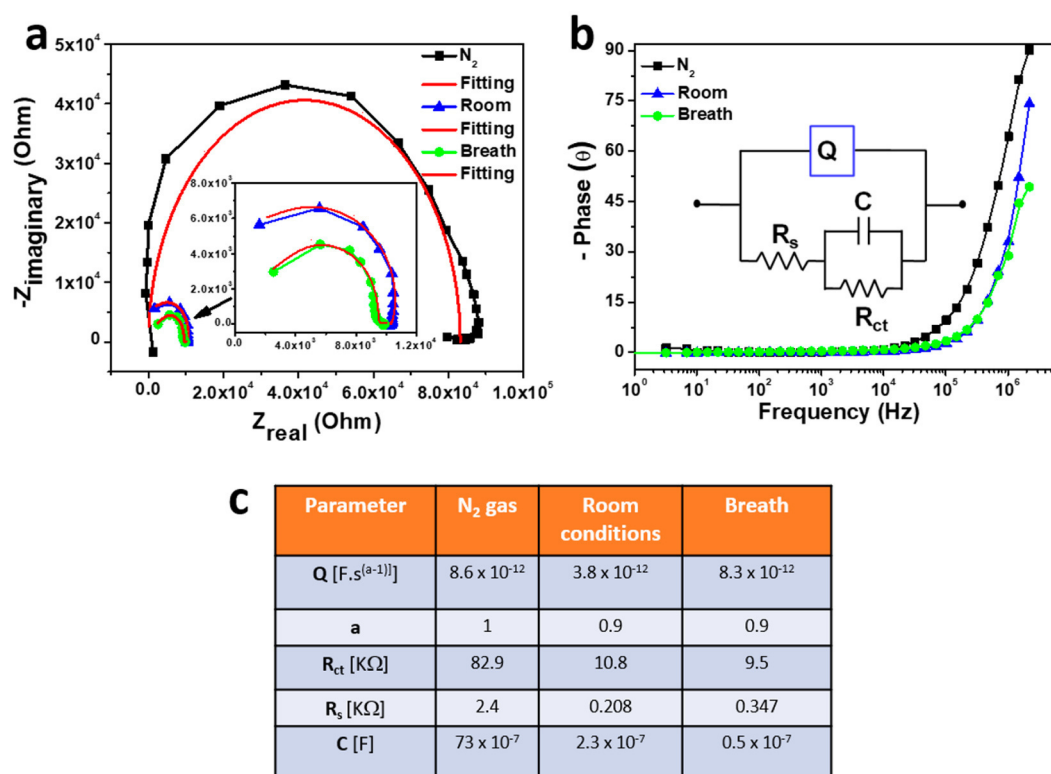
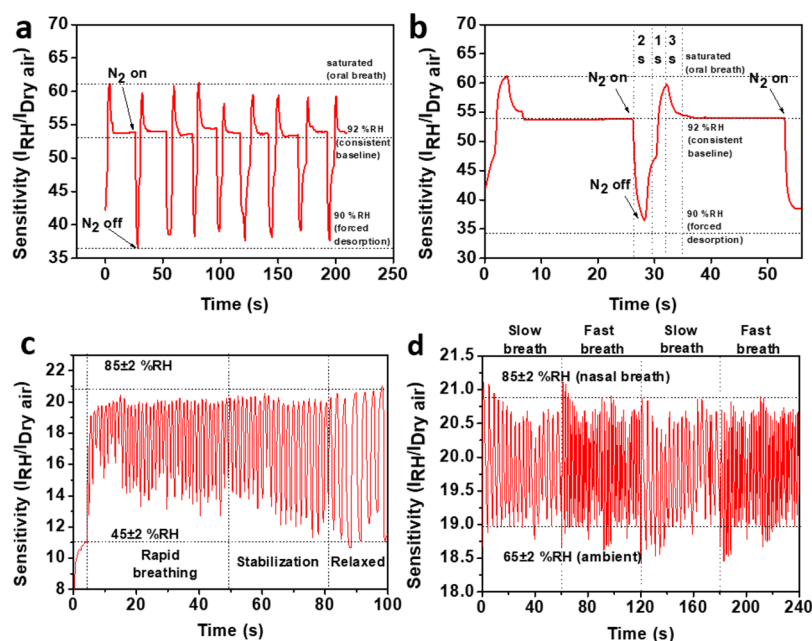


Figure 4. (a) Nyquist plot to determine the  $R_s$  and  $R_{ct}$  of the sensor under room (RH = 44%) and nasal breath (RH = 88%) conditions and under N<sub>2</sub> (absence of humidity RH = 0%). (b) Bode plot of the sensor to understand the phase of C capacitance. Inset: circuit arrangement used for fitting the Nyquist plot. (c) Capacitive and resistive parameters for the setup constant phase element (CPE) under various humidity conditions.

acceptor cluster.<sup>59</sup> We suggest that there could be a hydrogen bond between the  $-(\text{NH})^+-$  of PANi and H<sub>2</sub>O as it is necessary for proton hopping. The peaks at 1344 and 3002  $\text{cm}^{-1}$  support the adsorption and proton hopping mechanism. The decrease in the intensity might be due to the loss in hydrogen bonding as water desorbed. Time lapse Raman spectra were collected for a total duration of 15 s in which the decrease in the intensity of the peak at 3002  $\text{cm}^{-1}$  was observed (Figure 3a). This change is graphically shown in Figure 3b. The intensity decreased by ~ 66% within 1 s upon exposure to humidity. However, for a complete decrease in the peak intensity it took ~16 s. The prevailing temperature and % RH during the time of collecting the spectra were 20 °C and

50% RH, respectively. The low temperature during testing made it convenient to capture the entire sorption over time.

**IR/ATR Spectral Analysis of Nanofibers.** IR spectral data were obtained for the nanofiber sample before and after SILAR treatment to confirm the presence of PANi as shown in Figure S2. The peak at 1400  $\text{cm}^{-1}$  observed in both the samples can be assigned to C–F stretching. The peaks at 1065 and 880  $\text{cm}^{-1}$  indicate C=C trans-conformer of vinylidene and C–C–C asymmetrical stretching modes,<sup>51</sup> respectively. The characteristic peaks at 1566 and 2115  $\text{cm}^{-1}$  correspond to the N–H and the C=N stretching frequencies which are not visible in the PVDF/rGO sample. The C–N bond appears at 1299  $\text{cm}^{-1}$ . The presence of both C–N and C=N is a hallmark of PANi in the emeraldine base form as its polymeric backbone is



**Figure 5.** Chronoamperometric studies highlighting differences between (a) sensor response to nasal breath immediately after 15 min of moderate cardio exercise and (b) sensor response to alternating slow and fast nasal breath cycles (manually induced). (c, d) Testing the sensitivity at nearly saturated humidity levels caused by oral exhalation.

partly protonated. The broad peak at  $2690\text{ cm}^{-1}$  can be attributed to the intermolecular N–H stretch which is evident only in the PANi-coated fibers, indicating adsorption of atmospheric moisture post SILAR treatment. Additionally, an out-of-plane (oop) N–H bend was visualized at  $800\text{ cm}^{-1}$ . The weak signal at  $1995\text{ cm}^{-1}$  suggests the presence of a ketenimine  $\text{C}=\text{C}=\text{N}$  group.<sup>52</sup> All of these correspond to the PVDF backbone and the emeraldine structure of PANi.

**TEM Analysis of RGO and PVDF/RGO Nanofiber.** TEM micrographs of the as-prepared rGO and PVDF/rGO nanofiber are shown in Figure S3. Figure S3a shows a low-magnification TEM image of rGO. A single sheet is transparent to the electron beam, wrinkled, and also folded at the edges. The corresponding image in the inset shows a high-magnification TEM image of rGO; the transparency and wrinkles are evident. A low-magnification TEM of PVDF/rGO nanofiber is shown in Figure S3b; the fiber diameter from this image does match the fiber diameter from the SEM. A high-magnification TEM image of a nanofiber is shown in Figure S3c,d. We observe the rGO flake protruding out from the PVDF fiber. Because of the low concentration of rGO (8 mg), we do not observe a uniform covering of rGO on the PVDF fiber.

**PANi Phase Characterization by Cyclic Voltammetry (CV).** To phase characterize the PANi that was coated on the fibers, PANi was coated on indium-doped tin oxide (ITO)-coated glass via SILAR. This glass slide was subjected to cyclic voltammetry using  $0.5\text{ M H}_2\text{SO}_4$  as electrolyte, at a scan rate of  $50\text{ mV s}^{-1}$  and cycled between 0.4 and 0.8 V. The corresponding CV is shown in Figure S4; the corresponding voltammogram has two peaks at 0.7 and  $-0.2\text{ V}$ . The broad peaks could be due to nonuniform coating of PANi on ITO. Upon coating of PANi on ITO, a slight greenish coloration was observed on ITO glass, which confirmed the coating. The presence of a peak at  $0.7\text{ V}$  confirms the presence of PANi in the emeraldine salt form.<sup>49,50</sup>

**Contact Angle Measurements.** Optical images obtained during contact angle measurements for the nanofiber sample before and after PANi coating via SILAR are presented in Figures S8a and S8b, respectively. The corresponding contact angles were  $125^\circ$  and  $76^\circ$  without and with PANi coating. This confirms the change in physical affinity toward moisture from a hydrophobic backbone surface to a hydrophilic one.

**Impedance Measurements and Studies.** Impedance spectroscopy was conducted to investigate the conduction mechanism of humidity sensing, and results are shown in Figure 4a–c. A complex impedance spectrum was measured by applying an ac signal (20 mV) along with a dc voltage (2 V) between two silver metallic contacts formed on the PANi-coated nanofibers. The frequency of the ac signal was varied from 7 MHz to 10 Hz, and the subsequent change of impedance was recorded as a function of frequency. This sets up a constant phase element (CPE). Figure 4a shows the Nyquist plot which describes the charge transfer resistance between two electrodes in the absence/presence of humidity. Because of the adsorption of  $\text{N}_2$  gas onto the fiber mat, a double-layer capacitor is formed. This is attributed to high charge transfer resistance ( $R_{\text{ct}}$ ) as well high surface capacitance ( $C$ ) of the mat. Figure 4c displays these parameters along with the parameters  $Q$  and  $a$  which appear in the constant phase element's impedance equations. However, under room conditions ( $25^\circ\text{C}$ ,  $\text{RH} \sim 44\%$ ) and humid conditions ( $\text{RH} \sim 88\%$ ),  $R_{\text{ct}}$  was reduced drastically in the presence of exhaled nasal breath. The capacitance  $C$  in the absence of humidity was  $73 \times 10^{-7}\text{ F}$ , and this decreased drastically in the presence of humidity. We attribute  $R_s$  to the surface resistance of PANi fibers and  $R_{\text{ct}}$  to the resistance associated with proton hopping due to the aforementioned changes. In the presence of humidity, water molecules were adsorbed onto the electrode surface and formed an electrical double layer containing  $\text{OH}^-$ . The change in phase angle (Bode plot) as a function of frequency has been depicted in Figure 4b. Under  $\text{N}_2$  gas, the phase angle was found to be  $90^\circ$  at higher frequencies (close to

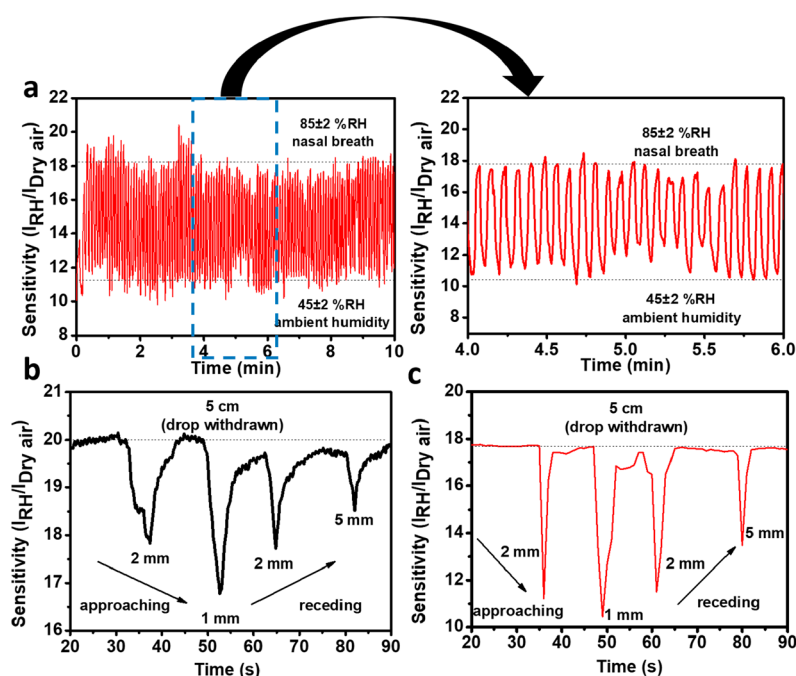


**Figure 6.** (a) Chronoamperometric studies of nasal breath indicating sensor's signal stability and response. Proximity drop test conducted for pure (b) acetone and (c) ethanol. In (b) and (c), the drop was shifted toward and then away from the sensor element. Sensor response was captured at the various elevations mentioned above.

7 MHz) and nearly zero at lower frequencies, exhibiting the capacitive nature of the material. Whereas, in humid conditions, the phase angle decreased, attributing to the resistive behavior of the active surface of the material. Thus, the sensing mechanism is mostly influenced by a change in resistance of the material in the presence of humidity. The sensor response is presented in terms of sensitivity, where sensitivity is obtained by dividing the  $I_{RH}$  with  $I_{Dry\ air}$ . Here,  $I_{RH}$  represents the current value obtained at that particular %RH, and  $I_{Dry\ air}$  represents the current value obtained by the sensor in the presence of pure  $N_2$  gas.

**Oral Breath Analysis.** Chronoamperometric testing was performed initially by alternating between three levels of relative humidity (%RH) to observe the response current range and response time hysteresis. Although oral breath presents a near humidity saturation, on shorter bursts, we achieved sensor response even at levels >90% RH. After each oral exhalation, the calibrated response measured at >95%. The sensor was then left undisturbed for desorption to occur. Although not complete due to possible saturation effects, the desorption occurred consistently to reach 92% RH in 3 s, which was subsequently marked as our baseline. Diffusing  $N_2$  gas onto the sensor surface caused a forced desorption to reach 90% RH. The response time was inversely proportional to the change in %RH exposure; i.e., sorption kinetics was faster when alternating between the “consistent baseline” (92% RH) and “oral breath” (>95% RH) when compared to switching between “forced desorption” (90% RH) and “consistent baseline” (92% RH) as shown in Figure 5a,b. Through these repeated cycles of switching, we were able to establish a full range of sensitivity toward humidity, specifically from 90% RH to saturation. Peng et al. fabricated a breath sensor for obtaining a static response from breath in the offline mode and analyzed it for detecting lung cancer.<sup>60</sup> We propose a real-time operating sensor relying on the continuous breath in contrast to static analysis. Hence, this range is highly crucial in

determining various health aspects tied to the breath rate. Furthermore, conducting oral breath measurements in addition to controlled humidity calibration experiments is crucial to establish the utility of the sensing element under exaggerated humidity and dynamic breath conditions. Experiments involving controlled humidity calibration can be found elsewhere (see Figure S5).

**Nasal Breath for Health Monitoring.** As the sensor setup was shown to provide quick and crisp data from breath tests, further examinations were conducted to verify its flexibility for health monitoring. Data were collected after 15 min of moderate cardiovascular exercise to study the changes in breath responses and are presented in Figure 5c. Sensor characteristics reveal a very clear demarcation of three stages of breathing post workout. Starting with the initial stage of rapid breathing, which is found to be at 56 breaths/min for a period of 45 s, a gradual decrease in breath rate as well as humidity saturation was observed. This decrease was attributed to a period of breath stabilization, lasting for around 15 s. Finally, the volunteer's breath rate returned to normal breathing as seen evidently. A blank was also conducted by manually alternating between fast and slow breath cycles and is presented in Figure 5d. Thus, a clear difference is observed between natural and artificially simulated breath cycles. This distinguishing ability is essential “smart” feature for wearable electronics. An image of the final setup layout during breath sensing is shown in Figure S7b. As the sensor responds appropriately to breath rate and regularity, it may find applications in various fields such as interrogation and polygraph testing.<sup>61</sup>

**Sensor Response and Material Stability.** Additional tests were performed to confirm sensor response and stability over time. Sensor data were collected for a longer duration of ~10 min of continuous monitoring as shown in Figure 6a. An expanded view of this data is shown in Figure 6a (right); the response between 4 and 6 min shows a consistent response in



current. The sensor was subjected to continuous breathing cycles for a period of 10 min during which the volunteer was relaxed. Data collected conformed to a fixed response range, indicating no drastic or sudden changes. Although minor variations were detected and can be attributed to the uniqueness of each breath cycle, this does not affect the breath rate and humidity levels visualized. The SILAR-treated nanofiber mat had been stored in atmospheric conditions for a period of 1 week before this experiment was conducted. In comparison to a freshly prepared sensor element, the sensor aged for a duration of 1 week under laboratory conditions showed the same characteristics because of the stability of polyaniline.

**Sensor Response Selectivity.** Proximity drop tests were conducted to check for other interfering commonplace volatile organic compounds (VOCs) such as acetone and ethanol as shown in Figures 6b and 6c, respectively, also present in traces in the oral breath of those who have recently imbibed alcohol and those who are diabetic, respectively.<sup>62,63</sup> Test results reveal that although we detected sensitivity toward the analytes, the signal was negligible compared to that of moisture. In contrast to the sensor response observed for humidity, we observe an increase in resistivity when either an acetone or ethanol drop is brought closer to the sensor element. This elucidates that the proton hopping mechanism is not at play while sensing these analytes and is valid only for atmospheric humidity. Testing settings and procedure can be found elsewhere (see the Supporting Information).

**Sensing Mechanism.** By embedding rGO within the PVDF structure, we observed better sensor characteristics in terms of both response time and current, confirming previous reports of Borini et al.<sup>64</sup> The current response originates from a charge transfer mechanism based on ionic conductance. As mentioned before, we believe that the underlying mechanism for sensing is to follow the Grotthuss method of proton hopping.<sup>65</sup> The adsorption is driven by intermolecular hydrogen bond formation followed by the completion of conduction channels throughout the surface for proton transport and, finally, quick desorption due to the hydrophobicity of the PVDF/rGO backbone. Out of the three phases of PANi, the emeraldine salt (ES) possesses partly positive and partly neutral charged polymeric backbone, which ultimately results in switch-like positions throughout its structure. Once the H<sub>2</sub>O molecules have adsorbed onto the surface, the switches close instantaneously, which results in a current increase with rising %RH levels. This occurs due to the transient formation of H<sub>3</sub>O<sup>+</sup> species. The proton is then transferred across to the next nitrogen atom, by what is characterized as a “hop”. This hop or exchange occurs due to an interplay between polarity and hydrophilicity and is necessary for the transfer of electrons within the network of PANi as explained through nuclear magnetic resonance (NMR) studies performed by Nechtschein et al.<sup>66</sup> Moreover, Stejskal et al. have elaborated on the variable-range hopping (VRH) mechanism which is observed in polyaniline and other amorphous semiconductors.<sup>67</sup> During the proton free induction decay study of PANi, they observed two peaks corresponding to the protons in the rigid polymer and also the protons of water absorbed in the polymer network. They proposed that electron conduction in PANi is by removal of one electron from one reduced unit and transferring to the oxidized unit.<sup>68</sup> For this transfer of electron, a proton must be exchanged between  $-(NH)^+-$  and H<sub>2</sub>O forming H<sub>3</sub>O<sup>+</sup> as

shown in Figure 1b,c. We have found rGO to play key roles in enhancing this conductance during the proton hop as previously discussed. Indeed, this two-pronged approach to increase ionic and electronic conductivity in our material has resulted in good selectivity at higher humidity levels. In the event that there are multiple conduction channels on the PANi surface, the proton hop occurs even via neighboring H<sub>2</sub>O molecules, resulting in the formation of H<sub>3</sub>O<sup>+</sup> and OH<sup>-</sup> species as explained by Farahani et al.<sup>69</sup> To understand the effect of rGO within the fibers, PVDF was spun without rGO and with 4 mg of rGO. These fibers were coated with PANi via SILAR and examined for humidity response by a chronoamperometric study. The response of fibers without rGO is shown in Figure S6a. The current output under 90% RH of oral breath was 10 nA with a response time of 25 s. However, there was a stark increase (~65%) in the current output in the presence of rGO (4 mg) and a decrease in response time to 7 s. This output along with the response time was further improved by doubling the concentration of rGO to 8 mg; the rise in current output was ~1000 times, and the response time for sensing humidity reduced to ~1 s. Additionally, a table comparing our sensor features with other reports is available in Table S1.

**Sensor Portability.** For personal use, the sensor was combined with a prototyping circuit board (Arduino) to perform the chronoamperometric study. Although the device can be powered externally by a small battery source (2 V), it was tethered to a laptop system via universal serial bus (USB) cable to acquire data. The chronoamperometric response collected in the presence of breath humidity is shown in Figure S7a. After a period of inactivity (100 s), breath cycles were suddenly initiated and continued for another 300 s to observe the response characteristics of the sensor. The current output rose to 0.8 mA as soon as the fibers were saturated with nasal breath. The increase in current output in the presence of rGO is appreciable in terms of response time. Because of increased current, the device may face higher power loads. Although not encountered while testing, future work involved reducing the bias voltage and reducing noise. The circuit diagram explaining the sensor element arrangement with Arduino is shown in Figure S7c. Further data refinement, in the form of long-term data acquisition, will provide a deeper understanding of various underlying patterns and parameters in our day-to-day breath cycles.

## ■ CONCLUSION AND OUTLOOK

The PANi-coated PVDF/rGO nanofibers have been shown to provide a robust response to humidity and can be calibrated to measure %RH levels from desiccated to saturated conditions (10–95% RH). Sensor characteristics reveal high sensitivity, especially under near-saturated conditions of 70–95% RH, confirming its viability for breath sensing. The sensor response can be sustained at higher current ranges (~mA– $\mu$ A). Moreover, based on materials optimization, small quantities of rGO (8 mg) can be used to fabricate up to 400 viable sensor elements, making it cost-effective on a large scale. A repeatable dynamic response has been recorded before and after physical activity which supports its use in health monitoring. In parallel, the device can replace most commercially available humidity sensors due to its superior characteristics and stability. We combined our sensing element with an Arduino module that can collect the chronoamperometric data, with the objective of using the device under lower operating voltages of <1 V.

Future work would involve collecting such breath data from multiple individuals for long spans of time, recognizing patterns, and tying the information to vital clinical conditions. The device may find applications in tracking calories burnt during exercise via breath rate and humidity levels, as well as in hospitals as low-cost and low-energy alternatives for patient monitoring.

## ■ ASSOCIATED CONTENT

### ● Supporting Information

The Supporting Information is available free of charge on the ACS Publications website at DOI: 10.1021/acsaelm.9b00123.

Materials and methods for preparing rGO; device fabrication methodology; Raman spectrum of PVDF/rGO composite; IR spectra of fibers; TEM of rGO and fiber composite; CV of PANi; breath analysis combined with a prototyping platform; water contact angle and sensor performance comparison between reported devices and present experiments (PDF)

## ■ AUTHOR INFORMATION

### Corresponding Author

\*E-mail [pradeep@iitm.ac.in](mailto:pradeep@iitm.ac.in); Fax +91-44-2257-0545.

### ORCID

Sourav Kanti Jana: 0000-0001-5772-7022

Thalappil Pradeep: 0000-0003-3174-534X

### Author Contributions

S.A.I. and P.S. contributed equally to this work.

### Notes

The authors declare no competing financial interest.

## ■ ACKNOWLEDGMENTS

The authors thank the Department of Science and Technology, Government of India, for supporting their research program on nanomaterials. P.S., S.K.J., T.A., and J.S.M. thank IIT Madras for their research fellowship. M.R.I. and J.S.M. thank the Council of Scientific and Industrial Research (CSIR), Government of India, for a research fellowship. We also thank the Sophisticated Analytical Instrument Facility (SAIF), IIT Madras, for performing the ATR/IR analysis. We acknowledge Prof. Pijush Ghosh, Department of Applied Mechanics, IIT Madras, for helping us with contact angle measurements.

## ■ REFERENCES

- (1) Vanhoestenbergh, A.; Donaldson, N. Corrosion of Silicon Integrated Circuits and Lifetime Predictions in Implantable Electronic Devices. *J. Neural Eng.* **2013**, *10* (3), 031002.
- (2) Paull, R. E. Effect of Temperature and Relative Humidity on Fresh Commodity Quality. *Postharvest Biol. Technol.* **1999**, *15* (3), 263–277.
- (3) Nolte, A. J.; Treat, N. D.; Cohen, R. E.; Rubner, M. F. Effect of Relative Humidity on the Young's Modulus of Polyelectrolyte Multilayer Films and Related Nonionic Polymers. *Macromolecules* **2008**, *41*, 5793–5798.
- (4) Rohde, F.; Normand, M. D.; Peleg, M. Effect of Equilibrium Relative Humidity on the Mechanical Signatures of Brittle Food Materials. *Biotechnol. Prog.* **1993**, *9* (5), 497–503.
- (5) Tang, J. W. The Effect of Environmental Parameters on the Survival of Airborne Infectious Agents. *J. R. Soc., Interface* **2009**, *6*, 737–746.
- (6) Zuo, Y. Y.; Gitiafroz, R.; Acosta, E.; Policova, Z.; Cox, P. N.; Hair, M. L.; Neumann, A. W. Effect of Humidity on the Adsorption Kinetics of Lung Surfactant at Air-Water Interfaces. *Langmuir* **2005**, *21* (23), 10593–10601.
- (7) Xu, P.; Kujundzic, E.; Peccia, J.; Schafer, M. P.; Moss, G.; Hernandez, M.; Miller, S. L. Impact of Environmental Factors on Efficacy of Upper-Room Air Ultraviolet Germicidal Irradiation for Inactivating Airborne Mycobacteria. *Environ. Sci. Technol.* **2005**, *39* (24), 9656–9664.
- (8) Tatara, T.; Tsuzaki, K. An Apnea monitor using a rapid-response hygrometer. *J. Clin. Monit.* **1997**, *13*, 5–9.
- (9) Oki, Y.; Kaneko, M.; Fujimoto, Y.; Sakai, H.; Misu, S.; Mitani, Y.; Yamaguchi, T.; Yasuda, H.; Ishikawa, A. Usefulness of the 6-minute Walk Test as a Screening Test for Pulmonary Arterial Enlargement in COPD. *Int. J. Chronic Obstruct. Pulm. Dis.* **2016**, *11* (1), 2869–2875.
- (10) Hirsch, J. A.; Bishop, B. Respiratory Sinus Arrhythmia in Humans: How Breathing Pattern Modulates Heart Rate. *Am. J. Physiol.* **1981**, *241* (4), 620–629.
- (11) Huang, Z.-M.; Zhang, Y.-Z.; Kotaki, M.; Ramakrishna, S. A Review on Polymer Nanofibers by Electrospinning and Their Applications in Nanocomposites. *Compos. Sci. Technol.* **2003**, *63* (15), 2223–2253.
- (12) Chinnappan, A.; Baskar, C.; Baskar, S.; Ratheesh, G.; Ramakrishna, S. An Overview of Electrospun Nanofibers and Their Application in Energy Storage, Sensors and Wearable/Flexible Electronics. *J. Mater. Chem. C* **2017**, *5* (48), 12657–12673.
- (13) Zhu, P.; Nair, A. S.; Shengjie, P.; Shengyuan, Y.; Ramakrishna, S. Facile Fabrication of TiO<sub>2</sub>-Graphene Composite with Enhanced Photovoltaic and Photocatalytic Properties by Electrospinning. *ACS Appl. Mater. Interfaces* **2012**, *4* (2), 581–585.
- (14) Binittha, G.; Soumya, M. S.; Madhavan, A. A.; Praveen, P.; Balakrishnan, A.; Subramanian, K. R. V.; Reddy, M. V.; Nair, S. V.; Nair, A. S.; Sivakumar, N. Electrospun  $\alpha$ -Fe<sub>2</sub>O<sub>3</sub> Nanostructures for Supercapacitor Applications. *J. Mater. Chem. A* **2013**, *1* (38), 11698–11704.
- (15) Wang, X.; Sun, F.; Yin, G.; Wang, Y.; Liu, B.; Dong, M. Tactile-Sensing Based on Flexible PVDF Nanofibers via Electrospinning: A Review. *Sensors* **2018**, *18* (2), 330.
- (16) Lee, H.; Wang, M.; Chen, P.; Gamelin, D. R.; Zakeeruddin, S. M.; Gratzel, M.; Nazeeruddin, M. K. Efficient CdSe Quantum Dot-Sensitized Solar Cells Prepared by an Improved Successive Ionic Layer Adsorption and Reaction Process. *Nano Lett.* **2009**, *9* (12), 4221–4227.
- (17) Trembl, B. E.; Savitzky, B. H.; Tirmzi, A. M.; Dasilva, J. C.; Kourkoutis, L. F.; Hanrath, T. Successive Ionic Layer Adsorption and Reaction for Postassembly Control over Inorganic Interdot Bonds in Long-Range Ordered Nanocrystal Films. *ACS Appl. Mater. Interfaces* **2017**, *9* (15), 13500–13507.
- (18) Navale, S. T.; Bandgar, D. K.; Chougule, M. A.; Patil, V. B. Facile Method of Preparation of PbS Films for NO<sub>2</sub> Detection. *RSC Adv.* **2015**, *5* (9), 6518–6527.
- (19) Shishiyuan, S. T.; Shishiyuan, T. S.; Lupan, O. I. Sensing Characteristics of Tin-Doped ZnO Thin Films as NO<sub>2</sub> Gas Sensor. *Sens. Actuators, B* **2005**, *107* (1), 379–386.
- (20) Esteves, C. H. A.; Iglesias, B. A.; Li, R. W. C.; Ogawa, T.; Araki, K.; Gruber, J. New Composite Porphyrin-Conductive Polymer Gas Sensors for Application in Electronic Noses. *Sens. Actuators, B* **2014**, *193*, 136–141.
- (21) Najjar, R.; Nematdoust, S. A Resistive-Type Humidity Sensor Based on Polypyrrole and ZnO Nanoparticles: Hybrid Polymers Vis-a-Vis Nanocomposites. *RSC Adv.* **2016**, *6* (113), 112129–112139.
- (22) Guo, Y. N.; Gao, Z. Y.; Wang, X. X.; Sun, L.; Yan, X.; Yan, S. Y.; Long, Y. Z.; Han, W. P. A Highly Stretchable Humidity Sensor Based on Spandex Covered Yarns and Nanostructured Polyaniline. *RSC Adv.* **2018**, *8* (2), 1078–1082.
- (23) Zhang, D.; Wang, D.; Li, P.; Zhou, X.; Zong, X.; Dong, G. Facile Fabrication of High-Performance QCM Humidity Sensor Based on Layer-by-Layer Self-Assembled Polyaniline/Graphene Oxide Nanocomposite Film. *Sens. Actuators, B* **2018**, *255*, 1869–1877.

- (24) Parvatikar, N.; Jain, S.; Khasim, S.; Revansiddappa, M.; Bhoraskar, S. V.; Prasad, M. V. N. A. Electrical and Humidity Sensing Properties of Polyaniline/WO<sub>3</sub> Composites. *Sens. Actuators, B* **2006**, *114* (2), 599–603.
- (25) Li, X. Z.; Liu, S. R.; Guo, Y. Polyaniline-Intercalated Layered Double Hydroxides: Synthesis and Properties for Humidity Sensing. *RSC Adv.* **2016**, *6* (68), 63099–63106.
- (26) Dhawale, D. S.; Salunkhe, R. R.; Jamadade, V. S.; Dubal, D. P.; Pawar, S. M.; Lokhande, C. D. Hydrophilic Polyaniline Nanofibrous Architecture Using Electrosynthesis Method for Supercapacitor Application. *Curr. Appl. Phys.* **2010**, *10* (3), 904–909.
- (27) Zhong, W.; Chen, X.; Liu, S.; Wang, Y.; Yang, W. Synthesis of Highly Hydrophilic Polyaniline Nanowires and Sub-Micro/Nanostructured Dendrites on Poly(Propylene) Film Surfaces. *Macromol. Rapid Commun.* **2006**, *27* (7), 563–569.
- (28) Feng, C.; Khulbe, C.; Matsuura, T.; Tabe, S.; Ismail, A. F. Preparation and Characterization of Electro-Spun Nanofiber Membranes and Their Possible Applications in Water Treatment. *Sep. Purif. Technol.* **2013**, *102*, 118–135.
- (29) Wang, S.; Zhao, X.; Yin, X.; Yu, J.; Ding, B. Electret Polyvinylidene Fluoride Nanofibers Hybridized by Polytetrafluoroethylene Nanoparticles for High-Efficiency Air Filtration. *ACS Appl. Mater. Interfaces* **2016**, *8* (36), 23985–23994.
- (30) Wang, L.-Y.; Yong, W. F.; Yu, L. E.; Chung, T.-S. Design of High Efficiency PVDF-PEG Hollow Fibers for Air Filtration of Ultrafine Particles. *J. Membr. Sci.* **2017**, *535*, 342–349.
- (31) Laroche, G.; Marois, Y.; Guidoin, R.; King, M. W.; Martin, L.; How, T.; Douville, Y. Polyvinylidene Fluoride (PVDF) as a Biomaterial: From Polymeric Raw Material to Monofilament Vascular Suture. *J. Biomed. Mater. Res.* **1995**, *29* (12), 1525–1536.
- (32) Zhang, S.; Cao, J.; Ma, N.; You, M.; Wang, X.; Meng, J. Fast and Facile Fabrication of Antifouling and Hemocompatible PVDF Membrane Tethered with Amino-Acid Modified PEG Film. *Appl. Surf. Sci.* **2018**, *428*, 41–53.
- (33) Al Halabi, F.; Gryshkov, O.; Kuhn, A. I.; Kapralova, V. M.; Glasmacher, B. Force Induced Piezoelectric Effect of Polyvinylidene Fluoride and Polyvinylidene Fluoride-Co-Trifluoroethylene Nanofibrous Scaffolds. *Int. J. Artif. Organs* **2018**, *41* (11), 811–822.
- (34) Kuang, Q.; Lao, C.; Wang, Z. L.; Xie, Z.; Zheng, L. High-Sensitivity Humidity Sensor Based on a Single SnO<sub>2</sub> Nanowire. *J. Am. Chem. Soc.* **2007**, *129* (19), 6070–6071.
- (35) Wang, Z.; Xiao, Y.; Cui, X.; Cheng, P.; Wang, B.; Gao, Y.; Li, X.; Yang, T.; Zhang, T.; Lu, G. Humidity-Sensing Properties of Urchinlike CuO Nanostructures Modified by Reduced Graphene Oxide. *ACS Appl. Mater. Interfaces* **2014**, *6* (6), 3888–3895.
- (36) Sreedhara, M. B.; Ghatak, J.; Bharath, B.; Rao, C. N. R. Atomic Layer Deposition of Ultrathin Crystalline Epitaxial Films of V<sub>2</sub>O<sub>5</sub>. *ACS Appl. Mater. Interfaces* **2017**, *9* (3), 3178–3185.
- (37) Zhao, H.; Zhang, T.; Qi, R.; Dai, J.; Liu, S.; Fei, T. Drawn on Paper: A Reproducible Humidity Sensitive Device by Handwriting. *ACS Appl. Mater. Interfaces* **2017**, *9* (33), 28002–28009.
- (38) Zhen, Z.; Li, Z.; Zhao, X.; Zhong, Y.; Zhang, L.; Chen, Q.; Yang, T.; Zhu, H. Formation of Uniform Water Microdroplets on Wrinkled Graphene for Ultrafast Humidity Sensing. *Small* **2018**, *14* (15), 1703848.
- (39) Güder, F.; Ainla, A.; Redston, J.; Mosadegh, B.; Glavan, A.; Martin, T. J.; Whitesides, G. M. Paper-Based Electrical Respiration Sensor. *Angew. Chem., Int. Ed.* **2016**, *55* (19), 5727–5732.
- (40) Zhang, Y.; Yu, K.; Jiang, D.; Zhu, Z.; Geng, H.; Luo, L. Zinc Oxide Nanorod and Nanowire for Humidity Sensor. *Appl. Surf. Sci.* **2005**, *242* (1–2), 212–217.
- (41) Chen, Z.; Lu, C. Humidity Sensors: A Review of Materials and Mechanisms. *Sens. Lett.* **2005**, *3* (4), 274–295.
- (42) Chen, M.; Zhang, C.; Li, L.; Liu, Y.; Li, X.; Xu, X.; Xia, F.; Wang, W.; Gao, J. Sn Powder as Reducing Agents and SnO<sub>2</sub> Precursors for the Synthesis of SnO<sub>2</sub>-Reduced Graphene Oxide Hybrid Nanoparticles. *ACS Appl. Mater. Interfaces* **2013**, *5* (24), 13333–13339.
- (43) Buvailo, A. I.; Xing, Y.; Hines, J.; Dollahon, N.; Borguet, E. TiO<sub>2</sub>/LiCl-Based Nanostructured Thin Film for Humidity Sensor Applications. *ACS Appl. Mater. Interfaces* **2011**, *3* (2), 528–533.
- (44) He, J.; Xiao, P.; Shi, J.; Liang, Y.; Lu, W.; Chen, Y.; Wang, W.; Théato, P.; Kuo, S. W.; Chen, T. High Performance Humidity Fluctuation Sensor for Wearable Devices via a Bioinspired Atomic-Precise Tunable Graphene-Polymer Heterogeneous Sensing Junction. *Chem. Mater.* **2018**, *30* (13), 4343–4354.
- (45) Mogera, U.; Sagade, A. A.; George, S. J.; Kulkarni, G. U. Ultrafast Response Humidity Sensor Using Supramolecular Nanofibre and Its Application in Monitoring Breath Humidity and Flow. *Sci. Rep.* **2015**, *4*, 1–9.
- (46) Tan, Y.; Fang, L.; Xiao, J.; Song, Y.; Zheng, Q. Grafting of Copolymers onto Graphene by Miniemulsion Polymerization for Conductive Polymer Composites: Improved Electrical Conductivity and Compatibility Induced by Interfacial Distribution of Graphene. *Polym. Chem.* **2013**, *4* (10), 2939–2944.
- (47) Yuan, B.; Wang, B.; Hu, Y.; Mu, X.; Hong, N.; Liew, K. M.; Hu, Y. Electrical Conductive and Graphitizable Polymer Nanofibers Grafted on Graphene Nanosheets: Improving Electrical Conductivity and Flame Retardancy of Polypropylene. *Composites, Part A* **2016**, *84*, 76–86.
- (48) Kano, S.; Dobashi, Y.; Fujii, M. Silica Nanoparticle-Based Portable Respiration Sensor for Analysis of Respiration Rate, Pattern, and Phase During Exercise. *IEEE Sensors Lett.* **2018**, *2* (1), 1–4.
- (49) Watanabe, A.; Mori, K.; Iwasaki, Y.; Nakamura, Y.; Niizuma, S. Electrochromism of Polyaniline Film Prepared by Electrochemical Polymerization. *Macromolecules* **1987**, *20* (8), 1793–1796.
- (50) Planes, G. A.; Rodríguez, J. L.; Miras, M. C.; García, G.; Pastor, E.; Barbero, C. A. Spectroscopic Evidence for Intermediate Species Formed during Aniline Polymerization and Polyaniline Degradation. *Phys. Chem. Chem. Phys.* **2010**, *12* (35), 10584–10593.
- (51) Gu, S.; He, G.; Wu, X.; Hu, Z.; Wang, L.; Xiao, G.; Peng, L. Preparation and Characterization of Poly(Vinylidene Fluoride)/Sulfonated Poly(Phthalazinone Ether Sulfone Ketone) Blends for Proton Exchange Membrane. *J. Appl. Polym. Sci.* **2009**, *116* (2), 852–860.
- (52) Trchová, M.; Stejskal, J. Polyaniline: The Infrared Spectroscopy of Conducting Polymer Nanotubes (IUPAC Technical Report). *Pure Appl. Chem.* **2011**, *83* (10), 1803–1817.
- (53) Constantino, C. J. L.; Job, A. E.; Simões, R. D.; Giacometti, J. A.; Zucolotto, V.; Oliveira, O. N.; Gozzi, G.; Chinaglia, D. L. Phase Transition in Poly(Vinylidene Fluoride) Investigated with Micro-Raman Spectroscopy. *Appl. Spectrosc.* **2005**, *59* (3), 275–279.
- (54) Zheng, J.; He, A.; Li, J.; Han, C. C. Polymorphism Control of Poly(Vinylidene Fluoride) through Electrospinning. *Macromol. Rapid Commun.* **2007**, *28* (22), 2159–2162.
- (55) Furukawa, T. Ferroelectric Properties of Vinylidene Fluoride Copolymers. *Phase Transitions* **1989**, *18* (3–4), 143–211.
- (56) Grzeszczuk, M.; Grańska, A.; Szostak, R. Raman Spectroelectrochemistry of Polyaniline Synthesized Using Different Electrolytic Regimes-Multivariate Analysis. *Int. J. Electrochem. Sci.* **2013**, *8* (7), 8951–8965.
- (57) Evans, J. C. The Vibrational Assignments and Configuration of Aniline, Aniline-NHD and Aniline-ND<sub>2</sub>. *Spectrochim. Acta* **1960**, *16* (4), 428–442.
- (58) Sun, Q. The Raman OH Stretching Bands of Liquid Water. *Vib. Spectrosc.* **2009**, *51* (2), 213–217.
- (59) Choe, C.; Lademann, J.; Darwin, M. E. Depth Profiles of Hydrogen Bound Water Molecule Types and Their Relation to Lipid and Protein Interaction in the Human Stratum Corneum in Vivo. *Analyst* **2016**, *141* (22), 6329–6337.
- (60) Peng, G.; Tisch, U.; Adams, O.; Hakim, M.; Shehada, N.; Broza, Y. Y.; Billan, S.; Abdah-Bortnyak, R.; Kuten, A.; Haick, H. Diagnosing Lung Cancer in Exhaled Breath Using Gold Nanoparticles. *Nat. Nanotechnol.* **2009**, *4* (10), 669–673.
- (61) Grubin, D.; Madsen, L. Lie Detection and the Polygraph: A Historical Review. *J. Forensic Psychiatry Psychol.* **2005**, *16* (2), 357–369.



- (62) Wu, L.; McIntosh, M.; Zhang, X.; Ju, H. Amperometric Sensor for Ethanol Based on One-Step Electropolymerization of Thionine-Carbon Nanofiber Nanocomposite Containing Alcohol Oxidase. *Talanta* **2007**, *74* (3), 387–392.
- (63) Choi, S. J.; Lee, I.; Jang, B. H.; Youn, D. Y.; Ryu, W. H.; Park, C. O.; Kim, I. D. Selective Diagnosis of Diabetes Using Pt-Functionalized WO<sub>3</sub> Hemitube Networks as a Sensing Layer of Acetone in Exhaled Breath. *Anal. Chem.* **2013**, *85* (3), 1792–1796.
- (64) Borini, S.; White, R.; Wei, D.; Astley, M.; Haque, S.; Spigone, E.; Harris, N.; Kivioja, J.; Ryhänen, T. Ultrafast Graphene Oxide Humidity Sensors. *ACS Nano* **2013**, *7* (12), 11166–11173.
- (65) Farahani, H.; Wagiran, R.; Hamidon, M. N. Humidity Sensors Principle, Mechanism, and Fabrication Technologies: A Comprehensive Review. *Sensors* **2014**, *14*, 7881–7939.
- (66) Nechtschein, M.; Santier, C. NMR Observation of Proton Exchange in the Conducting Polymer Polyaniline. *J. Phys. (Paris)* **1986**, *47* (6), 935–937.
- (67) Stejskal, J.; Trchová, M.; Bober, P.; Humpolíček, P.; Kašpárková, V.; Sapurina, I.; Shishov, M. A.; Varga, M. Conducting Polymers: Polyaniline. *Encyclopedia of Polymer Science and Technology*, 2015; p 1.
- (68) Travers, J.; Nechtschein, M. Water Effects in Polyaniline: A New Conduction Process. *Synth. Met.* **1987**, *21* (1–3), 135–141.
- (69) Doan, T. C. D.; Ramaneti, R.; Baggerman, J.; Tong, H. D.; Marcelis, A. T. M.; Van Rijn, C. J. M. Intrinsic and Ionic Conduction in Humidity-Sensitive Sulfonated Polyaniline. *Electrochim. Acta* **2014**, *127*, 106–114.

## Supporting Information

### **Surface Treated Nanofibers as High Current Yielding Breath Humidity Sensors for Wearable Electronics**

Sathvik Ajay Iyengar<sup>†</sup>, Pillalamarri Srikrishnarka<sup>†,‡</sup>, Sourav Kanti Jana, Md Rabiul Islam, Tripti Ahuja, Jyoti Sarita Mohanty and Thalappil Pradeep\*

DST Unit of Nanoscience, Thematic Unit of Excellence, Department of Chemistry, Indian Institute of Technology Madras, Chennai 600036, India.

<sup>‡</sup>Also at, Department of Chemical Engineering, Indian Institute of Technology Madras, Chennai 600036, India.

Corresponding author E-mail: pradeep@iitm.ac.in

<sup>†</sup>These authors contributed equally.

## Table of Contents

<b>Figure No.</b>	<b>Description</b>	<b>Page No.</b>
-	<b>Preparation of rGO</b>	<b>S-3</b>
-	<b>Fabrication and testing</b>	<b>S-4</b>
-	<b>Instrumentation</b>	<b>S-5</b>
<b>Figure S1</b>	<b>Raman spectra with features of <math>\alpha</math> and <math>\beta</math> phases of PVDF and rGO in the composite materials</b>	<b>S-7</b>
<b>Figure S2</b>	<b>IR/ATR spectra of electrospun nanofibers before and after PANi coating via SILAR</b>	<b>S-8</b>
<b>Figure S3</b>	<b>TEM image rGO in free and composite forms</b>	<b>S-9</b>
<b>Figure S4</b>	<b>Cyclic voltammogram of PANi coated on ITO</b>	<b>S-10</b>
<b>Figure S5</b>	<b>Calibration curve of humidity with respect to sensitivity and current</b>	<b>S-11</b>
<b>Figure S6</b>	<b>Chronoamperometric response of PANi treated PVDF and PVDF/rGO fibers</b>	<b>S-12</b>
<b>Figure S7</b>	<b>Breath analysis data and the sensor set-up</b>	<b>S-12</b>
-	<b>Arduino interface code</b>	<b>S-13</b>
<b>Figure S8</b>	<b>Contact angle measurements</b>	<b>S-14</b>
<b>Table S1</b>	<b>Comparison of performance of different sensors</b>	<b>S-15</b>
-	<b>References</b>	<b>S-16</b>

## Preparation of rGO

**Materials.** Poly[vinylidene fluoride] (PVDF) [commercial grade], aniline, ethanol, ammonium persulfate (APS) from RANKEM, India. Dimethylformamide (DMF) and hydrochloric acid (HCl) were purchased from Sigma Aldrich, hydrogen peroxide ( $\text{H}_2\text{O}_2$ ), sulfuric Acid ( $\text{H}_2\text{SO}_4$ ), sodium nitrate ( $\text{NaNO}_3$ ), potassium persulfate ( $\text{K}_2\text{S}_2\text{O}_8$ ), phosphorus pentoxide ( $\text{P}_2\text{O}_5$ ) and potassium permanganate ( $\text{KMnO}_4$ ) were obtained from Alfa Aesar. Millipore produced de-ionized water ( $\sim 18.2 \text{ M}\Omega$ ) was used throughout the experiments and all the chemicals were used without any further purification.

**Preparation of graphite oxide.** A modified version Hummer's method<sup>1</sup> was used to synthesize graphite oxide using graphite powder. Briefly, graphite powder (2 g) was added to  $\text{K}_2\text{S}_2\text{O}_8$  (4 g) and  $\text{P}_2\text{O}_5$  (4 g) in concentrated  $\text{H}_2\text{SO}_4$  (25 mL), and the mixture was heated to  $100^\circ\text{C}$ . The resulting dark blue oxidized mixture was isolated and slowly cooled to room temperature over a period of 6 h. The mixture was diluted, filtered and dried overnight at  $60^\circ\text{C}$ . About 2 g of this powder was added to  $\text{H}_2\text{SO}_4$  (92 mL) chilled in an ice bath, to which  $\text{KMnO}_4$  (12 g) was gradually added. After 15 min,  $\text{NaNO}_3$  (2 g) was added to the mixture. The solution was further stirred for 2 h at  $35^\circ\text{C}$  and distilled water (200 mL) was added. Finally,  $\text{H}_2\text{O}_2$  diluted to 30% in distilled water was added. The product was washed with HCl (1:10) and then with water. The resulting brown dispersion was extensively dialyzed and exfoliated via ultra-sonication for 2 h (300 W). Unexfoliated graphite oxide was removed by centrifugation (12000 rpm, 20 min) using a KUBOTA (Tokyo, Japan) centrifuge.

**Preparation of reduced graphene oxide (RGO).** About 1 g of the freeze-dried graphite oxide was taken and dispersed in 1 L of deionized water and ultrasonicated for 1 h. Then GO suspension was mixed with  $\text{NH}_3$  and aq. KOH to adjust the pH to 10. Under the effect of ultrasound and electrostatic repulsion, the layers of GO were separated. About 1 mL of hydrazine hydrate solution was added to the suspension and it was maintained at  $95^\circ\text{C}$  in an oil bath with reflux condenser



overnight.<sup>2-4</sup> The color change from brown to black confirms the formation of rGO. The solution was filtered and washed with deionized water. The washed rGO was dried under vacuum to obtain the desired rGO powder.

## **Fabrication and testing**

**Testing breath humidity.** The SILAR treated fiber mat was cut into pieces of dimensions, 2.5 cm x 1.5 cm to serve as the sensing element and to maximize the sensor response. Each piece was taped to a glass slide for support. Using commercial grade conducting silver paste, wire contact points were made at opposite ends of the sensing fiber element with a separation of 1 cm. The wire terminals were connected to a CH Instruments Electrochemical Workstation and testing was carried out under the chronoamperometry scan mode. All experiments were carried out at ambient conditions, recorded to be  $45 \pm 2$  %RH and 25 °C, respectively, by standard humidity and temperature sensors. For breath analysis, a standard respiratory mask fitted with holes at its periphery and a central connecting tube was used to carry the exhaled oral/nasal breath directly to the sensing element.

**Device fabrication.** To use the sensing element as an independent functioning unit for health monitoring purposes, a basic voltage divider circuit was prepared. The entire circuit was designed using a commercially available open-source electronic prototyping platform which can acquire real-time data and relaying it via universal serial bus wire cable or Bluetooth to a PC/mobile device. The data were collected periodically and plotted after basic noise filtration processes. The sensing element has been prepared in such a way that, the over dimension of the sensor are 2.5 x 1.5 cm. The distance between the electrodes is 1 cm. The electrode contact is considered as a point contact, but has a width of around 2-3 mm.

**Proximity drop tests.** To confirm increased sensitivity and specificity toward atmospheric moisture, pure ethanol and acetone droplets (5  $\mu$ L) were separately brought within proximity of the sensing material and current measurements were taken. All experiments were carried out at ambient conditions, recorded to be  $45 \pm 2$  %RH and 25 °C, respectively, by standard humidity and temperature sensors. The analytes were loaded in a 2 mL capacity syringe and the droplets from

the needle tip were initially suspended at a fixed distance of 5 cm. Soon after, the syringe was lowered so that the droplets were at 1, 2 and 5 mm above the surface of the sensing element. This was carried out in approaching-withdrawal and a receding-withdrawal fashion and the current response was noted accordingly.

## **Instrumentation**

**SEM (Scanning electron microscopy) of fibers.** To determine the size and morphology of the bare PVDF/rGO fibers and SILAR treated fibers, they were characterized using a FEI QUANTA 200 SEM.

**IR/ATR and real-time Raman spectral analysis.** In order to confirm the various organic functional groups present in the nanofibers, IR spectral data were collected using Perkin Elmer Spectrum System One FTIR in attenuated total reflectance (ATR) mode. Raman analysis was performed using WiTec GmbH confocal Raman microscope (alpha-300S). A 532 nm (Nd-YAG) laser was used for Raman excitation with a power of 0.2 - 0.5 mW, which was maintained throughout the experiment. Oral breath was exhaled onto the sensor to the point of humidity saturation and it was later placed under the objective lens for the collection of time lapse Raman spectra. Spectra were collected for a time period of 25 s, marked from the time of oral exhalation, at an interval of 2 s.

**Cyclic Voltammogram of PANi and LCR measurement.** To understand the redox states of PANi, CV of PANi was performed by using 0.5 M H<sub>2</sub>SO<sub>4</sub> aqueous solution as electrolyte. Indium doped tin oxide coated (ITO) glass was used as electrode and PANi was coated via SILAR. After 12 cycles, a greenish coat was observed on the ITO glass and after drying the ITO was used as electrode. Ag/AgCl electrode was used as reference and Platinum wire was used as anode. The electrode was cycled between -0.4 – 0.8 V with a sweep rate of 50 mVs<sup>-1</sup> using a CH Instruments Electrochemical Analyzer.

**Sensor calibration.** To study the sensitivity of the sensor towards various humidity levels, a standard calibration was performed by controlling the humidity of the chamber in which the sensor

was placed. Initially, the current during continuous purging of N<sub>2</sub> was noted as ( $I_{\text{Dry air}}$ ) and we observed the output to be 0.012 mA. Aqueous solutions of K<sub>2</sub>CO<sub>3</sub> and K<sub>2</sub>SO<sub>4</sub> and finally mist generated via nebulizing water was used to obtain humidity levels of 43±5 %, 85±5 % and ~100 %RH, respectively<sup>5</sup>. The sensor was placed in each of the humidity condition for calibration. The corresponding calibration curve is presented in Figure S5.

**TEM of rGO and the composite fiber.** In order to visualize the synthesized rGO, the rGO flakes were dispersed in DMF and it was drop-casted on transmission electron microscope (TEM) grid. Later this grid was placed inside a JEOL 3010 TEM operating at 300 kV. Similarly, PVDF/rGO nanofibers were directly electrospun on the TEM grid to visualize the surface morphology and location of rGO in PVDF matrix.

**Contact angle studies.** Surface contact angle measurements were performed using a sessile water droplet with a volume of 3 µL using a Holmarc contact angle meter. A fresh sample of PVDF/rGO was electrospun onto glass slides for a period of 20 min. SILAR was performed for one slide and the other was taken as is. These glass slides were placed under the syringe needle and the droplet was brought to make contact with the surface and the contact angle was measured. These tests were performed to confirm the hydrophobicity of PVDF nanofibers and its hydrophilicity in presence of a PANi coating.

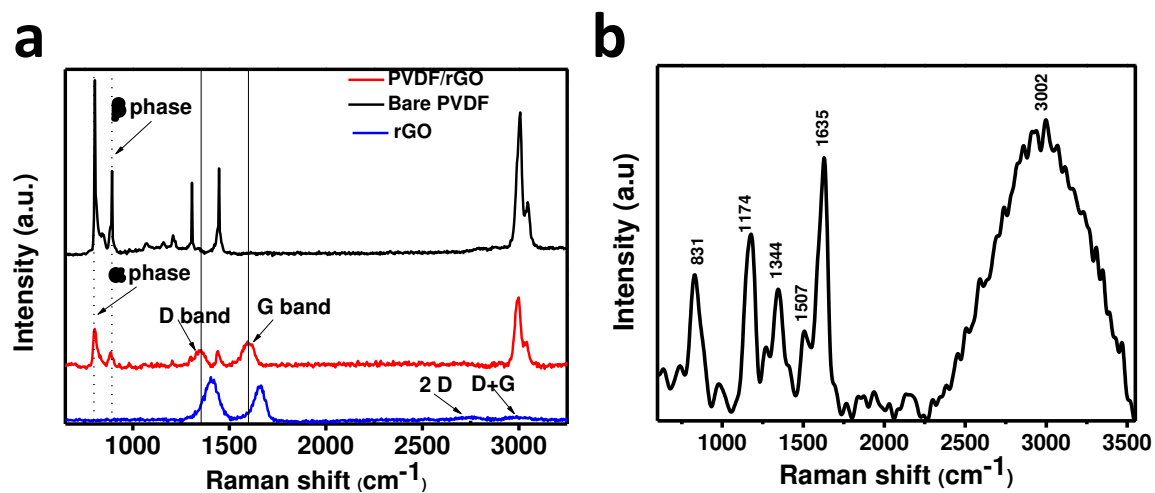


**Figure S1.** Raman spectra showing  $\alpha$  and  $\beta$  phases of PVDF and D & G bands of rGO. (a) Comparison of bare PVDF with rGO and PVDF/rGO. (b) Electrospun composite fiber saturated with humidity.

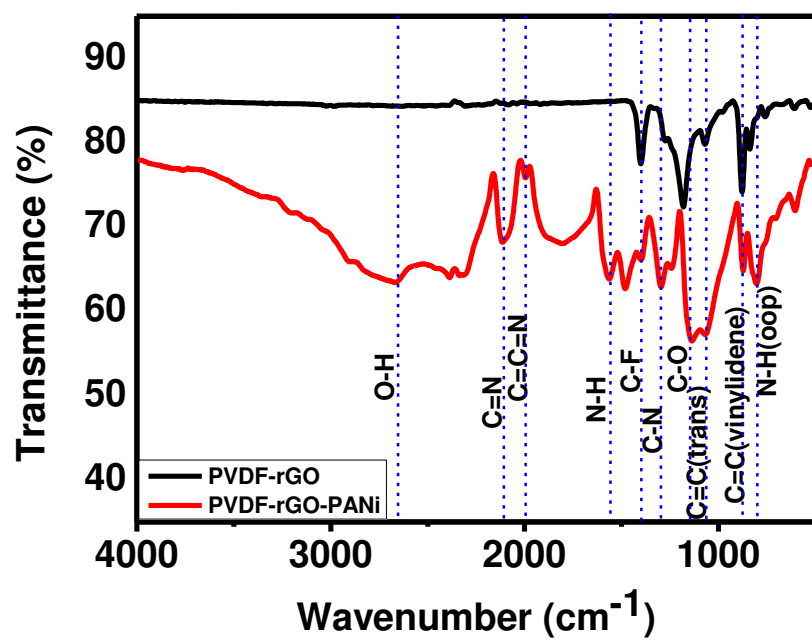


**Figure S2.** IR spectra of electrospun nanofibers before and after PANi coating via SILAR.

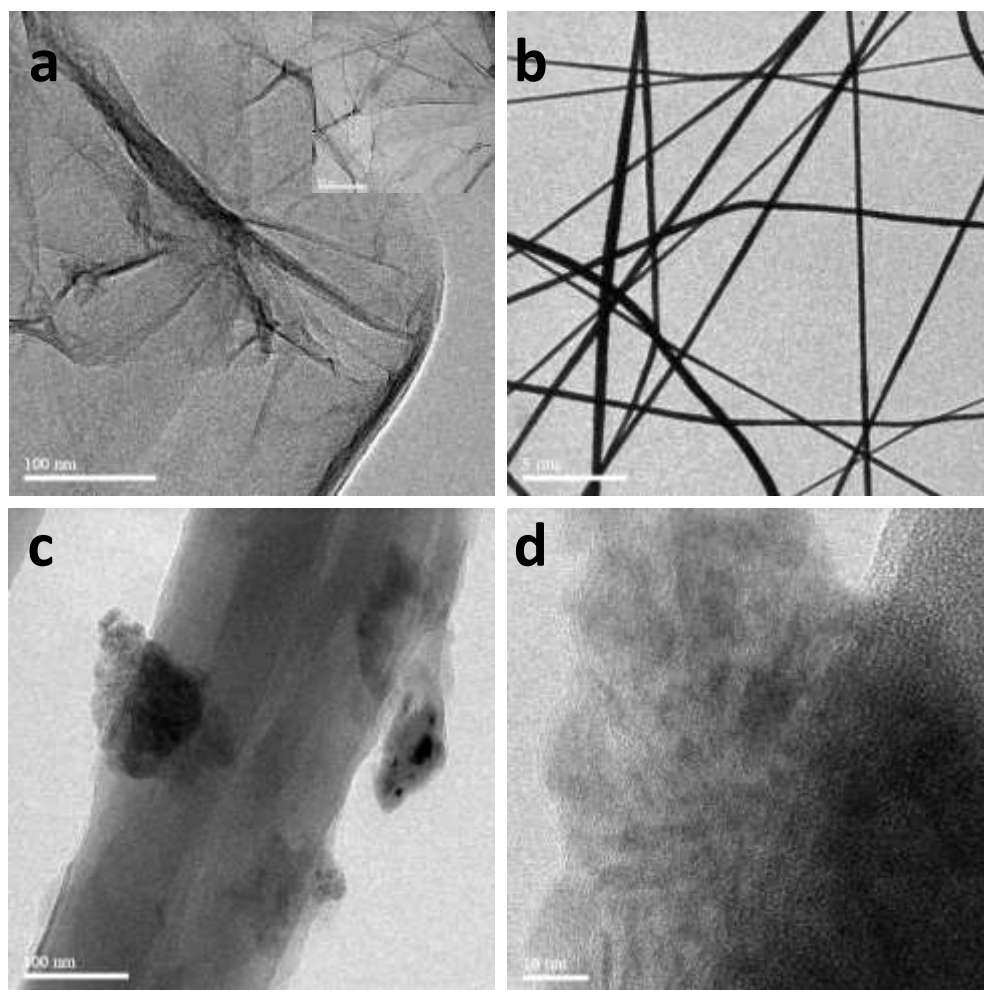


**Figure S3.** TEM images of (a) rGO and an expanded view of parent graphene shown in the inset. (b, c and d) PVDF/rGO nanofibers in different magnifications and expanded view of the fibers in (d) shows the embedded graphene.

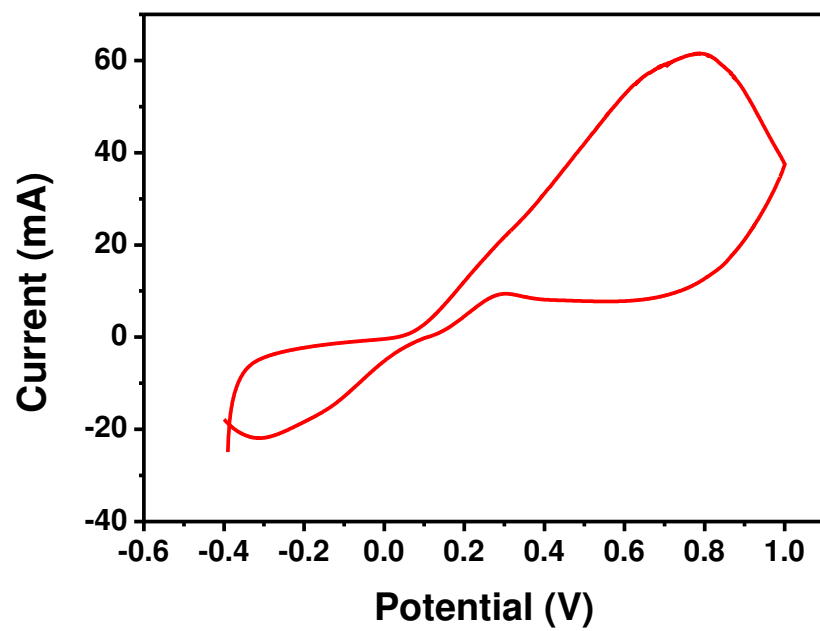


**Figure S4.** Cyclic voltammogram of PANi coated on ITO via SILAR, with a scan rate of 50 mVs<sup>-1</sup> using 0.5 M H<sub>2</sub>SO<sub>4</sub> as electrolyte.



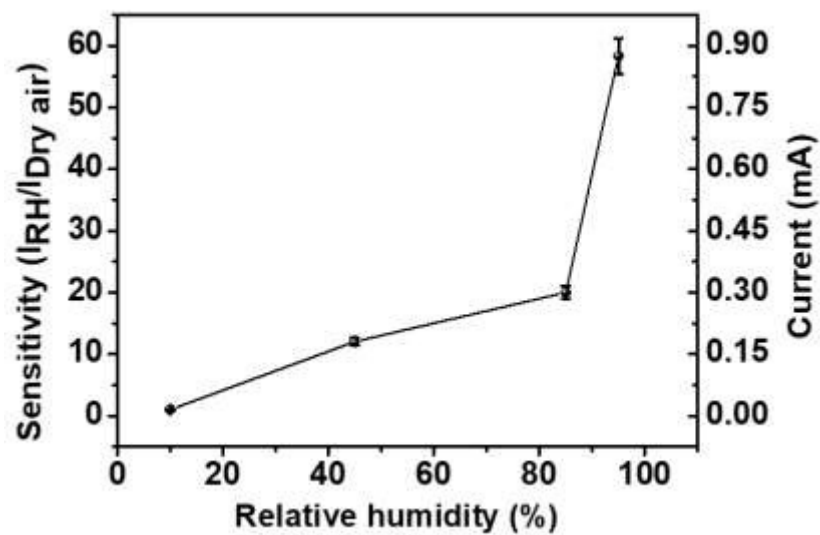


**Figure S5.** Calibration curve of humidity with respect to sensitivity and current.

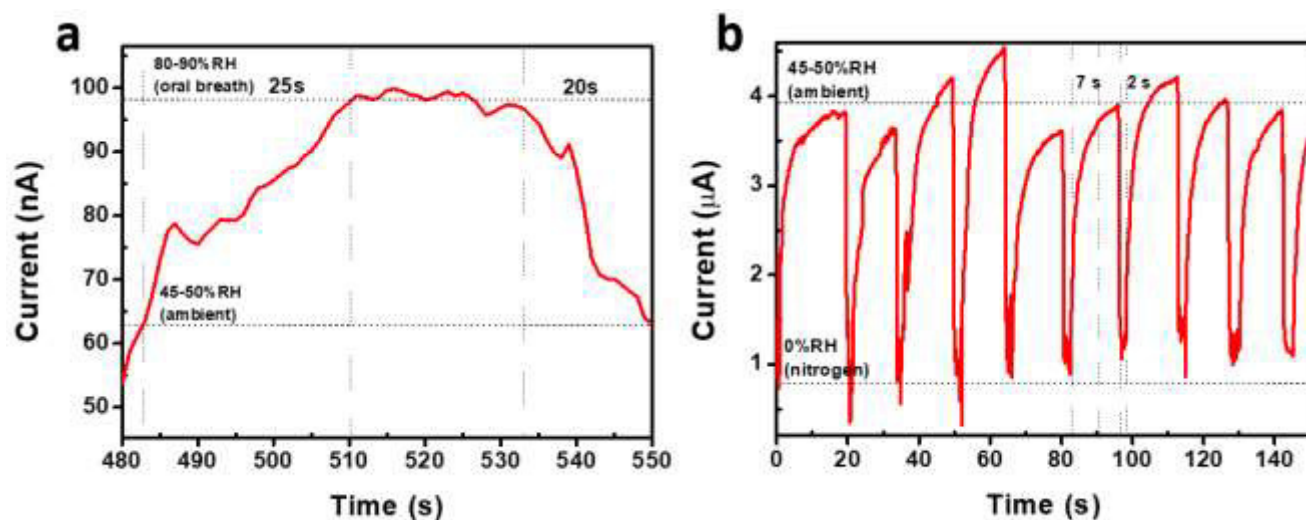


**Figure S6.** Chronoamperometric response of PANi-coated (a) PVDF and (b) PVDF/4 mg rGO.

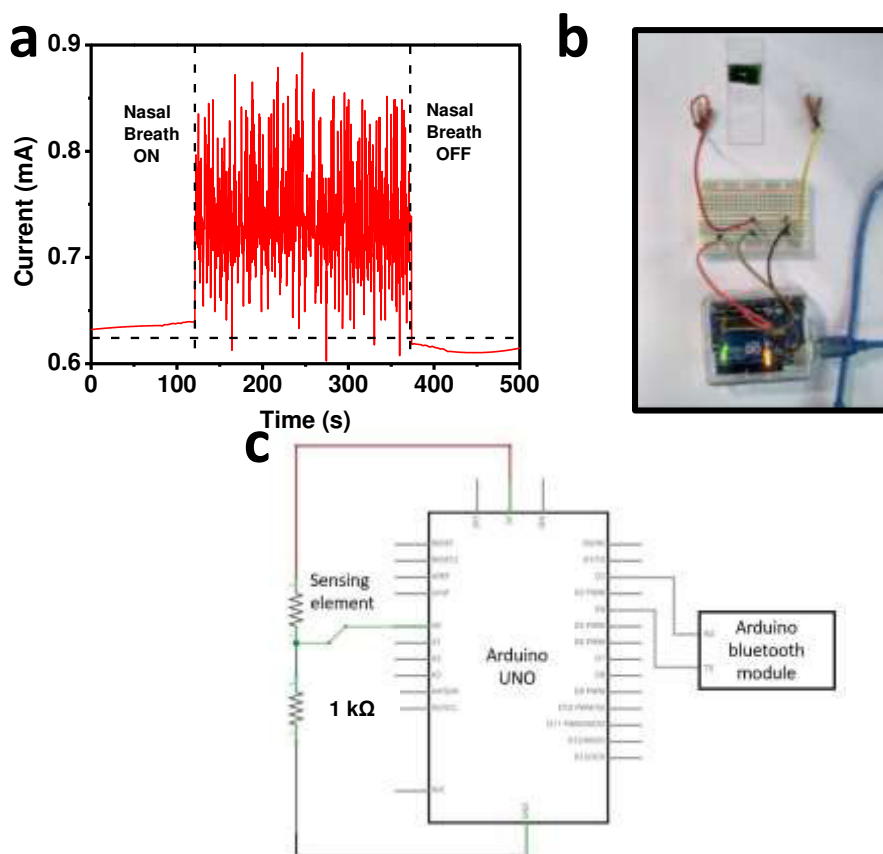


**Figure S7.** (a) Breath analysis data collected from the sensing element combined with the prototyping platform. (b) Sensor device set-up with circuit, (c) Circuit diagram of the sensor assembly using Arduino UNO and Bluetooth module for data transfer to mobile.

**The Arduino interface code used is shown below:**

```
int analogPin= 0;
int raw= 0;
int Vin= 5;
float Vout= 0;
float R1= 1000; //specifies the resistance rating of series load in Ohm
float R2= 0;
float buffer= 0;
void setup()
{
  Serial.begin(9600);
}
void loop()
{
  raw= analogRead(analogPin);
  if(raw)
  {
    buffer= raw * Vin;
    Vout= (buffer)/1024.0;
    buffer= (Vin/Vout) -1;
    R2= R1 * buffer;
    Serial.print("Vout: ");
    Serial.println(Vout);
    Serial.print("R2: ");
    Serial.println(R2);
    delay(1000); //specifies time interval between measurements in ms
  }
}
```

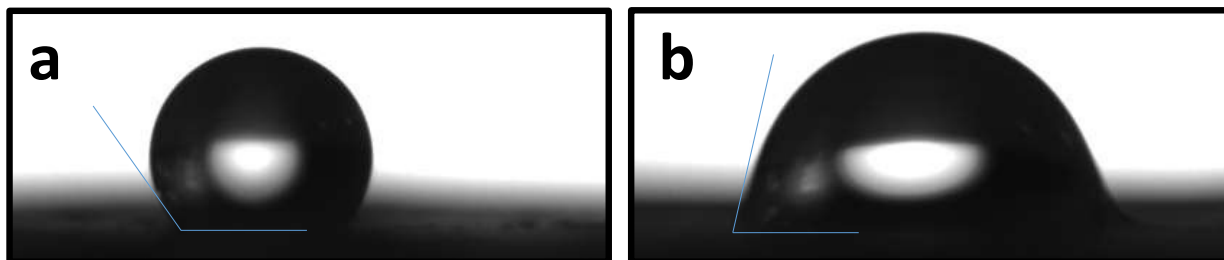


**Figure S8.** Contact angle measurements performed for PVDF/rGO nanofibers (a) before SILAR and (b) after SILAR treatment.

**Table S1.** Comparison of the sensing performance between our sensor and previously reported ones.

<b>Sensing element</b>	<b>Sensing Range (% RH)</b>	<b>Response time (s)</b>	<b>Sensitivity</b>	<b>Reference</b>
<b>Supramolecular nanofibers</b>	10-80	0.01	2200	6
<b>Graphene oxide</b>	35-80	0.03	10	7
<b>Polyaniline/poly (vinyl butyral) nanofibers</b>	20-90	1-2	1	8
<b>Amphiphilic Dyad fibers</b>	0-75	0.026	5	9
<b>MoS<sub>2</sub> modified ZnO quantum dots composite</b>	11-95	20	1000	5
<b>Graphene oxide/ polyelectrolyte nanofilm</b>	11-97	1	1000	10
<b>Supramolecular modified graphene oxide</b>	11-95	1	600	11
<b>PVDF/rGO/ PANi based nanofibers</b>	10-95	1	60	Present work
<b>Black phosphorus/ Al<sub>2</sub>O<sub>3</sub></b>	20-80	200	6	12
<b>rGO/GO/rGO</b>	6.3-100	1.9	8	13
<b>CNT/PVA filament</b>	60-100	40	220	14
<b>CNT/polyimide composite</b>	10-95	-	1.5	15
<b>CNT/cellulose paper</b>	10-90	6	0.67	16
<b>MWCNT</b>	25-95	3	1.4	17
<b>Silica nanoparticle</b>	10-80	2.4	0.001	18
<b>Paper based</b>	0-90	3	2	19
<b>Wrinkled graphene</b>	11-95	0.0125	1.1	20

## References

- (1) Wen, Y.; Xing, F.; He, S.; Song, S.; Wang, L.; Long, Y.; Li, D.; Fan, C. A Graphene-Based Fluorescent Nanoprobe for Silver(i) Ions Detection by Using Graphene Oxide and a Silver-Specific Oligonucleotide. *Chem. Commun.* **2010**, 46 (15), 2596–2598.
- (2) Chua, C. K.; Pumera, M. Chemical Reduction of Graphene Oxide: A Synthetic Chemistry Viewpoint. *Chem. Soc. Rev.* **2014**, 43 (1), 291–312.
- (3) Pei, S.; Cheng, H.-M. The Reduction of Graphene Oxide. *Carbon N. Y.* **2012**, 50 (9), 3210–3228.
- (4) Long, D.; Li, W.; Ling, L.; Miyawaki, J.; Mochida, I.; Yoon, S.-H. Preparation of Nitrogen-Doped Graphene Sheets by a Combined Chemical and Hydrothermal Reduction of Graphene Oxide. *Langmuir* **2010**, 26 (20), 16096–16102.
- (5) Ze, L.; Yueqiu, G.; Xujun, L.; Yong, Z. MoS<sub>2</sub>-Modified ZnO Quantum Dots Nanocomposite: Synthesis and Ultrafast Humidity Response. *Appl. Surf. Sci.* **2017**, 399, 330–336.
- (6) Mogera, U.; Sagade, A. A.; George, S. J.; Kulkarni, G. U. Ultrafast Response Humidity Sensor Using Supramolecular Nanofibre and Its Application in Monitoring Breath Humidity and Flow. *Sci. Rep.* **2014**, 4, 1–9.
- (7) Borini, S.; White, R.; Wei, D.; Astley, M.; Haque, S.; Spigone, E.; Harris, N.; Kivioja, J.; Ryhänen, T. Ultrafast Graphene Oxide Humidity Sensors. *ACS Nano* **2013**, 7 (12), 11166–11173.
- (8) Lin, Q.; Li, Y.; Yang, M. Highly Sensitive and Ultrafast Response Surface Acoustic Wave Humidity Sensor Based on Electrospun Polyaniline/Poly(Vinyl Butyral) Nanofibers. *Anal. Chim. Acta* **2012**, 748, 73–80.
- (9) Squillaci, M. A.; Ferlauto, L.; Zagranyski, Y.; Milita, S.; Müllen, K.; Samorì, P. Self-Assembly of an Amphiphilic  $\pi$ -Conjugated Dyad into Fibers: Ultrafast and Ultrasensitive Humidity Sensor. *Adv. Mater.* **2015**, 27 (20), 3170–3174.
- (10) Zhang, D.; Tong, J.; Xia, B.; Xue, Q. Ultrahigh Performance Humidity Sensor Based on Layer-by-Layer Self-Assembly of Graphene Oxide/Polyelectrolyte Nanocomposite Film. *Sensors Actuators B Chem.* **2014**, 203, 263–270.
- (11) Wang, S.; Chen, Z.; Umar, A.; Wang, Y.; Tian, T.; Shang, Y.; Fan, Y.; Qi, Q.; Xu, D.

- Supramolecularly Modified Graphene for Ultrafast Responsive and Highly Stable Humidity Sensor. *J. Phys. Chem. C* **2015**, *119* (51), 28640–28647.
- (12) Miao, J.; Cai, L.; Zhang, S.; Nah, J.; Yeom, J.; Wang, C. Air-Stable Humidity Sensor Using Few-Layer Black Phosphorus. *ACS Appl. Mater. Interfaces* **2017**, *9* (11), 10019–10026.
- (13) Cai, J.; Lv, C.; Aoyagi, E.; Ogawa, S.; Watanabe, A. Laser Direct Writing of a High-Performance All-Graphene Humidity Sensor Working in a Novel Sensing Mode for Portable Electronics. *ACS Appl. Mater. Interfaces* **2018**, *10* (28), 23987–23996.
- (14) Fei, T.; Jiang, K.; Jiang, F.; Mu, R.; Zhang, T. Humidity Switching Properties of Sensors Based on Multiwalled Carbon Nanotubes/Polyvinyl Alcohol Composite Films. *J. Appl. Polym. Sci.* **2014**, *131* (1), 1–7.
- (15) Yoo, K.-P.; Lim, L.-T.; Min, N.-K.; Lee, M. J.; Lee, C. J.; Park, C.-W. Novel Resistive-Type Humidity Sensor Based on Multiwall Carbon Nanotube/Polyimide Composite Films. *Sensors Actuators B Chem.* **2010**, *145* (1), 120–125.
- (16) Han, J.-W.; Kim, B.; Li, J.; Meyyappan, M. Carbon Nanotube Based Humidity Sensor on Cellulose Paper. *J. Phys. Chem. C* **2012**, *116* (41), 22094–22097.
- (17) Liu, L.; Ye, X.; Wu, K.; Han, R.; Zhou, Z.; Cui, T. Humidity Sensitivity of Multi-Walled Carbon Nanotube Networks Deposited by Dielectrophoresis. *Sensors* . 2009.
- (18) Kano, S.; Dobashi, Y.; Fujii, M. Silica Nanoparticle-Based Portable Respiration Sensor for Analysis of Respiration Rate, Pattern, and Phase During Exercise. *IEEE Sensors Lett.* **2018**, *2* (1), 1–4.
- (19) Güder, F.; Ainla, A.; Redston, J.; Mosadegh, B.; Glavan, A.; Martin, T. J.; Whitesides, G. M. Paper-Based Electrical Respiration Sensor. *Angew. Chemie - Int. Ed.* **2016**, *55* (19), 5727–5732.
- (20) Zhen, Z.; Li, Z.; Zhao, X.; Zhong, Y.; Zhang, L.; Chen, Q.; Yang, T.; Zhu, H. Formation of Uniform Water Microdroplets on Wrinkled Graphene for Ultrafast Humidity Sensing. *Small* **2018**, *14* (15), 1–8.



REPLY TO CHOUKROUN ET AL.:

# IR and TPD data suggest the formation of clathrate hydrates in laboratory experiments simulating ISM

Jyotirmoy Ghosh<sup>a</sup>, Rabin Rajan J. Methikkalam<sup>a,1</sup>, Radha Gobinda Bhui<sup>a,2</sup>, Gopi Ragupathy<sup>a</sup>, Nilesh Choudhary<sup>b</sup>, Rajnish Kumar<sup>b,3</sup>, and Thalappil Pradeep<sup>a,3</sup>

In their letter, Choukroun et al. (1) caution against our results (2) as definitive evidence for the formation of clathrate hydrates (CHs) in the interstellar medium (ISM). We show the emergence of an infrared (IR) feature at  $3,017\text{ cm}^{-1}$  in vapor-deposited  $\text{CH}_4$ -water mixture upon  $\sim 25\text{ h}$  of annealing, at  $30\text{ K}$  in ultrahigh vacuum (2). We attribute the blue-shifted feature (with respect to the  $3,009\text{ cm}^{-1}$  peak of condensed  $\text{CH}_4$ ) to  $\text{CH}_4$  hydrate of the  $5^{12}$  structure. Dartois et al. (3) also suggested a blue shift for  $\text{CH}_4$  trapped in the  $5^{12}$  cage. A microsecond molecular dynamics simulation of  $\text{CH}_4$  hydrate (4) predicted preferential formation of  $5^{12}$  cages during CH nucleation. In our experiment (2), the trapped  $\text{CH}_4$  desorbs along with the collapse of  $5^{12}$  cages, increasing the intensity of molecular volcano of  $\text{CH}_4$  at  $\sim 140\text{ K}$  in temperature programmed desorption (TPD). This is unexpected without CH being present. Thus, IR results, along with TPD and computations, support CH formation (2).

Because  $\text{CO}_2$  forms CH at  $120\text{ K}$ , confirmed by IR (5), we performed thermal annealing of the  $\text{CO}_2$ -ice mixture, and the characteristic  $2,346\text{ cm}^{-1}$  peak emerged corresponding to  $\text{CO}_2$  trapped in the  $5^{12}$  cage (2). Devlin et al. (6) reported the formation of pure  $\text{CO}_2$  CH by vapor deposition under vacuum, and the  $\nu_3(\text{CO}_2)$  due to  $5^{12}$  occupancy was seen at  $2,346\text{ cm}^{-1}$ . In our work (2), only the  $5^{12}$  cage was formed as the  $2,346\text{ cm}^{-1}$  peak alone was observed, and not the double peak feature due to the s-I structure (6).

$\text{CH}_3\text{OH}$  is a CH inhibitor (7), although it forms CH under certain conditions (8). Blake et al. (5) used  $\text{CO}_2$  as a local IR probe to sense  $\text{CH}_3\text{OH}$  hydrate. Additives

such as  $\text{CH}_3\text{OH}$ , tetrahydrofuran, etc., alter the rate of hydrate formation. However, our studies did not explore this aspect. It is unlikely that the presence of  $\text{CH}_3\text{OH}$  is absolutely necessary for the formation of  $\text{CO}_2$  hydrate.

It is known that  $\text{CO}_2$  interacts chemically with the  $5^{12}$  cage (9). However, this interaction is weak, although stronger than in  $\text{CH}_4$  hydrate. We studied the nature of this interaction using atoms-in-molecules analysis, which confirmed it to be H bonding (2). The small cavity size ( $3.95\text{ \AA}$ ) of the  $5^{12}$  cage (7), comparable to the van der Waals diameter ( $2.32\text{ \AA}$ ) of  $\text{CO}_2$ , may be enabling this (10). However, this interaction is not strong enough to distort the overall structure of the host lattice (10). When we correlated the experimental shifts with computed values, the influence of neighboring cages on an isolated cage was not considered. Moreover, we did not make a comparison with the  $2,353\text{ cm}^{-1}$  peak, since  $\text{CO}_2$  exhibits weak interaction with water of the ice matrix, while in  $\text{CH}_4$ , it is negligible.

The unit cells of hydrates are complex, and the water molecules reside in several inequivalent sites (11). For this reason, the O-H stretching band of the host ice network is broadened (11).

Ongoing investigations using other guest molecules by a similar method further support the existence of CHs under these conditions.

Although our experiments suggest the existence of CHs (primarily  $5^{12}$  cages) in ISM, further investigations with longer annealing time, supported by additional spectroscopic and diffraction data, are welcome to understand more details.

<sup>a</sup>Department of Science and Technology (DST) Unit of Nanoscience and Thematic Unit of Excellence (TUE), Department of Chemistry, Indian Institute of Technology Madras, Chennai 600036, India; and <sup>b</sup>Department of Chemical Engineering, Indian Institute of Technology Madras, Chennai 600036, India

Author contributions: J.G. and T.P. designed research; J.G. and R.R.J.M. performed research; J.G., R.R.J.M., and T.P. contributed new reagents/analytic tools; J.G., R.R.J.M., R.G.B., G.R., N.C., R.K., and T.P. analyzed data; and J.G., R.R.J.M., R.G.B., G.R., R.K., and T.P. wrote the paper.

The authors declare no conflict of interest.

Published under the PNAS license.

<sup>1</sup>Present address: Institute of Chemistry, The Hebrew University, Jerusalem 91904, Israel.

<sup>2</sup>Present address: Lehrstuhl für Physikalische Chemie II, Friedrich-Alexander-Universität Erlangen-Nürnberg, 91058 Erlangen, Germany.

<sup>3</sup>To whom correspondence may be addressed. Email: rajnish@iitm.ac.in or pradeep@iitm.ac.in.

Published online July 3, 2019.

- 1 M. Choukroun, T. H. Vu, E. C. Fayolle, No compelling evidence for clathrate hydrate formation under interstellar medium conditions over laboratory time scales. *Proc. Natl. Acad. Sci. U.S.A.* **116**, 14407–14408 (2019).
- 2 J. Ghosh et al., Clathrate hydrates in interstellar environment. *Proc. Natl. Acad. Sci. U.S.A.* **116**, 1526–1531 (2019).
- 3 E. Dartois, D. Deboffle, M. Bouzit, Methane clathrate hydrate infrared spectrum II. Near-infrared overtones, combination modes and cages assignments. *Astron. Astrophys.* **514**, 49 (2010).
- 4 M. R. Walsh, C. A. Koh, E. D. Sloan, A. K. Sum, D. T. Wu, Microsecond simulations of spontaneous methane hydrate nucleation and growth. *Science* **326**, 1095–1098 (2009).
- 5 D. Blake, L. Allamandola, S. Sandford, D. Hudgins, F. Freund, Clathrate hydrate formation in amorphous cometary ice analogs in vacuo. *Science* **254**, 548–551 (1991).
- 6 F. Fleyfel, J. P. Devlin, Carbon dioxide clathrate hydrate epitaxial growth: Spectroscopic evidence for formation of the simple type-II carbon dioxide hydrate. *J. Phys. Chem.* **95**, 3811–3815 (1991).
- 7 E. D. Sloan, Jr, C. A. Koh, *Clathrate Hydrates of Natural Gases* (CRC Press, 2008).
- 8 K. Shin et al., Methanol incorporation in clathrate hydrates and the implications for oil and gas pipeline flow assurance and icy planetary bodies. *Proc. Natl. Acad. Sci. U.S.A.* **110**, 8437–8442 (2013).
- 9 P. Warrier, M. N. Khan, V. Srivastava, C. M. Maupin, C. A. Koh, Overview: Nucleation of clathrate hydrates. *J. Chem. Phys.* **145**, 211705 (2016).
- 10 P. A. Siuda, “Dynamics and molecular properties of clathrate hydrates of carbon dioxide and hydrocarbons,” PhD thesis, University of Warsaw, Warsaw, Poland (2014).
- 11 V. Buch et al., Clathrate hydrates with hydrogen-bonding guests. *Phys. Chem. Chem. Phys.* **11**, 10245–10265 (2009).

REVIEW ARTICLE

Open Access

# The emerging interface of mass spectrometry with materials

Papri Chakraborty<sup>1</sup> and Thalappil Pradeep<sup>1</sup>

## Abstract

Mass spectrometry (MS), a hundred-year-old subject, has been a technique of profound importance to molecular science. Its impact in solid-state materials science has not been evident, although many materials of modern science, such as fullerenes, have their origins in MS. Of late, mass spectrometric interface with materials is increasingly strengthened with advances in atomically precise clusters of noble metals. Advances in instrumentation along with recent developments in synthetic approaches have expanded the chemistry of clusters, and new insights into matter at the nanoscale are emerging. High-resolution MS coupled with soft ionization techniques enable efficient characterization of atomically precise clusters. Apart from that, techniques such as ion mobility, tandem MS, etc. reveal structural details of these systems. Growth, nucleation, and reactivity of clusters are also probed by MS. Some of the recent advancements in this field include the development of new hyphenated techniques. Finer structural details may be obtained by coupling MS with spectroscopic tools, such as photoelectron spectroscopy, vacuum ultraviolet spectroscopy, etc. With such advancements in instrumentation, MS can evolve into a universal tool for the characterization of materials. The present review captures highlights of this area.

## Introduction

Mass spectrometry (MS), a century-old discipline concerning the investigation of matter using ions, is undergoing revolutionary changes. While the systems being examined went through systematic changes from atomic and molecular species to proteins and macromolecules in the course of evolution of MS, the perception of matter itself underwent a drastic transformation in this period. Materials science is becoming increasingly molecular today, and constituents of molecular matter are acquiring new properties leading to novel applications. Investigations require newer tools, and MS has evidently met the needs in this area. This has happened due to efficient methods of ionization of large molecular systems<sup>1,2</sup>.

The first use of MS dates back to a century ago when Sir J.J. Thomson measured the  $m/z$  values of gaseous ionized molecules<sup>3,4</sup>. He also found the first evidence of isotopes

of an element<sup>5</sup>. Later in 1922, Aston received a Nobel Prize in Chemistry for his discovery of isotopes in several nonradioactive elements<sup>5</sup>. Initially, MS gained importance in the analysis of organic molecules, and ionization techniques like electric discharge and electron impact (EI) were used in such studies. Slowly, scientists started using MS for the analysis of sugars, alkaloids, and peptides<sup>6</sup>. The development of hyphenated techniques like gas chromatography–mass spectrometry (GC–MS)<sup>7,8</sup> further strengthened the use of MS as an analytical tool. The use of tandem MS (MS/MS) techniques, where mass spectrum of a mass-selected species is analyzed, became a popular tool for understanding the structures of molecules. For extending MS/MS studies to larger molecules like proteins and peptides, Todd, McGilvery, and Baldwin constructed a high-resolution double-focussing mass spectrometer<sup>9</sup>. But still, MS/MS studies for large molecules were possible only with harsh ionization techniques like fast atom bombardment. For the study of large molecules like proteins, there was a need for the development of softer ionization techniques. Such needs led to

Correspondence: Thalappil Pradeep (pradeep@iitm.ac.in)

<sup>1</sup>DST Unit of Nanoscience (DST UNS) and Thematic Unit of Excellence (TUE), Department of Chemistry, Indian Institute of Technology Madras, Chennai 600036 Tamil Nadu, India

© The Author(s) 2019



**Open Access** This article is licensed under a Creative Commons Attribution 4.0 International License, which permits use, sharing, adaptation, distribution and reproduction in any medium or format, as long as you give appropriate credit to the original author(s) and the source, provide a link to the Creative Commons license, and indicate if changes were made. The images or other third party material in this article are included in the article's Creative Commons license, unless indicated otherwise in a credit line to the material. If material is not included in the article's Creative Commons license and your intended use is not permitted by statutory regulation or exceeds the permitted use, you will need to obtain permission directly from the copyright holder. To view a copy of this license, visit <http://creativecommons.org/licenses/by/4.0/>.

the development of electrospray ionization (ESI)<sup>1</sup>, and for this breakthrough development, a Nobel Prize was awarded to John Fenn in 2002. Koichi Tanaka was also awarded a Nobel Prize in the same year for his development of soft laser desorption (SLD) and its applications for ionization of macromolecules<sup>10</sup>. Moreover, for the analysis of complex mixtures, high-resolving power ( $m/\Delta m$ ) is desired<sup>11</sup>. The use of time-of-flight (TOF) mass analyzers came into use in the year 1948<sup>12</sup>. By using dual-stage reflectrons, the flight path of the ions could be extended by multiple reflections, and at present TOF analyzers can reach a resolving power of about 50,000 or more at  $m/z$  20–16,000. In 1974, Fourier-transform ion cyclotron resonance (FTICR) analyzers were introduced<sup>13</sup>, which exhibited higher-resolving power compared with the TOF analyzers<sup>14</sup>. The orbitrap was invented in 1999<sup>14</sup>, and at present, they can reach a resolution of 6,00,000 at  $m/z$  195<sup>15</sup>. The gas-phase ions generated inside the mass spectrometer can also be confined for a significant amount of time in “ion traps”, and properties of the trapped ions have been studied in the literature<sup>16</sup>. Though MS is mainly used for proteomics these days, it also became popular for studying materials. In this review, we have captured how MS has enriched the field of materials science.

Extended solids have been the materials of recent past. They had unique tools for structural characterization, principally revolving around diffraction techniques of various forms<sup>17</sup>. The molecular systems on the other extreme had MS as their integral or most essential tool for compositional (to a lesser degree structural as well) analysis. As extended solids became molecular in their building blocks, as evident from the recent advances in nanoscale matter, analytical requirements to understand composition reached newer scales. Molecular materials of the past were composed of smaller constituents weighing a few hundred mass units. Many of them were stable under the harsh conditions of electron impact MS, and therefore were investigated extensively using sector-based instruments. Coupled with methods of ion activation, fragmentation gave a wealth of information on molecular structure<sup>18</sup>. These studies were complemented by nuclear magnetic resonance (NMR) spectroscopy, and structural details of molecules with NMR active nuclei could be understood with precision<sup>19,20</sup>. This was expanded to even solution-state structure determination of macromolecules. The other extreme of structural insight came from electron diffraction, which was instrumental in understanding structures of simple molecules at the early part of the last century<sup>21</sup>. Soon, structural details of small molecules in the gas phase were understood mostly by spectroscopy, particularly for those molecules in the

atmosphere as well as in interstellar space. Electron diffraction of another kind became a prominent analytical tool with the advent of electron microscopy (EM). With cryo-EM in low-dose diffraction, structures were being solved at Angstrom ( $\text{\AA}$ ) resolution in conjunction with high-quality modeling. In addition to single-crystal diffraction, NMR, electron diffraction, and spectroscopy, there are a number of scattering and analytical tools involving X-rays, electrons, positrons, neutrons, photons, and ions to unravel the structure and properties of materials. While this review does not intend to cover comprehensively any of these techniques, we wish to note that the evolution of materials demands new kinds of techniques for compositional and structural analysis. This has happened because constituent units in advanced materials became more and more discrete while increasing in complexity. Along with this change, constituents of matter expanded from diatomics to polyatomics to macromolecules to nanoparticles. While the need to study all of them in isolation became intense, experimental methods of MS in ionization and ion analysis also got evolved.

The importance of MS as a tool for characterization of materials<sup>22–24</sup> has got strengthened with the advancement in the science of atomically precise nanoclusters (NCs)<sup>25,26</sup>, which are materials with atomic precision. Such clusters exhibit unique electronic and optical properties, and have precision in its compositional structure in the metal core and the protecting ligand layers. Till date, single-crystal X-ray crystallography has been used to resolve the structures of several clusters like  $\text{Au}_{25}\text{L}_{18}$ <sup>27</sup>,  $\text{Au}_{28}\text{L}_{20}$ <sup>28</sup>,  $\text{Au}_{38}\text{L}_{24}$ <sup>29</sup>,  $\text{Au}_{40}\text{L}_{24}$ <sup>30</sup>,  $\text{Au}_{52}\text{L}_{32}$ <sup>31</sup>,  $\text{Au}_{92}\text{L}_{44}$ <sup>32</sup>,  $\text{Au}_{102}\text{L}_{44}$ <sup>33</sup>,  $\text{Au}_{133}\text{L}_{52}$ <sup>34</sup>,  $\text{Ag}_{44}\text{L}_{30}$ <sup>35</sup>,  $\text{Ag}_{25}\text{L}_{18}$ <sup>36</sup>,  $\text{Ag}_{29}\text{L}_{12}$ <sup>37</sup>, etc., where L corresponds to different types of ligands. However, due to their extremely small size, size determination by other techniques like transmission electron microscopy (TEM) or powder XRD has been less reliable. In contrast, MS can accurately identify precision in their compositions. Techniques such as ion mobility–MS (IM–MS) and tandem MS (MS/MS) are becoming increasingly important for understanding the size, shape, and dynamics of cluster systems. Moreover, advancement in instrumentation has enabled the determination of inherent properties of clusters like electron affinity (EA), ionization energy (IE), electronic transitions, etc., through the development of new hyphenated techniques. In this review, we will discuss the recent advances in those emerging directions, and elucidate how MS is evolving into a promising tool for materials characterization.

This has become possible due to advancements in various areas of ionization, mass analysis, detection, sensitivity, resolution, etc. The landmark developments in these aspects are captured in Table 1.

**Table 1** Landmark events in the history of mass spectrometry and their importance in enabling the characterization of materials

Progress in instrumentation		Systems studied by MS	Resolution <sup>6,134*</sup>	Mass range (m/z) <sup>134,5</sup>
1912	Measurement of m/z values by Thomson <sup>3</sup>	Isotopes of elements Atomic weights using MS <sup>6</sup>	100 Aston (130) <sup>5</sup>	100 Aston (~100) <sup>5</sup>
1918	Electron ionization <sup>135</sup>			
1936-37	Secondary ion MS <sup>136</sup>			
1946	Time of flight <sup>139</sup>	1940s Organic mass spectrometry, Mixture of organic analytes could be separated by GC-MS <sup>6</sup>	TOF (4000-5000 at m/z ~100) <sup>137</sup>	Magnetic sector (~2000) <sup>138</sup>
1952	Double-focussing instruments <sup>140</sup>			
1955	Advanced TOF <sup>141</sup>			
1956	GC-MS, <sup>7,8</sup> high-resolution MS <sup>142</sup>			
1953-58	Quadrupole analyzers <sup>143</sup>			
1962	Ion mobility <sup>144</sup>			
1966	Chemical ionization <sup>145</sup>	1980s high molecular-weight polymers, peptides, proteins, nucleic acids, ESI for macromolecules <sup>6</sup> 1996 Analysis of intact live viruses <sup>156</sup>	W geometry ortho-TOF (70,000 at m/z 316) <sup>147</sup>	FTICR (~29,000) <sup>148</sup>
1967	Tandem MS <sup>146</sup>			
1968	Electrospray ionization (ESI) <sup>149</sup>			
1974	Fourier transform (FT) Ion cyclotron resonance <sup>13</sup> , Atmospheric pressure chemical ionization <sup>150</sup>			
1975	Surface-induced dissociation <sup>151</sup>			
1978	Triple quadrupole <sup>152</sup>			
1981	Fast atom bombardment MS <sup>153</sup>	1985 Discovery of fullerenes by laser-induced vaporization <sup>38</sup> 1996 LDI for characterization of thiol-protected clusters <sup>47</sup> 2008 MS of intact Au <sub>25</sub> (PET) <sub>18</sub> clusters <sup>52</sup> 2018 MS of Au-2000 NPs <sup>124</sup>	Orbitrap (6,00,000 at m/z 195) <sup>15</sup>	MALDI TOF (~2,00,000) <sup>158</sup>
1987	MALDI <sup>10,154</sup>			
1999	Orbitrap <sup>14</sup>			
2004	Desorption electrospray ionization <sup>155</sup>			
			10,00,000	10,00,000
			FTICR (20,00,000 at m/z 66,000) <sup>157</sup>	Cryo MALDI TOF (~20,00,000) <sup>159</sup>

\*Does not strictly correspond to the time evolution presented in the left column

### Role of MS in the discovery and characterization of materials

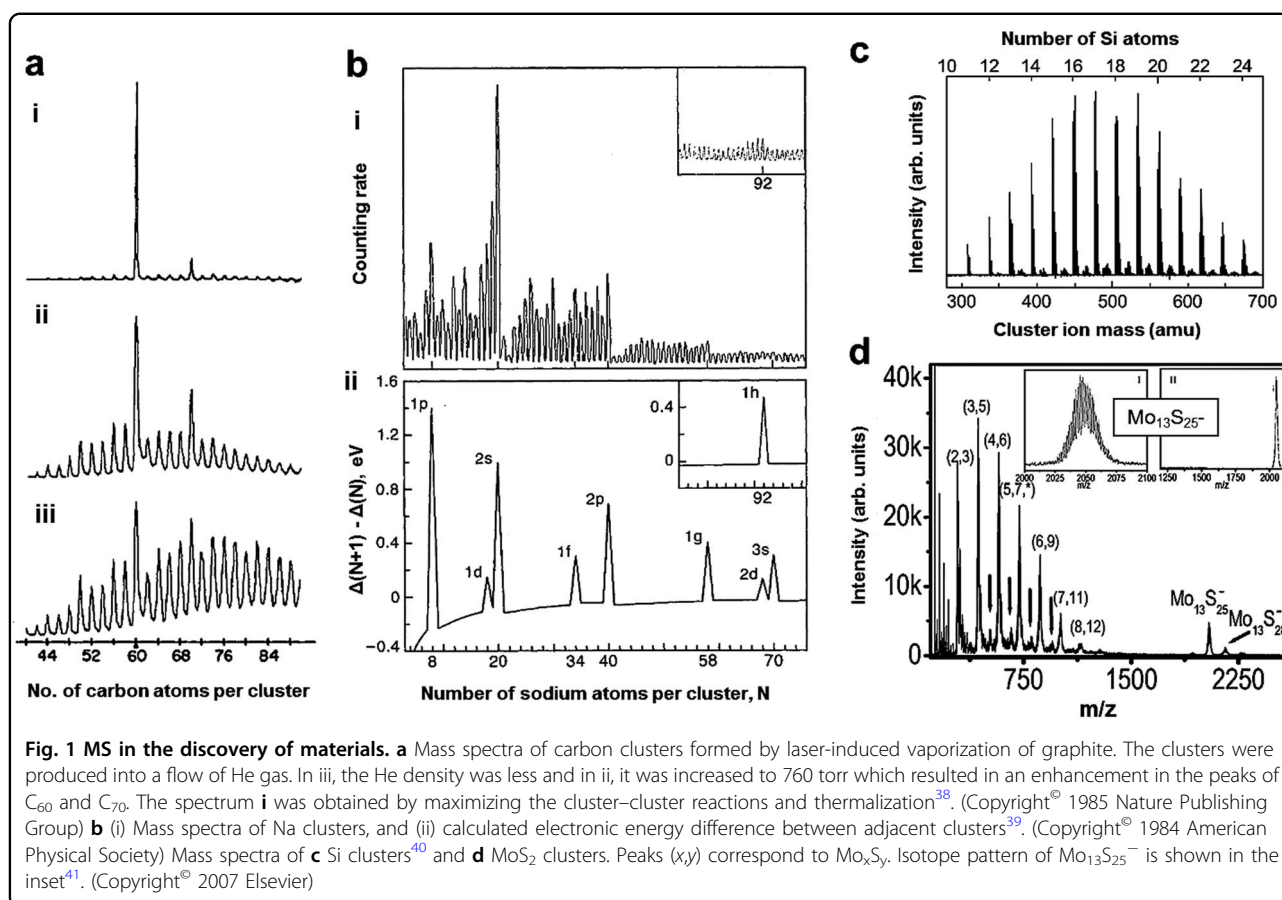
One of the most popular classes of materials of modern science, fullerenes, was discovered using a mass spectrometer<sup>38</sup>. When a pulsed laser evaporated a solid disk of graphite, cooling of the resulting carbon species by a high-density helium flow resulted in the formation of carbon clusters, which were then detected by a TOF MS (Fig. 1a)<sup>38</sup>. In low density of He gas, even numbered clusters, C<sub>n</sub> (*n* = 38–120) were formed (Fig. 1(iii)), with increase in the He pressure to ~760 torr, the abundances of the peaks due to C<sub>60</sub> and C<sub>70</sub> were increased (Fig. 1(ii)) and the peak for C<sub>60</sub> became predominant upon maximizing the cluster–cluster reactions and thermalization (Fig. 1(i)). Apart from fullerenes, MS was immensely used for the characterization of gas-phase metal clusters of Na, namely Na<sub>*n*</sub> (*n* = 4–100)<sup>39</sup>. The discontinuous intensities for the clusters of *n* = 8, 20, 40, 58, and 92 observed in MS (Fig. 1b)

were attributed to the stability of closed shell electronic configurations. Apart from that, there has been extensive research in the field of gas-phase semiconductor clusters like Si clusters (*n* = 8–24) (Fig. 1c)<sup>40</sup> and molecular clusters like MoS<sub>2</sub> clusters (Fig. 1d)<sup>41</sup>.

### Early stages of characterization of noble metal clusters by MS

Gas-phase clusters of noble metals like Au<sub>*n*</sub> or Ag<sub>*n*</sub> were also investigated by MS<sup>42</sup>. Furche et al. assigned the structures of Au<sub>*n*</sub> (*n* < 13) clusters by a combination of mass spectrometric and theoretical studies<sup>43</sup>. Lechtken et al. determined the structures of Au<sub>14</sub><sup>−</sup> – Au<sub>19</sub><sup>−</sup> clusters by trapped ion electron diffraction<sup>44</sup>. Later, in 2003, Li et al. observed that Au<sub>20</sub> cluster which possesses a tetrahedral structure, shows similar atomic packing but largely different properties compared with bulk gold<sup>45</sup>. By photoelectron spectroscopy (PES), the authors





demonstrated that the EA of  $Au_{20}$  cluster was comparable with that of  $C_{60}$ , as shown in Fig. 2a. Along with such studies on gas-phase bare metal clusters, MS slowly evolved into a powerful tool for the characterization of ligand-protected noble metal NCs also.

After Brust reported a new method of synthesis of thiol-protected gold NPs in 1994<sup>46</sup>, scientists started the synthesis of monodisperse NPs with molecule-like optical absorption features. In 1996, Whetten et al. used laser desorption ionization (LDI) for the characterization of dodecanethiol protected gold NCs having mass in the range of 27–93 kDa (Fig. 2b)<sup>47</sup>. The LDI measurements suggested that the gold cores consisted of 140–459 atoms, which was also consistent with their TEM measurements.

### Advances in the study of noble metal clusters

Though LDI was used as the primary characterization tool in the 1990s, softer techniques like matrix-assisted laser desorption ionization (MALDI) and ESI became more popular for the ionization of intact ligand-protected clusters. In 1998, Schaff et al. reported a 10.4 kDa Au-GSH (GSH = glutathione) cluster,  $Au_{28}(SG)_{16}^-$ . The composition was proposed from both MALDI MS and ESI MS. Following this, several other reports came on the

same cluster until in 2005, it was reassigned as  $Au_{25}(SG)_{18}$  by Negishi et al.<sup>49</sup>. With advancement in instrumentation, resolution of the mass spectral measurements improved, which enabled successful characterization of the cluster. MS has largely been used in the characterization of gold clusters, particularly due to their high stability under ambient conditions. Though ESI efficiently ionized water-soluble gold clusters, organic-soluble clusters often showed poor ionization efficiency in this technique. In order to overcome this, scientists implemented new approaches like ligand exchange with ionizable ligands<sup>50</sup>, using  $Ce(SO_4)_2$ <sup>51</sup>, or CsOAc to enhance the ionization<sup>52,53</sup>. In most cases, with the choice of appropriate matrices like sinapinic acid, cinnamic acid, etc., MALDI worked better for the ionization of NCs. In 2008, Dass et al. introduced the use of trans-2-[3-(4-tert-butylphenyl)-2-methyl-2-propenylidene] malononitrile (DCTB) matrix which proved to be more effective<sup>52</sup>, and MALDI MS of intact  $Au_{25}(PET)_{18}$  clusters was successfully measured (Fig. 3b). Comparison of MALDI MS of  $Au_{25}(PET)_{18}$  clusters in different matrices showed the superiority of using DCTB (Fig. 3a). Larger NCs like  $Au_{102}(pMBA)_{44}$ <sup>54</sup> were also characterized using a combination of ESI and MALDI MS. However, due to lesser

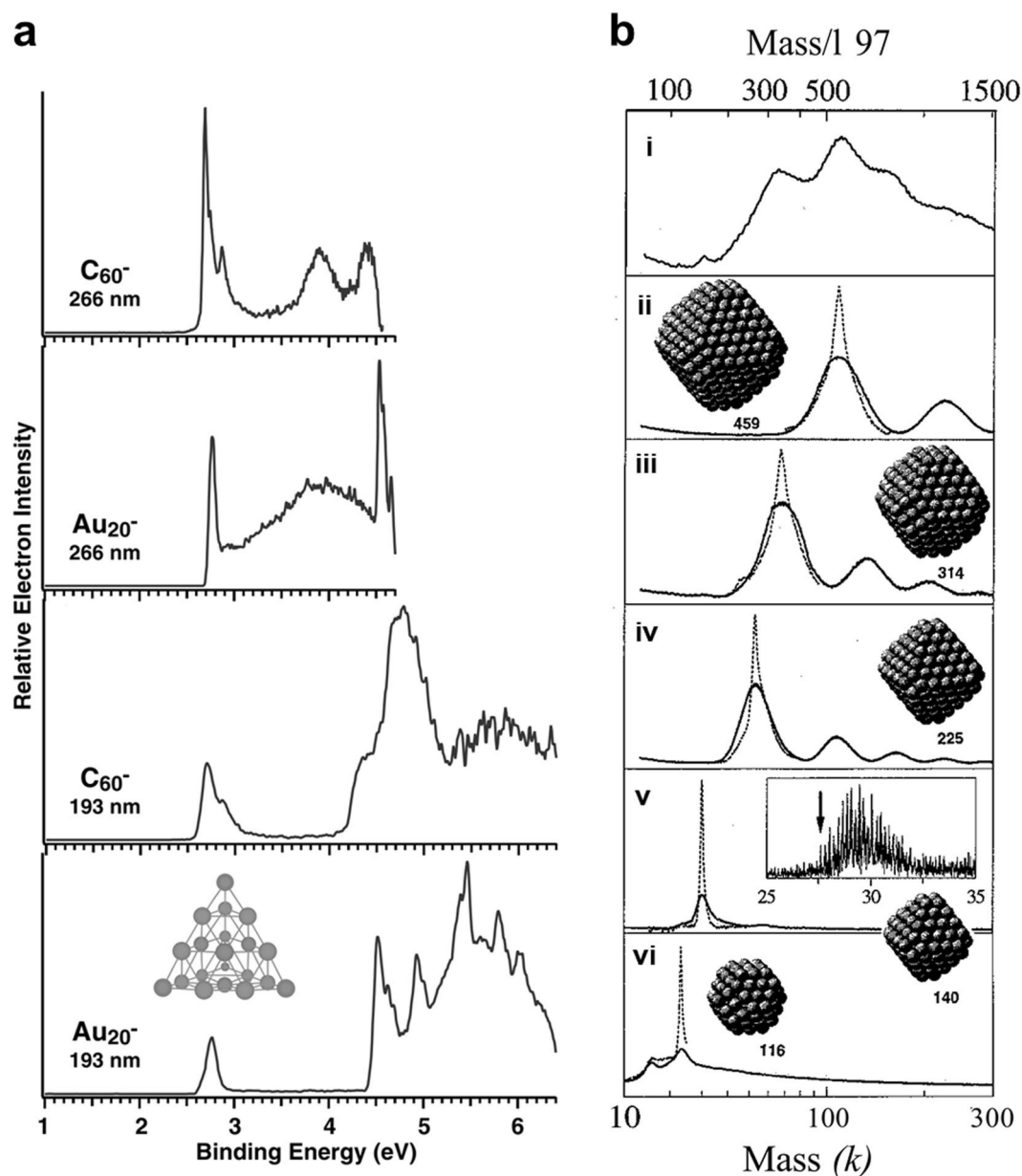
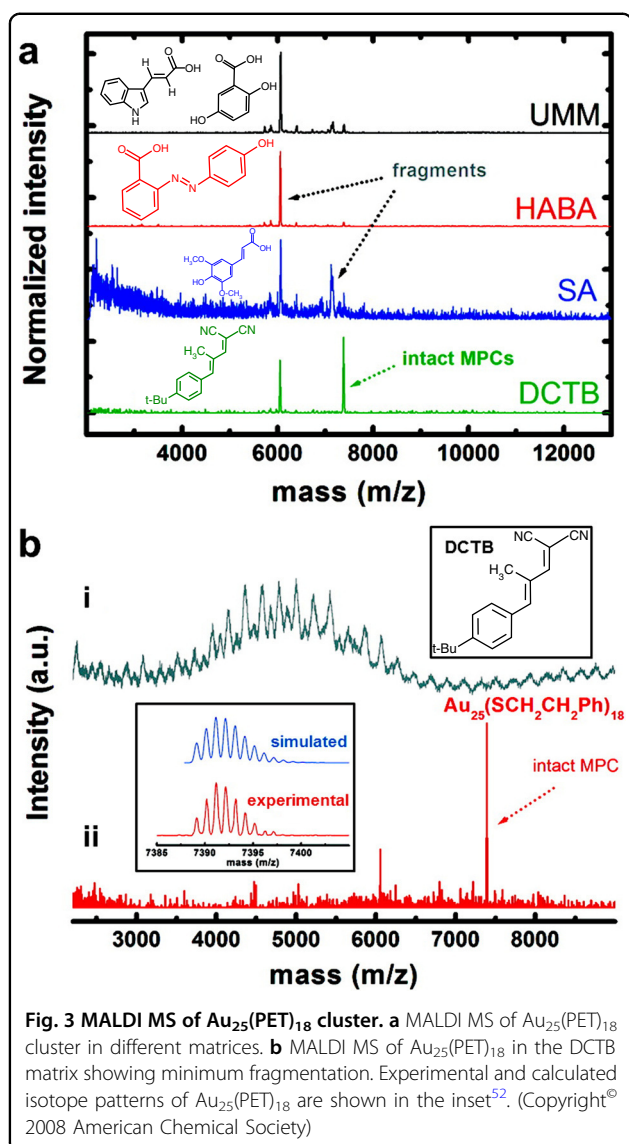


**Fig. 2** Early stages of MS of noble metal clusters. **a** Photoelectron spectra of  $Au_{20}^-$  cluster compared with  $C_{60}^-$  at 193 nm and 266 nm<sup>45</sup>. (Copyright © 2003 the American Association for the Advancement of Science) **b** Mass spectra obtained by laser desorption ionization of dodecanethiol thiol-protected gold clusters, (i) crude mixture of clusters and (ii–vi) separated fractions<sup>47</sup>. (Copyright © 1996 John Wiley and Sons)

stability, mass spectral characterization of silver clusters has always been challenging. As Ag has two isotopes (107 and 109), silver clusters show broader isotope patterns. At the initial stages of research in the field of Ag clusters, mercaptosuccinic acid ( $H_2MSA$ ) protected  $Ag_7$ ,  $Ag_8$ <sup>55,56</sup>, glutathione protected  $Ag_{11}(SG)_7$ <sup>57</sup>,  $Ag_{15}(SG)_{11}$ <sup>58</sup>,  $Ag_{31}(SG)_{19}$ <sup>58</sup>, and  $Ag_{32}(SG)_{19}$ <sup>59</sup>, etc., clusters were characterized by MS. In 2012, Harkness et al. reported the  $Ag_{44}(SR)_{30}$  NCs<sup>60</sup>, which was later crystallized in 2013 by Desiredy et al.<sup>35</sup> and Yang et al.<sup>61</sup>. Recently, in 2015,

Bakr et al. reported  $Ag_{25}(SR)_{18}$  NCs which exhibits identical structure as that of  $Au_{25}(SR)_{18}$ <sup>36</sup>. A luminescent Ag NC,  $[Ag_{29}(BDT)_{12}(TPP)_4]$ <sup>37</sup>, and a box-shaped  $[Ag_{67}(SPhMe_2)_{32}(PPh_3)_8]$ <sup>62</sup> were also reported from the same group. High-resolution ESI MS gave the accurate molecular formulae of these clusters, which matched exactly with their composition found in crystal structures. This highlights the importance of using MS as a versatile tool for the characterization of the NCs. Most recently it has been possible to characterize new types of silver





clusters, [Ag<sub>18</sub>H<sub>16</sub>(TPP)<sub>10</sub>]<sup>2+</sup>, [Ag<sub>25</sub>H<sub>22</sub>(DPPE)<sub>8</sub>]<sup>3+</sup>, and [Ag<sub>26</sub>H<sub>22</sub>(TFPP)<sub>13</sub>]<sup>2+</sup>, which are protected by hydrides and phosphines<sup>63</sup>. Hydride-doped gold cluster [Au<sub>9</sub>H(PPh<sub>3</sub>)<sub>8</sub>]<sup>2+</sup><sup>64</sup> and bimetallic [HPdAu<sub>9</sub>(PPh<sub>3</sub>)<sub>8</sub>]<sup>2+</sup> clusters<sup>65</sup> were also characterized by ESI MS. The crystal structures of many such clusters are not yet available.

Apart from research in the field of Au and Ag NCs, the applicability of MS has also been extended to the field of clusters of other noble metals, eg., Pt NCs<sup>66,67</sup>, Pd NCs<sup>68–70</sup>. MS has also been proved to be useful in case of non-noble metals; eg. Cu NCs like [Cu<sub>20</sub>H<sub>11</sub>(S<sub>2</sub>P(OiPr)<sub>2</sub>)<sub>9</sub>]<sup>71</sup>, Fe NCs like [Fe<sub>6</sub>H<sub>10</sub>(PMe<sub>3</sub>)<sub>8</sub>]<sup>+72</sup>, Ir NCs like Ir<sub>9</sub>(PET)<sub>6</sub><sup>73</sup>, etc.

### High-resolution mass spectrometry (HRMS)

Over the years, there has been a tremendous improvement in instrumentation, which has enabled to obtain HR mass spectra of clusters with minimum fragmentation. A

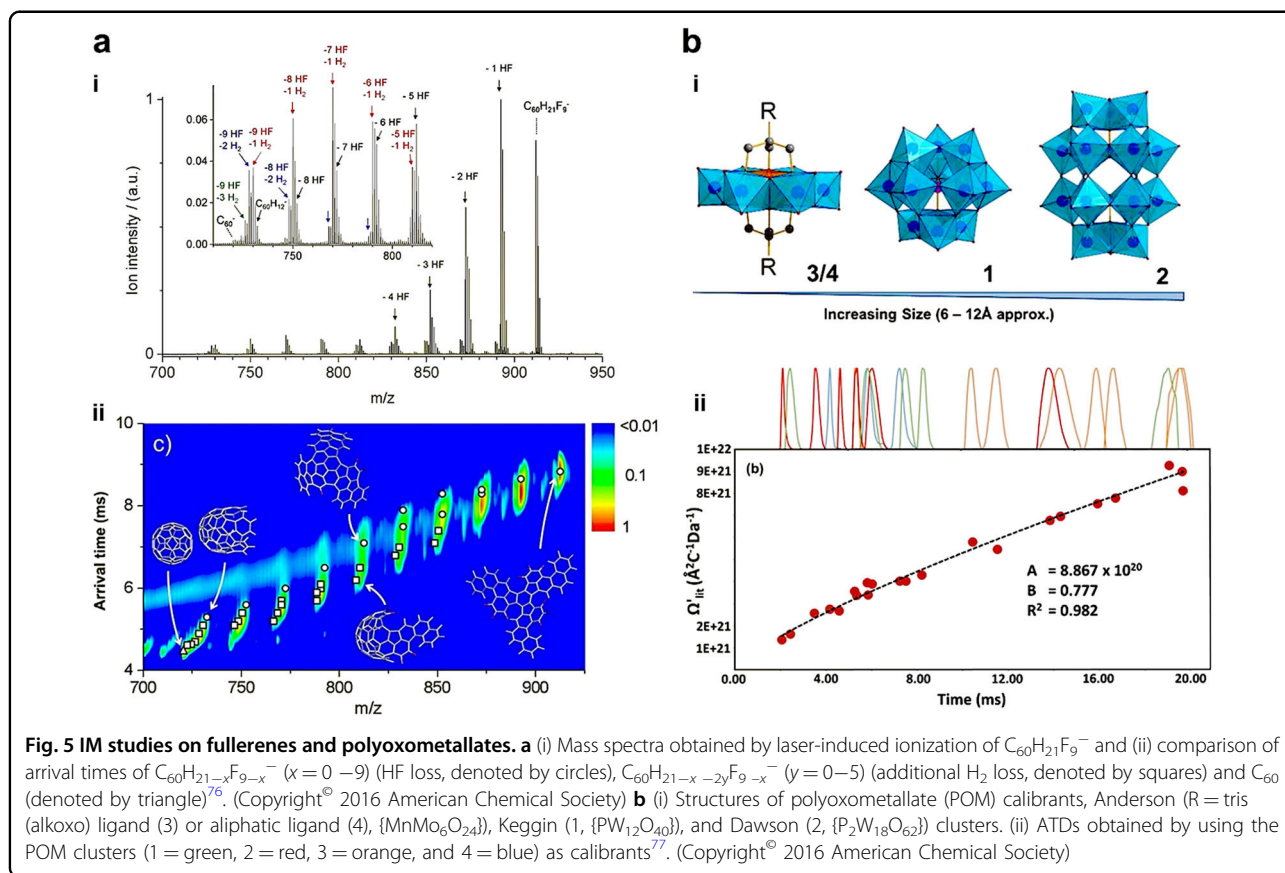
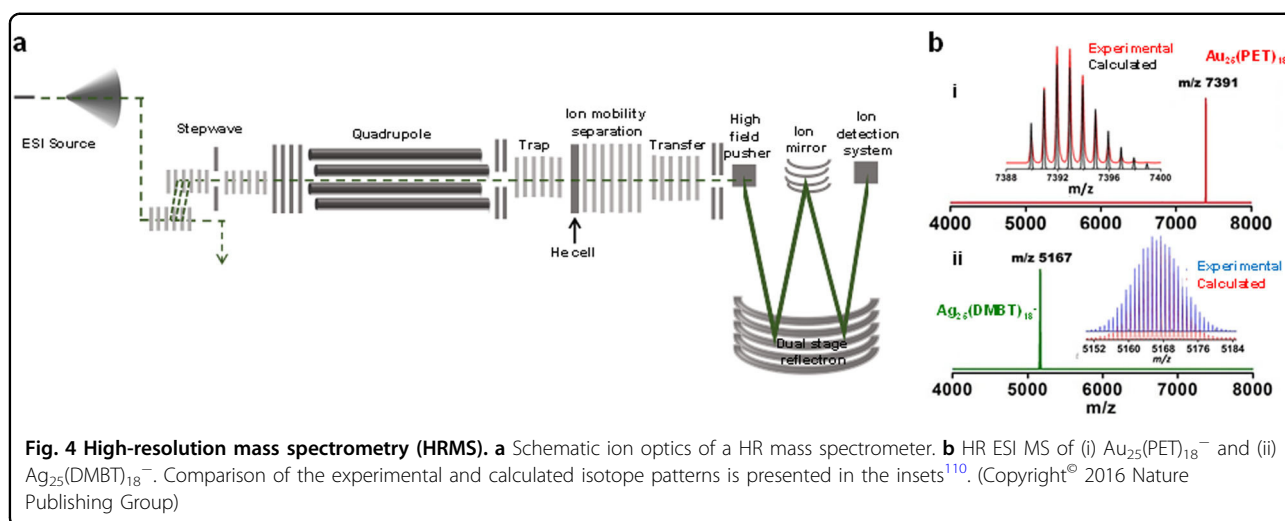
schematic of a HRMS instrument is shown in Fig. 4a. In the TOF analyzer, the trajectory of the ions can be controlled in a shorter “V” or a longer “W” path. With the increase in the path of the ions, the resolution ( $m/\Delta m$ ) increases from ~20,000–35,000 to ~35,000–50,000 in the  $m/z$  range of 20–16000. Additional parts like “stepwaves” are used to remove all contaminants before the ions enter the quadrupole of the mass spectrometer. This also increases the sensitivity of the measurement. Precise composition of the core and the ligands and charge states of the cluster can be determined accurately by using HRMS. The compositions are further confirmed from the isotope patterns of the metals (Au, Ag, Pt, Pd, etc.) and that of C, H, and S present in the ligands. HR ESI MS of Au<sub>25</sub>(PET)<sub>18</sub><sup>–</sup> (PET is phenyl ethane thiol) and Ag<sub>25</sub>(DMBT)<sub>18</sub><sup>–</sup> (DMBT is 2,4-dimethyl benzene thiol) are presented in Fig. 4b.

Apart from the conventional ESI MS analysis, HR mass spectrometers of the present day are also equipped with several other advanced features that enable further studies on the gas-phase cluster ions. Some such recent studies are summarized below.

### Ion mobility–mass spectrometry (IM-MS)

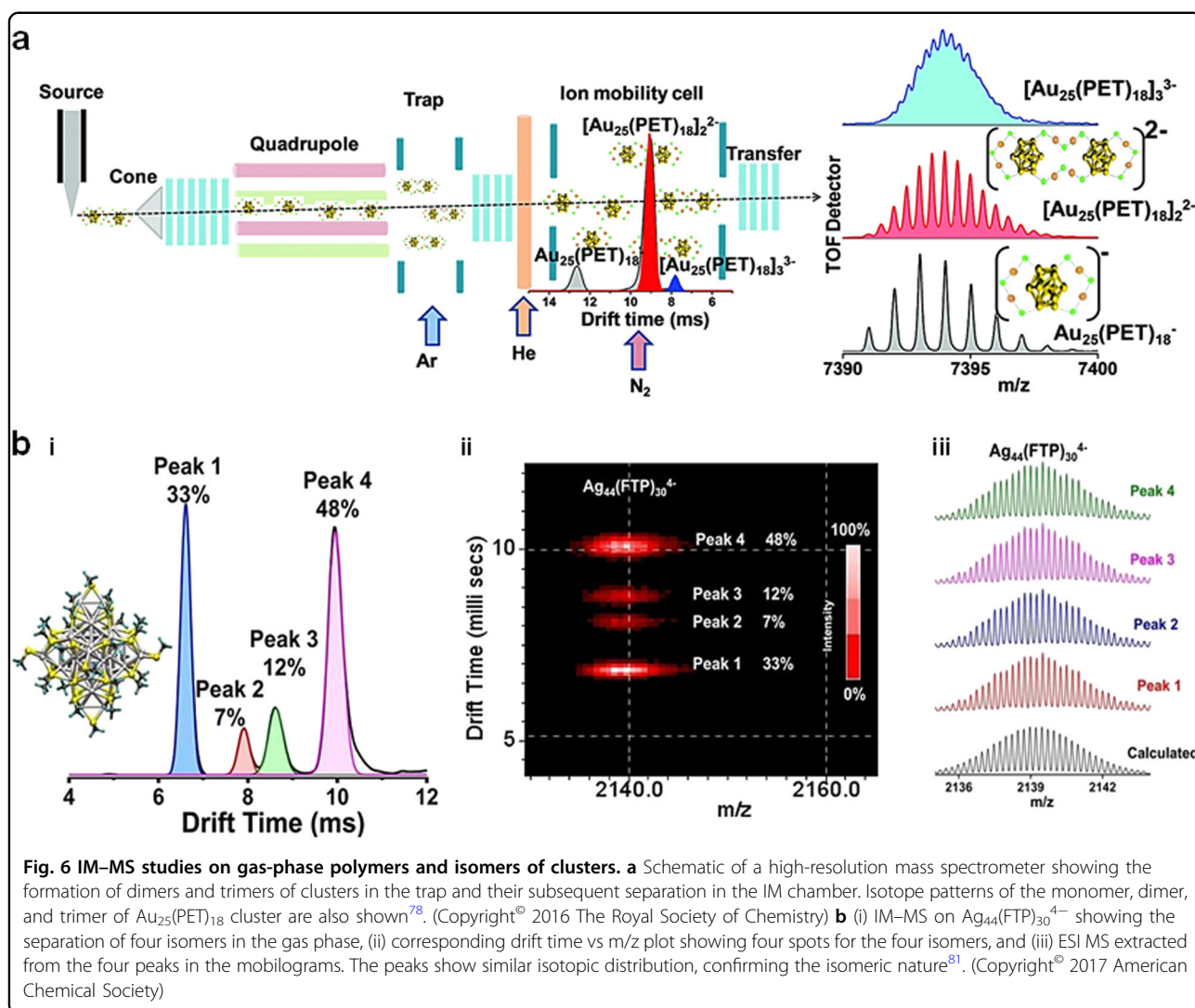
MS coupled with IM has proved to be an important tool for structural characterization, and has enhanced research in many areas of biochemical and biophysical studies<sup>74</sup>. In the IM cell, the ions are passed through buffer gases like He, N<sub>2</sub>, etc. As a result, species having the same mass but different size and shape exhibit different collision cross-section (CCS), hence show different drift times and get separated. IM–MS is capable of studying the conformational dynamics present in a system, and has largely been used to understand the folding and unfolding mechanism in proteins<sup>75</sup>. In materials science, IM–MS has been used to study the mechanism of formation of fullerenes from polycyclic aromatic hydrocarbons (PAH). Laser desorption of PAHs like C<sub>60</sub>H<sub>21</sub>F<sub>9</sub><sup>–</sup> causes stepwise loss of HF and H<sub>2</sub> (Fig. 5ai), which results in increasing curvature of the remaining PAH fragments and finally closed-cage fullerenes are formed<sup>76</sup>. To understand the mechanism, the extent of curvature in the structure of the products at each step was modeled by comparing the CCS of the computed structures with the experimental CCS observed in IM–MS (Fig. 5aii). IM–MS has also been largely used for understanding the structures of polyoxometallates. Surman et al. showed that Keggin or Dawson type POM clusters (structures are shown in Fig. 5bi) can be used as IM calibrants for high mass negatively charged ions, and using the calibration curves (Fig. 5bii), structures of other POM clusters can be determined<sup>77</sup>.

Recently, IM–MS has also gained importance in the field of protected noble metal NCs. Baksi et al. separated dimers and trimers of [Au<sub>25</sub>(SR)<sub>18</sub>]<sup>–</sup> using IM–MS<sup>78</sup>. A



schematic of the instrumental setup showing the formation of aggregates of the cluster under increased pressure conditions in the trap, and its subsequent separation in the IM chamber is presented in Fig. 6a. Chakraborty et al. have also shown that alkali metal ions can induce dimerization of  $[\text{Ag}_{29}(\text{BDT})_{12}]^{3-}$  NCs in a similar manner<sup>79</sup>. Baksi et al. identified isomerism in  $[\text{Ag}_{11}(\text{SG})_7]^-$

cluster in the gas phase<sup>80</sup>. However, as the crystal structure of  $[\text{Ag}_{11}(\text{SG})_7]^-$  is not known, the correlation with the condensed-phase structures could not be established. In another report, the authors showed that  $[\text{Ag}_{44}(\text{SR})_{30}]^{4-}$  and  $[\text{Ag}_{29}(\text{BDT})_{12}]^{3-}$  clusters also show isomerism in the gas phase<sup>81</sup>, which do not show any isomers in their crystal structure. Four distinct isomeric peaks were



observed in IM-MS of  $[\text{Ag}_{44}(\text{FTP})_{30}]^{4-}$  (Fig. 6b). However, two isomers were separated for  $[\text{Ag}_{44}(\text{FTP})_{30}]^{3-}$ , which indicated that isomerism is charge-state dependent. The influence of the ligand shell in isomerism was studied by using  $[\text{Ag}_{44}(\text{SR})_{30}]$  clusters protected by different ligands, which showed different number of isomers. Also,  $\text{Au}_{25}(\text{SR})_{18}$  and  $\text{Ag}_{25}(\text{SR})_{18}$  clusters showed a single peak in IM, suggesting that isomerism is highly selective to the structure and the symmetry of the cluster.

Kappes et al. performed IM studies on Au cluster cations  $\text{Au}_n^+$ . Comparison of experimental CCS with that of theoretical CCS from DFT-optimized structures revealed that  $\text{Au}_n^+$  have planar structures for  $n = 3-7$ , while for  $n = 8-10$ , they show three-dimensional structures<sup>82</sup>. In a recent study, Daly et al. characterized homometallic cluster ions,  $[\text{Ag}_{14}(\text{C}\equiv\text{C}^t\text{Bu})_{12}\text{Cl}]^+$ ,  $[\text{Ag}_{14}(\text{C}\equiv\text{C}^t\text{Bu})_{12}\text{Br}]^+$  and heterometallic clusters ions,  $[\text{Ag}_8\text{Cu}_6(\text{C}\equiv\text{C}^t\text{Bu})_{12}\text{Cl}]^+$ ,  $[\text{Ag}_8\text{Cu}_6(\text{C}\equiv\text{C}^t\text{Bu})_{12}\text{Br}]^+$  by

IM-MS<sup>83</sup>. These cluster ions showed a single peak in IM, and comparison of the CCS values derived from IM with the CCS values modeled from its X-ray crystal structure suggested that the gas-phase structures of the clusters resembled their condensed-phase structures (Fig. 7a, b). The shorter arrival time of the heterometallic cluster ions in comparison with that of the homometallic cluster ions was consistent with the observation from their crystal structures and DFT calculations (Fig. 7c). Thus, IM proved to be an effective tool not only for the separation of gas-phase entities but also for structural characterization of the clusters. In another study by Soleilhac et al., the size of GSH-protected clusters were compared in the solid, liquid, and gas phase by using X-ray powder diffraction (XRPD), time-resolved fluorescence anisotropy (TRFA), and IM-MS, respectively<sup>84</sup>. From the CCS values obtained from IM, the radii of the clusters were calculated as 1.22, 1.31, and 1.47 nm for  $\text{Au}_{15}(\text{SG})_{13}$ ,  $\text{Au}_{18}(\text{SG})_{14}$ , and

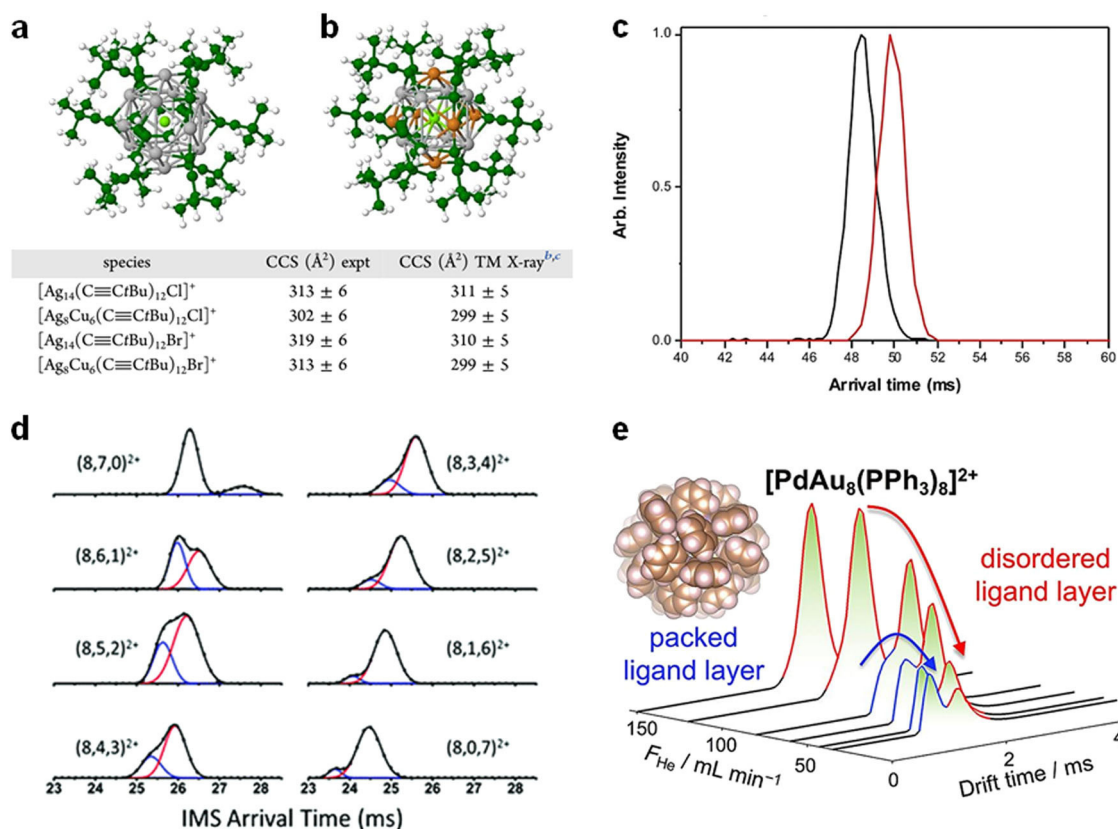


**Fig. 7** IM-MS studies of gas-phase cluster ions. DFT-optimized structures of **a**  $[\text{Ag}_{14}(\text{C}\equiv\text{CtBu})_{12}\text{Cl}]^+$  and **b**  $[\text{Ag}_8\text{Cu}_6(\text{C}\equiv\text{CtBu})_{12}\text{Cl}]^+$ . **c** IM arrival times of  $[\text{Ag}_{14}(\text{C}\equiv\text{CtBu})_{12}\text{Cl}]^+$  (red) and  $[\text{Ag}_8\text{Cu}_6(\text{C}\equiv\text{CtBu})_{12}\text{Cl}]^+$  (black)<sup>83</sup>. (Copyright© 2017 American Chemistry Society) **d** IM ATDs of  $[\text{Au}_8(\text{PPh}_3)_x(\text{MePPh}_2)_y]^{2+}$   $\{(8,x,y)^{2+}$ , where  $x$  = number of  $\text{PPh}_3$ , and  $y$  = number of  $\text{MePPh}_2$  ligands and  $x + y = 7\}$ <sup>85</sup>. (Copyright© 2017 The Royal Society of Chemistry) **e** ATDs of  $[\text{PdAu}_8(\text{PPh}_3)_8]^{2+}$  showing the interconversion of isomers as a function of He gas flow<sup>86</sup>. (Copyright© 2018 American Chemical Society)

$\text{Au}_{25}(\text{SG})_{18}$ , respectively. Though the absolute values differed, the trends in the size of the above NCs were similar in all the three phases. In comparison with techniques like XRPD and TRFA, IM-MS is expected to become a more convenient technique for determining the size of the clusters due to the ease of sample preparation and lower limit of error ( $\sim 2\%$ ) compared with other techniques.

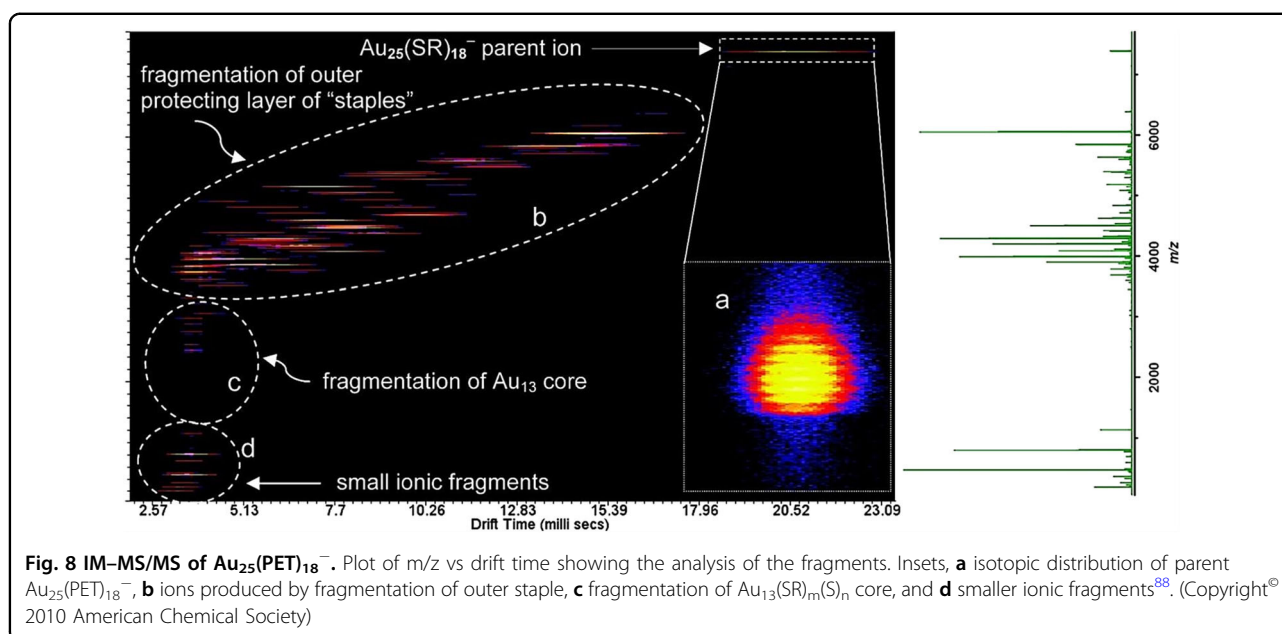
Ligare et al. used ESI IM-MS to study the structural changes upon systematic ligand exchange of  $[\text{Au}_8(\text{PPh}_3)_7]^{2+}$  and  $[\text{Au}_{11}(\text{PPh}_3)_9\text{H}]^{2+}$  with methyldiphenylphosphine ( $\text{MePPh}_2$ )<sup>85</sup>. Studies revealed that  $[\text{Au}_8(\text{PPh}_3)_7]^{2+}$  cluster showed two isomers, and on increasing ligand exchange with  $\text{MePPh}_2$ , these isomers underwent a change in relative population from a more compact structure showing lower arrival time to a more extended structure showing larger arrival time, as shown in Fig. 7d. In contrast,  $[\text{Au}_{11}(\text{PPh}_3)_9\text{H}]^{2+}$  cluster showed only one isomer. Recently, Hirata et al. showed that phosphine-protected gold clusters like  $[\text{Au}_9(\text{PPh}_3)_8]^{3+}$  and  $[\text{PdAu}_8(\text{PPh}_3)_8]^{2+}$  undergo conversion to more

compact isomers upon collisional excitation (Fig. 7e)<sup>86</sup>. Such studies help to understand the fluxionality in the structures of the NCs.

### Gas-phase dissociation studies of noble metal nanoclusters

While IM-MS reveals enormous information regarding the shape, size, and conformations of the cluster ions, more information regarding their structure and bonding can be obtained from dissociation studies. In collision-induced dissociation (CID), mass-selected ions are subjected to dissociation by collision with gases like Ar,  $\text{N}_2$ , He, etc. Fields-Zinna et al. reported CID studies on ligand-protected  $\text{Au}_{25}$  NCs and showed that the dissociation involved the  $\text{Au}_2\text{L}_3$  semirings, which are the staples motifs present in its crystal structure<sup>87</sup>. The authors used  $\text{Au}_{25}(\text{SC}_2\text{H}_4\text{Ph})_{18}$  cluster, and ligand-exchanged it with  $-\text{S}(\text{CH}_2\text{CH}_2\text{O})_5\text{CH}_3$  ( $-\text{SPEG}$ ) to facilitate ionization and studied CID on these mixed ligand-protected  $\text{Na}_x\text{Au}_{25}(\text{SC}_2\text{H}_4\text{Ph})_{18-y}(\text{S}(\text{C}_2\text{H}_4\text{O})_5\text{CH}_3)_y$  clusters using ESI TOF and ESI FTICR MS. CID produced





fragments such as  $[\text{Na}_2\text{Au}_2\text{L}_3]^{1+}$  representing the loss of a single semiring and fragments such as  $[\text{NaAu}_3\text{L}_3]^{1+}$  and  $[\text{NaAu}_4\text{L}_4]^{1+}$  representing the loss of multiple semirings<sup>87</sup>. Later, Angel et al. studied the fragmentation of  $\text{Au}_{25}\text{L}_{18}^-$  NCs using HR ESI MS<sup>88</sup>. The predominant fragmentation pathway involved the loss of  $\text{Au}_4\text{L}_4$  leading to the formation of fragment ions, such as  $\text{Au}_{21}\text{L}_{14}^-$  and  $\text{Au}_{17}\text{L}_{10}^-$ . They also introduced the use of IM-MS/MS, a technique where IM is coupled to CID, which could differentiate between fragmentation from the outer staples, fragmentation from the icosahedral core and the smaller ionic fragments, by separating them into distinct bands (Fig. 8). Black et al. carried out CID on larger Au NCs like  $\text{Au}_{144}(\text{SR})_{60}$  and  $\text{Au}_{130}(\text{SR})_{50}$ , and also showed that the extent of fragmentation is specific to the charge state of the cluster ions<sup>89</sup>. CID of mixed-ligand-protected cluster,  $[\text{Au}_{11}(\text{PPh}_3)_8\text{X}_2]^+$  ( $\text{X} = \text{Cl}, \text{C}\equiv\text{CPh}$ ), showed competing fragmentation channels involving sequential loss of  $\text{PPh}_3$  and  $\text{Au}_x(\text{PPh}_3)$ <sup>90</sup>.

The extent of fragmentation also depends on the internal energy distribution of the ions, and hence CID studies were used to understand the stabilities of the cluster ions. Taking  $\text{Ag}_{29}(\text{SR})_{12}$ ,  $\text{Ag}_{25}(\text{SR})_{18}$ , and  $\text{Ag}_{44}(\text{SR})_{30}$  NCs as examples, Chakraborty et al. demonstrated that the predominant fragmentation pathways of these NCs involved the loss of  $\text{Ag}_5(\text{SR})_6^-$ ,  $\text{Ag}(\text{SR})^-$ , or  $\text{Ag}_2(\text{SR})_3^-$  fragments<sup>91</sup>. By using survival yield analysis and comparing the values of  $E_{\text{com}50}$  ( $E_{\text{com}50}$  is center-of-mass energy corresponding to 50% dissociation of the cluster), the stabilities of these clusters were compared (Fig. 9a), and the order of gas-phase stability  $[\text{Ag}_{29}(\text{SR})_{12}]^{3-} > [\text{Ag}_{25}(\text{SR})_{18}]^- > [\text{Ag}_{44}(\text{SR})_{30}]^{3-}$  was similar to that observed in the solution phase.

Another technique that can be effectively used to study the energetics and kinetics of the fragmentation process is surface-induced dissociation (SID). In this process, mass-selected ions are collided with a surface (usually Au surfaces protected by monolayers of alkanethiols) and impact induced activation leads to dissociation. In comparison with CID, SID is a more convenient technique to extract thermodynamic parameters of the cluster ions, as here the applied CE can be varied through a large range to observe a small change in the threshold internal energies of large ions. Using SID, Johnson et al. quantified the stability and ligand-binding energies of small TPP-protected Au clusters,  $\text{Au}_7\text{L}_6^{2+}$ ,  $\text{Au}_8\text{L}_6^{2+}$ ,  $\text{Au}_8\text{L}_7^{2+}$ , and  $\text{Au}_9\text{L}_7^{2+}$ <sup>92</sup>. Collision energy-resolved fragmentation curves revealed that  $\text{Au}_8\text{L}_6^{2+}$  cluster was more stable toward dissociation (Fig. 9bi). SID enabled the quantitative estimation of the threshold energies and activation entropies of fragmentation. It also enabled to understand the kinetics of fragmentation by determining the microcanonical rate constants for the different fragmentation pathways (Fig. 9bii) and hence determining the kinetically and thermodynamically favored pathways. Moreover, taking  $\text{Ag}_{11}(\text{SG})_7^{7-}$  clusters as an example, Baksi et al. showed that CID and SID of the clusters occurred through different pathways. SID produced more fragments compared with CID, and charge stripping from 3- to 2- and 1- charge states of the cluster ions occurred<sup>80</sup>.

While both CID and SID produces a lesser number of fragments, extensive fragmentation can be observed by ultraviolet photodissociation (UVPD) as observed in the case of  $\text{Au}_{25}(\text{pMBA})_{18}$  and  $\text{Au}_{36}(\text{pMBA})_{24}$  NCs<sup>93</sup>. UVPD on these clusters using  $\lambda = 193$  nm involved high-energy fragmentation pathways and cleavage of Au-S and C-S

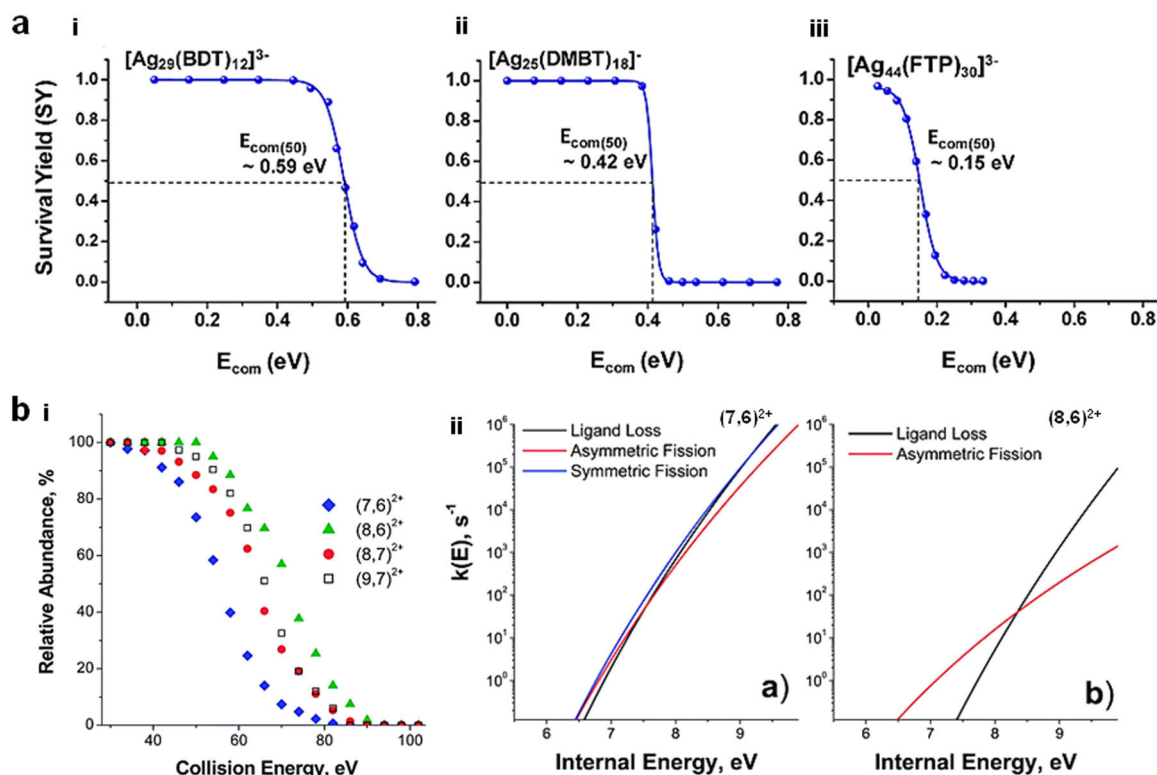


**Fig. 9** Collision energy-resolved fragmentation curves for comparison of stability of cluster ions. **a** Survival yield curves for CID of  $[Ag_{29}(BDT)_{12}]^{3-}$ ,  $[Ag_{25}(DMBT)_{18}]^{-}$ , and  $[Ag_{44}(FTP)_{30}]^{3-}$  cluster ions<sup>91</sup>. (Copyright© 2017 American Chemistry Society) **b** (i) Survival yield curves for SID on  $(xy)^{2+}$  ( $x$  = no. of Au,  $y$  = no. of PPH<sub>3</sub> ligands) cluster ions. (ii) Plot of the rate constant vs internal energy showing the competition between different fragmentation channels for  $(7,6)^{2+}$  and  $(8,6)^{2+}$  cluster ions<sup>92</sup>. (Copyright© 2014 The Royal Society of Chemistry)

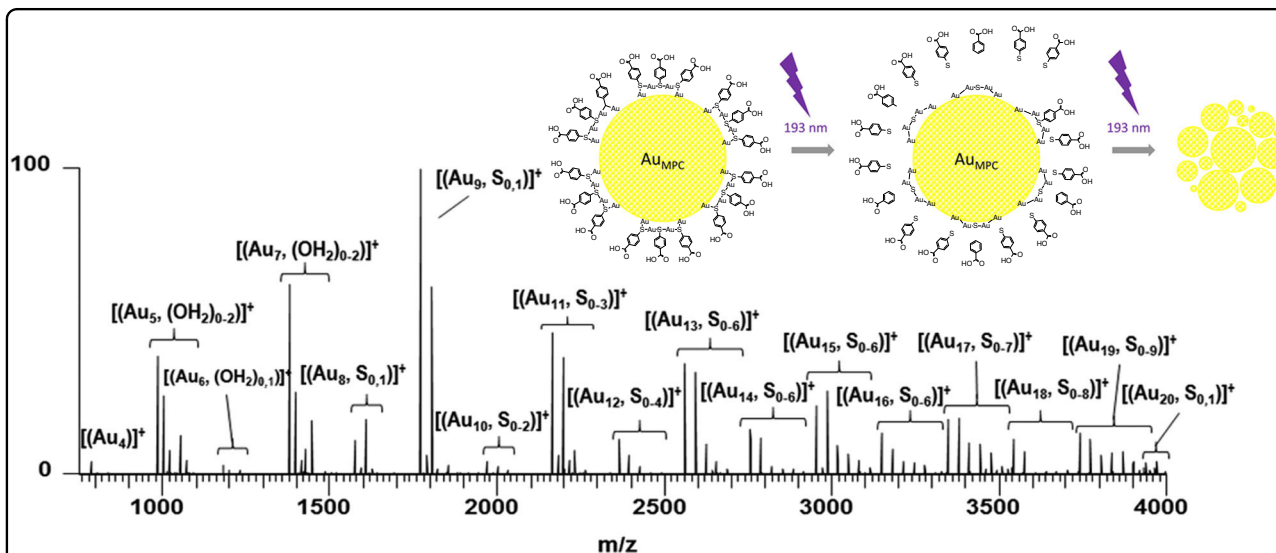
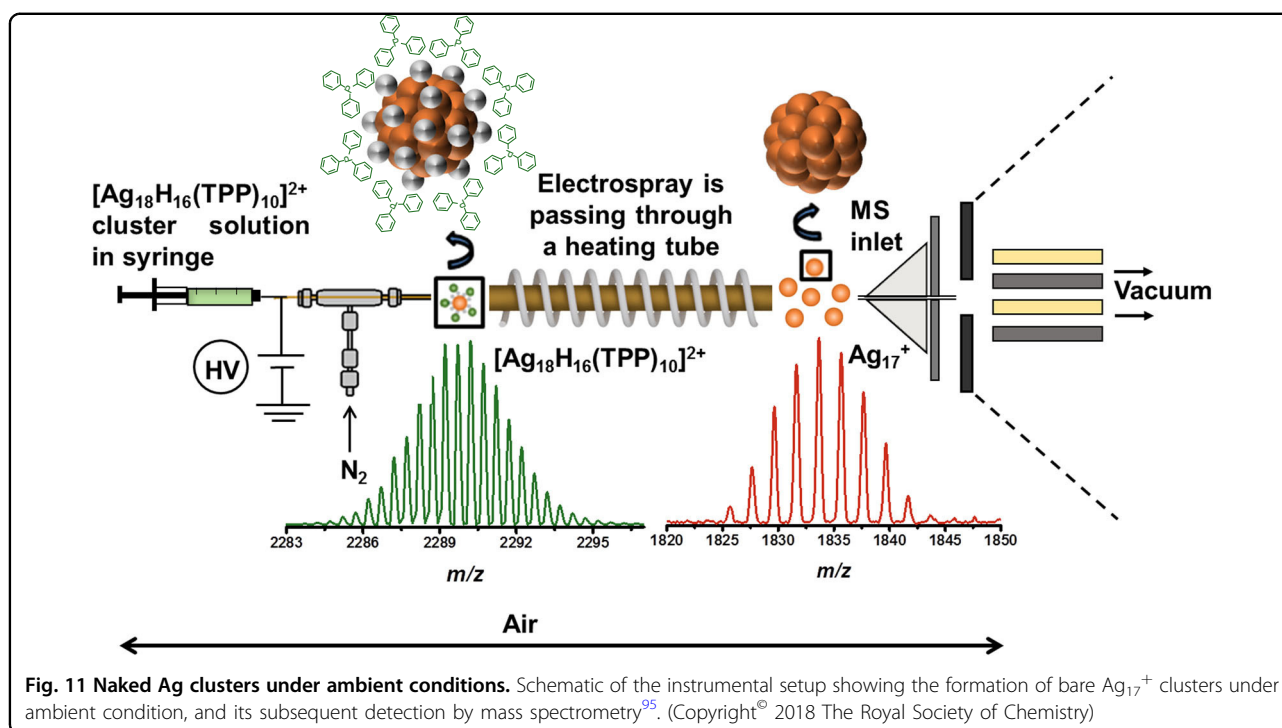


**Fig. 10** Ultraviolet photodissociation (UVPD) on gas-phase cluster ions. UVPD-MS of  $[Au_{25}(pMBA)_{18} + 4NH_4]^{3+}$  using  $\lambda = 193$  nm<sup>93</sup>. (Copyright© 2017 American Chemical Society)

bonds. When the cluster ions were exposed to multiple laser pulses, a series of bare Au cluster ions were formed by sequential evaporation of neutral Au atoms (Fig. 10).

Recently, Ghosh et al. showed that the bare cluster ion,  $Ag_{17}^+$ , can be produced selectively by CID of  $[Ag_{18}(TPP)_{10}H_{16}]^{2+}$  clusters and by further increasing the



collision energy, a series of  $\text{Ag}_n^+$  ( $n = 1-17$ ) clusters may be produced<sup>63,94</sup>. In a similar manner,  $[\text{Ag}_{25}(\text{DPPE})_8\text{H}_{22}]^{3+}$  and  $[\text{Ag}_{22}(\text{DPPE})_8\text{H}_{19}]^{3+}$  were also used as precursors for bare Ag clusters<sup>94</sup>. In a recent study by Jash et al., electro sprayed  $[\text{Ag}_{18}(\text{TPP})_{10}\text{H}_{16}]^{2+}$  clusters were passed through a heated tube, whereby all the ligand layers were desorbed leading to the formation of  $\text{Ag}_{17}^+$  under ambient conditions, and the product ions were subsequently detected by MS (Fig. 11)<sup>95</sup>.

### Spectroscopy on the mass-selected gas-phase cluster ions

The electronic properties of the NCs are probed experimentally by optical and electrochemical studies in solution. However, these experimental results are influenced by the solvents and the counter ions present in solution. So, there is a need to directly probe the energy levels of the isolated cluster ions in vacuum. Anion PES is usually used to determine HOMO–LUMO gaps and EAs. Such studies have been done for bare  $\text{Au}_n^-$  clusters<sup>96</sup>. Recently, Hirata et al. performed PES on isolated  $[\text{Au}_{25}(\text{SC}_{12}\text{H}_{25})_{18}]^-$  ions by coupling a magnetic bottle-type photoelectron spectrometer with a TOF mass spectrometer<sup>97</sup>. Schematic of the instrumental setup used for the study is presented in Fig. 12a. The photoelectron spectrum of  $[\text{Au}_{25}(\text{SC}_{12}\text{H}_{25})_{18}]^-$  showed two bands, A and B (Fig. 12b), corresponding to electron detachment from 1P superatomic and Au 5d orbitals localized on the core Au atoms. The vertical detachment

energy (VDE) and adiabatic electron affinity (AEA) of  $[\text{Au}_{25}(\text{SC}_{12}\text{H}_{25})_{18}]^-$  was determined to be 2.5 eV and 2.2 eV, which corresponds to the values of  $E_{\text{top}}$  and  $E_{\text{th}}$  in the photoelectron spectrum (Fig. 12b), respectively. Hamouda et al. studied photoexcitation of  $[\text{Au}_{25}(\text{SG})_{18-6}\text{H}]^{7-}$ , where the yield of electron detachment as a function of the laser wavelength gave the gas-phase optical action spectra, which was found to be similar to the solution-phase spectrum<sup>98</sup>. Daly et al. studied the photofragmentation and VUV photoionization of  $[\text{Ag}_{10}\text{D}_8\text{L}_6]^{2+}$  NCs in the gas phase by coupling a linear ion trap mass spectrometer with a beamline of synchrotron, capable of producing high flux of photons that could be tuned in the entire VUV range<sup>99</sup>. Upon photoexcitation of  $[\text{Ag}_{10}\text{D}_8\text{L}_6]^{2+}$ , a number of photofragments were produced, such as  $[\text{Ag}_{10}\text{D}_8\text{L}_6]^{3+}$ ,  $[\text{Ag}_{10}\text{D}_8\text{L}_5]^{2+}$ ,  $[\text{Ag}_{10}\text{D}_8\text{L}_4]^{2+}$ ,  $[\text{Ag}_9\text{D}_8\text{L}_4]^{2+}$ , and  $[\text{AgL}_2]^+$ . The ionization onset of  $[\text{Ag}_{10}\text{D}_8\text{L}_6]^{2+}$  was determined from the onsets in the yield of  $[\text{Ag}_{10}\text{D}_8\text{L}_6]^{3+}$  as a function of photon energy. Two ionization onsets were determined as ~9.3 eV and ~10.6 eV, which might be due to removal of electrons from orbitals of different energy levels. In another study, authors from the same group performed VUV and UV spectroscopy on  $[\text{Ag}_{14-n}\text{Cu}_n(\text{C}\equiv\text{CtBu})_{12}\text{X}]^+$  ( $\text{X} = \text{Cl}$  and  $\text{Br}$ ) cluster ions<sup>83</sup>. The ionization onsets of the cluster ions were determined to be ~8.8 eV, and this was similar for all the ions, irrespective of the nature of halides or the extent of Cu doping (Fig. 12c). Photofragmentation of the same



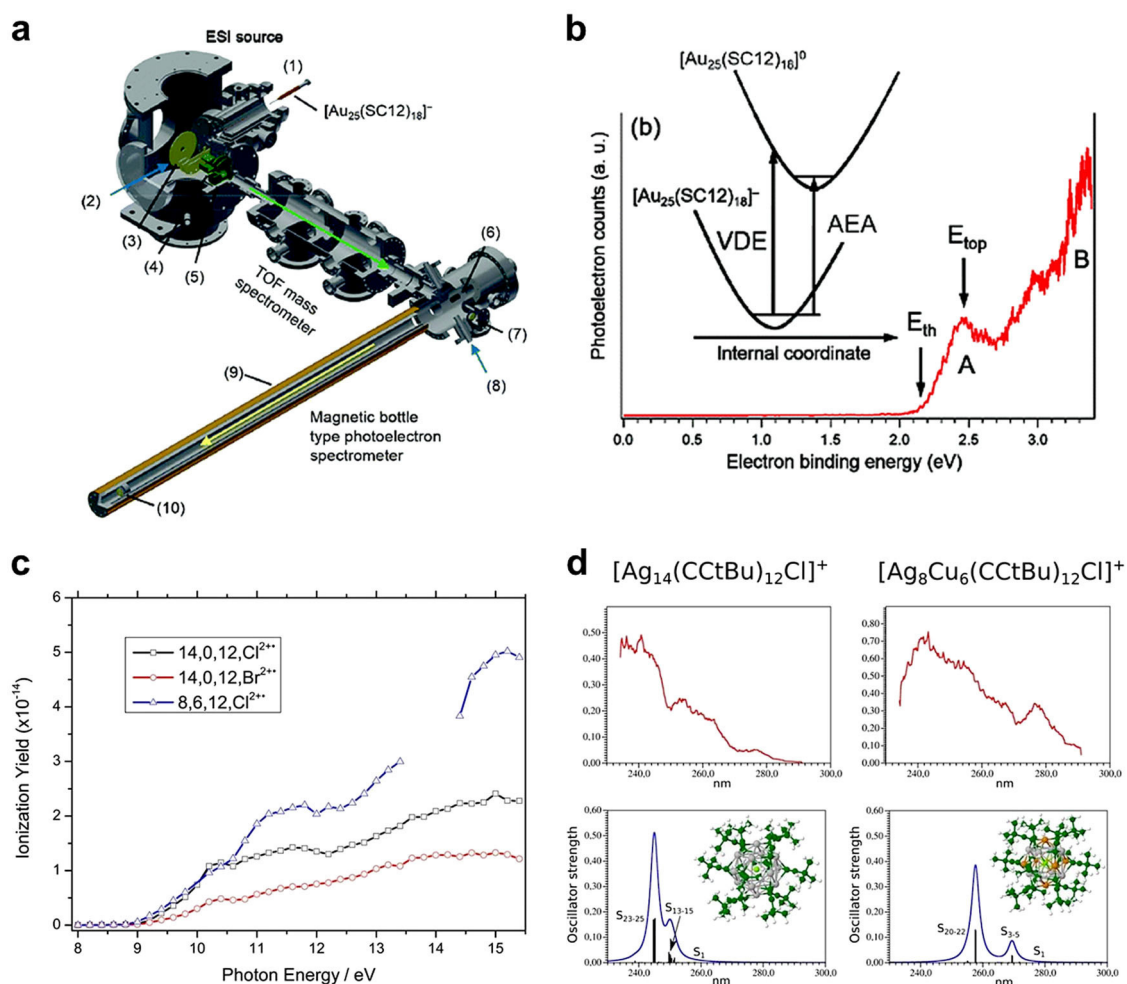


**Fig. 12 Spectroscopy on gas-phase cluster ions.** **a** Schematic of the instrumental setup showing the coupling of a magnetic bottle-type photoelectron spectrometer with a TOF mass spectrometer. (1) Syringe, (2) photodissociation laser, (3) acceleration grids, (4) deflectors, (5) einzel lens, (6) permanent magnet, (7) microsphere plate, (8) photodetachment laser, (9) coil, and (10) microchannel plate. **b** Photoelectron spectrum of  $[\text{Au}_{25}(\text{SC}_{12})_{18}]^{-}$  at 355 nm. Inset shows a schematic of the potential energy curves of the cluster ions<sup>97</sup>. (Copyright© 2017 The Royal Society of Chemistry) **c** Plot of ionization yield vs VUV energy of  $[\text{Ag}_{14}(\text{C}\equiv\text{CtBu})_{12}\text{Cl}]^{+}$ ,  $[\text{Ag}_8\text{Cu}_6(\text{C}\equiv\text{CtBu})_{12}\text{Cl}]^{+}$ , and  $[\text{Ag}_{14}(\text{C}\equiv\text{CtBu})_{12}\text{Br}]^{+}$  cluster ions showing their onsets of ionization. The yield of the product ions as a function of the photon energy is shown for  $[\text{Ag}_{14}(\text{C}\equiv\text{CtBu})_{12}\text{Cl}]^{2+}$ ,  $[\text{Ag}_8\text{Cu}_6(\text{C}\equiv\text{CtBu})_{12}\text{Cl}]^{2+}$ , and  $[\text{Ag}_{14}(\text{C}\equiv\text{CtBu})_{12}\text{Br}]^{2+}$ . **d** Gas-phase UV spectra of  $[\text{Ag}_{14}(\text{C}\equiv\text{CtBu})_{12}\text{Cl}]^{+}$  and  $[\text{Ag}_8\text{Cu}_6(\text{C}\equiv\text{CtBu})_{12}\text{Cl}]^{+}$  cluster ions. The TDDFT spectra are also presented, which shows similar trends in the shifts for  $\text{Ag}_{14}$  and  $\text{Ag}_8\text{Cu}_6$  cluster ions<sup>83</sup>. (Copyright© 2017 American Chemical Society)

clusters were studied in the wavelength range of 235–291 nm by coupling a laser with the ion trap. The plot of photofragmentation yield as a function of the wavelength of the radiation gave the UV spectra of the cluster ions in the gas phase (Fig. 12d). The experimental optical absorption spectra were also in accordance with TDDFT calculations (Fig. 12d).

### Resolving the solution-phase growth and nucleation of clusters

Apart from such studies on gas-phase cluster ions, MS also proved to be powerful in unveiling complex

solution-phase phenomena. Understanding the mechanism of nucleation and growth of clusters in solution has always remained challenging. In 2012, Yu et al. reported the size controlled growth of  $\text{Au}_{25}$  NCs where they slowed down the reduction rate by using CO as a mild reducing agent<sup>100</sup>. By using MALDI MS, the authors demonstrated that a mixture of  $\text{Au}_{10-15}$  NCs was produced within 5 min of reaction, followed by the formation of  $\text{Au}_{16-25}$  NCs over a period of 40 min, which finally size focussed to  $\text{Au}_{25}$  NCs after 24 h. However, due to fragmentation, only the core masses could be identified, and no information was obtained about the ligand shell of the intermediate

products. More recently, in 2014, in another report from the same group, ESI MS was used to trace all the stable intermediates involved in the formation of Au<sub>25</sub> clusters starting from Au thiolates. This study showed that the formation of Au NCs occurred by a 2e hopping process, which involved a fast reduction step followed by slow interconversion and size focussing steps<sup>101</sup>. All the intermediates involved in the process were detected by ESI MS, and the changes in the solution composition with gradual growth of the NCs were also in accordance with the changes in the optical absorption features (Fig. 13). Similar studies have been reported by the same group where ESI MS was used to understand the steps involved in the process of conversion of Au<sub>25</sub> to Au<sub>44</sub> NCs<sup>102</sup>. Isoelectronic conversion from [Au<sub>23</sub>(SR)<sub>16</sub>]<sup>−</sup> to [Au<sub>25</sub>(SR)<sub>18</sub>]<sup>−</sup> NCs was also studied by ESI MS. Careful mass spectrometric analysis of the system revealed the size-conversion reaction as [Au<sub>23</sub>(SR)<sub>16</sub>]<sup>−</sup> + 2 [Au<sub>2</sub>(SR)<sub>3</sub>]<sup>−</sup> → [Au<sub>25</sub>(SR)<sub>18</sub>]<sup>−</sup> + 2 [Au(SR)<sub>2</sub>]<sup>−</sup><sup>103</sup>. Based on HRMS measurements, Chen et al. have recently formulated a balanced equation for the stoichiometric synthesis of Au<sub>25</sub>(SR)<sub>18</sub> NCs as, 32/x [Au(SR)]<sub>x</sub> + 8e<sup>−</sup> = [Au<sub>25</sub>(SR)<sub>18</sub>]<sup>−</sup> + 7 [Au(SR)<sub>2</sub>]<sup>−</sup><sup>104</sup>. Similar studies have also been done to understand the growth of silver clusters like [Ag<sub>17</sub>(SPh-<sup>t</sup>Bu)<sub>12</sub>]<sup>3−</sup> and [Ag<sub>44</sub>(SPh-<sup>t</sup>Bu)<sub>30</sub>]<sup>4−</sup><sup>105</sup>, and step-by-step mechanism of ligand exchange induced cluster conversion reactions, e.g., the conversion from Ag<sub>44</sub> to Ag<sub>25</sub> clusters and vice versa<sup>106</sup>.

### Reactions between nanoparticles

Inter-cluster reactions are an emerging area in the field of NCs<sup>107</sup>. Krishnadas et al. demonstrated the reaction between Au<sub>25</sub>(FTP)<sub>18</sub> and Ag<sub>44</sub>(FTP)<sub>30</sub> NCs, which produces a mixture of alloy clusters in solution<sup>108,109</sup>. Exchange of Au–Ag atoms between the clusters were observed by using MALDI and ESI MS (Fig. 14a, b). In case of reaction between clusters protected by different ligands like Au<sub>25</sub>(PET)<sub>18</sub> and Ag<sub>44</sub>(FTP)<sub>30</sub>, ligand exchanges were also observed in MS. In another report from the same group, the authors demonstrated reaction between Au<sub>25</sub>(SR)<sub>18</sub> and Ag<sub>25</sub>(SR)<sub>18</sub> clusters leading to the formation of alloy clusters Ag<sub>m</sub>Au<sub>n</sub>(SR)<sub>18</sub> (*n* = 1–24) (Fig. 14c)<sup>110</sup>. The authors also detected a dianionic intermediate, [Ag<sub>25</sub>Au<sub>25</sub>(SR)<sub>36</sub>]<sup>2−</sup> (Fig. 14d) at the early stages of the reaction, which provided better insights into the mechanism of such reactions. Salassa et al. used MALDI MS and NMR spectroscopy to show that monolayers of clusters are dynamic in nature, and inter-cluster ligand exchanges can occur during collision between the NCs<sup>111</sup>. Using isotopically pure silver clusters made of <sup>107</sup>Ag and <sup>109</sup>Ag, Chakraborty et al. studied rapid isotopic exchange in silver clusters by HR ESI MS and found that the solution-state exchange dynamics of the clusters is similar to that occurring in water (H<sub>2</sub>O + D<sub>2</sub>O = 2HDO)<sup>112</sup>.

### Supramolecular chemistry of monolayer-protected noble metal NCs

MS has also been used for exploring supramolecular chemistry of clusters. Chakraborty et al. studied supramolecular functionalization of [Ag<sub>29</sub>(BDT)<sub>12</sub>]<sup>3−</sup> clusters with fullerenes (C<sub>60</sub> and C<sub>70</sub>) by HR ESI MS (Fig. 15a)<sup>113</sup>. The authors also used CID studies to gain further insights into the nature of the interaction and IM–MS (Fig. 15b) to study the structure of the adducts. Mathew et al. studied supramolecular functionalization of [Au<sub>25</sub>(SBB)<sub>18</sub>]<sup>−</sup> clusters with cyclodextrins (CD), the adducts [Au<sub>25</sub>(SBB)<sub>18</sub> ∩ CD<sub>*n*</sub>]<sup>−</sup> (*n* = 1–4) were characterized by using MALDI and ESI MS (Fig. 15c)<sup>114</sup>. Recently, Nag et al. separated isomers of the inclusion complexes [Ag<sub>29</sub>(BDT)<sub>12</sub> ∩ CD<sub>*n*</sub>]<sup>3−</sup> (*n* = 1–6) (Fig. 15d) by using IM–MS<sup>115</sup>. Two isomers were observed for *n* = 2, 3, and 4 while no isomerism was observed in the case of *n* = 1, 5, and 6 complexes, suggesting similar behavior to that observed in octahedral transition metal co-ordination complexes.

### Liquid chromatography (LC) -MS

Characterization, analysis, and separation of mixtures of clusters by chromatography have been pursued for long<sup>116</sup>. Some of the recent developments include directly coupling chromatographic techniques to MS. Black et al. coupled reversed-phase chromatography with mass spectrometry and separated gold clusters of varying core sizes from their mixtures<sup>117</sup>. The same group also coupled capillary LC to ESI and separated Au<sub>104</sub>L<sub>45</sub>, Au<sub>130</sub>L<sub>50</sub>, Au<sub>137</sub>L<sub>56</sub>, and Au<sub>144</sub>L<sub>60</sub> clusters from their mixtures (Fig. 16a)<sup>118</sup>. In another report, isomers of Ag<sub>29</sub>(LA)<sub>12</sub> (LA = (R)-α lipoic acid) clusters were separated using LC–MS (Fig. 16b)<sup>119</sup>.

### Toward nanoparticles

Though the atomically precise NCs have been extensively characterized by MS, plasmonic NPs are not atomically precise, and determination of their exact composition still remains challenging. Recently, with the tremendous advancement in instrumentation and using a combination of ESI, LDI, and MALDI MS, it has been possible to assign approximate composition to some such plasmonic NPs, e.g., Au<sub>333</sub>(SR)<sub>39</sub><sup>53</sup>, Au<sub>~500</sub>(SR)<sub>~120</sub><sup>120</sup>, Au<sub>~940</sub>(SR)<sub>~160</sub><sup>121</sup>, etc. NPs. Recently in 2017, the crystal structure of a plasmonic NP, Au<sub>279</sub>(SPh-<sup>t</sup>Bu)<sub>84</sub> was reported<sup>122</sup>. MS measurements also revealed the composition in accordance with the crystal structure. Even larger NPs, Au<sub>~1400</sub><sup>123</sup> with a mass of ~300 kDa (Fig. 17a) and Au<sub>~2000</sub><sup>124</sup> with a mass of ~400 kDa (Fig. 17b) were recently characterized by MALDI MS.

### Mass spectrometry as a tool for materials synthesis

Electrospray as a method of ionization has also been used for organic synthesis<sup>125,126</sup>. While synthesis of new molecules

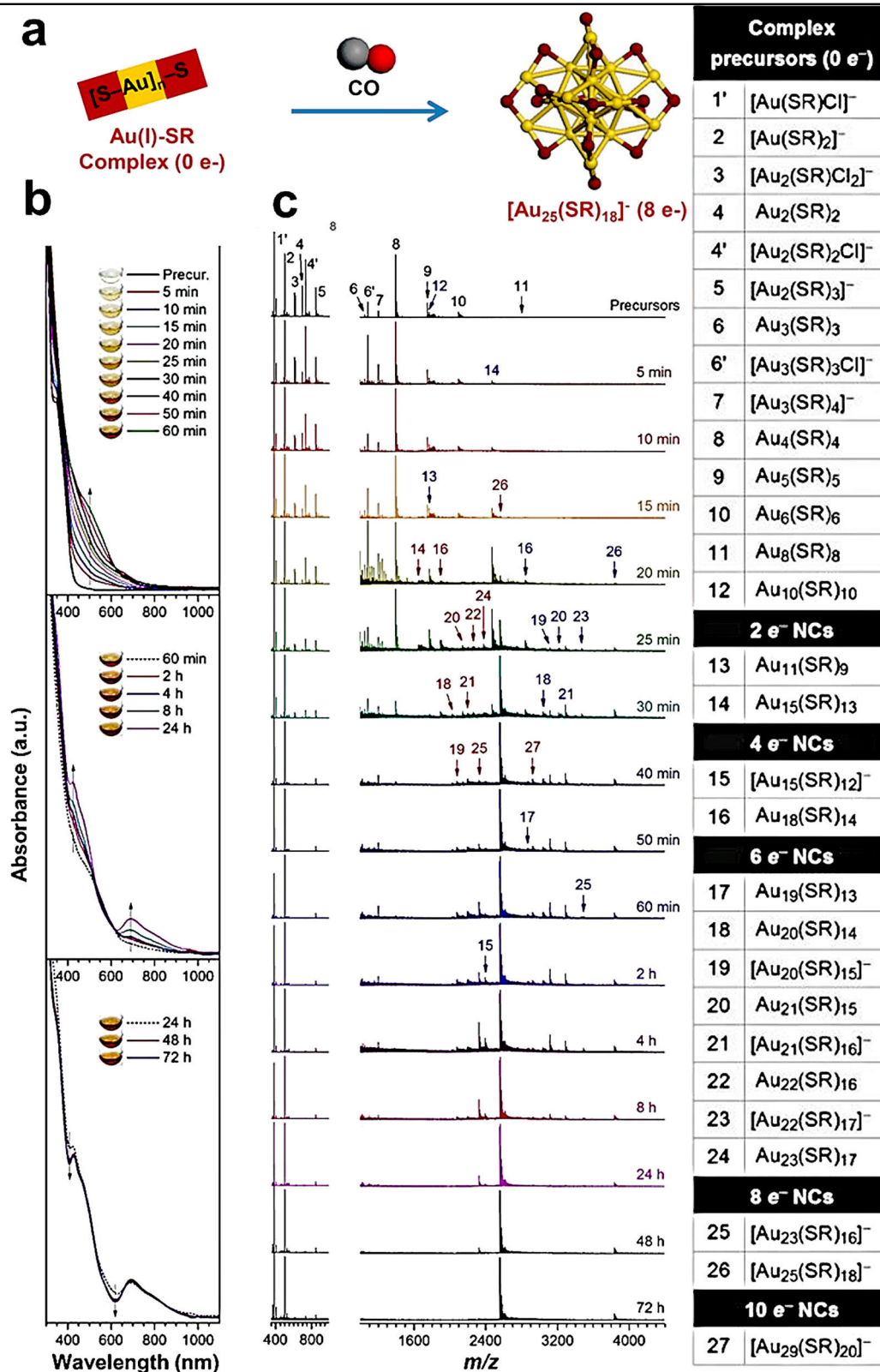


**Fig. 13** ESI MS showing stepwise growth of Au<sub>25</sub>(SR)<sub>18</sub> clusters. **a** Reaction scheme showing the formation of Au<sub>25</sub>(SR)<sub>18</sub> clusters from Au thiolates under the mild reducing environment of CO. **b** Time-dependent UV-vis spectra, and **c** ESI MS during the formation of Au<sub>25</sub>(SR)<sub>18</sub> clusters from Au thiolates. ESI MS shows detection of several intermediate species (numbered 1–27), which are listed in the table presented on the right<sup>101</sup>. (Copyright © 2014 American Chemical Society)

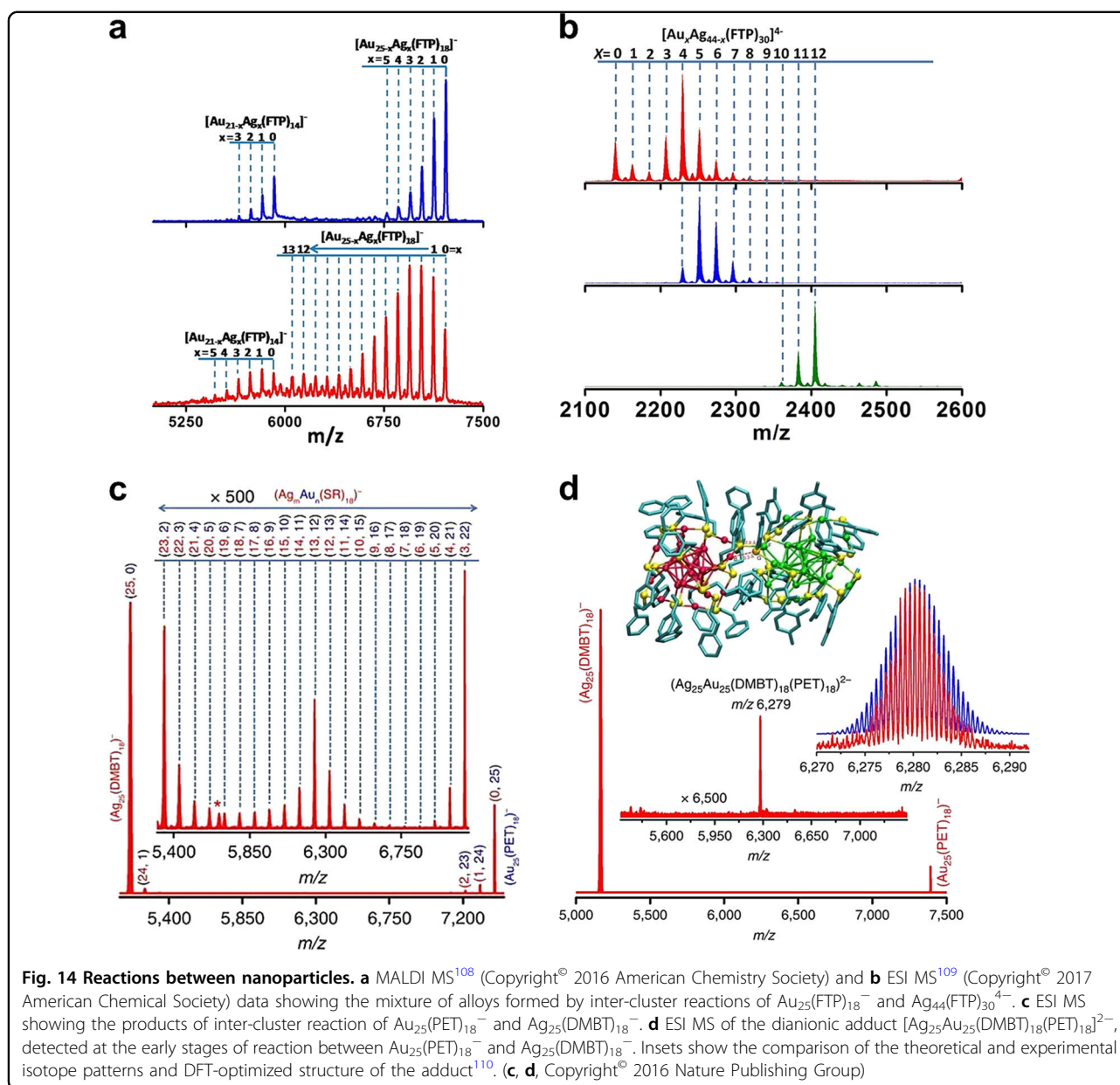


**Fig. 14** Reactions between nanoparticles. **a** MALDI MS<sup>108</sup> (Copyright© 2016 American Chemistry Society) and **b** ESI MS<sup>109</sup> (Copyright© 2017 American Chemical Society) data showing the mixture of alloys formed by inter-cluster reactions of  $\text{Au}_{25}(\text{FTP})_{18}^-$  and  $\text{Ag}_{44}(\text{FTP})_{30}^{4-}$ . **c** ESI MS showing the products of inter-cluster reaction of  $\text{Au}_{25}(\text{PET})_{18}^-$  and  $\text{Ag}_{25}(\text{DMBT})_{18}^-$ . **d** ESI MS of the dianionic adduct  $[\text{Ag}_{25}\text{Au}_{25}(\text{DMBT})_{18}(\text{PET})_{18}]^{2-}$ , detected at the early stages of reaction between  $\text{Au}_{25}(\text{PET})_{18}^-$  and  $\text{Ag}_{25}(\text{DMBT})_{18}^-$ . Insets show the comparison of the theoretical and experimental isotope patterns and DFT-optimized structure of the adduct<sup>110</sup>. (**c**, **d**, Copyright© 2016 Nature Publishing Group)

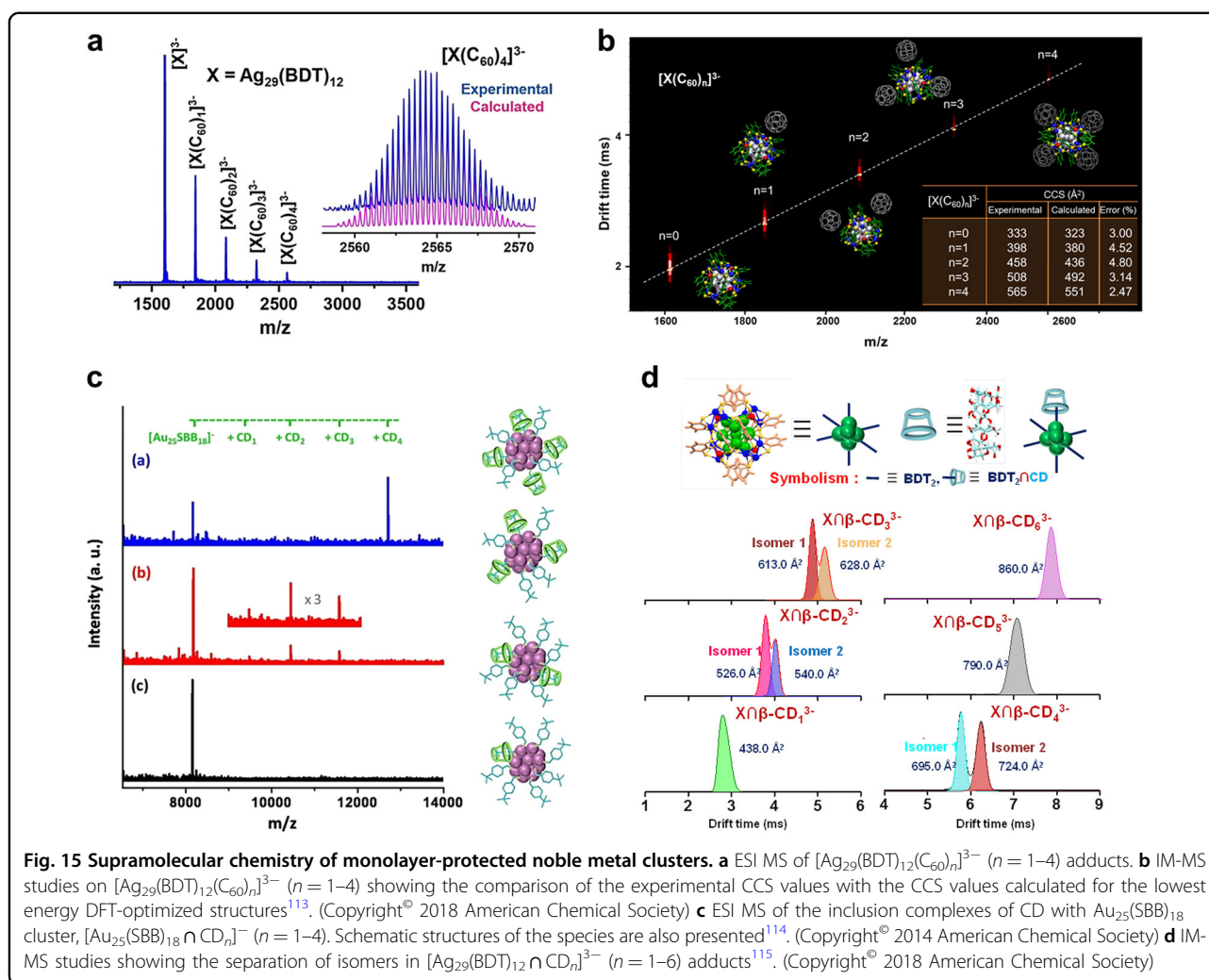
in sprays was observed before, bulk synthesis of molecules with which characterization is possible was not attempted earlier. Using a home-built nano-electrospray source, Sarkar et al.<sup>127</sup> showed that spraying an aqueous solution of silver acetate ( $\text{AgOAc}$ ) over a TEM grid, resulted in the formation of 1D nanowire structures of Ag NPs (Fig. 18). The precursors for the formation of the nanostructures were ions. Such studies unfold new routes of synthesis of materials using mass spectrometric interfaces<sup>127</sup>.

## Conclusions and future perspectives

In conclusion, we have presented how MS has enriched the field of materials science; in particular, the field of

monolayer-protected atomically precise NCs. From the discussion presented above, it becomes clear that MS has developed into a powerful tool for materials characterization, and it is expected to expand further in the future. MS as a technique is capable of building new interfaces which connects itself with independent disciplines. This has produced GC-MS, LC-MS, and their variations. New hyphenated methodologies and their power to understand structural details would expand further in the coming years. Combined with automation, synthesis of materials of atomic precision is expected to produce greater throughput in precision manufacture. Newer methods, utilizing the properties of molecular solids, and molecular building





blocks such as infrared (IR) absorption will be important to study molecular interactions on such materials. Interfaces such as ion chromatography or PES could be built with the mass spectrometer, which can produce new information related to structural changes and associated electronic structure. As the science of the noble metal clusters is enriched by MS, a thorough study on these systems also reveals their potential to be used as mass spectrometric standards<sup>128</sup>. Due to their high efficiency of ionization, distinct isotope patterns, stable intensities, and high  $m/z$  values, they can be used as calibrants for mass spectrometers. This might help in overcoming the limitations of the lack of proper calibrants in the high mass range, and especially in the negative ion mode<sup>128</sup>.

Gas-phase IR in combination with IM-MS has recently gained importance in revealing the structural details of proteins. It has also proved to be powerful in understanding the geometries of other molecules such as the aggregates of protoporphyrin IX where IR spectroscopy confirmed that the pairing of carboxylic groups occurred during the

formation of the stacked conformations<sup>129</sup>. Moreover, IM-MS in combination with IR has also been used in understanding the structures of isomers of small molecules like the N-protonated and O-protonated forms of benzocaine<sup>130</sup>, and structures of serine octamers<sup>129</sup>. In a similar manner, such studies may be extended in the case of clusters as well. Gas-phase IR can give more insights into the structure of the isomers or polymers of clusters. It can also be helpful for understanding interactions in the case of supramolecular adducts of clusters.

Spectroscopy and dynamics of trapped clusters ions, produced inside the mass spectrometer, can present new insights into their electronic structure. Trapped ion electron diffraction may be used for determining structures of noble metal NCs. Other possibilities include studies such as trapped ion laser-induced fluorescence. Spectroscopy of isolated cluster ions like electron detachment spectroscopy, PES, and single-particle fluorescence may be explored for a wide range of ligand-protected clusters. Such studies may even be done on

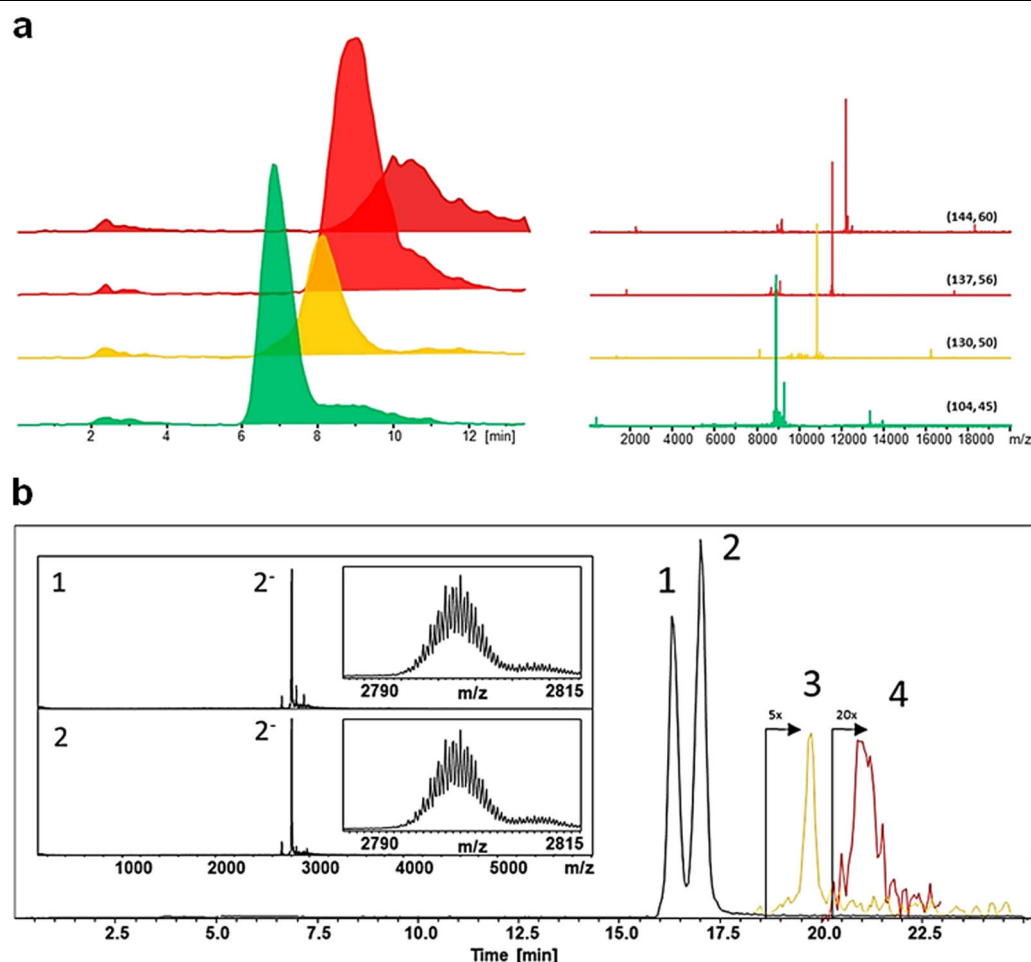


**Fig. 16 Liquid chromatography (LC) MS on clusters.** **a** Extracted ion chromatograms corresponding to  $\text{Au}_{104}\text{L}_{45}$ ,  $\text{Au}_{130}\text{L}_{50}$ ,  $\text{Au}_{137}\text{L}_{56}$ , and  $\text{Au}_{144}\text{L}_{60}$  clusters, respectively, obtained by LC–MS on their mixture<sup>118</sup>. (Copyright© 2016 American Chemistry Society) **b** LC–MS on  $\text{Ag}_{29}(\text{LA})_{12}$  clusters showing the separation of the two isomers. Peaks 3 and 4 correspond to dimer- and trimer-like species<sup>119</sup>. (Copyright© 2018 American Chemistry Society)

specific isomers of the clusters to obtain isomer-specific properties. Catalysis of isolated cluster ions may be studied. Ion soft landing may be used to deposit ligand-protected cluster ions on specific substrates.

Extensive studies can also be done with clusters synthesized in macromolecular templates like proteins<sup>131</sup>, DNAs<sup>132</sup>, etc., which are of particular interest because of their biocompatibility. Till now, most of the protein-protected clusters are mainly characterized by MS due to the difficulty in their crystallization. Though this aspect has not been discussed in detail in this review, enormous literature exists on the use of MS in understanding their composition, mechanism of growth, etc.<sup>131,133</sup>. MS has always been effective in revealing structural details of proteins. In a similar way such studies can be extended to clusters synthesized in protein templates.

With such enormous possibilities, the proliferation of MS into materials science could make it an indispensable

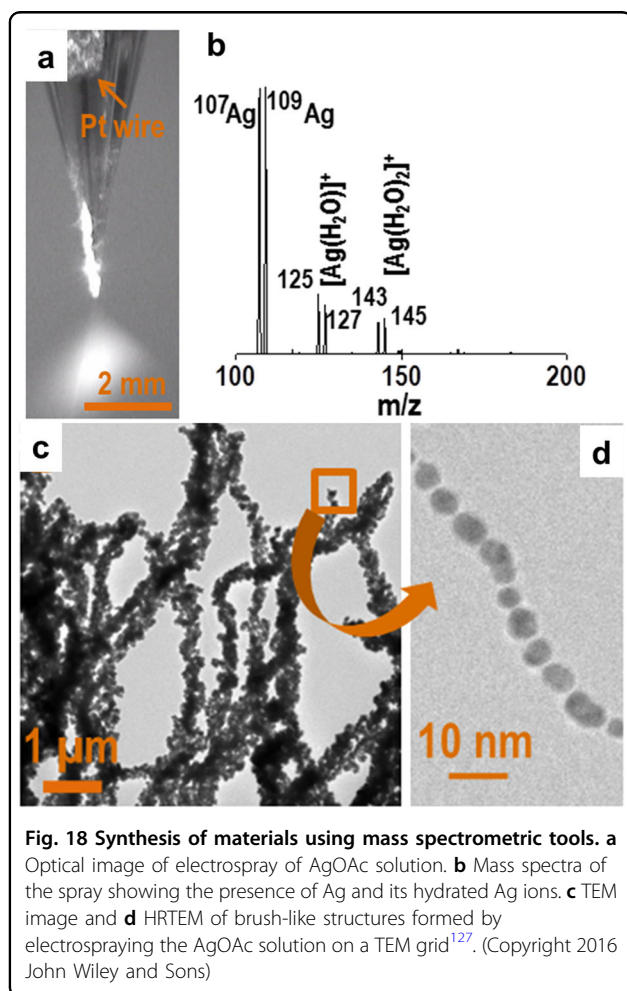
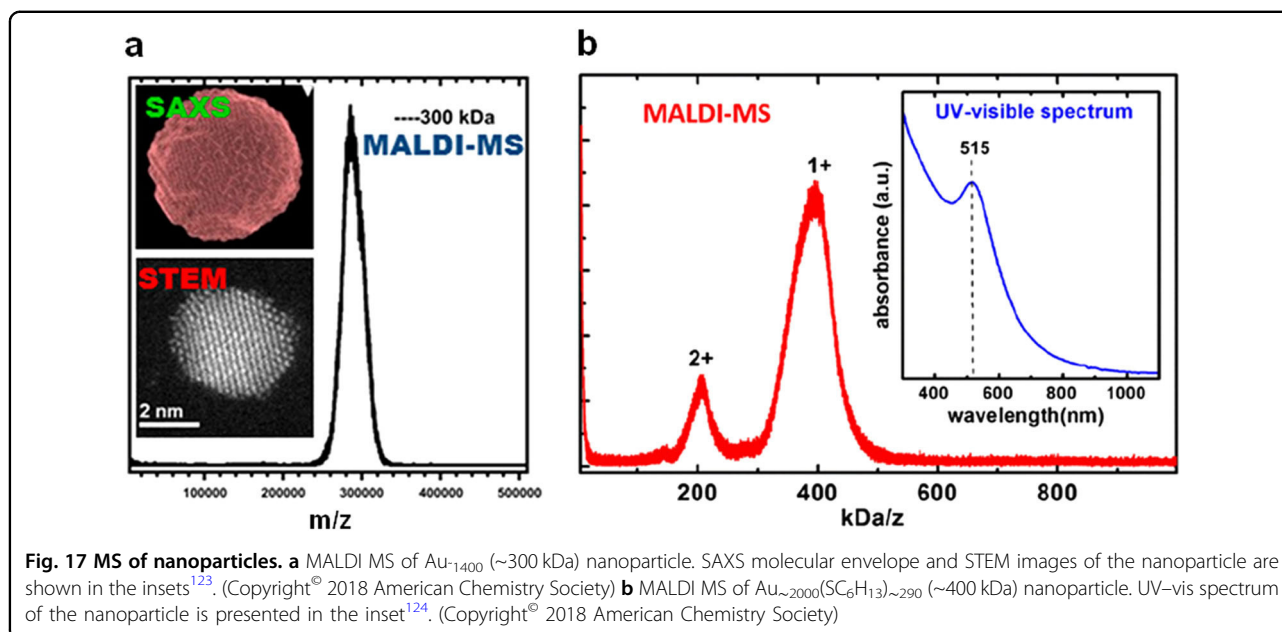
tool in that branch of science as has happened with TEM. This would produce new demands for instrumentation, associated interfaces, calibration standards, and associated needs. Expanding the limits of mass spectrometry in mass range and resolution would push traditional analytical methods further. Depending on the properties of such materials, possibilities to do catalysis, IR spectroscopy, fluorescence spectroscopy, and electron diffraction in mass spectrometers, as discussed above, could expand our understanding of phenomena to even greater detail.

#### Acknowledgements

P.C. thanks Council of Scientific and Industrial Research (CSIR) for her research fellowship. We acknowledge the Department of Science and Technology (DST), Government of India for supporting our research program.

#### Conflict of interest

The authors declare that they have no conflict of interest.



#### Publisher's note

Springer Nature remains neutral with regard to jurisdictional claims in published maps and institutional affiliations.

Received: 4 February 2019 Revised: 5 May 2019 Accepted: 20 May 2019  
Published online: 20 September 2019

#### References

- Fenn, J. B., Mann, M., Meng, C. K., Wong, S. F. & Whitehouse, C. M. Electrospray ionization for mass spectrometry of large biomolecules. *Science* **246**, 64 (1989).
- Wenzel, R. J., Matter, U., Schultheis, L. & Zenobi, R. Analysis of megadalton ions using cryodetection MALDI time-of-flight mass spectrometry. *Anal. Chem.* **77**, 4329–4337 (2005).
- Thomson, J. J. Bakerian lecture:—rays of positive electricity. *Proc. R. Soc. A* **89**, 1–20 (1913).
- Thomas, J. M. J. Thomson: winner of the Nobel Prize for physics 1906. *Angew. Chem. Int. Ed.* **45**, 6797–6800 (2006).
- Aston, F. W. *Isotopes*. London: Edward Arnold, 252 (E. Arnold & Company, London 1922).
- McLafferty, F. W. A century of progress in molecular mass spectrometry. *Ann. Rev. Anal. Chem.* **4**, 1–22 (2011).
- Gohlke, R. S. Time-of-flight mass spectrometry and gas-liquid partition chromatography. *Anal. Chem.* **31**, 535–541 (1959).
- Gohlke, R. S. & McLafferty, F. W. Early gas chromatography/mass spectrometry. *J. Am. Soc. Mass Spectrom.* **4**, 367–371 (1993).
- McLafferty, F. W., Todd, P. J., McGilvery, D. C. & Baldwin, M. A. Collisional activation and metastable ion characteristics. High-resolution tandem mass spectrometer (MS/MS) of increased sensitivity and mass range. *J. Am. Chem. Soc.* **102**, 3360–3363 (1980).
- Tanaka, K. et al. Protein and polymer analyses up to m/z 100 000 by laser ionization time-of-flight mass spectrometry. *Rapid Commun. Mass Spectrom.* **2**, 151–153 (1988).
- Xian, F., Hendrickson, C. L. & Marshall, A. G. High resolution mass spectrometry. *Anal. Chem.* **84**, 708–719 (2012).
- Cameron, A. E., Eggers Jr, D. F. An ion “Velocitron”. *Rev. Sci. Instrum.* **19**, 605–607 (1948).
- Cornisarow, M. B. & Marshall, A. G. Fourier transform ion cyclotron resonance spectroscopy. *Chem. Phys. Lett.* **25**, 282–283 (1974).






14. Makarov, A. Electrostatic axially harmonic orbital trapping: a high-performance technique of mass analysis. *Anal. Chem.* **72**, 1156–1162 (2000).
15. Makarov, A., Denisov, E. & Lange, O. Performance evaluation of a high-field orbitrap mass analyzer. *J. Am. Soc. Mass Spectrom.* **20**, 1391–1396 (2009).
16. Nolting, D., Malek, R. & Makarov, A. Ion traps in modern mass spectrometry. *Mass Spectrom. Rev.* **0**, 1–19 (2017).
17. Bunaciu, A. A., Udriștiu, E. G. & Aboul-Enein, H. Y. X-ray diffraction: instrumentation and applications. *Crit. Rev. Anal. Chem.* **45**, 289–299 (2015).
18. McLafferty, F. W. Tandem mass spectrometry (MS/MS): a promising new analytical technique for specific component determination in complex mixtures. *Acc. Chem. Res.* **13**, 33–39 (1980).
19. Elyashberg, M. Identification and structure elucidation by NMR spectroscopy. *TrAC Trends Anal. Chem.* **69**, 88–97 (2015).
20. Kwan, E. E. & Huang, S. G. Structural elucidation with NMR spectroscopy: practical strategies for organic chemists. *Eur. J. Org. Chem.* **2008**, 2671–2688 (2008).
21. Pauling, L. *The Nature of the Chemical Bond and the Structure of Molecules and Crystals: An Introduction to Modern Structural Chemistry*. Third Edition (Cornell University Press, Ithaca, New York, 1960).
22. Harkness, K. M., Cliffl, D. E. & McLean, J. A. Characterization of thiolate-protected gold nanoparticles by mass spectrometry. *Analyst* **135**, 868–874 (2010).
23. Lu, Y. & Chen, W. Application of mass spectrometry in the synthesis and characterization of metal nanoclusters. *Anal. Chem.* **87**, 10659–10667 (2015).
24. Johnson, G. E. & Laskin, J. Understanding ligand effects in gold clusters using mass spectrometry. *Analyst* **141**, 3573–3589 (2016).
25. Chakraborty, I. & Pradeep, T. Atomically precise clusters of noble metals: emerging link between atoms and nanoparticles. *Chem. Rev.* **117**, 8208–8271 (2017).
26. Jin, R., Zeng, C., Zhou, M. & Chen, Y. Atomically precise colloidal metal nanoclusters and nanoparticles: fundamentals and opportunities. *Chem. Rev.* **116**, 10346–10413 (2016).
27. Heaven, M. W., Dass, A., White, P. S., Holt, K. M. & Murray, R. W. Crystal structure of the gold nanoparticle  $[\text{N}(\text{C}_8\text{H}_{17})_4][\text{Au}_{25}(\text{SCH}_2\text{CH}_2\text{Ph})_{18}]$ . *J. Am. Chem. Soc.* **130**, 3754–3755 (2008).
28. Zeng, C., Li, T., Das, A., Rosi, N. L. & Jin, R. Chiral structure of thiolate-protected 28-gold-atom nanocluster determined by X-ray crystallography. *J. Am. Chem. Soc.* **135**, 10011–10013 (2013).
29. Qian, H., Eckenhoff, W. T., Zhu, Y., Pintauer, T. & Jin, R. Total structure determination of thiolate-protected  $\text{Au}_{38}$  nanoparticles. *J. Am. Chem. Soc.* **132**, 8280–8281 (2010).
30. Malola, S. et al.  $\text{Au}_{40}(\text{SR})_{24}$  cluster as a chiral dimer of 8-electron superatoms: structure and optical properties. *J. Am. Chem. Soc.* **134**, 19560–19563 (2012).
31. Zeng, C. et al. Gold tetrahedra coil up: Kekulé-like and double helical superstructures. *Sci. Adv.* **1**, e1500425 (2015).
32. Zeng, C., Liu, C., Chen, Y., Rosi, N. L. & Jin, R. Atomic structure of self-assembled monolayer of thiolates on a tetragonal  $\text{Au}_{52}$  nanocrystal. *J. Am. Chem. Soc.* **138**, 8710–8713 (2016).
33. Jadzinsky, P. D., Calero, G., Ackerson, C. J., Bushnell, D. A. & Kornberg, R. D. Structure of a thiol monolayer-protected gold nanoparticle at 1.1 Å resolution. *Science* **318**, 430–433 (2007).
34. Dass, A. et al.  $\text{Au}_{133}(\text{SPh}^t\text{Bu})_{52}$  nanomolecules: X-ray crystallography, optical, electrochemical, and theoretical analysis. *J. Am. Chem. Soc.* **137**, 4610–4613 (2015).
35. Desireddy, A. et al. Ultrastable silver nanoparticles. *Nature* **501**, 399 (2013).
36. Joshi, C. P., Bootharaju, M. S., Alhilaly, M. J. & Bakr, O. M.  $[\text{Ag}_{25}(\text{SR})_{18}]^-$ : the “Golden” silver nanoparticle. *J. Am. Chem. Soc.* **137**, 11578–11581 (2015).
37. AbdulHalim, L. G. et al.  $\text{Ag}_{29}(\text{BDT})_{12}(\text{TPP})_4$ : a tetravalent nanocluster. *J. Am. Chem. Soc.* **137**, 11970–11975 (2015).
38. Kroto, H. W., Heath, J. R., O’Brien, S. C., Curl, R. F. & Smalley, R. E.  $\text{C}_{60}$ : buckminsterfullerene. *Nature* **318**, 162 (1985).
39. Knight, W. D. et al. Electronic shell structure and abundances of sodium clusters. *Phys. Rev. Lett.* **52**, 2141–2143 (1984).
40. Maruyama, S., Kohno, M. & Inoue, S. FT-ICR study of chemical reaction of silicon clusters. *Therm. Sci. Eng.* **7**, 1–6 (1999).
41. Singh, D. M. D. J., Pradeep, T., Bhattacharjee, J. & Waghmare, U. V. Closed-cage clusters in the gaseous and condensed phases derived from sonochemically synthesized  $\text{MoS}_2$  nanoflakes. *J. Am. Soc. Mass Spectrom.* **18**, 2191–2197 (2007).
42. Katakuse, I. et al. Mass distributions of negative cluster ions of copper, silver, and gold. *Int. J. Mass Spectrom. Ion-Process.* **74**, 33–41 (1986).
43. Furche, F. et al. The structures of small gold cluster anions as determined by a combination of ion mobility measurements and density functional calculations. *J. Chem. Phys.* **117**, 6982–6990 (2002).
44. Lechtken, A., Neiss, C., Kappes, M. M. & Schooss, D. Structure determination of gold clusters by trapped ion electron diffraction:  $\text{Au}_{14}^-$ – $\text{Au}_{19}^-$ . *Phys. Chem. Chem. Phys.* **11**, 4344–4350 (2009).
45. Li, J., Li, X., Zhai, H.-J. & Wang, L.-S.  $\text{Au}_{20}$ : a tetrahedral cluster. *Science* **299**, 864 (2003).
46. Brust, M., Walker, M., Bethell, D., Schiffrin, D. J. & Whyman, R. Synthesis of thiol-derivatised gold nanoparticles in a two-phase liquid-liquid system. *J. Chem. Soc., Chem. Commun.*, 801–802 (1994).
47. Whetten, R. L. et al. Nanocrystal gold molecules. *Adv. Mat.* **8**, 428–433 (1996).
48. Schaaff, T. G., Knight, G., Shafigullin, M. N., Borkman, R. F. & Whetten, R. L. Isolation and selected properties of a 10.4 kDa gold:glutathione cluster compound. *J. Phys. Chem. B* **102**, 10643–10646 (1998).
49. Negishi, Y., Nobusada, K. & Tsukuda, T. Glutathione-protected gold clusters revisited: bridging the gap between gold(I)–thiolate complexes and thiolate-protected gold nanocrystals. *J. Am. Chem. Soc.* **127**, 5261–5270 (2005).
50. Tracy, J. B. et al. Poly(ethylene glycol) ligands for high-resolution nanoparticle mass spectrometry. *J. Am. Chem. Soc.* **129**, 6706–6707 (2007).
51. Negishi, Y., Chaki, N. K., Shichibu, Y., Whetten, R. L. & Tsukuda, T. Origin of magic stability of thiolated gold clusters: a case study on  $\text{Au}_{25}(\text{SC}_6\text{H}_{13})_{18}$ . *J. Am. Chem. Soc.* **129**, 11322–11323 (2007).
52. Dass, A., Stevenson, A., Dubay, G. R., Tracy, J. B. & Murray, R. W. Nanoparticle MALDI-TOF mass spectrometry without fragmentation:  $\text{Au}_{25}(\text{SCH}_2\text{CH}_2\text{Ph})_{18}$  and mixed monolayer  $\text{Au}_{25}(\text{SCH}_2\text{CH}_2\text{Ph})_{18-x}(\text{L})_x$ . *J. Am. Chem. Soc.* **130**, 5940–5946 (2008).
53. Qian, H., Zhu, Y. & Jin, R. Atomically precise gold nanocrystal molecules with surface plasmon resonance. *Proc. Natl. Acad. Sci.* **109**, 696–700 (2012).
54. Levi-Kalishman, Y. et al. Synthesis and characterization of  $\text{Au}_{102}(\text{p-MBA})_{44}$  nanoparticles. *J. Am. Chem. Soc.* **133**, 2976–2982 (2011).
55. Wu, Z. et al. High yield, large scale synthesis of thiolate-protected  $\text{Ag}_7$  clusters. *J. Am. Chem. Soc.* **131**, 16672–16674 (2009).
56. Udaya Bhaskara Rao, T. & Pradeep, T. Luminescent  $\text{Ag}_7$  and  $\text{Ag}_8$  clusters by interfacial synthesis. *Angew. Chem.* **49**, 3925–3929 (2010).
57. Baksi, A., Bootharaju, M. S., Chen, X., Häkkinen, H. & Pradeep, T.  $\text{Ag}_{11}(\text{SG})_7$ : a new cluster identified by mass spectrometry and optical spectroscopy. *J. Phys. Chem. C* **118**, 21722–21729 (2014).
58. Bertorello, F. et al. Synthesis, characterization and optical properties of low nuclearity liganded silver clusters:  $\text{Ag}_{31}(\text{SG})_{19}$  and  $\text{Ag}_{15}(\text{SG})_{11}$ . *Nanoscale* **5**, 5637–5643 (2013).
59. Udayabhaskararao, T., Bootharaju, M. S. & Pradeep, T. Thiolate-protected  $\text{Ag}_{32}$  clusters: mass spectral studies of composition and insights into the Ag-thiolate structure from NMR. *Nanoscale* **5**, 9404–9411 (2013).
60. Harkness, K. M. et al.  $\text{Ag}_{44}(\text{SR})_{30}^{4-}$ : a silver-thiolate superatom complex. *Nanoscale* **4**, 4269–4274 (2012).
61. Yang, H. et al. All-thiol-stabilized  $\text{Ag}_{44}$  and  $\text{Au}_{12}\text{Ag}_{32}$  nanoparticles with single-crystal structures. *Nat. Commun.* **4**, 2422 (2013).
62. Alhilaly, M. J. et al.  $[\text{Ag}_{67}(\text{SPhMe})_{32}(\text{PPh}_3)_8]^{3+}$ : synthesis, total structure, and optical properties of a large box-shaped silver nanocluster. *J. Am. Chem. Soc.* **138**, 14727–14732 (2016).
63. Bootharaju, M. S. et al. A new class of atomically precise, hydride-rich silver nanoclusters co-protected by phosphines. *J. Am. Chem. Soc.* **138**, 13770–13773 (2016).
64. Takano, S., Hirai, H., Muramatsu, S. & Tsukuda, T. Hydride-doped gold superatom  $(\text{Au}_6\text{H})^{2+}$ : synthesis, structure, and transformation. *J. Am. Chem. Soc.* **140**, 8380–8383 (2018).
65. Takano, S., Hirai, H., Muramatsu, S. & Tsukuda, T. Hydride-mediated controlled growth of a bimetallic  $(\text{Pd@Au}_6)^{2+}$  superatom to a hydride-doped  $(\text{HPd@Au}_6)^{3+}$  superatom. *J. Am. Chem. Soc.* **140**, 12314–12317 (2018).
66. Le Guével, X., Trouillet, V., Spies, C., Jung, G. & Schneider, M. Synthesis of yellow-emitting platinum nanoclusters by ligand etching. *J. Phys. Chem. C* **116**, 6047–6051 (2012).
67. Tanaka, S.-I., Miyazaki, J., Tiwari, D. K., Jin, T. & Inoue, Y. Fluorescent platinum nanoclusters: synthesis, purification, characterization, and application to bioimaging. *Angew. Chem.* **50**, 431–435 (2011).
68. Zamborini, F. P., Gross, S. M. & Murray, R. W. Synthesis, characterization, reactivity, and electrochemistry of palladium, monolayer protected clusters. *Langmuir* **17**, 481–488 (2001).

69. Negishi, Y., Murayama, H. & Tsukuda, T. Formation of  $\text{Pd}_n(\text{SR})_m$  clusters ( $n < 60$ ) in the reactions of  $\text{PdCl}_2$  and RSH ( $R = n\text{-C}_{18}\text{H}_{37}$ ,  $n\text{-C}_{12}\text{H}_{25}$ ). *Chem. Phys. Lett.* **366**, 561–566 (2002).
70. Chen, J., Pan, Y., Wang, Z. & Zhao, P. The fluorescence properties of tiara like structural thiolated palladium clusters. *Dalton Trans.* **46**, 12964–12970 (2017).
71. Dhayal, R. S. et al. Diselenophosphate-induced conversion of an achiral  $[\text{Cu}_{20}\text{H}_{11}(\text{S}_2\text{P}(\text{O}i\text{Pr})_2)_3]$  into a chiral  $[\text{Cu}_{20}\text{H}_{11}(\text{Se}_2\text{P}(\text{O}i\text{Pr})_2)_3]$  polyhydrido nanocluster. *Angew. Chem.* **54**, 13604–13608 (2015).
72. Araake, R., Sakadani, K., Tada, M., Sakai, Y. & Ohki, Y.  $[\text{Fe}_4]$  and  $[\text{Fe}_2]$  hydride clusters supported by phosphines: synthesis, characterization, and application in  $\text{N}_2$  reduction. *J. Am. Chem. Soc.* **139**, 5596–5606 (2017).
73. Bhat, S. et al. Atomically precise and monolayer protected iridium clusters in solution. *RSC Adv.* **6**, 26679–26688 (2016).
74. Lanucara, F., Holman, S. W., Gray, C. J. & Eyers, C. E. The power of ion mobility-mass spectrometry for structural characterization and the study of conformational dynamics. *Nat. Chem.* **6**, 281 (2014).
75. Canzani, D., Laszlo, K. J. & Bush, M. F. Ion mobility of proteins in nitrogen gas: effects of charge state, charge distribution, and structure. *J. Phys. Chem. A* **122**, 5625–5634 (2018).
76. Greisch, J.-F. et al. From planar to cage in 15 easy steps: resolving the  $\text{C}_{60}\text{H}_{21}\text{F}_9^- \rightarrow \text{C}_{60}^-$  transformation by ion mobility mass spectrometry. *J. Am. Chem. Soc.* **138**, 11254–11263 (2016).
77. Surman, A. J. et al. Sizing and discovery of nanosized polyoxometalate clusters by mass spectrometry. *J. Am. Chem. Soc.* **138**, 3824–3830 (2016).
78. Baksi, A., Chakraborty, P., Bhat, S., Natarajan, G. & Pradeep, T.  $[\text{Au}_{25}(\text{SR})_{18}]_2^{2-}$ : a noble metal cluster dimer in the gas phase. *Chem. Commun.* **52**, 8397–8400 (2016).
79. Chakraborty, P. et al. Understanding proton capture and cation-induced dimerization of  $[\text{Ag}_{29}(\text{BDT})_{12}]^{3-}$  clusters by ion mobility mass spectrometry. *Phys. Chem. Chem. Phys.* **20**, 7593–7603 (2018).
80. Baksi, A., Harvey, S. R., Natarajan, G., Wysocki, V. H. & Pradeep, T. Possible isomers in ligand protected  $\text{Ag}_{11}$  cluster ions identified by ion mobility mass spectrometry and fragmented by surface induced dissociation. *Chem. Commun.* **52**, 3805–3808 (2016).
81. Baksi, A. et al. Isomerism in monolayer protected silver cluster ions: an ion mobility-mass spectrometry approach. *J. Phys. Chem. C* **121**, 13421–13427 (2017).
82. Gilb, S., Weis, P., Furche, F., Ahlrichs, R. & Kappes, M. M. Structures of small gold cluster cations ( $\text{Au}_n^+$ ,  $n < 14$ ): ion mobility measurements versus density functional calculations. *J. Chem. Phys.* **116**, 4094–4101 (2002).
83. Daly, S. et al. Gas-phase structural and optical properties of homo- and heterobimetallic rhombic dodecahedral nanoclusters  $[\text{Ag}_{14-n}\text{Cu}_n(\text{C}\equiv\text{C}^*\text{Bu})_{12}\text{X}]^+$  ( $X = \text{Cl}$  and  $\text{Br}$ ): Ion mobility, VUV and UV spectroscopy, and DFT calculations. *J. Phys. Chem. C* **121**, 10719–10727 (2017).
84. Soleilhac, A. et al. Size characterization of glutathione-protected gold nanoclusters in the solid, liquid and gas phases. *J. Phys. Chem. C* **121**, 27733–27740 (2017).
85. Ligare, M. R., Baker, E. S., Laskin, J. & Johnson, G. E. Ligand induced structural isomerism in phosphine coordinated gold clusters revealed by ion mobility mass spectrometry. *Chem. Commun.* **53**, 7389–7392 (2017).
86. Hirata, K. et al. Interconversions of structural isomers of  $[\text{PdAu}_8(\text{PPh}_3)_6]^{2+}$  and  $[\text{Au}_9(\text{PPh}_3)_3]^{3+}$  revealed by ion mobility mass spectrometry. *J. Phys. Chem. C* **122**, 23123–23128 (2018).
87. Fields-Zinna, C. A. et al. Tandem mass spectrometry of thiolate-protected Au nanoparticles  $\text{Na}_x\text{Au}_{25}(\text{SC}_2\text{H}_4\text{Ph})_{18-y}(\text{S}(\text{C}_2\text{H}_4\text{O})_2\text{CH}_3)_y$ . *J. Am. Chem. Soc.* **131**, 13844–13851 (2009).
88. Angel, L. A., Majors, L. T., Dharmaratne, A. C. & Dass, A. Ion mobility mass spectrometry of  $\text{Au}_{25}(\text{SCH}_2\text{CH}_2\text{Ph})_{18}$  nanoclusters. *ACS Nano* **4**, 4691–4700 (2010).
89. Black, D. M., Bhattarai, N., Whetten, R. L. & Bach, S. B. H. Collision-induced dissociation of monolayer protected clusters  $\text{Au}_{144}$  and  $\text{Au}_{130}$  in an electrospray time-of-flight mass spectrometer. *J. Phys. Chem. A* **118**, 10679–10687 (2014).
90. Tomihara, R. et al. Collision-induced dissociation of undecagold clusters protected by mixed ligands  $[\text{Au}_{11}(\text{PPh}_3)_9\text{X}_2]^+$  ( $X = \text{Cl}$ ,  $\text{C}\equiv\text{CPh}$ ). *ACS Omega* **3**, 6237–6242 (2018).
91. Chakraborty, P. et al. Dissociation of gas phase ions of atomically precise silver clusters reflects their solution phase stability. *J. Phys. Chem. C* **121**, 10971–10981 (2017).
92. Johnson, G. E., Priest, T. & Laskin, J. Size-dependent stability toward dissociation and ligand binding energies of phosphine ligated gold cluster ions. *Chem. Sci.* **5**, 3275–3286 (2014).
93. Black, D. M., Crittenden, C. M., Brodbelt, J. S. & Whetten, R. L. Ultraviolet photodissociation of selected gold clusters: ultraefficient unstapling and ligand stripping of  $\text{Au}_{25}(\text{pMBA})_{18}$  and  $\text{Au}_{36}(\text{pMBA})_{24}$ . *J. Phys. Chem. Lett.* **8**, 1283–1289 (2017).
94. Ghosh, A. et al. Sequential dihydrogen desorption from hydride-protected atomically precise silver clusters and the formation of naked clusters in the gas phase. *ACS Nano* **11**, 11145–11151 (2017).
95. Jash, M. et al. Preparation of gas phase naked silver cluster cations outside a mass spectrometer from ligand protected clusters in solution. *Nanoscale* **10**, 15714–15722 (2018).
96. Wang, L.-M. & Wang, L.-S. Probing the electronic properties and structural evolution of anionic gold clusters in the gas phase. *Nanoscale* **4**, 4038–4053 (2012).
97. Hirata, K. et al. Anion photoelectron spectroscopy of free  $[\text{Au}_{25}(\text{SC}_2\text{H}_5)_{18}]^-$ . *Nanoscale* **9**, 13409–13412 (2017).
98. Hamouda, R. et al. Electron emission of gas-phase  $[\text{Au}_{25}(\text{SG})_{18-6\text{H}}]^{7-}$  gold cluster and its action spectroscopy. *J. Phys. Chem. Lett.* **1**, 3189–3194 (2010).
99. Daly, S. et al. Gas-phase VUV photoionisation and photofragmentation of the silver deuteride nanocluster  $[\text{Ag}_{10}\text{D}_8\text{L}_6]^{2+}$  ( $\text{L} = \text{bis}(\text{diphenylphosphino})\text{methane}$ ). A joint experimental and theoretical study. *Phys. Chem. Chem. Phys.* **17**, 25772–25777 (2015).
100. Yu, Y., Luo, Z., Yu, Y., Lee, J. Y. & Xie, J. Observation of cluster size growth in CO-directed synthesis of  $\text{Au}_{25}(\text{SR})_{18}$  nanoclusters. *ACS Nano* **6**, 7920–7927 (2012).
101. Luo, Z. et al. Toward understanding the growth mechanism: tracing all stable intermediate species from reduction of  $\text{Au}(\text{I})$ -thiolate complexes to evolution of  $\text{Au}_{25}$  nanoclusters. *J. Am. Chem. Soc.* **136**, 10577–10580 (2014).
102. Yao, Q. et al. Understanding seed-mediated growth of gold nanoclusters at molecular level. *Nat. Commun.* **8**, 927 (2017).
103. Yao, Q. et al. Revealing isoelectronic size conversion dynamics of metal nanoclusters by a noncrystallization approach. *Nat. Commun.* **9**, 1979 (2018).
104. Chen, T. et al. Synthesis of water-soluble  $[\text{Au}_{25}(\text{SR})_{18}]^-$  using a stoichiometric amount of  $\text{NaBH}_4$ . *J. Am. Chem. Soc.* **140**, 11370–11377 (2018).
105. Cao, Y. et al. Evolution of thiolate-stabilized Ag nanoclusters from Ag-thiolate cluster intermediates. *Nat. Commun.* **9**, 2379 (2018).
106. Bootharaju, M. S., Joshi, C. P., Alhilaly, M. J. & Bakr, O. M. Switching a nanocluster core from hollow to nonhollow. *Chem. Mat.* **28**, 3292–3297 (2016).
107. Krishnadas, K. R. et al. Interparticle reactions: an emerging direction in nanomaterials chemistry. *Acc. Chem. Res.* **50**, 1988–1996 (2017).
108. Krishnadas, K. R. et al. Intercluster reactions between  $\text{Au}_{25}(\text{SR})_{18}$  and  $\text{Ag}_{44}(\text{SR})_{30}$ . *J. Am. Chem. Soc.* **138**, 140–148 (2016).
109. Krishnadas, K. R., Baksi, A., Ghosh, A., Natarajan, G. & Pradeep, T. Manifestation of geometric and electronic shell structures of metal clusters in intercluster reactions. *ACS Nano* **11**, 6015–6023 (2017).
110. Krishnadas, K. R., Baksi, A., Ghosh, A., Natarajan, G. & Pradeep, T. Structure-conserving spontaneous transformations between nanoparticles. *Nat. Commun.* **7**, 13447 (2016).
111. Salassa, G., Sels, A., Mancin, F. & Bürgi, T. Dynamic nature of thiolate monolayer in  $\text{Au}_{25}(\text{SR})_{18}$  nanoclusters. *ACS Nano* **11**, 12609–12614 (2017).
112. Chakraborty, P. et al. Rapid isotopic exchange in nanoparticles. *Sci. Adv.* **5**, eaau7555 (2019).
113. Chakraborty, P., Nag, A., Paramasivam, G., Natarajan, G. & Pradeep, T. Fullerene-functionalized monolayer-protected silver clusters:  $[\text{Ag}_{29}(\text{BDT})_{12}(\text{C}_{60})_n]^{3-}$  ( $n = 1-9$ ). *ACS Nano* **12**, 2415–2425 (2018).
114. Mathew, A. et al. Supramolecular functionalization and concomitant enhancement in properties of  $\text{Au}_{25}$  clusters. *ACS Nano* **8**, 139–152 (2014).
115. Nag, A. et al. Isomerism in supramolecular adducts of atomically precise nanoparticles. *J. Am. Chem. Soc.* **140**, 13590–13593 (2018).
116. Niihori, Y., Uchida, C., Kurashige, W. & Negishi, Y. High-resolution separation of thiolate-protected gold clusters by reversed-phase high-performance liquid chromatography. *Phys. Chem. Chem. Phys.* **18**, 4251–4265 (2016).
117. Black, D. M., Bhattarai, N., Bach, S. B. H. & Whetten, R. L. Selection and identification of molecular gold clusters at the nano(gram) scale: reversed phase HPLC–ESI–MS of a mixture of Au-Peth MPCs. *J. Phys. Chem. Lett.* **7**, 3199–3205 (2016).

118. Black, D. M., Bach, S. B. H. & Whetten, R. L. Capillary liquid chromatography mass spectrometry analysis of intact monolayer-protected gold clusters in complex mixtures. *Anal. Chem.* **88**, 5631–5636 (2016).
119. Black, D. M. et al. Liquid chromatography separation and mass spectrometry detection of silver-lipoate Ag<sub>29</sub>(LA)<sub>12</sub> nanoclusters: evidence of isomerism in the solution phase. *Anal. Chem.* **90**, 2010–2017 (2018).
120. Kumara, C. et al. Super-stable, highly monodisperse plasmonic faradaurate-500 nanocrystals with 500 gold atoms: Au<sub>~500</sub>(SR)<sub>~120</sub>. *J. Am. Chem. Soc.* **136**, 7410–7417 (2014).
121. Kumara, C., Zuo, X., Cullen, D. A. & Dass, A. Faradaurate-940: synthesis, mass spectrometry, electron microscopy, high-energy X-ray diffraction, and X-ray scattering study of Au<sub>~940±20</sub>(SR)<sub>~160±4</sub> nanocrystals. *ACS Nano* **8**, 6431–6439 (2014).
122. Sakthivel, N. A., Theivendran, S., Ganeshraj, V., Oliver, A. G. & Dass, A. Crystal structure of faradaurate-279: Au<sub>279</sub>(SPh-Bu)<sub>84</sub> plasmonic nanocrystal molecules. *J. Am. Chem. Soc.* **139**, 15450–15459 (2017).
123. Kumara, C. et al. Isolation of a 300 kDa, Au<sub>~1400</sub> gold compound, the standard 3.6 nm capstone to a series of plasmonic nanocrystals protected by aliphatic-like thiolates. *J. Phys. Chem. Lett.* **9**, 6825–6832 (2018).
124. Vergara, S. et al. Synthesis, mass spectrometry, and atomic structural analysis of Au<sub>~2000</sub>(SR)<sub>~290</sub> nanoparticles. *J. Phys. Chem. C* **122**, 26733–26738 (2018).
125. Yan, X., Bain, R. M. & Cooks, R. G. Organic reactions in microdroplets: reaction acceleration revealed by mass spectrometry. *Angew. Chem. Int. Ed.* **55**, 12960–12972 (2016).
126. Ingram, A. J., Boeser, C. L. & Zare, R. N. Going beyond electrospray: mass spectrometric studies of chemical reactions in and on liquids. *Chem. Sci.* **7**, 39–55 (2016).
127. Sarkar, D. et al. Metallic nanobrushes made using ambient droplet sprays. *Adv. Mat.* **28**, 2223–2228 (2016).
128. Baksi, A. et al. Monolayer-protected noble-metal clusters as potential standards for negative-ion mass spectrometry. *Anal. Chem.* **90**, 11351–11357 (2018).
129. Seo, J., Warnke, S., Pagel, K., Bowers, M. T. & von Helden, G. Infrared spectrum and structure of the homochiral serine octamer-dichloride complex. *Nat. Chem.* **9**, 1263 (2017).
130. Warnke, S. et al. Protomers of benzocaine: solvent and permittivity dependence. *J. Am. Chem. Soc.* **137**, 4236–4242 (2015).
131. Xavier, P. L., Chaudhari, K., Baksi, A. & Pradeep, T. Protein-protected luminescent noble metal quantum clusters: an emerging trend in atomic cluster nanoscience. *Nano Rev.* **3**, 14767 (2012).
132. Gwinn, E., Schultz, D., Copp, S. M. & Swasey, S. DNA-protected silver clusters for nanophotonics. *Nanomaterials* **5**, 180–207 (2015).
133. Chaudhari, K., Xavier, P. L. & Pradeep, T. Understanding the evolution of luminescent gold quantum clusters in protein templates. *ACS Nano* **5**, 8816–8827 (2011).
134. Barner-Kowollik, C., Gruendling, T., Falkenhagen, J. & Weidner, S. *Mass Spectrometry in Polymer Chemistry* (Wiley-VCH Verlag GmbH & Co. KGaA, Weinheim, Germany, 2012).
135. Dempster, A. J. A new method of positive ray analysis. *Phys. Rev.* **11**, 316–325 (1918).
136. Arnot, F. L. & Beckett, C. Formation of negative ions at surfaces. *Nature* **141**, 1011 (1938).
137. Graus, M., Müller, M. & Hansel, A. High resolution PTR-TOF: quantification and formula confirmation of VOC in real time. *J. Am. Soc. Mass Spectrom.* **21**, 1037–1044 (2010).
138. Cody, R. B., Tamura, J. & Musselman, B. D. Electrospray ionization/magnetic sector mass spectrometry: calibration, resolution, and accurate mass measurements. *Anal. Chem.* **64**, 1561–1570 (1992).
139. E., S. W. A pulsed mass spectrometer with time dispersion. *Phys. Rev.* **69**, 674–674 (1946).
140. Johnson, E. G. & Nier, A. O. Angular aberrations in sector shaped electromagnetic lenses for focusing beams of charged particles. *Phys. Rev.* **91**, 10–17 (1953).
141. Wiley, W. C. & McLaren, I. H. Time-of-flight mass spectrometer with improved resolution. *Rev. Sci. Instrum.* **26**, 1150–1157 (1955).
142. Beynon, J. H. The use of the mass spectrometer for the identification of organic compounds. *Microchim. Acta* **44**, 437–453 (1956).
143. Paul, W. Electromagnetic traps for charged and neutral particles. *Rev. Mod. Phys.* **62**, 531–540 (1990).
144. McDaniel, E. W., Martin, D. W. & Barnes, W. S. Drift tube-mass spectrometer for studies of low-energy ion-molecule reactions. *Rev. Sci. Instrum.* **33**, 2–7 (1962).
145. Munson, M. S. B. & Field, F. H. Chemical ionization mass spectrometry. I. general introduction. *J. Am. Chem. Soc.* **88**, 2621–2630 (1966).
146. McLafferty, F. W. & Bryce, T. A. Metastable-ion characteristics: characterization of isomeric molecules. *Chem. Commun.*, 1215–1217 (1967).
147. Chernushevich, I. V., Merenbloom, S. I., Liu, S. & Bloomfield, N. A W-Geometry ortho-TOF MS with high resolution and up to 100% duty cycle for MS/MS. *J. Am. Soc. Mass Spectrom.* **28**, 2143–2150 (2017).
148. Weisbrod, C. R. et al. Front-end electron transfer dissociation coupled to a 21 Tesla FT-ICR mass spectrometer for intact protein sequence analysis. *J. Am. Soc. Mass Spectrom.* **28**, 1787–1795 (2017).
149. Dole, M. et al. Molecular beams of macroions. *J. Chem. Phys.* **49**, 2240–2249 (1968).
150. Horning, E. C. et al. Atmospheric pressure ionization (API) mass spectrometry. Solvent-mediated ionization of samples introduced in solution and in a liquid chromatograph effluent stream. *J. Chromatogr. Sci.* **12**, 725–729 (1974).
151. Cooks, R. G., Terwilliger, D. T., Ast, T., Beynon, J. H. & Keough, T. Surface modified mass spectrometry. *J. Am. Chem. Soc.* **97**, 1583–1585 (1975).
152. Yost, R. A. & Enke, C. G. Selected ion fragmentation with a tandem quadrupole mass spectrometer. *J. Am. Chem. Soc.* **100**, 2274–2275 (1978).
153. Barber, M., Bordoli, R. S., Sedgwick, R. D. & Tyler, A. N. Fast atom bombardment of solids (F.A.B.): a new ion source for mass spectrometry. *J. Chem. Soc., Chem. Commun.*, 325–327 (1981).
154. Karas, M., Bachmann, D., Bahr, U. & Hillenkamp, F. Matrix-assisted ultraviolet laser desorption of non-volatile compounds. *Int. J. Mass Spectrom. Ion-Process.* **78**, 53–68 (1987).
155. Takáts, Z., Wiseman, J. M., Gologan, B. & Cooks, R. G. Mass spectrometry sampling under ambient conditions with desorption electrospray ionization. *Science* **306**, 471 (2004).
156. Siuzdak, G. et al. Mass spectrometry and viral analysis. *Chem. Biol.* **3**, 45–48 (1996).
157. Hendrickson, C. L. et al. 21 Tesla fourier transform ion cyclotron resonance mass spectrometer: a national resource for ultrahigh resolution mass analysis. *J. Am. Soc. Mass Spectrom.* **26**, 1626–1632 (2015).
158. Ludwig, K., Habbach, S., Krieglstein, J., Klumpp, S. & König, S. MALDI-TOF high mass calibration up to 200 kDa using human recombinant 16 kDa protein histidine phosphatase aggregates. *PLoS One* **6**, e23612 (2011).
159. Aksenov, A. A. & Bier, M. E. The analysis of polystyrene and polystyrene aggregates into the mega dalton mass range by cryodetection MALDI TOF MS. *J. Am. Soc. Mass Spectrom.* **19**, 219–230 (2008).

## PAPER

[View Article Online](#)  
[View Journal](#) | [View Issue](#)Cite this: *Dalton Trans.*, 2019, **48**, 8664Formation of an NIR-emitting  $\text{Ag}_{34}\text{S}_3\text{SBB}_{20}(\text{CF}_3\text{COO})_6^{2+}$  cluster from a hydride-protected silver cluster†C. K. Manju,  Debasmita Ghosh, Mohammad Bodiuzzaman  and Thalappil Pradeep  \*

Recent reports have shown that the intercluster reaction is a new synthetic strategy to prepare alloy clusters. In this work, we performed an intercluster reaction between silver clusters and produced highly ionizable Ag–S-type clusters; we examined their formation by mass spectrometry.  $[\text{Ag}_{18}(\text{TPP})_{10}\text{H}_{16}]^{2+}$  ( $\text{Ag}_{18}$ ), a highly reactive hydride and phosphine-protected silver cluster, was used as a sacrificial cluster in this synthesis. An intercluster reaction between  $\text{Ag}_{18}$  and smaller silver-chalcogenolate clusters (SCC) resulted in a new cluster,  $[\text{Ag}_{34}\text{S}_3\text{SBB}_{20}(\text{CF}_3\text{COO})_6]^{2+}$ . The cluster showed an NIR emission at around 1100 nm. The cluster composition was confirmed by high-resolution electrospray ionization mass spectrometry (ESI-MS), thermogravimetry (TGA), and X-ray photoelectron spectroscopy (XPS).

Received 10th April 2019,  
Accepted 9th May 2019

DOI: 10.1039/c9dt01533g

[rsc.li/dalton](http://rsc.li/dalton)

## Introduction

Nanoclusters (NCs) of noble metals and semiconductors have been of significant interest in contemporary science due to their chemical and physical properties and a wide variety of applications.<sup>1–3</sup> NCs consisting of a few atoms have properties that are in between those of molecules and bulk materials. These NCs show size-dependent optical characteristics.<sup>3,4</sup> Different synthetic methodologies have been reported to prepare these NCs.<sup>1,5</sup> Various spectroscopic and spectrometric techniques have been employed to understand them in detail, including UV-visible spectroscopy (UV-vis), photoluminescence, nuclear magnetic resonance (NMR), matrix-assisted laser desorption ionization mass spectrometry (MALDI MS), electrospray ionization mass spectrometry (ESI-MS), and single crystal X-ray diffraction (XRD).<sup>2,5–10</sup>

Several chalcogenide clusters of silver, copper, cadmium, and zinc (Ag, Cu, Cd, and Zn) have been investigated.<sup>11–15</sup> Historically, a coordination chemistry approach has been followed for the synthesis of high-nuclearity metal chalcogenide clusters.<sup>11</sup> In this approach, the reaction of a metal salt (MX)

with a chalcogenide precursor or highly reactive thiolates and phosphines resulted in chalcogenide clusters. Silylated compounds such as  $\text{E}(\text{SiMe}_3)_2$  and  $\text{RESiMe}_3$  ( $\text{E} = \text{S}, \text{Se}, \text{Te}$ ) along with mono or diphosphines were used. The highly polarizable electrons and the anionic nature of these ligands helped the formation of clusters with different bridging modes. The choice of MX and the presence of phosphines were the critical factors in this method. A large number of crystal structures were reported using this method including that of the largest  $\text{Ag}_{490}\text{S}_{118}(\text{S}^t\text{C}_5\text{H}_{11})_{114}$ .<sup>14,16,17</sup> The inherent insoluble nature of these clusters made their solution phase studies difficult. This issue was recently resolved by the use of 4-*tert*-butylbenzyl mercaptan as a capping agent.<sup>18</sup>

The insertion reaction of  $\text{CS}_2$  into the M–S bond is another way to synthesize chalcogenide clusters.<sup>19</sup> Larger Cd–S clusters can be obtained by the reaction of cadmium thiolates with  $\text{CS}_2$ .<sup>20</sup> The slow release of  $\text{S}^{2-}$  is due to the reaction of  $\text{CS}_2$  with solvents.  $\text{S}^{2-}$  can be released into the reaction medium by the cleavage of the C–S bond, which results in the Ag–S cluster core.<sup>21,22</sup> Clusters such as  $\text{Ag}_{62}\text{S}_{13}(\text{S}^t\text{Bu})_{32}^{4+}$  and  $\text{Ag}_{62}\text{S}_{12}(\text{S}^t\text{Bu})_{32}^{2+}$  are formed by the cleavage of *t*-Butyl mercaptan ( $\text{S}^t\text{BuSH}$ ). A change in the number of core sulfur atoms has a large impact on the physical properties of these clusters.  $\text{Ag}_{62}\text{S}_{13}(\text{S}^t\text{Bu})_{32}^{4+}$  was highly red luminescent both in solution and in the solid state, while the luminescence was quenched in  $\text{Ag}_{62}\text{S}_{12}(\text{S}^t\text{Bu})_{32}^{2+}$ . Femtosecond transient absorption spectra suggested that the quenching of luminescence in the latter cluster was due to the free valence electrons available.<sup>22</sup>

Synthetic methods for noble metal clusters include the Brust–Schiffrin method and its modifications,<sup>23,24</sup> ligand-

DST Unit of Nanoscience (DST UNS) and Thematic Unit of Excellence, Department of Chemistry, Indian Institute of Technology Madras, Chennai 600036, India. E-mail: [pradeep@iitm.ac.in](mailto:pradeep@iitm.ac.in)

†Electronic supplementary information (ESI) available: UV-vis and ESI-MS spectra of  $\text{Ag}_{18}$ , ESI-MS spectrum of 30 min reaction product, comparative IR spectra of cluster and  $\text{CF}_3\text{COOAg}$ , XPS spectrum of cluster, SEM EDS spectrum and mapping, and UV-vis and ESI spectra of control experiments. See DOI: 10.1039/c9dt01533g

induced etching of NPs,<sup>25</sup> ligand exchange (thiolates with selenolates),<sup>26</sup> solid state,<sup>27</sup> and ligand exchange-induced size transformation (LEIST).<sup>28,29</sup> Recent reports have shown the intercluster reaction as a new pathway to produce alloy clusters.<sup>30,31</sup> Here, thiolate-protected clusters of two different metals were allowed to react. The reaction resulted in the exchange of metal ions and ligands. This methodology can also be extended to the clusters of same metals.

Fluorescence is one of the important properties of NCs, due to which they find applications in the field of chemical sensing, bioimaging, and drug delivery.<sup>32</sup> Most of the reported clusters emit in the red region.<sup>33</sup> There have been many efforts to tune the luminescence of NCs by changing the ligand composition and core size or by heteroatom doping. Near-infrared (NIR)-emitting materials find more applications in the field of biomedical science and energy conversion. Compared with optical imaging in the visible (450–700 nm) and NIR-I (700–950 nm) regions, the NIR-II (1000–1400 nm) region is optimal because of the lower auto-fluorescence and reduced scattering.<sup>32</sup> Silver chalcogenide semiconductors of a lower band gap, which emit in the NIR-II window, have been used for bio-imaging applications.<sup>32</sup>

In this work, we describe the synthesis of a new Ag-S cluster from a highly reactive silver cluster protected by phosphine and hydrides. The new cluster was assigned as  $[\text{Ag}_{34}\text{S}_3\text{SBB}_{20}(\text{CF}_3\text{COO})_6]^{2+}$  from the ESI-MS, TGA, and EDS data. An intercluster reaction of two silver clusters produced a cluster of different nuclearity. This protocol resulted in a charged cluster, which made the ESI-MS studies possible compared to our earlier efforts to make easily ionizable chalcogenide clusters. The cluster showed emission in solution and in the solid state at around 1100 nm.

## Materials and methods

### Materials

Silver nitrate ( $\text{AgNO}_3$ ), silver trifluoroacetate ( $\text{CF}_3\text{COOAg}$ ), 4-*tert*-butylbenzyl mercaptan (BBSH), triphenyl phosphine (TPP) and sodium borohydride ( $\text{NaBH}_4$ ) were purchased from Sigma Aldrich, India. Methanol (MeOH), chloroform, acetonitrile (ACN), hexane and dichloromethane (DCM) were obtained from Merck India.

### Synthesis of thiolate (Ag-SBB)

Silver thiolate was prepared by using a 1:5 mmol ratio of  $\text{AgNO}_3$  and BBSH. About 169 mg of  $\text{AgNO}_3$  was dissolved in 7 mL of MeOH by sonication for 5 minutes. Then, 933  $\mu\text{L}$  of BBSH was added drop by drop. The reaction mixture was stirred for 1 h. After that, the light yellowish product was centrifuged and washed with MeOH four times and dried using a rotavapor.

### Synthesis of $[\text{Ag}_{18}(\text{TPP})_{10}\text{H}_{16}]^{2+}$

$[\text{Ag}_{18}(\text{TPP})_{10}\text{H}_{16}]^{2+}$  was synthesized by following a previously reported method.<sup>34</sup> In a typical synthesis, 20 mg of  $\text{AgNO}_3$  (or

25 mg  $\text{CF}_3\text{COOAg}$ ) was dissolved in 1.5 mL of MeOH by sonication. This was added to a vial containing 3.5 mL of MeOH. Then, 70 mg of  $\text{PPh}_3$  dissolved in 10 mL of chloroform was added to the mixture under stirring conditions. After 20 minutes of stirring, 6.5 mg of  $\text{NaBH}_4$  dissolved in 0.5 mL cold water was added. The solution turned yellow immediately after the addition of  $\text{NaBH}_4$  solution. Green-colored  $\text{Ag}_{18}$  was obtained after 3 h of stirring. This green solution was dried and washed with water. After a water wash, the green precipitate was dried and dissolved in the required amount of MeOH and used for further synthesis.<sup>34</sup>

### Synthesis of $\text{Ag}_{34}\text{S}_3\text{SBB}_{20}(\text{CF}_3\text{COO})_6^{2+}$

About 0.35 mmol of Ag-SBB was suspended in 3 mL of ACN. ACN (1 mL) containing 0.45 mmol of  $\text{CF}_3\text{COOAg}$  was added to the above solution under continuous stirring. After 3 min of stirring, 2 mL of  $\text{Ag}_{18}$  (absorbance at 545 nm was kept as 0.9) was added to this mixture. The color of the solution changed from yellow to brown. Stirring was continued for 4.5 h, and the obtained suspension was centrifuged and washed with MeOH. The resulting precipitate was dissolved in hexane and centrifuged. A brown-colored supernatant was collected, and the precipitate was discarded. The purified cluster was soluble in DCM, hexane, toluene, and heptane.

### Instrumentation

Absorbance spectra were measured using a PerkinElmer Lambda 365 instrument in the range of 200–1100 nm. A Waters Synapt G2Si HDMS instrument consisting of an electrospray source, quadrupole ion guide/trap, ion mobility cell, and TOF analyzer was used for the ESI-MS measurements. CID measurements were obtained by colliding with high-purity Ar gas. All the ESI-MS spectra were measured in the positive mode. The ESI-MS sample was prepared by dissolving 1 mg of the cluster in 1 mL DCM. Then, 200  $\mu\text{L}$  of this was diluted to 2 mL and used for the electrospray measurements. Thermogravimetric (TG) analyses were carried out on a PerkinElmer TGA7 instrument under  $\text{N}_2$  atmosphere. A FEI quanta 200 scanning electron microscope fitted with a tungsten filament was used for the energy dispersive spectroscopy (EDS) measurements. X-ray photoelectron spectroscopy (XPS) was conducted using an Omicron ESCA probe spectrometer with polychromatic Mg K $\alpha$  X-rays ( $h\nu = 1253.6$  eV). IR measurements were obtained using a PerkinElmer Spectrum Two instrument. A Jobin Yvon NanoLog instrument was used for the photoluminescence measurements.

## Results and discussion

The recently reported hydride-protected  $[\text{Ag}_{18}(\text{TPP})_{10}\text{H}_{16}]^{2+}$  (abbreviated as  $\text{Ag}_{18}$  hereafter) was used as a sacrificial cluster for the synthesis of a new Ag-S cluster.<sup>34</sup>  $\text{Ag}_{18}$  was synthesized by a modified procedure previously reported by our group.<sup>35</sup> The purified  $\text{Ag}_{18}$  was dissolved in MeOH and characterized by UV-vis and ESI-MS (Fig. S1†).  $\text{Ag}_{18}$  showed two main UV-vis

absorption peaks at 545 nm and 614 nm. A peak at  $m/z$  2290 in the positive ion mode ESI-MS confirmed the formation of  $\text{Ag}_{18}$ .

In a typical synthesis, an MeOH solution of the  $\text{Ag}_{18}$  cluster was added to a mixture of  $\text{Ag-SBB}$  and  $\text{CF}_3\text{COOAg}$  in ACN. The addition of  $\text{Ag}_{18}$  to this mixture resulted in a color change from yellow to brown. The reaction was continued until the supernatant of the mixture became clear. A hexane solution of the new cluster showed two main peaks at 497 and 618 nm and two humps at 457 and 690 nm (Fig. 1A) in the UV-vis measurement. These features were different from those of  $\text{Ag}_{18}$  used as the reagent and other reported clusters.<sup>36–39</sup> The cluster showed an emission around 1100 nm when excited at 497 nm both in solution and in the solid state (inset of Fig. 1A). An ESI-MS measurement of the cluster dissolved in DCM showed an intense peak at 3676  $m/z$  in the positive mode (Fig. 1B). This peak is expanded in the inset of Fig. 1B, which shows a peak separation of 0.5 mass unit, confirming the 2+ charge state of the cluster ion. The composition of  $\text{Ag}_{34}\text{S}_3\text{SBB}_{20}^{2+}$  was assigned to this cluster from the isotopic distribution pattern, which is in good agreement with the observation of the theoretical spectrum (blue) shown in the inset of Fig. 1B.

A time-dependent experiment was also performed to monitor the synthesis process. The UV-vis spectrum of the time-dependent reaction showed a small peak shift from 30 min to 1 h of the reaction. After 1 h, there was no change in the UV-vis spectrum (Fig. 2A). The ESI-MS measurements of the time-dependent cluster synthesis showed an envelope of peaks with a 2+ charge state around  $m/z$  5000 after 30 minutes of reaction (Fig. 2B). From 1 h onwards, the species at  $m/z$  3676 became the intense one. This suggested that larger clusters were formed in the initial stages of the reaction and they decomposed to a stable smaller cluster. The higher intensity peak for the 30 min sample could be assigned to a compo-

sition of  $\text{Ag}_{47}\text{S}_7\text{SBB}_{28}^{2+}$  ( $m/z$  5156) (Fig. S2†). Two other peaks at  $m/z$  5013 and 4869 were assigned to the loss of the  $\text{Ag-SBB}$  group from the main peak. The lower mass range ESI-MS spectra showed peaks corresponding to thiolates with the general formula  $\text{Ag}_m\text{SBB}_m\text{S}_x\text{CF}_3\text{COO}_y$  (Fig. S3, Table S1†).

Tandem mass spectrometric (MS/MS) studies were performed to understand the cluster in more detail (Fig. 3A). The collision-induced dissociation (CID) of well-known silver nano-clusters showed that their solution phase stability is reflected in the gas phase dissociation.<sup>40</sup> The peak at  $m/z$  3676 was selected for CID experiments. Measurements were obtained by gradually increasing the collision energy (CE, in instrumental units) of the selected ions and after colliding with Ar. The first fragmentation started at CE 25. Two peaks were observed under this condition, which were assigned to the loss of  $\text{Ag}_3\text{SBB}_3$  and  $\text{Ag}_4\text{SBB}_4$  from the main cluster. The peak corresponding to the loss of  $\text{Ag}_4\text{SBB}_4$ , giving rise to  $\text{Ag}_{30}\text{S}_3(\text{SBB})_{16}^{2+}$ , was the dominant one. This observation was similar to the fragmentation of  $\text{Ag}_{25}(\text{SR})_{18}^-$ , where the loss of neutral  $\text{Ag}_4\text{SR}_4$  gives  $\text{Ag}_{21}(\text{SR})_{14}^-$  as the prominent species.<sup>41</sup> A fragmentation study of  $\text{Ag}_{25}(\text{SR})_{18}^-$  showed that upon increasing CE, the  $\text{Ag}_3\text{SR}_3$  unit was lost from  $\text{Ag}_{25}(\text{SR})_{18}^-$ .<sup>40</sup> In the present study, a further increase in the collision energy resulted in  $\text{Ag}_6\text{SBB}_6$  and  $\text{Ag}_7\text{SBB}_7$  losses from  $\text{Ag}_{34}\text{S}_3\text{SBB}_{20}^{2+}$ . The parent ion intensity started decreasing from CE 40 and at CE 50, the intensity of the peak  $\text{Ag}_{27}\text{S}_3\text{SBB}_{13}^{2+}$ , arising from the loss of  $\text{Ag}_7\text{SBB}_7$  became the prominent one. Ten  $\text{Ag-SBB}$  losses were observed in the MS/MS measurements. In the lower mass range, fragments such as  $\text{Ag}_5\text{SBB}_4^+$ ,  $\text{Ag}_6\text{SBB}_5^+$ ,  $\text{Ag}_7\text{SBB}_6^+$  and  $\text{Ag}_8\text{SBB}_7^+$  were also observed as the CE increased (Fig. S4).†  $\text{Ag}_6\text{SBB}_5^+$  was the dominant species in this region.

A careful analysis of the higher  $m/z$  region of the ESI-MS spectra showed less intense peaks, which could be assigned to the attachment of the trifluoroacetate ( $\text{CF}_3\text{COO}^-$ ) groups to the  $\text{Ag}_{34}\text{S}_3\text{SBB}_{20}^{2+}$  cluster (Fig. 3B). A maximum of six  $\text{CF}_3\text{COO}^-$

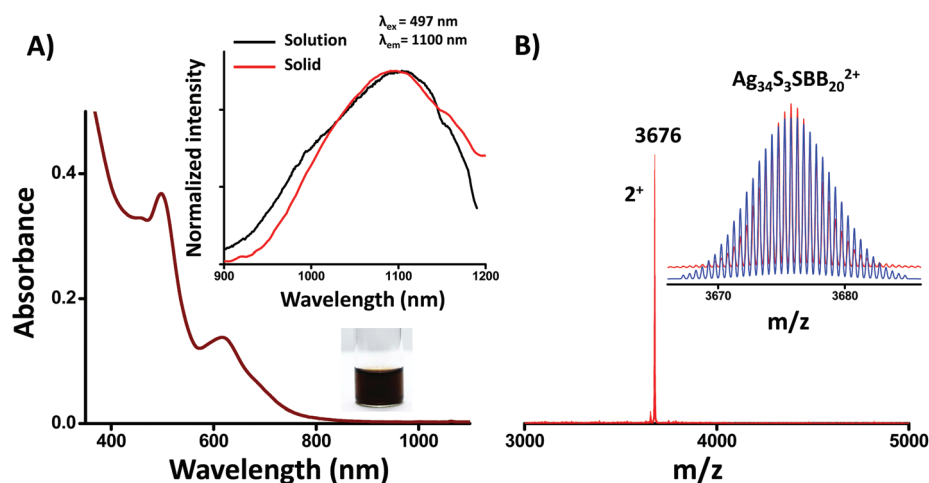


**Fig. 1** (A) UV-vis spectrum of the purified cluster in hexane showing absorption features at 457, 497, 618, and 690 nm. The luminescence spectrum of the cluster in the solution and solid state showing emission maxima around 1100 nm is given in the inset. A photograph of the cluster solution is also shown in the inset. (B) Positive mode ESI-MS spectrum of the cluster. The peak at  $m/z$  3676 is expanded and compared with the theoretical isotopic pattern (red-experimental and blue-theoretical), which matches with the composition of  $\text{Ag}_{34}\text{S}_3\text{SBB}_{20}^{2+}$ .



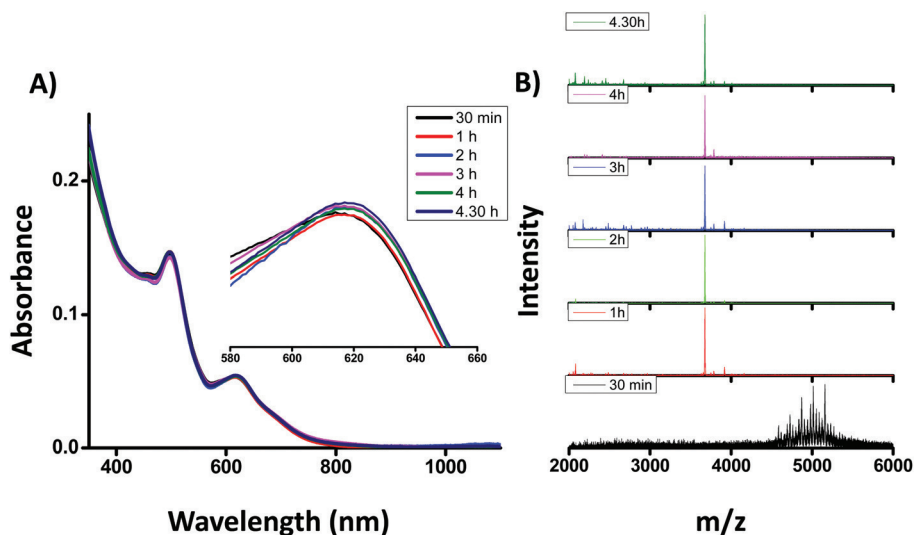


Fig. 2 (A) Time-dependent UV-vis absorption and (B) ESI-MS spectra of the cluster. The reaction was continued till 4.5 h. The absorption feature at the 618 nm region is expanded in the inset of (A), showing a small peak shift from 30 minutes to 1 h. Correspondingly, ESI-MS also showed certain changes (B).

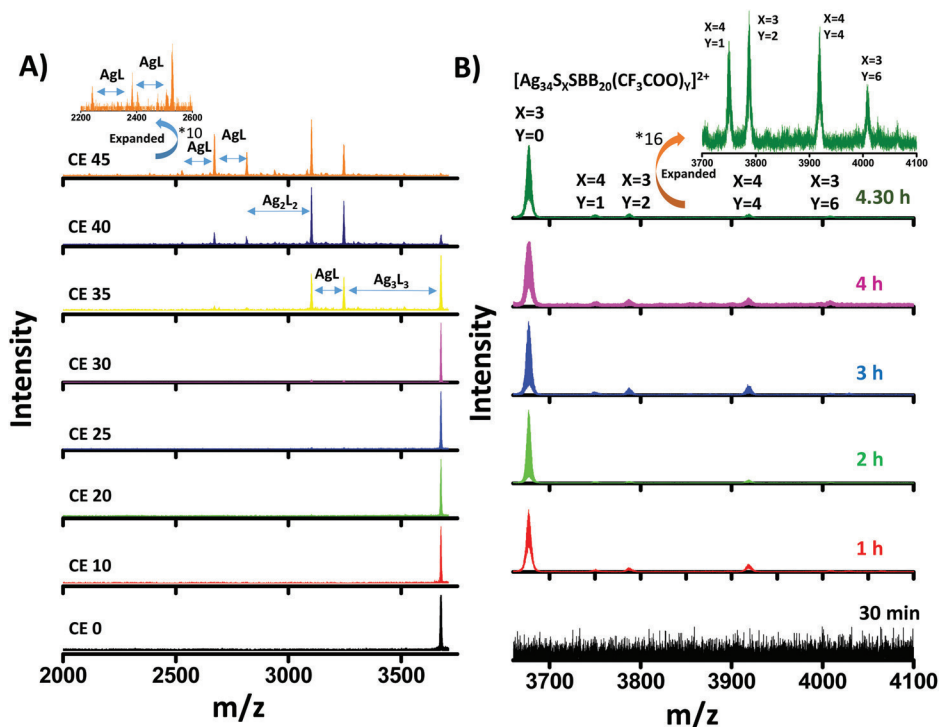


Fig. 3 Collision energy (CE)-dependent ESI-MS spectra of the  $m/z$  3676 peak (A). We have marked CE (in instrumental units). Loss of neutral  $\text{Ag}_n\text{SBB}_n$  units was observed during the measurement. Time-dependent ESI-MS spectra expanded in the higher  $m/z$  region are given in (B). Peaks corresponding to the  $\text{CF}_3\text{COO}^-$  group attachment to the main peak ( $m/z$  3676) were seen with low intensity in this region.  $\text{Ag}_{34}\text{S}_4\text{SBB}_{20}^{2+}$  formed as a by-product is also observed with the  $\text{CF}_3\text{COO}^-$  attachment.

attachments were observed. A small amount of  $\text{Ag}_{34}\text{S}_4\text{SBB}_{20}^{2+}$  formed as a byproduct was also seen with the  $\text{CF}_3\text{COO}^-$  attachment. This secondary ligand may be labile in nature and hence, it was less intense in the mass spectrum. We did not observe any change in the charge state after ligand desorption.

The charge of the cluster may be due to the cluster core arising from the magic number of electrons needed for electronic stability. It is likely that the ligand loss is not affecting the overall charge of the cluster as the ligands may be leaving as neutral entities. Carboxylates can undergo decarboxylation



and neutral species can be formed.<sup>42</sup> The decarboxylation of Ag-LA (LA = Lipoic acid) was observed during the ESI MS studies.<sup>43</sup> The fragmentation of thiolates as RH and RS-SR was also seen without a change in the charge state.<sup>44</sup> The four peaks observed in this region were assigned to  $[\text{Ag}_{34}\text{S}_4\text{SBB}_{20}(\text{CF}_3\text{COO})]^{2+}$ ,  $[\text{Ag}_{34}\text{S}_3\text{SBB}_{20}(\text{CF}_3\text{COO})_2]^{2+}$ ,  $[\text{Ag}_{34}\text{S}_4\text{SBB}_{20}(\text{CF}_3\text{COO})_4]^{2+}$ , and  $[\text{Ag}_{34}\text{S}_3\text{SBB}_{20}(\text{CF}_3\text{COO})_6]^{2+}$ . The intensity of the six  $\text{CF}_3\text{COO}^-$  attached peaks increased with time.

Infrared spectroscopic (IR) measurements were obtained to confirm the presence of  $\text{CF}_3\text{COO}^-$  as the secondary ligand. Comparative IR spectra of the cluster and the BBSH ligand and the cluster and  $\text{CF}_3\text{COOAg}$  are given in Fig. 4 and Fig. S5,<sup>†</sup> respectively. The IR spectrum of the cluster showed some new peaks along with BBSH features (Fig. 4A). New features at 720, 1137, and 1197  $\text{cm}^{-1}$  were assigned to the  $\text{CF}_3$  group. A strong peak at 1648  $\text{cm}^{-1}$  was due to the carbonyl ( $\text{C}=\text{O}$ ) stretching. The carbonyl stretching of the cluster showed a small shift towards a higher wavenumber in comparison to the observation for pure  $\text{CF}_3\text{COOAg}$ . The important difference between a thiol-protected cluster and a pure thiol is the disappearance of the S-H vibration at around 2562  $\text{cm}^{-1}$  (Fig. 4B). This confirmed the formation of the metal-sulfur bond. The aliphatic C-H stretching region is around 2850–2950  $\text{cm}^{-1}$  and the aromatic C-H stretching peaks appear at around 3000–3100  $\text{cm}^{-1}$ . After cluster formation, the aromatic C-H stretching was not prominent. An earlier study of thiol-protected gold clusters showed the overlap of aromatic and aliphatic C-H stretchings.<sup>45</sup>

XPS measurements confirmed the presence of silver, sulfur, and fluorine in the synthesized cluster. Silver showed a higher binding energy compared to  $\text{Ag}(0)$  (368.0 eV), which confirmed the presence of Ag in the univalent state (Fig. S6<sup>†</sup>). Thermogravimetric (TG) analysis of the cluster showed 54.3% weight loss due to organic ligands (Fig. 5). A cluster composition of  $[\text{Ag}_{34}\text{S}_3\text{SBB}_{20}(\text{CF}_3\text{COO})_6]^{2+}$  with two  $\text{CF}_3\text{COO}^-$  groups as the counter ions matched this mass loss. The SEM EDS

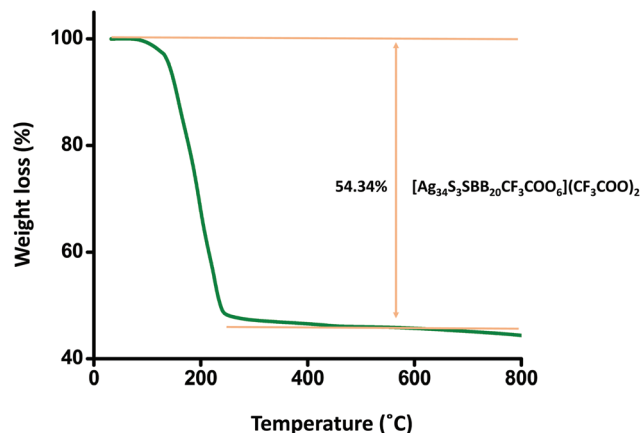


Fig. 5 TG curve of the cluster showing 54.3% weight loss. The loss corresponded to the composition of  $[\text{Ag}_{34}\text{S}_3\text{SBB}_{20}\text{CF}_3\text{COO}_6](\text{CF}_3\text{COO})_2$ .

result with an Ag:S:F ratio of 1:0.64:0.71 was also in good agreement with the assigned formula (Fig. S7<sup>†</sup>).

To understand the factors affecting cluster formation, different control experiments were performed. The first one involved the determination of the role of  $\text{CF}_3\text{COOAg}$  in synthesis. In this case,  $\text{Ag}_{18}$  was added to a suspension of Ag-SBB in ACN. The reaction was continued for 4.5 h. After that, the product was purified by hexane precipitation. The product formed was red in color and showed an absorption at 440 nm, which was different from that of the  $\text{CF}_3\text{COOAg}$ -added cluster (Fig. S8<sup>†</sup>). Similarly, we tried an experiment with  $\text{Ag}_{18}$  synthesized using  $\text{CF}_3\text{COOAg}$  as the precursor, which may have  $\text{CF}_3\text{COO}^-$  groups as counter ions. In this case, the product formed was also different and showed a broad absorption at 465 nm (Fig. S9<sup>†</sup>). From these control experiments, it was understood that the addition of  $\text{CF}_3\text{COOAg}$  was crucial in this synthesis. In order to understand the role of  $\text{CF}_3\text{COOAg}$  in the synthesis, the yellow solution formed after the addition  $\text{CF}_3\text{COOAg}$  to Ag-SBB was further investigated. The UV-vis

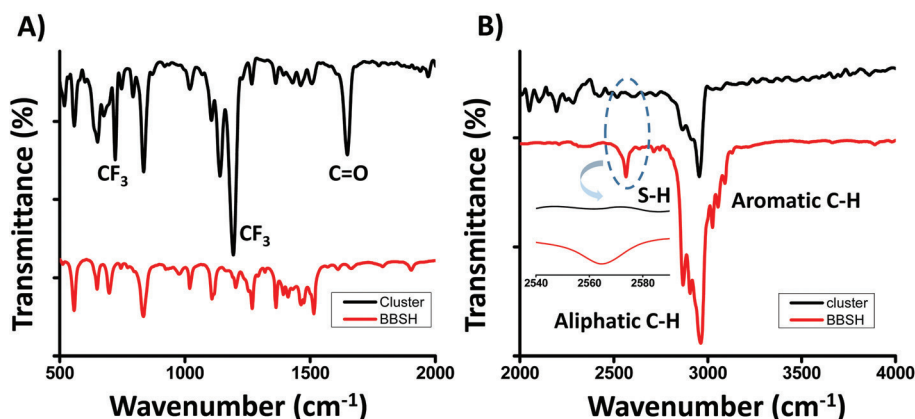


Fig. 4 Comparison of the IR spectra of the cluster and pure BBSH thiol. The cluster showed IR features of both thiol and  $\text{CF}_3\text{COO}^-$  groups (A and B). The IR features of the  $\text{CF}_3\text{COO}^-$  group were seen at 720, 1137 and 1197  $\text{cm}^{-1}$  (due to  $\text{CF}_3$ ) as well as at 1648  $\text{cm}^{-1}$  (due to  $\text{C}=\text{O}$ ). The formation of the metal-sulfur bond is clear from the absence of the S-H vibration at 2562  $\text{cm}^{-1}$  for the cluster; this region is expanded in the inset.

spectrum of this solution showed two humps at 235 and 290 nm (Fig. S10†). To obtain more details, ESI-MS of this solution was also measured. The ESI-MS studies (Fig. S11†) showed that smaller silver-chalcogenolate clusters (SCC) were formed in the solution by the reaction of thiolate and  $\text{CF}_3\text{COOAg}$ . The formation of SCC by the reaction of Ag-thiolates with  $\text{CF}_3\text{COOAg}$  is known in the case of SCC metal-organic frameworks (MOFs).<sup>46</sup> These SCCs formed were reacted with  $\text{Ag}_{18}$ , and new clusters were obtained.

## Conclusions

In conclusion, we synthesized a new Ag-S-type cluster and characterized it using various techniques including ESI-MS, UV-vis, TGA, IR, and XPS. A reaction between a hydride and phosphine-protected silver cluster and silver-chalcogenolate clusters produced the new cluster. The UV-vis spectrum showed four absorption features at 497, 457, 618, and 690 nm. The cluster showed NIR-II (1000–1400 nm) emission around the 1100 nm region, which is the ideal window for bio-imaging. The prominent ESI-MS peak at  $m/z$  3676 was assigned to the composition of  $\text{Ag}_{34}\text{S}_3\text{SBB}_{20}^{2+}$ . A detailed investigation using ESI-MS and other techniques such as TGA and EDS pointed to a composition of  $[\text{Ag}_{34}\text{S}_3\text{SBB}_{20}(\text{CF}_3\text{COO})_6]^{2+}$  for the cluster with  $\text{CF}_3\text{COO}^-$  as counter ions.

## Conflicts of interest

There are no conflicts to declare.

## Acknowledgements

We thank the Department of Science and Technology, Government of India for constantly supporting our research program on nanomaterials. C. K. M. thanks the CSIR for a research fellowship. D. G. thanks IITM for her fellowship and M. B. thanks UGC for his fellowship.

## References

- 1 A. Mathew and T. Pradeep, *Part. Part. Syst. Charact.*, 2014, **31**, 1017–1053.
- 2 R. Jin, C. Zeng, M. Zhou and Y. Chen, *Chem. Rev.*, 2016, **116**, 10346–10413.
- 3 J. F. Corrigan, O. Fuhr and D. Fenske, *Adv. Mater.*, 2009, **21**, 1867–1871.
- 4 V. N. Soloviev, A. Eichhoefer, D. Fenske and U. Banin, *J. Am. Chem. Soc.*, 2001, **123**, 2354–2364.
- 5 Y.-P. Xie, J.-L. Jin, G.-X. Duan, X. Lu and T. C. W. Mak, *Coord. Chem. Rev.*, 2017, **331**, 54–72.
- 6 A. Dass, A. Stevenson, G. R. Dubay, J. B. Tracy and R. W. Murray, *J. Am. Chem. Soc.*, 2008, **130**, 5940–5946.
- 7 A. Desireddy, B. E. Conn, J. Guo, B. Yoon, R. N. Barnett, B. M. Monahan, K. Kirschbaum, W. P. Griffith, R. L. Whetten, U. Landman and T. P. Bigioni, *Nature*, 2013, **501**, 399–402.
- 8 H. Yang, Y. Wang, H. Huang, L. Gell, L. Lehtovaara, S. Malola, H. Hakkinen and N. Zheng, *Nat. Commun.*, 2013, **4**, 2422.
- 9 M. Zhu, C. M. Aikens, F. J. Hollander, G. C. Schatz and R. Jin, *J. Am. Chem. Soc.*, 2008, **130**, 5883–5885.
- 10 P. D. Jadzinsky, G. Calero, C. J. Ackerson, D. A. Bushnell and R. D. Kornberg, *Science*, 2007, **318**, 430–433.
- 11 O. Fuhr, S. Dehnen and D. Fenske, *Chem. Soc. Rev.*, 2013, **42**, 1871–1906.
- 12 N. Herron, J. C. Calabrese, W. E. Farneth and Y. Wang, *Science*, 1993, **259**, 1426–1428.
- 13 I. G. Dance, A. Choy and M. L. Scudder, *J. Am. Chem. Soc.*, 1984, **106**, 6285–6295.
- 14 C. Anson, A. Eichhoefer, I. Issac, D. Fenske, O. Fuhr, P. Sevilano, C. Persau, D. Stalke and J. Zhang, *Angew. Chem., Int. Ed.*, 2008, **47**, 1326–1331.
- 15 Y. Wang, Y.-H. Liu, Y. Zhang, F. Wang, P. J. Kowalski, H. W. Rohrs, R. A. Loomis, M. L. Gross and W. E. Buhro, *Angew. Chem., Int. Ed.*, 2012, **51**, 6154–6157.
- 16 D. Fenske, C. E. Anson, A. Eichhoefer, O. Fuhr, A. Ingendoh, C. Persau and C. Richert, *Angew. Chem., Int. Ed.*, 2005, **44**, 5242–5246.
- 17 R. Langer, B. Breitung, L. Wuensche, D. Fenske and O. Fuhr, *Z. Anorg. Allg. Chem.*, 2011, **637**, 995–1006.
- 18 S. Bestgen, O. Fuhr, B. Breitung, V. S. Kiran Chakravadhanula, G. Guthausen, F. Hennrich, W. Yu, M. M. Kappes, P. W. Roesky and D. Fenske, *Chem. Sci.*, 2017, **8**, 2235–2240.
- 19 K. Tang, X. Xie, Y. Zhang, X. Zhao and X. Jin, *Chem. Commun.*, 2002, 1024–1025, DOI: 10.1039/b201116f.
- 20 X. Jin, K. Tang, S. Jia and Y. Tang, *Polyhedron*, 1996, **15**, 2617–2622.
- 21 G. Li, Z. Lei and Q.-M. Wang, *J. Am. Chem. Soc.*, 2010, **132**, 17678–17679.
- 22 S. Jin, S. Wang, Y. Song, M. Zhou, J. Zhong, J. Zhang, A. Xia, Y. Pei, M. Chen, P. Li and M. Zhu, *J. Am. Chem. Soc.*, 2014, **136**, 15559–15565.
- 23 M. Brust, M. Walker, D. Bethell, D. J. Schiffrin and R. Whyman, *J. Chem. Soc., Chem. Commun.*, 1994, 801–802, DOI: 10.1039/C39940000801.
- 24 R. L. Donkers, D. Lee and R. W. Murray, *Langmuir*, 2004, **20**, 1945–1952.
- 25 T. U. B. Rao and T. Pradeep, *Angew. Chem., Int. Ed.*, 2010, **49**, 3925–3929.
- 26 X. Meng, Q. Xu, S. Wang and M. Zhu, *Nanoscale*, 2012, **4**, 4161–4165.
- 27 T. U. B. Rao, B. Nataraju and T. Pradeep, *J. Am. Chem. Soc.*, 2010, **132**, 16304–16307.
- 28 M. Bodiuzzaman, A. Ghosh, K. S. Sugi, A. Nag, E. Khatun, B. Varghese, G. Paramasivam, S. Antharjanam, G. Natarajan and T. Pradeep, *Angew. Chem., Int. Ed.*, 2019, **58**, 189–194.

- 29 C. Zeng, Y. Chen, A. Das and R. Jin, *J. Phys. Chem. Lett.*, 2015, **6**, 2976–2986.
- 30 K. R. Krishnadas, A. Ghosh, A. Baksi, I. Chakraborty, G. Natarajan and T. Pradeep, *J. Am. Chem. Soc.*, 2016, **138**, 140–148.
- 31 S. Bhat, A. Baksi, S. K. Mudedla, G. Natarajan, V. Subramanian and T. Pradeep, *J. Phys. Chem. Lett.*, 2017, **8**, 2787–2793.
- 32 R. Gui, H. Jin, Z. Wang and L. Tan, *Coord. Chem. Rev.*, 2015, **296**, 91–124.
- 33 X. Kang and M. Zhu, *Chem. Soc. Rev.*, 2019, **48**, 2422–2457.
- 34 M. S. Bootharaju, R. Dey, L. E. Gevers, M. N. Hedhili, J.-M. Basset and O. M. Bakr, *J. Am. Chem. Soc.*, 2016, **138**, 13770–13773.
- 35 A. Ghosh, M. Bodiuzzaman, A. Nag, M. Jash, A. Baksi and T. Pradeep, *ACS Nano*, 2017, **11**, 11145–11151.
- 36 C. P. Joshi, M. S. Bootharaju, M. J. Alhilaly and O. M. Bakr, *J. Am. Chem. Soc.*, 2015, **137**, 11578–11581.
- 37 L. G. AbdulHalim, M. S. Bootharaju, Q. Tang, S. Del Gobbo, R. G. AbdulHalim, M. Eddaoudi, D.-e. Jiang and O. M. Bakr, *J. Am. Chem. Soc.*, 2015, **137**, 11970–11975.
- 38 B. Li, R.-W. Huang, J.-H. Qin, S.-Q. Zang, G.-G. Gao, H.-W. Hou and T. C. W. Mak, *Chem. – Eur. J.*, 2014, **20**, 12416–12420.
- 39 X.-J. Xi, J.-S. Yang, J.-Y. Wang, X.-Y. Dong and S.-Q. Zang, *Nanoscale*, 2018, **10**, 21013–21018.
- 40 P. Chakraborty, A. Baksi, E. Khatun, A. Nag, A. Ghosh and T. Pradeep, *J. Phys. Chem. C*, 2017, **121**, 10971–10981.
- 41 C. A. Fields-Zinna, J. S. Sampson, M. C. Crowe, J. B. Tracy, J. F. Parker, A. M. de Ney, D. C. Muddiman and R. W. Murray, *J. Am. Chem. Soc.*, 2009, **131**, 13844–13851.
- 42 G. Kataby, M. Cojocaru, R. Prozorov and A. Gedanken, *Langmuir*, 1999, **15**, 1703–1708.
- 43 M. van der Linden, A. Barendregt, A. J. van Bunningen, P. T. K. Chin, D. Thies-Weesie, F. M. F. de Groot and A. Meijerink, *Nanoscale*, 2016, **8**, 19901–19909.
- 44 D. M. Black, N. Bhattarai, R. L. Whetten and S. B. H. Bach, *J. Phys. Chem. A*, 2014, **118**, 10679–10687.
- 45 M. Farrag, M. Tschurl, A. Dass and U. Heiz, *Phys. Chem. Chem. Phys.*, 2013, **15**, 12539–12542.
- 46 R.-W. Huang, Y.-S. Wei, X.-Y. Dong, X.-H. Wu, C.-X. Du, S.-Q. Zang and T. C. W. Mak, *Nat. Chem.*, 2017, **9**, 689–697.

## Electronic Supplementary Information (ESI):

### Formation of a new $\text{Ag}_{34}\text{S}_3\text{SBB}_{20}(\text{CF}_3\text{COO})_6^{2+}$ cluster from a hydride protected silver cluster

C. K. Manju, Debasmita Ghosh, Mohammad Bodiuzzaman, and Thalappil Pradeep\*

*DST Unit of Nanoscience (DST UNS) and Thematic Unit of Excellence,*

*Department of Chemistry, Indian Institute of Technology Madras,*

*Chennai 600036, India*

*Email:pradeep@iitm.ac.in*

#### Table of contents

No	Description	Page No
S1	Characterization of $\text{Ag}_{18}$	2
S2	ESI MS spectrum of 30 min reaction product	3
S3	Lower mass region of time-dependent cluster sunthesis	4
S4	ESI MS/MS spectra of the cluster at higher collition energy	5
S5	Comparative IR spectrum of cluster and $\text{CF}_3\text{COOAg}$	6
S6	XPS spectrum of the cluster	7
S7	SEM EDS spectrum and mapping of the cluster	8
S8	UV-vis spectrum of the control experiment without the addition of $\text{CF}_3\text{COOAg}$	9
S9	UV-vis spectrum of the control experiment with $\text{Ag}_{18}$ synthesized using $\text{CF}_3\text{COOAg}$ as a precursor	10
S10	UV-vis spectrum of the reaction between Ag-SBB and $\text{CF}_3\text{COOAg}$	11
S11	ESI MS spectrum of the reaction between Ag-SBB with $\text{CF}_3\text{COOAg}$	12

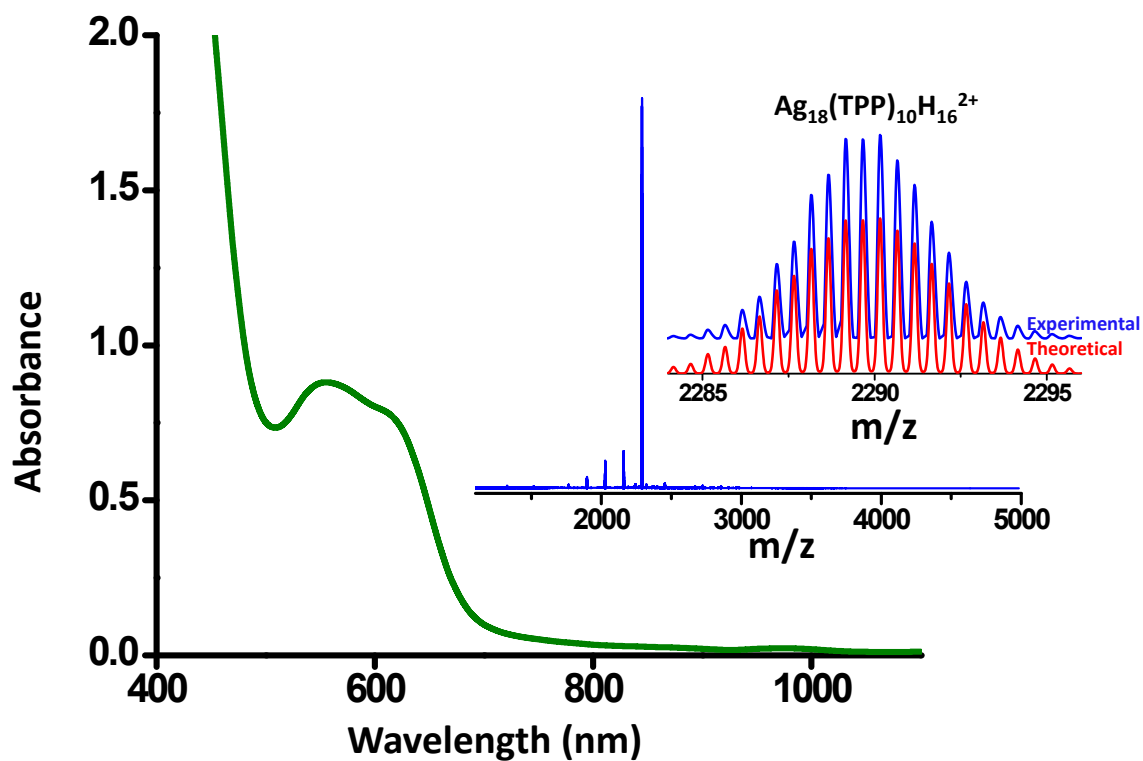


**Fig. S1** UV-vis spectrum of  $\text{Ag}_{18}$  showed two main peaks at 545 and 614 nm. ESI MS spectrum is given inset. The peak at  $m/z$  2290 is expanded and compared with the theoretical spectrum of  $\text{Ag}_{18}(\text{TPP})_{10}\text{H}_{16}^{2+}$ .

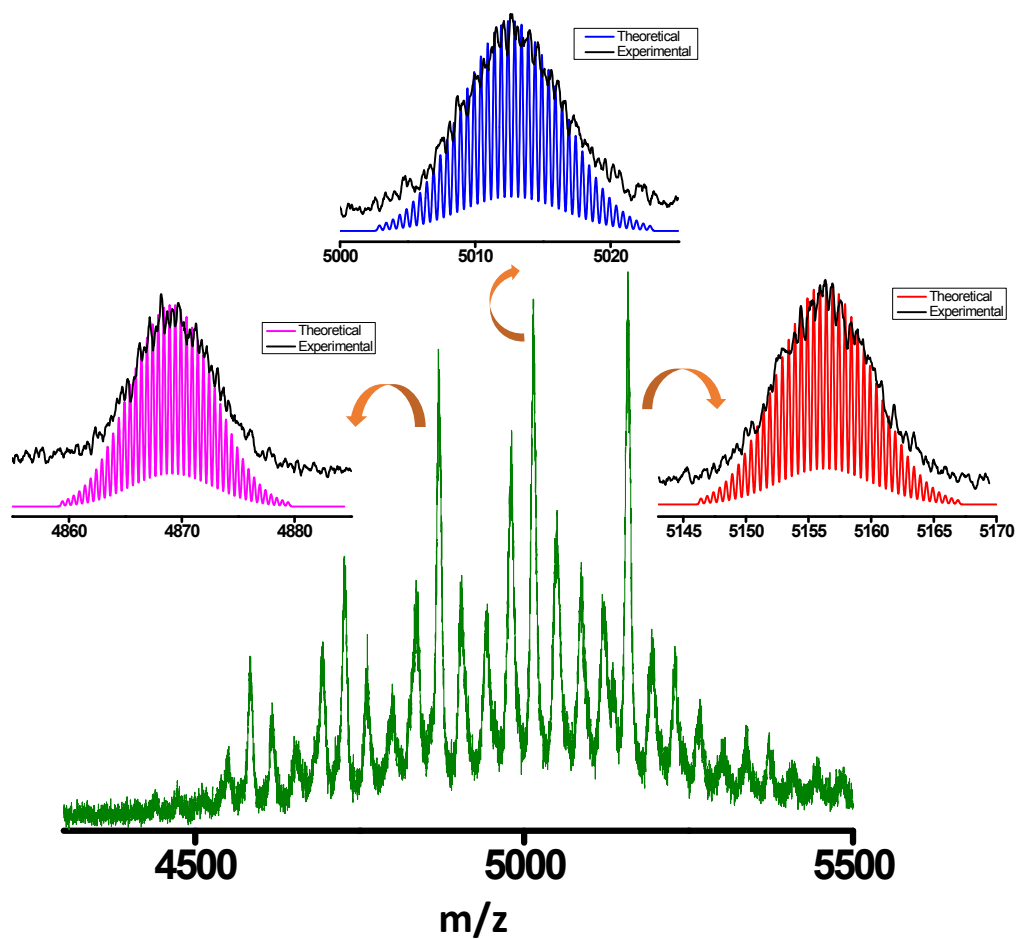


**Fig. S2** ESI MS spectrum of 30 min reaction product. Three major peaks are seen at  $m/z$  5156, 5013, and 4869 and are assigned as  $\text{Ag}_{47}\text{S}_7\text{SBB}_{28}^{2+}$ ,  $\text{Ag}_{46}\text{S}_7\text{SBB}_{27}^{2+}$ , and  $\text{Ag}_{45}\text{S}_7\text{SBB}_{26}^{2+}$  respectively.

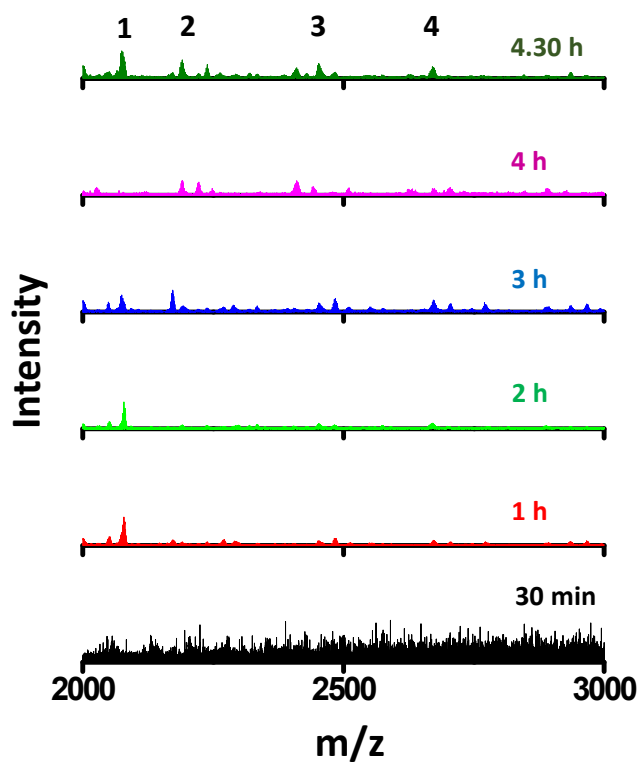


**Fig. S3** Lower mass region of time-dependent cluster synthesis. Assignments for the species 1, 2, 3 and 4 are given in table S2.

No	Assignment	m/z
1	$\text{Ag}_6\text{SSBB}_7\text{CF}_3\text{COO}^+$	2045
2	$\text{Ag}_6\text{S}_2\text{SBB}_7\text{CF}_3\text{COO}^+$	2077
3	$\text{Ag}_6\text{S}_2\text{SBB}_7(\text{CF}_3\text{COO})_2^+$	2189
4	$\text{Ag}_8\text{SBB}_7(\text{CF}_3\text{COO})_5^+$	2677

**Table. S1** Thiolates species present in the lower mass region of time-dependent ESI MS.



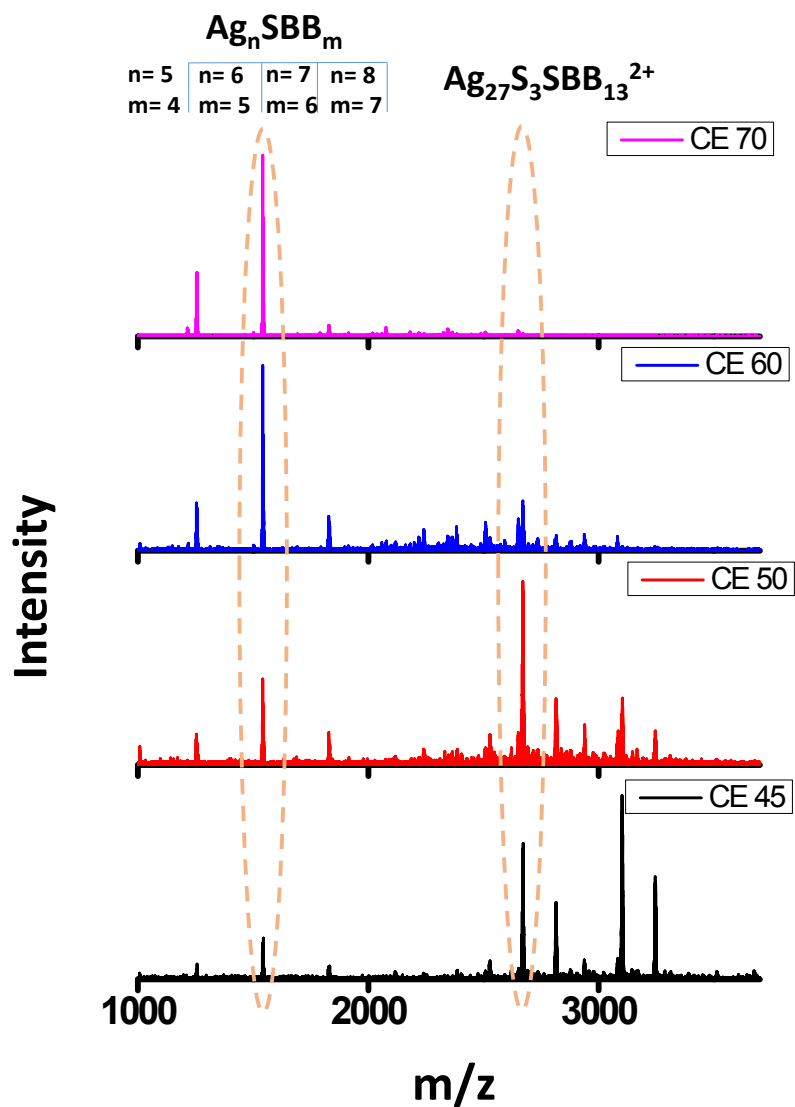
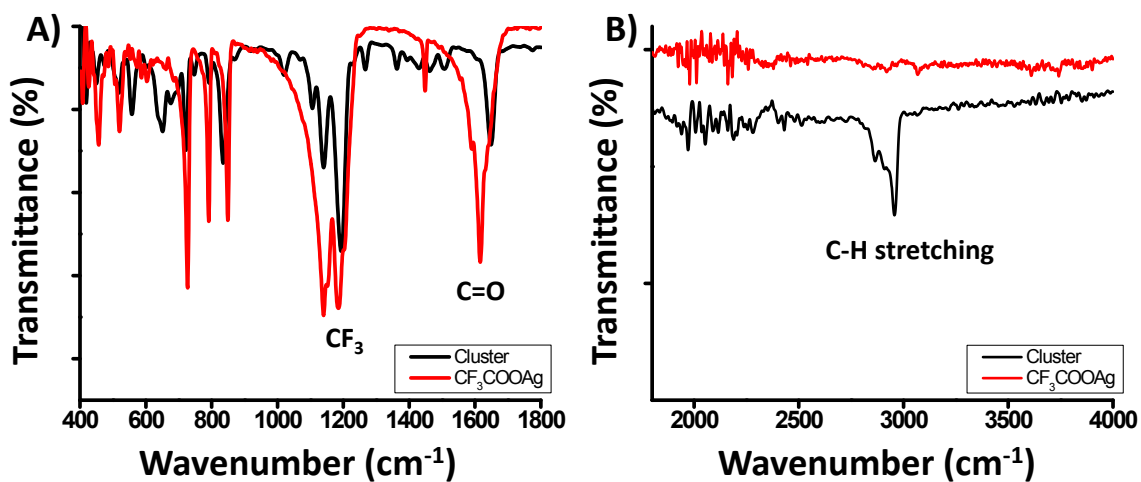


**Fig. S4** ESI MS/MS spectrum of the cluster at higher collision energy (CE, in instrumental unit). Intensity of  $\text{Ag}_{27}\text{S}_3\text{SBB}_{13}^{2+}$  peak increased as the CE increased. At higher CE,  $\text{Ag}_8\text{SBB}_7^+$ ,  $\text{Ag}_7\text{SBB}_6^+$ ,  $\text{Ag}_6\text{SBB}_5^+$  and  $\text{Ag}_5\text{SBB}_4^+$  were also observed in the lower mass region.



**S5** Comparison of the IR spectrum of cluster and  $\text{CF}_3\text{COOAg}$  (A and B). Cluster showed peaks corresponding to  $\text{CF}_3$  and  $\text{C=O}$  groups.

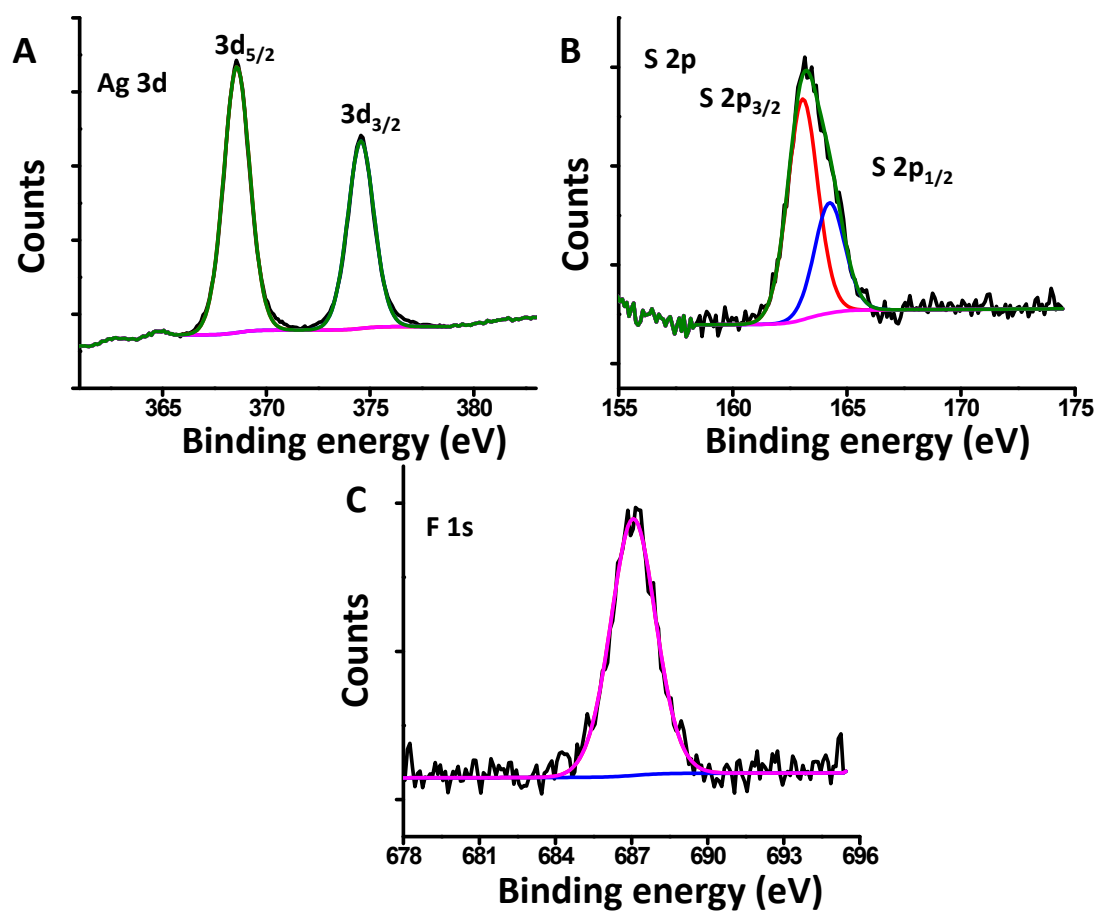


**Fig. S6** XPS spectrum of cluster showed the presence of Ag, S and F. Expanded region for (A) Ag 3d, (B) S 2p, and (C) F 1s.

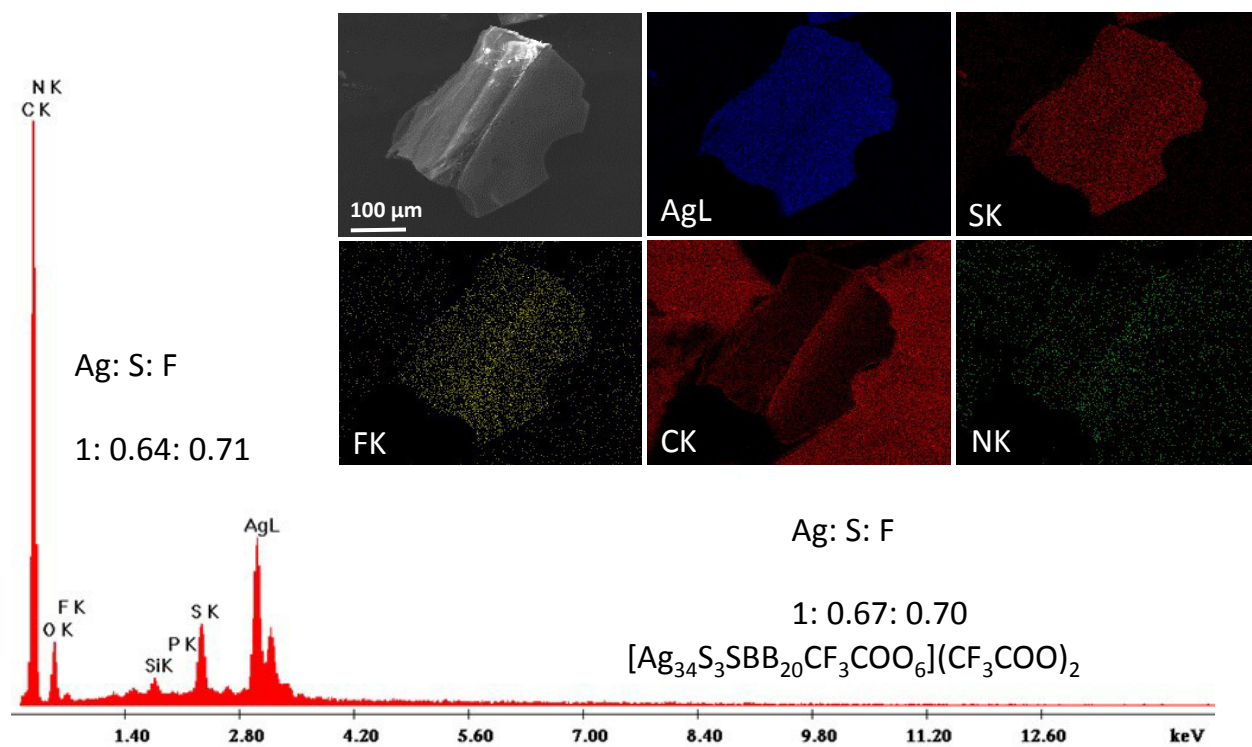


**Fig. S7** SEM EDS spectrum and elemental mapping of the cluster.

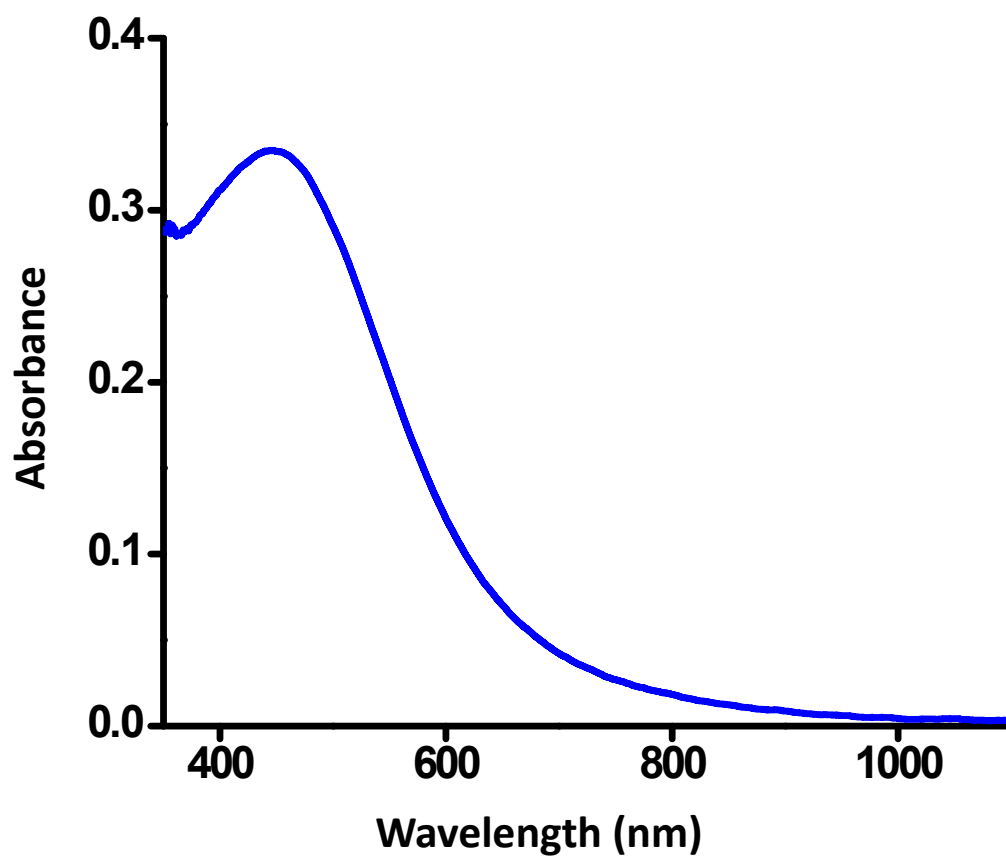


**Fig. S8** UV-vis spectrum of the control experiment without the addition of  $\text{CF}_3\text{COOAg}$ . A hexane solution of this showed a peak at 440 nm.

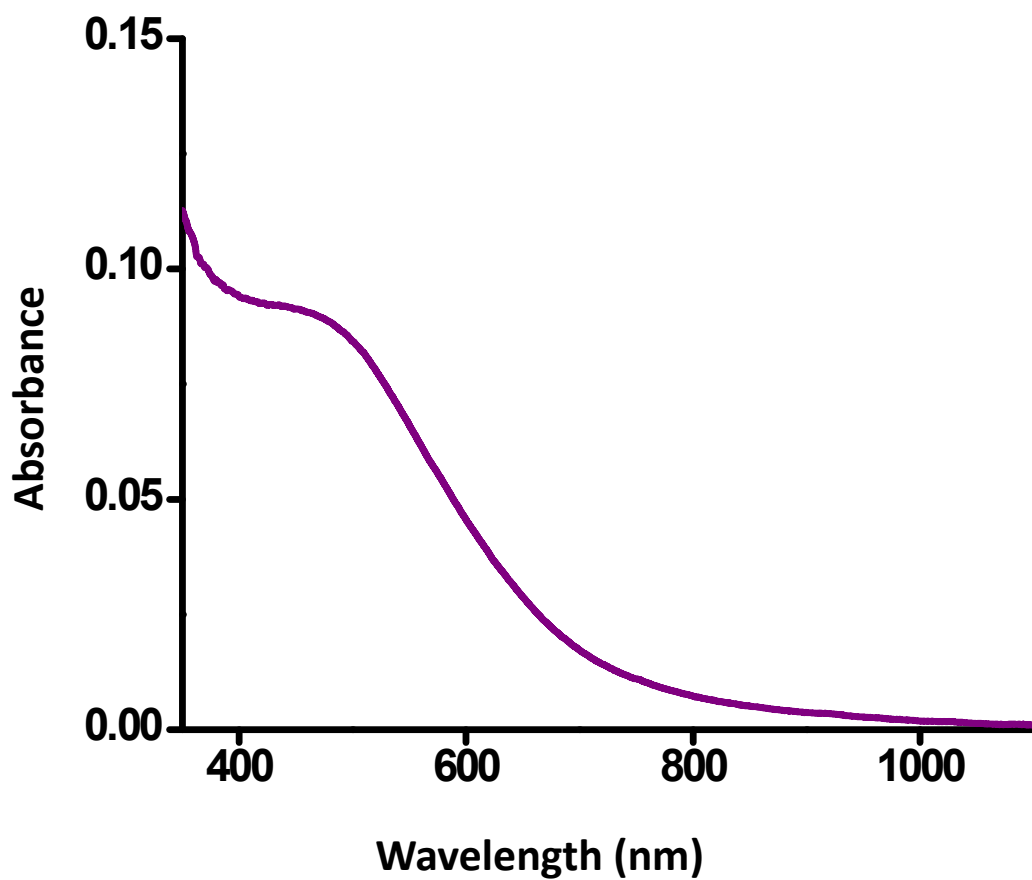


**Fig. S9** UV-vis spectrum of the control experiment with Ag<sub>18</sub> synthesized using CF<sub>3</sub>COOAg as a precursor. This sample in hexane showed a broad peak at 465 nm.

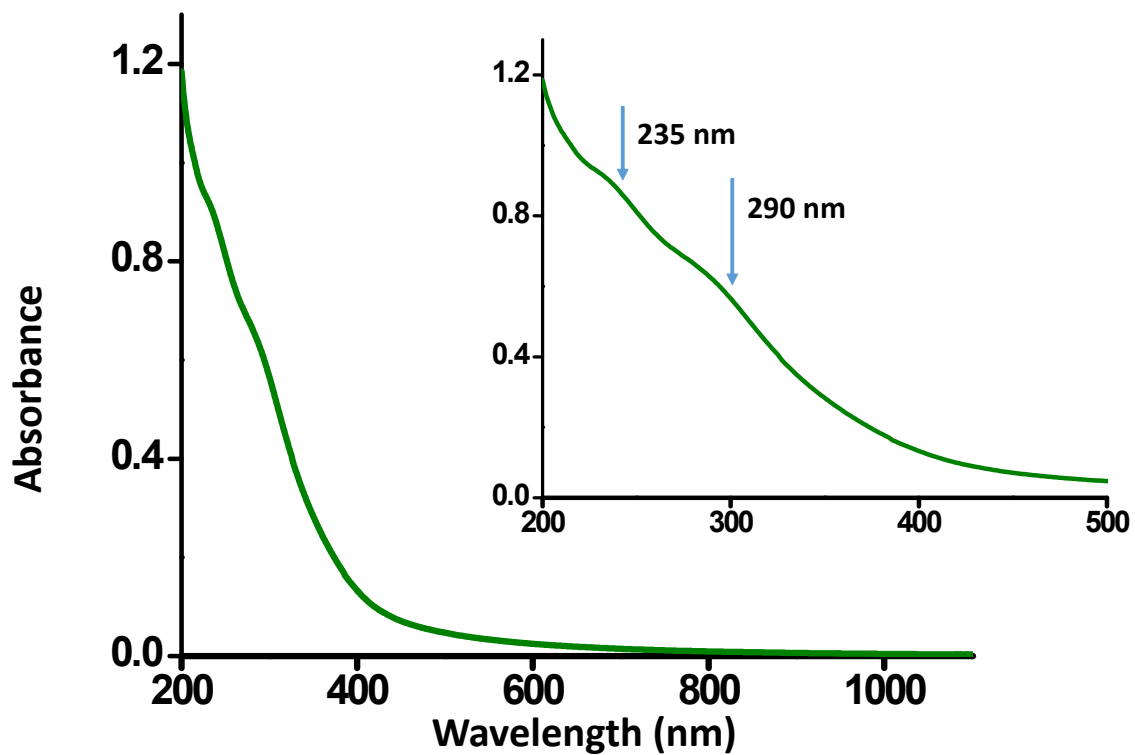


**Fig. S10** UV-vis spectrum of the reaction between Ag-SBB and  $\text{CF}_3\text{COOAg}$ . The 200-500 nm region is expanded in the inset. Two humps were observed at 235 nm and 290 nm.



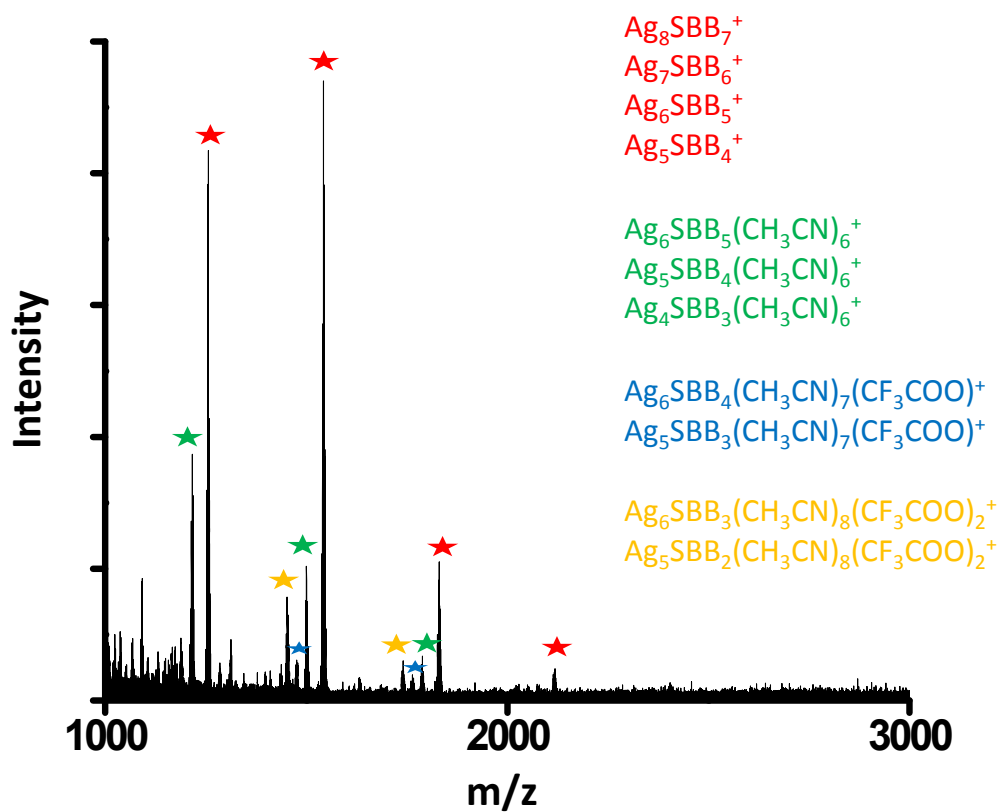


**Fig. S11** ESI MS spectrum of the reaction between Ag-SBB and  $CF_3COOAg$ . Formation of smaller silver-chalcogenolate clusters were observed.

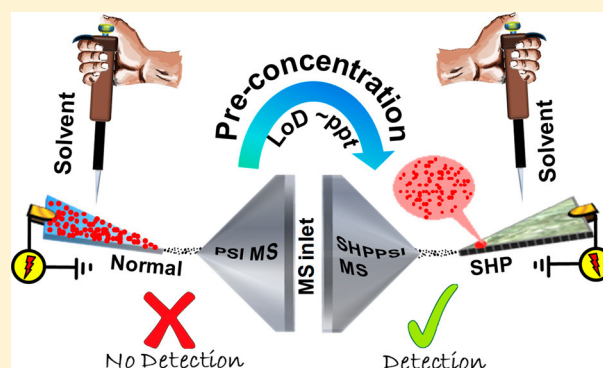
# Sub-Parts-per-Trillion Level Detection of Analytes by Superhydrophobic Preconcentration Paper Spray Ionization Mass Spectrometry (SHPPSI MS)

Pallab Basuri, Avijit Baidya,<sup>1b</sup> and Thalappil Pradeep\*<sup>1b</sup>

DST Unit of Nanoscience (DST UNS), Thematic Unit of Excellence (TUE), Department of Chemistry, Indian Institute of Technology Madras, Chennai 600036, India

## S Supporting Information

**ABSTRACT:** A new kind of ambient ionization method named superhydrophobic preconcentration paper spray ionization mass spectrometry (SHPPSI MS) is introduced, where superhydrophobicity and paper spray mass spectrometry (PS MS) are coupled. The SHPPSI MS requires only microliter amounts of analyte solutions, allows easy sampling procedure, and provides high sensitivity for a diverse array of analytes. It can be used to detect food adulteration at extremely low concentrations. The experimental methodology involves modifying one of the surfaces of a triangularly cut filter paper to make it acquire low surface energy by drop casting a green and ecofriendly superhydrophobic coating material over it followed by drying. A micrometer scale defect was made at close proximity to one of the tips of the paper using a pin. Preconcentration of the sample was accomplished by allowing a 10  $\mu$ L droplet of an aqueous solution of the analyte to stand at the defect followed by drying naturally. The dried paper was used as the substrate for paper spray mass spectrometry by eluting the analyte with a suitable solvent. This novel technique was used to detect melamine in adulterated milk, whose detection at the ppt level in milk normally needs sophisticated instruments, a larger amount of sample, and a complex sampling procedure, including further purification and separation. The SHPPSI MS detects melamine directly from milk at the sub-ppb level by simply putting a microdroplet of adulterated milk at the substrate and eluting the sample with methanol. This paper-based technique can be a promising tool for direct sensing of analytes such as drugs in body fluids, pesticides in water and soil, etc.



Ambient ionization mass spectrometry is one of the fast evolving areas of analytical mass spectrometry. Electrospray ionization (ESI),<sup>1</sup> desorption electrospray ionization (DESI),<sup>2–4</sup> low-temperature plasma ionization (LTP)<sup>5–7</sup> and atmospheric pressure chemical ionization (APCI)<sup>8–10</sup> are examples of ambient ionization techniques. Paperspray ionization (PSI),<sup>11,12</sup> where a sample in the form of a solution is ionized from the tip of a paper using an applied electric field in air, is one of the variants of the electrospray ionization method. Paper spray in diverse forms such as leaf spray,<sup>13</sup> cloth spray,<sup>14</sup> spray from polymer,<sup>15</sup> or glass<sup>16</sup> are used for the analysis of blood clots,<sup>17,18</sup> body fluids,<sup>19</sup> forensic specimens,<sup>20</sup> food stuff,<sup>21</sup> and catalytic reactions.<sup>22</sup> Inherent properties of the paper can be modified by incorporating nanostructures<sup>23–25</sup> leading to low-voltage ionization, and the technique has been used for the analysis of small molecules, such as drugs, pesticides, adulterating agents, etc., present in body fluids, food, and water.

While a paper modified by nanostructures<sup>26,27</sup> can enhance ionization as demonstrated by us previously, it can also be a platform for preconcentration. This can be done effectively by concentrating the analyte at the tip of a triangularly cut paper

by drop casting droplets at the tip and evaporating the solvent leading to the deposition of the analyte and by repeating the process. The process of preconcentration can be achieved spontaneously on a superhydrophobic (SHP) paper. By doing this, preconcentration and ionization steps can be combined on the paper, making sample preparation simpler and rapid, which leads to improved limits of detection for a chosen analyte in solution.

The use of hydrophobic paper in paperspray ionization has already been demonstrated by Badu-Tawiah et al., which results in better ionization as well as lower detection limits. The method involves a silane coated hydrophobic paper spray technique to enhance the sensitivity of the detection. Going to the limit of detection in the range of the sub-ppt level is indeed a challenge.<sup>28,29</sup>

Herein, we demonstrate that the preconcentration technique can be used efficiently for mass spectrometric detection of an analyte from a complex mixture, at a low concentration, down

Received: January 9, 2019

Accepted: May 9, 2019

Published: May 9, 2019

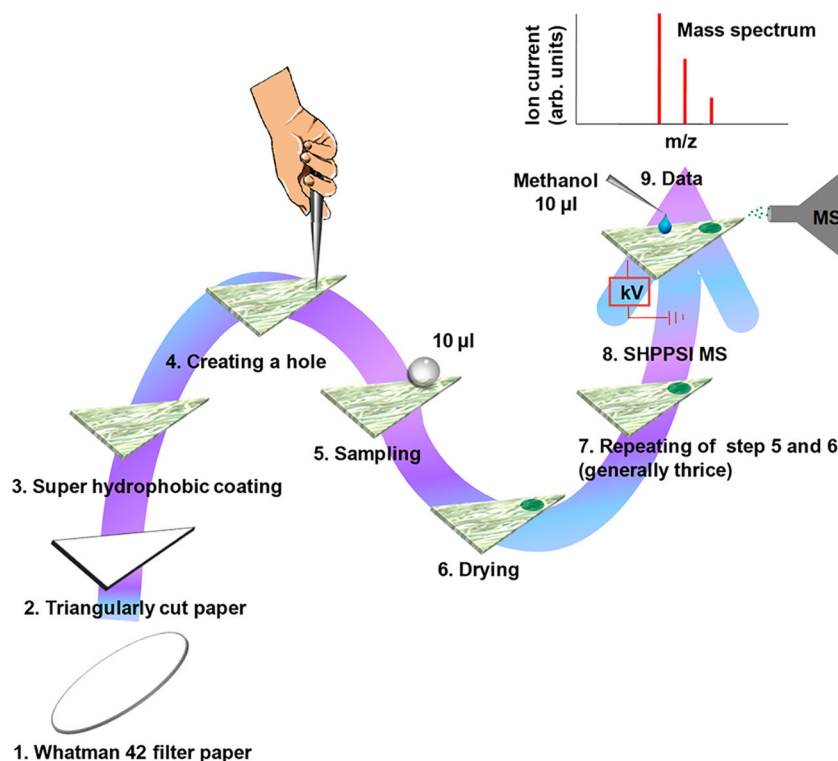


**Figure 1.** Schematic representation of the consecutive steps involved in the experimental setup for SHPPSI MS. The SHP coating can be made by any of the methods commonly used for making such surfaces.

to picomolar or sub-ppt levels. We combine selective localization and ionization of the analyte to achieve ultralow detection without sample preparation. The aforementioned modified paperspray ionization technique named superhydrophobic preconcentration paperspray ionization mass spectrometry (SHPPSI MS) is introduced here. In SHPPSI MS, the position of sample preconcentration over the substrate, which affects the ionization efficiency, can be manipulated depending upon the user's wish. Application of SHPPSI MS is demonstrated with analytes having different functionalities. The paper also illustrates application of the methodology for the detection of melamine, an adulterant in commercial milk. Melamine is a trimer of cyanamide which contains 66% nitrogen in its molecular mass. It is used as one of the major adulterants in commercially available milk to make false quantification of protein content in milk due to enhanced nitrogen, which increases the market value of the product. Detection of melamine in very low concentration needs sophisticated instruments, e.g., high-pressure liquid chromatography (HPLC),<sup>30</sup> gas chromatography/mass spectrometry (GC/MS),<sup>31</sup> nuclear magnetic resonance (NMR),<sup>32</sup> fluorescence polarization immunoassay (FPIA),<sup>33</sup> enzyme-linked immunosorbent assay (ELISA),<sup>34,35</sup> etc. It also requires complex sample preparation, purification, and pretreatment.

Prolonged melamine uptake leads to an adverse effect on human health. Renal dysfunction as well as kidney and bladder stones due to crystallization of melamine have been demonstrated in animals.<sup>36–38</sup>

## MATERIALS AND METHODS

**Chemicals and Materials.** Caffeine, rhodamine 6G, and methyl orange were purchased from Sigma-Aldrich, and HPLC grade methanol was purchased either from Sigma or Rankem.

Diazepam was purchased as a medicine. All the chemicals were used without further pretreatment and purification. Milk was purchased from the local market for all the studies.

**Synthesis of the Superhydrophobic Material.** Synthesis protocol of the superhydrophobic material followed a recent publication from our group.<sup>39</sup> Briefly, a mixture of different functionalized silanes, aminosilane (0.92 v/v%) and fluorosilane (0.61 v/v%), was stirred in water in room temperature for 6 to 7 h. Finally, the well-dispersed composite suspension was used directly for the preparation of the substrate.

**Preparation of the Paper.** Superhydrophobic paper was prepared by the spray coating technique where the triangularly cut Whatman 42 filter paper was spray coated with the as-synthesized clay material. Finally, the coated paper was dried under ambient conditions and was used directly for SHPPSI MS.

**SHPPSI MS.** This method combines preconcentration and ionization on the substrate, useful in many analytical situations. Figure 1 schematically represents the steps involved. These steps include (1) preconcentration of analyte (steps 1–7) and (2) ionization leading to detection (steps 8 and 9).

**Preconcentration Steps.** To obtain preconcentration at a position of interest (1 mm away from the tip), a micrometer-sized point defect was made manually at the tip of the coated paper with a sharp pin. This designed paper was used for the experiments, where a 10 µL droplet of analyte solution was carefully drop-casted at the point defect using a micropipette keeping the paper on a planar surface. Due to the superhydrophobic property of the paper, the solution forms a perfect sphere and sits at the desired position. It was then dried in laboratory air at 30–35 °C by spontaneous evaporation of the solvent. The process was repeated thrice or more times to deposit more analyte. The same procedure

was also followed for the normal paper. Interestingly, while the sample was observed to spread over the normal paper, it stayed as a droplet over the modified paper and dried slowly. Hence, the droplet formation and slow evaporation of solvent led to the accumulation of analyte molecules at the micrometer-sized point defect. Figure 2 shows the schematic and photographic

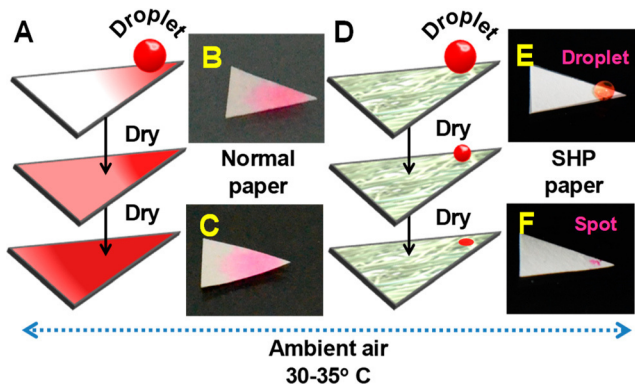


**Figure 2.** Liquid droplet behavior on (A) Whatman 42 filter paper and (D) superhydrophobic paper. B, C and E, F are optical images of the wet and dry paper samples.

representation of sampling over superhydrophobic and normal paper samples. The analyte used here was rhodamine 6G of 1 mM concentration to visually demonstrate the preconcentration technique in the picture. In Figure 2E, we can see a standing droplet which gets dried and accumulated in a smaller area shown in Figure 2F. However, Figure 2B,C shows that the dye got spread as soon as it was drop-casted over a normal paper. Similar images in Figure S1 show a distinct red dot on the superhydrophobic paper, which is a result of three times drop-casting of 25  $\mu$ L of nanomolar concentration of the same dye. Only a faint color was visible on the normal paper due to the dispersion. In this case, a higher order of preconcentration was done for visual detection over the papers.

**Detection Step.** The sample loaded triangular paper was finally placed in front of a mass spectrometer, pointing the tip toward the inlet, at a distance of 1 cm apart. The paper was connected to a high voltage dc power supply for the experiments. The analyte was eluted by 10  $\mu$ L of methanol.

The Thermo Scientific LTQ XL mass spectrometer was used for the mass spectrometric detection of analytes. The average size of the paper was chosen as 35 mm<sup>2</sup> with 7 mm at the base and 10 mm in height. The point defect was made approximately 0.5–1 mm away from the tip. The spray voltage was varied within the range of 3–5 kV depending on the analyte of interest. The capillary and tube lens voltages were set to  $\pm 45$  and  $\pm 100$  V in all the cases for positive and negative modes, respectively. The capillary temperature and the sheath gas pressure were set to be 275 °C and 0 psi, respectively. Collision induced dissociation (CID) was used in all cases to understand the fragmentation pattern of the molecules through a MS<sup>n</sup> study. Helium was used to effect collisions in CID. All these optimized conditions were chosen based on the trial and error method.

**Preparation of the Standard Samples.** Caffeine, rhodamine 6G, methyl orange, and melamine were chosen to characterize the system. All the samples were prepared in Milli Q water with different concentrations ranging from 1 mM to 1

pM using dilution methodology. Methanol was used to elute the analyte from the paper in all cases.

## RESULTS AND DISCUSSION

**Characterization of the SHP Coated Paper.** Coated filter paper was used directly without additional treatment. Figure S2A,B represents the scanning electron microscopy (SEM) image of normal Whatman 42 filter paper and the SHP coated paper at different magnifications. The fibrous nature of the paper remained intact after the coating. The fibrous nature of the substrate plays an important role to generate a large electric field between the fibers, which leads to the formation of electrospray from the tip.

**Characterization of SHPPSI MS.** Analysis of molecules having low concentrations such as the sub-ppt level is difficult to be detected in standard PSI mass spectrometry due to diffusion of the analyte over the paper. Hence, during elution of the analyte, only a small fraction of the total analyte gets detected. By changing the wettability of the paper surface, diffusion of the analytes can be restricted by a substantial amount that allows localization of the analyte molecules in a micrometer region at close proximity to the tip. Figure 3

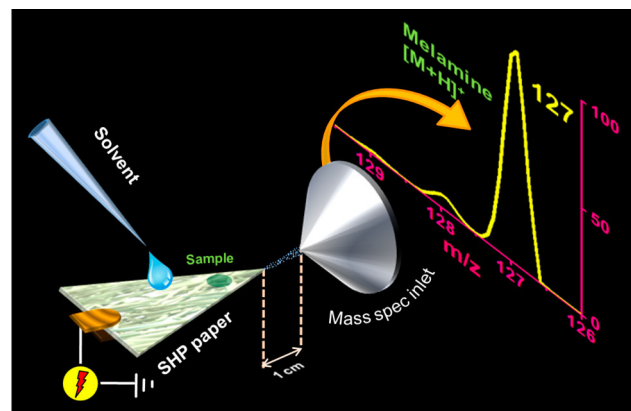


**Figure 3.** Schematic of the experimental setup used for superhydrophobic paper spray ionization mass spectrometry (SHPPSI MS). The triangularly cut SHP paper acts as the substrate to ionize the molecule. The inset shows the mass spectrum of melamine at 10 pM (1.2 ppt) concentration. The analyte containing the analyte is preconcentrated on the paper.

schematically represents the setup along with the mass spectrum of the analyte, melamine, at a concentration of 10 pM ( $10^{-11}$  M or 1.2 ppt). The peak  $m/z$  127 corresponds to the protonated cation of the analyte in positive ion mode. This peak was further confirmed by the MS<sup>2</sup> data, which are shown in Figure S3. The peak at  $m/z$  127 (Figure S3a) upon CID gives a major peak at  $m/z$  85 (Figure S3b), which corresponds to the loss of the H<sub>2</sub>NCN fragment. This forms the C<sub>2</sub>N<sub>4</sub>H<sub>5</sub><sup>+</sup> cation. Further fragmentation of the peak at  $m/z$  85 gives  $m/z$  65 (Figure S3c), which corresponds to the NH<sub>3</sub> loss of the four member ring.

The same preconcentration technique was adopted for the sampling of other analytes to demonstrate the applicability of the methodology toward any analyte. The mass spectra of all the analytes are shown in Figure 4 and Figure S7. Figure 4 shows the mass spectra of three different analytes of interest, such as caffeine (positive ion mode), rhodamine 6G (positive ion mode), and methyl orange (negative ion mode) at



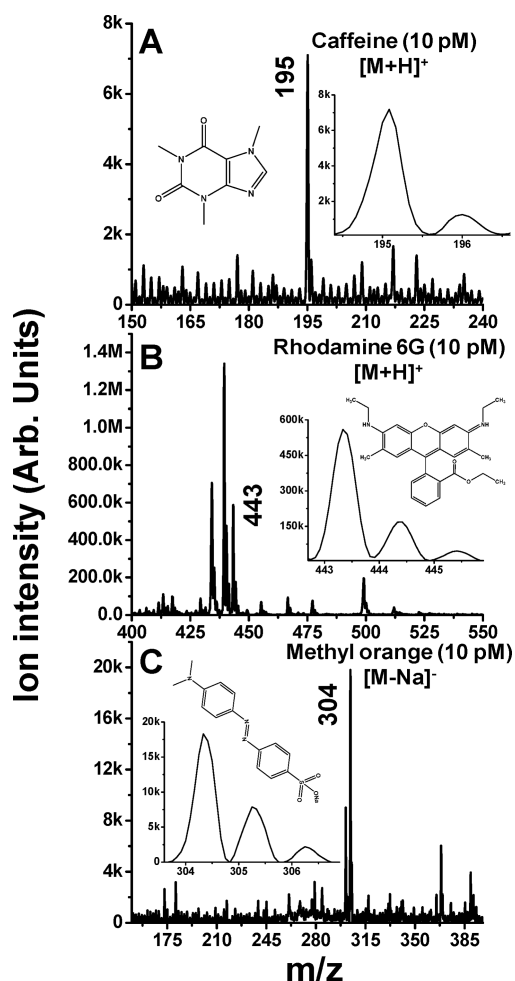


**Figure 4.** SHPPSI MS spectra of (A) caffeine, (B) rhodamine 6G, and (C) methyl orange in picomolar or ppt concentrations. Insets show the isotope distributions and structures of the analytes. The label, “k” represents  $10^3$ .

picomolar concentrations. The peaks  $m/z$  195, 443, and 304 present in Figure 4 correspond to the protonated cations of caffeine and rhodamine 6G and the deprotonated anion of methyl orange. From the ion intensity of the corresponding peaks, it is clear that SHPPSI MS has a capability to detect extremely low concentrations of analytes in solution and it works for different kinds of analytes irrespective of their functionality.

The MS<sup>2</sup> spectrum of caffeine is presented in Figure S4. Fragmentation of the peak at  $m/z$  195 (S4a) (also in Figure 4A) gives the major peak at  $m/z$  138 (S4b), which corresponds to the loss of one  $\text{CH}_3\text{NCO}$ . Fragmentation of  $m/z$  138 gives  $m/z$  110 due to the fragment shown in the structure S4c, as a result of the loss of one CO. In addition to this, two weak fragments at  $m/z$  85 and 68 are due to the loss of one CHN and CHN +  $\text{CH}_3$  group from Figure S4c. Structures corresponding to the ions are presented in Figure S4d,e. The fragmentation patterns of rhodamine 6G and methyl orange are also presented in Figures S5 and S6.

Similarly, Figure S7 represents the mass spectra of isoleucine, adenine, and urea at concentrations of 1.3, 1.4, and 0.6 ppt. Mass peaks at  $m/z$  131, 135, and 61 correspond to the molecular ions of isoleucine, adenine, and the protonated peak of urea.

The fragmentation pattern of the peak at  $m/z$  131 is shown in Figure S8. Other peaks corresponding to adenine and urea could not be studied due to ion loss in the trap at that concentration. Additionally, we have analyzed diazepam, a well-known antianxiety drug at 10 pM in water (Figure S10). To show the stability of the ionization methodology, the total ion chromatogram (TIC) and selected ion chromatogram (SIC) are shown in Figure S11. It also provides the information about the background current. As we see in the TIC, the ion current is of the order of 8M, whereas the peak that corresponds to isoleucine has an intensity up to 40k. This is due to the fact that there are more ions in the background which either come from the paper or from the instrument and are shown in the inset of Figure S11A. However, from the SIC, it is clear that the ionization of the preconcentrated analytes at the ppt level is stable for a certain time interval until the maximum number of ion ejections has happened.

To compare with standard PSI MS, rhodamine 6G and glucose were chosen as potential candidates, as they can be detected in paper spray mode easily. The experiment was conducted by putting the same amount of analyte (10  $\mu\text{L}$  each, thrice) on both the superhydrophobic paper and normal paper using similar sampling methodologies. Comparison of the mass spectrum of rhodamine 6G by SHPPSI MS and PSI MS are shown in Figure 5, where almost a 13-fold enhancement of the

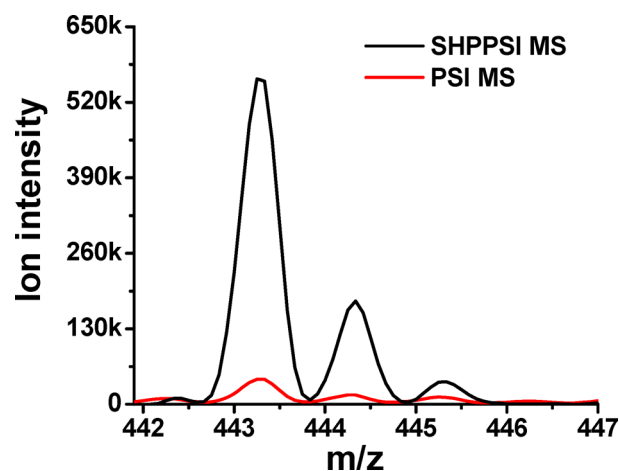


**Figure 5.** Comparison of the ion intensity for a chosen analyte (rhodamine 6G) in SHPPSI MS and by standard PSI MS. The same quantity of analyte was used in both the cases.

ion intensity was observed. The ion current of the selected peak at  $m/z$  443 in PSI MS is 43.26k, whereas in SHPPSI MS, the ion current for the same peak is 563.46k. The mass spectrum recorded for the two times preconcentrated sample has an ion current of 273.33k (Figure S12). In the case of glucose, the ion current in the normal paper is only 5.44k, whereas the superhydrophobic paper gives 48.14k for the peak at  $m/z$  181 (Figure S13).

We have also compared the ion current of the selected peak at  $m/z$  127, corresponding to protonated melamine in PSI, ESI, and SHPPSI, at 10 pM concentration. Figure S14 represents the comparative mass spectrum, in which we have not observed this peak at  $m/z$  127 in the case of PSI and ESI, whereas SHPPSI provides a distinct peak of melamine in the mass spectrum.

For further characterization of the method, five different concentrations of the analytes were chosen and the peak

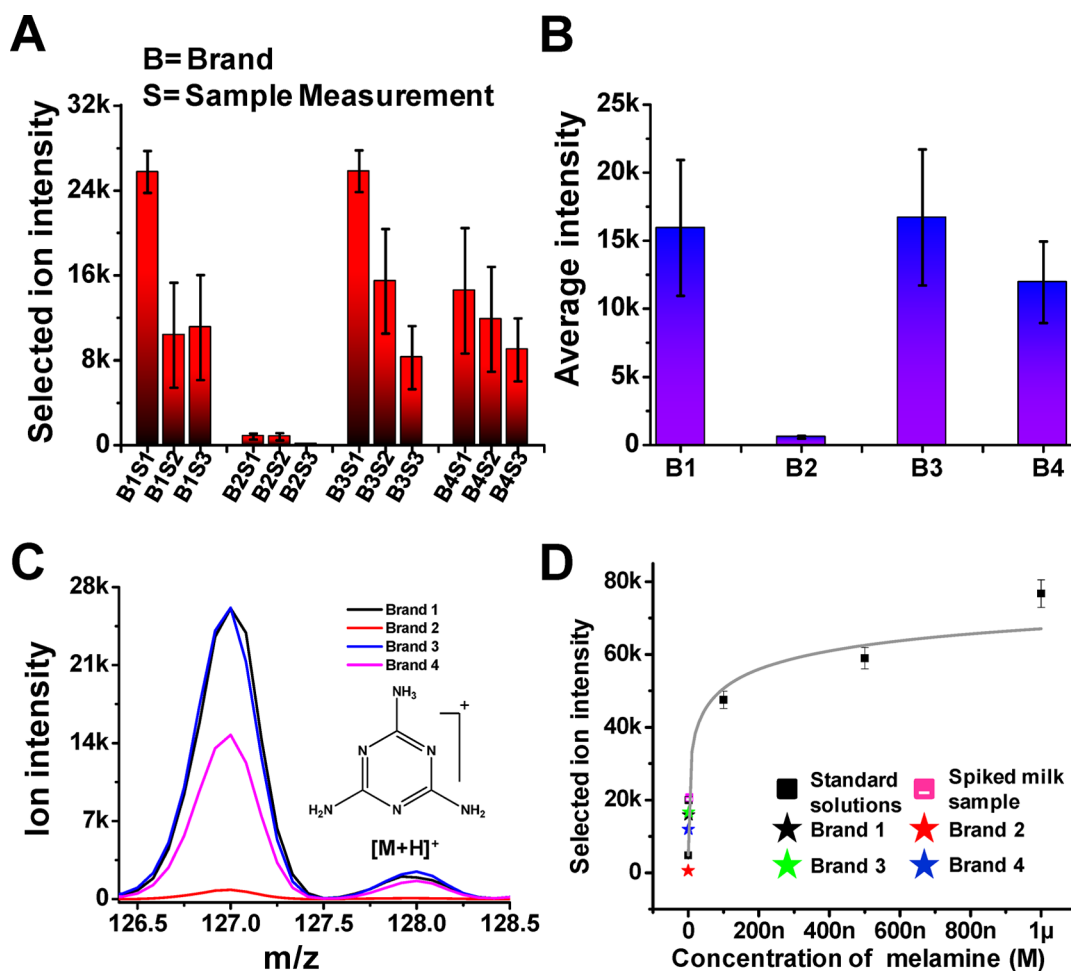


**Figure 6.** Mass spectrum of melamine found in commercial milk. (A) Selected ion intensity of each brand milk samples of three independent experiments, (B) average ion intensity of each brand, (C) mass spectra of the melamine in the commercially available milk brands, and (D) calibration curve based on the selected ion current for melamine in spiked milk, due to the peak at  $m/z$  127. The concentration of melamine in commercial milk was found to be in the nanomolar range for brands 1, 3, and 4. Brand 2 does not contain melamine.

intensity was compared. Figure S17 represents the SHPPSI MS spectra of five different concentrations of melamine ranging from picomolar to millimolar. The observed ion intensity change is from 3k to 1M. By correlating the ion intensity of the peak at  $m/z$  127, with the given concentration of the analyte in the solution, it can be concluded that the peak intensity gets saturated at higher concentration (Figure S18). Hence the methodology for preconcentrating a molecule and simultaneously detecting the same is both qualitative as well as quantitative.

**Detection of Melamine in Adulterated Milk.** To show the utility of the invention in an analytical context of societal relevance, we have chosen the detection of melamine in a sample of milk. Detection of melamine is important to know the actual nitrogen content of the milk. The commercial value of the milk is related to the total protein content, which is measured by quantifying the total nitrogen content in it. The melamine skeleton contains six nitrogen atoms. Hence by mixing it, the nitrogen content of milk can be enhanced.

The limit of daily melamine uptake is set to be 0.2 mg/kg or 1.6  $\mu$ M by the World Health Organization (WHO) in 2008.<sup>40</sup> The reported melamine content in commercially available milk sample from the state Tamilnadu in India is 0.028–0.071 mg/kg or in the range of 0.2–0.58  $\mu$ M.<sup>41</sup>

SHPPSI MS provides an easy and direct detection method of melamine in milk samples without having the sample processing step (Figure 6). The experiment was conducted by arbitrarily spiking a 5 nM (or 0.63 ppb) concentration of melamine in a melamine free milk sample, purchased from the local market. Figure S15 represents the mass spectrum of the milk before spiking which shows no melamine contamination. The prepared milk sample was directly used for SHPPSI MS analysis without further dilution. The intensity of the peak corresponding to melamine cation was 20.67k (Figure S16). Figure 6D shows the calibration curve of ion intensity vs solution phase concentration of standard samples of melamine in milk. Shape of the calibration curve shows a similar trend as shown in Figure S18. This seems to be related to the solubility of the analyte in the eluting solvent. At the lowest detectable concentration, almost all the analyte molecules can be eluted by methanol at the retention time scale, which subsequently gets ionized. Here, the retention time scale refers to the time taken for methanol to dissolve the analyte at that location and to get sprayed from the tip. With an increased concentration of melamine, part of it may get detected by one time drop casting of the methanol solution and the remaining part may stay at the groove and hence the overall intensity of the analyte become saturated after certain concentration. By correlating the ion intensity of the selected ion of  $m/z$  127 with the

calibration curve, we can conclude that the level of adulteration is in the nanomolar (or ppb) range. We have chosen four other brands to measure the level of contamination. Figure 6A represents the bar diagram of selected ion intensity vs brands. Each sample was tested three times to get an average ion intensity shown in Figure 6B. The average intensity was related to the fitted calibration curve. Brands 1, 3, and 4 had nanomolar concentrations of melamine, whereas brand 2 did not contain melamine. Figure 6C shows the mass spectra of all the brands. The data presented in Figure S17 also shows that analysis at even lower concentrations, down to the ppt, is possible. The minimum concentration of melamine in water with measurable ion count was 1.2 ppt (10 pM).

## CONCLUSION

In this article, we demonstrate a method of ionization in which ion intensity was increased by selective localization of analyte molecules at the tip of a superhydrophobic paper and simultaneously detecting it with an ion detector. This methodology named as superhydrophobic preconcentration paper spray ionization mass spectrometry (SHPPSI MS) is demonstrated for a variety of analytes with different functionalities. This technique requires less volume of sample and involves easy sample preparation. The actual amounts of the analytes used are at the femtogram level; e.g., 38, 18, 39.1, 40.5, 58.2 fg of melamine, urea, isolucine, adenine, and caffeine, respectively. We achieved detection at the 0.6 ppt level in water using SHPPSI MS for which urea was chosen as the analyte of choice. Detection of the 1.2 ppt (10 pM) level of melamine has been demonstrated here with standard samples in water. Qualitative and quantitative detection of melamine is also shown with a commercial milk sample.

SHPPSI MS can be utilized for the detection of many socially relevant analytes, e.g., pesticides, drugs, and toxic chemicals in an environment at lowest possible levels. This methodology can also be coupled with other excitation sources such as light, heat, etc. to enhance the ionization probability.

## ASSOCIATED CONTENT

### Supporting Information

The Supporting Information is available free of charge on the ACS Publications website at DOI: 10.1021/acs.analchem.9b00144.

Part of the experimental data, optical images of the preconcentration technique, SEM of the normal and superhydrophobic papers, MS<sup>n</sup> data of the analytes, chronogram of the analytes, and mass spectra of standard melamine samples (PDF)

## AUTHOR INFORMATION

### Corresponding Author

\*E-mail: [pradeep@iitm.ac.in](mailto:pradeep@iitm.ac.in). Phone: +91-44-22574208. Fax: +91-44-2257 0509/0545.

### ORCID

Avijit Baidya: 0000-0001-5215-2856

Thalappil Pradeep: 0000-0003-3174-534X

### Notes

The authors declare no competing financial interest.

## ACKNOWLEDGMENTS

The authors thank the Department of Science and Technology, Government of India, for equipment support through the Nano Mission. P.B. acknowledges IIT Madras for providing the Institute Doctoral Fellowship.

## REFERENCES

- (1) Yamashita, M.; Fenn, J. B. *J. Phys. Chem.* **1984**, *88* (20), 4451–9.
- (2) Takats, Z.; Wiseman, J. M.; Gologan, B.; Cooks, R. G. *Science (Washington, DC, U. S.)* **2004**, *306* (5695), 471–473.
- (3) Chen, H.; Talaty, N. N.; Takats, Z.; Cooks, R. G. *Anal. Chem.* **2005**, *77* (21), 6915–6927.
- (4) Cotte-Rodriguez, I.; Takats, Z.; Talaty, N.; Chen, H.; Cooks, R. G. *Anal. Chem.* **2005**, *77* (21), 6755–6764.
- (5) Harper, J. D.; Charipar, N. A.; Mulligan, C. C.; Zhang, X.; Cooks, R. G.; Ouyang, Z. *Anal. Chem. (Washington, DC, U. S.)* **2008**, *80* (23), 9097–9104.
- (6) Spencer, S. E.; Santiago, B. G.; Glish, G. L. *Anal. Chem. (Washington, DC, U. S.)* **2015**, *87* (23), 11887–11892.
- (7) Kuklya, A.; Engelhard, C.; Uteschil, F.; Kerpen, K.; Marks, R.; Telgheder, U. *Anal. Chem. (Washington, DC, U. S.)* **2015**, *87* (17), 8932–8940.
- (8) Nagy, K.; Pollreis, F.; Takats, Z.; Vekey, K. *Rapid Commun. Mass Spectrom.* **2004**, *18* (20), 2473–2478.
- (9) van Bavel, B.; Geng, D.; Cherta, L.; Nacher-Mestre, J.; Portoles, T.; Abalos, M.; Saulo, J.; Abad, E.; Dunstan, J.; Jones, R.; Kotz, A.; Winterhalter, H.; Malisch, R.; Traag, W.; Hagberg, J.; Ericson Jogsten, I.; Beltran, J.; Hernandez, F. *Anal. Chem. (Washington, DC, U. S.)* **2015**, *87* (17), 9047–9053.
- (10) Zuth, C.; Vogel, A. L.; Ockenfeld, S.; Huesmann, R.; Hoffmann, T. *Anal. Chem.* **2018**, *90*, 8816–8823.
- (11) Wang, H.; Liu, J.; Cooks, R. G.; Ouyang, Z. *Angew. Chem., Int. Ed.* **2010**, *49* (5), 877–880.
- (12) Ren, Y.; Wang, H.; Liu, J.; Zhang, Z.; McLuckey, M. N.; Ouyang, Z. *Chromatographia* **2013**, *76* (19–20), 1339–1346.
- (13) Sarkar, D.; Srimany, A.; Pradeep, T. *Analyst (Cambridge, U. K.)* **2012**, *137* (19), 4559–4563.
- (14) Jackson, S.; Swiner, D. J.; Capone, P. C.; Badu-Tawiah, A. K. *Anal. Chim. Acta* **2018**, *1023*, 81–88.
- (15) Wang, T.; Zheng, Y.; Wang, X.; Austin, D. E.; Zhang, Z. *Anal. Chem. (Washington, DC, U. S.)* **2017**, *89* (15), 7988–7995.
- (16) Jiang, J.; Zhang, H.; Li, M.; Dulay, M. T.; Ingram, A. J.; Li, N.; You, H.; Zare, R. N. *Anal. Chem. (Washington, DC, U. S.)* **2015**, *87* (16), 8057–8062.
- (17) Espy, R. D.; Teunissen, S. F.; Manicke, N. E.; Ren, Y.; Ouyang, Z.; van Asten, A.; Cooks, R. G. *Anal. Chem. (Washington, DC, U. S.)* **2014**, *86* (15), 7712–7718.
- (18) Yannell, K. E.; Kesely, K. R.; Chien, H. D.; Kissinger, C. B.; Cooks, R. G. *Anal. Bioanal. Chem.* **2017**, *409* (1), 121–131.
- (19) Yang, Q.; Wang, H.; Maas, J. D.; Chappell, W. J.; Manicke, N. E.; Cooks, R. G.; Ouyang, Z. *Int. J. Mass Spectrom.* **2012**, *312*, 201–207.
- (20) Amador, V. S.; Pereira, H. V.; Sena, M. M.; Augusti, R.; Piccin, E. *J. Am. Soc. Mass Spectrom.* **2017**, *28* (9), 1965–1976.
- (21) Wang, Q.; Zheng, Y.; Zhang, X.; Han, X.; Wang, T.; Zhang, Z. *Analyst (Cambridge, U. K.)* **2015**, *140* (23), 8048–8056.
- (22) Banerjee, S.; Basheer, C.; Zare, R. N. *Angew. Chem., Int. Ed.* **2016**, *55* (41), 12807–12811.
- (23) Narayanan, R.; Sarkar, D.; Som, A.; Wlekinski, M.; Cooks, R. G.; Pradeep, T. *Anal. Chem.* **2015**, *87* (21), 10792–10798.
- (24) Narayanan, R.; Pradeep, T. *Anal. Chem.* **2017**, *89* (20), 10696–10701.
- (25) Narayanan, R.; Sarkar, D.; Cooks, R. G.; Pradeep, T. *Angew. Chem., Int. Ed.* **2014**, *53* (23), 5936–5940.
- (26) Basuri, P.; Sarkar, D.; Paramasivam, G.; Pradeep, T. *Anal. Chem.* **2018**, *90* (7), 4663–4668.
- (27) Sarkar, D.; Som, A.; Pradeep, T. *Anal. Chem.* **2017**, *89* (21), 11378–11382.



- (28) Damon, D. E.; Davis, K. M.; Moreira, C. R.; Capone, P.; Cruttenden, R.; Badu-Tawiah, A. K. *Anal. Chem. (Washington, DC, U. S.)* **2016**, 88 (3), 1878–1884.
- (29) Damon, D. E.; Yin, M.; Allen, D. M.; Maher, Y. S.; Tanny, C. J.; Oyola-Reynoso, S.; Smith, B. L.; Maher, S.; Thuo, M. M.; Badu-Tawiah, A. K. *Anal. Chem. (Washington, DC, U. S.)* **2018**, 90 (15), 9353–9358.
- (30) Filazi, A.; Sireli, U. T.; Ekici, H.; Can, H. Y.; Karagoz, A. J. *Dairy Sci.* **2012**, 95 (2), 602–608.
- (31) Li, J.; Qi, H.-Y.; Shi, Y.-P. *J. Chromatogr. A* **2009**, 1216 (29), 5467–5471.
- (32) Harnly, J.; Bergana, M. M.; Adams, K. M.; Xie, Z.; Moore, J. C. *J. Agric. Food Chem.* **2018**, 66, 8478–8488.
- (33) Wang, Q.; Haughey, S. A.; Sun, Y.-M.; Eremin, S. A.; Li, Z.-F.; Liu, H.; Xu, Z.-L.; Shen, Y.-D.; Lei, H.-T. *Anal. Bioanal. Chem.* **2011**, 399 (6), 2275–2284.
- (34) Cao, B.; Yang, H.; Song, J.; Chang, H.; Li, S.; Deng, A. *Talanta* **2013**, 116, 173–180.
- (35) Lei, H.; Su, R.; Haughey, S. A.; Wang, Q.; Xu, Z.; Yang, J.; Shen, Y.; Wang, H.; Jiang, Y.; Sun, Y. *Molecules* **2011**, 16, 5591–5603.
- (36) Lee, I.-C.; Ko, J.-W.; Park, S.-H.; Shin, I.-S.; Moon, C.; Kim, S.-H.; Kim, Y.-B.; Kim, J.-C. *Food Chem. Toxicol.* **2016**, 96, 254–262.
- (37) Bandle, O. J.; Stine, C. B.; Ferguson, M.; Black, T.; Olejnik, N.; Keltner, Z.; Evans, E. R.; Crosby, T. C.; Reimschuessel, R.; Sprando, R. L. *Food Chem. Toxicol.* **2014**, 74, 301–308.
- (38) Xu, C.-F.; Gao, X.-L.; Du, Y.-X.; Ren, S.-T. *Food Chem. Toxicol.* **2011**, 49 (12), 3013–3017.
- (39) Baidya, A.; Ganayee, M. A.; Jakka Ravindran, S.; Tam, K. C.; Das, S. K.; Ras, R. H. A.; Pradeep, T. *ACS Nano* **2017**, 11 (11), 11091–11099.
- (40) World Health Organization. *Melanin and Cyanuric Acid: Toxicity, Preliminary Risk Assessment and Guidance on Levels in Food*. October 30, 2008.
- (41) Niraimathi, V.; Jerad Suresh, A.; Ananthakumar, T. *Indo Am. J. Pharm. Res.* **2015**, 5 (1), 271–276.

#### ■ NOTE ADDED AFTER ASAP PUBLICATION

This paper was originally published ASAP on May 22, 2019. Due to a production error, there was an error in the title. The corrected version was reposted on May 23, 2019.

# Supporting Information

## Sub-Parts-per-Trillion Level Detection of Analytes by Superhydrophobic Preconcentration Paper Spray Ionization Mass Spectrometry (SHPPSI MS)

Pallab Basuri, Avijit Baidya, and Thalappil Pradeep\*

*DST Unit of Nanoscience (DST UNS) and Thematic Unit of Excellence,*

*Department of Chemistry, Indian Institute of Technology Madras,*

*Chennai 600036, India.*

\*E-mail: [pradeep@iitm.ac.in](mailto:pradeep@iitm.ac.in),

Fax: 91-44-2257 0545

### Table of contents

Number	Description	Page Number
Figure S1	Optical images of the pre-concentration steps involved in SHPPSI MS using normal paper and superhydrophobic paper.	2
Figure S2	Comparative SEM images of the normal paper and superhydrophobic paper at different magnification.	3
Figure S3	MS <sup>2</sup> and MS <sup>3</sup> spectra of melamine at 1.2 ppt level in solution.	4
Figure S4	MS <sup>2</sup> and MS <sup>3</sup> spectra of caffeine at 2 ppt level in solution.	5
Figure S5	MS <sup>2</sup> and MS <sup>3</sup> spectra of rhodamine 6g at 4.7 ppt level in solution.	6
Figure S6	MS <sup>2</sup> and MS <sup>3</sup> spectra of methyl orange at 3.2 ppt level in solution.	7
Figure S7	Mass spectra of A) isoleucine, B) adenine, and C) urea at 1.3, 1.4 and 0.6 ppt concentration.	8
Figure S8	MS <sup>2</sup> spectrum of isolucine at 1.3 ppt level in solution.	9
Figure S9	Blank mass spectrum with 10 µl methanol.	10
Figure S10	MS <sup>1</sup> , MS <sup>2</sup> , and MS <sup>3</sup> spectra of diazepam.	11
Figure S11	Total ion chromatogram (TIC) and Selected ion chromatogram of (SIC) of isoleucine.	12
Figure S12	Full mass range mass spectrum of rhodamine 6G with two times drop cast. The intensity corresponds to the peak 443 is almost half of the peak intensity shown in figure 4B.	13
Figure S13	Comparative mass spectra of glucose in A) normal paper and B) superhydrophobic paper. The used glucose conc. here is 10 picomolar.	14
Figure S14	Comparative mass spectra of melamine at 10 picomolar in A) PSI, B) ESI, and C) SHPPSI MS.	15
Figure S15	Mass spectrum of milk sample before spiking with melamine.	16
Figure S16	Mass spectrum of melamine found in laboratory-made artificially adulterated milk. Melamine concentration in the milk was 0.63 ppb.	17
Figure S17	Chart of 5 different concentrations of melamine in water, ranging from millimolar to picomolar.	18
Figure S18	Calibration curve of melamine in water.	19

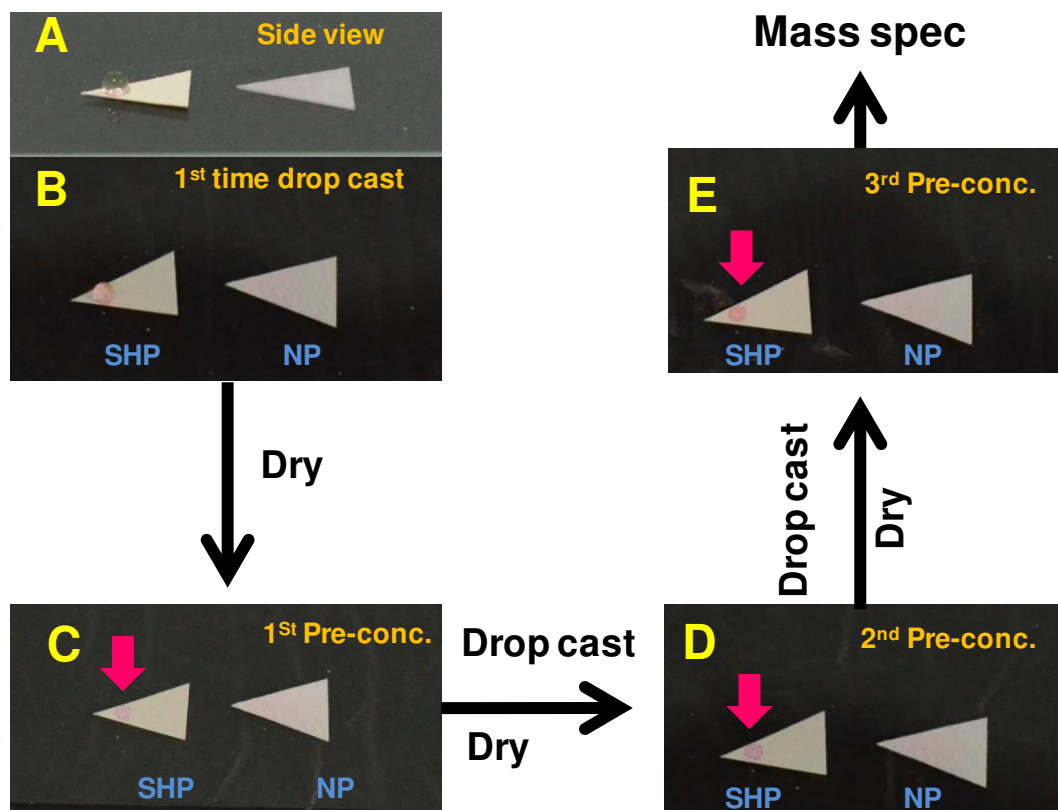


**Figure S1.** Optical images of the pre-concentration steps involved in SHPPSI MS using normal paper and superhydrophobic paper.

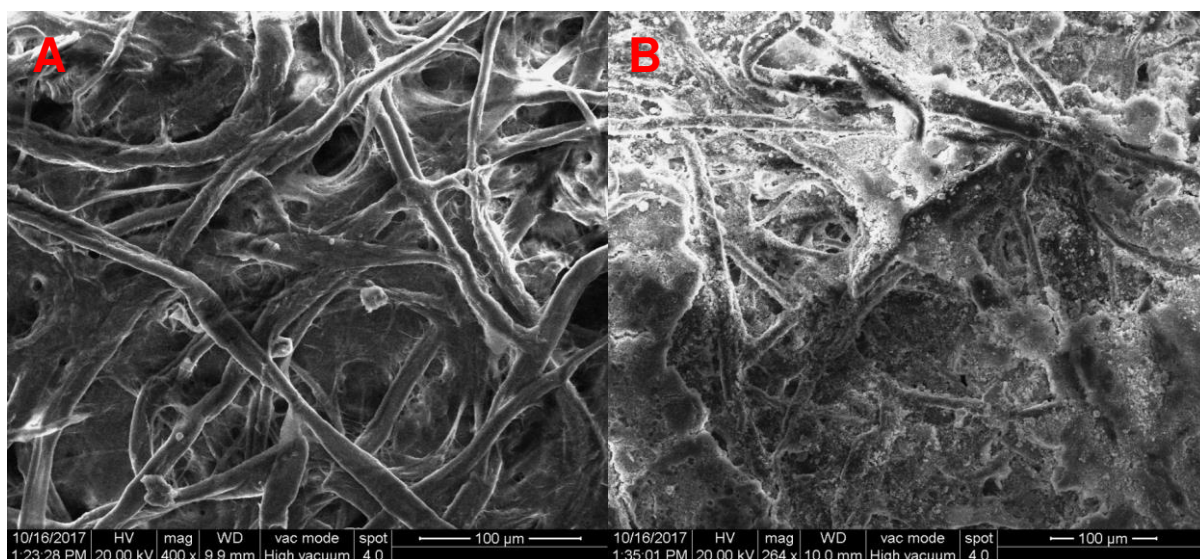


**Figure S2.** Comparative SEM images of a A) normal paper and B) superhydrophobic paper at different magnifications.

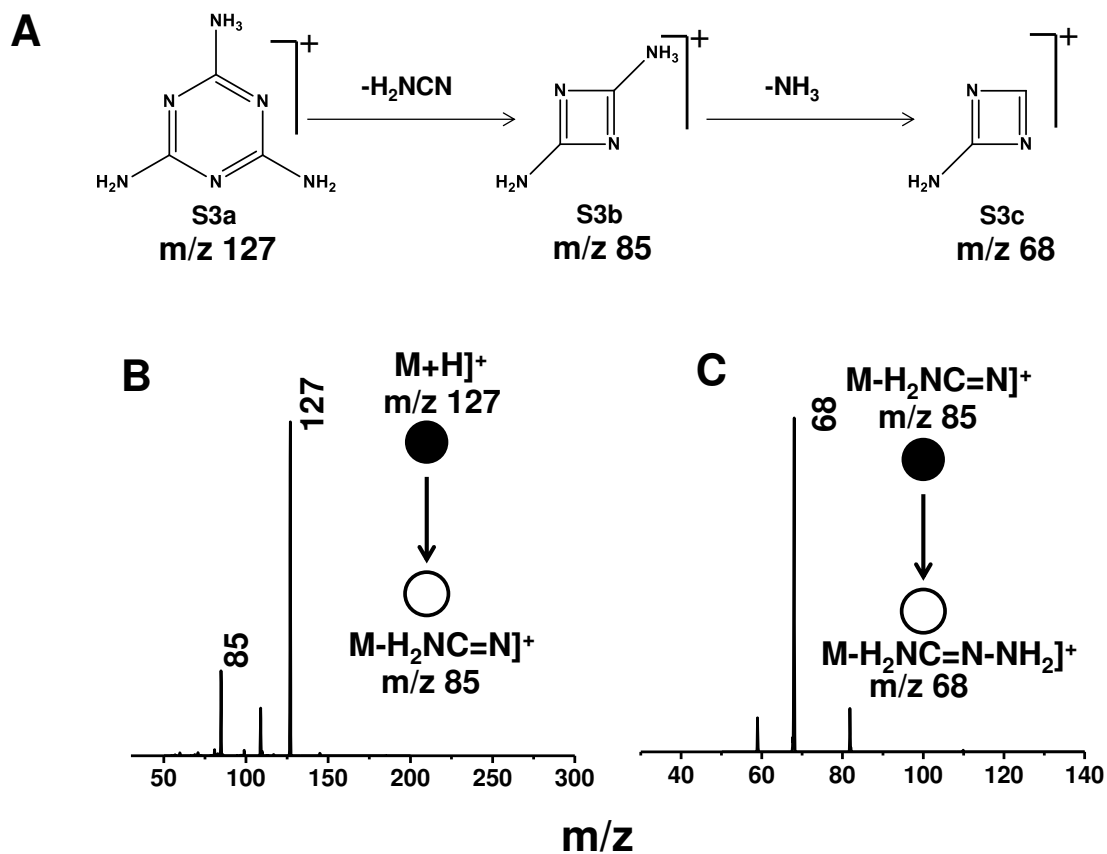


**Figure S3.** MS<sup>2</sup> and MS<sup>3</sup> spectra of melamine at 1.2 ppt (10 pM) in solution. A) Structures of the fragments; B) and C) are the MS<sup>2</sup> and MS<sup>3</sup> spectra of peaks at m/z 127 and 85. The fragmentation patterns and the structures of the fragmented ions were confirmed from the literature.<sup>1</sup>

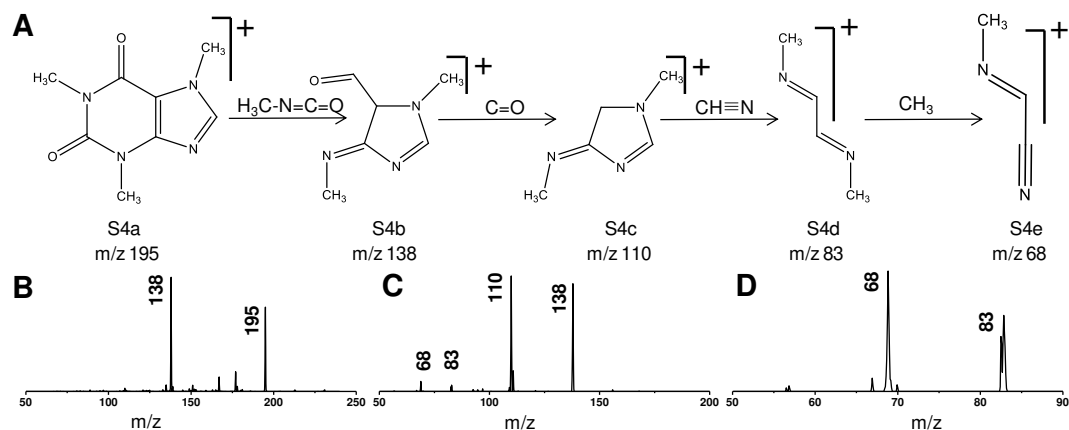


**Figure S4.**  $MS^2$  and  $MS^3$  spectra of caffeine at 2 ppt (10 pM) in solution. A) Structures of the fragments; B), C) and D) are the  $MS^2$  and  $MS^3$  spectra of peaks at  $m/z$  195 and 138. Fragmentation patterns were matched with the literature.<sup>2</sup>

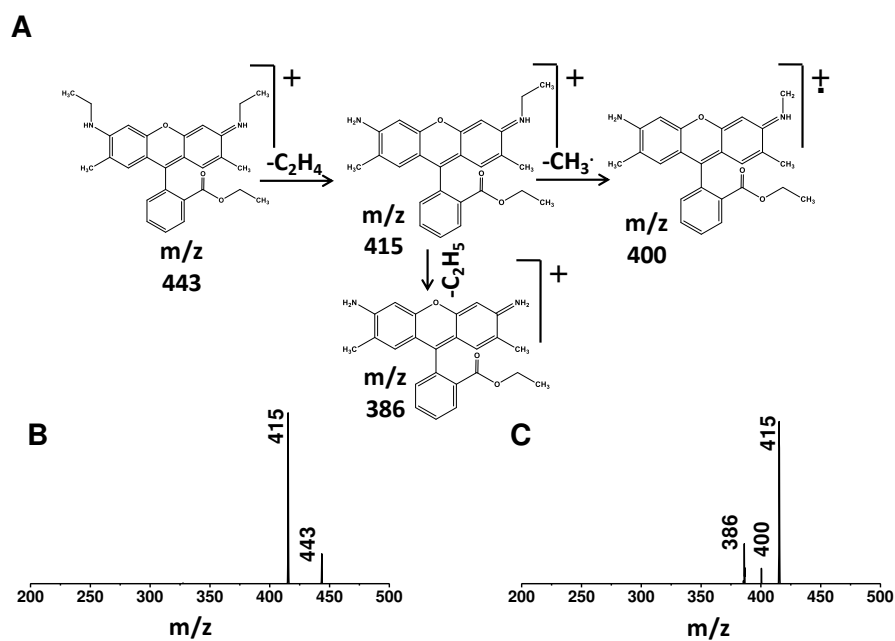


**Figure S5.** MS<sup>2</sup> and MS<sup>3</sup> spectra of rhodamine 6g at 4.7 ppt (10 pM) in solution. A) Structures of the fragments; B) and C) are the MS<sup>2</sup> and MS<sup>3</sup> spectra of peaks at m/z 443 and 415. The fragmentation patterns and the structures of the fragmented ions were confirmed from the literature.<sup>3</sup>



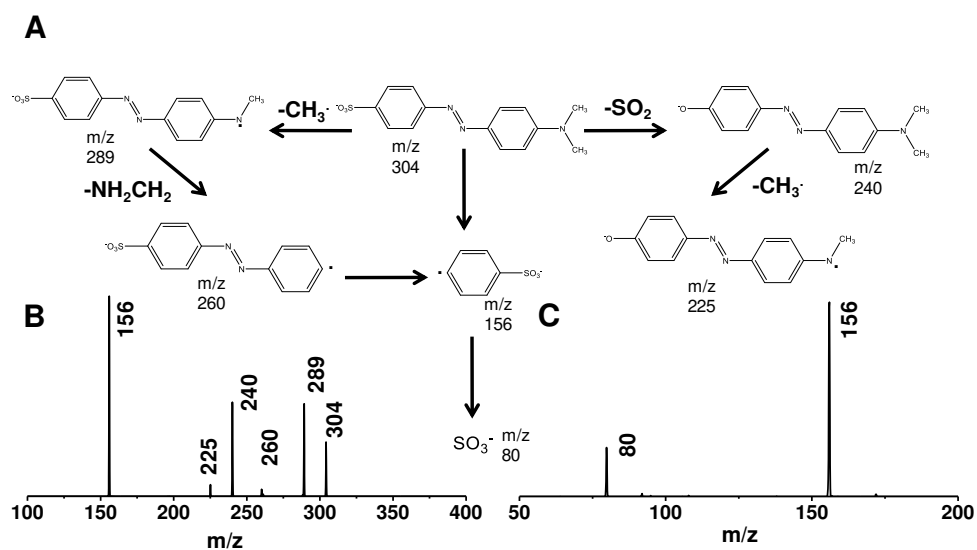


**Figure S6.** MS<sup>2</sup> and MS<sup>3</sup> spectra of methyl orange at 3.3 ppt (10 pM) in solution. A) Structures of the fragments; B) and C) are the MS<sup>2</sup> and MS<sup>3</sup> spectra of peaks at m/z 304 and 156. The fragmentation patterns and the structures of the fragmented ions were confirmed from the literature.<sup>4</sup>

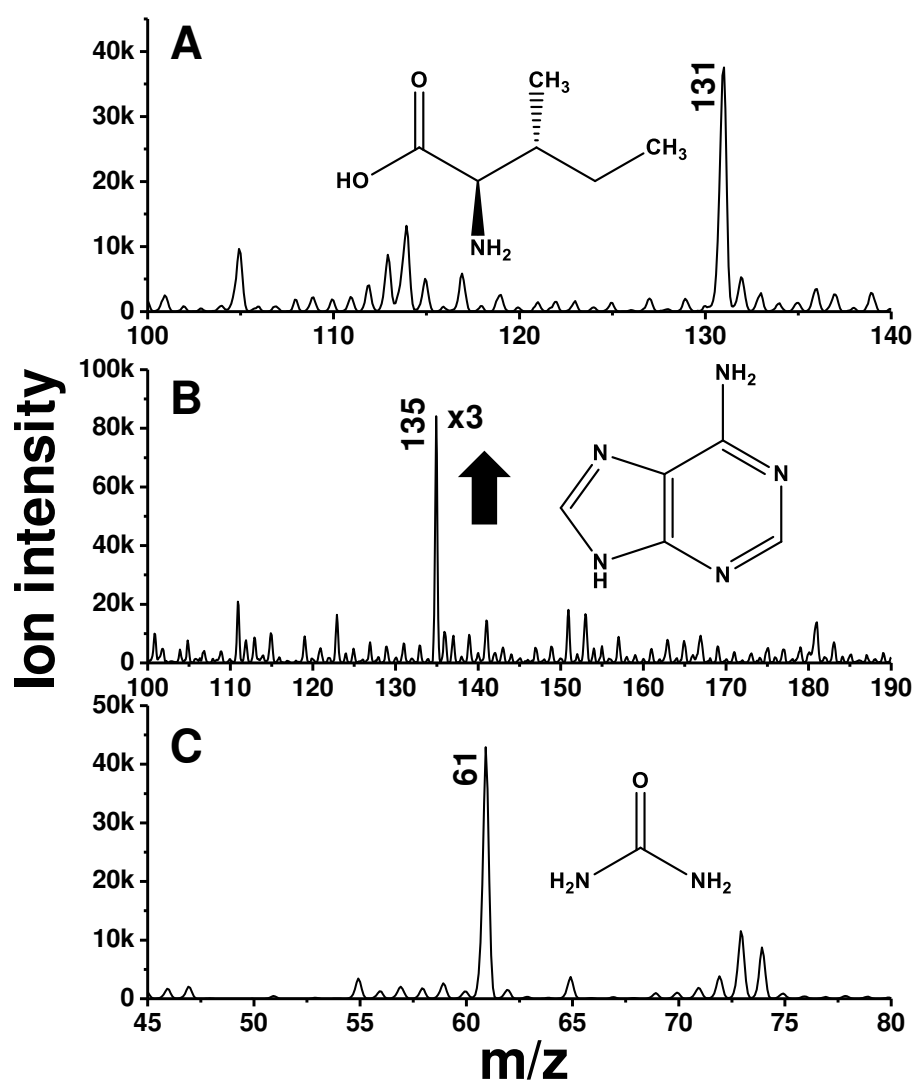


**Figure S7.** Mass spectra of A) isoleucine, B) adenine, and C) urea at 1.3, 1.4 and 0.6 ppt (or 10 pM) concentration.

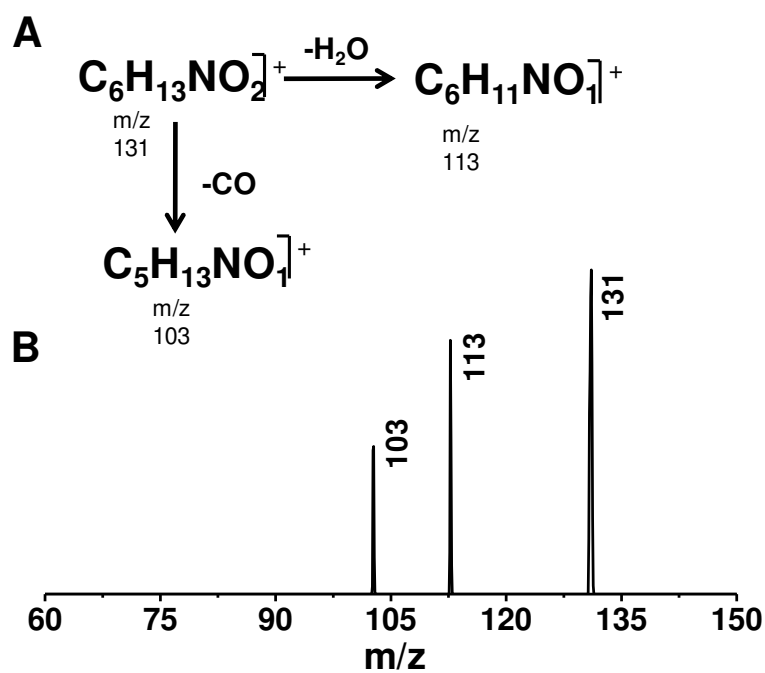


**Figure S8.** MS<sup>2</sup> spectrum of isoleucine at 1.3 ppt (10 pM) level in solution. A) Structures of the fragments and B) MS<sup>2</sup> spectrum of the peak at m/z 131. The fragmentation pattern and the structure of the fragmented ions were confirmed from the literature.<sup>5</sup>

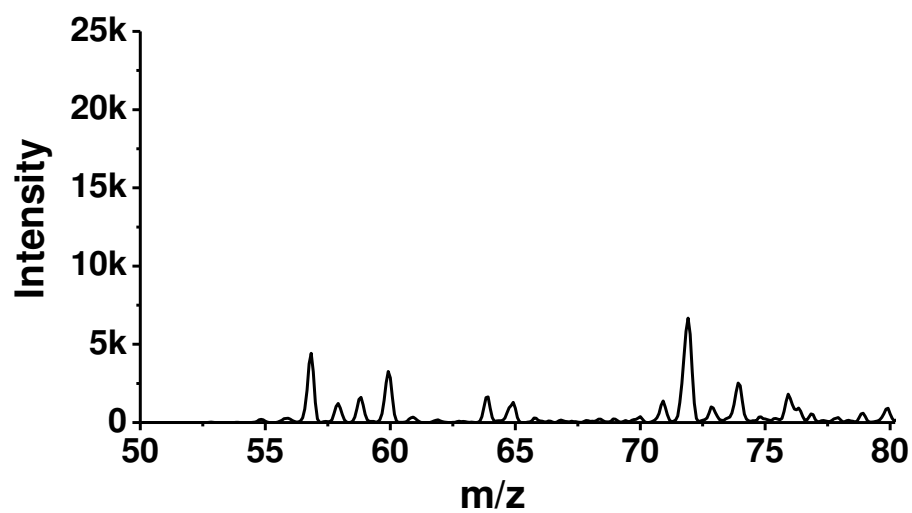


**Figure S9.** Blank SHPPSI mass spectrum collected by drop casting 10  $\mu$ l of methanol. Mass spectrum shows absence of peak at m/z 61 in the background.

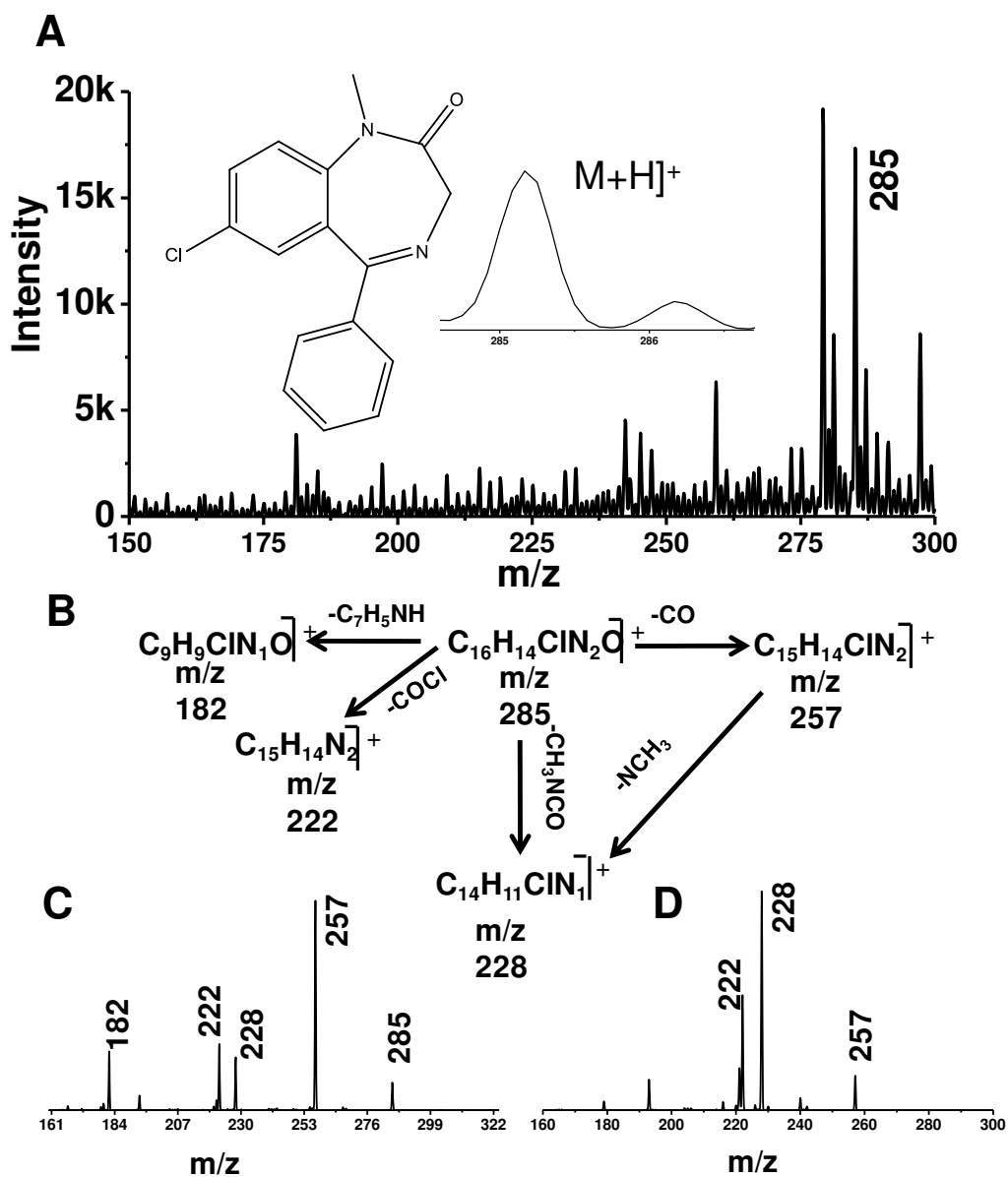


**Figure S10.** MS<sup>1</sup>, MS<sup>2</sup> and MS<sup>3</sup> spectra of diazepam at 10 pM in solution. A) MS<sup>1</sup> spectrum of the solution; B) Structures of the fragments; C) and D) are the MS<sup>2</sup> and MS<sup>3</sup> spectra of peaks at  $m/z$  285 and 257.<sup>6</sup>

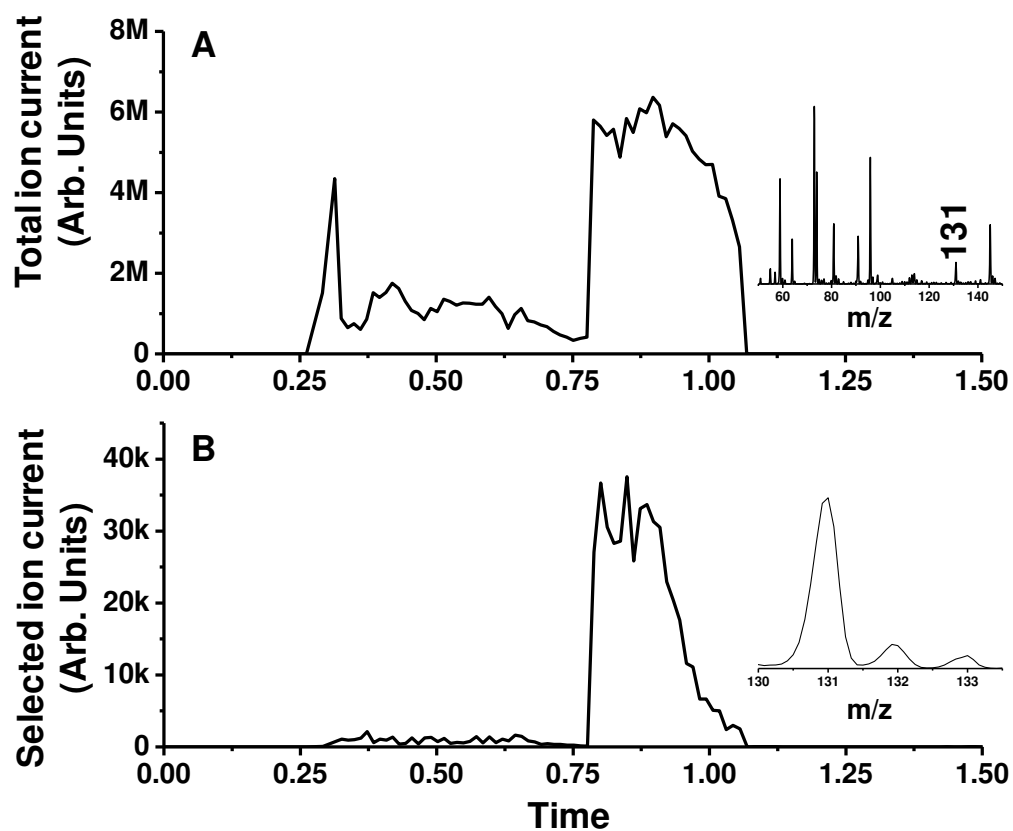


**Figure S11.** A) Total ion chromatogram (TIC) and B) selected ion chromatogram of (SIC) of isoleucine. Inset shows the full range mass spectrum and the spectrum in selected range.

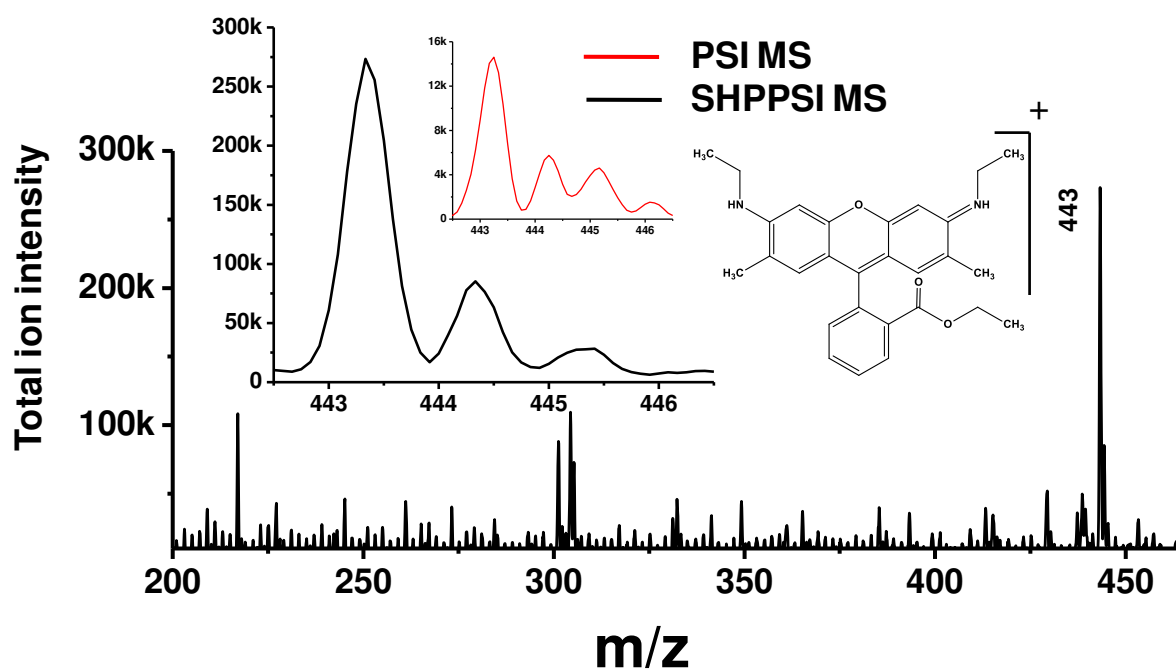


**Figure S12.** Full mass range mass spectrum of rhodamine 6G upon drop casting twice. The intensity corresponds to the peak 443 is almost half of the peak intensity shown in Figure 4B. It indicates that the peak intensity can be further enhanced by putting more analytes in a restricted area. Inset shows the selected area mass spectrum of the peak at  $m/z$  443 by SHPPSI (black trace) and PSI (red trace). The intensity corresponds to two times and three times drop casting (Figure 5) in normal paper are similar due to diffusion.



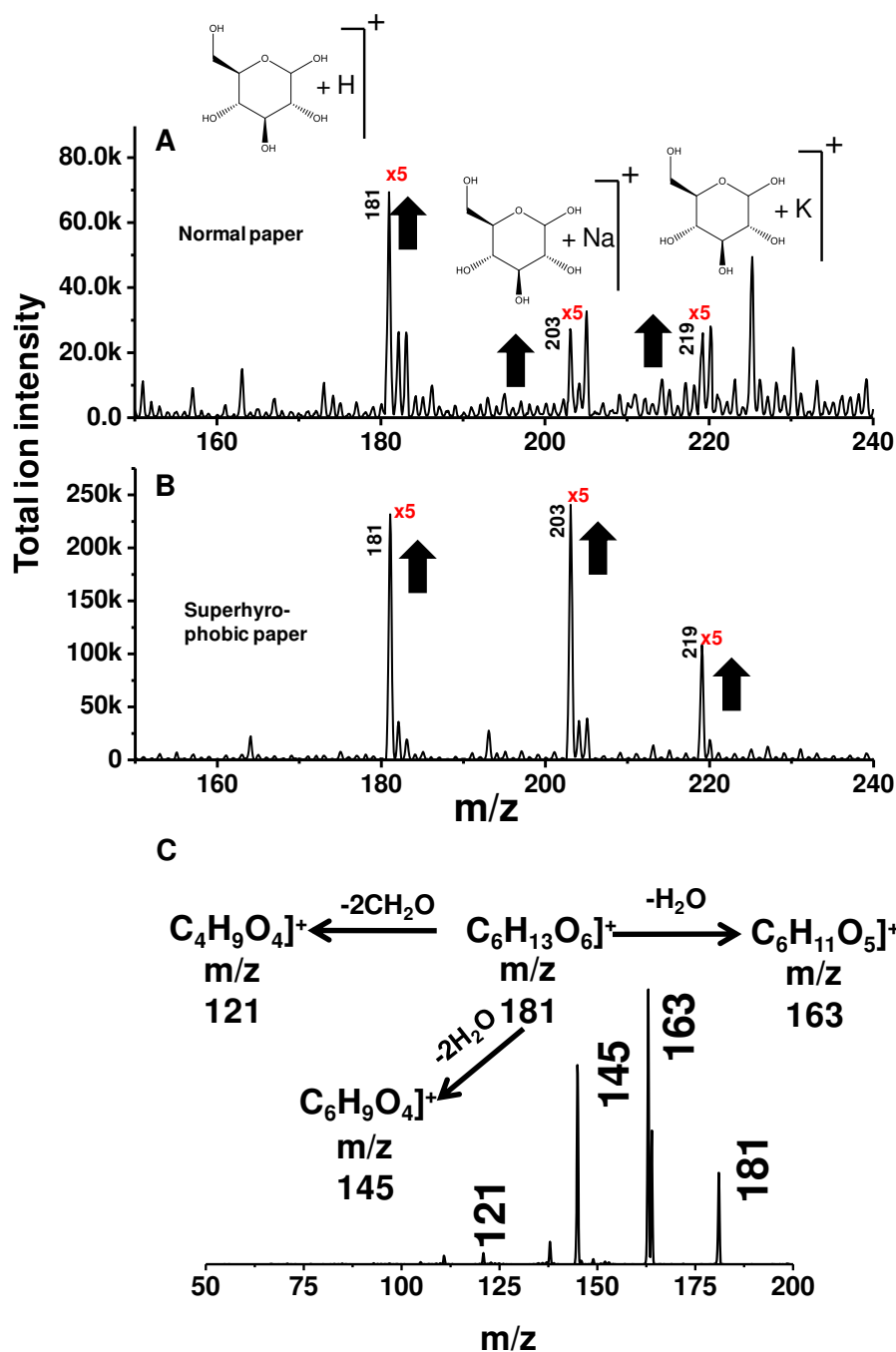


**Figure S13.** Comparative mass spectra of glucose in A) normal paper and B) superhydrophobic paper. C) MS<sup>2</sup> spectrum and the fragmentation pattern of the peak at  $m/z$  181.<sup>7</sup> The intensity of the mass peaks corresponding to proton, sodium and potassium added glucose are much lower in case of normal paper than that of superhydrophobic paper. To emphasize the peak positions, the peaks have been multiplied with a factor of 5 which are indicated by upward arrows. The glucose concentration used here was 2 ppt (10 pM).

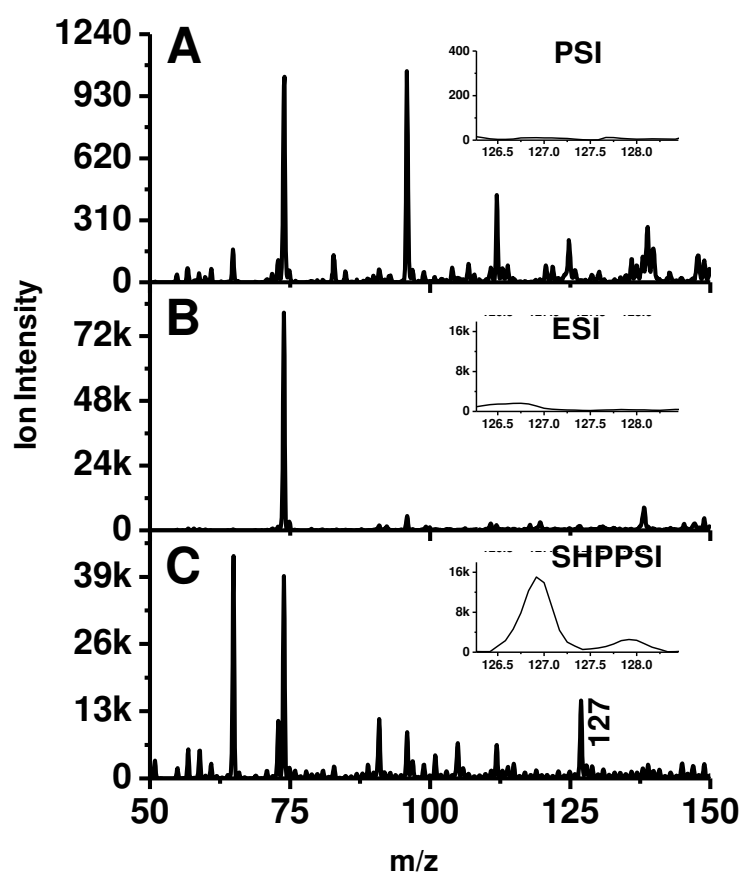


**Figure S14.** A) PSI, B) ESI, and C) SHPPSI mass spectra of melamine in water at 10 pM (1.2 ppt) concentration. Inset of each spectrum shows the zoomed in view of the selected peak at  $m/z$  127, due to protonated melamine.

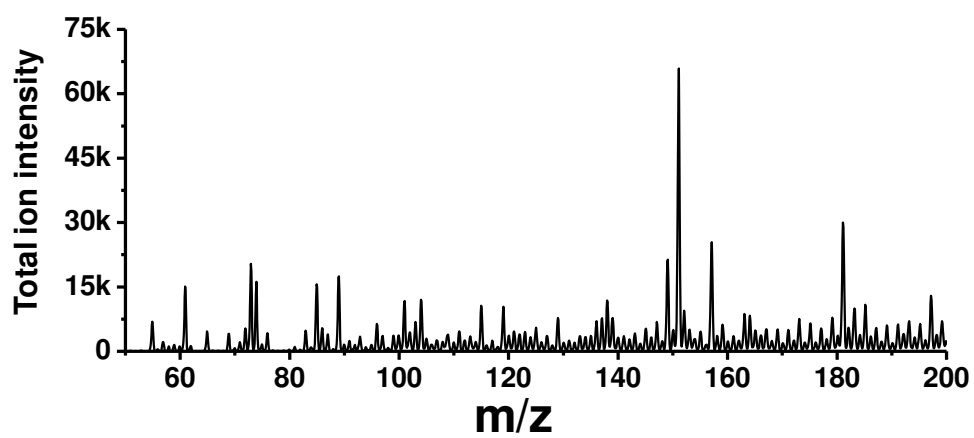


**Figure S15.** Mass spectrum of milk sample before spiking with melamine.

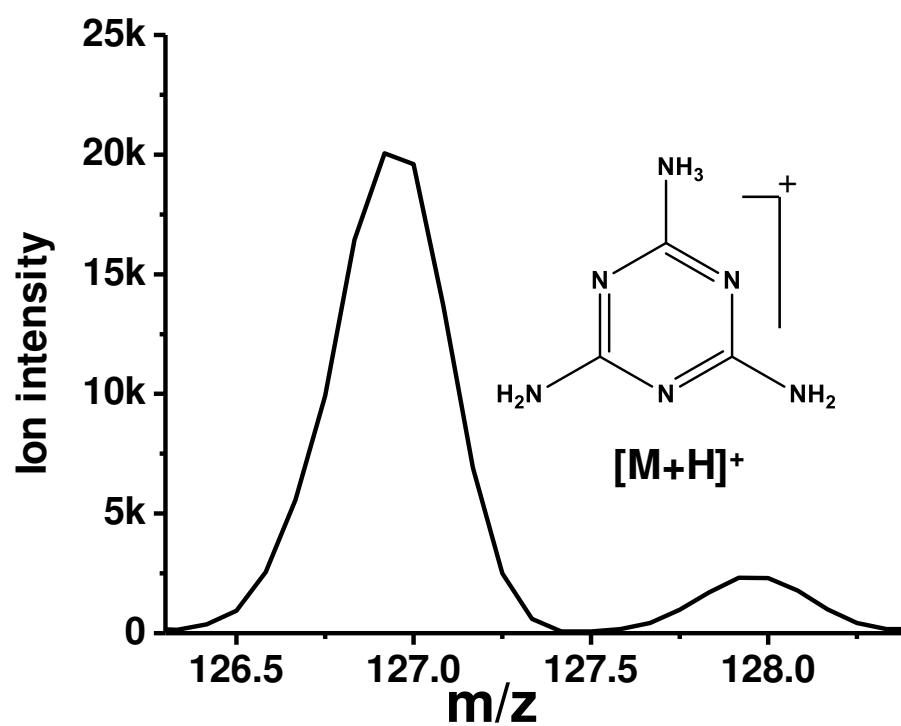


**Figure S16.** Mass spectrum of melamine found in laboratory-made artificially adulterated milk. Melamine concentration in the milk was 0.63 ppb (10 pM).

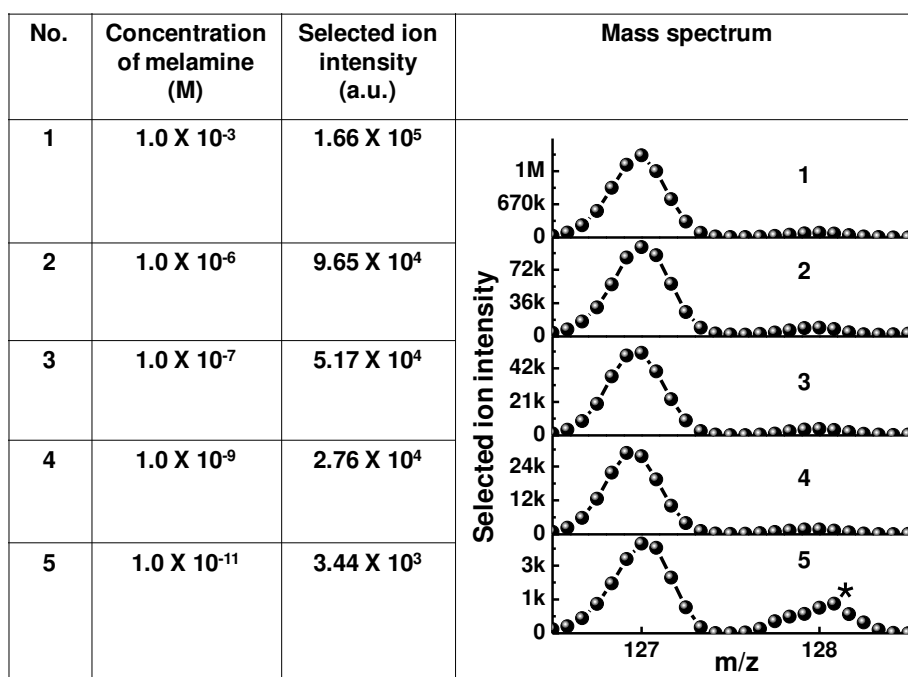


**Figure S17.** Mass spectra of 5 different concentrations of melamine, ranging from millimolar to picomolar. Peak labelled ‘\*’ is larger at a reduced concentration. May be it has an impurity in addition to the  $^{13}\text{C}$  isotopic peak of melamine. The chart represents the concentration of each solution and the peak intensity of melamine at the corresponding concentration.

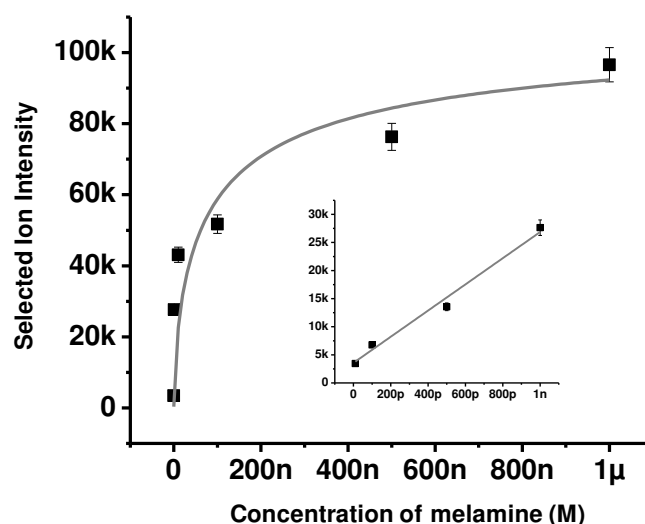


**Figure S18.** Calibration curve of melamine in water. Inset shows the graph at low concentrations of melamine.

## References

1. Kokotou, M. G.; Thomaidis, N. S., Behavior and retention models of melamine and its hydrolysis products. *Chromatographia* **2012**, 75 (9-10), 457-467.
2. Bianco, G.; Abate, S.; Labella, C.; Cataldi, T. R. I., Identification and fragmentation pathways of caffeine metabolites in urine samples via liquid chromatography with positive electrospray ionization coupled to a hybrid quadrupole linear ion trap (LTQ) and Fourier transform ion cyclotron resonance mass spectrometry and tandem mass spectrometry. *Rapid Commun Mass Spectrom* **2009**, 23 (7), 1065-74.
3. Ferreira, B. R. V.; Correa, D. N.; Eberlin, M. N.; Vendramini, P. H., Fragmentation reactions of rhodamine B and 6G as revealed by high accuracy orbitrap tandem mass spectrometry. *J. Braz. Chem. Soc.* **2017**, 28 (1), 136-142.
4. Baiocchi, C.; Brussino, M. C.; Pramauro, E.; Prevot, A. B.; Palmisano, L.; Marcì, G., Characterization of methyl orange and its photocatalytic degradation products by HPLC/UV-VIS diode array and atmospheric pressure ionization quadrupole ion trap mass spectrometry. *International Journal of Mass Spectrometry* **2002**, 214 (2), 247-256.
5. Choi, S.-S.; Song, M. J.; Kim, O.-B.; Kim, Y., Fragmentation patterns of protonated amino acids formed by atmospheric pressure chemical ionization. *Rapid Commun. Mass Spectrom.* **2013**, 27 (1), 143-151.
6. Soparawalla, S.; Salazar, G. A.; Sokol, E.; Perry, R. H.; Cooks, R. G., Trace detection of non-uniformly distributed analytes on surfaces using mass transfer and large-area desorption electrospray ionization (DESI) mass spectrometry. *Analyst* **2010**, 135 (8), 1953-1960.
7. Taylor, V. F.; March, R. E.; Longerich, H. P.; Stadey, C. J., A mass spectrometric study of glucose, sucrose, and fructose using an inductively coupled plasma and electrospray ionization. *International Journal of Mass Spectrometry* **2005**, 243 (1), 71-84.

# Confining an Ag<sub>10</sub> Core in an Ag<sub>12</sub> Shell: A Four-Electron Superatom with Enhanced Photoluminescence upon Crystallization

Esma Khatun,<sup>†</sup> Mohammad Bodiuzzaman,<sup>†</sup> Korath Shivan Sugi,<sup>†</sup> Papri Chakraborty,<sup>†</sup> Ganesan Paramasivam,<sup>†</sup> Wakeel Ahmed Dar,<sup>†</sup> Tripti Ahuja,<sup>†</sup> Sudhadevi Antharjanam,<sup>‡</sup> and Thalappil Pradeep<sup>\*,†</sup>

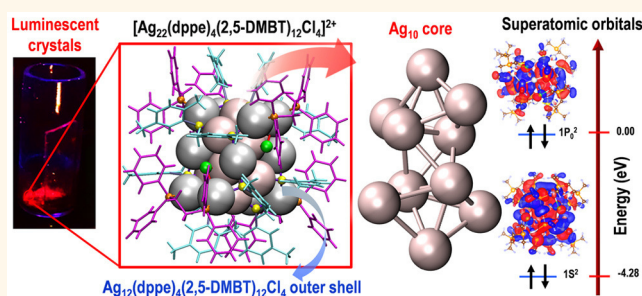
<sup>†</sup>Department of Chemistry, DST Unit of Nanoscience (DST UNS) and Thematic Unit of Excellence (TUE), Indian Institute of Technology Madras, Chennai 600036, India

<sup>‡</sup>Sophisticated Analytical Instruments Facility, Indian Institute of Technology Madras, Chennai 600036, India

## Supporting Information

**ABSTRACT:** We introduce a cluster coprotected by thiol and diphosphine ligands, [Ag<sub>22</sub>(dppe)<sub>4</sub>(2,5-DMBT)<sub>12</sub>Cl<sub>4</sub>]<sup>2+</sup> (dppe = 1,2-bis(diphenylphosphino)ethane; 2,5-DMBT = 2,5-dimethylbenzenethiol), which has an Ag<sub>10</sub> core encapsulated by an Ag<sub>12</sub>(dppe)<sub>4</sub>(2,5-DMBT)<sub>12</sub>Cl<sub>4</sub> shell. The Ag<sub>10</sub> core comprises two Ag<sub>5</sub> distorted trigonal bipyramidal units and is uncommon in Au and Ag nanoclusters. The electrospray ionization mass spectrum reveals that the cluster is divalent and contains four free electrons. An uncommon crystallization-induced enhancement of emission is observed in the cluster. The emission is weak in the solution and amorphous states. However, it is enhanced 12 times in the crystalline state compared to the amorphous state. A detailed investigation of the crystal structure suggests that well-arranged C–H⋯π and π⋯π interactions between the ligands are the major factors for this enhanced emission. Further, in-depth structural elucidation and density functional theory calculations suggest that the cluster is a superatom with four magic electrons.

**KEYWORDS:** nanocluster, crystallization induced emission enhancement, 1,2-bis(diphenylphosphino)ethane, 2,5-dimethylbenzenethiol, superatom, magic electron, photoluminescence



Atomically precise analogues of noble metals, also called as nanoclusters (NCs), have become an emerging category of nanomaterials, shown to be important in diverse applications such as sensing, catalysis, energy storage, drug delivery, cancer treatment, etc.<sup>1–8</sup> NCs have been used as nanoscale building blocks for creating solid-state materials.<sup>9,10</sup> Among these, Au NCs have been long studied due to their higher stability and biocompatibility. The synthesis of stable Ag NCs with well-defined structure and luminescence has drawn intense attention of researchers in the recent past.<sup>11–15</sup> Precision in their compositions and their structural diversity suggest possible structure–property relationships.<sup>16,17</sup> The properties of NCs can be tuned by changing the core structure as in the case of Au<sub>38</sub>(PET)<sub>24</sub> (PET = 2-phenylethanethiol) NCs.<sup>18</sup> Two isomeric Au<sub>38</sub>(PET)<sub>24</sub> NCs having different core structures exhibit different stability and catalytic activity. The sphere (icosahedral core) and rodlike (biicosahedral core) Au<sub>25</sub> NCs also display different catalytic activity for CO<sub>2</sub> electroreduction.<sup>19</sup> The protecting ligands such as thiols,<sup>20,21</sup> phosphines,<sup>22</sup> alkynyls,<sup>23</sup> calixarenes,<sup>24</sup> etc. also control the

properties of NCs.<sup>25–29</sup> Enhancement of photoluminescence (PL) after ligand modification in [Au<sub>22</sub>(SG)<sub>18</sub>] (SG = glutathione)<sup>30</sup> and [Au<sub>23</sub>(SR)<sub>16</sub>]<sup>31</sup> has been noted. Other than these, NCs are also protected with mixed ligands as in [Ag<sub>67</sub>(2,4-DMBT)<sub>32</sub>(PPh<sub>3</sub>)<sub>8</sub>]<sup>3+</sup> (2,4-DMBT = 2,4-dimethylbenzenethiol),<sup>32</sup> [Ag<sub>50</sub>(dppm)<sub>6</sub>(SR)<sub>30</sub>] (dppm = 1,1-bis(diphenylphosphino)methane),<sup>33</sup> [Ag<sub>14</sub>(SC<sub>6</sub>H<sub>3</sub>F<sub>2</sub>)<sub>12</sub>-(PPh<sub>3</sub>)<sub>8</sub>],<sup>34</sup> [Ag<sub>29</sub>(BDT)<sub>12</sub>(PPh<sub>3</sub>)<sub>4</sub>]<sup>3–</sup> (BDT = 1,3-benzenedithiol),<sup>35</sup> etc.<sup>36</sup> The mixed-ligand-protected NCs exhibit higher stability with enhanced properties as compared to single ligand protected ones.<sup>34,35,37</sup> Such an example is [Ag<sub>29</sub>(BDT)<sub>12</sub>-(PPh<sub>3</sub>)<sub>4</sub>]<sup>3–</sup>, which is less reactive to [Au<sub>25</sub>(PET)<sub>18</sub>]<sup>–</sup> compared to [Ag<sub>25</sub>(2,4-DMBT)<sub>18</sub>]<sup>–</sup> and [Ag<sub>44</sub>(SR)<sub>30</sub>]<sup>4–</sup>.<sup>38</sup> Further, by varying the secondary ligands, one can modulate the PL of this kind of NCs by keeping the cluster atomicity unaltered.<sup>39</sup>

**Received:** February 12, 2019

**Accepted:** April 24, 2019

**Published:** April 24, 2019



The stability of NCs is expressed in terms of the superatom structure which has been described by the jellium model. According to the spherical jellium model, shell-closing electron counts are 2, 8, 18, 20, 34, 40, 58, 68, 70, *etc.*, which are known as magic numbers. But change in shape and dimensionality result in other magic numbers such as 4 and 6 electrons for prolate and oblate systems, respectively.<sup>40</sup> Due to mixed ligand protection, NCs can show different shapes and structures. Hence, the underlying diversity of mixed ligand protected Ag NCs need to be explored in terms of their structures and properties and also to discover cluster systems with unknown geometric and electronic structures.

Herein, we report the synthesis, crystal structure, optical and electronic properties of  $[\text{Ag}_{22}(\text{dppe})_4(2,5\text{-DMBT})_{12}\text{Cl}_4]^{2+}$  (**I**) (dppe = 1,2-bis(diphenylphosphino)ethane), also referred to as  $\text{Ag}_{22}$  in the subsequent text. The cluster crystallizes in a tetragonal crystal system with an  $I4_1/a$  space group. The cluster has three characteristics: (i) it contains an uncommon  $\text{Ag}_{10}$  core which is formed by the combination of two perpendicularly connected  $\text{Ag}_5$  distorted trigonal bipyramidal (tbp) units, (ii) the 4e cluster displays  $1\text{S}^21\text{P}^2$  electronic shell closure as it has a prolate shaped structure which has not been observed in previously published Ag NCs,<sup>41</sup> and (iii) it exhibits crystallization-induced emission enhancement (CIEE). Apart from single-crystal X-ray diffraction study, **I** was thoroughly characterized by high-resolution electrospray ionization mass spectrometry (HRESI MS), scanning electron microscopy/energy dispersive spectroscopy (SEM/EDS), X-ray photoelectron spectroscopy (XPS), and infrared spectroscopy (IR). In addition, the electronic structure and optical properties are understood in detail by density functional theory (DFT) calculations.

## RESULTS AND DISCUSSION

The cluster **I** was prepared by a one-pot synthetic method which involved the reduction of silver–thiol–phosphine complexes (a detailed synthetic procedure is given in the [Experimental Section](#)). Briefly,  $\text{AgNO}_3$  was reduced by  $\text{NaBH}_4$  in the presence of 2,5-DMBT and dppe in MeOH/DCM (DCM = dichloromethane) under ice-cold conditions. Upon stirring the reaction product with  $\text{PPh}_4\text{Cl}$  and triethylamine for 12 h, absorption spectrum of the crude product was measured and exhibited distinct features at 415 and 497 nm along with a small hump at 635 nm, as presented in [Figure S1A](#). HRESI MS in the positive mode revealed that a mixture of clusters was present in the solution ([Figure S1B](#)). Hence, the solution was kept for size focusing for 2–3 days at 4 °C, and the final purified cluster was obtained in MeOH. The optical absorption spectrum of **I** presented in [Figure 1A](#) manifests well-defined sharp peaks at 368 and 512 nm along with two broad shoulder peaks centered at 445 and 670 nm. The cluster shows a sharp peak at  $m/z$  2876 in the HRESI MS, which suggests the formation of a monodispersed cluster ([Figure 1B](#)). No other prominent features were observed up to  $m/z$  10000. The cluster was divalent as confirmed by the characteristic difference between two successive peaks of the isotopic distribution, which was 0.5 ([Figure S2A](#)). Therefore, the peak at  $m/z$  2876 was assigned as  $[\text{Ag}_{22}(\text{dppe})_4(2,5\text{-DMBT})_{12}\text{Cl}_4]^{2+}$  whose experimental isotopic pattern matched well with the theoretical one ([Figure 1B](#)). The assignment was consistent with the single-crystal X-ray diffraction (SCXRD) data.

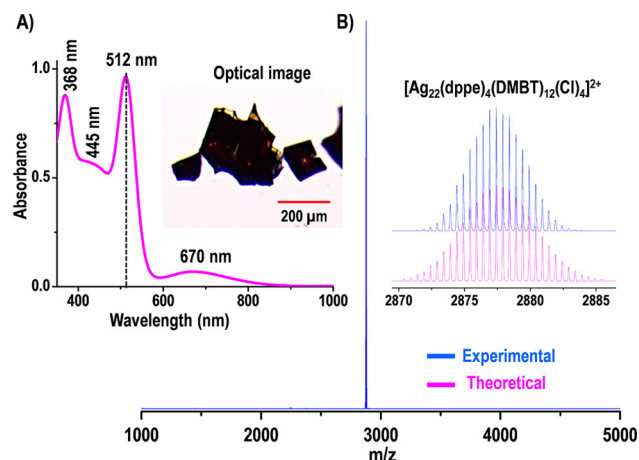


**Figure 1.** (A) Optical absorption spectrum of **I**. Inset: image of single crystals under a microscope. (B) HRESI MS of **I** which displays a peak at  $m/z$  2876. Inset: Comparison of the theoretical and the experimental isotopic distributions of **I**.

The collision-induced dissociation (CID) study of  $[\text{Ag}_{22}(\text{dppe})_4(2,5\text{-DMBT})_{12}\text{Cl}_4]^{2+}$  ( $m/z$  2876) is presented in [Figure S2B](#). A systematic loss of four dppe ligands is shown. Initially, two dppe ligands were lost followed by a  $[\text{Ag}(\text{dppe})]^+$  unit (panel b of [Figure S2B](#)). Hence, the cluster became singly charged (the formed species is  $[\text{Ag}_{21}(\text{dppe})(2,5\text{-DMBT})_{12}\text{Cl}_4]^+$  which was abbreviated as **II**), and a further increase in collision energy (CE) resulted in the removal of the remaining one dppe ligand which gave rise to a peak at  $m/z$  4052 (panel c of [Figure S2B](#)). At higher collision energies, detachments of Ag–Cl (panel b) and Ag–DMBT (panel c) units from **II** were observed. The crystals of **I** were obtained by layering hexane on the surface of the DCM/MeOH solution (1:1 v/v) and was kept for 2 weeks at 4 °C (a photograph of the crystals is shown in [Figure 1A](#)). Rectangular-shaped crystals appeared black in color and were of 150–300  $\mu\text{m}$  in dimension. Cluster **I** crystallizes in a body-centered tetragonal unit cell under the  $I4_1/a$  space group (detailed crystallographic analysis is given in the [Supporting Information \(SI\)](#)) containing four clusters per unit cell ([Figure S3A](#)). The atomic structure of **I** is presented in [Figure S3B,C](#).

The structural anatomy of **I** shows that it possesses an  $\text{Ag}_{10}$  core ([Figure 2A,B](#)) which has not been observed in previous reports of Au and Ag NCs (a list of known Ag structures is given in [Table S2](#)). The  $\text{Ag}_{10}$  core is made up of two  $\text{Ag}_5$  units having distorted trigonal bipyramidal (tbp) geometry ([Figure 2C](#)) which are connected to each other in a perpendicular fashion through the four axial Ag atoms forming a tetrahedron. The  $\text{Ag}_5$  units can also be viewed as a combination of two face-shared tetrahedra ([Figure S4](#)). Hence, the alternate structure of the  $\text{Ag}_{10}$  can be described as a combination of five edge and face-shared tetrahedra ([Figure S4](#)). The  $\text{Ag}_5$  units possess a chiral  $C_2$  point group while the  $\text{Ag}_{10}$  core unveils an achiral  $S_4$  point group.

The  $\text{Ag}_{10}$  core is encapsulated by an  $\text{Ag}_{12}(\text{dppe})_4(\text{DMBT})_{12}\text{Cl}_4$  shell ([Figure 2E–G](#)) which is formed by four  $\text{Ag}_2\text{SP}_2\text{Cl}$  and four  $\text{Ag}_2\text{S}$  staple motifs ([Figure 2G](#)). The shell can also be viewed as a combination of four  $\text{Ag}_2\text{S}_3\text{P}_2\text{Cl}$  and four Ag atoms ([Figure 2H](#)). Out of the four  $\text{Ag}_2\text{S}_3\text{P}_2\text{Cl}$  staples, two connect the first three layers of the core and the remaining two connect the last three layers in a similar

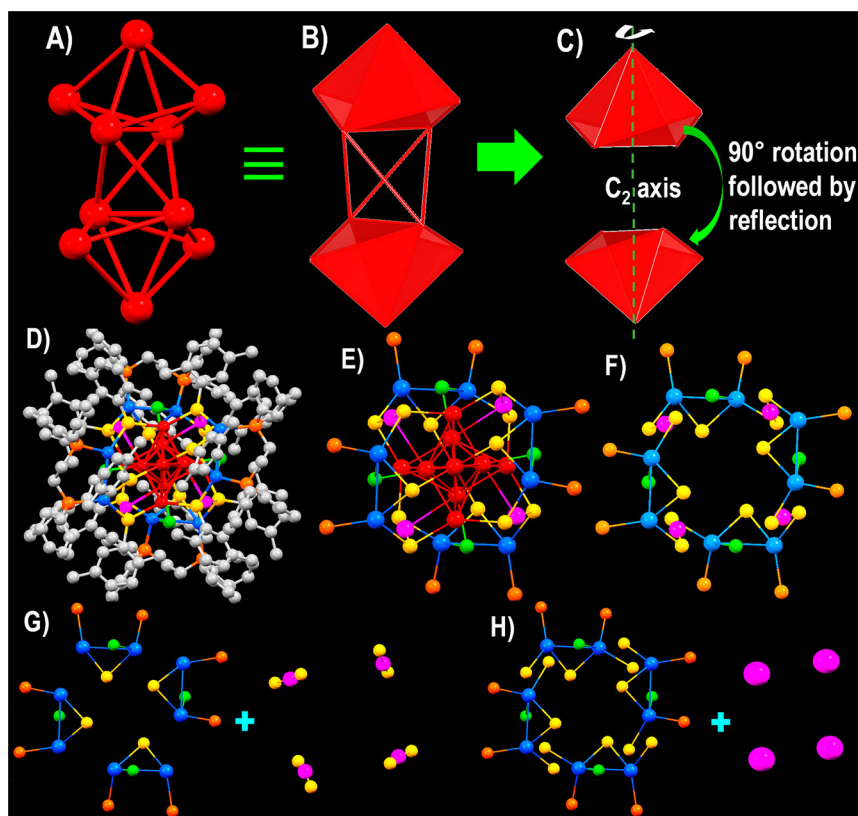


**Figure 2.** (A, B) Ball and stick and polyhedral representations of the  $\text{Ag}_{10}$  core, (C)  $\text{Ag}_5$  units having tbp geometry, (D, E) total structure of **I** with and without C and H atoms of ligands, (F) structure of  $\text{Ag}_{12}\text{P}_8\text{S}_{12}\text{Cl}_4$  shell, (G) four  $\text{Ag}_2\text{SP}_2\text{Cl}$  and  $\text{AgS}_2$  motifs, and (H) four  $\text{Ag}_2\text{S}_3\text{P}_2\text{Cl}$  and Ag atoms. Labels: red, blue, and pink = Ag; yellow = S; orange = P; green = Cl; gray = C; H atoms are omitted for clarity.

fashion, but rotated  $\sim 90^\circ$  along the  $C_2$  axis (Figure S5). The remaining four silver atoms are connected with the third and fourth layers of the  $\text{Ag}_{10}$  core and also act as bridging atoms between the tetrameric staples of the first three and the last three layers. Staples are connected to the core in such a way that  $S_4$  symmetry is maintained (Figure S6). The counterions that could be nitrates were not identified due to the disorder present in the crystal. However, the IR spectrum of **I** display peaks corresponding to N–O and N=O stretching frequencies (Figure S7A). In addition, the HRESI MS of **I** shows a peak corresponding to  $\text{NO}_3^-$  (Figure S7B). Therefore, the results of HRESI MS and IR confirm the presence of  $\text{NO}_3^-$  as the counterion.

The Ag–Ag bond lengths present in the  $\text{Ag}_{10}$  core range between 2.704 and 3.031 Å, which is similar to other thiol/phosphine-coprotected clusters.<sup>33,34,42</sup> The Ag–Ag distance in  $\text{Ag}_2\text{SP}_2\text{Cl}$  staple motifs is 3.144 Å, which is shorter than that of the other dppe-protected clusters.<sup>42</sup> The remaining four  $\text{AgS}_2$  staples where Ag atoms are directly bonded to the  $\text{Ag}_{10}$  core also display a shorter Ag–Ag distance (3.063 Å). The average Ag–S distance is 2.508 Å, which is shorter than that of monothiol-protected clusters<sup>20,21,27,42</sup> and almost similar to that of the dithiol-protected clusters.<sup>35</sup> The Ag–P bond length is 2.417 Å with a distorted P–C–C–P linkage.<sup>42</sup> The two P–C bonds are 1.861 and 1.777 Å because of the stronger C–H $\cdots\pi$  interactions between the benzene rings of dppe and 2,5-DMBT on one side (3.266, 2.852, 2.851 Å) than on another side (3.292, 3.072, 3.246 Å) (Figure S8). Other than dppe and 2,5-DMBT, the cluster is stabilized by Cl ligands which connect the Ag atoms of core and staples. In this cluster, Cl is strongly bonded to the metal core (2.491 Å) which is stronger

than bulk AgCl (2.77 Å), though the distance between Ag atoms of staples and Cl is slightly longer than that of the core (2.855 and 3.066 Å). Because of these strong interactions, **I** exhibits high stability at room temperature (Figure S9). The Cl atoms can be substituted by Br atoms using  $\text{PPh}_4\text{Br}$  which formed  $[\text{Ag}_{22}(\text{dppe})_4(\text{DMBT})_{12}\text{Cl}_{4-n}\text{Br}_n]$  with  $n = 0-4$  (Figure S10). This showed the anion-exchange capability of **I**. Further, the cluster was analyzed by SEM/EDS elemental mapping, which confirms the presence of Ag, S, Cl, and P (Figure S11). In addition, elemental characterization of **I** was performed using XPS (Figure S12). Peaks corresponding to Ag 3d<sub>5/2</sub>, S 2p<sub>3/2</sub>, P 2p<sub>3/2</sub>, and Cl 2p<sub>3/2</sub> appear at  $\sim 367.9$ ,  $\sim 162.2$ ,  $\sim 131.3$ , and  $\sim 198.0$  eV, respectively. Both Ag(0) and Ag(1) should be present in the spectrum, but it is hard to separate them.

Cluster **I** emitted in the red region with an emission maximum at  $\sim 670$  nm as shown in Figure 3A. The crystal displayed intense red photoluminescence (PL); however, when it was dissolved in MeOH, the intensity was reduced (QY of **I** in MeOH is  $5.3 \times 10^{-4}$ ). In addition, the amorphous powder made by evaporation of MeOH solution of **I** showed very weak emission. We have compared the luminescence intensities of the amorphous and crystalline forms of **I**. The densities of these forms are approximately the same. The experiments were done similarly with the same illumination volume and keeping all experimental parameters the same (details are given in the Experimental Section). The crystalline state exhibits 12 times more luminescence intensity than the amorphous powder. Detailed structural investigations showed the presence of strong intramolecular noncovalent C–H $\cdots\pi$  and  $\pi\cdots\pi$  interactions between the benzene rings of 2,5-DMBT and dppe in

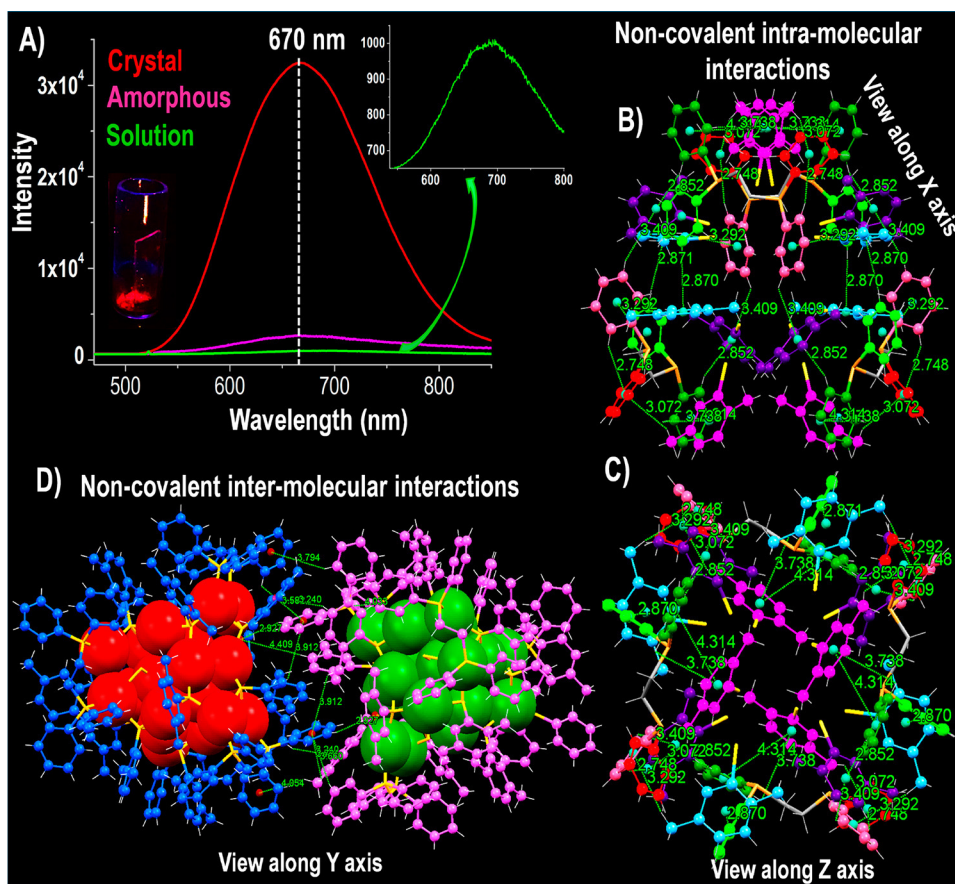


Figure 3. (A) Emission spectra of I in the crystalline (red), amorphous (pink), and solution (green) states. Inset: photograph under UV light shows red emission. (B, C) Intramolecular noncovalent interactions between protective ligands (metal atoms are omitted). (D) Noncovalent intermolecular interactions between protective ligands of two adjacent clusters.

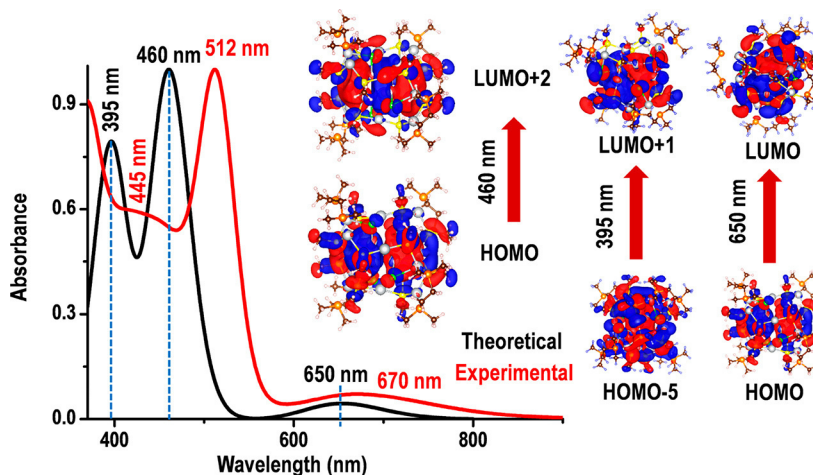


Figure 4. Experimental (red) and the theoretical (black) absorption spectra of I and the model cluster  $[\text{Ag}_{22}(\text{SMe})_{12}(\text{Me}_4\text{P}_2\text{C}_2\text{H}_4)_4\text{Cl}_4]^{2+}$ , respectively. K–S MOs are shown in the inset.

the crystal of I (Figure 3B,C). In addition, the clusters are strongly bonded to the neighboring one through strong C–H $\cdots\pi$  interactions between the ligands (Figure 3D). The packing diagrams shown in Figure S13 display that the clusters are packed in a rectangle and square 2D lattices along X/Y and Z axes, respectively. This extended intermolecular interaction gives rise to higher PL intensity in the crystalline state. The lower emission intensity in the amorphous state is because of the random arrangement of clusters which do not allow

formation of regular intermolecular as well as intramolecular interactions. Crystallization-induced emission enhancement is one type of aggregation induced emission (AIE) where the aggregation occurs in the crystalline state and molecules are arranged systematically.<sup>43</sup>

The electronic structure and optical spectrum of I were studied by density functional theory (DFT) and time-dependent DFT (TDDFT) calculations using the Gaussian G09 software. For calculations, the reduced model cluster,



$[\text{Ag}_{22}(\text{SMe})_{12}(\text{Me}_2\text{PCH}_2\text{CH}_2\text{PMe}_2)_4\text{Cl}_4]^{2+}$  was used where benzene groups of each 2,5-DMBT and dppe were simplified using  $-\text{CH}_3$  (or  $-\text{Me}$ ) groups (Figure S14). Further details of the computations are included in the Experimental Section. The theoretical and experimental absorption spectra presented in Figure 4 demonstrate that the theoretical spectrum is blue-shifted and is consistent with the experimental one (peaks at  $\sim 460$  and  $\sim 395$  nm are  $\sim 50$  nm blue-shifted while the peak at  $\sim 650$  nm is  $\sim 25$  nm blue-shifted), which is due to the reduced structure.<sup>32,35</sup> To analyze the contributions of atomic orbitals (AOs) in the molecular orbitals (MOs), the Kohn–Sham (K–S) MOs (inset of Figure 4) and the density of states (DOS) were calculated (Figure 5). The electronic transitions related

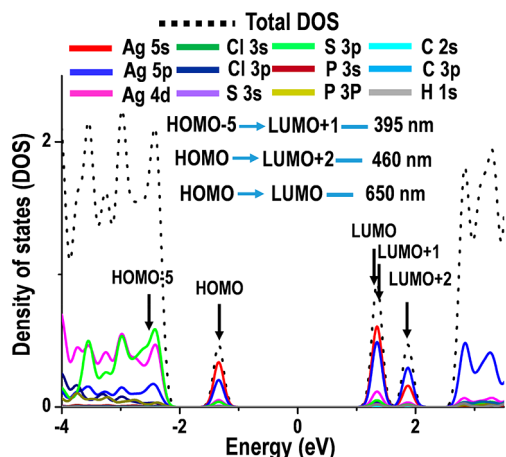


Figure 5. (B) The DOS analysis of MOs of the model cluster,  $[\text{Ag}_{22}(\text{SMe})_{12}(\text{Me}_4\text{P}_2\text{C}_2\text{H}_4)_4\text{Cl}_4]^{2+}$ .

to the peak at  $\sim 650$  nm originate from the highest occupied molecular orbital (HOMO) to the lowest unoccupied molecular orbital (LUMO). Hence, the theoretical energy gap is 1.9 eV, which is in accordance with  $\text{Au}_{22}$  and is higher than that of recently published  $\text{Ag}_{23}$  (1.4 eV).<sup>44,45</sup> The features at  $\sim 460$  and  $395$  nm arose due to the transitions between HOMO to LUMO+2 and HOMO–5 to LUMO+1, respectively (K–S MOs are given in the inset of Figure 4). The partial DOS spectra shown in Figure 5 show that HOMO, LUMO, LUMO+1, and LUMO+2 are mainly composed of 5s and 5p AOs of Ag, while HOMO–5 exhibits predominant contributions from Ag 4d and S 3p. Thus, the peaks at 650 and 460 nm are attributed to sp to sp interband transition while that of 395 nm is attributed to  $\pi$  to sp transition.

The jellium electron count of I gives 4e, which do not correspond to a shell-closing structure according to the spherical jellium model as electrons cannot be stabilized in spherical geometry. However, the 4e systems having a  $1\text{S}^21\text{P}^2$  configuration can be stabilized in a prolate geometry, which was explained by Mingos on the basis of the structural jellium model.<sup>46</sup> According to the hypothesis, the stabilization energy to place 2e in  $p_0$  is double that required for placing them in  $p_{\pm 1}$ , and hence, they have a preference for prolate geometry.<sup>40</sup> The silver framework in I possesses a prolate geometry similar to the previously reported 4e gold NCs (Figure S15).<sup>46</sup> The DFT calculation showed that I is a superatom with 4e and the electronic distributions in superatomic orbitals are presented in Figure S16 along with the isosurfaces of superatomic orbitals (analysis of superatomic orbitals are described in the Experimental Section). The higher stability of I may be due

to the presence of four magic electrons. The magic stability of I can also be described in terms of the superatom network (SAN) model which has been used to explain the stability of 4e gold NCs such as  $[\text{Au}_{18}(\text{SR})_{14}]$ ,  $[\text{Au}_{20}(\text{SR})_{16}]$ ,  $[\text{Au}_{24}(\text{SR})_{20}]$ , etc.<sup>47</sup> Cluster I is composed of the  $\text{Ag}_{10}^{6+}$  core, which is a combination of two 2e  $\text{tbp Ag}_5^{3+}$  units. Thus, the core can be viewed as a network of  $\text{Ag}_5^{3+}$  superatoms according to the SAN model.

## CONCLUSION

In conclusion, we have presented a silver cluster,  $\text{Ag}_{22}$ , with an  $\text{Ag}_{10}$  core which was formed by two orthogonal  $\text{Ag}_5$  distorted trigonal bipyramid units connected to each other to form an  $\text{Ag}_4$  tetrahedron. The  $\text{Ag}_5$  units were also expressed as two face-shared  $\text{Ag}_4$  tetrahedra. Thus, the  $\text{Ag}_{10}$  core was described as an arrangement of five  $\text{Ag}_4$  tetrahedra, and it was encapsulated by an outer shell,  $\text{Ag}_{12}(\text{dppe})_4(2,5\text{-DMBT})_{12}\text{Cl}_4$ . Though the cluster was feebly luminescent in solution, the crystal is highly luminescent due to extended C–H $\cdots\pi$  and  $\pi\cdots\pi$  interactions. This enhancement has rarely been observed in a pure Ag NC. Theoretical calculations showed that the cluster contains superatomic orbitals with four magic electrons which contribute to the magic stability of  $\text{Ag}_{22}$ . This work highlights the unknown aspects of mixed ligand protected silver NCs and suggests additional possibilities with them.

## EXPERIMENTAL SECTION

**Chemicals and Materials.** Silver nitrate ( $\text{AgNO}_3$ ), triethylamine, and dppe were purchased from Rankem Chemicals. Tetraphenylphosphonium chloride ( $\text{PPh}_4\text{Cl}$ ), 2,5-DMBT, sodium borohydride ( $\text{NaBH}_4$ , 98%), and triphenylphosphine ( $\text{PPh}_3$ ) were purchased from Sigma-Aldrich. All chemicals were used as received without further purification. All the solvents such as DCM, MeOH, *n*-hexane, *N,N*-dimethylformamide (DMF), acetonitrile (ACN), and  $\text{CHCl}_3$  were purchased from Rankem Chemicals and were of analytical grade.

**Synthesis of  $[\text{Ag}_{22}(\text{dppe})_4(2,5\text{-DMBT})_{12}\text{Cl}_4]^{2+}$  (I).** In a typical one-pot synthesis,  $\sim 20$  mg of  $\text{AgNO}_3$  was dissolved in MeOH/DCM (5/9 v/v) followed by the addition of 10  $\mu\text{L}$  of 2,5-DMBT. Then 10 mg of dppe was added to the reaction mixture and kept stirring. After 15–20 min, 20 mg of  $\text{NaBH}_4$  (in 1 mL of ice-cold water) was added dropwise to the mixture, which changed the color from yellow to dark brown. After that, 10 mg of  $\text{PPh}_4\text{Cl}$  and 30  $\mu\text{L}$  of triethylamine were added. The reaction was kept under stirring for 12 h under ice-cold conditions. After completion of the reaction, it was kept for 2–3 days at 4  $^\circ\text{C}$ . The mixture was then thoroughly washed with MeOH/ $\text{H}_2\text{O}$  followed by complete solvent evaporation. Then the cluster was extracted using MeOH and dried on a rotavapor. The obtained purified NC showed high solubility in various organic solvents such as MeOH, DCM, DMF, ACN,  $\text{CHCl}_3$ , etc. All measurements were performed in MeOH.

**Crystallization of  $[\text{Ag}_{22}(\text{dppe})_4(2,5\text{-DMBT})_{12}\text{Cl}_4]^{2+}$  (I).** About 45 mg of the purified cluster was dissolved in 1.5 mL of DCM and 0.5 mL of MeOH. Then the cluster solution was filtered by a syringe filter of 0.22  $\mu\text{m}$  pore size, and it was layered by 2 mL of hexane. The sample was kept at 4  $^\circ\text{C}$ , and the black crystals were formed after 2 weeks. Distilled solvents were used for crystallization.

**Characterization.** UV–vis spectra were measured using a PerkinElmer Lambda 25 spectrometer. HRESI MS were recorded using a Waters Synapt G2-Si high-resolution mass spectrometer in the positive-ion mode. Emission spectra of the cluster were collected in a Witec GmbH, Alpha-SNOM alpha300S confocal Raman instrument equipped with 532 nm laser as the excitation source. A laser power of 500  $\mu\text{W}$  with integration time of 0.1 s and two accumulations were used throughout the experiments. IR spectra were recorded using a JASCO-FT/IR-4100 spectrometer. XPS measurements were carried out with an Omicron ESCA Probe spectrometer with polychromatic

Al K $\alpha$  X-rays ( $h\nu = 1486.7$  eV). During the measurement, pass energy for the survey scans was kept at 50 eV, which was changed to 20 eV for specific regions. Binding energies (BE) of the core levels were calibrated with C 1s BE set at 285 eV. SEM measurements were performed using FEI Quanta 200 operating at 30 kV equipped with EDS. X-ray data collection was performed with Bruker AXS Kappa Apex III CMOS diffractometer equipped with graphite monochromated Mo (K $\alpha$ ) ( $\lambda = 0.71073$  Å) radiation at 273 K (further details are presented in the SI).

**Quantum Yield Measurements.** The PL quantum yield (QY) of I in solution (MeOH) was calculated by the integrated luminescence intensity method where emission intensity of I was compared to that of rhodamine 6G (QY is 1 in MeOH). The PL QY of a sample can be calculated from the following equation

$$\varphi_s = \frac{F_s}{A_s} \times \frac{A_r}{F_r} \times \frac{n_s^2}{n_r^2} \times \varphi_r$$

where “s” and “r” refer to the clusters and the reference;  $\varphi_s$  and  $\varphi_r$  are the QY of the sample and that of the reference;  $F_s$  and  $F_r$  are the integrated intensity of the samples and the reference;  $A_s$  and  $A_r$  are the absorbance of the sample and the reference at the excitation wavelength; and  $n_s$  and  $n_r$  are the refractive indices of the sample and reference solution, respectively.

**Computational Details.** The structural, electronic, and optical properties of I were computationally studied using DFT and TDDFT. All of the calculations were performed using the Gaussian09 software package.<sup>48</sup> Initially, all of the phenyl rings of I in its crystal form were replaced by the reduced model ligands (CH<sub>3</sub>), and then the structure was optimized by allowing only relaxation of the C and H atoms in the DFT formalism with a PBE1PBE exchange-correlation functional,<sup>49</sup> which is extensively used for electronic structure calculations, along with the Los Alamos double- $\zeta$  effective core potential (LANL2DZ) basis set.<sup>50</sup> Further, the vibrational frequency calculations were performed at the same level of theory to check that the structures have any saddle points. The absorption spectrum of the [Ag<sub>22</sub>(SMe)<sub>12</sub>(P<sub>2</sub>(CH<sub>2</sub>)<sub>2</sub>(Me)<sub>4</sub>)<sub>4</sub>Cl<sub>4</sub>]<sup>2+</sup> cluster was calculated by the TD-DFT at the same level of theory. The electronic properties such as superatomic orbital analysis, the total DOS, and partial DOS (PDOS) were also calculated and analyzed by using the Multiwfn3.3.5 package.<sup>51</sup> The natural population analysis was utilized to identify the character of superatomic orbital using the NBO 3.1 software.<sup>52</sup> For all of the spectra, the Fermi level (EF) was centered at the middle of the HOMO–LUMO gap. Superatomic orbitals were analyzed following a recent publication of Jiang et al.<sup>53</sup> According to this report, all superatomic orbitals should have higher s orbital contribution over the p and d orbital contributions. This is an important requirement as it describes the state of free electrons. The nature of the superatomic orbitals is usually confirmed by the computation of the superatomic DOS, which is obtained by projection of the Kohn–Sham states onto cluster-centered spherical harmonic functions (Y<sub>lm</sub>( $\theta, \varphi$ )), which was beyond our present capabilities. Still, the superatomic orbital assignments made by NBO 3.1 software show the essential superatomic properties of the cluster.

## ASSOCIATED CONTENT

### Supporting Information

The Supporting Information is available free of charge on the ACS Publications website at DOI: 10.1021/acsnano.9b01189.

Crystallographic analysis and structure of [Ag<sub>22</sub>(dppe)<sub>4</sub>(2,5-DMBT)<sub>12</sub>Cl<sub>4</sub>]<sup>2+</sup> (CIF)  
IR, SEM, and XPS data and theoretical analysis (PDF)

## AUTHOR INFORMATION

### Corresponding Author

\*E-mail: pradeep@iitm.ac.in.

### ORCID

Thalappil Pradeep: 0000-0003-3174-534X

## Notes

The authors declare no competing financial interest.

## ACKNOWLEDGMENTS

We thank the Department of Science and Technology (DST) for supporting our research program. We thank the Sophisticated Analytical Instruments Facility, Indian Institute of Technology Madras, for SCXRD data collection. E.K. and T.A. thank IIT Madras for institute doctoral fellowships. M.B. and K.S.S. thank U.G.C. for their research fellowships. P.C. thanks the Council of Scientific and Industrial Research (CSIR) for a research fellowship. G.P. thanks IITM for an Institute Postdoctoral Fellowship. W.A.D. thanks SERB-DST for the award of a National Postdoctoral fellowship.

## REFERENCES

- (1) Chakraborty, I.; Pradeep, T. Atomically Precise Clusters of Noble Metals: Emerging Link between Atoms and Nanoparticles. *Chem. Rev.* **2017**, *117*, 8208–8271.
- (2) Mathew, A.; Sajanlal, P. R.; Pradeep, T. Selective Visual Detection of TNT at the Sub-Zeptomole Level. *Angew. Chem., Int. Ed.* **2012**, *51*, 9596–9600.
- (3) Tyo, E. C.; Vajda, S. Catalysis by Clusters with Precise Numbers of Atoms. *Nat. Nanotechnol.* **2015**, *10*, 577–588.
- (4) Mathew, A.; Pradeep, T. Noble Metal Clusters: Applications in Energy, Environment, and Biology. *Part. Part. Syst. Charact.* **2014**, *31*, 1017–1053.
- (5) Lin, C.-A. J.; Yang, T.-Y.; Lee, C.-H.; Huang, S. H.; Sperling, R. A.; Zanella, M.; Li, J. K.; Shen, J.-L.; Wang, H.-H.; Yeh, H.-I.; Parak, W. J.; Chang, W. H. Synthesis, Characterization, and Bioconjugation of Fluorescent Gold Nanoclusters toward Biological Labeling Applications. *ACS Nano* **2009**, *3*, 395–401.
- (6) Ghosh, A.; Jeseentharani, V.; Ganayee, M. A.; Hemalatha, R. G.; Chaudhari, K.; Vijayan, C.; Pradeep, T. Approaching Sensitivity of Tens of Ions Using Atomically Precise Cluster-Nanofiber Composites. *Anal. Chem.* **2014**, *86*, 10996–11001.
- (7) Gross, E.; Liu, J. H.; Alayoglu, S.; Marcus, M. A.; Fakra, S. C.; Toste, F. D.; Somorjai, G. A. Asymmetric Catalysis at the Mesoscale: Gold Nanoclusters Embedded in Chiral Self-Assembled Monolayer as Heterogeneous Catalyst for Asymmetric Reactions. *J. Am. Chem. Soc.* **2013**, *135*, 3881–3886.
- (8) Draz, M. S.; Fang, B. A.; Li, L.; Chen, Z.; Wang, Y.; Xu, Y.; Yang, J.; Killeen, K.; Chen, F. Hybrid Nanocluster Plasmonic Resonator for Immunological Detection of Hepatitis B Virus. *ACS Nano* **2012**, *6*, 7634.
- (9) Pinkard, A.; Champsaur, A. M.; Roy, X. Molecular Clusters: Nanoscale Building Blocks for Solid-State Materials. *Acc. Chem. Res.* **2018**, *51*, 919–929.
- (10) Chakraborty, P.; Nag, A.; Chakraborty, A.; Pradeep, T. Approaching Materials with Atomic Precision Using Supramolecular Cluster Assemblies. *Acc. Chem. Res.* **2019**, *52*, 2–11.
- (11) Jin, R.; Zeng, C.; Zhou, M.; Chen, Y. Atomically Precise Colloidal Metal Nanoclusters and Nanoparticles: Fundamentals and Opportunities. *Chem. Rev.* **2016**, *116*, 10346–10413.
- (12) Zeng, C. Precision at the Nanoscale: On the Structure and Property Evolution of Gold Nanoclusters. *Pure Appl. Chem.* **2018**, *90*, 1409–1427.
- (13) Yao, Q.; Chen, T.; Yuan, X.; Xie, J. Toward Total Synthesis of Thiolate-Protected Metal Nanoclusters. *Acc. Chem. Res.* **2018**, *51*, 1338–1348.
- (14) Udayabhaskararao, T.; Pradeep, T. New Protocols for the Synthesis of Stable Ag and Au Nanocluster Molecules. *J. Phys. Chem. Lett.* **2013**, *4*, 1553–1564.
- (15) Song, Y.; Lambright, K.; Zhou, M.; Kirschbaum, K.; Xiang, J.; Xia, A.; Zhu, M.; Jin, R. Large-Scale Synthesis, Crystal Structure, and Optical Properties of the Ag<sub>146</sub>Br<sub>2</sub>(SR)<sub>80</sub> Nanocluster. *ACS Nano* **2018**, *12*, 9318–9325.

- (16) Joshi, C. P.; Bootharaju, M. S.; Bakr, O. M. Tuning Properties in Silver Clusters. *J. Phys. Chem. Lett.* **2015**, *6*, 3023–3035.
- (17) Negishi, Y.; Sakamoto, C.; Ohya, T.; Tsukuda, T. Synthesis and the Origin of the Stability of Thiolate-Protected Au<sub>130</sub> and Au<sub>187</sub> Clusters. *J. Phys. Chem. Lett.* **2012**, *3*, 1624–1628.
- (18) Tian, S.; Li, Y.-Z.; Li, M.-B.; Yuan, J.; Yang, J.; Wu, Z.; Jin, R. Structural Isomerism in Gold Nanoparticles Revealed by X-Ray Crystallography. *Nat. Commun.* **2015**, *6*, 8667.
- (19) Zhao, S.; Austin, N.; Li, M.; Song, Y.; House, S. D.; Bernhard, S.; Yang, J. C.; Mpourmpakis, G.; Jin, R. Influence of Atomic-Level Morphology on Catalysis: The Case of Sphere and Rod-Like Gold Nanoclusters for CO<sub>2</sub> Electoreduction. *ACS Catal.* **2018**, *8*, 4996–5001.
- (20) Yang, H.; Wang, Y.; Huang, H.; Gell, L.; Lehtovaara, L.; Malola, S.; Häkkinen, H.; Zheng, N. All-Thiol-Stabilized Ag<sub>44</sub> and Au<sub>12</sub>Ag<sub>32</sub> Nanoparticles with Single-Crystal Structures. *Nat. Commun.* **2013**, *4*, 2422.
- (21) Joshi, C. P.; Bootharaju, M. S.; Alhilaly, M. J.; Bakr, O. M. [Ag<sub>25</sub>(SR)<sub>18</sub>]<sup>−</sup>: The “Golden” Silver Nanoparticle Silver Nanoparticle. *J. Am. Chem. Soc.* **2015**, *137*, 11578–11581.
- (22) Bootharaju, M. S.; Dey, R.; Gevers, L. E.; Hedhili, M. N.; Basset, J. M.; Bakr, O. M. A New Class of Atomically Precise, Hydride-Rich Silver Nanoclusters Co-Protected by Phosphines. *J. Am. Chem. Soc.* **2016**, *138*, 13770–13773.
- (23) Qu, M.; Li, H.; Xie, L. H.; Yan, S. T.; Li, J. R.; Wang, J. H.; Wei, C. Y.; Wu, Y. W.; Zhang, X. M. Bidentate Phosphine-Assisted Synthesis of an All-Alkynyl-Protected Ag<sub>74</sub> Nanocluster. *J. Am. Chem. Soc.* **2017**, *139*, 12346–12349.
- (24) Guan, Z. J.; Zeng, J. L.; Nan, Z. A.; Wan, X. K.; Lin, Y. M.; Wang, Q. M. Thiacalix[4]Arene: New Protection for Metal Nanoclusters. *Sci. Adv.* **2016**, *2*, 1–8.
- (25) Li, B.; Huang, R.-W.; Qin, J.-H.; Zang, S.-Q.; Gao, G.-G.; Hou, H.-W.; Mak, T. C. W. Thermochromic Luminescent Nest-Like Silver Thiolate Cluster. *Chem. - Eur. J.* **2014**, *20*, 12416–12420.
- (26) Li, G.; Lei, Z.; Wang, Q.-M. Luminescent Molecular Ag-S Nanocluster [Ag<sub>62</sub>S<sub>13</sub>(SBU)<sub>32</sub>](BF<sub>4</sub>)<sub>4</sub>. *J. Am. Chem. Soc.* **2010**, *132*, 17678–17679.
- (27) Zou, X.; Jin, S.; Du, W.; Li, Y.; Li, P.; Wang, S.; Zhu, M. Multi-Ligand-Directed Synthesis of Chiral Silver Nanoclusters. *Nanoscale* **2017**, *9*, 16800–16805.
- (28) Khatun, E.; Ghosh, A.; Ghosh, D.; Chakraborty, P.; Nag, A.; Mondal, B.; Chennu, S.; Pradeep, T. [Ag<sub>50</sub>(2,5-DCBT)<sub>32</sub>]<sup>3−</sup>: A New Cluster and a Precursor for Three Well-Known Clusters. *Nanoscale* **2017**, *9*, 8240–8248.
- (29) Li, G.; Abroshan, H.; Liu, C.; Zhuo, S.; Li, Z.; Xie, Y.; Kim, H. J.; Rosi, N. L.; Jin, R. Tailoring the Electronic and Catalytic Properties of Au<sub>25</sub> Nanoclusters via Ligand Engineering. *ACS Nano* **2016**, *10*, 7998–8005.
- (30) Pyo, K.; Thanthirige, V. D.; Yoon, S. Y.; Ramakrishna, G.; Lee, D. Enhanced Luminescence of Au<sub>22</sub>(SG)<sub>18</sub> Nanoclusters via Rational Surface Engineering. *Nanoscale* **2016**, *8*, 20008–20016.
- (31) Li, Q.; Wang, S.; Zhu, X.; Song, Y.; Jin, R.; Luo, T.-Y.; Rosi, N. L.; Taylor, M. G.; Mpourmpakis, G. Molecular “Surgery” on a 23-Gold-Atom Nanoparticle. *Sci. Adv.* **2017**, *3*, No. e1603193.
- (32) Alhilaly, M. J.; Bootharaju, M. S.; Joshi, C. P.; Besong, T. M.; Emwas, A. H.; Juarez-Mosqueda, R.; Kaappa, S.; Malola, S.; Adil, K.; Shkurenko, A.; Häkkinen, H.; Eddaoudi, M.; Bakr, O. M. [Ag<sub>67</sub>(SPhMe<sub>2</sub>)<sub>32</sub>(PPh<sub>3</sub>)<sub>8</sub>]<sup>3+</sup>: Synthesis, Total Structure, and Optical Properties of a Large Box-Shaped Silver Nanocluster. *J. Am. Chem. Soc.* **2016**, *138*, 14727–14732.
- (33) Du, W.; Jin, S.; Xiong, L.; Chen, M.; Zhang, J.; Zou, X.; Pei, Y.; Wang, S.; Zhu, M. Ag<sub>50</sub>(Dppm)<sub>6</sub>(SR)<sub>30</sub> and Its Homologue Au<sub>x</sub>Ag<sub>50-x</sub>(Dppm)<sub>6</sub>(SR)<sub>30</sub> Alloy Nanocluster: Seeded Growth, Structure Determination, and Differences in Properties. *J. Am. Chem. Soc.* **2017**, *139*, 1618–1624.
- (34) Yang, H.; Lei, J.; Wu, B.; Wang, Y.; Zhou, M.; Xia, A.; Zheng, L.; Zheng, N. Crystal Structure of a Luminescent Thiolated Ag Nanocluster with an Octahedral Ag<sub>64+</sub> Core. *Chem. Commun.* **2013**, *49*, 300–302.
- (35) AbdulHalim, L. G.; Bootharaju, M. S.; Tang, Q.; Del Gobbo, S.; AbdulHalim, R. G.; Eddaoudi, M.; Jiang, D.; Bakr, O. M. Ag<sub>29</sub>(BDT)<sub>12</sub>(TPP)<sub>4</sub>: A Tetravalent Nanocluster. *J. Am. Chem. Soc.* **2015**, *137*, 11970–11975.
- (36) Bodiuzzaman, M.; Ghosh, A.; Shivan Sugi, K.; Nag, A.; Khatun, E.; Varghese, B.; Paramasivam, G.; Antharjanam, S.; Natarajan, G.; Pradeep, T. Camouflaging Structural Diversity: Co-Crystallization of Two Different Nanoparticles Having Different Cores but the Same Shell. *Angew. Chem., Int. Ed.* **2019**, *58*, 189–194.
- (37) Chen, T.; Yang, S.; Chai, J.; Song, Y.; Fan, J.; Rao, B.; Sheng, H.; Yu, H.; Zhu, M. Crystallization-Induced Emission Enhancement: A Novel Fluorescent Au-Ag Bimetallic Nanocluster with Precise Atomic Structure. *Sci. Adv.* **2017**, *3*, No. e1700956.
- (38) Ghosh, A.; Ghosh, D.; Khatun, E.; Chakraborty, P.; Pradeep, T. Unusual Reactivity of Dithiol Protected Clusters in Comparison to Monothiol Protected Clusters: Studies Using Ag<sub>31</sub>(BDT)<sub>19</sub>(TPP)<sub>3</sub> and Ag<sub>29</sub>(BDT)<sub>12</sub>(TPP)<sub>4</sub>. *Nanoscale* **2017**, *9*, 1068–1077.
- (39) Khatun, E.; Ghosh, A.; Chakraborty, P.; Singh, P.; Bodiuzzaman, M.; Ganesan, P.; Natarajan, G.; Ghosh, J.; Pal, S. K.; Pradeep, T. A Thirty-Fold Photoluminescence Enhancement Induced by Secondary Ligands in Monolayer Protected Silver Clusters. *Nanoscale* **2018**, *10*, 20033–20042.
- (40) Mingos, D. M. P.; Slee, T.; Zhenyang, L. Bonding Models for Ligated and Bare Clusters. *Chem. Rev.* **1990**, *90*, 383–402.
- (41) Goh, J.-Q.; Akola, J. Superatom Model for Ag–S Nanocluster with Delocalized Electrons. *J. Phys. Chem. C* **2015**, *119*, 21165–21172.
- (42) Yang, H.; Wang, Y.; Zheng, N. Stabilizing Subnanometer Ag(0) Nanoclusters by Thiolate and Diphosphine Ligands and Their Crystal Structures. *Nanoscale* **2013**, *5*, 2674–2677.
- (43) Wu, Z.; Mo, S.; Tan, L.; Fang, B.; Su, Z.; Zhang, Y.; Yin, M. Crystallization-Induced Emission Enhancement of a Deep-Blue Luminescence Material with Tunable Mechano- and Thermochromism. *Small* **2018**, *14*, 1802524.
- (44) Liu, C.; Li, T.; Abroshan, H.; Li, Z.; Zhang, C.; Kim, H. J.; Li, G.; Jin, R. Chiral Ag<sub>23</sub> Nanocluster with Open Shell Electronic Structure and Helical Face-Centered Cubic Framework. *Nat. Commun.* **2018**, *9*, 744.
- (45) Chen, J.; Zhang, Q.-F.; Bonaccorso, T. A.; Williard, P. G.; Wang, L.-S. Controlling Gold Nanoclusters by Diphosphine Ligands. *J. Am. Chem. Soc.* **2014**, *136*, 92–95.
- (46) Shichibu, Y.; Zhang, M.; Kamei, Y.; Konishi, K. [Au<sub>7</sub>]<sup>3+</sup>: A Missing Link in the Four-Electron Gold Cluster Family. *J. Am. Chem. Soc.* **2014**, *136*, 12892–12895.
- (47) Cheng, L.; Yuan, Y.; Zhang, X.; Yang, J. Superatom Networks in Thiolate-Protected Gold Nanoparticles. *Angew. Chem., Int. Ed.* **2013**, *52* (34), 9035–9039.
- (48) Frisch, M. J.; Trucks, G. W.; Schlegel, H. B.; Scuseria, G. E.; Robb, M. A.; Cheeseman, J. R.; Scalmani, G.; Barone, V.; Mennucci, B.; Petersson, G. A.; Nakatsuji, H.; Caricato, M.; Li, X.; Hratchian, H. P.; Izmaylov, A. F.; Bloino, J.; Zheng, G.; Sonnenberg, J. L.; Hada, M.; Ehara, M. et al. *Gaussian 09*, Revision B.01; Gaussian, Inc.: Wallingford, CT, 2009.
- (49) Stephens, P. J.; Devlin, F. J.; Chabalowski, C. F.; Frisch, M. J. *Ab Initio* Calculation of Vibrational Absorption and Circular Dichroism Spectra Using Density Functional Force Fields. *J. Phys. Chem.* **1994**, *98*, 11623–11627.
- (50) Hay, P. J.; Wadt, W. R. *Ab Initio* Effective Core Potentials for Molecular Calculations. Potentials for the Transition Metal Atoms Sc to Hg. *J. Chem. Phys.* **1985**, *82*, 270–283.
- (51) Lu, T.; Chen, F. Multiwfn: A Multifunctional Wavefunction Analyzer. *J. Comput. Chem.* **2012**, *33*, 580–592.
- (52) Glendening, E. D.; Reed, A. E.; Carpenter, J. E.; Weinhold, F. *NBO*, version 3.1, 2009.
- (53) Jiang, W.; Gao, Y.; Xu, D.; Liu, F.; Wang, Z. Structural Influence on Superatomic Orbitals of Typical Gold Nanostructure Building Blocks. *J. Electron. Mater.* **2017**, *46*, 3938–3941.



## Supporting Information

### Confining an Ag<sub>10</sub> Core in an Ag<sub>12</sub> Shell: A Four-Electron Superatom with Enhanced Photoluminescence upon Crystallization

Esma Khatun,<sup>a</sup> Mohammad Bodiuzzaman,<sup>a</sup> Korath Shivan Sugi,<sup>a</sup> Papri Chakraborty,<sup>a</sup> Ganesan Paramasivam,<sup>a</sup> Wakeel Ahmed Dar,<sup>a</sup> Tripti Ahuja,<sup>a</sup> Sudhadevi Antharjanam<sup>b</sup> and Thalappil Pradeep<sup>a\*</sup>

a. Department of Chemistry, DST Unit of Nanoscience (DST UNS) and Thematic Unit of Excellence (TUE), Indian Institute of Technology Madras, Chennai 600036, India.

b. Sophisticated Analytical Instruments Facility, Indian Institute of Technology Madras, Chennai 600036, India.

E-mail: pradeep@iitm.ac.in

#### Table of contents

List of tables and figures	Description	Page number
	Crystallographic analysis	3-4



<b>Table S1</b>	Crystal data and structure refinement for $[\text{Ag}_{22}(\text{dppe})_4(2,5\text{-DMBT})_{12}\text{Cl}_4]^{2+}$	4-5
<b>S1</b>	UV-vis absorption spectrum and ESI MS of $[\text{Ag}_{22}(\text{dppe})_4(2,5\text{-DMBT})_{12}\text{Cl}_4]^{2+}$ before size focusing	5
<b>S2</b>	Expanded view of the ESI MS peak at m/z 2876 and its collision induced dissociation mass spectrum	6-7
<b>S3</b>	The overall structure of $[\text{Ag}_{22}(\text{dppe})_4(2,5\text{-DMBT})_{12}\text{Cl}_4]^{2+}$	7
<b>S4</b>	Anatomy of the $\text{Ag}_{10}$ core	8
<b>S5</b>	Formation of the $\text{Ag}_{12}(\text{dppe})_4(\text{DMBT})_{12}\text{Cl}_4$ shell by four $\text{Ag}_2\text{S}_3\text{P}_2\text{Cl}$ and four Ag atoms	8
<b>S6</b>	Symmetry and orientations in $[\text{Ag}_{22}(\text{dppe})_4(2,5\text{-DMBT})_{12}\text{Cl}_4]^{2+}$	9
<b>Table S2</b>	A list of reported silver nanoclusters having crystal structures	10-11
<b>S7</b>	IR spectrum and HRESI MS of $[\text{Ag}_{22}(\text{dppe})_4(2,5\text{-DMBT})_{12}\text{Cl}_4]^{2+}$	12
<b>S8</b>	C-H... $\pi$ interactions between benzene rings of dppe and 2,5-DMBT	12
<b>S9</b>	Time-dependent absorption spectra of $[\text{Ag}_{22}(\text{dppe})_4(2,5\text{-DMBT})_{12}\text{Cl}_4]^{2+}$	13
<b>S10</b>	Replacement of $\text{Cl}^-$ by $\text{Br}^-$ using $\text{PPh}_4\text{Br}$ which form $[\text{Ag}_{22}(\text{dppe})_4(\text{DMBT})_{12}\text{Cl}_{4-n}\text{Br}_n]^{2+}$ where $n=0-4$ .	13
<b>S11</b>	SEM image and EDS mapping of $[\text{Ag}_{22}(\text{dppe})_4(2,5\text{-DMBT})_{12}\text{Cl}_4]^{2+}$	14
<b>S12</b>	XPS spectrum of $[\text{Ag}_{22}(\text{dppe})_4(2,5\text{-DMBT})_{12}\text{Cl}_4]^{2+}$	15
<b>S13</b>	Packing diagram of $[\text{Ag}_{22}(\text{dppe})_4(2,5\text{-DMBT})_{12}\text{Cl}_4]^{2+}$	15

<b>S14</b>	The reduced model structure, $[\text{Ag}_{22}(\text{SMe})_{12}(\text{Me}_2\text{PCH}_2\text{-CH}_2\text{PMe}_2)_4\text{Cl}_4]^{2+}$	16
<b>S15</b>	Schematic of the geometrical structure of the $\text{Ag}_{10}$ core in $[\text{Ag}_{22}(\text{dppe})_4(2,5\text{-DMBT})_{12}\text{Cl}_4]^{2+}$	17
<b>S16</b>	Energy vs. density of states graph of $[\text{Ag}_{22}(\text{dppe})_4(2,5\text{-DMBT})_{12}\text{Cl}_4]^{2+}$ and the isosurfaces of superatomic orbitals in $[\text{Ag}_{22}(\text{dppe})_4(2,5\text{-DMBT})_{12}\text{Cl}_4]^{2+}$	17

### Crystallographic analysis

X-ray data collection was performed with Bruker AXS Kappa Apex III CMOS Diffractometer equipped with graphite monochromated Mo ( $K_\alpha$ ) ( $\lambda = 0.71073 \text{ \AA}$ ) radiation at 273K. The automatic cell determination routine, with 24 frames at two different orientations of the detector was employed to collect reflections for unit cell determination. Further, intensity data for structure determination were collected through an optimized strategy which gave an average 4-fold redundancy. The program APEX3-SAINT (Bruker, 2016) was used for integrating the frames. Four-fold redundancy per reflection was utilized for achieving good multi-scan absorption correction using the program SADABS (Bruker, 2016). The structure was solved by SHELXT-2014 (Sheldrick, 2014) and refined by full-matrix least squares techniques using the same program. Hydrogens on all carbon atoms were fixed at calculated positions and refined as riding model with  $\text{C-H} = 0.93 \text{ \AA}$  ( $\text{C-H} = 0.96 \text{ \AA}$  for  $\text{CH}_3$ ),  $\text{Uiso}(\text{H}) = 1.2\text{Ueq}(\text{C})$  ( $\text{Uiso}(\text{H}) = 1.5\text{Ueq}(\text{C})$  for  $\text{CH}_3$ ). The molecule is crystallized in body-centered tetragonal crystal system with  $I4(1)/a$  space group. The asymmetric unit contains one-fourth of the silver cluster with one silver atom ( $\text{Ag}_3$ ) at the 4-fold axis of symmetry. Solvent and counter

ions were not modeled due to difficulty in locating and refining their positions satisfactorily. One of the 2,5-DMBT moieties is disordered by 180° rotation through the S2-C43 bond over two positions with a site-occupancy ratio of 60:40. The disorder was resolved by successive Fourier electron density maps and least squares refinements. Sum of the occupancies of the disordered components was restrained as 1 during refinement. The corresponding bond distances of disordered groups were restrained to be equal within an allowed standard deviation of 0.02 Å. Similar restraints were applied to the thermal parameters of the disordered components of the molecule. Thermal parameters of the atoms of the moiety were restrained to show approximate isotropic behaviour within an effective standard deviation of 0.02 Å.

## Crystal Information

**Table S1.** Crystal data and structure refinement for [Ag<sub>22</sub>(dppe)<sub>4</sub>(2,5-DMBT)<sub>12</sub>Cl<sub>4</sub>]<sup>2+</sup>.

Identification code	ag22	
Empirical formula	C <sub>200</sub> H <sub>204</sub> Ag <sub>22</sub> Cl <sub>4</sub> P <sub>8</sub> S <sub>12</sub>	
Formula weight	5755.04	
Temperature	273(2) K	
Wavelength	0.71073 Å	
Crystal system	Tetragonal	
Space group	I4 <sub>1</sub> /a	
Unit cell dimensions	a = 19.4007(9) Å	a = 90°.
	b = 19.4007(9) Å	b = 90°.
	c = 57.9021(18) Å	g = 90°.
Volume	21794(2) Å <sup>3</sup>	
Z	4	
Density (calculated)	1.754 Mg/m <sup>3</sup>	
Absorption coefficient	2.194 mm <sup>-1</sup>	
F(000)	11272.0	
Crystal size	0.250 x 0.200 x 0.150 mm <sup>3</sup>	
Theta range for data collection	2.934 to 20.864°.	
Index ranges	-19 ≤ h ≤ 19, -19 ≤ k ≤ 19, -57 ≤ l ≤ 57	
Reflections collected	42397	
Independent reflections	5629 [R(int) = 0.0718]	

Completeness to theta = 20.864°	97.7 %
Absorption correction	Semi-empirical from equivalents
Max. and min. transmission	0.7446 and 0.5734
Refinement method	Full-matrix least-squares on F <sup>2</sup>
Data / restraints / parameters	5629 / 311 / 628
Goodness-of-fit on F <sup>2</sup>	1.135
Final R indices [I>2sigma(I)]	R1 = 0.1267, wR2 = 0.2562
R indices (all data)	R1 = 0.1950, wR2 = 0.3121
Extinction coefficient	n/a
Largest diff. peak and hole	1.467 and -1.525 e.Å <sup>-3</sup>

## Supporting information 1

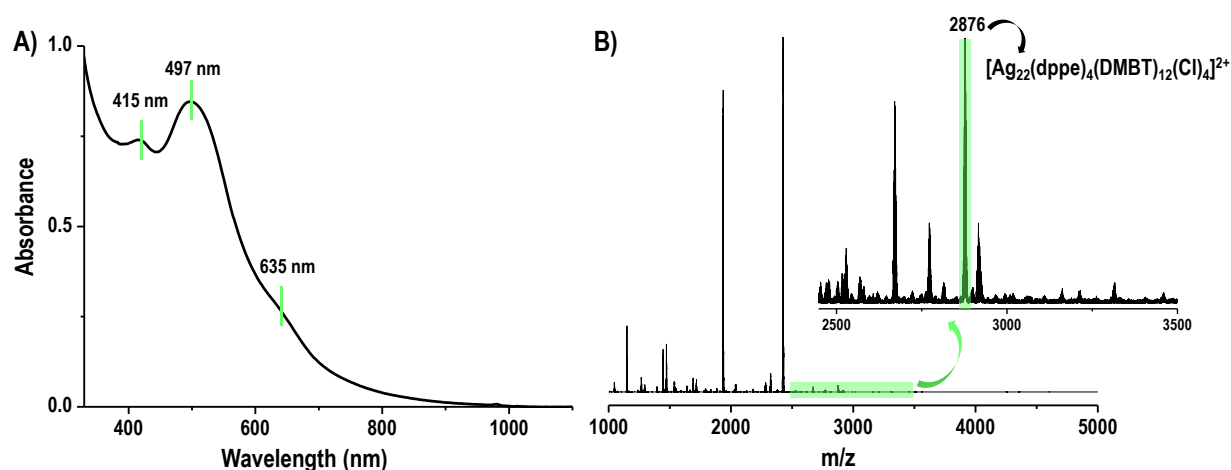


**Figure S1.** (A) UV-vis absorption spectrum and (B) HRESI MS of  $[Ag_{22}(dppe)_4(2,5-DMBT)_{12}Cl_4]^{2+}$  before size focusing. The absorption spectrum of the crude product shows two features at ~415 and 497 nm along with a small hump at 635 nm. The feature at m/z 2876 is due to  $[Ag_{22}(dppe)_4(2,5-DMBT)_{12}Cl_4]^{2+}$ .

## Supporting information 2

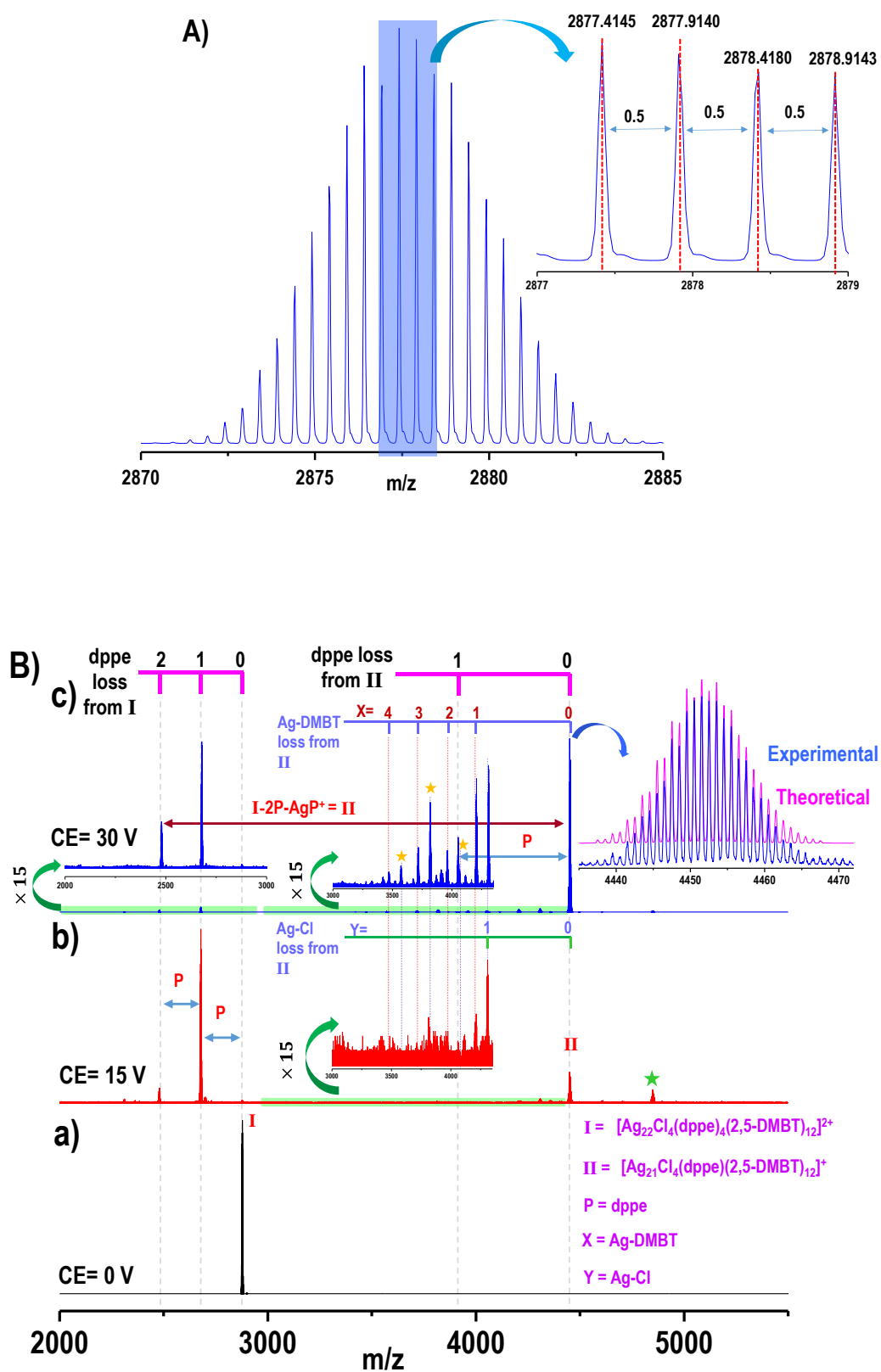


**Figure S2.** (A) Expanded view of the peak at  $m/z$  2876. Separation between two successive peaks is 0.5 which confirms the  $2^+$  charge state. (B) Collision-induced dissociation (CID) mass spectrum of the peak at 2876 which is assigned as  $[\text{Ag}_{22}(\text{dppe})_4(2,5\text{-DMBT})_{12}\text{Cl}_4]^{2+}$  (panel a). It shows systematic loss of four dppe ligands upon increase in collision energy along with the loss of some Ag-DMBT and AgCl units. Various species involved are marked in the inset of panel a. After the loss of one Ag-Cl from **II** (panel b), the formed species undergoes systematic Ag-DMBT losses which are denoted by yellow asterisks (panel c). The peak marked with green asterisk in panel b is assigned as  $[\text{Ag}_{21}(\text{dppe})_2(2,5\text{-DMBT})_{12}\text{Cl}_4]^+$ . Theoretical and experimental isotopic distributions of **II** are expanded in the inset of panel c.

### Supporting information 3:

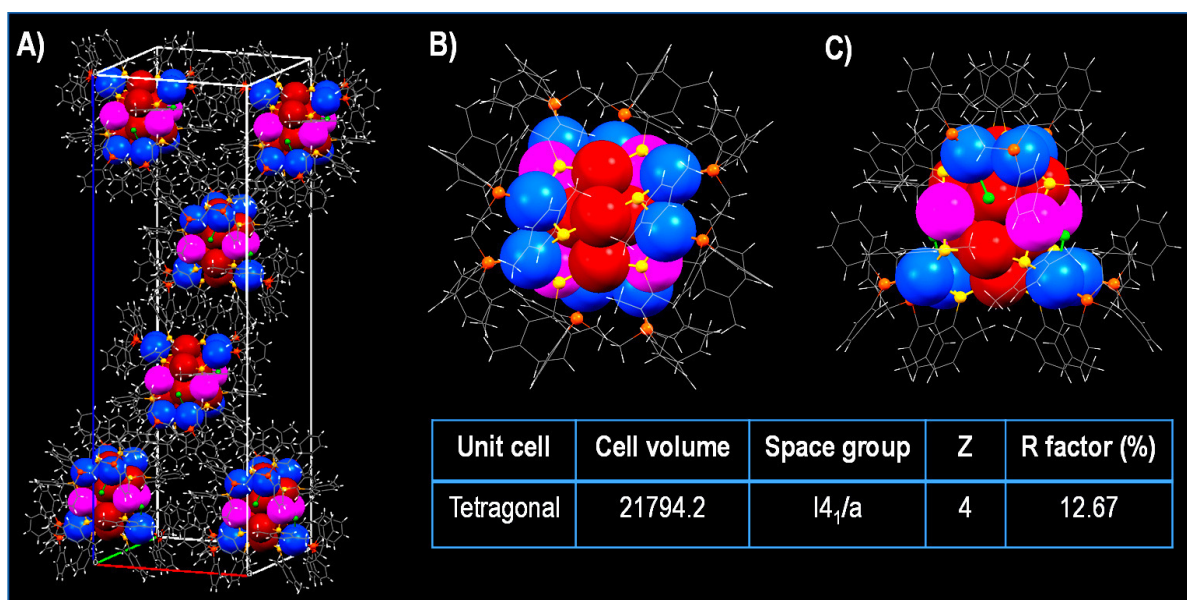


**Figure S3.** The overall structure of  $[\text{Ag}_{22}(\text{dppe})_4(2,5\text{-DMBT})_{12}\text{Cl}_4]^{2+}$ : A) Unit cell with a tetragonal arrangement; B) top view; C) side view. Labels: red, blue and pink = Ag, yellow = S, orange = P, green = Cl, gray = C and white = H.

## Supporting information 4

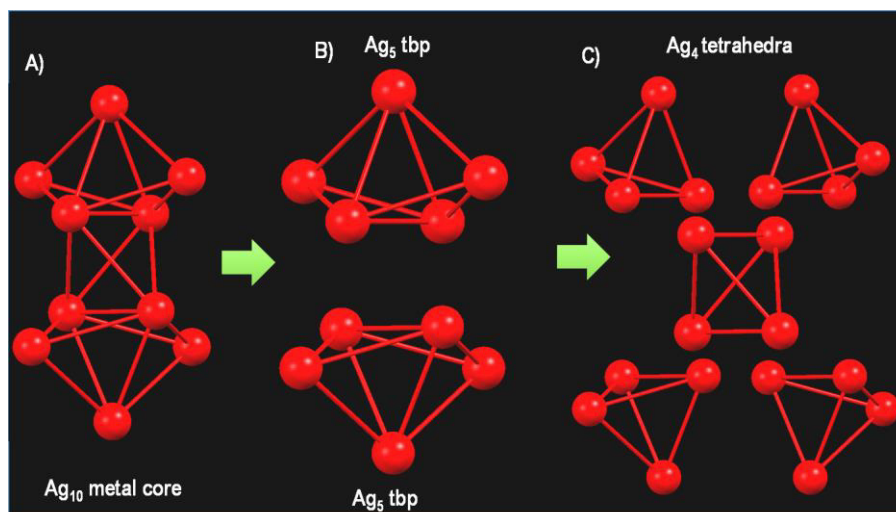


**Figure S4.** Anatomy of the  $\text{Ag}_{10}$  core: (A)  $\text{Ag}_{10}$  core, (B)  $\text{Ag}_{10}$  is composed of two perpendicular  $\text{Ag}_5$  units having trigonal bipyramidal (tbp) geometry, (C)  $\text{Ag}_{10}$  can also be viewed as a combination of five edge and face shared  $\text{Ag}_4$  tetrahedra.

## Supporting information 5

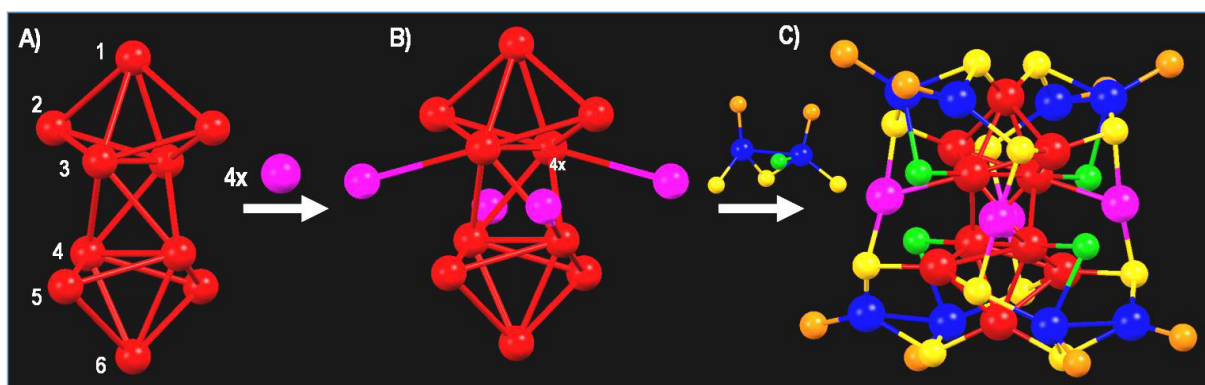


**Figure S5.** (A)  $\text{Ag}_{10}$  metal core, (B)  $\text{Ag}_{14}$  unit, (C)  $\text{Ag}_{22}\text{P}_8\text{S}_{12}\text{Cl}_4$ .

The shell is formed by four  $\text{Ag}_2\text{S}_3\text{P}_2\text{Cl}$  and four Ag atoms. Out of the four  $\text{Ag}_2\text{S}_3\text{P}_2\text{Cl}$  staples, two connect the first three layers of the core and remaining two connect the last three layers perpendicularly. The remaining four silver atoms are connected with the third and fourth layer



of the  $\text{Ag}_{10}$  core and also act as bridging atoms between the  $\text{Ag}_2\text{S}_3\text{P}_2\text{Cl}$  staples of the first three and the last three layers.

Labels: red, blue and pink = Ag, yellow = S, orange = P, green = Cl, C and H atoms are omitted here for clarity.

### Supporting information 6

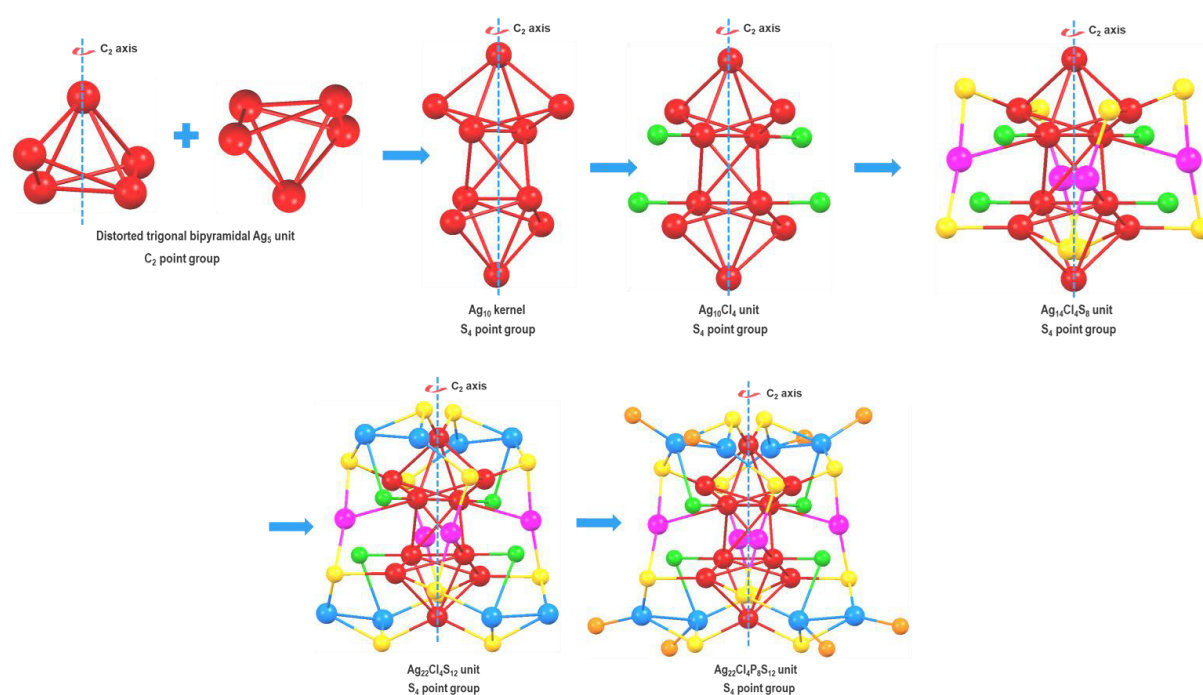


**Figure S6.** Symmetry and orientations in  $[\text{Ag}_{22}(\text{dppe})_4(2,5\text{-DMBT})_{12}\text{Cl}_4]^{2+}$ . The  $\text{Ag}_5$  units possess a chiral  $C_2$  point group while the  $\text{Ag}_{10}$  core unveils an achiral  $S_4$  point group. Staples are connected to the core in such a way that  $S_4$  symmetry is maintained. Labels: red, blue and pink = Ag, yellow = S, orange = P, green = Cl. C and H atoms are omitted here for clarity.

**Table S2.** A list of reported silver nanoclusters having crystal structures.

Cluster composition	Inner core	Shell	Unit cell	Nominal electron count	References
[Ag <sub>14</sub> (DFBT) <sub>12</sub> (PPh <sub>3</sub> ) <sub>8</sub> ]	Ag <sub>6</sub> (octahedron)	Ag <sub>8</sub> S <sub>12</sub> P <sub>8</sub>	Primitive	2	1
[Ag <sub>15</sub> (N-triphos) <sub>4</sub> (Cl <sub>4</sub> ) <sup>3+</sup>	Ag <sub>9</sub> (centered cube)	Ag <sub>6</sub> N <sub>4</sub> P <sub>12</sub> Cl <sub>4</sub>	C2221 Orthorhombic	8	2
[Ag <sub>16</sub> (DPPE) <sub>4</sub> (DFBT) <sub>14</sub> ]	Ag <sub>8</sub> (Ag <sub>4</sub> rhombus capped by Ag <sub>2</sub> unit)	Ag <sub>8</sub> P <sub>8</sub> S <sub>14</sub>	I 4 <sub>1</sub> /a Tetragonal	2	3
[Ag <sub>21</sub> [S <sub>2</sub> P(O <sup>i</sup> Pr) <sub>2</sub> ] <sub>12</sub> ] <sup>+</sup>	Ag <sub>13</sub> (centered icosahedron)	Ag <sub>8</sub> S <sub>24</sub> P <sub>12</sub>	P2 <sub>1</sub> /n Monoclinic	8	4
[Ag <sub>23</sub> (PET) <sub>18</sub> (PPh <sub>3</sub> ) <sub>8</sub> ]	Ag <sub>12</sub> (two connected rhombic bipyramidal)	Ag <sub>12</sub> S <sub>18</sub> P <sub>8</sub>	Cc Monoclinic	5	5
[Ag <sub>25</sub> (DMBT) <sub>18</sub> ] <sup>-</sup>	Ag <sub>13</sub> (centered icosahedra)	Ag <sub>12</sub> S <sub>18</sub>	P-1 Triclinic	8	6
[Ag <sub>29</sub> (BDT) <sub>12</sub> (PPh <sub>3</sub> ) <sub>4</sub> ] <sup>3-</sup>	Ag <sub>13</sub> (centered icosahedra)	Ag <sub>16</sub> S <sub>24</sub> P <sub>8</sub>	Pa-3 Cubic	8	7
[Ag <sub>32</sub> (DPPE) <sub>5</sub> (SC <sub>6</sub> H <sub>3</sub> F <sub>2</sub> ) <sub>24</sub> ] <sup>2-</sup>	Ag <sub>22</sub> (pentagon face-sharing bi-pentagonal antiprism)	Ag <sub>10</sub> P <sub>10</sub> S <sub>24</sub>	C 2/c Monoclinic	10	3
[Ag <sub>32</sub> (Dppm) <sub>5</sub> (SAdm) <sub>13</sub> Cl <sub>8</sub> ] <sup>3+</sup>	Ag <sub>13</sub> (centered icosahedra)	Ag <sub>19</sub> P <sub>10</sub> S <sub>13</sub> Cl <sub>8</sub>	P-1 Triclinic	8	8
[Ag <sub>35</sub> (H <sub>2</sub> L) <sub>2</sub> (L)(C≡CBu <sup>t</sup> ) <sub>16</sub> ] <sup>3+</sup>	Ag <sub>13</sub> (centered icosahedra)	Ag <sub>22</sub> S <sub>12</sub> (C≡CBu <sup>t</sup> ) <sub>16</sub>	P-1 Triclinic	8	9
[Ag <sub>38</sub> (SPhF <sub>2</sub> ) <sub>26</sub> (PPh <sub>3</sub> ) <sub>8</sub> ]	Ag <sub>14</sub> (fcc)	Ag <sub>24</sub> S <sub>26</sub> P <sub>8</sub>	P-1 Triclinic	12	10
[Ag <sub>40</sub> (SPhMe <sub>2</sub> ) <sub>24</sub> (PPh <sub>3</sub> ) <sub>8</sub> ] <sup>2+</sup>	Ag <sub>8</sub> (cube)	Ag <sub>32</sub> S <sub>24</sub> P <sub>8</sub>	C2/m Monoclinic	14	11
[Ag <sub>44</sub> (FTP) <sub>30</sub> ] <sup>4-</sup>	Ag <sub>12</sub> (hollow icosahedra)	Ag <sub>32</sub> S <sub>30</sub>	P-1 Triclinic	18	12
[Ag <sub>45</sub> (Dppm) <sub>4</sub> (SAdm) <sub>16</sub> Br <sub>12</sub> ] <sup>3+</sup>	Ag <sub>23</sub> (face shared biicosahedra)	Ag <sub>22</sub> S <sub>16</sub> P <sub>8</sub> Br <sub>12</sub>	C12/c1 Monoclinic	14	8
[Ag <sub>46</sub> (SPhMe <sub>2</sub> ) <sub>24</sub> (PPh <sub>3</sub> ) <sub>8</sub> ] <sup>2+</sup>	Ag <sub>14</sub> (fcc)	Ag <sub>32</sub> S <sub>24</sub> P <sub>8</sub>	C2/m Monoclinic	20	11
Ag <sub>50</sub> (DPPM) <sub>6</sub> (TBBM) <sub>30</sub>	Ag <sub>12</sub> (hollow icosahedra)	Ag <sub>38</sub> S <sub>30</sub> P <sub>6</sub>	P-1 Triclinic	20	13
[Ag <sub>62</sub> (S <sup>t</sup> Bu) <sub>32</sub> S <sub>12</sub> ] <sup>2+</sup>	Ag <sub>14</sub> (fcc)	Ag <sub>48</sub> S <sub>44</sub>	P-1 Triclinic	4*	14

$[\text{Ag}_{63}(\text{SPhF}_2)_{36}(\text{PR}'_3)_8]^+$	$\text{Ag}_{14}$ (fcc)	$\text{Ag}_{49}\text{S}_{36}\text{P}_8$	R-3 Trigonal	26	10
$[\text{Ag}_{67}(\text{SPhMe}_2)_{32}(\text{PPh}_3)_8]^{3+}$	$\text{Ag}_{23}$ (centred cuboctahedra)	$\text{Ag}_{44}\text{S}_{32}\text{P}_8$	Ccc2 Orthorhombic	32	15
$[\text{Ag}_{78}(\text{BDPP})_6(\text{SR})_{42}]$	$\text{Ag}_{22}$ (three mutually interpenetrating icosahedra)	$\text{Ag}_{56}\text{S}_{42}\text{P}_6$	Ccc2 Orthorhombic	36	16
$[\text{Ag}_{141}\text{X}_{12}(\text{SAdm})_{40}]^{3+}$ (X=Cl, Br, I)	$\text{Ag}_{19}$ (interpenetrating biicosahedra)	$\text{Ag}_{122}\text{S}_{40}\text{X}_{12}$	Pbcn Orthorhombic	86	17
$[\text{Ag}_{136}(\text{SR})_{64}\text{Cl}_3\text{Ag}_{0.45}]^-$	$\text{Ag}_{54}$ (pentagonal bipyramids)	$\text{Ag}_{82}\text{S}_{64}$	P-1 Triclinic	70	18
$\text{Ag}_{374}(\text{SR})_{113}\text{Br}_2\text{Cl}_2$	$\text{Ag}_{207}$ (elongated pentagonal bipyramids)	$\text{Ag}_{167}\text{S}_{113}\text{Br}_2\text{Cl}_2$	R-3c rhombohedral	257	18
$[\text{Ag}_{22}(\text{dppe})_4(\text{DMBT})_{12}\text{Cl}_4]^{2+}$	$\text{Ag}_{10}$ (two tbp units connected to each other perpendicularly)	$\text{Ag}_{12}\text{S}_{12}\text{P}_8\text{Cl}_4$	I4 <sub>1</sub> /a Tetragonal	4	

\*Although the nominal electron count is 4, the superatom electron count calculated is 2.<sup>14</sup>

Acronyms of ligands used:

DFBT: 3,4-difluoro-benzenethiol

N-triphos: tris((diphenylphosphino)methyl)amine

DPPE: 1,2-bis(diphenylphosphino)ethane

PET: 2-phenylethanethiol

DMBT: 2,4-dimethylbenzenethiol

BDT: 1,3-benzenedithiol

Dppm: 1,1-bis(diphenylphosphino)methane

H<sub>4</sub>L: p-tert-butylthiacalix[4]-arene

FTP: 4-fluorothiophenol

SAdm: Adamantanethiol

S<sup>t</sup>Bu: tert-butylbenzenethiol

BDPP: 2,4-bis(diphenylphosphino)pentane

TBBM: 4-tert-butylbenzylmercaptant

## Supporting information 7

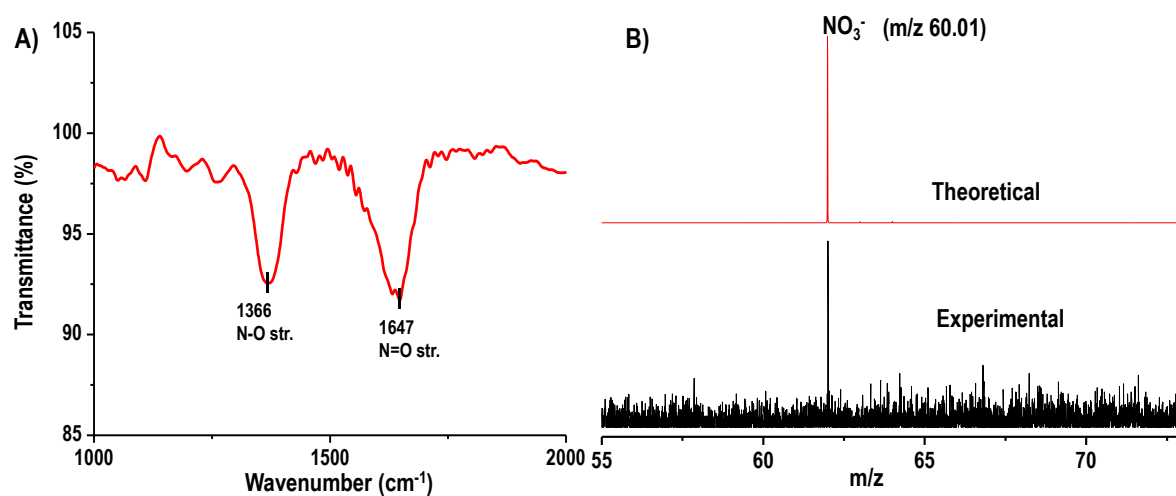


**Figure S7.** (A) IR spectrum of  $[\text{Ag}_{22}(\text{dppe})_4(2,5\text{-DMBT})_{12}\text{Cl}_4]^{2+}$  which shows two peaks corresponds to N-O stretching and N=O stretching frequencies. (B) HRESI MS of  $[\text{Ag}_{22}(\text{dppe})_4(2,5\text{-DMBT})_{12}\text{Cl}_4]^{2+}$  shows peak corresponding to  $\text{NO}_3^-$ . These two experiments confirm the presence of  $\text{NO}_3^-$  as the counterion.

## Supporting information 8

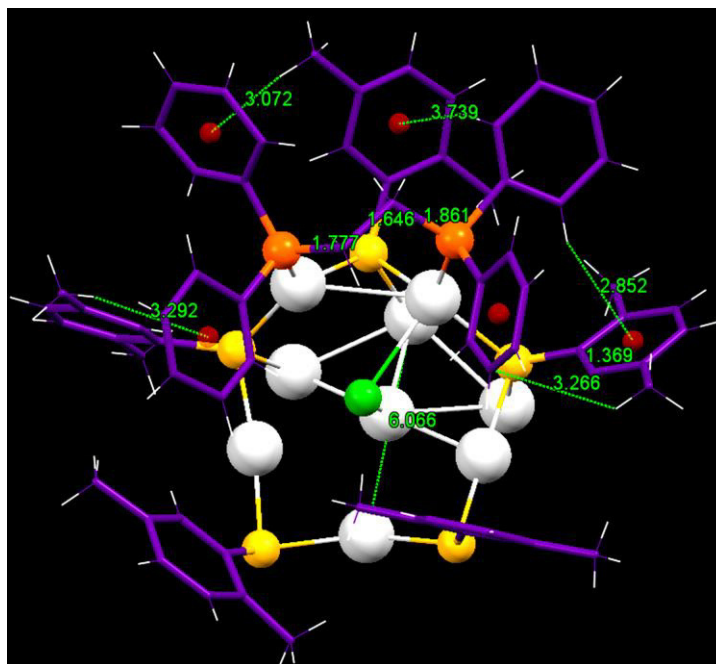


**Figure S8.** C-H...  $\pi$  interactions between benzene rings of dppe and 2,5-DMBT.

## Supporting information 9

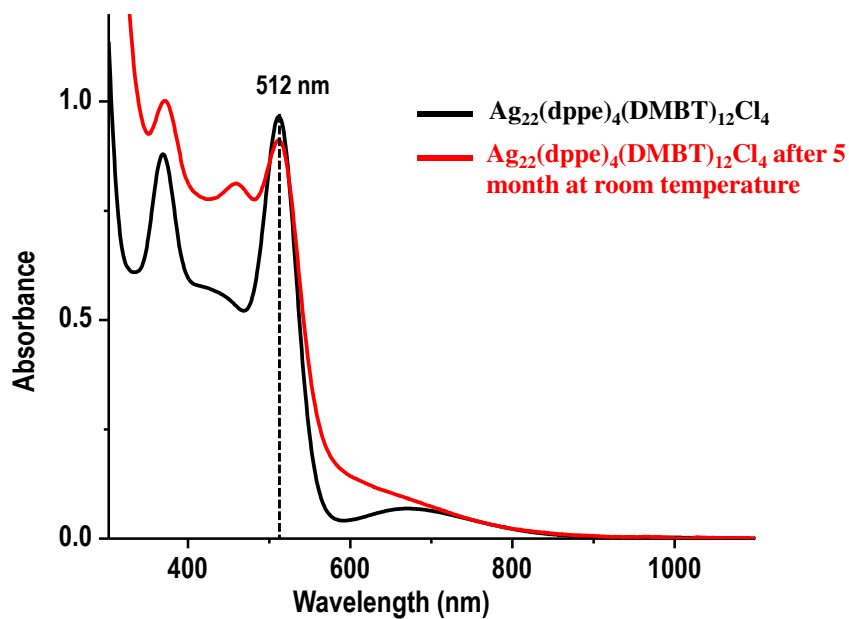


**Figure S9.** Time-dependent absorption spectra of  $[\text{Ag}_{22}(\text{dppe})_4(2,5\text{-DMBT})_{12}\text{Cl}_4]^{2+}$  at room temperature. The absorption features are similar in both the spectra after 5 months at room temperature which suggest the stability of the cluster.

## Supporting information 10

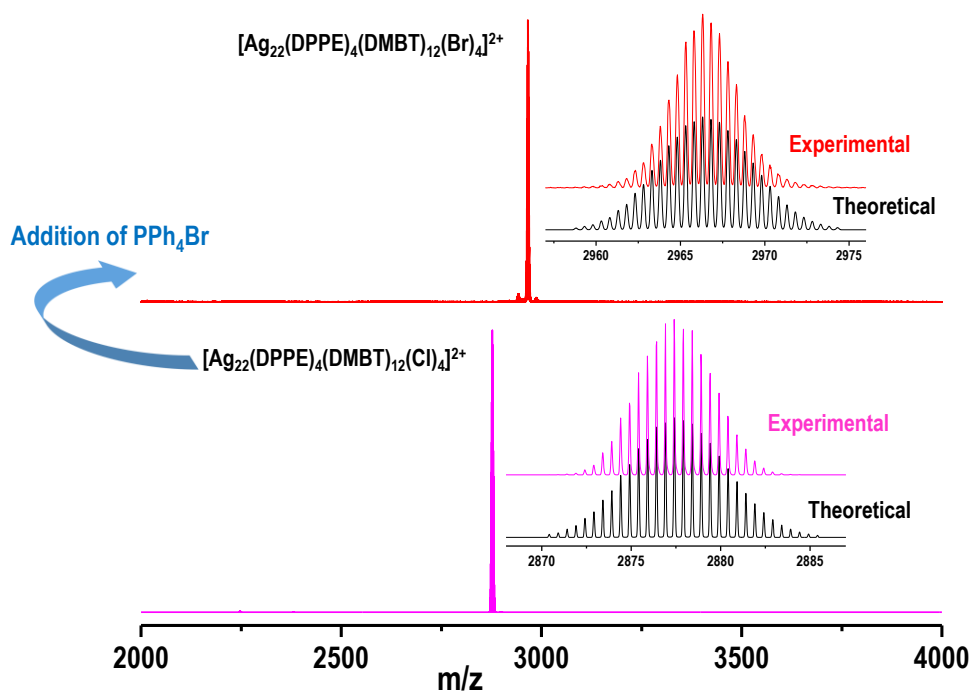


**Figure S10.** Replacement of  $\text{Cl}^-$  by  $\text{Br}^-$  using  $\text{PPh}_4\text{Br}$ . The lower panel shows the ESI MS of  $[\text{Ag}_{22}(\text{dppe})_4(2,5\text{-DMBT})_{12}\text{Cl}_4]^{2+}$  and upper panel corresponds to the ESI MS of Br substituted product,  $[\text{Ag}_{22}(\text{dppe})_4(\text{DMBT})_{12}\text{Cl}_{4-n}\text{Br}_n]^{2+}$  where  $n=0-4$ .

### Supporting information 11

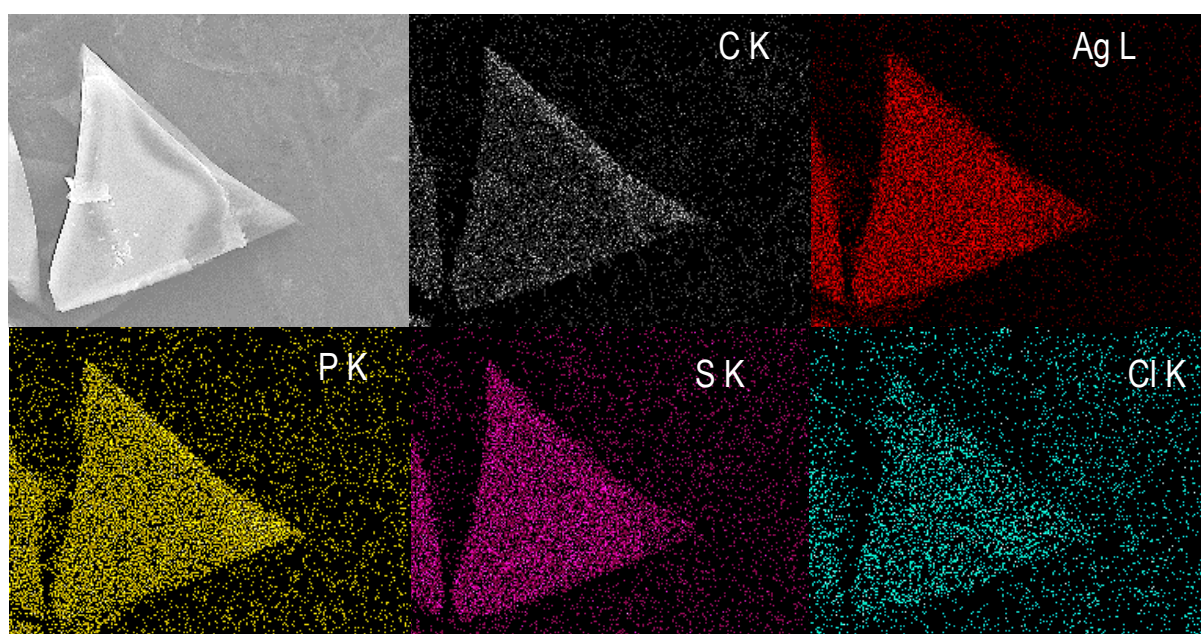


**Figure S11.** SEM image and EDS mapping of  $[\text{Ag}_{22}(\text{dppe})_4(2,5\text{-DMBT})_{12}\text{Cl}_4]^{2+}$ . C, Ag, P, S and Cl are represented by white, red, yellow, purple and light blue colors, respectively.

## Supporting information 12

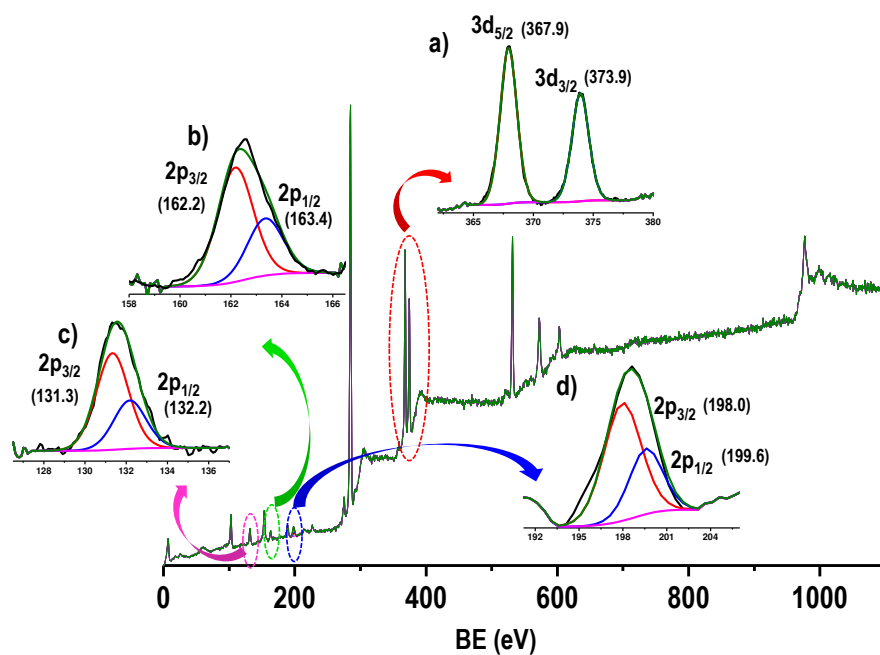


**Figure S12.** XPS spectrum of  $[\text{Ag}_{22}(\text{dppe})_4(2,5\text{-DMBT})_{12}\text{Cl}_4]^{2+}$ . Expanded area of (a) Ag 3d, (b) S 2p, (c) P 2p and (d) Cl 2p.

## Supporting information 13

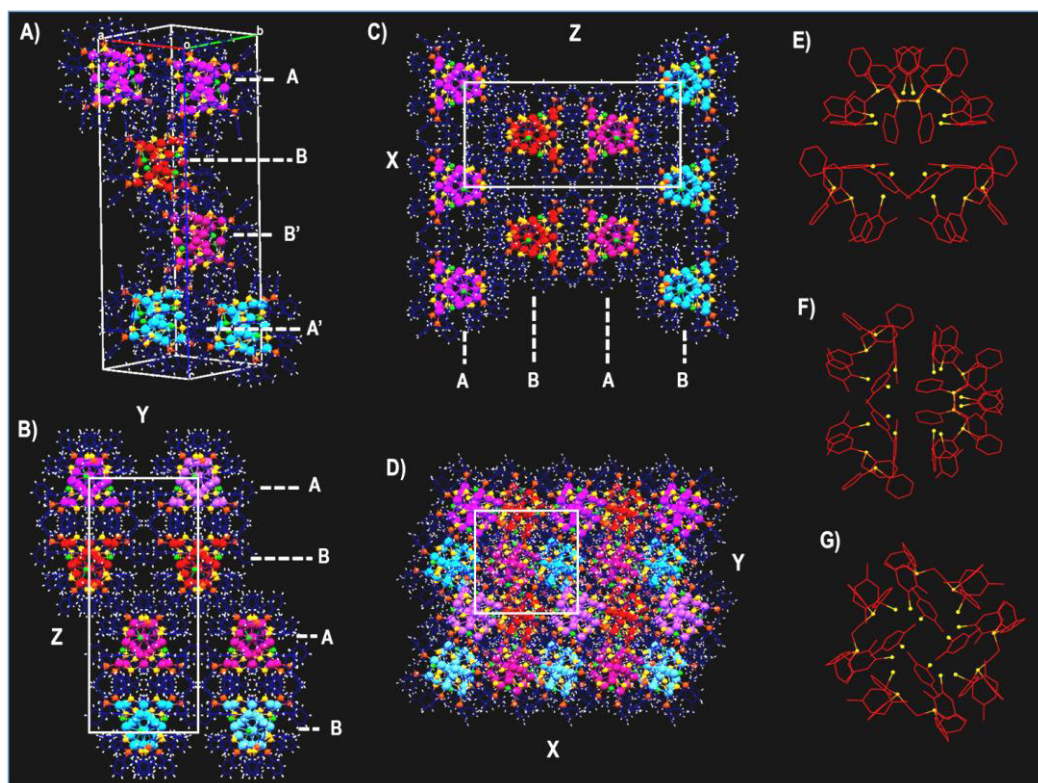




**Figure S13.** Packing diagram of  $[\text{Ag}_{22}(\text{dppe})_4(2,5\text{-DMBT})_{12}\text{Cl}_4]^{2+}$ : (A) Organization of clusters in a unit cell; (B) and (C) Packing diagrams along X and Y-axes, respectively display rectangular 2D lattice; (D) Packing diagram along Z-axis presents square 2D lattice; (E-G) The arrangement of ligands in  $[\text{Ag}_{22}(\text{dppe})_4(2,5\text{-DMBT})_{12}\text{Cl}_4]^{2+}$  along x, y and z-axes.

#### Supporting information 14

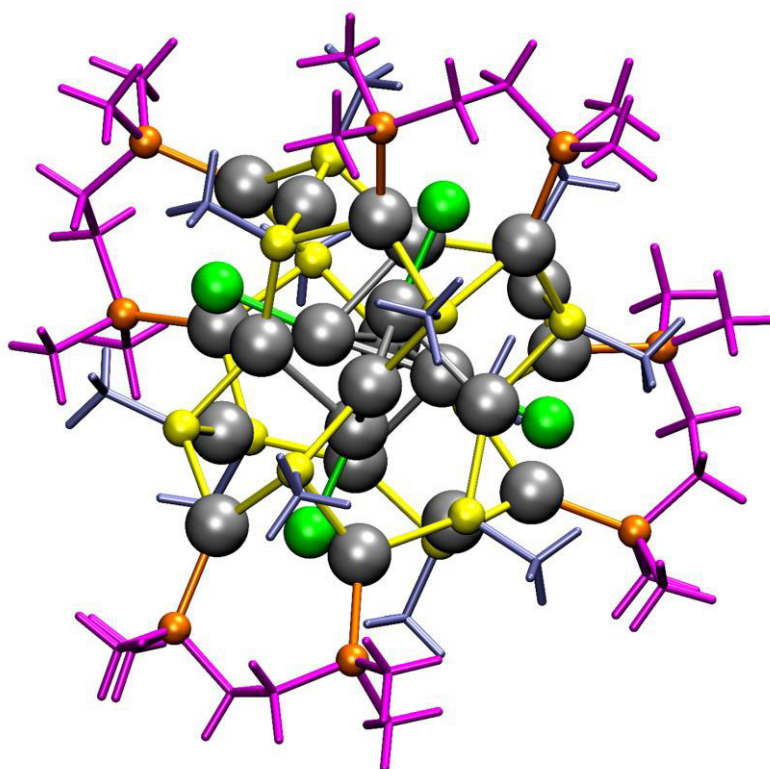


**Figure S14.** The reduced model structure,  $[\text{Ag}_{22}(\text{SMe})_{12}(\text{Me}_2\text{PCH}_2\text{-CH}_2\text{PMe}_2)_4\text{Cl}_4]^{2+}$  where benzene groups of each 2,5-DMBT and dppe were simplified using  $-\text{CH}_3$  groups to reduce the cost of computation.

## Supporting information 15

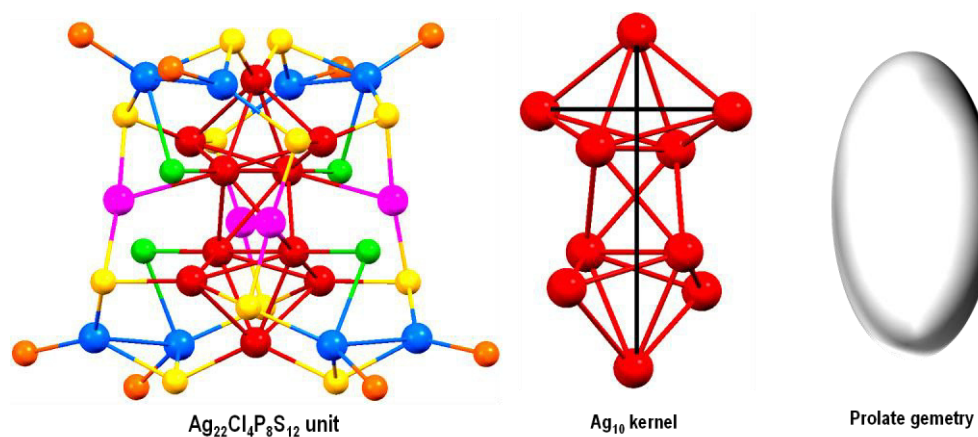


**Figure S15.** Schematic of the geometrical structure of the  $\text{Ag}_{10}$  core in  $[\text{Ag}_{22}(\text{dppe})_4(2,5\text{-DMBT})_{12}\text{Cl}_4]^{2+}$  which possesses a prolate geometry.

## Supporting information 16

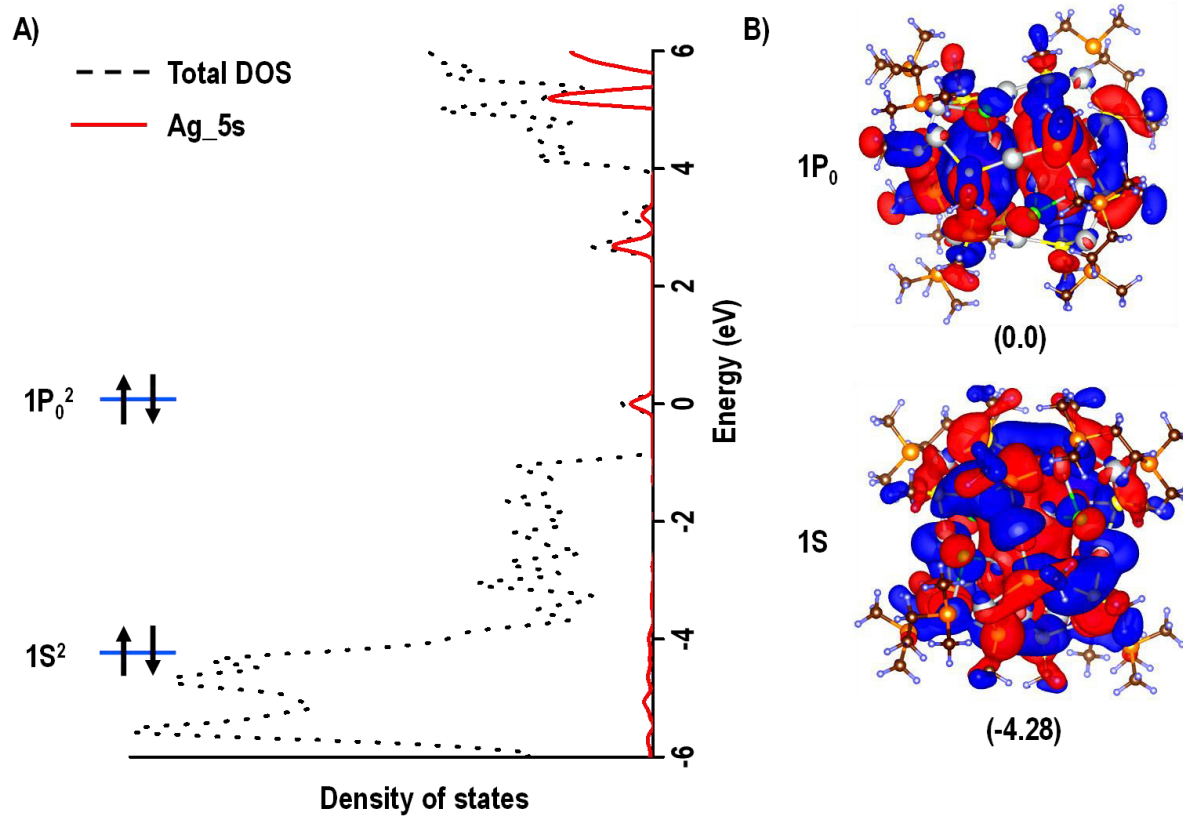


**Figure S16.** (A) Energy vs. density of states graph of  $[\text{Ag}_{22}(\text{dppe})_4(2,5\text{-DMBT})_{12}\text{Cl}_4]^{2+}$  and the filling of 4e in the superatomic orbitals. (B) The isosurfaces of superatomic orbitals in  $[\text{Ag}_{22}(\text{dppe})_4(2,5\text{-DMBT})_{12}\text{Cl}_4]^{2+}$ . The highest molecular orbital is set to be at zero.

## References

- (1) Yang, H.; Lei, J.; Wu, B.; Wang, Y.; Zhou, M.; Xia, A.; Zheng, L.; Zheng, N. Crystal Structure of a Luminescent Thiolated Ag Nanocluster with an Octahedral  $\text{Ag}_6^{4+}$  Core. *Chem. Commun. (Cambridge, United Kingdom)* **2013**, 49, 300–302.
- (2) Shen, X.-T.; Ma, X.-L.; Ni, Q.-L.; Ma, M.-X.; Gui, L.-C.; Hou, C.; Hou, R.-B.; Wang, X.-J.  $[\text{Ag}_{15}(\text{N-Triphos})_4(\text{Cl}_4)](\text{NO}_3)_3$ : A Stable Ag–P Superatom with Eight Electrons (N-Triphos = Tris((Diphenylphosphino)Methyl)Amine). *Nanoscale* **2018**, 10, 515–519.
- (3) Yang, H.; Wang, Y.; Zheng, N. Stabilizing Subnanometer Ag(0) Nanoclusters by Thiolate and Diphosphine Ligands and Their Crystal Structures. *Nanoscale* **2013**, 5, 2674–2677.
- (4) Dhayal, R. S.; Liao, J. H.; Liu, Y. C.; Chiang, M. H.; Kahlal, S.; Saillard, J. Y.; Liu, C. W.  $\text{Ag}_{21}\{\text{S}_2\text{P}(\text{OiPr})_2\}_{12}^+$ : An Eight-Electron Superatom. *Angew. Chemie - Int. Ed.* **2015**, 54, 3702–3706.
- (5) Liu, C.; Li, T.; Abroshan, H.; Li, Z.; Zhang, C.; Kim, H. J.; Li, G.; Jin, R. Chiral  $\text{Ag}_{23}$  Nanocluster with Open Shell Electronic Structure and Helical Face-Centered Cubic Framework. *Nat. Commun.* **2018**, 9, 744.

- (6) Joshi, C. P.; Bootharaju, M. S.; Alhilaly, M. J.; Bakr, O. M.  $[\text{Ag}_{25}(\text{SR})_{18}]^-$ : The “Golden” Silver Nanoparticle Silver Nanoparticle. *J. Am. Chem. Soc.* **2015**, *137*, 11578–11581.
- (7) AbdulHalim, L. G.; Bootharaju, M. S.; Tang, Q.; Del Gobbo, S.; AbdulHalim, R. G.; Eddaoudi, M.; Jiang, D.; Bakr, O. M.  $\text{Ag}_{29}(\text{BDT})_{12}(\text{TPP})_4$ : A Tetravalent Nanocluster. *J. Am. Chem. Soc.* **2015**, *137*, 11970–11975.
- (8) Zou, X.; Jin, S.; Du, W.; Li, Y.; Li, P.; Wang, S.; Zhu, M. Multi-Ligand-Directed Synthesis of Chiral Silver Nanoclusters. *Nanoscale* **2017**, *9*, 16800–16805.
- (9) Guan, Z. J.; Zeng, J. L.; Nan, Z. A.; Wan, X. K.; Lin, Y. M.; Wang, Q. M. Thiocalix[4]Arene: New Protection for Metal Nanoclusters. *Sci. Adv.* **2016**, *2*, 1–8.
- (10) Yang, H.; Yan, J.; Wang, Y.; Su, H.; Gell, L.; Zhao, X.; Xu, C.; Teo, B. K.; Häkkinen, H.; Zheng, N. Embryonic Growth of Face-Center-Cubic Silver Nanoclusters Shaped in Nearly Perfect Half-Cubes and Cubes. *J. Am. Chem. Soc.* **2017**, *139*, 31–34.
- (11) Bodiuzzaman, M.; Ghosh, A.; Shivan Sugi, K.; Nag, A.; Khatun, E.; Varghese, B.; Paramasivam, G.; Antharjanam, S.; Natarajan, G.; Pradeep, T. Camouflaging Structural Diversity: Co-Crystallization of Two Different Nanoparticles Having Different Cores but the Same Shell. *Angew. Chem. Int. Ed* **2018**, *57*, 1–7.
- (12) Yang, H.; Wang, Y.; Huang, H.; Gell, L.; Lehtovaara, L.; Malola, S.; Häkkinen, H.; Zheng, N. All-Thiol-Stabilized  $\text{Ag}_{44}$  and  $\text{Au}_{12}\text{Ag}_{32}$  Nanoparticles with Single-Crystal Structures. *Nat. Commun.* **2013**, *4*, 2422.
- (13) Du, W.; Jin, S.; Xiong, L.; Chen, M.; Zhang, J.; Zou, X.; Pei, Y.; Wang, S.; Zhu, M.  $\text{Ag}_{50}(\text{Dppm})_6(\text{SR})_{30}$  and Its Homologue  $\text{Au}_x\text{Ag}_{50-x}(\text{Dppm})_6(\text{SR})_{30}$  Alloy Nanocluster: Seeded Growth, Structure Determination, and Differences in Properties. *J. Am. Chem.*

- Soc.* **2017**, *139*, 1618–1624.
- (14) Jin, S.; Wang, S.; Song, Y.; Zhou, M.; Zhong, J.; Zhang, J.; Xia, A.; Pei, Y.; Chen, M.; Li, P.; Zhu, M. Crystal Structure and Optical Properties of the  $[\text{Ag}_{62}\text{S}_{12}(\text{SBu}^t)_{32}]^{2+}$  Nanocluster with a Complete Face-Centered Cubic Kernel. *J. Am. Chem. Soc.* **2014**, *136*, 15559–15565.
- (15) Alhilaly, M. J.; Bootharaju, M. S.; Joshi, C. P.; Besong, T. M.; Emwas, A. H.; Juarez-Mosqueda, R.; Kaappa, S.; Malola, S.; Adil, K.; Shkurenko, A.; Häkkinen, H.; Eddaoudi, M.; Bakr, O. M.  $[\text{Ag}_{67}(\text{SPhMe}_2)_{32}(\text{PPh}_3)_8]^{3+}$ : Synthesis, Total Structure, and Optical Properties of a Large Box-Shaped Silver Nanocluster. *J. Am. Chem. Soc.* **2016**, *138*, 14727–14732.
- (16) Yang, H.; Yan, J.; Wang, Y.; Deng, G.; Su, H.; Zhao, X.; Xu, C.; Teo, B. K.; Zheng, N. From Racemic Metal Nanoparticles to Optically Pure Enantiomers in One Pot. *J. Am. Chem. Soc.* **2017**, *139*, 16113–16116.
- (17) Ren, L.; Yuan, P.; Su, H.; Malola, S.; Lin, S.; Tang, Z.; Teo, B. K.; Häkkinen, H.; Zheng, L.; Zheng, N. Bulky Surface Ligands Promote Surface Reactivities of  $[\text{Ag}_{141}\text{X}_{12}(\text{S-Adm})_{40}]^{3+}$  (X = Cl, Br, I) Nanoclusters: Models for Multiple-Twinned Nanoparticles. *J. Am. Chem. Soc.* **2017**, *139*, 13288–13291.
- (18) Yang, H.; Wang, Y.; Chen, X.; Zhao, X.; Gu, L.; Huang, H.; Yan, J.; Xu, C.; Li, G.; Wu, J.; Edwards, A. J.; Dittrich, B.; Tang, Z.; Wang, D.; Lehtovaara, L.; Häkkinen, H.; Zheng, N. Plasmonic Twinned Silver Nanoparticles with Molecular Precision. *Nat. Commun.* **2016**, *7*, 12809.



Cite this: *Chem. Commun.*, 2019, 55, 5025

Received 14th February 2019,  
Accepted 2nd April 2019

DOI: 10.1039/c9cc01289c

rsc.li/chemcomm

## A covalently linked dimer of $[\text{Ag}_{25}(\text{DMBT})_{18}]^{-\dagger}$

Mohammad Bodiuzzaman,<sup>a</sup> Abhijit Nag,<sup>a</sup> Raghu Pradeep Narayanan,<sup>a</sup>  
Ankush Chakraborty,<sup>b</sup> Ranjit Bag,<sup>b</sup> Ganesan Paramasivam,<sup>a</sup> Ganapati Natarajan,<sup>a</sup>  
Govindasamy Sekar,<sup>b</sup> Sundargopal Ghosh<sup>b</sup> and Thalappil Pradeep<sup>\*,a</sup>

**We report the first example of a covalently bound dimer of monolayer protected atomically precise silver nanocluster  $[\text{Ag}_{25}(\text{DMBT})_{18}]^{-}$  (DMBT stands for 2,4-dimethylbenzenethiol). Covalently linked dimers could be important to design new cluster assembled materials with composite properties.**

Atomically precise noble metal nanoclusters protected with ligands have emerged as a new research frontier in nanoscience, due to their unique optical and chemical properties as well as promising applications.<sup>1–4</sup> Out of these, the molecular systems studied in detail include  $[\text{Au}_{102}(\text{p-MBA})_{44}]$ ,  $[\text{Au}_{25}(\text{SCH}_2\text{CH}_2)_{18}]$ ,  $[\text{Au}_{38}(\text{SCH}_2\text{CH}_2)_{24}]$ ,  $[\text{Ag}_{44}(\text{p-MBA})_{30}]$ ,  $[\text{Ag}_{25}(\text{SPhMe}_2)_{18}]$ ,  $[\text{Ag}_{29}(\text{BDT})_{12}(\text{PPh}_3)_4]$ ,  $[\text{Ag}_{40}(\text{SPhMe}_2)_{24}(\text{PPh}_3)_8]$ ,  $[\text{Ag}_{46}(\text{SPhMe}_2)_{24}(\text{PPh}_3)_8]$  etc.,<sup>5–12</sup> which exist in various charge states (the abbreviations used are presented in the ESI†). Single crystal X-ray diffraction has been utilized for their structural analysis while mass spectrometry is an important tool to understand their formulae and supramolecular interactions.<sup>13,14</sup> Dimers of  $\text{Au}_{25}(\text{SR})_{18}$  (SR: phenyl ethanethiolate and butane thiolate) were first reported by our group using studies in the gas phase.<sup>15</sup> This kind of dimer was not observed for structurally similar  $[\text{Ag}_{25}(\text{DMBT})_{18}]^{-}$  clusters due to the lack of metallophilic interactions.

Recently, synthesis of new superstructures by the assembly of molecular pieces of metals has attracted great attention.<sup>16–18</sup> The creation of superstructures using clusters without changing the original structure of the building block is a challenging task. The ligand exchange reaction is suitable in this regard and various studies have been done on gold clusters to create superstructures.<sup>16,18</sup> Ligands containing two reactive rigid thiol groups can be efficient to create the assembly of building blocks. This aspect of creating superstructures has not been explored in the case of silver nanoclusters.

In this communication, we demonstrate the synthesis of a covalently linked dimer of a monolayer protected cluster (MPC),

$[\text{Ag}_{25}(\text{DMBT})_{18}]^{-}$  via a ligand-exchange reaction, wherein a complex of ruthenium bipyridyl-4-4'-dithiol  $[\text{Ru}(\text{bpy})_2\text{bpy}(\text{CH}_2\text{SH})_2]^{2+}$  replaces two dimethylbenzenethiol ligands and creates a dimer. The products were characterized by optical absorption spectroscopy, infrared spectroscopy and detailed high resolution electrospray ionization mass spectrometry (HR ESI MS).

$[\text{Ag}_{25}(\text{DMBT})_{18}]^{-}$  and  $[\text{Ru}(\text{bpy})_2\text{bpy}(\text{CH}_2\text{SH})_2](\text{PF}_6)_2$  were synthesized by following reported procedures<sup>6,19</sup> and characterized by optical absorption spectroscopy and HR ESI MS (Fig. S1 and S2, ESI†). The ligand exchange reaction which leads to dimerization of  $[\text{Ag}_{25}(\text{DMBT})_{18}]^{-}$  was carried out by mixing  $[\text{Ru}(\text{bpy})_2\text{bpy}(\text{CH}_2\text{SH})_2]^{2+}$  and  $[\text{Ag}_{25}(\text{DMBT})_{18}]^{-}$  in acetonitrile (see the Experimental section of the ESI† for details). The cleaned product obtained from the ligand exchange reaction was analysed via UV-vis spectroscopy. The optical absorption spectra of  $[\text{Ag}_{25}(\text{DMBT})_{18}]^{-}$ , its dimer and  $[\text{Ru}(\text{bpy})_2\text{bpy}(\text{CH}_2\text{SH})_2]^{2+}$  are compared as shown in Fig. 1. The spectrum of the dimer changed slightly compared to the parent cluster from which we infer that the cluster core remains intact. There is a slight red shift of 600 nm and a change was observed close to absorption at 400 nm which indicates optical coupling between  $[\text{Ru}(\text{bpy})_2\text{bpy}(\text{CH}_2\text{SH})_2]^{2+}$  and the cluster. This type of minor change in the optical absorption spectrum ensures that the building blocks are intact which is essential for creating superstructures.

HR ESI MS was used to show the formation of the dimer of  $[\text{Ag}_{25}(\text{DMBT})]^{-}$ . Sample preparation and instrumental details are given in the ESI.† Under optimized conditions for collecting the data, full range HR ESI MS shows two peaks, at an  $m/z$  value of 5167 and an  $m/z$  value of 5504. Expansion of the peak at an  $m/z$  value of 5167 exhibits a characteristic peak to peak separation of 1 which confirms its unit charge. This species is  $[\text{Ag}_{25}(\text{DMBT})]^{-}$ , confirmed by its perfect match of experimental and theoretical mass spectra. Similarly, the expanded peak at  $m/z$  5504 shows the characteristic peak to peak separation of 0.5 which confirms its doubly charged state. This peak is assigned as the dimer of  $[\text{Ag}_{25}(\text{DMBT})_{18}]^{-}$  linked by the  $[\text{Ru}(\text{bpy})_2\text{bpy}(\text{CH}_2\text{SH})_2]^{2+}$  linker. The assignment of the peak was supported by the well matching of simulated and experimental isotopic distributions (Fig. 1).

<sup>a</sup> Department of Chemistry, DST Unit of Nanoscience (DST UNS) and Thematic Unit of Excellence (TUE), Indian Institute of Technology Madras, Chennai 600036, India. E-mail: pradeep@iitm.ac.in

<sup>b</sup> Department of Chemistry, Indian Institute of Technology Madras, Chennai 600036, India

† Electronic supplementary information (ESI) available. See DOI: 10.1039/c9cc01289c

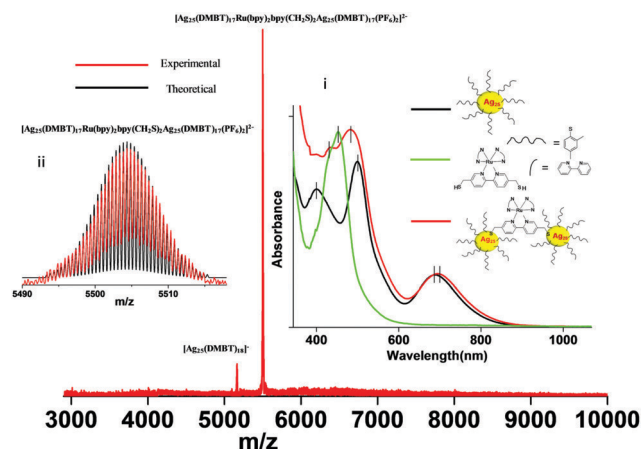


Fig. 1 Full range ESI MS in negative ion mode. The major peak at an  $m/z$  value of 5504 is assigned as  $[\text{Ag}_{25}(\text{DMBT})_{17}\text{Ru}(\text{bpy})_2\text{bpy}(\text{CH}_2\text{S})_2\text{Ag}_{25}(\text{DMBT})_{17}(\text{PF}_6)_2]^{2-}$ . Comparison of the optical absorption spectra of  $\text{Ag}_{25}$ , its dimer and  $[\text{Ru}(\text{bpy})_2\text{bpy}(\text{CH}_2\text{SH})_2]^{2+}$  is shown in the inset (i). The features in the spectra are marked. The experimental isotopic distribution is compared with the simulated spectrum in the inset (ii). Red and black traces correspond to experimental and theoretical spectra, respectively.

The presence of  $[\text{Ag}_{25}(\text{DMBT})]^-$  in the full spectrum is most likely to be due to the fragmentation of the dimeric species. This was further proven by the collision induced dissociation (CID) experiment. This experiment was performed by selecting the ion at an  $m/z$  value of 5504 and colliding it at various laboratory collision energies. Upon increasing the laboratory collision energy (CE) from 0 to 30 V, the dimeric species is fragmented into monomeric species  $[\text{Ag}_{25}(\text{DMBT})]^-$  and  $[\text{Ru}(\text{bpy})_2\text{bpy}(\text{CH}_2\text{S})_2(\text{PF}_6)]^-$  (Fig. 2). Furthermore, an increase in collision energy resulted in the formation of  $[\text{Ag}_{22}\text{L}_{15}]^-$ ,  $[\text{Ag}_{21}\text{L}_{14}]^-$ ,  $[\text{Ag}_5\text{L}_6]^-$ , and  $[\text{Ag}_2\text{L}_3]^-$  (L corresponds to DMBT) which represents the regular fragmentation of  $[\text{Ag}_{25}(\text{DMBT})_{18}]^-$  and this matches well with the previously reported fragmentation pattern.<sup>20</sup> Similar reactions were attempted by using only the dithiols,  $[\text{Bpy}(\text{CH}_2\text{SH})_2]$ , 1,4-BDT and biphenyl-4,4-dithiol but they were unsuccessful as after the mixing of dithiols and the cluster, the optical absorption spectra became featureless. It is likely to be due to the decomposition of  $[\text{Ag}_{25}(\text{DMBT})_{18}]^-$  clusters (Fig. S3A and B, ESI†).

The product was further analyzed *via* infrared spectroscopy (IR) to get further insights. IR spectra of  $[\text{Ru}(\text{bpy})_2\text{bpy}(\text{CH}_2\text{SH})_2]^{2+}$  and the cluster dimer were compared as shown in Fig. S4 (ESI†) which revealed that the peak at wavenumber  $2558\text{ cm}^{-1}$  is absent in the dimer. To get a clear view, the window of  $2530\text{--}2580\text{ cm}^{-1}$  is expanded as shown in Fig. S4 (ESI†). This region corresponds to the characteristic S–H frequency. This observation suggests that the thiol group of  $[\text{Ru}(\text{bpy})_2\text{bpy}(\text{CH}_2\text{SH})_2]^{2+}$  is linked with two clusters to form the dimer, by the loss of thiol protons. Similar experiments were performed using  $[\text{Au}_{25}(\text{SR})_{18}]^-$  (SR: butane thiolate) but no dimer was observed. Upon addition of  $[\text{Ru}(\text{bpy})_2\text{bpy}(\text{CH}_2\text{SH})_2]^{2+}$  to  $[\text{Au}_{25}(\text{SR})_{18}]^-$  cluster solution, an instant colour change was observed and an oxidised feature of  $\text{Au}_{25}$  was observed in UV-vis spectroscopy (Fig. S5D, ESI†). We failed to get any signal in the ESI MS in negative ion mode but in positive ion mode, good intensity was observed at  $m/z$  6527 which corresponds to  $[\text{Au}_{25}(\text{BT})_{18}]^+$

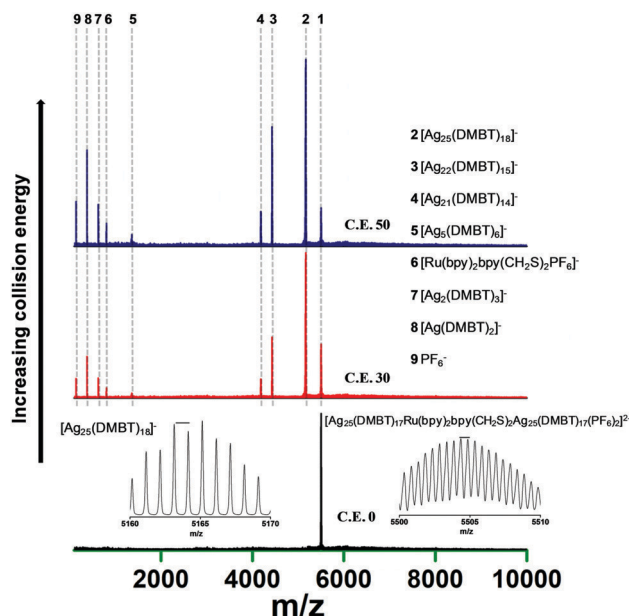


Fig. 2 Collision induced dissociation of  $m/z$  5504 at various collision energies. With increasing collision energy, the species like  $[\text{Ag}_{22}\text{L}_{15}]^-$ ,  $[\text{Ag}_{21}\text{L}_{14}]^-$ ,  $[\text{Ag}_5\text{L}_6]^-$ , and  $[\text{Ag}_2\text{L}_3]^-$  (L correspond to DMBT) were detected. All the fragments are marked and assigned. Most of the fragments are similar to the reported fragmentation of  $[\text{Ag}_{25}\text{L}_{18}]^-$ . The expansion of isotopic distributions of  $[\text{Ag}_{25}\text{L}_{18}]^-$  and its dimer in the  $1^-$  and  $2^-$  charge states shows the characteristic peak to peak separation of  $m/z$  1 and 0.5, respectively.

(BT stands for 1-butanethiolate), as confirmed by the perfect match of the theoretical and experimental isotopic distributions. It is important to note that in both the ion modes, no peak was detected corresponding to  $[\text{Ru}(\text{bpy})_2\text{bpy}(\text{CH}_2\text{SH})_2]$  in any charge state (Fig. S5A–C, ESI†). Seemingly, instead of forming the dimer, an electron transfer reaction has taken place.  $[\text{Au}_{25}(\text{SR})_{18}]^-$  was oxidised to  $[\text{Au}_{25}(\text{SR})_{18}]^+$  and consequently  $[\text{Ru}(\text{bpy})_2\text{bpy}(\text{CH}_2\text{SH})_2]^{2+}$  was reduced to  $[\text{Ru}(\text{bpy})_2\text{bpy}(\text{CH}_2\text{SH})_2]$ . In order to check the influence of steric hindrance, similar experiments were performed using phenyl ethanethiol (PET) protected  $\text{Au}_{25}$ . In this case also, similar results were observed as discussed earlier. We have not studied the electron transfer process in detail as it is beyond the scope of this work.

We were not able to grow single crystals of the dimer to get structural insights. However, powder X-ray diffraction of the dimer was performed and data are compared with the monomer as shown in Fig. S6 (ESI†). The peaks shift to the lower side of  $2\theta$  in the dimer which reveals an increase in the interplanar distances ( $d$ ). The extent of increase in  $d$  spacing is  $5.2\text{ \AA}$ , comparable to the difference in ligand dimensions. The dimer was further characterized by SEM EDS to correlate the metal percentage in between Ru and Ag (Fig. S7, ESI†). It shows that the ratio of atomic percentage of Ag and Ru is  $97.72:2.28 = 1:0.023$ . This ratio is close (actual ratio, Ag:Ru =  $1:0.02$ ) to the most probable composition of the dimer. To get further insights, the structure of the dimer was computed by density functional theory (DFT). The initial structure of the  $[\text{Ag}_{25}(\text{DMBT})_{18}]^-$  monomer was obtained from its crystal structure and subsequently, it was optimized using complete ligands as well as using the reduced model ligands (Fig. S8A and B, ESI†). Full theoretical



details of the methods are given in the ESI†. The structure of  $[\text{Ag}_{25}(\text{DMBT})_{18}]^-$  is composed of an  $\text{Ag}_{13}$  icosahedral core, which is further covered by six  $\text{Ag}_2(\text{SR})_3$  v-shaped staple units. Depending on their location and connectivity, there are two different types of sulphur atoms. The two possible locations where ligand exchange can take place are (i) at the apex sulphur atom of a staple and (ii) at the sulphur atom between a staple silver atom and the inner icosahedral core of the silver atom (marked in Fig. S8C, ESI†). We used the Borromean ring diagram and the aspicule system of nomenclature<sup>21</sup> to precisely identify binding sites and orientations of the clusters. Previous studies have shown that the sulphur locations ii are amenable for ligand exchange.<sup>22</sup> This might be due to the weaker interactions of ligands present at these sites or due to the greater solvent accessible area in this region.<sup>22</sup> Therefore, to find the appropriate locations for ligand exchange on the surface of the  $[\text{Ag}_{25}(\text{DMBT})_{18}]^-$  cluster, the linker molecule was connected to either clusters by replacing the ligands which are interacting between the staple and the inner icosahedral core atoms. The binding energy was obtained by subtracting the sum of energies of an isolated  $[\text{Ag}_{25}(\text{DMBT})_{18}]^-$  cluster and the linker,  $[\text{Ru}(\text{bpy})_2\text{bpy}(\text{CH}_2\text{SH})_2]^{2+}$  derived from the total energy of the complex,  $[\text{Ag}_{25}(\text{DMBT})_{17}\text{Ru}(\text{bpy})_2\text{bpy}(\text{CH}_2\text{S})_2]^+$  and an isolated DMBT ligand. Based on the binding energies of the linker among three possible

combinations of non-apex binding sites  $\{(\text{D5-5}), (\text{D3'-1'})\}$ ,  $\{(\text{D5-5}), (\text{D2'-5'})\}$  and  $\{(\text{D5-5}), (\text{D6'-1'})\}$ , (Fig. 3, see below), the sites with the higher binding affinity were identified as being the most probable for the ligand exchange to form the dimer structure.

The lowest energy isomer of the dimer, A is shown in Fig. 3A. The structure of isomer A using the Borromean ring diagram is shown in Fig. 3C. Full details of our method and the structures of other isomers are given in the ESI†. We formed the dimer structure by attaching, *via* the linker molecule, cluster 1 (on the left in Fig. 3A) to a rotated and translated copy of itself, which is referred to as cluster 2 (shown on the right side in Fig. 3A). We first placed cluster 1 in standard orientation and labelled its locants. Next, we assigned the locants of cluster 2 and especially the sulphur locants required for describing the second binding site in the following way. We identified which sulphur atoms in each cluster are equivalent to each other, and thereby assigned similar aspicule locants to those sulphur atoms with primes used for locants on cluster 2. For example, sulphur atom D3-1 in cluster 1 is equivalent to sulphur atom D3'-1' in cluster 2 and so on.

Five possible isomers, A, B, C, D and E for the dimer structure were generated by connecting the site of the sulphur atom (D5-5) of the first cluster with three different sites of the second one as shown in Fig. S9 (ESI†). Isomers D and E have the

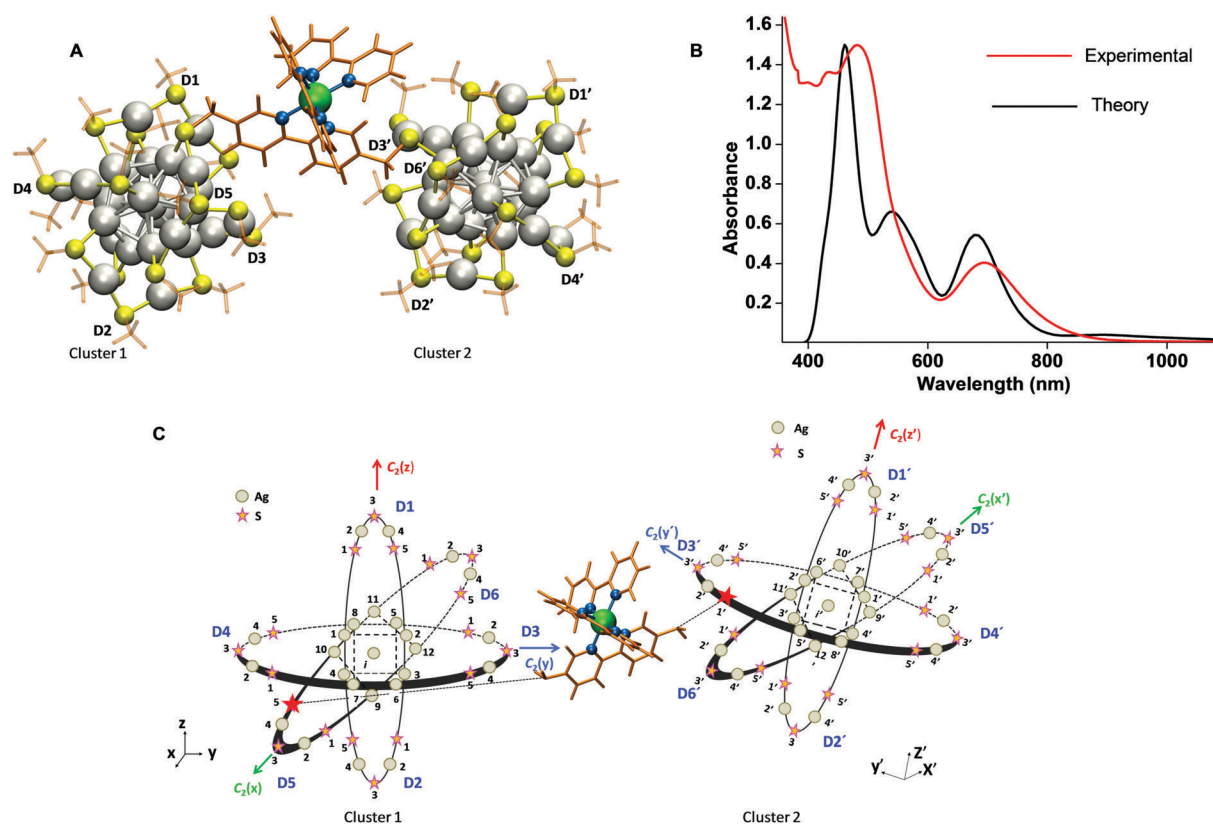


**Fig. 3** (A) Density functional theory (DFT) optimized structure of the most stable isomer A of the dimer. Depending on the connectivity, different isomers were observed. (B) The optical spectrum of the most stable isomer was calculated by time-dependent DFT and it is compared with the experimental data. The comparison shows a reasonable match, particularly in the 680 nm region. (C) The most stable isomer of the dimer in the aspicule (Borromean rings) representation. The bonding between  $[\text{Ru}(\text{bpy})_2\text{bpy}(\text{CH}_2\text{SH})_2]$  and  $[\text{Ag}_{25}(\text{DMBT})_{18}]$  clusters is shown by dotted lines. The ligand sites, denoted by the locants (D5-5) and (D3'-1') marked by the larger red stars are those which are involved in the ligand exchange and have been chosen on the basis of their calculated lower binding energies. Color codes: gray, silver; blue, nitrogen; yellow, sulphur; and green, ruthenium.

same binding sites as isomers A and B, respectively, but slightly different conformations for the linker molecule. The energies of the five dimer structures (A–E) are given in Table S2 (ESI†).

The most stable structure of the dimer, A was formed by the interaction of the linker between the sites (D5-5) and (D3'-1') of the  $[\text{Ag}_{25}(\text{DMBT})_{18}]^-$  monomers (Fig. 3A and C). On the other hand, the dimer in isomer C links between the sites (D5-5) and (D2'-5') of the  $[\text{Ag}_{25}(\text{DMBT})_{18}]^-$  clusters and exhibits the least stability. Overall stability decreases in the order,  $A < D < B < E < C$ , where the locants of the linker binding are,  $A = \{(D5-5), (D3'-1')\}$ ,  $B = \{(D5-5), (D3'-1')\}$ ,  $C = \{(D5-5), (D2'-5')\}$ ,  $D = \{(D5-5), (D6'-1')\}$ , and  $E = \{(D5-5), (D6'-1')\}$ . The lowest energy isomer, A has fewer DMBT ligands close to the exchanged site on both clusters, which minimizes steric hindrance and thereby increases the conformational freedom of the linker. This leads to a closer inter-cluster distance, as measured between their central Ag atoms, and therefore, lowers the total energy due to the decrease in steric hindrance and shorter atomic contacts between the linker atoms and the cluster ligand atoms. Besides the covalent linkage, there is a contribution of non-covalent interactions comprising the inter-cluster ligand–ligand van der Waals interactions. A  $\pi$ – $\pi$  interaction was observed between the pyridyl groups and the phenyl groups of the DMBT ligand in the second lowest energy isomer, D. This implies that the orientation of the clusters, the environment of the two exchange sites, and their associated degrees of steric hindrance play very important roles during the formation of such covalently-linked dimer structures. The total energy and aspicule locants (site position labels) of the sites of attachment of different isomers are presented in Fig. S9 (ESI†). Based on the structure computed, the aspicule name of the dimer is  $\mu$ -(D5-5, D3'-1')-(5,5')-di(mercaptomethyl) ruthenium tris(bipyridine), di((DMBT)<sub>17</sub>-argento-25 aspicule), where the binding sites on the clusters have been indicated in the prefix, and the  $\mu$  notation introduced here indicates that the linker bridges the two clusters between the D5-5 sulphur site on cluster 1 and D3'-1' sulphur site on cluster 2, as shown in Fig. 3C. The binding sites of methyl groups of DMBT are omitted from this name for simplicity. The electronic and optical absorption properties were also studied using the linear-response time dependent density functional theory (LR-TDDFT).<sup>23</sup> Electronic structures of the monomer and the dimer revealed that the transition taking place between the frontier orbitals in the monomer is altered to deeper lying orbitals, especially the unoccupied levels. This implies that the linker plays a vital role in the electronic structure of the dimer. Bader charge analysis of the dimer and the monomer showed that the structural changes of the dimer are minor after the incorporation of the linker. Hence, it is clear that the alteration in the electronic structure of the dimer resulted in changes in the UV/vis spectrum of the dimer (see the ESI†). The predicted spectrum of the most stable structure (Fig. 3B) showed a reasonable agreement with the experimental spectrum, which supports our calculated structure.

In conclusion, a covalently linked dimer of a silver nanocluster was synthesised using a ligand exchange methodology.

The formation of the dimer was confirmed by optical absorption spectroscopy, HR ESI MS and DFT. Theoretical prediction of the most stable binding site was made and identified using the aspicule positional notation and diagrams. It is worth noting that the combined properties of the nanoclusters and the chromophoric linker would be useful in the amplification of properties of individual constituents.

We thank the Department of Science and Technology for supporting our research project. M. B. thanks U. G. C. for his doctoral fellowship. A. N. and R. B. thank IITM for their fellowships. G. P. thanks IITM for an Institute Postdoctoral Fellowship.

## Conflicts of interest

There are no conflicts to declare.

## Notes and references

- 1 I. Chakraborty and T. Pradeep, *Chem. Rev.*, 2017, **117**, 8208–8271.
- 2 R. Jin, C. Zeng, M. Zhou and Y. Chen, *Chem. Rev.*, 2016, **116**, 10346–10413.
- 3 A. Mathew and T. Pradeep, *Part. Part. Syst. Charact.*, 2014, **31**, 1017–1053.
- 4 C. P. Joshi, M. S. Bootharaju and O. M. Bakr, *J. Phys. Chem. Lett.*, 2015, **6**, 3023–3035.
- 5 P. D. Jadzinsky, G. Calero, C. J. Ackerson, D. A. Bushnell and R. D. Kornberg, *Science*, 2007, **318**, 430–433.
- 6 C. P. Joshi, M. S. Bootharaju, M. J. Alhilaly and O. M. Bakr, *J. Am. Chem. Soc.*, 2015, **137**, 11578–11581.
- 7 L. G. AbdulHalim, M. S. Bootharaju, Q. Tang, S. Del Gobbo, R. G. AbdulHalim, M. Eddaoudi, D.-e. Jiang and O. M. Bakr, *J. Am. Chem. Soc.*, 2015, **137**, 11970–11975.
- 8 M. J. Alhilaly, M. S. Bootharaju, C. P. Joshi, T. M. Besong, A.-H. Emwas, R. Juarez-Mosqueda, S. Kaappa, S. Malola, K. Adil, A. Shkurenko, H. Häkkinen, M. Eddaoudi and O. M. Bakr, *J. Am. Chem. Soc.*, 2016, **138**, 14727–14732.
- 9 H. Qian, W. T. Eckenhoff, Y. Zhu, T. Pintauer and R. Jin, *J. Am. Chem. Soc.*, 2010, **132**, 8280–8281.
- 10 H. Yang, Y. Wang, H. Huang, L. Gell, L. Lehtovaara, S. Malola, H. Häkkinen and N. Zheng, *Nat. Commun.*, 2013, **4**, 2422.
- 11 B. Mohammad, A. Ghosh, K. S. Sugi, A. Nag, E. Khatun, B. Varghese, G. Paramasivam, S. Antharjanam, G. Natarajan and T. Pradeep, *Angew. Chem., Int. Ed.*, 2019, **58**, 189–194.
- 12 J. Chai, S. Yang, Y. Lv, T. Chen, S. Wang, H. Yu and M. Zhu, *J. Am. Chem. Soc.*, 2018, **140**, 15582–15585.
- 13 A. Mathew, G. Natarajan, L. Lehtovaara, H. Häkkinen, R. M. Kumar, V. Subramanian, A. Jaleel and T. Pradeep, *ACS Nano*, 2014, **8**, 139–152.
- 14 A. Nag, P. Chakraborty, G. Paramasivam, M. Bodiuazzaman, G. Natarajan and T. Pradeep, *J. Am. Chem. Soc.*, 2018, **140**, 13590–13593.
- 15 A. Baksi, P. Chakraborty, S. Bhat, G. Natarajan and T. Pradeep, *Chem. Commun.*, 2016, **52**, 8397–8400.
- 16 T. Lahtinen, E. Hulkko, K. Sokolowska, T.-R. Tero, V. Saarnio, J. Lindgren, M. Pettersson, H. Häkkinen and L. Lehtovaara, *Nanoscale*, 2016, **8**, 18665–18674.
- 17 A. Sels, G. Salassa, F. Cousin, L.-T. Lee and T. Bürgi, *Nanoscale*, 2018, **10**, 12754–12762.
- 18 R. Ho-Wu, K. Sun and T. Goodson, *J. Phys. Chem. C*, 2018, **122**, 2315–2329.
- 19 P. Bertoncello, E. T. Kefalas, Z. Pikramenou, P. R. Unwin and R. J. Forster, *J. Phys. Chem. C*, 2006, **110**, 10063–10069.
- 20 P. Chakraborty, A. Baksi, E. Khatun, A. Nag, A. Ghosh and T. Pradeep, *J. Phys. Chem. C*, 2017, **121**, 10971–10981.
- 21 G. Natarajan, A. Mathew, Y. Negishi, R. L. Whetten and T. Pradeep, *J. Phys. Chem. C*, 2015, **119**, 27768–27785.
- 22 C. L. Heinecke, T. W. Ni, S. Malola, V. Mäkinen, O. A. Wong, H. Häkkinen and C. J. Ackerson, *J. Am. Chem. Soc.*, 2012, **134**, 13316–13322.
- 23 M. Walter, H. Häkkinen, L. Lehtovaara, M. Puska, J. Enkovaara, C. Rostgaard and J. J. Mortensen, *J. Chem. Phys.*, 2008, **128**, 244101.

## A covalently linked dimer of $[\text{Ag}_{25}(\text{DMBT})_{18}]^-$

Mohammad Bodiuzzaman<sup>a</sup>, Abhijit Nag<sup>a</sup>, Raghu Narayanan Pradeep<sup>a</sup>, Ankush Chakraborty<sup>b</sup>,  
Ranjit Bag<sup>b</sup>, Ganesan Paramasivam<sup>a</sup>, Ganapati Natarajan<sup>a</sup> Govindasamy Sekar<sup>b</sup>, Sundargopal  
Ghosh<sup>b</sup> and Thalappil Pradeep<sup>\*a</sup>

<sup>a</sup> Department of Chemistry, DST Unit of Nanoscience (DST UNS) and Thematic Unit of Excellence (TUE), Indian Institute of Technology Madras, Chennai 600036, India

<sup>b</sup> Department of Chemistry, Indian Institute of Technology Madras, Chennai 600036, India

\*Email: pradeep@iitm.ac.in

### A Isomer

Ag	15.164230000	16.096740000	22.226480000
Ag	12.727850000	15.021010000	23.176390000
Ag	13.483520000	14.759360000	20.392940000
Ag	13.834040000	17.460790000	24.322190000
Ag	12.766070000	17.373320000	21.492310000
Ag	16.816960000	17.464530000	24.029390000
Ag	17.510780000	17.225240000	21.104580000
Ag	16.532310000	14.680470000	20.223010000
Ag	15.017160000	17.277320000	19.645320000
Ag	15.301200000	15.054980000	24.849740000
Ag	17.504840000	14.742200000	22.992020000
Ag	15.306640000	18.922330000	22.024170000
Ag	15.072930000	13.262430000	22.312620000
Ag	12.937960000	19.730660000	19.771280000
Ag	12.237750000	15.193050000	26.082070000
Ag	17.749090000	16.317370000	18.039410000
Ag	18.246000000	15.368660000	25.935960000
Ag	12.330530000	12.185950000	21.789460000

Ag	10.885850000	17.583970000	23.941020000
Ag	19.719310000	15.282100000	20.485830000
Ag	16.649170000	12.439860000	24.821290000
Ag	18.169040000	19.808590000	22.894040000
Ag	15.279850000	20.080140000	24.765440000
Ag	14.751890000	12.228000000	19.326800000
Ag	12.620650000	16.731030000	18.007390000
S	17.431570000	21.220870000	24.745850000
S	11.231740000	13.081360000	23.764470000
S	18.293530000	17.796590000	26.105620000
S	15.594190000	17.105950000	17.199110000
S	12.595820000	14.299940000	18.092730000
S	14.176100000	13.876870000	26.764140000
S	12.949990000	19.617570000	25.324230000
S	14.077450000	21.050910000	21.517980000
S	10.054550000	16.236190000	25.790180000
S	15.085490000	11.060560000	23.549490000
S	10.833360000	18.957060000	21.910190000
S	16.615970000	13.287750000	18.142030000
S	20.006530000	14.562790000	22.809970000
S	19.580710000	18.671870000	21.244060000
S	12.247420000	19.085840000	17.514690000
S	20.044840000	15.481990000	18.080870000
S	18.480420000	12.981760000	26.344100000
S	12.823560000	10.825250000	19.841590000
C	17.072770000	22.819540000	24.011830000
C	18.127400000	23.617700000	23.481190000

C	17.807920000	24.879740000	22.938350000
C	16.492670000	25.387990000	22.903470000
C	15.467940000	24.592680000	23.463070000
C	15.753200000	23.331390000	24.008260000
C	19.550890000	23.118810000	23.440030000
C	16.181850000	26.707320000	22.234680000
C	9.557960000	13.426240000	23.211260000
C	8.570610000	12.401930000	23.321360000
C	7.237510000	12.723900000	22.986290000
C	6.842970000	14.008560000	22.550890000
C	7.840670000	15.000140000	22.432030000
C	9.175260000	14.705680000	22.749750000
C	8.928510000	11.005490000	23.769850000
C	5.403610000	14.303260000	22.189850000
C	15.871290000	18.740260000	16.518820000
C	16.248000000	18.850850000	15.146650000
C	16.410390000	20.143030000	14.601390000
C	16.192640000	21.323090000	15.347770000
C	15.800370000	21.187190000	16.697640000
C	15.652490000	19.914690000	17.273690000
C	16.431170000	17.627290000	14.280000000
C	16.390540000	22.687780000	14.723710000
C	10.853590000	13.874950000	18.166660000
C	10.117850000	13.764200000	16.947240000
C	8.771640000	13.348670000	17.016790000
C	8.127760000	13.025960000	18.233450000
C	8.873290000	13.148920000	19.424630000

C	10.211870000	13.574630000	19.387240000
C	10.754370000	14.064970000	15.611740000
C	6.688600000	12.557300000	18.250720000
C	14.635660000	14.632090000	28.324360000
C	14.057480000	14.123470000	29.527680000
C	14.475790000	14.676960000	30.756120000
C	15.440890000	15.705460000	30.845830000
C	15.991230000	16.198150000	29.642490000
C	15.594240000	15.667070000	28.403460000
C	13.041070000	13.007670000	29.499830000
C	15.889870000	16.232600000	32.191490000
C	13.027510000	19.494750000	27.112760000
C	12.891700000	20.675970000	27.899510000
C	12.855460000	20.539680000	29.304630000
C	12.941910000	19.291190000	29.955500000
C	13.088050000	18.137920000	29.153680000
C	13.135680000	18.242010000	27.756720000
C	12.800700000	22.043150000	27.265170000
C	12.846410000	19.176220000	31.460680000
C	15.150910000	22.124750000	20.569080000
C	14.605360000	23.289190000	19.946140000
C	15.482090000	24.147490000	19.246930000
C	16.872310000	23.911410000	19.150470000
C	17.390220000	22.761810000	19.784980000
C	16.540000000	21.881850000	20.472280000
C	13.129360000	23.597080000	20.015010000
C	17.770240000	24.827180000	18.347730000

C	9.776200000	17.383110000	27.137840000
C	9.660780000	16.897130000	28.473140000
C	9.340680000	17.815380000	29.496030000
C	9.127350000	19.188480000	29.255960000
C	9.232960000	19.645660000	27.922860000
C	9.551580000	18.757990000	26.883640000
C	9.903990000	15.446890000	28.807170000
C	8.836860000	20.142950000	30.393020000
C	16.248680000	9.931440000	22.773570000
C	16.601240000	8.722360000	23.447230000
C	17.477750000	7.824360000	22.798620000
C	18.010180000	8.066280000	21.512760000
C	17.649340000	9.269660000	20.869100000
C	16.790440000	10.187740000	21.493620000
C	16.074080000	8.405610000	24.826250000
C	18.921000000	7.068850000	20.830490000
C	9.429280000	18.305460000	21.003680000
C	8.152750000	18.919870000	21.174020000
C	7.070820000	18.436190000	20.406220000
C	7.202360000	17.379170000	19.478870000
C	8.477120000	16.792560000	19.323750000
C	9.569550000	17.248120000	20.076360000
C	7.948410000	20.051880000	22.151810000
C	6.015550000	16.861090000	18.697030000
C	18.001660000	12.160560000	18.242930000
C	18.222910000	11.246830000	17.169910000
C	19.373910000	10.429330000	17.216570000



C	20.311700000	10.484340000	18.270470000
C	20.061910000	11.384850000	19.329580000
C	18.921900000	12.202110000	19.315020000
C	17.259030000	11.141800000	16.011780000
C	21.557790000	9.625600000	18.262710000
C	20.621620000	12.883960000	22.726030000
C	21.983050000	12.644500000	22.367650000
C	22.464120000	11.319350000	22.404900000
C	21.658900000	10.223140000	22.790840000
C	20.313850000	10.483420000	23.129680000
C	19.803610000	11.791320000	23.087900000
C	22.895970000	13.769490000	21.944390000
C	22.229960000	8.823740000	22.852770000
C	19.768900000	19.798310000	19.868730000
C	20.816700000	20.766650000	19.908970000
C	21.011300000	21.582400000	18.775260000
C	20.234060000	21.457570000	17.600960000
C	19.200870000	20.496260000	17.589470000
C	18.967030000	19.684960000	18.712120000
C	21.732450000	20.894880000	21.105530000
C	20.534090000	22.302780000	16.383880000
C	10.486560000	19.150810000	17.177770000
C	9.649740000	20.216600000	17.620270000
C	8.305910000	20.234020000	17.187580000
C	7.759780000	19.263340000	16.320950000
C	8.611570000	18.224090000	15.885660000
C	9.946500000	18.167620000	16.313180000

C	10.160730000	21.318920000	18.513620000
C	6.326650000	19.359930000	15.844960000
C	21.127310000	16.864690000	17.736490000
C	21.167230000	17.434540000	16.429740000
C	22.128190000	18.435710000	16.162650000
C	23.051640000	18.898310000	17.124290000
C	22.984580000	18.325810000	18.415400000
C	22.038540000	17.333520000	18.711040000
C	20.199800000	17.005770000	15.354190000
C	24.059680000	19.980500000	16.805750000
C	17.772100000	12.592480000	27.946710000
C	18.260600000	13.201870000	29.139520000
C	17.725810000	12.777170000	30.375310000
C	16.748180000	11.767700000	30.485920000
C	16.287870000	11.167820000	29.292520000
C	16.784530000	11.580550000	28.047520000
C	19.304370000	14.290790000	29.110100000
C	16.204860000	11.345190000	31.832470000
C	13.368710000	9.267100000	20.532890000
C	14.230980000	8.404560000	19.792990000
C	14.551720000	7.148040000	20.348440000
C	14.051230000	6.703690000	21.590540000
C	13.184590000	7.567710000	22.296250000
C	12.852040000	8.827810000	21.775920000
C	14.808840000	8.808470000	18.459620000
C	14.465880000	5.367660000	22.163380000
H	18.630470000	25.490460000	22.511840000

H	14.422780000	24.960940000	23.466280000
H	14.933140000	22.710070000	24.423460000
H	19.917510000	22.818430000	24.450180000
H	20.231680000	23.894910000	23.024170000
H	19.623000000	22.208650000	22.793980000
H	17.075190000	27.369640000	22.193040000
H	15.366550000	27.254180000	22.760040000
H	15.841350000	26.539270000	21.184390000
H	6.466940000	11.930770000	23.080240000
H	7.576680000	16.016870000	22.079900000
H	9.948970000	15.494100000	22.640860000
H	9.618240000	10.519670000	23.038070000
H	8.020500000	10.370450000	23.865590000
H	9.467030000	11.016080000	24.745040000
H	5.211730000	14.110760000	21.106180000
H	5.145820000	15.368370000	22.384090000
H	4.696260000	13.664340000	22.765020000
H	16.706840000	20.228310000	13.534500000
H	15.615910000	22.085590000	17.319490000
H	15.352670000	19.828210000	18.338360000
H	17.131120000	16.895320000	14.746430000
H	16.822600000	17.904140000	13.276470000
H	15.466160000	17.083390000	14.147180000
H	17.446880000	23.037720000	14.831010000
H	15.743040000	23.453000000	15.208240000
H	16.159720000	22.677500000	13.634580000
H	8.203720000	13.262020000	16.066700000

H	8.402090000	12.925350000	20.401680000
H	10.776790000	13.686410000	20.335930000
H	11.246480000	15.066170000	15.611690000
H	9.999960000	14.035540000	14.794760000
H	11.559900000	13.331590000	15.372420000
H	6.007250000	13.301470000	17.775190000
H	6.335950000	12.383220000	19.291250000
H	6.563980000	11.602010000	17.687850000
H	14.030120000	14.271510000	31.689320000
H	16.732730000	17.022170000	29.663520000
H	16.033260000	16.069910000	27.467590000
H	12.162260000	13.269120000	28.864200000
H	12.677620000	12.773360000	30.524790000
H	13.479190000	12.084720000	29.052890000
H	15.044830000	16.296300000	32.915030000
H	16.344210000	17.244200000	32.100760000
H	16.656430000	15.562330000	32.650730000
H	12.753760000	21.459160000	29.918190000
H	13.169820000	17.141100000	29.629610000
H	13.248170000	17.326090000	27.137850000
H	13.730570000	22.283790000	26.694800000
H	12.652660000	22.829990000	28.037950000
H	11.962290000	22.099760000	26.532410000
H	13.051000000	20.147430000	31.963390000
H	13.564950000	18.422230000	31.855990000
H	11.826200000	18.845600000	31.771530000
H	15.050750000	25.042300000	18.750110000

H	18.473180000	22.537710000	19.726780000
H	16.959710000	20.969500000	20.948980000
H	12.527430000	22.756900000	19.593840000
H	12.886590000	24.522790000	19.448080000
H	12.786370000	23.722860000	21.068890000
H	17.759330000	24.549030000	17.265830000
H	18.826430000	24.760580000	18.692770000
H	17.445860000	25.890390000	18.417040000
H	9.252040000	17.432770000	30.533990000
H	9.066600000	20.717040000	27.691280000
H	9.644540000	19.137280000	25.845810000
H	9.243670000	14.767040000	28.220290000
H	9.746740000	15.251850000	29.890460000
H	10.953290000	15.157040000	28.549220000
H	8.523700000	19.598250000	31.311680000
H	8.031990000	20.867190000	30.130790000
H	9.742840000	20.742420000	30.651840000
H	17.758690000	6.892420000	23.333270000
H	18.059170000	9.505990000	19.868230000
H	16.528590000	11.135610000	20.975890000
H	16.444880000	9.145840000	25.576160000
H	16.397660000	7.392220000	25.152370000
H	14.960820000	8.455720000	24.856410000
H	19.509340000	6.473690000	21.564820000
H	19.634220000	7.577740000	20.143490000
H	18.337440000	6.342530000	20.215110000
H	6.080110000	18.919400000	20.540600000

H	8.623170000	15.963000000	18.605610000
H	10.562890000	16.771300000	19.940880000
H	8.162900000	19.724590000	23.197360000
H	6.902320000	20.428550000	22.112460000
H	8.640210000	20.901130000	21.943470000
H	5.502740000	16.036070000	19.248320000
H	6.335150000	16.451710000	17.712370000
H	5.257920000	17.656740000	18.517420000
H	19.544930000	9.721410000	16.379060000
H	20.757760000	11.440490000	20.188760000
H	18.723170000	12.884510000	20.167900000
H	16.227140000	10.907110000	16.363540000
H	17.578940000	10.346080000	15.303910000
H	17.182150000	12.103550000	15.453840000
H	21.798170000	9.243760000	19.281490000
H	22.445350000	10.212470000	17.922780000
H	21.452430000	8.753810000	17.578230000
H	23.521550000	11.138490000	22.118180000
H	19.641260000	9.651980000	23.418350000
H	18.739620000	11.974560000	23.343820000
H	22.445130000	14.344720000	21.097900000
H	23.886290000	13.380100000	21.618800000
H	23.052100000	14.497720000	22.775710000
H	22.796590000	8.564680000	21.928230000
H	21.425920000	8.066990000	22.983920000
H	22.939920000	8.712490000	23.707250000
H	21.820460000	22.342410000	18.809880000

H	18.556510000	20.380320000	16.695990000
H	18.147200000	18.936610000	18.693770000
H	21.154710000	20.927360000	22.059010000
H	22.358680000	21.812600000	21.030430000
H	22.414530000	20.013090000	21.185300000
H	20.669350000	23.377060000	16.647000000
H	19.717160000	22.229030000	15.633050000
H	21.476430000	21.964220000	15.889150000
H	7.654330000	21.056820000	17.548970000
H	8.225490000	17.441150000	15.202110000
H	10.603980000	17.347450000	15.962220000
H	10.569810000	20.912880000	19.471390000
H	9.349010000	22.038600000	18.761670000
H	10.989110000	21.882930000	18.023410000
H	5.656010000	19.756270000	16.640700000
H	5.934390000	18.367850000	15.527590000
H	6.237480000	20.047290000	14.969360000
H	22.155820000	18.873050000	15.143330000
H	23.682900000	18.674970000	19.202600000
H	21.965220000	16.903670000	19.729610000
H	20.248140000	15.907130000	15.171610000
H	20.397730000	17.539150000	14.398270000
H	19.148530000	17.225320000	15.665270000
H	24.048140000	20.246090000	15.726050000
H	25.098880000	19.663570000	17.056830000
H	23.848180000	20.906940000	17.392320000
H	18.094860000	13.265280000	31.301130000



H	15.521130000	10.368030000	29.336350000
H	16.391040000	11.115590000	27.120360000
H	20.249360000	13.941360000	28.631830000
H	19.536010000	14.647640000	30.137970000
H	18.949050000	15.164620000	28.508200000
H	16.593890000	10.344430000	32.137890000
H	15.093480000	11.269200000	31.813780000
H	16.483660000	12.070260000	32.629000000
H	15.228840000	6.482760000	19.772840000
H	12.756590000	7.249250000	23.268060000
H	12.175720000	9.498260000	22.343840000
H	14.010000000	9.065260000	17.725660000
H	15.438310000	7.995830000	18.034270000
H	15.447460000	9.721690000	18.561180000
H	14.760320000	4.652710000	21.362740000
H	13.647820000	4.903050000	22.758300000
H	15.343980000	5.482560000	22.843450000
C	20.000260000	18.468200000	26.308200000
H	20.326790000	18.191370000	27.338910000
H	19.852950000	19.577360000	26.304580000
C	21.117790000	18.138540000	25.335380000
C	20.916670000	17.563030000	24.068740000
C	22.450870000	18.449910000	25.689190000
C	22.006540000	17.381920000	23.200910000
N	23.515610000	18.276230000	24.866470000
C	23.303030000	17.759820000	23.598160000
H	22.682110000	18.862270000	26.690690000

H	21.823340000	16.931650000	22.208870000
C	24.501090000	17.626790000	22.736490000
N	25.703090000	18.047040000	23.275440000
C	26.858790000	17.839930000	22.561320000
H	27.796300000	18.179750000	23.044390000
C	26.912310000	17.211020000	21.293130000
C	25.659680000	16.867940000	20.724190000
H	25.622140000	16.407890000	19.715640000
C	24.472780000	17.066300000	21.442070000
H	23.512890000	16.761170000	20.992990000
H	26.250950000	13.498990000	25.387160000
C	26.101900000	14.396620000	26.015350000
C	26.078850000	14.324020000	27.427150000
C	25.937710000	15.643290000	25.401910000
C	25.878480000	15.501690000	28.155800000
N	25.757700000	16.802270000	26.097350000
C	25.711640000	16.737460000	27.483280000
H	26.214390000	13.357560000	27.948810000
H	25.960730000	15.742080000	24.300800000
H	25.849880000	15.469290000	29.260430000
C	25.468750000	18.015270000	28.153160000
N	25.289980000	19.103300000	27.306910000
C	25.018880000	20.317180000	27.868090000
H	24.873050000	21.149520000	27.154450000
C	24.926860000	20.526040000	29.247690000
C	25.117610000	19.425310000	30.116210000
H	25.051630000	19.551350000	31.213350000

C	25.386890000	18.171960000	29.558020000
H	25.540040000	17.297850000	30.217610000
C	29.900500000	18.976290000	25.614290000
C	30.157150000	20.293070000	25.169820000
C	28.575180000	18.532660000	25.674360000
C	29.073320000	21.108550000	24.825090000
N	27.510400000	19.312570000	25.332770000
C	27.749570000	20.616620000	24.922270000
H	31.195370000	20.667820000	25.081120000
H	28.328980000	17.502840000	25.994460000
H	29.253810000	22.138940000	24.468150000
C	26.552190000	21.392970000	24.575410000
N	25.353400000	20.698030000	24.657830000
C	24.202010000	21.342730000	24.313570000
H	23.275930000	20.740500000	24.372680000
C	24.165820000	22.681540000	23.908630000
C	25.378220000	23.404910000	23.841990000
H	25.388160000	24.468020000	23.534500000
C	26.571150000	22.749830000	24.172960000
H	27.532500000	23.294020000	24.125890000
H	24.712300000	21.539670000	29.633480000
H	30.719740000	18.291080000	25.898480000
H	23.193460000	23.141290000	23.649870000
Ru	25.522380000	18.713800000	25.270720000
C	28.182100000	16.740650000	20.580190000
H	28.542250000	15.827850000	21.117860000
H	27.890930000	16.407750000	19.558860000

H	19.893830000	17.258220000	23.771460000
Ag	32.840440000	16.752110000	15.970260000
Ag	34.895910000	18.642900000	15.502530000
Ag	34.301290000	16.642870000	13.496670000
Ag	34.320630000	17.645650000	18.180980000
Ag	35.532050000	15.868060000	16.018640000
Ag	31.428230000	16.951820000	18.515340000
Ag	30.901930000	14.761910000	16.350460000
Ag	31.306220000	15.923930000	13.753730000
Ag	33.427820000	14.148680000	15.003580000
Ag	32.298860000	19.309420000	17.004480000
Ag	30.188540000	17.661600000	15.870640000
Ag	33.356790000	14.727390000	17.852220000
Ag	32.266400000	18.649310000	13.966440000
Ag	36.082450000	13.035960000	16.497400000
Ag	35.184250000	20.726010000	17.553470000
Ag	30.659590000	13.028350000	13.516430000
Ag	29.379710000	19.181180000	18.446460000
Ag	34.732570000	19.616540000	12.531040000
Ag	37.251590000	17.832330000	17.623040000
Ag	28.383620000	15.074710000	14.900840000
Ag	30.368920000	20.644270000	15.255490000
Ag	30.700420000	14.208950000	19.325220000
Ag	33.500720000	15.871230000	20.542320000
Ag	32.655100000	17.352290000	11.086870000
Ag	35.816810000	13.870070000	13.187530000
S	31.645150000	14.646470000	21.531510000

S	35.873330000	20.696950000	14.399400000
S	29.678120000	17.836460000	20.464630000
S	33.013800000	12.448700000	13.196620000
S	35.303000000	15.520740000	11.468150000
S	32.967170000	21.725090000	17.276530000
S	35.591300000	17.102930000	20.300960000
S	35.075720000	13.137430000	18.752720000
S	37.551690000	20.234520000	17.889490000
S	31.704700000	20.995590000	13.246780000
S	37.765930000	15.477310000	17.159770000
S	31.201340000	15.401520000	11.302530000
S	27.734700000	17.126160000	16.070560000
S	29.065070000	13.552400000	17.622440000
S	36.793150000	11.992330000	14.400390000
S	28.244360000	13.231740000	13.317470000
S	28.616600000	20.937500000	16.924420000
S	34.175000000	19.055790000	10.226880000
C	32.359000000	13.078240000	22.041340000
C	31.512900000	11.962680000	22.309820000
C	32.104460000	10.766250000	22.767320000
C	33.493000000	10.628740000	22.977130000
C	34.309260000	11.751840000	22.715580000
C	33.752180000	12.954120000	22.253680000
C	30.024060000	12.026140000	22.078970000
C	34.094430000	9.314820000	23.422410000
C	37.619200000	20.413510000	14.082190000
C	38.359040000	21.385670000	13.346480000

C	39.754260000	21.202240000	13.218220000
C	40.443040000	20.108850000	13.788600000
C	39.685130000	19.147740000	14.492970000
C	38.296570000	19.296910000	14.621190000
C	37.682850000	22.577180000	12.712610000
C	41.936570000	19.940790000	13.618820000
C	33.188110000	10.797940000	13.871560000
C	32.882060000	9.679050000	13.039290000
C	33.092170000	8.385690000	13.563210000
C	33.614250000	8.155580000	14.856130000
C	33.916160000	9.279360000	15.656050000
C	33.694620000	10.578660000	15.172060000
C	32.371710000	9.861090000	11.629380000
C	33.826700000	6.748920000	15.372450000
C	36.887000000	16.251390000	11.040450000
C	37.689460000	15.621080000	10.040120000
C	38.899590000	16.244340000	9.665570000
C	39.340320000	17.465630000	10.224840000
C	38.525670000	18.073050000	11.204020000
C	37.328260000	17.464110000	11.613640000
C	37.261270000	14.329050000	9.386420000
C	40.637510000	18.107780000	9.783190000
C	32.567400000	22.257360000	18.937000000
C	32.978760000	23.554550000	19.368070000
C	32.589800000	23.987350000	20.653840000
C	31.798920000	23.200980000	21.518920000
C	31.406300000	21.919330000	21.074930000

C	31.791550000	21.456960000	19.807150000
C	33.776830000	24.466530000	18.469370000
C	31.342550000	23.742710000	22.856440000
C	35.289300000	18.441610000	21.459020000
C	35.629080000	18.255850000	22.831600000
C	35.473410000	19.348640000	23.711760000
C	35.006670000	20.610800000	23.285970000
C	34.657620000	20.764140000	21.926330000
C	34.798240000	19.694830000	21.029000000
C	36.139080000	16.926630000	23.333060000
C	34.933470000	21.783800000	24.238570000
C	34.316260000	11.527150000	18.936430000
C	35.138780000	10.405260000	19.259570000
C	34.517600000	9.153170000	19.458120000
C	33.121090000	8.967730000	19.364690000
C	32.327490000	10.093590000	19.054880000
C	32.917080000	11.347770000	18.837180000
C	36.635430000	10.547830000	19.384900000
C	32.494530000	7.602480000	19.543000000
C	37.963400000	20.504820000	19.608350000
C	37.841160000	21.805720000	20.180260000
C	38.260330000	21.994060000	21.514080000
C	38.794260000	20.953820000	22.303670000
C	38.925130000	19.678830000	21.708870000
C	38.517420000	19.459710000	20.384860000
C	37.261070000	22.958320000	19.401250000
C	39.171250000	21.185590000	23.749370000



C	30.406980000	20.939460000	12.007870000
C	29.791260000	22.164060000	11.607870000
C	28.810800000	22.118980000	10.595230000
C	28.425850000	20.921760000	9.952330000
C	29.043930000	19.723100000	10.368350000
C	30.013080000	19.732930000	11.385510000
C	30.159250000	23.480170000	12.248990000
C	27.400620000	20.928370000	8.838390000
C	39.046450000	15.582980000	15.905870000
C	40.411580000	15.546420000	16.318380000
C	41.411190000	15.558560000	15.320170000
C	41.111970000	15.590550000	13.939850000
C	39.752470000	15.618470000	13.557240000
C	38.738470000	15.620790000	14.526760000
C	40.790890000	15.477350000	17.778810000
C	42.205340000	15.609420000	12.893940000
C	29.595140000	15.901330000	10.688350000
C	29.305750000	15.753320000	9.299530000
C	27.999390000	16.059620000	8.856710000
C	26.976260000	16.490840000	9.728170000
C	27.289700000	16.632460000	11.098760000
C	28.579860000	16.349080000	11.565300000
C	30.345980000	15.261500000	8.321320000
C	25.582920000	16.798540000	9.224760000
C	26.806010000	17.946000000	14.766820000
C	25.489220000	17.497250000	14.440990000
C	24.762940000	18.220710000	13.470930000

C	25.280540000	19.359090000	12.808820000
C	26.594270000	19.765150000	13.127020000
C	27.342070000	19.059410000	14.084100000
C	24.889990000	16.266660000	15.074470000
C	24.448260000	20.107730000	11.790630000
C	29.296310000	11.786470000	17.402970000
C	28.451180000	10.887690000	18.121670000
C	28.577980000	9.505560000	17.867570000
C	29.482990000	8.979980000	16.917760000
C	30.312230000	9.888120000	16.225610000
C	30.225920000	11.268160000	16.473840000
C	27.419490000	11.393080000	19.102080000
C	29.540960000	7.497890000	16.622300000
C	38.539910000	12.072600000	14.003990000
C	39.560480000	11.803040000	14.962650000
C	40.896590000	11.735360000	14.513230000
C	41.268270000	11.908360000	13.162440000
C	40.240520000	12.172300000	12.231100000
C	38.902970000	12.253280000	12.647400000
C	39.248910000	11.577660000	16.422120000
C	42.713280000	11.788440000	12.731050000
C	27.416390000	11.898220000	14.178400000
C	27.601640000	10.545190000	13.766170000
C	26.799240000	9.548760000	14.363420000
C	25.827470000	9.830910000	15.345700000
C	25.666050000	11.177260000	15.742020000
C	26.448470000	12.191400000	15.169170000

C	28.628750000	10.165120000	12.728710000
C	25.012260000	8.727200000	15.980260000
C	29.031950000	22.526560000	17.634950000
C	28.511210000	22.922780000	18.901970000
C	28.835840000	24.208470000	19.386580000
C	29.642410000	25.120450000	18.670830000
C	30.119570000	24.717310000	17.404500000
C	29.823820000	23.442480000	16.900800000
C	27.669350000	21.986150000	19.732520000
C	29.990420000	26.478560000	19.239170000
C	33.257700000	20.482380000	9.649690000
C	32.297360000	20.353240000	8.603440000
C	31.679860000	21.524130000	8.114690000
C	31.975770000	22.813030000	8.607160000
C	32.943010000	22.919220000	9.632550000
C	33.568490000	21.772250000	10.146340000
C	31.925620000	19.010050000	8.027250000
C	31.251540000	24.030740000	8.078370000
H	31.444270000	9.895520000	22.960590000
H	35.404990000	11.682410000	22.865060000
H	34.412250000	13.820300000	22.039100000
H	29.547770000	12.842890000	22.670860000
H	29.535580000	11.062100000	22.341750000
H	29.801010000	12.250950000	21.005900000
H	33.347640000	8.672360000	23.940110000
H	34.952900000	9.469070000	24.114980000
H	34.478870000	8.738770000	22.546200000

H	40.329530000	21.962410000	12.650470000
H	40.179540000	18.265260000	14.943950000
H	37.709050000	18.526470000	15.162840000
H	36.934880000	22.253360000	11.949500000
H	38.424710000	23.240350000	12.215340000
H	37.119760000	23.173510000	13.466690000
H	42.166670000	19.182390000	12.831940000
H	42.417230000	19.578500000	14.555850000
H	42.431570000	20.890810000	13.318260000
H	32.853620000	7.516590000	12.916250000
H	34.324050000	9.146660000	16.677410000
H	33.923990000	11.451460000	15.818810000
H	31.493560000	10.547200000	11.597600000
H	32.076150000	8.887050000	11.181520000
H	33.145640000	10.328780000	10.976050000
H	32.885880000	6.320870000	15.796570000
H	34.590000000	6.728110000	16.181880000
H	34.160110000	6.060250000	14.563000000
H	39.528640000	15.746150000	8.898400000
H	38.840390000	19.023040000	11.678510000
H	36.721370000	17.935030000	12.414850000
H	36.991770000	13.557410000	10.145560000
H	38.066420000	13.924100000	8.734310000
H	36.345550000	14.473290000	8.766150000
H	41.443640000	17.351990000	9.637380000
H	40.989320000	18.850700000	10.533670000
H	40.517250000	18.648440000	8.813710000

H	32.914470000	24.994590000	20.988250000
H	30.798340000	21.261270000	21.728890000
H	31.476170000	20.448840000	19.465090000
H	34.671360000	23.951420000	18.050180000
H	34.112280000	25.373620000	19.019030000
H	33.169950000	24.784070000	17.589330000
H	32.038960000	24.515990000	23.252490000
H	31.268320000	22.931910000	23.618430000
H	30.334230000	24.220690000	22.774120000
H	35.746570000	19.207380000	24.778260000
H	34.276940000	21.735950000	21.556190000
H	34.532640000	19.835390000	19.958600000
H	35.362450000	16.131660000	23.212490000
H	36.425310000	16.978880000	24.406750000
H	37.021030000	16.587520000	22.741520000
H	34.838960000	21.452640000	25.297140000
H	34.073870000	22.451530000	23.999390000
H	35.855720000	22.411460000	24.169190000
H	35.159980000	8.281100000	19.700250000
H	31.229740000	9.986900000	18.965680000
H	32.276530000	12.216700000	18.569550000
H	37.079690000	10.926840000	18.433370000
H	37.114230000	9.576090000	19.638460000
H	36.905590000	11.297940000	20.165450000
H	32.339460000	7.101650000	18.556900000
H	31.495720000	7.673860000	20.029450000
H	33.134670000	6.931140000	20.158140000

H	38.159860000	23.007860000	21.956130000
H	39.346200000	18.836530000	22.293490000
H	38.619440000	18.452540000	19.932280000
H	37.837180000	23.157450000	18.467790000
H	37.236340000	23.886030000	20.014310000
H	36.216280000	22.725870000	19.076360000
H	39.349580000	22.264630000	23.956860000
H	40.090280000	20.622660000	24.030670000
H	38.357300000	20.843200000	24.434820000
H	28.330330000	23.071670000	10.290360000
H	28.756270000	18.762320000	9.898920000
H	30.476280000	18.776860000	11.710820000
H	29.913000000	23.483660000	13.338100000
H	29.615310000	24.321270000	11.765050000
H	31.253360000	23.672730000	12.169860000
H	26.564190000	21.634410000	9.051370000
H	26.969260000	19.914030000	8.683590000
H	27.854660000	21.248720000	7.868710000
H	42.472460000	15.527250000	15.645810000
H	39.480350000	15.636580000	12.483950000
H	37.674860000	15.638460000	14.207150000
H	40.419480000	16.366740000	18.341440000
H	41.894510000	15.420030000	17.903350000
H	40.334650000	14.587680000	18.273010000
H	42.427150000	16.652910000	12.560860000
H	41.904140000	15.034100000	11.988800000
H	43.153530000	15.173630000	13.281480000

H	27.767900000	15.930260000	7.779300000
H	26.518530000	16.971540000	11.816710000
H	28.815510000	16.476940000	12.643020000
H	31.229530000	15.941710000	8.281610000
H	29.919220000	15.183410000	7.297120000
H	30.739500000	14.263340000	8.622230000
H	25.343070000	17.883510000	9.332900000
H	24.810920000	16.243170000	9.806510000
H	25.463140000	16.531710000	8.151400000
H	23.744580000	17.860340000	13.215290000
H	27.055150000	20.632000000	12.611910000
H	28.378860000	19.379960000	14.314300000
H	25.475990000	15.358950000	14.787590000
H	23.838800000	16.120830000	14.745720000
H	24.908050000	16.325410000	16.186600000
H	24.080930000	19.432820000	10.981620000
H	25.036080000	20.924880000	11.316810000
H	23.544520000	20.564400000	12.259620000
H	27.926020000	8.811040000	18.437040000
H	31.053380000	9.516120000	15.492420000
H	30.900320000	11.967110000	15.935500000
H	27.877400000	12.046450000	19.881020000
H	26.904370000	10.546900000	19.607790000
H	26.652320000	12.015250000	18.583930000
H	29.537620000	6.880010000	17.550060000
H	30.454260000	7.245100000	16.039250000
H	28.658290000	7.179710000	16.016990000



H	41.685840000	11.530980000	15.265400000
H	40.487900000	12.321660000	11.160510000
H	38.106670000	12.455820000	11.904420000
H	38.743890000	12.466570000	16.874420000
H	40.176080000	11.374520000	17.002250000
H	38.555310000	10.714700000	16.556370000
H	43.402740000	12.256170000	13.470500000
H	42.884530000	12.276010000	11.745510000
H	43.020410000	10.719580000	12.631070000
H	26.938860000	8.498700000	14.031550000
H	24.906570000	11.441940000	16.505040000
H	26.311260000	13.243890000	15.489440000
H	28.450880000	10.688350000	11.760240000
H	28.628080000	9.067830000	12.547500000
H	29.653380000	10.462050000	13.063690000
H	25.005530000	7.809620000	15.350510000
H	23.956420000	9.041510000	16.147010000
H	25.431440000	8.444070000	16.975700000
H	28.441840000	24.507060000	20.381490000
H	30.744980000	25.407590000	16.802130000
H	30.249850000	23.132190000	15.924550000
H	26.767300000	21.641190000	19.174230000
H	27.339440000	22.472150000	20.677800000
H	28.240520000	21.059780000	19.995250000
H	29.283100000	27.266500000	18.884750000
H	31.014180000	26.792420000	18.931100000
H	29.954740000	26.471220000	20.351830000

H	30.930130000	21.418940000	7.302820000
H	33.215860000	23.914820000	10.038310000
H	34.322150000	21.868680000	10.953780000
H	32.811210000	18.484670000	7.598900000
H	31.154220000	19.118170000	7.233910000
H	31.514570000	18.337990000	8.821600000
H	30.847550000	23.853980000	7.056720000
H	31.918390000	24.921930000	8.038950000
H	30.386830000	24.293960000	8.734340000

#### B Isomer

Ag	14.331050000	14.747390000	19.909370000
Ag	11.571060000	14.779290000	20.488750000
Ag	13.153430000	12.383280000	20.887310000
Ag	12.663810000	16.381280000	18.314520000
Ag	12.592220000	13.360250000	18.178500000
Ag	15.509750000	17.056570000	18.877750000
Ag	17.076000000	14.517060000	19.264920000
Ag	15.997680000	13.221920000	21.585030000
Ag	15.262100000	12.341130000	18.718170000
Ag	13.378650000	17.193480000	20.970410000
Ag	16.003530000	16.145920000	21.693610000
Ag	15.058140000	14.789060000	17.152790000
Ag	13.702110000	14.624410000	22.678510000
Ag	13.735860000	11.959720000	15.880520000

Ag	10.182870000	17.382490000	20.274690000
Ag	18.058920000	11.601610000	20.208400000
Ag	15.793600000	19.163350000	21.227990000
Ag	11.142820000	13.183340000	23.180810000
Ag	10.087230000	15.066900000	17.591670000
Ag	18.857550000	14.592110000	21.674270000
Ag	14.215230000	17.473380000	23.777670000
Ag	17.521600000	16.621400000	16.773710000
Ag	14.329140000	17.446040000	15.997390000
Ag	14.219050000	11.649460000	23.616270000
Ag	13.532180000	9.948950000	18.716190000
S	16.510330000	18.254520000	15.262980000
S	9.635570000	14.757610000	22.101100000
S	16.203520000	19.497890000	18.851380000
S	16.550580000	10.173320000	18.924940000
S	13.081830000	9.888210000	21.106210000
S	11.508010000	18.578680000	21.943870000
S	11.899970000	17.191470000	16.046240000
S	14.470610000	14.072570000	14.830260000
S	8.483300000	16.451350000	18.790110000
S	12.959470000	15.677450000	24.847570000
S	10.966090000	13.218040000	16.241490000
S	16.545790000	11.210590000	22.979050000
S	18.329110000	16.876370000	22.354660000
S	19.146410000	15.409830000	18.153490000
S	13.739900000	9.554260000	16.321910000
S	19.942550000	12.421740000	21.530020000

S	15.507160000	19.539020000	23.614110000
S	11.995450000	11.408700000	24.599040000
C	16.699110000	17.577890000	13.608040000
C	17.985740000	17.544860000	12.995800000
C	18.099830000	17.016660000	11.693140000
C	16.993210000	16.532980000	10.964480000
C	15.721240000	16.615470000	11.573760000
C	15.576770000	17.126780000	12.873020000
C	19.217210000	18.013380000	13.729750000
C	17.173070000	15.884990000	9.610720000
C	8.352450000	13.686570000	21.443640000
C	7.222350000	13.382190000	22.258870000
C	6.172830000	12.631070000	21.685460000
C	6.195830000	12.170490000	20.350640000
C	7.335420000	12.466000000	19.570310000
C	8.396150000	13.204800000	20.115530000
C	7.141790000	13.832300000	23.697940000
C	5.049260000	11.363620000	19.783210000
C	17.326460000	9.777960000	17.358060000
C	18.125590000	8.600120000	17.265340000
C	18.659560000	8.258380000	16.002990000
C	18.421730000	9.018580000	14.836600000
C	17.619270000	10.175410000	14.952870000
C	17.089350000	10.550100000	16.197200000
C	18.379850000	7.715120000	18.463360000
C	19.029020000	8.620070000	13.509080000
C	11.372000000	9.352260000	21.222910000

C	11.081840000	7.954000000	21.209850000
C	9.740820000	7.549950000	21.380130000
C	8.680500000	8.465400000	21.573470000
C	8.991530000	9.841460000	21.576150000
C	10.316040000	10.273360000	21.393410000
C	12.172630000	6.926750000	21.024930000
C	7.259300000	7.981840000	21.764870000
C	11.560870000	20.237300000	21.265940000
C	10.556710000	21.174490000	21.658300000
C	10.644690000	22.494130000	21.164760000
C	11.681260000	22.926120000	20.307820000
C	12.657700000	21.978930000	19.928870000
C	12.595900000	20.658440000	20.401030000
C	9.427540000	20.774520000	22.578060000
C	11.753030000	24.360900000	19.832400000
C	11.354350000	18.897920000	16.166620000
C	11.214910000	19.673880000	14.978770000
C	10.668110000	20.971380000	15.091710000
C	10.254920000	21.525790000	16.321680000
C	10.426320000	20.745120000	17.486570000
C	10.970150000	19.455240000	17.406650000
C	11.642010000	19.141800000	13.631570000
C	9.624420000	22.898640000	16.396500000
C	15.950900000	13.619880000	13.929270000
C	15.821330000	12.944640000	12.676790000
C	16.992480000	12.644910000	11.949230000
C	18.284630000	13.000510000	12.398010000

C	18.388480000	13.679280000	13.630570000
C	17.240950000	13.974250000	14.384570000
C	14.470910000	12.549740000	12.134150000
C	19.517270000	12.635460000	11.600030000
C	7.949410000	17.705070000	17.630300000
C	7.276760000	18.870290000	18.100640000
C	6.781060000	19.787750000	17.149530000
C	6.926850000	19.604460000	15.759340000
C	7.588580000	18.437070000	15.315790000
C	8.084760000	17.501700000	16.235450000
C	7.115290000	19.149840000	19.573250000
C	6.424210000	20.637830000	14.776920000
C	14.091100000	15.239980000	26.171870000
C	14.015670000	15.940040000	27.414790000
C	14.875190000	15.540330000	28.461600000
C	15.791470000	14.471660000	28.336090000
C	15.840350000	13.789270000	27.102470000
C	15.009200000	14.174860000	26.038740000
C	13.055150000	17.086910000	27.614150000
C	16.674790000	14.048420000	29.488500000
C	9.854540000	11.859080000	16.621190000
C	8.709180000	11.646120000	15.797980000
C	7.889140000	10.528990000	16.074410000
C	8.162880000	9.615790000	17.116190000
C	9.304420000	9.847240000	17.914580000
C	10.132360000	10.952650000	17.670330000
C	8.367940000	12.583590000	14.663000000

C	7.254730000	8.439500000	17.398570000
C	17.610610000	11.710150000	24.329130000
C	18.101440000	10.699070000	25.207130000
C	19.023730000	11.075520000	26.207970000
C	19.481110000	12.400620000	26.370450000
C	18.963630000	13.388950000	25.504300000
C	18.039230000	13.046410000	24.505760000
C	17.660540000	9.260350000	25.074910000
C	20.503060000	12.757660000	27.426850000
C	18.660450000	16.878300000	24.115330000
C	20.005930000	17.010770000	24.576880000
C	20.230090000	17.107110000	25.965210000
C	19.180980000	17.084150000	26.913330000
C	17.862540000	16.934610000	26.433390000
C	17.608890000	16.825500000	25.055730000
C	21.168990000	17.023440000	23.613500000
C	19.467720000	17.219370000	28.392690000
C	19.929100000	14.220600000	17.071490000
C	20.981230000	14.654000000	16.211260000
C	21.638930000	13.686920000	15.423620000
C	21.337210000	12.307880000	15.493050000
C	20.300430000	11.903930000	16.360060000
C	19.594800000	12.850170000	17.122980000
C	21.429830000	16.096100000	16.174350000
C	22.123090000	11.296190000	14.688770000
C	12.238190000	8.661660000	15.923030000
C	11.496160000	8.883100000	14.726390000



C	10.410880000	8.024750000	14.447280000
C	10.038500000	6.951870000	15.284130000
C	10.790100000	6.750080000	16.462030000
C	11.865590000	7.593490000	16.774960000
C	11.840470000	9.986380000	13.756040000
C	8.898770000	6.031310000	14.910160000
C	21.290210000	12.563700000	20.363870000
C	21.889990000	11.386010000	19.828370000
C	22.975900000	11.533850000	18.937030000
C	23.486130000	12.790750000	18.549840000
C	22.889120000	13.939540000	19.115470000
C	21.817910000	13.827110000	20.011070000
C	21.350640000	10.015240000	20.157150000
C	24.605400000	12.934880000	17.547870000
C	14.247750000	20.794610000	23.850530000
C	14.400990000	22.101600000	23.302850000
C	13.430430000	23.077030000	23.618330000
C	12.324330000	22.820550000	24.454200000
C	12.194560000	21.519070000	24.988680000
C	13.135390000	20.524170000	24.685290000
C	15.549350000	22.455900000	22.390100000
C	11.316520000	23.900490000	24.777480000
C	12.005100000	12.145220000	26.231720000
C	12.877310000	11.636710000	27.239470000
C	12.789270000	12.183170000	28.536830000
C	11.875430000	13.201000000	28.883490000
C	11.005340000	13.672570000	27.875610000

C	11.072510000	13.155570000	26.571800000
C	13.887170000	10.555740000	26.944700000
C	11.870140000	13.799460000	30.272130000
H	19.108030000	16.972130000	11.230940000
H	14.824560000	16.261120000	11.027110000
H	14.573430000	17.149920000	13.346040000
H	19.128060000	19.076990000	14.053850000
H	20.125190000	17.902810000	13.094640000
H	19.361490000	17.413800000	14.660270000
H	18.101920000	16.232190000	9.104890000
H	16.312530000	16.090170000	8.935200000
H	17.245330000	14.775940000	9.724420000
H	5.288280000	12.403610000	22.316340000
H	7.405100000	12.110150000	18.523480000
H	9.287500000	13.425800000	19.491320000
H	7.957220000	13.368460000	24.303440000
H	6.167060000	13.546590000	24.152070000
H	7.272270000	14.935020000	23.792060000
H	5.263500000	10.268220000	19.824320000
H	4.861170000	11.619340000	18.716180000
H	4.108840000	11.537640000	20.352300000
H	19.281400000	7.341960000	15.929900000
H	17.410770000	10.805410000	14.065750000
H	16.467550000	11.466040000	16.274910000
H	18.784350000	8.293760000	19.326480000
H	19.100420000	6.906060000	18.211290000
H	17.435520000	7.246040000	18.827530000

H	19.929820000	9.237610000	13.273450000
H	18.310360000	8.765560000	12.670970000
H	19.348160000	7.554080000	13.512100000
H	9.519200000	6.462300000	21.368390000
H	8.188870000	10.593800000	21.705670000
H	10.540880000	11.359850000	21.369710000
H	12.769060000	7.130630000	20.103680000
H	11.747660000	5.901100000	20.955890000
H	12.901000000	6.953710000	21.868890000
H	6.917810000	7.361380000	20.902860000
H	6.556400000	8.837970000	21.870960000
H	7.161110000	7.347410000	22.677000000
H	9.863870000	23.221430000	21.471250000
H	13.478450000	22.266630000	19.241830000
H	13.361850000	19.923620000	20.079870000
H	8.802850000	19.964520000	22.131170000
H	8.765960000	21.641350000	22.801020000
H	9.822180000	20.363890000	23.536400000
H	10.740280000	24.811480000	19.726600000
H	12.270880000	24.437490000	18.850630000
H	12.319860000	24.999870000	20.552320000
H	10.559480000	21.574620000	14.166140000
H	10.132400000	21.149490000	18.474920000
H	11.087380000	18.844610000	18.327650000
H	12.733930000	18.908150000	13.624020000
H	11.439950000	19.884790000	12.828260000
H	11.118330000	18.190420000	13.378600000

H	9.737030000	23.454840000	15.439630000
H	10.078250000	23.513630000	17.207800000
H	8.532630000	22.827030000	16.620170000
H	16.883030000	12.107860000	10.983460000
H	19.382950000	13.970370000	14.020930000
H	17.342240000	14.493630000	15.361540000
H	13.920050000	11.911120000	12.864610000
H	14.571730000	11.990210000	11.178150000
H	13.826740000	13.443410000	11.959280000
H	19.806890000	11.569300000	11.764570000
H	20.386850000	13.264700000	11.894540000
H	19.351540000	12.761370000	10.505430000
H	6.255530000	20.692170000	17.521790000
H	7.724100000	18.256630000	14.230920000
H	8.604740000	16.591810000	15.871720000
H	6.587410000	18.321070000	20.100630000
H	6.554350000	20.094910000	19.743470000
H	8.116080000	19.243330000	20.065050000
H	5.742860000	21.367870000	15.267020000
H	5.872820000	20.165220000	13.931920000
H	7.272000000	21.213690000	14.334610000
H	14.820320000	16.094630000	29.422480000
H	16.546700000	12.947950000	26.961830000
H	15.068280000	13.634580000	25.069640000
H	13.313730000	17.945410000	26.948340000
H	13.074800000	17.447190000	28.666680000
H	12.013510000	16.787740000	27.354130000

H	16.990460000	14.916140000	30.111420000
H	17.589470000	13.530830000	29.121980000
H	16.142840000	13.337620000	30.165170000
H	6.998440000	10.362080000	15.432790000
H	9.555210000	9.153600000	18.740320000
H	11.030050000	11.116040000	18.303950000
H	8.113260000	13.601320000	15.045500000
H	7.499910000	12.203160000	14.080270000
H	9.231030000	12.720040000	13.970040000
H	6.544970000	8.670480000	18.229780000
H	7.842940000	7.546700000	17.710310000
H	6.646530000	8.163230000	16.508500000
H	19.409830000	10.287270000	26.886880000
H	19.270580000	14.446070000	25.622020000
H	17.622230000	13.840130000	23.850660000
H	16.551350000	9.163180000	25.152890000
H	18.126780000	8.629630000	25.863790000
H	17.937230000	8.842880000	24.078650000
H	20.206940000	13.674570000	27.987280000
H	21.498100000	12.967390000	26.967540000
H	20.640930000	11.932400000	28.159770000
H	21.276780000	17.204110000	26.322820000
H	17.012870000	16.887410000	27.142410000
H	16.567950000	16.693880000	24.694570000
H	21.194020000	16.077830000	23.017420000
H	22.137060000	17.124320000	24.153530000
H	21.075700000	17.856480000	22.877130000

H	20.239580000	16.489620000	28.731060000
H	18.548420000	17.048840000	28.994600000
H	19.854760000	18.235130000	28.647530000
H	22.439790000	14.032370000	14.737820000
H	20.027090000	10.833520000	16.435440000
H	18.767060000	12.522020000	17.786480000
H	20.564860000	16.795850000	16.242340000
H	22.002490000	16.313070000	15.244280000
H	22.086890000	16.327900000	17.048060000
H	22.147380000	11.557380000	13.605360000
H	21.683280000	10.279670000	14.791490000
H	23.182850000	11.247770000	15.038660000
H	9.829570000	8.208110000	13.520230000
H	10.529180000	5.922820000	17.152040000
H	12.451280000	7.421140000	17.699500000
H	11.806510000	10.989090000	14.249180000
H	11.127330000	9.997980000	12.901900000
H	12.871170000	9.861880000	13.348110000
H	8.100740000	6.574250000	14.355740000
H	8.437870000	5.561660000	15.807860000
H	9.251050000	5.203190000	14.249540000
H	23.433190000	10.616840000	18.510390000
H	23.264890000	14.939690000	18.822040000
H	21.333820000	14.729600000	20.437290000
H	21.271030000	9.853060000	21.257480000
H	21.986820000	9.214380000	19.719180000
H	20.313510000	9.897930000	19.752170000

H	24.952680000	11.954370000	17.159660000
H	25.491510000	13.444750000	17.994670000
H	24.279110000	13.550490000	16.677800000
H	13.549640000	24.089950000	23.181690000
H	11.339990000	21.274160000	25.651280000
H	13.005150000	19.503470000	25.098290000
H	16.534640000	22.290040000	22.885340000
H	15.483110000	23.517990000	22.065650000
H	15.544070000	21.810910000	21.475500000
H	11.475320000	24.315310000	25.801940000
H	10.275760000	23.504500000	24.745620000
H	11.383350000	24.747730000	24.059610000
H	13.471190000	11.787170000	29.317700000
H	10.260440000	14.458360000	28.113630000
H	10.390860000	13.547180000	25.789660000
H	13.397880000	9.636510000	26.546230000
H	14.465920000	10.291760000	27.856960000
H	14.613020000	10.886090000	26.158170000
H	12.215370000	13.067730000	31.036970000
H	10.858010000	14.158110000	30.564890000
H	12.559530000	14.676870000	30.324730000
C	17.851440000	20.246720000	18.518300000
H	17.774000000	21.308370000	18.854060000
H	17.921740000	20.271720000	17.401590000
C	19.156000000	19.675600000	19.044240000
C	19.350420000	18.382570000	19.563670000
C	20.303670000	20.493510000	18.952900000



C	20.646920000	17.944430000	19.904150000
N	21.552780000	20.090360000	19.282430000
C	21.756070000	18.798660000	19.744600000
H	20.225200000	21.533110000	18.578800000
H	20.774000000	16.913460000	20.281320000
C	23.177120000	18.435390000	19.989280000
N	24.086940000	19.435760000	19.708820000
C	25.416720000	19.199210000	19.868130000
H	26.084590000	20.046350000	19.628070000
C	25.968610000	17.987670000	20.321570000
C	25.038290000	16.956350000	20.612350000
H	25.402750000	15.966720000	20.953530000
C	23.656610000	17.188870000	20.458930000
H	22.939930000	16.384920000	20.711900000
H	22.574750000	20.951220000	24.333330000
C	22.501550000	21.613850000	23.451320000
C	21.969910000	22.919270000	23.544890000
C	22.949200000	21.156040000	22.206310000
C	21.893260000	23.697640000	22.384500000
N	22.884800000	21.904320000	21.068130000
C	22.336070000	23.177080000	21.144180000
H	21.605480000	23.314990000	24.511410000
H	23.385530000	20.144890000	22.096670000
H	21.449200000	24.708470000	22.427090000
C	22.187260000	23.875760000	19.862890000
N	22.454220000	23.111680000	18.731380000
C	22.268980000	23.682600000	17.508540000

H	22.487680000	23.031860000	16.640890000
C	21.838560000	25.002910000	17.333350000
C	21.595090000	25.796200000	18.478200000
H	21.272880000	26.850270000	18.379590000
C	21.774270000	25.224900000	19.742180000
H	21.611250000	25.830430000	20.653320000
C	27.110420000	23.361440000	19.605770000
C	27.656590000	23.295610000	18.304510000
C	25.853360000	22.790820000	19.837710000
C	26.919660000	22.654600000	17.301470000
N	25.137620000	22.140730000	18.874770000
C	25.674340000	22.054220000	17.598250000
H	28.649780000	23.727410000	18.075950000
H	25.383460000	22.831310000	20.838430000
H	27.317700000	22.606700000	16.272360000
C	24.905540000	21.239980000	16.644390000
N	23.719890000	20.713900000	17.133130000
C	23.019450000	19.843450000	16.352640000
H	22.096160000	19.430320000	16.801310000
C	23.432520000	19.467630000	15.068190000
C	24.622940000	20.023580000	14.548240000
H	24.988300000	19.745880000	13.540870000
C	25.353680000	20.916210000	15.342270000
H	26.297990000	21.344830000	14.960480000
H	21.708500000	25.405730000	16.311900000
H	27.649920000	23.852940000	20.437160000
H	22.824700000	18.743900000	14.493530000

Ru	23.291800000	21.243240000	19.121240000
C	27.470060000	17.936560000	20.551850000
H	27.940190000	18.816810000	20.059550000
H	27.655060000	18.054910000	21.648090000
H	18.476820000	17.713620000	19.690740000
Ag	33.276640000	15.227890000	19.122800000
Ag	32.970330000	12.442850000	19.123070000
Ag	33.103120000	13.938180000	16.612550000
Ag	31.810240000	14.033150000	21.250590000
Ag	30.780060000	14.163800000	18.336560000
Ag	33.387280000	16.422920000	21.654040000
Ag	33.516190000	18.024420000	19.093780000
Ag	34.889720000	16.385220000	17.108670000
Ag	31.781500000	16.693790000	17.247800000
Ag	34.725950000	13.900520000	21.144630000
Ag	35.857750000	16.214690000	19.804720000
Ag	30.954500000	16.672970000	19.998730000
Ag	35.555780000	13.790270000	18.183810000
Ag	28.702230000	16.226650000	17.657670000
Ag	33.166990000	11.159180000	21.794270000
Ag	34.268450000	19.039560000	15.980000000
Ag	36.503780000	16.055490000	22.692830000
Ag	34.772380000	11.240360000	16.867530000
Ag	30.054670000	11.805760000	20.458030000
Ag	36.193990000	19.134410000	18.379870000
Ag	37.595680000	13.693520000	20.494940000
Ag	32.469960000	19.235340000	21.606730000

Ag	30.570720000	16.522330000	22.923150000
Ag	35.671550000	13.991910000	15.042140000
Ag	30.873200000	15.162260000	14.947250000
S	31.133160000	18.786290000	23.594640000
S	33.889190000	10.118690000	18.845820000
S	34.767510000	17.637190000	23.368130000
S	32.310290000	17.880920000	15.068340000
S	32.646830000	13.722380000	14.116370000
S	35.490060000	11.794480000	22.262550000
S	29.896380000	14.191850000	22.905770000
S	28.333340000	16.376790000	20.067530000
S	31.037600000	9.957220000	21.675280000
S	37.525500000	12.253560000	18.529070000
S	28.592820000	13.084390000	18.991250000
S	35.655120000	16.417830000	14.714590000
S	37.394680000	18.146580000	20.288140000
S	33.993010000	20.343200000	20.038310000
S	28.762130000	16.368470000	15.227920000
S	36.252730000	20.418590000	16.278950000
S	38.616920000	14.888120000	22.350720000
S	35.750130000	11.577820000	14.670740000
C	29.645640000	19.774650000	23.597530000
C	29.714350000	21.192530000	23.446770000
C	28.522010000	21.938410000	23.576250000
C	27.273810000	21.350810000	23.864320000
C	27.227720000	19.945810000	24.021610000
C	28.393120000	19.175880000	23.890370000

C	31.012050000	21.906130000	23.163320000
C	26.032790000	22.199890000	24.013460000
C	32.579180000	9.082160000	18.194670000
C	32.881490000	7.742120000	17.811090000
C	31.813430000	6.902310000	17.421720000
C	30.469760000	7.334220000	17.396960000
C	30.201390000	8.677490000	17.743120000
C	31.242270000	9.535550000	18.126030000
C	34.300600000	7.226220000	17.808380000
C	29.342170000	6.406990000	16.998940000
C	34.313190000	17.100600000	25.016010000
C	35.059540000	17.594720000	26.128030000
C	34.655550000	17.208890000	27.425090000
C	33.536520000	16.381260000	27.666370000
C	32.812840000	15.908290000	26.549080000
C	33.205580000	16.254510000	25.247270000
C	36.241130000	18.516370000	25.936130000
C	33.103260000	16.034120000	29.074410000
C	31.231210000	19.235720000	14.641350000
C	31.499510000	19.974460000	13.448710000
C	30.642040000	21.046070000	13.118740000
C	29.528940000	21.406080000	13.907990000
C	29.278810000	20.647860000	15.075450000
C	30.118440000	19.583920000	15.440350000
C	32.667480000	19.624740000	12.558870000
C	28.632350000	22.559890000	13.508950000
C	31.860050000	12.136050000	13.825750000

C	31.324280000	11.851040000	12.531660000
C	30.803690000	10.559620000	12.295950000
C	30.809740000	9.540340000	13.275560000
C	31.338850000	9.849090000	14.545730000
C	31.845320000	11.129340000	14.817370000
C	31.333070000	12.880550000	11.423730000
C	30.287000000	8.153550000	12.971230000
C	35.525920000	12.038380000	24.038050000
C	35.857910000	10.927450000	24.872100000
C	35.956820000	11.142480000	26.263500000
C	35.757530000	12.407530000	26.860290000
C	35.428080000	13.489580000	26.015770000
C	35.308150000	13.303770000	24.628510000
C	36.131730000	9.562620000	24.287210000
C	35.929250000	12.607500000	28.350540000
C	30.472260000	13.615950000	24.505620000
C	29.677880000	13.859370000	25.665130000
C	30.097210000	13.301510000	26.893370000
C	31.263470000	12.514910000	27.018280000
C	32.047140000	12.309250000	25.861400000
C	31.655930000	12.852700000	24.629040000
C	28.430330000	14.705620000	25.598550000
C	31.652930000	11.879470000	28.334380000
C	30.284650000	9.941190000	23.298560000
C	30.889940000	9.186690000	24.345830000
C	30.227870000	9.118210000	25.590870000
C	29.000990000	9.767500000	25.844150000

C	28.415410000	10.499200000	24.786080000
C	29.044480000	10.580540000	23.534750000
C	32.215550000	8.494340000	24.149680000
C	28.351170000	9.719150000	27.208570000
C	38.957800000	12.863930000	17.631730000
C	40.231470000	12.261280000	17.870710000
C	41.330440000	12.693200000	17.098520000
C	41.221600000	13.679380000	16.092420000
C	39.957300000	14.271230000	15.885840000
C	38.847430000	13.873440000	16.650030000
C	40.421660000	11.202270000	18.929500000
C	42.415350000	14.074150000	15.250100000
C	28.143620000	11.879300000	17.739000000
C	27.264540000	10.797440000	18.060860000
C	26.824380000	9.962250000	17.009630000
C	27.222260000	10.144330000	15.665100000
C	28.112650000	11.200780000	15.381480000
C	28.564910000	12.054230000	16.401080000
C	26.815000000	10.530160000	19.478240000
C	26.737370000	9.216840000	14.572030000
C	37.373790000	16.912350000	14.619710000
C	38.029120000	16.891570000	13.353000000
C	39.353090000	17.380380000	13.280490000
C	40.042270000	17.895710000	14.399470000
C	39.370620000	17.905180000	15.643850000
C	38.061810000	17.413450000	15.749290000
C	37.329150000	16.394170000	12.110560000



C	41.454580000	18.425920000	14.280810000
C	39.020760000	17.872160000	19.580830000
C	39.908380000	18.981620000	19.417080000
C	41.215440000	18.727400000	18.952930000
C	41.683000000	17.428700000	18.645810000
C	40.785460000	16.351440000	18.801260000
C	39.473820000	16.575080000	19.252430000
C	39.461310000	20.398280000	19.686350000
C	43.096390000	17.212030000	18.152720000
C	32.983930000	21.564790000	19.205370000
C	32.992900000	22.904960000	19.702190000
C	32.285730000	23.890460000	18.982450000
C	31.600010000	23.614030000	17.778380000
C	31.591660000	22.279930000	17.317590000
C	32.263810000	21.268700000	18.026190000
C	33.779740000	23.284770000	20.933790000
C	30.957790000	24.724240000	16.972700000
C	27.609070000	15.237350000	14.449270000
C	26.209870000	15.307240000	14.708090000
C	25.351980000	14.480620000	13.951990000
C	25.812010000	13.577190000	12.967920000
C	27.201180000	13.536280000	12.720210000
C	28.078340000	14.355890000	13.446660000
C	25.653810000	16.232100000	15.763370000
C	24.853050000	12.658150000	12.245070000
C	35.779530000	22.100540000	16.671200000
C	35.016500000	22.878500000	15.750580000

C	34.824150000	24.249360000	16.028340000
C	35.356460000	24.884420000	17.168920000
C	36.113570000	24.095490000	18.064650000
C	36.316680000	22.728520000	17.821760000
C	34.412430000	22.270070000	14.510600000
C	35.096770000	26.349380000	17.441190000
C	38.881360000	13.609030000	23.574180000
C	38.945230000	13.932200000	24.961160000
C	39.254970000	12.901690000	25.874160000
C	39.513860000	11.573990000	25.476400000
C	39.466970000	11.281960000	24.094260000
C	39.151890000	12.281250000	23.161520000
C	38.668670000	15.328090000	25.459080000
C	39.826360000	10.500220000	26.495080000
C	37.426250000	10.974460000	14.853960000
C	38.459230000	11.442570000	13.987980000
C	39.739900000	10.861750000	14.098770000
C	40.043820000	9.837800000	15.021600000
C	39.004430000	9.386640000	15.864800000
C	37.719870000	9.947680000	15.782950000
C	38.209880000	12.535260000	12.979150000
C	41.443890000	9.275710000	15.126040000
H	28.578490000	23.041650000	23.463380000
H	26.268020000	19.445170000	24.264780000
H	28.349790000	18.077200000	24.040430000
H	31.796590000	21.641710000	23.909490000
H	30.870960000	23.009520000	23.169450000

H	31.421370000	21.615250000	22.162450000
H	26.259540000	23.279160000	23.866090000
H	25.571550000	22.087230000	25.023290000
H	25.247510000	21.908490000	23.278550000
H	32.050700000	5.858210000	17.130940000
H	29.166360000	9.068820000	17.703270000
H	31.015220000	10.593610000	18.377850000
H	34.931120000	7.799730000	17.086760000
H	34.338820000	6.151740000	17.522900000
H	34.780790000	7.349380000	18.806410000
H	28.839860000	6.759270000	16.066920000
H	28.554110000	6.365230000	17.786720000
H	29.703300000	5.370470000	16.821230000
H	35.244130000	17.584740000	28.287500000
H	31.940220000	15.242160000	26.691430000
H	32.645020000	15.848780000	24.378490000
H	37.012850000	18.059600000	25.272260000
H	36.716500000	18.764660000	26.910190000
H	35.933520000	19.465790000	25.438620000
H	33.960510000	16.038720000	29.784600000
H	32.620920000	15.031570000	29.112940000
H	32.356920000	16.769700000	29.459580000
H	30.858770000	21.627250000	12.198840000
H	28.433440000	20.904440000	15.742520000
H	29.926740000	19.010620000	16.369780000
H	33.611900000	19.548030000	13.148280000
H	32.802810000	20.381560000	11.756700000

H	32.523680000	18.623210000	12.089010000
H	28.493850000	23.291290000	14.341130000
H	27.615820000	22.212380000	13.204200000
H	29.053390000	23.122290000	12.646870000
H	30.387750000	10.341140000	11.289660000
H	31.340800000	9.083670000	15.345340000
H	32.237940000	11.361500000	15.830230000
H	30.928090000	13.862890000	11.762680000
H	30.735560000	12.532830000	10.551760000
H	32.371030000	13.086460000	11.072810000
H	29.294400000	8.183570000	12.466450000
H	30.185630000	7.553920000	13.902540000
H	30.980790000	7.600980000	12.294460000
H	36.220540000	10.278020000	26.907590000
H	35.244730000	14.493180000	26.445830000
H	35.033250000	14.162470000	23.979870000
H	35.289690000	9.212790000	23.644990000
H	36.302920000	8.810720000	25.089230000
H	37.030570000	9.589770000	23.627510000
H	35.552710000	11.735820000	28.933520000
H	35.390870000	13.517560000	28.698730000
H	37.005450000	12.736860000	28.620860000
H	29.478540000	13.492940000	27.795130000
H	32.980760000	11.715890000	25.924100000
H	32.276280000	12.669740000	23.725780000
H	28.677860000	15.743860000	25.267720000
H	27.931300000	14.762330000	26.590710000

H	27.705540000	14.305230000	24.852070000
H	31.178110000	12.393550000	29.200280000
H	32.756730000	11.896230000	28.480150000
H	31.337000000	10.808600000	28.367720000
H	30.703130000	8.528670000	26.402400000
H	27.452440000	11.024850000	24.943960000
H	28.574950000	11.165660000	22.718360000
H	32.177530000	7.766070000	23.306500000
H	32.531960000	7.958270000	25.071210000
H	33.010580000	9.235180000	23.883580000
H	28.785560000	8.914210000	27.841720000
H	27.253240000	9.545290000	27.138090000
H	28.492180000	10.685500000	27.750600000
H	42.320090000	12.230540000	17.298050000
H	39.834910000	15.064480000	15.123290000
H	37.863270000	14.360680000	16.484580000
H	40.226950000	11.618230000	19.947110000
H	41.460340000	10.803830000	18.910640000
H	39.711260000	10.355780000	18.789020000
H	43.330850000	14.223040000	15.868590000
H	42.217510000	15.015320000	14.690310000
H	42.658230000	13.283200000	14.500290000
H	26.133320000	9.129530000	17.258720000
H	28.464600000	11.359730000	14.344700000
H	29.258430000	12.885280000	16.156380000
H	27.694060000	10.322490000	20.138640000
H	26.136290000	9.649980000	19.522380000

H	26.285750000	11.406330000	19.920050000
H	27.282860000	8.242590000	14.588500000
H	26.896260000	9.663710000	13.565400000
H	25.654400000	8.979990000	14.678930000
H	39.863390000	17.368620000	12.294670000
H	39.876770000	18.295380000	16.548680000
H	37.548620000	17.421090000	16.733530000
H	36.896840000	15.376670000	12.259740000
H	38.028930000	16.358400000	11.246830000
H	36.470680000	17.054290000	11.841680000
H	42.157700000	17.848390000	14.926780000
H	41.517920000	19.488500000	14.612810000
H	41.830410000	18.369660000	13.235440000
H	41.900490000	19.590980000	18.821620000
H	41.107810000	15.320220000	18.556540000
H	38.773100000	15.720560000	19.354800000
H	38.672220000	20.697520000	18.953440000
H	40.309750000	21.110790000	19.589320000
H	39.008340000	20.506680000	20.698430000
H	43.310740000	17.829820000	17.249040000
H	43.272690000	16.146250000	17.888160000
H	43.848530000	17.504080000	18.922560000
H	32.299720000	24.929590000	19.372900000
H	31.065040000	22.020500000	16.378530000
H	32.257450000	20.226630000	17.642880000
H	33.579520000	22.591450000	21.782570000
H	33.544710000	24.325300000	21.249690000

H	34.874640000	23.219680000	20.733230000
H	30.337840000	25.404620000	17.603310000
H	30.316870000	24.317070000	16.157910000
H	31.731960000	25.364600000	16.486330000
H	24.262560000	14.552650000	14.143060000
H	27.614150000	12.846490000	11.955590000
H	29.167440000	14.310330000	13.241600000
H	26.095560000	16.002630000	16.765870000
H	24.548220000	16.136100000	15.840740000
H	25.910500000	17.296960000	15.549190000
H	24.615390000	11.765390000	12.869580000
H	25.280130000	12.287790000	11.286560000
H	23.886780000	13.167320000	12.019470000
H	34.236180000	24.851010000	15.304360000
H	36.562890000	24.561360000	18.964150000
H	36.915060000	22.123940000	18.531970000
H	35.184750000	21.774970000	13.877320000
H	33.886000000	23.038990000	13.902300000
H	33.672880000	21.476720000	14.781780000
H	34.748490000	26.879530000	16.527340000
H	36.008040000	26.870550000	17.813920000
H	34.308520000	26.478810000	18.222320000
H	39.287020000	13.153850000	26.954100000
H	39.669790000	10.252400000	23.737800000
H	39.098330000	12.031200000	22.082380000
H	39.362390000	16.071560000	25.001620000
H	38.761070000	15.384450000	26.565700000



H	37.635280000	15.649680000	25.178450000
H	40.917910000	10.268840000	26.531930000
H	39.299960000	9.548640000	26.252540000
H	39.516850000	10.812960000	27.517210000
H	40.540140000	11.233680000	13.425670000
H	39.200350000	8.580380000	16.600050000
H	36.916970000	9.584820000	16.455900000
H	37.426630000	12.243610000	12.241310000
H	39.140950000	12.792300000	12.428430000
H	37.836160000	13.461080000	13.482470000
H	41.966730000	9.294290000	14.143150000
H	41.440510000	8.226690000	15.497500000
H	42.061000000	9.875890000	15.837670000

#### C Isomer

Ag	14.642820000	16.559010000	20.590430000
Ag	12.058570000	16.707390000	21.743390000
Ag	12.991500000	14.278890000	20.468650000
Ag	13.293400000	19.045360000	20.537060000
Ag	12.416380000	16.670260000	18.869270000
Ag	16.270650000	18.829340000	20.660790000
Ag	17.137330000	16.294790000	19.267280000
Ag	16.023770000	14.118510000	20.792720000
Ag	14.757260000	15.109270000	18.150040000
Ag	14.499860000	18.105230000	22.954250000
Ag	16.800470000	16.439210000	22.381250000
Ag	15.030200000	18.001810000	18.171070000
Ag	14.303600000	15.017460000	22.956820000

Ag	12.887820000	16.637370000	15.970280000
Ag	11.382020000	19.191960000	23.196600000
Ag	17.417900000	13.250740000	18.315110000
Ag	17.339560000	19.227340000	23.608550000
Ag	11.516180000	13.989720000	23.252120000
Ag	10.397960000	18.805890000	19.873980000
Ag	19.142930000	14.714740000	20.840030000
Ag	15.645140000	16.616000000	25.215360000
Ag	17.885170000	19.236500000	18.238200000
Ag	14.892160000	20.915040000	18.773660000
Ag	14.134840000	11.971420000	22.064640000
Ag	12.432680000	13.463280000	17.377900000
S	17.132620000	21.550650000	18.060060000
S	10.352070000	16.114260000	23.502820000
S	17.579630000	20.749860000	21.727760000
S	15.443460000	13.015650000	16.913060000
S	12.221930000	12.144210000	19.416130000
S	13.149460000	19.005100000	24.876760000
S	12.510560000	21.099060000	19.288550000
S	14.055690000	18.811130000	16.007520000
S	9.324420000	19.553730000	21.928970000
S	14.071910000	14.771830000	25.459290000
S	10.603540000	17.901010000	17.601000000
S	16.175780000	11.614210000	20.751400000
S	19.281410000	16.250070000	22.734010000
S	19.307580000	17.246020000	18.376070000
S	12.279190000	14.421810000	15.143410000

S	19.571710000	12.827450000	19.373390000
S	17.409750000	18.190950000	25.801720000
S	12.051670000	11.619140000	23.285280000
C	16.964820000	21.874760000	16.300530000
C	18.119720000	21.909930000	15.465510000
C	17.953670000	22.206020000	14.096780000
C	16.695310000	22.475090000	13.519560000
C	15.568090000	22.459140000	14.369740000
C	15.699530000	22.163340000	15.735540000
C	19.493120000	21.595170000	16.004070000
C	16.550480000	22.715080000	12.034410000
C	8.755280000	15.828710000	22.729800000
C	7.686050000	15.319420000	23.526100000
C	6.408330000	15.209720000	22.933880000
C	6.145450000	15.581230000	21.596530000
C	7.223730000	16.066150000	20.824090000
C	8.505740000	16.179000000	21.383780000
C	7.903100000	14.896830000	24.959520000
C	4.764110000	15.429410000	20.997390000
C	15.941160000	13.404770000	15.236860000
C	16.433020000	12.353610000	14.406970000
C	16.760510000	12.661900000	13.068720000
C	16.589540000	13.948810000	12.512900000
C	16.081190000	14.967460000	13.349980000
C	15.773410000	14.698440000	14.692810000
C	16.566770000	10.939630000	14.918920000
C	16.955770000	14.231160000	11.072130000

C	10.453530000	11.953570000	19.648160000
C	9.784800000	10.884280000	18.978270000
C	8.409900000	10.697850000	19.230230000
C	7.676320000	11.514010000	20.122640000
C	8.357540000	12.567280000	20.767750000
C	9.722980000	12.787430000	20.522070000
C	10.522440000	9.964090000	18.035300000
C	6.207640000	11.262220000	20.384900000
C	13.589710000	20.712960000	25.191370000
C	12.914730000	21.416310000	26.234570000
C	13.313670000	22.740970000	26.513140000
C	14.351590000	23.395150000	25.813000000
C	14.996960000	22.682050000	24.778850000
C	14.618330000	21.364920000	24.474490000
C	11.818110000	20.768160000	27.044590000
C	14.785010000	24.793710000	26.193110000
C	12.485880000	22.514640000	20.390950000
C	12.428070000	23.826300000	19.834540000
C	12.294110000	24.919530000	20.717500000
C	12.211170000	24.764500000	22.117610000
C	12.291480000	23.456440000	22.644390000
C	12.430630000	22.351310000	21.792670000
C	12.513080000	24.057580000	18.345130000
C	12.009730000	25.951730000	23.032030000
C	15.281670000	18.656460000	14.708640000
C	14.880160000	18.841540000	13.349870000
C	15.866660000	18.773110000	12.342240000

C	17.233680000	18.549260000	12.621610000
C	17.610240000	18.383600000	13.971380000
C	16.647060000	18.426770000	14.992970000
C	13.437460000	19.099000000	12.990560000
C	18.251240000	18.441450000	11.506740000
C	9.057250000	21.314140000	21.743960000
C	8.824010000	22.124500000	22.893550000
C	8.520830000	23.489020000	22.700500000
C	8.441980000	24.083810000	21.424820000
C	8.669260000	23.259550000	20.298880000
C	8.968500000	21.898570000	20.457000000
C	8.924480000	21.563820000	24.289300000
C	8.155440000	25.559700000	21.265670000
C	15.187360000	13.494660000	26.053690000
C	15.399790000	13.358830000	27.459940000
C	16.242120000	12.320260000	27.912420000
C	16.872050000	11.406820000	27.037380000
C	16.642100000	11.556620000	25.653750000
C	15.818330000	12.588020000	25.172290000
C	14.765500000	14.302520000	28.452890000
C	17.760200000	10.298380000	27.558040000
C	9.217630000	16.768200000	17.485450000
C	7.982050000	17.237450000	16.949060000
C	6.927330000	16.310850000	16.796880000
C	7.048080000	14.948870000	17.148760000
C	8.280710000	14.509040000	17.678640000
C	9.344290000	15.407260000	17.846310000

C	7.792030000	18.681470000	16.550820000
C	5.892040000	13.987490000	16.986460000
C	17.446970000	11.062560000	21.887520000
C	17.681110000	9.660070000	22.009540000
C	18.749910000	9.229740000	22.824530000
C	19.597880000	10.123560000	23.515170000
C	19.334360000	11.506190000	23.396290000
C	18.270640000	11.963340000	22.600910000
C	16.822800000	8.649290000	21.286290000
C	20.766100000	9.614930000	24.332100000
C	19.761050000	15.199600000	24.102510000
C	21.124170000	14.794730000	24.234310000
C	21.493890000	14.048040000	25.372190000
C	20.573300000	13.689050000	26.383530000
C	19.229010000	14.086840000	26.221250000
C	18.829790000	14.823550000	25.094540000
C	22.151610000	15.130060000	23.179540000
C	21.017780000	12.913780000	27.604440000
C	19.687570000	16.767250000	16.696320000
C	20.787530000	17.392390000	16.036020000
C	21.124280000	16.951110000	14.739380000
C	20.442640000	15.897150000	14.089990000
C	19.366640000	15.287570000	14.770350000
C	18.986360000	15.725410000	16.049640000
C	21.614110000	18.462470000	16.710730000
C	20.882930000	15.408960000	12.728030000
C	10.558770000	14.166820000	14.708340000

C	9.792770000	15.114900000	13.968930000
C	8.499050000	14.739950000	13.544400000
C	7.937800000	13.471300000	13.802870000
C	8.713500000	12.551890000	14.542550000
C	9.995330000	12.898890000	14.991040000
C	10.328060000	16.481640000	13.617280000
C	6.570190000	13.096790000	13.277380000
C	20.815580000	13.290180000	18.175420000
C	21.027300000	12.467520000	17.029870000
C	22.059650000	12.817280000	16.133150000
C	22.887790000	13.942860000	16.320690000
C	22.668200000	14.735820000	17.469220000
C	21.654300000	14.409130000	18.380940000
C	20.138240000	11.283760000	16.742840000
C	23.944200000	14.332730000	15.314380000
C	16.591470000	19.265890000	26.980480000
C	17.064830000	20.587900000	27.222380000
C	16.428720000	21.354380000	28.223850000
C	15.356020000	20.867480000	28.999520000
C	14.919110000	19.545770000	28.756810000
C	15.522640000	18.763240000	27.762170000
C	18.194360000	21.182070000	26.418680000
C	14.685360000	21.724800000	30.050330000
C	12.409940000	11.285070000	25.007940000
C	13.236560000	10.184120000	25.381320000
C	13.407870000	9.911870000	26.755280000
C	12.796470000	10.673840000	27.772440000



C	11.970010000	11.749350000	27.378670000
C	11.783920000	12.051100000	26.021740000
C	13.937700000	9.326990000	24.357290000
C	13.050290000	10.374470000	29.232300000
H	18.854470000	22.219110000	13.448510000
H	14.563070000	22.671700000	13.953620000
H	14.796230000	22.129440000	16.378810000
H	19.775410000	22.275670000	16.842080000
H	20.259260000	21.669600000	15.199970000
H	19.520010000	20.557640000	16.420370000
H	17.478350000	23.137570000	11.587750000
H	15.710930000	23.410880000	11.809520000
H	16.334370000	21.755190000	11.505850000
H	5.575160000	14.822910000	23.557060000
H	7.067330000	16.354920000	19.766020000
H	9.343060000	16.554550000	20.759270000
H	8.641580000	14.061170000	25.020100000
H	6.951790000	14.557270000	25.425900000
H	8.326020000	15.727830000	25.570310000
H	4.658910000	14.452860000	20.465240000
H	4.555370000	16.228650000	20.251150000
H	3.970790000	15.465400000	21.777090000
H	17.146710000	11.845030000	12.424200000
H	15.929560000	15.991510000	12.955400000
H	15.382600000	15.510290000	15.340600000
H	17.151890000	10.894810000	15.866760000
H	17.060890000	10.287820000	14.165010000

H	15.567670000	10.504500000	15.156960000
H	17.995550000	14.630830000	10.983760000
H	16.278770000	14.992780000	10.624120000
H	16.905180000	13.311810000	10.446480000
H	7.891230000	9.867330000	18.706970000
H	7.814330000	13.240130000	21.459560000
H	10.241090000	13.635790000	21.017100000
H	11.076170000	10.539180000	17.255380000
H	9.820620000	9.263900000	17.531040000
H	11.292640000	9.363880000	18.573980000
H	5.612650000	11.264980000	19.441690000
H	5.784750000	12.039100000	21.059960000
H	6.043710000	10.269570000	20.866790000
H	12.785470000	23.283460000	27.324970000
H	15.799120000	23.161750000	24.182620000
H	15.126330000	20.824420000	23.650360000
H	11.010330000	20.361630000	26.391980000
H	11.365530000	21.495850000	27.754140000
H	12.212930000	19.902250000	27.625290000
H	13.932210000	25.408800000	26.560370000
H	15.251310000	25.326360000	25.334250000
H	15.541950000	24.765070000	27.014090000
H	12.250700000	25.940680000	20.284060000
H	12.249280000	23.294210000	23.739520000
H	12.485390000	21.327840000	22.221790000
H	13.503470000	23.731870000	17.943940000
H	12.374700000	25.134280000	18.102420000

H	11.744630000	23.465570000	17.795560000
H	12.315670000	26.905250000	22.546260000
H	12.592370000	25.839930000	23.975010000
H	10.936040000	26.053870000	23.323110000
H	15.547060000	18.899840000	11.286090000
H	18.670970000	18.203000000	14.234540000
H	16.957360000	18.265120000	16.048120000
H	12.780990000	18.269220000	13.346750000
H	13.308680000	19.204570000	11.890980000
H	13.056800000	20.022590000	13.486750000
H	18.254340000	17.417320000	11.060870000
H	19.280540000	18.641380000	11.879040000
H	18.036380000	19.154630000	10.678290000
H	8.339480000	24.117780000	23.597190000
H	8.620130000	23.690640000	19.278530000
H	9.151990000	21.263650000	19.566290000
H	8.219230000	20.715000000	24.446400000
H	8.721130000	22.346700000	25.052410000
H	9.949200000	21.153910000	24.472460000
H	7.855930000	26.025840000	22.230860000
H	7.339310000	25.744400000	20.529660000
H	9.056180000	26.102430000	20.892290000
H	16.416720000	12.229950000	29.005300000
H	17.131050000	10.869650000	24.936450000
H	15.660990000	12.705530000	24.078140000
H	15.159420000	15.340540000	28.332340000
H	14.973340000	13.972270000	29.494690000

H	13.662320000	14.362570000	28.308380000
H	18.406510000	10.642520000	28.398080000
H	18.420080000	9.905890000	26.752120000
H	17.155950000	9.443710000	27.945710000
H	5.968080000	16.674650000	16.372390000
H	8.417340000	13.449520000	17.968310000
H	10.307430000	15.041320000	18.261670000
H	7.952320000	19.362230000	17.420720000
H	6.766380000	18.852530000	16.154730000
H	8.528200000	18.991040000	15.772180000
H	5.348870000	13.841110000	17.951230000
H	6.248920000	12.985590000	16.656020000
H	5.152020000	14.357230000	16.241970000
H	18.933420000	8.138520000	22.909470000
H	19.954420000	12.240520000	23.945510000
H	18.056590000	13.051550000	22.544370000
H	15.747210000	8.752490000	21.564480000
H	17.150170000	7.614000000	21.525750000
H	16.870250000	8.793610000	20.181810000
H	20.964740000	10.270200000	25.210600000
H	21.702290000	9.589410000	23.723630000
H	20.587640000	8.579790000	24.701320000
H	22.553110000	13.731080000	25.468740000
H	18.470410000	13.803160000	26.976480000
H	17.766050000	15.116580000	24.974260000
H	21.836670000	14.731470000	22.183230000
H	23.142890000	14.694090000	23.436360000

H	22.263470000	16.233920000	23.057750000
H	21.667070000	12.049720000	27.333170000
H	20.144030000	12.523210000	28.170240000
H	21.609580000	13.554100000	28.301530000
H	21.967230000	17.451130000	14.218280000
H	18.800190000	14.468590000	14.285900000
H	18.128480000	15.245220000	16.565630000
H	20.972710000	19.234800000	17.196050000
H	22.291940000	18.958820000	15.980510000
H	22.241800000	18.026180000	17.525450000
H	21.161680000	16.251180000	12.053820000
H	20.079230000	14.819760000	12.233410000
H	21.776730000	14.743780000	12.811020000
H	7.904100000	15.482140000	12.972820000
H	8.309440000	11.545790000	14.773970000
H	10.594110000	12.166980000	15.568720000
H	10.634550000	17.050250000	14.530420000
H	9.560560000	17.080530000	13.078370000
H	11.231820000	16.407390000	12.966640000
H	5.866640000	13.959080000	13.306880000
H	6.122860000	12.266070000	13.867360000
H	6.623630000	12.754080000	12.216370000
H	22.219770000	12.173520000	15.243740000
H	23.300530000	15.629880000	17.643960000
H	21.461820000	15.047330000	19.266810000
H	20.069620000	10.592200000	17.614360000
H	20.495840000	10.716110000	15.855410000

H	19.095090000	11.633560000	16.539990000
H	24.143090000	13.520280000	14.580640000
H	24.908130000	14.592700000	15.809590000
H	23.619180000	15.233840000	14.739470000
H	16.791210000	22.389450000	28.398430000
H	14.083660000	19.121420000	29.349460000
H	15.144150000	17.739610000	27.563720000
H	19.109010000	20.546280000	26.464380000
H	18.446520000	22.202330000	26.782570000
H	17.914420000	21.254920000	25.337550000
H	14.939070000	21.379890000	31.081140000
H	13.575400000	21.679530000	29.956960000
H	14.994430000	22.789840000	29.963530000
H	14.058280000	9.059890000	27.041640000
H	11.460330000	12.364230000	28.147410000
H	11.138540000	12.904010000	25.730420000
H	13.217080000	8.852980000	23.651190000
H	14.533230000	8.528370000	24.851490000
H	14.636330000	9.940100000	23.733010000
H	13.389390000	9.325160000	29.382320000
H	12.138450000	10.536300000	29.851070000
H	13.846280000	11.042690000	29.641670000
C	19.340560000	21.247080000	21.512230000
H	19.575890000	21.936400000	22.357670000
H	19.330620000	21.875330000	20.586110000
C	20.468870000	20.240670000	21.372360000
C	20.310690000	18.881710000	21.046700000

C	21.796750000	20.703790000	21.504950000
C	21.440690000	18.073610000	20.813340000
N	22.895660000	19.943900000	21.271920000
C	22.735980000	18.616870000	20.903650000
H	22.000410000	21.751340000	21.801400000
H	21.292000000	17.013300000	20.540840000
C	23.999600000	17.904390000	20.607760000
N	25.118570000	18.701860000	20.698710000
C	26.341720000	18.169810000	20.460120000
H	27.198800000	18.858010000	20.568140000
C	26.580680000	16.819760000	20.162860000
C	25.433870000	15.993200000	20.034870000
H	25.544100000	14.919340000	19.783030000
C	24.155260000	16.540240000	20.255640000
H	23.265360000	15.887190000	20.181120000
H	25.441520000	17.821560000	25.690290000
C	25.261950000	18.837580000	25.294890000
C	25.157630000	19.957560000	26.150180000
C	25.148930000	19.031110000	23.913840000
C	24.938310000	21.216350000	25.581870000
N	24.944350000	20.255370000	23.344410000
C	24.825900000	21.356190000	24.178580000
H	25.250670000	19.847930000	27.247370000
H	25.236610000	18.178940000	23.213600000
H	24.855360000	22.106660000	26.230990000
C	24.572690000	22.626100000	23.497440000
N	24.490370000	22.544150000	22.113850000



C	24.224440000	23.689600000	21.419960000
H	24.164120000	23.583540000	20.320630000
C	24.035830000	24.933630000	22.032140000
C	24.126730000	25.024220000	23.440270000
H	23.991110000	25.991400000	23.960320000
C	24.395020000	23.860510000	24.166550000
H	24.477380000	23.902320000	25.267440000
C	29.222820000	21.135860000	21.764280000
C	29.605210000	21.629730000	20.496060000
C	27.864470000	20.914140000	22.017390000
C	28.609910000	21.869750000	19.539720000
N	26.886870000	21.133270000	21.091770000
C	27.251370000	21.610340000	19.841550000
H	30.673250000	21.799200000	20.256290000
H	27.523650000	20.517110000	22.992190000
H	28.888870000	22.239870000	18.535620000
C	26.153710000	21.741330000	18.872210000
N	24.913650000	21.297760000	19.311010000
C	23.863470000	21.331410000	18.442610000
H	22.901170000	20.953070000	18.836970000
C	23.964880000	21.825260000	17.136610000
C	25.215560000	22.308830000	16.690060000
H	25.336900000	22.718890000	15.669680000
C	26.308580000	22.258550000	17.563770000
H	27.296710000	22.624750000	17.231410000
H	23.827520000	25.822350000	21.409100000
H	29.967640000	20.907430000	22.547970000

H	23.070830000	21.830420000	16.485500000
Ru	24.859510000	20.660190000	21.306290000
C	28.020990000	16.377920000	20.241880000
H	28.659430000	17.270610000	20.418240000
H	28.103510000	15.753130000	21.169690000
H	19.286600000	18.464750000	20.972980000
Ag	33.440820000	13.464050000	18.988010000
Ag	31.333590000	15.226380000	19.545430000
Ag	33.237630000	15.818790000	17.423360000
Ag	32.830740000	13.798380000	21.716690000
Ag	34.212330000	15.918980000	20.095950000
Ag	33.641530000	11.235510000	20.707590000
Ag	35.527080000	11.669860000	18.335140000
Ag	34.082710000	13.067050000	16.274970000
Ag	35.938710000	14.544560000	18.154060000
Ag	31.020950000	12.283580000	19.992800000
Ag	32.562080000	11.070730000	17.825930000
Ag	35.679780000	13.309750000	20.747760000
Ag	31.368000000	13.596740000	17.033820000
Ag	37.125990000	16.244390000	20.528910000
Ag	29.988260000	14.550340000	22.034200000
Ag	36.938150000	12.658650000	15.568740000
Ag	31.299460000	9.247770000	19.863510000
Ag	30.010360000	16.315750000	17.090290000
Ag	32.522240000	16.659750000	22.376970000
Ag	34.999890000	9.934540000	16.026460000
Ag	29.453400000	11.288630000	17.664360000

Ag	36.420510000	10.220430000	20.977160000
Ag	34.975780000	12.300520000	23.417270000
Ag	32.421400000	15.379600000	14.637990000
Ag	36.123650000	17.425390000	17.536210000
S	36.292270000	10.255780000	23.413760000
S	28.745600000	15.323360000	18.924190000
S	33.322420000	8.789530000	21.153970000
S	37.507770000	14.948040000	16.215710000
S	34.277150000	17.609220000	15.953900000
S	28.736970000	12.671710000	21.030840000
S	33.521990000	14.129930000	24.138730000
S	37.377860000	14.441840000	22.209680000
S	30.171100000	16.840730000	22.997000000
S	28.972320000	13.249960000	16.310660000
S	34.844220000	17.415940000	22.080960000
S	34.345780000	14.022980000	13.974070000
S	33.093530000	8.758140000	16.999900000
S	36.825300000	9.537860000	18.662080000
S	38.099680000	17.811780000	18.903960000
S	36.668150000	10.556200000	14.371130000
S	29.272200000	9.033500000	18.533170000
S	30.651380000	17.076620000	14.867310000
C	37.910960000	10.721540000	24.027970000
C	39.039290000	9.883750000	23.779300000
C	40.277240000	10.240770000	24.353750000
C	40.447580000	11.385400000	25.160580000
C	39.313200000	12.190640000	25.406440000

C	38.067070000	11.863260000	24.849930000
C	38.942890000	8.663040000	22.898480000
C	41.809740000	11.764770000	25.694110000
C	32.726060000	8.544530000	22.827240000
C	32.349350000	7.226590000	23.225500000
C	31.933780000	7.027240000	24.559780000
C	31.892700000	8.066570000	25.515440000
C	32.277750000	9.360900000	25.099860000
C	32.678270000	9.593020000	23.774360000
C	32.393460000	6.068250000	22.256800000
C	31.463170000	7.797230000	26.941430000
C	39.216160000	14.868730000	16.749280000
C	40.247820000	14.976950000	15.766950000
C	41.587460000	14.977210000	16.208140000
C	41.947150000	14.894430000	17.572650000
C	40.908660000	14.798440000	18.523880000
C	39.564570000	14.775850000	18.114380000
C	39.927730000	15.115430000	14.297800000
C	43.401110000	14.893340000	17.992680000
C	33.519650000	19.187350000	16.330730000
C	34.064890000	20.373480000	15.750230000
C	33.422590000	21.602700000	16.011340000
C	32.254660000	21.705750000	16.799490000
C	31.723770000	20.515840000	17.344270000
C	32.352290000	19.280240000	17.122040000
C	35.281110000	20.317090000	14.859080000
C	31.593140000	23.048160000	17.027390000

C	28.382860000	11.521170000	22.355490000
C	27.118540000	11.595960000	23.016990000
C	26.838950000	10.659340000	24.034760000
C	27.745340000	9.641200000	24.405550000
C	28.979970000	9.575840000	23.724610000
C	29.295300000	10.506590000	22.722500000
C	26.076640000	12.618550000	22.624110000
C	27.392320000	8.620880000	25.464980000
C	32.366160000	13.293770000	25.226690000
C	32.743920000	13.029510000	26.577620000
C	31.776120000	12.475940000	27.445930000
C	30.458360000	12.174060000	27.036440000
C	30.117390000	12.412320000	25.686930000
C	31.062190000	12.952370000	24.801310000
C	34.145670000	13.297740000	27.069180000
C	29.439150000	11.623640000	28.009590000
C	38.995300000	13.749840000	21.869820000
C	40.149110000	14.380100000	22.426390000
C	41.409540000	13.778200000	22.217650000
C	41.577620000	12.577850000	21.494150000
C	40.422500000	11.971630000	20.953530000
C	39.158400000	12.553180000	21.134050000
C	40.041610000	15.662260000	23.214000000
C	42.948600000	11.981540000	21.260810000
C	30.126790000	16.525720000	24.759620000
C	28.927190000	16.049040000	25.366050000
C	28.919070000	15.835960000	26.760110000

C	30.046600000	16.067660000	27.576020000
C	31.216500000	16.559600000	26.954990000
C	31.254620000	16.789470000	25.571610000
C	27.708370000	15.712310000	24.543320000
C	30.021430000	15.739280000	29.051630000
C	28.907460000	12.585460000	14.647600000
C	27.733750000	11.899300000	14.210780000
C	27.657600000	11.506660000	12.856840000
C	28.694840000	11.751400000	11.928650000
C	29.862910000	12.393190000	12.394580000
C	29.961670000	12.804000000	13.732780000
C	26.622020000	11.546880000	15.169210000
C	28.555220000	11.352530000	10.476940000
C	34.607980000	19.117560000	21.564340000
C	34.719710000	20.154440000	22.537180000
C	34.608900000	21.493500000	22.102220000
C	34.399690000	21.844720000	20.751840000
C	34.291700000	20.799290000	19.807450000
C	34.392380000	19.459510000	20.209760000
C	34.962460000	19.844260000	23.995410000
C	34.304050000	23.291120000	20.317850000
C	33.758090000	12.802710000	12.801550000
C	33.782010000	13.117250000	11.411500000
C	33.403630000	12.110800000	10.494160000
C	33.012750000	10.815320000	10.895510000
C	32.996290000	10.529240000	12.279470000
C	33.358870000	11.510140000	13.212760000

C	34.217710000	14.477420000	10.920160000
C	32.634640000	9.754470000	9.884720000
C	32.138810000	8.428690000	15.515860000
C	32.508320000	7.337580000	14.671340000
C	31.689090000	7.044500000	13.560000000
C	30.531740000	7.790990000	13.240410000
C	30.201340000	8.880960000	14.074130000
C	30.995490000	9.191080000	15.189860000
C	33.762120000	6.535690000	14.922870000
C	29.667700000	7.429190000	12.051790000
C	38.557590000	9.871090000	18.335260000
C	39.498430000	8.807560000	18.497710000
C	40.845390000	9.049570000	18.153080000
C	41.296500000	10.287480000	17.641090000
C	40.350700000	11.324190000	17.496750000
C	39.004540000	11.118090000	17.845380000
C	39.068400000	7.448260000	18.995710000
C	42.743540000	10.484500000	17.245300000
C	37.967420000	19.550750000	19.328300000
C	38.349430000	20.059930000	20.605650000
C	38.358900000	21.459090000	20.792620000
C	38.021310000	22.377390000	19.775110000
C	37.642990000	21.851900000	18.520400000
C	37.617330000	20.465480000	18.305580000
C	38.750400000	19.149970000	21.740950000
C	38.096720000	23.868950000	20.017940000
C	38.069900000	9.475230000	14.645360000



C	39.370130000	9.859780000	14.203490000
C	40.414260000	8.912460000	14.287230000
C	40.229060000	7.607410000	14.787700000
C	38.932510000	7.250420000	15.224020000
C	37.873960000	8.169020000	15.156720000
C	39.646480000	11.243200000	13.671240000
C	41.381780000	6.632360000	14.881180000
C	27.813020000	9.078890000	19.568100000
C	27.616190000	8.084010000	20.571150000
C	26.402830000	8.092730000	21.289800000
C	25.372890000	9.026910000	21.048890000
C	25.583340000	9.992010000	20.039400000
C	26.787430000	10.022580000	19.318250000
C	28.672990000	7.053630000	20.881060000
C	24.081980000	8.980400000	21.835800000
C	29.208020000	16.533240000	13.947630000
C	29.305520000	16.087150000	12.595810000
C	28.122520000	15.704950000	11.927430000
C	26.846300000	15.770510000	12.523970000
C	26.768200000	16.265200000	13.844460000
C	27.927760000	16.627320000	14.545600000
C	30.625170000	15.993240000	11.873650000
C	25.617140000	15.288050000	11.786780000
H	41.152630000	9.588590000	24.151230000
H	39.406030000	13.093980000	26.042220000
H	37.188380000	12.511740000	25.043650000
H	38.157850000	7.955280000	23.253270000

H	39.915230000	8.125020000	22.847240000
H	38.654260000	8.954360000	21.857060000
H	42.464070000	10.873510000	25.821950000
H	41.738400000	12.286940000	26.674320000
H	42.325720000	12.457780000	24.985810000
H	31.630130000	6.004520000	24.865860000
H	32.246340000	10.207780000	25.813700000
H	32.955130000	10.620400000	23.456780000
H	31.750940000	6.257580000	21.363990000
H	32.049930000	5.130450000	22.746350000
H	33.424550000	5.909670000	21.862870000
H	30.761440000	6.934520000	27.002100000
H	30.961700000	8.684600000	27.388960000
H	32.338370000	7.553050000	27.590050000
H	42.388400000	15.067160000	15.444840000
H	41.146540000	14.728900000	19.603510000
H	38.759860000	14.679850000	18.872660000
H	39.251310000	14.301580000	13.945990000
H	40.855100000	15.091510000	13.684670000
H	39.388870000	16.070180000	14.092660000
H	43.894380000	13.918870000	17.759150000
H	43.506980000	15.065640000	19.086190000
H	43.982410000	15.681040000	17.460380000
H	33.853880000	22.523740000	15.566070000
H	30.804940000	20.545160000	17.963240000
H	31.934460000	18.352440000	17.564560000
H	36.134720000	19.809030000	15.366720000

H	35.603790000	21.333760000	14.544950000
H	35.073800000	19.711990000	13.945650000
H	32.330460000	23.879920000	16.971170000
H	31.106070000	23.104170000	18.028630000
H	30.807250000	23.255480000	16.260640000
H	25.858020000	10.723490000	24.550570000
H	29.718120000	8.794880000	23.990280000
H	30.278780000	10.453060000	22.209750000
H	26.474570000	13.659500000	22.672420000
H	25.184140000	12.548200000	23.286890000
H	25.745760000	12.454660000	21.571070000
H	26.730130000	9.050010000	26.250440000
H	28.304450000	8.219140000	25.960500000
H	26.852400000	7.751460000	25.018120000
H	32.074760000	12.263200000	28.493890000
H	29.105850000	12.157200000	25.313360000
H	30.788480000	13.102190000	23.732720000
H	34.883990000	12.675550000	26.506800000
H	34.244340000	13.059340000	28.151000000
H	34.444240000	14.358520000	26.903830000
H	29.928390000	11.146380000	28.888030000
H	28.778530000	10.869700000	27.523530000
H	28.774950000	12.433240000	28.399150000
H	42.302760000	14.280390000	22.643940000
H	40.509740000	11.037370000	20.366200000
H	38.264180000	12.065850000	20.689740000
H	39.566920000	16.463340000	22.599260000

H	41.043910000	16.014220000	23.546460000
H	39.390270000	15.535880000	24.110600000
H	43.333280000	12.250100000	20.247490000
H	42.924220000	10.869030000	21.312970000
H	43.691220000	12.347600000	22.005110000
H	27.988780000	15.451610000	27.228870000
H	32.120790000	16.757730000	27.563900000
H	32.184980000	17.156790000	25.093670000
H	27.355490000	16.585250000	23.943590000
H	26.875440000	15.346900000	25.185020000
H	27.950430000	14.909520000	23.801870000
H	28.983670000	15.733250000	29.454750000
H	30.622590000	16.463180000	29.647290000
H	30.456880000	14.727240000	29.233620000
H	26.747970000	10.968050000	12.516590000
H	30.714660000	12.566610000	11.706720000
H	30.883250000	13.308780000	14.091800000
H	26.986090000	10.822470000	15.938330000
H	25.763730000	11.080730000	14.635270000
H	26.261920000	12.438420000	15.730950000
H	27.865550000	10.487680000	10.351920000
H	29.540130000	11.081250000	10.035260000
H	28.139860000	12.188990000	9.864140000
H	34.717720000	22.299490000	22.857100000
H	34.145990000	21.033380000	18.735400000
H	34.326490000	18.651640000	19.451130000
H	34.126490000	19.244790000	24.429610000

H	35.068170000	20.778850000	24.589540000
H	35.883170000	19.231020000	24.133010000
H	33.247810000	23.598070000	20.121480000
H	34.869960000	23.463090000	19.373740000
H	34.710650000	23.978640000	21.092660000
H	33.429860000	12.355660000	9.411820000
H	32.685650000	9.529490000	12.640210000
H	33.336180000	11.270260000	14.296600000
H	33.575910000	15.288780000	11.337960000
H	34.173950000	14.534580000	9.810610000
H	35.257270000	14.711990000	11.248790000
H	31.641650000	9.307220000	10.123880000
H	33.369960000	8.915580000	9.885480000
H	32.591940000	10.167500000	8.852740000
H	31.980390000	6.192780000	12.909960000
H	29.323080000	9.515410000	13.841590000
H	30.731050000	10.060200000	15.828700000
H	34.667600000	7.178310000	14.795290000
H	33.841420000	5.685940000	14.209540000
H	33.802830000	6.140200000	15.963370000
H	30.277540000	7.190740000	11.150270000
H	28.976310000	8.262360000	11.793400000
H	29.042960000	6.529090000	12.263590000
H	41.574100000	8.222510000	18.285830000
H	40.667630000	12.317860000	17.125680000
H	38.278750000	11.952760000	17.745680000
H	38.512760000	7.519170000	19.959720000

H	39.946070000	6.779950000	19.139390000
H	38.372040000	6.961610000	18.272740000
H	43.442440000	10.176840000	18.058130000
H	42.948700000	11.548870000	16.996230000
H	43.002270000	9.872610000	16.347990000
H	38.655000000	21.850530000	21.787730000
H	37.367300000	22.537110000	17.693260000
H	37.332390000	20.065170000	17.313010000
H	37.929920000	18.435180000	21.997470000
H	39.000620000	19.736160000	22.652770000
H	39.637330000	18.531520000	21.465510000
H	37.726880000	24.140140000	21.033220000
H	37.496200000	24.435550000	19.271730000
H	39.147020000	24.240130000	19.945400000
H	41.422440000	9.216760000	13.935270000
H	38.743570000	6.233460000	15.622450000
H	36.865150000	7.874180000	15.510400000
H	38.981280000	11.496840000	12.813150000
H	40.705330000	11.345620000	13.345670000
H	39.450020000	12.012680000	14.458730000
H	42.244590000	6.961020000	14.259740000
H	41.083230000	5.613750000	14.543050000
H	41.745220000	6.534100000	15.932380000
H	26.256950000	7.325080000	22.077170000
H	24.790860000	10.733300000	19.810080000
H	26.944680000	10.797880000	18.540930000
H	28.954460000	6.468230000	19.974770000

H	28.326780000	6.349240000	21.668950000
H	29.610230000	7.544650000	21.244970000
H	23.317550000	8.344240000	21.328810000
H	23.637930000	9.995330000	21.949090000
H	24.243750000	8.555220000	22.852230000
H	28.212430000	15.333200000	10.885340000
H	25.781650000	16.359100000	14.338870000
H	27.849180000	16.992670000	15.589830000
H	31.149870000	16.975860000	11.833650000
H	30.483380000	15.619320000	10.836450000
H	31.319230000	15.287320000	12.397460000
H	25.708180000	15.446330000	10.688640000
H	24.696400000	15.809200000	12.135270000
H	25.462140000	14.193410000	11.948770000

#### D Isomer

Ag	14.407380000	15.970970000	19.030500000
Ag	11.693810000	15.358070000	19.582460000
Ag	13.483790000	13.356370000	18.467930000
Ag	12.486160000	18.032890000	18.740560000
Ag	12.633720000	15.648640000	16.867610000
Ag	15.325740000	18.565510000	19.542130000
Ag	17.108360000	16.487700000	18.313830000
Ag	16.329810000	13.957340000	19.426000000
Ag	15.418370000	14.843840000	16.639290000
Ag	13.382460000	17.240280000	21.340560000
Ag	16.104930000	16.239950000	21.261890000

Ag	14.885380000	17.686920000	16.815100000
Ag	14.019870000	14.188400000	21.193930000
Ag	13.695160000	16.021000000	14.162080000
Ag	10.071420000	17.455990000	20.898190000
Ag	18.454530000	13.719590000	17.329820000
Ag	15.662740000	18.963960000	22.685400000
Ag	11.575890000	12.490690000	20.851010000
Ag	9.962220000	17.126970000	17.437410000
Ag	19.155500000	15.358920000	20.205390000
Ag	14.330990000	15.878880000	23.760670000
Ag	17.207830000	19.639380000	17.576870000
Ag	13.858560000	20.394460000	17.462050000
Ag	14.806940000	11.287050000	20.230870000
Ag	13.822230000	12.701810000	15.355560000
S	15.912130000	21.693200000	17.296530000
S	9.856170000	14.217250000	20.884290000
S	15.971920000	20.623830000	20.941180000
S	16.888090000	13.113510000	15.556010000
S	13.549080000	11.173620000	17.224490000
S	11.447950000	17.587360000	22.912490000
S	11.462490000	19.911130000	17.382180000
S	14.207270000	18.403080000	14.504700000
S	8.309060000	17.400810000	19.207160000
S	13.301180000	13.682030000	23.552820000
S	10.871310000	16.474240000	15.250190000
S	17.079540000	11.566690000	19.364790000
S	18.424920000	16.632620000	22.157580000



S	19.050110000	18.072230000	17.986280000
S	13.899520000	13.794790000	13.186980000
S	20.401260000	13.814810000	18.797780000
S	15.414790000	17.797190000	24.796730000
S	12.680300000	10.326510000	20.943060000
C	16.049290000	22.083500000	15.548400000
C	17.303160000	22.484510000	15.000730000
C	17.361820000	22.829100000	13.634840000
C	16.235900000	22.792080000	12.786020000
C	15.000980000	22.407200000	13.353130000
C	14.909320000	22.060910000	14.710420000
C	18.559710000	22.500330000	15.835940000
C	16.365160000	23.098220000	11.311850000
C	8.601430000	13.602150000	19.755200000
C	7.568660000	12.756540000	20.259930000
C	6.529500000	12.378820000	19.380260000
C	6.470460000	12.798660000	18.032860000
C	7.512780000	13.620900000	17.552680000
C	8.560820000	14.006580000	18.401920000
C	7.581940000	12.250170000	21.682690000
C	5.350470000	12.349430000	17.120150000
C	17.590780000	13.743690000	14.034540000
C	18.507020000	12.919800000	13.314520000
C	19.002060000	13.397430000	12.082530000
C	18.611070000	14.635990000	11.526400000
C	17.693790000	15.427190000	12.252980000
C	17.197710000	14.987690000	13.491230000

C	18.926640000	11.562980000	13.829310000
C	19.182000000	15.112040000	10.208390000
C	11.886910000	10.526550000	17.023520000
C	11.686810000	9.382970000	16.191330000
C	10.387550000	8.839210000	16.105330000
C	9.285500000	9.367190000	16.816680000
C	9.509410000	10.494480000	17.634100000
C	10.788380000	11.068780000	17.724590000
C	12.827430000	8.752520000	15.428550000
C	7.912190000	8.739050000	16.713170000
C	11.318040000	19.315790000	23.368660000
C	10.263110000	19.718780000	24.242870000
C	10.210470000	21.070950000	24.643970000
C	11.155300000	22.034090000	24.227160000
C	12.185790000	21.612880000	23.358420000
C	12.262850000	20.275540000	22.937230000
C	9.241030000	18.733380000	24.757890000
C	11.088680000	23.457150000	24.735570000
C	10.813740000	21.164590000	18.490270000
C	10.518020000	22.460150000	17.973740000
C	9.897220000	23.392510000	18.834200000
C	9.558680000	23.095240000	20.171370000
C	9.885960000	21.812930000	20.665700000
C	10.505220000	20.866680000	19.836940000
C	10.850830000	22.846210000	16.551290000
C	8.837280000	24.096870000	21.045820000
C	15.681350000	18.651130000	13.516110000

C	15.558140000	18.809690000	12.101510000
C	16.723110000	19.079960000	11.351310000
C	18.001370000	19.213410000	11.939680000
C	18.098910000	19.057850000	13.339100000
C	16.958430000	18.775650000	14.108160000
C	14.219940000	18.697460000	11.414790000
C	19.229000000	19.472220000	11.094550000
C	7.630440000	19.042390000	18.999700000
C	6.953320000	19.677590000	20.081010000
C	6.340140000	20.926890000	19.846780000
C	6.376440000	21.575090000	18.594950000
C	7.043720000	20.921130000	17.534610000
C	7.654790000	19.675110000	17.733250000
C	6.912280000	19.062830000	21.456650000
C	5.758090000	22.939710000	18.396020000
C	14.546470000	12.675680000	24.366580000
C	14.453990000	12.467910000	25.776960000
C	15.400760000	11.620870000	26.391290000
C	16.423360000	10.962350000	25.672040000
C	16.498180000	11.188130000	24.281460000
C	15.576940000	12.035330000	23.642880000
C	13.389590000	13.141900000	26.608900000
C	17.396710000	10.039050000	26.370500000
C	9.879490000	15.050880000	14.784540000
C	8.716110000	15.250300000	13.983220000
C	7.992150000	14.112650000	13.562930000
C	8.374650000	12.794940000	13.893510000

C	9.527460000	12.623560000	14.690360000
C	10.263370000	13.734020000	15.129900000
C	8.259050000	16.631330000	13.576680000
C	7.571930000	11.600310000	13.429570000
C	18.196250000	11.271210000	20.735080000
C	18.748910000	9.965880000	20.896170000
C	19.701260000	9.765630000	21.920160000
C	20.129600000	10.798510000	22.781870000
C	19.558210000	12.079220000	22.611290000
C	18.603160000	12.305310000	21.609170000
C	18.337400000	8.822850000	19.998750000
C	21.175730000	10.557280000	23.848470000
C	18.857260000	15.625300000	23.573130000
C	20.215180000	15.559000000	24.011880000
C	20.498000000	14.850090000	25.198040000
C	19.497090000	14.208570000	25.964730000
C	18.168040000	14.263960000	25.493910000
C	17.857040000	14.958460000	24.313810000
C	21.330170000	16.205220000	23.223920000
C	19.842450000	13.501800000	27.256510000
C	19.900670000	17.816140000	16.436070000
C	20.948910000	18.711540000	16.066920000
C	21.667840000	18.444010000	14.884200000
C	21.411910000	17.313290000	14.075630000
C	20.374290000	16.440640000	14.465620000
C	19.621010000	16.696660000	15.622590000
C	21.330080000	19.887090000	16.936680000

C	22.249520000	17.025680000	12.851460000
C	12.450120000	13.148790000	12.351840000
C	11.630490000	13.938810000	11.494200000
C	10.605850000	13.291170000	10.769490000
C	10.365610000	11.903050000	10.841280000
C	11.185500000	11.141410000	11.702990000
C	12.202660000	11.756530000	12.446760000
C	11.839730000	15.423800000	11.323150000
C	9.290870000	11.254970000	9.997830000
C	21.712060000	14.688630000	17.940650000
C	22.398530000	14.045270000	16.868710000
C	23.521370000	14.689270000	16.302520000
C	23.998320000	15.937800000	16.749820000
C	23.291670000	16.566650000	17.800490000
C	22.171910000	15.951720000	18.381710000
C	21.934110000	12.720070000	16.320570000
C	25.206970000	16.593520000	16.117820000
C	14.090200000	18.530570000	25.757750000
C	14.122700000	19.905440000	26.131850000
C	13.111400000	20.390610000	26.990050000
C	12.080620000	19.576280000	27.501840000
C	12.074290000	18.214160000	27.126370000
C	13.055410000	17.704180000	26.263920000
C	15.189260000	20.844930000	25.624710000
C	11.015170000	20.136610000	28.416610000
C	12.733150000	9.937620000	22.689010000
C	13.706760000	9.029940000	23.203320000

C	13.640200000	8.682380000	24.569190000
C	12.651690000	9.185690000	25.441930000
C	11.684300000	10.063150000	24.904430000
C	11.727590000	10.435450000	23.552470000
C	14.788920000	8.444630000	22.330220000
C	12.657380000	8.835200000	26.911950000
H	18.341230000	23.132810000	13.210470000
H	14.090880000	22.369810000	12.721680000
H	13.935340000	21.741970000	15.134260000
H	18.446630000	23.142350000	16.740780000
H	19.428670000	22.863190000	15.241910000
H	18.793230000	21.471630000	16.209110000
H	17.225790000	23.773720000	11.107310000
H	15.445220000	23.575920000	10.905970000
H	16.533870000	22.158200000	10.732960000
H	5.723430000	11.726650000	19.775890000
H	7.517450000	13.962800000	16.498910000
H	9.377510000	14.644850000	18.004820000
H	8.471310000	11.598880000	21.861730000
H	6.667640000	11.656020000	21.903850000
H	7.652910000	13.084750000	22.417840000
H	5.642910000	11.440230000	16.540750000
H	5.089960000	13.135320000	16.376180000
H	4.432180000	12.092550000	17.694620000
H	19.713830000	12.755700000	11.522280000
H	17.358570000	16.404980000	11.853810000
H	16.479520000	15.621090000	14.052480000

H	19.361430000	11.627250000	14.854770000
H	19.678970000	11.098670000	13.154050000
H	18.053410000	10.874400000	13.912550000
H	20.116190000	15.705350000	10.362560000
H	18.463500000	15.768050000	9.667860000
H	19.443860000	14.259820000	9.541770000
H	10.235270000	7.952430000	15.454840000
H	8.672120000	10.946410000	18.200250000
H	10.941530000	11.969340000	18.354820000
H	13.376550000	9.507720000	14.817740000
H	12.459140000	7.947720000	14.754550000
H	13.583480000	8.314930000	16.121970000
H	7.575790000	8.649940000	15.653700000
H	7.156290000	9.342890000	17.262730000
H	7.899810000	7.710640000	17.146000000
H	9.391100000	21.381550000	25.324940000
H	12.934060000	22.341410000	22.986900000
H	13.073690000	19.961620000	22.248500000
H	8.745520000	18.176110000	23.928640000
H	8.458700000	19.253140000	25.354630000
H	9.726740000	17.961610000	25.399710000
H	10.042890000	23.774130000	24.947570000
H	11.526740000	24.175460000	24.006520000
H	11.660910000	23.566790000	25.687990000
H	9.660560000	24.399250000	18.429580000
H	9.651420000	21.544640000	21.714980000
H	10.749800000	19.859480000	20.237960000

H	11.953010000	22.821660000	16.370710000
H	10.483180000	23.870790000	16.323820000
H	10.399560000	22.134820000	15.821030000
H	8.899420000	25.127420000	20.630990000
H	9.256910000	24.110600000	22.077980000
H	7.755100000	23.836370000	21.140050000
H	16.620700000	19.197670000	10.251810000
H	19.081610000	19.147450000	13.842210000
H	17.055610000	18.638290000	15.206790000
H	13.753770000	17.700680000	11.601150000
H	14.321200000	18.841710000	10.316830000
H	13.500000000	19.450330000	11.812910000
H	19.630860000	18.525160000	10.659130000
H	20.045530000	19.926860000	11.698920000
H	19.005920000	20.153290000	10.241870000
H	5.817690000	21.421490000	20.692490000
H	7.095960000	21.400750000	16.536590000
H	8.182210000	19.175480000	16.895380000
H	6.463710000	18.042520000	21.445010000
H	6.335520000	19.700720000	22.162030000
H	7.947410000	18.944060000	21.863850000
H	5.114950000	23.228980000	19.256290000
H	5.134530000	22.976910000	17.473170000
H	6.546600000	23.723210000	18.288910000
H	15.333470000	11.467850000	27.489350000
H	17.295290000	10.706520000	23.682480000
H	15.659530000	12.215580000	22.548920000



H	13.531280000	14.250280000	26.623390000
H	13.420470000	12.775410000	27.659100000
H	12.372490000	12.956220000	26.192580000
H	17.761820000	10.471570000	27.330640000
H	18.280290000	9.826770000	25.729260000
H	16.919600000	9.061330000	26.621160000
H	7.090620000	14.269830000	12.935170000
H	9.860150000	11.606840000	14.974890000
H	11.169610000	13.575570000	15.751750000
H	8.051780000	17.269310000	14.468410000
H	7.334020000	16.574470000	12.961540000
H	9.042150000	17.164020000	12.987810000
H	6.891830000	11.231790000	14.235340000
H	8.240390000	10.753210000	13.153230000
H	6.940190000	11.848500000	12.547520000
H	20.135860000	8.751460000	22.041480000
H	19.849380000	12.912000000	23.279820000
H	18.144010000	13.311100000	21.508610000
H	17.237640000	8.643210000	20.048240000
H	18.859990000	7.883430000	20.284160000
H	18.564440000	9.046370000	18.930170000
H	20.892870000	11.048000000	24.808670000
H	22.163220000	10.981750000	23.546430000
H	21.324410000	9.471700000	24.042400000
H	21.553820000	14.798660000	25.538810000
H	17.358010000	13.748820000	26.047160000
H	16.810440000	14.985360000	23.947940000

H	21.352100000	15.809490000	22.178020000
H	22.320670000	16.009340000	23.692140000
H	21.183140000	17.308790000	23.142610000
H	20.731620000	12.839870000	27.140100000
H	18.992990000	12.880390000	27.616700000
H	20.088310000	14.233540000	28.062950000
H	22.476630000	19.145860000	14.590620000
H	20.134820000	15.553710000	13.847050000
H	18.797880000	16.009600000	15.910720000
H	20.435480000	20.473770000	17.251340000
H	22.039230000	20.560830000	16.404800000
H	21.822600000	19.540990000	17.877520000
H	22.390040000	17.935200000	12.223010000
H	21.778070000	16.239280000	12.222200000
H	23.265370000	16.661970000	13.139200000
H	9.962970000	13.909470000	10.109320000
H	11.024340000	10.048720000	11.798690000
H	12.837970000	11.147750000	13.121050000
H	11.753420000	15.969040000	12.295660000
H	11.089230000	15.849660000	10.620610000
H	12.856930000	15.642960000	10.921010000
H	8.445440000	11.953520000	9.807980000
H	8.879150000	10.342700000	10.484600000
H	9.691390000	10.944950000	9.002780000
H	24.054240000	14.181410000	15.471560000
H	23.629350000	17.557350000	18.166140000
H	21.605200000	16.459940000	19.187810000

H	21.838650000	11.952930000	17.123250000
H	22.633290000	12.343610000	15.542020000
H	20.920580000	12.824270000	15.860530000
H	25.680590000	15.933060000	15.357940000
H	25.984910000	16.838870000	16.879650000
H	24.929380000	17.548570000	15.611550000
H	13.136830000	21.464140000	27.270940000
H	11.282260000	17.540700000	27.512190000
H	13.019060000	16.638080000	25.961160000
H	16.211350000	20.477380000	25.877120000
H	15.056660000	21.861700000	26.056230000
H	15.151470000	20.929270000	24.509890000
H	11.133740000	19.758160000	29.460130000
H	9.995940000	19.839150000	28.076700000
H	11.053540000	21.248090000	28.452520000
H	14.402700000	7.980950000	24.968550000
H	10.881220000	10.465360000	25.554300000
H	10.967040000	11.133270000	23.146760000
H	14.359080000	7.886950000	21.465650000
H	15.437930000	7.754080000	22.912430000
H	15.437030000	9.247120000	21.895500000
H	13.123350000	7.841360000	27.095780000
H	11.629600000	8.822950000	27.339230000
H	13.246800000	9.585490000	27.492680000
C	17.537470000	21.577180000	21.151310000
H	17.383190000	22.220420000	22.050130000
H	17.558950000	22.264000000	20.267540000

C	18.904900000	20.920620000	21.248420000
C	19.193960000	19.591070000	20.893550000
C	20.001230000	21.714990000	21.651980000
C	20.525600000	19.135400000	20.895770000
N	21.290810000	21.291990000	21.662840000
C	21.577610000	19.997210000	21.262920000
H	19.844940000	22.765190000	21.965340000
H	20.726890000	18.094960000	20.583430000
C	23.018520000	19.649150000	21.224480000
N	23.884780000	20.686410000	21.517900000
C	25.226440000	20.448650000	21.507970000
H	25.866480000	21.317870000	21.758470000
C	25.816640000	19.196470000	21.226550000
C	24.926440000	18.141260000	20.921780000
H	25.339390000	17.140850000	20.677210000
C	23.538010000	18.370900000	20.924650000
H	22.848690000	17.538380000	20.690660000
H	23.346480000	19.399800000	26.377550000
C	22.953350000	20.362490000	25.998860000
C	22.245600000	21.260600000	26.829610000
C	23.164030000	20.712810000	24.660600000
C	21.797320000	22.468100000	26.284830000
N	22.726460000	21.884000000	24.112990000
C	22.042950000	22.775120000	24.925260000
H	22.048350000	21.016470000	27.890390000
H	23.716360000	20.036630000	23.981710000
H	21.242710000	23.185230000	26.915650000

C	21.609220000	24.009950000	24.267810000
N	21.892370000	24.093020000	22.909760000
C	21.498320000	25.213810000	22.238730000
H	21.736510000	25.234540000	21.159020000
C	20.834600000	26.281900000	22.850600000
C	20.553050000	26.209360000	24.234520000
H	20.037850000	27.037820000	24.754530000
C	20.942960000	25.065060000	24.935370000
H	20.739300000	24.980420000	26.017760000
C	26.707460000	24.286220000	23.498430000
C	27.104250000	25.050970000	22.376330000
C	25.518300000	23.554050000	23.425320000
C	26.297690000	25.037220000	21.233610000
N	24.721560000	23.526720000	22.316380000
C	25.113510000	24.261160000	21.204980000
H	28.037230000	25.644470000	22.397440000
H	25.158200000	22.952190000	24.281340000
H	26.585070000	25.632360000	20.347520000
C	24.239030000	24.129200000	20.036780000
N	23.142880000	23.293210000	20.215070000
C	22.315470000	23.077160000	19.153620000
H	21.467420000	22.391050000	19.335200000
C	22.497640000	23.679210000	17.903960000
C	23.598910000	24.546910000	17.718910000
H	23.774270000	25.044070000	16.745940000
C	24.468170000	24.766560000	18.793400000
H	25.339910000	25.435420000	18.673170000

H	20.545880000	27.160600000	22.246960000
H	27.311870000	24.262830000	24.423950000
H	21.776810000	23.464380000	17.093610000
Ru	22.947980000	22.470720000	22.119650000
C	27.335980000	19.066380000	21.306330000
H	27.804040000	19.840160000	20.655140000
H	27.640130000	19.298500000	22.356810000
H	18.365520000	18.918720000	20.598340000
Ag	33.102330000	15.481620000	21.506210000
Ag	33.379240000	13.295050000	23.257060000
Ag	30.809770000	13.906340000	22.012990000
Ag	34.942860000	15.708000000	23.664450000
Ag	31.897150000	15.667690000	24.020480000
Ag	35.459360000	17.010780000	21.137640000
Ag	32.779220000	17.705180000	19.859650000
Ag	31.372030000	15.219210000	19.308140000
Ag	30.627980000	16.972710000	21.645260000
Ag	35.597020000	14.123230000	21.328770000
Ag	34.302210000	15.167340000	18.957270000
Ag	33.202030000	18.050090000	22.679160000
Ag	32.932340000	12.944170000	20.267440000
Ag	30.656300000	18.249270000	24.564230000
Ag	36.163040000	12.797710000	24.217150000
Ag	29.403270000	17.531570000	18.896210000
Ag	37.303700000	15.404860000	19.004510000
Ag	31.850630000	10.881210000	22.121140000
Ag	34.030010000	14.698000000	26.269290000

Ag	32.625500000	16.979620000	17.042090000
Ag	35.744760000	12.405530000	18.942390000
Ag	34.895870000	19.890470000	20.608810000
Ag	35.913900000	18.664400000	23.738440000
Ag	29.902410000	12.382840000	19.601100000
Ag	28.626740000	15.769980000	23.384730000
S	36.509530000	20.546430000	22.316110000
S	33.663680000	10.836420000	23.759550000
S	37.360200000	17.756100000	19.677620000
S	28.009490000	17.400710000	20.888290000
S	28.333280000	13.567260000	22.371790000
S	37.138130000	12.270550000	22.029310000
S	36.022970000	17.027950000	25.542460000
S	32.705750000	19.605340000	24.597320000
S	35.584980000	12.851300000	26.595350000
S	33.997330000	10.799140000	19.489370000
S	32.128850000	16.232820000	26.470950000
S	29.271150000	14.329970000	18.260980000
S	34.916150000	16.210560000	16.743340000
S	33.544230000	19.729610000	18.576200000
S	28.239430000	17.881120000	24.587340000
S	30.317190000	17.632440000	16.639120000
S	37.660620000	13.331810000	17.767840000
S	29.914040000	10.253800000	20.788040000
C	35.849100000	21.975950000	23.167060000
C	35.661850000	23.201670000	22.462820000
C	35.215390000	24.328760000	23.184370000

C	34.954650000	24.296500000	24.570010000
C	35.164900000	23.076140000	25.249980000
C	35.602280000	21.935510000	24.560110000
C	35.901100000	23.301080000	20.977800000
C	34.425550000	25.513300000	25.295110000
C	32.815320000	10.497710000	25.304070000
C	32.665990000	9.144540000	25.728080000
C	32.086140000	8.901630000	26.993840000
C	31.656700000	9.937150000	27.852620000
C	31.800970000	11.268400000	27.403850000
C	32.363640000	11.538000000	26.147710000
C	33.094230000	7.993810000	24.849520000
C	31.031690000	9.636040000	29.197090000
C	38.885910000	17.904570000	20.608560000
C	40.088140000	18.205840000	19.901250000
C	41.273740000	18.380220000	20.648310000
C	41.313420000	18.286670000	22.056900000
C	40.108970000	17.992950000	22.735240000
C	38.919150000	17.796010000	22.017180000
C	40.101550000	18.351330000	18.398070000
C	42.602250000	18.513980000	22.816200000
C	28.082630000	12.420110000	23.726240000
C	26.758470000	12.203720000	24.218620000
C	26.568920000	11.225670000	25.217690000
C	27.627850000	10.447070000	25.739170000
C	28.927610000	10.687150000	25.246710000
C	29.148320000	11.664700000	24.262750000



C	25.579200000	12.982500000	23.685280000
C	27.374350000	9.392630000	26.794850000
C	38.834730000	12.841630000	22.132460000
C	39.836510000	11.922960000	22.574840000
C	41.179120000	12.356910000	22.593510000
C	41.575170000	13.646220000	22.173180000
C	40.568090000	14.535990000	21.742360000
C	39.219790000	14.140260000	21.730010000
C	39.489140000	10.513710000	22.990740000
C	43.034330000	14.048240000	22.157150000
C	37.782890000	16.677750000	25.604010000
C	38.632760000	17.529710000	26.370600000
C	39.992240000	17.170630000	26.507050000
C	40.540980000	16.008960000	25.920480000
C	39.685870000	15.197680000	25.141520000
C	38.333220000	15.534380000	24.980980000
C	38.106170000	18.785910000	27.020700000
C	41.987860000	15.622920000	26.137910000
C	32.140230000	21.163180000	23.917300000
C	31.560190000	22.135510000	24.785270000
C	31.198750000	23.389540000	24.243720000
C	31.403640000	23.725110000	22.888980000
C	31.973140000	22.744230000	22.046090000
C	32.326850000	21.486420000	22.553480000
C	31.349810000	21.849590000	26.251130000
C	31.039980000	25.088450000	22.342320000
C	36.978110000	13.489780000	27.523750000

C	38.221900000	12.790700000	27.525420000
C	39.260420000	13.271710000	28.352540000
C	39.121560000	14.405120000	29.179020000
C	37.876520000	15.074360000	29.171020000
C	36.825610000	14.623960000	28.357410000
C	38.457260000	11.585550000	26.649370000
C	40.278190000	14.909410000	30.012670000
C	33.409430000	10.414630000	17.836040000
C	34.047260000	9.373860000	17.095410000
C	33.526320000	9.037330000	15.827180000
C	32.399710000	9.677730000	15.265350000
C	31.797350000	10.716850000	16.007340000
C	32.299990000	11.080530000	17.267220000
C	35.255820000	8.647820000	17.633640000
C	31.833990000	9.248420000	13.929050000
C	30.918800000	15.222950000	27.329150000
C	30.928020000	15.195190000	28.755850000
C	29.947810000	14.422880000	29.415750000
C	28.963720000	13.683780000	28.721600000
C	28.964850000	13.740940000	27.310470000
C	29.928480000	14.498900000	26.627640000
C	31.966410000	15.950560000	29.549740000
C	27.958990000	12.824540000	29.458210000
C	29.569550000	13.888060000	16.549200000
C	28.510050000	13.294880000	15.800020000
C	28.727670000	13.041650000	14.426050000
C	29.934090000	13.363880000	13.767510000

C	30.972490000	13.938540000	14.535260000
C	30.792550000	14.185090000	15.903660000
C	27.189180000	12.943820000	16.443750000
C	30.121850000	13.112220000	12.286970000
C	34.707910000	15.050440000	15.388420000
C	34.647760000	15.550000000	14.051360000
C	34.563500000	14.618900000	12.994760000
C	34.531360000	13.221280000	13.201540000
C	34.577760000	12.751800000	14.532600000
C	34.664270000	13.654400000	15.605570000
C	34.630170000	17.031220000	13.758770000
C	34.468560000	12.261730000	12.033090000
C	32.271260000	20.977360000	18.746330000
C	32.494280000	22.262530000	18.161330000
C	31.446460000	23.206580000	18.191810000
C	30.189460000	22.935900000	18.776460000
C	30.005950000	21.674150000	19.377830000
C	31.025950000	20.707570000	19.359240000
C	33.807170000	22.609400000	17.503430000
C	29.067590000	23.949680000	18.719540000
C	27.567390000	17.301030000	26.148480000
C	28.021310000	17.746480000	27.424090000
C	27.369770000	17.242710000	28.570910000
C	26.284310000	16.343140000	28.512680000
C	25.834760000	15.937200000	27.236380000
C	26.471970000	16.405360000	26.077490000
C	29.158990000	18.724570000	27.581090000

C	25.617650000	15.843150000	29.774200000
C	30.409290000	19.304840000	16.017800000
C	29.245030000	20.126520000	15.966820000
C	29.346290000	21.398320000	15.360870000
C	30.540550000	21.884770000	14.790010000
C	31.677150000	21.046080000	14.839010000
C	31.614860000	19.787010000	15.451840000
C	27.926330000	19.658710000	16.527620000
C	30.619030000	23.261920000	14.169400000
C	39.051290000	12.401390000	18.406210000
C	40.369590000	12.944210000	18.369420000
C	41.442940000	12.123690000	18.778580000
C	41.270480000	10.794860000	19.218090000
C	39.956740000	10.275660000	19.236680000
C	38.868270000	11.066740000	18.842300000
C	40.631920000	14.362500000	17.930340000
C	42.448240000	9.950840000	19.651820000
C	30.553150000	8.971920000	19.713530000
C	29.907850000	8.667750000	18.478320000
C	30.401750000	7.588980000	17.713670000
C	31.491040000	6.790800000	18.124250000
C	32.098350000	7.096750000	19.361870000
C	31.639140000	8.170610000	20.139600000
C	28.744660000	9.482120000	17.970240000
C	32.024920000	5.680080000	17.246950000
H	35.063070000	25.278390000	22.629960000
H	34.975660000	23.013430000	26.340140000

H	35.749420000	20.981570000	25.107100000
H	36.928090000	22.969260000	20.699290000
H	35.746950000	24.340540000	20.613590000
H	35.198190000	22.627680000	20.424760000
H	34.653960000	26.450500000	24.740790000
H	34.855400000	25.602910000	26.318530000
H	33.316190000	25.453490000	25.409110000
H	31.968170000	7.849030000	27.325230000
H	31.460090000	12.109860000	28.038110000
H	32.459050000	12.589140000	25.803400000
H	32.498140000	7.971360000	23.905300000
H	32.955430000	7.022370000	25.372250000
H	34.160620000	8.086850000	24.541280000
H	29.920300000	9.735510000	29.154310000
H	31.390500000	10.343000000	29.979180000
H	31.259720000	8.600810000	29.535230000
H	42.210010000	18.610150000	20.098100000
H	40.098100000	17.894500000	23.838650000
H	37.984520000	17.540880000	22.558890000
H	39.679810000	17.449290000	17.894330000
H	41.135400000	18.516840000	18.023990000
H	39.465330000	19.206580000	18.069510000
H	43.493000000	18.341170000	22.171240000
H	42.677160000	17.844030000	23.703040000
H	42.667920000	19.561720000	23.195120000
H	25.539470000	11.056740000	25.598320000
H	29.785870000	10.112280000	25.644860000

H	30.179040000	11.852720000	23.893790000
H	25.762380000	14.082170000	23.736250000
H	24.656440000	12.748710000	24.261370000
H	25.390180000	12.751720000	22.610920000
H	26.863680000	9.823510000	27.688040000
H	28.327310000	8.929390000	27.135120000
H	26.719500000	8.575050000	26.410440000
H	41.953290000	11.642280000	22.943930000
H	40.833990000	15.563980000	21.428290000
H	38.438520000	14.861180000	21.409690000
H	38.711740000	10.496450000	23.790180000
H	40.389460000	9.974470000	23.360610000
H	39.061380000	9.942450000	22.134120000
H	43.585970000	13.635020000	23.032470000
H	43.149940000	15.155080000	22.161220000
H	43.548460000	13.666670000	21.241640000
H	40.651530000	17.836510000	27.102710000
H	40.081300000	14.291330000	24.642170000
H	37.674920000	14.888310000	24.361650000
H	37.740010000	19.510070000	26.252880000
H	38.895540000	19.286440000	27.623440000
H	37.236110000	18.563890000	27.681040000
H	42.589450000	16.477360000	26.522270000
H	42.459450000	15.256420000	25.196900000
H	42.071140000	14.795650000	26.883850000
H	30.755460000	24.145750000	24.926280000
H	32.144600000	22.963480000	20.973790000

H	32.771880000	20.726190000	21.876010000
H	30.723150000	20.938920000	26.398520000
H	30.859090000	22.709090000	26.760260000
H	32.318830000	21.637640000	26.761040000
H	30.338060000	25.000620000	21.479920000
H	31.937280000	25.631990000	21.962550000
H	30.564650000	25.732260000	23.116260000
H	40.228640000	12.728260000	28.349410000
H	37.727060000	15.967680000	29.810040000
H	35.856740000	15.163010000	28.354080000
H	37.699770000	10.787410000	26.826910000
H	39.471250000	11.158260000	26.816050000
H	38.369810000	11.864120000	25.569050000
H	41.083470000	14.145810000	30.094250000
H	39.956510000	15.182200000	31.044160000
H	40.729130000	15.823940000	29.556340000
H	34.034550000	8.235410000	15.251090000
H	30.931380000	11.264930000	15.587830000
H	31.822550000	11.908800000	17.833600000
H	36.110680000	9.350070000	17.784650000
H	35.582670000	7.849360000	16.932030000
H	35.041260000	8.188580000	18.626070000
H	32.624340000	8.847010000	13.254620000
H	31.327880000	10.095490000	13.413740000
H	31.071350000	8.442180000	14.056160000
H	29.958650000	14.402930000	30.526000000
H	28.210250000	13.173720000	26.731360000

H	29.920700000	14.528170000	25.516970000
H	32.987210000	15.539580000	29.359350000
H	31.762930000	15.882100000	30.641210000
H	32.005300000	17.024970000	29.255030000
H	28.383900000	11.818260000	29.690640000
H	27.047210000	12.661500000	28.841470000
H	27.649110000	13.277220000	30.427720000
H	27.908570000	12.572010000	13.842270000
H	31.943820000	14.183030000	14.063020000
H	31.625350000	14.617200000	16.497310000
H	27.328780000	12.258640000	17.313660000
H	26.510050000	12.449850000	15.714170000
H	26.677180000	13.847830000	16.848680000
H	31.063890000	12.550310000	12.084890000
H	30.194450000	14.071440000	11.722060000
H	29.275340000	12.532190000	11.856720000
H	34.515920000	15.013130000	11.958450000
H	34.529410000	11.665320000	14.745290000
H	34.689680000	13.267260000	16.645390000
H	33.691710000	17.497500000	14.148150000
H	34.683460000	17.223760000	12.664630000
H	35.471710000	17.560770000	14.260860000
H	33.855530000	12.669720000	11.197400000
H	34.035160000	11.282930000	12.337160000
H	35.485730000	12.058920000	11.621070000
H	31.622300000	24.197260000	17.722320000
H	29.045840000	21.444200000	19.881170000



H	30.858200000	19.718170000	19.834900000
H	34.661960000	22.487400000	18.209630000
H	33.801530000	23.658180000	17.133110000
H	34.018220000	21.930390000	16.645160000
H	29.430190000	24.980720000	18.939970000
H	28.262840000	23.698070000	19.446420000
H	28.602990000	23.975180000	17.704090000
H	27.744020000	17.567050000	29.563480000
H	24.986260000	15.229160000	27.145620000
H	26.128200000	16.068180000	25.078980000
H	30.112790000	18.322480000	27.157410000
H	29.335940000	18.959910000	28.654110000
H	28.946080000	19.677900000	27.043140000
H	26.360410000	15.667280000	30.584500000
H	25.076560000	14.888630000	29.591840000
H	24.871980000	16.576260000	30.165480000
H	28.435870000	22.032090000	15.320710000
H	32.632330000	21.383210000	14.390140000
H	32.524150000	19.154070000	15.503350000
H	27.563290000	18.740980000	16.006640000
H	27.149020000	20.449900000	16.437680000
H	28.023690000	19.379760000	17.607970000
H	29.609330000	23.711470000	14.041240000
H	31.110840000	23.236790000	13.169710000
H	31.218170000	23.955410000	14.807490000
H	42.465060000	12.556010000	18.761330000
H	39.776830000	9.236930000	19.577380000

H	37.842820000	10.647540000	18.883390000
H	40.227980000	14.558240000	16.910320000
H	41.721510000	14.585780000	17.933900000
H	40.128090000	15.087260000	18.616410000
H	42.771640000	9.251100000	18.844810000
H	42.190450000	9.327490000	20.538250000
H	43.323700000	10.583410000	19.918520000
H	29.903210000	7.360790000	16.748940000
H	32.944240000	6.482010000	19.729130000
H	32.136270000	8.406910000	21.102240000
H	27.927240000	9.551080000	18.725120000
H	28.331090000	9.048150000	17.033640000
H	29.061340000	10.533070000	17.751210000
H	31.231050000	5.244680000	16.599620000
H	32.468420000	4.857780000	17.851770000
H	32.827880000	6.063030000	16.571150000

#### E Isomer

Ag	14.870350000	17.499300000	19.932980000
Ag	12.152760000	16.774370000	20.332600000
Ag	13.933700000	15.069680000	18.810200000
Ag	12.939080000	19.565790000	20.093290000
Ag	13.102630000	17.658230000	17.740170000
Ag	15.771550000	19.936950000	20.996210000
Ag	17.565350000	18.140980000	19.323780000
Ag	16.755300000	15.421300000	19.910540000
Ag	15.867690000	16.888230000	17.343860000

Ag	13.833390000	18.211340000	22.459140000
Ag	16.567420000	17.270210000	22.165090000
Ag	15.345460000	19.641440000	18.130530000
Ag	14.455530000	15.275630000	21.664640000
Ag	14.141690000	18.585580000	15.148920000
Ag	10.573470000	18.503500000	22.140770000
Ag	18.755040000	15.642720000	17.776570000
Ag	16.104980000	19.694360000	24.093930000
Ag	12.048530000	13.653150000	20.896420000
Ag	10.400040000	18.913710000	18.674500000
Ag	19.495060000	16.574240000	21.012260000
Ag	14.838830000	16.354810000	24.510630000
Ag	17.691550000	21.359080000	19.255250000
Ag	14.308010000	22.156140000	19.353460000
Ag	15.210310000	12.643630000	20.042690000
Ag	14.275240000	15.130470000	15.553220000
S	16.392630000	23.421020000	19.445160000
S	10.343490000	15.331750000	21.338580000
S	16.215650000	21.745860000	22.780180000
S	17.275260000	15.421510000	15.843110000
S	14.005870000	13.251400000	17.080590000
S	11.945510000	18.183230000	24.130670000
S	11.911920000	21.703270000	19.200190000
S	14.627760000	20.829410000	16.036580000
S	8.794400000	18.795280000	20.500750000
S	13.780550000	14.250330000	23.874600000
S	11.297170000	18.798920000	16.394440000

S	17.497760000	13.098710000	19.298580000
S	18.859650000	17.460790000	23.208050000
S	19.531610000	19.739180000	19.274330000
S	14.322100000	16.663990000	13.656460000
S	20.684500000	15.378160000	19.251910000
S	15.958230000	18.042170000	25.878790000
S	13.103120000	11.502220000	20.498210000
C	16.505820000	24.226060000	17.842070000
C	17.732280000	24.816360000	17.418720000
C	17.768140000	25.472820000	16.170340000
C	16.643520000	25.574690000	15.326020000
C	15.433460000	25.000530000	15.774120000
C	15.366310000	24.338790000	17.009590000
C	18.987960000	24.720270000	18.250250000
C	16.743230000	26.235490000	13.970470000
C	9.073070000	14.993480000	20.115310000
C	8.020020000	14.087300000	20.441810000
C	6.976660000	13.912710000	19.506540000
C	6.929050000	14.597040000	18.271650000
C	7.986510000	15.481380000	17.967450000
C	9.043290000	15.664640000	18.872650000
C	8.014520000	13.315790000	21.739450000
C	5.806620000	14.355620000	17.286120000
C	17.962550000	16.392760000	14.503560000
C	18.810340000	15.745940000	13.555910000
C	19.307720000	16.510890000	12.477420000
C	18.981230000	17.870800000	12.284880000

C	18.118960000	18.481940000	13.223780000
C	17.626220000	17.753690000	14.317930000
C	19.152450000	14.278380000	13.661240000
C	19.549840000	18.656240000	11.122800000
C	12.349580000	12.647150000	16.751690000
C	12.161630000	11.702710000	15.696850000
C	10.867660000	11.181030000	15.491030000
C	9.759690000	11.535170000	16.294910000
C	9.972530000	12.461150000	17.336280000
C	11.245780000	13.015680000	17.550350000
C	13.310460000	11.251890000	14.827420000
C	8.391540000	10.940430000	16.042350000
C	11.832390000	19.780590000	24.938720000
C	10.797740000	20.006550000	25.896490000
C	10.768830000	21.248060000	26.570090000
C	11.720270000	22.267020000	26.345100000
C	12.724580000	22.025160000	25.381970000
C	12.774120000	20.805060000	24.690370000
C	9.767450000	18.947890000	26.207320000
C	11.680280000	23.559830000	27.130430000
C	11.281910000	22.676510000	20.570900000
C	10.973930000	24.053450000	20.366250000
C	10.370900000	24.765450000	21.425420000
C	10.058010000	24.171690000	22.666390000
C	10.397030000	22.813400000	22.853560000
C	11.001930000	22.081770000	21.821210000
C	11.280660000	24.750570000	19.062470000

C	9.353060000	24.950500000	23.753450000
C	16.077340000	21.349720000	15.121250000
C	15.929740000	21.853900000	13.792650000
C	17.075670000	22.342510000	13.127400000
C	18.357290000	22.363100000	13.721700000
C	18.480070000	21.858060000	15.033880000
C	17.359990000	21.355270000	15.714310000
C	14.587630000	21.872880000	13.102710000
C	19.568580000	22.867100000	12.966780000
C	8.102570000	20.437120000	20.662150000
C	7.408040000	20.801630000	21.852410000
C	6.790580000	22.069410000	21.905380000
C	6.833600000	22.988000000	20.836140000
C	7.519160000	22.600250000	19.662520000
C	8.140500000	21.346080000	19.577620000
C	7.348930000	19.879230000	23.044440000
C	6.195300000	24.353460000	20.951770000
C	15.024730000	13.084130000	24.438510000
C	14.972490000	12.615290000	25.787130000
C	15.914550000	11.649430000	26.199000000
C	16.895730000	11.117190000	25.332190000
C	16.931380000	11.598680000	24.006750000
C	16.012650000	12.568590000	23.570500000
C	13.952350000	13.141410000	26.766040000
C	17.863070000	10.054200000	25.804930000
C	10.320220000	17.513530000	15.610120000
C	9.135870000	17.880820000	14.904170000

C	8.422590000	16.868840000	14.224200000
C	8.829190000	15.516200000	14.218310000
C	10.004060000	15.178580000	14.924930000
C	10.735920000	16.162050000	15.607700000
C	8.642920000	19.307960000	14.874720000
C	8.019550000	14.449640000	13.514350000
C	18.613030000	12.501910000	20.567030000
C	19.223540000	11.223120000	20.394710000
C	20.179010000	10.806370000	21.346200000
C	20.564110000	11.602790000	22.447040000
C	19.936710000	12.857030000	22.606220000
C	18.969540000	13.290340000	21.685040000
C	18.875570000	10.331020000	19.226570000
C	21.640030000	11.142510000	23.403830000
C	19.325110000	16.148760000	24.337550000
C	20.696950000	15.995640000	24.707920000
C	21.030590000	15.014150000	25.664130000
C	20.064200000	14.178520000	26.270930000
C	18.717420000	14.338240000	25.879640000
C	18.356550000	15.305300000	24.925610000
C	21.779890000	16.836580000	24.077060000
C	20.468180000	13.152770000	27.307600000
C	20.333460000	19.906790000	17.682410000
C	21.316860000	20.928120000	17.506070000
C	21.987210000	21.008950000	16.267690000
C	21.754040000	20.097670000	15.212380000
C	20.792230000	19.086270000	15.419860000

C	20.084110000	18.998640000	16.630890000
C	21.683240000	21.875900000	18.624280000
C	22.532720000	20.187150000	13.917970000
C	12.850660000	16.241380000	12.723660000
C	12.018970000	17.214090000	12.098210000
C	10.978070000	16.759480000	11.257720000
C	10.735250000	15.394580000	10.996160000
C	11.573540000	14.448860000	11.628180000
C	12.605800000	14.867970000	12.478240000
C	12.229200000	18.694350000	12.298960000
C	9.641730000	14.957120000	10.046800000
C	21.911430000	16.477680000	18.551410000
C	22.428810000	16.236850000	17.245690000
C	23.423940000	17.108080000	16.750160000
C	23.962920000	18.175560000	17.498340000
C	23.440670000	18.386120000	18.793430000
C	22.432680000	17.555220000	19.303840000
C	21.905450000	15.119550000	16.377280000
C	25.072270000	19.046710000	16.958620000
C	14.663510000	18.536400000	27.021030000
C	14.712880000	19.789920000	27.697880000
C	13.723100000	20.069690000	28.665290000
C	12.696540000	19.163930000	29.001370000
C	12.672200000	17.923670000	28.325080000
C	13.631550000	17.621980000	27.348210000
C	15.776610000	20.815550000	27.395180000
C	11.650020000	19.508570000	30.036860000



C	13.202020000	10.748370000	22.118410000
C	14.185430000	9.752400000	22.392450000
C	14.164200000	9.122960000	23.654670000
C	13.217890000	9.433090000	24.653300000
C	12.240330000	10.407560000	24.352130000
C	12.235400000	11.054990000	23.107300000
C	15.246590000	9.375740000	21.389250000
C	13.285260000	8.783040000	26.016100000
H	18.727340000	25.923460000	15.839640000
H	14.526010000	25.061130000	15.140610000
H	14.412930000	23.872230000	17.332860000
H	18.844560000	25.153220000	19.268730000
H	19.833450000	25.245000000	17.750010000
H	19.278620000	23.651910000	18.398190000
H	17.638200000	26.893440000	13.901240000
H	15.844740000	26.853790000	13.746230000
H	16.825800000	25.467280000	13.163990000
H	6.157380000	13.209390000	19.764460000
H	7.995480000	16.031290000	17.005860000
H	9.875150000	16.350560000	18.608610000
H	8.893420000	12.629910000	21.798020000
H	7.089810000	12.705460000	21.834450000
H	8.088580000	13.994100000	22.620650000
H	6.053930000	13.516630000	16.590650000
H	5.618730000	15.254060000	16.657090000
H	4.858490000	14.082800000	17.801360000
H	19.968970000	16.004880000	11.743160000

H	17.834900000	19.546910000	13.111960000
H	16.955630000	18.248870000	15.050310000
H	19.558410000	14.013220000	14.664700000
H	19.900420000	13.991740000	12.889170000
H	18.245860000	13.644470000	13.520750000
H	20.383980000	19.322410000	11.452700000
H	18.778840000	19.312870000	10.658900000
H	19.954650000	17.982420000	10.335180000
H	10.725040000	10.451350000	14.666670000
H	9.131550000	12.771560000	17.986170000
H	11.386250000	13.765410000	18.356280000
H	13.822310000	12.116010000	14.339810000
H	12.958460000	10.553610000	14.036500000
H	14.093470000	10.737260000	15.431850000
H	8.031900000	11.163150000	15.010010000
H	7.643950000	11.346130000	16.758960000
H	8.398760000	9.830350000	16.150380000
H	9.961570000	21.422480000	27.312270000
H	13.475510000	22.806330000	25.148940000
H	13.559090000	20.637890000	23.924920000
H	9.269960000	18.572390000	25.282660000
H	8.985710000	19.340940000	26.895090000
H	10.246870000	18.059330000	26.681030000
H	10.649230000	23.807070000	27.469600000
H	12.060920000	24.416150000	26.528660000
H	12.318330000	23.494280000	28.044930000
H	10.133820000	25.838630000	21.265830000

H	10.186940000	22.316080000	23.821030000
H	11.256690000	21.011690000	21.977590000
H	12.374970000	24.726640000	18.841240000
H	10.953690000	25.813700000	19.095280000
H	10.777680000	24.249420000	18.202580000
H	9.489380000	26.048380000	23.630800000
H	9.729790000	24.664030000	24.761350000
H	8.255660000	24.744290000	23.744570000
H	16.955190000	22.728570000	12.093330000
H	19.468120000	21.850960000	15.534420000
H	17.478800000	20.947410000	16.741110000
H	14.148770000	20.848840000	13.050780000
H	14.673840000	22.273650000	12.068630000
H	13.851660000	22.493030000	13.665830000
H	20.017410000	22.061410000	12.336430000
H	20.361880000	23.212940000	13.666700000
H	19.315160000	23.711960000	12.286310000
H	6.252030000	22.350880000	22.834520000
H	7.572110000	23.292980000	18.798750000
H	8.683990000	21.057580000	18.654810000
H	6.937080000	18.879270000	22.773350000
H	6.728550000	20.314200000	23.859140000
H	8.375350000	19.693610000	23.449470000
H	5.547250000	24.422690000	21.853500000
H	5.571480000	24.596280000	20.060650000
H	6.973130000	25.150330000	21.031650000
H	15.874470000	11.299030000	27.252150000

H	17.695850000	11.218210000	23.301460000
H	16.061490000	12.944800000	22.525890000
H	14.117070000	14.226680000	26.972040000
H	14.009160000	12.592770000	27.732040000
H	12.919610000	13.051240000	26.358070000
H	18.262760000	10.278440000	26.821350000
H	18.726380000	9.958900000	25.109550000
H	17.366820000	9.055620000	25.866870000
H	7.508810000	17.159790000	13.665350000
H	10.355900000	14.129210000	14.946480000
H	11.660340000	15.875490000	16.152810000
H	8.427480000	19.684080000	15.903450000
H	7.714370000	19.391240000	14.268360000
H	9.407620000	19.997010000	14.445650000
H	7.313670000	13.951160000	14.222070000
H	8.678650000	13.655430000	13.096800000
H	7.412730000	14.872060000	12.682200000
H	20.653230000	9.812430000	21.209740000
H	20.196450000	13.502660000	23.467290000
H	18.457790000	14.263430000	21.842440000
H	17.797870000	10.042240000	19.238360000
H	19.487300000	9.401840000	19.242890000
H	19.046360000	10.853160000	18.256770000
H	21.495390000	11.577330000	24.418780000
H	22.647800000	11.462170000	23.044680000
H	21.663130000	10.033540000	23.496680000
H	22.099270000	14.895070000	25.943970000

H	17.932150000	13.686140000	26.311350000
H	17.294730000	15.407430000	24.620710000
H	21.783930000	16.699510000	22.967320000
H	22.784580000	16.559180000	24.467370000
H	21.607420000	17.923950000	24.260450000
H	21.329470000	12.534660000	26.961730000
H	19.626560000	12.466050000	27.545610000
H	20.785760000	13.642220000	28.258960000
H	22.738430000	21.815550000	16.130400000
H	20.577650000	18.353630000	14.618090000
H	19.323680000	18.201630000	16.769500000
H	20.778020000	22.314490000	19.106410000
H	22.330680000	22.700000000	18.248630000
H	22.236240000	21.336950000	19.431830000
H	22.522800000	21.219730000	13.496990000
H	22.113220000	19.497360000	13.152660000
H	23.602910000	19.906780000	14.069280000
H	10.329200000	17.521210000	10.777990000
H	11.419420000	13.365060000	11.450640000
H	13.260480000	14.117700000	12.963430000
H	12.178380000	18.971230000	13.381070000
H	11.458860000	19.284280000	11.755160000
H	13.234090000	19.013450000	11.933450000
H	8.849630000	15.732900000	9.949480000
H	9.157260000	14.012630000	10.383460000
H	10.047320000	14.766370000	9.024680000
H	23.791390000	16.943680000	15.718290000

H	23.828040000	19.226020000	19.403240000
H	21.996020000	17.740300000	20.305020000
H	21.968680000	14.131920000	16.891800000
H	22.468990000	15.058880000	15.419770000
H	20.823530000	15.282480000	16.137180000
H	25.220510000	18.906150000	15.865580000
H	26.043310000	18.796210000	17.449900000
H	24.867640000	20.125260000	17.146250000
H	13.759590000	21.051090000	29.182730000
H	11.885830000	17.178650000	28.561390000
H	13.576440000	16.655020000	26.807580000
H	16.799680000	20.394770000	27.536890000
H	15.662530000	21.708710000	28.048320000
H	15.719270000	21.153490000	26.329700000
H	11.714140000	18.834800000	30.923620000
H	10.621470000	19.400130000	29.621020000
H	11.763430000	20.554060000	30.398470000
H	14.933250000	8.351150000	23.864990000
H	11.470290000	10.668240000	25.106100000
H	11.472380000	11.829940000	22.890670000
H	14.803270000	9.005360000	20.435810000
H	15.918620000	8.591190000	21.801050000
H	15.874550000	10.261790000	21.119740000
H	13.841740000	7.820050000	25.980500000
H	12.273070000	8.584020000	26.435820000
H	13.818440000	9.447720000	26.738210000
C	17.764690000	22.714820000	23.041870000

H	17.624310000	23.292470000	23.986340000
H	17.759070000	23.463000000	22.208680000
C	19.126300000	22.046880000	23.052370000
C	19.373470000	20.776120000	22.501290000
C	20.242560000	22.741720000	23.578190000
C	20.687760000	20.291870000	22.419420000
N	21.520900000	22.280810000	23.516980000
C	21.759020000	21.060460000	22.909500000
H	20.116500000	23.728110000	24.068830000
H	20.863900000	19.304560000	21.958110000
C	23.174710000	20.652720000	22.787770000
N	24.108750000	21.534530000	23.292100000
C	25.435420000	21.236280000	23.139580000
H	26.137790000	21.984220000	23.558300000
C	25.930800000	20.069620000	22.505640000
C	24.960120000	19.161830000	22.027290000
H	25.298290000	18.236060000	21.517350000
C	23.596110000	19.456070000	22.173800000
H	22.844590000	18.743870000	21.792550000
H	22.622200000	19.016030000	27.450770000
C	22.503970000	20.113950000	27.386760000
C	21.884350000	20.860470000	28.413630000
C	22.979050000	20.790330000	26.256040000
C	21.749860000	22.243980000	28.246900000
N	22.861960000	22.136630000	26.078630000
C	22.215860000	22.868680000	27.065860000
H	21.493800000	20.361750000	29.320920000

H	23.485070000	20.238070000	25.442910000
H	21.245560000	22.849820000	29.021790000
C	21.998320000	24.287440000	26.764570000
N	22.317140000	24.679280000	25.473680000
C	22.149840000	25.989300000	25.131730000
H	22.433520000	26.257340000	24.096680000
C	21.670900000	26.959830000	26.018690000
C	21.334770000	26.567370000	27.334420000
H	20.957460000	27.305410000	28.067470000
C	21.499810000	25.227280000	27.699580000
H	21.257600000	24.902740000	28.728400000
C	27.054870000	24.548150000	26.111340000
C	27.574600000	25.421370000	25.127400000
C	25.824090000	23.925130000	25.875820000
C	26.822200000	25.650100000	23.970850000
N	25.095960000	24.103860000	24.736740000
C	25.576850000	24.998180000	23.789230000
H	28.545940000	25.931670000	25.271410000
H	25.375300000	23.247350000	26.625200000
H	27.197530000	26.346420000	23.197580000
C	24.701870000	25.206200000	22.635820000
N	23.526390000	24.466780000	22.652190000
C	22.672450000	24.592650000	21.595230000
H	21.759470000	23.969100000	21.638480000
C	22.911630000	25.447610000	20.513240000
C	24.096760000	26.218960000	20.500290000
H	24.322250000	26.907460000	19.663840000



C	24.990500000	26.089570000	21.567860000
H	25.926520000	26.676850000	21.583080000
H	21.572120000	28.009030000	25.681910000
H	27.596780000	24.346580000	27.053630000
H	22.168700000	25.502970000	19.696000000
Ru	23.250310000	23.208950000	24.293130000
C	27.436080000	19.810660000	22.388560000
H	27.928220000	20.717400000	21.965870000
H	27.848870000	19.655910000	23.415010000
H	18.518860000	20.176480000	22.127950000
Ag	32.397470000	15.636410000	20.057310000
Ag	31.649650000	14.240430000	17.727810000
Ag	33.200890000	16.704450000	17.559040000
Ag	29.917870000	14.289990000	20.101580000
Ag	30.437940000	16.792250000	18.449490000
Ag	31.521460000	14.516010000	22.457360000
Ag	33.160100000	17.122700000	22.318840000
Ag	34.944380000	16.876730000	20.078250000
Ag	32.304130000	18.439150000	19.896220000
Ag	32.420710000	12.805600000	20.317150000
Ag	34.473290000	14.463330000	21.595820000
Ag	30.314290000	17.080350000	21.476940000
Ag	34.533660000	14.369560000	18.679210000
Ag	29.232590000	19.258280000	19.516890000
Ag	30.368510000	11.598980000	18.165940000
Ag	35.158640000	19.531170000	21.420630000
Ag	33.638950000	12.118440000	23.207910000

Ag	34.036780000	14.222260000	15.771170000
Ag	28.552970000	14.411090000	17.524940000
Ag	35.994690000	16.916000000	23.125180000
Ag	35.187820000	11.756650000	20.253030000
Ag	31.260120000	16.547730000	24.500380000
Ag	28.462700000	15.266810000	22.816200000
Ag	36.147350000	16.556880000	17.045840000
Ag	32.062530000	19.663030000	17.217230000
S	29.067380000	15.669070000	25.137510000
S	32.195710000	12.619820000	15.855680000
S	32.147400000	13.427740000	24.630510000
S	33.674250000	20.537020000	19.752510000
S	33.851530000	18.579400000	15.990700000
S	32.201950000	10.489340000	19.350070000
S	27.492200000	14.296960000	20.798580000
S	27.879230000	18.327720000	21.356030000
S	28.433090000	12.113510000	16.754760000
S	35.783550000	12.316120000	17.953660000
S	28.116080000	16.818370000	17.523870000
S	36.712940000	18.124520000	18.841940000
S	35.949340000	14.519780000	23.631170000
S	33.501550000	17.508650000	24.806640000
S	30.262980000	21.018620000	18.151600000
S	37.086580000	19.083700000	22.847310000
S	35.419310000	10.658730000	22.416820000
S	35.960050000	15.420640000	14.891830000
C	28.229280000	17.114590000	25.759800000

C	28.756290000	17.787810000	26.903480000
C	28.062030000	18.907330000	27.397770000
C	26.863910000	19.378170000	26.828160000
C	26.335620000	18.671350000	25.724490000
C	27.011190000	17.560120000	25.195270000
C	30.030710000	17.350870000	27.572990000
C	26.181250000	20.599210000	27.397000000
C	31.229250000	13.055750000	14.408150000
C	31.392510000	12.290310000	13.215980000
C	30.591690000	12.614360000	12.098450000
C	29.639640000	13.653690000	12.117410000
C	29.496230000	14.398060000	13.309150000
C	30.279850000	14.102980000	14.433820000
C	32.394790000	11.163720000	13.133680000
C	28.809130000	13.990710000	10.898680000
C	30.875200000	12.257190000	25.102620000
C	31.089720000	11.448900000	26.259290000
C	30.071670000	10.549110000	26.638920000
C	28.853000000	10.427540000	25.935000000
C	28.658710000	11.249060000	24.802360000
C	29.659400000	12.144370000	24.390910000
C	32.364020000	11.548170000	27.064160000
C	27.780460000	9.465990000	26.399870000
C	32.799800000	21.867200000	20.570470000
C	33.362450000	23.177270000	20.531520000
C	32.645080000	24.232390000	21.138810000
C	31.395800000	24.045000000	21.768050000

C	30.849890000	22.740600000	21.777080000
C	31.544150000	21.671180000	21.191890000
C	34.682390000	23.442450000	19.846970000
C	30.657830000	25.195980000	22.417420000
C	33.195670000	18.213440000	14.362310000
C	33.353350000	19.184690000	13.327490000
C	32.929730000	18.847580000	12.024780000
C	32.371810000	17.589450000	11.701890000
C	32.218300000	16.649620000	12.742750000
C	32.615230000	16.963890000	14.053080000
C	33.960310000	20.538220000	13.610440000
C	31.969160000	17.253390000	10.282620000
C	31.374000000	9.416240000	20.524110000
C	31.047140000	8.082030000	20.128750000
C	30.473140000	7.223050000	21.091010000
C	30.226480000	7.620920000	22.423750000
C	30.547750000	8.946560000	22.787580000
C	31.106530000	9.830110000	21.849080000
C	31.334380000	7.574510000	18.735110000
C	29.684280000	6.641990000	23.442250000
C	27.096860000	12.636710000	21.357090000
C	26.002760000	12.421290000	22.246310000
C	25.670550000	11.088320000	22.583380000
C	26.367350000	9.970450000	22.072440000
C	27.458360000	10.211400000	21.206310000
C	27.814160000	11.522340000	20.860930000
C	25.227120000	13.569730000	22.845900000

C	25.964380000	8.557260000	22.431470000
C	26.973660000	11.424400000	17.528520000
C	26.826030000	10.009600000	17.619640000
C	25.638720000	9.498780000	18.186920000
C	24.599870000	10.324390000	18.665420000
C	24.759850000	11.723610000	18.543680000
C	25.924980000	12.262670000	17.979630000
C	27.914260000	9.065380000	17.170510000
C	23.369890000	9.739490000	19.320430000
C	37.553850000	12.569910000	18.124220000
C	38.429500000	11.452140000	17.968440000
C	39.821500000	11.680310000	18.018090000
C	40.384120000	12.962280000	18.208500000
C	39.498730000	14.048620000	18.377030000
C	38.108070000	13.851560000	18.339830000
C	37.895860000	10.054720000	17.765240000
C	41.883540000	13.168970000	18.209020000
C	28.265170000	17.213700000	15.780860000
C	27.277060000	16.753280000	14.856460000
C	27.331690000	17.234500000	13.531520000
C	28.353630000	18.095100000	13.068630000
C	29.361800000	18.465530000	13.980570000
C	29.305870000	18.047090000	15.319290000
C	26.258260000	15.710780000	15.243780000
C	28.368590000	18.590790000	11.640310000
C	38.324210000	17.619830000	19.435240000
C	39.481200000	18.160250000	18.801160000

C	40.747260000	17.815830000	19.324280000
C	40.909820000	16.969660000	20.442320000
C	39.747040000	16.448880000	21.054250000
C	38.476890000	16.766880000	20.552400000
C	39.363160000	19.078990000	17.608770000
C	42.283150000	16.622790000	20.972900000
C	37.627640000	14.016720000	23.250240000
C	38.668480000	14.279500000	24.194630000
C	39.957560000	13.775500000	23.925090000
C	40.264040000	13.029020000	22.763330000
C	39.225950000	12.802760000	21.834870000
C	37.932780000	13.296150000	22.075160000
C	38.416880000	15.104090000	25.433600000
C	41.660720000	12.498740000	22.522080000
C	33.233550000	19.249190000	25.142700000
C	33.342420000	19.705920000	26.492150000
C	33.211720000	21.087620000	26.742140000
C	33.011140000	22.036650000	25.716040000
C	32.905910000	21.561800000	24.393060000
C	33.003640000	20.188060000	24.112600000
C	33.622420000	18.753530000	27.629830000
C	32.935580000	23.514890000	26.028350000
C	29.221120000	21.461100000	16.766300000
C	27.864680000	21.865280000	16.957660000
C	27.116880000	22.260110000	15.827310000
C	27.657550000	22.302130000	14.523020000
C	29.015290000	21.950750000	14.368390000

C	29.778660000	21.535280000	15.469940000
C	27.233010000	21.891220000	18.328490000
C	26.802780000	22.685560000	13.334360000
C	36.893180000	19.954730000	24.398990000
C	36.814060000	21.378760000	24.423500000
C	36.796120000	22.028020000	25.676950000
C	36.863260000	21.332190000	26.901490000
C	36.965590000	19.923260000	26.853000000
C	36.972420000	19.247270000	25.624060000
C	36.747950000	22.188420000	23.152900000
C	36.800340000	22.069030000	28.220610000
C	34.795770000	9.011200000	22.102530000
C	34.205440000	8.243310000	23.148040000
C	33.825560000	6.914170000	22.863860000
C	34.019280000	6.311140000	21.603800000
C	34.622330000	7.087050000	20.588300000
C	34.996390000	8.416030000	20.833570000
C	33.961840000	8.826520000	24.517680000
C	33.599420000	4.881070000	21.350740000
C	37.195800000	14.127430000	14.761400000
C	38.585870000	14.446290000	14.788580000
C	39.513400000	13.407700000	14.560320000
C	39.128240000	12.075160000	14.301440000
C	37.746930000	11.782900000	14.276460000
C	36.799210000	12.792550000	14.504520000
C	39.072270000	15.846850000	15.065700000
C	40.163820000	10.992840000	14.094550000

H	28.488250000	19.447330000	28.267390000
H	25.389610000	18.998800000	25.248180000
H	26.604370000	17.031000000	24.309700000
H	29.986510000	16.284400000	27.889670000
H	30.252710000	17.987420000	28.456850000
H	30.893930000	17.424180000	26.865670000
H	25.344850000	20.331200000	28.085620000
H	25.749440000	21.225370000	26.583950000
H	26.898340000	21.222600000	27.977410000
H	30.719520000	12.020970000	11.169860000
H	28.772290000	15.233440000	13.359240000
H	30.161740000	14.706170000	15.358810000
H	33.439490000	11.544860000	13.234690000
H	32.310300000	10.627400000	12.162550000
H	32.249450000	10.431800000	13.961320000
H	29.123510000	14.963670000	10.451520000
H	27.730450000	14.087850000	11.158740000
H	28.906470000	13.217410000	10.106180000
H	30.239800000	9.913520000	27.533320000
H	27.723030000	11.176470000	24.214640000
H	29.506870000	12.764510000	23.482400000
H	33.261320000	11.355460000	26.429900000
H	32.362140000	10.818510000	27.903300000
H	32.498910000	12.572620000	27.483660000
H	28.220650000	8.574390000	26.901770000
H	27.153000000	9.113560000	25.550190000
H	27.093700000	9.949300000	27.135920000



H	33.087840000	25.249980000	21.113230000
H	29.873430000	22.552740000	22.268930000
H	31.108010000	20.651340000	21.211240000
H	35.490720000	22.791900000	20.255630000
H	34.989820000	24.505280000	19.960940000
H	34.624280000	23.203520000	18.759370000
H	30.413880000	24.968850000	23.482470000
H	29.691170000	25.402370000	21.898440000
H	31.258700000	26.131920000	22.398510000
H	33.057720000	19.603560000	11.221480000
H	31.768420000	15.659000000	12.535700000
H	32.462660000	16.223050000	14.866140000
H	33.357370000	21.103350000	14.360630000
H	34.027640000	21.150930000	12.684930000
H	34.979560000	20.443270000	14.052160000
H	31.370310000	18.070130000	9.816050000
H	31.365600000	16.319820000	10.249930000
H	32.863290000	17.094470000	9.634440000
H	30.226070000	6.185360000	20.782310000
H	30.351790000	9.303760000	23.817680000
H	31.350340000	10.871020000	22.149250000
H	30.938470000	8.263690000	17.952620000
H	30.886390000	6.567930000	18.577790000
H	32.433460000	7.505420000	18.556470000
H	28.970430000	5.920280000	22.983840000
H	29.165280000	7.167310000	24.275440000
H	30.507620000	6.039510000	23.897710000

H	24.829810000	10.922240000	23.290260000
H	28.047690000	9.364480000	20.799040000
H	28.664630000	11.697930000	20.167840000
H	25.899750000	14.219190000	23.460460000
H	24.405160000	13.198130000	23.497820000
H	24.789420000	14.227040000	22.058730000
H	25.176620000	8.546050000	23.218480000
H	26.836080000	7.966520000	22.800370000
H	25.560790000	8.017110000	21.540840000
H	25.529220000	8.397120000	18.265690000
H	23.964420000	12.406080000	18.905480000
H	26.039860000	13.362500000	17.897660000
H	28.211110000	9.244720000	16.111380000
H	27.593520000	8.005820000	17.278950000
H	28.841280000	9.215620000	17.778330000
H	23.294690000	8.643640000	19.142520000
H	22.437500000	10.220180000	18.945190000
H	23.393610000	9.900960000	20.425020000
H	40.497100000	10.807230000	17.899680000
H	39.897680000	15.066460000	18.553430000
H	37.426640000	14.716520000	18.485810000
H	37.350580000	9.697940000	18.672120000
H	38.721490000	9.339740000	17.554190000
H	37.165750000	10.021080000	16.924400000
H	42.418150000	12.337830000	18.724290000
H	42.158910000	14.122430000	18.712340000
H	42.284600000	13.216810000	17.167660000

H	26.549380000	16.894660000	12.820820000
H	30.210810000	19.089120000	13.643810000
H	30.085130000	18.380290000	16.036130000
H	26.768220000	14.735490000	15.446760000
H	25.524880000	15.544750000	14.423470000
H	25.708080000	15.979830000	16.172220000
H	28.369140000	17.743850000	10.913050000
H	29.268700000	19.215100000	11.440990000
H	27.465610000	19.207840000	11.415070000
H	41.648640000	18.238560000	18.834340000
H	39.829260000	15.774910000	21.930030000
H	37.572170000	16.341500000	21.035910000
H	38.868850000	18.566210000	16.749080000
H	40.361500000	19.438490000	17.276930000
H	38.725060000	19.961080000	17.846230000
H	42.438860000	15.518620000	21.001730000
H	42.421090000	16.993250000	22.015470000
H	43.087600000	17.065390000	20.344930000
H	40.761090000	13.980220000	24.663480000
H	39.426880000	12.243850000	20.899950000
H	37.130300000	13.120270000	21.329700000
H	38.143690000	16.150050000	25.151370000
H	39.322180000	15.145380000	26.078280000
H	37.563870000	14.706280000	26.030180000
H	42.415250000	13.320570000	22.493110000
H	41.719560000	11.949150000	21.556680000
H	41.978640000	11.799730000	23.331080000


H	33.291470000	21.438880000	27.792390000
H	32.744920000	22.273220000	23.561040000
H	32.908170000	19.830580000	23.065910000
H	32.886810000	17.918340000	27.659040000
H	33.596320000	19.287380000	28.605650000
H	34.625140000	18.280370000	27.516540000
H	32.080590000	23.753100000	26.705400000
H	32.817530000	24.116950000	25.100130000
H	33.859730000	23.866680000	26.544690000
H	26.056620000	22.557730000	15.973570000
H	29.485180000	21.986060000	13.365710000
H	30.840170000	21.244440000	15.329820000
H	27.165500000	20.866300000	18.771520000
H	26.205520000	22.315370000	18.284810000
H	27.840270000	22.497400000	19.041330000
H	26.036520000	21.901670000	13.117560000
H	27.422810000	22.810380000	12.418700000
H	26.248880000	23.638940000	13.504900000
H	36.732990000	23.136410000	25.692050000
H	37.037130000	19.341790000	27.794200000
H	37.042730000	18.141210000	25.601080000
H	37.604360000	21.957410000	22.477630000
H	36.746300000	23.278800000	23.372180000
H	35.820810000	21.947230000	22.575130000
H	36.965850000	23.160640000	28.084630000
H	37.561230000	21.691160000	28.941260000
H	35.803510000	21.939760000	28.707300000

H	33.351030000	6.321940000	23.673310000
H	34.798260000	6.646950000	19.585950000
H	35.446680000	9.023410000	20.022770000
H	34.906650000	9.195020000	24.981100000
H	33.498890000	8.077670000	25.197370000
H	33.276710000	9.708900000	24.455810000
H	34.474510000	4.187750000	21.360410000
H	33.108720000	4.771220000	20.356580000
H	32.884300000	4.528870000	22.127030000
H	40.594140000	13.658860000	14.580910000
H	37.402970000	10.748850000	14.072170000
H	35.718250000	12.546890000	14.487700000
H	38.653750000	16.578960000	14.336150000
H	40.182490000	15.898710000	15.030990000
H	38.740730000	16.185770000	16.078480000
H	41.105290000	11.406550000	13.668330000
H	39.793610000	10.197520000	13.408700000
H	40.427590000	10.499220000	15.061130000



Cite this: *J. Mater. Chem. A*, 2019, 7, 6387

## Electrospray deposition-induced ambient phase transition in copper sulphide nanostructures†

Arijit Jana,  Sourav Kanti Jana,  Depanjan Sarkar,  Tripti Ahuja, Pallab Basuri,  Biswajit Mondal, Sandeep Bose,  Jyotirmoy Ghosh  and Thalappil Pradeep \*

We introduce a new and simple method for synthesizing different phases of copper sulphide nanostructures using electrospray deposition (ESD) of molecular sulphur in the form of droplets on metallic copper surfaces under ambient conditions. Different phases of copper sulphide nanostructures were created by controlling the deposition time. Time dependent electron microscopy reveals conversion of the  $\text{Cu}_2\text{S}$  nanopyramids to  $\text{Cu}_{1.8}\text{S}$  platelets during the course of ESD. In the beginning of deposition, direct interaction between sulphur ions and metallic copper creates  $\text{Cu}_2\text{S}$  nanopyramids followed by subsequent slow diffusion of sulphur leading to the formation of copper deficient  $\text{Cu}_{1.8}\text{S}$  platelets. A detailed characterization of both the nanostructures was performed by using different microscopic and spectroscopic tools such as scanning electron microscopy (SEM), transmission electron microscopy (TEM), Raman spectroscopy, powder X-ray diffraction (PXRD) and X-ray photoelectron spectroscopy (XPS). We have also studied the optical properties of these nanostructures in both UV-Vis and near infrared (NIR) regions. The characteristic broad peaks in the UV-Vis region of  $\text{Cu}_2\text{S}$  nanopyramids indicate the photosensitive nature of the material. A positive photocurrent response was observed from the  $\text{Cu}_2\text{S}$  nanopyramids under electrochemical conditions, while  $\text{Cu}_{1.8}\text{S}$  nanostructure shows an intense localized surface plasmon (LSPR) peak in the NIR region indicating its metallic nature. Current–voltage ( $I$ – $V$ ) measurements showed metallic conductivity in them.

Received 1st January 2019  
Accepted 15th February 2019

DOI: 10.1039/c9ta00003h

rsc.li/materials-a

## Introduction

Among the different types of transition metals in the periodic table, copper (Cu) shows a great tendency to form different types of chalcogenides due to its high chalcogenicity.<sup>1</sup> Different types of main group metals (In, Ga, and Sn) as well as transition metals (Fe, Zn, and Cr) also form copper chalcogenide-based tertiary as well as multinary crystal structures.<sup>2–4</sup> Among all of these copper based multinary chalcogenides, binary chalcogenides such as  $\text{Cu}_{2-x}\text{S}$ ,  $\text{Cu}_{2-x}\text{Se}$ , and  $\text{Cu}_{2-x}\text{Te}$  are an interesting class of compounds due to their different electronic, magnetic and optical properties.<sup>5–8</sup> The electronic structure associated with their previous crystal phase and atomic dislocation within the lattice leads to variable energy bands.<sup>9</sup> Visible range optical absorption associated with the energy gap and NIR absorption due to defect-based charge carrier availability make them acquire different electronic properties such as semiconductivity and even metallicity.<sup>10,11</sup> Owing to their size, shape and composition-dependent tunable band gap and associated optical and plasmonic properties, they are promising

candidates for different applications such as optical limiting, thermoelectrics, photocatalysis, photoacoustics, metal ion batteries, sensors, photothermal therapies and biomedical applications.<sup>12–19</sup>

Among all of these binary copper chalcogenides, copper sulphide is an interesting one due to its several stoichiometric and nonstoichiometric crystal phases, associated with different properties.<sup>20</sup> Copper sulphide, a well-known p-type semiconducting material with a direct band gap ranging from 1.2 to 2.5 eV, exhibits various crystallographic forms, due to facile diffusion of copper and sulphur ions.<sup>21</sup> They form different stoichiometric copper sulphide phases such as covellite ( $\text{CuS}$ ) and chalcocite ( $\text{Cu}_2\text{S}$ ) as well as various nonstoichiometric phases such as djurleite ( $\text{Cu}_{1.94}\text{S}$ ), digenite ( $\text{Cu}_{1.8}\text{S}$ ), anilite ( $\text{Cu}_{1.75}\text{S}$ ), geerite ( $\text{Cu}_{1.6}\text{S}$ ), *etc.*<sup>22–26</sup> Thermal annealing and temperature dependent phase transitions among different copper sulphide phases make them prone to form mixed phases.<sup>27,28</sup> Therefore, it is important to find new synthetic ways to create different copper sulphide nanostructures under ambient conditions with a suitable morphology, shape and crystal structures.

Over the past few decades, significant progress has been made in the solution phase synthesis such as solvothermal methods, microfluidic synthesis, template directed synthesis, microwave assisted synthesis and colloidal phase hot injection

DST Unit of Nanoscience (DST UNS), Thematic Unit of Excellence (TUE), Department of Chemistry, Indian Institute of Technology Madras, Chennai – 600036, India. E-mail: pradeep@iitm.ac.in

† Electronic supplementary information (ESI) available. See DOI: 10.1039/c9ta00003h

methods for making different copper sulphide nanostructures.<sup>29–33</sup> Based on the molecular precursor, solvent and temperature associated with the synthetic conditions, different types of crystal phases and microstructural morphologies such as nanowires, nanosheets, nanocubes, nanowalls and hollow spheres were formed.<sup>34–38</sup> Since the solution phase synthesis of copper sulphide nanostructures, researchers were trying to make them in the solid state. Chemical vapor deposition (CVD) is the most common synthetic method which was extensively used for making high quality atomic layer thin films of copper sulphide for different applications.<sup>39,40</sup> Common CVD is a high temperature method which requires a copper plate as the source of copper and solid sulphur or hydrogen sulphide gas as the source of sulphur. High temperature processing is needed for making such materials for electronic applications.<sup>41</sup> Therefore, it is important to develop specific copper sulphide nanostructures under ambient conditions for practically viable applications.

Here, we introduce a completely new synthetic procedure for creating different copper sulphide nanostructures by an electrospray deposition (ESD) process under ambient conditions. ESD is an ionic charge droplet based synthetic tool for making different types of nanostructures under ambient conditions.<sup>42</sup> We have already shown that ESD can create metallic nanobrushes and nanoparticle assembled nanosheets which exhibit the highest water harvesting capacity, while being an excellent catalyst.<sup>43–45</sup> Previous studies have shown that ESD can produce surface enhanced Raman active nanoparticles.<sup>46</sup> In the present paper, we have used an ambient electrospray deposition technique for creating copper sulphide nanostructures under ambient conditions by interacting metallic copper with molecular sulphur ions. During the ESD process, Cu<sub>2</sub>S nanopyramids were formed initially on top of the metallic copper surface and after subsequent continuous sulphur spray, Cu<sub>1.8</sub>S platelets were formed on top of the Cu<sub>2</sub>S nanopyramids. After successful synthesis of these two nanostructures at different times of sulphur spray, we further demonstrated the phase-dependent change of optical properties. Based on the optical and charge carrier-based plasmonic properties of the materials, we further demonstrate the change in the electrical properties of the nanostructures. We show that the semiconducting Cu<sub>2</sub>S nanopyramids were gradually converted to metallic Cu<sub>1.8</sub>S platelets during the ESD process.

## Experimental section

### 1. Electrospray deposition technique

A home built electrospray source was used for delivering toluene-solvated charged droplets of sulphur towards the copper surface which was grounded. The electrospray source was made by pulling a borosilicate glass capillary (1.5 mm outer diameter and 0.86 mm inner diameter) by using a micropipette puller (P-97, Sutter Instruments, USA). The inner diameter of the formed glass capillary tip was 20 to 25  $\mu\text{m}$ . A spray plume was generated from the tip of the glass capillary by applying a DC potential of 1.50 to 1.80 kV between a platinum wire placed inside the capillary and the ground which produced a current of

10–15 nA. The capillary tip was manually placed over the copper plate at a distance of 5 to 8 mm and deposition was done. Although droplet dimensions have not been measured, they have been estimated to be in the range of 100 to 150 nm with a solution flow rate of 8 to 10  $\text{nL min}^{-1}$ , from various studies.<sup>47</sup> Detailed electrospray deposition experiments are described in the ESI.<sup>†</sup>

### 2. Materials used

The borosilicate glass capillary was purchased from Sutter instruments, USA. Both the copper TEM grid (without carbon coating) and the pure copper plate used as a copper source were purchased from SPI supplies and a local source, respectively. Copper plates were ultrasonically cleaned with acetone and isopropanol sequentially to remove organic contaminants. Platinum electrodes of 0.2 mm diameter were purchased from Sigma Aldrich, India. Sulphur powder (100 mesh, 99.5%) was purchased from Sigma Aldrich, India. Toluene (99.5%) and methanol (99.5%) were purchased from Merck, India and Finar, India, respectively. All the chemicals were commercially available and used without further purification.

### 3. Preparation of sulphur solution

Sulphur solution was made by refluxing 10 mg sulphur powder in 10 mL toluene at 120 °C under an argon atmosphere. After 10 hours of refluxion, a homogeneous solution was formed. Sulphur solution in toluene was mixed with 2 mL methanol for our electrospray deposition experiments.

## Results and discussion

For the synthesis of copper sulphide nanostructures under ambient conditions, ESD was carried out by spraying sulphur solution on a copper plate. The experimental set-up used for electrospray deposition (ESD) is shown in Fig. 1a. Ejection of the spray plume during the electrospray deposition process is shown in the inset of Fig. 1a. To understand the chemical nature of the as-synthesized sulphur solution, a mass spectrum was collected from the solvated spray plume by using a similar ESI source. Fig. 1b shows a feature assigned to  $[\text{S}_{24}(\text{C}_7\text{H}_8)]^+$ . The isotopic distribution pattern of the spectrum was well matched with the theoretical spectrum. During the preparation of sulphur solution in toluene at 120 °C, a toluene solvated trimer of S<sub>8</sub> was formed.<sup>48,49</sup> After the spray of sulphur, a black circular spot was formed over the copper surface. Fig. 1c shows an optical image of the copper plate after different times of sulphur deposition. From the optical image, it was observed that in the course of deposition, a dark black circular spot evolved with time on top of the copper plate. Sulphur ions ejected from the capillary tip interact with the copper on the surface and form chalcocite (Cu<sub>2</sub>S) nanopyramids initially due to superionic diffusion between copper and charged sulphur microdroplets and further continuous sulphur spray over the Cu<sub>2</sub>S nanopyramids creates digenite (Cu<sub>1.8</sub>S) platelets due to slow ionic diffusion of sulphur ions through the vacancy of the upper surface of Cu<sub>2</sub>S nanopyramids.<sup>50</sup> Fig. 1d shows the time

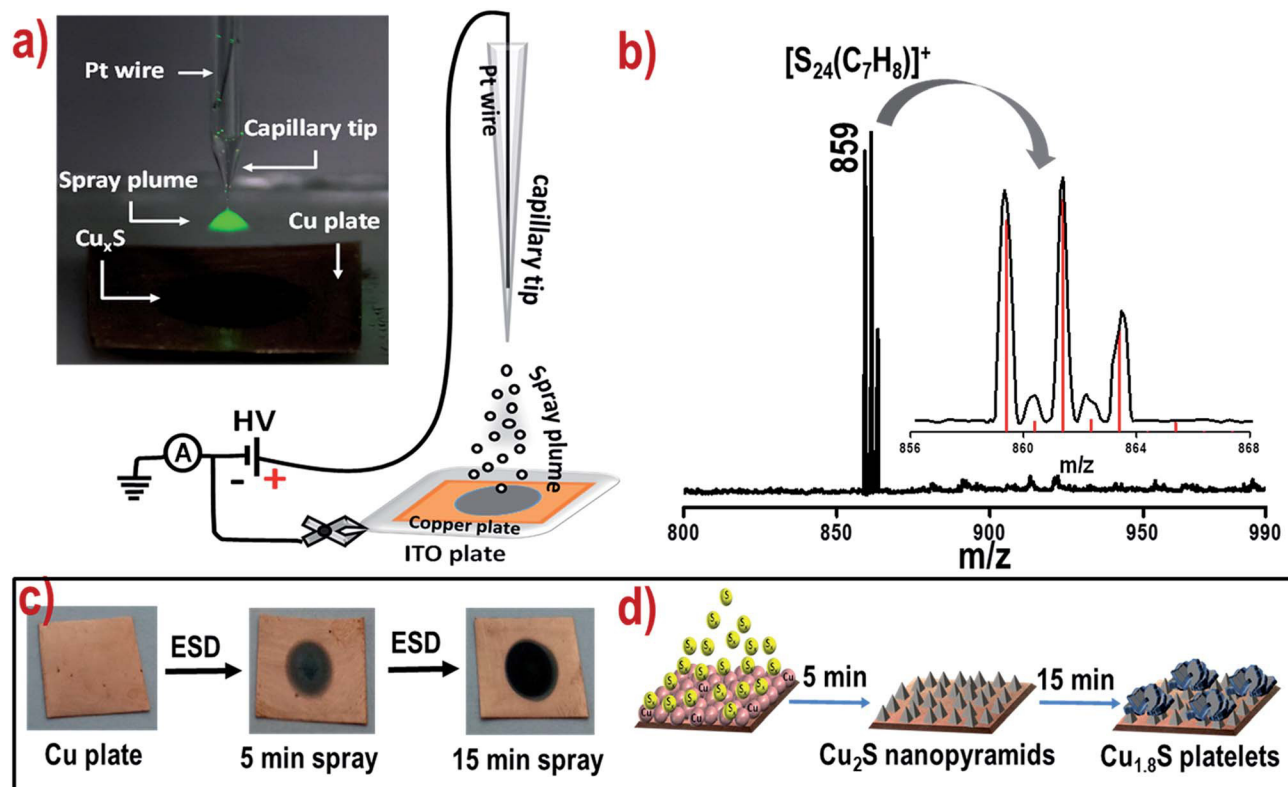


Fig. 1 (a) Schematic representation of the ESD set-up (inset shows the optical image of the spray plume), (b) ESI-MS spectrum of sulphur solution (inset spectrum in black shows the experimental spectrum and red lines show the theoretical spectrum), (c) time-dependent evolution of a black circular spot during ESD, and (d) schematic representation of the growth mechanism of chalcocite ( $\text{Cu}_2\text{S}$ ) nanopryramids and digenite ( $\text{Cu}_{1.8}\text{S}$ ) platelets during ESD.

dependent growth mechanism of both  $\text{Cu}_2\text{S}$  nanopryramids and  $\text{Cu}_{1.8}\text{S}$  platelets during the electro spray deposition process.

To observe the growth of different copper sulphide nanostructures during the ESD process, we have performed time-dependent scanning electron microscopy (SEM) measurements. Fig. 2a–c show SEM micrographs of the nanostructures grown over the copper surface with varying times of sulphur spray. After 2 to 5 min of S spray, a highly dense pyramidal morphology was formed with a 1 to 2  $\mu\text{m}$  edge length on the copper surface (Fig. 2a and b). More than 5 min of S spray creates randomly oriented platelets and their assembled dendritic structures.

Fig. S3† shows the time-dependent evolution of different copper sulphide nanostructures on copper plates as well as copper TEM grids. Both the copper surfaces show similar types of growth. Fig. S4 and S5† present the elemental composition of the nanopryramids and platelets through the point EDAX spectrum, which shows a copper to sulphur atomic ratio of 1.93 for nanopryramids and 1.80 for platelet nanostructures, respectively.

For further characterization of the as-prepared nanostructures, transmission electron microscopy (TEM) followed by Raman spectroscopy, powder X-ray diffraction (PXRD) and X-ray photoelectron spectroscopy (XPS) studies were performed. The TEM image shown in Fig. 2d reveals that the as-grown nanopryramids have a smooth surface with sharp edges. The high resolution TEM (HRTEM) image of the pyramidal surface shows

a lattice spacing of 0.24 nm, assigned to the (102) plane of the hexagonal chalcocite ( $\text{Cu}_2\text{S}$ ) phase (reference code 00-026-01116). A nanopryramid with 0.24 nm lattice spacing was seen along the surface indicating that the growth occurs along the (102) direction. More than 5 min of S spray creates randomly oriented platelets on top of the pyramids. From the TEM image in Fig. 2f, we observed crystalline growth of small particles on the outer surface of the platelets which indicates the possibility of further growth of the platelets. Well resolved lattice fringes observed in the HRTEM image under these conditions correspond to 0.32, 0.28 and 0.19 nm, attributed to the (111), (200) and (220) planes respectively, of cubic digenite ( $\text{Cu}_{1.8}\text{S}$ ) (reference code 01-072-1966).

Raman spectroscopic measurements were performed *ex situ* to understand the phase transformation from chalcocite ( $\text{Cu}_2\text{S}$ ) to digenite ( $\text{Cu}_{1.8}\text{S}$ ) during the electro spray deposition process. Fig. 3a shows the time-dependent Raman spectrum after different times of S spray. The characteristic S–S stretching peak at  $474\text{ cm}^{-1}$  indicates the formation of  $\text{Cu}_2\text{S}$  nanopryramids after 5 min of S spray. Raman imaging using the  $474\text{ cm}^{-1}$  mode in Fig. 3a (inset) clearly indicates  $\text{Cu}_2\text{S}$  growth on the copper surface. After more time (more than 5 min) of S spray, the  $474\text{ cm}^{-1}$  peak vanishes and a new peak at  $469\text{ cm}^{-1}$  arises, which indicates further growth of  $\text{Cu}_{1.8}\text{S}$  nanostructures on top of the nanopryramids. For the electro spray deposited sample, there was no additional impurity peak for copper oxide or excess



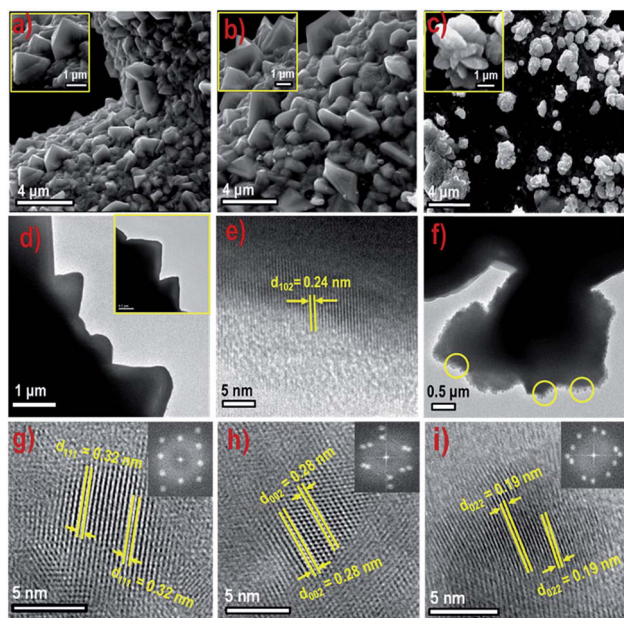


Fig. 2 (a–c) Large area SEM images at different times of deposition: (a) 2 min spray, (b) 5 min spray, and (c) 15 min spray (inset shows a higher magnification SEM image), (d) low magnification TEM image of  $\text{Cu}_2\text{S}$  nanoplatelets (inset depicts the higher magnification TEM image), (e) HRTEM of  $\text{Cu}_2\text{S}$  nanoplatelets, (f) TEM image of  $\text{Cu}_{1.8}\text{S}$  platelets, and (g–i) HRTEM image of  $\text{Cu}_{1.8}\text{S}$  platelets. Lattice parameters are marked and inset images show the corresponding FFT patterns.

sulphur on the copper surface which indicated uniformity in the crystal phase of both  $\text{Cu}_2\text{S}$  nanoplatelets and  $\text{Cu}_{1.8}\text{S}$  platelets.

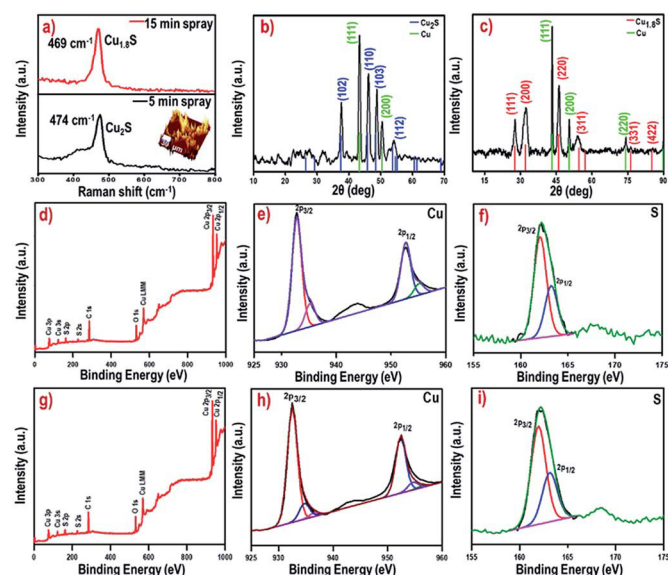


Fig. 3 (a) Raman spectra of copper sulphide nanostructures at different spray times (inset shows the Raman image corresponding to the  $474\text{ cm}^{-1}$  peak), (b) powder XRD pattern of  $\text{Cu}_2\text{S}$  nanoplatelets over the copper plate after 5 min of S spray, (c) powder XRD pattern of  $\text{Cu}_{1.8}\text{S}$  platelets, (d) survey XPS spectrum after 5 min of S spray and XPS spectra in the (e) Cu 2p and (f) S 2p regions, (g) survey XPS spectrum after 15 min of S spray and the corresponding XPS spectra in the (h) Cu 2p and (i) S 2p regions.

The phase and crystal structure of copper sulphide nanostructures were determined by powder X-ray diffraction (PXRD). To understand the time-dependent phase transformation during the electrospray deposition process, PXRD was performed by extracting the sample after different times of electrospray. Fig. 3b shows the PXRD pattern of blackish copper sulphide after 5 min of sulphur spray. From the PXRD pattern, we observed four prominent diffraction peaks at  $2\theta$  values of  $37.70^\circ$ ,  $46.21^\circ$ ,  $48.64^\circ$  and  $54.20^\circ$ . These four primary peaks were indexed to the (102), (110), (103) and (112) lattice planes, respectively of the chalcocite ( $\text{Cu}_2\text{S}$ ) phase with the space group of  $P6_3/mmc$  (reference code 00-026-1116). After confirming the chalcocite  $\text{Cu}_2\text{S}$  phase, we performed PXRD of the platelet nanostructures and the corresponding spectrum is shown in Fig. 3c. In Fig. 3c, we observed four prominent diffraction peaks at  $27.74^\circ$ ,  $32.46^\circ$ ,  $46.19^\circ$  and  $54.08^\circ$ . Upon careful analysis of the data and matching with a previous database, these peaks were indexed to the (111), (002), (022) and (113) planes of cubic digenite ( $\text{Cu}_9\text{S}_5$  or  $\text{Cu}_{1.8}\text{S}$ ) with the space group  $Fm\bar{3}m$  (reference code 01-072-1966). According to the previous literature, for digenite  $\text{Cu}_{1.8}\text{S}$ , both cubic and rhombohedral phases are closely related and it is very difficult to separate them.<sup>51</sup> Therefore, there is a chance of coexistence of both these phases.

In order to analyze the chemical binding states of different elements on the as-grown copper sulphide nanostructures, a time-dependent XPS study was performed. Copper plates were electrosprayed at different times and XPS spectra were measured. Fig. 3d shows the total XPS spectrum of the copper plate after 5 min of S spray. The total XPS spectrum shown in Fig. 3d contains Cu and S as well as carbon and oxygen, may be due to the adsorbed oxygen on the copper plate, which was exposed to ambient conditions. Fig. 3e shows the XPS spectrum of Cu 2p regions. Two primary peaks centered at 932.8 and 952.7 eV were assigned to Cu  $2p_{3/2}$  and Cu  $2p_{1/2}$ , respectively. After peak fitting, we got two peaks at 932.8 eV and 935.3 eV, due to the existence of Cu(0) as well as Cu(I) species. Similarly, two peaks at 952.7 eV and 955.2 eV were assigned to Cu  $2p_{1/2}$  of Cu(0) and Cu(I), respectively. This Cu(I) state represents the Cu(I) species present in the  $\text{Cu}_2\text{S}$  nanoplatelets. In the S 2p spectrum in Fig. 3f, we saw two peaks centered at 162.1 and 163.2 eV which were assigned to S  $2p_{3/2}$  and S  $2p_{1/2}$  of the  $\text{S}^{2-}$  species present in the  $\text{Cu}_2\text{S}$  nanoplatelets. Fig. 3g–j show the XPS spectra of  $\text{Cu}_{1.8}\text{S}$  platelets synthesized by 15 min sulphur spray. The survey spectrum shown in Fig. 3g presents the Cu, S, C and O peaks. In the Cu 2p XPS, two main peaks centered at 932.5 eV and 952.3 eV were seen, assigned to Cu  $2p_{3/2}$  and Cu  $2p_{1/2}$ , respectively, of the  $\text{Cu}_{1.8}\text{S}$  platelets. Shoulder peaks associated with these two primary peaks appear at 934.8 & 936.7 eV and 954.6 & 956.3 eV, due to the coexistence of Cu(I) and Cu(II)  $2p_{3/2}$  and  $2p_{1/2}$  doublets, respectively. Thus the formation of both Cu(I) and Cu(II) mixed states in  $\text{Cu}_{1.8}\text{S}$  platelets was clearly distinguishable in the XPS spectrum. Fig. 3i shows the XPS spectrum of sulphur showing peaks at 161.9 and 163.2 eV, due to S  $2p_{3/2}$  and S  $2p_{1/2}$  of the sulphide ( $\text{S}^{2-}$ ) in  $\text{Cu}_{1.8}\text{S}$ . Based on the Raman spectra, PXRD and XPS analysis, we can conclude that during electrospray deposition, chalcocite ( $\text{Cu}_2\text{S}$ ) nanoplatelets were formed first and  $\text{Cu}_{1.8}\text{S}$  platelets were grown subsequently.

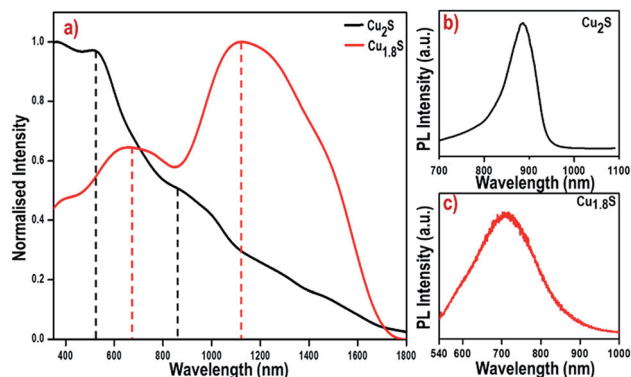


Fig. 4 (a) UV-Vis-NIR absorption spectrum of  $\text{Cu}_2\text{S}$  nanopyramids and  $\text{Cu}_{1.8}\text{S}$  platelets; (b and c) solid state photoluminescence spectrum collected by excitation with a 532 nm laser.

For gaining better insight into the electronic properties as well as band structure of the as-synthesized copper sulphide nanostructures, we studied their time-dependent solid-state UV-Vis NIR and solid-state photoluminescence. After spraying sulphur on the copper plate at different times, we have studied the optical response from the as-grown copper sulphide nanostructures in the solid state in the reflectance mode. For  $\text{Cu}_2\text{S}$  nanopyramids, there was a broad absorption maximum at 540 nm (2.29 eV) in the lower wavelength region, which indicated the indirect band gap of the semiconducting  $\text{Cu}_2\text{S}$  nanopyramids. There was a weak absorption offset in the 906 nm (1.36 eV) region, which indicated the direct band gap of the  $\text{Cu}_2\text{S}$  nanopyramids. Both these bandgaps were well matched with the previous literature.<sup>52,53</sup> Surprisingly, there was no NIR

absorption peak for the  $\text{Cu}_2\text{S}$  nanopyramids due to the unavailability of localized surface plasmons in the near infrared region. Fig. 4b shows the solid-state photoluminescence spectrum of  $\text{Cu}_2\text{S}$  nanopyramids. A 532 nm green laser (5 mW at the sample) was used as the excitation source for measuring solid-state photoluminescence from the nanostructures. A sharp photoluminescence emission peak observed at 890 nm (1.39 eV) due to indirect band to band transition for the nanopyramids. The sharpness of the emission peak is increased due to the well defined crystallinity of the nanopyramids.

After studying the optical properties of  $\text{Cu}_2\text{S}$  nanopyramids, we explored the optical properties of  $\text{Cu}_{1.8}\text{S}$  platelets grown by 15 min sulphur spray on a copper plate. From the UV visible NIR spectrum, we can see a broad absorption maximum at 712 nm (1.74 eV) which clearly indicates the band gap of  $\text{Cu}_{1.8}\text{S}$  platelets. In addition to the visible range absorption, there was a broad absorption maximum at 1134 nm (1.09 eV) in the NIR region. This NIR absorption band was attributed to the localized surface plasmon resonance (LSPR) due to the accumulation of a large number of free charge carriers, *i.e.*, holes within the nonstoichiometric  $\text{Cu}_{1.8}\text{S}$  phase. Copper deficiency in  $\text{Cu}_{1.8}\text{S}$  creates several holes which are responsible for the creation of surface plasmons in the NIR region.<sup>54,55</sup>  $\text{Cu}_{1.8}\text{S}$  platelets also show a broad photoluminescence peak in the 710 nm (1.74 eV) region due to the emissive band gap of  $\text{Cu}_{1.8}\text{S}$  platelets.

In addition to the detailed characterization of the different copper sulphide nanostructures, we have also investigated the photoelectrochemical properties of the chalcocite ( $\text{Cu}_2\text{S}$ ) nanopyramids and *I*-*V* characteristics of the digenite ( $\text{Cu}_{1.8}\text{S}$ ) platelets. To measure the photoelectrochemical properties of the as-synthesized  $\text{Cu}_2\text{S}$  nanopyramids, linear sweep voltammetry (LSV) was performed in 0.01 M  $\text{Na}_2\text{SO}_4$  solution. Prior to the measurement of the photoelectrochemical response, a copper plate ( $\sim 1 \text{ cm}^2$ ) was electro sprayed for 5 min with sulphur solution and subsequently, it was used as an electrode material for measuring the electrochemical response. During this electro-spray, mostly  $\text{Cu}_2\text{S}$  nanopyramids were formed on the substrate as already shown in the SEM micrographs. Fig. 5a shows the LSV plot of the photocurrent response under dark and light illumination conditions. A sharp increase of the photocurrent in the negative potential window (0 V to  $-0.55$  V) is observed from the above plot. The photocurrent increases sharply up to  $-0.12$  mA after light illumination; however, the current decreases within 1 s after turning off the light source. Fig. 5b shows the time resolved reversible photocurrent response measured by the chronoamperometry technique performed at  $-0.4$  V up to three cycles. The efficient photocurrent response from the  $\text{Cu}_2\text{S}$  nanopyramids results from the photoelectron transfer from the  $\text{Cu}_2\text{S}$  nanopyramids to the working electrode. Furthermore, to investigate the interfacial charge transfer behavior upon light illumination, we performed Electrochemical Impedance Spectroscopy (EIS) at  $-0.4$  V with frequency ranging from 1 MHz to 1 mHz with and without light illumination. From the Nyquist plot, we have found that there is a significant decrease of charge transfer resistance from  $170 \Omega$  to  $130 \Omega$  which indicates photocurrent generation upon light illumination.

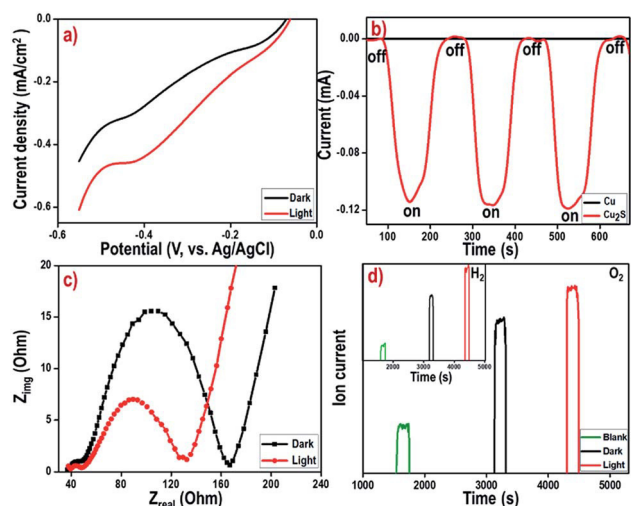


Fig. 5 (a) *I*-*V* characteristics of the as-grown  $\text{Cu}_2\text{S}$  nanopyramids under dark (black trace) and light illumination (red trace) in the presence of 0.01 (M)  $\text{Na}_2\text{SO}_4$  solution (light power 195 W), (b) chronoamperometric reversible photocurrent response from the as-grown electrode before and after light illumination (applied potential  $-0.4$  V vs. Ag/AgCl), (c) Nyquist plot of  $\text{Cu}_2\text{S}$  nanopyramids recorded at a fixed potential of  $-0.4$  V with respect to Ag/AgCl and (d) oxygen and hydrogen (inset) removal under dark and light conditions.

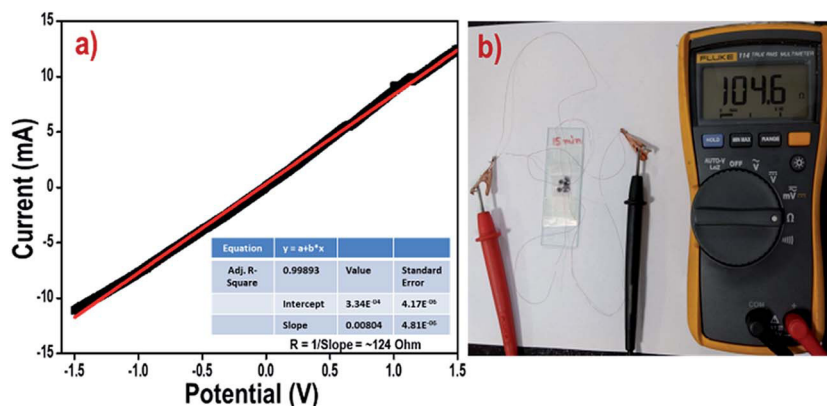


Fig. 6 Solid state electrical measurements of  $\text{Cu}_{1.8}\text{S}$  platelets: metallic behavior is shown by  $\text{Cu}_{1.8}\text{S}$  platelets. (a) Metallic  $I$ – $V$  characteristics of  $\text{Cu}_{1.8}\text{S}$  films with 124 ohm resistance and (b) resistance of the film measured by using a multimeter.

During the photoelectrochemical measurements, we observed gas evolution from both the working and counter electrodes, which is presumably due to the photoelectrochemical water splitting by the  $\text{Cu}_2\text{S}$  electrode. Photoelectrochemical total water splitting was also confirmed by mass spectrometry (MS) measurements. The mechanism of total water splitting can be realized with the help of an energy level diagram at the electrode electrolyte interface as shown in Fig. S6 of the ESI.† Both the optical band gap and energy level of both the conduction and valence bands are well matched for total water splitting, *i.e.* the conduction band should be above the thermodynamic potential of the  $\text{H}_2$  evolution (0 V) reaction ( $\text{H}^+ + \text{e}^- \rightarrow 1/2\text{H}_2$ ) and the valence band should be below the thermodynamic potential of the oxygen evolution (1.23 V) reaction ( $\text{OH}^- + \text{h}^+ \rightarrow 1/2\text{O}_2$ ). Upon photoexcitation of the working electrode ( $\text{Cu}_2\text{S}$ ), the photo-generated electrons flow towards the counter electrode (Pt) and react with  $\text{H}^+$  ions and produce  $\text{H}_2$  gas at the Pt electrode. Simultaneously, photogenerated holes react with  $\text{OH}^-$  anions and generate  $\text{O}_2$  at the working electrode. Fig. 5d shows the MS ion current data under dark as well as light illumination conditions. There is a sharp increase of ion current for both oxygen and hydrogen under light illumination conditions indicating that during light illumination, more amount of water splitting happens than that in the dark. Photo-induced charge carriers reduce the barrier height of this metal–semiconductor junction which increases the photocatalytic efficiency.

After studying the photoelectrochemical response of the  $\text{Cu}_2\text{S}$  nanoplatelets, we measured the  $I$ – $V$  characteristics of  $\text{Cu}_{1.8}\text{S}$  platelets. For that, we used a simple scotch tape technique to peel off the  $\text{Cu}_{1.8}\text{S}$  platelets and a film was prepared. Fig. S7† shows a schematic representation of the peeled off film. The continuity and the surface morphology of the film were confirmed through optical and scanning electron microscopy images. Fig. S8 and S9† show the optical images and SEM images of the platelet assembled film which show that it is continuous. We performed the electrical response measurement of the film by making four probe electrical connection using fine copper wires and silver paste. Fig. 6a shows the  $I$ – $V$  data of the film. During the voltage sweep from  $-1.5$  V to  $+1.5$  V at room temperature, we observed the ohmic conductivity of the

thin film and the linear fitting in the  $I$ – $V$  characteristics proved that  $\text{Cu}_{1.8}\text{S}$  platelets are metallic in nature. Reciprocal of the slope calculated from the  $I$ – $V$  characteristics shows a resistance of 124 ohm which clearly matches with the resistance measured by using a multimeter as shown in Fig. 6b.

## Conclusions

In conclusion, we have synthesized two different copper sulphide nanostructures by using ambient electrospray deposition techniques. Without using any solvent and harsh synthetic conditions, we selectively synthesized stoichiometric chalcocite ( $\text{Cu}_2\text{S}$ ) nanoplatelets and nonstoichiometric digenite ( $\text{Cu}_{1.8}\text{S}$ ) platelet structures, exclusively. The important issue in our experiment is tuning the morphology and proper structural control among a variety of copper sulphide phases ( $\text{Cu}_2\text{S}$  and  $\text{Cu}_{1.8}\text{S}$ ) by varying electrospray deposition time under ambient conditions. Gradual decrease of the diffusion rate of sulphur ions as well as surface energy barrier of copper atoms is most probably the reason for this phase transition from  $\text{Cu}_2\text{S}$  to  $\text{Cu}_{1.8}\text{S}$  nanostructures. Complete characterization of both the nanostructures was performed by using several spectroscopic tools. From optical measurements, we observed that due to the phase transition from  $\text{Cu}_2\text{S}$  nanoplatelets to  $\text{Cu}_{1.8}\text{S}$  platelets, there is a significant increase of localized surface plasmon absorption in the NIR region due to increase in copper deficiency in the  $\text{Cu}_{1.8}\text{S}$  crystal structure. For gaining better insight into the electrical properties of the nanostructures, we measured the photocurrent response of the  $\text{Cu}_2\text{S}$  nanoplatelets electrochemically. We observed that a positive photocurrent response arose from  $\text{Cu}_2\text{S}$  nanoplatelets under electrochemical conditions. We studied the electrical response of the  $\text{Cu}_{1.8}\text{S}$  platelets showing a sharp metallic conductance due to the accumulation of free charge carriers.

## Conflicts of interest

There are no conflicts to declare.



## Acknowledgements

The authors would like to thank Sophisticated Analytical Instrument Facility, Indian Institute of Technology Madras for solid state UV-Vis-NIR spectroscopic measurements. AJ, TA, PB, BM, and SB acknowledge financial support from IIT Madras. DS and JG thanks UGC, Govt. of India for their research fellowships. TP thanks the Department of Science and Technology, Govt. of India for supporting his research through the grant, SR/NM/TP-92/2016(G).

## References

- 1 P. Lukashev, W. R. L. Lambrecht, T. Kotani and M. Van Schilfgaarde, *Phys. Rev. B: Condens. Matter Mater. Phys.*, 2007, **76**, 1–14.
- 2 C. Coughlan, M. Ibáñez, O. Dobrozhan, A. Singh, A. Cabot and K. M. Ryan, *Chem. Rev.*, 2017, **117**, 5865–6109.
- 3 Z. Guan, A. Tang, P. Lv, Z. Liu, X. Li, Z. Tan, T. Hayat, A. Alsaedi, C. Yang and F. Teng, *Adv. Opt. Mater.*, 2018, **6**, 1–13.
- 4 K. E. Knowles, K. H. Hartstein, T. B. Kilburn, A. Marchioro, H. D. Nelson, P. J. Whitham and D. R. Gamelin, *Chem. Rev.*, 2016, **116**, 10820–10851.
- 5 P. Roy and S. K. Srivastava, *CrystEngComm*, 2015, **17**, 7801–7815.
- 6 G. Gariano, V. Lesnyak, R. Brescia, G. Bertoni, Z. Dang, R. Gaspari, L. De Trizio and L. Manna, *J. Am. Chem. Soc.*, 2017, **139**, 9583–9590.
- 7 C. M. Hessel, V. P. Pattani, M. Rasch, M. G. Panthani, B. Koo, J. W. Tunnell and B. A. Korgel, *Nano Lett.*, 2011, **11**, 2560–2566.
- 8 W. Li, R. Zamani, P. Rivera Gil, B. Pelaz, M. Ibáñez, D. Cadavid, A. Shavel, R. A. Alvarez-Puebla, W. J. Parak, J. Arbiol and A. Cabot, *J. Am. Chem. Soc.*, 2013, **135**, 7098–7101.
- 9 Y. Sun, L. Xi, J. Yang, L. Wu, X. Shi, L. Chen, J. Snyder, J. Yang and W. Zhang, *J. Mater. Chem. A*, 2017, **5**, 5098–5105.
- 10 Y. Wu, C. Wadia, W. Ma, B. Sadtlir, A. P. Alivisatos, M. Science, V. Di and L. Berkeley, *Nano Lett.*, 2008, **8**, 2551–2555.
- 11 S. C. Riha, D. C. Johnson and A. L. Prieto, *J. Am. Chem. Soc.*, 2011, **133**, 1383–1390.
- 12 X. Yu, C. Cao, H. Zhu, Q. Li, C. Liu and Q. Gong, *Adv. Funct. Mater.*, 2007, **17**, 1397–1401.
- 13 Z. H. Ge, B. P. Zhang, Y. X. Chen, Z. X. Yu, Y. Liu and J. F. Li, *Chem. Commun.*, 2011, **47**, 12697–12699.
- 14 (a) W. Fu, M. Liu, F. Xue, X. Wang, Z. Diao and L. Guo, *RSC Adv.*, 2016, **6**, 80361–80367; (b) Y. Yu, L. Pan, M. Son, M. T. Mayer and W. Zhang, *ACS Energy Lett.*, 2018, **3**, 760–766.
- 15 G. Ku, M. Zhou, S. Song, Q. Huang, J. Hazle and C. Li, *ACS Nano*, 2012, **6**, 7489–7496.
- 16 H. Park, J. Kwon, H. Choi, D. Shin, T. Song, X. Wen and D. Lou, *ACS Nano*, 2018, **12**, 2827–2837.
- 17 (a) X. Zhang, G. Wang, A. Gu, Y. Wei and B. Fang, *Chem. Commun.*, 2008, **45**, 5945–5947; (b) P. Sahatiya, A. Kadu, H. Gupta, P. T. Gomathi and S. Badhulika, *ACS Appl. Mater. Interfaces*, 2018, **10**, 9048–9059.
- 18 (a) M. Zhou, S. Song, J. Zhao, M. Tian and C. Li, *J. Mater. Chem. B*, 2015, **3**, 8939–8948; (b) Z. Zhang, H. Suo, X. Zhao, D. Sun, L. Fan and C. Guo, *ACS Appl. Mater. Interfaces*, 2018, **10**, 14570–14576.
- 19 S. Goel, F. Chen and W. Cai, *Small*, 2014, **10**, 631–645.
- 20 I. Grozdanov and M. Najdoski, *J. Solid State Chem.*, 1995, **114**, 469–475.
- 21 J. M. Luther, P. K. Jain, T. Ewers and A. P. Alivisatos, *Nat. Mater.*, 2011, **10**, 361–366.
- 22 M. Liu, X. Xue, C. Ghosh, X. Liu, Y. Liu, E. P. Furlani, M. T. Swihart and P. N. Prasad, *Chem. Mater.*, 2015, **27**, 2584–2590.
- 23 M. Lotfipour, T. MacHani, D. P. Rossi and K. E. Plass, *Chem. Mater.*, 2011, **23**, 3032–3038.
- 24 X. Zhang, Y. Xu, C. Pang, Y. Wang, L. Shen, A. Gupta and N. Bao, *CrystEngComm*, 2018, **20**, 2351–2356.
- 25 M. Shahriar Zaman, G. Bernard Grajeda and E. D. Haberer, *J. Appl. Phys.*, 2014, **115**, 144311.
- 26 H. Chen, M. Song, J. Tang, G. Hu, S. Xu, Z. Guo, N. Li, J. Cui, X. Zhang, X. Chen and L. Wang, *ACS Nano*, 2016, **10**, 1355–1362.
- 27 L. Liu, B. Zhou, L. Deng, W. Fu, J. Zhang, M. Wu, W. Zhang and B. Zou, *J. Phys. Chem. C*, 2014, **118**, 26964–26972.
- 28 P. Leidinger, R. Popescu, D. Gerthsen, H. Lünsdorf and C. Feldmann, *Nanoscale*, 2011, **3**, 2544–2551.
- 29 (a) Q. Lu, F. Gao and D. Zhao, *Nano Lett.*, 2002, **2**, 725–728; (b) F. Wang, Q. Li, L. Lin, H. Peng, Z. Liu and D. Xu, *J. Am. Chem. Soc.*, 2015, **137**, 12006–12012; (c) S. Han, C. Gu, S. Zhao, S. Xu, M. Gong, Z. Li and S. Yu, *J. Am. Chem. Soc.*, 2016, **138**, 12913–12919; (d) X. Chen, J. Yang, T. Wu, L. Li, W. Luo, W. Jiang and L. Wang, *Nanoscale*, 2018, **10**, 15130–15163.
- 30 I. Ortiz De Solorzano, M. Prieto, G. Mendoza, T. Alejo, S. Irusta, V. Sebastian and M. Arruebo, *ACS Appl. Mater. Interfaces*, 2016, **8**, 21545–21554.
- 31 S. Sun, S. Wang, D. Deng and Z. Yang, *New J. Chem.*, 2013, **37**, 3679–3684.
- 32 Y. Wang, X. Ai, D. Miller, P. Rice, T. Topuria, L. Krupp, A. Kellock and Q. Song, *CrystEngComm*, 2012, **14**, 7560–7562.
- 33 L. Liu, H. Zhong, Z. Bai, T. Zhang, W. Fu, L. Shi, H. Xie, L. Deng and B. Zou, *Chem. Mater.*, 2013, **25**, 4828–4834.
- 34 F. Zhang and S. S. Wong, *Chem. Mater.*, 2009, **21**, 4541–4554.
- 35 M. Ye, X. Wen, N. Zhang, W. Guo, X. Liu and C. Lin, *J. Mater. Chem. A*, 2015, **3**, 9595–9600.
- 36 W. Jiang, F. Wu, Y. Jiang, M. Sun, K. Zhang, Y. Xia, D. Wang and A. Xie, *Nanoscale*, 2017, **9**, 10961–10965.
- 37 P. Kar, S. Farsinezhad, X. Zhang and K. Shankar, *Nanoscale*, 2014, **6**, 14305–14318.
- 38 J. Gao, Q. Li, H. Zhao, L. Li, C. Liu, Q. Gong and L. Qi, *Chem. Mater.*, 2008, **20**, 6263–6269.
- 39 M. Xu, H. Wu, P. Da, D. Zhao and G. Zheng, *Nanoscale*, 2012, **4**, 1794.
- 40 L. Reijnen, B. Meester, F. De Lange, J. Schoonman and A. Goossens, *Chem. Mater.*, 2005, **17**, 2724–2728.
- 41 A. Itzhak, E. Teblum, O. Girshevitz, S. Okashy, Y. Turkulets, L. Burlaka, G. Cohen-taguri, E. S. Avraham, M. Noked, I. Shalish and G. D. Nessim, *Chem. Mater.*, 2018, **30**, 2379–2388.

- 42 A. Li, Q. Luo, S. Park and R. G. Cooks, *Angew. Chem., Int. Ed.*, 2014, **53**, 3147–3150.
- 43 D. Sarkar, M. K. Mahitha, A. Som, A. Li, M. Wlekinski, R. G. Cooks and T. Pradeep, *Adv. Mater.*, 2016, **28**, 2223–2228.
- 44 D. Sarkar, R. Singh, A. Som, C. K. Manju, M. A. Ganayee, R. Adhikari and T. Pradeep, *J. Phys. Chem. C*, 2018, **122**, 17777–17783.
- 45 D. Sarkar, A. Mahapatra, A. Som, R. Kumar, A. Nagar, A. Baidya and T. Pradeep, *Adv. Mater. Interfaces*, 2018, **5**, 1800667.
- 46 A. Li, Z. Baird, S. Bag, D. Sarkar, A. Prabhath, T. Pradeep and R. G. Cooks, *Angew. Chem., Int. Ed.*, 2014, **53**, 12528–12531.
- 47 A. Schmidt, M. Karas and T. Du, *J. Am. Soc. Mass Spectrom.*, 2003, **0305**, 492–500.
- 48 B. Meyer, *Chem. Rev.*, 1976, **76**, 367–388.
- 49 T. P. Martin, *J. Chem. Phys.*, 1984, **81**, 4426–4432.
- 50 (a) Q. Zhang, Z. Shi, K. Yin, H. Dong, F. Xu, X. Peng, K. Yu, H. Zhang, C. Chen, I. Valov, H. Zheng and L. Sun, *Nano Lett.*, 2018, **18**, 5070–5077; (b) X. Liu, M. T. Mayer and D. Wang, *Angew. Chem., Int. Ed.*, 2010, **49**, 3165–3168.
- 51 G. Will, E. Hinze and A. R. M. Abdelrahman, *Eur. J. Mineral.*, 2002, **14**, 591–598.
- 52 S. C. Riha, R. D. Schaller, D. J. Gosztola, G. P. Wiederrecht and A. B. F. Martinson, *J. Phys. Chem. Lett.*, 2014, **5**, 4055–4061.
- 53 P. Lukashev, W. R. L. Lambrecht, T. Kotani and M. van Schilfgaarde, *Phys. Rev. B*, 2007, **76**, 195202.
- 54 Y. Zhao, H. Pan, Y. Lou, X. Qiu, J. Zhu and C. Burda, *J. Am. Chem. Soc.*, 2009, **131**, 4253–4261.
- 55 Y. Liu, M. Liu and M. T. Swihart, *J. Phys. Chem. C*, 2017, **121**, 13435–13447.

## Supplementary Information

### Electrospray Deposition-Induced Ambient Phase Transition in Copper Sulphide Nanostructures

Arijit Jana, Sourav Kanti Jana, Depanjan Sarkar, Tripti Ahuja, Pallab Basuri, Biswajit Mondal, Sandeep Bose, Jyotirmoy Ghosh, Thalappil Pradeep\*

DST Unit of Nanoscience (DST UNS) and Thematic Unit of Excellence (TUE), Department of Chemistry, Indian Institute of Technology, Madras, Chennai – 600036, India.

\*Email: [pradeep@iitm.ac.in](mailto:pradeep@iitm.ac.in)

#### Table of Contents

Item	Description	Page No.
	Experimental section	2-3
	Instrumentation	3
Fig. S1	Optical images of the capillary tip	4
Fig. S2	TEM images of sulphur spray over a TEM grid	5
Table S1	Voltage and distance dependent spray current measurements during ESD	6
Fig. S3	SEM image of copper sulphide growth at different copper substrate	7
Fig. S4	EDAX spectrum of Cu <sub>2</sub> S nanopyramids	7
Fig. S5	EDAX spectrum of Cu <sub>1.8</sub> S platelets	8
Fig. S6	Schematic representation of the photoelectrochemical process on Cu <sub>2</sub> S nanopyramids	9
Fig. S7	Schematic representation of scotch tape peeled off method of Cu <sub>1.8</sub> S platelets	10
Fig. S8	Optical microscopic images of Cu <sub>1.8</sub> S platelets assembled film	10
Fig. S9	SEM images of Cu <sub>1.8</sub> S platelets assembled film	11

## Experimental Section

### 1) Electrospray deposition:

Electrospray deposition experiments were carried out using a home-made nanospray emitter. For all the ESD experiments, a glass capillary emitter was tailored by pulling borosilicate glass capillary of proper dimension (0.86 mm inner diameter, 1.5 mm outer diameter and 1.5 cm length) using a micropipette puller instrument (P-97) purchased from Sutter instruments, USA. A platinum filament was used to cut the glass capillary into two parts. Prior to making ultrafine capillary tip (20 to 25  $\mu\text{m}$ ), operating conditions of the micropipette puller were set as heating temperature of 565  $^{\circ}\text{C}$ , initial and final pull velocities of 11  $\mu\text{m}/\text{sec}$  and 9  $\mu\text{m}/\text{sec}$ , respectively. Optical microscopic images of the as prepared capillary tips are shown in the Fig. S1. Sulphur solution in toluene: methanol mixture (8:2, v/v) was filled in the capillary tip, by using a capillary injector. Finally, a platinum wire connected with the positive terminal of the high voltage DC power supply was inserted inside the capillary and while the negative terminal was connected to the copper plate to generate the spray plume. Formation of spherical sulphur was observed during ESD. Fig. S2 shows the TEM images of the sulphur particles with diameters of 100 to 150 nm, after 1 min sulphur spray over the TEM grid. A  $532 \pm 10$  nm ( $\leq 10$  mW) green laser pointer was used for confirming the generation of the spray plume. This laser pointer was purchased from UKTECHLAB, UK. During ESD, spray current was measured by using a Keithley Picoammeter. All the spray current data are summarized in Table S1. To confirm the chemical nature of the spray plume, mass spectrum was collected using an ion trap LTQ XL (Thermo Scientific) mass spectrometer.

### 2) Solution phase photoconductivity measurements of $\text{Cu}_2\text{S}$ nanopyramids:

For the photoelectrochemical measurements of the  $\text{Cu}_2\text{S}$  nanopyramids, a CHI600A potentiostat was used, while impedance spectroscopic measurements were carried out by using a Bio-Logic SP-200 instrument. Both the electrochemical measurements were performed in 0.01 (M)  $\text{Na}_2\text{SO}_4$  solution, used as an electrolyte. A 195 W white light source from Newport, India was used as a source for solar energy irradiation. The formation of the gas bubbles during photo-electrochemical process was analyzed by a ThermoStar Balzer MS instrument. Quadstar 32 Bit software was used to record the data.

### 3) Solid state conductivity measurements of $\text{Cu}_{1.8}\text{S}$ platelets assembled film:

For studying the electrical property of the  $\text{Cu}_{1.8}\text{S}$  platelets, we peeled off the platelets by using a Scotch tape. Basic schematic representation of the peeled off methods was shown in Fig. S8. After etching the platelets from the copper plate, a black thin film was formed on the Scotch-tape. Continuous

arrangements of the platelets was confirmed by using optical and SEM images, shown in Fig. S9 and S10, respectively. This film was used to measure the electrical conductivity. Afterwards, we made four probe contacts on the film by using silver paste and ultrafine copper wires. Among four contacts, two contacts were connected to the positive terminal and while the other two contacts were connected to the negative terminal of the potentiostat. A CHI600A instrument was used to study the current-voltage (I-V) response of the film in a wide potential range (-1.5V to +1.5V).

## **Instrumentation**

### **1) Microscopic characterization:**

All the SEM measurements were performed using a FEI Quanta environmental scanning electron microscope (ESEM) in the high vacuum mode. EDAX spectra were recorded using the same instrument. TEM measurements were performed using a JEOL 3010 high resolution transmission electron microscope (HRTEM) operated at 200 kV. A Gatan 794 multiscan CCD camera was used for image collection. All the optical microscopic images were collected using a LEICA optical microscope with LAS V4.8 software.

### **2) Spectroscopic characterization:**

Raman spectroscopic measurements were carried out by using a confocal Raman microscope, CRM Alpha 300 S, WITec GmbH, Germany by using 532 nm frequency doubled Nd: YAG laser with 40 mW output power (sample power was used  $\leq 5$  mW). X Ray photoelectron spectroscopy (XPS) measurements were carried out using an ESCA probe TPD equipped with polychromatic Mg K $\alpha$  X ray light source ( $h\nu = 1253.6$  eV). Powder XRD measurements were conducted using a D8 Advance Bruker, using Cu K $\alpha$  as the X Ray source ( $h\nu = 8047.8$  eV).

Optical absorption spectroscopic measurements were carried out in the solid state, by using a Perkin Elmer LAMBDA 950 UV-VIS-NIR spectrophotometer. Spectrum was collected in the diffuse reflectance mode (% R) using 60 mm integrating sphere. Perkin Elmer UV Win-lab 6.4.0.973 software was used to collect the spectrum in reflectance mode and the spectrum was converted to Kubelka Munk (K-M) absorption spectrum. Solid state photoluminescence spectral measurements were carried out using the same Raman microscope.



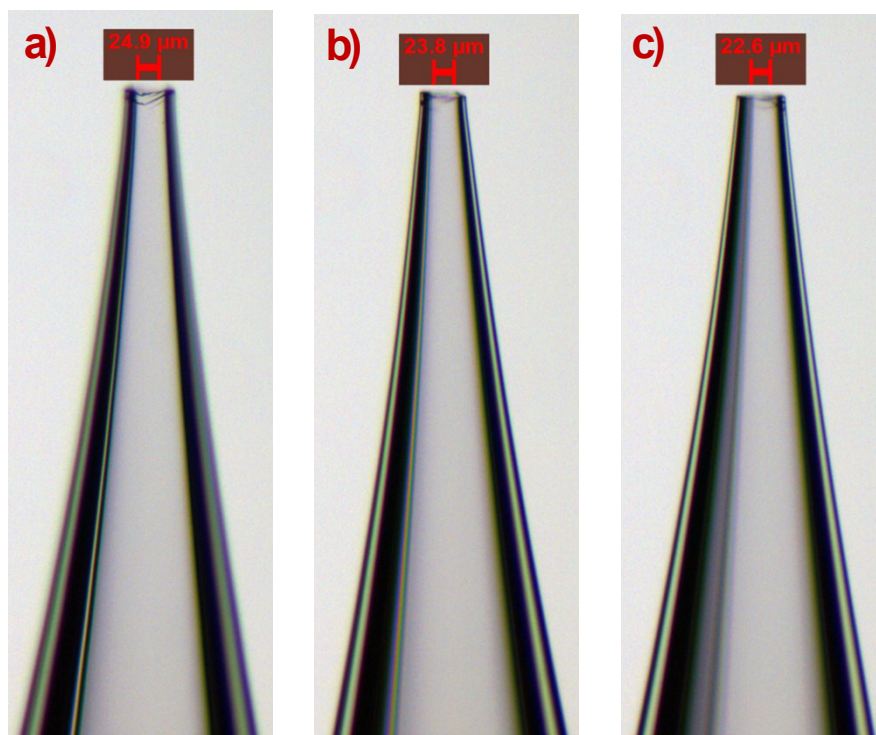


**Fig. S1** Optical microscopic images of three different capillary tips, made separately with tip diameters of a) 24.9, b) 23.8 and c) 22.6  $\mu\text{m}$ .

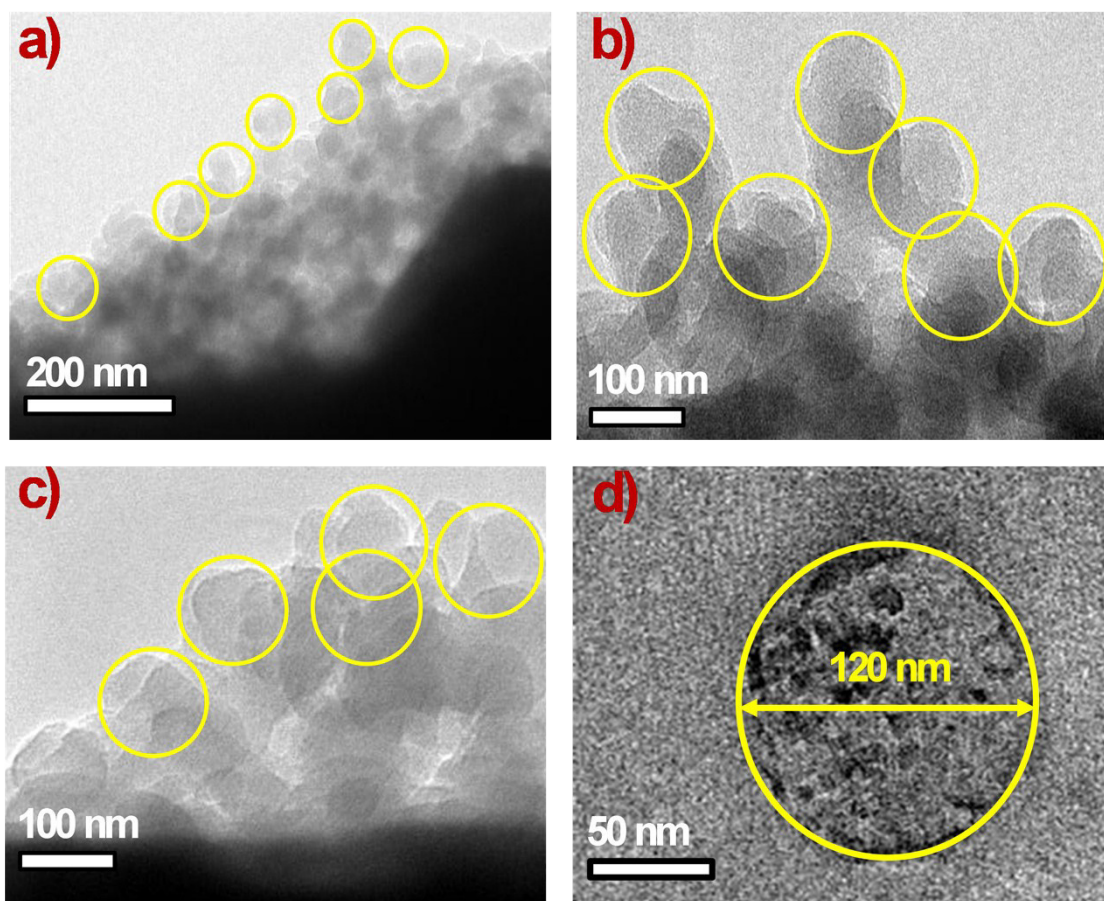


**Fig. S2** TEM images of the sulphur particles forms during ESD over a TEM grid after 1 min of deposition, a) image at lower magnification, b, c) images at higher magnification at two different regions, d) Single particle of amorphous sulphur.

**Table S1** Spray current measurements at varying applied voltages and tip to collector distances.

Tip to collector distance	Applied voltage	Spray current	Remarks
6 mm	1.3 kV	0.01440 nA	no spray
	1.4 kV	0.03084 nA	no spray
	1.5 kV	9.93265 nA	spray plume
	1.6 kV	11.6066 nA	spray plume
	1.7 kV	12.0823 nA	spray plume
	1.8 kV	14.5945 nA	spray plume
	1.9 kV	23.3021 nA	liquid Jet spray
	2.0 kV	28.9206 nA	liquid Jet spray
	2.1 kV	37.837 nA	liquid Jet spray
	2.2 kV	49.499 nA	liquid Jet spray
2 mm	1.65 kV	36.205 nA	liquid jet spray
4 mm		20.2080 nA	liquid jet spray
6 mm		10.3652 nA	spray plume
8 mm		9.5611 nA	spray plume
10 mm		0.2356 nA	no spray
12 mm		0.01249 nA	no spray

- ❖ Spray current in the range of 10 to 15 nA is suitable for gentle spray emission. Spray currents more than 20 nA is due to liquid jet formation and it is inappropriate for the experiments.

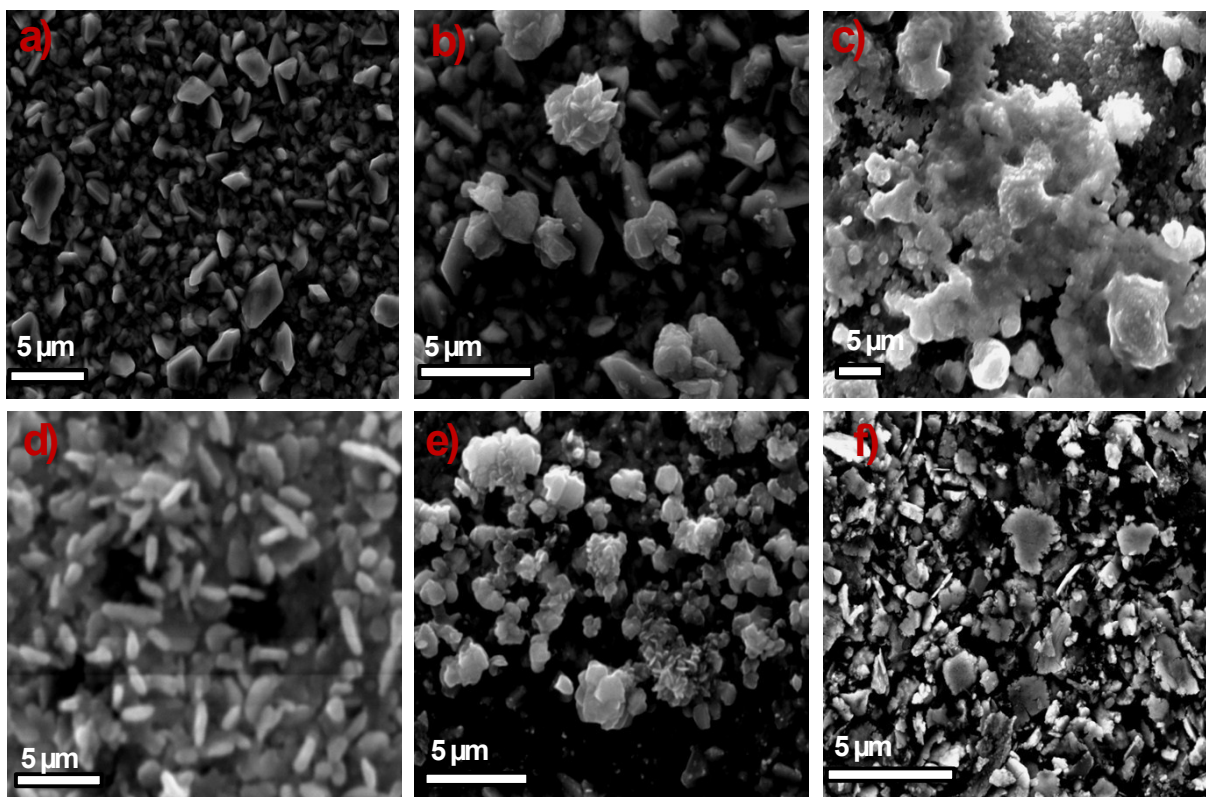


**Fig. S3** a, b, c) SEM images of the TEM grid after different times of sulphur spray (a) 3 min, (b) 7 min, (c) 30 min. d, e, f) SEM images of the copper plate after different time of spray, (d) 7 min, (e) 15 min and (f) toluene extracted platelets after 15 mins of spray.

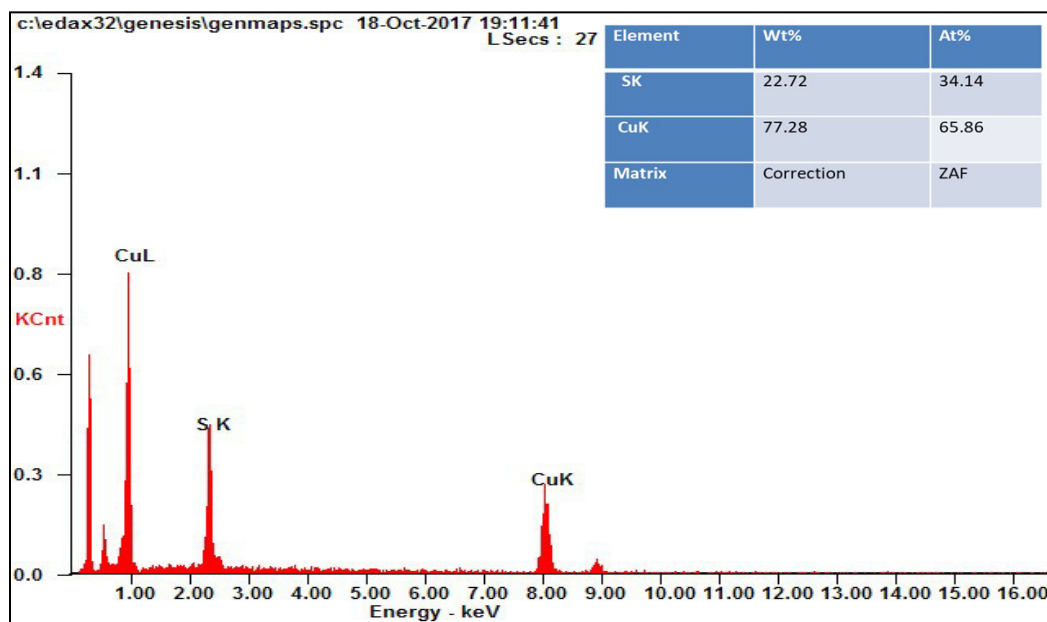


**Fig. S4** EDAX spectrum of the  $\text{Cu}_2\text{S}$  nanoplatelets (inset shows the elemental distribution of the  $\text{Cu}_2\text{S}$  nanoplatelets).

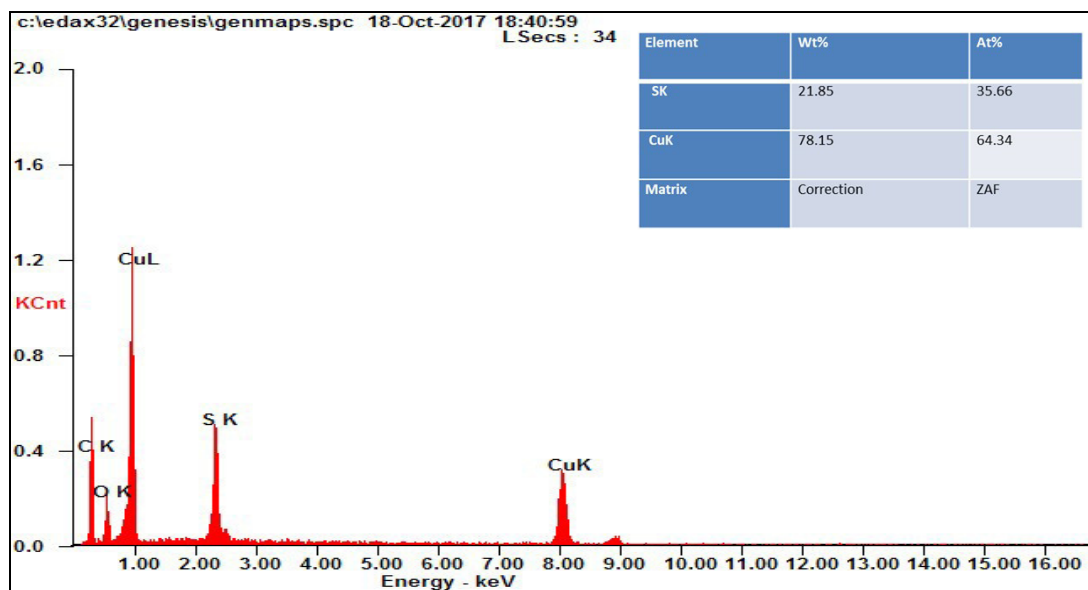


**Fig. S5** EDAX spectrum of the  $\text{Cu}_{1.8}\text{S}$  platelets (inset shows the elemental distribution for the  $\text{Cu}_{1.8}\text{S}$  platelets).

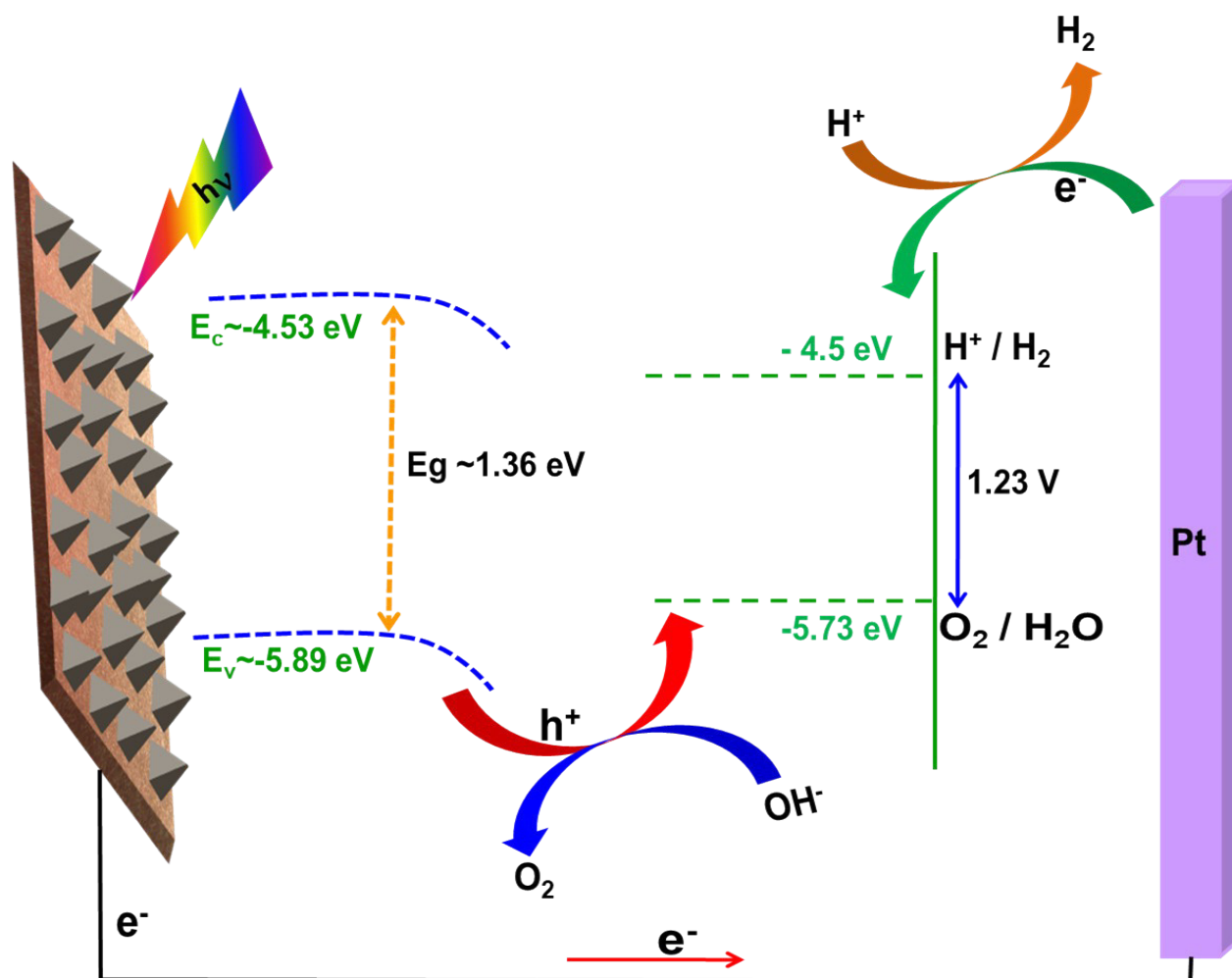


**Fig. S6** Schematic representation of the photoelectrochemical process at Cu<sub>2</sub>S nanopyramids.



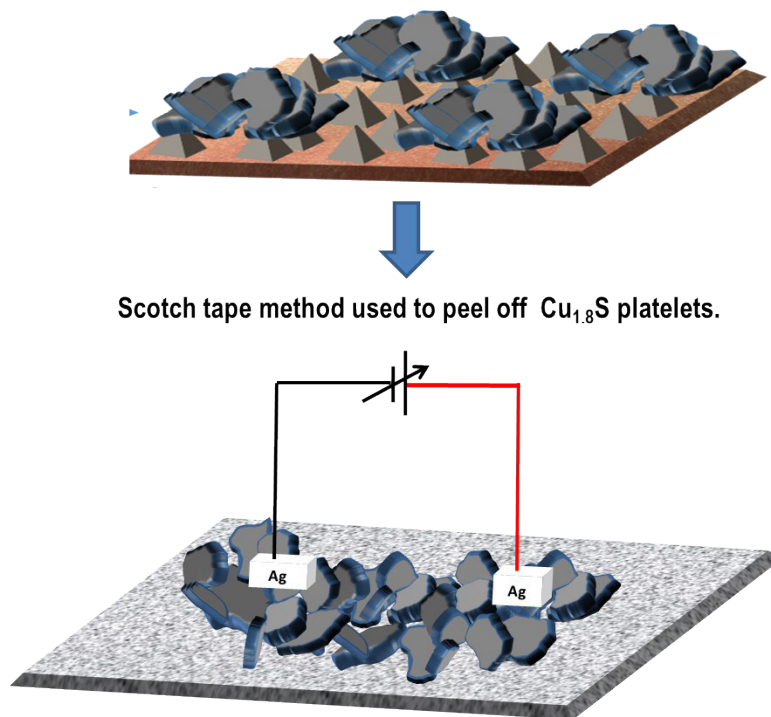


**Fig. S7** Schematic representation of the scotch tape peeled off method of Cu<sub>1.8</sub>S platelets and electrical circuit preparation for solid state conductivity measurements.

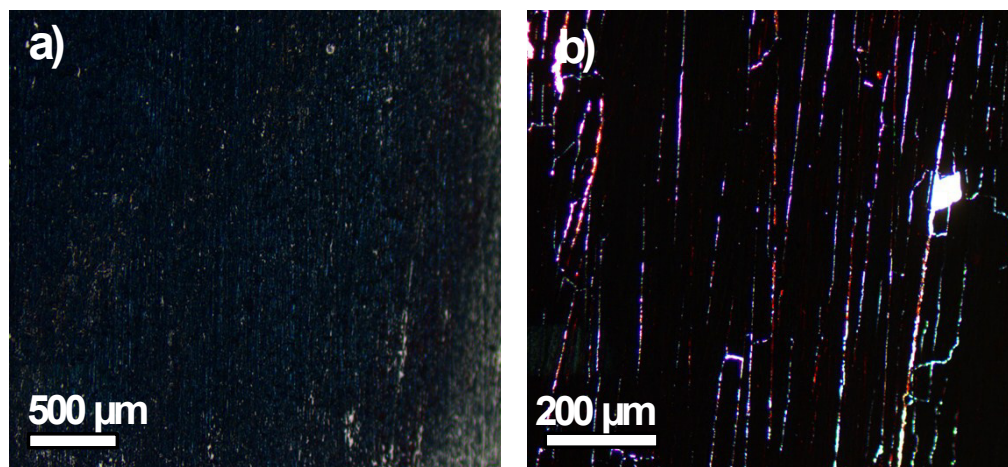


**Fig. S8** Optical microscopic images of the film made by Cu<sub>1.8</sub>S platelets at different a) 10X and b) 40X magnification.



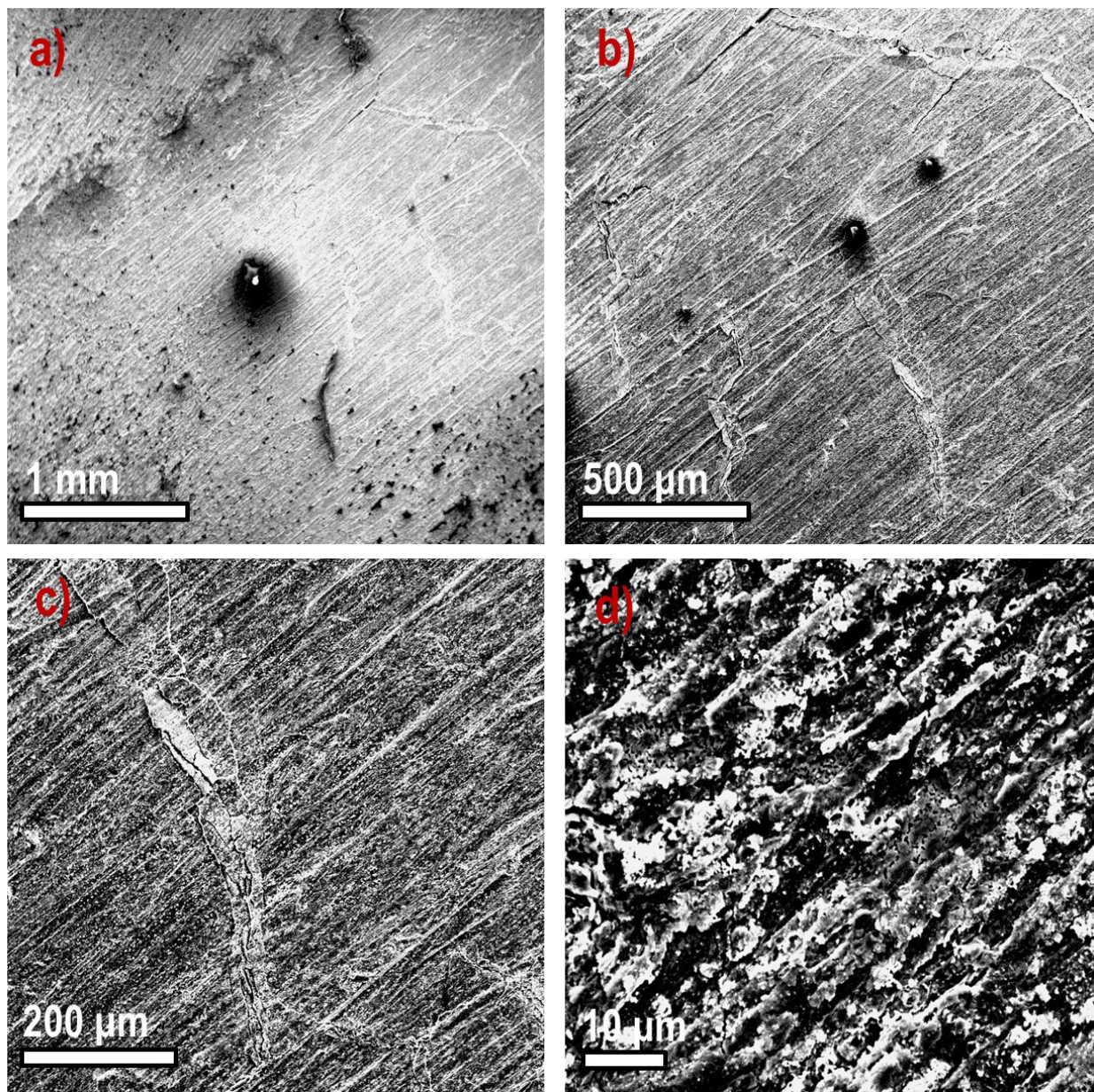


**Fig. S9** SEM images of the film under different magnification, a, b) lower magnification and c, d) higher magnification.



## RESEARCH ARTICLE

# Spatial distribution mapping of molecules in the grains of different rice landraces, using desorption electrospray ionization mass spectrometry

Arunan Suganya<sup>1</sup>  | Debal Deb<sup>2</sup>  | Thalappil Pradeep<sup>1</sup> 

<sup>1</sup>DST Unit of Nanoscience, and Thematic Unit of Excellence, Department of Chemistry, Indian Institute of Technology Madras, Chennai 600 036, India

<sup>2</sup>Centre for Interdisciplinary Studies, Barrackpore, Kolkata 700 123, India

**Correspondence**

Thalappil Pradeep, DST Unit of Nanoscience, and Thematic Unit of Excellence, Department of Chemistry, Indian Institute of Technology Madras, Chennai 600 036, India.  
Email: pradeep@iitm.ac.in

**Funding information**

Department of Science and Technology

**Rationale:** Documentation of the metabolite profiles of rice landraces is essential as most of them have been lost due to the conventional practices of cultivation. Therefore, application of mass spectrometry imaging (MSI) will be an appropriate analytical platform for molecular profiling, as it can provide a detailed understanding of the site-specific localization patterns of biomolecules, and the cues concerning metabolic pathways in organisms.

**Methods:** Desorption electrospray ionization mass spectrometry (DESI-MS) is a relatively non-destructive analytical technique for surface sampling in natural conditions. Here, we report the spatial distribution of diverse molecules in the grains of different rice landraces of India using DESI-MSI. Molecules were identified by ESI-MS and tandem MS analysis of rice extracts. Scanning electron microscopy (SEM) and energy-dispersive X-ray spectroscopy (EDS) were used for the elemental mapping on the rice grains.

**Results:** DESI-MSI showed a uniform distribution of choline ( $m/z$  104.1), sucrose in the form of its sodium ( $m/z$  365.1) and potassium ( $m/z$  381.0) adducts, linoleic acid ( $m/z$  279.2), 13-HODE-9-HODE ( $m/z$  295.2), unidentified molecules with  $m/z$  535.3, 559.5, and 561.5 and isoschaftoside ( $m/z$  563.1) in the endosperm of rice grains. Gluconic acid ( $m/z$  195.0) and signalling phospholipid intermediate molecules were localized in the embryo whereas oryzanol A ( $m/z$  601.5) and oryzanol C ( $m/z$  615.5) had a restricted localization in the bran region of the grain. SEM-EDS mapping showed the localization of potassium and phosphorus along the bran and embryo.

**Conclusions:** DESI-MSI revealed the distribution of lipids and sugar molecules in the specific regions of the rice grains. Thus, molecules unique to some rice varieties were identified with this analytical platform. Mass spectrometry imaging of rice along with the elemental mapping by SEM-EDS will be of use in understanding the localization pattern of certain molecules in the context of metals present in the grain.

## 1 | INTRODUCTION

Metabolomics is one of the rapidly evolving key “omics strategies” employed in plant research. Understanding the complex metabolome of a biological sample is feasible today with the availability of various forms of mass spectrometry. The capability to combine the spatial information along with the chemical fingerprints of the specimen makes imaging mass spectrometry a useful, and much preferred, analytical platform for plantomics.<sup>1</sup> Based on the nature of ionization, a number of imaging mass spectrometry methods such as matrix-assisted laser desorption/ionization mass spectrometry (MALDI-MS), secondary ion mass spectrometry (SIMS), desorption electrospray ionization mass spectrometry (DESI-MS) and several other variants of these broad techniques are available for capturing the site-specific molecular mapping of biological samples.

Rice is the staple cereal of about half of the world's population.<sup>2</sup> Adverse environmental effects and the use of toxic agrochemicals have resulted in the accumulation of metals in rice which are issues of serious concern. Arsenic accumulation in rice has led to stringent quality restrictions on its imports in many parts of Europe. Besides such environmental effects, natural bioaccumulation of prevalent minerals such as silver has also been reported.<sup>3</sup> Although environmental effects have been significant and have been studied largely from the point of view of toxicity, mineral fortification and other dietary enhancements of rice are also important.<sup>4</sup> A rapid fingerprinting of molecular species expressed in rice and their spatial distribution in the rice grain would help build up an important dietary database for rice consumers. Vitamins and mineral fortification in specific regions of rice grain, along with socio-cultural practices involved in the processing of rice, will contribute to health benefits.<sup>5</sup> The natural accumulation of organic osmolytes such as glycine betaine, proline, trehalose, mannitol, and fructan will enable the plant to thrive under adverse environmental conditions.<sup>6</sup> Some rice landraces inherently possess heritable traits for tolerance of diseases and edapho-climatic stress such as drought and salinity.<sup>7</sup> Application of molecular imaging platforms to scout for such rice varieties and an understanding of the key molecules linked with their inherent stress tolerant properties will be useful in crop improvement.

Previous reports on rice grain imaging using MALDI-MS provided information about the spatial distribution of phospholipids and anthocyanins.<sup>8–10</sup> Although MALDI-MSI allows identification of macromolecules like proteins, it is not efficient to image the molecules in the low molecular weight range due to the interferents from the matrices applied on the sample. Therefore, any imaging tool of this kind employed on biological materials would be more beneficial if performed under natural conditions. This would enable such studies at various developmental stages of the tissue such as during germination. Mass spectrometry, especially using ambient ionization methods, can be advantageous in undertaking such studies. One of the most prominent methods of ambient ionization imaging mass spectrometry is desorption electrospray ionization mass spectrometry (DESI-MS) where ionization is achieved by the impingement of charged solvent

droplets at surfaces.<sup>11</sup> DESI-MSI was widely used to study the molecules expressed on the surfaces of delicate plant or animal tissues.<sup>12,13</sup> Compared with imaging of lipids in mammalian samples, the lipid imaging in plant samples is not well addressed by DESI-MSI.<sup>14</sup> This is the first work to report the localization of lipids and other unknown molecular entities on rice grains by DESI-MSI. We present a systematic investigation of this imaging methodology performed on several rice landraces of India.

## 2 | EXPERIMENTAL

### 2.1 | Chemicals and materials

Commercially available methanol (MeOH) (Honeywell Riedel-de Haen LC/MS ultra chromasolv tested for UHPLC/MS, Sigma Aldrich) was used in our experiments without any further purification. HPLC grade *N,N*-dimethyl formamide (DMF), acetonitrile (ACN) and propan-2-ol (IP) were purchased from Rankem. Samples of ten rice (*Oryza sativa* ssp. *indica*) landraces G2 (Garib-sal), G28 (Gouri sundari), G38 (Gazep xali), H24 (Hugi bhatta), H34 (Hende baihar), K11 (Kataribhog), K86 (Kala nuniya), R09 (Radha tilak), T05 (Tiki), and T11 (Tike churi) were obtained from the seed bank of the Centre for Interdisciplinary Studies, Kolkata (<http://www.cintdis.org/basudha>). G28, H24, K11, K86 and R09 are aromatic. All these rice varieties are cultivated and conserved in Basudha farm in the southern Odisha district, Rayagada (19°42'32.0"N, 83°28'8.4"E), and grown in an organic environment without application of chemical fertilizers and pesticides.

### 2.2 | Sample preparation

Dehusked, unpolished rice grains were used for our study. To remove moisture, the rice grains were vacuum desiccated for 2 days at 10<sup>−2</sup> mbar. For embedding, two parts of epoxy resin (Technovit EPOX resin and EPOX hardener regular (A) procured from Chennai Metco, India, Cat. No: TECH001 & TECH002) mixed with one part of hardener was poured over the desiccated rice samples aligned on a silicone mould. The embedded samples were air cured at room temperature for 24 h. A rotary cutter (Discoplan TS, Struers, Denmark) was used to cut the resin blocks to a thickness of 3 mm. The cut resin blocks were further polished to a flat surface for DESI-MS imaging using a belt sander machine. The resin block with embedded rice grains was fixed directly on to the DESI-MS stage using double-sided adhesive tape.

### 2.3 | Metabolite extraction

Fresh rice samples were frozen in liquid nitrogen and ground to form a powder. The powdered rice samples were stored at −20°C until further analysis. The ground rice samples were extracted with methanol, and centrifuged at 20,000 g for 20 min, and refrigerated at −20°C for 2 days to precipitate the large molecules. The samples

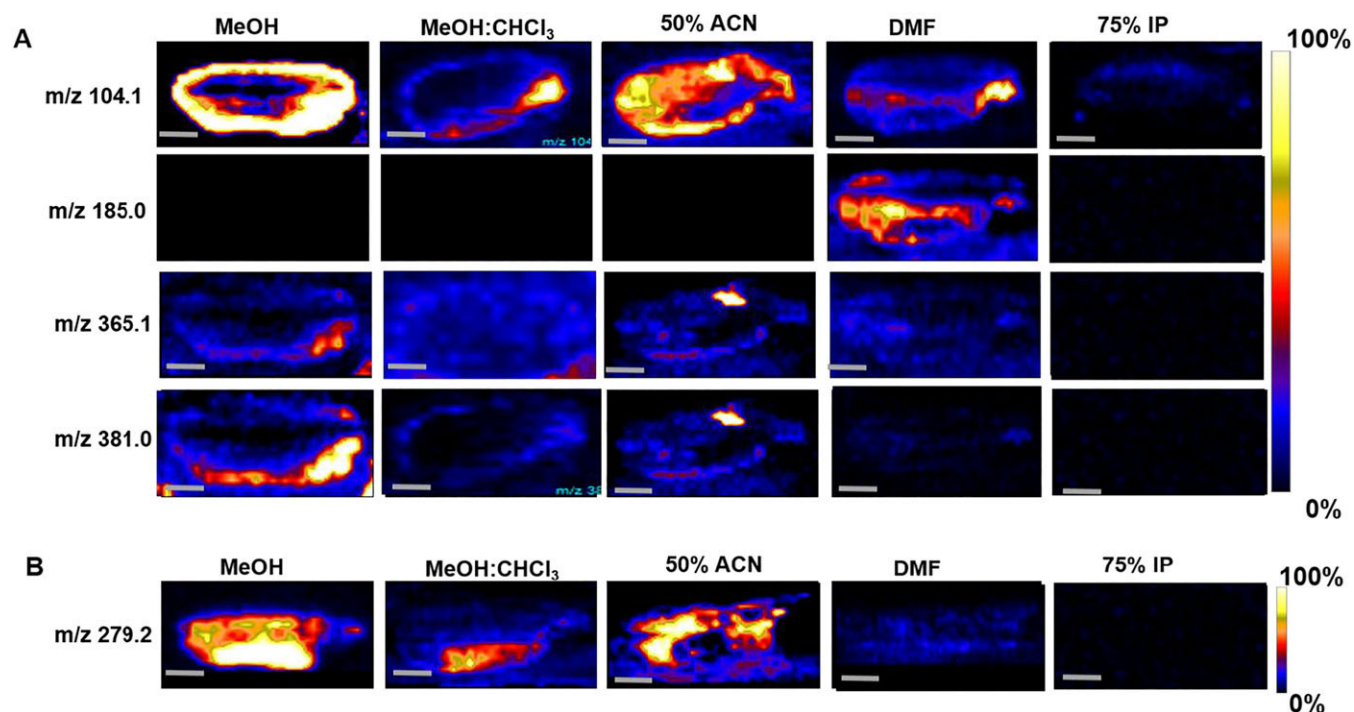


**FIGURE 1** DESI-MS imaging of H24 rice using different solvents as spray solvent. Molecular images from A) positive and B) negative ion mode imaging. The ion intensities of the images are normalized across the rows. All the images have a uniform scale bar of 1 mm [Color figure can be viewed at [wileyonlinelibrary.com](http://wileyonlinelibrary.com)]

were centrifuged again at 20,000 *g* for 20 min and metabolites were concentrated using a rotary evaporator. The concentrated samples were diluted 100 times prior to MS analysis.

### 3 | INSTRUMENTATION

#### 3.1 | DESI-MS imaging of rice grains

A LTQ XL linear ion trap mass spectrometer (Thermo Scientific, San Jose, CA, USA) fitted with a DESI source (Prosolia, Indianapolis, IN, USA) was used for the imaging experiments. The flat rice sections

were mounted directly onto the 2D moving stage of the mass spectrometer using double-sided tape. The samples were scanned over a mass range of *m/z* 50–1000. Methanol was the spray solvent for imaging in both positive and negative ionization mode. The operating conditions were as follows: spray tip to sample distance 2 mm, tip to mass spectrometer inlet 2 mm, solvent spray angle 60°, solvent flow rate 5  $\mu$ L/min, spray voltage  $\pm 5$  kV, capillary temperature 250°C, capillary voltage  $\pm 45$  V, tube-lens voltage  $\pm 100$  V and nebulizing gas pressure ( $N_2$ ) 100 psi. The area of imaging was fixed depending on the rice grain size ( $\sim 3$  mm). The pixel size (spatial resolution) was set to 200  $\mu$ m  $\times$  200  $\mu$ m. Imaging was performed on the single rice grains of different varieties

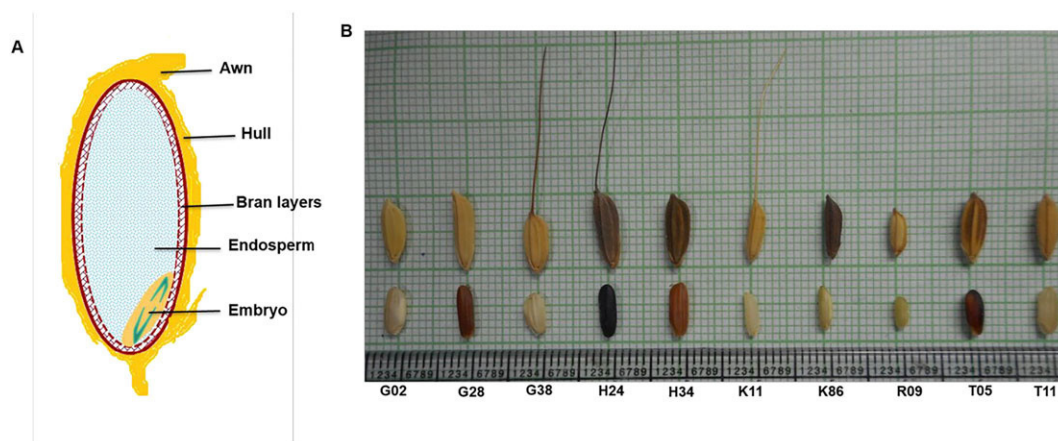


**FIGURE 2** A, Schematic representation of the anatomy of the rice grain. B, Photograph of the spikelets (top row) and dehulled (bottom row) grains of ten rice landraces of India used in this study. The grains were placed on a graph paper with grid lines of 1 mm width [Color figure can be viewed at [wileyonlinelibrary.com](http://wileyonlinelibrary.com)]

individually. For DESI-MSI experiments, the auto gain control (AGC) was off. Each line scan spectrum obtained as an Xcalibur raw file was processed using the Firefly software for creating an image file. The constructed 2D ion images were visualized in BioMap software (<http://www.maldi-msi.org>) in an interpolate display method.

### 3.2 | ESI-MS analysis

The electrospray ionization (ESI) source of the Thermo LTQ mass spectrometer was used for analysis. The data were acquired using Xcalibur Quant software. The diluted samples were sprayed by applying a voltage of 5 kV in both the ionization modes with a mass range of  $m/z$  50–1000. The capillary temperature was set to 250°C,  $N_2$  sheath gas flow rate was 10 arbitrary units, solvent flow rate was

set at 5  $\mu\text{L}/\text{min}$ , and tube lens voltage was  $\pm 100\text{ V}$ . Collision-induced dissociation (CID) fragmentation was carried out for the specific ion peaks from the MS analysis with an isolation width of 1.0  $m/z$ . Utilizing the spectral details, the metabolites were annotated using several publicly available databases such as METLIN, ReSpec, LipidMaps, KEGG, MassBank, and also published literature.

### 3.3 | Electron microscopy imaging and elemental characterization.

The surface morphology imaging by scanning electron microscopy (SEM) and energy-dispersive X-ray spectroscopy (EDS) analysis for the elemental composition and mapping on the rice grain surface was performed using a FEI QUANTA 200 scanning electron microscope.

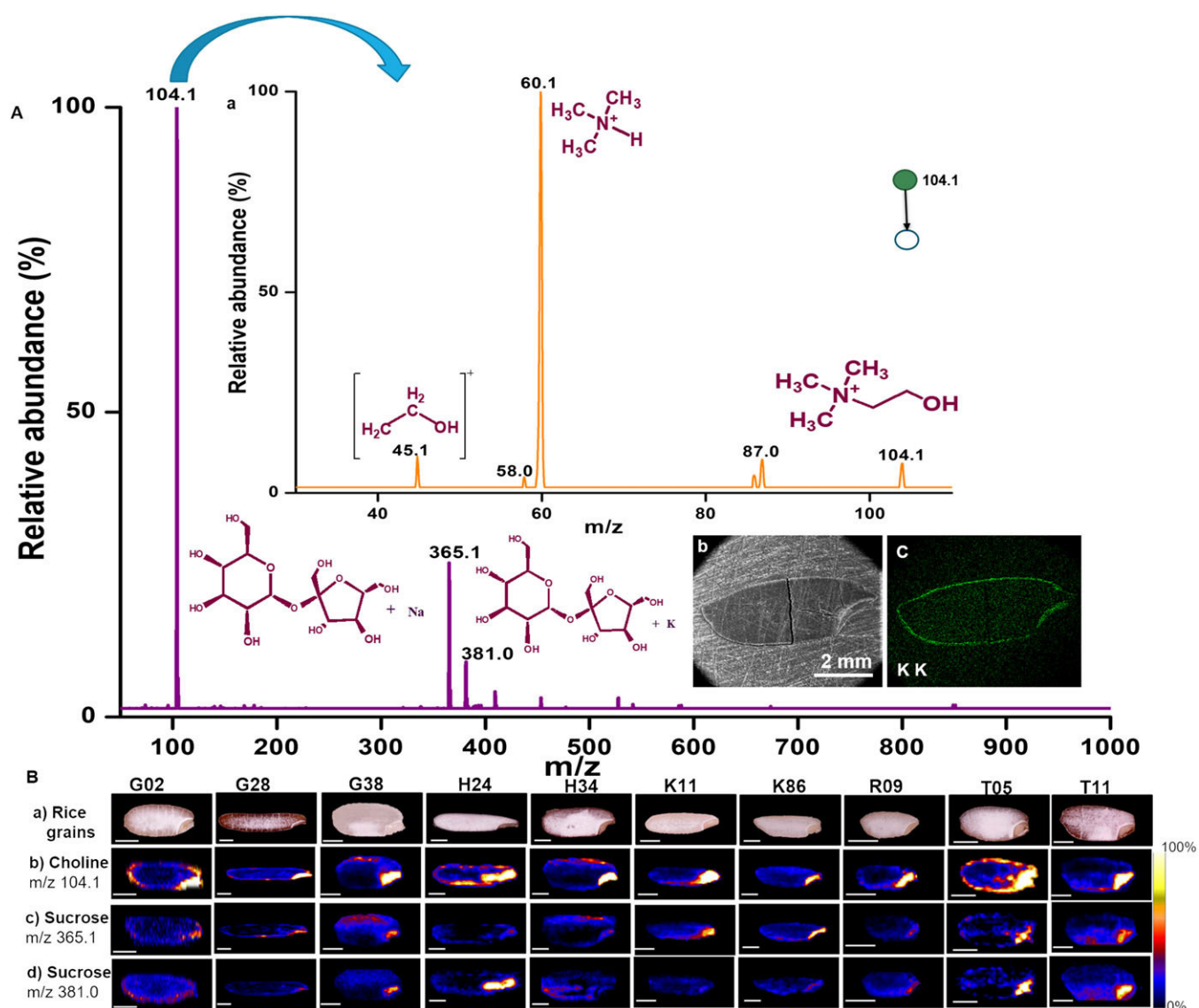


**FIGURE 3** A, A representative line scan spectrum collected from the grain surface in positive ion mode of DESI-MS, the inset represents: a) tandem MS spectrum of choline at  $m/z$  104.1, b) SEM image of G2 rice grain section, and c) EDAX image showing the distribution of potassium in the G2 grain. B, a) optical images of rice grain cut surface, molecular images of b) protonated choline, c) sodiated sucrose, and d) potassiated sucrose. The scale bars in the images correspond to 1 mm [Color figure can be viewed at [wileyonlinelibrary.com](http://wileyonlinelibrary.com)]



## 4 | RESULTS AND DISCUSSION

DESI-MSI aids in the direct detection of metabolites expressed on a tissue/organ surface under ambient atmospheric conditions without tedious sample preparation protocols. However, in the present case, embedding and sectioning of rice grain was necessary to obtain a flat cross section of the specimen and rice otherwise is too hard to cut. The charged solvent spray based ionization of DESI-MSI is nearly non-destructive to the sample as it does not use high-energy lasers as in MALDI-MSI. The literature suggests that mounting of the sample with epoxy resin does not generate any interfering mass signals.<sup>14</sup> Figure S1 (supporting information), showing the DESI-MS spectrum collected from the embedded grain surface, proves that the resin does not interfere with the molecular imaging of rice. The imaging resolution in DESI-MS is greatly influenced by its operating parameters like the shape of the emitter, gas flow rate, the distance

between the spray tip and mass spectrometer inlet, the nature of the spray solvent, and so on. A number of modifications were made to the shape and size of the emitter tip in order to achieve a resolution below 100  $\mu\text{m}$  in DESI-MS.<sup>15-17</sup> In our work, we tried to image rice grain features using a typical DESI-MS spray emitter without any modifications. The composition of solvent and the influence of solvent on surface wettability are other crucial factors which influence the signal ion intensity and the image quality.<sup>18</sup> Although most of the studies employ organic solvent mixtures as spray solvent, 100% methanol gave good signal ion intensity for rice metabolites compared with 50% and 95% methanol (Figure S2, supporting information). We tested an array of solvents, e.g. 100% MeOH, 50% ACN, DMF, 75% IP and MeOH:CHCl<sub>3</sub>(1:1 v/v). (Figure 1) 50% ACN, DMF, MeOH:CHCl<sub>3</sub> and MeOH gave almost the same chemical information in positive ion mode. DMF is considered to be a morphologically friendly spray solvent as the

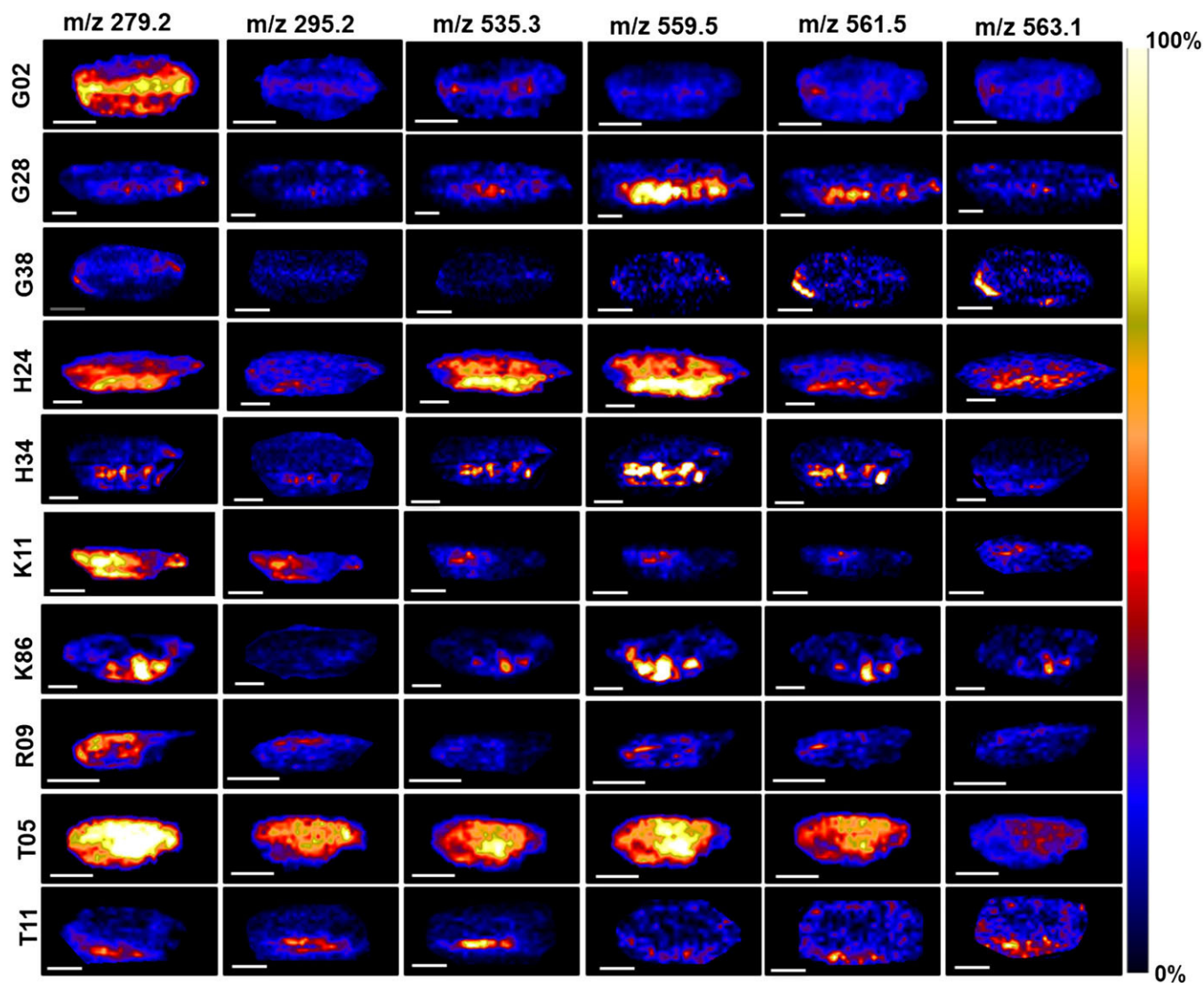


**FIGURE 4** Negative ion mode DESI-MS images of rice grains showing the distribution of linoleic acid ( $m/z$  279.2), 13-HODE-9-HODE ( $m/z$  295.2), and unidentified molecules at  $m/z$  535.3, 559.5, 561.5 and isoschaftoside ( $m/z$  563.1) along the endosperm regions. The ion intensity is normalized along the columns and all the images have a uniform scale bar of 1 mm [Color figure can be viewed at [wileyonlinelibrary.com](http://wileyonlinelibrary.com)]

samples analyzed with DMF can be further used for histopathology studies.<sup>18</sup> However, in our study, a slight disturbance in the specimen was noticed when DMF was electrosprayed over the rice grain surface. The molecular images obtained in negative ion mode were relatively better with MeOH in comparison with other solvents tested. Table S1 (supporting information) presents the characteristic features of the rice grains based on which they were selected for our study. The grain morphologies of the rice varieties used in this investigation are presented in Figure 2.

#### 4.1 | Distribution of choline and sugar molecules

The positive ion mode DESI-MS spectrum from the rice grain surface in Figure 3A and molecular images in Figure 3B show the expression of choline and sucrose with their sodium and potassium adducts in the whole grain of ten different rice landraces. Choline ( $m/z$  104.1) is a water-soluble *N*-methyl-substituted molecule which plays a role in both glycine betaine and phosphatidyl choline biosynthetic pathways in plants.<sup>19</sup> As rice is a non-natural accumulator of glycine betaine, the role of choline is restricted to phospholipid biosynthesis.

Endosperm, the storage tissue of the mature cereal grain, is chiefly composed of starch and a minor amount of soluble sugars such as glucose, fructose, sucrose, etc.<sup>20,21</sup> The soluble sugar content in rice is known to vary between the cultivars.<sup>22</sup> Carbohydrates are mainly transported in the form of sucrose in the plant system through the phloem.<sup>23</sup> In Figure 3B, the accumulation of sucrose is seen to be uniform in the endosperm of G02, G38, K11, K86, R09 and T11 rice varieties. Sucrose is known to form adducts with cations. The literature suggests that potassiated sucrose does not fragment easily as compared with sodiated and lithiated sucrose under the same applied collision energy, and thus the potassiated sucrose imparts structural integrity to sucrose during molecular transport unlike its other cationic adducts.<sup>24</sup> The DESI-MS images of potassiated sucrose shows enhanced signal intensity in the embryo of the G38, H24, T05, and T11 rice varieties. SEM-EDAX mapping of G2 rice in the inset of Figure 3A showed a strong localization of potassium in the embryo. Interestingly there may be a correlation between molecular localization and metal ion distribution, especially in rice grown in areas where surface water is contaminated with heavy metals such as arsenic, mercury, etc. Figure S3 (supporting information) shows the results from a quick experiment performed

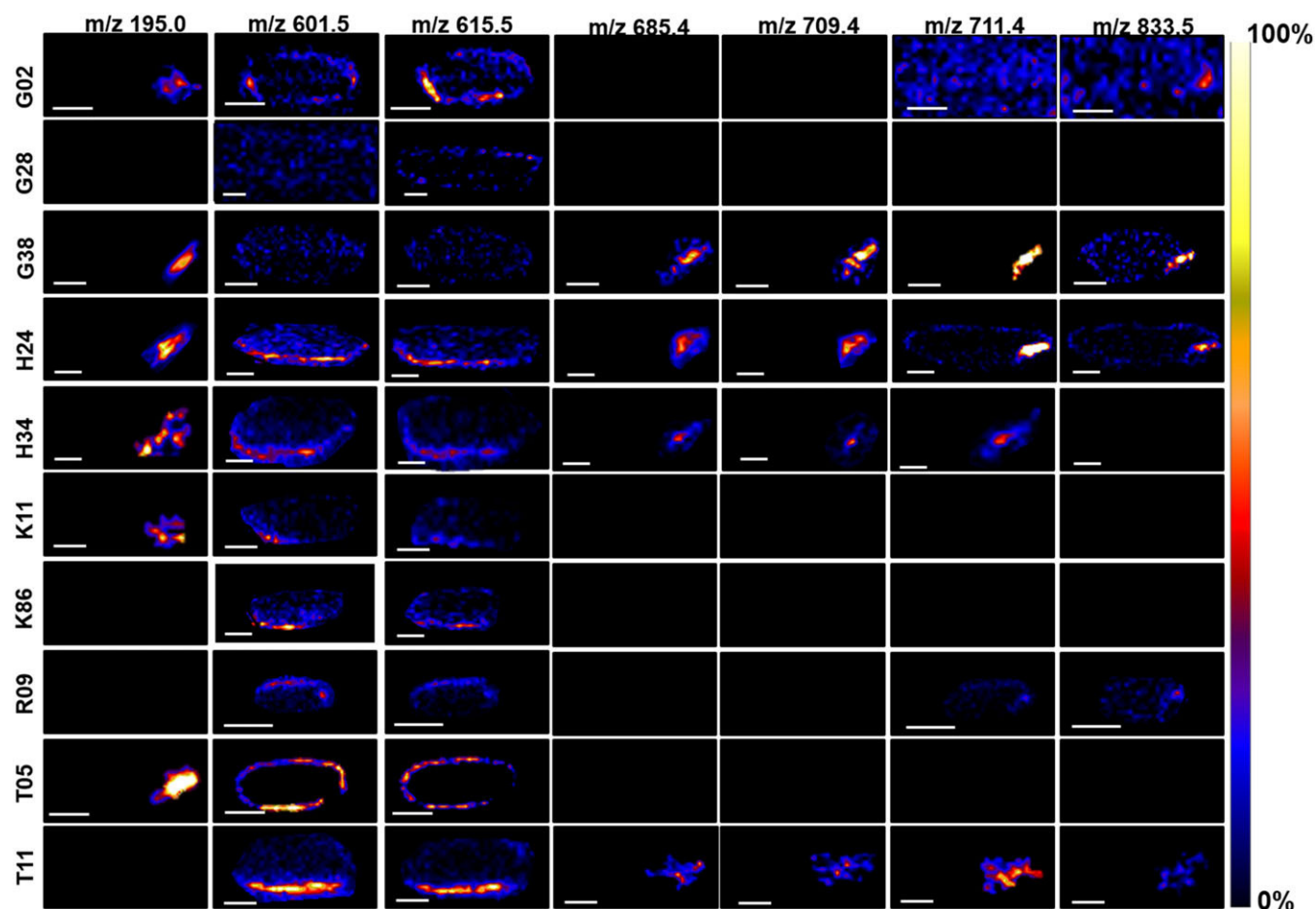


**FIGURE 5** Negative ion mode DESI-MS images of rice grains showing the distribution of gluconic acid ( $m/z$  195.0), oryzanol A ( $m/z$  601.5), oryzanol C ( $m/z$  615.5), methyl phosphoesters of PA 34:2 ( $m/z$  685.4), PA 36:4 ( $m/z$  709.4), PA 36:3 ( $m/z$  711.4) and PI 34:2 ( $m/z$  833.5) along the bran and embryo regions. All the images have a uniform scale bar of 1 mm [Color figure can be viewed at [wileyonlinelibrary.com](http://wileyonlinelibrary.com)]

by soaking G2 rice grains in  $10 \text{ mg g}^{-1}$  of  $\text{Cr}^{3+}$  metal ion solutions for 5 h and checking for bioaccumulation of chromium in the rice grains. SEM-EDS mapping showed the distribution of chromium along the bran and embryo of the rice grain. The metal picking efficiency of the cereal grains depends on many factors such as form of the metal ions (organic or inorganic), rice variety, nature of the soil and water where the rice grows, temperature, susceptibility to stress, and so on. Therefore, an elaborate experiment has to be performed by screening a large number of rice samples. Certain molecules expressed on the bran or embryo surface did not have enough signal intensity when subjected to fragmentation in DESI-MS. Therefore, ESI-MS/MS analysis of rice extracts was performed to identify the molecule. Figure S4 (supporting information) shows the tandem MS data obtained from ESI-MS and DESI-MS for a representative molecular ion in positive and negative ion mode. The metabolite profile obtained from the ESI-MS analysis of rice extracts in positive ionization mode is shown in Figure S5 (supporting information). Data from ten rice varieties are presented.

#### 4.2 | Distribution of endosperm-specific molecules

Figures 4 and 5 represent the distribution of molecules in the rice varieties from the negative ion mode of imaging. The composition and distribution of lipids in rice are not uniform as they vary with their genotypes and environmental conditions. Palmitic acid, linoleic acid, and oleic acid are known to be the major free fatty acids in rice.<sup>25</sup> Linoleic acid ( $m/z$  279.2), also referred to as omega-6 fatty acid, is an essential fatty acid required for the normal growth and development of humans. Hydroxyoctadecadienoic acids (HODEs) are the stable oxidative derivatives of omega-6 fatty acid. In Figure 4, the free fatty acids linoleic acid ( $m/z$  279.2), 13-HODE-9-HODE ( $m/z$  295.2), three other unidentified molecules with  $m/z$  535.3, 559.5, and 561.5, and isoschaftoside, a C-glycosylflavonoid ( $m/z$  563.1), present a strong localization in the starchy endosperm of the rice varieties.

#### 4.3 | Distribution of embryo-specific molecules

In Figure 5, gluconic acid, a glucose oxidation product ( $m/z$  195.0), is seen to be localized in the embryo of G02, G38, H24, H34, K11 and T05 rice varieties. The multiple components of  $\gamma$ -oryzanol are made up of the esters of triterpene alcohol ferulates and sterol ferulates.<sup>26,27</sup> Two of the major  $\gamma$ -oryzanol components of the rice bran oil such as cycloartenyl ferulate (oryzanol A,  $m/z$  601.5) and 24-methyl cycloartenyl ferulate (oryzanol C,  $m/z$  615.5) were mapped along the bran region of the rice varieties. Oryzanol distribution is more pronounced in the T05 rice variety than the other rice landraces. A review suggests that the dietary intake of  $\gamma$ -oryzanol from rice bran oil helps in the treatment of hypercholesterolemia by lowering the plasma cholesterol levels, and, also, the ferulate part of oryzanol offers antioxidant properties.<sup>28</sup> Phosphatidyl inositol is a regulatory membrane lipid from the

glycerophospholipid class with an inositol head group. The literature suggests the distribution and expression of specific molecular species of PIs will vary with external conditions such as stress states or the molecular function which has to be regulated.<sup>29</sup> PI 34:2 ( $m/z$  833.5), a molecular species of PI, was localized along the bran and embryo.

#### 4.4 | Methylation of phosphatidic acids

Phosphatidic acids (PAs), a minor class of total phospholipids, are known to be the key signalling molecules involved in plant development and metabolic pathways. The ions at  $m/z$  685.4, 709.4, and 711.4 exhibit a site-specific localization in the embryo of G38, H24, H34 and T11. The DESI-MS spectrum shown in Figure 6 collected from the rice grain cross sections further confirmed that those molecules are from the grain surface. A study on maize embryo imaging by MALDI-MS reported that the ions at  $m/z$  685.4 and 709.4 are methyl phosphoesters of PA 34:2 ( $m/z$  671.4) and PA 36:4 ( $m/z$  695.4), respectively. It was also mentioned that the phosphoesterification of phosphatidic acid was detected only when 5% methanol was used as the solvent for matrix recrystallization.<sup>30</sup>

To further confirm the influence of spray solvent on the methylation of phosphatidic acids, imaging was performed with an array of non-methanolic solvents. Figure 7 shows the absence of methylated PA species when non-methanolic solvents were used as spray solvents. Therefore, the methylation of PA molecules in our study is from methanol. The product ion mass spectra of unidentified molecules by ESI MS are shown in Figure S6 (supporting information).

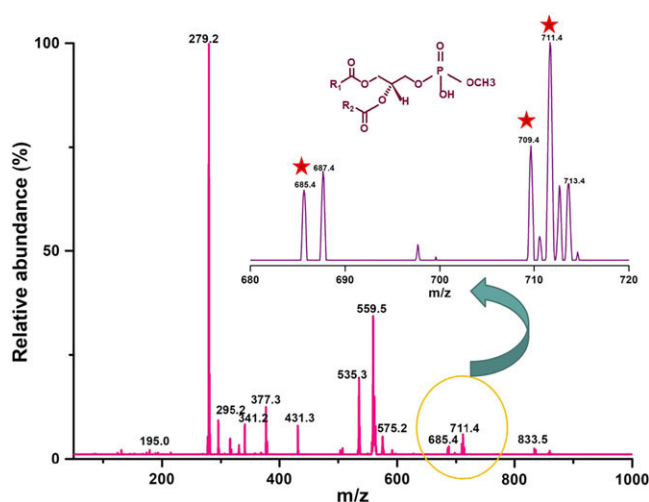


**FIGURE 6** Negative ion mode DESI-MS spectrum collected from H24 rice section. The inset shows the molecular distribution pattern of methyl phosphoester of phosphatidic acids in the zoomed region of  $m/z$  680–720 [Color figure can be viewed at [wileyonlinelibrary.com](http://wileyonlinelibrary.com)]

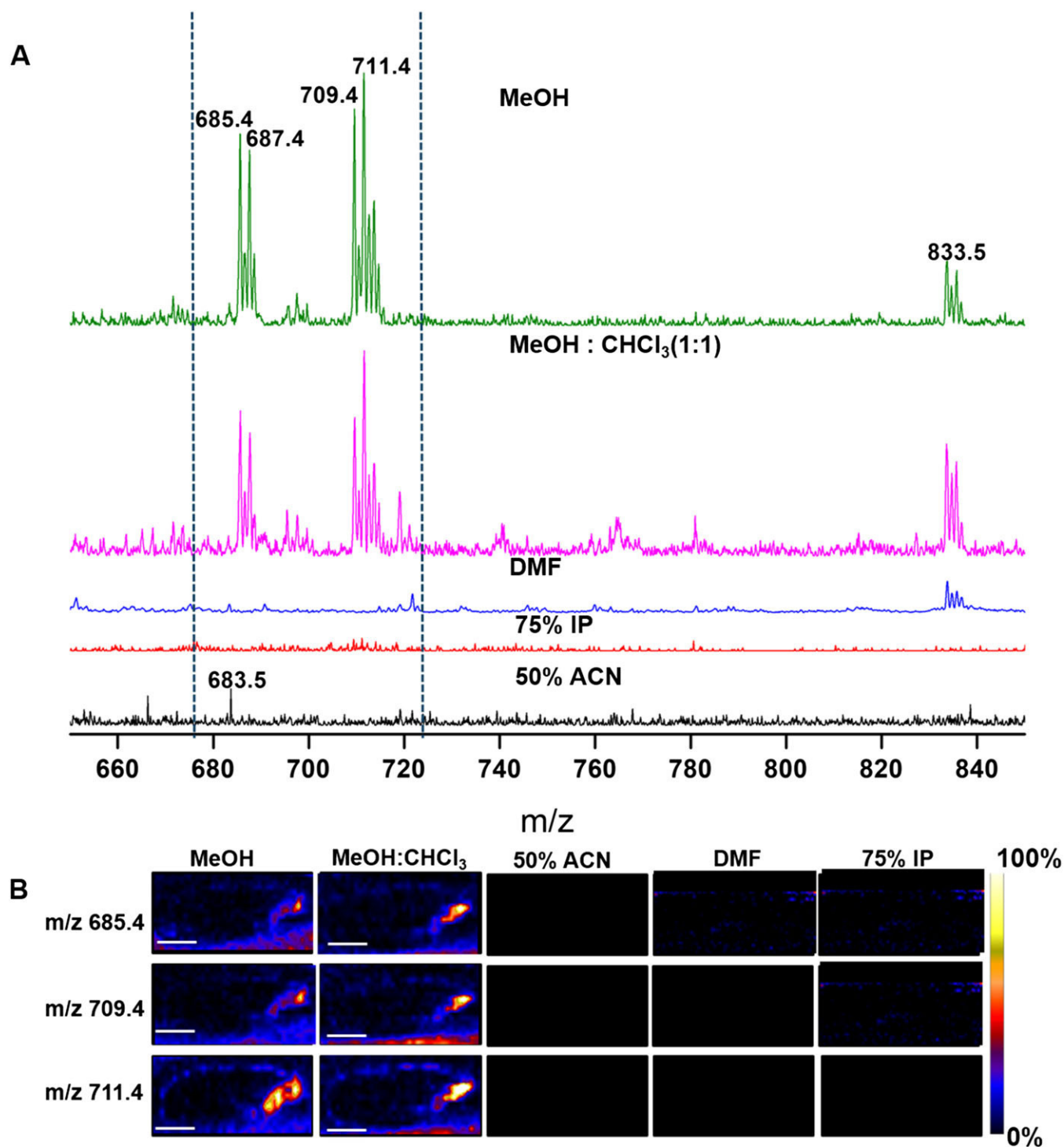


**FIGURE 7** A, Negative ion mode DESI-MS spectrum collected from H24 rice section using an array of solvent systems. B, Molecular ion distribution pattern of methyl phosphoester of phosphatidic acids in H24 rice using different spray solvents. All the images have a uniform scale bar of 2 mm [Color figure can be viewed at [wileyonlinelibrary.com](http://wileyonlinelibrary.com)]

## 5 | CONCLUSIONS

In this study, we reported the spatial mapping of different molecules of physiological importance in rice grains under ambient conditions. We introduced a systematic investigation into some of the rarest,

traditional, and contemporary rice varieties. The DESI-MS based chemical imaging technique is non-invasive, and, therefore, the samples can be reused for imaging with further polishing to understand the details of molecular distribution at different depths of the sample. This approach can be advanced to studying tissues at the



developmental stages. The identification of molecules was made possible with tandem ESI MS analysis. An undesirable effect of spray solvent on the embryo-specific phosphatidic acid molecules was observed. Further optimization of spray solvents is necessary for obtaining lipid signals without interferences. The identified metabolites are not only important for human nutrition, but they also provide significant information regarding their role in plant metabolism. Thus, screening of rice samples by DESI-MS aided in understanding the distribution patterns of dietary metabolites and signalling molecules, which would be helpful in crop improvement for nutritional qualities. A compendium of metabolite distribution data of this kind along with the metal profile of rice grains may help people across the world to have the most appropriate rice varieties for consumption. A study correlating the metabolite expression under stress by different metal contaminants will be addressed in our upcoming work.

## ACKNOWLEDGEMENTS

The authors acknowledge the financial support by the Department of Science and Technology, Government of India, for nanomaterials research. A.S. thanks the Indian Institute of Technology Madras for a research fellowship. They would also like to thank Mr. Priyabrata Roy for his timely support in sample collection.

## ORCID

Arunan Suganya  <https://orcid.org/0000-0002-2990-1916>

Debal Deb  <https://orcid.org/0000-0002-7230-659X>

Thalappil Pradeep  <https://orcid.org/0000-0003-3174-534X>

## REFERENCES

- Gemperline E, Keller C, Li L. Mass spectrometry in plant-omics. *Anal Chem*. 2016;88(7):3422-3434. <https://doi.org/10.1021/acs.analchem.5b02938>
- Khush GS. Origin, dispersal, cultivation and variation of rice. *Plant Mol Biol*. 1997;35(1):25-34. <https://doi.org/10.1023/A:1005810616885>
- Sen Gupta S, Bakshi A, Roy P, Deb D, Pradeep T. Unusual accumulation of silver in the Aleurone layer of an Indian rice (*Oryza sativa*) landrace and sustainable extraction of the metal. *ACS Sustain Chem Eng*. 2017;5(9):8310-8315. <https://doi.org/10.1021/acssuschemeng.7b02058>
- Bouis HE, Saltzman A. Improving nutrition through biofortification: A review of evidence from HarvestPlus, 2003 through 2016. *Glob Food Sec*. 2017;12:49-58. <https://doi.org/10.1016/j.gfs.2017.01.009>
- De Moura FF, Moursi M, Donahue Angel M, et al. Biofortified  $\beta$ -carotene rice improves vitamin A intake and reduces the prevalence of inadequacy among women and young children in a simulated analysis in Bangladesh, Indonesia, and the Philippines. *Am J Clin Nutr*. 2016;104(3):769-775. <https://doi.org/10.3945/ajcn.115.129270>
- Ks H, Nihal A, Faizan A, Raj K. Naturally occurring organic osmolytes: From cell physiology to disease prevention. *IUBMB Life*. 2010;62(12):891-895. <https://doi.org/10.1002/iub.406>
- Deb D. Folk rice varieties, traditional knowledge and nutritional security in South Asia. In: Poyyamoli G, ed. *Agroecology, Ecosystems, and Sustainability in the Tropics*. Delhi: Studera Press, 2017; 2017:117-134. <http://www.studeraapress.com/wp-content/uploads/2017/06/6-Folk-Rice-Varieties-Traditional-Knowledge-and-Nutritional-Security-in-South-Asia.pdf>
- Zaima N, Goto-Inoue N, Hayasaka T, Setou M. Application of imaging mass spectrometry for the analysis of *Oryza sativa* rice. *Rapid Commun Mass Spectrom*. 2010;24(18):2723-2729. <https://doi.org/10.1002/rcm.4693>
- Yoshimura Y, Zaima N, Moriyama T, Kawamura Y. Different localization patterns of anthocyanin species in the pericarp of black rice revealed by imaging mass spectrometry. *PLoS One*. 2012;7(2):e31285. <https://doi.org/10.1371/journal.pone.0031285>
- Zaima N, Yoshimura Y, Kawamura Y, Moriyama T. Distribution of lysophosphatidylcholine in the endosperm of *Oryza sativa* rice. *Rapid Commun Mass Spectrom*. 2014;28(13):1515-1520. <https://doi.org/10.1002/rcm.6927>
- Wiseman JM, Iffa DR, Venter A, Cooks RG. Ambient molecular imaging by desorption electrospray ionization mass spectrometry. *Nat Protoc*. 2008;3(3):517-524.
- Claude E, Jones EA, Pringle SD. DESI Mass Spectrometry Imaging (MSI) In: Cole LM, ed. *Imaging Mass Spectrometry: Methods and Protocols*. New York, NY: Humana Press; 2017:65-75. [https://doi.org/10.1007/978-1-4939-7051-3\\_7](https://doi.org/10.1007/978-1-4939-7051-3_7)
- Boughton BA, Thinagaran D, Sarabia D, Bacic A, Roessner U. Mass spectrometry imaging for plant biology: A review. *Phytochem Rev*. 2016;15(3):445-488. <https://doi.org/10.1007/s11101-015-9440-2>
- Dong Y, Li B, Malitsky S, et al. Sample preparation for mass spectrometry imaging of plant tissues: A review. *Front Plant Sci*. 2016;7:60. <https://doi.org/10.3389/fpls.2016.00060>
- Kertesz V, Van Berkel GJ. Improved imaging resolution in desorption electrospray ionization mass spectrometry. *Rapid Commun Mass Spectrom*. 2008;22(17):2639-2644. <https://doi.org/10.1002/rcm.3662>
- Campbell DI, Ferreira CR, Eberlin LS, Cooks RG. Improved spatial resolution in the imaging of biological tissue using desorption electrospray ionization. *Anal Bioanal Chem*. 2012;404(2):389-398. <https://doi.org/10.1007/s00216-012-6173-6>
- Tillner J, Wu V, Jones EA, et al. Faster, more reproducible DESI-MS for biological tissue imaging. *J Am Soc Mass Spectrom*. 2017;28(10):2090-2098. <https://doi.org/10.1007/s13361-017-1714-z>
- Green FM, Salter TL, Gilmore IS, Stokes P, O'Connor G. The effect of electrospray solvent composition on desorption electrospray ionisation (DESI) efficiency and spatial resolution. *Analyst*. 2010;135(4):731-737. <https://doi.org/10.1039/B924208B>
- Rhodes D, Hanson AD. Quaternary ammonium and tertiary sulfonium compounds in higher plants. *Annu Rev Plant Physiol Plant Mol Biol*. 1993;44(1):357-384. <https://doi.org/10.1146/annurev.pp.44.060193.002041>
- Smyth DA, Prescott HE. Sugar content and activity of sucrose metabolism enzymes in milled rice grain. *Plant Physiol*. 1989;89(3):893-896.
- Singh R, Juliano BO. Free sugars in relation to starch accumulation in developing rice grain. *Plant Physiol*. 1977;59(3):417-421.
- Smyth DA, Repetto BM, Seidel NE. Cultivar differences in soluble sugar content of mature rice grain. *Physiol Plant*. 1986;68(3):367-374. <https://doi.org/10.1111/j.1399-3054.1986.tb03367.x>
- Truernit E. Plant physiology: The importance of sucrose transporters. *Curr Biol*. 2001;11(5):R169-R171. [https://doi.org/10.1016/S0960-9822\(01\)00085-9](https://doi.org/10.1016/S0960-9822(01)00085-9)
- Yuan H, Wu Y, Liu W, et al. Mass spectrometry-based method to investigate the natural selectivity of sucrose as the sugar transport form for plants. *Carbohydr Res*. 2015;407:5-9. <https://doi.org/10.1016/j.carres.2015.01.011>
- Fujino Y. Rice lipids. *Cereal Chem*. 1978;55(5):559-571. [https://www.aaccnet.org/publications/cc/backissues/1978/Documents/chem55\\_559.pdf](https://www.aaccnet.org/publications/cc/backissues/1978/Documents/chem55_559.pdf)
- Aladedunye F, Przybylski R, Rudzinska M, Klensporf-Pawlik D.  $\gamma$ -Oryzanol of north American wild rice (*Zizania palustris*). *J Am Oil Chem Soc*. 2013;90(8):1101-1109. <https://doi.org/10.1007/s11746-013-2252-x>

27. Xu Z, Godber JS. Purification and identification of components of  $\gamma$ -oryzanol in rice bran oil. *J Agric Food Chem.* 1999;47(7):2724-2728. <https://doi.org/10.1021/jf981175j>
28. Patel M, Naik SN. gamma-Oryzanol from rice bran oil – A review 2004; 63:569–578. <https://pdfs.semanticscholar.org/a78c/6655599f92e7732a066c03ad07b33b0b32f6.pdf>
29. Heilmann I. Phosphoinositide signaling in plant development. *Development.* 2016;143(12):2044 LP-2055. <https://doi.org/10.1242/dev.136432>
30. Dueñas ME, Carlucci L, Lee YJ. Matrix recrystallization for MALDI-MS imaging of maize lipids at high-spatial resolution. *J Am Soc Mass Spectrom.* 2016;27(9):1575-1578. <https://doi.org/10.1007/s13361-016-1422-0>

## SUPPORTING INFORMATION

Additional supporting information may be found online in the Supporting Information section at the end of the article.

**How to cite this article:** Suganya A, Deb D, Pradeep T. Spatial distribution mapping of molecules in the grains of different rice landraces, using desorption electrospray ionization mass spectrometry. *Rapid Commun Mass Spectrom.* 2019;33: 727–736. <https://doi.org/10.1002/rcm.8397>

## Supplementary information

### Spatial distribution mapping of molecules in the grains of different rice landraces, using desorption electrospray ionization mass spectrometry

Arunan Suganya<sup>1</sup>, Debal Deb<sup>2</sup>, and Thalappil Pradeep<sup>1\*</sup>

<sup>1</sup> DST Unit of Nanoscience, and Thematic Unit of Excellence, Department of Chemistry, Indian Institute of Technology Madras, Chennai 600 036, India

<sup>2</sup> Centre for Interdisciplinary Studies, Barrackpore 700 123, India

\*Corresponding author: Thalappil Pradeep

Tel: +91-44-2257 4208, E-mail: [pradeep@iitm.ac.in](mailto:pradeep@iitm.ac.in)

#### Table of contents:

Particulars	Title	Page No.
Table S1	Morphological characteristics of the rice landraces examined	2
Figure S1	DESI MS spectrum from resin and grain surface	2
Figure S2	DESI MS imaging using different concentrations of methanol	3
Figure S3	SEM and EDAX characterization of H24 rice whole grain section	4
Figure S4	Tandem MS data of representative molecular ions using ESI MS and DESI MS	5
Figure S5	Metabolite chart of molecule identified in positive ion mode DESI MSI	6
Figure S6	Product ion MS/MS of unidentified molecules	7

<b>Rice landrace</b>	<b>Code</b>	<b>Phenol reaction</b>	<b>Grain aroma</b>	<b>Grain pericarp colour</b>
Garib-sal	G02	Strong	Absent	White
Gouri sundari	G28	Strong	Strong	Dark brown
Gazepxali	G38	Absent	Strong	White
Huggi bhatta	H24	Strong	Strong	Dark purple
Hendebaihar	H34	Absent	Absent	Light brown
Kataribhog	K11	Strong	Mild	White
Kala Nuniya	K86	Strong	Strong	White
Radha Tilak	R09	Absent	Mild	White
Tikki	T05	Strong	Absent	Black
Tike Churi	T11	Weak	Absent	Dark brown

**Table S1.** Morphological Characteristics of the Rice Landraces Examined.

Rice fragrance is tested olfactorily, by a group of people, who report the strength of aroma they perceive. Phenol reaction was tested by soaking the rice seeds in 2% phenol for 6 hours, when the rice hull colour becomes dark (strong reaction), light purple (weak) or remains unchanged (no reaction).

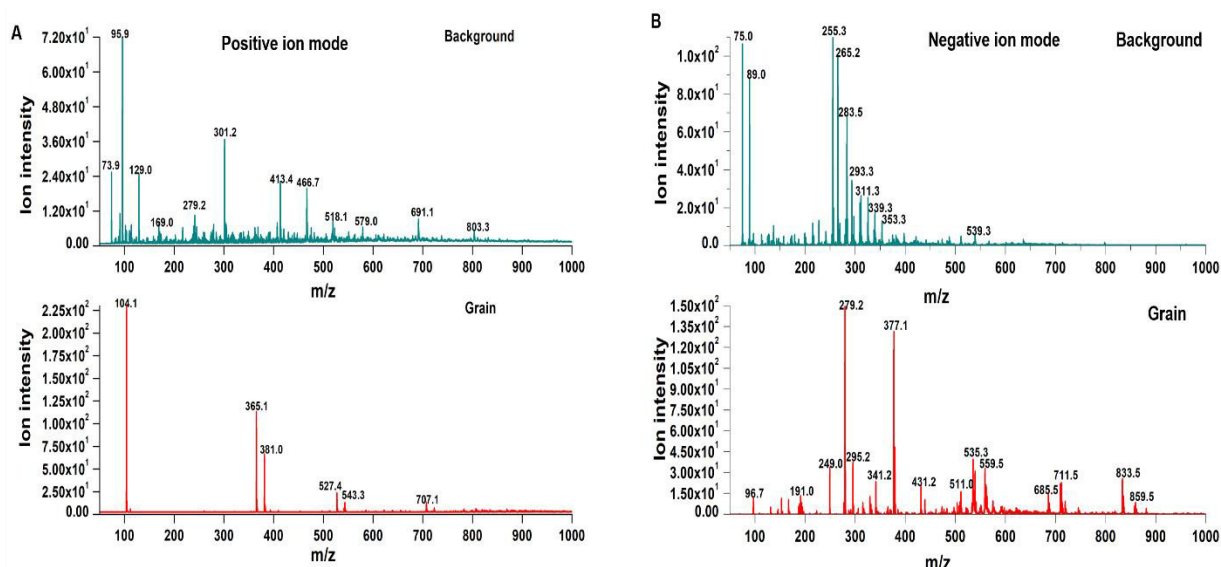


**Figure S1:** DESI MS spectra collected from the background and grain surface of H24 rice in the A) positive, and B) negative ion mode.

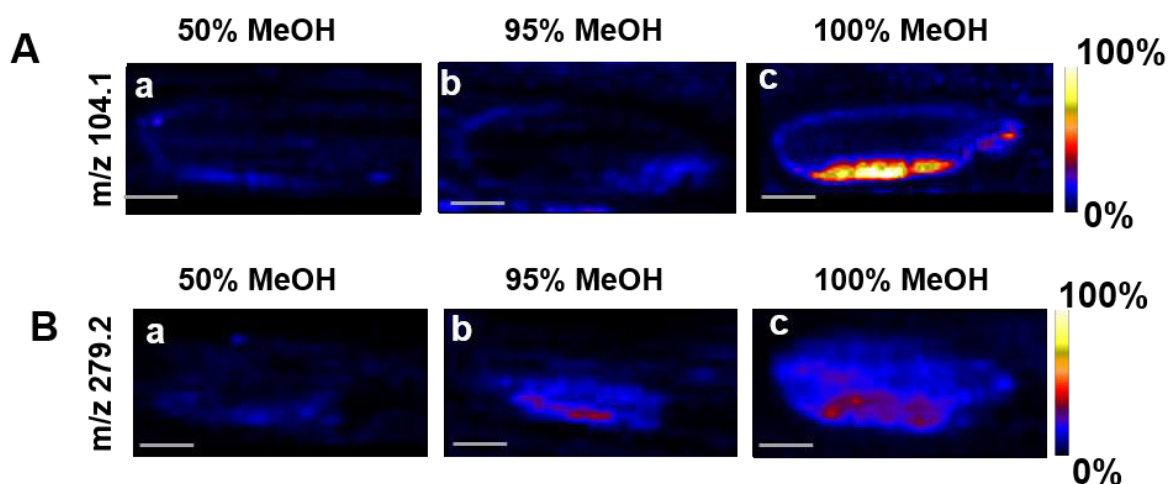


**Figure S2:** DESI MS imaging of H24 rice using different concentrations of methanol as spray solvent. A & B) molecular ion image of choline and linoleic acid obtained from positive and negative ion mode imaging, respectively. a) 50% MeOH, b) 95% MeOH and c) 100% MeOH.

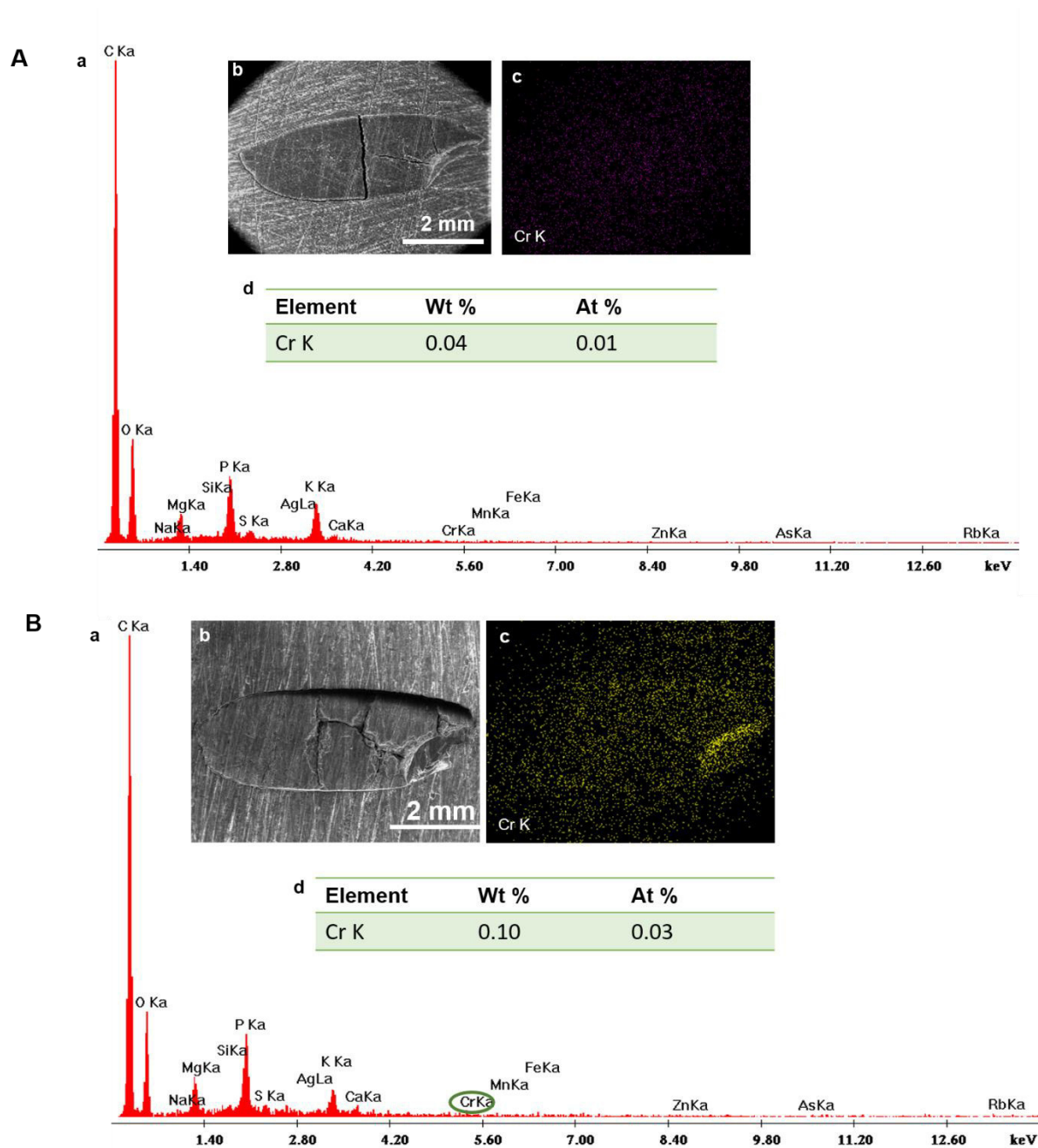


**Figure S3:** SEM-EDAX mapping of G2 rice A) Control, and B) treated with chromium ( $\text{Cr}^{3+}$ ) metal ion solution. In both A & B, a) EDAX spectrum, b) SEM image of G2 rice, c) EDAX image and e) elemental ratio of chromium.

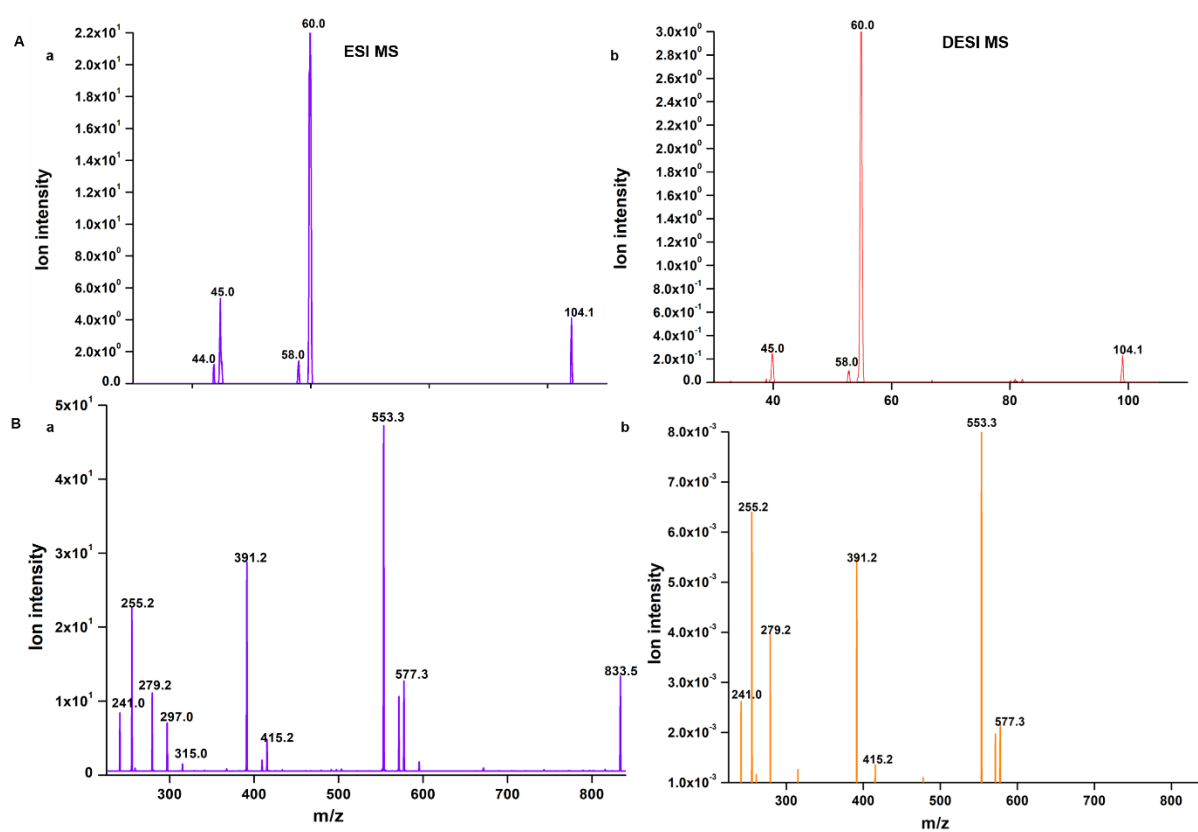


**Figure S4:** Tandem MS/MS data of A) choline and B) PI (34:2) in positive and negative ion mode, respectively using a) ESI MS and b) DESI MS.



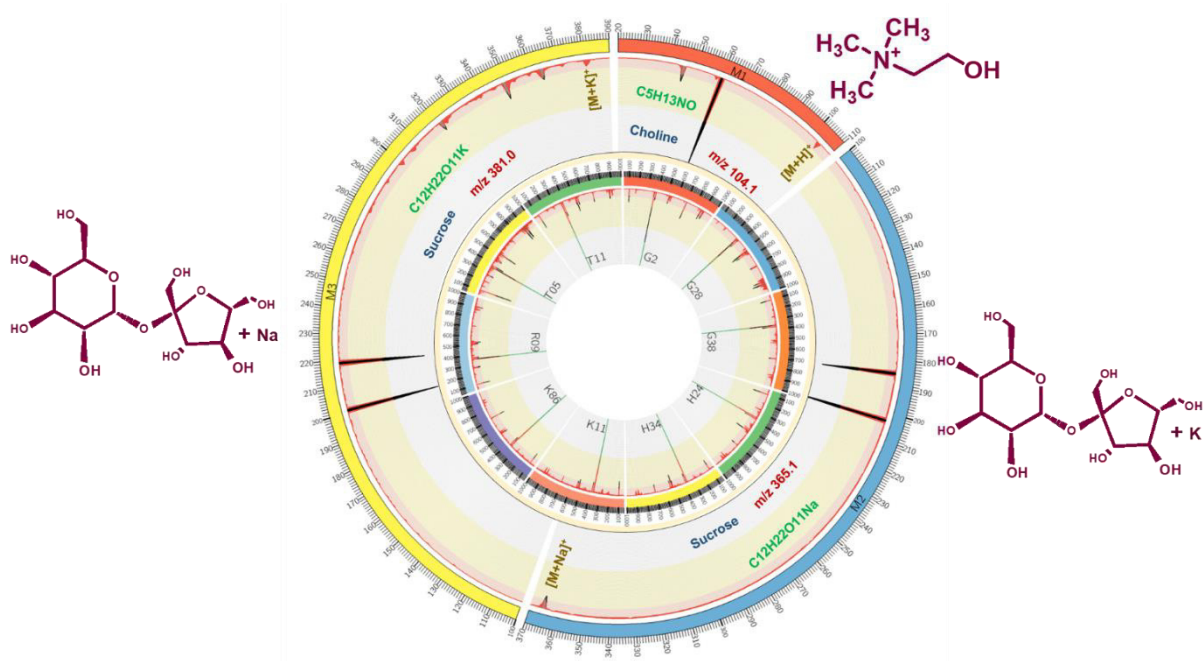
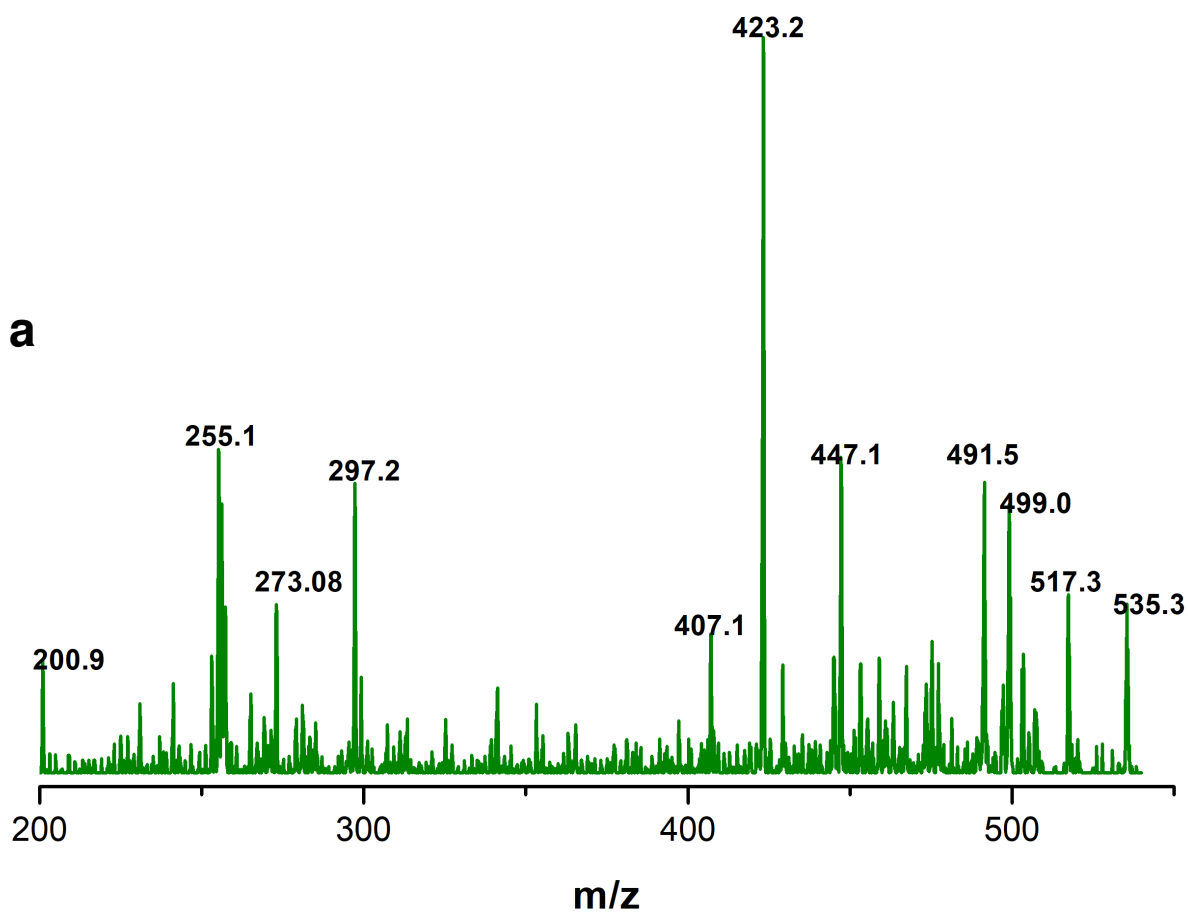


**Figure S5:** The metabolite chart representing the MS, MS/MS, and chemical information data from the ESI MS analysis of the rice grain extracts of various landraces corresponding to the molecules identified by DESI MS imaging, in positive ion mode. Inner circle represents MS data and the outer circle denotes the tandem MS data.

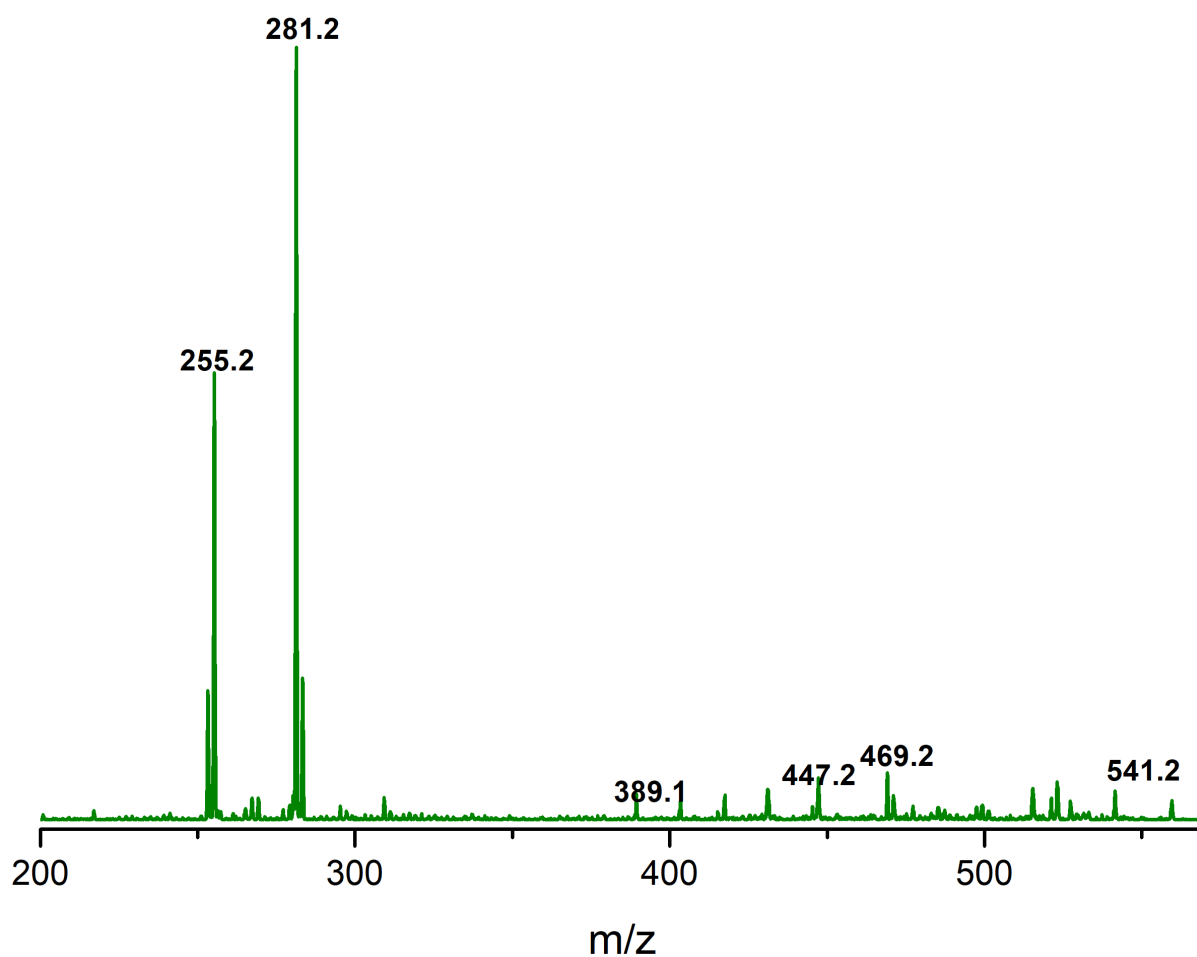
In the positive ionization mode, protonated choline ( $m/z$  104.1,  $[C_5H_{14}NO]^+$ ) was identified by its characteristic fragment ions at  $m/z$  60.1  $[(CH_3)_3NH]^+$ , and  $m/z$  45.1  $[C_2H_5O]^+$  as a result of  $H_2C-N$  bond cleavage. The disaccharide, sucrose was identified from its characteristic CID spectrum. The glycosidic cleavage produced fragment ions at  $m/z$  203.0 and 185.0 from sodiated sucrose and  $m/z$  219.0 and 201.0 from potassiated sucrose ion. The fragments at  $m/z$  203.0 and 219.0 and  $m/z$  185.0 and 201.0 correspond to the neutral loss of 162 and 180 mass units from their molecular ion peaks, respectively. The identified molecules were further confirmed by comparison with the mass spectrum from the METLIN database (Choline, id: 56; sucrose, id: 137).



**a**



**b**



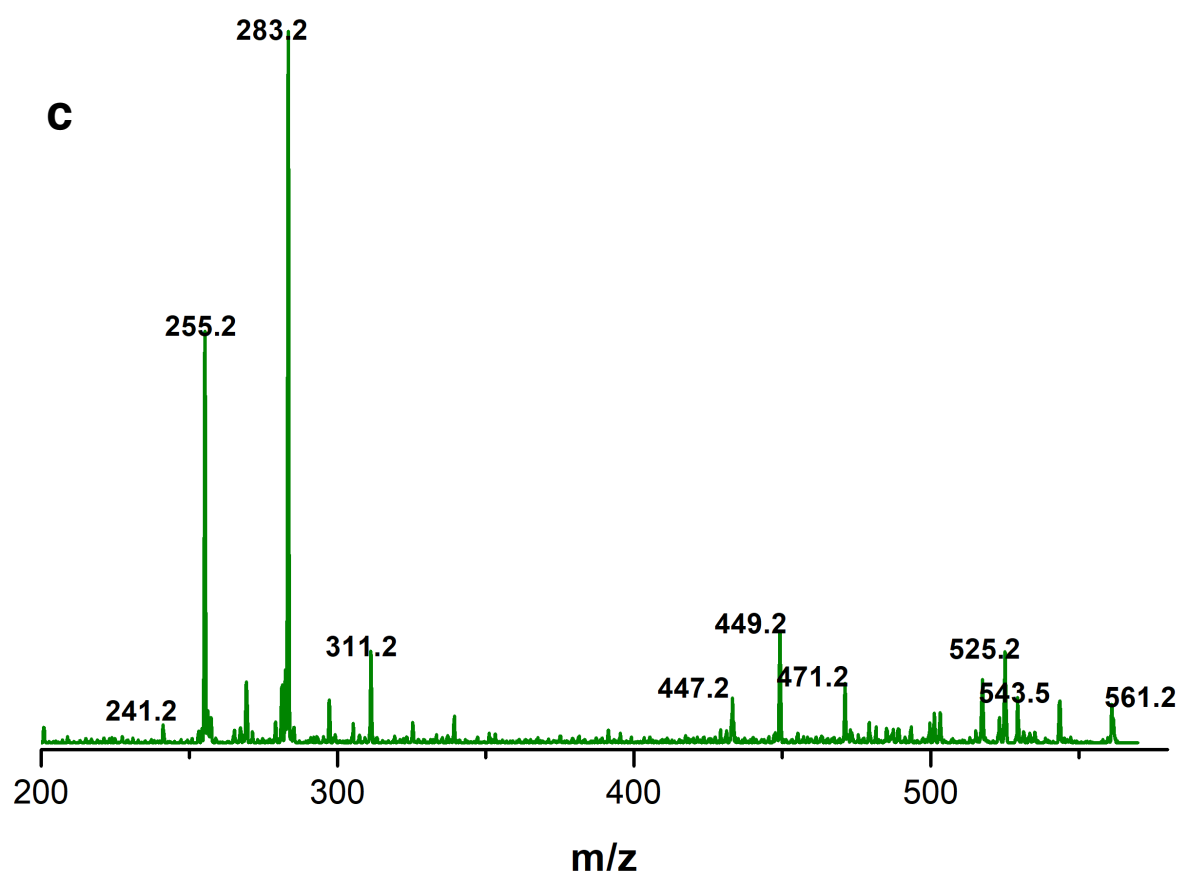


Figure S6. The product ion MS/MS data of unidentified molecules a) 535, b) 559 c)561

# Clathrate hydrates in interstellar environment

Jyotirmoy Ghosh<sup>a</sup>, Rabin Rajan J. Methikkalam<sup>a,1</sup>, Radha Gobinda Bhuin<sup>a,2</sup>, Gopi Ragupathy<sup>a</sup>, Nilesh Choudhary<sup>b</sup>, Rajnish Kumar<sup>b,3</sup>, and Thalappil Pradeep<sup>a,3</sup>

<sup>a</sup>Department of Science and Technology (DST) Unit of Nanoscience and Thematic Unit of Excellence (TUE), Department of Chemistry, Indian Institute of Technology Madras, Chennai 600036, India; and <sup>b</sup>Department of Chemical Engineering, Indian Institute of Technology Madras, Chennai 600036, India

Edited by Francois Forget, Laboratoire de Météorologie Dynamique, Paris, France, and accepted by Editorial Board Member Jean Jouzel December 10, 2018 (received for review August 18, 2018)

**Clathrate hydrates (CHs) are ubiquitous in earth under high-pressure conditions, but their existence in the interstellar medium (ISM) remains unknown. Here, we report experimental observations of the formation of methane and carbon dioxide hydrates in an environment analogous to ISM. Thermal treatment of solid methane and carbon dioxide–water mixture in ultrahigh vacuum of the order of  $10^{-10}$  mbar for extended periods led to the formation of CHs at 30 and 10 K, respectively. High molecular mobility and H bonding play important roles in the entrapment of gases in the in situ formed  $5^{12}$  CH cages. This finding implies that CHs can exist in extreme low-pressure environments present in the ISM. These hydrates in ISM, subjected to various chemical processes, may act as sources for relevant prebiotic molecules.**

clathrate hydrate | interstellar medium | ISM | ultra-high vacuum | amorphous solid water

**C**lathrate hydrates (CHs) are crystalline inclusion compounds in which different guest molecules are encased in H-bonded water cages (1). These trapped molecules are generally small such as  $\text{CH}_4$ ,  $\text{CO}_2$ ,  $\text{N}_2$ ,  $\text{H}_2$ , etc. Among several such known CHs, those of  $\text{CH}_4$  and  $\text{CO}_2$  have drawn close attention of the scientific community due to their use as potential future source of energy (1, 2) and in  $\text{CO}_2$  sequestration (3), respectively. Natural methane and carbon dioxide hydrates are found in permafrost and marine sediments on the outer continental shelves (4) at ambient temperatures ( $<300$  K) and moderately high pressures (6 atm) (1). They could also exist in many solar system bodies such as in the Martian permafrost (5–7), on the surface of Titan (8), and on other icy satellites due to the prevalent thermodynamic (high P, low T) conditions (9). The stabilizing conditions (generally high pressures) of methane hydrate suggest that it is nonexistent in ultrahigh vacuum (UHV). Near zero diffusion prevents molecular rearrangements at cryogenic conditions, making the formation of cage structures impossible for water at interstellar temperatures. Therefore, it is not surprising that there is no report of its existence in conditions of relevance to space. Using thermodynamic data of methane hydrate available in the literature, its stability was extrapolated to low T, P region as shown (*SI Appendix, Fig. S1*), which suggests stability up to  $2 \times 10^{-6}$  mbar at 30 K. This temperature and pressure range is very close to nebular pressures, which could reach as high as  $10^{-3}$  mbar, and the temperature range can vary from 4 to 100 K (9). Equilibrium condensation curve of methane hydrate in protostellar nebula also suggests its stability  $\sim 1 \times 10^{-8}$  mbar at 45 K (10).

Experimentally, in situ formation of CHs in UHV, and cryogenic interstellar conditions has not been explored. However, it was proposed that at low pressure, CH may be grown epitaxially on other preformed CHs or by annealing the condensed gas–water mixture (11). CH of  $\text{CO}_2$  was obtained in a vacuum of  $10^{-6}$  torr, but at 120 K (12). We have adopted the annealing method to obtain CHs. In experiments conducted in the temperature window of 10–160 K and at  $10^{-10}$  mbar pressure, we observed  $\text{CH}_4$  and  $\text{CO}_2$  hydrates at temperatures near 30 and 10 K, respectively. Molecular mobility and structural rearrangement observed in these experiments at cryogenic conditions suggest unusual processes in water. The anomalous eruption of  $\text{CH}_4$ ,

$\text{CO}_2$ , or other volatile gases in cold interstellar clouds or in comets could possibly be explained by the existence of such hydrates in gas-forming regions of the interstellar space (10, 12). Irradiation or annealing leads to the chemical evolution of ice in ISM, forming new species (13). CHs could be one such new chemical system in the ISM, which may be subjected to additional processing.

## Results and Discussion

Fig. 14 displays time-dependent reflection absorption infrared (RAIR) spectra of 300 monolayers (MLs; 1 monolayer is equivalent to  $\sim 1.0 \times 10^{15}$  molecules  $\cdot \text{cm}^{-2}$ ) of a codeposited mixture (1:1) of  $\text{CH}_4$  and water at the C–H antisymmetric stretching region at three different temperatures (10, 20, and 30 K) and two different annealing times (0 and 25 h) under UHV. The annealing time is crucial for the success of the experiment. The figure clearly shows no change in peak position for the C–H antisymmetric stretching band of solid  $\text{CH}_4$  ( $3,009 \text{ cm}^{-1}$ ) with time, at 10 and 20 K. This peak is due to the untrapped  $\text{CH}_4$ ; in other words,  $\text{CH}_4$  hydrate was not observed at 10 and 20 K. A completely new IR peak ( $3,017 \text{ cm}^{-1}$ ) appears alongside the peak at  $3,009 \text{ cm}^{-1}$  after 25 h of annealing at 30 K. This new peak ( $3,017 \text{ cm}^{-1}$ ) is attributed to the  $\text{CH}_4$  hydrate, where  $\text{CH}_4$  is trapped in the CH cage. The rest of the untrapped  $\text{CH}_4$  remained in the pores of amorphous ice. The experimental blue shift of  $8 \text{ cm}^{-1}$  is due to the entrapment of  $\text{CH}_4$  in the hydrate cage. Here, the trapped  $\text{CH}_4$  inside the CH cage behaves more

## Significance

**Formation of clathrate hydrate (CH) requires high pressures and moderate temperatures, which enable their existence in marine sediments and the permafrost region of earth. The presence of CHs in interstellar medium (ISM) is still in question due to the extreme high vacuum and ultracold conditions present there. Here, we conclusively identified methane and carbon dioxide hydrates in conditions analogous to ISM. We found that molecular mobility and interactions play crucial roles in the formation of CHs, even though there is no external pressure to force cage formation. Various chemical processes on these hydrates in ISM may lead to relevant prebiotic molecules.**

Author contributions: J.G. and T.P. designed research; J.G. and R.R.J.M. performed research; J.G., R.R.J.M., and T.P. contributed new reagents/analytic tools; J.G., R.R.J.M., R.G.B., G.R., N.C., R.K., and T.P. analyzed data; and J.G., R.R.J.M., R.G.B., G.R., R.K., and T.P. wrote the paper.

The authors declare no conflict of interest.

This article is a PNAS Direct Submission. F.F. is a guest editor invited by the Editorial Board.

This open access article is distributed under [Creative Commons Attribution-NonCommercial-NoDerivatives License 4.0 \(CC BY-NC-ND\)](#).

<sup>1</sup>Present address: Institute of Chemistry, The Hebrew University, Jerusalem 91904, Israel.

<sup>2</sup>Present address: Lehrstuhl für Physikalische Chemie II, Friedrich-Alexander-Universität Erlangen-Nürnberg, 91058 Erlangen, Germany.

<sup>3</sup>To whom correspondence may be addressed. Email: rajnish@iitm.ac.in or pradeep@iitm.ac.in.

This article contains supporting information online at [www.pnas.org/lookup/suppl/doi:10.1073/pnas.1814293116/-DCSupplemental](http://www.pnas.org/lookup/suppl/doi:10.1073/pnas.1814293116/-DCSupplemental).

Published online January 10, 2019.

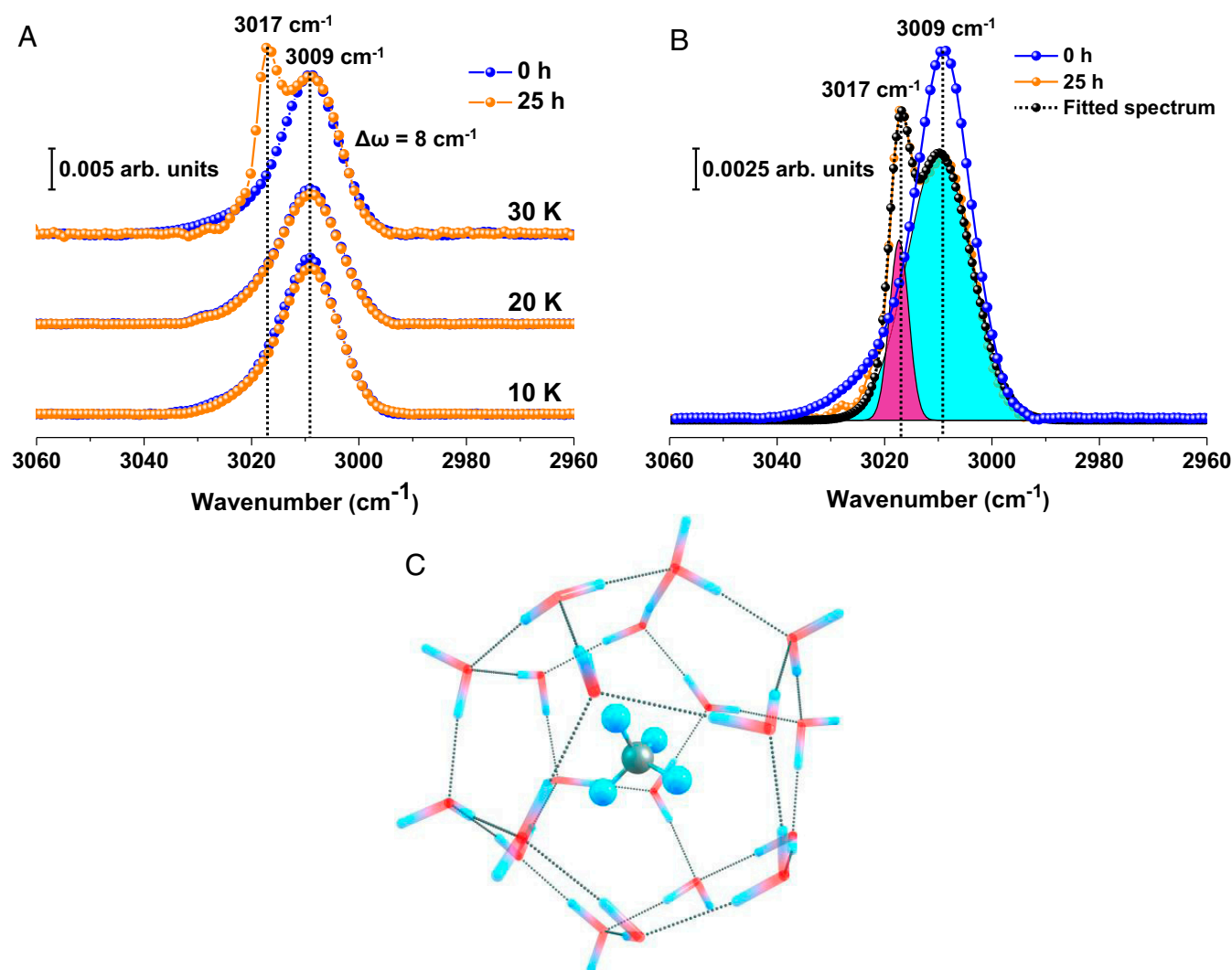


**Fig. 1.** CH<sub>4</sub> hydrate formation as studied by RAIR spectroscopy and quantum chemical calculations. (A) Normalized time-dependent RAIR spectra of 300 MLs CH<sub>4</sub>+H<sub>2</sub>O (1:1) mixed ice at 10, 20, and 30 K at the C–H antisymmetric stretching region. (B) Time-dependent RAIR spectra of the same system at 30 K. Here, the blue trace was divided by a factor of 7 to match the intensity of orange trace. Difference in intensity is due to desorption of CH<sub>4</sub> at 30 K, near its desorption temperature. Deconvoluted IR peaks are shown by cyan (3,009 cm<sup>-1</sup>) and pink shade (3,017 cm<sup>-1</sup>). (C) DFT-optimized structure of CH<sub>4</sub> trapped within CH (5<sup>12</sup> cage). Here, water cage and guest molecule (CH<sub>4</sub>) are shown. Color code used: gray, C; red, O; cyan, H.

like gaseous CH<sub>4</sub> as expected. It is known that vibrational frequency of free guest molecules in CH fall in between their vapor and condensed phase frequencies (14). The IR peak was deconvoluted to show the actual concentration of CH<sub>4</sub> trapped inside the hydrate cages and pores of amorphous solid water (ASW). The peak widths were calculated upon deconvolution, and the values were 14.1 and 4.2 cm<sup>-1</sup> for the peaks at 3,009 and 3,017 cm<sup>-1</sup>, respectively. Note the reduced width (4.2) of 3,017 cm<sup>-1</sup> for the hydrate peak, characteristic of a unique structure. Taking the IR intensity, the extent of CH<sub>4</sub> in the hydrate form was estimated to be 12.71% of the total CH<sub>4</sub> at this condition. As the annealing temperature is close to that of desorption, about 6/7 of the adsorbed CH<sub>4</sub> desorbs during annealing. Furthermore, we confirmed the formation of CH<sub>4</sub> hydrate by quantum chemical calculations. Density functional theory (DFT) calculations of the CH<sub>4</sub> hydrate revealed that the small cage (5<sup>12</sup>) as shown in Fig. 1C is favorable to form at this particular condition. Our computationally determined shift in the C–H antisymmetric mode during hydrate formation closely matches with the experimental value (*SI Appendix, Table S1*). A microsecond molecular dynamics simulation of CH<sub>4</sub> hydrate nucleation

predicts preferential formation of smaller 5<sup>12</sup> cages in the initial stages of CH<sub>4</sub> hydrate nucleation, supporting our observation (2).

Keeping the CH<sub>4</sub> and water ice mixture at 30 K for more than 25 h results in the formation of CH<sub>4</sub> hydrate. The long experimental time scale and the temperature (30 K), very near to the desorption temperature of CH<sub>4</sub>, are two crucial factors for the formation of CH<sub>4</sub> hydrate under UHV conditions. We propose that prolonged subjugation of CH<sub>4</sub>–water mixture at 30 K enhances the mobility of CH<sub>4</sub> molecules and leads to its insertion within the cages formed simultaneously. In a time-dependent study of 150 MLs of pure solid CH<sub>4</sub> at 25 K (*SI Appendix, Fig. S2*), the additional peak (3,017 cm<sup>-1</sup>) was not observed. This is again a piece of evidence that the above peak is due to CH<sub>4</sub> hydrate.

To support our claim of the formation of CH in ISM, we have chosen a more stable hydrate, namely that of CO<sub>2</sub>, which is already known to form CH at 120 K and 10<sup>-6</sup> torr (12). Fig. 2A represents the temperature-dependent RAIR spectra of 300 MLs of the codeposited mixture (1:5 ratio) of CO<sub>2</sub> and water in the C = O antisymmetric stretching region. The figure shows two IR peaks for the C = O antisymmetric stretching band of solid CO<sub>2</sub> at 10 K. The peak at 2,353 cm<sup>-1</sup> is attributed to the untrapped CO<sub>2</sub> that exists

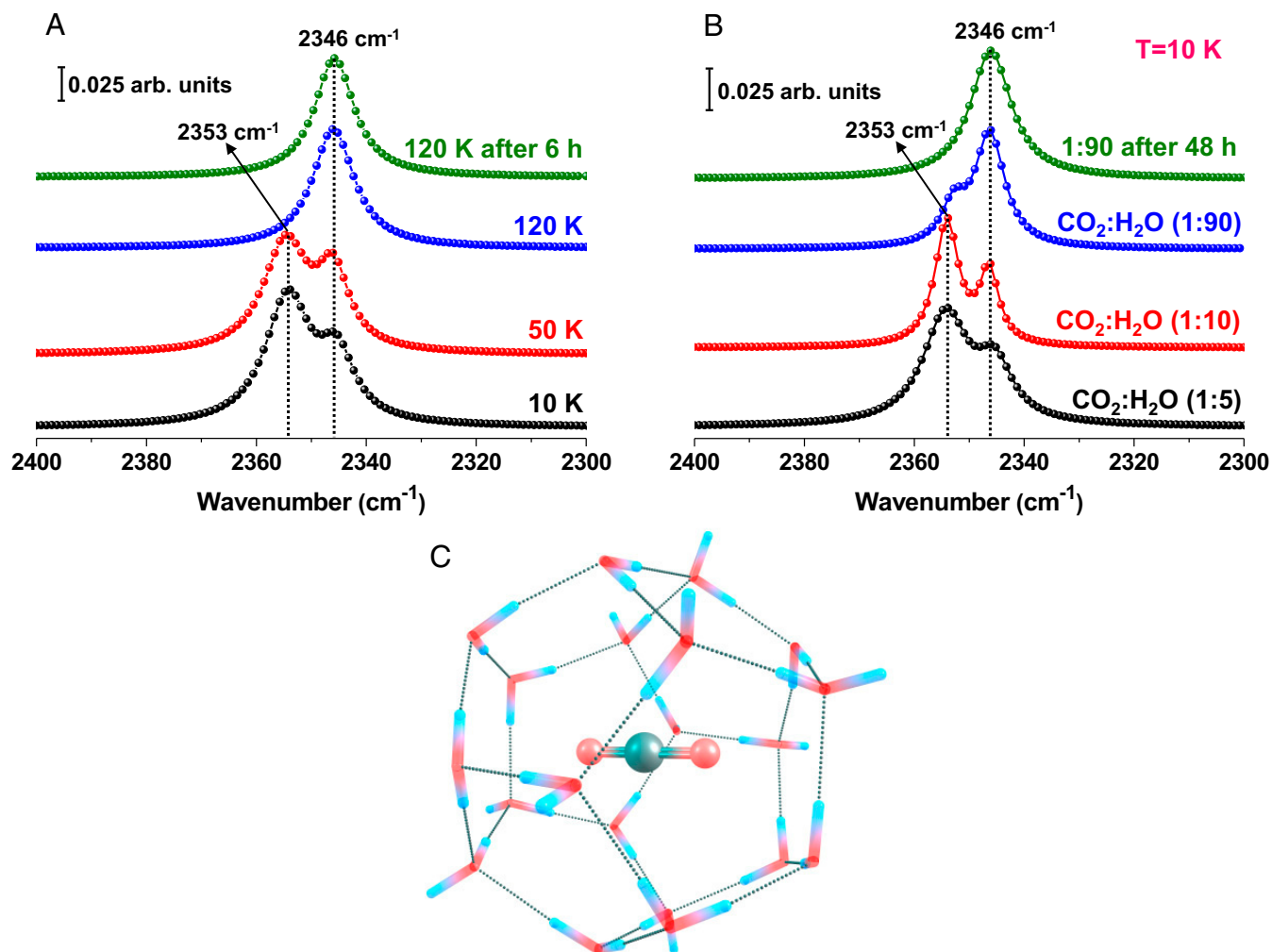


**Fig. 2.** CO<sub>2</sub> hydrate formation as studied by RAIR spectroscopy and quantum mechanical calculations. (A) Normalized temperature dependent RAIR spectra of 300 MLs CO<sub>2</sub>+H<sub>2</sub>O (1:5) mixed ice at C = O antisymmetric stretching region. A new peak at 2,346 cm<sup>-1</sup> arises due to the formation of CO<sub>2</sub> hydrate. (B) Ratio-dependent RAIR spectra of 300 MLs CO<sub>2</sub>+H<sub>2</sub>O at 10 K (normalized). (C) DFT-optimized structure of CO<sub>2</sub> trapped inside CH (5<sup>12</sup>) cage. Here, water cage and guest molecule (CO<sub>2</sub>) are shown. Color code used: gray, C; red, O; cyan, H.

outside of the CH cage, and in the amorphous pores of water ice. The other peak, positioned at 2,346 cm<sup>-1</sup>, is due to the CO<sub>2</sub> entrapped in the CH cage (15, 16). Now, as the system was annealed further to 50 K (heating rate = 2 K · min<sup>-1</sup>), the intensity of the CO<sub>2</sub> hydrate peak (2,346 cm<sup>-1</sup>) increased and that of the free CO<sub>2</sub> peak (2,353 cm<sup>-1</sup>) decreased. At 120 K, the untrapped CO<sub>2</sub> peak vanished completely and only the CO<sub>2</sub> hydrate peak remained. It indicates that the annealing of CO<sub>2</sub> mixed ice leads to the gradual formation of CO<sub>2</sub> hydrate and the transformation is complete at 120 K. Furthermore, no change in CO<sub>2</sub> hydrate peak position (2,346 cm<sup>-1</sup>) was observed when the system was kept at 120 K for 6 h (Fig. 2A). This confirms that the CO<sub>2</sub> hydrate is quite stable in these analogous astrochemical conditions. It is also clear that CO<sub>2</sub> hydrate forms even at 10 K during deposition itself.

The stoichiometric ratio of water and guest molecules is an essential aspect of controlling the formation of CH (12). The ideal ratio of water and guest molecules is 20:1 for CH<sub>3</sub>OH hydrate formed at 130 K and at 10<sup>-6</sup> torr pressure (12). Fig. 2B shows the comparative formation of CO<sub>2</sub> hydrate at different ratios of CO<sub>2</sub>:H<sub>2</sub>O at 10 K under UHV. The figure clearly indicates that the intensity of 2,346 cm<sup>-1</sup> peak is maximum for a 1:90 mixture compared with the other ratios. This suggests the optimum ratio needed for CO<sub>2</sub> hydrate formation at 10 K, which is a very diluted mixed

ice. The shoulder at 2,353 cm<sup>-1</sup> vanished upon keeping the ice at 10 K for over 48 h as shown in Fig. 2B, suggesting that all of the remaining free CO<sub>2</sub> forms hydrate structure over time.

We confirmed the formation of CO<sub>2</sub> hydrate by quantum chemical calculations. These calculations revealed that the small cage (5<sup>12</sup>), as shown in Fig. 2C, is favorable to form. Our computationally determined shift in the C = O antisymmetric mode closely matches with the experimental vibrational shift upon hydrate formation. Here, CO<sub>2</sub> is interacting with the water cage through hydrogen bonding, and consequently, there is a red shift. This result agrees well with the experimental shift (SI Appendix, Table S1). Other possible cages computed (5<sup>12</sup>6<sup>2</sup> and 5<sup>12</sup>6<sup>4</sup>) have reduced or opposite shift, respectively (SI Appendix, Table S1). In SI Appendix, Table S2, we have presented the coordinates of optimized geometries of CH<sub>4</sub> and CO<sub>2</sub> in 5<sup>12</sup>, 5<sup>12</sup>6<sup>2</sup>, and 5<sup>12</sup>6<sup>4</sup> CH cages. In SI Appendix, Table S3, we have added the harmonic frequencies calculated for different cages of CH<sub>4</sub>, CH, and CO<sub>2</sub>.

The rapid formation of CO<sub>2</sub> hydrate compared with the slow kinetics seen for CH<sub>4</sub> hydrate is because of the induced polarity of CO<sub>2</sub>. Nucleation mechanism of CH formation varies for different guest molecules and can depend on their chemical nature (17). During the nucleation of CO<sub>2</sub> hydrate structure, it interacts

with water through stronger interaction, whereas  $\text{CH}_4$  is unable to interact similarly. We extended the analysis using Bader's theory of atoms in molecules (AIM) to confirm the nature of interaction of guest molecules with hydrate cages. The electron density  $\rho(\mathbf{r}_c)$  values obtained for the critical points between a particular atom of the guest species and the hydrate cage along with the corresponding Laplacian of the electron density ( $\nabla^2\rho(\mathbf{r}_c)$ ) are listed in *SI Appendix, Table S4*. The higher value of electron density ( $\rho(\mathbf{r}_c)$ ) for the critical point between the O atom of  $\text{CO}_2$  and the hydrate cage (0.01563 a.u.) compared with that between the H atom of  $\text{CH}_4$  (0.00598 a.u.) and the hydrate cage suggests that the interaction for  $\text{CO}_2$  is stronger than that for methane.

In the previous experiments, codeposition of  $\text{CO}_2$  and water results in CH. Sequential deposition was also carried out. Annealing of this sequentially deposited system,  $\text{CO}_2\text{:H}_2\text{O}$  (1:5 ratio), did not result in  $\text{CO}_2$  hydrate and the  $2,346\text{ cm}^{-1}$  peak was not observed (*SI Appendix, Fig. S3*). Here, the peak at  $2,381\text{ cm}^{-1}$  is attributed to pure multilayer  $\text{CO}_2$ . This phenomenon strongly supports the fact that proper mixing of water and  $\text{CO}_2$  is a crucial step for the formation of  $\text{CO}_2$  hydrate. The codeposition method allows better mixing of  $\text{CO}_2$  molecules with water, whereas sequential deposition does not. Sequential deposition of water over

$\text{CO}_2$  may result in diffusional mixing, but this does not lead to the formation of CH.

About 1% of  $^{13}\text{CO}_2$  is present along with  $^{12}\text{CO}_2$  naturally as shown (*SI Appendix, Fig. S4*). During the  $^{12}\text{CO}_2$  hydrate experiment,  $^{13}\text{CO}_2$  also shows CH upon annealing to 120 K. Temperature-dependent RAIR spectra in the  $^{13}\text{C}=\text{O}$  antisymmetric stretching region (*SI Appendix, Fig. S5*), where the  $2,282\text{ cm}^{-1}$  peak is due to untrapped  $^{13}\text{CO}_2$  and that at  $2,278\text{ cm}^{-1}$  is due to  $^{13}\text{CO}_2$  hydrate (15).

The formation of CHs in ISM condition is further confirmed by temperature programmed desorption-mass spectrometry (TPD-MS). The trapped guest molecules within ASW are released when amorphous to crystalline ice transition occurs at 140 K. Fig. 3A represents the comparative TPD spectra before and after the formation of  $\text{CH}_4$  hydrate. The spectra correspond to  $\text{CH}_4$  desorption and were monitored using the intensity of  $\text{CH}_3^+$  alone. Peaks at 38 and 46 K correspond to multilayer  $\text{CH}_4$  and  $\text{CH}_4$  trapped in ASW ( $\text{CH}_4\cdot\text{ASW}$ ), respectively. These TPD peaks are assigned by a control study as shown (*SI Appendix, Fig. S6*). The  $\text{CH}_4$  hydrate was formed by annealing a codeposited mixture at 30 K for 25 h, and during this course, most of the free  $\text{CH}_4$  got desorbed, as observed from TPD. Desorption of  $\text{CH}_4$  in trapped ASW got shifted to 53 K after the formation of CH. The abrupt release of trapped gases from ASW at 140 K is termed as

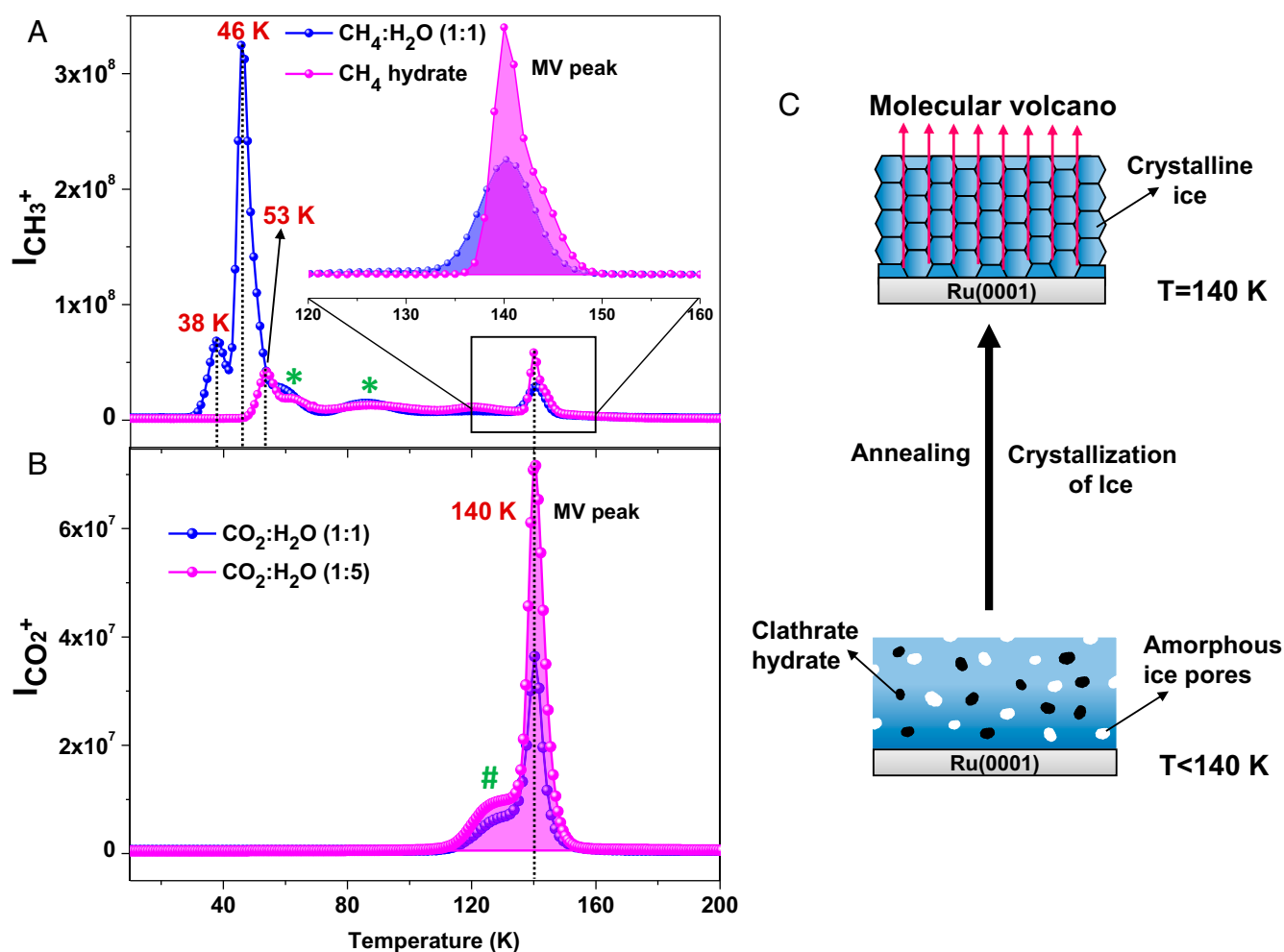


**Fig. 3.** TPD mass spectra of 300 MLs of codeposited ice systems at different ratio (heating rate =  $30\text{ K} \cdot \text{min}^{-1}$ ). Here, the intensities of  $\text{CH}_3^+$  ( $m/z = 15$ ), and  $\text{CO}_2^+$  ( $m/z = 44$ ) are plotted. (A) Desorption of  $\text{CH}_4$  after hydrate formation (magenta line) and before hydrate formation (blue line). MV peaks are shown in the *insets*. \*, peaks are attributed to desorption due to structural transitions of ASW upon annealing. (B) Desorption of  $\text{CO}_2$  after hydrate formation at different ratios, as indicated. #, the peak is due to the predissociation of  $\text{CO}_2$  hydrate cage. (C) Schematic representation of MV upon crystallization of ice.



molecular volcano (MV) (18, 19). The intensity of MV peak (at 140 K) increases, upon the formation of CH<sub>4</sub> hydrate. Before the formation of CH<sub>4</sub> hydrate, the MV peak is due to the trapped CH<sub>4</sub> in ASW. The reason for the enhancement of MV peak intensity is the simultaneous release of trapped CH<sub>4</sub> from ASW pores as well as from the CH<sub>4</sub> hydrate cage (Fig. 3C). Note that the amount of gases deposited is the same in both the cases. Slight distortion in the MV peak is attributed to the modification of ASW pores due to CH formation (Fig. 3A). The amount of desorption due to CH is estimated to be 14.53% of the total CH<sub>4</sub> at this condition, and it is correlated to the amount of CH calculated from the IR data (Fig. 1B).

In Fig. 3B, we compared the TPD spectra of 300 MLs of CO<sub>2</sub>+H<sub>2</sub>O at two ratios, 1:1 and 1:5, which were deposited at 10 K. Then, these two systems were annealed at 120 K for the complete formation of CO<sub>2</sub> hydrate. After that, they were cooled back to 10 K, and TPD mass spectra were taken. The heating rate for TPD was 30 K · min<sup>-1</sup>. The peak at 140 K corresponds to MV of CO<sub>2</sub>. Fig. 3B shows that the intensity of MV increased as the ratio of CO<sub>2</sub> and H<sub>2</sub>O was changed from 1:1 to 1:5. Taking the area under the MV peaks, the amount of CH formed was found 1.7 times higher for (1:5) than the former. As previously explained, the extent of formation of CO<sub>2</sub> hydrate is greater for the latter ratio (Fig. 2). Here again, the enhancement agrees with the IR data. No additional desorption of CH<sub>4</sub> and CO<sub>2</sub> above this temperature suggest that the hydrates have been decomposed.

## Conclusion

We have shown that CHs can form in UHV and they can exist in the ISM conditions down to 10 K and 10<sup>-10</sup> mbar. The anomalous eruption of volatile gases in ISM could be explained by the existence of hydrates. Enclathration of these gases and additional processing (e.g., irradiation, heating, etc.) may result in complex organic or prebiotic molecules. We believe that the present report may have an impact on both astronomy and chemistry.

## Materials and Methods

**Experimental Setup.** Experiments were conducted in an ultrahigh vacuum instrument (base pressure ~10<sup>-10</sup> mbar), which was described elsewhere (20, 21). Briefly, the instrument consists of a UHV chamber made of stainless steel, equipped with RAIR spectroscopy and TPD mass spectrometry. The spectrometer can also perform low energy ion scattering and secondary ion mass spectrometry, which have not been used in the present work (20). Vacuum of the order of ~10<sup>-10</sup> mbar is an essential condition for simulating the condition of ISM. Vacuum was maintained by three oil-free Turbo molecular pumps backed by diaphragm pumps (Pfeiffer Vacuum). The system has a collective pumping speed of ~400 L/s. The UHV system is fully covered with a heating jacket, which allows an easy bake out over the weekend. The pressure of the experimental chamber is monitored by a Bayard-Alpert gauge (Pfeiffer Vacuum), controlled by a "MaxiGauge" vacuum gauge controller (Pfeiffer, Model TPG 256 A).

A thin film of ice was grown on top of a Ru(0001) single crystal that was mounted on a copper holder, which in turn was attached at the tip of a closed cycle helium cryostat (Coldedge Technologies). The substrate temperature could be controlled from 8 to 1,000 K. Comprehensive heat shielding and excellent thermal contact between the substrate holder and the cryofinger allowed us to achieve 8 K in 2 h. For the present study, the temperature was measured by a thermocouple sensor attached to the substrate. Repeated heating to 300 K before vapor deposition ensured surface cleanliness, adequate for the present experiments. Temperature ramping was controlled and monitored by a temperature controller (Lakeshore 336) (20).

**Sample Preparation.** For the formation of methane hydrate, ~99.99% pure methane gas, purchased from Rana Industrial Gases & Products, was used. The gas lines were connected to the experimental chamber through a high-precision all-metal leak valve through which the flow rate or deposition pressure of different gases was controlled. These two deposition tubes or gas lines were directed to the center of the substrate. Out of the two sample inlet lines, one was used exclusively for methane or carbon dioxide while the

other line was used exclusively for water vapor deposition. Here, Millipore water (H<sub>2</sub>O of 18.2 MΩ resistivity), taken in a test tube, connected to the sample line through a glass-to-metal seal was used for the experiment. The Millipore water was further purified through several freeze-pump-thaw cycles before introduction into the UHV chamber. During the exposure of different samples into the UHV chamber, mass spectra were recorded with a residual gas analyzer (RGA) attached near to the sample inlet line. Recorded mass spectra were used as an indication of the purity of the samples as well as to measure the ratio of the mixtures. The ratio of the mixed ice was achieved by the proper adjustment of flow or inlet pressure of the sample gas by regulating the leak valves. The substrate was kept at a perpendicular position for the uniform growth of ice. Here, most of the experiments were performed using 300 MLs coverage of the mixed ice. One point to be noted is that all of the experiments were performed under multilayer deposition conditions, and therefore, the substrate does not play any significant role in the formation of CH. The deposition of molecular solids was controlled through leak valves, and ML coverage was calculated (18, 22) assuming that 1.33 × 10<sup>-6</sup> mbar · s = 1 ML, which was estimated to contain ~1.1 × 10<sup>15</sup> molecules · cm<sup>-2</sup>. Surface coverages mentioned were quantitative by following a similar deposition method adopted elsewhere (23). The inlet pressure during the sample deposition was decided based on the coverage desired at the time of the experiment.

**Typical Experimental Protocol.** For the deposition of 300 MLs of 1:1 mixed methane and ice, the chamber was backfilled at a total pressure of ~5 × 10<sup>-7</sup> mbar (where methane pressure was 2.5 × 10<sup>-7</sup> mbar and water pressure was 2.5 × 10<sup>-7</sup> mbar) and the mixture was exposed to the surface for 10 min. Evacuation of residual water from the experimental chamber is one of the most common issues with UHV experiments, particularly when we deposit large amounts of water. After deposition, we waited for a few minutes to reach the background pressure before starting the spectroscopic measurements. Periodic bake out of the chamber during weekends ensures the cleanliness of the chamber.

This 1:1 mixed methane and ice was slowly (heating rate = 2 K · min<sup>-1</sup>) heated to 30 K, near the desorption temperature of methane. At this temperature, most of the methane sublimed, which was observed in the mass spectra recorded by the residual gas analyzer. After that, the remaining mixed ice was maintained at 30 K for over 25 h. The ice sample was constantly monitored by IR spectroscopy. In other words, time-dependent RAIRS were recorded over a period of 25 h. During such measurements, a few monolayers of additional water could be deposited but this is rather negligible to be reflected in the spectra. Variation of a few monolayers in coverage does not change the observed phenomena. During the time-dependent measurements, we maintained identical conditions from the beginning to the end. The position of the substrate, the external IR detector (mercury cadmium telluride; MCT), and the environment (dry N<sub>2</sub>) in the IR spectrometer were kept constant throughout the experiment. A similar time-dependent RAIR study was carried out at 10 and 20 K also, and the spectra were collected for over 25 h as a separate set of experiments. IR exposure over extended periods did not have an effect on CH formation as revealed by studies at lower temperatures.

For the CO<sub>2</sub> hydrate study, 300 MLs of mixed ice was made by the codeposition of a mixture of CO<sub>2</sub>:H<sub>2</sub>O at 10 K. Different ratios (1:5, 1:10, and 1:90) of CO<sub>2</sub>:H<sub>2</sub>O were used. For each of the ratios, the total inlet pressure was kept at ~5 × 10<sup>-7</sup> mbar, whereas the inlet pressures of CO<sub>2</sub> and water were varied according to the desired ratio. For the temperature-dependent measurements, after deposition of 1:5 ratio of CO<sub>2</sub>:H<sub>2</sub>O at 10 K, the sample was slowly heated (heating rate = 2 K · min<sup>-1</sup>) up to 160 K. In another set of experiments, sequential deposition of CO<sub>2</sub> and water was carried out, where at first 150 MLs of CO<sub>2</sub> were deposited, which was followed by the deposition of 150 MLs of water at 10 K. By this way, we generated a sequentially deposited (CO<sub>2</sub>@H<sub>2</sub>O) film of equal coverage. A similar temperature-dependent IR study was carried out as described before, with this sequentially deposited film to observe the formation of CO<sub>2</sub> CH.

**RAIRS Setup.** RAIR spectra were recorded using a Bruker FT-IR spectrometer, Vertex 70. The external IR beam was focused onto the substrate using gold-plated mirrors through ZnSe windows (transparent to IR beam), attached to the vacuum chamber. The reflected IR beam from the substrate was refocused using another gold-plated mirror to a liquid N<sub>2</sub> cooled external MCT IR detector. The spectra were collected in the 4,000–550 cm<sup>-1</sup> range with 2 cm<sup>-1</sup> resolution. Each spectrum was an average of 512 scans to get a better signal-to-noise ratio. The IR beam path outside the UHV chamber was purged with dry N<sub>2</sub>.

**TPD-MS Setup.** The clathrate hydrates were further characterized by TPD-MS analysis. For this, after ice deposition or clathrate hydrate formation (by following the method described earlier), the substrate was moved to a fixed position by using the sample manipulator to ensure that the surface is close to the mass spectrometer inlet. During TPD-MS measurements, the substrate was heated at a constant heating rate ( $30\text{ K} \cdot \text{min}^{-1}$ ). Suitable mass of the desorbed species was selected by the RGA and the intensity of the desorbed species was plotted as a function of substrate temperature. Mass spectrometers were supplied by Extrel CMS (20). For TPD, the inlet of the mass spectrometer was positioned 50 mm from the center of the Ru substrate.

**Computational Details.** We examined the stability of clathrate hydrate cages and their  $\text{CO}_2$ ,  $\text{CH}_4$  inclusion complexes computationally. All of the considered cages of clathrate hydrates have been fully optimized at the B3LYP/6-311++G (d, p) level of theory using the Gaussian 09 program package (24). Frequency calculations characterize the obtained stationary points as minima on the potential energy surface. We sequentially added  $\text{CO}_2$  and  $\text{CH}_4$  molecules in  $5^{12}$ ,  $5^{12}6^2$ , and  $5^{12}6^4$  clathrate hydrate cages and probed their

cage occupancy. In general, the optimizations of clathrate hydrate cages were found to be quite challenging with the Gaussian programs. Normally, most optimizations of clathrate cages take a large number of steps and it was difficult to reach convergence. The B3LYP/6-311++G (d, p) level of theory was found to be reasonable for optimizations of clathrate hydrates and various other water clusters (14). The quantum theory of atoms in molecules methodology (25) was capable of revealing bonding interactions between individual functional groups and atoms in a molecule by the electron density distribution analysis.

All possible cages were considered in the present study. It was found that the  $5^{12}$  clathrate hydrate cage was more stable; stability also depended on the size of the guest molecule. These results were also compared with the computational studies reported (14).

**ACKNOWLEDGMENTS.** J.G. thanks the University Grants Commission (UGC) for his research fellowship. We thank the Department of Science and Technology, Government of India, for supporting our research.

- Sloan ED, Jr (2003) Fundamental principles and applications of natural gas hydrates. *Nature* 426:353–363.
- Walsh MR, Koh CA, Sloan ED, Sum AK, Wu DT (2009) Microsecond simulations of spontaneous methane hydrate nucleation and growth. *Science* 326:1095–1098.
- Park Y, et al. (2006) Sequestering carbon dioxide into complex structures of naturally occurring gas hydrates. *Proc Natl Acad Sci USA* 103:12690–12694.
- Boswell R (2009) Engineering. Is gas hydrate energy within reach? *Science* 325: 957–958.
- Chastain BK, Chevrier V (2007) Methane clathrate hydrates as a potential source for martian atmospheric methane. *Planet Space Sci* 55:1246–1256.
- Swindle TD, Thomas C, Mousis O, Lunine JL, Picaud S (2009) Incorporation of argon, krypton and xenon into clathrates on Mars. *Icarus* 203:66–70.
- Thomas C, Mousis O, Picaud S, Ballenegger V (2009) Variability of the methane trapping in martian subsurface clathrate hydrates. *Planet Space Sci* 57:42–47.
- Tobie G, Lunine JL, Sotin C (2006) Episodic outgassing as the origin of atmospheric methane on Titan. *Nature* 440:61–64.
- Mousis O, Lunine JL, Picaud S, Cordier D (2010) Volatile inventories in clathrate hydrates formed in the primordial nebula. *Faraday Discuss* 147:509–525, 527–552.
- Luspay-Kuti A, et al. (2016) The presence of clathrates in comet 67P/Churyumov-Gerasimenko. *Sci Adv* 2:e1501781.
- Mao WL, et al. (2002) Hydrogen clusters in clathrate hydrate. *Science* 297:2247–2249.
- Blake D, Allamandola L, Sandford S, Hudgins D, Freund F (1991) Clathrate hydrate formation in amorphous cometary ice analogs in vacuo. *Science* 254:548–551.
- Allamandola LJ, Bernstein MP, Sandford SA, Walker RL (1999) Evolution of interstellar ices. *Space Sci Rev* 90:219–232.
- Buch V, et al. (2009) Clathrate hydrates with hydrogen-bonding guests. *Phys Chem Chem Phys* 11:10245–10265.
- Fleyfel F, Devlin JP (1991) Carbon dioxide clathrate hydrate epitaxial growth: Spectroscopic evidence for formation of the simple type-II carbon dioxide hydrate. *J Phys Chem* 95:3811–3815.
- Kumar R, Lang S, Englezos P, Ripmeester J (2009) Application of the ATR-IR spectroscopic technique to the characterization of hydrates formed by  $\text{CO}_2$ ,  $\text{CO}_2/\text{H}_2$  and  $\text{CO}_2/\text{H}_2/\text{C}_3\text{H}_8$ . *J Phys Chem A* 113:6308–6313.
- Warrier P, Khan MN, Srivastava V, Maupin CM, Koh CA (2016) Overview: Nucleation of clathrate hydrates. *J Chem Phys* 145:211705.
- Ghosh J, Hariharan AK, Bhuin RG, Methikkalam RRJ, Pradeep T (2018) Propane and propane-water interactions: A study at cryogenic temperatures. *Phys Chem Chem Phys* 20:1838–1847.
- Smith RS, Petrik NG, Kimmel GA, Kay BD (2012) Thermal and nonthermal physicochemical processes in nanoscale films of amorphous solid water. *Acc Chem Res* 45: 33–42.
- Bag S, et al. (2014) Development of ultralow energy (1–10 eV) ion scattering spectrometry coupled with reflection absorption infrared spectroscopy and temperature programmed desorption for the investigation of molecular solids. *Rev Sci Instrum* 85: 014103.
- Bhuin RG, Methikkalam RRJ, Sivaraman B, Pradeep T (2015) Interaction of acetonitrile with water-ice: An infrared spectroscopic study. *J Phys Chem C* 119:11524–11532.
- Eui-Seong M, Heon K, Yasuhiro O, Naoki W, Akira K (2010) Direct evidence for ammonium ion formation in ice through ultraviolet-induced acid-base reaction of  $\text{NH}_3$  with  $\text{H}_3\text{O}^+$ . *Astrophys J* 713:906–911.
- Kimmel GA, Petrik NG, Dohnálek Z, Kay BD (2005) Crystalline ice growth on PT(111): Observation of a hydrophobic water monolayer. *Phys Rev Lett* 95:166102.
- Frisch MJ, et al. (2009) *Gaussian 09, Revision A.1* (Gaussian, Inc., Wallingford, CT).
- Bader RFW (1990) *Atoms in Molecules. A Quantum Theory* (Oxford Univ Press, Oxford).





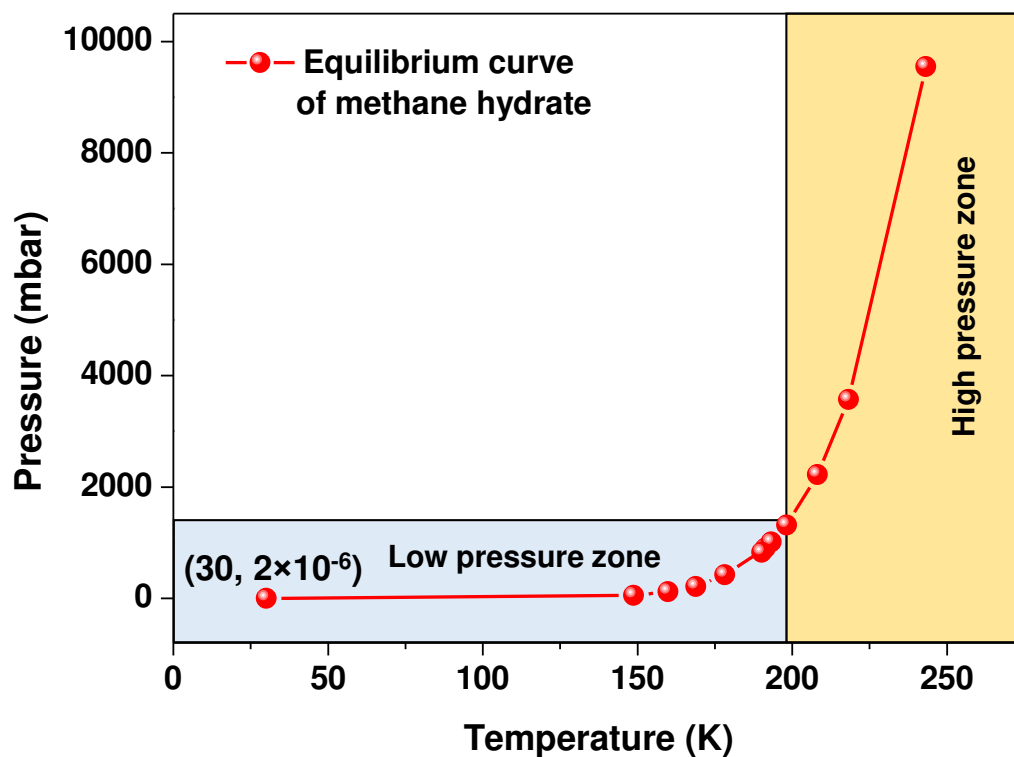
Supplementary Information for  
Clathrate hydrates in interstellar environment

Jyotirmoy Ghosh<sup>a</sup>, Rabin Rajan J. Methikkalam<sup>a</sup>, Radha Gobinda Bhuin<sup>a</sup>, Gopi  
Ragupathy<sup>a</sup>, Nilesh Choudhary<sup>b</sup>, Rajnish Kumar<sup>b,1</sup>, Thalappil Pradeep<sup>a,1</sup>

Corresponding author: Thalappil Pradeep and Rajnish Kumar  
Email: [pradeep@iitm.ac.in](mailto:pradeep@iitm.ac.in), and [rajnish@iitm.ac.in](mailto:rajnish@iitm.ac.in)

**This PDF file includes:**

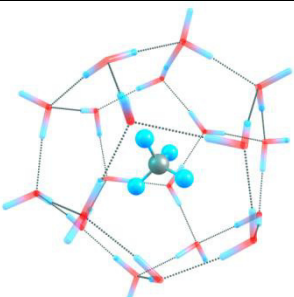
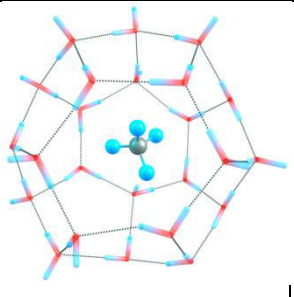
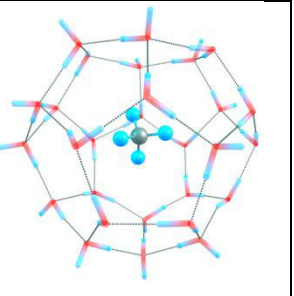
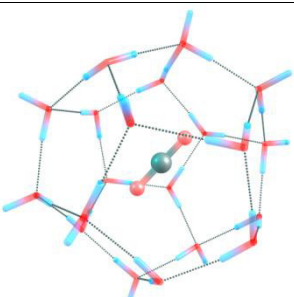
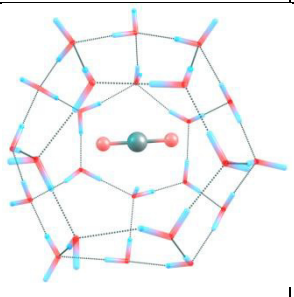
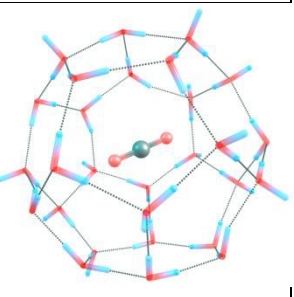
Supplementary text  
Figs. S1 to S6  
Tables S1 to S4



**Fig. S1.** Equilibrium curve for CH<sub>4</sub> clathrate hydrate. The curve depicts the stability of CH<sub>4</sub> clathrate hydrate as a function of temperature and pressure. Extrapolation of the curve to 30 K, denotes that CH<sub>4</sub> hydrate could be stable up to 2×10<sup>-6</sup> mbar pressure. Two different pressure zones of the equilibrium curve are indicated with different colours.

**Table S1**

Comparison of the computational and experimental vibrational shift of CH<sub>4</sub> and CO<sub>2</sub> clathrate hydrate compared to free CH<sub>4</sub> and CO<sub>2</sub> using the B3LYP level of theory with 6-311++G (d, p) basis set. Optimized structures are shown.

	<b>5<sup>12</sup> cage</b>	<b>5<sup>12</sup> 6<sup>2</sup> cage</b>	<b>5<sup>12</sup> 6<sup>4</sup> cage</b>
<b>CH<sub>4</sub> Clathrate hydrate</b>			
<b>Experimental shift</b>	8.0 cm <sup>-1</sup>	-	-
<b>Computational shift</b>	9.3 cm <sup>-1</sup>	-9.2 cm <sup>-1</sup>	-9.1 cm <sup>-1</sup>
<b>CO<sub>2</sub> Clathrate hydrate</b>			
<b>Experimental shift</b>	-36.0 cm <sup>-1</sup>	-	-
<b>Computational al shift</b>	-86.0 cm <sup>-1</sup>	-16.6 cm <sup>-1</sup>	15.8 cm <sup>-1</sup>

**Table S2**

Cartesian coordinates of CH<sub>4</sub> and CO<sub>2</sub> hydrate of 5<sup>12</sup>, 5<sup>12</sup>6<sup>2</sup>, and 5<sup>12</sup>6<sup>4</sup> cages. The structure is optimized by using B3LYP level of theory and 6-311G (d, p) basis set.

**1. Cartesian coordinates of CH<sub>4</sub> hydrate, 5<sup>12</sup> Cage:**

O	-3.113799000	1.008215000	-2.047060000
H	-2.381895000	0.992378000	-2.714133000
H	-3.218239000	0.092361000	-1.737059000
O	0.761157000	-0.854957000	3.737123000
H	1.560278000	-0.913295000	3.191474000
H	0.148218000	-1.525272000	3.382112000
O	-1.002868000	0.947991000	-3.756640000
H	-0.309583000	1.569863000	-3.462264000
H	-0.578668000	0.068649000	-3.767502000
O	3.236217000	-0.955734000	2.135120000
H	3.165067000	-1.629113000	1.426215000
H	3.958821000	-1.235974000	2.706513000
O	-2.887629000	1.244738000	2.323347000
H	-2.864259000	1.802526000	1.528887000
H	-2.060639000	1.440855000	2.816443000
O	3.377885000	1.359687000	-1.664637000
H	3.390890000	1.479109000	-0.669870000
H	4.148373000	1.829781000	-2.000028000
O	-3.128400000	-1.415490000	1.789380000
H	-3.087569000	-0.450695000	2.003609000
H	-3.283298000	-1.476211000	0.831714000

O	2.934977000	-1.253851000	-2.282868000
H	3.114524000	-0.298037000	-2.098165000
H	3.468989000	-1.484359000	-3.050455000
O	-0.392260000	3.941626000	-0.321881000
H	-1.300177000	3.541485000	-0.260272000
H	-0.524169000	4.853345000	-0.602208000
O	-1.315789000	-3.368020000	-1.793775000
H	-0.766874000	-3.555981000	-0.981288000
H	-1.479818000	-4.222051000	-2.206772000
O	1.274060000	3.320629000	1.800109000
H	0.676657000	3.585035000	1.064246000
H	1.488010000	4.128382000	2.278270000
O	0.169003000	-3.814487000	0.364703000
H	-0.238946000	-3.488499000	1.197401000
H	1.064810000	-3.442266000	0.323879000
O	-2.826177000	2.787763000	-0.173036000
H	-2.934327000	2.091445000	-0.898850000
H	-3.618404000	3.333407000	-0.214224000
O	-1.055651000	-2.776069000	2.622687000
H	-1.388378000	-3.388609000	3.286796000
H	-1.855960000	-2.248031000	2.311115000
O	0.248875000	-1.605446000	-3.500857000
H	-0.291977000	-2.196372000	-2.949011000
H	1.080021000	-1.487073000	-3.016487000
O	3.377580000	1.642717000	0.955655000

H	3.325899000	0.801116000	1.444402000
H	2.669365000	2.221709000	1.300892000
O	2.888590000	-2.759494000	0.015226000
H	3.477233000	-3.513445000	-0.097366000
H	2.928022000	-2.253620000	-0.830955000
O	0.935500000	2.696090000	-2.620765000
H	1.742558000	2.253160000	-2.312497000
H	0.528794000	3.081979000	-1.827324000
O	-0.442940000	1.678091000	3.581632000
H	-0.011264000	0.807131000	3.705067000
H	0.163645000	2.190341000	3.026261000
O	-3.430939000	-1.707732000	-1.081963000
H	-2.720572000	-2.319774000	-1.376262000
H	-4.261351000	-2.100719000	-1.369631000
C	0.021699000	0.014389000	-0.004436000
H	0.102928000	-1.071075000	-0.064084000
H	-0.278043000	0.408448000	-0.974906000
H	0.984345000	0.437479000	0.283329000
H	-0.722369000	0.274011000	0.747594000

**2. Cartesian coordinates of CO<sub>2</sub> hydrate, 5<sup>12</sup> Cage:**

O	-0.868021000	3.588583000	-1.062084000
H	0.066218000	3.438070000	-1.408937000
H	-1.430117000	2.919226000	-1.508264000
O	-1.706223000	-2.946539000	2.022264000
H	-0.770471000	-3.035377000	1.755662000

H	-2.171975000	-2.696231000	1.191943000
O	1.596326000	3.122198000	-1.934612000
H	2.186276000	2.918271000	-1.169796000
H	1.624434000	2.318089000	-2.504875000
O	1.040272000	-3.445759000	1.251327000
H	1.080443000	-3.488309000	0.263060000
H	1.111111000	-4.360300000	1.563830000
O	-3.071044000	1.240215000	2.040835000
H	-2.352366000	1.862651000	1.806185000
H	-2.630359000	0.554553000	2.609979000
O	3.820642000	-0.340356000	0.262704000
H	3.423565000	-0.820900000	1.074377000
H	4.775571000	-0.307884000	0.426195000
O	-3.889176000	0.127430000	-0.240429000
H	-3.634618000	0.543466000	0.638883000
H	-3.459546000	0.689488000	-0.919834000
O	2.916361000	-1.388227000	-1.994854000
H	3.314869000	-1.004684000	-1.156094000
H	3.642988000	-1.470212000	-2.630746000
O	1.299069000	2.625576000	2.498043000
H	0.400986000	2.879855000	2.108578000
H	1.586053000	3.384128000	3.028280000
O	-1.096637000	-0.132027000	-3.637858000
H	-1.187205000	-1.051178000	-3.209203000
H	-1.310462000	-0.266456000	-4.573538000

O	1.098934000	0.151735000	3.562278000
H	1.180338000	1.088266000	3.236013000
H	1.116802000	0.201161000	4.529891000
O	-1.340796000	-2.497246000	-2.570136000
H	-1.970098000	-2.436408000	-1.803130000
H	-0.489404000	-2.775385000	-2.172927000
O	-1.038061000	3.174905000	1.441572000
H	-0.949613000	3.321711000	0.415082000
H	-1.488139000	3.970026000	1.766134000
O	-2.952018000	-2.254904000	-0.391508000
H	-3.755968000	-2.794278000	-0.446434000
H	-3.300324000	-1.285945000	-0.316151000
O	1.592742000	0.749874000	-3.423629000
H	0.652483000	0.484801000	-3.511696000
H	1.982256000	0.062811000	-2.849519000
O	2.838088000	-1.586054000	2.308754000
H	2.226577000	-2.283377000	1.979844000
H	2.258337000	-0.965752000	2.813275000
O	1.168056000	-3.356005000	-1.486938000
H	1.409354000	-4.148468000	-1.990155000
H	1.850759000	-2.664779000	-1.716536000
O	3.117526000	2.443550000	0.301684000
H	3.315088000	1.486219000	0.258949000
H	2.488449000	2.526490000	1.047734000
O	-1.694213000	-0.618757000	3.500779000



H	-1.766148000	-1.490403000	3.035732000
H	-0.754396000	-0.372599000	3.401749000
O	-2.559414000	1.650173000	-2.227732000
H	-2.050242000	1.012432000	-2.796781000
H	-3.187348000	2.092683000	-2.818208000
C	-0.236975000	-0.022832000	-0.055102000
O	0.569452115	0.641156553	0.470020419
O	-1.043403816	-0.686813492	-0.580231437

### 3. Cartesian coordinates of CH<sub>4</sub> hydrate, 5<sup>12</sup>6<sup>2</sup> Cage:

O	-1.670912000	-4.226009000	-1.082352000
H	-2.375524000	-3.766957000	-0.603643000
H	-2.959334000	-2.320575000	1.911485000
O	3.529092000	2.803767000	1.029338000
H	-1.351771000	-3.578305000	-1.739442000
H	-2.569391000	-2.645506000	3.386338000
O	-3.825508000	-2.802754000	0.442226000
H	2.929516000	3.374599000	0.509101000
H	-5.468080000	-0.476336000	-1.297831000
O	1.675003000	4.357287000	-0.462631000
H	4.288235000	3.348667000	1.261625000
H	-4.426153000	0.220910000	-0.353308000
O	4.139684000	-1.822405000	0.869087000
H	-4.547179000	-3.439336000	0.475345000
H	-0.981477000	5.165787000	1.386092000
O	-4.100843000	1.509095000	0.645082000

H	-4.152398000	-2.036879000	-0.088426000
H	-1.472644000	4.135872000	0.310204000
O	2.754696000	-3.524800000	-1.148957000
H	0.821835000	4.395381000	0.033043000
H	1.390268000	3.342589000	-2.065515000
O	-2.709958000	3.585579000	-0.704716000
H	1.911470000	5.272815000	-0.647189000
H	1.490020000	3.250005000	-3.612671000
O	-2.744559000	0.731707000	3.040679000
H	3.633583000	-1.680969000	1.697571000
H	-1.998216000	1.501647000	-2.910970000
O	2.229125000	1.390499000	3.194198000
H	4.929342000	-2.315907000	1.112625000
H	-0.744828000	2.479495000	-2.858839000
O	4.353905000	0.558668000	-0.693508000
H	-3.609881000	2.239531000	0.222207000
H	2.223599000	-1.362192000	-3.409527000
O	2.624222000	-1.238043000	3.147085000
H	-3.636143000	1.295966000	1.475066000
H	2.218476000	-2.751014000	-2.703744000
O	-2.471293000	-1.980180000	2.696660000
H	3.194764000	-2.945362000	-0.509959000
H	0.592452000	-4.140968000	1.200296000
O	-4.579206000	-0.571005000	-0.940033000
H	2.062654000	-3.995233000	-0.634114000

H	-0.123889000	-4.625560000	-0.086935000
O	-0.709102000	4.380655000	0.899103000
H	-2.306692000	3.123411000	-1.524305000
H	-0.341601000	-1.612857000	-1.657252000
O	1.122959000	2.810480000	-2.838108000
H	-3.333393000	4.233540000	-1.050255000
H	0.234227000	-2.116329000	-2.985975000
O	-1.711676000	2.439102000	-2.755956000
H	-2.632211000	-0.244876000	2.975008000
H	-1.137195000	1.788790000	3.046958000
O	1.802672000	-2.243961000	-3.435423000
H	-3.253054000	0.885301000	3.844124000
H	-0.512036000	3.000628000	2.303422000
O	0.726252000	-4.665817000	0.391856000
H	1.310371000	1.731422000	3.207575000
H	-1.890831000	-0.791522000	-3.007814000
O	-0.636408000	-1.982559000	-2.497875000
H	2.685233000	1.881333000	2.489575000
H	-3.256373000	-0.341073000	-2.411504000
O	-0.373664000	2.391835000	3.046281000
H	4.094280000	1.264692000	-0.082898000
H	3.437823000	0.428194000	-2.285335000
O	-2.577228000	-0.090461000	-3.057271000
H	4.324432000	-0.265563000	-0.174937000
H	2.208278000	1.072719000	-2.963687000

O	2.862669000	0.369477000	-3.074985000
H	2.459143000	-0.254212000	3.165096000
H	1.068282000	-2.297241000	2.811159000
O	0.330133000	-2.914756000	2.665132000
H	2.970538000	-1.460402000	4.017548000
H	-0.467690000	-2.376841000	2.566654000
C	0.273774000	0.028734000	0.124279000
H	0.247314000	-1.019981000	0.427699000
H	1.075606000	0.172601000	-0.600784000
H	0.463833000	0.641570000	1.005234000
H	-0.680662000	0.318927000	-0.319142000

**4. Cartesian coordinates of CO<sub>2</sub> hydrate, 5<sup>12</sup>6<sup>2</sup> Cage:**

O	0.924327000	-4.271216000	-1.002928000
H	0.117919000	-4.127666000	-0.489932000
H	-1.145871000	-3.412845000	2.055052000
O	1.485002000	4.299181000	0.902052000
H	0.860379000	-3.642443000	-1.746774000
H	-0.618827000	-3.437657000	3.517730000
O	-1.595810000	-4.312127000	0.612579000
H	0.666072000	4.439132000	0.389312000
H	-4.370677000	-3.460119000	-1.063668000
O	-0.918089000	4.510434000	-0.560126000
H	1.796279000	5.172287000	1.162723000
H	-3.810366000	-2.244442000	-0.248867000
O	4.556701000	0.834186000	0.836470000

H	-1.652190000	-5.271066000	0.548338000
H	-3.569920000	3.810540000	1.330457000
O	-4.208194000	-0.945854000	0.721561000
H	-2.330449000	-3.940048000	0.074625000
H	-3.476551000	2.664970000	0.268110000
O	4.397838000	-1.439490000	-1.099305000
H	-1.651706000	4.096084000	-0.048420000
H	-0.651556000	3.378515000	-2.082013000
O	-4.284931000	1.517126000	-0.702504000
H	-1.248593000	5.372562000	-0.835036000
H	-0.127150000	3.105896000	-3.524321000
O	-2.675457000	-0.783823000	3.139978000
H	4.061790000	0.682406000	1.669739000
H	-2.626512000	0.141540000	-2.931559000
O	1.151354000	2.440252000	3.109620000
H	5.486847000	0.891199000	1.077303000
H	-2.114796000	1.621420000	-2.927138000
O	3.371151000	2.829900000	-0.797838000
H	-4.228803000	-0.078109000	0.278439000
H	2.780148000	-0.049862000	-3.413861000
O	2.979907000	0.518745000	3.111220000
H	-3.690206000	-0.835611000	1.540206000
H	3.515440000	-1.175917000	-2.636865000
O	-0.922532000	-2.842374000	2.823957000
H	4.417246000	-0.686008000	-0.490709000

H	2.836439000	-3.029222000	1.236715000
O	-3.548801000	-3.024117000	-0.815092000
H	4.048153000	-2.189809000	-0.570516000
H	2.478621000	-3.804023000	-0.053318000
O	-2.939589000	3.282082000	0.828980000
H	-3.738088000	1.336909000	-1.540270000
H	0.214978000	-1.502215000	-2.331876000
O	-0.661011000	2.737727000	-2.811563000
H	-5.178640000	1.708922000	-1.006373000
H	1.478903000	-1.811849000	-3.163727000
O	-2.912810000	1.071654000	-2.832473000
H	-2.032597000	-1.525377000	3.089947000
H	-1.916372000	0.976551000	3.108154000
O	2.921256000	-1.013355000	-3.403145000
H	-3.242091000	-0.971337000	3.895796000
H	-2.023365000	2.277905000	2.276867000
O	3.230295000	-3.428795000	0.443017000
H	0.196768000	2.212985000	3.129825000
H	-1.449901000	-2.019742000	-3.321833000
O	0.597318000	-2.195804000	-2.880566000
H	1.263372000	3.081360000	2.389559000
H	-2.630423000	-2.186872000	-2.298298000
O	-1.584034000	1.889483000	3.046487000
H	2.792935000	3.329876000	-0.200309000
H	2.673902000	2.143459000	-2.325081000

O	-2.199404000	-1.565376000	-2.908164000
H	3.823983000	2.170298000	-0.243938000
H	1.275135000	1.685598000	-2.748633000
O	2.179542000	1.750217000	-3.075471000
H	2.283661000	1.230852000	3.111445000
H	2.254027000	-1.213976000	2.813420000
O	1.958656000	-2.131674000	2.702163000
H	3.379574000	0.547887000	3.986700000
H	0.998975000	-2.101258000	2.605737000
C	-0.299000000	-0.053692000	0.072084000
O	-0.825551000	1.023644000	-0.532867000
O	0.225129000	-1.130569000	0.675788000

**5. Cartesian coordinates of CH<sub>4</sub> hydrate, 5<sup>12</sup>6<sup>4</sup> Cage:**

O	-1.605874000	4.327345000	1.091007000
H	-0.654904000	4.407629000	0.894300000
H	4.240880000	0.680906000	-1.253611000
O	1.233495000	4.441217000	0.673175000
H	-2.034107000	4.065372000	0.259580000
H	4.480701000	-0.767814000	-0.759697000
O	-2.056668000	2.784311000	3.368236000
H	1.513626000	4.169658000	-0.214507000
H	-4.444734000	-1.192308000	0.417931000
O	2.705554000	2.928418000	2.718463000
H	1.691220000	3.853647000	1.294587000
H	-5.572570000	-0.294812000	0.990577000

O	-2.874993000	3.695924000	-1.473950000
H	-1.163278000	2.570836000	3.676758000
H	-0.987716000	-1.466298000	4.048379000
O	1.895069000	3.860804000	-2.103425000
H	-1.935305000	3.355548000	2.579668000
H	-2.409912000	-0.948528000	3.549798000
O	0.606333000	2.048822000	4.405162000
H	3.264189000	2.163176000	2.446792000
H	3.239813000	-0.849629000	2.774491000
O	-0.745370000	3.468092000	-3.305074000
H	3.315039000	3.605709000	3.030048000
H	2.884539000	-2.358665000	2.721381000
O	-3.398682000	0.421657000	3.080969000
H	-3.397667000	2.847257000	-1.548749000
H	-2.230601000	0.163339000	-3.940207000
O	4.219506000	0.756811000	1.990518000
H	-3.505033000	4.402630000	-1.648458000
H	-2.636723000	-1.076249000	-3.096173000
O	3.469582000	1.595749000	-2.799803000
H	2.467083000	3.109831000	-2.354693000
H	1.962820000	-1.149562000	-3.893241000
O	-4.257056000	1.444682000	-1.756283000
H	2.297519000	4.648681000	-2.483857000
H	1.918542000	-0.261234000	-5.175820000
O	0.544487000	-0.874416000	4.614731000



H	1.345024000	2.393503000	3.866115000
H	-3.187659000	-3.228967000	0.896130000
O	-0.772966000	1.018254000	-4.521579000
H	0.679144000	2.472813000	5.266724000
H	-4.566967000	-3.592812000	0.253793000
O	4.717913000	0.160548000	-0.585984000
H	0.076719000	3.653591000	-2.826103000
H	3.357457000	-2.718420000	-1.839087000
O	-4.722620000	-0.265511000	0.538887000
H	-1.473930000	3.594558000	-2.664691000
H	4.681411000	-3.205331000	-1.185147000
O	-1.875353000	-1.757685000	3.727678000
H	-2.966247000	1.303071000	3.182815000
H	-1.978711000	-2.837672000	2.753840000
O	2.935260000	-1.586080000	3.323035000
H	-3.668930000	0.363306000	2.154304000
H	-2.386425000	-4.376539000	2.643973000
O	-3.001014000	-0.299826000	-3.539573000
H	4.409631000	0.574759000	1.033410000
H	3.100205000	-3.264608000	0.596776000
O	1.933968000	-0.224859000	-4.213202000
H	5.044014000	0.597337000	2.462156000
H	1.901992000	-3.990620000	1.254997000
O	-3.826361000	-2.983336000	0.160478000
H	2.926743000	0.968464000	-3.326700000

H	-3.077576000	-3.004971000	-1.461877000
O	3.961160000	-2.573327000	-1.085948000
H	4.247552000	1.782165000	-3.337163000
H	-3.358176000	-3.237996000	-2.980485000
O	-2.118740000	-3.636620000	2.087794000
H	-3.869394000	0.835977000	-2.420132000
H	1.246287000	-3.243811000	-2.866705000
O	2.798806000	-3.643142000	1.434631000
H	-4.442885000	0.900718000	-0.973779000
H	2.359088000	-3.495501000	-3.917251000
O	-2.657193000	-3.031014000	-2.352912000
H	1.374381000	-1.190133000	4.201493000
H	0.053421000	-4.193386000	-0.205613000
O	2.086042000	-2.871771000	-3.234887000
H	0.583603000	0.093715000	4.565807000
H	-0.517509000	-4.176128000	1.229564000
O	0.223361000	-4.513301000	0.691120000
H	0.042339000	0.616402000	-4.196206000
H	-1.068476000	-3.680186000	-2.349020000
O	-0.160157000	-4.048155000	-2.215880000
H	-0.785060000	1.923773000	-4.127641000
H	-0.237369000	-4.999070000	-2.351085000
C	0.381333000	-0.246902000	-0.139731000
H	0.268241000	-1.056677000	-0.863370000
H	-0.540807000	-0.144842000	0.433693000

H	0.577766000	0.689340000	-0.663475000
---	-------------	-------------	--------------

H	1.199761000	-0.472262000	0.543971000
---	-------------	--------------	-------------

**6. Cartesian coordinates of CO<sub>2</sub> hydrate, 5<sup>12</sup>6<sup>4</sup> Cage:**

C	-0.550460000	0.498600000	-0.096952000
---	--------------	-------------	--------------

O	-1.145201000	-0.417503000	-0.484701000
---	--------------	--------------	--------------

O	0.040166000	1.425588000	0.290450000
---	-------------	-------------	-------------

O	1.082845000	-3.985558000	2.360476000
---	-------------	--------------	-------------

H	1.843465000	-3.387649000	2.473499000
---	-------------	--------------	-------------

H	3.328391000	2.699927000	1.002441000
---	-------------	-------------	-------------

O	3.323752000	-2.196294000	2.509719000
---	-------------	--------------	-------------

H	0.326129000	-3.543707000	2.778462000
---	-------------	--------------	-------------

H	3.035841000	3.327263000	-0.387179000
---	-------------	-------------	--------------

O	0.826312000	-4.812167000	-0.290227000
---	-------------	--------------	--------------

H	3.109558000	-1.345108000	2.921842000
---	-------------	--------------	-------------

H	-3.962353000	-2.146585000	-0.743573000
---	--------------	--------------	--------------

O	4.567539000	-1.785603000	-0.135342000
---	-------------	--------------	--------------

H	3.669184000	-1.996440000	1.626401000
---	-------------	--------------	-------------

H	-4.277706000	-3.636801000	-0.431233000
---	--------------	--------------	--------------

O	-1.139664000	-2.767234000	3.839162000
---	--------------	--------------	-------------

H	1.568986000	-4.376439000	-0.733826000
---	-------------	--------------	--------------

H	-0.025539000	-2.219308000	-3.812846000
---	--------------	--------------	--------------

O	2.639252000	0.163912000	4.067027000
---	-------------	-------------	-------------

H	0.906897000	-4.576584000	0.658940000
---	-------------	--------------	-------------

H	-1.112681000	-3.004221000	-2.955189000
---	--------------	--------------	--------------

O	3.030826000	-3.512784000	-1.778790000
---	-------------	--------------	--------------

H	4.581901000	-0.881471000	-0.529158000
H	3.302119000	0.572848000	-2.889269000
O	-0.146643000	-0.328137000	4.844819000
H	5.482998000	-2.006409000	0.065273000
H	2.308208000	1.247033000	-3.870466000
O	-1.461706000	-4.075461000	-1.600126000
H	-1.985262000	-2.543001000	3.351054000
H	-3.071568000	1.093057000	3.110235000
O	4.544150000	0.707807000	-1.262840000
H	-1.389496000	-3.417766000	4.503116000
H	-3.688675000	1.060709000	1.677818000
O	2.637483000	2.707051000	2.824773000
H	2.678808000	1.059139000	3.677278000
H	-0.201764000	4.067327000	1.813120000
O	-3.350096000	-2.089127000	2.558355000
H	3.205333000	0.178822000	4.845885000
H	-0.268389000	4.356737000	3.343362000
O	1.705636000	-2.044115000	-3.957043000
H	3.608034000	-2.962489000	-1.214814000
H	-3.707321000	-0.564164000	-2.515879000
O	-1.693658000	1.760848000	3.996086000
H	3.581157000	-4.231004000	-2.108399000
H	-5.226665000	-0.758674000	-2.228463000
O	3.712572000	2.844221000	0.121121000
H	0.785251000	-0.262441000	4.587191000

H	0.901983000	4.425392000	-0.849178000
O	-3.723820000	-2.895306000	-0.165832000
H	-0.461812000	-1.196620000	4.522802000
H	1.981672000	5.090096000	-1.747902000
O	-0.994509000	-2.361557000	-3.693403000
H	-0.662814000	-4.378186000	-1.106269000
H	-1.910035000	-1.226475000	-3.723785000
O	2.910870000	0.481866000	-3.769422000
H	-2.019727000	-3.622067000	-0.952441000
H	-3.003083000	-0.555552000	-4.667349000
O	-3.769993000	0.670732000	2.557774000
H	4.245265000	1.484324000	-0.716283000
H	1.308032000	3.153156000	-2.977356000
O	0.070176000	3.732213000	2.692267000
H	5.318336000	1.007483000	-1.751056000
H	0.222056000	2.493160000	-3.852374000
O	-4.386415000	-0.610882000	-1.779895000
H	1.723211000	3.070395000	2.803983000
H	-4.398840000	0.823809000	-0.708806000
O	1.716022000	4.249505000	-1.359645000
H	3.177952000	3.378565000	3.255465000
H	-5.243798000	1.756435000	0.223020000
O	-2.621116000	-0.454904000	-3.788458000
H	-3.546116000	-1.128619000	2.563078000
H	-1.400594000	4.200142000	-0.314769000

O	1.178534000	2.690636000	-3.816980000
H	-3.486148000	-2.399928000	1.647228000
H	-0.961360000	5.610188000	0.154543000
O	-4.366288000	1.640111000	-0.157325000
H	2.104179000	-1.149701000	-3.958760000
H	-1.915402000	2.469763000	-2.752932000
O	-0.669999000	4.691564000	0.134280000
H	2.166162000	-2.532104000	-3.257276000
H	-1.880095000	1.264675000	-3.722875000
O	-1.601040000	2.196055000	-3.625305000
H	-1.086697000	2.239357000	3.415911000
H	-3.372609000	2.878141000	-0.796480000
O	-2.727424000	3.493659000	-1.224271000
H	-1.163910000	1.013200000	4.364138000
H	-3.246424000	4.083672000	-1.781829000

**Table S3**

Comparison of the computational and experimental vibrational frequency of CH<sub>4</sub> and CO<sub>2</sub> Clathrate hydrate using the B3LYP level of theory and 6-311++G(d, p) basis.

<b>B3LYP/6-311++G(d, p) Level</b>	<b>Free CH<sub>4</sub>/CO<sub>2</sub></b>	<b>5<sup>12</sup> cage</b>	<b>5<sup>12</sup> 6<sup>2</sup> cage</b>	<b>5<sup>12</sup> 6<sup>4</sup> cage</b>
<b>CH<sub>4</sub> hydrate</b>	3129.6 (26)	3138.9 (24) 3144.1 (12) 3151.6 (10)	3120.4 (6) 3128.9 (10) 3141.3 (3)	3120.5 (22) 3132.2 (11) 3138.9 (16)
<b>CO<sub>2</sub> hydrate</b>	2420.0 (712)	2333.5 (295)	2403.4 (580)	2435.8 (546)

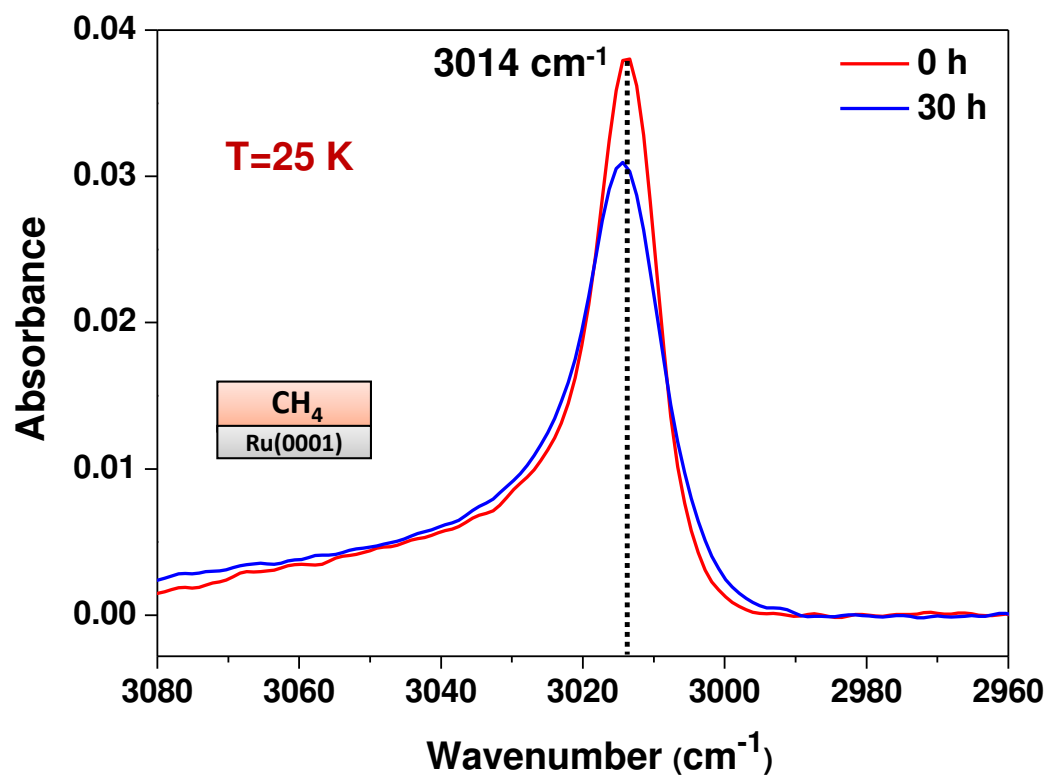


**Fig. S2.** Time dependent RAIR spectra of 150 MLs of solid CH<sub>4</sub> in the C-H antisymmetric stretching region at 25 K. The decrease in the intensity of the IR peak is due to desorption of CH<sub>4</sub> in UHV. This experiment was performed at 25 K instead of 30 K, as at this temperature (30 K), most of the CH<sub>4</sub> desorbed from the surface after 30 hours.



**Table S4**

Properties of (3,-1) bond critical points in CH<sub>4</sub> and CO<sub>2</sub> clathrate hydrate computed at B3LYP level of theory with 6-311++G (d, p) basis set.

Clathrate Hydrate (5 <sup>12</sup> )	Type of bonding	Bonds	$\rho(r_C)$	$\nabla^2\rho(r_C)$
CH <sub>4</sub>	van der Waals interaction	-C-H of free CH <sub>4</sub>	0.27217	-0.89913
		-C-H of CH <sub>4</sub> hydrate	0.27199	-0.89544
		-C-H $\cdots$ H <sub>2</sub> O interaction	0.00598	0.01601
CO <sub>2</sub>	Hydrogen bonding	-C=O of free CO <sub>2</sub>	0.45773	-0.08650
		-C=O of CO <sub>2</sub> hydrate	0.44922	-0.07620
		-C=O $\cdots$ H <sub>2</sub> O interaction	0.01563	0.07161

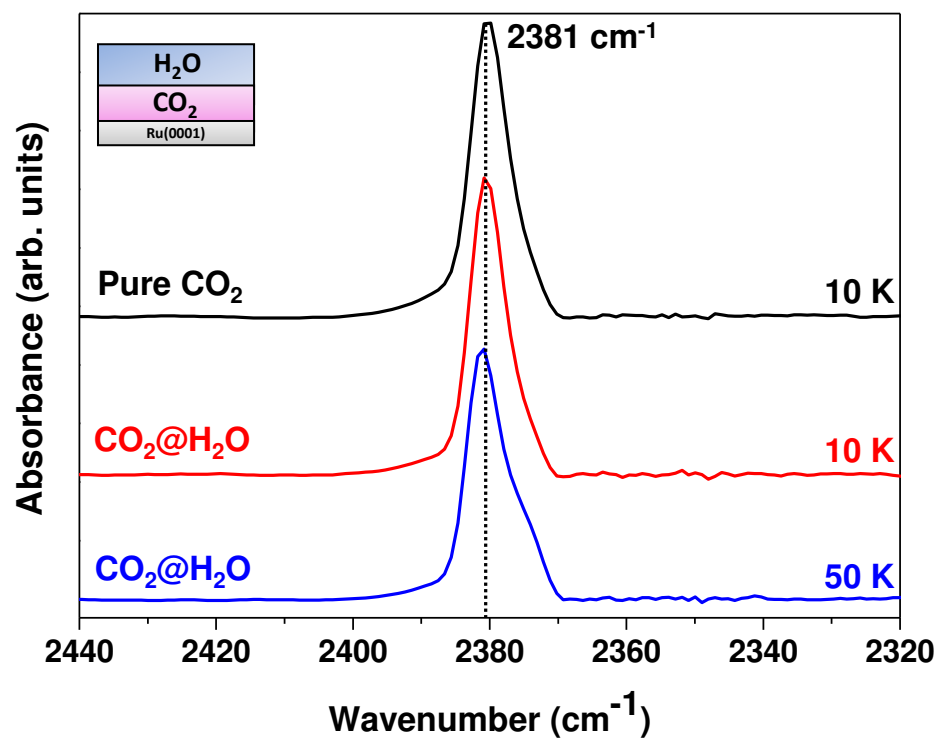


**Fig. S3.** Temperature dependent RAIR spectra of 300 MLs of CO<sub>2</sub>@H<sub>2</sub>O (1:5 ratio) in the C=O antisymmetric stretching region. Spectrum for pure solid CO<sub>2</sub> was added for comparison. The CO<sub>2</sub>@H<sub>2</sub>O symbolism implies that H<sub>2</sub>O was deposited over CO<sub>2</sub>. The spectra were translated vertically for the clarity.

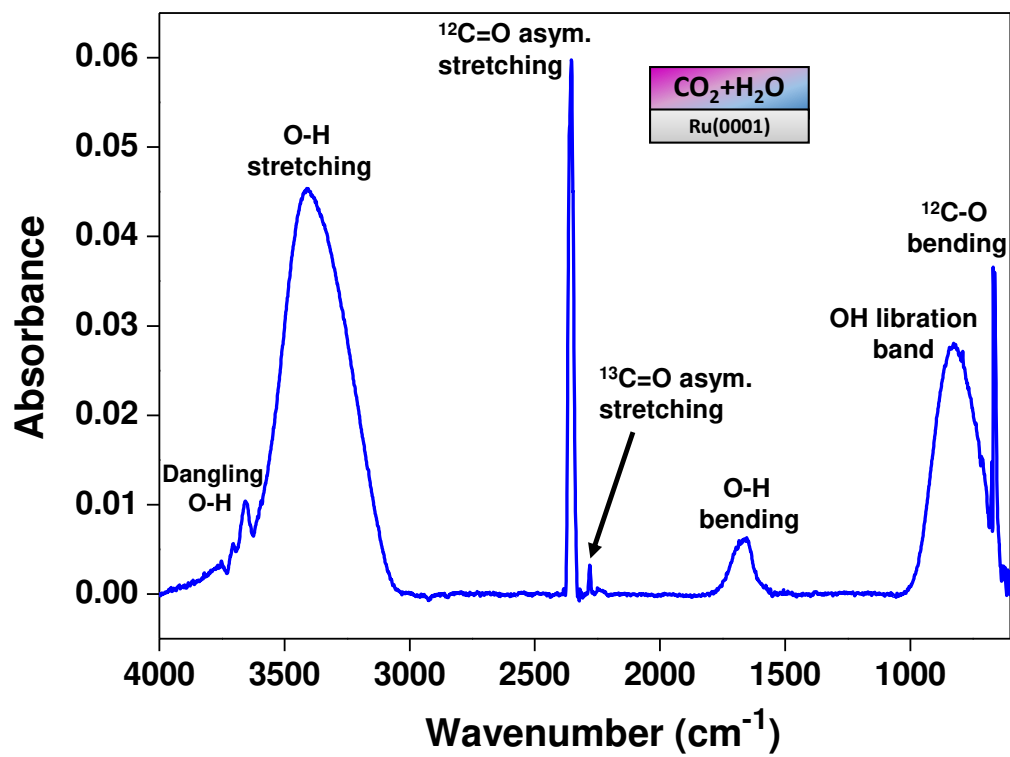


**Fig. S4.** Full scale RAIR spectrum of 300 MLs of  $\text{CO}_2+\text{H}_2\text{O}$  (1:5 ratio) at 10 K.

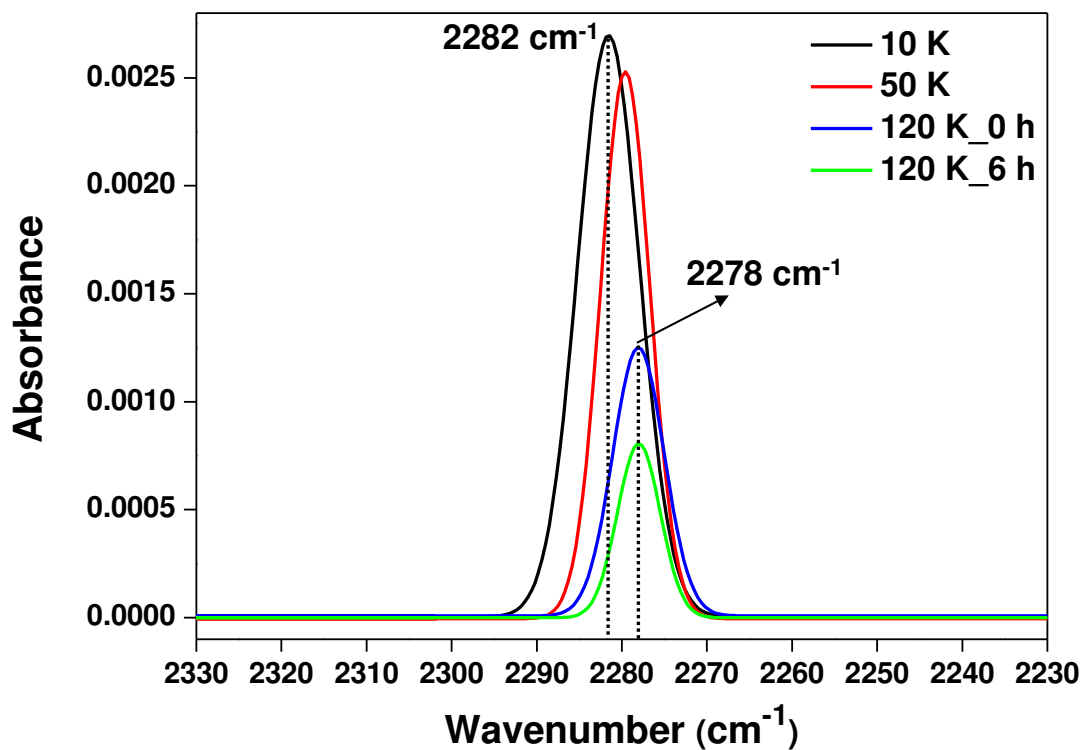


**Fig. S5.** Temperature dependent RAIR spectra of 300 MLs of CO<sub>2</sub>+H<sub>2</sub>O (1:5 ratio) in the <sup>13</sup>C=O antisymmetric region. Reduction in intensity with time is due to partial desorption.

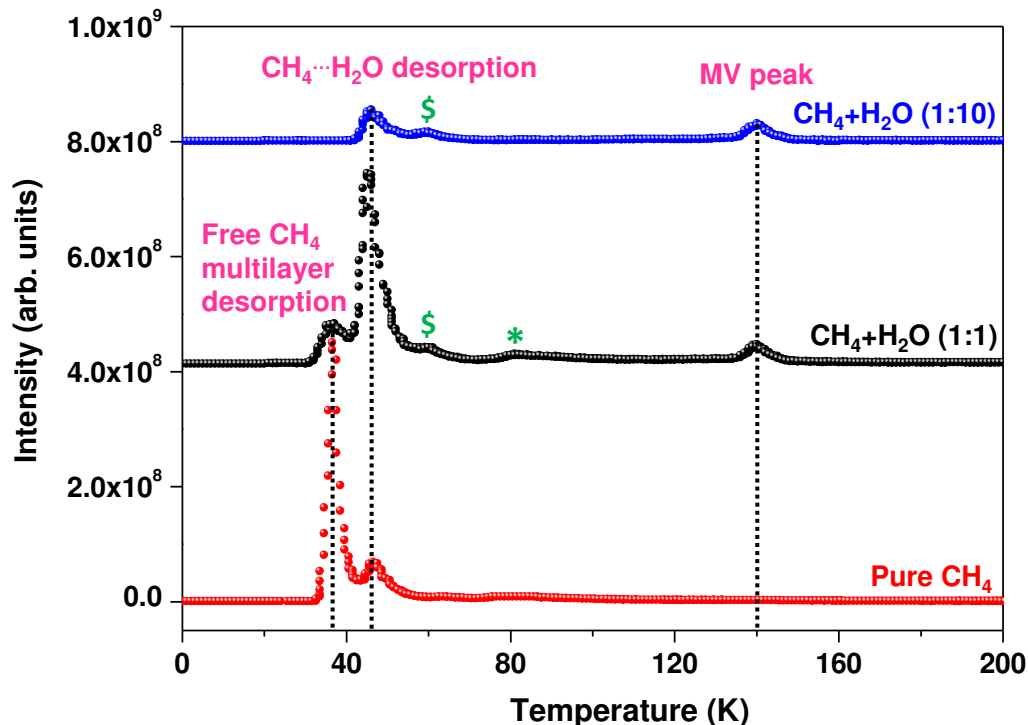


**Fig. S6.** TPD mass spectra of 150 MLs of solid  $\text{CH}_4$  and  $\text{CH}_4+\text{H}_2\text{O}$  co-deposited ice systems at different ratios (heating rate of  $30 \text{ K}\cdot\text{min}^{-1}$ ). Here, the intensities of  $\text{CH}_3^+$  ( $m/z=15$ ) under these conditions are plotted. After the deposition at 10 K, these ice systems were annealed and simultaneously the mass spectra were recorded. The marked desorption (\*, \$) peaks are due to the structural transitions of amorphous ice during annealing (1).

#### References:

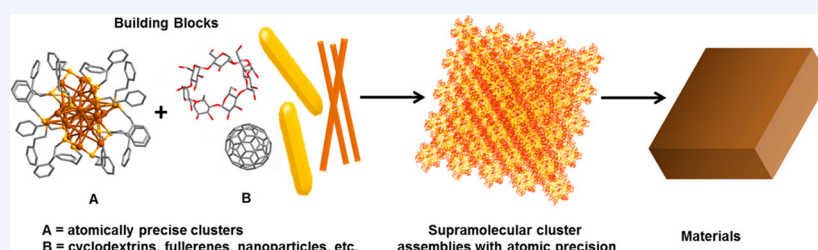
1. Jenniskens P & Blake DF (1994) Structural transitions in amorphous water ice and astrophysical implications. *Science* 265(5173):753.

## Approaching Materials with Atomic Precision Using Supramolecular Cluster Assemblies

Published as part of the *Accounts of Chemical Research* special issue “*Toward Atomic Precision in Nanoscience*”.

Papri Chakraborty, Abhijit Nag, Amrita Chakraborty, and Thalappil Pradeep\*

DST Unit of Nanoscience (DST UNS) and Thematic Unit of Excellence (TUE), Department of Chemistry, Indian Institute of Technology Madras, Chennai 600 036, India



**CONSPECTUS:** Supramolecular chemistry is a major area of chemistry that utilizes weaker non-covalent interactions between molecules, including hydrogen bonding, van der Waals, electrostatic,  $\pi\cdots\pi$ , and C–H $\cdots\pi$  interactions. Such forces have been the basis of several molecular self-assemblies and host–guest complexes in organic, inorganic, and biological systems. Atomically precise nanoclusters (NCs) are materials of growing interest that display interesting structure–property correlations. The evolving science of such systems reaffirms their molecular behavior. This gives a possibility of exploring their supramolecular chemistry, leading to assemblies with similar or dissimilar cluster molecules. Such assemblies with compositional, structural, and conformational precision may ultimately result in cluster-assembled hybrid materials. In this Account, we present recent advancements on different possibilities of supramolecular interactions in atomically precise cluster systems that can occur at different length scales. We first present a brief discussion of the aspicule model of clusters, considering  $\text{Au}_{25}(\text{SR})_{18}$  as an example, that can explain various aspects of its atomic precision and distinguish the similar or dissimilar interacting sites in their structures. The supramolecular interaction of 4-*tert*-butylbenzyl mercaptan (BBSH)-protected  $[\text{Au}_{25}(\text{SBB})_{18}]^-$  NCs with cyclodextrins (CD) to form  $\text{Au}_{25}\text{SBB}_{18}\cap\text{CD}_n$  ( $n = 1-4$ ) and that of  $[\text{Ag}_{29}(\text{BDT})_{12}]^{3-}$  with fullerenes to form  $[\text{Ag}_{29}(\text{BDT})_{12}(\text{C}_{60})_n]^{3-}$  ( $n = 1-9$ ) (BDT = 1,3-benzenedithiolate) are discussed subsequently. The formation of these adducts was studied by electrospray ionization mass spectrometry (ESI MS), optical absorption and NMR spectroscopy. In the subsequent sections, we discuss how variation in intercluster interactions can lead to polymorphic crystals, which are observable in single-crystal X-ray diffraction. Taking  $[\text{Ag}_{29}(\text{BDT})_{12}(\text{TPP})_4]^{3-}$  (TPP = triphenylphosphine) clusters as an example, we discuss how the different patterns of C–H $\cdots\pi$  and  $\pi\cdots\pi$  interactions between the secondary ligands can alter the packing of the NCs into cubic and trigonal lattices. Finally, we discuss how the supramolecular interactions of atomically precise clusters can result in their hybrid assemblies with plasmonic nanostructures. The interaction of *p*-mercaptobenzoic acid (*p*-MBA)-protected  $\text{Ag}_{44}(\text{p-MBA})_{30}$  NCs with tellurium nanowires (Te NWs) can form crossed-bilayer precision assemblies with a woven-fabric-like structure with an angle of  $81^\circ$  between the layers. Similar crossed-bilayer assemblies show an angle of  $77^\circ$  when  $\text{Au}_{102}(\text{p-MBA})_{44}$  clusters are used to form the structure. Such assemblies were studied by transmission electron microscopy (TEM). Precision in these hybrid assemblies of Te NWs was highly controlled by the geometry of the ligands on the NC surface. Moreover, we also present how  $\text{Ag}_{44}(\text{p-MBA})_{30}$  clusters can encapsulate gold nanorods to form cage-like nanostructures. Such studies involved TEM, scanning transmission electron microscopy (STEM), and three-dimensional tomographic reconstructions of the nanostructures. The hydrogen bonding interactions of the –COOH groups of the *p*-MBA ligands were the major driving force in both of these cases. An important aspect that is central to the advancement of the area is the close interplay of molecular tools such as MS with structural tools such as TEM along with detailed computational modeling. We finally conclude this Account with a future perspective on the supramolecular chemistry of clusters. Advancements in this field will help in developing new materials with potential optical, electrical, and mechanical properties.

### ■ INTRODUCTION

Atomically precise nanoclusters (NCs) present rich diversity in their structures and properties.<sup>1,2</sup> A large variety of clusters made of noble metals like Au, Ag, etc. and protected by ligands<sup>3,4</sup> such as thiols and phosphines are known in the literature, and many of

their structures have been determined from single-crystal studies. Precise composition, precision in molecular structure,

Received: July 28, 2018

Published: December 3, 2018



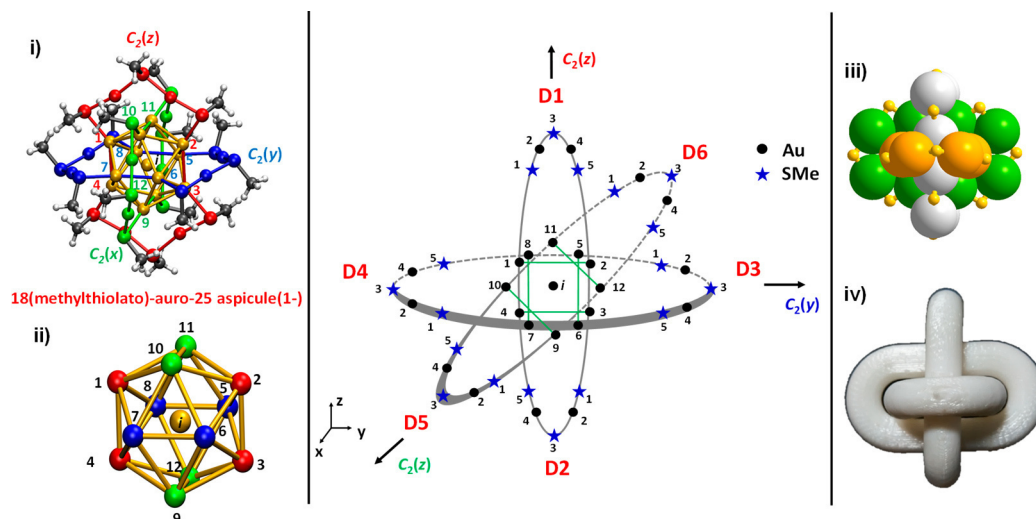


**Figure 1.** Representation of the  $\text{Au}_{25}(\text{SMe})_{18}$  cluster in the Borromean ring model. Three ellipses encompassing six  $\text{Au}_2(\text{SR})_3$  staples are represented as nearly coplanar rings. These staples are labeled as D1 to D6. The rings include core Au atoms (numbered 1 to 12). The atoms in the staples are numbered 1 to 5 in the clockwise direction. Inset (i) shows these aspicule rings in the standard structure of  $\text{Au}_{25}(\text{SMe})_{18}$ . The three rings are shown in red, green, and blue, while the Au atoms in the icosahedron are shown in gold. Inset (ii) shows an expanded view of the icosahedral core, where the icosahedral central atom alone is shown in gold. A cluster composed of Au (green, orange, and gray) and S (yellow) atoms is shown in inset (iii), and a photograph of a Borromean ring structure is shown in inset (iv). The ring structure enables the cluster to be disassembled completely just by detaching one bond; a break in one ring separates the other two. Reproduced from ref 12. Copyright 2015 American Chemical Society.

electronic energy levels, optical absorption and emission, chemical reactivity,<sup>5,6</sup> catalysis,<sup>3</sup> and an expanding body of emerging properties increasingly reaffirm the molecular nature of such systems. This expanding science makes one wonder about the distinct possibilities of supramolecular chemistry of such molecules. While supramolecular interactions play important roles in cluster crystallization, phase transfer, reaction chemistry, etc., these interactions can also be important for the synthesis of new cluster compounds, e.g., in the formation of cluster assemblies. Recently, Jin and co-workers reported that protecting ligands on clusters can organize in specific patterns that may direct their assembly, which can match the level of atomic precision in biomolecules.<sup>7</sup> The forces guiding the organization of the NCs may vary from weak intermolecular forces like  $\text{C}-\text{H}\cdots\pi$ ,  $\pi\cdots\pi$ , van der Waals, hydrogen bonding, and electrostatic interactions to strong covalent bonding. While molecular interactions between clusters result in their crystallization, interactions with heteromolecules as well as those between clusters forming homomolecular adducts such as dimers,<sup>8</sup> trimers,<sup>8</sup> and polymers<sup>9</sup> can create specific building blocks. Clusters, which have nanometric dimensions, can interact with other systems to form supramolecular architectures of larger dimensions. Such assemblies could also occur in organized biological systems such as viruses and bacteria, leading to bio–nano conjugates or synthetic superstructures of unprecedented diversity.<sup>10,11</sup> This Account briefly illustrates this emerging body of science and projects its growth to suggest future possibilities.

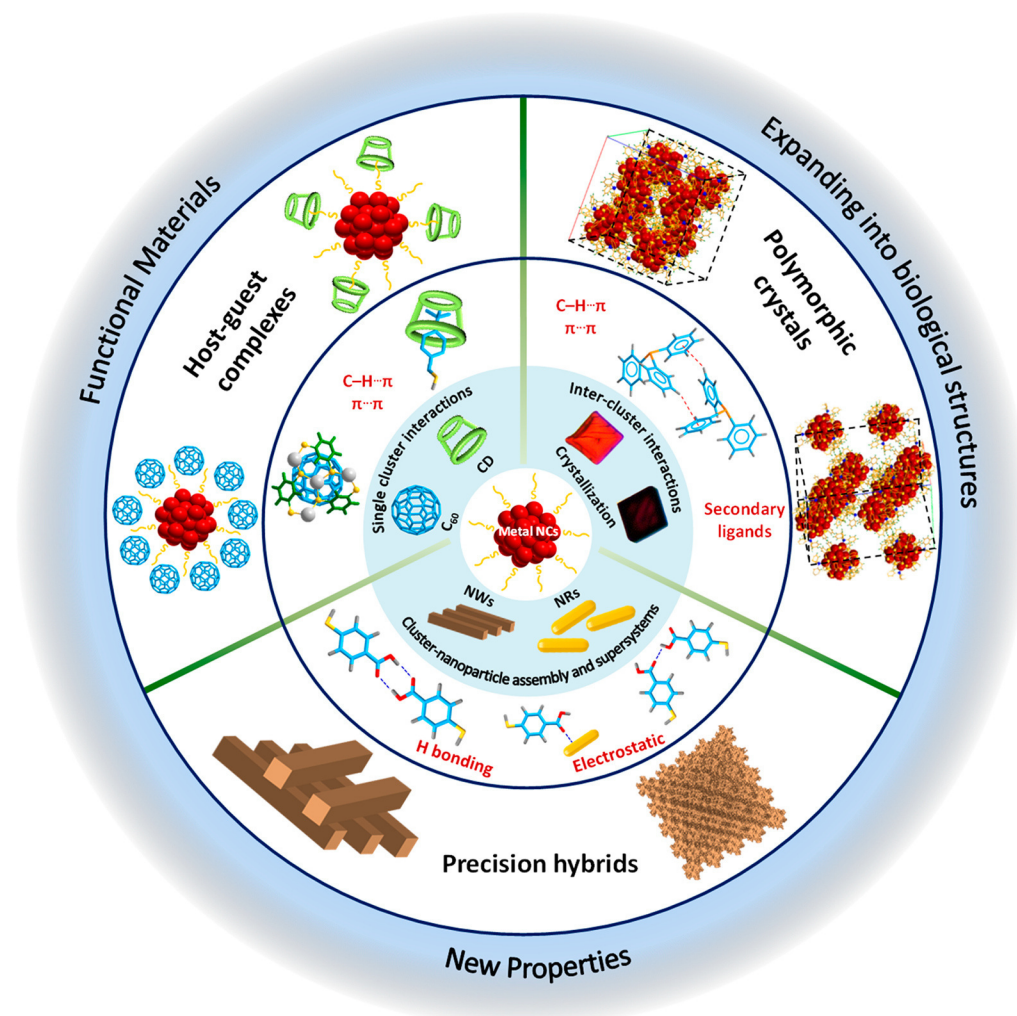
The precision in structures is captured elegantly in the aspicule nomenclature,<sup>12</sup> wherein the cluster is composed of a core and distinct staples having precise labels. The overall structure of  $\text{Au}_{25}(\text{SMe})_{18}$  can be drawn precisely, leading to the name 18(methylthiolato)-auro-25 aspicule(1–) to represent the molecule, as shown in Figure 1. This molecular structure presents symmetry-equivalent sites where interactions are similar or dissimilar. It also indicates the limits or limitations of molecular access and presents the possibilities of interactions

at distinct sites leading to structural transformation, particularly ligand exchange,<sup>13</sup> exchange of core atoms, creation of alloys,<sup>5,14</sup> and supramolecular functionalization.<sup>15</sup> Intercluster interactions between similar or different clusters as well as those with nanoparticles may also be visualized. In this Account, we discuss the different possibilities of supramolecular interactions in the atomically precise clusters and classify them into the following specific categories:

- (A) single cluster interactions (with small molecules)
- (B) intercluster interactions
- (C) cluster–nanoparticle assembly and supersystems

In each of these, the essential interaction is intermolecular in nature, but they occur at different length scales. Consequently, they are explored with different tools. In the first case, single cluster interactions, supramolecular interactions of the clusters with molecules like cyclodextrins (CDs) and fullerenes are studied principally using mass spectrometry (MS). Such results are supplemented by complementary studies using optical and NMR spectroscopy. In the second case, supramolecular interactions lead to intercluster organizations, which are observed by single-crystal diffraction. In the third case, interactions occur on substrates or at surfaces of much larger (bulk-like) phases, so the integrated systems are currently above the limit of regular MS. Here the formation of assemblies around nanostructures such as nanowires and nanorods mediated by supramolecular interactions with NCs is discussed.<sup>16</sup> Such systems are examined with microscopy. All of these systems are examined with computational methods with varying degrees of sophistication. Each of these subclasses is separately presented below, and Scheme 1 presents a schematic of the possible types of supramolecular interactions in the atomically precise clusters, as discussed above. While the interactions and structures derived are atomically precise in detail, a thorough understanding of structural and conformational precision has been possible only for A and B. We hope that more definitive understanding of all three types will be available in the years ahead.



Scheme 1. Schematic Capturing Some of the Supramolecular Interactions Possible in Atomically Precise Clusters<sup>a</sup>

<sup>a</sup>New directions shown at the periphery are not captured in this Account. The size of each component is not to scale.

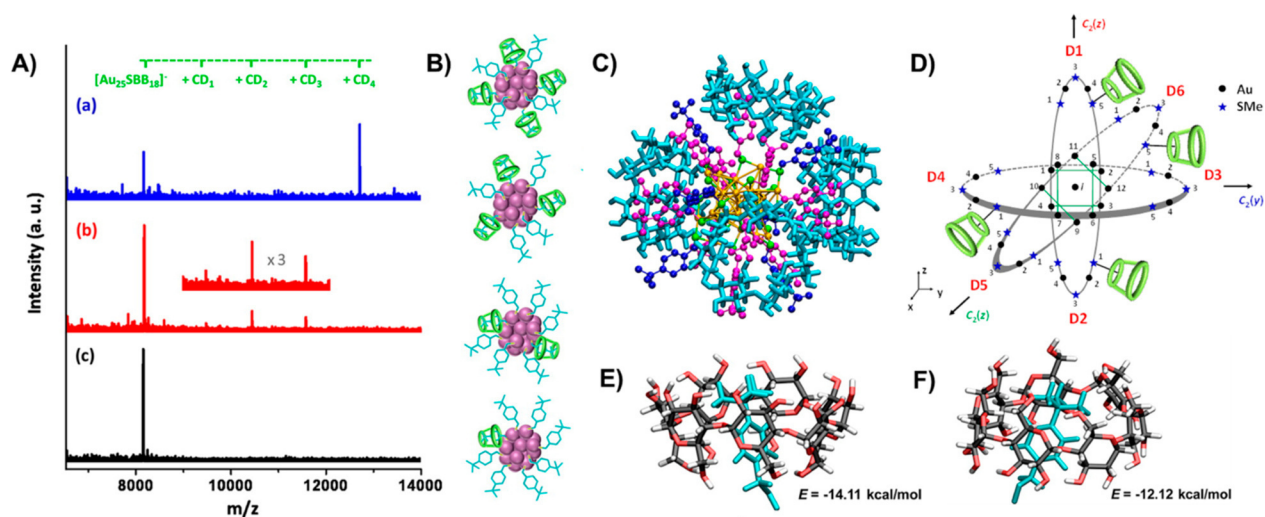


**Figure 2.** (A) Negative ion ESI MS spectra for the  $\text{Au}_{25}\text{SBB}_{18}$  cluster and its CD adducts. Spectra a, b, and c are at SBB/CD molar ratios of 1:1.2, 1:1, and 1:0, respectively. Part of a spectrum is expanded in (b). (B) Schematic representations of  $\text{Au}_{25}\text{SBB}_{18}\text{CD}_n$  ( $n = 1-4$ ). (C) Computed structure of  $\text{Au}_{25}\text{SBB}_{18}\text{CD}_4$  with nearly tetrahedral binding of the four CDs (shown in cyan). H atoms of the SBB ligands have been omitted for clarity. (D) Aspicule representation of  $\text{Au}_{25}\text{SBB}_{18}\text{CD}_4$ . (E, F) BBSH/CD inclusion complexes where the *tert*-butyl group of BBSH undergoes complexation through the (E) narrower and (F) wider rims of  $\beta$ -CD. In (E) and (F), all of the atoms of BBSH are colored cyan for clarity, whereas atoms of CD are colored differently. Reproduced from ref 15. Copyright 2014 American Chemical Society.



## A. SINGLE CLUSTER INTERACTIONS

## Supramolecular Interactions of NCs with CDs

The interactions of a cluster with other molecules may be tuned to precisely functionalize the surface of the NCs. We used the 4-*tert*-butylbenzyl mercaptan (BBSH)-protected  $[\text{Au}_{25}(\text{SBB})_{18}]^-$  cluster<sup>15</sup> and studied its supramolecular functionalization with  $\beta$ -CD. CDs are water-soluble cyclic oligosaccharides having hydrophobic cavities that form inclusion complexes with specific molecules.<sup>17</sup> Several host–guest complexes of  $\beta$ -CDs with inorganic complexes containing thiol groups like BBSH have been reported in the literature.<sup>18</sup> We utilized such a molecular recognition process to synthesize  $\text{Au}_{25}\text{SBB}_{18}\cap\text{CD}_n$  ( $n = 1-4$ ), where  $\text{X}\cap\text{Y}$  denotes an inclusion complex between the substrate X and receptor Y.<sup>15</sup> The CD-encapsulated clusters were synthesized from a mixture of the cluster and  $\beta$ -CD in THF/water medium by constant stirring followed by intermittent sonication, and they were characterized using different techniques such as UV–vis, fluorescence, and NMR spectroscopy. The formation of  $\text{Au}_{25}\text{SBB}_{18}\cap\text{CD}_n$  ( $n = 1-4$ ) was observed in electrospray ionization mass spectrometry (ESI MS) (Figure 2A). Schematic structures of  $\text{Au}_{25}\text{SBB}_{18}\cap\text{CD}_n$  ( $n = 1-4$ ) are presented in Figure 2B. Although a mixture of adducts ( $n = 1-4$ ) existed in solution, the amount of  $\text{Au}_{25}\text{SBB}_{18}\cap\text{CD}_4$  was increased by careful control of the SBB/CD molar ratio at 1:1.2. The nature of the interaction was explained using computational studies. In the structure of  $\text{Au}_{25}\text{SBB}_{18}$ , surrounding the icosahedral core there are six  $\text{Au}_2(\text{SR})_3$  staples, corresponding to the six staples D1 to D6 in the aspicule model (Figure 1). In each staple, there are two nonbridging S (positions 1 and 5) joining a core Au to a staple Au and one bridging S (position 3) joining only two exterior Au atoms. The ligands anchored at positions 1 and 5, being less crowded, remain more accessible for encapsulation with CDs. This appears to be counterintuitive, as position 3 appears to be less crowded in the aspicule picture. However, Figure 1(iv) suggests that positions 1 and 5 are indeed accessible. NMR data also revealed the interactions between aromatic protons of SBB and  $\text{H}^3$  and  $\text{H}^5$  (inner protons) of CD. The theoretical structure of  $\text{Au}_{25}\text{SBB}_{18}\cap\text{CD}_4$  (Figure 2C) shows four CDs bound at tetrahedral locations, minimizing the inter-CD interactions. A representation in the aspicule model is shown in Figure 2D. Complexation through the narrower rim of CD facing the cluster core was more favorable than complexation through the wider rim (Figure 2E,F).

The formation of these inclusion complexes was specific to the precise orientation of the SBB ligands, which pointed outward from the core. In the case of  $\text{Au}_{25}(\text{PET})_{18}$  (PET = 2-phenylethyl thiolate),<sup>19,20</sup> which presents a different orientation of the PET ligands, no CD inclusion was observed. CD encapsulation resulted in an enhancement in the luminescence of the cluster and shielded the metal core from incoming ions or ligands and consequently increased its stability. Inclusion complexes of other thiols such as adamantanethiol (SAdm) with CD are also well-known.<sup>21–23</sup> Yan et al.<sup>24</sup> showed the surface functionalization of  $\text{Au}_{38}\text{S}_2(\text{SAdm})_{20}$  NCs with  $\alpha$ -,  $\beta$ -, and  $\gamma$ -CD. This unfolds the possibility of functionalizing other Adm-protected clusters like  $\text{Au}_{30}(\text{SAdm})_{18}$ ,<sup>25</sup>  $\text{Pt}_1\text{Ag}_{28}(\text{SAdm})_{18}(\text{PPh}_3)_4$ ,<sup>26</sup>  $\text{Au}_{24}(\text{SAdm})_{16}$ ,<sup>27</sup> etc. with CDs in a similar fashion. In a recent report, Au NC-grafted CD superstructures were used to develop fluorescence on–off composites.<sup>28</sup> Xie and co-workers used a CD–AuNC– $\text{TiO}_2$  hybrid system to enhance photocatalytic decomposition of organic pollutants.<sup>29</sup>

## Supramolecular Interactions of NCs with Fullerenes

Fullerenes are another important class of molecules for exploration of the supramolecular chemistry of clusters. Fullerenes show electron-accepting properties and form a wide range of supramolecular self-assembled structures.<sup>30</sup> We observed the formation of  $[\text{Ag}_{29}(\text{BDT})_{12}(\text{C}_{60})_n]^{3-}$  ( $n = 1-9$ )<sup>31</sup> (BDT = 1,3-benzenedithiolate) adducts in solution through the interaction of  $[\text{Ag}_{29}(\text{BDT})_{12}]^{3-}$  NCs<sup>32</sup> with  $\text{C}_{60}$ . Twelve Ag atoms cover the icosahedral core, forming four trigonal prisms. The  $\text{Ag}_{13}$  core is further covered by four Ag atoms at tetrahedral positions.<sup>32</sup> Addition of  $\text{C}_{60}$  to the cluster at a cluster: $\text{C}_{60}$  molar ratio of 1:4 resulted in the formation of  $[\text{Ag}_{29}(\text{BDT})_{12}(\text{C}_{60})_n]^{3-}$  ( $n = 1-4$ ) adducts, which were observed by ESI MS (Figure 3). The BDT ligands are arranged

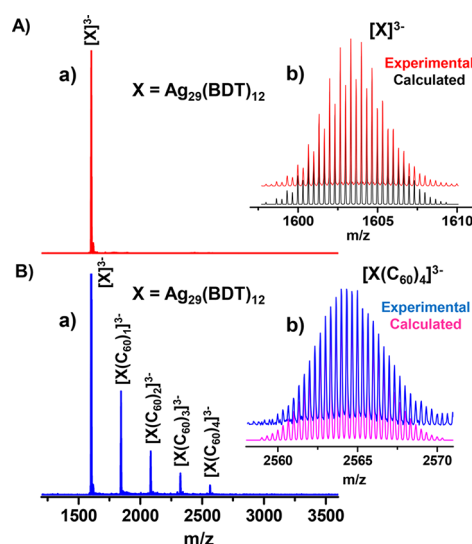


**Figure 3.** ESI MS spectra of (A)  $[\text{Ag}_{29}(\text{BDT})_{12}]^{3-}$  and (B)  $[\text{Ag}_{29}(\text{BDT})_{12}(\text{C}_{60})_n]^{3-}$  ( $n = 1-4$ ). Experimental and theoretical isotopic distributions of the peaks are compared in the insets. Reproduced from ref 31. Copyright 2018 American Chemical Society.

in such a way that they form a cavity, encapsulating the curved surface of fullerenes (Figure 4A,B). This structural compatibility facilitated the supramolecular host–guest complexation. Detailed insights into the structures of  $[\text{Ag}_{29}(\text{BDT})_{12}(\text{C}_{60})_n]^{3-}$  ( $n = 1-4$ ) were obtained from computational studies. In the structure of  $[\text{Ag}_{29}(\text{BDT})_{12}(\text{C}_{60})]^{3-}$  (Figure 4A),  $\text{C}_{60}$  has weak binding interactions with the vertex Ag atom at a distance of about 3.40–3.53 Å and stabilizes the unpassivated Ag atom by  $\eta^2$  interactions. The adduct  $[\text{Ag}_{29}(\text{BDT})_{12}(\text{C}_{60})_4]^{3-}$  (Figure 4C) retains a tetrahedral symmetry in its structure with four  $\text{C}_{60}$  molecules bound at four vertex sites. The primary interactions are  $\pi\cdots\pi$  and van der Waals interactions between the  $\pi$  surface of the fullerene and the aromatic rings of BDT. In the crystal structure of the NC, triphenylphosphine (TPP) ligands are bound at the vertex Ag sites.<sup>32</sup> When TPP was added to  $[\text{Ag}_{29}(\text{BDT})_{12}(\text{C}_{60})_n]^{3-}$  ( $n = 1-4$ ), TPP replaced  $\text{C}_{60}$ , forming  $[\text{Ag}_{29}(\text{BDT})_{12}(\text{TPP})_4]^{3-}$  ( $n = 1-4$ ), which reaffirmed the binding sites of the fullerenes to the cluster. Addition of excess  $\text{C}_{60}$  resulted in an even higher number of  $\text{C}_{60}$  additions to the cluster ( $n > 4$ ). Additional  $\text{C}_{60}$  may bind over the four trigonal faces formed by the  $\text{Ag}_3\text{S}_3$  motifs. The likely structure of  $[\text{Ag}_{29}(\text{BDT})_{12}(\text{C}_{60})_8]^{3-}$  (Figure 4D) shows fullerenes bound at all of the face and vertex positions of the cluster with a slightly distorted cube-like overall geometry. Additional fullerene–

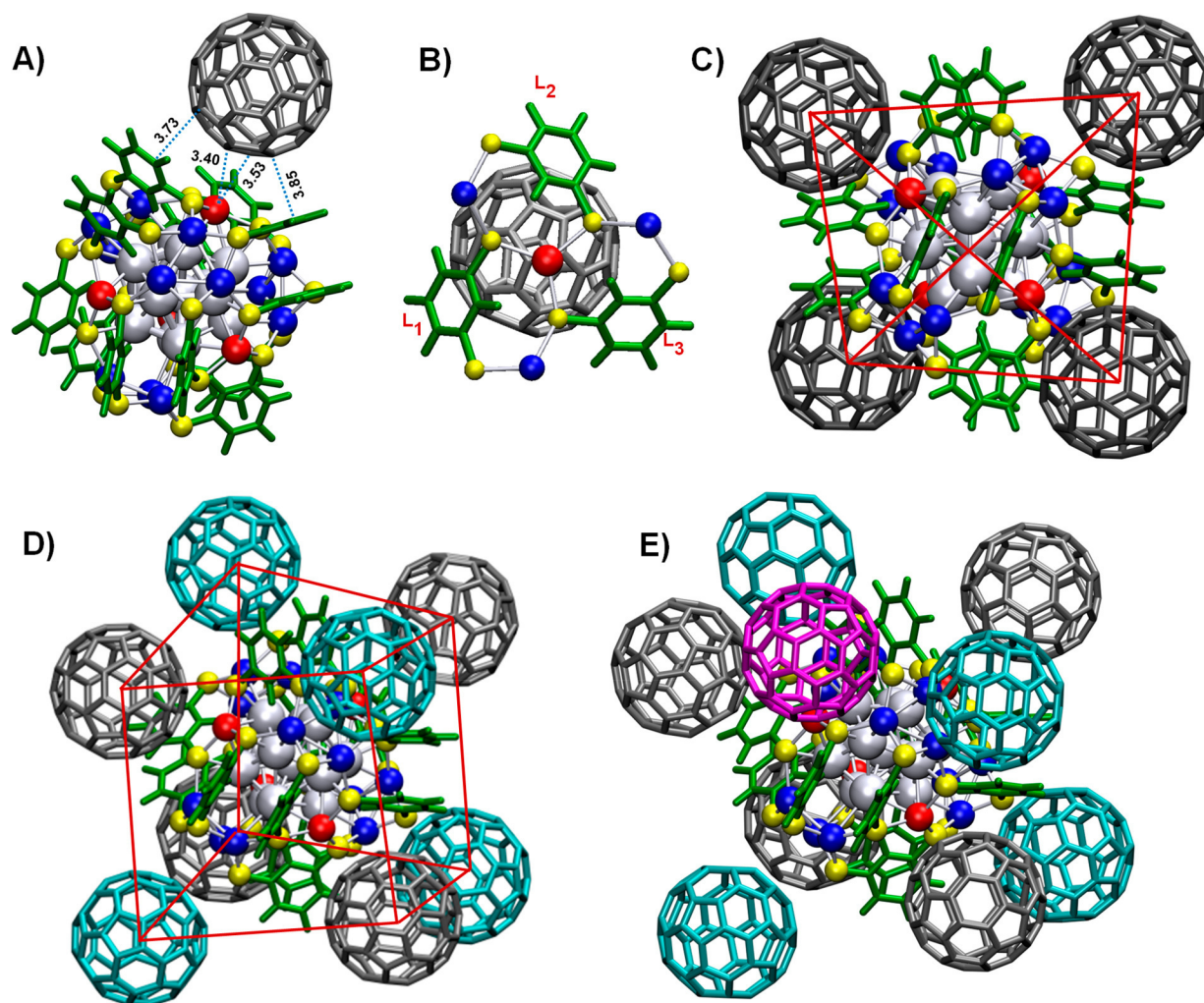


**Figure 4.** (A) Results of DFT calculations on the minimum-energy geometry of  $[\text{Ag}_{29}(\text{BDT})_{12}(\text{C}_{60})]^{3-}$ . Interaction distances (in Å) are marked in the figure. (B) Interactions between the fullerene and the ligands are shown in an expanded view. (C–E) Lowest-energy structures of (C)  $[\text{Ag}_{29}(\text{BDT})_{12}(\text{C}_{60})_4]^{3-}$ , (D)  $[\text{Ag}_{29}(\text{BDT})_{12}(\text{C}_{60})_8]^{3-}$ , and (E)  $[\text{Ag}_{29}(\text{BDT})_{12}(\text{C}_{60})_9]^{3-}$ . Color code: yellow, S; gray, Ag of the icosahedral core; red, tetrahedral sites of four Ag atoms; blue,  $\text{Ag}_3\text{S}_3$  staple motifs composed of 12 Ag atoms making four trigonal planes; green, BDT ligands; black,  $\text{C}_{60}$  at vertex positions; cyan,  $\text{C}_{60}$  at face positions; purple, an additional fullerene located between the face and vertex positions. Reproduced from ref 31. Copyright 2018 American Chemical Society.

fullerene interactions may also favor further attachment of  $\text{C}_{60}$  (Figure 4E) such that the latter may form a sphere covering the entire cluster surface. Similar results were observed with  $\text{C}_{70}$ , which exhibited stronger  $\pi\cdots\pi$  interactions and closer contacts with the aromatic ligands of the cluster. The importance of intermolecular interactions in the formation of intercluster compounds of fullerides with gold NCs,  $[\text{Au}_7(\text{PPh}_3)_7]\text{C}_{60}\cdot\text{THF}$  and  $[\text{Au}_8(\text{PPh}_3)_8](\text{C}_{60})_2$ , was also demonstrated by Schulz-Dobrick et al.<sup>33</sup> The interactions of a cluster may also be utilized to form atomically precise supramolecular assemblies with other molecules such as catenanes, calixarenes, rotaxanes, porphyrins, etc.

## B. INTERCLUSTER INTERACTIONS

Supramolecular interactions also play a crucial role in arranging the NCs in their crystal lattice. In the crystal lattice of *p*-mercaptobenzoic acid (*p*-MBA)-protected  $\text{Ag}_{44}(\text{p-MBA})_{30}$  NCs, the  $-\text{COOH}$  groups of the *p*-MBA ligands show strong hydrogen bonding between the neighboring NCs.<sup>34</sup> Similar non-covalent interactions have also been observed in the crystal lattices of  $\text{Au}_{102}$ ,<sup>35</sup>  $\text{Au}_{246}$ ,<sup>7</sup>  $\text{Au}_{103}$ ,<sup>36</sup> etc. Interesting packing

patterns such as the 4H phase array of  $\text{Au}_{92}(\text{TBBT})_{44}\text{NCs}$ <sup>37</sup> and the 6H left-handed helical arrangement of  $\text{Au}_{60}\text{S}_6(\text{SCH}_2\text{Ph})_{36}\text{NCs}$ <sup>38</sup> in their crystal lattices were also observed. Considering  $[\text{Ag}_{29}(\text{BDT})_{12}(\text{TPP})_4]^{3-}\text{NCs}$ <sup>32</sup> as an example, we demonstrated how the intercluster interactions may be tuned to create polymorphic crystals. In the structure reported by Bakr and co-workers,<sup>32</sup> evaporation of DMF formed orange crystals in a cubic (C) lattice with space group  $Pa\bar{3}$  (Figure 5A). In our vapor diffusion method (MeOH diffusing into DMF solution of the NCs), dark-red crystals in a trigonal (T) lattice with space group  $R\bar{3}$  were formed (Figure 5D).<sup>39</sup> The difference in packing of the two polymorphic forms is largely due to the difference in the supramolecular interactions of the BDT and TPP ligands. These interactions for the T and C systems may be classified into two categories:

- (i) In a single NC, the C–H groups of the TPP subunits interact with the  $\pi$  system of the aromatic rings of BDT in an intracluster fashion. Moreover, the C–H groups of BDT and the aromatic rings of TPP also interact strongly through intercluster C–H $\cdots\pi$  interactions in both the C



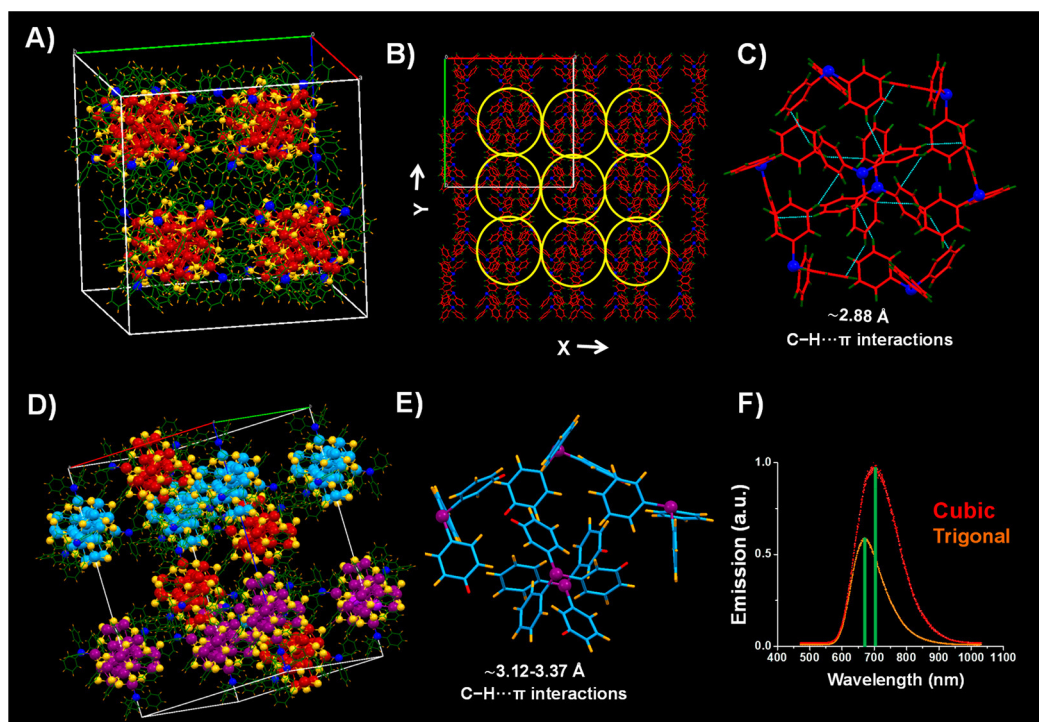


**Figure 5.** (A) Cubic unit cell of  $\text{Ag}_{29}(\text{BDT})_{12}(\text{TPP})_4^{3-}$  NCs. (B) Packing of the TPP subunits viewed from the Z axis in the C system. (C) Strong C-H... $\pi$  interactions (T-shaped) between the eight TPP subunits forming a hexagonal shape in the C system. (D) Trigonal unit cell of the NCs. (E) C-H... $\pi$  interactions between the TPP subunits in the T system. (F) Emission spectra obtained from single crystals of the C and T lattices. The C structure exhibits stronger and slightly red-shifted ( $\sim 30 \text{ nm}$ ) luminescence compared with the T structure. Reproduced with permission from ref 39. Copyright 2018 Royal Society of Chemistry.

and the T systems at distances of  $\sim 3.07\text{--}3.39$  and  $2.92 \text{ \AA}$ , respectively.

- (ii) In the C lattice, the C-H... $\pi$  interactions within the TPP subunits are stronger, forming polymeric chains (Figure 5B) to directly or indirectly connect every NC with others. These distances are comparable to the C-H... $\pi$  distances of  $2.88 \pm 0.42 \text{ \AA}$  seen in  $\text{Au}_{246}$  NCs protected by -SPh-*p*- $\text{CH}_3$  ligands<sup>7</sup> but slightly longer than the interaction distances of  $2.76 \pm 0.05 \text{ \AA}$  in  $\text{Au}_{103}$  NCs protected by -S-Nap.<sup>36</sup> The interaction distances for the TPP subunits are larger in the T system (Figure 5E) compared with the C system, and hence, these interactions are discontinuous and do not form polymeric chains.

It is evident from the crystal packing of the two polymorphs of the clusters that the intercluster interactions of TPP ligands are more favored in C than in T. The C lattice, being more rigid, exhibits a higher luminescence efficiency than the T NCs with a slight red shift ( $30 \text{ nm}$ ) (Figure 5F). This also reveals how the luminescence efficiencies of the NCs in the solid state are controlled by interactions of their secondary ligands.

## C. CLUSTER-NANOPARTICLE ASSEMBLY AND SUPERSYSTEMS

### Cluster-Mediated Precision Assemblies of Nanowires

The interactions of NCs are very different from those of nanoparticles or ionic salts of metals.<sup>40</sup> Small thiol-protected clusters like  $\text{Ag}_{32}(\text{SG})_{19}$ <sup>41</sup> tend to coalesce on the surface of one-dimensional (1D) nanomaterials like tellurium nanowires (Te NWs). This finally leads to the decoration of the NWs with Ag nodules, whereas the interactions of Ag(I) ions and Ag NPs lead

to the formation of  $\text{Ag}_2\text{Te}$  NWs.<sup>40</sup> Inspired by this result, in a particular study we modified the surface of Te NWs with  $\text{Ag}_{44}(\text{p-MBA})_{30}$  (abbreviated as  $\text{Ag}_{44}$ ). Next, the  $\text{Ag}_{44}@\text{Te}$  NWs were dispersed in 1-butanol, which was then spread over water, followed by solvent evaporation.<sup>16</sup> The pristine Te NWs formed the usual monolayer assembly when subjected to this process, whereas  $\text{Ag}_{44}@\text{Te}$  NWs led to a crossed-bilayer structure. Upon detailed TEM investigation, the pattern was found to be a woven-fabric-like structure in which NWs in the same layer were parallel but adjacent layers were arranged at an unusual angle of  $81^\circ$  (Figure 6C). To explain the origin of the unusual assembly, we modeled the hydrogen bonding between neighboring  $\text{Ag}_{44}$  units in the cluster superlattice. The *p*-MBA ligands on individual  $\text{Ag}_{44}$  clusters are present in the form of bundles of two ( $L_2$ ) or three ( $L_3$ ) units (Figure 6D). Either two  $L_2$  pairs or two  $L_3$  pairs are known to form hydrogen bonds in the  $\text{Ag}_{44}$  crystal. In  $\text{Ag}_{44}@\text{Te}$  NWs, the clusters attach themselves on the surfaces of the Te NWs via the  $-\text{COO}^-$  groups of some of their *p*-MBA ligands (Figure 6A). Upon solvent evaporation, the  $\text{Ag}_{44}@\text{Te}$  NWs come closer, and hydrogen bonding may occur between free *p*-MBA ligands, which are not bound on the NWs, of two neighboring  $\text{Ag}_{44}$  clusters attached to adjacent NWs. Computational modeling further explained that the greatest number of hydrogen bonds was possible when the two layers were arranged at an angle of  $81^\circ$ , thereby giving the most stable and most symmetrical structure (Figure 6E). When  $\text{Au}_{102}(\text{p-MBA})_{44}$ <sup>35</sup> was used instead of  $\text{Ag}_{44}(\text{p-MBA})_{30}$ , a similar crossed-bilayer structure was observed with an angle of  $77^\circ$  between the two layers, which is due to the difference in the geometrical arrangement of the ligands of the two clusters. Thus, precise angular control between highly ordered Te NW assemblies could be achieved by using atomically precise NCs.

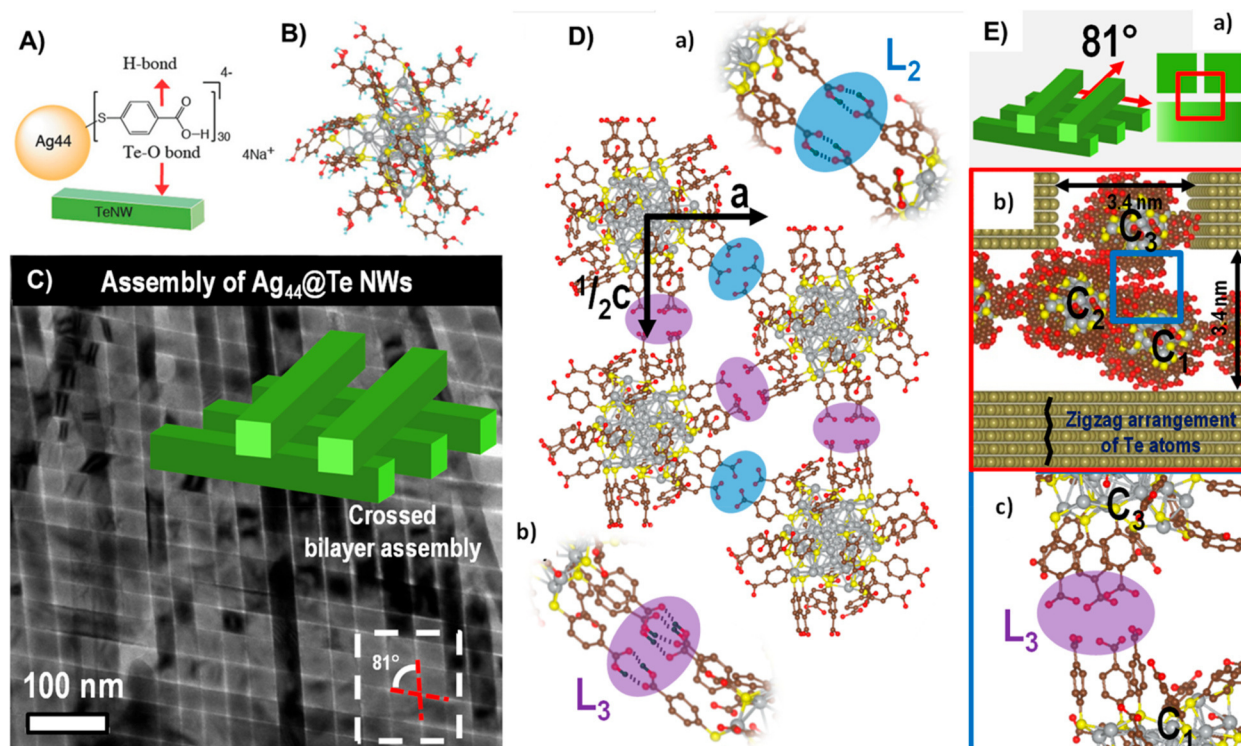


**Figure 6.** (A) Schematic of the bonding of  $\text{Ag}_{44}(\text{p-MBA})_{30}$  clusters to Te NWs. (B) Structure of  $\text{Ag}_{44}(\text{p-MBA})_{30}$  modeled from its crystal structure. (C) TEM image of the crossed bilayer assembly of  $\text{Ag}_{44}(\text{p-MBA})_{30}$  Te NWs. A schematic showing the crossed-bilayer structure of the assembly is presented in the inset. (D) Hydrogen bonding between the  $-\text{COOH}$  groups of the  $\text{p-MBA}$  ligands of neighboring NCs in the  $\text{Ag}_{44}(\text{p-MBA})_{30}$  superlattice. The neighboring clusters interact via hydrogen bonding with  $\text{L}_2$  (inset a) and  $\text{L}_3$  (inset b) types of ligands. (E) (a) Schematic of the crossed bilayer assembly. (b) Expanded view of the region modeled in (a). Further details are shown in (c). Clusters assembled on the surfaces of the Te NWs, which were kept at a distance of 3.4 nm, in three different planes, labeled as  $\text{C}_1$ ,  $\text{C}_2$ , and  $\text{C}_3$ . Reproduced with permission from refs 16 and 45. Copyright 2016 and 2018 Wiley.

### Nanoparticle-Templated Cluster Supersystems

Once the clusters were known to interact with anisotropic nanoparticles leading to structures of interesting morphology, we expanded the study using similar nanomaterials. Gold nanorods (GNRs) have been at the center of interest for decades because of their unique surface plasmonic properties. Recent studies have revealed that because of their nanometric dimensions, GNRs can accommodate quantum dots on their surfaces and significantly alter the optoelectronic properties of the quantum dots by plasmon–exciton coupling in these systems.<sup>43</sup> Using  $\text{p-MBA}$ -protected gold NCs, Nonappa and co-workers demonstrated the formation of monolayer-thick 2D nanosheets and spherical capsids by tuning the supramolecular interactions such as intercluster hydrogen bonding.<sup>44,45</sup> We placed atomically precise clusters on GNRs to explore the possibility of supramolecular-chemistry-driven hybrid nanostructures.<sup>46</sup> Specifically, GNRs were functionalized with  $\text{p-MBA}$  at neutral pH. These GNRs were then incubated with  $\text{Ag}_{44}(\text{p-MBA})_{30}$  in DMF for 20 h, during which the  $\text{p-MBA}$  groups of the clusters formed hydrogen bonds within themselves as well as with the  $\text{p-MBA}$  groups on the GNR surface (scheme in Figure 7A). This created a multilayer shell encapsulating the individual GNRs within a cage-like nanostructure. Transmission electron microscopy (TEM), scanning transmission electron microscopy (STEM), and 3D tomographic reconstructions of these nanostructures revealed that the final morphology of the hybrid material is octahedral (Figure 7C–E), possibly because of the preferable anchoring of the clusters on the four alternative  $\langle 110 \rangle$  facets over the  $\langle 100 \rangle$  facets on the octagonal GNR

surfaces. Interestingly, the intrinsic properties of the constituent materials, namely, the GNR and  $\text{Ag}_{44}$ , were retained in the final nanostructure which shows remarkable ambient stability. Next, we reacted the  $\text{p-MBA}$ -functionalized GNRs with water-dispersible  $\text{Au}_{102}(\text{p-MBA})_{44}$ <sup>35</sup> and  $\text{Au}_{250}(\text{p-MBA})_{47}$ <sup>47</sup> in a similar fashion to check the generic nature of the scheme in terms of the NCs and the solvents used. Here also we observed encapsulation of the GNRs by the NCs, although in these cases the cluster moieties were less closely packed (Figure 7F). This was attributed to the fact that in the water-soluble state, some of the  $\text{p-MBA}$  ligands of the gold clusters had to be deprotonated, making fewer ligands available for hydrogen bonding and thus making the final structures less compact. We expect that with the rightly chosen NC, this hybrid system can significantly improve the stability and detection limit of cluster-based sensing devices by plasmon-assisted enhancement of cluster properties.

### FUTURE PERSPECTIVES

In this Account, we have presented a glimpse into the various supramolecular interactions possible in atomically precise clusters. While supramolecular functionalization of the NCs with molecules like CD and  $\text{C}_{60}$  highlights the precision in their structures to selectively favor the formation of the host–guest complexes, exploring such composite structures in the solid state would lead to new materials. Although we have observed a mixture of adducts in solution, better control of the polydispersity of the supramolecular adducts to accomplish atomic precision and consequent crystallization are challenging areas. Furthermore, the site of attachment and binding modes of



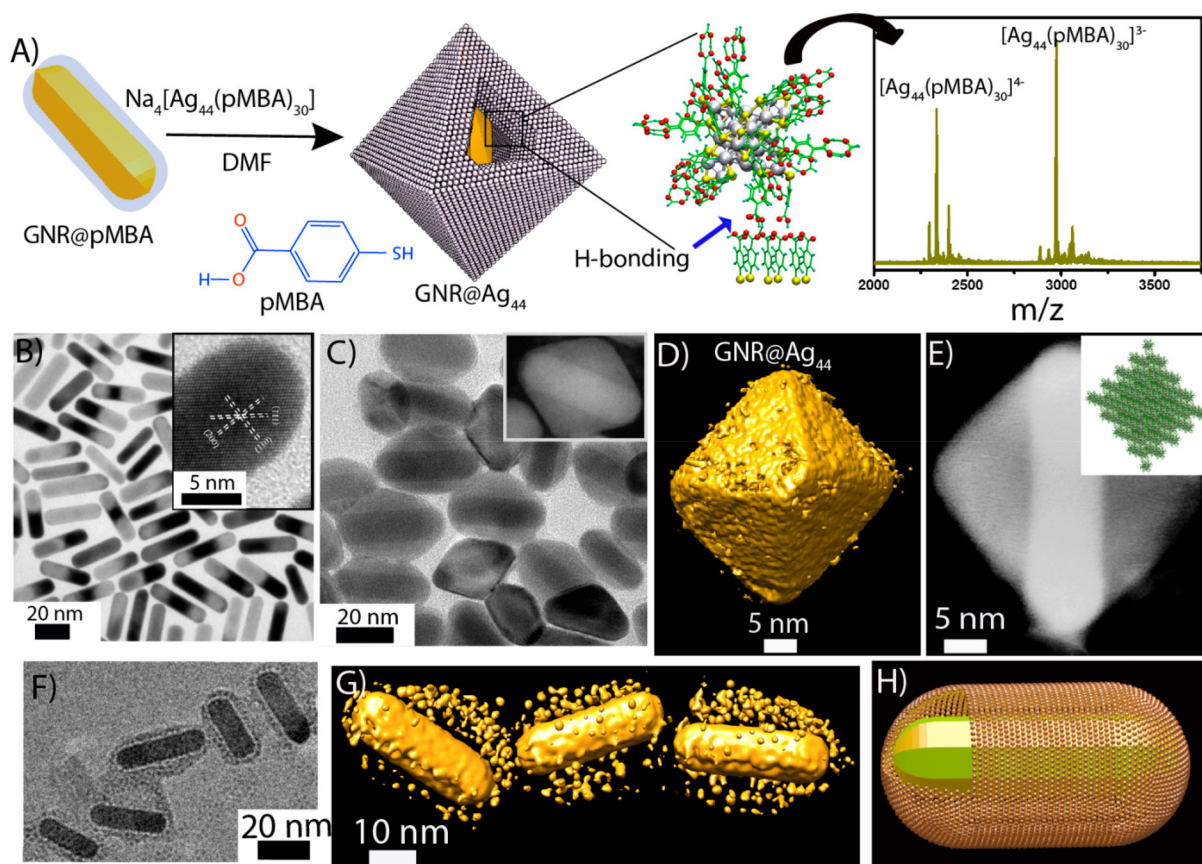


**Figure 7.** (A) Assembly of  $\text{Ag}_{44}$  NCs on the  $\text{GNR}@p\text{-MBA}$  surface. The ESI MS spectrum of  $\text{Ag}_{44}$  is shown as the inset. (b) TEM image of  $\text{GNR}@p\text{-MBA}$ . HRTEM image of the tip of a GNR is shown in the inset. (C) TEM image of  $\text{GNR}@Ag_{44}$ . A dark-field STEM image is shown in the inset. (D, E) TEM tomographic and dark-field STEM images of  $\text{GNR}@Ag_{44}$ . The image shows that the clusters make a nanocage and encapsulate the GNR. A theoretical model of the assembly of  $\text{Ag}_{44}$  clusters forming an octahedral shape is presented in the inset. (F) TEM image of  $\text{GNR}@Au_{250}$ . (G, H) 3D reconstructed structures and 3D graphical representation of  $\text{GNR}@Au_{250}$ , respectively. Reproduced with permission from ref 46. Copyright 2018 Wiley-VCH.

CD and  $C_{60}$  to the clusters may vary, which may lead to isomerism in the resulting structures. Such isomerism could extend to novel optical properties as well. With an appropriate choice of the host and guest molecules, chirality may also be introduced in supramolecular assemblies of certain clusters. Functionalized fullerenes or CDs may also be used to modify cluster binding. The development of functional cluster-based materials may also include modifying the ligand shell of the cluster with suitable bidentate or multidentate linkers, allowing the creation of cluster-assembled metal–organic frameworks.<sup>48</sup> The observation of polymorphic crystal lattices of NCs also enfold a new area in nanoparticle engineering. Supramolecular interactions may also favor crystallization of dimers or oligomers of clusters. Furthermore, the self-organization of nanostructures with macrostructures leading to architectures of larger dimensions constitutes new types of precision hybrids with diverse possibilities. These derived materials, especially low-dimensional building blocks, may lead to anisotropic solids with unprecedented properties. The self-assembly of NCs leading to spherical capsids<sup>44,45</sup> is a direction toward larger assemblies similar to biological systems. Cluster-assembled hybrid materials may result in a new paradigm of conductive or magnetic luminescent materials.

The choice of supramolecular building blocks presented here has been dominated by the consideration of interactions. However, such building blocks can also be chosen on the basis of

new properties such as magnetism, chirality, energy transfer, etc. that they provide. A unique aspect of clusters is that their size is comparable to the dimensions of biomolecules, which are also building blocks with atomic precision. Thus, structures incorporating biomolecules or synthetic polymers along with clusters is another strategy to create functional materials. In comparison with supramolecular assemblies solely composed of biomolecules, cluster-based assemblies can introduce new optical, magnetic, or electrical properties.

A closer analysis of this area shows that the molecule–materials interface is enriched by MS in its diverse forms. Compositional precision revealed by MS, in conjunction with structural and conformational precision revealed by diffraction and spectroscopy, coupled with computational studies enabling better insights into the properties, are essential components of this area. Several of the finer details of these materials such as the atomistic steps involved in the formation of these assemblies and their time scales are not accessible presently by experimental methods, and therefore, computations become the only credible methodology for exploration. This MS–diffraction–theory combination in the context of novel properties of atomically precise matter is expected to expand into even more larger systems in the years ahead, which should result in a fuller appreciation of materials with atomic precision.

## AUTHOR INFORMATION

### Corresponding Author

\*E-mail: [pradeep@iitm.ac.in](mailto:pradeep@iitm.ac.in).

### ORCID

Thalappil Pradeep: 0000-0003-3174-534X

### Notes

The authors declare no competing financial interest.

### Biographies

**Papri Chakraborty** is a Ph.D. student in the group of Prof. T. Pradeep at Indian Institute of Technology Madras. Her research is focused on mass spectrometric studies of noble metal clusters.

**Abhijit Nag** is a Ph.D. student in the group of Prof. T. Pradeep at Indian Institute of Technology Madras. His research is focused on supramolecular chemistry of clusters and biomolecules.

**Amrita Chakraborty** is a Ph.D. student in the group of Prof. T. Pradeep at Indian Institute of Technology Madras. Her research is focused on cluster–nanoparticle composite systems.

**Thalappil Pradeep** is a Professor at Indian Institute of Technology Madras. He works on molecular and nanoscale materials. Some of his findings have been translated to products through startup companies.

## ACKNOWLEDGMENTS

We thank all of the coauthors of previous publications from our group, who made this Account possible. P.C. and A.C. thank the Council of Scientific and Industrial Research (CSIR) for their research fellowships. A.N. thanks IIT Madras for an Institute Doctoral Fellowship. We acknowledge the financial support of the Department of Science and Technology (DST), Government of India.

## REFERENCES

- (1) Chakraborty, I.; Pradeep, T. Atomically Precise Clusters of Noble Metals: Emerging Link between Atoms and Nanoparticles. *Chem. Rev.* **2017**, *117*, 8208–8271.
- (2) Jin, R.; Zeng, C.; Zhou, M.; Chen, Y. Atomically Precise Colloidal Metal Nanoclusters and Nanoparticles: Fundamentals and Opportunities. *Chem. Rev.* **2016**, *116*, 10346–10413.
- (3) Fang, J.; Zhang, B.; Yao, Q.; Yang, Y.; Xie, J.; Yan, N. Recent Advances in the Synthesis and Catalytic Applications of Ligand-protected, Atomically Precise Metal Nanoclusters. *Coord. Chem. Rev.* **2016**, *322*, 1–29.
- (4) Maity, P.; Xie, S.; Yamauchi, M.; Tsukuda, T. Stabilized Gold Clusters: From Isolation toward Controlled Synthesis. *Nanoscale* **2012**, *4*, 4027–4037.
- (5) Krishnadas, K. R.; Baksi, A.; Ghosh, A.; Natarajan, G.; Som, A.; Pradeep, T. Interparticle Reactions: An Emerging Direction in Nanomaterials Chemistry. *Acc. Chem. Res.* **2017**, *50*, 1988–1996.
- (6) Yao, Q.; Feng, Y.; Fung, V.; Yu, Y.; Jiang, D.-e.; Yang, J.; Xie, J. Precise Control of Alloying Sites of Bimetallic Nanoclusters via Surface Motif Exchange Reaction. *Nat. Commun.* **2017**, *8*, 1555.
- (7) Zeng, C.; Chen, Y.; Kirschbaum, K.; Lambright, K. J.; Jin, R. Emergence of Hierarchical Structural Complexities in Nanoparticles and their Assembly. *Science* **2016**, *354*, 1580.
- (8) Baksi, A.; Chakraborty, P.; Bhat, S.; Natarajan, G.; Pradeep, T.  $[\text{Au}_{25}(\text{SR})_{18}]_2^{2-}$ : A Noble Metal Cluster Dimer in the Gas Phase. *Chem. Commun.* **2016**, *52*, 8397–8400.
- (9) De Nardi, M.; Antonello, S.; Jiang, D.-e.; Pan, F.; Rissanen, K.; Ruzzi, M.; Venzo, A.; Zoleo, A.; Maran, F. Gold Nanowired: A Linear  $(\text{Au}_{25})_n$  Polymer from  $\text{Au}_{25}$  Molecular Clusters. *ACS Nano* **2014**, *8*, 8505–8512.
- (10) Fontana, J.; Dressick, W. J.; Phelps, J.; Johnson, J. E.; Rendell, R. W.; Sampson, T.; Ratna, B. R.; Soto, C. M. Virus-Templated Plasmonic

Nanoclusters with Icosahedral Symmetry via Directed Self-Assembly. *Small* **2014**, *10*, 3058–3063.

(11) Berry, V.; Saraf, R. F. Self-Assembly of Nanoparticles on Live Bacterium: An Avenue To Fabricate Electronic Devices. *Angew. Chem., Int. Ed.* **2005**, *44*, 6668–6673.

(12) Natarajan, G.; Mathew, A.; Negishi, Y.; Whetten, R. L.; Pradeep, T. A Unified Framework for Understanding the Structure and Modifications of Atomically Precise Monolayer Protected Gold Clusters. *J. Phys. Chem. C* **2015**, *119*, 27768–27785.

(13) Fernando, A.; Aikens, C. M. Ligand Exchange Mechanism on Thiolate Monolayer Protected  $\text{Au}_{25}(\text{SR})_{18}$  Nanoclusters. *J. Phys. Chem. C* **2015**, *119*, 20179–20187.

(14) Jin, R.; Nobusada, K. Doping and Alloying in Atomically Precise Gold Nanoparticles. *Nano Res.* **2014**, *7*, 285–300.

(15) Mathew, A.; Natarajan, G.; Lehtovaara, L.; Häkkinen, H.; Kumar, R. M.; Subramanian, V.; Jaleel, A.; Pradeep, T. Supramolecular Functionalization and Concomitant Enhancement in Properties of  $\text{Au}_{25}$  Clusters. *ACS Nano* **2014**, *8*, 139–152.

(16) Som, A.; Chakraborty, I.; Maark, T. A.; Bhat, S.; Pradeep, T. Cluster-Mediated Crossed Bilayer Precision Assemblies of 1D Nanowires. *Adv. Mater.* **2016**, *28*, 2827–2833.

(17) Rekharsky, M. V.; Inoue, Y. Complexation Thermodynamics of Cyclodextrins. *Chem. Rev.* **1998**, *98*, 1875–1918.

(18) May, B. L.; Gerber, J.; Clements, P.; Buntine, M. A.; Brittain, D. R. B.; Lincoln, S. F.; Easton, C. J. Cyclodextrin and Modified Cyclodextrin Complexes of *E*-4-*tert*-butylphenyl-4'-oxyazobenzene: UV–visible,  $^1\text{H}$  NMR and ab Initio Studies. *Org. Biomol. Chem.* **2005**, *3*, 1481–1488.

(19) Heaven, M. W.; Dass, A.; White, P. S.; Holt, K. M.; Murray, R. W. Crystal Structure of the Gold Nanoparticle  $[\text{N}(\text{C}_8\text{H}_{17})_4]_4\text{[Au}_{25}(\text{SCH}_2\text{CH}_2\text{Ph})_{18}]$ . *J. Am. Chem. Soc.* **2008**, *130*, 3754–3755.

(20) Zhu, M.; Aikens, C. M.; Hollander, F. J.; Schatz, G. C.; Jin, R. Correlating the Crystal Structure of a Thiol-Protected  $\text{Au}_{25}$  Cluster and Optical Properties. *J. Am. Chem. Soc.* **2008**, *130*, 5883–5885.

(21) Park, J. H.; Hwang, S.; Kwak, J. Nanosieving of Anions and Cavity-Size-Dependent Association of Cyclodextrins on a 1-Adamantanethiol Self-Assembled Monolayer. *ACS Nano* **2010**, *4*, 3949–3958.

(22) Böhm, I.; Isenbügel, K.; Ritter, H.; Branscheid, R.; Kolb, U. Cyclodextrin and Adamantane Host–Guest Interactions of Modified Hyperbranched Poly(ethylene imine) as Mimetics for Biological Membranes. *Angew. Chem., Int. Ed.* **2011**, *50*, 7896–7899.

(23) Harries, D.; Rau, D. C.; Parsegian, V. A. Solutes Probe Hydration in Specific Association of Cyclodextrin and Adamantane. *J. Am. Chem. Soc.* **2005**, *127*, 2184–2190.

(24) Yan, C.; Liu, C.; Abroshan, H.; Li, Z.; Qiu, R.; Li, G. Surface Modification of Adamantane-Terminated Gold Nanoclusters using Cyclodextrins. *Phys. Chem. Chem. Phys.* **2016**, *18*, 23358–23364.

(25) Higaki, T.; Liu, C.; Zeng, C.; Jin, R.; Chen, Y.; Rosi, N. L.; Jin, R. Controlling the Atomic Structure of  $\text{Au}_{30}$  Nanoclusters by a Ligand-Based Strategy. *Angew. Chem., Int. Ed.* **2016**, *55*, 6694–6697.

(26) Kang, X.; Zhou, M.; Wang, S.; Jin, S.; Sun, G.; Zhu, M.; Jin, R. The Tetrahedral Structure and Luminescence Properties of Bi-metallic  $\text{Pt}_1\text{Ag}_{28}(\text{SR})_{18}(\text{PPh}_3)_4$  Nanocluster. *Chem. Sci.* **2017**, *8*, 2581–2587.

(27) Crasto, D.; Barcaro, G.; Stener, M.; Sementa, L.; Fortunelli, A.; Dass, A.  $\text{Au}_{24}(\text{SAdm})_{16}$  Nanomolecules: X-ray Crystal Structure, Theoretical Analysis, Adaptability of Adamantane Ligands To Form  $\text{Au}_{23}(\text{SAdm})_{16}$  and  $\text{Au}_{25}(\text{SAdm})_{16}$ , and its Relation to  $\text{Au}_{25}(\text{SR})_{18}$ . *J. Am. Chem. Soc.* **2014**, *136*, 14933–14940.

(28) Bhunia, S.; Kumar, S.; Purkayastha, P. Gold Nanocluster-Grafted Cyclodextrin Suprastructures: Formation of Nanospheres to Nanocubes with Intriguing Photophysics. *ACS Omega* **2018**, *3*, 1492–1497.

(29) Zhu, H.; Goswami, N.; Yao, Q.; Chen, T.; Liu, Y.; Xu, Q.; Chen, D.; Lu, J.; Xie, J. Cyclodextrin–Gold Nanocluster Decorated  $\text{TiO}_2$  Enhances Photocatalytic Decomposition of Organic Pollutants. *J. Mater. Chem. A* **2018**, *6*, 1102–1108.

(30) Diederich, F.; Gomez-Lopez, M. Supramolecular Fullerene Chemistry. *Chem. Soc. Rev.* **1999**, *28*, 263–277.

(31) Chakraborty, P.; Nag, A.; Paramasivam, G.; Natarajan, G.; Pradeep, T. Fullerene-Functionalized Monolayer-Protected Silver

Clusters:  $[\text{Ag}_{29}(\text{BDT})_{12}(\text{C}_{60})_n]^{3-}$  ( $n = 1-9$ ). *ACS Nano* **2018**, *12*, 2415–2425.

(32) AbdulHalim, L. G.; Bootharaju, M. S.; Tang, Q.; Del Gobbo, S.; AbdulHalim, R. G.; Eddaoudi, M.; Jiang, D.-e.; Bakr, O. M.  $\text{Ag}_{29}(\text{BDT})_{12}(\text{TPP})_4$ : A Tetravalent Nanocluster. *J. Am. Chem. Soc.* **2015**, *137*, 11970–11975.

(33) Schulz-Dobrick, M.; Jansen, M. Intercluster Compounds Consisting of Gold Clusters and Fullerides:  $[\text{Au}_7(\text{PPh}_3)_7]\text{C}_{60}\cdot\text{THF}$  and  $[\text{Au}_8(\text{PPh}_3)_8](\text{C}_{60})_2$ . *Angew. Chem., Int. Ed.* **2008**, *47*, 2256–2259.

(34) Yoon, B.; Luedtke, W. D.; Barnett, R. N.; Gao, J.; Desiredy, A.; Conn, B. E.; Bigioni, T.; Landman, U. Hydrogen-Bonded Structure and Mechanical Chiral Response of a Silver Nanoparticle Superlattice. *Nat. Mater.* **2014**, *13*, 807.

(35) Jadzinsky, P. D.; Calero, G.; Ackerson, C. J.; Bushnell, D. A.; Kornberg, R. D. Structure of a Thiol Monolayer-Protected Gold Nanoparticle at 1.1 Å Resolution. *Science* **2007**, *318*, 430.

(36) Higaki, T.; Liu, C.; Zhou, M.; Luo, T.-Y.; Rosi, N. L.; Jin, R. Tailoring the Structure of 58-Electron Gold Nanoclusters:  $\text{Au}_{103}\text{S}_2(\text{S-Nap})_{41}$  and Its Implications. *J. Am. Chem. Soc.* **2017**, *139*, 9994–10001.

(37) Liao, L.; Chen, J.; Wang, C.; Zhuang, S.; Yan, N.; Yao, C.; Xia, N.; Li, L.; Bao, X.; Wu, Z. Transition-Sized  $\text{Au}_{92}$  Nanoparticle Bridging Non-fcc-structured Gold Nanoclusters and fcc-structured Gold Nanocrystals. *Chem. Commun.* **2016**, *52*, 12036–12039.

(38) Gan, Z.; Chen, J.; Wang, J.; Wang, C.; Li, M.-B.; Yao, C.; Zhuang, S.; Xu, A.; Li, L.; Wu, Z. The Fourth Crystallographic Closest Packing Unveiled in the Gold Nanocluster Crystal. *Nat. Commun.* **2017**, *8*, 14739.

(39) Nag, A.; Chakraborty, P.; Bodiuzzaman, M.; Ahuja, T.; Antharjanam, S.; Pradeep, T. Polymorphism of  $\text{Ag}_{29}(\text{BDT})_{12}(\text{TPP})_4^{3-}$  Cluster: Interactions of Secondary Ligands and their Effect on Solid State Luminescence. *Nanoscale* **2018**, *10*, 9851–9855.

(40) Som, A.; Samal, A. K.; Udayabhaskararao, T.; Bootharaju, M. S.; Pradeep, T. Manifestation of the Difference in Reactivity of Silver Clusters in Contrast to Its Ions and Nanoparticles: The Growth of Metal Tipped Te Nanowires. *Chem. Mater.* **2014**, *26*, 3049–3056.

(41) Udayabhaskararao, T.; Bootharaju, M. S.; Pradeep, T. Thiolate-Protected  $\text{Ag}_{32}$  Clusters: Mass Spectral Studies of Composition and Insights into the Ag–thiolate Structure from NMR. *Nanoscale* **2013**, *5*, 9404–9411.

(42) Desiredy, A.; Conn, B. E.; Guo, J.; Yoon, B.; Barnett, R. N.; Monahan, B. M.; Kirschbaum, K.; Griffith, W. P.; Whetten, R. L.; Landman, U.; Bigioni, T. P. Ultrastable Silver Nanoparticles. *Nature* **2013**, *501*, 399.

(43) Nepal, D.; Drummy, L. F.; Biswas, S.; Park, K.; Vaia, R. A. Large Scale Solution Assembly of Quantum Dot–Gold Nanorod Architectures with Plasmon Enhanced Fluorescence. *ACS Nano* **2013**, *7*, 9064–9074.

(44) Nonappa; Lahtinen, T.; Haataja, J. S.; Tero, T.-R.; Häkkinen, H.; Ikkala, O. Template-Free Supracolloidal Self-assembly of Atomically Precise Gold Nanoclusters: From 2D Colloidal Crystals to Spherical Capsids. *Angew. Chem., Int. Ed.* **2016**, *55*, 16035–16038.

(45) Nonappa; Ikkala, O. Hydrogen Bonding Directed Colloidal Self-Assembly of Nanoparticles into 2D Crystals, Capsids, and Supracolloidal Assemblies. *Adv. Funct. Mater.* **2018**, *28*, 1704328.

(46) Chakraborty, A.; Fernandez, A. C.; Som, A.; Mondal, B.; Natarajan, G.; Paramasivam, G.; Lahtinen, T.; Häkkinen, H.; Nonappa; Pradeep, T. Atomically Precise Nanocluster Assemblies Encapsulating Plasmonic Gold Nanorods. *Angew. Chem., Int. Ed.* **2018**, *57*, 6522–6526.

(47) Lahtinen, T.; Hulkko, E.; Sokolowska, K.; Tero, T.-R.; Saarnio, V.; Lindgren, J.; Pettersson, M.; Häkkinen, H.; Lehtovaara, L. Covalently Linked Multimers of Gold Nanoclusters  $\text{Au}_{102}(\text{p-MBA})_{44}$  and  $\text{Au}_{250}(\text{p-MBA})_n$ . *Nanoscale* **2016**, *8*, 18665–18674.

(48) Huang, R.-W.; Wei, Y.-S.; Dong, X.-Y.; Wu, X.-H.; Du, C.-X.; Zang, S.-Q.; Mak, T. C. W. Hypersensitive Dual-Function Luminescence Switching of a Silver–Chalcogenolate Cluster-Based Metal–Organic Framework. *Nat. Chem.* **2017**, *9*, 689.



## CONDENSED MATTER PHYSICS

## Rapid isotopic exchange in nanoparticles

Papri Chakraborty<sup>1</sup>, Abhijit Nag<sup>1</sup>, Ganapati Natarajan<sup>1</sup>, Nayanika Bandyopadhyay<sup>1</sup>,  
Ganesan Paramasivam<sup>1</sup>, Manoj Kumar Panwar<sup>1</sup>, Jaydeb Chakrabarti<sup>2</sup>, Thalappil Pradeep<sup>1\*</sup>

Rapid solution-state exchange dynamics in nanoscale pieces of matter is revealed, taking isotopically pure atomically precise clusters as examples. As two isotopically pure silver clusters made of <sup>107</sup>Ag and <sup>109</sup>Ag are mixed, an isotopically mixed cluster of the same entity results, similar to the formation of HDO, from H<sub>2</sub>O and D<sub>2</sub>O. This spontaneous process is driven by the entropy of mixing and involves events at multiple time scales.

Copyright © 2019  
The Authors, some  
rights reserved;  
exclusive licensee  
American Association  
for the Advancement  
of Science. No claim to  
original U.S. Government  
Works. Distributed  
under a Creative  
Commons Attribution  
NonCommercial  
License 4.0 (CC BY-NC).

## INTRODUCTION

Since the discovery of deuterium (D) (1) and the isolation of D<sub>2</sub>O (2), isotopic exchange in molecules has served as a characteristic signature of their dynamic chemical bonds (3). The rate of isotopic exchange in water (H<sub>2</sub>O + D<sub>2</sub>O = 2HDO) is fast with an equilibrium constant of  $3.75 \pm 0.07$  at room temperature (4), and it occurs at measurable speeds down to cryogenic temperatures (5). H/D exchange in proteins has been an important tool to understand their surface structure (6). Moreover, isotopic exchange in systems like H<sub>2</sub>/D<sub>2</sub> has high activation barrier and occurs at very high temperatures (~1000 K) or over heated catalytic metal surfaces (7). The existence of nanomaterials of noble metals with precise composition (8, 9) allows the feasibility of their isotopic exchange to be tested. Using high-resolution electrospray ionization mass spectrometry (ESI MS), we show that atomically precise monolayer-protected nanoclusters, made of isotopically pure silver (<sup>107</sup>Ag and <sup>109</sup>Ag), despite their well-defined structures and ligand protection, undergo rapid exchange of the isotopes of the metal atoms. The exchange approaches a dynamic equilibrium within a minute in solution at room temperature. Using two archetypal examples of Ag nanoparticles of precise composition, [Ag<sub>25</sub>(SR)<sub>18</sub>]<sup>−</sup> (10) and [Ag<sub>25</sub>(S<sub>2</sub>R)<sub>12</sub>(TPP)<sub>4</sub>]<sup>3−</sup> (11), where SR, S<sub>2</sub>R, and TPP are protecting ligands, we demonstrate that the rapid isotopic exchange reflects their solution-state dynamics. In addition, we show the ability to control the exchange dynamics by controlling the temperature. Time-resolved measurements further reveal that the mechanism of exchange involves several processes that occur at different time scales. The spontaneity in such reactions is mainly driven by the mixing entropy contribution to the free energy. Such an exchange mechanism, reminiscent of isotopic exchange between H<sub>2</sub>O and D<sub>2</sub>O, presents intriguing insights into the nature of nanoscale matter.

## RESULTS

To study isotopic exchange, we chose [Ag<sub>25</sub>(SR)<sub>18</sub>]<sup>−</sup> clusters (10) initially. Two identical but isotopically different clusters, [<sup>107</sup>Ag<sub>25</sub>(DMBT)<sub>18</sub>]<sup>−</sup> and [<sup>109</sup>Ag<sub>25</sub>(DMBT)<sub>18</sub>]<sup>−</sup> (DMBT = 2,4-dimethyl benzene thiol), were prepared starting from isotopically pure metals and extensively characterized to ensure their chemical purity and isotopic identity.

The isotopic clusters showed identical optical absorption spectra (fig. S1A). ESI MS of [<sup>107</sup>Ag<sub>25</sub>(DMBT)<sub>18</sub>]<sup>−</sup> and [<sup>109</sup>Ag<sub>25</sub>(DMBT)<sub>18</sub>]<sup>−</sup> are presented in Fig. 1A, a and b, respectively. The peak maxima of the spectra are separated by *m/z* (mass/charge ratio) 50 because of the interchange of 25 atoms of <sup>107</sup>Ag with <sup>109</sup>Ag. The mass spectral distributions of the isotopic clusters are narrower than those of a sample with natural Ag (fig. S1B). The isotope patterns (fig. S1, C and D) are purely due to the isotopes of S, C, and H in the ligands, and therefore, they are similar to those of the [Au<sub>25</sub>(PET)<sub>18</sub>]<sup>−</sup> cluster (12, 13) [PET (phenyl ethane thiol) has the same atomic composition (C<sub>8</sub>H<sub>10</sub>S) as DMBT], as Au has only one isotope. The minor differences with calculated patterns (fig. S1, C and D) are due to the slight isotopic impurity, as the isotope enrichment was ~98%. Upon mixing an equimolar mixture of [<sup>107</sup>Ag<sub>25</sub>(DMBT)<sub>18</sub>]<sup>−</sup> and [<sup>109</sup>Ag<sub>25</sub>(DMBT)<sub>18</sub>]<sup>−</sup> in solution at room temperature, the spectrum changed instantaneously, and the resulting distribution is shown in Fig. 1B. No peaks due to the parent clusters were observed, indicating that they were totally exchanged in this process. The mass spectral distribution calculated (fig. S2A) considering a system where each isotope of Ag (107/109) has a probability of occupying 50% of the total sites of the cluster is similar to the distribution observed in Fig. 1B. It is nearly identical to that of the ion [Ag<sub>25</sub>(DMBT)<sub>18</sub>]<sup>−</sup>, having the natural isotope distribution (<sup>107</sup>Ag: 51.839%, <sup>109</sup>Ag: 48.161%), and the minor differences arise as the <sup>107</sup>Ag/<sup>109</sup>Ag ratio is not exactly 1:1 in nature (fig. S2B). The two isotopically pure clusters were further mixed at varying molar ratios, and in each case, rapid exchange between the two clusters resulted in a binomial mass spectral distribution (fig. S3), in agreement with the calculated isotope pattern considering the relative abundance of each isotope from their initial molar ratio of mixing (fig. S4). Such an equilibrium statistical distribution is expected for a system where there are nearly equivalent sites that have equal probability of exchange.

Control over the exchange dynamics was achieved by lowering the temperature. The parent solutions were cooled to −20°C and mixed in a 1:1 molar ratio, and ESI MS was measured instantly. The source and desolvation temperatures were lowered to 30°C, and the sample was infused from an external syringe, which was also cooled to −20°C to reduce the effect of temperature during injection. In Fig. 2 (A to D), we presented the intermediate stages involving stepwise exchange of the isotopes of the atoms between the two clusters. Although the reaction kinetics was slower at lower temperatures, the equilibrium distribution was attained in about 30 s. Rapid exchange occurred even in alloys of the cluster (14), such as [Ag<sub>24</sub>Au(SR)<sub>18</sub>]<sup>−</sup> (fig. S5).

To probe how the dynamics of the exchange process is controlled by the inherent structures of the cluster, we performed a similar study

<sup>1</sup>DST Unit of Nanoscience (DST UNS) and Thematic Unit of Excellence (TUE), Department of Chemistry, Indian Institute of Technology Madras, Chennai 600 036, India. <sup>2</sup>Department of Chemical, Biological and Macromolecular Sciences, S. N. Bose National Centre for Basic Sciences, Sector III, Block JD, Salt Lake, Kolkata 700098, India.

\*Corresponding author. Email: pradeep@iitm.ac.in



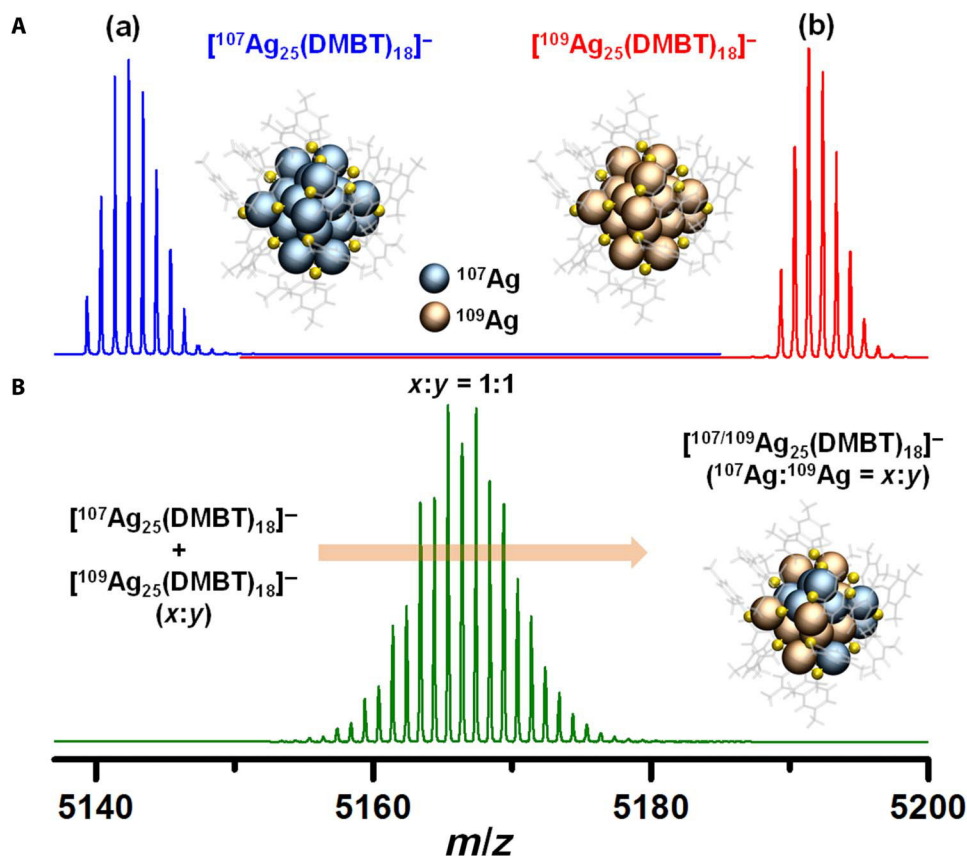


**Fig. 1. Mass spectra of the parent isotope clusters and the product of mixing.** (A) ESI MS of the as-synthesized isotopically pure clusters, (a)  $[^{107}\text{Ag}_{25}(\text{DMBT})_{18}]^-$  and (b)  $[^{109}\text{Ag}_{25}(\text{DMBT})_{18}]^-$ . (B) Mass spectral distribution of the product obtained by mixing the two isotopic clusters at 1:1 molar ratio. The spectrum was collected within 1 min after mixing the solutions of the clusters at room temperature. A representation of the clusters is shown. Comparison with the calculated mass spectrum is presented in figs. S1 and S2. Yellow, S; transparent gray, ligands.

with  $[\text{Ag}_{29}(\text{BDT})_{12}(\text{TPP})_4]^{3-}$ , where the dithiolate protection provides a very different structure (11) as compared to that of  $[\text{Ag}_{25}(\text{DMBT})_{18}]^-$ . Isotopically pure  $[^{107}\text{Ag}_{29}(\text{BDT})_{12}(\text{TPP})_4]^{3-}$  (BDT = benzene dithiol) and  $[^{109}\text{Ag}_{29}(\text{BDT})_{12}(\text{TPP})_4]^{3-}$  clusters were synthesized and characterized using optical absorption (fig. S6C) and ESI MS (fig. S6, A and B). We observed a reduced exchange rate compared to that of  $[\text{Ag}_{25}(\text{DMBT})_{18}]^-$ . At room temperature, an equimolar mixture of the two isotopic  $[\text{Ag}_{29}(\text{BDT})_{12}(\text{TPP})_4]^{3-}$  clusters, at a concentration of  $1.5 \times 10^{-3}$  mM, showed stepwise exchanges reaching a dynamic equilibrium over a period of 3 hours (fig. S7A). Although the labile TPP ligands were lost during ionization, the use of soft ionization conditions enabled us to observe that exchange occurred at a similar rate to that in the intact TPP-protected clusters that exist in solution (fig. S7B). The clusters mixed at any arbitrary molar ratios also attained equilibrium in a similar manner, and in all cases, the relative abundance of the isotopes in the final product was in accordance with their initial molar ratio of mixing (fig. S8).

The slower exchange rates seen here encouraged us to analyze the dynamics in greater detail. A kinetic plot of the percentage of unexchanged parent isotopic cluster ( $C_t$ ) versus time ( $t$ ) is shown in Fig. 3. At a given time, the percentage of exchange on either of the two isotopic clusters was similar when mixed in equimolar quantities. Therefore, monitoring the kinetics with respect to either of them gave identical results. In this plot, we included a hypothetical data point at  $t = 0$  min and  $C_t = 100\%$ , assuming that at 0 min, that is, in an

ideal situation before mixing, the abundance of a particular isotope ( $^{107}\text{Ag}/^{109}\text{Ag}$ ) in the clusters is 100%. Figure 3 shows that at room temperature ( $25^\circ\text{C}$ ), the  $^{107}\text{Ag}/^{109}\text{Ag}$  exchange rate was initially fast, and within 8 to 10 min, about 30% exchange occurred. Later, the exchange progressed slowly, and after about 250 min, the rate slowed down further, approaching an equilibrium corresponding to a state of 50% exchange. A triexponential effectively fitted the data points, suggesting at least three different rates for the exchange process with rate constants of  $5.9 \times 10^{-1} \text{ min}^{-1}$ ,  $1.4 \times 10^{-2} \text{ min}^{-1}$ , and  $7.1 \times 10^{-18} \text{ min}^{-1}$ , respectively. Similar exchange was studied at higher temperatures of  $40^\circ$  and  $60^\circ\text{C}$  (fig. S9, A and B), and the kinetic plots are shown in the inset of Fig. 3. The rate increased substantially at higher temperatures, and the reaction was complete within 60 min, whereas upon cooling the reaction mixture to  $0^\circ\text{C}$  the rate was drastically reduced and the process took around 3 days to attain equilibrium (fig. S9, C and D). Similar features were also observed for H/D exchange in supramolecular polymers in water (15). The three stages of exchange suggest that possibly the isotopic exchange in nanoparticles proceeds through (i) rapid exchange of their surface atoms, (ii) slower diffusion of the exchanged atoms within the core, and (iii) subsequent equilibration in the whole cluster. The reaction rates were dependent on the concentration of the clusters, which was evident from the kinetic studies at lower ( $1.5 \times 10^{-5}$  mM) and higher ( $1.5 \times 10^{-1}$  mM) concentrations compared to the above case ( $1.5 \times 10^{-3}$  mM) (fig. S10). At a given concentration of the parent clusters, we also

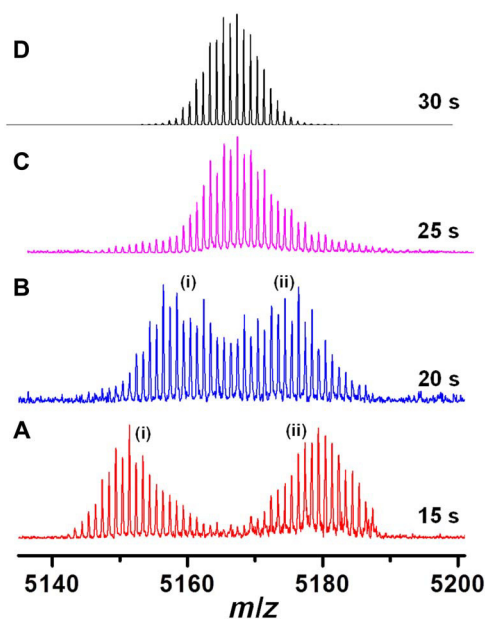


**Fig. 2. Low-temperature reaction showing the intermediate steps of exchange.** Exchange between the two isotopic  $[\text{Ag}_{25}(\text{DMBT})_{18}]^-$  clusters at  $-20^\circ\text{C}$  showing the intermediate stages of exchange (A) to (D) with mixing time (s). Distributions (i) and (ii) denote exchange at the  $^{107}\text{Ag}_{25}(\text{DMBT})_{18}^-$  and  $^{109}\text{Ag}_{25}(\text{DMBT})_{18}^-$  sides, respectively. Noise in the spectrum is due to the short acquisition time.

investigated the reaction rates at different molar ratios of mixing. Keeping the total number of moles of the mixture as constant, and starting from an excess concentration of  $^{107}\text{Ag}_{29}(\text{BDT})_{12}(\text{TPP})_4^{3-}$ , the rate increases with an increase in the concentration of  $^{109}\text{Ag}_{29}(\text{BDT})_{12}(\text{TPP})_4^{3-}$ , reaching a maximum at 1:1 condition. As the relative concentration of  $^{109}\text{Ag}_{29}(\text{BDT})_{12}(\text{TPP})_4^{3-}$  in the reaction mixture increases, the number of effective collisions between the isotopically different entities increases, and hence, the rate of exchange increases. Similar results were obtained starting from an excess concentration of  $^{109}\text{Ag}_{29}(\text{BDT})_{12}(\text{TPP})_4^{3-}$  and slowly increasing the concentration of  $^{107}\text{Ag}_{29}(\text{BDT})_{12}(\text{TPP})_4^{3-}$  in the mixture. Kinetic studies at different molar ratios showing the rate constants (fig. S11) and corresponding time-dependent ESI MS (fig. S12) are included in the Supplementary Materials. Reaction rates were independent of solvents such as dimethyl formamide (DMF), acetonitrile (ACN), and dichloromethane (DCM).

To investigate the mechanism and the driving forces of the isotopic exchange reaction, we carried out molecular docking studies and free-energy calculations. The mechanism of atom exchange is expected to be initiated through intercluster collisions (16), and this expectation is consistent with the temperature dependence of the rate constants. We have carried out molecular docking simulations for studying the interaction between two  $[\text{Ag}_{25}(\text{DMBT})_{18}]^-$  and two  $[\text{Ag}_{29}(\text{BDT})_{12}(\text{TPP})_4]^{3-}$  clusters. In each case, docking generated 10 different possible orientations, and the lowest-energy geometries for the approach of two  $[\text{Ag}_{25}(\text{DMBT})_{18}]^-$  and two  $[\text{Ag}_{29}(\text{BDT})_{12}(\text{TPP})_4]^{3-}$  clusters are represented in Fig. 4 (A and B). However, the other possible geometries were also similar in both cases, where the two clusters approach along the same orientation or along other symmetry equivalent orientations such that they interact at similar sites and generate the same configuration. The other possibilities were also energetically

similar within 0.01 to 0.07 kcal/mol. As all the possible structures obtained from docking were geometrically and energetically equivalent, it is likely that exchange reaction will be more favorable when the clusters approach along this specific geometry. The FFGMG obtained by docking two  $[\text{Ag}_{25}(\text{DMBT})_{18}]^-$  clusters indicates that after collision, the clusters may bind together supramolecularly in the initial steps of the reaction with an interaction energy of  $-23.7$  kcal/mol between the two clusters (Fig. 4A). The rapid exchange and the structural changes in  $[\text{Ag}_{25}(\text{DMBT})_{18}]^-$  can also be viewed from their topologically simplified structure (referred to as the aspicule model) (17), which considers the structure of an  $\text{M}_{25}\text{L}_{18}$  cluster (where  $\text{M} = \text{Au}, \text{Ag}$ ;  $\text{L} = \text{ligand}$ ) as a system of three interlocked Borromean rings of  $\text{M}_8(\text{SR})_6$  around a central  $\text{M}$  atom. Rapid exchange of isolobal  $\text{Ag}_2(\text{SR})_3$  and  $\text{Ag}(\text{SR})_2$  entities may occur. The opening of the rings can also make the core more exposed and facilitate spontaneous exchange of  $\text{Ag}$  or  $\text{Ag-SR}$  units between the core and staples of the two clusters. In comparison,  $[\text{Ag}_{29}(\text{BDT})_{12}(\text{TPP})_4]^{3-}$  does not contain any interlocked rings or chain structures. It has a rigid surface network with cross-linking dithiolates in the outer shell. In the lowest-energy geometry of two  $[\text{Ag}_{29}(\text{BDT})_{12}(\text{TPP})_4]^{3-}$  clusters (Fig. 4B), the proximity of  $\text{Ag}_3\text{S}_6$  or  $\text{AgS}_3\text{P}$  motifs of the two clusters may result in opening up of these staples. Molecular docking reveals an interaction energy of  $-7.8$  kcal/mol between two  $[\text{Ag}_{29}(\text{BDT})_{12}(\text{TPP})_4]^{3-}$  clusters (Fig. 4B). The supramolecular interactions between the clusters mainly include van der Waals and  $\text{C-H}\cdots\pi$  interactions. In the case of  $[\text{Ag}_{25}(\text{DMBT})_{18}]^-$  clusters, the  $\text{H}$  of the benzene ring and  $-\text{CH}_3$  group of one ligand on a cluster can interact with the  $\pi$ -system of the benzene ring of another cluster to facilitate the binding. These  $\text{C-H}\cdots\pi$  interaction distances are in the range of 2.99 to 4.16 Å, which are comparable with the  $\text{C-H}\cdots\pi$  distances observed in the crystal structures of  $\text{Au}_{246}$  (18) and  $\text{Ag}_{29}$  (19) nanoclusters. Interactions are also similar in the case of  $[\text{Ag}_{29}(\text{BDT})_{12}(\text{TPP})_4]^{3-}$  clusters. The  $\text{C-H}\cdots\pi$  interactions exist between  $-\text{H}$  of BDT of one cluster with benzene ring of BDT of another cluster at a distance of about 3.46 to 4.39 Å. The interactions are greater in the  $[\text{Ag}_{25}(\text{DMBT})_{18}]^-$  cluster, leading to higher binding energy. The interactions between the ligands are indicated in fig. S13. The reduced intercluster interaction energy and higher rigidity in the structure of  $[\text{Ag}_{29}(\text{BDT})_{12}(\text{TPP})_4]^{3-}$  might result in a slower exchange rate as compared to that of  $[\text{Ag}_{25}(\text{DMBT})_{18}]^-$ . However, more detailed computations are required to understand the complete mechanism of the atom exchange process.

We considered the thermodynamics of the reaction to identify the main driving force of the isotopic exchange reaction. The energy barrier for an intercluster isotopic exchange represents the energy cost of breaking and reforming bonds and any intermediate barriers, which must be crossed while the atoms travel along the path from their initial to final positions. We computed the enthalpic [electronic energy, zero-point energy (ZPE), and specific heat] and the entropic (electronic, translational, rotational, and vibrational) contributions to the free energy. Computational details are mentioned in Materials and Methods, and detailed results are presented in table S2. The total electronic energies of the clusters do not vary when different isotopes of the atoms are exchanged and rearranged because their bonding interactions are identical. Hence, any differences in enthalpy will be due to ZPE. Furthermore, the vibrational contribution to enthalpy and entropy will also contribute to the free energy. However, we found that there were only very small differences in the free energy of the clusters ( $\sim 0.01$  eV) due to isotopic exchange, and moreover, these differences cancel out when the reaction free energy  $[\Delta G_{\text{react}} = G(\text{products}) - G(\text{reactants})]$  is computed for the 1:1 ratio. In this calculation, we

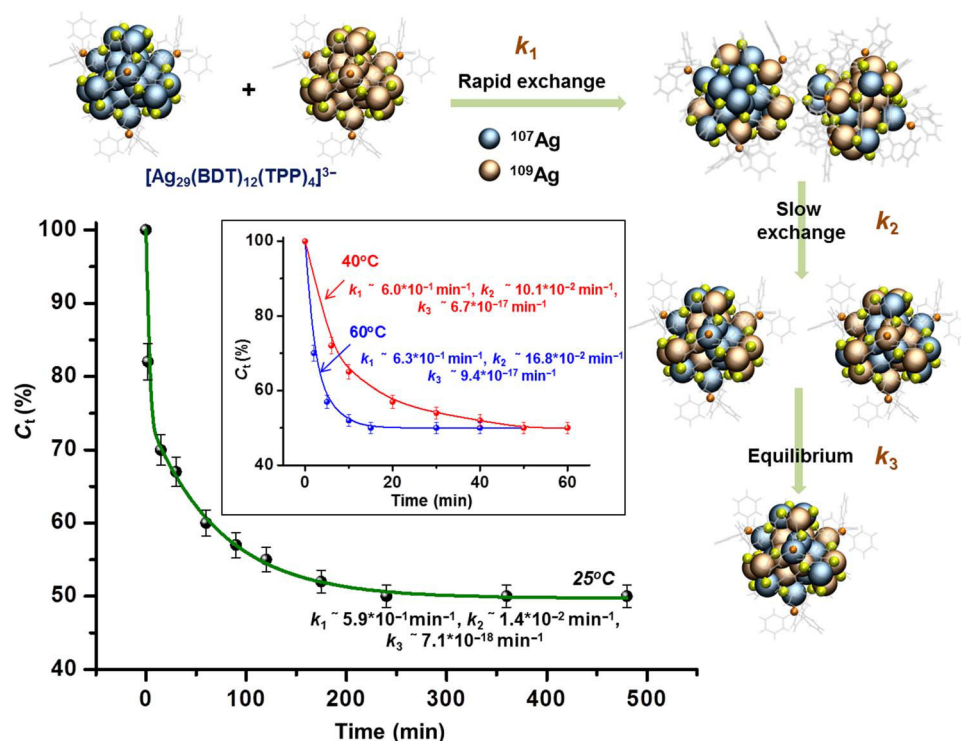


**Fig. 3. Kinetic study of isotopic exchange in  $[\text{Ag}_{29}(\text{BDT})_{12}(\text{TPP})_4]^{3-}$  clusters.** Plot of percentage of unexchanged parent isotopic cluster ( $C_t$ ) versus time (min) of reaction at room temperature (25°C). Kinetics at 40° and 60°C are presented in the inset. Average of three kinetic measurements is plotted, and the error bar is indicated at each point. A schematic showing the different stages of isotopic exchange is also shown in the figure. Yellow, S; orange, P; transparent gray, ligands.

have assumed that the parent clusters are the isotopically pure reactants and that the products are the two mixed isotope clusters with the following compositions:  $(m,n) = (12,13)$  and  $(13,12)$  in the case of  $[\text{Ag}_m^{107}\text{Ag}_n^{109}(\text{DMBT})_{18}]^-$  and  $(m,n) = (14,15)$  and  $(15,14)$  in the case of  $[\text{Ag}_m^{107}\text{Ag}_n^{109}(\text{BDT})_{12}(\text{TPP})_4]^{3-}$ . Thus, in the absence of other contributions to the reaction free energy, the contribution from the mixing of isotopic clusters is expected to be of central importance in understanding the driving force of the reaction.

We now describe how we estimated the mixing contribution to the free energy. Application of the concept of entropy to a single cluster is not proper due to the small number of atoms ( $10^2$  to  $10^3$ ) in an individual cluster; however, we may apply it to the macroscopically large ensemble of  $N$  clusters, and the ensemble configuration is defined by the positions of  $^{107}\text{Ag}$  and  $^{109}\text{Ag}$  atoms in  $N$  clusters, where  $N$  is taken to be in the thermodynamic limit. The final equilibrium state of the cluster ensemble will be that in which the number of isotopic substituents is maximum for a given molar ratio so that the whole ensemble of clusters has the highest entropy ( $S$ ), which is defined as  $S = k \log W$ , where  $W$  is the total number of ways of arranging the two isotopes of Ag atoms (microstates) in the total available sites of the clusters, and  $k$  is the Boltzmann constant. For the equimolar composition, this will occur for the half-mixed compositions of each clusters, that is,  $n = (12, 13)$  and  $(13, 12)$  for  $\text{Ag}_{25}$ , and  $(14, 15)$  and  $(15, 14)$  for  $\text{Ag}_{29}$ , where these compositions have the identical maximum degeneracy in positional arrangements.

We approximate the ensemble of clusters with two crystalline lattices, one consisting of  $^{107}\text{Ag}$  and the other of  $^{109}\text{Ag}$ , which are fused together, and then assume random thermal exchanges of atoms in the joint lattice. In this simplification, we considered only the Ag atoms,

neglecting the cluster structure and symmetry and all interatomic interactions, and this situation is identical to the mixing of two ideal gases. Hence, the expression for mixing or configurational entropy is simply that of mixing two different ideal gases, which is known from statistical mechanics, and is given by

$$\Delta S_{\text{mix}} = -n_{\text{mol}} R [p \ln p + (1 - p) \ln (1 - p)]$$

where  $p$  is the mole fraction of  $^{107}\text{Ag}$ ,  $(1 - p)$  is the mole fraction of  $^{109}\text{Ag}$ , and  $n_{\text{mol}}$  is the total number of moles of the mixture.  $\Delta S_{\text{mix}}$  attains its maximum negative value for the half-and-half mixture, that is,  $p = 0.5$ , for a given total number of moles of the mixture (20). For a 1:1 ratio of mixing,  $\Delta S_{\text{mix}}$  is  $R \ln 2 = 5.76 \text{ J K}^{-1} \text{ mol}^{-1}$ , which is  $1.37 \text{ cal K}^{-1} \text{ mol}^{-1}$ , and  $\Delta G_{\text{mix}} = -T^* \Delta S_{\text{mix}} = -408.26 \text{ cal mol}^{-1}$  ( $T = 298 \text{ K}$  and  $n_{\text{mol}} = 1$ ). Because the calculated reaction free energies are negligible, the mixing entropic contribution to the free energy must be the main driving force of the observed spontaneous reaction. We remark that the mixing entropy term would also be important in spontaneous bimetallic intercluster reactions, where there are larger enthalpic changes due to the bonding interactions such as those between  $\text{Ag}_{25}(\text{DMBT})_{18}$  and  $\text{Au}_{25}(\text{PET})_{18}$  (16).

## DISCUSSION

The results presented establish that spontaneous isotopic exchange can occur between atomically precise silver nanoclusters. While it is rapid in  $[\text{Ag}_{25}(\text{SR})_{18}]^-$ , it is relatively slower in  $[\text{Ag}_{29}(\text{S}_2\text{R})_{12}(\text{TPP})_4]^{3-}$ , reflecting the differences in their chemical structures. Spontaneity in such reactions, driven by their entropy of mixing, reflects the dynamic



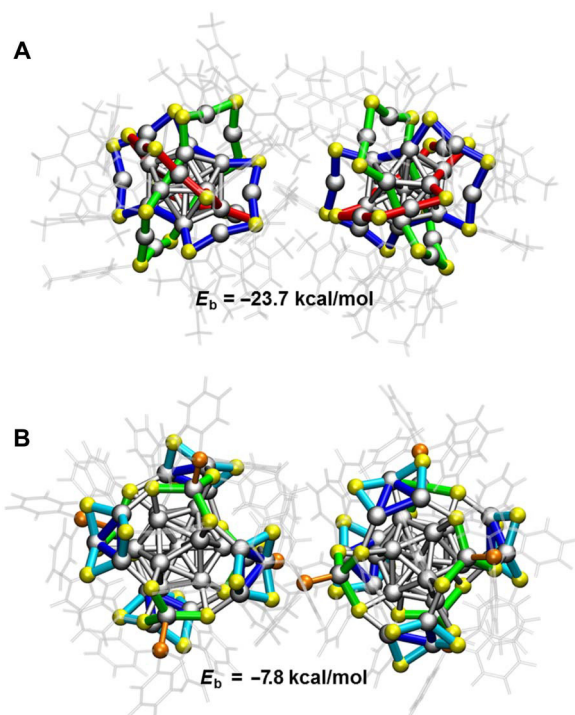


**Fig. 4. Molecular docking studies.** Force-field global minimum geometry (FFGMG) of two (A)  $[Ag_{25}(DMBT)_{18}]^{-}$  and (B)  $[Ag_{29}(BDT)_{12}(TPP)_4]^{3-}$  clusters, lying in close proximity. Gray, Ag; yellow, S; orange, P. The overlapping Borromean rings are shown in blue, green, and red in (A); staple units are shown in green and blue in (B); and ligand shell is shown in transparent gray. Atomic diameters were reduced to show the bonding.

nature of nanoparticles in solution. However, our study is restricted only to subnanometer-sized clusters, where exchange is shown to be dependent on their inherent structures. In a similar manner, the study may also be extended to classic nanomaterials of various sizes. Future possibilities include investigating the correlation between the extent of exchange with the size of the nanoparticles and the nature of their ligands or the constituent metal atoms.

The fundamental significance of this study is to understand the dynamics in nanoscale systems, which is comparable to solution-state dynamics of many simpler molecules like  $H_2O$ . This study has the potential to answer questions regarding the rigidity of the structures and rapid interconversions between the subunits that constitute nanosystems. Nanoparticle dynamics contributing to catalysis is of relevance to applications. In homogeneous catalysis involving nanoparticles, the site at which chemistry occurs could be changing continuously. This characteristic implies associated dynamics for the anchored ligands and therefore may contribute to their solution-state availability. This phenomenon may also be important in biology, where nanoparticles are used as carriers of molecular cargo.

Moreover, isotopic exchanges like H/D exchanges in  $H_2O/D_2O$  (21) can alter physical and chemical properties of the materials. Isotopic exchange affects the vibrational modes. In the case of clusters also, there will be changes in the vibrations, although these were found to be very small from our calculations. The change in properties is small in this particular case probably because the mass ratio of the two isotopes of Ag (109/107) is 1.019 (in contrast, the mass ratio for other isotopes like D/H is  $\sim 2$ ), and hence, the effect will be

less compared to the total mass of the cluster. However, the effect of isotopic exchange may become significant to alter the properties with the appropriately chosen cluster system and appropriately chosen metal or ligand isotopes. Isotopic modification can introduce a change in both the spatial distribution of nuclear mass and the nuclear spins in the clusters. Because the x-ray diffraction pattern of mixed isotope clusters and single isotope clusters would be identical, the use of neutron scattering could be useful to probe the structure and dynamics of these clusters. The change in the nuclear spins would affect the nuclear magnetic resonance (NMR) spectrum, and in the case of clusters with an unpaired electronic spin, isotopic modification would change the electron spin resonance properties through the electron-nuclear hyperfine interactions, which depend on the values of the nuclear spins. For example, in the case of isotopes of metals such as Pd ( $^{102}Pd$ ,  $^{104}Pd$ ,  $^{105}Pd$ ,  $^{106}Pd$ ,  $^{108}Pd$ , and  $^{110}Pd$ ),  $^{105}Pd$  has a nuclear spin of  $(5/2)^+$ , while other isotopes have 0 nuclear spin. This is similar in the case for the isotopes of Pt ( $^{192}Pt$ ,  $^{194}Pt$ ,  $^{195}Pt$ ,  $^{196}Pt$ ,  $^{198}Pt$ ), where  $^{195}Pt$  has a nuclear spin of  $(1/2)^-$ , while other isotopes have 0 nuclear spin. Such isotopic modification in clusters and their crystals might have applications in magnetic devices.

## MATERIALS AND METHODS

### Reagents and materials

Isotopically pure Ag foils,  $^{107}Ag$  (98%) and  $^{109}Ag$  (98%), were purchased from Cambridge Isotope Laboratories Inc. 2,4-DMBT, 1,3-BDT, sodium borohydride ( $NaBH_4$ ), and tetraphenyl phosphonium bromide ( $PPh_4Br$ ) were purchased from Sigma-Aldrich. Triphenyl phosphine (TPP) was purchased from Spectrochem, India. All the solvents [DCM, methanol (MeOH), DMF, and ACN] were of the high-performance liquid chromatography grade and were used without further purification.

### Synthesis of isotopically pure silver nitrate ( $^{107}AgNO_3$ and $^{109}AgNO_3$ ) from isotopically pure metal foils ( $^{107}Ag$ and $^{109}Ag$ )

About 50 mg of the metal foils of the isotopes of Ag ( $^{107}Ag$  and  $^{109}Ag$ ) was separately reacted with about 2 ml of concentrated nitric acid (70%) in a 5-ml reaction vessel and heated at  $70^\circ C$  inside a fume hood. The heating was continued until the evolution of nitrogen oxide gases was complete and the solution turned colorless. The solution was then diluted with water, and heating was continued. The process of addition of water was continued for a few times, and lastly, 0.5 ml of a concentrated solution of  $AgNO_3$  was kept for crystallization. For crystallization, the solution was kept inside an airtight dark box in the presence of solid  $P_2O_5$  and NaOH pellets (kept separately in the same box) to enhance the evaporation of water and remove excess acid. Colorless crystals of  $AgNO_3$  were obtained within 5 to 7 days. The yield of the reaction was around 95%.

### Synthesis of isotopically pure $[^{107}Ag_{25}(DMBT)_{18}]^{-}[PPh_4]^{+}$ and $[^{109}Ag_{25}(DMBT)_{18}]^{-}[PPh_4]^{+}$ clusters

Isotopically pure clusters were synthesized using the isotopically pure  $AgNO_3$  salt, which was synthesized according to the above mentioned method. The clusters were synthesized following a reported protocol (9). About 38 mg of  $^{107}AgNO_3$ / $^{109}AgNO_3$  was dissolved in a mixture of 2 ml of methanol and 17 ml of DCM. To this reaction mixture, about 90  $\mu l$  of 2,4-DMBT was added. The mixture was kept under stirring condition at  $0^\circ C$ . About 6 mg of  $PPh_4Br$  in 0.5 ml of methanol was added after about 15 to 20 min. Next, about 15 mg of  $NaBH_4$  in 0.5 ml of ice-cold water was added to the solution in a dropwise fashion. The stirring was continued for about 7 to 8 hours; the solution was then stored at  $4^\circ C$  for about 2 days. For purification, the sample

was centrifuged and DCM was removed by rotary evaporation. The precipitate was washed twice with methanol. Then, the cluster was redissolved in DCM and centrifuged to remove any further insoluble impurities. Further removal of DCM by rotary evaporation led to the formation of the purified clusters ( $[^{107}\text{Ag}_{25}(\text{DMBT})_{18}]^{-}[\text{PPh}_4]^{+}$  /  $[^{109}\text{Ag}_{25}(\text{DMBT})_{18}]^{-}[\text{PPh}_4]^{+}$ ) in their powder form.

#### Synthesis of isotopically pure $[^{107}\text{Ag}_{29}(\text{BDT})_{12}(\text{TPP})_4]^{3-}$ and $[^{109}\text{Ag}_{29}(\text{BDT})_{12}(\text{TPP})_4]^{3-}$ clusters

Isotopically pure clusters were synthesized using the isotopically pure  $\text{AgNO}_3$  salt following a reported method (10). About 20 mg of  $^{107}\text{AgNO}_3$  /  $^{109}\text{AgNO}_3$  was dissolved in a mixture of 5 ml of MeOH and 10 ml of DCM. To this solution, about 13.5  $\mu\text{l}$  of 1,3-BDT ligand was added, and the reaction mixture was kept under stirring condition. Addition of the thiol immediately resulted in a turbid yellow solution, which turned clear upon addition of about 200 mg of  $\text{PPh}_3$ . After about 15 min, a freshly prepared solution of 10.5 mg of  $\text{NaBH}_4$  in 500  $\mu\text{l}$  of water was added. The stirring was continued under dark conditions for 3 to 5 hours. During the course of the reaction, the dark brown color of the solution changed to orange. After completion of the reaction, the mixture was centrifuged and the supernatant was discarded. The precipitate consisting of the  $\text{Ag}_{29}$  cluster was washed repeatedly with methanol. The sample was dissolved in DMF and again centrifuged to remove any further insoluble contaminants. The supernatant was vacuum dried, and the purified clusters ( $[^{107}\text{Ag}_{29}(\text{BDT})_{12}(\text{TPP})_4]^{3-}$  /  $[^{109}\text{Ag}_{29}(\text{BDT})_{12}(\text{TPP})_4]^{3-}$ ) were obtained in powder form.

#### Synthesis of isotopically pure $[^{107}\text{Ag}_{24}\text{Au}(\text{DMBT})_{18}]^{-}$ and $[^{109}\text{Ag}_{24}\text{Au}(\text{DMBT})_{18}]^{-}$ clusters

Isotopically pure  $[^{107}\text{Ag}_{25}(\text{DMBT})_{18}]^{-}$  and  $[^{109}\text{Ag}_{25}(\text{DMBT})_{18}]^{-}$  clusters were used as the precursor to which  $\text{Au}^{+}$  was added in a controlled manner such that galvanic replacement of a Ag atom with Au resulted in the formation of  $[^{107}\text{Ag}_{24}\text{Au}(\text{DMBT})_{18}]^{-}$  and  $[^{109}\text{Ag}_{24}\text{Au}(\text{DMBT})_{18}]^{-}$  clusters (13), respectively.

#### Reaction of the isotopically pure clusters

In each case, stock solutions of parent isotopically pure clusters were prepared at a concentration of  $1.5 \times 10^{-3}$  mM. Then, they were mixed in different molar ratios, and their reaction was monitored by ESI MS.

#### Instrumentation

The optical absorption spectra were measured in PerkinElmer Lambda 25 ultraviolet-visible spectrophotometer. All the mass spectrometric measurements were done in a Waters SYNAPT G2-Si instrument. The instrument is well equipped with ESI, and all spectra were measured in the negative ion and resolution mode. The instrument is capable of measuring ESI MS with high-resolution touching orders of 50,000 ( $m/\Delta m$ ). The instrument was calibrated using NaI. An optimized condition involving a capillary voltage of 3 kV, a cone voltage of 20 V, a desolvation gas flow of 400 liters/hour, a source temperature of 100°C, a desolvation temperature of 150°C, and a sample infusion rate of 30  $\mu\text{l}$ /hour was used for all measurements. For low-temperature measurements, the source and desolvation temperatures were lowered to 30°C, and the sample was infused by an external syringe, which was also cooled at  $-20^\circ\text{C}$ .

#### Computational methods

##### Free-energy calculations

The exchange effect of silver isotopes ( $^{107}\text{Ag}$  and  $^{109}\text{Ag}$ ) was computationally studied in  $[\text{Ag}_{25}(\text{DMBT})_{18}]^{-}$  and  $[\text{Ag}_{29}(\text{BDT})_{12}(\text{PPh}_3)_4]^{3-}$  clusters by calculating free energy and thermochemistry parameters such as ZPE, enthalpy (H), and entropy (S) using density functional theory (DFT), as implemented in real-space grid-based projector

augmented wave (PAW) package (22). The PAW setup  $\text{Ag}(4d^{10}5s^1)$ ,  $\text{S}(3s^23p^4)$ ,  $\text{P}(3s^23p^3)$ ,  $\text{C}(2s^22p^2)$ , and  $\text{H}(1s^1)$  was considered to include only the valence electronic structure for the constituent atoms including the scalar-relativistic effects for Ag. Further, a reduced model was used considering  $-\text{CH}_3$  instead of the benzene rings in DMBT, BDT, and TPP ligands to reduce the high computational time of frequency calculations. The real-space calculation in finite difference mode, along with Perdew-Burke-Ernzerhof (PBE) functional, was applied for the geometry optimizations with a grid spacing of 0.2 Å, and the minimization criterion was the residual forces of 0.05 eV/Å, without considering any symmetry constraints. The atomic masses of Ag isotopes were taken as 106.905 and 108.905 for  $^{107}\text{Ag}$  and  $^{109}\text{Ag}$ , respectively. The vibrational modes were calculated only for Ag, S, and P atoms using the finite difference approximation of the Hessian matrix by considering the two displacements ( $+\Delta$  and  $-\Delta$ ) per atom in each Cartesian coordinate. Further, the calculated vibrational energies were used to calculate the thermodynamic quantities like H, S, and Gibbs free energy (G).

The calculation of G is made in the ideal gas approximation. It includes the electronic energy ( $E_{\text{pot}}$ ), ZPE ( $E_{\text{ZPE}}$ ), translational, rotational, and vibrational components of H and S, which are based on DFT calculations. An additional entropy of mixing component was calculated separately from statistical mechanics.

Enthalpy (H) is calculated within the atomistic simulation environment as

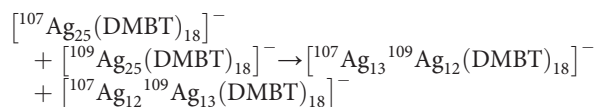
$$H = E_{\text{pot}} + E_{\text{ZPE}} + C_{\text{v,trans}} + C_{\text{v,rot}} + C_{\text{v,vib}}, \text{ and entropy is } S = S_{\text{trans}} + S_{\text{rot}} + S_{\text{elec}} + S_{\text{vib}}$$

Hence, the Gibbs free energy at temperature  $T$  and pressure  $P$  is calculated as

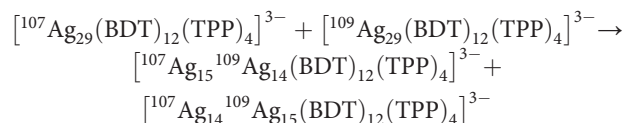
$$G = H - T^*S$$

The structural isomers of each isotopically substituted cluster arising from the different possible ways of arranging  $n$  Ag isotopic substituent atoms among the total number of Ag atoms are all degenerate as far as their total electronic energy is concerned, with a small difference of only 0.01 eV for both  $\text{Ag}_{29}$  and  $\text{Ag}_{25}$  in the value of G of the parent and isotopic substituent clusters, in terms of their enthalpic and the vibrational entropic components (see table S2).

We may write the reaction equations for the 1:1 ratio of mixing as follows, and in doing so, we assume that both products,  $(m,n) = (12,13)$  and  $(13,12)$  for  $\text{Ag}_{25}$  and  $(m,n) = (14,15)$  and  $(15,14)$  for  $\text{Ag}_{29}$ , are equally likely to form.



For the case of  $[\text{Ag}_{29}(\text{BDT})_{12}(\text{TPP})_4]^{3-}$



For  $(m,n) = (12,13)$ ,  $(13,12)$  in  $[\text{Ag}_{25}(\text{DMBT})_{18}]^{-}$  and  $(m,n) = (14,15)$ ,  $(15,14)$  in  $[\text{Ag}_{29}(\text{BDT})_{12}(\text{TPP})_4]^{3-}$  substituent cases (1:1 molar ratio), we have computed the reaction molar Gibbs free energy ( $\Delta G_{\text{react}}$ ) at standard temperature (298 K) and pressure (1 atm). The reaction free

energies ( $\Delta G_{\text{react}}$ ) are zero for both  $\text{Ag}_{29}$  and  $\text{Ag}_{25}$  clusters (see table S2), and the overall free energy of reaction is given by

$$\Delta G = \Delta G_{\text{react}} + \Delta G_{\text{mix}} = G(\text{products}) - G(\text{reactants}) + \Delta G_{\text{mix}}$$

For  $[\text{Ag}_{25}(\text{DMBT})_{18}]^-$ ,

$$G(\text{products}) = G \text{ of } {}^{107}\text{Ag}^{109}\text{Ag}(12, 13) + G \text{ of } {}^{107}\text{Ag}^{109}\text{Ag}(13, 12)$$

$$G(\text{reactants}) = G \text{ of parent } {}^{107}\text{Ag}_{25} + G \text{ of parent } {}^{109}\text{Ag}_{25}$$

and similarly for  $\text{Ag}_{29}$ .

The expression for mixing or configurational entropy is simply that of mixing two different ideal gases, which is known from statistical mechanics, and is given by

$$\Delta S_{\text{mix}} = -n_{\text{mol}} R [p \ln p + (1 - p) \ln (1 - p)]$$

where  $p$  is the mole fraction of  ${}^{107}\text{Ag}$ ,  $(1 - p)$  is the mole fraction of  ${}^{109}\text{Ag}$ , and  $n_{\text{mol}}$  is the total number of moles of the mixture (17). We note that the mixing entropy is independent of the cluster size and only depends on the mixing ratio; hence, we expect the half-and-half-mixture to have the largest mixing free energy. For the 1:1 mixture, we have  $p = 0.5$ , and hence,  $\Delta S_{\text{mix}}$  is  $R \ln 2$  ( $n_{\text{mol}} = 1$ ) and  $\Delta G_{\text{mix}} = -T \Delta S_{\text{mix}} = -RT \ln 2$ , where  $R$  is the gas constant in joules per mole and  $n_{\text{mol}} = 1$ . This analysis reveals that the entropy of isotopic mixing is the largest and most significant contribution to the Gibbs free energy. Because of the fractional mixing ratio, the mixing entropy is always positive, and therefore,  $\Delta G_{\text{mix}}$  is always negative and is larger than the other terms in the free energy. Hence,  $\Delta G_{\text{mix}}$ , being the largest contribution to the overall reaction, causes  $\Delta G$  to be always negative, which makes the reaction spontaneous.

The mixing ratio  $x = 0.5$  corresponds to the nearest integer numbers of exchanged Ag atoms to half of the total number of Ag atoms in the cluster, because both clusters have an odd number of Ag atoms, for example,  $(25/2) = 12.5$ , hence, (13,12) or (12,13), where these compositions both have the identical maximum degeneracy in arrangements as a function of the number of substituents  $n$  in the  $\text{Ag}_{25}$  cluster. Similarly, for the  $\text{Ag}_{29}$  cluster,  $(29/2) = 14.5$  and, hence, (14,15) or (15,14) are the most entropically favorable compositions in  $\text{Ag}_{29}$ .

### Molecular docking

To understand the intermolecular interactions in  $[\text{Ag}_{25}(\text{SR})_{18}]^-$  clusters, molecular docking studies were performed using AutoDock4.2 and its associated tools (23). DFT-optimized geometry and partial charges of  $[\text{Ag}_{25}(\text{SR})_{18}]^-$  were used for this study. We used  $[\text{Ag}_{25}(\text{SR})_{18}]^-$  as both “ligand” and “receptor.” Receptor grids were generated using  $126 \times 126 \times 126$  grid points in  $xyz$ , with a grid spacing of 0.375 Å, and map types were created using AutoGrid-4.2. The grid parameter file (.gpf) was saved using MGL Tools-1.4.6.50. The docking parameter files (.dpf) were generated using MGLTools-1.4.6.50. The results of AutoDock generated an output file (.dlg), and the generated conformers were scored and ranked as per the interaction energy. Ten lowest-energy conformers were obtained. We used the Lamarckian genetic algorithm for the output file using MGLTools-1.4.6. The binding free energy of the FFGMG of the dimeric cluster adduct was  $-23.7$  kcal/mol. Similar study was done with  $[\text{Ag}_{29}(\text{S}_2\text{R})_{12}(\text{TPP})_4]^{3-}$  clusters, where  $[\text{Ag}_{29}(\text{S}_2\text{R})_{12}(\text{TPP})_4]^{3-}$  was used as both ligand and receptor. In this case, the binding free energy of FFGMG of the dimeric adduct was  $-7.8$  kcal/mol.

### Calculation of theoretical isotope patterns with varying composition of ${}^{107}\text{Ag}/{}^{109}\text{Ag}$

We calculated the theoretical isotope patterns of  $[\text{Ag}_{25}(\text{DMBT})_{18}]^-$  and  $[\text{Ag}_{29}(\text{BDT})_{12}(\text{TPP})_4]^{3-}$  by varying the abundance of each isotope ( ${}^{107}\text{Ag}/{}^{109}\text{Ag}$ ) in them by 1% change so that the composition is  $(x,y)$ , that is,  $\{(100,0), (99,1), (98,2), \dots, (0,100)\}$ , where  $x$  and  $y$  are the abundance of  ${}^{107}\text{Ag}$  and  ${}^{109}\text{Ag}$ , respectively. The experimental spectra were compared with the calculated spectra to find the best match and hence confirm the composition.

### Details of fitting the kinetic data

The triexponential fitting in Fig. 3 was performed using the Origin 8.5 software package. The equation  $y = k_1 \exp(-t^*a) + k_2 \exp(-t^*b) + k_3 \exp(-t^*c)$  was used for the triexponential fits. The parameters  $k_1$ ,  $k_2$ ,  $k_3$ ,  $a$ ,  $b$ , and  $c$  were varied during the fitting, and  $t$  was used as the independent variable. Both monoexponential and biexponential fits were inadequate, and only a triexponential fit could successfully fit the data points.

### SUPPLEMENTARY MATERIALS

Supplementary material for this article is available at <http://advances.sciencemag.org/cgi/content/full/5/1/eaau7555/DC1>

Fig. S1. Characterization of isotopically pure  $[\text{Ag}_{25}(\text{DMBT})_{18}]^-$  and  $[\text{Ag}_{25}(\text{DMBT})_{18}]^-$  clusters.

Fig. S2. Isotope patterns of the product obtained by reaction of  $[\text{Ag}_{25}(\text{DMBT})_{18}]^-$  and  $[\text{Ag}_{25}(\text{DMBT})_{18}]^-$  at 1:1 molar ratio.

Fig. S3. ESI MS of reaction product obtained by mixing the two isotopic  $[\text{Ag}_{25}(\text{DMBT})_{18}]^-$  and  $[\text{Ag}_{25}(\text{DMBT})_{18}]^-$  clusters at various molar ratios.

Fig. S4. Comparison of the experimental and calculated isotope patterns of the products obtained by mixing  $[\text{Ag}_{25}(\text{DMBT})_{18}]^-$  and  $[\text{Ag}_{25}(\text{DMBT})_{18}]^-$  at various molar ratios.

Fig. S5. Isotope exchange in  $[\text{Ag}_{24}\text{Au}(\text{DMBT})_{18}]^-$  clusters.

Fig. S6. Characterization of isotopically pure  $[\text{Ag}_{29}(\text{BDT})_{12}(\text{TPP})_4]^{3-}$  and  $[\text{Ag}_{29}(\text{BDT})_{12}(\text{TPP})_4]^{3-}$  clusters.

Fig. S7. Reaction between  $[\text{Ag}_{29}(\text{BDT})_{12}(\text{TPP})_4]^{3-}$  and  $[\text{Ag}_{29}(\text{BDT})_{12}(\text{TPP})_4]^{3-}$  clusters in 1:1 molar ratio at room temperature.

Fig. S8. ESI MS of reaction product obtained by mixing the two isotopic  $[\text{Ag}_{29}(\text{BDT})_{12}(\text{TPP})_4]^{3-}$  and  $[\text{Ag}_{29}(\text{BDT})_{12}(\text{TPP})_4]^{3-}$  clusters at various molar ratios.

Fig. S9. Time-dependent study of reaction between  $[\text{Ag}_{29}(\text{BDT})_{12}(\text{TPP})_4]^{3-}$  and  $[\text{Ag}_{29}(\text{BDT})_{12}(\text{TPP})_4]^{3-}$  in 1:1 molar ratio at various temperatures.

Fig. S10. Kinetic study of isotopic exchange at different concentrations of  $[\text{Ag}_{29}(\text{BDT})_{12}(\text{TPP})_4]^{3-}$  clusters.

Fig. S11. Kinetic study of isotopic exchange in  $[\text{Ag}_{29}(\text{BDT})_{12}(\text{TPP})_4]^{3-}$  clusters at different molar ratios of mixing.

Fig. S12. Time-dependent study of reaction between  $[\text{Ag}_{29}(\text{BDT})_{12}(\text{TPP})_4]^{3-}$  and  $[\text{Ag}_{29}(\text{BDT})_{12}(\text{TPP})_4]^{3-}$  at various molar ratios.

Fig. S13. Molecular docking studies.

Table S1. Abundance of  ${}^{107}\text{Ag}$  in product =  $\{x/(x + y)\} \times 100$  and  ${}^{109}\text{Ag}$  in product =  $\{y/(x + y)\} \times 100$ .

Table S2. Table showing ZPE and Gibbs free energy ( $G$ ) values of the isotopic clusters.

### REFERENCES AND NOTES

1. H. C. Urey, F. G. Brickwedde, G. M. Murphy, A hydrogen isotope of mass 2. *Phys. Rev.* **39**, 164–165 (1932).
2. G. N. Lewis, R. T. Macdonald, Concentration of  $\text{H}^2$  isotope. *J. Chem. Phys.* **1**, 341–344 (1933).
3. A. Thibblin, P. Ahlberg, Reaction branching and extreme kinetic isotope effects in the study of reaction mechanisms. *Chem. Soc. Rev.* **18**, 209–224 (1989).
4. J. W. Pyper, R. S. Newbury, G. W. Barton Jr., Study of the isotopic disproportionation reaction between light and heavy water using a pulsed-molecular-beam mass spectrometer. *J. Chem. Phys.* **46**, 2253–2257 (1967).
5. S.-C. Park, K.-H. Jung, H. Kang, H/D isotopic exchange between water molecules at ice surfaces. *J. Chem. Phys.* **121**, 2765–2774 (2004).
6. L. Konermann, J. Pan, Y.-H. Liu, Hydrogen exchange mass spectrometry for studying protein structure and dynamics. *Chem. Soc. Rev.* **40**, 1224–1234 (2011).
7. G. Pratt, D. Rogers, Homogeneous isotope exchange reactions.  $\text{H}_2/\text{D}_2$ . *J. Chem. Soc. Faraday Trans. 1* **72**, 1589–1600 (1976).

8. I. Chakraborty, T. Pradeep, Atomically precise clusters of noble metals: Emerging link between atoms and nanoparticles. *Chem. Rev.* **117**, 8208–8271 (2017).
9. R. Jin, C. Zeng, M. Zhou, Y. Chen, Atomically precise colloidal metal nanoclusters and nanoparticles: Fundamentals and opportunities. *Chem. Rev.* **116**, 10346–10413 (2016).
10. C. P. Joshi, M. S. Bootharaju, M. J. Alhilaly, O. M. Bakr,  $[\text{Ag}_{25}(\text{SR})_{18}]^-$ : The “Golden” silver nanoparticle. *J. Am. Chem. Soc.* **137**, 11578–11581 (2015).
11. L. G. AbdulHalim, M. S. Bootharaju, Q. Tang, S. Del Gobbo, R. G. AbdulHalim, M. Eddaoudi, D.-E. Jiang, O. M. Bakr,  $\text{Ag}_{25}(\text{BDT})_{12}(\text{TPP})_4$ : A tetravalent nanocluster. *J. Am. Chem. Soc.* **137**, 11970–11975 (2015).
12. M. Zhu, C. M. Aikens, F. J. Hollander, G. C. Schatz, R. Jin, Correlating the crystal structure of a thiol-protected  $\text{Au}_{25}$  cluster and optical properties. *J. Am. Chem. Soc.* **130**, 5883–5885 (2008).
13. M. W. Heaven, A. Dass, P. S. White, K. M. Holt, R. W. Murray, Crystal structure of the gold nanoparticle  $[\text{N}(\text{C}_8\text{H}_{17})_4][\text{Au}_{25}(\text{SCH}_2\text{CH}_2\text{Ph})_{18}]$ . *J. Am. Chem. Soc.* **130**, 3754–3755 (2008).
14. M. S. Bootharaju, C. P. Joshi, M. R. Parida, O. F. Mohammed, O. M. Bakr, Templated atom-precise galvanic synthesis and structure elucidation of a  $[\text{Ag}_{24}\text{Au}(\text{SR})_{18}]^-$  nanocluster. *Angew. Chem. Int. Ed.* **55**, 922–926 (2016).
15. X. Lou, R. P. M. Lafleur, C. M. A. Leenders, S. M. C. Schoenmakers, N. M. Matsumoto, M. B. Baker, J. L. J. van Dongen, A. R. A. Palmans, E. W. Meijer, Dynamic diversity of synthetic supramolecular polymers in water as revealed by hydrogen/deuterium exchange. *Nat. Commun.* **8**, 15420 (2017).
16. K. R. Krishnadas, A. Baksi, A. Ghosh, G. Natarajan, T. Pradeep, Structure-conserving spontaneous transformations between nanoparticles. *Nat. Commun.* **7**, 13447 (2016).
17. G. Natarajan, A. Mathew, Y. Negishi, R. L. Whetten, T. Pradeep, A unified framework for understanding the structure and modifications of atomically precise monolayer protected gold clusters. *J. Phys. Chem. C* **119**, 27768–27785 (2015).
18. C. Zeng, Y. Chen, K. Kirschbaum, K. J. Lambright, R. Jin, Emergence of hierarchical structural complexities in nanoparticles and their assembly. *Science* **354**, 1580–1584 (2016).
19. A. Nag, P. Chakraborty, M. Bodiuzzaman, T. Ahuja, S. Antharjanam, T. Pradeep, Polymorphism of  $\text{Ag}_{29}(\text{BDT})_{12}(\text{TPP})_4^{3-}$  cluster: Interactions of secondary ligands and their effect on solid state luminescence. *Nanoscale* **10**, 9851–9855 (2018).
20. P. Atkins, J. De Paula, *Atkins’ Physical Chemistry* (Oxford Univ. Press, 2006).
21. J. D. Bernal, G. Tamm, Zero point energy and physical properties of  $\text{H}_2\text{O}$  and  $\text{D}_2\text{O}$ . *Nature* **135**, 229–230 (1935).
22. J. J. Mortensen, L. B. Hansen, K. W. Jacobsen, Real-space grid implementation of the projector augmented wave method. *Phys. Rev. B* **71**, 035109 (2005).
23. G. M. Morris, R. Huey, W. Lindstrom, M. F. Sanner, R. K. Belew, D. S. Goodsell, A. J. Olson, AutoDock4 and AutoDockTools4: Automated docking with selective receptor flexibility. *J. Comput. Chem.* **30**, 2785–2791 (2009).

**Acknowledgments:** P.C. thanks the Council of Scientific and Industrial Research (CSIR) for a research fellowship. A.N. thanks IIT Madras for an Institute Doctoral fellowship. G.P. thanks IIT Madras for an Institute Postdoctoral fellowship. We thank the Department of Science and Technology (DST), Government of India for continuous support of our research program. We thank D. Frenkel, University of Cambridge, UK, for useful discussions on the computational part of the work. **Funding:** This work was supported by the Council of Scientific and Industrial Research (CSIR), Indian Institute of Technology Madras and Department of Science and Technology (DST), Government of India. **Author contributions:** P.C. carried out the synthesis and designed and conducted the experiments. P.C. and A.N. carried out the ESI MS measurements. A.N. carried out the molecular docking studies. G.N. and G.P. carried out the DFT calculations. N.B. participated in the experiments. M.K.P. calculated the theoretical mass spectral distributions. G.N. and J.C. supervised the computational part. T.P. proposed the project and supervised the progress. The manuscript was written through contributions of all the authors. **Competing interests:** P.C., A.N., G.N., G.P., and T.P. are inventors of an Indian patent application related to this work (no. 201741037349, filed on 23 October 2017). The other authors declare that they have no competing interests. **Data and materials availability:** All data needed to evaluate the conclusions in the paper are present in the paper and/or the Supplementary Materials. Additional data related to this paper may be requested from the authors.

Submitted 12 July 2018  
 Accepted 27 November 2018  
 Published 2 January 2019  
 10.1126/sciadv.aau7555

**Citation:** P. Chakraborty, A. Nag, G. Natarajan, N. Bandyopadhyay, G. Paramasivam, M. K. Panwar, J. Chakrabarti, T. Pradeep, Rapid isotopic exchange in nanoparticles. *Sci. Adv.* **5**, eaau7555 (2019).



## Rapid isotopic exchange in nanoparticles

Papri Chakraborty, Abhijit Nag, Ganapati Natarajan, Nayanika Bandyopadhyay, Ganesan Paramasivam, Manoj Kumar Panwar, Jaydeb Chakrabarti and Thalappil Pradeep

*Sci Adv* **5** (1), eaau7555.  
DOI: 10.1126/sciadv.aau7555

### ARTICLE TOOLS

<http://advances.sciencemag.org/content/5/1/eaau7555>

### SUPPLEMENTARY MATERIALS

<http://advances.sciencemag.org/content/suppl/2018/12/21/5.1.eaau7555.DC1>

### REFERENCES

This article cites 22 articles, 1 of which you can access for free  
<http://advances.sciencemag.org/content/5/1/eaau7555#BIBL>

### PERMISSIONS

<http://www.sciencemag.org/help/reprints-and-permissions>

Use of this article is subject to the [Terms of Service](#)

---

*Science Advances* (ISSN 2375-2548) is published by the American Association for the Advancement of Science, 1200 New York Avenue NW, Washington, DC 20005. 2017 © The Authors, some rights reserved; exclusive licensee American Association for the Advancement of Science. No claim to original U.S. Government Works. The title *Science Advances* is a registered trademark of AAAS.



## Supplementary Materials for

### Rapid isotopic exchange in nanoparticles

Papri Chakraborty, Abhijit Nag, Ganapati Natarajan, Nayanika Bandyopadhyay, Ganesan Paramasivam, Manoj Kumar Panwar, Jaydeb Chakrabarti, Thalappil Pradeep\*

\*Corresponding author. Email: pradeep@iitm.ac.in

Published 4 January 2019, *Sci. Adv.* **5**, eaau7555 (2019)  
DOI: 10.1126/sciadv.aau7555

#### This PDF file includes:

Fig. S1. Characterization of isotopically pure  $[^{107}\text{Ag}_{25}(\text{DMBT})_{18}]^-$  and  $[^{109}\text{Ag}_{25}(\text{DMBT})_{18}]^-$  clusters.

Fig. S2. Isotope patterns of the product obtained by reaction of  $[^{107}\text{Ag}_{25}(\text{DMBT})_{18}]^-$  and  $[^{109}\text{Ag}_{25}(\text{DMBT})_{18}]^-$  at 1:1 molar ratio.

Fig. S3. ESI MS of reaction product obtained by mixing the two isotopic  $[^{107}\text{Ag}_{25}(\text{DMBT})_{18}]^-$  and  $[^{109}\text{Ag}_{25}(\text{DMBT})_{18}]^-$  clusters at various molar ratios.

Fig. S4. Comparison of the experimental and calculated isotope patterns of the products obtained by mixing  $[^{107}\text{Ag}_{25}(\text{DMBT})_{18}]^-$  and  $[^{109}\text{Ag}_{25}(\text{DMBT})_{18}]^-$  at various molar ratios.

Fig. S5. Isotope exchange in  $[\text{Ag}_{24}\text{Au}(\text{DMBT})_{18}]^-$  clusters.

Fig. S6. Characterization of isotopically pure  $[^{107}\text{Ag}_{29}(\text{BDT})_{12}(\text{TPP})_4]^{3-}$  and  $[^{109}\text{Ag}_{29}(\text{BDT})_{12}(\text{TPP})_4]^{3-}$  clusters.

Fig. S7. Reaction between  $[^{107}\text{Ag}_{29}(\text{BDT})_{12}(\text{TPP})_4]^{3-}$  and  $[^{109}\text{Ag}_{29}(\text{BDT})_{12}(\text{TPP})_4]^{3-}$  clusters in 1:1 molar ratio at room temperature.

Fig. S8. ESI MS of reaction product obtained by mixing the two isotopic  $[^{107}\text{Ag}_{29}(\text{BDT})_{12}(\text{TPP})_4]^{3-}$  and  $[^{109}\text{Ag}_{29}(\text{BDT})_{12}(\text{TPP})_4]^{3-}$  clusters at various molar ratios.

Fig. S9. Time-dependent study of reaction between  $[^{107}\text{Ag}_{29}(\text{BDT})_{12}(\text{TPP})_4]^{3-}$  and  $[^{109}\text{Ag}_{29}(\text{BDT})_{12}(\text{TPP})_4]^{3-}$  in 1:1 molar ratio at various temperatures.

Fig. S10. Kinetic study of isotopic exchange at different concentrations of  $[\text{Ag}_{29}(\text{BDT})_{12}(\text{TPP})_4]^{3-}$  clusters.

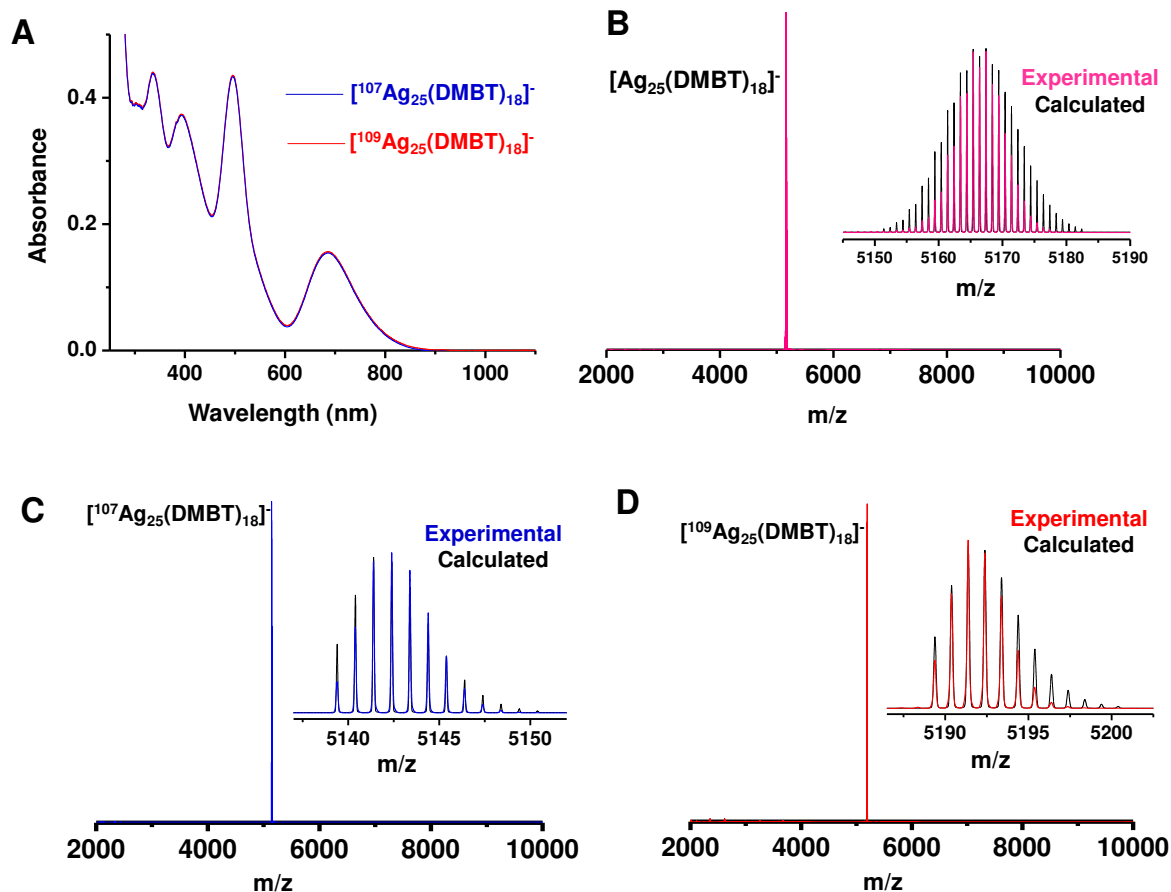
Fig. S11. Kinetic study of isotopic exchange in  $[\text{Ag}_{29}(\text{BDT})_{12}(\text{TPP})_4]^{3-}$  clusters at different molar ratios of mixing.

Fig. S12. Time-dependent study of reaction between  $[^{107}\text{Ag}_{29}(\text{BDT})_{12}(\text{TPP})_4]^{3-}$  and  $[^{109}\text{Ag}_{29}(\text{BDT})_{12}(\text{TPP})_4]^{3-}$  at various molar ratios.

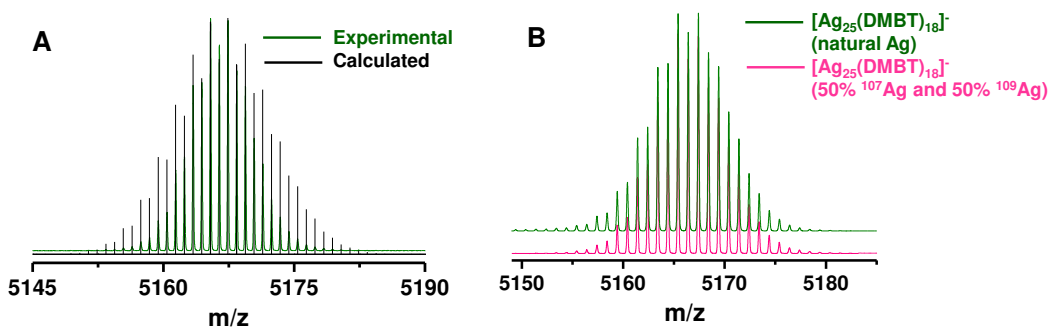
Fig. S13. Molecular docking studies.

Table S1. Abundance of  $^{107}\text{Ag}$  in product =  $\{x/(x+y)\} \times 100$  and  $^{109}\text{Ag}$  in product =  $\{y/(x+y)\} \times 100$ .

Table S2. Table showing ZPE and Gibbs free energy ( $G$ ) values of the isotopic clusters.



**Fig. S1. Characterization of isotopically pure  $[^{107}\text{Ag}_{25}(\text{DMBT})_{18}]^-$  and  $[^{109}\text{Ag}_{25}(\text{DMBT})_{18}]^-$  clusters.** (A) UV-vis spectra of  $[^{107}\text{Ag}_{25}(\text{DMBT})_{18}]^-$  and  $[^{109}\text{Ag}_{25}(\text{DMBT})_{18}]^-$  clusters showing identical features. ESI MS of (B)  $[\text{Ag}_{25}(\text{DMBT})_{18}]^-$  made from natural Ag, (C)  $[^{107}\text{Ag}_{25}(\text{DMBT})_{18}]^-$  and (D)  $[^{109}\text{Ag}_{25}(\text{DMBT})_{18}]^-$ . Insets show the comparison of the experimental and calculated isotope patterns of the peaks. The minor differences in the experimental spectra (in C and D) in comparison to the calculated spectra are due to the slight contribution of the other isotope in each sample as the isotope enrichment was 98%.



**Fig. S2. Isotope patterns of the product obtained by reaction of  $[^{107}\text{Ag}_{25}(\text{DMBT})_{18}]^-$  and  $[^{109}\text{Ag}_{25}(\text{DMBT})_{18}]^-$  at 1:1 molar ratio.** Experimental isotope distribution of the product obtained by mixing  $[^{107}\text{Ag}_{25}(\text{DMBT})_{18}]^-$  and  $[^{109}\text{Ag}_{25}(\text{DMBT})_{18}]^-$  at 1:1 molar ratio. The isotope pattern is compared with (A) the distribution computed considering 50% abundance of each isotope in  $[\text{Ag}_{25}(\text{DMBT})_{18}]^-$  and (B) experimental isotope patterns of  $[\text{Ag}_{25}(\text{DMBT})_{18}]^-$  synthesized from natural Ag.

**N.B.** In this case, the overall isotope distribution has contribution from the isotopes of the metal Ag and also C, H and S in the ligands. For the two parent clusters (Fig. 1 and S1) which are isotopically pure there is only one isotope of Ag. However, the product, which is a 1:1 mixture of the two isotopic clusters, has an isotope abundance of  $^{107}\text{Ag}$ :  $\frac{1}{2}$  and  $^{109}\text{Ag}$ :  $\frac{1}{2}$  and the isotope pattern for Ag will follow the binomial distribution and as a result will be broader compared to the monoisotopic case. This contribution from the isotopic abundance of Ag will be reflected in the overall isotope distribution and thus the product distribution is obviously broader than the two parent clusters.

Moreover natural abundance of Ag is  $^{107}\text{Ag}$  (51.84%) and  $^{109}\text{Ag}$  (48.16%). Hence the ratio of their abundances is 1.08, i.e.  $\sim 1$ , hence product distribution is similar to the cluster made of naturally abundant Ag.

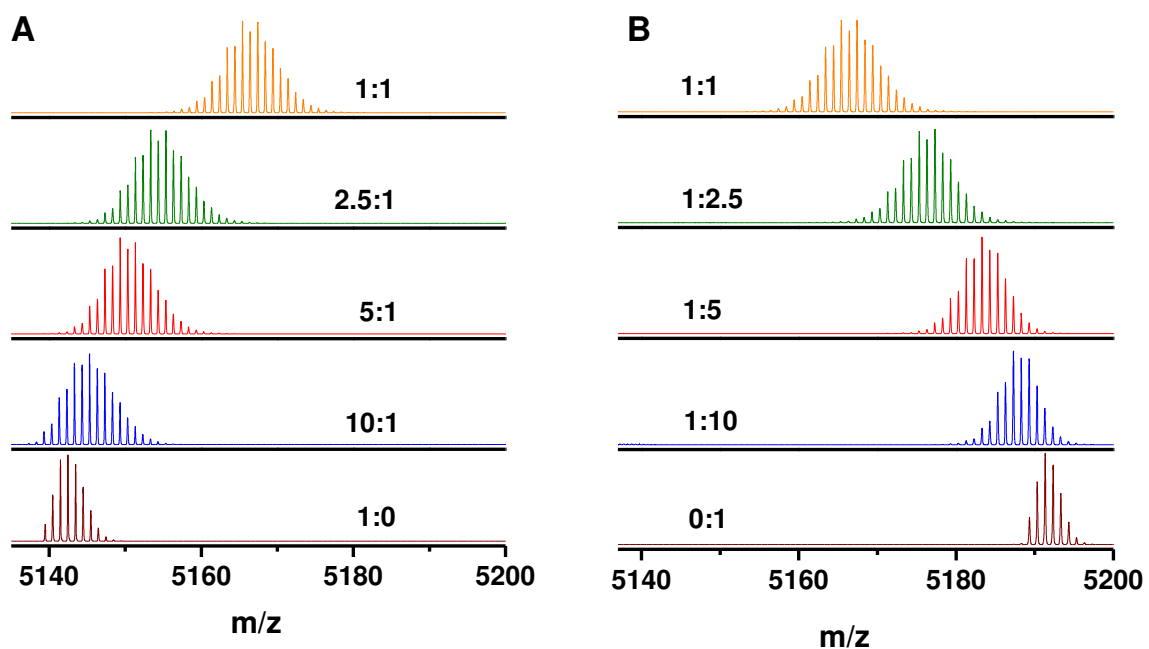


**Fig. S3. ESI MS of reaction product obtained by mixing the two isotopic  $^{107}\text{Ag}_{25}(\text{DMBT})_{18}^-$  and  $^{109}\text{Ag}_{25}(\text{DMBT})_{18}^-$  clusters at various molar ratios.** Product obtained by mixing  $^{107}\text{Ag}_{25}(\text{DMBT})_{18}^-$  and  $^{109}\text{Ag}_{25}(\text{DMBT})_{18}^-$  at varying molar ratios where in (A)  $^{107}\text{Ag}_{25}(\text{DMBT})_{18}^-$  cluster is kept in higher concentration and in (B)  $^{109}\text{Ag}_{25}(\text{DMBT})_{18}^-$  cluster is kept in higher concentration. The initial molar ratio of mixing the two clusters ( $^{107}\text{Ag}_{25}(\text{DMBT})_{18}^- : ^{109}\text{Ag}_{25}(\text{DMBT})_{18}^-$ ) is indicated for each product observed.

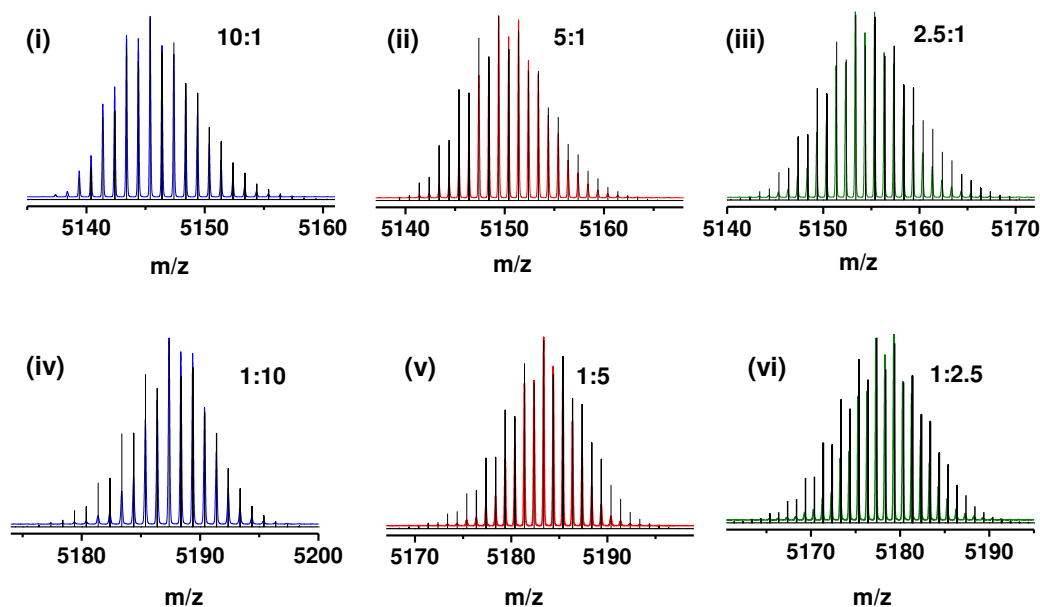


**Fig. S4. Comparison of the experimental and calculated isotope patterns of the products obtained by mixing  $[^{107}\text{Ag}_{25}(\text{DMBT})_{18}]^-$  and  $[^{109}\text{Ag}_{25}(\text{DMBT})_{18}]^-$  at various molar ratios.** Comparison of the experimental isotope patterns of the products obtained at different molar ratios of mixing the two isotopic clusters ( $[^{107}\text{Ag}_{25}(\text{DMBT})_{18}]^- : [^{109}\text{Ag}_{25}(\text{DMBT})_{18}]^-$ ) with the calculated patterns. The experimental patterns showed best match with the calculated patterns considering the abundances of each isotope in the cluster from their initial molar ratio of mixing.

Note. Molar ratio of mixing ( $[^{107}\text{Ag}_{25}(\text{DMBT})_{18}]^- : [^{109}\text{Ag}_{25}(\text{DMBT})_{18}]^-$ ) = x:y

**Table S1. Abundance of  $^{107}\text{Ag}$  in product =  $\{x/(x + y)\} \times 100$  and  $^{109}\text{Ag}$  in product =  $\{y/(x + y)\} \times 100$ .**

Sl. No.	x:y	Abundance ( $^{107}\text{Ag}$ : $^{109}\text{Ag}$ )	Sl. No.	x:y	Abundance ( $^{107}\text{Ag}$ : $^{109}\text{Ag}$ )
1	10:1	90.909:9.091	5	1:10	9.091:90.909
2	5:1	83.333:16.667	6	1:5	16.667:83.333
3	2.5:1	71.428:28.571	7	1:2.5	28.571:71.428
4	1:1	50:50	8	1:1	50:50

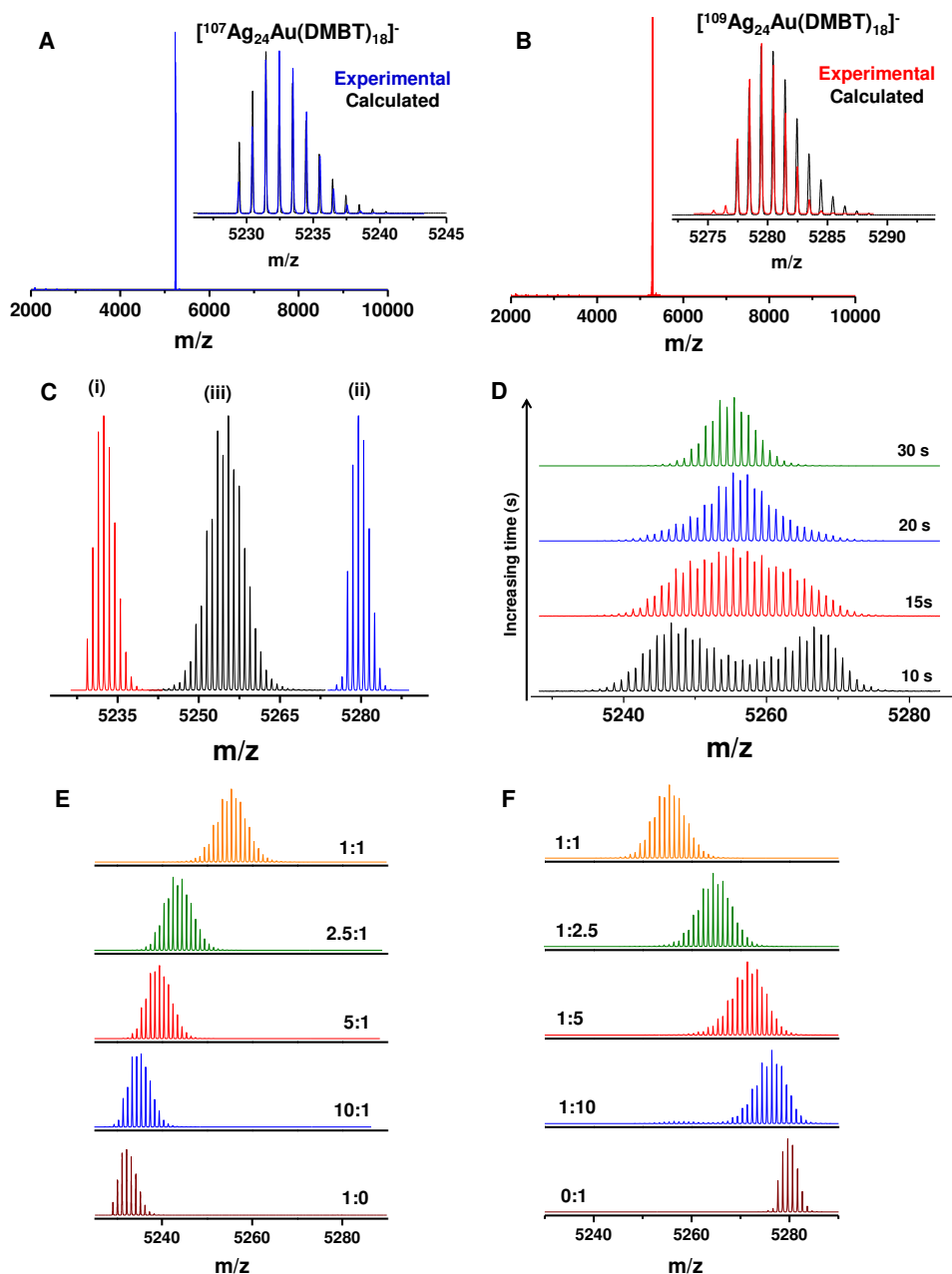


**Fig. S5. Isotope exchange in  $[\text{Ag}_{24}\text{Au}(\text{DMBT})_{18}]^-$  clusters.** ESI MS of (A)  $[\text{}^{107}\text{Ag}_{24}\text{Au}(\text{DMBT})_{18}]^-$  and (B)  $[\text{}^{109}\text{Ag}_{24}\text{Au}(\text{DMBT})_{18}]^-$ . Insets show the comparison of the experimental and calculated isotope patterns. (C) Reaction of  $[\text{}^{107}\text{Ag}_{24}\text{Au}(\text{DMBT})_{18}]^-$  and  $[\text{}^{109}\text{Ag}_{24}\text{Au}(\text{DMBT})_{18}]^-$  in 1:1 molar ratio at room temperature, where (i), (ii) and (iii) denotes ESI MS of  $[\text{}^{107}\text{Ag}_{24}\text{Au}(\text{DMBT})_{18}]^-$ ,  $[\text{}^{109}\text{Ag}_{24}\text{Au}(\text{DMBT})_{18}]^-$  and the product (50% abundance of each isotope), respectively. All the spectra are shown in the same scale. (D) Intermediates stages of reaction in 1:1 molar ratio at  $-20\text{ }^{\circ}\text{C}$ . (E) and (F) Reaction at various molar ratios,  $[\text{}^{107}\text{Ag}_{24}\text{Au}(\text{DMBT})_{18}]^- : [\text{}^{109}\text{Ag}_{24}\text{Au}(\text{DMBT})_{18}]^-$  ratio is indicated in the figure.

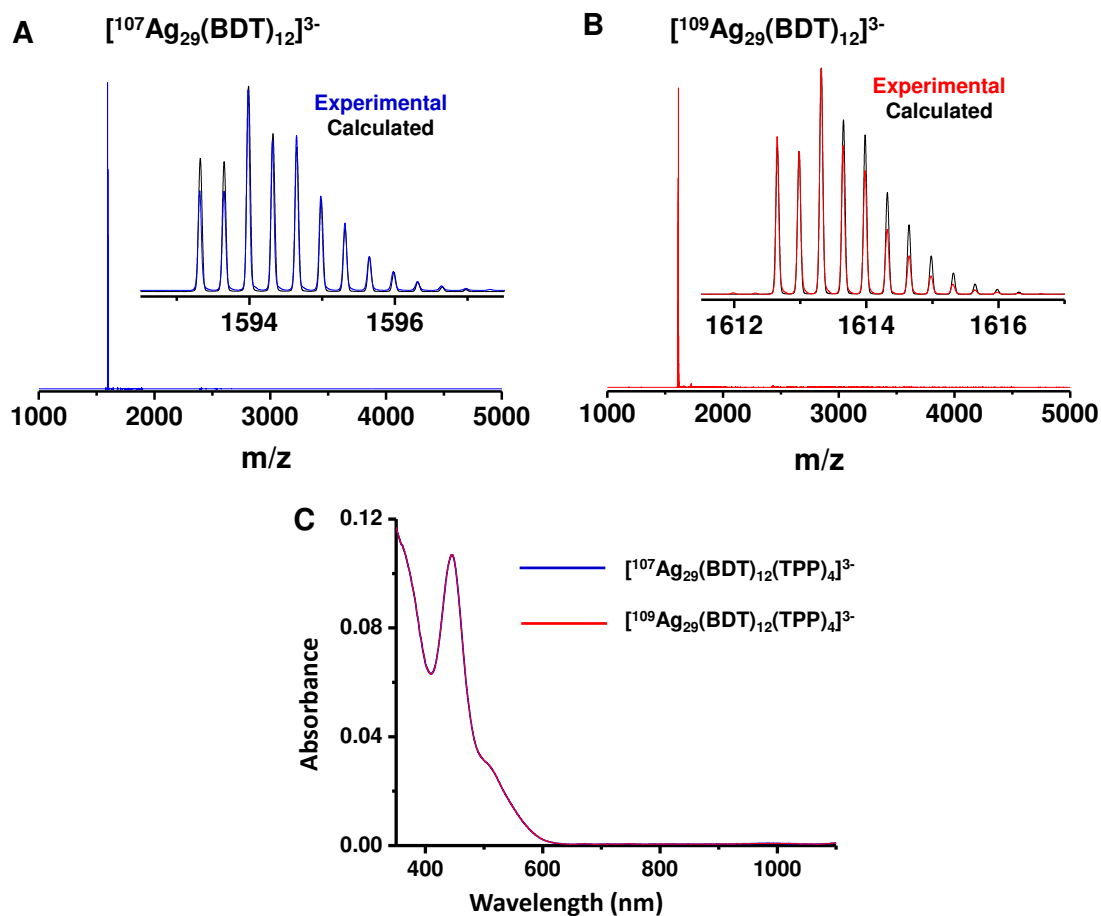


**Fig. S6. Characterization of isotopically pure  $[^{107}\text{Ag}_{29}(\text{BDT})_{12}(\text{TPP})_4]^{3-}$  and  $[^{109}\text{Ag}_{29}(\text{BDT})_{12}(\text{TPP})_4]^{3-}$  clusters.** ESI MS of (A)  $[^{107}\text{Ag}_{29}(\text{BDT})_{12}]^{3-}$  and (B)  $[^{109}\text{Ag}_{29}(\text{BDT})_{12}]^{3-}$  clusters. The labile TPP ligands were lost during ionization. Insets show the comparison of the experimental and calculated isotope patterns of the peaks. The minor differences in the experimental spectra in comparison to the calculated spectra are due to the slight contribution of the other isotope in each sample as the isotope enrichment was 98%. (C), UV-vis spectra of  $[^{107}\text{Ag}_{29}(\text{BDT})_{12}(\text{TPP})_4]^{3-}$  and  $[^{109}\text{Ag}_{29}(\text{BDT})_{12}(\text{TPP})_4]^{3-}$  clusters showing identical features.

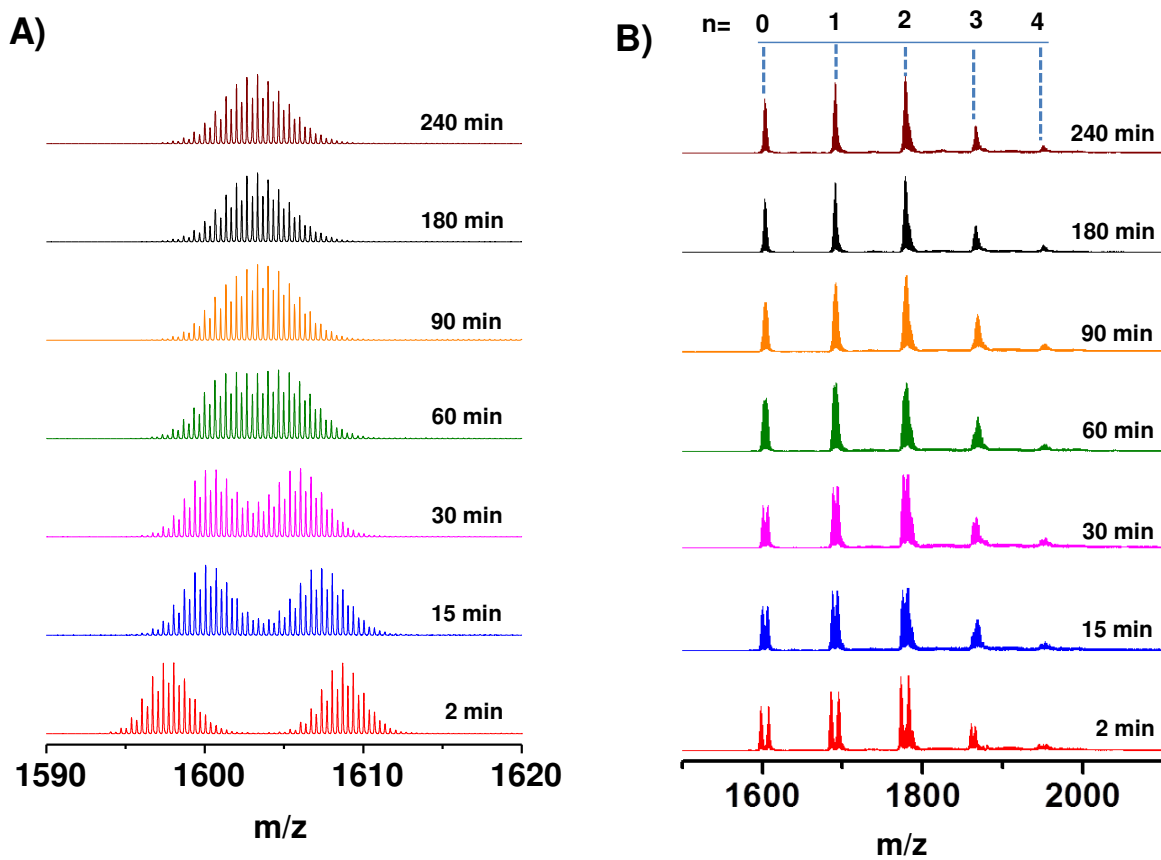


**Fig. S7. Reaction between  $[^{107}\text{Ag}_{29}(\text{BDT})_{12}(\text{TPP})_4]^{3-}$  and  $[^{109}\text{Ag}_{29}(\text{BDT})_{12}(\text{TPP})_4]^{3-}$  clusters in 1:1 molar ratio at room temperature.** (A) Intermediates stages of reaction between  $[^{107}\text{Ag}_{29}(\text{BDT})_{12}]^{3-}$  and  $[^{109}\text{Ag}_{29}(\text{BDT})_{12}]^{3-}$  in 1:1 molar ratio at room temperature. The mixture reaches equilibrium over a period of 2 h. (B) Intermediates stages of reaction between  $[^{107}\text{Ag}_{29}(\text{BDT})_{12}(\text{TPP})_n]^{3-}$  ( $n=0-4$ ) and  $[^{109}\text{Ag}_{29}(\text{BDT})_{12}(\text{TPP})_n]^{3-}$  ( $n=0-4$ ) in 1:1 molar ratio at room temperature, showing the intact TPP attached clusters in ESI MS. The mixture reaches equilibrium at similar time scales.



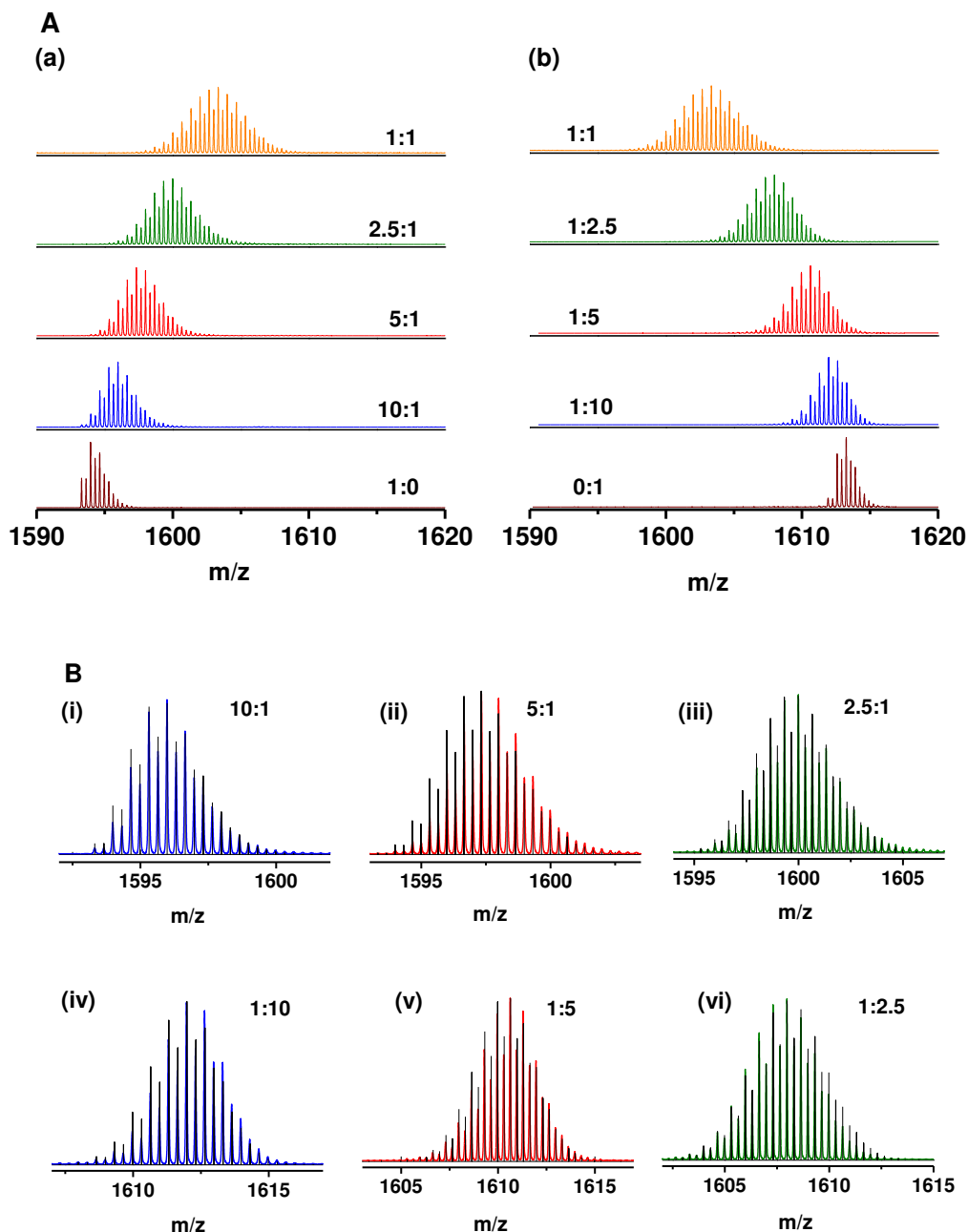


**Fig. S8. ESI MS of reaction product obtained by mixing the two isotopic  $[^{107}\text{Ag}_{29}(\text{BDT})_{12}(\text{TPP})_4]^{3-}$  and  $[^{109}\text{Ag}_{29}(\text{BDT})_{12}(\text{TPP})_4]^{3-}$  clusters at various molar ratios. (A)** Product obtained by mixing the two isotopic clusters  $[^{107}\text{Ag}_{29}(\text{BDT})_{12}]^{3-}$  and  $[^{109}\text{Ag}_{29}(\text{BDT})_{12}]^{3-}$  at varying molar ratios where in (a)  $[^{107}\text{Ag}_{29}(\text{BDT})_{12}]^{3-}$  is kept in higher concentration and in (b)  $[^{109}\text{Ag}_{29}(\text{BDT})_{12}]^{3-}$  is kept in higher concentration. The initial molar ratio of mixing the two clusters ( $[^{107}\text{Ag}_{29}(\text{BDT})_{12}]^{3-} : [^{109}\text{Ag}_{29}(\text{BDT})_{12}]^{3-}$ ) is indicated for each product observed. **(B)** Comparison of the experimental isotope patterns of the products with the calculated isotope patterns considering the abundances of each isotope from their initial molar ratio of mixing.

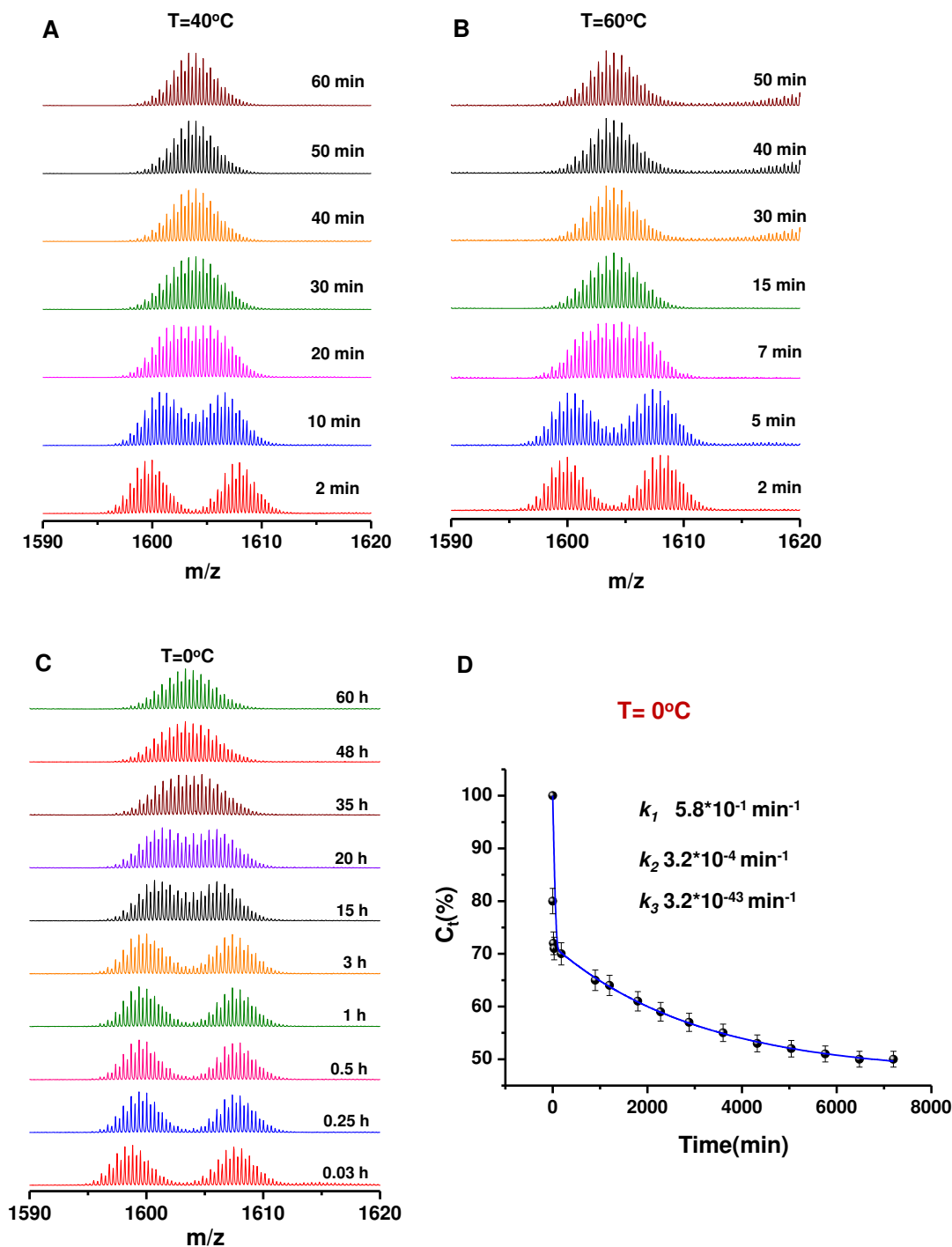


**Fig. S9. Time-dependent study of reaction between  $[\text{}^{107}\text{Ag}_{29}(\text{BDT})_{12}(\text{TPP})_4]^{3-}$  and  $[\text{}^{109}\text{Ag}_{29}(\text{BDT})_{12}(\text{TPP})_4]^{3-}$  in 1:1 molar ratio at various temperatures.** Time-dependent study showing the intermediates stages of reaction between  $[\text{}^{107}\text{Ag}_{29}(\text{BDT})_{12}]^{3-}$  and  $[\text{}^{109}\text{Ag}_{29}(\text{BDT})_{12}]^{3-}$  in 1:1 molar ratio at (A)  $40^{\circ}\text{C}$ , (B)  $60^{\circ}\text{C}$  and (C)  $0^{\circ}\text{C}$ . (D) Kinetic plot of the percentage of un-exchanged parent cluster ( $C_i$ ) versus time at  $0^{\circ}\text{C}$ . The rate constants obtained from tri-exponential fitting are indicated in the figure.

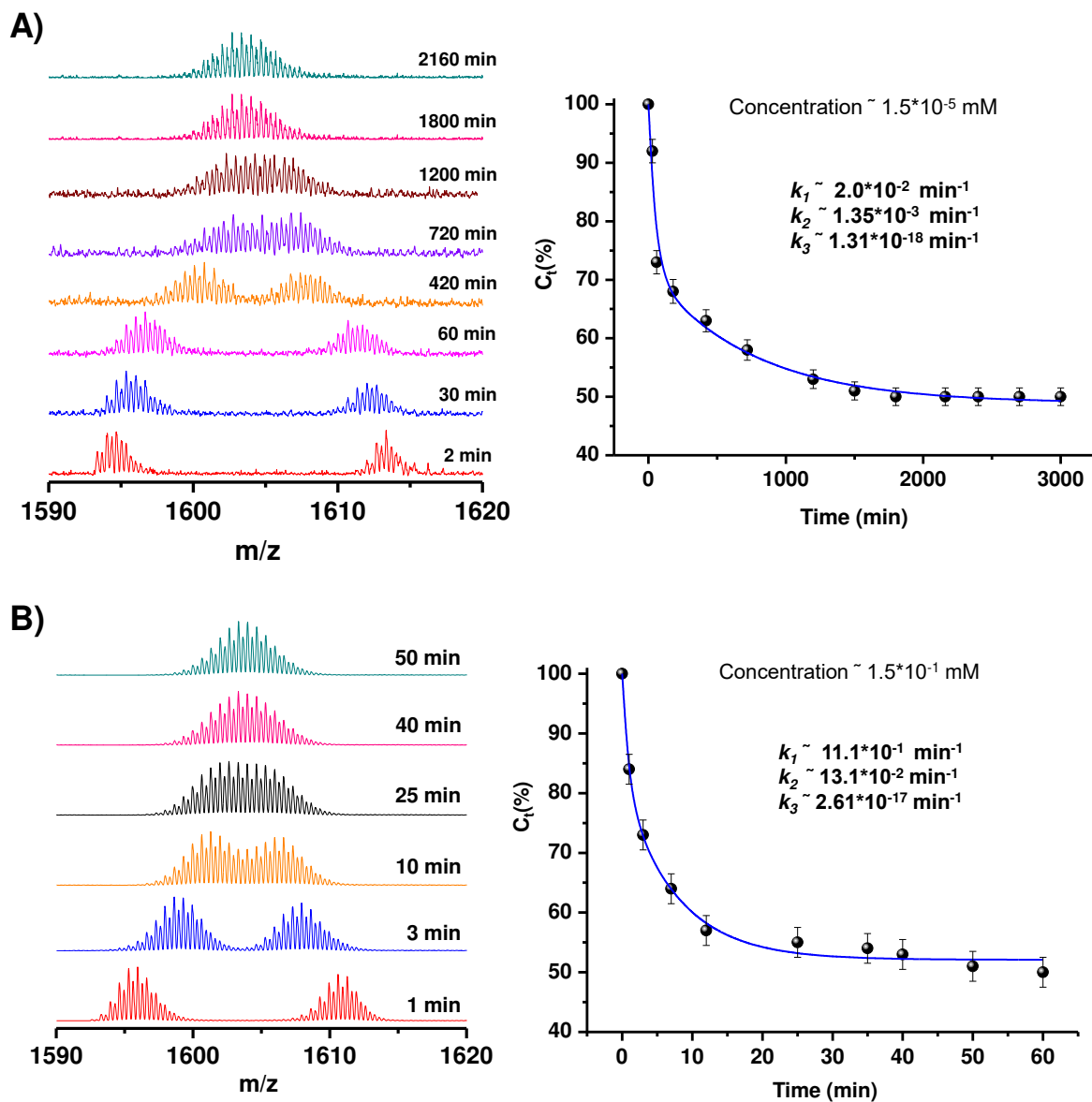


**Fig. S10. Kinetic study of isotopic exchange at different concentrations of  $[\text{Ag}_{29}(\text{BDT})_{12}(\text{TPP})_4]^{3-}$  clusters.** Time-dependent ESI MS and corresponding kinetic study showing the rate constants of the reaction at **A)**  $1.5 \cdot 10^{-5}$  mM and **B)**  $1.5 \cdot 10^{-1}$  mM concentration.

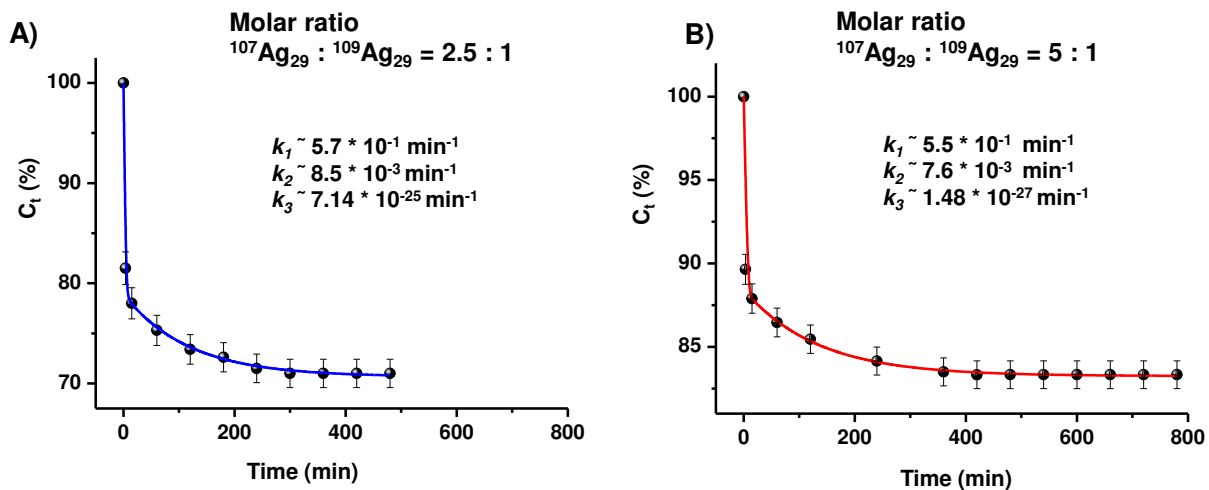


**Fig. S11. Kinetic study of isotopic exchange in  $[\text{Ag}_{29}(\text{BDT})_{12}(\text{TPP})_4]^{3-}$  clusters at different molar ratios of mixing.** Kinetic study of isotopic exchange at molar ratios of mixing of  $^{107}\text{Ag}_{29} : ^{109}\text{Ag}_{29}$  clusters, (A) 2.5:1 and (B) 5:1. The rate constants of the three stages of exchange in each case are denoted in the figure.

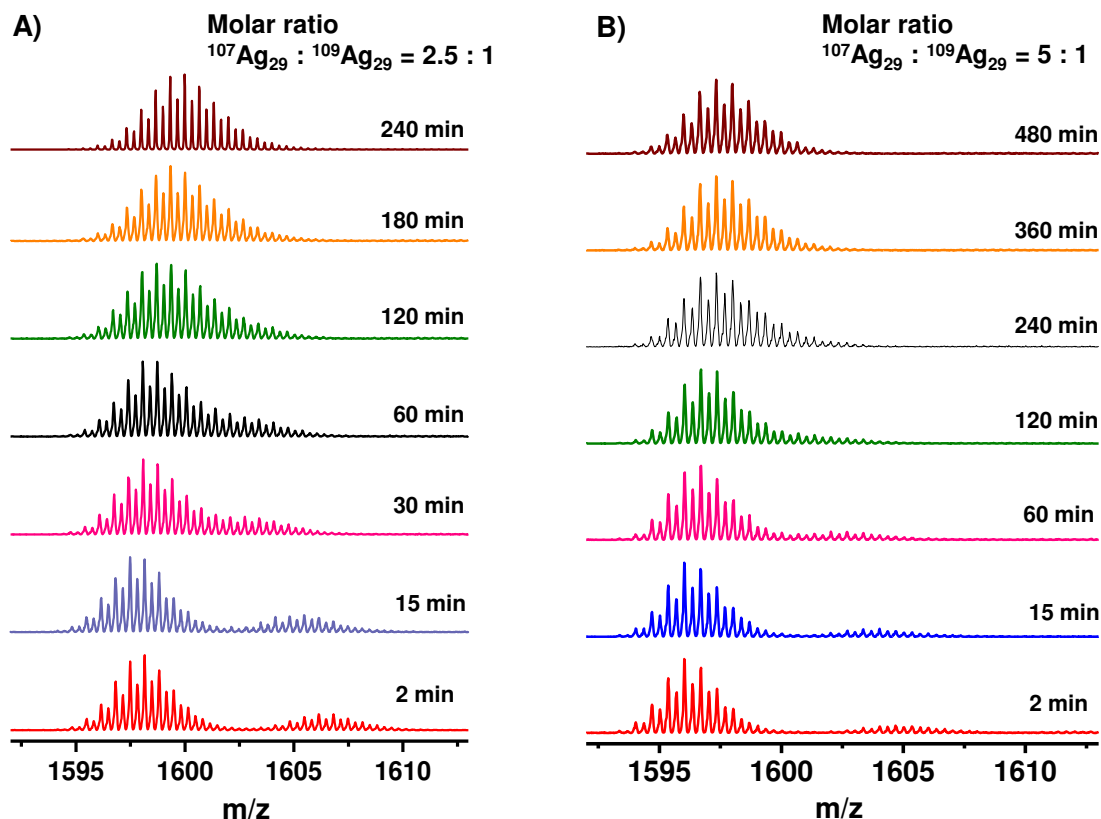


**Fig. S12. Time-dependent study of reaction between  $[\text{}^{107}\text{Ag}_{29}(\text{BDT})_{12}(\text{TPP})_4]^{3-}$  and  $[\text{}^{109}\text{Ag}_{29}(\text{BDT})_{12}(\text{TPP})_4]^{3-}$  at various molar ratios.** Time-dependent study showing the intermediate stages of reaction at  $^{107}\text{Ag}_{29} : ^{109}\text{Ag}_{29}$  molar ratios of (A) 2.5:1 and (B) 5:1.

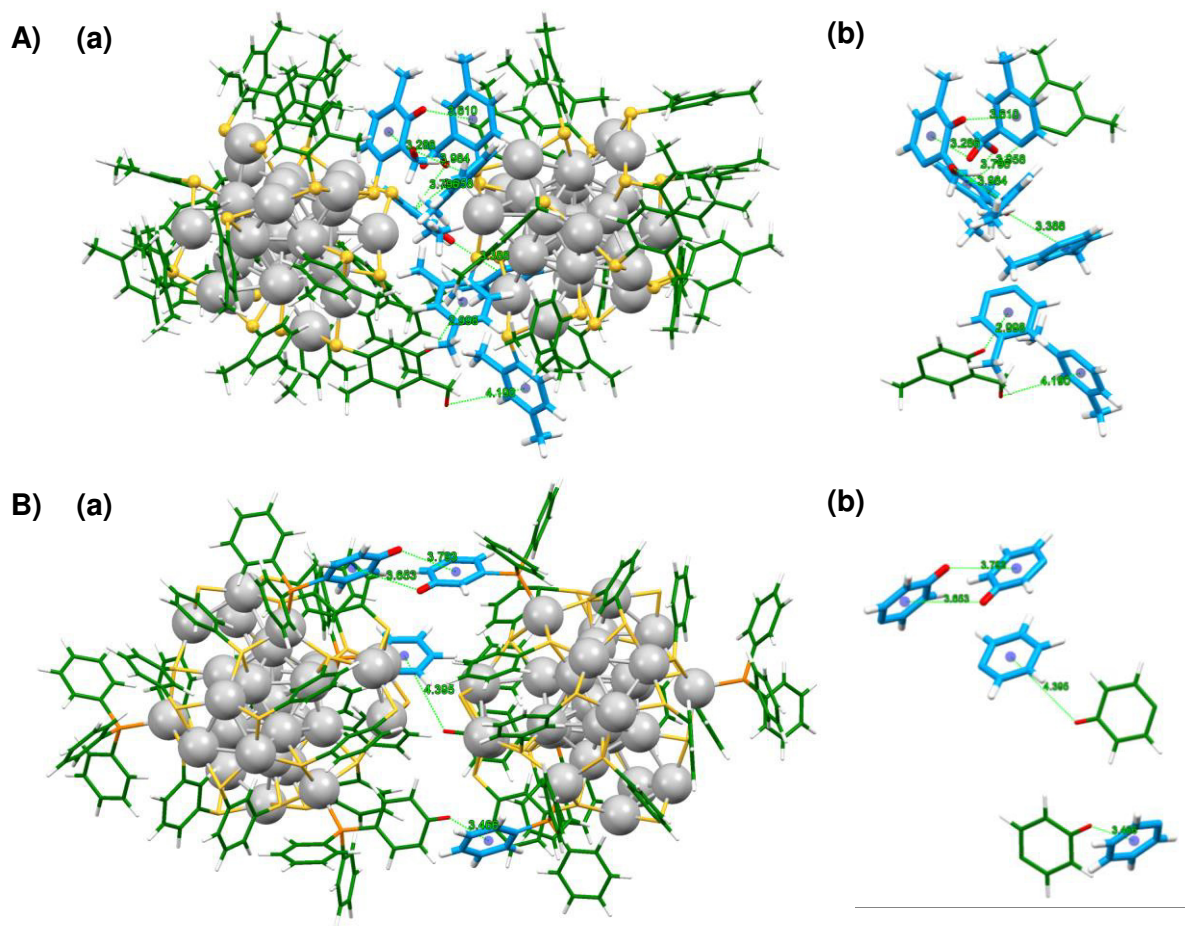


**Fig. S13. Molecular docking studies.** Lowest energy geometry obtained from docking two A)  $[Ag_{25}(DMBT)_{18}]^{-}$  and B)  $[Ag_{29}(BDT)_{12}(TPP)_4]^{3-}$  clusters. C-H... $\pi$  interactions are indicated in the figure. Color codes: grey: Ag, yellow: S, orange: P, green: ligands. The H atoms involved in these interactions are shown in red and the benzene rings involved are shown in blue. Expanded view of the ligands involved in these C-H... $\pi$  interactions are shown in the insets b.

**Table S2. Table showing ZPE and Gibbs free energy (*G*) values of the isotopic clusters.**

(a) For  $[\text{Ag}_{29}(\text{BDT})_{12}(\text{TPP})_4]^{3-}$  clusters

(i) Isotopically pure reactants

Cluster	ZPE (eV)	G (eV)
$[\text{}^{107}\text{Ag}_{29}(\text{BDT})_{12}(\text{TPP})_4]^{3-}$	2.400	-1262.250
$[\text{}^{109}\text{Ag}_{29}(\text{BDT})_{12}(\text{TPP})_4]^{3-}$	2.394	-1262.271

(ii) Mixed isotope product clusters with composition (m,n) = (15,14) and (14,15) in  $[\text{}^{107}\text{Ag}_m\text{}^{109}\text{Ag}_n(\text{BDT})_{12}(\text{TPP})_4]^{3-}$ .

(m,n) = (15,14)				(m,n) = (14,15)			
Position of $^{107}\text{Ag}$ atoms	Position of $^{109}\text{Ag}$ atoms	ZPE (eV)	G (eV)	Position of $^{107}\text{Ag}$ atoms	Position of $^{109}\text{Ag}$ atoms	ZPE (eV)	G (eV)
C-1 I-12 S-2	S-14	2.397	-1262.260	S-14	C-1 I-12 S-2	2.397	-1262.261
S-15	C-1 I-12 S-1	2.397	-1262.260	C-1 I-12 S-1	S-15	2.397	-1262.261
C-1 I-6 S-8	I-6 S-8	2.397	-1262.260	I-6 S-8	C-1 I-6 S-8	2.397	-1262.261

(b) For  $[\text{Ag}_{25}(\text{DMBT})_{18}]^-$  clusters

(i) Isotopically pure reactants

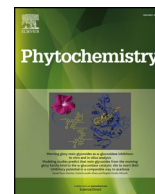
Cluster	Zero-point energy (ZPE) (eV)	Free Energy (G) (eV)
$[\text{}^{107}\text{Ag}_{25}(\text{DMBT})_{18}]^-$	1.655	-502.919
$[\text{}^{109}\text{Ag}_{25}(\text{DMBT})_{18}]^-$	1.650	-502.938

- (ii) Mixed isotope product clusters with composition (m,n) = (13,12) and (12,13) in  $[^{107}\text{Ag}_m^{109}\text{Ag}_n(\text{DMBT})_{18}]^-$

(m,n) = (13,12)				(m,n) = (12,13)			
Position of $^{107}\text{Ag}$ atoms	Position of $^{109}\text{Ag}$ atoms	ZPE (eV)	G (eV)	Position of $^{107}\text{Ag}$ atoms	Position of $^{109}\text{Ag}$ atoms	ZPE (eV)	G (eV)
C-1 I-12	S-12	1.652	-502.928	S-12	C-1 I-12	1.652	-502.929
S-12 C/I-1	C/I-12	1.652	-502.928	C/I-12	S-12 C/I-1	1.652	-502.929
C-1 I-6 S-6	I-6 S-6	1.652	-502.928	I-6 S-6	C-1 I-6 S-6	1.652	-502.929

**N.B.** C, I and S refers to centre, icosahedron and staple positions, respectively.





# UPLC and ESI-MS analysis of metabolites of *Rauvolfia tetraphylla* L. and their spatial localization using desorption electrospray ionization (DESI) mass spectrometric imaging

P. Mohana Kumara<sup>a,c,\*</sup>, R. Uma Shaanker<sup>b</sup>, T. Pradeep<sup>a,\*</sup>

<sup>a</sup> DST Unit of Nanoscience and Thematic Unit of Excellence, Department of Chemistry, Indian Institute of Technology Madras, Chennai, 600036, India

<sup>b</sup> School of Ecology and Conservation, Department of Crop Physiology, University of Agricultural Sciences, GKVK, Bengaluru, 560065, India

<sup>c</sup> Center for Ayurveda Biology and Holistic Nutrition, The University of Trans-Disciplinary Health Sciences and Technology (TDU), Bengaluru, 560064, India

## ARTICLE INFO

### Keywords:

*Rauvolfia tetraphylla*  
Apocynaceae  
Indole alkaloids  
DESI-MS  
Ajmaline  
Reserpine  
Yohimbine

## ABSTRACT

*Rauvolfia tetraphylla* L. (family Apocynaceae), often referred to as the wild snakeroot plant, is an important medicinal plant and produces a number of indole alkaloids in its seeds and roots. The plant is often used as a substitute for *Rauvolfia serpentina* (L.) Benth. ex Kurz known commonly as the Indian snakeroot plant or sarphagandha in the preparation of Ayurvedic formulations for a range of diseases including hypertension. In this study, we examine the spatial localization of the various indole alkaloids in developing fruits and plants of *R. tetraphylla* using desorption electrospray ionization mass spectrometry imaging (DESI-MSI). A semi-quantitative analysis of the various indole alkaloids was performed using UPLC-ESI/MS. DESI-MS images showed that the distribution of ajmaline, yohimbine, demethyl serpentine and mitoridine are largely localized in the fruit coat while that for ajmaline is restricted to mesocarp of the fruit. At a whole plant level, the ESI-MS intensities of many of the ions were highest in the roots and lesser in the shoot region. Within the root tissue, except sarpagine and ajmaline, all other indole alkaloids occurred in the epidermal and cortex tissues. In leaves, only serpentine, ajmaline, reserpiline and yohimbine were present. Serpentine was restricted to the petiolar region of leaves. Principal component analysis based on the presence of the indole alkaloids, clearly separated the four tissues (stem, leaves, root and fruits) into distinct clusters. In summary, the DESI-MSI results indicated a clear tissue localization of the various indole alkaloids, in fruits, leaves and roots of *R. tetraphylla*. While it is not clear of how such localization is attained, we discuss the possible pathways of indole alkaloid biosynthesis and translocation during fruit and seedling development in *R. tetraphylla*. We also briefly discuss the functional significance of the spatial patterns in distribution of metabolites.

## 1. Introduction

*Rauvolfia tetraphylla* L. (Family Apocynaceae) (Fig. 1a) is an economically important medicinal plant, often used as a substitute for its conspecific plant, *Rauvolfia serpentina* (L.) Benth. ex Kurz commonly referred to as the Indian snakeroot plant or sarphaganda (Gupta et al., 2012). The latex of both species of plants are used in a variety of cures in folk medicine and several indigenous or traditional medicine systems (Gupta et al., 2012). The white latex is used as emetic, cathartic and expectorant for treating dropsy (Gupta et al., 2012; Kaushik et al., 2013). Both the species of *Rauvolfia* produce a variety of monoterpene indole alkaloids (MIAs) such as reserpine, serpentine,

deserpidine, ajmaline, ajmaline, yohimbine that have been reported to have important pharmaceutical and biological activities. All these compounds originate from strictosidine (Fig. 2), formed by the condensation of tryptamine with secologanin (Hagel et al., 2008; Pan et al., 2015). Little is known about the downstream biosynthetic pathway of these compounds from strictosidine (Fig. 2) (Faisal et al., 2005).

Considering the importance of many of the monoterpene indole alkaloids (MIAs) in pharmaceutical applications, a number of studies have explored to unravel the pathway genes involved in the biosynthesis of these compounds. Using an integrated transcriptomics and proteomics approach for gene discovery, Miettinen et al. (2014) discovered the last four missing steps of the (seco)iridoid biosynthesis pathway in

\* Corresponding author.

\*\* Corresponding author. DST Unit of Nanoscience and Thematic Unit of Excellence, Department of Chemistry, Indian Institute of Technology Madras, Chennai, 600036, India.

E-mail addresses: [monapatelpgatti@gmail.com](mailto:monapatelpgatti@gmail.com) (P. Mohana Kumara), [pradeep@iitm.ac.in](mailto:pradeep@iitm.ac.in) (T. Pradeep).

<https://doi.org/10.1016/j.phytochem.2018.11.009>

Received 4 June 2018; Received in revised form 15 November 2018; Accepted 16 November 2018

Available online 17 December 2018

0031-9422/ © 2018 Elsevier Ltd. All rights reserved.

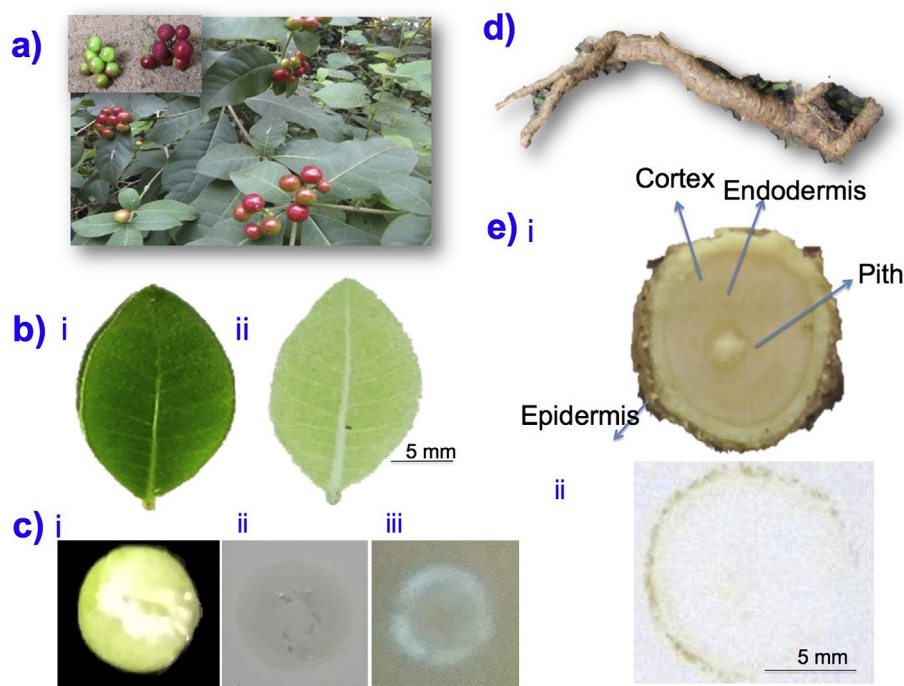


**Fig. 1.** a) Fruit bearing *Rauvolfia tetraphylla* plant. Insert in shows the different stages of fruit b) leaf and its TLC imprint, c) Fruit cross section (i) and its TLC imprint (ii) TLC imprint photo taken with UV light (iii) d) Root and e) Root cross section (i) and its TLC imprint (ii).

*Catharanthus roseus*. More recently, the entire MIA pathway up to strictosidine was engineered in *Nicotiana benthamiana* by heterologous expression of newly identified genes in combination with the previously known biosynthesis genes (Miettinen et al., 2014). Interestingly the biosynthetic pathways of many plant specialised metabolites often involve multiple cell types that are biochemically and morphologically distinct (Hagel et al., 2008; Pan et al., 2015). *In situ* RNA hybridization and immuno-cytochemical studies have shown the localization of MIA pathway enzymes to a number of cell types (St-Pierre et al., 1999). For example, studies in *C. roseus* have shown that secoiridoid metabolism begins in phloem-associated parenchyma cells (IPAP) cells and that loganic acid produced in IPAP cells is transferred to epidermal cells (ECs). Further synthesis involving secologanin and tryptamine occurs in the ECs. Finally, a MIA intermediate, deacetoxyvindoline, moves to the idioblast cells (ICs) and laticifer cells (LCs) and MIAs begin to accumulate in the vacuole of these cells (St-Pierre et al., 1999; Mahroug et al., 2006; Dug   de Bernonville et al., 2015; Burlat et al., 2004).

In a more recent study on a Mediterranean plant, *Thapsia garganica* (dicot, Apiaceae), using MALDI MSI, it was shown that the metabolite, thapsigargin was stored in the secretory ducts in the roots. Transcripts of *TgTPS2* (epikunzeol synthase) and *TgCYP76AE2* in roots were found only in the epithelial cells lining these secretory ducts (Andersen et al., 2017). Similarly, in *Vitex agnuscastus* L, MALDI-MSI analysis showed that the diterpenoids were localized in trichomes on the surface of fruit and leaves. Analysis of a trichome-specific transcriptome database, coupled with expression studies, identified seven candidate genes involved in diterpenoid biosynthesis (Heskes et al., 2018; Boughton et al., 2016).

Unraveling the localization of pathway gene expression and their products or metabolites can profoundly help in understanding, both the regulatory and functional basis of metabolite synthesis in plants (Miettinen et al., 2014). While traditionally, studies have relied on techniques such as *in situ* RNA hybridization and immuno-cytochemical studies, in recent years there has been increasing attempts to use mass spectrometry imaging techniques for localizing plant metabolites. These techniques, such as MALDI-MSI or DESI-MSI are rapid, easy to use and have been used in a number of studies to understand the spatial

context of metabolite accumulation and localization (Bjarnholt et al., 2014; Lee et al., 2012; Ifa et al., 2011; Korte et al., 2012; Hemalatha and Pradeep, 2013; Kueger et al., 2012; Boughton et al., 2016; Andersen et al., 2017; Zifkin et al., 2012). Coupled with tissue-based transcriptomic analysis, the technique can potentially be used in unraveling biosynthetic pathway genes responsible for the synthesis and accumulation of specialised metabolites (Bjarnholt et al., 2014; Zifkin et al., 2012; Andersen et al., 2017).

In this study, using a DESI-MSI approach, we have developed a spatially explicit map of the indole alkaloids in developing fruits and plants of *R. tetraphylla*. We rationalize the results based on both the functional significance of such patterns as well as the possible metabolic regulatory processes that might have resulted in these patterns.

## 2. Results and discussion

ESI MS analysis of the different parts (root, stem, leaf and fruits: Fig. 1) of *R. tetraphylla* showed the presence of prominent metabolites in the range of  $m/z$  300–611 (Table 1). Among the different tissues, by far the roots contained relatively large number of indole alkaloids compared to the stem, leaves and fruits (Fig. S1). Structural characterization of these indole alkaloids were done by both accurate mass measurement and mass fragmentation analysis (Fig. S2) (Smith et al., 2005). Mass fragmentation analysis was done mainly by comparing the observed fragment ions with those retrieved from earlier publications (Fig. S2). Where not available, the patterns were annotated using the fragments core structural features (Supplementary information; Fig. S2). A list of  $m/z$  values of the parent and fragment ions and their chemical formulae are given in Table 1. Based on these masses, the identity and the spatial location of the compounds were established in different parts of the fruit and plant using DESI-MS imaging facility. Principal component analysis (PCA) based on the presence of MIAs clearly separated the four tissues (stem, leaves, root and fruits) in to distinct clusters (Fig. S2). The first and second PC axis respectively explained 66.5% and 30.5% of the variance. The eigenvector contributions for the two axes are: PC1 Leaf-L1 (2.0994) L2 (4.827) L3 (4.827) and PC2 (L1 3.990, Root-R2 0.29, R3- 0.217) (Fig. S3).

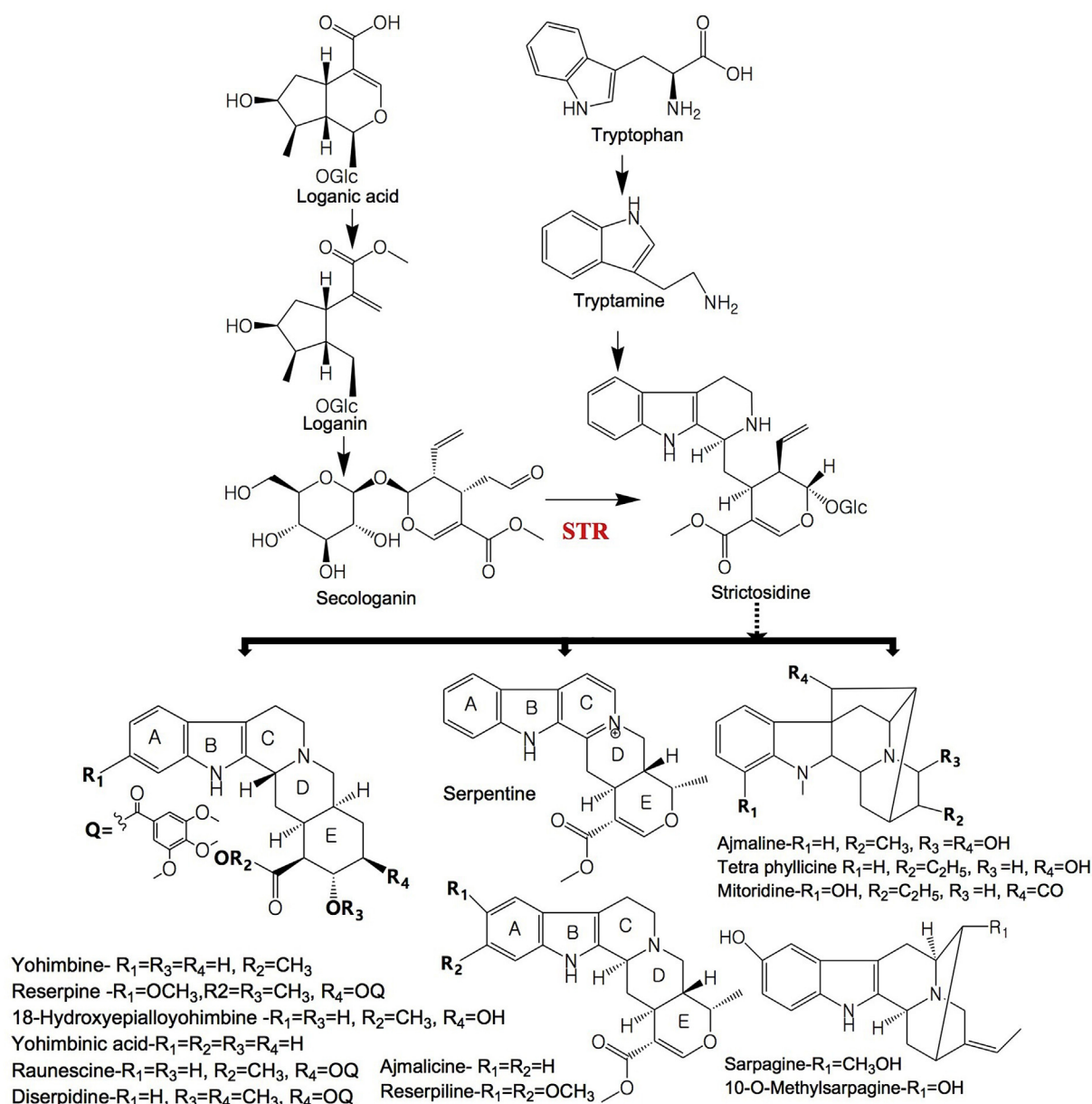


Fig. 2. Pathway of monoterpenoid indole alkaloid biosynthesis. Strictosidine synthase (STR) is a key gene responsible for the biosynthesis of strictosidine. Strictosidine is a major precursor for the biosynthesis of a diversity of MIAs in *Rauvolfia tetraphylla*.

### 2.1. MIAs during fruit development

The spatial locations of different MIAs in cross section of developing fruits were established using DESI-MS. Among the various indole alkaloids, prominent were mitoridine, ajmaline, demethyl serpentine, ajmalicine and yohimbine (Fig. 3). The molecular ion intensities were higher in early stage fruits compared to mature fruit. The alkaloids, mitoridine, 12-methoxyvellosimine, demethyl serpentine, ajmalicine and yohimbine were restricted to the fruit coat (exocarp), while ajmaline was largely restricted to mesocarp of the fruit (Fig. 3). Demethyl serpentine was detected only in fruits and not in other parts of the plant.

### 2.2. MIAs in root and shoot

Cross-sections of root and shoot of the plant showed distinct spatial distribution patterns of the various ions. In roots, most of the indole alkaloids were present and showed tissue specific localization.

Tetraphyllicine, raunescine and deserpidine were present only in epidermis; mitoridine and ajmalicine were present in cortex while reserpine was restricted to the pith region only. Sarpagine, 10-O-methylsarpagine, ajmaline, serpentine, yohimbine and 18-hydroxy-yohimbine were present in higher abundance in epidermis and pith region. Stem contained, sarpagine, ajmaline, serpentine, ajmalicine, yohimbine and 18-hydroxy-yohimbine with a localization pattern similar to that in the root (Fig. 4).

### 2.3. MIAs in leaves

In leaves, only serpentine, ajmalicine, reserpiline and yohimbine were found. Specifically, serpentine was found only in the leaf petiole while the other metabolites were abundant in the leaf blade (Fig. 5).

Intensities of many of these metabolites were highest in the roots upwards to the collar region, representing the transition from the root to the shoot (Figs. 3–5, Fig. S5). For example, reserpine content on dry weight basis, was highest in the main roots ( $0.50\% \pm 0.10$ ) and lateral

**Table 1**  
Details of  $m/z$  values of the ions, fragment ions and chemical formulae of monoterpene alkaloids identified in *Rauvolfia tetraphylla*.

Serial number	Metabolite	Ion type	Exact mass (calculated)	$m/z$ obtained from ESI MS (Orbitrap)	Error (ppm)	Chemical Formula	Mass fragments <sup>a</sup>	Metabolite tissue localization		
								Root/stem	Leaves	Fruit
1	Strictosidine	[M + H] <sup>+</sup>	531.2337	531.2337	0	C <sub>27</sub> H <sub>35</sub> N <sub>2</sub> O <sub>9</sub>	514, 352, 334, 320, 302, 282, 251, 222, 223, 144			
<b>Reserpine type of alkaloids</b>										
2	Yohimbine	[M + H] <sup>+</sup>	355.2016	355.2007	-2.5	C <sub>21</sub> H <sub>27</sub> N <sub>2</sub> O <sub>3</sub>	337, 323, 224, 212, 194, 144	Epidermis and pith	Leaf blade	-
3	Deserpidine	[M + H] <sup>+</sup>	579.2701	579.2698	-0.5	C <sub>32</sub> H <sub>39</sub> N <sub>2</sub> O <sub>8</sub>	547, 448, 367, 335, 195, 144	Epidermis	-	-
4	Reserpine	[M + H] <sup>+</sup>	609.2807	609.2802	-0.8	C <sub>33</sub> H <sub>41</sub> N <sub>2</sub> O <sub>9</sub>	577, 448, 436, 397, 365, 336, 236, 224, 195	Pith	-	-
5	18-Hydroxyepialloyohimbine	[M + H] <sup>+</sup>	371.1965	371.1961	-1.0	C <sub>21</sub> H <sub>27</sub> N <sub>2</sub> O <sub>4</sub>	353, 339, 240, 2281, 58, 223, 144	Epidermis and pith	-	-
6	Yohimbic acid	[M + H] <sup>+</sup>	341.1865	341.1862	-0.8	C <sub>20</sub> H <sub>25</sub> N <sub>2</sub> O <sub>3</sub>	32, 32, 11, 19, 61, 58, 144	Epidermis and pith	-	-
7	Raunesine	[M + H] <sup>+</sup>	565.2544	565.2542	-0.3	C <sub>31</sub> H <sub>35</sub> N <sub>2</sub> O <sub>8</sub>	547, 448, 353, 321, 195, 144	Epidermis	-	-
<b>Ajmalicine type of alkaloids</b>										
8	Ajmalicine	[M + H] <sup>+</sup>	353.186	353.1851	-2.5	C <sub>21</sub> H <sub>25</sub> N <sub>2</sub> O <sub>3</sub>	321, 293, 210, 222, 144	Cortex	Leaf blade	Outer part
9	Reserpiline	[M + H] <sup>+</sup>	413.2071	413.2068	-0.7	C <sub>23</sub> H <sub>29</sub> N <sub>2</sub> O <sub>5</sub>	381, 222, 204, 144	-	Leaf blade	-
<b>Ajmaline type of alkaloids</b>										
10	Ajmaline	[M + H] <sup>+</sup>	327.2067	327.2063	-1.2	C <sub>20</sub> H <sub>27</sub> N <sub>2</sub> O <sub>2</sub>	309, 238, 210, 194, 182, 158, 144	Epidermis and pith	-	Endosperm
11	Tetraphyllicine	[M + H] <sup>+</sup>	309.1961	309.1957	-1.3	C <sub>20</sub> H <sub>25</sub> N <sub>2</sub> O	291, 238, 182, 158, 144	Epidermis	-	-
12	Sarpagine	[M + H] <sup>+</sup>	311.176	311.175	-3.2	C <sub>19</sub> H <sub>23</sub> N <sub>2</sub> O <sub>2</sub>	293, 276, 165, 145, 138	Epidermis and pith	-	-
13	Mitoridine	[M + H] <sup>+</sup>	323.176	323.1749	-3.4	C <sub>20</sub> H <sub>23</sub> N <sub>2</sub> O <sub>2</sub>	305, 291, 279, 263, 144	Cortex	-	Outer part
14	10-O-Methylsarpagine	[M + H] <sup>+</sup>	325.1911	325.1907	-3.4	C <sub>20</sub> H <sub>25</sub> N <sub>2</sub> O <sub>2</sub>	307, 293, 160, 144	Epidermis and pith	-	-
<b>Others</b>										
15	Serpentine	[M + H] <sup>+</sup>	349.1547	349.1537	-2.8	C <sub>21</sub> H <sub>21</sub> N <sub>2</sub> O <sub>3</sub>	317, 293, 277, 263, 235	Epidermis and pith	Leaf petiole	-
16	Demethyl serpentine	[M + H] <sup>+</sup>	335.1396	335.1382	-4.1	C <sub>20</sub> H <sub>19</sub> N <sub>2</sub> O <sub>3</sub>	317, 293, 277, 263, 235	-	-	Outer part

- Below detection threshold.

<sup>a</sup> The mass fragments used to infer the chemical identities of the various compounds are based on published literature provided for each of the alkaloids in the supplementary information.



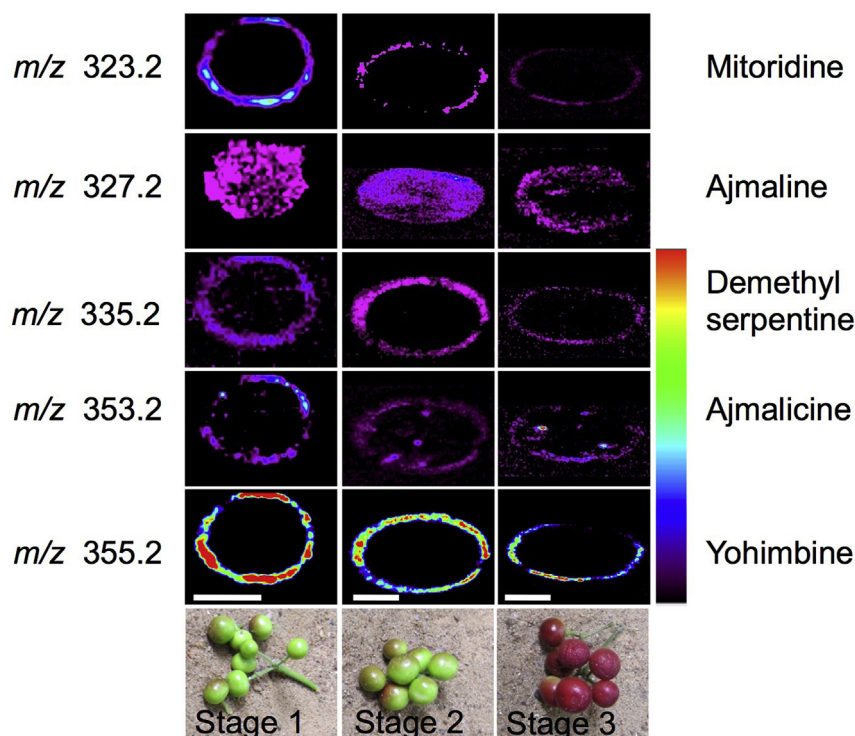


**Fig. 3.** DESI MS images showing the distribution of indole alkaloids in fruit sections of *R. tetraphylla*. Scale bars correspond to 5 mm and apply to all the images of a row.

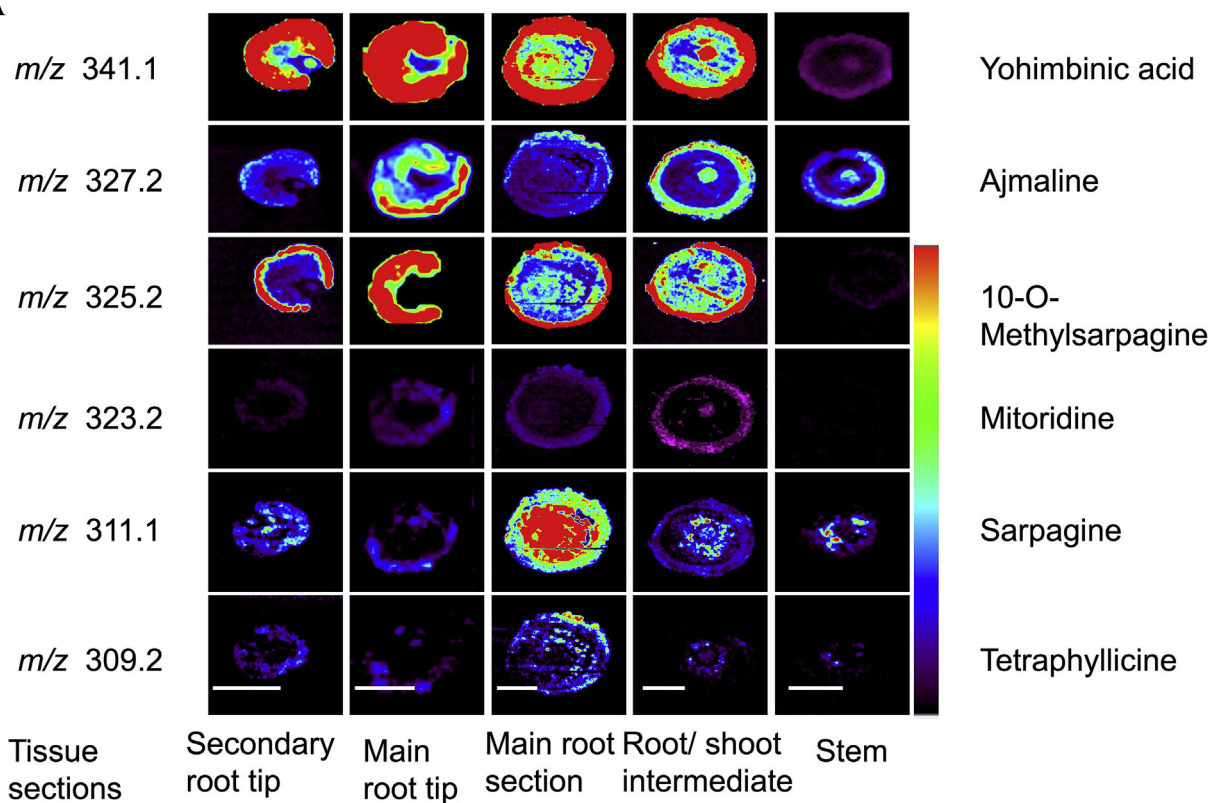
roots ( $0.44\% \pm 0.09$ ), followed by stem ( $0.31\% \pm 0.09$ ), and least in fruits ( $0.02\% \pm 0.02$ ) and absent in leaves (Fig. 6).

In summary, our results show that the MIAs in *R. tetraphylla* exhibit a distinct localization patterns, both, across and within different tissues (Figs. 3 and 4). For example, while roots contained most of the MIAs, the stems contained only sarpagine, ajmaline, serpentine, ajmalicine, yohimbine and 18-hydroxy-yohimbine. Similarly, the leaves had only serpentine, ajmalicine, reserpiline and yohimbine. Within each tissue as well, there were distinct patterns of occurrence. In fruits, several of the MIAs were restricted to the fruit coat, while others were restricted to the mesocarp. Similarly, within roots, there was a clear spatial separation of several of the MIA between the epidermal and cortex tissues. These results add to the now growing literature that suggests there could be spatial patterning of occurrence of specialised metabolites, across and within tissues (Dueñas et al., 2017; Bhandari et al., 2015; Mohana Kumara et al., 2016; Sturtevant et al., 2017). These are now increasingly becoming evident, especially through studies, involving non-invasive, imaging analysis including MALDI MSI and DESI MSI (Bjarnholt et al., 2014; Lee et al., 2012; Ifa et al., 2011; Korte et al., 2012; Hemalatha and Pradeep, 2013; Kueger et al., 2012; Dopstadt et al., 2017; Woodfield et al., 2017). The spatial patterning of MIAs also raises interesting questions, both proximate and ultimate, of such occurrence. Proximately, the patterns are best explained by studying the underlying gene expression patterns, and examining, if there is indeed any spatial correlation between the expression and the occurrence. A few studies have attempted to examine such correlation by analyzing cell and tissue specific transcriptome data. For example, in flaxseed (*Linum usitatissimum*), expression of the key genes involved in the synthesis of pinorensin and the subsequent downstream pathway intermediate were correlated with the spatial distribution of metabolite (Dalisay et al., 2015). Similarly, in highbush blueberry (*Vaccinium corymbosum*), occurrence of major classes of flavonoids was correlated to the transcript abundance. Proanthocyanidins (PAs) and corresponding transcripts encoding anthocyanidin reductase and leucoanthocyanidin reductase were mostly concentrated in young fruits

and localized predominantly to the inner fruit tissue containing the seeds and placentae (Zifkin et al., 2012). In *Calotropis procera*, tissue specific expression analysis of 30 putative transcripts involved in terpenoid, steroid and cardenolide pathways were correlated with metabolite and transcript accumulation (Pandey et al., 2016). In tea leaves, the expression patterns of genes in C2-2-1 and C2-2-2-1 groups were found to be probably responsible for the development-dependent accumulation of phenolic compounds in the leaves (Jiang et al., 2013). In *Sorghum bicolor*, during accumulation was reported to be correlated with transcript abundance of genes involved in biosynthesis of cyanogenic glycosides (Nielsen et al., 2016). It would be interesting to examine such association between the spatial distribution of the metabolites in tissues with the corresponding gene expression in *R. tetraphylla* as well. Where such correlation between spatial localization and gene expression is not evident, it is likely that the spatial patterns could be due to a disconnect between the sites of synthesis and sites of accumulation of the metabolites. For example, in pea and carrot, cytokinins biosynthesized in cambium of the root is finally exported to the shoot (Chen et al., 1985).

While the above studies may help explain the proximate basis of spatial patterning of metabolites, it is also interesting to examine, the ultimate functional significance of such patterning. One of the earliest studies is due to Berenbaum (1995) who proposed the concept of apparency in the synthesis and accumulation of specialised metabolites by plant tissue. According to this theory, plants bet-hedge on deploying defense responses and investing carbon to synthesizing specialised metabolites. Thus, instead of uniformly investing in synthesis and accumulation of specialised metabolites in all leaves, plants may accumulate the compound in only a proportion of the leaves and within a leaf, only in some parts of the leaf (Hansen et al., 2016). In *R. tetraphylla*, it is interesting to note that ajmaline is specifically distributed in the mesocarp of the fruit and increases through the fruit developmental phase. Ajmaline is a potent inhibitor of  $\text{Na}^+/\text{K}^+$  channel (Kiesecker et al., 2004) and it is likely that the accumulation pattern in the mesocarp could help defend the fruit from insect herbivores. On the

A



B

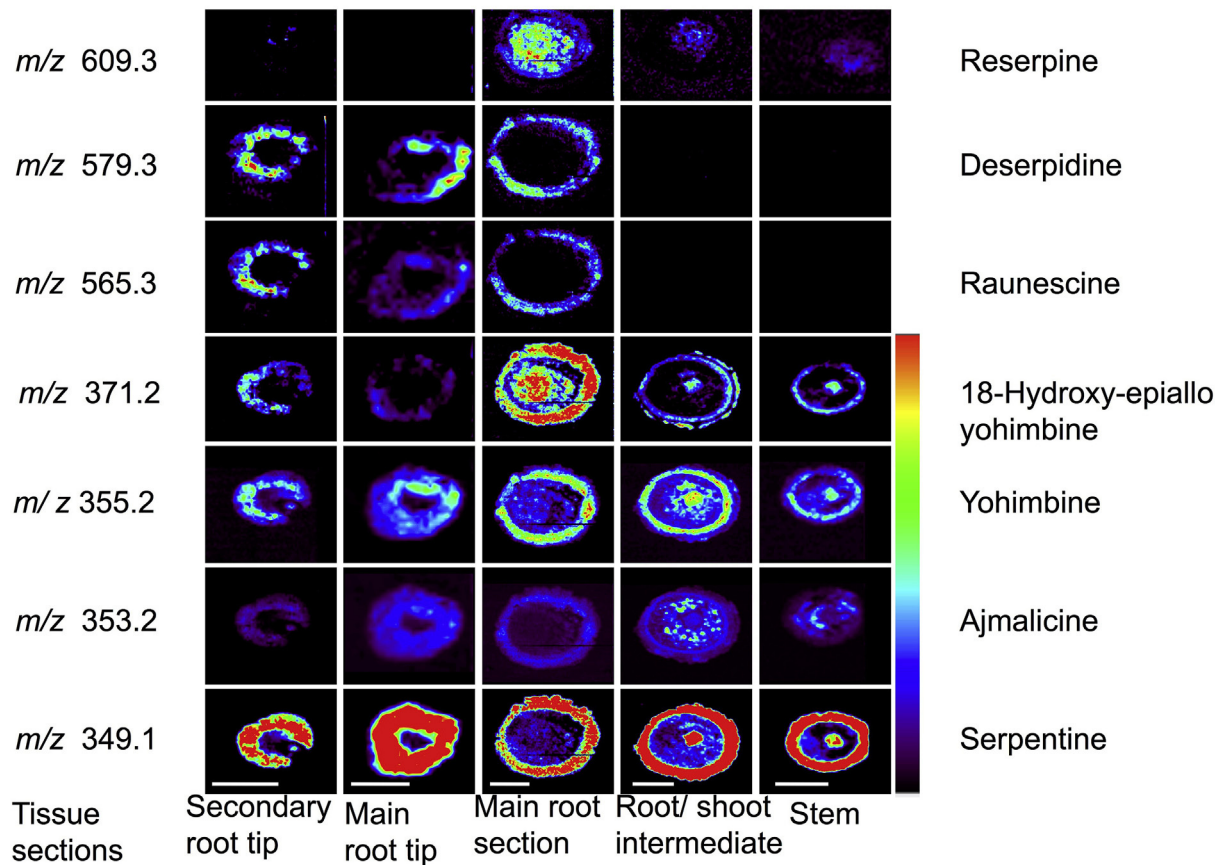


Fig. 4. DESI MS images showing the indole alkaloid distribution in root and stem sections of *R. tetraphylla*. Scale bars correspond to 5 mm and apply to all the images of a row.

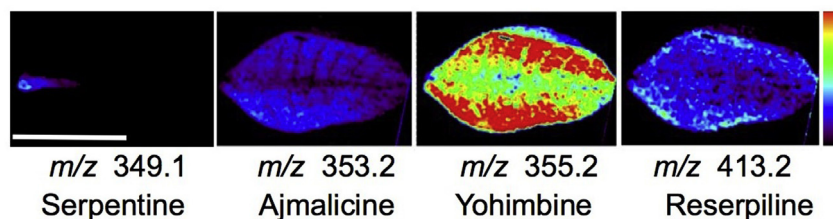


Fig. 5. DESI MS images showing the indole alkaloid distribution in leaf of *R. tetraphylla*. Scale bars correspond to 5 mm and apply to all the images of a row.

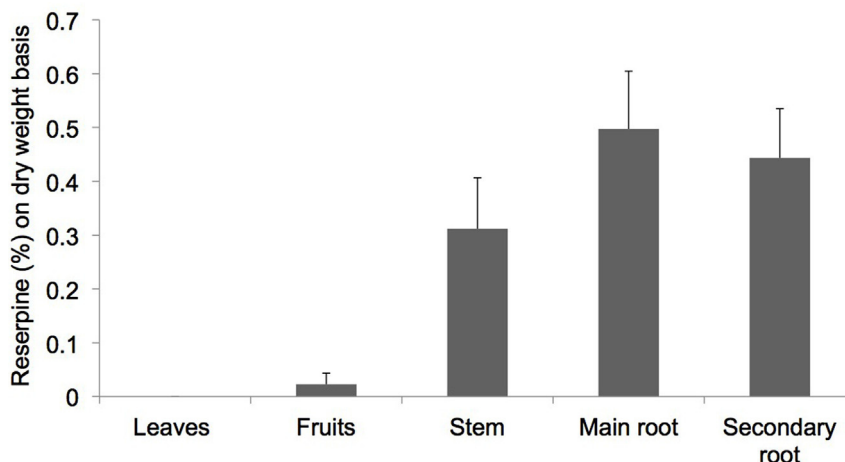


Fig. 6. Reserpine content (on dry weight basis) in different parts of *Rauvolfia tetraphylla* plant. Error bars indicates standard deviation.

other hand, ion intensities of many other compounds such as mitroline, yohimbine that was located in the fruit epidermis decreased with fruit ripening. The functional significance of many of these compounds is unknown, though some of them might serve as intermediates of biosynthesis of indole alkaloids. Yohimbine is an alpha adrenoreceptor inhibitor and could possibly also function in defense. Sarpagine, an ajmaline type monoterpene indole alkaloid, is a  $\text{Na}^+$  channel blocker and is concentrated in the cortex and pith of the root. Reserpine, also abundant in the main root cortex, is a monoamine transport blocker (Mahata et al., 1996). Ajmalicine, an andregnic receptor antagonist, is concentrated in the epidermis and cortex. The functional significance of most of these compounds are yet unknown and clearly more research is required to unravel their significance to plant growth and defense.

Like other terpene alkaloids, the synthesis of MIA begins with the condensation of tryptamine and secologanin to yield strictosidine. Strictosidine is converted into 4,21-dehydrogeissoschizine and thereafter through cyclization and reduction, ajmalicine is formed (KEGG pathway). However, in our study, we failed to recover the primary precursors of the different MIAs. An earlier study (Yamamoto et al., 2016) employing nano-DESI was successful in locating some of the precursors, such as strictosidine, indicating perhaps the need for high-resolution imaging to capture such molecules. It is also likely that our failure to spatially detect them could be due to them not being readily ionized as well as because of their inherently poor stability.

It is now well acknowledged that the primary site of synthesis of the MIAs is the root (Schlutenhofer et al., 2014; O'Connor and Maresh, 2006) and from there perhaps, a few are transported elsewhere in the plant (El-Sayed and Verpoorte, 2007; Liu et al., 2017; Pathania and Acharya, 2016). We have made a preliminary attempt to explore if there exist a tacit relationship between the spatial patterning of the specialised metabolites and their biosynthetic pathway (Figs. 7 and 8). Understandably, the root sections have the largest diversity of MIAs, perhaps representing the pathway intermediaries as well. However there is a clear narrowing of such diversity in the root:stem collar region and thereafter in the stem region, only to be partially restored in

the leaf and fruits. That there is an active transport is supported by the fact that transporters of ajmalicine and other MIAs have been reported (Liu et al., 2017; Zhu et al., 2015; Pathania and Acharya, 2016; Yu and De Luca, 2013).

In conclusion, the study provides a spatial framework of MIAs in different parts of *R. tetraphylla* plants. These results could serve as valuable inputs for further studies to address, both the proximate causes and the ultimate selective advantage of such patterning. Combined with other omics approaches, including transcriptomics/metabolomics, DESI MS imaging of specialised metabolites can offer exciting opportunities to explore tissue specific, and in some cases, cell specific gene expression to validate the spatial occurrences of metabolites.

### 3. Materials and methods

#### 3.1. Plant material

*R. tetraphylla* plants were raised and maintained at IIT Madras Nursery, Chennai (13.0052° N, 80.2420°E). *R. tetraphylla* produces brightly colored fruits, green during early stage, yellowish to red during maturity and shiny black during fully matured stage. The seeds take approximately 30–50 days to mature. Different plant parts were collected from the two-year-old plant during winter season (19-01-2015). Plant was up rooted, segmented into different parts, namely, root, stem and leaves (Fig. 1). Root and stem were further segmented in four different sections, namely, epidermis, cortex endodermis and pith region respectively (Fig. 1e). Different developmental stages of the fruit were collected from the two-year-old plants.

#### 3.2. ESI-MS/MS, orbitrap analysis and assigning the metabolites

Different sections of the root, shoot, and leaves (corresponding to regions that were used for the imaging) were cut into small pieces and soaked in methanol for 12 h. The solution was filtered and centrifuged at 10,000 rpm for 10 min. The supernatant was analyzed by ESI MS/MS



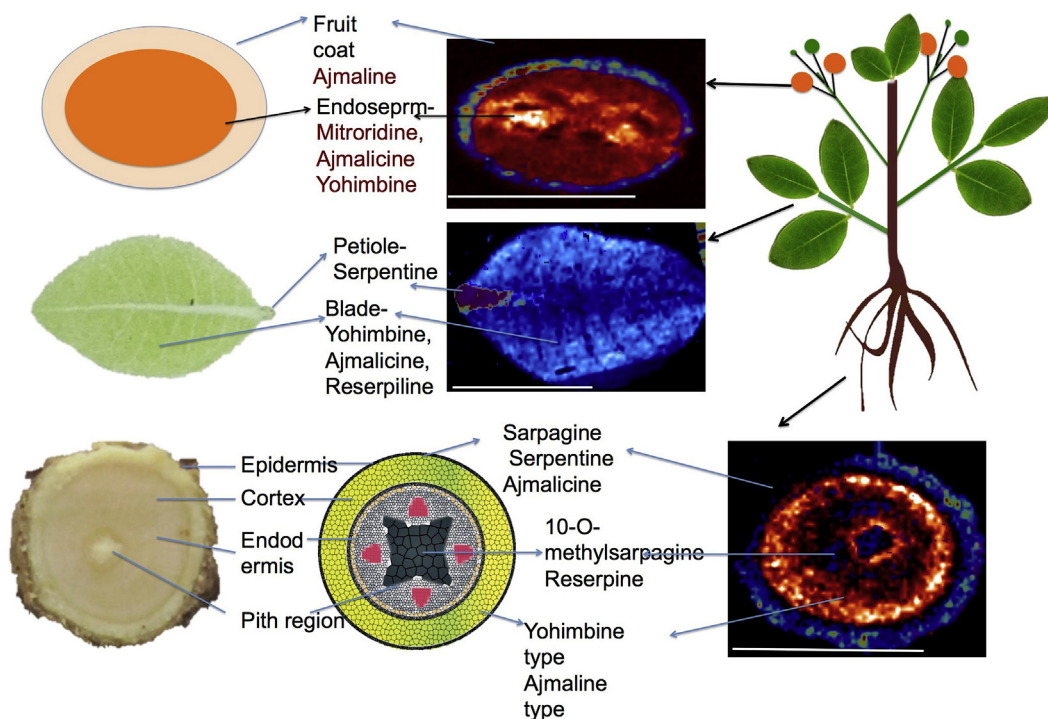


Fig. 7. Superimposed images of root, leaf and fruit sections of *R. tetraphylla* showing the tissue localization of indole alkaloids.

using Thermo Scientific LTQ XL (Thermo Scientific, San Jose, CA, USA) mass spectrometer, and exact mass was analyzed using Thermo Scientific Orbitrap Elite (Thermo Scientific, San Jose, CA, USA) mass spectrometer. The data was acquired in positive ion mode with a spray voltage of 3 kV. Collision induced dissociation (CID) was used for fragmentation of the ions during MS/MS measurements. The identities

of the ions were established based on both, the fragmentation patterns and exact masses of the ions obtained using METLIN and MassBank metabolite database. The mass window tolerance of  $\pm 3$  ppm was used for database search. The MS/MS data was used to infer the compound identity by comparing the fragment ion  $m/z$  with published literature and database. All the spectra were represented in the profile mode.

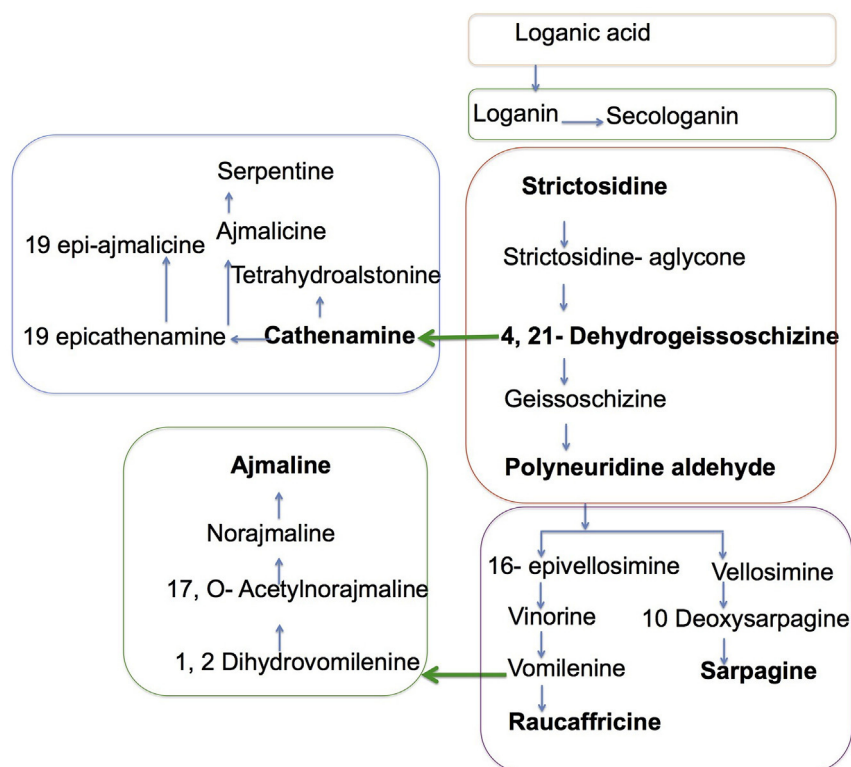


Fig. 8. Schematic illustration of the biosynthesis of monoterpene indole alkaloids (modified from KEGG pathways and Yamamoto et al., 2016).



### 3.3. Extraction and quantification of reserpine using UPLC analysis

Different sections of the root, shoot, and leaves of *R. tetraphylla* were collected from the nursery and oven dried for 3 days at 70 °C (Fig. 1). Tissues were powdered and extracted using 5 mL of methanol (Merck), centrifuged at 10,000 rpm for 5 min and filtered with 0.2 µm filters. Filtered sample (2 µL) was analyzed using UPLC Waters ACQUITY UPLC™ system SYNAPT G2-Si equipped with a binary solvent delivery system, an autosampler, column manager, and a tunable MS detector. Chromatographic separation was performed on a Waters ACQUITY UPLC™ BEH, C18 (130 Å, 1.7 µm, 2.1 mm × 50 mm, 1/pkg) column at 40 ± 5 °C. The mobile phase employed for UPLC analysis consisted of water; methanol (50:50 v/v) in a gradient mode, which was degassed, previously. The flow rate of the mobile phase was kept at 0.50 mL/min and 2 µL of sample solution was injected in each run. The total chromatographic run time was 5 min in resolution mode. The column and autosampler were maintained at 40 ± 5 and 4 ± 5 °C, respectively and pressure of the system was set to 15,000 psi. Care was exercised to ensure that the initial and final volumes of the extract were maintained constant for the sample. Standard curve was developed for the concentration range of 0.125 mg/mL to 1 mg/mL of standard reserpine (Sigma). The best fit ( $R^2 = 0.99$ ) was used in calculating the amount of reserpine in the sample (Fig. S4). All estimates were done on 3 replicates. Semi-quantitative analyses of other indole alkaloids were determined based on the extracted ion chromatogram for the specific ions (Fig. S5).

### 3.4. DESI MS analysis

Plant was uprooted and washed with running tap water and later with distilled water to remove all the debris from the root and other parts (Fig. 1a). Plants were segregated in different parts such as root, stem, leaves and fruits. Stem and roots were cross-sectioned (about 2 mm thick) using surgical blade (Fig. 1e). Fruits were collected at three developmental stages, namely immature (green), mature (green) and ripened (orange to red). Cross sections were made at mid-axis of the fruit and imprinted on flat surface of TLC plate for 10 s to obtain the imprint (TLC Silica gel 60 F<sub>254</sub>, Merck KGaA, Germany). Prior to imprinting, the TLC plates were pre-wetted with methanol and kept on a heating mantle (~70 °C) to obtain molecules present on the cut-end of the sections (Cabral et al., 2013; Mohana Kumara et al., 2015). Young leaves were imprinted on a TLC plate with 2 ton pressure for 15–30 s using a hydraulic pelletizer.

Imaging experiments were conducted using Thermo Scientific LTQ XL (Thermo Scientific, San Jose, CA, USA) mass spectrometer with 2D DESI ion source (Omni Spray Ion Source) from ProSolia, Inc., Indianapolis, IN, USA. The DESI source conditions were as follows; nebulizing gas (dry nitrogen) pressure: 150 psi, spray angle: 60°, tip of spray to surface: 1 mm, tip to inlet distance: 3 mm, spray solvent: methanol, solvent flow rate: 5 µL, spray voltage: 5 kV, and ionization mode: positive (+ve). The image area was chosen according to the sample dimensions and the spatial resolution used was 250 µm × 250 µm. Imaging 1 cm × 1 cm area of tissue sample took approximately 30 min. Imaging time varied with area of the tissue samples. Image files (IMG File) were created using FireFly software from the acquired data and Biomap 3 software was used to process the image files to create images.

### 3.5. Principal component analysis (PCA)

Principal component analysis (PCA) was done based on the exact masses of the compounds ( $m/z$  150–1000 range) recovered from fruits, leaves, and roots to examine if there is a differentiation of the tissues based on their metabolite content. Three representatives mid-point DESI MS spectra corresponding to the different tissues were collected and the masses were extracted for PCA analysis. The analysis was

performed using the statistical software PAST 3.08 (Hammer et al., 2001). The PCA analysis was based on a variance-covariance matrix.

### Conflicts of interest

The authors declare no conflict of interest.

### Acknowledgements

We thank Department of Science and Technology (DST), Government of India for the financial support to carry out this work. P.M.K. thanks IIT Madras, Chennai for a postdoctoral fellowship CY14IPF02 and SERB-DST Fast track grant File No SB/YS/LS-361/2013 for financial support.

### Appendix A. Supplementary data

Supplementary data to this article can be found online at <https://doi.org/10.1016/j.phytochem.2018.11.009>.

### References

- Andersen, T.B., Martinez-Swatson, K.A., Rasmussen, S.A., Boughton, B.A., Jørgensen, K., Andersen-Ranberg, J., Nyberg, N., Christensen, S.B., Simonsen, H.T., 2017. Localization and in-vivo characterization of *Thapsia garganica* CYP76AE2 indicates a role in thapsigargin biosynthesis. *Plant Physiol.* 174, 56–72.
- Berenbaum, M.R., 1995. The chemistry of defense: theory and practice. *Proc. Natl. Acad. Sci. U. S. A.* 92, 2–8.
- Bhandari, D.R., Wang, Q., Friedt, W., Spengler, B., Gottwald, S., Rompp, A., 2015. High resolution mass spectrometry imaging of plant tissues: towards a plant metabolite atlas. *Analyst* 140, 7696–7709.
- Bjarnholt, N., Li, B., D'Alvise, J., Janfelt, C., 2014. Mass spectrometry imaging of plant metabolites - principles and possibilities. *Nat. Prod. Rep.* 31, 818–837.
- Boughton, B.A., Thinakaran, D., Sarabia, D., Bacic, A., Roessner, U., 2016. Mass spectrometry imaging for plant biology: a review. *Phytochemistry Rev.* 15, 445–488.
- Burlat, V., Oudin, A., Courtois, M., Rideau, M., St-Pierre, B., 2004. Co-expression of three MEP pathway genes and geraniol 10-hydroxylase in internal phloem parenchyma of *Catharanthus roseus* implicates multicellular translocation of intermediates during the biosynthesis of monoterpene indole alkaloids and isoprenoid-derived primary metabolites. *Plant J.* 38, 131–141.
- Cabral, E., Mirabelli, M., Perez, C., Ifa, D., 2013. Blotting assisted by heating and solvent extraction for DESI-MS imaging. *J. Am. Soc. Mass Spectrom.* 24, 956–965.
- Chen, C.M., Ertl, J.R., Leisner, S.M., Chang, C.C., 1985. Localization of cytokinin biosynthetic sites in pea plants and carrot roots. *Plant Physiol.* 78, 510–513.
- Dalisy, D.S., Kim, K.W., Lee, C., Yang, H., Rübel, O., Bowen, B.P., Davin, L.B., Lewis, N.G., 2015. Dirigent protein-mediated lignan and cyanogenic glucoside formation in flax seed: integrated omics and MALDI mass spectrometry imaging. *J. Nat. Prod.* 78, 1231–1242.
- Dopstadt, J., Vens-Cappell, S., Neubauer, L., Tudzynski, P., Cramer, B., Dreisewerd, K., Humpf, H.U., 2017. Localization of ergot alkaloids in sclerotia of *Claviceps purpurea* by matrix-assisted laser desorption/ionization mass spectrometry imaging. *Anal. Bioanal. Chem.* 409, 1221–1230.
- Dueñas, M.E., Klein, A.T., Alexander, L.E., Yandean-Nelson, M.D., Nikolau, B.J., Lee, Y.J., 2017. High spatial resolution mass spectrometry imaging reveals the genetically programmed, developmental modification of the distribution of thylakoid membrane lipids among individual cells of maize leaf. *Plant J.* 89, 825–838.
- Dug   de Bernonville, T., Clastre, M., Besseau, S.B., Oudin, A., Burlat, V., Gl  evarec, G.L., Lanoue, A., Papon, N., Giglioli-Guivarc'h, N., St-Pierre, B., Courdavault, V., 2015. Phytochemical genomics of the Madagascar periwinkle: unravelling the last twists of the alkaloid engine. *Phytochemistry* 113, 9–23.
- El-Sayed, M., Verpoorte, R., 2007. *Catharanthus* terpenoid indole alkaloids: biosynthesis and regulation. *Phytochemistry Rev.* 6, 277–305.
- Faisal, M., Ahmad, N., Anis, M., 2005. Shoot multiplication in *Rauwolfia tetraphylla* L. using thidiazuron. *Plant Cell Tissue Organ Cult.* 80, 187–190.
- Gupta, S., Khanna, V.K., Maurya, A., Bawankule, D.U., Shukla, R.K., Pal, A., Srivastava, S.K., 2012. Bioactivity guided isolation of antipsychotic constituents from the leaves of *Rauwolfia tetraphylla* L. *Fitoterapia* 83, 1092–1099.
- Hagel, J.M., Yeung, E.C., Facchini, P.J., 2008. Got milk? The secret life of laticifers. *Trends Plant Sci.* 13, 631–639.
- Hammer, Ø., Harper, D.A.T., Ryan, P.D., 2001. PAST: paleontological statistics software package for education and data analysis. *Palaeontol. Electron.* 4 9pp.
- Hansen, A.C., Glassmire, A.E., Dyer, L.A., Smilanich, A.M., 2016. Patterns in parasitism frequency explained by diet and immunity. *Ecography* 40, 803–805.
- Hemalatha, R.G., Pradeep, T., 2013. Understanding the molecular signatures in leaves and flowers by desorption electrospray ionization mass spectrometry (DESI MS) imaging. *J. Agric. Food Chem.* 61, 7477–7487.
- Heskes, A.M., Sundram, T.C.M., Boughton, A., B.A. Jensen, N.B., Hansen, N.L., Crocoll, C., Cozzi, F., Rasmussen, S., Hamberger, B., Hamberger, B., Staerk, D., Moller, B.L., Pateraki, I., 2018. Biosynthesis of bioactive diterpenoids in the medicinal plant *Vitex*

- agnus-castus*. Plant J. 93, 943–958.
- Ifa, D.R., Srimany, A., Eberlin, L.S., Naik, H.R., Bhat, V., Cooks, R.G., Pradeep, T., 2011. Tissue imprint imaging by desorption electrospray ionization mass spectrometry. Anal. Methods 3, 1910–1912.
- Jiang, X., Liu, Y., Li, W., Zhao, L., Meng, F., Wang, Y., Tan, H., Yang, H., Wei, C., Wan, X., Gao, L., Xia, T., 2013. Tissue-Specific, Development-Dependent Phenolic Compounds Accumulation Profile and Gene Expression Pattern in Tea Plant *Camellia sinensis*. PLoS One 8, e62315.
- Kaushik, N., Kaushik, N., Attri, P., Kumar, N., Kim, C., Verma, A., Choi, E., 2013. Biomedical importance of indoles. Molecules 18, 6620.
- Kiesecker, C., Zitron, E., Lück, S., Bloehs, R., Scholz, E.P., Kathöfer, S., Thomas, D., Kreye, V.A.W., Katus, H.A., Schoels, W., Karle, C.A., Kiehn, J., 2004. Class Ia anti-arrhythmic drug ajmaline blocks HERG potassium channels: mode of action. Naunyn-Schmiedeberg's Arch. Pharmacol. 370, 423–435.
- Korte, A.R., Song, Z., Nikolau, B.J., Lee, Y.J., 2012. Mass spectrometric imaging as a high-spatial resolution tool for functional genomics: tissue-specific gene expression of TT7 inferred from heterogeneous distribution of metabolites in Arabidopsis flowers. Anal. Methods 4, 474–481.
- Kueger, S., Steinhäuser, D., Willmitzer, L., Giavalisco, P., 2012. High-resolution plant metabolomics: from mass spectral features to metabolites and from whole-cell analysis to subcellular metabolite distributions. Plant J. 70, 39–50.
- Lee, Y.J., Perdian, D.C., Song, Z., Yeung, E.S., Nikolau, B.J., 2012. Use of mass spectrometry for imaging metabolites in plants. Plant J. 70, 81–95.
- Liu, J., Cai, J., Wang, R., Yang, S., 2017. Transcriptional regulation and transport of terpenoid indole alkaloid in *Catharanthus roseus*: exploration of new research directions. Int. J. Mol. Sci. 18, 53.
- Mahata, M., Mahata, S.K., Parmer, R.J., O'Connor, D.T., 1996. Vesicular monoamine transport inhibitors: novel action at calcium channels to prevent catecholamine secretion hypertension. 28, 414–420.
- Mahroug, S., Courdavaud, V., Thiersault, M., St-Pierre, B., Burlat, V., 2006. Epidermis is a pivotal site of at least four secondary metabolic pathways in *Catharanthus roseus* aerial organs. Planta 223, 1191–1200.
- Miettinen, K., Dong, L., Navrot, N., Schneider, T., Burlat, V., Pollier, J., Woittiez, L., van der Krol, S., Lugan, R.L., Ilc, T., Verpoorte, R., Oksman-Caldentey, K.M., Martinoia, E., Bouwmeester, H., Goossens, A., Memelink, J., Werck-Reichhart, D.L., 2014. The secoiridoid pathway from *Catharanthus roseus*. Nat. Commun. 5, 3606.
- Mohana Kumara, P., Srimany, A., Ravikanth, G., Uma Shaanker, R., Pradeep, T., 2015. Ambient ionization mass spectrometry imaging of rohitukine, a chromone anti-cancer alkaloid, during seed development in *Dysoxylum binectariferum* Hook.f (Meliaceae). Phytochemistry 116, 104–110.
- Mohana Kumara, P., Srimany, A., Arunan, S., Ravikanth, G., Uma Shaanker, R., Pradeep, T., 2016. Desorption Electrospray Ionization (DESI) Mass Spectrometric Imaging of the Distribution of Rohitukine in the Seedling of *Dysoxylum binectariferum* Hook. F. PLoS One 11 (6), e0158099.
- Nielsen, L.J., Stuart, P., Pičmanová, M., Rasmussen, S., Olsen, C.E., Harholt, J., Møller, B.L., Bjarnholt, N., 2016. Dhurrin metabolism in the developing grain of *Sorghum bicolor* (L.) Moench investigated by metabolite profiling and novel clustering analyses of time-resolved transcriptomic data. BMC Genomics 17, 1021.
- O'Connor, S.E., Maresh, J.J., 2006. Chemistry and biology of monoterpene indole alkaloid biosynthesis. Nat. Prod. Rep. 23, 532–547.
- Pan, Q., Mustafa, N.R., Tang, K., Choi, Y.H., Verpoorte, R., 2015. Monoterpenoid indole alkaloids biosynthesis and its regulation in *Catharanthus roseus*: a literature review from genes to metabolites. Phytochemistry Rev. 15, 221–250.
- Pandey, A., Swarnkar, V., Pandey, T., Srivastava, P., Kanojia, S., Mishra, D.K., Tripathi, V., 2016. Transcriptome and Metabolite analysis reveal candidate genes of the cardiac glycoside biosynthetic pathway from *Calotropis procera*. Sci. Rep. 6, 34464.
- Pathania, S., Acharya, V., 2016. Computational analysis of “-omics” data to identify transcription factors regulating secondary metabolism in *Rauvolfia serpentina*. Plant Mol. Biol. Rep. 34, 283–302.
- Schluttenhofer, C., Pattanaik, S., Patra, B., Yuan, L., 2014. Analyses of *Catharanthus roseus* and Arabidopsis thaliana WRKY transcription factors reveal involvement in jasmonate signaling. BMC Genomics 15, 502.
- Smith, C.A., I'Maille, G., Want, E.J., Qin, C., Trauger, S.A., Brandon, T.R., Custodio, D.E., Abagyan, R., Siuzdak, G., 2005. METLIN: a metabolite mass spectral database. Ther. Drug Monit. 27, 747–751.
- St-Pierre, B., Vazquez-Flota, F.A., De Luca, V., 1999. Multicellular compartmentation of *catharanthus roseus* alkaloid biosynthesis predicts intercellular translocation of a pathway intermediate. Plant Cell 11, 887–900.
- Sturtevant, D., Dueñas, M.E., Lee, Y.J., Chapman, K.D., 2017. Three-dimensional visualization of membrane phospholipid distributions in Arabidopsis thaliana seeds: a spatial perspective of molecular heterogeneity. BBA. Mol. Cell Biol. Lipids 1862, 268–281.
- Woodfield, H.K., Sturtevant, D., Borisjuk, L., Munz, E., Guschina, I.A., Chapman, K., Harwood, J.L., 2017. Spatial and temporal mapping of key lipid species in *Brassica napus* seeds. Plant Physiol. 173, 1998–2009.
- Yamamoto, K., Takahashi, K., Mizuno, H., Anegawa, A., Ishizaki, K., Fukaki, H., Ohnishi, M., Yamazaki, M., Masujima, T., Mimura, T., 2016. Cell-specific localization of alkaloids in *Catharanthus roseus* stem tissue measured with Imaging MS and Single-cell MS. Proc. Natl. Acad. Sci. U. S. A. 113, 3891–3896.
- Yu, F., De Luca, V., 2013. ATP-binding cassette transporter controls leaf surface secretion of anticancer drug components in *Catharanthus roseus*. Proc. Natl. Acad. Sci. U. S. A. 110, 15830–15835.
- Zhu, J., Wang, M., Wen, W., Yu, R., 2015. Biosynthesis and regulation of terpenoid indole alkaloids in *Catharanthus roseus*. Phcog. Rev. 9 (17), 24–28.
- Zifkin, M., Jin, A., Ozga, J.A., Zaharia, L.I., Scherthaner, J.P., Gesell, A., Abrams, S.R., Kennedy, J.A., Constabel, C.P., 2012. Gene expression and metabolite profiling of developing highbush blueberry fruit indicates transcriptional regulation of flavonoid metabolism and activation of abscisic acid metabolism. Plant Physiol. 158, 200–224.

**UPLC and ESI-MS analysis of metabolites of *Rauvolfia tetraphylla* L. and their spatial localization using desorption electrospray ionization (DESI) mass spectrometric imaging**

P. Mohana Kumara<sup>\*a,c</sup>, R. Uma Shaanker<sup>b</sup> and T. Pradeep<sup>\*a</sup>

<sup>a</sup> *DST Unit of Nanoscience and Thematic Unit of Excellence, Department of Chemistry, Indian Institute of Technology Madras, Chennai, 600036, India,*

<sup>b</sup> *School of Ecology and Conservation, Department of Crop Physiology, University of Agricultural Sciences, GKVK, Bengaluru, 560065, India*

<sup>c</sup> *Center for Ayurveda Biology and Holistic Nutrition, The University of Trans-Disciplinary Health Sciences and Technology (TDU), Bengaluru, 560064*

**Corresponding authors:**

**Prof. T. Pradeep**

[pradeep@iitm.ac.in](mailto:pradeep@iitm.ac.in)

Phone: +91-44-2257 4208

Fax: +91-44-2257 0509/0545

and

**Dr. P. Mohana Kumara**

[monapatelpgatti@gmail.com](mailto:monapatelpgatti@gmail.com)

Mobile: 9790464058, Fax; +91-80-28567926

### Identification of indole alkaloids using exact mass and ESI MS/MS analysis

ESI MS analysis of the different parts (root, stem, leaf and fruits) of *R. tetraphylla* showed the presence of prominent metabolite signatures in the range of  $m/z$  150-1000 (**Table1**). Among the different tissues, roots contained relatively large number of indole alkaloids (Fig S2). Structural characterization of these indole alkaloids were done by both mass fragmentation analysis and accurate mass measurement (**Fig S2**) (Smith et al., 2005). A list of  $m/z$  values of the parent and fragment ions and their chemical formulae are given in **Table 1**.

Based on the masses obtained, we present below the salient results pertaining to exact masses and to the fragmentation ions.

Strictosidine ( $C_{27}H_{34}N_2O_9$ ; exact mass  $m/z$  531.2337), a key metabolic precursor in the synthesis of indole alkaloids was identified by ESI MS analysis in root and leaf. The identity was also confirmed by the characteristic fragmentations: at  $m/z$  514 due to loss of  $H_2O$ ,  $m/z$  499 due to loss of  $CH_3OH$ ,  $m/z$  351 is due loss of glucose,  $m/z$  222, 223 and  $m/z$  144 is due to breakage of C ring. These fragmentations corresponded with the published literatures and metabolite databases (Yamamoto et al., 2016) (**Fig S2a**). Here we present briefly the major alkaloids represented under three broad categories, namely, reserpine type, ajmalcine type and serpentine type of alkaloids.

#### Reserpine type of alkaloids

Yohimbine ( $C_{21}H_{26}N_2O_3$ ),  $m/z$  355.2 and exact mass of  $m/z$  355.2007, has a pentacyclic ring system with substitution at C16 and C17. The MS/MS spectrum showed five characteristic fragment ions at  $m/z$  337, 323, 224, 212 and 144. The product ions at  $m/z$  323 and 337 were produced due to the loss of  $CH_3OH$  and  $H_2O$  in terpene moiety, whereas the product ions at  $m/z$  224, 212 and 144 produced due to cleavage of C ring (**Fig S2b**). Correspondingly, the ion at  $m/z$  609.2 and exact mass  $m/z$  609.2802 was identified as reserpine ( $C_{33}H_{41}O_9N_2$ ). ESI MS fragmentation pattern of  $m/z$  609.2 showed the characteristic fragment ions at  $m/z$  397.2 due to loss of trimethoxybenzoic acid moiety and  $m/z$  195.0 due to cleavage of ester bond between trimethoxybenzoic acid from the rest of moiety. Further, fragment ion at  $m/z$  397.2 fragmented to  $m/z$  365.2 due to loss of methanol, and  $m/z$  236.01 due to loss of methanol followed by cleavage of C-ring. Fragment ion at  $m/z$  448.2 was also produced due to cleavage of C ring from the precursor ion (**Fig S2c**). The ion at  $m/z$  144 showed the presence of indole moiety fragmentation, this is one of the characteristic fragment confirming the molecule is the indole group of compounds (Bindu et al., 2014; Kumar et al., 2016a).

Similarly, few other reserpine like molecules  $m/z$  341.2, 371.2, 565.2, 579.2 were identified as yohimbic acid, 18-hydroxyepialloyohimbine, raunescine, deserpidine

respectively based on the exact mass and their mass fragmentation (**Fig S2d-i**). Yohimbic acid ( $m/z$  341.1862;  $C_{20}H_{25}N_2O_3$ ; **Fig S2d**) mass fragmented to  $m/z$  323 due to the loss of  $H_2O$  in terpene moiety, whereas the product ions at  $m/z$  196, 212 and 144 produced due to cleavage of C ring (**Fig S2b**). 18-hydroxyepialloyohimbine ( $m/z$  371.1961;  $C_{21}H_{26}N_2O_4$ ; **Fig S2e**) fragmented to  $m/z$  353 and 339, were due to the loss of  $CH_3OH$  and  $H_2O$  in terpene moiety, whereas the product ions at  $m/z$  240, 228 and 144 produced due to cleavage of C ring (**Fig S2c**). Deserpidine ( $m/z$  579.2698;  $C_{32}H_{38}N_2O_8$ ; **Fig S2 f-g**) and raunescine ( $m/z$  565.2542;  $C_{31}H_{36}N_2O_8$ ; **Fig S2h-i**) and showed the characteristic mass fragmentations similar to reserpine,  $m/z$  321.2 and  $m/z$  367.2 due to loss of trimethoxybenzoic acid moiety and  $m/z$  195.0 due to cleavage of ester bond between trimethoxybenzoic acid from the rest of moiety. Fragment ion at  $m/z$  448.2 was also produced due to cleavage of C ring from the precursor ion, respectively (**Fig S2 d-i**). Further, fragment ion of deserpidine at  $m/z$  397.2 fragmented to  $m/z$  365.2 due to loss of methanol, and  $m/z$  236.01 due to loss of methanol followed by cleavage of C-ring (**Fig S2d-i**) (Kumar et al., 2016a; Kumar et al., 2016b; Pandey et al., 2016).

### Ajmalcine type of alkaloids

The ion at  $m/z$  353.2 was identified as ajmalcine ( $m/z$  353.1851;  $C_{21}H_{25}N_2O_3$ ; **Fig S2j**). The product ions at  $m/z$  321 was produced due to the loss of  $CH_3OH$  in terpene moiety, whereas the product ions at  $m/z$  210, 222 and 144 were produced due to cleavage of C ring (**Fig S2j-k**). Similarly,  $m/z$  413.2 identified as reserpiline ( $m/z$  413.2068;  $C_{23}H_{29}N_2O_5$ ; **Fig S2k**). The mass fragmentation of  $m/z$  413.2 showed five characteristic fragment ions at  $m/z$  337, 224, 204 and 144. The product ions at  $m/z$  339 produced due to the loss of  $CH_3OH$  in terpene moiety, whereas the product ions at  $m/z$  224, 204 and 144 produced due to cleavage of C ring (**Fig S2i-k**) (Bindu et al., 2014; Kumar et al., 2015; Kumar et al., 2016b; Kumar et al., 2016c; Pandey et al., 2016; Sagi et al., 2016).

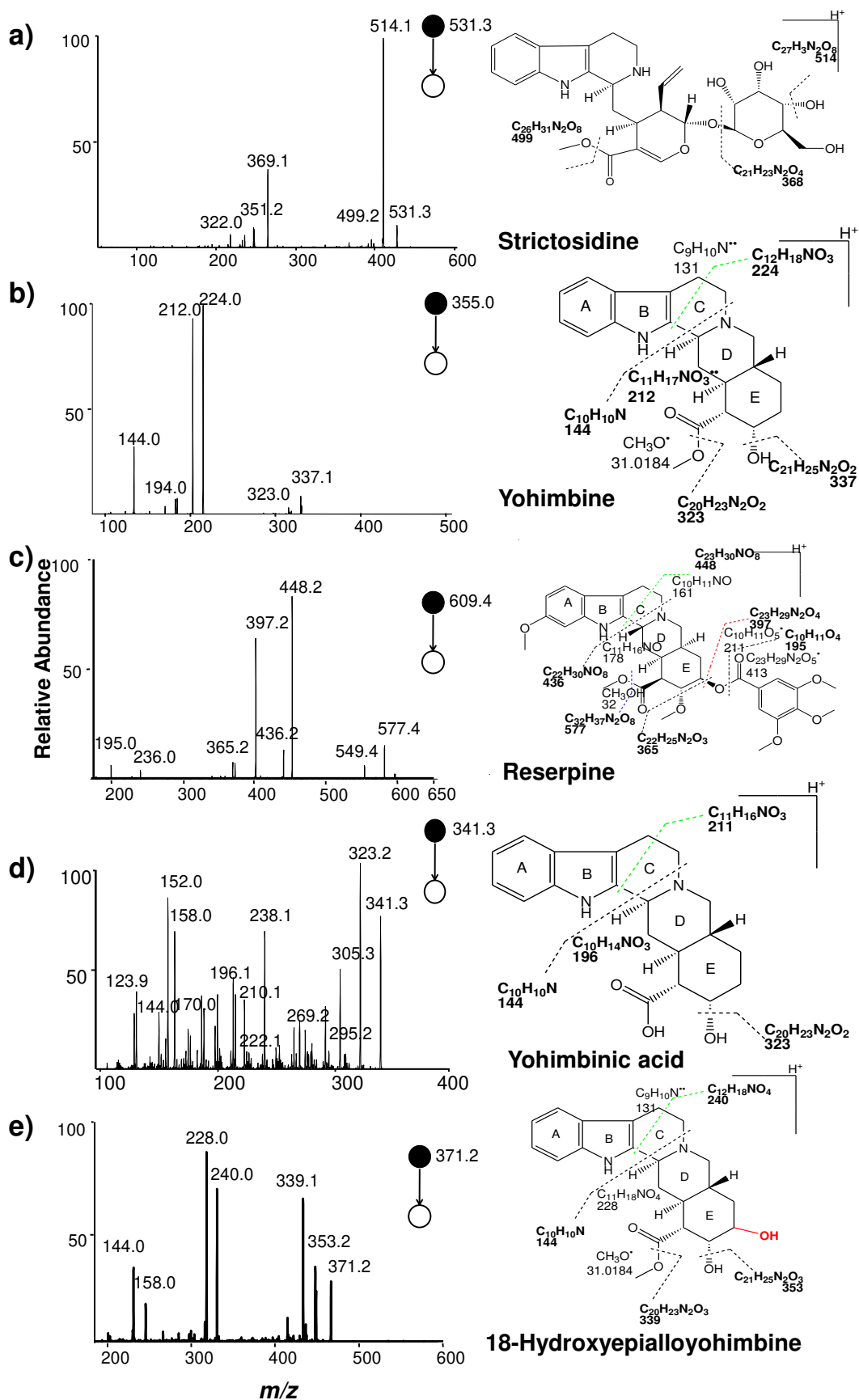
### Ajmaline type of alkaloids

The ion  $m/z$  327.2 at ajmaline ( $m/z$  327.2063;  $C_{20}H_{27}N_2O_2$ ; **Fig S2l**) showed the fragment ions at  $m/z$  309, 238, 210, 194, 182, 158, 144. The product ions at  $m/z$  309 and  $m/z$  291 were produced due to the successive losses of  $H_2O$  in terpene moiety, whereas the product ions at  $m/z$  238, 212, 194 and 144 were produced due to cleavage of C ring. Methyl indole derivative ( $m/z$  158) is formed by ring cleavage at C-ring and further loss of methyl group from nitrogen atom yields the base peak at  $m/z$  144 [ $C_{10}H_{10}N$ ]<sup>+</sup>. Loss of  $C_8H_7NO$  from protonated ion gives  $m/z$  194 [ $C_{12}H_{21}NO$ ]<sup>+</sup> (**Fig S2l-q**). Similarly, ions at  $m/z$  309.2, 311.1, 313.2, 323.2, 325.2 identified as sarpagine ( $m/z$  311.175;  $C_{19}H_{23}N_2O_2$ ; **Fig S2m**), 10-O-methylsarpagine ( $m/z$  325.1907;  $C_{20}H_{25}N_2O_2$ ; **Fig S2n-o**), tetraphyllicine ( $m/z$  309.1957;  $C_{20}H_{25}N_2O$ ; **Fig S2p**), mitoridine ( $m/z$  323.1749;  $C_{20}H_{23}N_2O_2$ ; **Fig S2q**) respectively. Identity of these

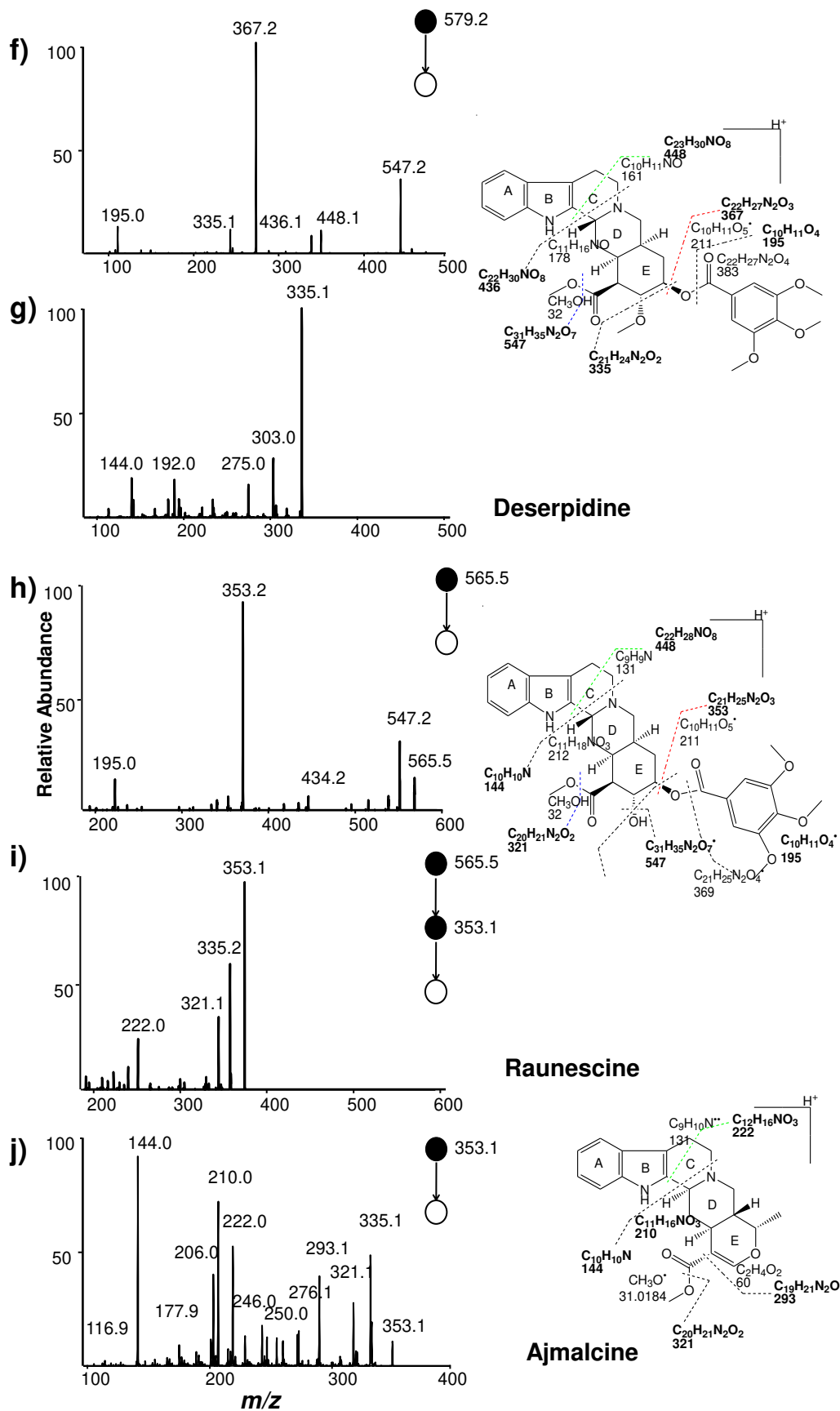
molecules was assigned based on the fragmentation patterns at C-ring cleavage (**Fig S2m-q**) (Bindu et al., 2014; Kumar et al., 2015; Kumar et al., 2016b; Kumar et al., 2016c; Pandey et al., 2016).

The ions at  $m/z$  349.1 were identified as serpentine ( $m/z$  349.1537;  $C_{21}H_{20}N_2O_3$ ). Serpentine showed the characteristic fragment ions at  $m/z$  317, 289, 277 and 263. The product ions at  $m/z$  317, 289 produced were due to the loss of  $CH_3OH$  and  $CO$  respectively, in terpene moiety, whereas the product ions at  $m/z$  277 and 263 produced were due to cleavage of E ring. One of the derivative of serpentine, demethyl serpentine was identified based on similar fragmentations (**Fig S2s-u**) (Kumar et al., 2016b).

# Supplementary information

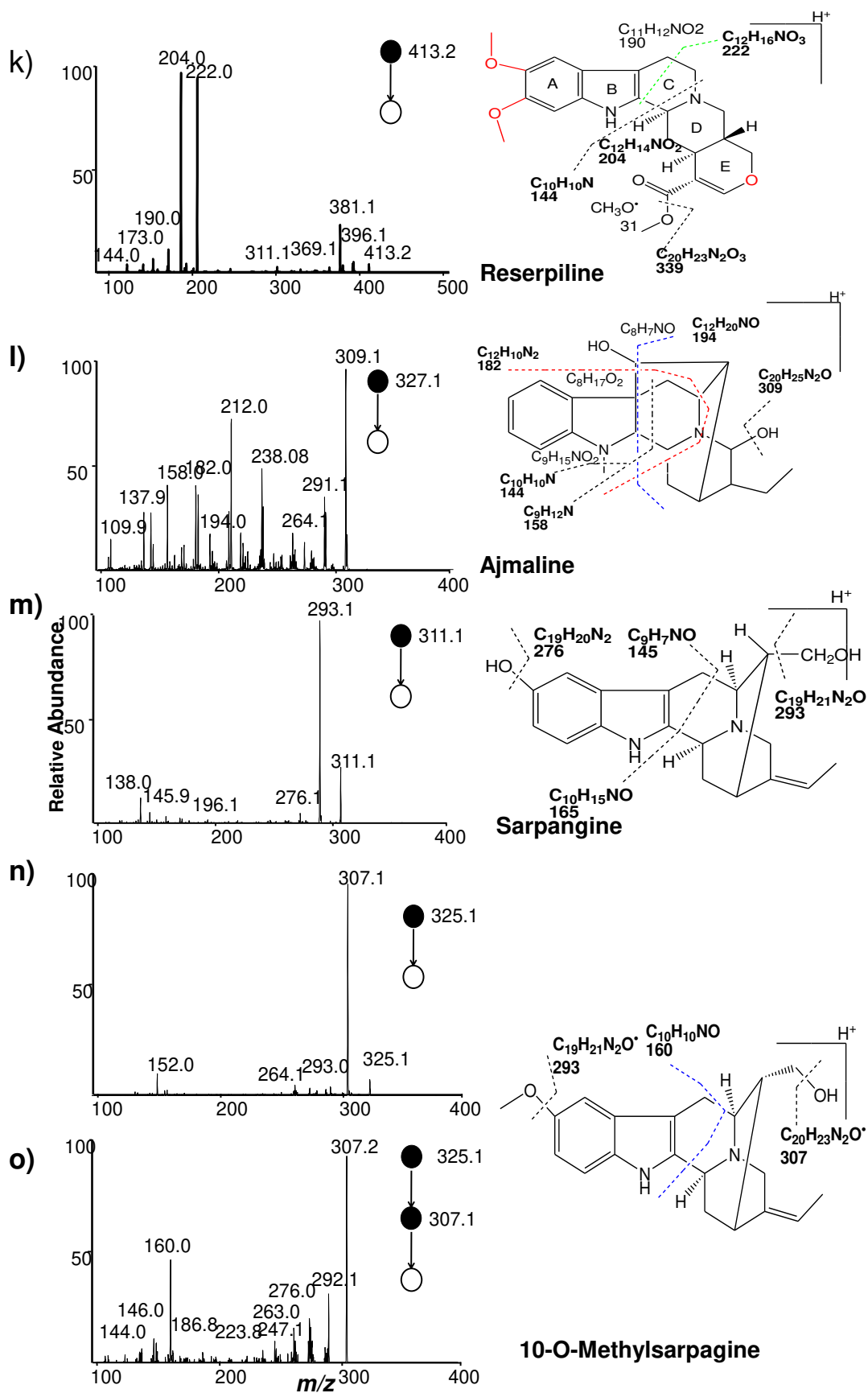


# Supplementary information

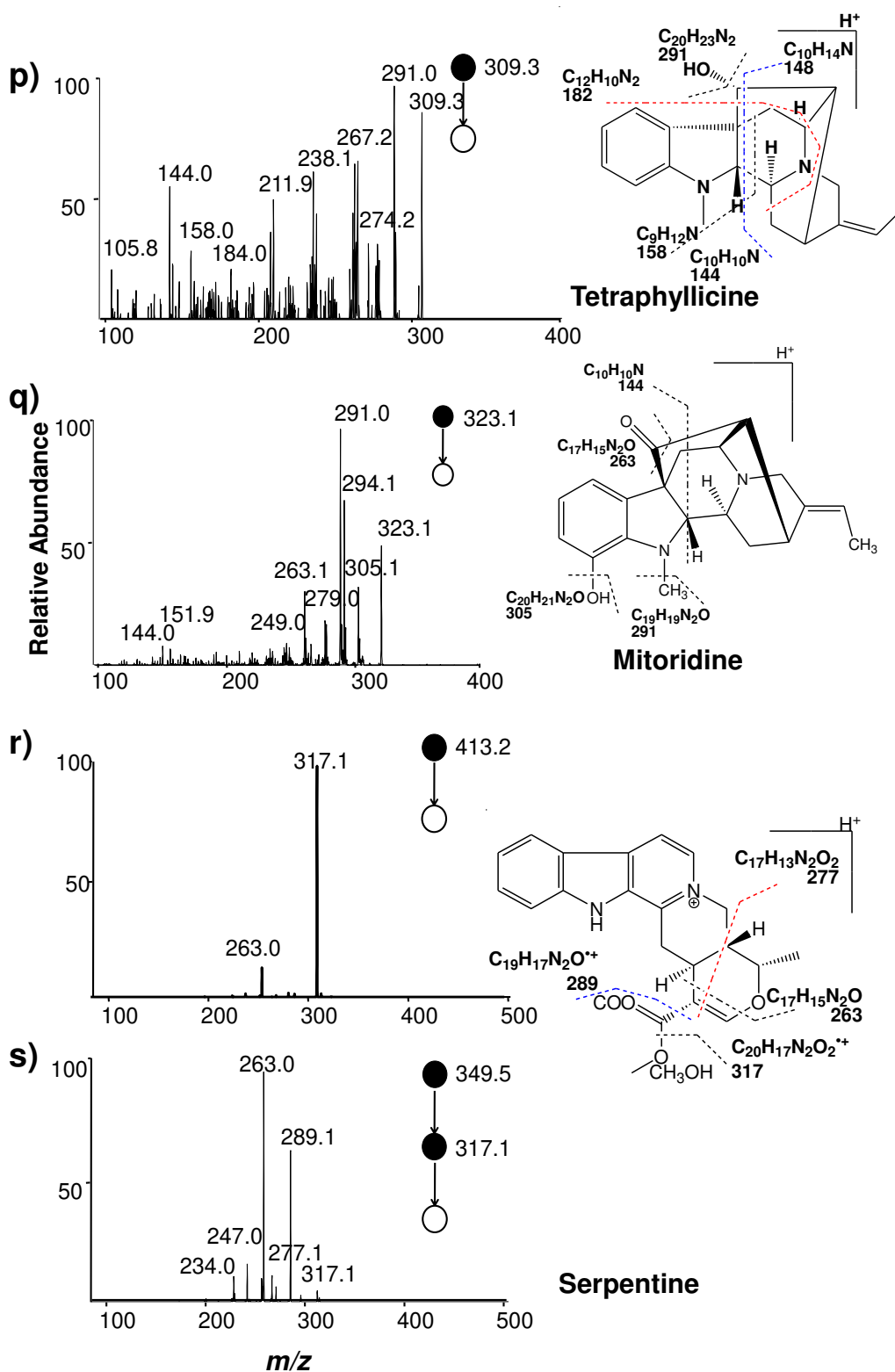




# Supplementary information



# Supplementary information



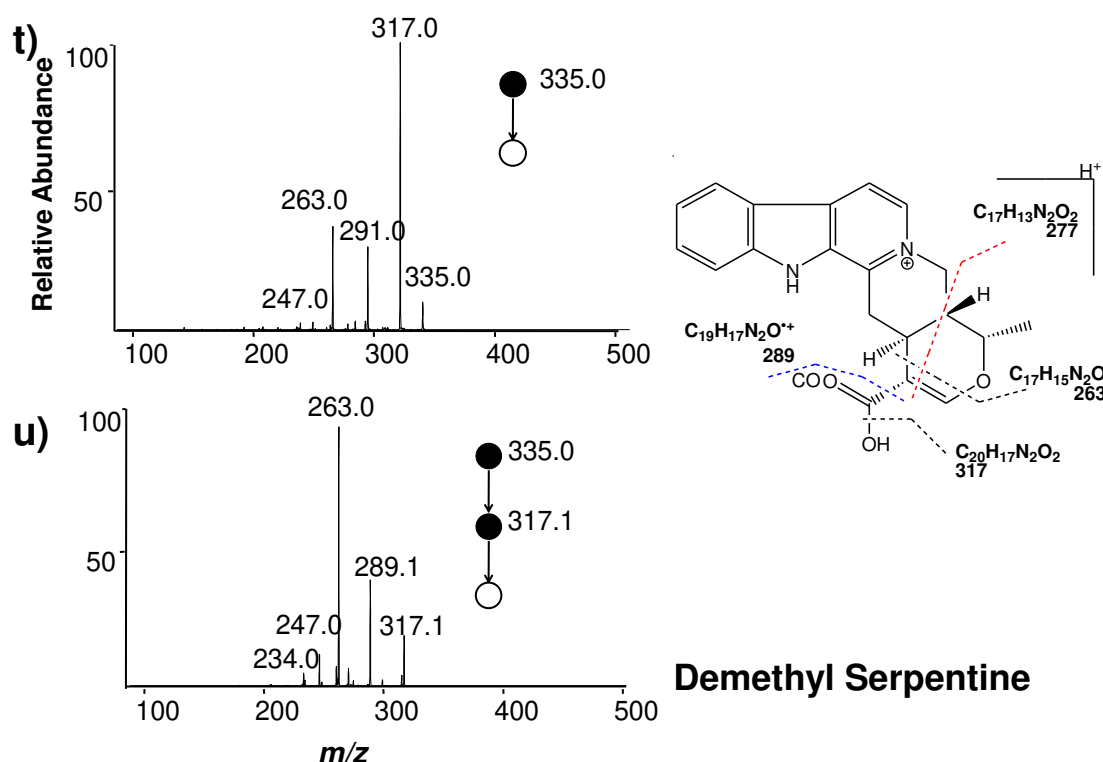


**Fig S2.** ESI MS/MS analysis of monoterpenoid indole alkaloids and their respective chemical structure and mass fragmentation patterns.

## References

- Bindu, S., Rameshkumar, K.B., Kumar, B., Singh, A., Anilkumar, C., 2014. Distribution of reserpine in *Rauwolfia* species from India“ HPTLC and LC-MS studies. *Ind Crops and Prod.* 62, 430-436.
- Kumar, S., Bajpai, V., Singh, A., Bindu, S., Srivastava, M., Rameshkumar, K.B., Kumar, B., 2015. Rapid fingerprinting of *Rauwolfia* species using direct analysis in real time mass spectrometry combined with principal component analysis for their discrimination. *Anal Methods.* 7, 6021-6026.
- Kumar, S., Singh, A., Bajpai, V., Kumar, B., 2016a. Identification, characterization and distribution of monoterpene indole alkaloids in *Rauwolfia* species by Orbitrap Velos Pro mass spectrometer. *J Pharma Biomed Anal* 118, 183-194.
- Kumar, S., Singh, A., Bajpai, V., Srivastava, M., Singh, B.P., Kumar, B., 2016b. Structural characterization of monoterpene indole alkaloids in ethanolic extracts of *Rauwolfia* species by liquid chromatography with quadrupole time-of-flight mass spectrometry. *J Pharma Anal.*
- Kumar, S., Singh, A., Bajpai, V., Srivastava, M., Singh, B.P., Ojha, S., Kumar, B.C.P.C.A.R., 2016c. Simultaneous Determination of Bioactive Monoterpene Indole Alkaloids in Ethanolic Extract of Seven *Rauwolfia* Species using UHPLC with Hybrid Triple Quadrupole Linear Ion Trap Mass Spectrometry. *Phytochem Anal.* 27, 296-303.

- Pandey, D.K., Radha, Dey, A., 2016. A validated and densitometric HPTLC method for the simultaneous quantification of reserpine and ajmalicine in *Rauvolfia serpentina* and *Rauvolfia tetraphylla*. *Revista Brasileira de Farmacognosia*.
- Sagi, S., Avula, B., Wang, Y.-H., Khan, I.A., 2016. Quantification and characterization of alkaloids from roots of *Rauvolfia serpentina* using ultra-high performance liquid chromatography-photo diode array-mass spectrometry. *Anal Bioanal Chem.*408, 177-190.
- Smith, C.A., I'Maille, G., Want, E.J., Qin, C., Trauger, S.A., Brandon, T.R., Custodio, D.E., Abagyan, R., Siuzdak, G., 2005. METLIN: a metabolite mass spectral database. *Ther Drug Monit.* 27, 747-751.
- Yamamoto, K., Takahashi, K., Mizuno, H., Anegawa, A., Ishizaki, K., Fukaki, H., Ohnishi, M., Yamazaki, M., Masujima, T., Mimura, T., 2016. Cell-specific localization of alkaloids in *Catharanthus roseus* stem tissue measured with Imaging MS and Single-cell MS. *Proc Natl Acad Sci U S A.* 113, 3891-3896.

# Publications with Other Groups

OPEN

# Effects of Chloride Concentration on the Water Disinfection Performance of Silver Containing Nanocellulose-based Composites

Janika Lehtonen<sup>1</sup>, Jukka Hassinen<sup>2\*</sup>, Riina Honkanen<sup>3</sup>, Avula Anil Kumar<sup>4</sup>, Heli Viskari<sup>1</sup>, Anu Kettunen<sup>3</sup>, Nikolaos Pahimanolis<sup>5</sup>, Thalappil Pradeep<sup>4</sup>, Orlando J. Rojas<sup>1,2</sup> & Olli Ikkala<sup>1,2</sup>

The availability of microbially-safe drinking water is a challenge in many developing regions. Due to the well-known antibacterial effect of silver ions, materials used for their controlled release have been widely studied for point-of-use water disinfection. However, even if it is in principle known that chloride anions can suppress the antibacterial efficiency of silver, the majority of previous studies, surprisingly, have not focused on chloride concentrations relevant for freshwaters and thus for practical applications. Here, we prepared low-cost nanocellulose-aluminium oxyhydroxide nanocomposites functionalized with silver nanoparticles. Field samples obtained from Chennai, India were used as a guideline for choosing relevant chloride concentrations for the antibacterial studies, i.e., 10, 90, and 290 ppm. The antibacterial performance of the material against *Escherichia coli* and *Bacillus subtilis* was demonstrated and the influence of chloride concentration on the antibacterial effect was studied with *E. coli*. A 1 h contact time led to bacterial reductions of 5.6 log<sub>10</sub>, 2.9 log<sub>10</sub>, and 2.2 log<sub>10</sub>, respectively. This indicates that an increase of chloride concentration leads to a substantial reduction of antibacterial efficiency, even within chloride concentrations found in freshwaters. This work enables further insights for designing freshwater purification systems that utilize silver-releasing materials.

Waterborne diseases caused by micro-organisms are a major cause of death worldwide and a grand challenge remains to find sustainable solutions for their control and elimination<sup>1</sup>. The need for affordable, efficient, eco-friendly, and easily applicable technologies for removing micro-organisms is urgent. Point-of-use (POU) water treatment is often used when drinking water is retrieved from untreated natural sources<sup>2</sup> where centralized water treatment facilities are not available<sup>3</sup>. Chlorine treatment is a generic method for household water disinfection, but the formation of toxic byproducts makes it problematic<sup>4</sup>, resulting in a need for alternative methods. Nanotechnology and especially nanoparticles have been studied as a possible solution to challenges related to water disinfection<sup>5,6</sup>. The use of silver as an antibacterial agent dates back already to the first century BC<sup>7</sup>. Nowadays, nanosilver is used in a variety of consumer products<sup>8,9</sup> and these products are generally based on silver nanoparticles (AgNPs) that can be produced by chemical reduction of silver salts<sup>10</sup>. Several different materials containing silver in its colloidal form, particularly nanoparticles, have been studied for POU water treatment<sup>3,11,12</sup>. Chitosan cryogels<sup>13</sup>, cellulosic material such as paper filters<sup>14</sup>, alginate beads<sup>3</sup>, ceramic cubes<sup>15</sup> and filters<sup>16,17</sup>, poly (sodium acrylate) cryogels<sup>18</sup>, and cotton textiles<sup>6</sup> loaded with AgNPs have been demonstrated for POU water treatment. However, research in the field still involves subtleties of e.g. controlling the concentration of released silver ions and the economic feasibility of the materials.

A low-cost material based on chitosan and aluminium oxyhydroxide embedded with AgNPs has previously been developed for a gravity-driven filtration unit<sup>19</sup>. Inspired by that work, and to improve the economic feasibility of the product, we synthesized and characterized a composite material comprising of commercially available

<sup>1</sup>Department of Bioproducts and Biosystems, School of Chemical Engineering, Aalto University, P. O. Box 16300, FI-00076, Aalto, Espoo, Finland. <sup>2</sup>Department of Applied Physics, School of Science, Aalto University, P. O. Box 16300, FI-00076, Aalto, Espoo, Finland. <sup>3</sup>Industrial Water Ltd., Moreenikatu 2 B, FI-04600, Mäntsälä, Finland. <sup>4</sup>DST Unit of Nanoscience (DST UNS) and Thematic Unit of Excellence (TUE), Department of Chemistry, Indian Institute of Technology Madras, Chennai, 600036, India. <sup>5</sup>Betulum Ltd., Tekniikantie 2, FI-02150, Espoo, Finland. \*email: [jukka.hassinen@aalto.fi](mailto:jukka.hassinen@aalto.fi)

cationic cellulose nanofibrils (cCNF) and aluminium oxyhydroxide, which can retain AgNPs. Nanocellulose, including cellulose nanofibrils (CNF), is a renewable high strength nanoscopic material with interesting properties such as relatively high aspect ratio and broad range of easily applicable chemical modifications<sup>20</sup>, making it, e.g., an attractive reinforcing component for nanocomposites. CNFs are commonly prepared by mechanical treatments combined with chemical treatments and the resulting nanofibrils have lateral dimension in the order of 5–50 nm, depending on the source and preparation method. The chemical modification results in functionalization of the fibrils<sup>21</sup>, as for example in this work, with cationic quaternary ammonium groups. Importantly, cCNF was chosen as the starting material instead of unmodified CNF due to its inherent antibacterial properties<sup>21,22</sup>, thus further promoting the intended function of the composite material. The fabricated materials act as carriers for the AgNPs and release  $\text{Ag}^+$  when brought into contact with water.

The mechanism of action of AgNPs for causing antibacterial effect is not yet fully understood<sup>10,23</sup>. However, there is consensus that the oxidation of metallic silver to silver ions ( $\text{Ag}^+$ ) is required for achieving an antibacterial effect<sup>7,24,25</sup>, although nanoparticle-specific effects have also been considered as one cause of toxicity<sup>10,26</sup>. AgNPs have been shown to be non-toxic to *Escherichia coli* when conducting tests under strictly anaerobic conditions, where  $\text{Ag}^+$  release is precluded, thus suggesting that antibacterial activity of AgNPs would solely be due to  $\text{Ag}^+$  release<sup>27</sup>. Factors affecting the release kinetics of  $\text{Ag}^+$  from AgNPs include size of particles, temperature, shape<sup>28</sup>, the surface ligand<sup>29</sup>, and the composition of the surrounding medium<sup>7</sup>.

Silver ions can form complexes with different anions commonly present in freshwaters, thereby reducing the amount of free  $\text{Ag}^+$  in water. Chloride concentration ( $[\text{Cl}^-]$ ) has been recognized as a significant factor decreasing the antibacterial performance of silver ions due to the low solubility product of AgCl. In addition, complexation with e.g. sulfide and organic matter in freshwaters can result in decrease of free  $\text{Ag}^+$  concentration<sup>30</sup>. In freshwaters,  $[\text{Cl}^-]$  can vary significantly. Still, this factor has not been properly considered when investigating the efficiency of silver-releasing materials for POU water purification. An objective of this study was first to screen realistic chloride concentrations relevant for applications and then to explore the effect of salinity in simulated freshwaters and more specifically,  $[\text{Cl}^-]$ , on the antibacterial effect of the composites on *Escherichia coli*, a bacterium typically used as a biological indicator of drinking water safety<sup>31</sup>. *Bacillus subtilis* was also used as a reference for a gram-positive model bacterium.

Unfortunately, the antibacterial tests of silver-releasing materials in laboratory conditions are often conducted in solutions with  $[\text{Cl}^-]$  irrelevant to freshwaters in rural areas. The tests are often performed in very low  $[\text{Cl}^-]$ , such as highly diluted buffer solution or deionized water<sup>4,32</sup>, or very high  $[\text{Cl}^-]$  such as undiluted PBS buffer where  $[\text{Cl}^-]$  is typically around 5000 ppm<sup>33</sup>. When silver concentration is high, charged silver polychloride complexes are formed, which can contribute to the antibacterial activity<sup>34</sup>. Additionally, several studies where the influence of  $[\text{Cl}^-]$  on AgNP toxicity has been considered, do not use  $[\text{Cl}^-]$  occurring in freshwaters as a basis for choosing the studied conditions, resulting in studies with low concentrations such as 12.5 ppm and high concentrations such as around 5000 ppm<sup>24,25,35</sup>. Therefore, the fact that  $[\text{Cl}^-]$  can vary significantly in freshwater sources and that this can affect silver-based water disinfection is the main issue we highlight in this work.

In this work, we used simulated freshwaters with  $[\text{Cl}^-]$  in the range relevant to possible rural drinking water sources. Two different contact times (1 h and 2 h) between the composite and water were used. First, the antibacterial activity against *E. coli* and *B. subtilis* was compared and tests were continued with *E. coli* to study the influence of  $[\text{Cl}^-]$  on the antibacterial activity. Silver release from the composite as a function of time was also studied. Finally, based on our observations, we give an evaluation of the potential of the composites for use in water disinfection.

## Results

**Characterization.** The cCNF (see Methods) was provided by Betulium Ltd. and was first imaged by transmission electron microscopy (TEM) (Fig. 1a). The material was found to consist of fibrils with widths ranging from 5 to 20 nm and lengths up to few  $\mu\text{m}$ . Data from the quantification of ammonium groups on the fibrils by conductometric titration was provided by the manufacturer (0.63 mmol/g).  $\zeta$ -potential measurements (Supplementary Fig. S1) confirmed the positive surface charge of cCNF in the whole pH range tested (pH 3–11). FTIR analysis of cCNF (Fig. 1b) revealed typical absorption peaks of cellulose ( $\nu(\text{O}-\text{H})$  at  $3330\text{ cm}^{-1}$ ,  $\nu_{\text{asym}}(\text{C}-\text{H})$  and  $\nu_{\text{sym}}(\text{C}-\text{H})$  at  $2900\text{ cm}^{-1}$ ,  $\delta(\text{H}_2\text{O})$  at  $1630\text{ cm}^{-1}$  and  $\nu(\text{C}-\text{O})$  at  $1130\text{ cm}^{-1}$ ). The absorption at  $1480\text{ cm}^{-1}$  was assigned to the methyl group of quaternary ammonium units. cCNF was chosen as the starting material due to its inherent antibacterial properties and economic feasibility. Composites were also prepared from unmodified CNF but preliminary tests indicated possible promotion of bacterial growth, thus suggesting to select cCNF.

cCNF together with  $\text{Al}_2(\text{SO}_4)_3$  was used to produce both composites without AgNPs (cCNFAl) and with AgNPs (cCNFAl<sub>Ag</sub>). Aluminium is present as hydrated  $\text{Al}^{3+}$  ions at low pH. An alkali treatment during the synthesis of the composite results in the formation of aluminium hydroxide, and aging the precipitate leads to the formation of aluminium oxyhydroxide ( $\text{AlOOH}$ )<sup>36</sup>. The synthesis process is described in Fig. 2. The phases in the cCNFAl<sub>Ag</sub> composite were identified by X-ray diffraction (XRD) (Supplementary Fig. S2). The XRD pattern of the cCNFAl<sub>Ag</sub> composite prepared from high purity  $\text{Al}_2(\text{SO}_4)_3$  hydrate shows reflections coinciding with the crystalline  $\text{AlOOH}$  boehmite phase<sup>37</sup>. The widths of the diffraction peaks suggest the size of the crystallites to be in the range of 4–5 nm based on the Scherrer equation. To ensure the economic feasibility of the end product, further experiments were focused on a composite prepared from technical grade  $\text{Al}_2(\text{SO}_4)_3$  hydrate. Therein, the precipitate was in an amorphous form<sup>37</sup>. However, both these materials could accommodate AgNPs and thus worked in the antibacterial test. The reflections from AgNPs were not resolved due to the small concentration of silver in the composite (0.67 wt-%). However, from a sample containing 1.12 wt-% silver, the reflections could be detected, and the size of silver crystallites could be estimated to be 15 nm based on the Scherrer equation.

Scanning electron microscope (SEM) images of both the composites (Fig. 3a,b) showed qualitatively similar porous structures indicating that the *in situ* AgNP synthesis did not cause any significant overall changes

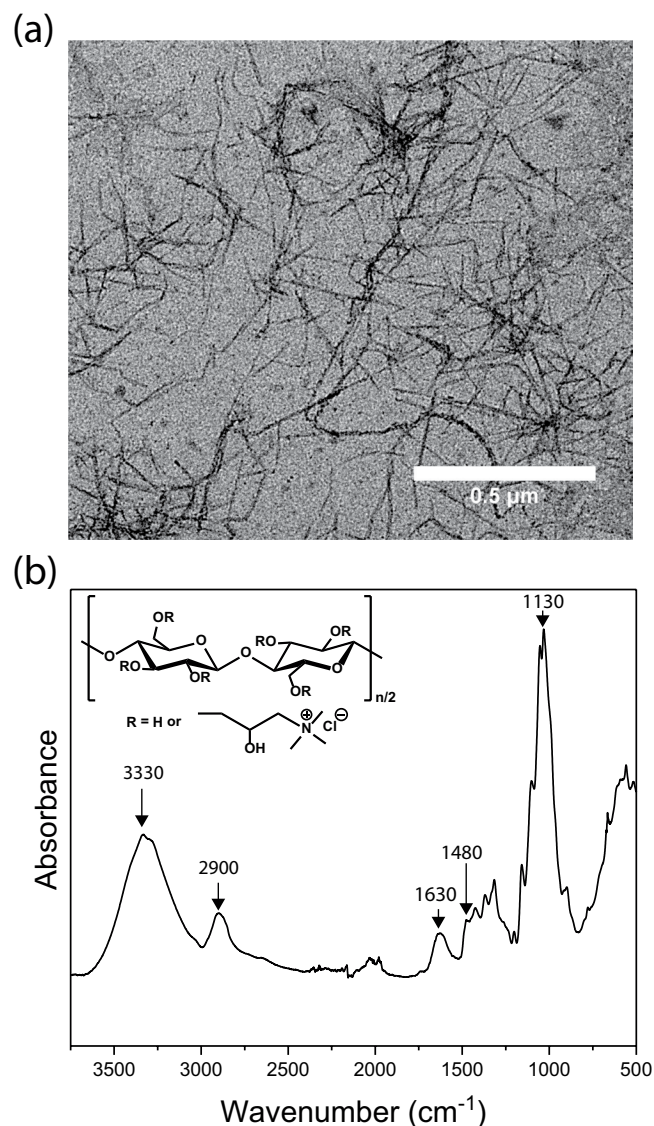


**Figure 1.** Characterization of cationic CNF (cCNF). (a) TEM image and (b) FTIR spectrum of cCNF (inset: chemical structure of cCNF).

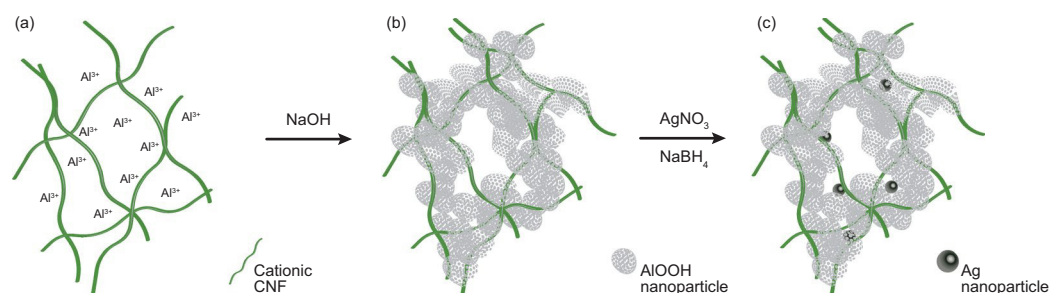


**Figure 2.** Synthesis of the cCNFAl and cCNFAl<sub>Ag</sub> composites. (a) Solution of  $\text{Al}_2(\text{SO}_4)_3$  and cationic CNF, where  $\text{Al}^{3+}$  complexes with the fibrils. (b) Precipitation of the material with NaOH and the formation of AlOOH. (c) Synthesis of embedded AgNPs into the composite matrix.

to the morphology of the material. More concrete proof of the similarities of the porous structure was provided by the high BET surface areas of the composites, which were  $150 \text{ m}^2/\text{g}$  for both compositions. SEM with energy-dispersive X-ray spectroscopy (EDX) (Fig. 3c and Supplementary Fig. S3) was used for elemental analysis and the elemental mapping confirmed the presence of silver in the composite. The surface charge of the composite



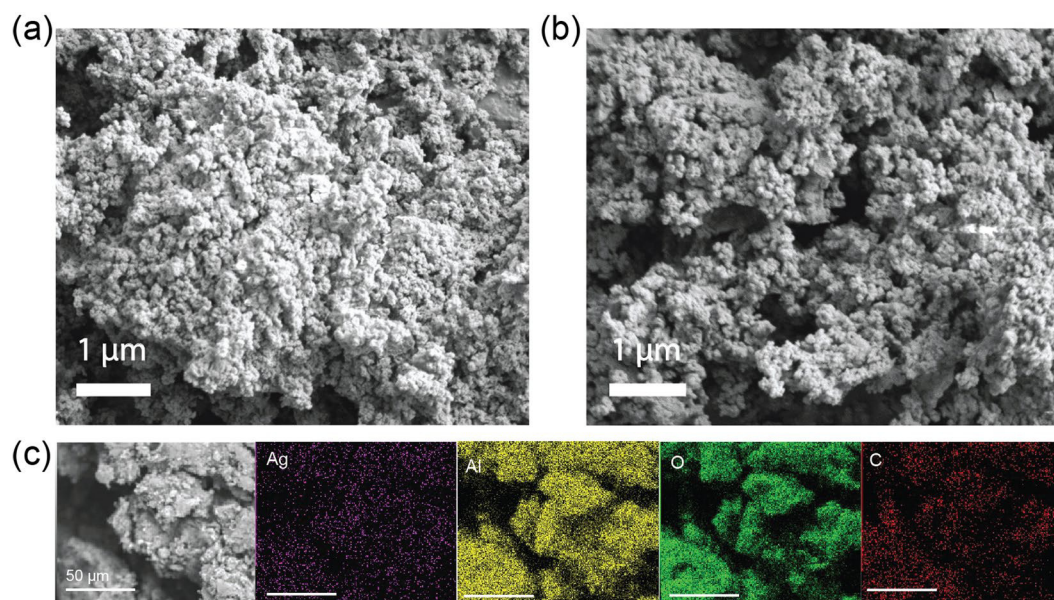


**Figure 3.** SEM images of composite materials. (a) cCNFAl nanocomposite, (b) cCNFAl<sub>Ag</sub> nanocomposite and (c) SEM-EDX elemental mapping of cCNFAl<sub>Ag</sub> nanocomposite (all scale bars are 50 μm).

was determined by conductometric titration from the cCNFAl composite to avoid interference from the Ag<sup>+</sup> dissolution from the AgNPs. The charge was 0.8 mmol/g indicating a positive surface charge of the composite (Supplementary Fig. S4).

**Antibacterial tests.** The antibacterial effect of AgNPs against various Gram-negative and Gram-positive bacteria is well known<sup>38–41</sup>. However, the precise mechanism of the action of AgNPs on micro-organisms is not yet fully understood but protein inactivation and DNA damage have been suggested as possible causes<sup>1,8,38</sup>. Especially, interaction with thiol groups has been related to the antibacterial mechanism of silver<sup>5,42</sup>. Ag<sup>+</sup> has also been shown to damage the cell membrane<sup>1,5,43,44</sup>. Both model organisms used in this work, Gram-negative *E. coli* and Gram-positive *B. subtilis*, are widely used in antibacterial studies. *E. coli* is a common cause of diarrheal diseases<sup>45</sup> and can survive in various environments<sup>46</sup> and is therefore a good reference bacterium to test materials for water purification. The compositions of the simulated freshwaters used for the antibacterial tests in this work are presented in Supplementary Table S1.

**Antibacterial tests in simulated freshwater using *E. coli* and *B. subtilis*.** First, the antibacterial effectiveness of the cCNFAl<sub>Ag</sub> composite on the two different bacteria was compared in simulated freshwater with 1% of Luria Bertani (LB) medium (Fig. 4). The small amount of medium introduced into the simulated freshwater with the inoculation of bacteria was found to be necessary to ensure the viability of *B. subtilis* for the duration of the experiment. This resulted in a final [Cl<sup>−</sup>] of 120 ppm, referred to as Cl<sup>−</sup><sub>120ppm+nutrient</sub>. The data indicates that the antibacterial effect was more pronounced in the case of *B. subtilis* compared to *E. coli* (6.6 log<sub>10</sub> reduction compared to 2 log<sub>10</sub> reduction after 2 h, respectively). It can be also observed that the small amount of nutrient caused bacterial growth in the control tests without the composite. Interestingly, the growth of *B. subtilis* was faster than the growth of *E. coli* in the control tests. The lower initial concentration and faster growth rate of *B. subtilis* compared to *E. coli* could have enhanced the antibacterial effect. Stronger antibacterial activity of AgNPs or AgNP-embedded materials against *B. subtilis* compared to *E. coli* has also been observed in some previous studies<sup>18,43,47</sup>. However, also contradictory results, such as better activity of AgNP-containing methacrylic acid copolymer beads on Gram-negative bacteria compared to Gram-positive bacteria, have been reported<sup>48</sup>.

**Effect of [Cl<sup>−</sup>] on antibacterial activity.** In this study, the goal was to focus on [Cl<sup>−</sup>] relevant to freshwaters and typical drinking water sources. Therefore, the [Cl<sup>−</sup>] and *E. coli* concentrations were analyzed from samples collected from possible drinking water sources in the Indian Institute of Technology Madras campus, Chennai, India (Supplementary Table S2). These results indicate that there can be significant variations in [Cl<sup>−</sup>] of possible drinking water sources. Based on the collected data, 10 ppm, 90 ppm and 290 ppm, referred to as Cl<sup>−</sup><sub>10ppm</sub>, Cl<sup>−</sup><sub>90ppm</sub>, and Cl<sup>−</sup><sub>290ppm</sub>, respectively, were selected to represent typical [Cl<sup>−</sup>] in purified drinking water, surface water, and well water, respectively. In addition, Cl<sup>−</sup><sub>290ppm</sub> coincides with the taste threshold of Cl<sup>−</sup>, therefore being the highest concentration relevant to drinking water purposes<sup>49</sup>.

Tests were continued with *E. coli* by studying the situation with no culture medium added in Cl<sup>−</sup><sub>10ppm</sub>, Cl<sup>−</sup><sub>90ppm</sub>, and Cl<sup>−</sup><sub>290ppm</sub> simulated freshwaters (Fig. 5). As a background, antibacterial tests with AgNPs and silver-releasing materials have previously been performed in different bacterial culture media<sup>50,51</sup>, phosphate buffer<sup>3,16</sup>, PBS buffer<sup>18,33</sup>, simple aquatic media (for example containing only NaCl and KCl<sup>52</sup>), dechlorinated tap water<sup>53</sup> or

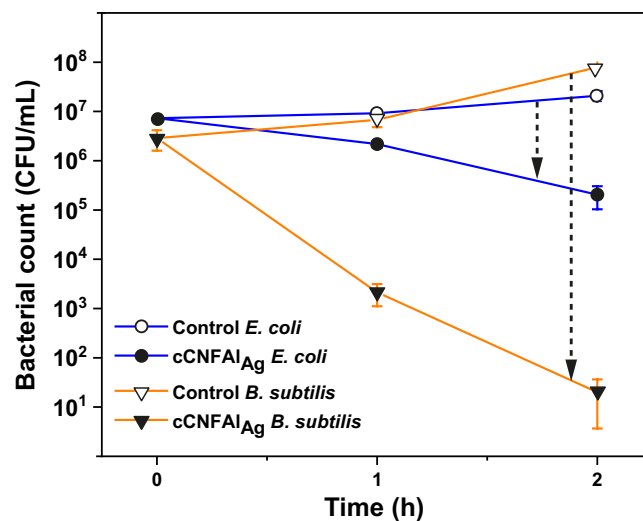


**Figure 4.** Antibacterial effect of the cCNFAI<sub>Ag</sub> composite against *E. coli* and *B. subtilis* in simulated freshwater ( $\text{Cl}^-$  120ppm + nutrient).

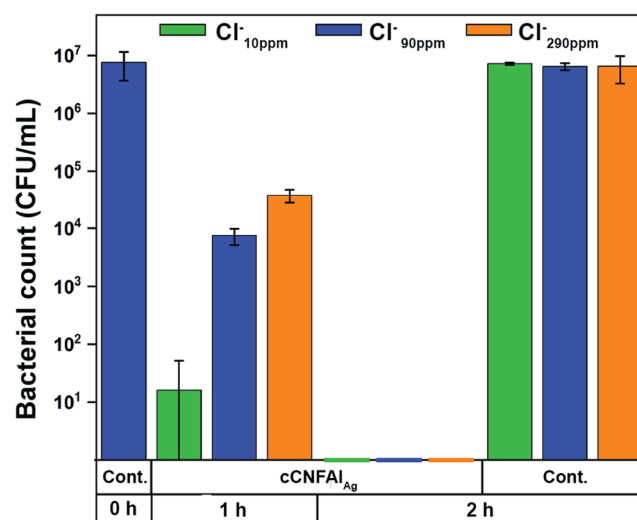


**Figure 5.** Influence of chloride concentration. The antibacterial activity of cCNFAI<sub>Ag</sub> composite against *E. coli* in  $\text{Cl}^-$  10ppm,  $\text{Cl}^-$  90ppm, and  $\text{Cl}^-$  290ppm simulated freshwaters.

deionized water<sup>32</sup>. However, in these cases,  $[\text{Cl}^-]$  is typically either very high or very low compared to freshwaters. Several studies have also been conducted using natural drinking waters or freshwaters<sup>54–56</sup>. However,  $[\text{Cl}^-]$  is often not reported or considered when interpreting results. Since the composition of water strongly affects the antibacterial efficiency, it is difficult to compare the results of these studies, thus urging the present studies.

The results in Fig. 5 indicate that, as expected, the absence of residual culture medium enhanced the antibacterial activity against *E. coli* compared to the situation where nutrients were present. After 1 h of incubation in the absence of nutrients in  $\text{Cl}^-$  90ppm, the cCNFAI<sub>Ag</sub> composite caused 2.9 log<sub>10</sub> reduction in bacterial plate count compared to 0.6 log<sub>10</sub> reduction in the presence of nutrients. When nutrients were present, it can be assumed that both the bacteria growth and complexation of  $\text{Ag}^+$  with the organic components of LB medium could reduce the antibacterial effect. In natural waters, bacterial growth is typically limited by low concentrations of appropriate carbon and energy sources<sup>57</sup>. Therefore, the conditions without nutrients are assumed to be closer to the state of bacteria populations in natural waters compared to water with added nutrients. The results also indicated good viability of bacteria in the control samples for the duration of the experiments, thus confirming that the antibacterial effects observed were due to the cCNFAI<sub>Ag</sub> composite.

For achieving an antibacterial effect in water with silver, the release of  $\text{Ag}^+$  is crucial. Water chemistry can impact the kinetics of the release and speciation of  $\text{Ag}^+$ .  $\text{Ag}^+$  can form complexes with  $\text{Cl}^-$  leading to the formation of both insoluble and soluble  $\text{AgCl}_x^{(x-1)-}$  species depending on the  $\text{Cl}/\text{Ag}$  ratio<sup>58</sup>. Thus, presence of  $\text{Cl}^-$  can reduce the amount of free  $\text{Ag}^+$  and consequently the antibacterial effect can be reduced<sup>59</sup>. Therefore, the influence

of  $[\text{Cl}^-]$  on the antibacterial activity of  $\text{cCNFAl}_{\text{Ag}}$  against *E. coli* was evaluated by comparing the antibacterial activity of the composite in  $\text{Cl}^-_{10\text{ppm}}$ ,  $\text{Cl}^-_{90\text{ppm}}$ , and  $\text{Cl}^-_{290\text{ppm}}$  simulated freshwaters. The amount of viable bacteria after 1 h contact time increases with increasing  $[\text{Cl}^-]$ , as observed in Fig. 5. This clearly indicates that decrease of  $[\text{Cl}^-]$  increases the antibacterial efficacy of the  $\text{cCNFAl}_{\text{Ag}}$  composite. After 2 h contact time the live bacteria count in all the simulated freshwaters was 0, indicating that with longer contact times the  $[\text{Cl}^-]$  is not as crucial for the antibacterial efficiency of  $\text{cCNFAl}_{\text{Ag}}$  as with shorter contact times, thus demonstrating potential for water disinfection.

Several studies have investigated the influence of  $[\text{Cl}^-]$  on the antibacterial activity of free AgNPs in the colloidal form<sup>24,25,35,58</sup>. Increased  $[\text{Cl}^-]$  was found to shift the dominant aqueous silver species to  $\text{AgCl}_x^{(x-1)-}$  which were found to be less toxic to *E. coli*, thus reducing the antibacterial efficiency of AgNPs. As the charge on the dominant species  $\text{AgCl}_x^{(x-1)-}$  decreased, the antibacterial efficiency also decreased<sup>35</sup>. Low concentrations of  $\text{Cl}^-$  (12.5 ppm) have been reported to have no effect on the antibacterial properties of AgNPs<sup>24</sup>. The antibacterial effect of polyvinylpyrrolidone coated AgNPs on *E. coli* was significantly decreased in  $[\text{Cl}^-]$  of 350 ppm<sup>25</sup>. This concentration is in the same range as the  $[\text{Cl}^-]$  of the  $\text{Cl}^-_{290\text{ppm}}$  simulated freshwater used in this study. Another study showed significant reduction in antibacterial activity against *E. coli* in phosphate buffer with 12 ppb  $\text{Ag}^+$  when  $[\text{Cl}^-]$  was 75–150 ppm compared to 0–50 ppm<sup>15</sup>.

Typical contact times used in experiments for testing antimicrobial activity of AgNP containing materials in water are less than 1 h<sup>33</sup>, but longer contact times up to 24 h have also been reported<sup>48,60</sup>. In this study, relatively long contact times, 1 h and 2 h, were chosen to see the influence of  $[\text{Cl}^-]$  on the antibacterial effectiveness of the  $\text{cCNFAl}_{\text{Ag}}$  composite. However, it should be noted that the initial bacterial concentrations in this study were high compared to typical reported concentrations in natural waters (for instance  $10^2$ – $10^3$  CFU/mL in rural India<sup>59</sup> and around  $1$ – $2 \times 10^2$  total coliforms/mL and  $10^2$ – $10^6$  CFU/mL heterotrophic bacteria in river waters in South Africa<sup>61</sup>). Considering this, it can be argued that shorter contact times could be sufficient in real life applications to achieve satisfactory antibacterial effects. The amount of material used in the experiments also influences the antibacterial effect and in this study we used contact times that were suitable to show the antibacterial effect with the material amount used (4 g/L). It should also be noted that the experiment was conducted within two weeks after the preparation of the material. The antibacterial activity of the material was found to decrease during long-term storage of the composite in ambient conditions, which is likely explained by the oxidation of AgNPs over time leading to passivation of the AgNP surfaces. This was evident based on an experiment conducted after one month of the composite preparation. No viable bacteria were detected in  $\text{Cl}^-_{10\text{ppm}}$  and  $\text{Cl}^-_{90\text{ppm}}$  after 2 h contact time, but viable bacteria were observed in  $\text{Cl}^-_{290\text{ppm}}$ .

In addition to  $[\text{Cl}^-]$ , there are several other factors that can influence the antibacterial effect of AgNPs. In natural waters, binding can occur to dispersed organic matter such as humic acid, which reduces the amount of dissolved silver<sup>7</sup>. Thiols present in organic matter have been predicted to compete with  $\text{Cl}^-$ <sup>62</sup>. Sunlight irradiation<sup>23</sup>, other electrolytes, pH, carbonate concentration<sup>59</sup>, and dissolved oxygen have also been shown to affect antibacterial efficiency of silver<sup>63</sup>. In this work, we used simulated freshwaters instead of real water samples to quantify the influence of  $[\text{Cl}^-]$  to the antibacterial effect of silver-releasing materials based on AgNPs. To apply silver-releasing materials for real-life water purification applications, many other factors including preservation of the AgNPs during storage and the microflora composition of the water to be purified need to be considered as well. These would be interesting aspects to focus on in future studies on silver-based materials for POU water disinfection.

The  $\text{cCNFAl}$  composite not containing AgNPs was used as a reference material and was found to slightly decrease the bacterial count in  $\text{Cl}^-_{90\text{ppm}}$  (0.5  $\log_{10}$  reduction after 1 h incubation) (Supplementary Fig. S5). This could have been caused by the adsorption of bacteria on the positively charged composite material (surface charge 0.8 mmol/g at pH 7.4). Another possibility is that  $\text{cCNFAl}$  has minor antibacterial properties due to the inherent cationic charge of the material, as shown in the case of  $\text{cCNF}$  matrix<sup>21,22</sup>. The antibacterial effect of positively charged materials is based on their interaction with the negatively charged phospholipids in the cell membranes of bacteria. Even though  $\text{cCNFAl}$  caused a minor decrease of the bacterial count, the antibacterial activity of  $\text{cCNFAl}_{\text{Ag}}$  was significantly higher.

**Silver release and speciation.** The United States Environmental Protection Agency indicates 100 ppb as a health advisory lifetime maximum level of silver in its secondary drinking water regulations<sup>64</sup>. On the other hand, it has been reported that a minimum concentration of silver of 50 ppb is needed to achieve antibacterial effect in typical natural waters<sup>59</sup>. Therefore, a major challenge in silver-based water purification is to develop a material that releases the required amount of  $\text{Ag}^+$  to achieve antibacterial effect but restricts the concentrations to a level regarded safe for human health. Silver dissolution from the  $\text{cCNFAl}_{\text{Ag}}$  composite was determined by inductively coupled plasma mass spectrometry (ICP-MS) in separate tests without bacteria present in  $\text{Cl}^-_{90\text{ppm}}$  and  $\text{Cl}^-_{120\text{ppm}+\text{nutrient}}$  using the composite concentration of 4 g/L. Figure 6 shows the release of silver from  $\text{cCNFAl}_{\text{Ag}}$  as a function of time, showing that silver dissolution is clearly time dependent and that the silver concentration saturates to below 100 ppb in both  $\text{Cl}^-_{90\text{ppm}}$  and  $\text{Cl}^-_{120\text{ppm}+\text{nutrient}}$  after 24 h contact time. It can be observed that the amount of dissolved silver species was higher from  $\text{Cl}^-_{90\text{ppm}}$  than  $\text{Cl}^-_{120\text{ppm}+\text{nutrient}}$ . This indicates that components from the culture medium decrease the amount of dissolved silver species from the composite. Free  $\text{Ag}^+$  ion percentages 64.9, 15.3 and 3.9 of total Ag, for  $\text{Cl}^-_{10\text{ppm}}$ ,  $\text{Cl}^-_{90\text{ppm}}$ , and  $\text{Cl}^-_{290\text{ppm}}$  waters, respectively, were calculated based on a computational speciation analysis (Supplementary Table S3). Thus, the amount of free  $\text{Ag}^+$  strongly depends on the composition of the water to be purified, and particularly its  $\text{Cl}^-$  content.

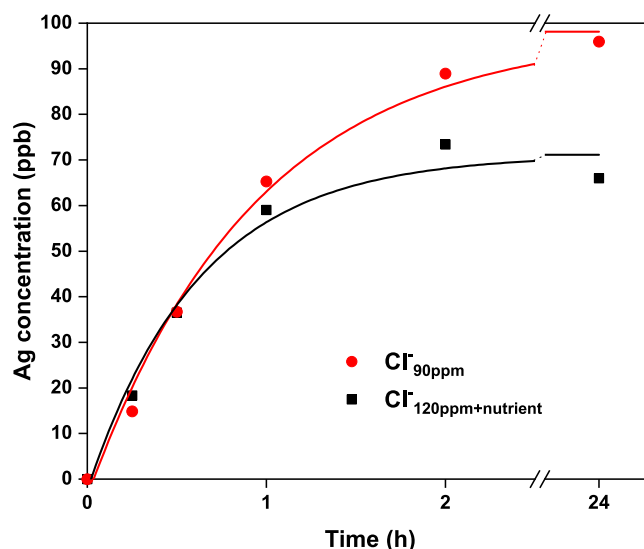


**Figure 6.** Silver release from cCNF<sub>Ag</sub> composite (4 g/L) in  $\text{Cl}^-_{90\text{ppm}}$  and  $\text{Cl}^-_{120\text{ppm}+\text{nutrient}}$  simulated freshwaters. Exponential decay curves (increasing form) have been plotted to the data to guide the eye.

## Discussion

Based on the collected field samples, the  $[\text{Cl}^-]$  of potential drinking water sources can vary significantly, thus influencing the antibacterial effect of AgNP embedded materials. In this study, efficient antibacterial activity was achieved when  $[\text{Cl}^-]$  was in the low range of concentrations present in possible freshwater sources, e.g. 10 ppm. If the  $[\text{Cl}^-]$  was high, the contact time of the material with water needed to be at least 2 h to reach a significant reduction of bacterial load. We see that in order to utilize AgNP embedded materials, it needs to be ensured that the contact time is sufficient or that  $[\text{Cl}^-]$  is at a low enough level, which could be achieved by auxiliary methods such as ion exchange or biosorption. In this study, the composite was directly brought into contact with water. For field applications, solutions such as loading the composite into a column or a filter unit of a gravity driven device could be considered. Further studies should also be conducted on the antibacterial capacity of the composite to determine when re-loading of the composite with silver or replacing the material would be necessary.

The results of this study indicate that the conditions of the aqueous environment need to be considered carefully when applying silver-releasing materials to POU water purification. We feel there is a lack of consideration in the case of POU water purification materials based on embedded nanosilver. This often leads to studies of limited significance in terms of real-life applications. We also want to address that mimicking natural aquatic environments in laboratory conditions is challenging, due to which field tests are necessary for actual applications. However, the complexity of natural waters presents several additional challenges. Therefore, conducting laboratory tests with reproducible simulated water compositions, as demonstrated here, is useful when identifying the effects of individual variables, such as  $[\text{Cl}^-]$ .

## Methods

**Materials and preparation of simulated freshwaters.** The cCNF containing quaternary ammonium groups was provided by Betulium Ltd., Finland. The average degree of substitution provided by the manufacturer was 0.1, determined as the amount of substituted glucose units or 0.63 mmol/g of cationic groups.  $\text{Al}_2(\text{SO}_4)_3 \bullet 18 \text{H}_2\text{O}$ , was purchased from Sigma-Aldrich (>97%) and  $\text{Al}_2(\text{SO}_4)_3 \bullet 14 \text{H}_2\text{O}$  from Aqua Nova Oy (technical grade, >90%). Chemicals used to prepare simulated freshwater ( $\text{NaCl}$ ,  $\text{MgSO}_4$ ,  $\text{KNO}_3$ ,  $\text{NaHCO}_3$ , and  $\text{CaCl}_2$ ),  $\text{AgNO}_3$ , and  $\text{NaBH}_4$  were purchased from Sigma-Aldrich. The water was prepared by dissolving the chemicals into Milli-Q water (Millipore) to achieve the ion composition typical for freshwaters and the pH was adjusted to 7.2–7.4 with 6 M HCl. The composition of  $\text{Cl}^-_{90\text{ppm}}$  water was formulated using the natural drinking water composition from Sankar *et al.* as a basis, omitting the silicate and fluoride and with the addition of carbonates<sup>19</sup>. Due to this, the chloride and magnesium concentrations are lower than those used by Sankar *et al.* The addition of 1% culture medium with bacteria inoculation resulted in higher sodium and chloride concentrations in  $\text{Cl}^-_{120\text{ppm}+\text{nutrient}}$  compared to  $\text{Cl}^-_{90\text{ppm}}$ .

**Preparation of composites.** For the preparation of cCNF-based composites, a method reported for the preparation of chitosan-based composites with embedded AgNPs<sup>19</sup> was used as a basis. 1.5 L of 1.5 wt-% dispersion of cCNF was prepared and 1.25 L of 0.5 M  $\text{Al}_2(\text{SO}_4)_3$  was added dropwise under stirring. The mixture was kept under stirring for 3 h. Further, 2 M NaOH was added dropwise to reach pH 9 and stirring was continued for 1 h. The suspension was filtered to collect the precipitate, which was washed extensively with water. Part of the precipitate was separated to act as a control material having no Ag. To form a composite embedded with AgNPs, a part of the above-described precipitate (dry mass of 86 g) was resuspended in 2 L of water and 1.07 L 5 mM  $\text{AgNO}_3$  was added. The solution was kept under stirring for 1.5 h. Then 1.07 L 10 mM  $\text{NaBH}_4$  was added dropwise at <10 °C. The mixture was stirred for 20 min and then left to stand for 20 min. The suspension was filtered to



collect the precipitate. The precipitate was washed extensively with water, collected, and dried to a paste with a solid content of 20–30 wt-%. The paste was extruded through a syringe and dried to form pellets noted as cCNF- $\text{FAL}_{\text{Ag}}$ . Pellets were also formed with the same method from the above-described precipitate without Ag (noted as cCNFAL).

**Characterization of cationic cellulose nanofibrils and composites.** The structure of cCNF was imaged with a FEI Tecnai 12 TEM operating at 120 kV. For sample preparation, 3  $\mu\text{L}$  0.01 wt-% dispersion of cCNF was drop-casted on a copper grid with an ultrathin carbon support film and the excess solution was blotted with a filter paper after 1 min contact time, followed by drying under ambient conditions. Thereafter, 3  $\mu\text{L}$  of 2% uranyl acetate was drop-casted onto the dried cCNF sample to stain the sample. The excess solution was blotted with a filter paper after 1 min of contact time, followed by drying under ambient conditions. FTIR spectra of freeze-dried cCNF samples were recorded with Nicolet 380 FTIR Spectrometer using an attenuated total reflectance (ATR) sampling accessory. The spectra were recorded in the 500–4000  $\text{cm}^{-1}$  range with 0.5  $\text{cm}^{-1}$  intervals. Adjacent averaging with 10 point window was applied to the data. The pH-dependence of  $\zeta$ -potential of cCNF was measured from 0.05 wt-% dispersions of cCNF with Zetasizer Nano-ZS90 (Malvern).

The composites were crushed into powder using a mortar and pestle for the SEM imaging, XRD analysis, EDX analysis, and charge determination. The SEM images were taken with a field emission SEM (Zeiss Sigma VP, Zeiss). The crushed samples were mounted on carbon tape on aluminium stubs and images were taken using an acceleration voltage of 1.6 kV with a working distance of 8 mm. Samples were sputtered with 10 nm gold before imaging. EDX analysis was done with a field emission SEM with EDX (JSM-7500F, JEOL). Before analysis the samples were mounted on carbon stubs with copper tape and sputter-coated with 10 nm layer of iridium. The XRD patterns were measured with a Rigaku SmartLab X-ray diffractometer and recorded in the  $2\theta$  range of  $10^\circ$ – $100^\circ$  with a scan step of  $0.01^\circ$ . The charge of the composites containing no silver was determined by conductometric titration. The composites were repeatedly washed with 10% NaCl solution to change the counter ions to  $\text{Cl}^-$ . The ion-exchanged composites were washed repeatedly with water, dried, and subjected to conductometric titration with 10 mM  $\text{AgNO}_3$ . Brunauer-Emmett-Teller (BET) surface areas were measured with a nitrogen sorption apparatus (Tristar II, Micrometrics). Samples were kept in a  $105^\circ\text{C}$  oven overnight and then outgassed for 1 h at  $120^\circ\text{C}$  under nitrogen flow before measurements.

**Bacteria strains.** *E. coli* (DSM 1116, ATCC 9637) and *B. subtilis* (1012M15, details provided elsewhere<sup>65</sup>) were used as Gram-negative and Gram-positive model bacteria, respectively. In all antibacterial tests and related sample preparation, the glassware was autoclaved to avoid bacterial contamination.

**Antibacterial tests.** Before tests the simulated freshwaters were sterilized by filtering with 0.2  $\mu\text{m}$  sterile syringe filters. *E. coli* and *B. subtilis* cultures were maintained on LB agar plates at  $4^\circ\text{C}$ . 4 mL of LB medium was activated with the *E. coli* and *B. subtilis* cultures and incubation was carried on overnight at  $37^\circ\text{C}$  and  $30^\circ\text{C}$ , respectively, and 220 rpm. For tests comparing the antibacterial activity on the two bacteria strains,  $\text{OD}_{600}$  values were adjusted by diluting the inocula with LB to a total volume of 0.5 mL to reach starting bacterial concentration between  $10^6$  and  $10^7$  CFU (colony forming unit)/mL and then suspended in 49.5 mL of  $\text{Cl}^-_{90\text{ppm}}$  simulated freshwater.

For tests with *E. coli* in the three different simulated freshwaters, 0.2 mL of the preculture was centrifuged (2 min, 5000 rcf) and the medium was carefully removed and the cells were resuspended in 0.5 mL of  $\text{Cl}^-_{10\text{ppm}}$ ,  $\text{Cl}^-_{90\text{ppm}}$ , and  $\text{Cl}^-_{290\text{ppm}}$  simulated freshwaters. The centrifuging was repeated and the cells were suspended in the simulated freshwaters (resulting in a total volume of 50 mL). Similar pretreatment of inocula was attempted with *B. subtilis* but the viability of the bacteria was found to suffer due to complete removal of the nutrients.

The antibacterial tests were conducted in 250 mL Erlenmeyer flasks using a composite concentration of 4 g/L. Controls without any composite were also conducted for each test. The flasks were shaken at 100 rpm at  $37^\circ\text{C}$  and  $30^\circ\text{C}$  for *E. coli* and *B. subtilis*, respectively. For plating, dilutions were made if needed in simulated freshwater to achieve countable colonies. 50  $\mu\text{L}$  of sample was spread onto LB agar plates and three parallel plates were made for each sampling. The plates were incubated overnight at  $37^\circ\text{C}$  and  $30^\circ\text{C}$  for *E. coli* and *B. subtilis*, respectively, and the colonies were counted. No significant change in pH of the simulated freshwaters was observed after 2 h contact with the cCNFAL $_{\text{Ag}}$  composite and *E. coli* (pH change was less than  $\pm 0.1$  units).

**Dissolution of silver from composites.** The Ag dissolution was determined in separate experiments without bacteria using 4 g/L cCNFAL $_{\text{Ag}}$  concentration in  $\text{Cl}^-_{90\text{ppm}}$  and  $\text{Cl}^-_{120\text{ppm}+\text{nutrient}}$ . The flasks were incubated at  $37^\circ\text{C}$  and 100 rpm. Samples were taken at 15, 30, 60, 120 min, and 24 h. Ag concentrations of all samples were analyzed with ICP-MS (PerkinElmer, NexION 300X). The samples were acidified with 5% (vol.) concentrated  $\text{HNO}_3$  (68–70%) before analysis.

The amounts of free  $\text{Ag}^+$  in the simulated freshwaters were calculated using an ion speciation software (PHREEQC). The calculations were made with total Ag concentration of 100 ppb.

Received: 13 September 2019; Accepted: 28 November 2019;

Published online: 20 December 2019

## References

- Pradeep, T. & Anshup. Noble metal nanoparticles for water purification: A critical review. *Thin Solid Films* **517**, 6441–6478 (2009).
- Chen, L. & Peng, X. Silver nanoparticle decorated cellulose nanofibrous membrane with good antibacterial ability and high water permeability. *Appl. Mater. Today* **9**, 130–135 (2017).
- Lin, S. *et al.* Silver nanoparticle-alginate composite beads for point-of-use drinking water disinfection. *Water Res.* **47**, 3959–3965 (2013).

4. Garcia Peña, L. V. *et al.* Hybrid chitosan-silver nanoparticles enzymatically embedded on cork filter material for water disinfection. *Ind. Eng. Chem. Res.* **56**, 3599–3606 (2017).
5. Li, Q. *et al.* Antimicrobial nanomaterials for water disinfection and microbial control: Potential applications and implications. *Water Res.* **42**, 4591–4602 (2008).
6. Liu, H., Tang, X. & Liu, Q. A novel point-of-use water treatment method by antimicrobial nanosilver textile material. *J. Water Health* **12**, 670–677 (2014).
7. Chernousova, S. & Eppele, M. Silver as antibacterial agent: Ion, nanoparticle, and metal. *Angew. Chemie - Int. Ed.* **52**, 1636–1653 (2013).
8. Dobias, J. & Bernier-Latmani, R. Silver release from silver nanoparticles in natural waters. *Environ. Sci. Technol.* **47**, 4140–4146 (2013).
9. Fabrega, J., Fawcett, S. R., Renshaw, J. C. & Lead, J. R. Silver nanoparticle impact on bacterial growth: Effect of pH, concentration, and organic matter. *Environ. Sci. Technol.* **43**, 7285–7290 (2009).
10. Zhang, C., Hu, Z. & Deng, B. Silver nanoparticles in aquatic environments: Physiochemical behavior and antimicrobial mechanisms. *Water Res.* **88**, 403–427 (2016).
11. Dankovich, T. A., Levine, J. S., Potgieter, N., Dillingham, R. & Smith, J. A. Inactivation of bacteria from contaminated streams in Limpopo, South Africa by silver- or copper-nanoparticle paper filters. *Environ. Sci. Water Res. Technol.* **2**, 85–96 (2016).
12. Ehdaie, B., Krause, C. & Smith, J. A. Porous ceramic tablet embedded with silver nanopatches for low-cost point-of-use water purification. *Environ. Sci. Technol.* **48**, 13901–13908 (2014).
13. Fan, M., Gong, L., Huang, Y., Wang, D. & Gong, Z. Facile preparation of silver nanoparticle decorated chitosan cryogels for point-of-use water disinfection. *Sci. Total Environ.* **613–614**, 1317–1323 (2018).
14. Dankovich, T. A. & Gray, D. G. Bactericidal paper impregnated with silver nanoparticles for point-of-use water treatment. *Environ. Sci. Technol.* **45**, 1992–1998 (2011).
15. Kahler, D. M., Koerner, N. T., Reichl, A. R., Samie, A. & Smith, J. A. Performance and acceptance of novel silver-impregnated ceramic cubes for drinking water treatment in two field sites: Limpopo province, South Africa and Dodoma Region, Tanzania. *Water (Switzerland)* **8**, (2016).
16. Oyanedel-Craver, V. A. & Smith, J. A. Sustainable colloidal-silver-impregnated ceramic filter for point-of-use water treatment. *Environ. Sci. Technol.* **42**, 927–933 (2008).
17. Rayner, J. *et al.* Laboratory investigation into the effect of silver application on the bacterial removal efficacy of filter material for use on locally produced ceramic water filters for household drinking water treatment. *ACS Sustain. Chem. Eng.* **1**, 737–745 (2013).
18. Loo, S. L. *et al.* Superabsorbent cryogels decorated with silver nanoparticles as a novel water technology for point-of-use disinfection. *Environ. Sci. Technol.* **47**, 9363–9371 (2013).
19. Sankar, M. U. *et al.* Biopolymer-reinforced synthetic granular nanocomposites for affordable point-of-use water purification. *Proc. Natl. Acad. Sci.* **110**, 8459–8464 (2013).
20. Moon, R. J., Martini, A., Nairn, J., Simonsen, J. & Youngblood, J. Cellulose nanomaterials review: Structure, properties and nanocomposites. *Chemical Society Reviews*, **40**, (2011).
21. Chaker, A. & Boufi, S. Cationic nanofibrillar cellulose with high antibacterial properties. *Carbohydr. Polym.* **131**, 224–232 (2015).
22. Littunen, K. *et al.* Synthesis of cationized nanofibrillated cellulose and its antimicrobial properties. *Eur. Polym. J.* **75**, 116–124 (2016).
23. Zhang, W., Xiao, B. & Fang, T. Chemical transformation of silver nanoparticles in aquatic environments: Mechanism, morphology and toxicity. *Chemosphere* **191**, 324–334 (2018).
24. Guo, Z. *et al.* Are silver nanoparticles always toxic in the presence of environmental anions? *Chemosphere* **171**, 318–323 (2017).
25. Levard, C. *et al.* Effect of chloride on the dissolution rate of silver nanoparticles and toxicity to *E. coli*. *Environ. Sci. Technol.* **47**, 5738–5745 (2013).
26. Stabryla, L. M., Johnston, K. A., Millstone, J. E. & Gilbertson, L. M. Emerging investigator series: It's not all about the ion: Support for particle-specific contributions to silver nanoparticle antimicrobial activity. *Environ. Sci. Nano* **5**, 2047–2068 (2018).
27. Xiu, Z. M., Zhang, Q. B., Puppala, H. L., Colvin, V. L. & Alvarez, P. J. J. Negligible particle-specific antibacterial activity of silver nanoparticles. *Nano Lett.* **12**, 4271–4275 (2012).
28. Pal, S., Tak, Y. K. & Song, J. M. Does the antibacterial activity of silver nanoparticles depend on the shape of the nanoparticle? A study of the gram-negative bacterium *Escherichia coli*. *J. Biol. Chem.* **290**, 1712–1720 (2015).
29. Long, Y. M. *et al.* Surface ligand controls silver ion release of nanosilver and its antibacterial activity against *Escherichia coli*. *Int. J. Nanomedicine* **12**, 3193–3206 (2017).
30. Choi, O. *et al.* The inhibitory effects of silver nanoparticles, silver ions, and silver chloride colloids on microbial growth. *Water Res.* **42**, 3066–3074 (2008).
31. Edberg, S. C., Rice, E. W., Karlin, R. J. & Allen, M. J. *Escherichia coli*: the best biological drinking water indicator for public health protection. *J. Appl. Microbiol.* **88**, 106S–116S (2000).
32. Praveena, S. M., Han, L. S., Than, L. T. L. & Aris, A. Z. Preparation and characterisation of silver nanoparticle coated on cellulose paper: evaluation of their potential as antibacterial water filter. *J. Exp. Nanosci.* **11**, 1307–1319 (2016).
33. Biswas, P. & Bandyopadhyaya, R. Water disinfection using silver nanoparticle impregnated activated carbon: *Escherichia coli* cell-killing in batch and continuous packed column operation over a long duration. *Water Res.* **100**, 105–115 (2016).
34. Le Ouay, B. & Stellacci, F. Antibacterial activity of silver nanoparticles: A surface science insight. *Nano Today* **10**, 339–354 (2015).
35. Chambers, B. A. *et al.* Effects of chloride and ionic strength on physical morphology, dissolution, and bacterial toxicity of silver nanoparticles. *Environ. Sci. Technol.* **48**, 761–769 (2014).
36. Wefers, K. & Misra, C. Oxides and Hydroxides of Aluminum. Alcoa Technical Paper No. 19. *Alum. Co. Am.* **92** (1987).
37. Shen, L., Hu, C., Sakka, Y. & Huang, Q. Study of phase transformation behaviour of alumina through precipitation method. *J. Phys. D: Appl. Phys.* **45**, (2012).
38. Li, W.-R. *et al.* Antibacterial effect of silver nanoparticles on *Staphylococcus aureus*. *BioMetals* **24**, 135–141 (2011).
39. Amato, E. *et al.* Synthesis, characterization and antibacterial activity against gram positive and gram negative bacteria of biomimetically coated silver nanoparticles. *Langmuir* **27**, 9165–9173 (2011).
40. Greulich, C. *et al.* The toxic effect of silver ions and silver nanoparticles towards bacteria and human cells occurs in the same concentration range. *RSC Adv.* **2**, 6981–6987 (2012).
41. Doody, M. A., Wang, D., Bais, H. P. & Jin, Y. Differential antimicrobial activity of silver nanoparticles to bacteria *Bacillus subtilis* and *Escherichia coli*, and toxicity to crop plant *Zea mays* and beneficial *B. subtilis*-inoculated *Z. mays*. *J. Nanoparticle Res.* **18**, 1–19 (2016).
42. Jung, W. K. *et al.* Antibacterial activity and mechanism of action of the silver ion in *Staphylococcus aureus* and *Escherichia coli*. *Appl. Environ. Microbiol.* **74**, 2171–2178 (2008).
43. Ruparelia, J. P., Chatterjee, A. K., Duttgupta, S. P. & Mukherji, S. Strain specificity in antimicrobial activity of silver and copper nanoparticles. *Acta Biomater.* **4**, 707–716 (2008).
44. Marambio-Jones, C. & Hoek, E. M. V. A review of the antibacterial effects of silver nanomaterials and potential implications for human health and the environment. *J. Nanoparticle Res.* **12**, 1531–1551 (2010).
45. Gross, A., Stangl, F., Hoenes, K., Sift, M. & Hessling, M. Improved drinking water disinfection with UVC-LEDs for *Escherichia coli* and *Bacillus subtilis* utilizing quartz tubes as light guide. *Water (Switzerland)* **7**, 4605–4621 (2015).

46. Van Elsas, J. D., Semenov, A. V., Costa, R. & Trevors, J. T. Survival of *Escherichia coli* in the environment: Fundamental and public health aspects. *ISME J.* **5**, 173–183 (2011).
47. Yoon, K. Y., Hoon Byeon, J., Park, J. H. & Hwang, J. Susceptibility constants of *Escherichia coli* and *Bacillus subtilis* to silver and copper nanoparticles. *Sci. Total Environ.* **373**, 572–575 (2007).
48. Gangadharan, D. *et al.* Polymeric microspheres containing silver nanoparticles as a bactericidal agent for water disinfection. *Water Res.* **44**, 5481–5487 (2010).
49. World Health Organization. Guidelines for drinking-water quality. 4<sup>th</sup> edition (2011).
50. Sondi, I. & Salopek-Sondi, B. Silver nanoparticles as antimicrobial agent: A case study on *E. coli* as a model for Gram-negative bacteria. *J. Colloid Interface Sci.* **275**, 177–182 (2004).
51. Johnston, K. A. *et al.* Impacts of broth chemistry on silver ion release, surface chemistry composition, and bacterial cytotoxicity of silver nanoparticles. *Environ. Sci. Nano* **5**, 304–312 (2018).
52. Ramalingam, B., Khan, M. M. R., Mondal, B., Mandal, A. B. & Das, S. K. Facile synthesis of silver nanoparticles decorated magnetic-chitosan microsphere for efficient removal of dyes and microbial contaminants. *ACS Sustain. Chem. Eng.* **3**, 2291–2302 (2015).
53. Bielefeldt, A. R., Kowalski, K. & Summers, R. S. Bacterial treatment effectiveness of point-of-use ceramic water filters. *Water Res.* **43**, 3559–3565 (2009).
54. Praveena, S. M., Karuppiiah, K. & Than, L. T. L. Potential of cellulose paper coated with silver nanoparticles: a benign option for emergency drinking water filter. *Cellulose* **25**, 2647–2658 (2018).
55. Quang, D. V. *et al.* Effective water disinfection using silver nanoparticle containing silica beads. *Appl. Surf. Sci.* **266**, 280–287 (2013).
56. Van der Laan, H. *et al.* Bacteria and virus removal effectiveness of ceramic pot filters with different silver applications in a long term experiment. *Water Res.* **51**, 47–54 (2014).
57. Jannasch, H. W. Estimations of Bacterial Growth Rates in Natural Waters. *J. Bacteriol.* **99**, 156–160 (1969).
58. Levard, C. *et al.* Sulfidation of silver nanoparticles: Natural antidote to their toxicity. *Environ. Sci. Technol.* **47**, 13440–13448 (2013).
59. Swathy, J. R. *et al.* Antimicrobial silver: An unprecedented anion effect. *Sci. Rep.* **11**, (2014).
60. Pinto, R. J. B. *et al.* Antibacterial activity of nanocomposites of silver and bacterial or vegetable cellulosic fibers. *Acta Biomater.* **5**, 2279–2289 (2009).
61. Obi, C. L., Potgieter, N., Bessong, P. O. & Matsaung, G. Scope of potential bacterial agents of diarrhoea and microbial assessment of quality of river water sources in rural Venda communities in South Africa. *Water Sci. Technol.* **47**, 59–64 (2003).
62. Gondikas, A. P. *et al.* Cysteine-induced modifications of zero-valent silver nanomaterials: Implications for particle surface chemistry, aggregation, dissolution, and silver speciation. *Environ. Sci. Technol.* **46**, 7037–7045 (2012).
63. Loo, S. L., Krantz, W. B., Hu, X., Fane, A. G. & Lim, T. T. Impact of solution chemistry on the properties and bactericidal activity of silver nanoparticles decorated on superabsorbent cryogels. *J. Colloid Interface Sci.* **461**, 104–113 (2016).
64. U.S. Environmental Protection Agency. 2012 Edition of the Drinking Water Standards and Health Advisories (2012).
65. Kallio, P. T. & Bailey, J. E. Intracellular expression of *Vitreoscilla* hemoglobin (VHb) enhances total protein secretion and improves the production of alpha-amylase and neutral protease in *Bacillus subtilis*. *Biotechnol. Prog.* **12**, 31–39 (1996).

## Acknowledgements

Business Finland is acknowledged for the funding of this work under the CelluClean project. The Academy of Finland Center of Excellence on Molecular Engineering of Biosynthetic Hybrid Materials Research (HYBER) is also acknowledged for supporting this work. We are grateful for the support by the FinnCERES Materials Bioeconomy Ecosystem. Amanda Eklund is acknowledged for the XRD measurements and Professor Alexander Frey for providing the *B. subtilis* strain. We acknowledge the facilities and technical support by Aalto University OtaNano Nanomicroscopy Center (Aalto-NMC).

## Author contributions

J.L. and J.H. wrote the main manuscript text, prepared all figures and performed material characterization experiments. J.L. performed antibacterial experiments and H.V., R.H., and A.K. assisted in the design of the antibacterial experiments. R.H. and A.A.K. collected field samples from India. A.A.K. performed ICP-MS measurements. N.P. provided the cationic cellulose nanofibrils on behalf of Betulium Ltd. R.H., A.A.K., H.V., A.K., N.P., T.P., O.J.R. and O.I. reviewed the manuscript. All authors approved the final manuscript.

## Competing interests

The authors declare no competing interests.

## Additional information

**Supplementary information** is available for this paper at <https://doi.org/10.1038/s41598-019-56009-6>.

**Correspondence** and requests for materials should be addressed to J.H.

**Reprints and permissions information** is available at [www.nature.com/reprints](http://www.nature.com/reprints).

**Publisher's note** Springer Nature remains neutral with regard to jurisdictional claims in published maps and institutional affiliations.



**Open Access** This article is licensed under a Creative Commons Attribution 4.0 International License, which permits use, sharing, adaptation, distribution and reproduction in any medium or format, as long as you give appropriate credit to the original author(s) and the source, provide a link to the Creative Commons license, and indicate if changes were made. The images or other third party material in this article are included in the article's Creative Commons license, unless indicated otherwise in a credit line to the material. If material is not included in the article's Creative Commons license and your intended use is not permitted by statutory regulation or exceeds the permitted use, you will need to obtain permission directly from the copyright holder. To view a copy of this license, visit <http://creativecommons.org/licenses/by/4.0/>.

© The Author(s) 2019

## Supporting Information

### Effects of Chloride Concentration on the Drinking Water Disinfection Performance of Silver Containing Nanocellulose-based Composites

*Janika Lehtonen<sup>1</sup>, Jukka Hassinen<sup>\*2</sup>, Riina Honkanen<sup>3</sup>, Avula Anil Kumar<sup>4</sup>, Heli Viskari<sup>1</sup>, Anu Kettunen<sup>3</sup>, Nikolaos Pahimanolis<sup>5</sup>, Thalappil Pradeep<sup>4</sup>, Orlando J. Rojas<sup>1,2</sup> and Olli Ikkala<sup>\*1,2</sup>*

<sup>1</sup> Department of Bioproducts and Biosystems, School of Chemical Engineering, Aalto University, P. O. Box 16300, FI-00076 Aalto, Espoo, Finland.

<sup>2</sup> Department of Applied Physics, School of Science, Aalto University, P. O. Box 16300, FI-00076 Aalto, Espoo, Finland.

<sup>3</sup> Industrial Water Ltd., Moreenikatu 2 B, FI-04600, Mäntsälä, Finland.

<sup>4</sup> DST Unit of Nanoscience (DST UNS) and Thematic Unit of Excellence (TUE), Department of Chemistry, Indian Institute of Technology Madras, Chennai 600036, India.

<sup>5</sup> Betulium Ltd., Tekniikantie 2, FI-02150, Espoo, Finland.

\* Corresponding authors

E-mail: [olli.ikkala@aalto.fi](mailto:olli.ikkala@aalto.fi)

E-mail: [jukka.hassinen@aalto.fi](mailto:jukka.hassinen@aalto.fi)

#### SUPPORTING INFORMATION CONTENT

Total number of pages: 12

Total number of figures: 5

Total number of tables: 3



## TABLE OF CONTENTS

Supporting items	Title	Page no.
Table S1	The ionic compositions of simulated drinking waters used for antibacterial tests	S3
Table S2	Cl <sup>-</sup> concentration, <i>E. coli</i> count, and total plate count present in the samples collected from IITM campus	S4-S5
Table S3	Silver speciation in simulated freshwaters used in the study	S6
Figure S1	ζ-potential of cationic CNF in pH range 3-11	S7
Figure S2	X-ray powder diffraction patterns of cCNFAI <sub>Ag</sub> composites	S8
Figure S3	SEM-EDX elemental mapping of cCNFAI <sub>Ag</sub> composite	S9
Figure S4	Titration curve for cCNFAI composite	S10
Figure S5	Antibacterial test with cCNFAI	S11
Supporting References	References used for Supporting Information	S12

## Supporting Table 1

### Ionic compositions used for the preparation of simulated freshwaters

**Table S1.** The ionic compositions of simulated freshwaters used for antibacterial tests.

	Cl <sup>-</sup> <sub>10ppm</sub>	Cl <sup>-</sup> <sub>90ppm</sub>	Cl <sup>-</sup> <sub>290ppm</sub>	Cl <sup>-</sup> <sub>120ppm+nutrient</sub> *
Ion	ppm	ppm	ppm	ppm
Cl <sup>-</sup>	10	89	290	120
SO <sub>4</sub> <sup>2-</sup>	33	33	33	33
NO <sub>3</sub> <sup>-</sup>	1.8	1.8	1.8	1.8
Carbonates	54	54	54	54
Na <sup>+</sup>	21	46	180	66
Mg <sup>2+</sup>	8.3	8.3	8.3	8.3
K <sup>+</sup>	1.2	1.2	1.2	1.2
Ca <sup>2+</sup>	5.6	28	28	28

\*Addition of 1% LB medium with bacteria inoculation was taken into account. This composition was used for the test shown in Figure 4.

## Supporting Table 2

### **Sample collection from IITM campus area and the determination of Cl<sup>-</sup> concentration and bacterial count**

Water samples were collected in September 2017 from various sources in the campus area of Indian Institute of Technology Madras (IITM) based in Chennai, India. Samples were collected into sterile plastic bottles and delivered to CVR Labs Pvt. Ltd., Chennai, India for the analyses of Cl<sup>-</sup> concentration, *Escherichia coli* count and total plate count of bacteria, which are presented in Table S2. The IITM Temple lake sample represents a surface water source. The metro water input sample represents potable inlet water that consists mainly of water brought by trucks to the campus. The water in these trucks originates from different sources and is difficult to track back. The inlet water may also consist of water supplied by the Chennai Metropolitan Water Supply and Sewerage Board (CMWSSB). The metro output sample consists of the same water as metro water input but may also consist of the bore well water. For both open well waters, the main source was rainwater but they also consisted partly of incoming filtrates through the walls of the open wells. The lake water sample and both open well waters represented a typical type of water wherein point-of-use water disinfection could be applied to produce potentially potable water. These waters were found to contain *E. coli*.

**Table S2.** Cl<sup>-</sup> concentration, *E. coli* count, and total plate count in the samples collected from IITM campus area, Chennai, India. MPN = most probable number.

<b>Sampling place</b>	<b>Cl<sup>-</sup> concentration (ppm)</b>	<b><i>E. coli</i> (MPN/100 mL)</b>	<b>Total plate count 22 °C (CFU/mL)</b>
<b>IITM Temple lake</b>	92	70	1500
<b>Open well water (near IITM swimming pool)</b>	1132	110	31000
<b>Open well water (near Ocean Engineering Department)</b>	132	280	57000
<b>Main gate Metro water input</b>	125	0	64
<b>Main gate Metro water output</b>	254	0	67000
<b>Bore well (main gate)</b>	157	0	100
<b>Output IITM drinking water facility</b>	19	0	3500

### Supporting Table 3

#### Silver speciation in simulated drinking waters used in the study

The speciation analysis of silver was performed with PHREEQC Interactive, version 3.3.12.12704 (Table S3). The additional ions (mainly  $\text{Na}^+$  and  $\text{Cl}^-$ ) originating from LB medium were separately considered. It should be noted that LB medium also contains organic components that can effect silver speciation, due to possible complexation between the organic components and silver. However, this was not considered in the speciation analysis. Silver concentration of 100 ppb was used in the speciation analysis. It was observed that the concentration of silver did not affect the speciation in the range between 0-200 ppb.

**Table S3.** Silver speciation in simulated drinking waters used in the study.

	Simulated drinking waters used in the study			
	$\text{Cl}^-_{120\text{ppm}+\text{nutrient}}$ % of total Ag	$\text{Cl}^-_{10\text{ppm}}$	$\text{Cl}^-_{90\text{ppm}}$ % of total Ag	$\text{Cl}^-_{290\text{ppm}}$
$\text{Ag}^+$	11.4	64.5	15.3	3.9
$\text{AgCl}$	68.2	34.3	69.2	55.1
$\text{AgCl}_2^-$	20.3	0.9	15.4	40.6
$\text{AgSO}_4^-$	0.0	0.3	0.1	0.0
$\text{AgCl}_3^{2-}$	0.1	0.0	0.0	0.4
<b>Ag (total)</b>	100.0	100.0	100.0	100.0

## Supporting Information 1

### $\zeta$ -potential of cationic cellulose nanofibrils

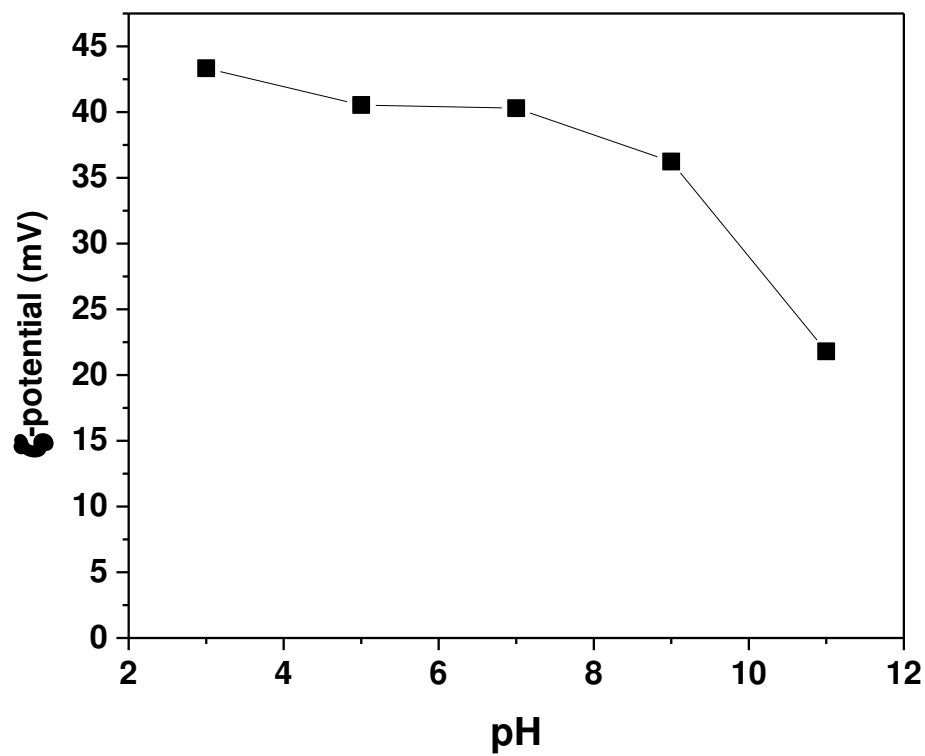


**Figure S1.**  $\zeta$ -potential of cationic CNF in pH range 3-11.

## Supporting Information 2

### Powder X-ray diffraction of cCNFAI<sub>Ag</sub>

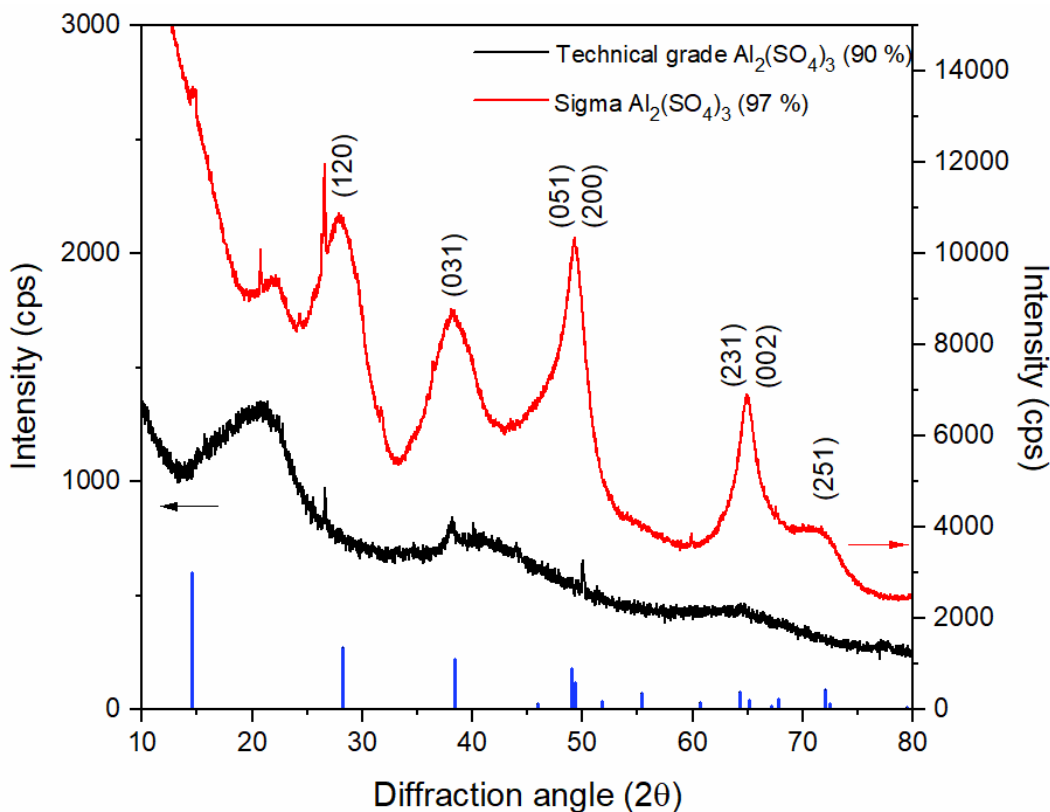


**Figure S2.** X-ray powder diffraction patterns of cCNFAI<sub>Ag</sub> composites prepared from high purity Al<sub>2</sub>(SO<sub>4</sub>)<sub>3</sub> (red curve) and technical grade, Al<sub>2</sub>(SO<sub>4</sub>)<sub>3</sub> (black curve). The reflections from the sample prepared from high-purity Al<sub>2</sub>(SO<sub>4</sub>)<sub>3</sub> originate from nanocrystalline boehmite phase (reflection positions from literature marked by blue lines<sup>1</sup>). The broad reflections from the sample prepared from technical grade Al<sub>2</sub>(SO<sub>4</sub>)<sub>3</sub> indicated presence of an amorphous form of the material.<sup>2</sup> The reflections from silver nanoparticles are absent due to the small concentration of silver in the composite (theoretically 0.67 wt%).

### Supporting Information 3

#### SEM-EDX spectrum of cCNFAl<sub>Ag</sub>

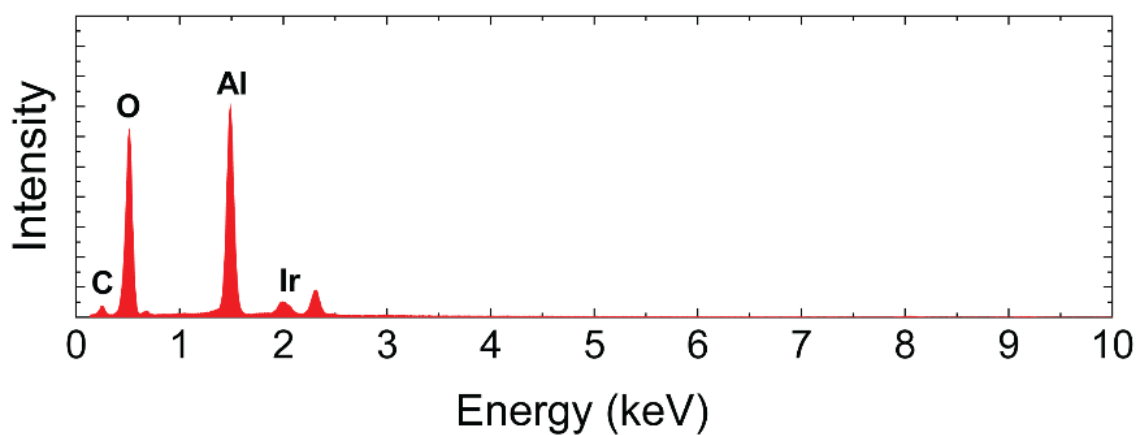


**Figure S3.** SEM-EDX spectrum of cCNFAl<sub>Ag</sub> composite. Silver could not be detected on the measured EDX spectrum due to its small concentration in the composite (theoretically 0.67 wt%). Iridium was used for coating the sample.



## Supporting Information 4

### Charge of the cCNFAl composite

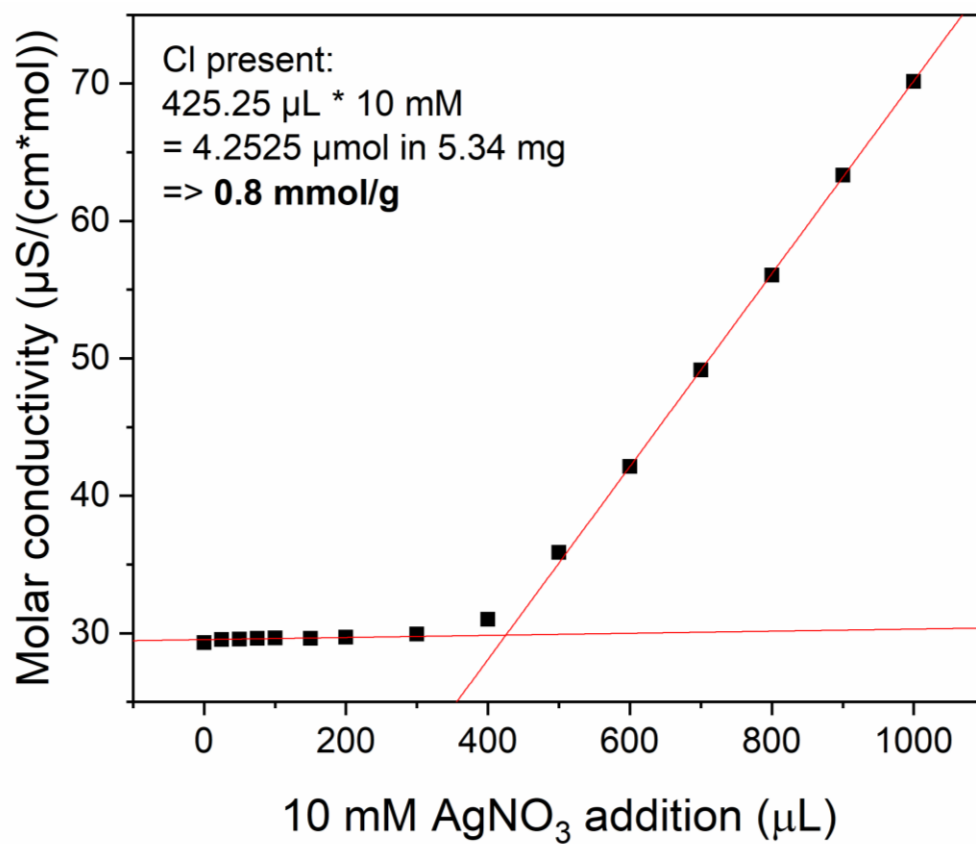


**Figure S4.** Titration curve for cCNFAl composite.

## Supporting Information 5

### Antibacterial test with cCNFAI

To test the antibacterial performance of the composite without AgNPs (cCNFAI), 4 g/L of the composite was incubated in  $\text{Cl}^-_{90\text{ppm}}$  simulated drinking water and samples were taken at 15 min and 1 h contact times. For inoculation of *E. coli* and plating of the samples, the same procedure was followed as described in the methods section.

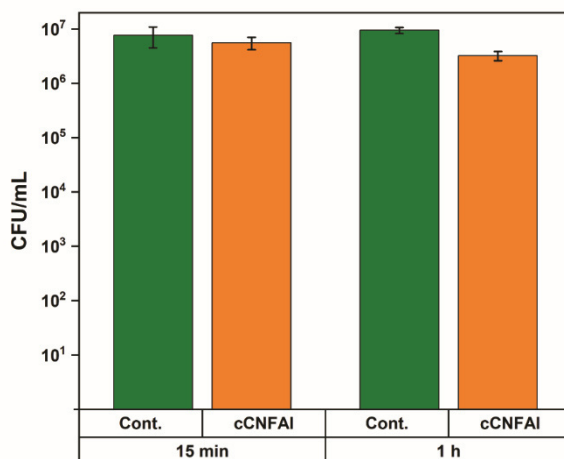


**Figure S5.** Antibacterial activity against *E. coli* of cCNFAI composite (4 g/L) in  $\text{Cl}^-_{90\text{ppm}}$  simulated drinking water.

## Supporting references

- (1) Hill, R. J. Hydrogen Atoms in Boehmite. a Single Crystal X-Ray Diffraction and Molecular Orbital Study. *CLAYS CLAY MINER. Clays Clay Miner.* **1981**, 29 (6), 435.  
<https://doi.org/10.1346/CCMN.1981.0290604>.
- (2) Shen, L.; Hu, C.; Sakka, Y.; Huang, Q. Study of Phase Transformation Behaviour of Alumina through Precipitation Method. *J. Phys. D. Appl. Phys.* **2012**, 45 (21).  
<https://doi.org/10.1088/0022-3727/45/21/215302>.

# Nanogymnastics: Visualization of Intercluster Reactions by High-Resolution Trapped Ion Mobility Mass Spectrometry

Ananya Baksi,<sup>†,‡,§</sup> Erik Karsten Schneider,<sup>‡</sup> Patrick Weis,<sup>‡,§</sup> K. R. Krishnadas,<sup>§</sup> Debasmita Ghosh,<sup>§</sup> Horst Hahn,<sup>\*,†,§</sup> Thalappil Pradeep,<sup>\*,§,§</sup> and Manfred M. Kappes<sup>\*,†,‡,§</sup>

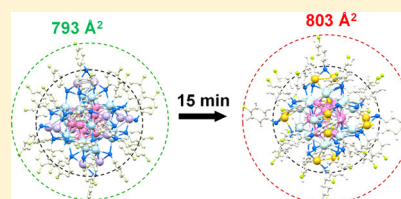
<sup>†</sup>Institute of Nanotechnology, Karlsruhe Institute of Technology, 76344 Eggenstein-Leopoldshafen, Baden-Württemberg, Germany

<sup>‡</sup>Institute of Physical Chemistry, Karlsruhe Institute of Technology, 76131 Karlsruhe, Baden-Württemberg, Germany

<sup>§</sup>DST Unit of Nanoscience and Thematic Unit of Excellence, Indian Institute of Technology Madras, Chennai, Tamil Nadu 600036, India

## Supporting Information

**ABSTRACT:** Although single-crystal X-ray diffraction is a proven technique to determine the structure of monolayer-protected coinage metal clusters in solid state, it is not readily applicable to the characterization of such cluster structures in solution. The complexity of the characterization problem increases further when *intercluster* reactions are studied, in which two reactive cluster ions interact to form final products using a sequence of structural changes involving exchange of metal atoms and ligands. Here, we present the first time-resolved structural study of such processes which occur when solutions of  $[\text{TOA}]^+[\text{Au}_{25}(\text{PET})_{18}]^-$  and  $[\text{PPh}_4]_4^+[\text{Ag}_{44}(\text{FTP})_{30}]^{4-}$  react upon mixing (PET: phenylethanethiolate; FTP: 4-fluorothiophenolate; and TOA: tetraoctylammonium ion). This is achieved using high-resolution trapped ion mobility mass spectrometry (TIMS). Specifically, we have used electrospray transfer to the TIMS apparatus followed by ion mobility measurements to probe the time-dependent structure of mass-selected  $\text{Au}_x\text{Ag}_{44-x}(\text{FTP})_{30}^{4-}$  ( $x = 0-12$ ) exchange products, with limited FTP for PET exchanges, formed in the reaction medium. Over the roughly 40 min reaction time before equilibration, with a product distribution centered around  $\text{Au}_{12}\text{Ag}_{32}(\text{FTP})_{30}^{4-}$ , we observe intermediate species,  $\text{Au}_x\text{Ag}_{44-x}(\text{FTP})_{30}^{4-}$ , whose collision cross sections (CCSs) at a given  $x$  increase first relative to that of the  $\text{Ag}_{44}(\text{FTP})_{30}^{4-}$  parent and decrease subsequently. We attribute this to an energy-driven migration of the incorporated Au atoms from the ligated “staples” at the cluster surface to its icosahedral core. Upon collisional heating of  $\text{Au}_x\text{Ag}_{44-x}(\text{FTP})_{30}^{4-}$ , analogous back-migration of the heavier Au atoms from the core to the staples was observed in tandem mass spectrometry. To support our experimental observations, several isomeric structures (with all ligands) were calculated using density functional theory, and their CCS values were modeled using trajectory method calculations.



## 1. INTRODUCTION

The size-dependent chemical physics of unprotected and therefore extremely reactive atomically precise metal clusters has been studied systematically in molecular beams for more than 50 years.<sup>1–4</sup> By contrast, it is only after the development of scalable cluster growth and monolayer protection about 20 years ago that a homologous series of ligand-protected homometallic clusters with a wide range of differently sized cores became available to mainstream chemistry.<sup>5–8</sup> Among clusters of coinage metals, these approaches were first developed for gold and later extended to silver and copper. Most recently, monolayer-protected bimetallic alloy nanoclusters comprising all coinage metals have also become available. Monolayer-protected, atomically precise, core–shell bimetallic nanoclusters are presently of great interest because of their unique shape and size-/composition-dependent reactivity.<sup>9–13</sup> Being size-selected with atomic precision, bimetallic clusters have a measurable molecular formula and can thus be considered as bridges between metal alloy nanoparticles and the (smaller) molecular regime.<sup>14</sup>

Synthesis of monolayer-protected alloy clusters is generally carried out by using two different metal precursors which react to form a new alloy cluster with defined nuclearity and composition.<sup>15</sup> In many cases, the position of the heteroatom(s) is analyzed by X-ray crystallography.<sup>16,17</sup> Galvanic and antigalvanic exchange has also been used to dope a single or a few heteroatoms (also noncoinage metals) into the presynthesized homonuclear clusters. Adding metal thiolates to a homonuclear cluster followed by reduction using  $\text{NaBH}_4$  has also been shown to allow the formation of alloy clusters.<sup>17–21</sup>

A newly emerging technique to make alloy clusters which has attracted a lot of attention recently is intercluster reactions.<sup>12,13,22–25</sup> Remarkably, two atomically precise homonuclear clusters, each containing a different coinage metal, can interact with each other in solution under ambient conditions to form alloy clusters by exchange of metals and ligands. Various types of interactions have been reported,<sup>26,27</sup> leading

**Received:** September 12, 2019

**Revised:** October 24, 2019

**Published:** October 27, 2019

to both alloys with variable atomic compositions—without changing the overall nuclearities of the respective cores—and dimers.<sup>13,26</sup> Recent reports of such reactions between Ag and Au clusters have shown rapid exchange of Au/Ag in the respective clusters independent of whether the reactant species have the same or different nuclearities. The first such report showed reaction between  $\text{Ag}_{44}(\text{SR})_{30}$  clusters with  $\text{Au}_{25}(\text{SR})_{18}$  clusters being added to the same solution (where SR corresponds to one of several different possible thiolate ligands). This was probed by UV–vis absorption spectroscopy and mass spectrometry.<sup>23,24</sup> Although multiple Ag atom exchanges were seen in the gold cluster upon adding a small amount of  $\text{Ag}_{44}(\text{SR}')_{30}$  to an excess of  $\text{Au}_{25}(\text{SR})_{18}$ , up to 12 Au atoms were found to be exchanged into the  $\text{Ag}_{44}(\text{SR}')_{30}$  cluster in parallel—along with the exchange of a few ligands on both sides. Density functional theory (DFT) calculations of the corresponding energetics suggested that eventually all the 12 Au atoms should go to the icosahedral core of the 44-atom cluster, which is the most stable substitutional isomer of  $\text{Au}_{12}\text{Ag}_{32}(\text{SR})_{30}$ .<sup>23</sup> The cluster consists of six ligand-terminated “staples” comprising two silver atoms (and five ligands) each. The staples sit on top of a 20-atom shell of silver atoms which in turn contains a 12-atom hollow icosahedral core of gold atoms (i.e., without a central atom).

The DFT structure is in agreement with the crystal structure of  $\text{Au}_{12}\text{Ag}_{32}(\text{SR})_{30}$  directly prepared from mononuclear precursors by Zheng et al.<sup>28,29</sup> In a recent report of alloy clusters formed in a related “one-pot ab initio synthesis”, Zheng et al. showed by X-ray crystallography that any number of Au doping (from 0 to 12) in  $\text{Ag}_{44}(\text{SR})_{30}$  clusters leads to Au exchange in the icosahedral core.<sup>29</sup> By contrast, Xie et al. have suggested that 12 Au atoms exchange on the surface (staple) of the preformed  $\text{Ag}_{44}(\text{SR})_{30}$  clusters (rather than in its core) when the exchange is mediated by  $\text{Au}(\text{SR})_2\text{Cl}$ -type thiolates.<sup>30</sup> In a related study, Bürgi et al. have inferred that over longer times, silver exchange occurs preferentially in the core of a  $\text{Au}_{38}(\text{SR})_{24}$  cluster rather than on its staples.<sup>31</sup>

Although the latter studies give some first information about the structural consequences of the exchange reaction, they do not provide extensive insight into its mechanism. In all cases of Au exchange into preformed silver clusters, it seems clear that the reaction must start from the outside, that is, start at the staples with the exchanged Au atoms perhaps subsequently migrating to the core. If this is indeed the case, then the associated rearrangement process must be associated with transitory volume and packing changes as the molecule isomerizes in a “nanogymnastics” fashion to allow for subsurface diffusional exchange. The comparatively high mobility of coinage metal atoms in such clusters under ambient conditions is highlighted in a recent report by Pradeep et al. who showed that rapid exchange between  $\text{Ag}^{107}$  and  $\text{Ag}^{109}$  (to the respective statistical limits) can happen when mixing the two corresponding isotopically pure clusters—for both  $\text{Ag}_{25}(\text{SR})_{18}$  and  $\text{Ag}_{29}(\text{SR})_{12}$ .<sup>32</sup>

In the present study, we show the first time-resolved visualization of the structural changes of  $\text{Ag}_{44}(\text{SR})_{30}$  cluster ions (SR = FTP; 4-fluorothiophenolate) during intercluster reaction with  $\text{Au}_{25}(\text{SR})_{18}$  cluster (SR' = PET; phenylethanethiolate). We obtain this information using high-resolution trapped ion mobility mass spectrometry (TIMS) coupled with electrospray ionization (ESI) to probe solution composition at selected times after starting the exchange reaction.<sup>33–37</sup> We show that the initial interaction of the

$\text{Ag}_{44}(\text{FTP})_{30}$  clusters with  $\text{Au}_{25}(\text{PET})_{18}$  leads to distortion/expansion of the  $\text{Ag}_{44}(\text{FTP})_{30}$  precursors as Ag/Au exchange proceeds. By analyzing all of the intermediate ions, we were able to probe the concerted migration mechanism transporting Au atoms from the surface to the cluster core (and correspondingly silver atoms from core to the surface). Collision-induced dissociation (CID) measurements of the Au-exchanged ions show that as the Au content of the system increases, Au can also diffuse back to the surface of the energized clusters—as indicated by the respective Au-containing fragments. To support the inferences from TIMS measurements, DFT was used to calculate (isomeric) structures of selected  $\text{Au}_x\text{Ag}_{44-x}(\text{FTP})_{30}^{4-}$  species ( $x = 0–12$ ). These DFT structures in turn formed the basis for trajectory method (TM) calculations, which were used to model the collision cross sections (CCSs) resulting from the ion mobility measurements.

## 2. EXPERIMENTAL SECTION

**2.1. Synthesis Details.** The clusters  $\text{Au}_{25}(\text{PET})_{18}$ <sup>38</sup> and  $[\text{PPh}_4]_4[\text{Ag}_{44}(\text{FTP})_{30}]$ <sup>37</sup> were synthesized and characterized following the previously reported methods (see the [Supporting Information](#) for details and Figures S1 and S2).

**2.2. Instrumental Details.** The time dependence of intercluster reactions in solution was studied by recording the ESI mass spectra using three different mass spectrometers, namely, a Bruker timsTOF, a Thermo Fisher Orbitrap, and a Waters SYNAPT G2S HDMS. In spite of the different ESI sources and spray conditions used, mass spectra were in good qualitative agreement across the three different platforms. The SYNAPT was used for CID measurements. The timsTOF was used to obtain  $^{\text{TIMS}}\text{CCS}_{\text{N}_2}$  values. Details of the instruments and typical operating parameters are also given in the [Supporting Information](#).

**2.3. Computational Details.** All ion geometries were obtained using DFT with the BP-86 functional<sup>39,40</sup> and the def-SV(P) basis set<sup>41</sup> as implemented in the TURBOMOLE<sup>42</sup> package. We used the experimental geometry (X-ray structure) of  $[\text{PPh}_4]_4\text{Ag}_{44}(\text{FTP})_{30}$  as the starting point and removed the  $[\text{PPh}_4]^+$  counterions to obtain an initial  $\text{Ag}_{44}(\text{FTP})_{30}^{4-}$  structure. This structure was then fully optimized without any symmetry restrictions. For the mixed Au/Ag systems, we replaced the respective silver atoms by gold atoms in the optimized structure and performed a new geometry optimization, again without symmetry restrictions. Partial charges on each atom (necessary for the CCS calculation) were assigned with a natural bond orbital (NBO) population analysis<sup>43</sup> unless otherwise noted. The optimized ion geometries and partial charges (see [Tables S1–S4](#)) formed the basis of systematic TM calculations as implemented in the IMoS 1.09 package.<sup>44,45</sup> For each CCS, we ran  $3 \times 10^6$  trajectories at a temperature of 300 K with the “carbon first” optimized Lennard-Jones parameters of Wu et al.,<sup>46</sup> that is, the default parameters of IMoS 1.09.

## 3. RESULTS AND DISCUSSION

The reaction kinetics of Au exchange and the resulting formation of  $\text{Au}_x\text{Ag}_{44-x}(\text{SR})_{30}^{4-}$  cluster ions,  $x = 1–12$  (SR = FTP or PET)<sup>23</sup> were monitored in-line generally using a high-resolution trapped ion mobility mass spectrometer (Bruker timsTOF) equipped with an ESI source. Dilute solutions (10  $\mu\text{M}$  and below) of both  $[\text{PPh}_4]_4[\text{Ag}_{44}(\text{FTP})_{30}]$  and  $[\text{TOA}]$ -



[Au<sub>25</sub>(PET)<sub>18</sub>]<sup>−</sup> were mixed in dimethyl formamide solvent and the products formed under ambient conditions were monitored continuously (at a temperature of ca. 298 K). We estimate the “dead time” between the start of the reaction upon mixing and the earliest timsTOF detection of products to be about 60 s. Note that we have optimized the ESI source conditions such that Au<sub>x</sub>Ag<sub>44−x</sub>(SR)<sub>30</sub><sup>4−</sup> is the most abundant Ag<sub>44</sub>-based multianion species. Under these conditions, the relative trianion intensity is less than 5%. We therefore regard the relative intensity of Au<sub>x</sub>Ag<sub>44−x</sub>(SR)<sub>30</sub><sup>4−</sup> intermediates as a representative of the progression of the exchange reaction.

A three-dimensional “heat-map” plot of *m/z* versus reaction time showing the relative intensities of the Ag<sub>44</sub>(SR)<sub>30</sub><sup>4−</sup> starting clusters as well as the intermediate alloy cluster products is shown in Figure 1 (deconvoluted mass peaks are

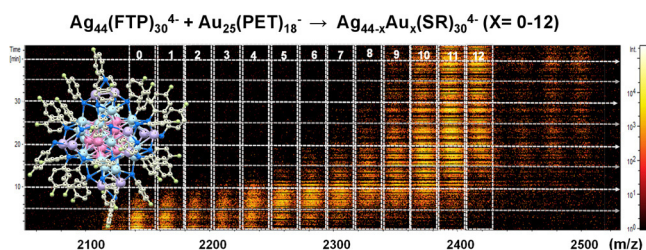


**Figure 1.** Time-dependent overview mass spectra of intercluster reaction showing slow formation of Au<sub>12</sub>Ag<sub>32</sub>(SR)<sub>30</sub><sup>4−</sup> over 40 min reaction time for 5:1 Ag<sub>44</sub>/Au<sub>25</sub> molar ratio (5 μM:1 μM); note the logarithmic intensity scale. Corresponding higher-resolution mass spectra are shown in Figure S1. The DFT-optimized structure of Ag<sub>44</sub>(FTP)<sub>30</sub><sup>4−</sup> is shown in the inset. See Figure 4 for structural details. Colors: Ag on the staple: light purple, Ag in shell: light cyan, Ag in the core: light pink, S: blue, C: light gray, and F: light green. Numbers 0, 1, 2...12 in the figure refer to the number of exchanges (*x*) in the reaction mentioned on the top.

shown in Figure S3). It is clear from the heat map that the initial reaction proceeds primarily via formation and subsequent consumption of intermediates with stepwise

exchange of silver by gold atoms (together with some exchange of ligands—see below). After a reaction time of 40 min, the composition change is essentially completed with predominantly Au<sub>12</sub>Ag<sub>32</sub>(SR)<sub>30</sub><sup>4−</sup> cluster ions being detected. We infer that this corresponds to an exchange equilibrium in solution. This is supported by (i) the observation of reverse exchange upon adding more Ag<sub>44</sub>(SR)<sub>30</sub><sup>4−</sup> starting clusters at later reaction times and (ii) previous mass spectrometric probes of the corresponding Au<sub>25−x</sub>Ag<sub>x</sub>(SR)<sub>18</sub><sup>−</sup> side of the reaction.<sup>24</sup>

Several measurement series at different starting concentration ratios were conducted, and the typical kinetic plots are shown in Figures S4 and S5. A full kinetic analysis will be reported elsewhere. Here, we only note that as in previous reports, we find a highly nonstatistical, Au<sub>x</sub>Ag<sub>44−x</sub>(SR)<sub>30</sub><sup>4−</sup> final product distribution. In particular, we find a 6-fold enrichment in average gold content relative to a binomial distribution weighted with the initial Ag/Au atomic concentration ratio. Furthermore, the mixed cluster mass distribution is much narrower than binomial and essentially cut off beyond 12 substituted Au atoms (Figure S6). The predominance of Au<sub>12</sub>Ag<sub>32</sub>(SR)<sub>30</sub><sup>4−</sup> supports previous conclusions that this composition is an island of low relative free energy among Au<sub>x</sub>Ag<sub>44−x</sub>(SR)<sub>30</sub><sup>4−</sup> species accessed.

Among the initial Ag<sub>44</sub>/Au<sub>25</sub> concentration ratios studied, ranging from 5:1 to 20:1, 5:1 resulted in maximum equilibrium conversion to Ag<sub>32</sub>Au<sub>12</sub>(SR)<sub>30</sub><sup>4−</sup> and was therefore chosen for further study. After recording the reaction kinetics by measuring mass-resolved ion intensity versus time, detailed trapped ion mobility measurements (TIMS) were performed to observe corresponding structural changes. Interestingly, we found that the CCSs of specific Au<sub>x</sub>Ag<sub>44−x</sub>(SR)<sub>30</sub><sup>4−</sup> cluster ions, *x* = 1–12, changed measurably during the course of the reaction.

Figure 2 shows representative contour plots of Au<sub>x</sub>Ag<sub>44−x</sub>(SR)<sub>30</sub><sup>4−</sup> ion intensity as functions of composition (*x* = 0–12) and CCS—for eight different reaction time intervals, A–H. These are based on the extracted TIMS

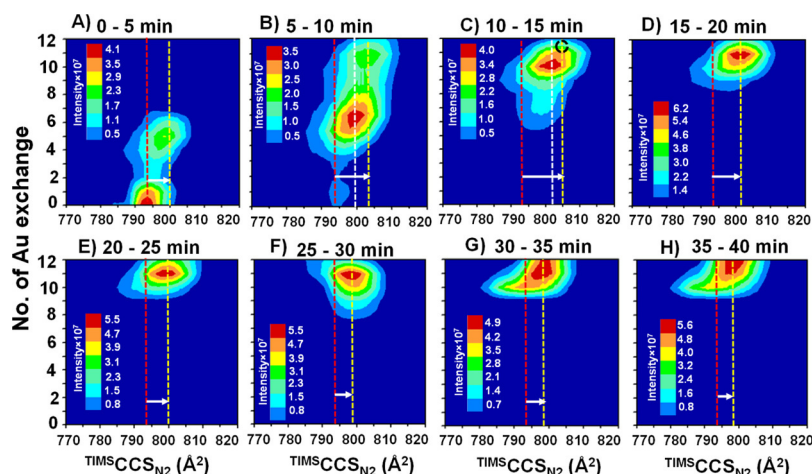


**Figure 2.** (A–H) Two-dimensional plots of time-dependent change in CCS during Au exchange into Ag<sub>44</sub>(SR)<sub>30</sub><sup>4−</sup> clusters to form Au<sub>x</sub>Ag<sub>44−x</sub>(SR)<sub>30</sub><sup>4−</sup>, *x* = 1–12. Initially, the CCS of all intermediate *x* species increases till ca. 20 min of reaction time whereupon their CCS gradually shrinks as exchange equilibrium is approached (with a product distribution centered at *x* = 11 and 12). The red dashed line corresponds to the CCS (peak maximum in corresponding mobilogram) of unreacted Ag<sub>44</sub>(SR)<sub>30</sub><sup>4−</sup> (793 Å<sup>2</sup>). The yellow dashed lines correspond to the peak maximum CCS of the exchange product with the largest CCS in that time interval. The white dashed lines in (B,C) correspond to the peak maximum CCS of the most intense Au exchange product in the specified time interval. The position of the CCS peak maximum for 12 Au-exchanged product has been circled for clarity. Corresponding mobilograms (i.e., intensity vs CCS) are shown in Figure S7.

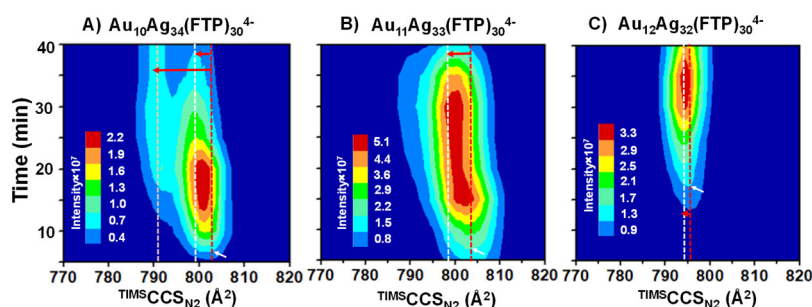


**Figure 3.** Time-dependent changes in the CCS of (A)  $\text{Au}_{10}\text{Ag}_{34}(\text{FTP})_{30}^{4-}$ , (B)  $\text{Au}_{11}\text{Ag}_{33}(\text{FTP})_{30}^{4-}$ , and (C)  $\text{Au}_{12}\text{Ag}_{32}(\text{FTP})_{30}^{4-}$  are shown as contour plots. Each of the mobilograms was extracted for the corresponding mass range to include only contributions from 0 to 1 ligand-exchange products. The CCS values of  $\text{Au}_{10}\text{Ag}_{34}(\text{FTP})_{30}^{4-}$  and  $\text{Au}_{11}\text{Ag}_{33}(\text{FTP})_{30}^{4-}$  change significantly with time while the CCS of  $\text{Au}_{12}\text{Ag}_{32}(\text{FTP})_{30}^{4-}$  remained almost constant. The red dashed lines correspond to the CCS of the respective products at the earliest reaction times at which they are detectable. The white/yellow dashed lines correspond to their final CCS. The initial CCS peak maximum of each species is indicated with a white arrow for clarity. Corresponding CCS vs normalized intensity plots are shown in Figure S11.

mobilograms (inverse mobility vs intensity plots) in  $\text{N}_2$  collision gas (shown in Figure S7) obtained for each of the different  $\text{Au}_x\text{Ag}_{44-x}(\text{SR})_{30}^{4-}$  masses, that is, for each discrete exchange product, at various reaction times following mixing of the silver and gold cluster reactants [under the same optimum solution reaction conditions as used for Figure 1 (5:1  $\text{Ag}_{44}/\text{Au}_{25}$  ratio)]. Corresponding instrumental details are described in a separate section below and further in the Supporting Information. Here, it is only important to realize that under our experimental conditions, we typically achieved ion mobility resolutions of 160 or better—with relative accuracies sufficient to distinguish  $\text{TIMS CCS}_{\text{N}_2}$  differences of 0.2%.<sup>47</sup>

Unreacted  $\text{Ag}_{44}(\text{SR})_{30}^{4-}$  ions in gas phase have an experimental CCS of  $793 \text{ \AA}^2$ . We assume that this corresponds to that of the most stable isomer/conformer under the given experimental conditions. It is unclear to what extent the isolated  $\text{Ag}_{44}(\text{SR})_{30}^{4-}$  structure (determined by TIMS, some milliseconds after electrospraying) differs from that of the same species in solution. For simplicity, we shall assume that any such differences between solution and gas-phase structures are similar for all  $\text{Au}_x\text{Ag}_{44-x}(\text{SR})_{30}^{4-}$ , that is, changes in CCS reflect changes to the cluster structures during reaction in solution.

During the reaction, we first observe a sequential increase in CCS with increasing Au exchange. Specifically, we find that at reaction times of 10–15 min, the experimental CCS has increased from  $793 \text{ \AA}^2$  for the  $\text{Ag}_{44}(\text{SR})_{30}^{4-}$  reactant up to  $805 \text{ \AA}^2$  for  $\text{Au}_{10}\text{Ag}_{34}(\text{SR})_{30}^{4-}$  (~1.5% increase). Also, the corresponding mobilograms become significantly broader with increasing Au exchange compared to the unreacted  $\text{Ag}_{44}(\text{SR})_{30}^{4-}$  (both effects can be seen more clearly in Figure S7, which plots ion intensity vs CCS for various reaction times and compositions). Interestingly, as the reaction proceeds further, we observe that the trend in CCS increases and the peak broadening reverses slightly (Figure 3). Specifically, the final CCS for  $\text{Au}_{12}\text{Ag}_{32}(\text{SR})_{30}^{4-}$  was  $799 \text{ \AA}^2$ . By contrast, the less abundant products with 9 and 10 Au exchanges retain a significantly broader mobilogram till the end of the reaction at 40 min.

There are two aspects which could lead to broadening of the mobilograms. First,  $\text{Au}_{25}(\text{PET})_{18}^{-}$  clusters have a slightly larger ligand than  $\text{Ag}_{44}(\text{FTP})_{30}^{4-}$ . Hence,  $\text{FTP} \rightarrow \text{PET}$  ligand exchange on the cluster surface<sup>24</sup> would be expected to increase the effective cross section of the ion by approximately  $2 \text{ \AA}^2$  per ligand (Figure S8). Consequently, for a  $12 \text{ \AA}^2$  increase, at least six ligand exchanges are necessary. To avoid

this issue, the mobilograms shown in Figures S9 and S10 which are used for the contour plots shown in Figures 2 and 3 were extracted from the lower mass flanks (left side) of the specific  $\text{Au}_x\text{Ag}_{44-x}(\text{SR})_{30}^{4-}$  envelopes, that is, they correspond to 0–2 ligand exchanges (see Figure S7 in the Supporting Information for details). Therefore, the observed increase in CCS of up to  $12 \text{ \AA}^2$  from  $\text{Ag}_{44}(\text{SR})_{30}^{4-}$  to  $\text{Au}_{10}\text{Ag}_{34}(\text{SR})_{30}^{4-}$  can not only be due to ligand exchange. As a corollary, this increase and the associated broadening of the respective mobilograms (see also Figures S7 and S8 in the Supporting Information) must reflect the structural change in order to accommodate the incoming Au and outgoing Ag. It seems likely that this would be associated with multiple isomeric forms having slightly different CCS simultaneously present during the reaction. As the Au/Ag exchange must start from the surface, the initial broadening is likely due to structural distortion of the staples. Over time, the Au atoms migrate from the “surface” and are collected in the core. Most likely as a result of this, the mobilograms of the 12 Au exchange product again becomes narrower and comparable with that of the unreacted  $\text{Ag}_{44}(\text{FTP})_{30}^{4-}$  ion.

To obtain further information on the migration of Au atoms from the surface to the core and the associated (consecutive) structural reorganization, we analyzed the time-dependent CCS of the main products,  $\text{Au}_x\text{Ag}_{44-x}(\text{SR})_{30}^{4-}$  ( $x = 10$ –12) more carefully. The respective measurements are shown in Figure 3. Again, to avoid effects due to ligand exchange, mobilograms were extracted only over a mass range comprising at most one exchanged ligand. Upon its initial formation (at ca. 15 min), the CCS of  $\text{Au}_{10}\text{Ag}_{34}(\text{SR})_{30}^{4-}$  was found to be  $803 \text{ \AA}^2$ , shifting to lower values over time. After a reaction time of around 30 min, the peak maximum has decreased to  $799 \text{ \AA}^2$ . Along with this shift in CCS of the main peak, another peak started to appear, which intensified over time. Its CCS value was found to be  $791 \text{ \AA}^2$ , which is close to the CCS of the unreacted  $\text{Ag}_{44}(\text{FTP})_{30}^{4-}$ . This clearly shows the presence of two isomeric forms of  $\text{Au}_{10}\text{Ag}_{34}(\text{SR})_{30}^{4-}$ . The larger, less-compact one is likely distorted because of nonuniform Au exchange in different layers of the cluster (see later). Note that the differences in Au–Au/Au–S/Au–Ag bond lengths versus the corresponding Ag–Ag/and Ag values are quite small. Therefore, a compact, high-symmetry form of  $\text{Au}_{10}\text{Ag}_{32}(\text{SR})_{30}^{4-}$  with all Au atoms in the core would be expected to have an overall CCS very similar to that of  $\text{Ag}_{44}(\text{FTP})_{30}^{4-}$  ( $793 \text{ \AA}^2$ ). The slight decrease ( $2 \text{ \AA}^2$ ) in the



overall CCS for the more compact isomer could be due to different charge distributions among 10 Au and 2 Ag in the core. A similar trend was also observed for  $\text{Au}_{11}\text{Ag}_{33}(\text{SR})_{30}^{4-}$ , where after 15 min, the overall CCS and peak width decreased with further reaction time to yield a final CCS of  $799 \text{ \AA}^2$  with a shoulder at  $790 \text{ \AA}^2$ . Note that such shifts in CCS are also likely contributed to reorientation of the FTP ligands. Presumably, these rearrange slightly upon migration of Au from the surface to the core (the bond lengths and angles associated with Au–S vs Ag–S links are slightly different).

While  $x = 10$  and 11 exchange products were formed almost immediately after mixing,  $\text{Au}_{12}\text{Ag}_{32}(\text{SR})_{30}^{4-}$  began to be observed in significant amounts only after 20 min. Interestingly, this product does not show any significant change in its CCS [the final CCS was found to be  $794 \text{ \AA}^2$  comparable to  $793 \text{ \AA}^2$  for the parent  $\text{Ag}_{44}(\text{FTP})_{30}^{4-}$ ]. Note that this observation is consistent with the time-dependent structural change of  $x = 10$  and 11. After 20 min, the CCS of both the compact isomer of  $\text{Au}_{10}\text{Ag}_{34}(\text{SR})_{30}^{4-}$  and the main part of  $\text{Au}_{11}\text{Ag}_{33}(\text{SR})_{30}^{4-}$  was already comparable with their final CCS values. Hence, we infer that some clusters can already exchange and rearrange on this timescale to achieve a compact 12 gold atom core structure.

Next, we consider the molecular structure of  $\text{Ag}_{44}(\text{FTP})_{30}$  in more detail. As already pointed out in the introduction, it comprises 12 Ag atoms in an inner hollow icosahedral core, which is surrounded by a shell of another 20 Ag atoms together forming a 32 (12@20) Ag atom core–shell entity. The remaining 12 Ag atoms are situated on the outer protecting staples as  $6 \times \text{Ag}_2(\text{FTP})_5$  mounts.<sup>48</sup> In the simple Jellium model based on s-electron counting scheme initially proposed to explain local stability islands among bare alkali cluster sizes,<sup>3,4</sup> which is also extensively used for monolayer-protected metal clusters,  $\text{Ag}_{44}(\text{SR})_{30}^{4-}$  is a *closed electronic shell species* comprising  $12 + 20 + 12 - 30 + 4 = 18$  s-electrons, that is, having the configuration  $1\text{S}^2 + 1\text{P}^6 + 1\text{D}^{10}$  in the nomenclature of the spherical Jellium model. Our TIMS measurements suggest that the exchange of 12 Ag by 12 Au atoms starts at the surface and leads finally to a stable  $\text{Au}_{12}\text{Ag}_{32}(\text{FTP})_{30}^{4-}$  isomer in which all 12 Au atoms reside in the hollow icosahedral core. To explore this further, we calculated three different isomers of  $\text{Au}_{12}\text{Ag}_{32}(\text{FTP})_{30}^{4-}$  by DFT—using starting geometries based on the known crystal structure of  $[\text{PPh}_4]_4\text{Ag}_{44}(\text{FTP})_{30}$ . For the first isomer (I), all Au atoms were assumed to occupy the hollow icosahedral core. For the second isomer (S—“statistically” distributed), the 12 Au atoms were equally, but otherwise randomly, distributed throughout the three different regions of the metal cluster (in the core, in the middle shell, and among the outer staples—four atoms each). In the final isomer (M), all 12 Au atoms were positioned in the outer staples (mount position) (Figure 4).

Isomer I is the most stable one ( $E = 0 \text{ eV}$ ) followed by isomer S ( $E = 2.8 \text{ eV}$ ) and then isomer M ( $E = 5.8 \text{ eV}$ ) as also predicted by previous DFT calculations and consistent with the crystal structure determination of  $[\text{PPh}_4]_4[\text{Au}_{12}\text{Ag}_{32}(\text{FTP})_{30}]$ .<sup>28</sup> Based on the DFT results, the CCS of each of these isomers in  $\text{N}_2$  as well as that of the parent  $\text{Ag}_{44}(\text{FTP})_{30}^{4-}$  were modeled by trajectory calculations using IMoS 1.09<sup>44</sup> with the default Lennard-Jones parameters and charges based on NBO analysis (see the Experimental Section and ref 39). For  $\text{Ag}_{44}(\text{FTP})_{30}^{4-}$ ,  $\text{CCS}_{\text{NBO}}$  was found to be  $902.5 \text{ \AA}^2$ , while for the I-, M-, S-isomers of  $\text{Au}_{12}\text{Ag}_{32}(\text{FTP})_{30}^{4-}$ , the calculated CCS values were 901.3, 911.0, and  $908.7 \text{ \AA}^2$ ,

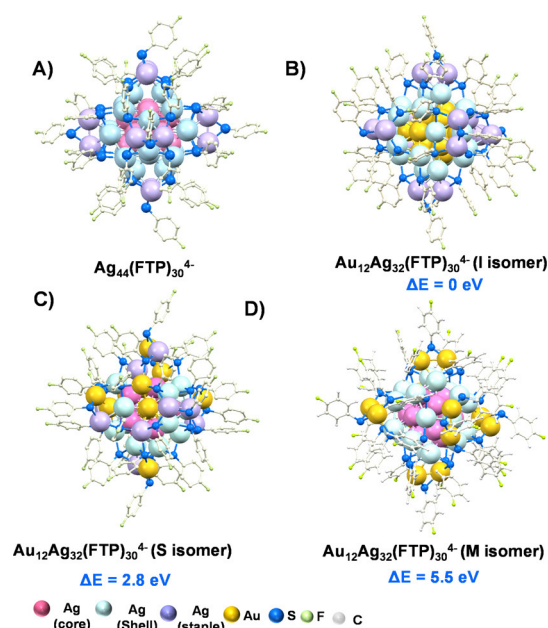


**Figure 4.** DFT-optimized structures of  $\text{Ag}_{44}(\text{FTP})_{30}^{4-}$  and three different isomers of  $\text{Au}_{12}\text{Ag}_{32}(\text{SR})_{30}^{4-}$  (relative energies in red). In all cases, 12 metal atoms are in the six staples (each terminated by five ligands), 20 metal atoms form a shell underneath within which 12 metal atoms reside in a hollow icosahedral core. Isomer I: all 12 Au atoms in the hollow inner icosahedron. Isomer S: four Au atoms statistically distributed in each of the three cluster layers. Isomer M: all 12 Au atoms in the staples.

respectively. The calculated  $\text{CCS}_{\text{NBO}}$  of  $\text{Ag}_{44}(\text{FTP})_{30}^{4-}$  is 14% larger than the experimental value  $^{\text{TIMS}}\text{CCS}_{\text{N}_2}$  ( $902.5 \text{ \AA}^2$  vs  $793 \text{ \AA}^2$ ), which is a significantly larger difference than one might expect. The calculated CCS for highly charged species depends crucially on the partial charge distribution within the ion. The NBO analysis places quite high partial charges on each atom (up to 0.6, see the Supporting Information). Therefore, the calculation was repeated with two different charge distributions: first, the Mulliken population analysis was used which predicted even higher partial charges (up to 1.5). This resulted in  $\text{CCS}_{\text{Mul}}$  values of  $905.9 \text{ \AA}^2$  for  $\text{Ag}_{44}(\text{FTP})_{30}^{4-}$  and 905.9, 920.5, and  $914.7 \text{ \AA}^2$  for the I-, M-, and S-isomers of  $\text{Au}_{12}\text{Ag}_{32}(\text{FTP})_{30}^{4-}$ , respectively, that is, between 0.4 and 1.0% larger than the NBO-based  $\text{CCS}_{\text{NBO}}$ . Second, the 4-fold negative charge was put into the (hollow) center of the cluster, leaving the individual atoms uncharged. Under this extreme assumption,  $\text{CCS}_{\text{center}}$  was found to be 860.5 for  $\text{Ag}_{44}(\text{FTP})_{30}^{4-}$  and 858.6, 875.5, and  $867.1 \text{ \AA}^2$  for the I-, M-, and S-isomers of  $\text{Au}_{12}\text{Ag}_{32}(\text{FTP})_{30}^{4-}$ , that is, roughly 8% above the experimental values. In other words, these calculations show that the charge distribution has a large effect on the calculated CCS and that  $\text{CCS}_{\text{center}}$  fits better than NBO or Mulliken. However, the CCS difference between experiment and calculation remains rather large, independent of the charge placement algorithm. This is possibly a reflection of other systematic errors in the TM calculations (e.g., because of default parameterized metal atoms). To take this into account, an empirical scaling factor (0.879) was used to calibrate the calculated  $\text{CCS}_{\text{NBO}}$  of  $902.5 \text{ \AA}^2$  against the experimental  $^{\text{TIMS}}\text{CCS}_{\text{N}_2}$   $793 \text{ \AA}^2$  value. Using the same scaling factor for the three isomers of  $\text{Au}_{12}\text{Ag}_{32}(\text{FTP})_{30}^{4-}$ ,  $^{\text{corr}}\text{CCS}_{\text{NBO}}$  was found to be 793.1, 800.8, and  $798.7 \text{ \AA}^2$  for isomers I, M, and S, respectively.



**Table 1.** Comparison of Experimental  $^{TIMS}CCS_{N_2}$  Values with CCS Trajectory Calculations Based on DFT-Optimized Structures as Shown in Figure 4<sup>a</sup>

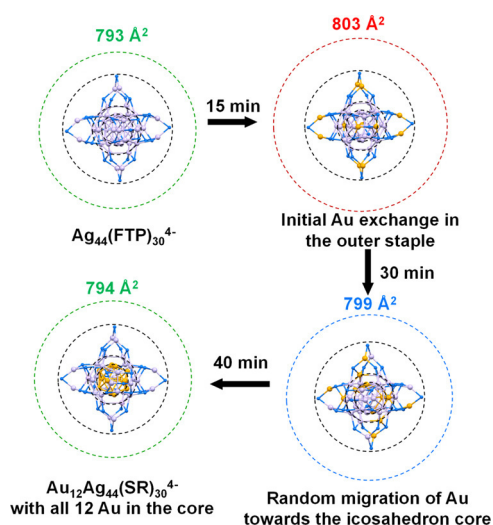
ions	experimental CCS (Å <sup>2</sup> )	calculated CCS <sub>NBO</sub> (Å <sup>2</sup> )	calculated CCS <sub>center</sub> (Å <sup>2</sup> )	calculated <sup>corr</sup> CCS <sub>NBO</sub> (Å <sup>2</sup> )	calculated <sup>corr</sup> CCS <sub>center</sub> (Å <sup>2</sup> )
Ag <sub>44</sub> (FTP) <sub>30</sub> <sup>4−</sup>	793	902.5	860.5	793.3	793.4
Au <sub>12</sub> Ag <sub>32</sub> (FTP) <sub>30</sub> <sup>4−</sup> (I) (0 eV)	794	901.3	858.6	793.1	791.6
Au <sub>12</sub> Ag <sub>32</sub> (FTP) <sub>30</sub> <sup>4−</sup> (S) (2.8 eV)		911.0	875.5	800.8	807.2
Au <sub>12</sub> Ag <sub>32</sub> (FTP) <sub>30</sub> <sup>4−</sup> (M) (5.5 eV)		908.7	867.1	798.7	799.5

<sup>a</sup>The trajectory calculations using IMoS 1.09 were performed with two different assumptions concerning (excess) charge localization, CCS<sub>NBO</sub>, and CCS<sub>center</sub>; see main text for details. <sup>corr</sup>CCS values were scaled against the experimental value for Ag<sub>44</sub>(FTP)<sub>30</sub><sup>4−</sup>. Using exact hard spheres scattering method which completely neglects charges, similar CCS values as with the TM (with the charge localized in the center) were obtained.

Apparently, the lowest energy isomer I fits best to the experimental  $^{TIMS}CCS_{N_2}$  value of 794 Å<sup>2</sup>. Scaling the CCS calculated with the central charge (CCS<sub>center</sub>) in an analogous fashion by 0.922 (to match the experimental  $^{TIMS}CCS_{N_2}$  of Ag<sub>44</sub>(FTP)<sub>30</sub><sup>4−</sup>) results in <sup>corr</sup>CCS<sub>center</sub> values of 791.6, 807.2, and 799.5 Å<sup>2</sup> (I, M, and S)—again isomer I fits the best. Therefore, the isomer assignment is rather robust with respect to the method used. The results are summarized in Table 1.

The DFT + IMoS-based modeling of the CCS measurements therefore supports our inference that the approximately 1% increase in the CCS observed for Au<sub>x</sub>Ag<sub>44−x</sub>(SR)<sub>30</sub><sup>4−</sup> ( $x = 10, 11$ ) at a reaction time of 10 min—relative to the CCS of the parent cluster—reflects the initial Au/Ag exchange on the staples. This CCS increase is similar to the 1.2% larger CCS of the M isomer of Au<sub>12</sub>Ag<sub>32</sub>(SR)<sub>30</sub><sup>4−</sup> versus Au<sub>44</sub>(SR)<sub>30</sub><sup>4−</sup>. Similarly, the significant CCS decrease subsequently observed in particular for  $x = 10$  and 11 can be related to the S isomer of Au<sub>12</sub>Ag<sub>32</sub>(SR)<sub>30</sub><sup>4−</sup>. This is 0.7% larger than the parent Ag<sub>44</sub>(FTP)<sub>30</sub><sup>4−</sup>. Note that S isomer is considered as a model for an intermediate rather than the actual one. Once the reaction reaches equilibrium and the 12 Au atom exchange product dominates in intensity, the CCS of Au<sub>12</sub>Ag<sub>32</sub>(SR)<sub>30</sub><sup>4−</sup> was found to be 794 Å<sup>2</sup>, which is almost identical to that of the parent Ag<sub>44</sub>(FTP)<sub>30</sub><sup>4−</sup> and is in good agreement with isomer I. Consequently, we experimentally resolve the migration of Au atoms from the staples to the cluster core (see Scheme 1)—a process which can apparently occur on a ca. 10 min timescale in room-temperature solutions.

To obtain further insight into Au atom migration, CID measurements were performed for each of the Au exchange products, Au<sub>x</sub>Ag<sub>44−x</sub>(SR)<sub>30</sub><sup>4−</sup> ( $x = 0–12$ ), with varying collision energy. Solution concentrations, concentration ratios, and reaction times differed slightly from those used for timsTOF so as to obtain optimal signal intensities. Typically,  $x = 1–5$  exchange products were probed by CID after relatively short reaction times to obtain sufficient signals and for  $x = 6–12$  after longer reaction times allowing for structural equilibration. All the CID experiments were performed on the Waters' SYNAPT G2S platform in slightly higher than regular trap gas flow (5 mL/min instead of regular 2 mL/min) to access a larger lab frame collision energy range.<sup>49</sup> To analyze the data, the laboratory collision energy settings were converted to center-of-mass energy (assuming a single ion/Ar collision) and the energy values corresponding to 50% survival yield were then determined ( $=E_{com(50)}$ ). The corresponding numbers are shown in Figures S12–S15. Note that in the absence of calibration measurements with structurally related thermometer ions,<sup>50</sup> the collision energy settings and thus the resulting  $E_{com(50)}$  values are only relative

**Scheme 1.** Schematic of Au Atom Migration from the Outer Staple to the Inner core<sup>a</sup>

<sup>a</sup>Ligands are not shown for clarity (apart from the S atoms). The ligand layer is represented by the outermost dashed circle to signify the range of the ligand shell whose diameter increases in the order green → blue → red during Au exchange and subsequent migration. Colors: Ag: purple, Au: orange, and S: blue.

numbers, that is, for comparison between different  $x = 0–12$ . They are not absolute dissociation energy determinations. With this caveat in mind, the  $E_{com(50)}$  values of 0.225 and 0.286 eV for Ag<sub>44</sub>(FTP)<sub>30</sub><sup>4−</sup> and Au<sub>12</sub>Ag<sub>32</sub>(SR)<sub>30</sub><sup>4−</sup>, respectively, confirm the lower relative stability of the parent Ag<sub>44</sub>(FTP)<sub>30</sub><sup>4−</sup>. The corresponding  $E_{com(50)}$  determination for Au<sub>12</sub>Ag<sub>32</sub>(SR)<sub>30</sub><sup>4−</sup> is shown in Figure S12B. A plot of  $E_{com(50)}$  values versus  $x = 0–12$  is shown in Figure S12C. Although there is no clear monotonic dependence on  $x$  (within the noise of the measurements),  $E_{com(50)}$  values are systematically >0.225 eV, that is, Au exchange always leads to stabilization relative to Ag<sub>44</sub>(FTP)<sub>30</sub><sup>4−</sup>.

For Ag<sub>44</sub>(FTP)<sub>30</sub><sup>4−</sup>, the main fragmentation pathway involves Ag(FTP)<sub>2</sub><sup>−</sup> ( $m/z$  362) loss (see Figure S12A). In all Au exchange products, an additional fragment peak appears at  $m/z$  451, which can be assigned to the corresponding Au(FTP)<sub>2</sub><sup>−</sup> loss channel. In Figure S12D, we have plotted the normalized intensity of the  $m/z$  451 fragment signal (at a constant laboratory collision energy setting of 6 V) against  $x = 0–12$ . It is evident that for higher  $x$ , the Au(FTP)<sub>2</sub><sup>−</sup> fragment intensity increases. This is surprising at first glance: if all Au atoms occupy the I position (i.e., located in the central icosahedron) and only the “staples” at the clusters surface are

involved in fragmentation, one would expect to see just  $\text{Ag}(\text{FTP})_2^-$  loss. Clearly, some Au atoms must be transported back to the staples after collisional energization. Our experimental time window during which subsequent fragmentation can be detected is likely on the order of 100  $\mu\text{s}$ . Consequently, we infer that at the vibrational temperatures generated upon collisions with Ar, the cluster forms a nanoalloy in which the heavier Au atoms can diffuse from the core to the cluster surface (staple) on the measurement timescale. In future work, it will be interesting to more quantitatively compare such observations to analogous in situ transmission electron microscopy studies of T-dependent redistribution upon alloying core–shell silver–gold nanoparticles.<sup>51</sup>

#### 4. CONCLUSIONS

In summary, we have used time-dependent TIMS to probe the intercluster reactions between  $\text{Ag}_{44}(\text{FTP})_{30}^{4-}$  and  $\text{Au}_{25}(\text{PET})_{18}^-$  in room-temperature solutions. As silver and gold atoms are very similar in size, there is very little scope to understand the structural changes in such cluster systems arising from Ag/Au exchange. Nevertheless, we show here for the first time that the high resolution and relative accuracy of TIMS is sufficient to observe systematic, time-dependent changes in the CCSs of  $\text{Au}_x\text{Ag}_{44-x}(\text{SR})_{30}^{4-}$  species. These can be assigned to migration of exchanging Au atoms from the cluster surface (staples/mount position) via the shell to the core on the 0–40 min timescale in the room-temperature solution mixture. Note that we have presented the simplest explanation which is still consistent with the experimental data. For this, the following set of assumptions has been made: (i) the electrosprayable  $\text{Au}_x\text{Ag}_{44-x}(\text{SR})_{30}^{4-}$  tetra-anions probed (without fragmentation) are assumed to be representative intermediates in a complicated kinetic scheme; (ii) in particular, intermediates with only 0–1 ligand exchange have been considered for interpretation of experimental CCS changes while more ligand exchange is usual; and (iii) the reaction proceeds via single Ag/Au exchange at a time (no strong “even/odd” effect was found in the time-dependent mass spectra). In future work on this system, it will be interesting to look more closely at early stage exchange events by comparing the present results with analogous measurements on clusters carrying the same SR ligands.

Apparently, about two or more Au exchanges in the staples lead to a measurable increase in the CCS mainly because of the differences in Ag–S–ligand and Au–S–ligand arrangement. This effect reverts when Au atoms “submerge” into the intermediate shell/icosahedral core whereupon the Ag–S–ligand reassumes its original arrangement on the surface. The interdiffusion of Au/Ag in the shell  $\rightarrow$  core is observed at the resolution limit of TIMS. We do however see two isomers for  $\text{Au}_{10}\text{Ag}_{34}(\text{SR})_{30}^{4-}$  and a low cross-sectional shoulder on  $\text{Au}_{11}\text{Ag}_{33}(\text{SR})_{30}^{4-}$ . By contrast, the CCS of  $\text{Au}_{12}\text{Ag}_{32}(\text{SR})_{30}^{4-}$  does not change significantly over the reaction time of 20–40 min, and hence, here diffusion of Au from the shell to the core is not clearly visible (or perhaps for the  $x = 12$  free energy minimum, it is just too fast to be observed by timsTOF). Upon collisional heating during tandem mass spectrometry, we observed predominantly  $\text{Au}(\text{FTP})_2^-$  fragment which might imply analogous back-migration of the heavier Au atoms from the core to the staples. Our experimental observations are supported by DFT calculations of different isomeric structures. By determining the corresponding CCS values and comparing

them to experiment, we have been able to draw some first inferences concerning the migration mechanism. Thus, this study establishes high-resolution TIMS as a very useful method to study heteroatom doping of monolayer-protected atomically precise metal clusters in condensed phase.

#### ■ ASSOCIATED CONTENT

##### Supporting Information

The Supporting Information is available free of charge on the ACS Publications website at DOI: 10.1021/acs.jpcc.9b08686.

Synthesis of  $[\text{TOA}][\text{Au}_{25}(\text{PET})_{18}]$  and  $[\text{PPh}_4][\text{Ag}_{44}(\text{FTP})_{30}]$ , instrumental parameters, concentration-dependent kinetics, plots of 50% survival yields of different Au-exchanged products, coordinates of DFT-optimized structures of  $\text{Ag}_{44}(\text{FTP})_{30}^{4-}$ , and different isomers of  $\text{Au}_{12}\text{Ag}_{32}(\text{FTP})_{30}^{4-}$  with corresponding partial charges (PDF)

#### ■ AUTHOR INFORMATION

##### Corresponding Authors

\*E-mail: horst.hahn@kit.edu (H.H.).

\*E-mail: pradeep@iitm.ac.in (T.P.).

\*E-mail: manfred.kappes@kit.edu (M.M.K.).

##### ORCID

Ananya Bakshi: 0000-0003-3328-4399

Patrick Weis: 0000-0001-7006-6759

Horst Hahn: 0000-0001-9901-3861

Thalappil Pradeep: 0000-0003-3174-534X

Manfred M. Kappes: 0000-0002-1199-1730

##### Author Contributions

A.B. and E.K.S. have performed the experiments and analyzed the data. DFT optimization and calculation of CCS were performed by P.W., A.B., and E.K.S. M.M.K. and A.B. have written the manuscript, which was refined by other authors. D.G. and K.R.K. have synthesized the clusters and helped in initial characterization of the clusters. The work was done in collaboration with T.P. and his group. All authors participated in the discussion and interpretation of the data. The whole project was supervised by M.M.K.

##### Notes

The authors declare no competing financial interest.

#### ■ ACKNOWLEDGMENTS

M.M.K. and H.H. acknowledge the research support from the Helmholtz Association of German Research Centers through Program STN (Science and Technology of Nanosystems). Additionally, P.W. and M.M.K. thank KIT as well as the DFG-funded collaborative research center “3MET” (Project C6) for supporting the timsTOF implementation. T.P. thanks the Department of Science and Technology, India, for funding. H.H. acknowledges the financial support from German Academic Exchange Service (DAAD).

#### ■ REFERENCES

- (1) Foster, P. J.; Leckenby, R. E.; Robbins, E. J. Ionization potentials of clustered alkali metal atoms. *Proc. Phys. Soc., London, At. Mol. Phys.* **1969**, *2*, 478–483.
- (2) Dietz, T. G.; Duncan, M. A.; Powers, D. E.; Smalley, R. E. Laser production of supersonic metal cluster beams. *J. Chem. Phys.* **1981**, *74*, 6511–6512.

- (3) Kappes, M. M.; Kunz, R. W.; Schumacher, E. Production of large sodium clusters ( $N_{\text{ax}}, x \leq 65$ ) by seeded beam expansions. *Chem. Phys. Lett.* **1982**, *91*, 413–418.
- (4) Knight, W. D.; Clemenger, K.; De Heer, W. A.; Saunders, W. A.; Chou, M. Y.; Cohen, M. L. Electronic shell structure and abundances of sodium clusters. *Phys. Rev. Lett.* **1984**, *52*, 2141–2143.
- (5) Heaven, M. W.; Dass, A.; White, P. S.; Holt, K. M.; Murray, R. W. Crystal Structure of the Gold Nanoparticle  $[\text{N}(\text{C}_8\text{H}_{17})_4][\text{Au}_{25}(\text{SCH}_2\text{CH}_2\text{Ph})_{18}]$ . *J. Am. Chem. Soc.* **2008**, *130*, 3754–3755.
- (6) Zhu, M.; Aikens, C. M.; Hollander, F. J.; Schatz, G. C.; Jin, R. Correlating the Crystal Structure of A Thiol-Protected Au<sub>25</sub> Cluster and Optical Properties. *J. Am. Chem. Soc.* **2008**, *130*, 5883–5885.
- (7) Negishi, Y.; Chaki, N. K.; Shichibu, Y.; Whetten, R. L.; Tsukuda, T. Origin of Magic Stability of Thiolated Gold Clusters: A Case Study on Au<sub>25</sub>(SC<sub>6</sub>H<sub>13</sub>)<sub>18</sub>. *J. Am. Chem. Soc.* **2007**, *129*, 11322–11323.
- (8) Brust, M.; Walker, M.; Bethell, D.; Schiffrin, D. J.; Whyman, R. Synthesis of thiol-derivatized gold nanoparticles in a two-phase liquid-liquid system. *J. Chem. Soc., Chem. Commun.* **1994**, 801–802.
- (9) Gilroy, K. D.; Ruditskiy, A.; Peng, H.-C.; Qin, D.; Xia, Y. Bimetallic Nanocrystals: Syntheses, Properties, and Applications. *Chem. Rev.* **2016**, *116*, 10414–10472.
- (10) Jin, R.; Zeng, C.; Zhou, M.; Chen, Y. Atomically Precise Colloidal Metal Nanoclusters and Nanoparticles: Fundamentals and Opportunities. *Chem. Rev.* **2016**, *116*, 10346–10413.
- (11) Yan, J.; Teo, B. K.; Zheng, N. Surface Chemistry of Atomically Precise Coinage-Metal Nanoclusters: From Structural Control to Surface Reactivity and Catalysis. *Acc. Chem. Res.* **2018**, *51*, 3084–3093.
- (12) Krishnadas, K. R.; Natarajan, G.; Bakshi, A.; Ghosh, A.; Khatun, E.; Pradeep, T. Metal-Ligand Interface in the Chemical Reactions of Ligand-Protected Noble Metal Clusters. *Langmuir* **2019**, *35*, 11243.
- (13) Krishnadas, K. R.; Bakshi, A.; Ghosh, A.; Natarajan, G.; Som, A.; Pradeep, T. Interparticle Reactions: An Emerging Direction in Nanomaterials Chemistry. *Acc. Chem. Res.* **2017**, *50*, 1988–1996.
- (14) Chakraborty, I.; Pradeep, T. Atomically Precise Clusters of Noble Metals: Emerging Link between Atoms and Nanoparticles. *Chem. Rev.* **2017**, *117*, 8208–8271.
- (15) Wang, S.; Li, Q.; Kang, X.; Zhu, M. Customizing the Structure, Composition, and Properties of Alloy Nanoclusters by Metal Exchange. *Acc. Chem. Res.* **2018**, *51*, 2784–2792.
- (16) Hossain, S.; Ono, T.; Yoshioka, M.; Hu, G.; Hosoi, M.; Chen, Z.; Nair, L. V.; Niihori, Y.; Kurashige, W.; Jiang, D.-e.; Negishi, Y. Thiolate-protected trimetallic Au<sub>20</sub>Ag<sub>4</sub>Pd and Au<sub>20</sub>Ag<sub>4</sub>Pt alloy clusters with controlled chemical composition and metal positions. *J. Phys. Chem. Lett.* **2018**, *9*, 2590–2594.
- (17) Wang, S.; Song, Y.; Jin, S.; Liu, X.; Zhang, J.; Pei, Y.; Meng, X.; Chen, M.; Li, P.; Zhu, M. Metal Exchange Method Using Au<sub>25</sub> Nanoclusters as Templates for Alloy Nanoclusters with Atomic Precision. *J. Am. Chem. Soc.* **2015**, *137*, 4018–4021.
- (18) Yang, S.; Wang, S.; Jin, S.; Chen, S.; Sheng, H.; Zhu, M. A metal exchange method for thiolate-protected tri-metal M<sub>1</sub>Ag<sub>x</sub>Au<sub>24-x</sub>(SR)<sub>18</sub> (M = Cd/Hg) nanoclusters. *Nanoscale* **2015**, *7*, 10005–10007.
- (19) Li, Q.; Luo, T.-Y.; Taylor, M. G.; Wang, S.; Zhu, X.; Song, Y.; Mpourmpakis, G.; Rosi, N. L.; Jin, R. Molecular “surgery” on a 23-gold-atom nanoparticle. *Sci. Adv.* **2017**, *3*, No. e1603193.
- (20) Alkan, F.; Pandeya, P.; Aikens, C. M. Understanding the Effect of Doping on Energetics and Electronic Structure for Au<sub>25</sub>, Ag<sub>25</sub>, and Au<sub>38</sub> Clusters. *J. Phys. Chem. C* **2019**, *123*, 9516–9527.
- (21) Li, Y.; Luo, T.-Y.; Zhou, M.; Song, Y.; Rosi, N. L.; Jin, R. A Correlated Series of Au/Ag Nanoclusters Revealing the Evolutionary Patterns of Asymmetric Ag Doping. *J. Am. Chem. Soc.* **2018**, *140*, 14235–14243.
- (22) Krishnadas, K. R.; Bakshi, A.; Ghosh, A.; Natarajan, G.; Pradeep, T. Structure-conserving spontaneous transformations between nanoparticles. *Nat. Commun.* **2016**, *7*, 13447.
- (23) Krishnadas, K. R.; Bakshi, A.; Ghosh, A.; Natarajan, G.; Pradeep, T. Manifestation of Geometric and Electronic Shell Structures of Metal Clusters in Intercluster Reactions. *ACS Nano* **2017**, *11*, 6015–6023.
- (24) Krishnadas, K. R.; Ghosh, A.; Bakshi, A.; Chakraborty, I.; Natarajan, G.; Pradeep, T. Intercluster Reactions between Au<sub>25</sub>(SR)<sub>18</sub> and Ag<sub>44</sub>(SR)<sub>30</sub>. *J. Am. Chem. Soc.* **2016**, *138*, 140–148.
- (25) Krishnadas, K. R.; Ghosh, D.; Ghosh, A.; Natarajan, G.; Pradeep, T. Structure-Reactivity Correlations in Metal Atom Substitutions of Monolayer-Protected Noble Metal Alloy Clusters. *J. Phys. Chem. C* **2017**, *121*, 23224–23232.
- (26) Bakshi, A.; Chakraborty, P.; Bhat, S.; Natarajan, G.; Pradeep, T. [Au<sub>25</sub>(SR)<sub>18</sub>]<sub>22</sub>: a noble metal cluster dimer in the gas phase. *Chem. Commun.* **2016**, *52*, 8397–8400.
- (27) Chakraborty, P.; Bakshi, A.; Mudedla, S. K.; Nag, A.; Paramasivam, G.; Subramanian, V.; Pradeep, T. Understanding proton capture and cation-induced dimerization of [Ag<sub>29</sub>(BDT)<sub>12</sub>]<sub>3</sub> clusters by ion mobility mass spectrometry. *Phys. Chem. Chem. Phys.* **2018**, *20*, 7593–7603.
- (28) Yang, H.; Wang, Y.; Huang, H.; Gell, L.; Lehtovaara, L.; Malola, S.; Hakkinen, H.; Zheng, N. All-thiol-stabilized Ag<sub>44</sub> and Au<sub>12</sub>Ag<sub>32</sub> nanoparticles with single-crystal structures. *Nat. Commun.* **2013**, *4*, 2422.
- (29) Su, H.; Wang, Y.; Ren, L.; Yuan, P.; Teo, B. K.; Lin, S.; Zheng, L.; Zheng, N. Fractal Patterns in Nucleation and Growth of Icosahedral Core of [Au<sub>n</sub>Ag<sub>44-n</sub>(SC<sub>6</sub>H<sub>3</sub>F<sub>2</sub>)<sub>30</sub>]<sub>4</sub> (n = 0–12) via ab Initio Synthesis: Continuously Tunable Composition Control. *Inorg. Chem.* **2019**, *58*, 259–264.
- (30) Yao, Q.; Feng, Y.; Fung, V.; Yu, Y.; Jiang, D.-e.; Yang, J.; Xie, J. Precise control of alloying sites of bimetallic nanoclusters via surface motif exchange reaction. *Nat. Commun.* **2017**, *8*, 1555.
- (31) Zhang, B.; Salassa, G.; Bürgi, T. Silver migration between Au<sub>38</sub>(SC<sub>2</sub>H<sub>4</sub>Ph)<sub>24</sub> and doped Ag<sub>x</sub>Au<sub>38-x</sub>(SC<sub>2</sub>H<sub>4</sub>Ph)<sub>24</sub> nanoclusters. *Chem. Commun.* **2016**, *52*, 9205–9207.
- (32) Chakraborty, P.; Nag, A.; Natarajan, G.; Bandyopadhyay, N.; Paramasivam, G.; Panwar, M. K.; Chakrabarti, J.; Pradeep, T. Rapid isotopic exchange in nanoparticles. *Sci. Adv.* **2019**, *5*, No. eaau7555.
- (33) Bertorelle, F.; Russier-Antoine, I.; Comby-Zerbino, C.; Chiro, F.; Dugourd, P.; Brevet, P.-F.; Antoine, R. Isomeric Effect of Mercaptobenzoic Acids on the Synthesis, Stability, and Optical Properties of Au<sub>25</sub>(MBA)<sub>18</sub> Nanoclusters. *ACS Omega* **2018**, *3*, 15635–15642.
- (34) Comby-Zerbino, C.; Bertorelle, F.; Chiro, F.; Dugourd, P.; Antoine, R. Structural insights into glutathione-protected gold Au<sub>10-12</sub>(SG)<sub>10-12</sub> nanoclusters revealed by ion mobility mass spectrometry. *Eur. Phys. J. D* **2018**, *72*, 144.
- (35) Daly, S.; Choi, C. M.; Zavras, A.; Krstić, M.; Chiro, F.; Connell, T. U.; Williams, S. J.; Donnelly, P. S.; Antoine, R.; Giuliani, A.; Bonacić-Koutecký, V.; Dugourd, P.; O’Hair, R. A. J. Gas-Phase Structural and Optical Properties of Homo- and Heterobimetallic Rhombic Dodecahedral Nanoclusters [Ag<sub>14-n</sub>Cu<sub>n</sub>(C≡tBu)<sub>12</sub>X]<sup>+</sup> (X = Cl and Br): Ion Mobility, VUV and UV Spectroscopy, and DFT Calculations. *J. Phys. Chem. C* **2017**, *121*, 10719–10727.
- (36) Bakshi, A.; Harvey, S. R.; Natarajan, G.; Wysocki, V. H.; Pradeep, T. Possible isomers in ligand protected Ag<sub>11</sub> cluster ions identified by ion mobility mass spectrometry and fragmented by surface induced dissociation. *Chem. Commun.* **2016**, *52*, 3805–3808.
- (37) Bakshi, A.; Ghosh, A.; Mudedla, S. K.; Chakraborty, P.; Bhat, S.; Mondal, B.; Krishnadas, K. R.; Subramanian, V.; Pradeep, T. Isomerism in Monolayer Protected Silver Cluster Ions: An Ion Mobility-Mass Spectrometry Approach. *J. Phys. Chem. C* **2017**, *121*, 13421–13427.
- (38) Bhat, S.; Bakshi, A.; Mudedla, S. K.; Natarajan, G.; Subramanian, V.; Pradeep, T. Au<sub>22</sub>Ir<sub>3</sub>(PET)<sub>18</sub>: An Unusual Alloy Cluster through Intercluster Reaction. *J. Phys. Chem. Lett.* **2017**, *8*, 2787–2793.
- (39) Becke, A. D. Density-functional exchange-energy approximation with correct asymptotic behavior. *Phys. Rev. A: At., Mol., Opt. Phys.* **1988**, *38*, 3098–3100.
- (40) Perdew, J. P. Density-functional approximation for the correlation energy of the inhomogeneous electron gas. *Phys. Rev. B: Condens. Matter Mater. Phys.* **1986**, *33*, 8822–8824.



- (41) Weigend, F.; Ahlrichs, R. Balanced basis sets of split valence, triple zeta valence and quadruple zeta valence quality for H to Rn: Design and assessment of accuracy. *Phys. Chem. Chem. Phys.* **2005**, *7*, 3297–3305.
- (42) Furche, F.; Ahlrichs, R.; Hättig, C.; Klopper, W.; Sierka, M.; Weigend, F. Turbomole. *Wiley Interdiscip. Rev.: Comput. Mol. Sci.* **2014**, *4*, 91–100.
- (43) Reed, A. E.; Weinstock, R. B.; Weinhold, F. Natural population analysis. *J. Chem. Phys.* **1985**, *83*, 735–746.
- (44) Larriba, C.; Hogan, C. J. Ion Mobilities in Diatomic Gases: Measurement versus Prediction with Non-Specular Scattering Models. *J. Phys. Chem. A* **2013**, *117*, 3887–3901.
- (45) Larriba, C.; Hogan, C. J. Free molecular collision cross section calculation methods for nanoparticles and complex ions with energy accommodation. *J. Comput. Phys.* **2013**, *251*, 344–363.
- (46) Wu, T.; Derrick, J.; Nahin, M.; Chen, X.; Larriba-Andaluz, C. Optimization of long range potential interaction parameters in ion mobility spectrometry. *J. Chem. Phys.* **2018**, *148*, 074102.
- (47) Hennrich, F.; Schneider, E.; Weis, P.; Kappes, M. M. Comparing Empty and Filled Fullerene Cages with High-Resolution Trapped Ion Mobility Spectrometry. *J. Am. Soc. Mass Spectrom.* **2019**, *30*, 1973.
- (48) Desireddy, A.; Conn, B. E.; Guo, J.; Yoon, B.; Barnett, R. N.; Monahan, B. M.; Kirschbaum, K.; Griffith, W. P.; Whetten, R. L.; Landman, U.; Bigioni, T. P. Ultrastable silver nanoparticles. *Nature* **2013**, *501*, 399–402.
- (49) Chakraborty, P.; Baksi, A.; Khatun, E.; Nag, A.; Ghosh, A.; Pradeep, T. Dissociation of Gas Phase Ions of Atomically Precise Silver Clusters Reflects Their Solution Phase Stability. *J. Phys. Chem. C* **2017**, *121*, 10971–10981.
- (50) Brendle, K.; Kordel, M.; Schneider, E.; Wagner, D.; Bräse, S.; Weis, P.; Kappes, M. M. Collision Induced Dissociation of Benzylpyridinium-Substituted Porphyrins: Towards a Thermometer Scale for Multiply Charged Ions? *J. Am. Soc. Mass Spectrom.* **2018**, *29*, 382–392.
- (51) van der Hoeven, J. E. S.; Welling, T. A. J.; Silva, T. A. G.; van den Reijen, J. E.; La Fontaine, C.; Carrier, X.; Louis, C.; van Blaaderen, A.; de Jongh, P. E. In Situ Observation of Atomic Redistribution in Alloying Gold-Silver Nanorods. *ACS Nano* **2018**, *12*, 8467–8476.

# Supporting Information

## Nano-Gymnastics: Visualisation of Inter-Cluster Reactions by High Resolution Trapped Ion Mobility Mass Spectrometry

Ananya Bakshi<sup>1,2</sup>, Erik Karsten Schneider<sup>2</sup>, Patrick Weis<sup>2</sup>, K. R. Krishnadas<sup>3</sup>, Debasmita Ghosh<sup>3</sup>, Horst Hahn,<sup>1\*</sup> Thalappil Pradeep<sup>3\*</sup> and Manfred M. Kappes<sup>1,2\*</sup>

<sup>1</sup>*Institute of Nanotechnology, Karlsruhe Institute of Technology, 76344 Eggenstein-Leopoldshafen, Germany*

<sup>2</sup>*Institute of Physical Chemistry, Karlsruhe Institute of Technology, 76131 Karlsruhe, Germany*

<sup>3</sup>*DST Unit of Nanoscience and Thematic Unit of Excellence, Indian Institute of Technology Madras, India*

\*Email: [manfred.kappes@kit.edu](mailto:manfred.kappes@kit.edu) ; [pradeep@iitm.ac.in](mailto:pradeep@iitm.ac.in) ; [horst.hahn@kit.edu](mailto:horst.hahn@kit.edu)

### Contents

S/N	Description	Page Number
	<i>Experimental Details</i>	<b>S2-S3</b>
<b>Figure S1</b>	<i>ESI MS and UV-vis absorption spectra of Ag<sub>44</sub>(FTP)<sub>30</sub></i>	<b>S4</b>
<b>Figure S2</b>	<i>ESI MS and UV-vis absorption spectra of Au<sub>25</sub>(PET)<sub>18</sub></i>	<b>S5</b>
<b>Figure S3</b>	<i>Time dependent mass spectra for 5:1 molar ratio of Ag<sub>44</sub>(FTP)<sub>30</sub> : Au<sub>25</sub>(PET)<sub>18</sub></i>	<b>S6</b>
<b>Figure S4</b>	<i>Time dependence of different Au<sub>x</sub>Ag<sub>44-x</sub>(SR)<sub>30</sub><sup>4-</sup> ion signals at 15:1 molar ratio of Ag<sub>44</sub>(FTP)<sub>30</sub> : Au<sub>25</sub>(PET)<sub>18</sub></i>	<b>S7</b>
<b>Figure S5</b>	<i>Time dependence of different Au<sub>x</sub>Ag<sub>44-x</sub>(SR)<sub>30</sub><sup>4-</sup> ion signals at 5:1 molar ratio of Ag<sub>44</sub>(FTP)<sub>30</sub> : Au<sub>25</sub>(PET)<sub>18</sub></i>	<b>S8</b>
<b>Figure S6</b>	<i>Predicted and experimentally observed Au<sub>x</sub>Ag<sub>44-x</sub>(SR)<sub>30</sub><sup>4-</sup> intensity distribution at equilibrium for an initial Ag<sub>44</sub>:Au<sub>25</sub> mixing ratio of 5:1</i>	<b>S9</b>
<b>Figure S7</b>	<i>Reaction time dependent TIMS mobilograms of Au<sub>x</sub>Ag<sub>44-x</sub>(SR)<sub>30</sub><sup>4-</sup> (x=0-12)</i>	<b>S10</b>
<b>Figure S8</b>	<i>TIMS mobilograms of different ligand exchange products Au<sub>12</sub>Ag<sub>32</sub>(FTP)<sub>30-y</sub>(PET)<sub>y</sub><sup>4-</sup></i>	<b>S11</b>
<b>Figure S9</b>	<i>Reaction time dependent high resolution mass spectra of Ag<sub>44</sub>(FTP)<sub>30-x</sub>(PET)<sub>x</sub><sup>4-</sup>Au<sub>6</sub>Ag<sub>38</sub>(FTP)<sub>30-x</sub>(PET)<sub>x</sub><sup>4-</sup></i>	<b>S12</b>
<b>Figure S10</b>	<i>Reaction time dependent high resolution mass spectra of Ag<sub>44</sub>(FTP)<sub>30-x</sub>(PET)<sub>x</sub><sup>4-</sup>Au<sub>6</sub>Ag<sub>38</sub>(FTP)<sub>30-x</sub>(PET)<sub>x</sub><sup>4-</sup></i>	<b>S13</b>
<b>Figure S11</b>	<i>Reaction time dependent TIMS mobilograms of Ag<sub>44-x</sub>Au<sub>x</sub>(SR)<sub>30</sub><sup>4-</sup> (x = 10-12)</i>	<b>S14</b>
<b>Figure S12</b>	<i>CID measurements for Ag<sub>44-x</sub>Au<sub>x</sub>(SR)<sub>30</sub><sup>4-</sup> (x = 0-12)</i>	<b>S15</b>
<b>Figure S13</b>	<i>50% survival yield for Ag<sub>44-x</sub>Au<sub>x</sub>(SR)<sub>30</sub><sup>4-</sup> (x = 0-3)</i>	<b>S16</b>
<b>Figure S14</b>	<i>50% survival yield Ag<sub>44-x</sub>Au<sub>x</sub>(SR)<sub>30</sub><sup>4-</sup> (x = 4-7)</i>	<b>S17</b>
<b>Figure S15</b>	<i>50% survival yield Ag<sub>44-x</sub>Au<sub>x</sub>(SR)<sub>30</sub><sup>4-</sup> (x = 8-11)</i>	<b>S18</b>
<b>Table S1</b>	<i>Co-ordinates of Ag<sub>44</sub>(FTP)<sub>30</sub><sup>4-</sup></i>	<b>S19-S27</b>
<b>Table S2</b>	<i>Co-ordinates of Au<sub>12</sub>Ag<sub>32</sub>(FTP)<sub>30</sub><sup>4-</sup> (I isomer)</i>	<b>S28-S36</b>
<b>Table S3</b>	<i>Co-ordinates of Au<sub>12</sub>Ag<sub>32</sub>(FTP)<sub>30</sub><sup>4-</sup> (M isomer)</i>	<b>S37-S45</b>
<b>Table S4</b>	<i>Co-ordinates of Au<sub>12</sub>Ag<sub>32</sub>(FTP)<sub>30</sub><sup>4-</sup> (S isomer)</i>	<b>S46-S54</b>

## Experimental Details

### Synthesis of $[\text{PPh}_4][\text{Ag}_{44}(\text{4-FTP})_{30}]$

$[\text{PPh}_4][\text{Ag}_{44}(\text{4-FTP})_{30}]$  clusters were synthesized following a room temperature solid state synthesis route.<sup>1</sup> For this about 20 mg of  $\text{AgNO}_3$  was ground with 12 mg of  $\text{PPh}_4\text{Br}$  in an agate mortar and pestle and 76  $\mu\text{L}$  of 4-FTP was added to the mixture and ground again to obtain silver thiolates. About 45 mg of dry  $\text{NaBH}_4$  was then added in order to reduce the thiolates to clusters. A color change to brown indicated successful reduction and formation of the cluster. The reaction mixture was extracted immediately with 7 mL of dichloromethane (DCM) and the resulting solution kept undisturbed at room temperature for a few hours. From time-to-time UV-vis absorption spectra were recorded until all the characteristic absorption features of the clusters appeared. The clusters were then cleaned repeatedly with dimethylformamide (DMF) and toluene by centrifugation and finally rotavapored to achieve powdered clusters. The powder was dissolved in DMF for further study

### Synthesis of $[\text{TOA}][\text{Au}_{25}(\text{PET})_{18}]$ cluster

$[\text{TOA}][\text{Au}_{25}(\text{PET})_{18}]$  clusters were synthesized following the previously reported method.<sup>1</sup> Briefly, about 40 mg of  $\text{HAuCl}_4 \cdot 3\text{H}_2\text{O}$  in 7.5 ml THF was mixed with 65 mg of  $\text{TAOBr}$  and stirred for around 15 min at room temperature until the color of the solution changed to orange red. To that, 68  $\mu\text{L}$  of PET was added and stirred for another hour. The resulting thiolate was reduced by 39 mg of  $\text{NaBH}_4$  in ice-cold water. The color changed from yellow to brown indicating reduction. The solution was stirred for another 5 hours for complete conversion of the thiolates to clusters and size focusing was applied to get  $[\text{TOA}][\text{Au}_{25}(\text{PET})_{18}]$ . The as-synthesized clusters were vacuum dried by rotavapor following precipitation using excess MeOH. This step removes free thiol and excess thiolate and was repeated several times. The resulting solid was then dissolved in acetone and centrifuged. The supernatant solution was collected and the precipitate containing larger clusters was discarded. The acetone solution containing  $[\text{TOA}][\text{Au}_{25}(\text{PET})_{18}]$  was vacuum dried and then dissolved in dichloromethane (DCM). Following centrifugation at 1500 rpm the supernatant solution was collected and used for further study.

## Instrumental details

Measurements were performed in Nano-ESI mode (NESI) on both the Waters Synapt G2S and the Thermo Fischer Orbitrap instruments. A regular ESI source was used in the Bruker timsTOF measurements. All the measurements were performed in negative ion mode. Both clusters were dissolved in DMF and dilute solutions (10  $\mu\text{M}$  and below) as well as dilute solution mixtures were sprayed. For NESI mode, a 2 kV capillary voltage was applied in the Synapt G2S measurements, while a 3 kV spray voltage was needed to get a stable spray in the case of the Orbitrap platform. All CID experiments were performed on the Synapt G2S platform in ESI mode. To get reasonable signal intensity in regular MS and in CID using ESI mode, the following parameters were used: capillary voltage: 1 kV, cone voltage: 10 V, source offset: 15 V, desolvation temperature 80 °C, desolvation gas flow: 600 L/h, nebulizer: 2.5 bar. Laboratory collision energy (CE) was varied from nominally 0 to 80 V at 5 mL/min trap gas flow rate. All other parameters were kept the same during CID measurements apart from the CE.

All the ion mobility measurements were performed using a Bruker timsTOF mass spectrometer. The optimized source parameters were as follows: capillary voltage of 2.5 kV, a nebuliser pressure of 0.3 bar, dry gas temperature of 200 °C and a dry gas flow of 3.5 l/min. Briefly, in trapped ion mobility spectrometry (TIMS)<sup>2</sup> the ions are held by an electric field gradient (EFG) while exposed to a constant  $\text{N}_2$  flow. The source of the flow is a pressure difference between the entrance and the exit of the TIMS-tunnel (here, a pressure difference,  $\Delta p$ , of 2 mbar was attained). Lowering the EFG results in the elution

of the analyte according to its inverse mobility ( $1/K_0$ ). Depending on the difference between start-EFG and end-EFG ( $\Delta\text{EFG}$ ) as well as the duration of this reduction (ramp time =  $t_r$ ), rather high ion mobility resolutions can be achieved. Resolutions of 250 and more have been reported.<sup>3</sup> In this study resolutions were better than 160 throughout. In front of the trapping part of the TIMS-tunnel, a second ramp accumulates the ions for a given period of time (accumulation time =  $t_a$ ) in order to enhance the overall duty cycle. Since TIMS doesn't operate on first principles, a calibration is necessary. For calibration, Agilent Tune-Mix<sup>TM</sup> was used as purchased and the reported drift tube  $^{DT}\text{CCS}_{\text{N}_2}$ -values published by Stow *et al.* have been used.<sup>4</sup> TIMS determines (calibrated) inverse mobilities which were converted to the tabulated  $^{TIMS}\text{CCS}_{\text{N}_2}$  values following Mason-Schamp-equation<sup>5</sup>

$$CCS = \left(\frac{3}{16N}\right) \left(\frac{2\pi}{kT}\right)^{0.5} \frac{q}{\sqrt{\mu}K_0}$$

where,  $q$  is the charge of the ion,  $N$  the number density of the collision gas,  $\mu$  is the reduced mass of the ion and the  $\text{N}_2$  collision gas,  $k$  the Boltzmann's constant,  $T$  the temperature in Kelvin. Both the analyte solution and the calibrants have been electrosprayed in anionic mode with the same experimental conditions ( $\Delta\text{EFG} = 0.1 \text{ V s cm}^{-2}$ ,  $t_r = 420 \text{ ms}$ ,  $t_a = 10 \text{ ms}$ ). After elution from the TIMS tunnel, the ions are focused into a hexapole ion guide, and can be selected by their  $m/z$  in a further quadrupole. Before entering the TOF-region, the ions have to pass a second quadrupole (the collision cell).

## Reference

1. Krishnadas, K. R.; Baksi, A.; Ghosh, A.; Natarajan, G.; Pradeep, T. Manifestation of Geometric and Electronic Shell Structures of Metal Clusters in Intercluster Reactions. *ACS Nano* **2017**, *11* (6), 6015-6023.
2. Michelmann, K.; Silveira, J. A.; Ridgeway, M. E.; Park, M. A. Fundamentals of Trapped Ion Mobility Spectrometry. *J. Am. Soc. Mass Spectrom.* **2015**, *26* (1), 14-24.
3. Ridgeway, M. E.; Silveira, J. A.; Meier, J. E.; Park, M. A. Microheterogeneity within conformational states of ubiquitin revealed by high resolution trapped ion mobility spectrometry. *Analyst* **2015**, *140* (20), 6964-6972.
4. Stow, S. M.; Causon, T. J.; Zheng, X.; Kurulugama, R. T.; Mairinger, T.; May, J. C.; Rennie, E. E.; Baker, E. S.; Smith, R. D.; McLean, J. A.; Hann, S.; Fjeldsted, J. C. An Interlaboratory Evaluation of Drift Tube Ion Mobility-Mass Spectrometry Collision Cross Section Measurements. *Anal. Chem.* **2017**, *89* (17), 9048-9055.
5. Revercomb, H. E.; Mason, E. A. Theory of plasma chromatography/gaseous electrophoresis. Review. *Anal. Chem.* **1975**, *47* (7), 970-83.

## Supporting Information 1

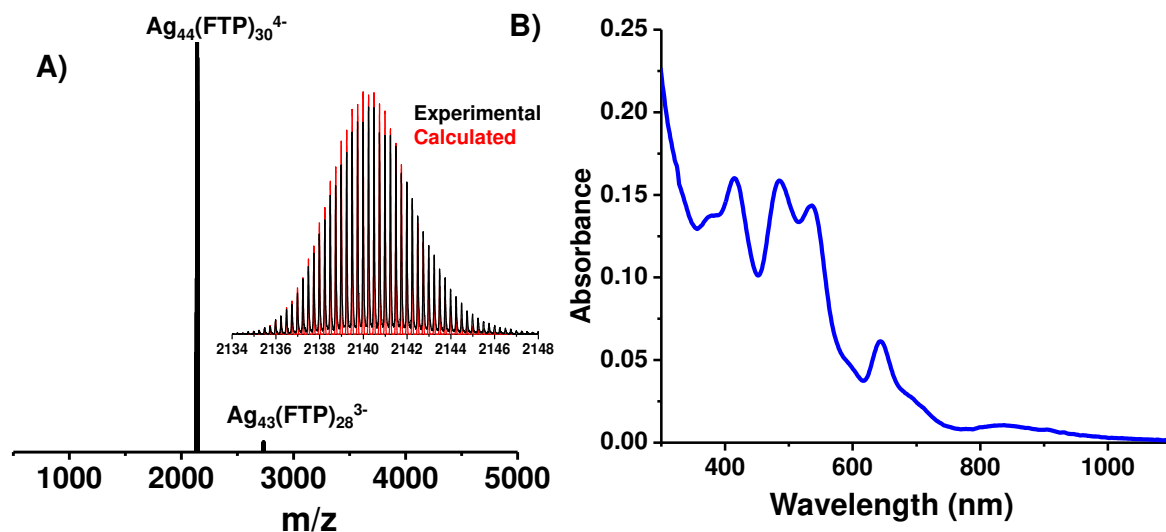


**Figure S1.** A) Negative ion ESI-MS of pure  $[\text{PPh}_4]_4[\text{Ag}_{44}(\text{FTP})_{30}]$  dissolved in DMF – as obtained under standard ESI conditions<sup>1</sup> (see Experimental Section for details) showing predominantly the 4-charged ion. The peak  $\text{Ag}_{43}(\text{FTP})_{28}^{3-}$  is a standard fragment formed by  $\text{Ag}(\text{FTP})_2^-$  loss during electrospray. Experimental isotope pattern exactly matches with the calculated pattern of  $\text{Ag}_{44}(\text{FTP})_{30}^{4-}$  as shown in inset. No other peaks were found confirming purity of the cluster. B) UV-vis absorption spectrum of the solution in the inset shows all the characteristic bands known from the literature.



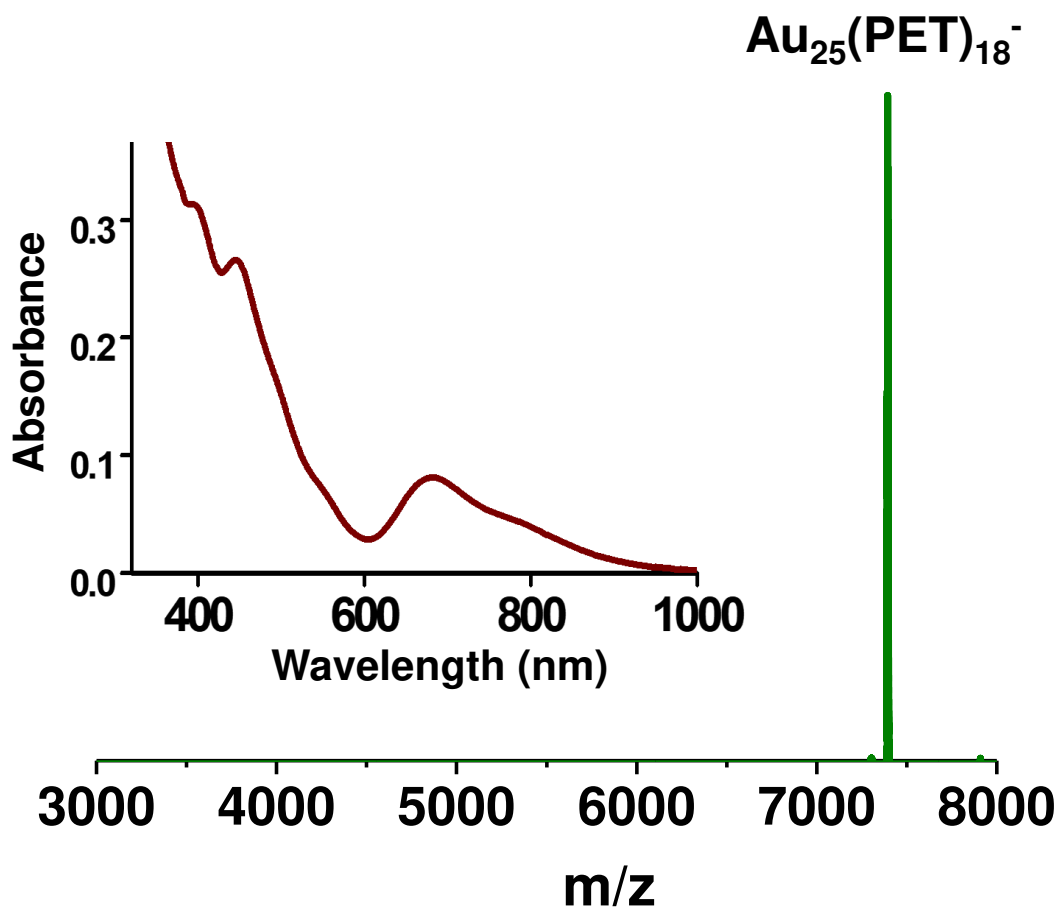


**Figure S2.** Negative ion ESI-MS of pure  $[\text{TOA}][\text{Au}_{25}(\text{PET})_{18}]$  dissolved in DMF - as obtained under standard ESI conditions<sup>1</sup> showing corresponding peak. The inset shows a UV-vis absorption spectrum of the solution showing all the characteristic bands. No other peaks were found confirming the purity of the cluster.

### Supporting Information 3

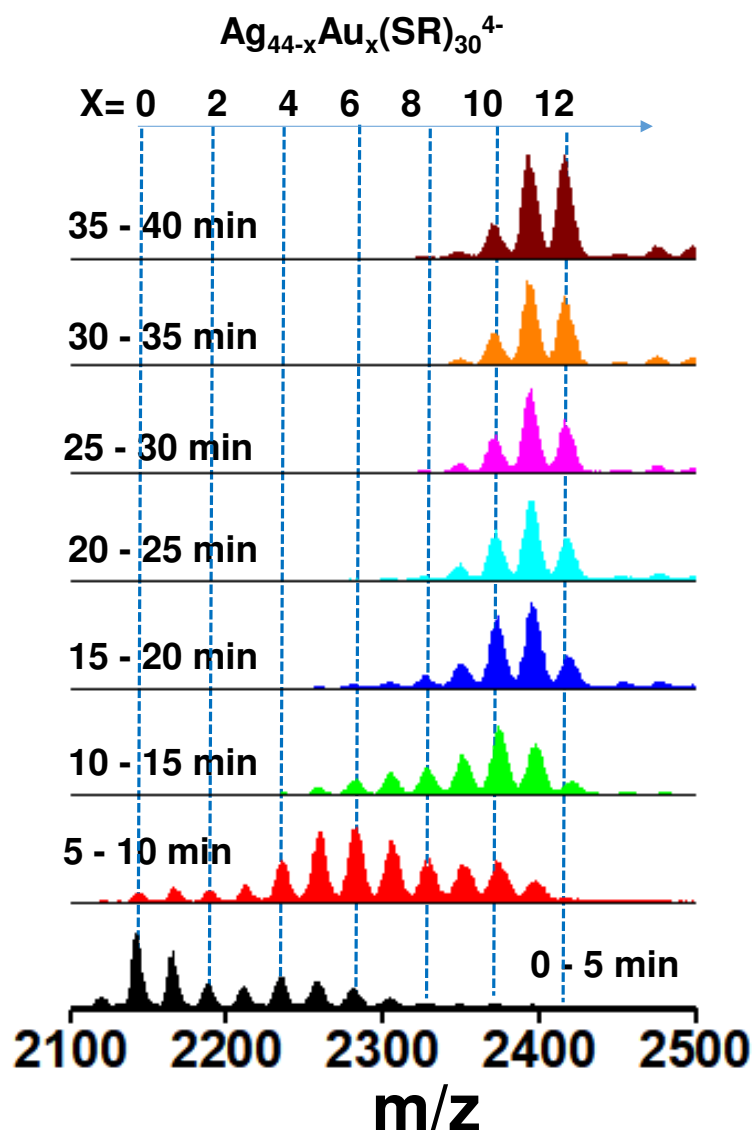


**Figure S3.** Time-dependent mass spectra (measured in Bruker timsTOF) of *inter-cluster* reaction showing gradual formation of  $\text{Au}_{12}\text{Ag}_{32}(\text{SR})_{30}^{4-}$  over a reaction time of 40 min for 5:1  $\text{Ag}_{44} : \text{Au}_{25}$  molar ratio ( $5\mu\text{M} : 1\mu\text{M}$ ). See also the corresponding “heat map” shown in Figure 1 of the main text. Mass spectra were collected at 1 scan/s and 300 mass spectra were averaged per 5 min reaction time interval. Dashed vertical blue lines are  $\Delta m/z = 45$  apart which corresponds to replacement of two silver atoms by two gold atoms. Selected  $\text{Au}_x\text{Ag}_{44-x}(\text{SR})_{30}^{4-}$  intermediate signals are zoomed in Figures S8-S9 to show their silver isotopomer and ligand compositions. Mass resolution,  $m/\Delta m$ , was  $\sim 36,400$  in this mass range.

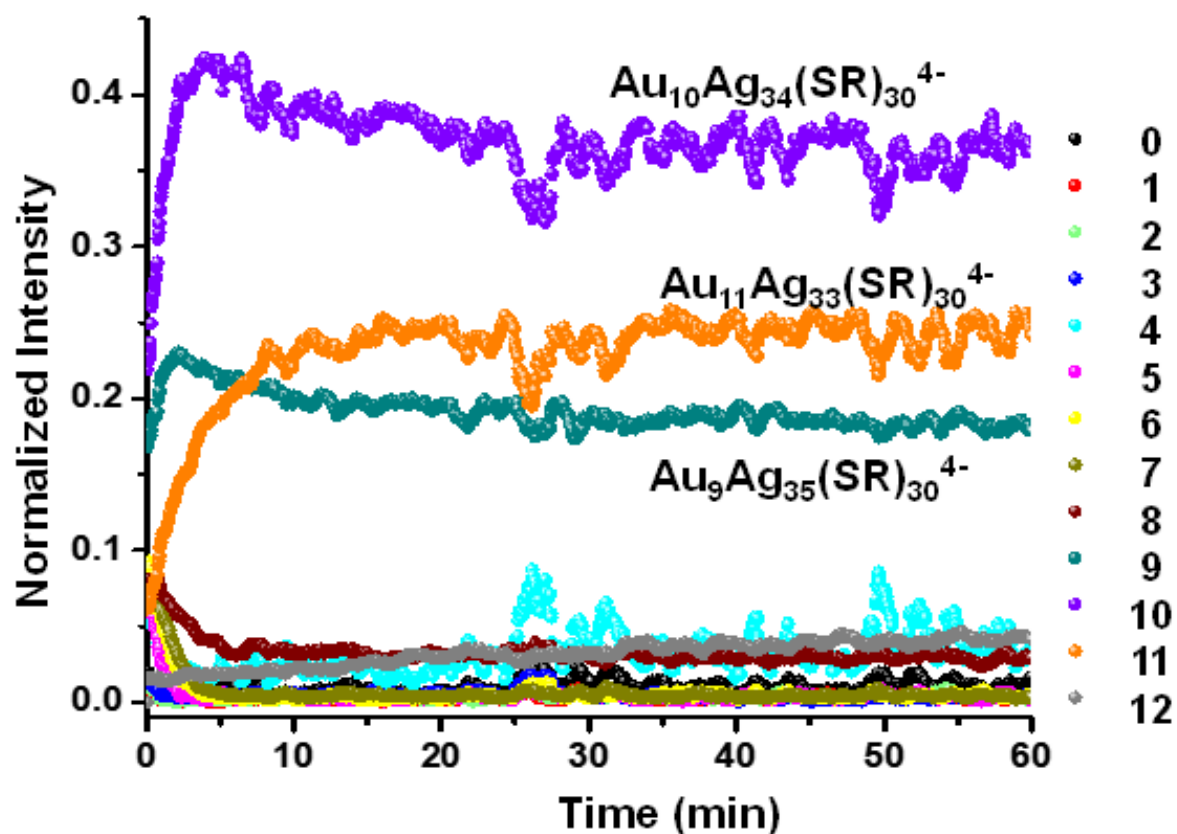


**Figure S4.** Reaction time dependent variation of total ion intensity of different reaction products  $\text{Au}_x\text{Ag}_{44-x}(\text{SR})_{30}^{4-}$ ,  $x=0-12$ , for an 15:1 molar ratio of  $\text{Ag}_{44}(\text{FTP})_{30}$  ( $1.5\ \mu\text{M}$ ) :  $\text{Au}_{25}(\text{PET})_{18}$  ( $100\ \text{nM}$ ). See also the Figure S2 caption. The reaction was probed using a Thermo Fischer Orbitrap in NESI mode. The time dependent change in intensity of each ion was extracted and was normalized to the total ion intensity (from “TIC” = total ion current) for a mass window of  $\Delta m/z = 3$  corresponding to 0-2 ligand exchanges.

## Supporting Information 5

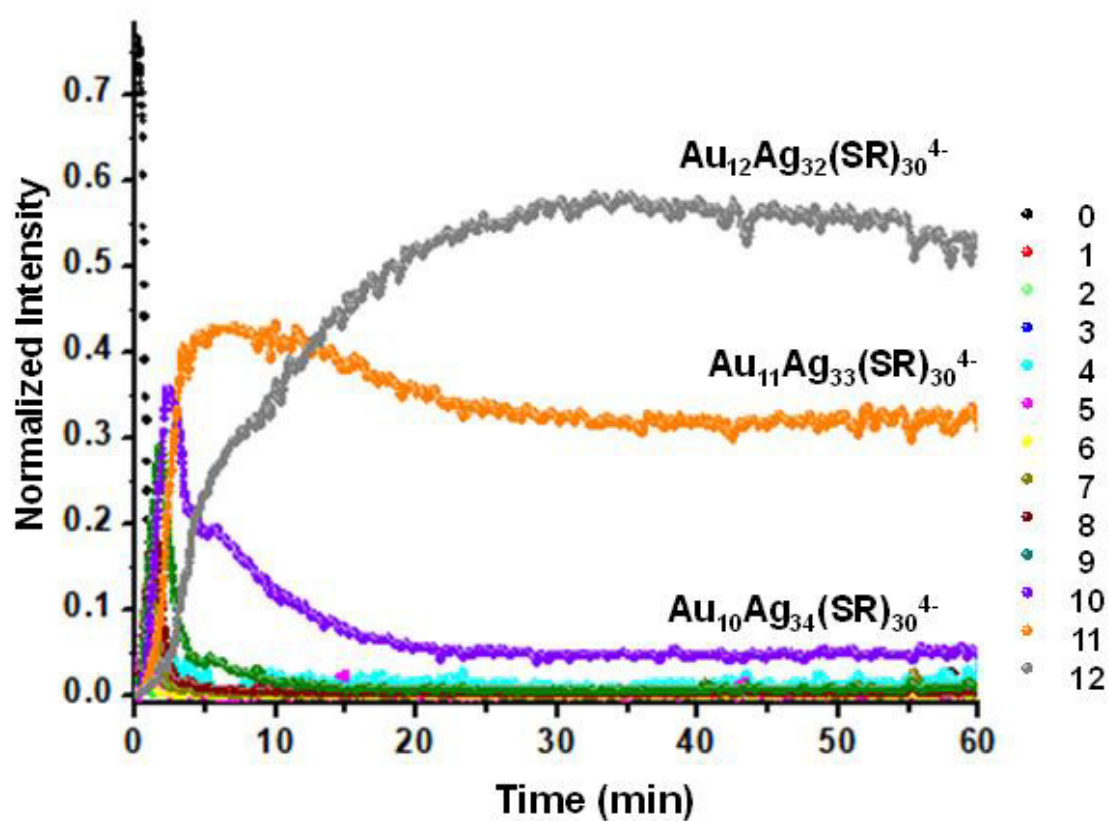


**Figure S5.** Reaction time dependent variation of total ion intensity of different reaction products  $\text{Au}_x\text{Ag}_{44-x}(\text{SR})_{30}^{4-}$ ,  $x=0-12$ , for an 5:1 molar ratio of  $\text{Ag}_{44}(\text{FTP})_{30}$  ( $5\ \mu\text{M}$ ) :  $\text{Au}_{25}(\text{PET})_{18}$  ( $1\ \mu\text{M}$ ). See also the Figure S2 caption.

## Supporting Information 6

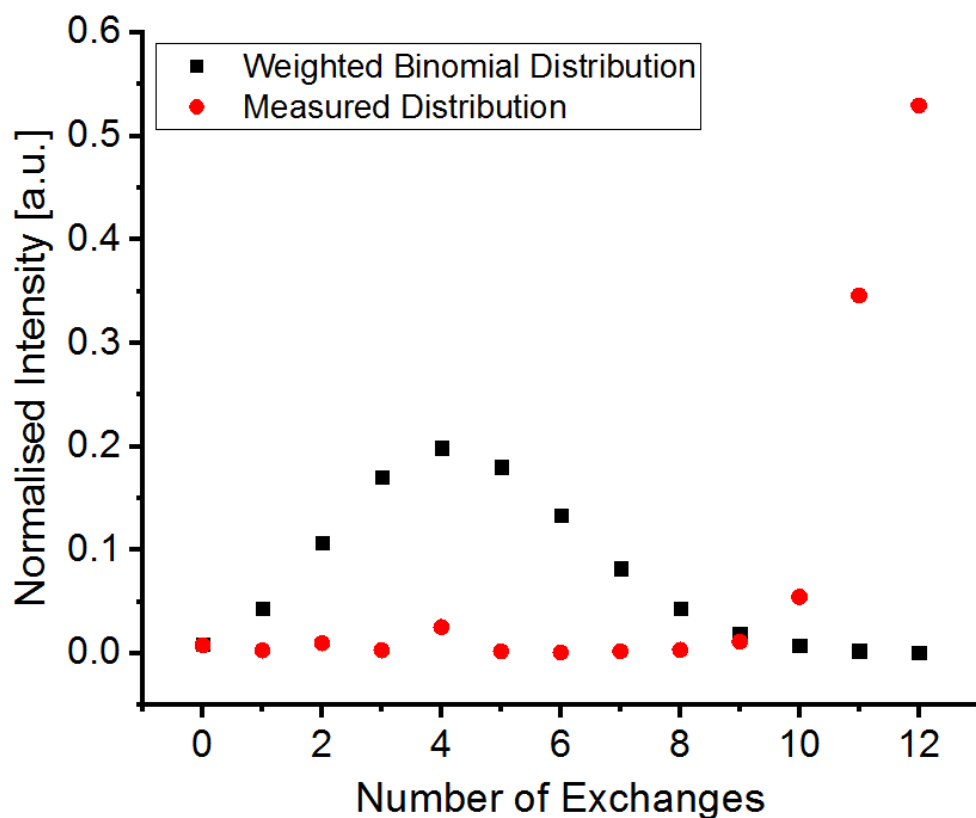


**Figure S6.** Comparison between the Au exchange distribution at equilibrium determined from the  $\text{Au}_x\text{Ag}_{44-x}(\text{SR})_{30}^{4+}$  ion intensity distribution at 40 minute reaction time (red line) with the weighted binomial distribution calculated for an initial  $\text{Ag}_{44}:\text{Au}_{25}$  mixing ratio of 5:1 (black line) using  $\binom{n}{k} p^k (1-p)^{n-k}$  where  $n=44$ ,  $k$  is the number of exchanged gold atoms and  $p$  is the statistical weight of Au, i.e.  $25/245=0.102$ . Corresponding mass spectra are presented in Figure S1.

## Supporting Information 7

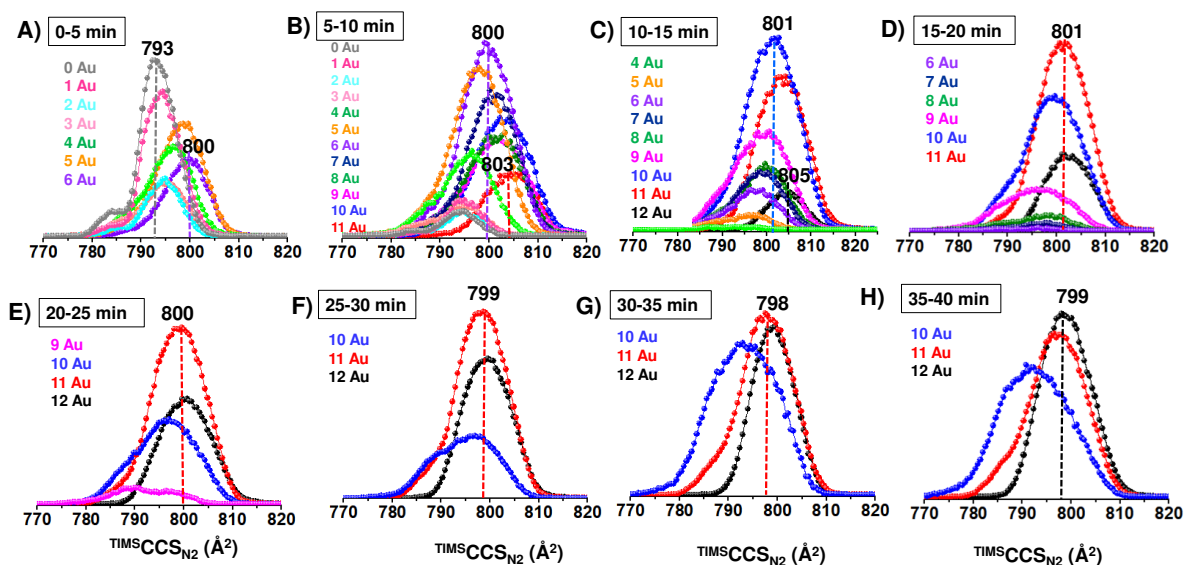


**Figure S7.** A-H) Change in TIMS CCS<sub>N2</sub> for different Au exchange products, Au<sub>x</sub>Ag<sub>44-x</sub>(SR)<sub>30</sub><sup>4+</sup> (x=0-12), over eight different reaction time ranges. Mobilograms were averaged for 5 min and 2 mobilograms were collected per second. Ion mobility resolution was calculated to be 160. Note, the initial increase in CCS for the Au exchange products. Consequently, the corresponding cluster collision cross sections increase significantly during the first 20 min after mixing. For the final products with x=10 and 11 the CCS then decreases again. The same information is shown in the form of contour plots in Figure 2 of the main text. The vertical dashed lines correspond to the CCS maximum of the most intense ion peak in the specific window. If two vertical dashed lines are shown (A-C), the first corresponds to the CCS of the highest intensity Au<sub>x</sub>Ag<sub>44-x</sub>(SR)<sub>30</sub><sup>4+</sup> exchange product whereas the second corresponds to the CCS peak maximum of the product with highest CCS - in that time interval. In each plot, the dashed vertical lines bear the same color code as their respective Au<sub>x</sub>Ag<sub>44-x</sub>(SR)<sub>30</sub><sup>4+</sup> (x=0-12) mobilograms.

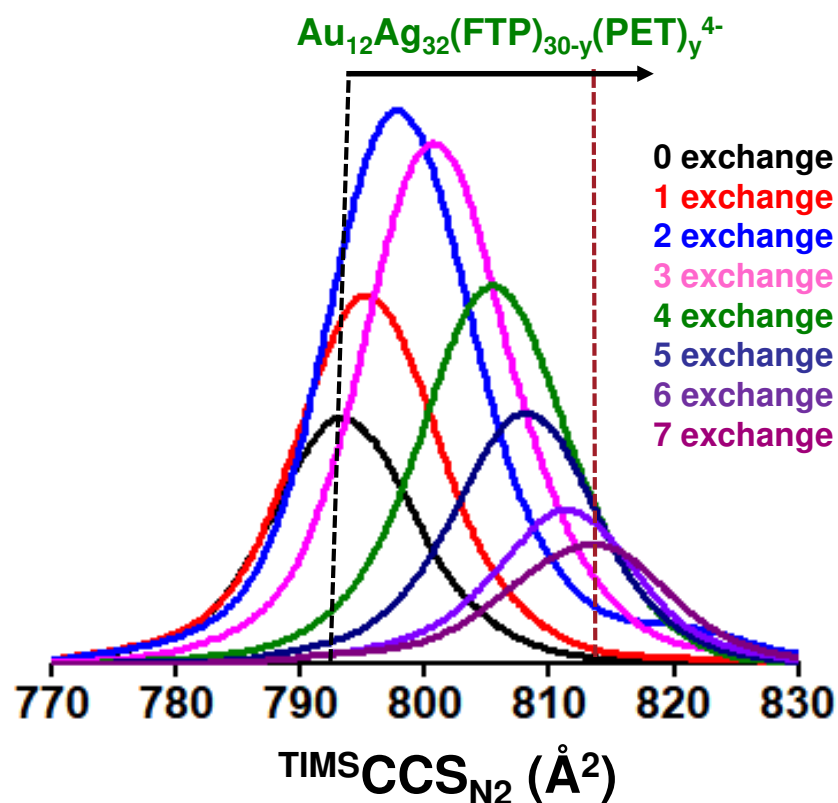


**Figure S8.**  $\text{TIMS CCS}_{\text{N}_2}$  of different ligand exchange products of  $\text{Au}_{12}\text{Ag}_{32}(\text{SR})_{30}^{4-}$  showing a sequential increase in overall cross section as FTP ligands are exchanged by PET ligands. Each such ligand exchange leads to an increase in  $\text{TIMS CCS}_{\text{N}_2}$  of roughly  $2 \text{ \AA}^2$ .

## Supporting Information 9

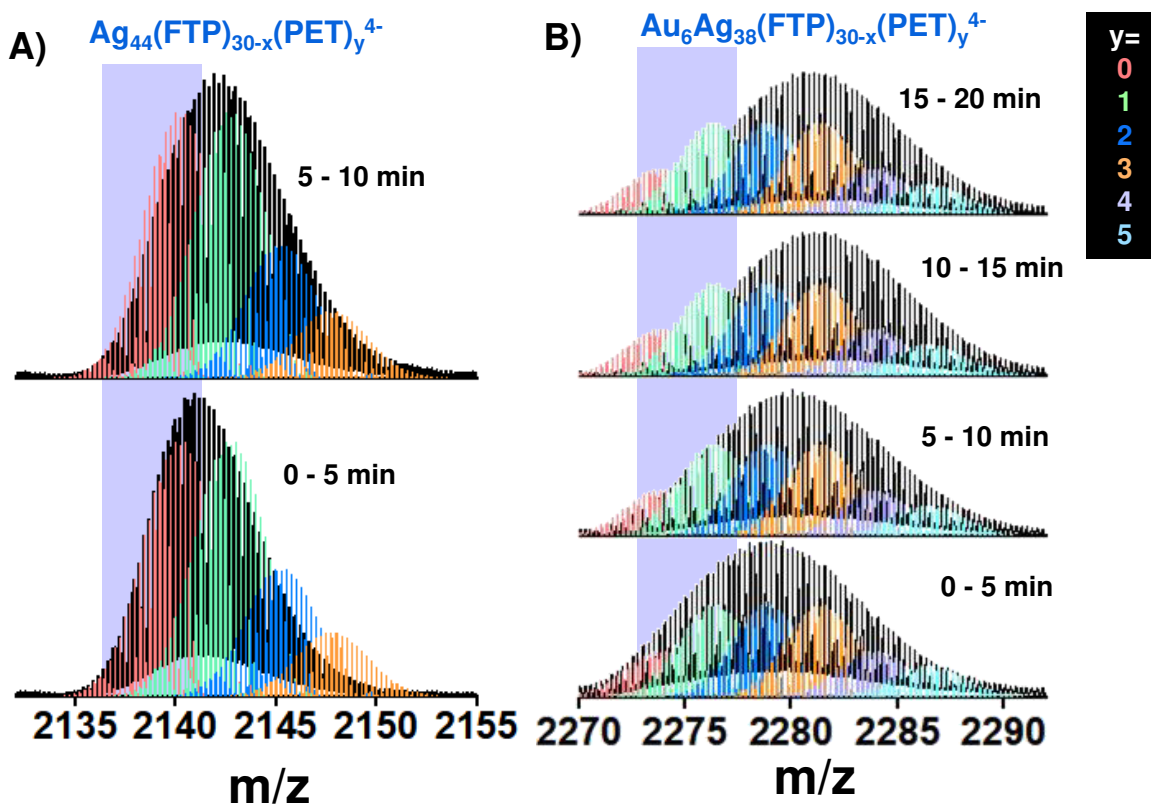


**Figure S9.** Time-dependent, high-resolution mass spectra of A)  $\text{Ag}_{44}(\text{SR})_{30}^{4-}$  and B)  $\text{Au}_6\text{Ag}_{38}(\text{SR})_{30}^{4-}$ , recorded with the Bruker timsTOF over different reaction time intervals between 0 and 20 min after mixing the cluster reagents (black traces). The calculated isotope patterns for different numbers of ligand exchange,  $x$ , are overlaid on the plots (colored traces). The mass range used to extract the mobilograms (and hence  $^{\text{TIMS}}\text{CCS}_{\text{N}_2}$ ) shown in Figure 2 and Figure S5 are highlighted (purple rectangle). This corresponds to 0-1 ligand exchanges.



## Supporting Information 10

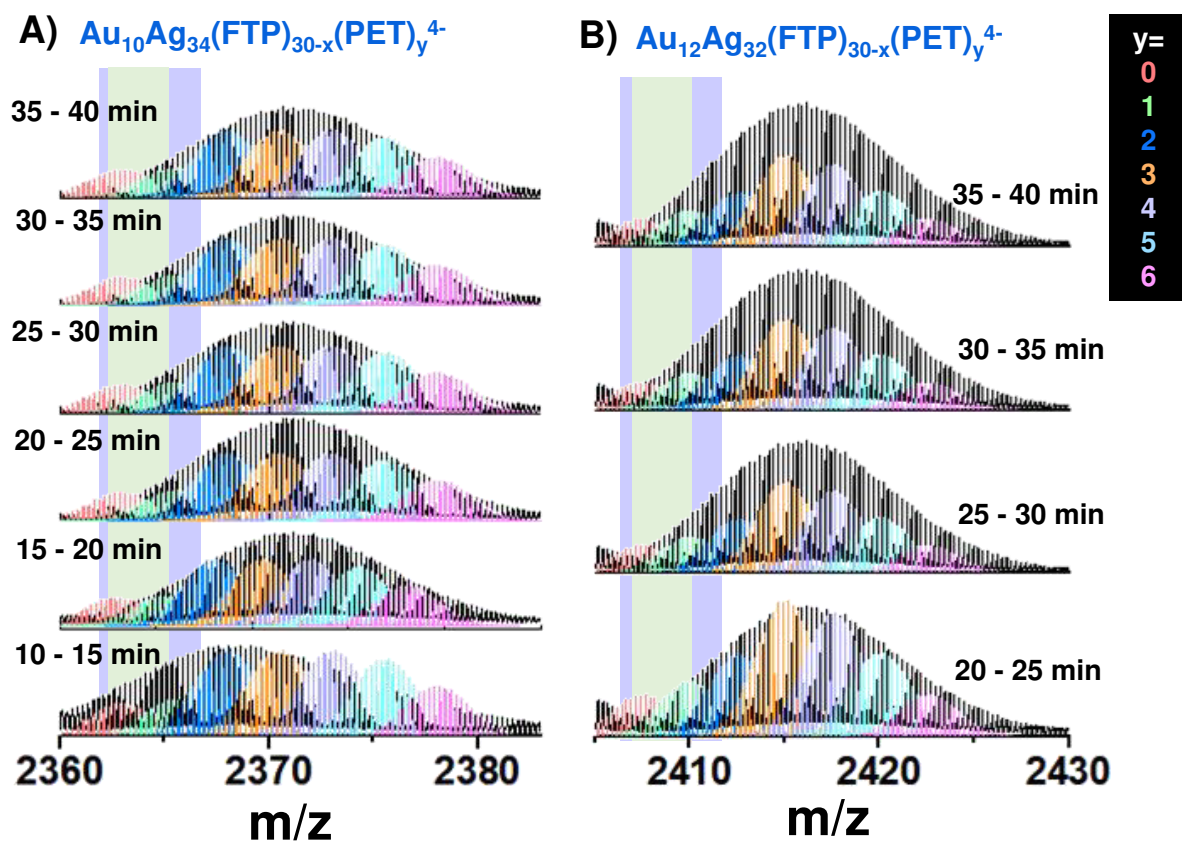


**Figure S10.** Time-dependent, high-resolution mass spectra of A)  $\text{Au}_{10}\text{Ag}_{34}(\text{SR})_{30}^{4-}$  and B)  $\text{Au}_{12}\text{Ag}_{32}(\text{SR})_{30}^{4-}$  recorded with the Bruker timsTOF over different reaction time intervals between 0 and 40 min after mixing the cluster reagents (black traces). The calculated isotope patterns for different numbers of ligand exchange,  $x$ , are overlaid on the plots (colored traces). Mass range used to extract the mobilograms (and hence  $^{\text{TIMS}}\text{CCS}_{\text{N}_2}$ ) shown in Figure 2 and Figure S6 are highlighted in purple (0-2 ligand exchange). The mass ranges used in Figure 3 and Figure S11 are highlighted in green (0-1 ligand exchange).

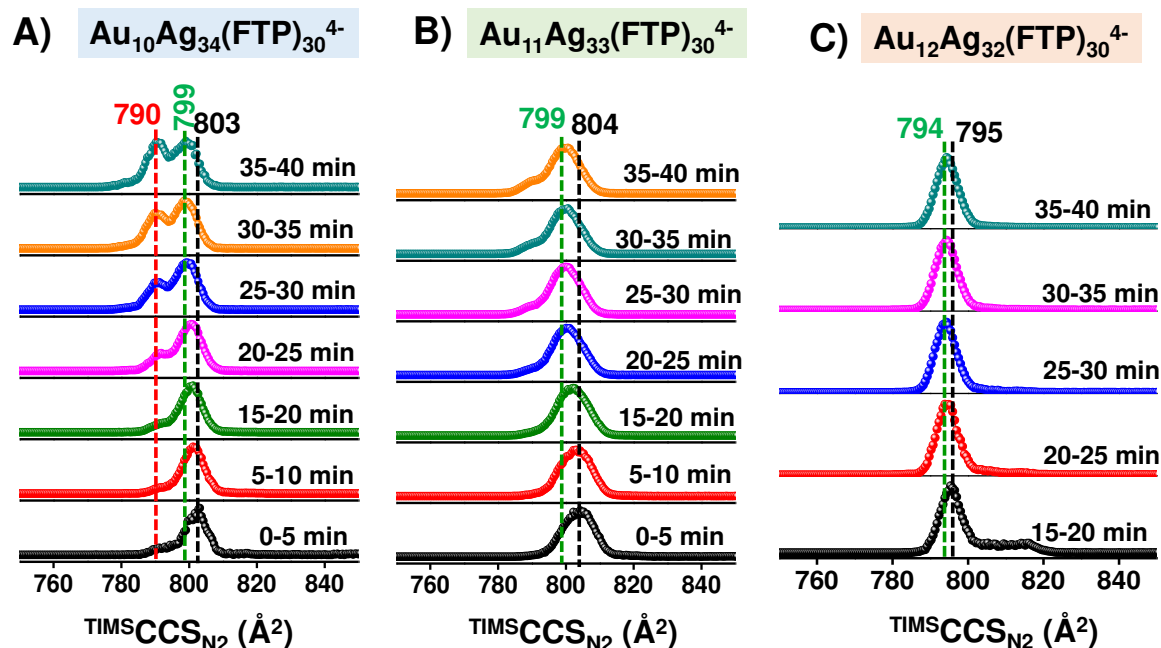


**Figure S11.** Time dependent change in  $\text{TIMS CCS}_{\text{N}_2}$  of A)  $\text{Au}_{10}\text{Ag}_{34}(\text{SR})_{30}^{4-}$ , B)  $\text{Au}_{11}\text{Ag}_{33}(\text{SR})_{30}^{4-}$  and C)  $\text{Au}_{12}\text{Ag}_{32}(\text{SR})_{30}^{4-}$ . Each of the mobilograms was extracted for the corresponding mass range taking into account only contributions from 0-1 ligand exchange products (see Fig. S9 and S10 as well as Fig. 3 in the main text). Note that  $\text{TIMS CCS}_{\text{N}_2}$  of  $\text{Au}_{10}\text{Ag}_{34}(\text{SR})_{30}^{4-}$  and  $\text{Au}_{11}\text{Ag}_{33}(\text{SR})_{30}^{4-}$  change significantly with time while  $\text{TIMS CCS}_{\text{N}_2}$  of  $\text{Au}_{12}\text{Ag}_{32}(\text{SR})_{30}^{4-}$  remains almost the same after it begins to be formed 15 min into the reaction. The black and green dashed lines in each plot correspond to the initial and final CCS, respectively. The red dotted line in A) is for the second isomer. Mobilograms are plotted normalized to the respective signal maxima.

## Supporting Information 12

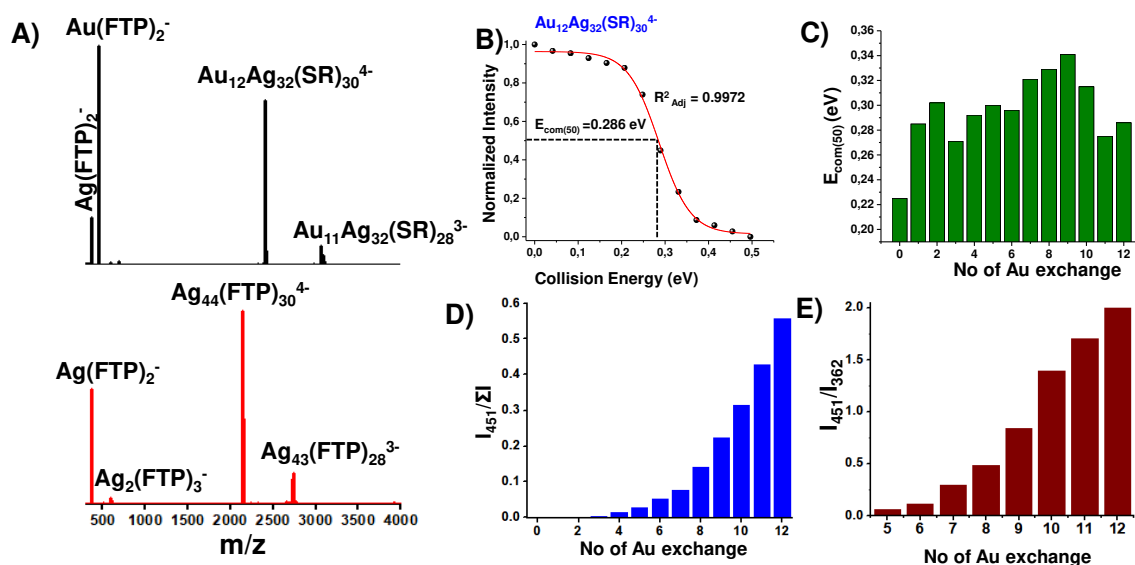


**Figure S12.** A) Collision induced dissociation measurements in Ar for mass-selected  $\text{Ag}_{44}(\text{FTP})_{30}^{4-}$   $\text{Au}_{12}\text{Ag}_{32}(\text{SR})_{30}^{4-}$ . Mass spectrum of primary anionic fragments resulting at a lab frame collision energy setting of 6 V. B) Residual  $\text{Au}_{12}\text{Ag}_{32}(\text{SR})_{30}^{4-}$  parent ion intensity after collision with Ar at systematically increasing centre of mass collision energy (normalized to the intensity at CE=0 eV). The collision energy providing 50% survival yield ( $E_{\text{com}(50)}$ ) was determined from a fit to the data of the function  $y = (a-b)/(1 + \exp((x-x_0)/dx)) + b$ .<sup>6</sup> Relative intensity of parent ion was calculated as:

$$I_p = \frac{I_p}{I_p + \frac{\Sigma I_f}{n}}$$

Where,  $I_p$  is the intensity of the parent ion and  $\Sigma I_f$  is sum of intensities of the fragment ions and  $n$  represents to the number of fragments. C) Plot of  $E_{\text{com}(50)}$  versus the number of Au atom exchanged ( $x=0-12$  Au). The main fragmentation channels correspond to  $\text{Ag}(\text{FTP})_2^-$  and for Au containing ions also  $\text{Au}(\text{FTP})_2^-$  loss. D) Plots of the relative  $\text{Au}(\text{FTP})_2^-$  fragment intensity ( $m/z = 451$ ) after background subtraction at 0 V normalized to the intensity of the mass selected  $\text{Au}_x\text{Ag}_{44-x}(\text{SR})_{30}^{4-}$  ion subjected to CID versus  $x$  -- for a nominal lab frame collision energy setting of 6 V. E) Shows the  $\text{Au}(\text{FTP})_2^-/\text{Ag}(\text{FTP})_2^-$  0 V background subtracted fragment intensity ratio ( $I_{m/z451}/I_{m/z362}$ ) for 5-12 Au exchange products at the same lab frame collision energy setting of 6 V. Note that at  $x=12$ , this observed ratio is larger than expected for a random distribution of 12 Au and 32 Ag atoms throughout the cluster – assuming dissociation only from the staple regions. However, the  $x=10-12$  measurements are subject to significant contributions from “upstream” fragmentation (presumably during ion transfer from the Synapt quadrupole mass filter to the collision cell region) which causes large  $\text{M}(\text{FTP})_2^-$  background signals even for low nominal collision energies. Therefore quantitative inferences concerning the  $\text{Au}(\text{FTP})_2^-/\text{Ag}(\text{FTP})_2^-$  ratio cannot be drawn at this stage.

## Reference

6. Chakraborty, P.; Bakshi, A.; Khatun, E.; Nag, A.; Ghosh, A.; Pradeep, T., Dissociation of Gas Phase Ions of Atomically Precise Silver Clusters Reflects Their Solution Phase Stability. *J. Phys. Chem. C* **2017**, *121* (20), 10971-10981.

# Supporting Information 13

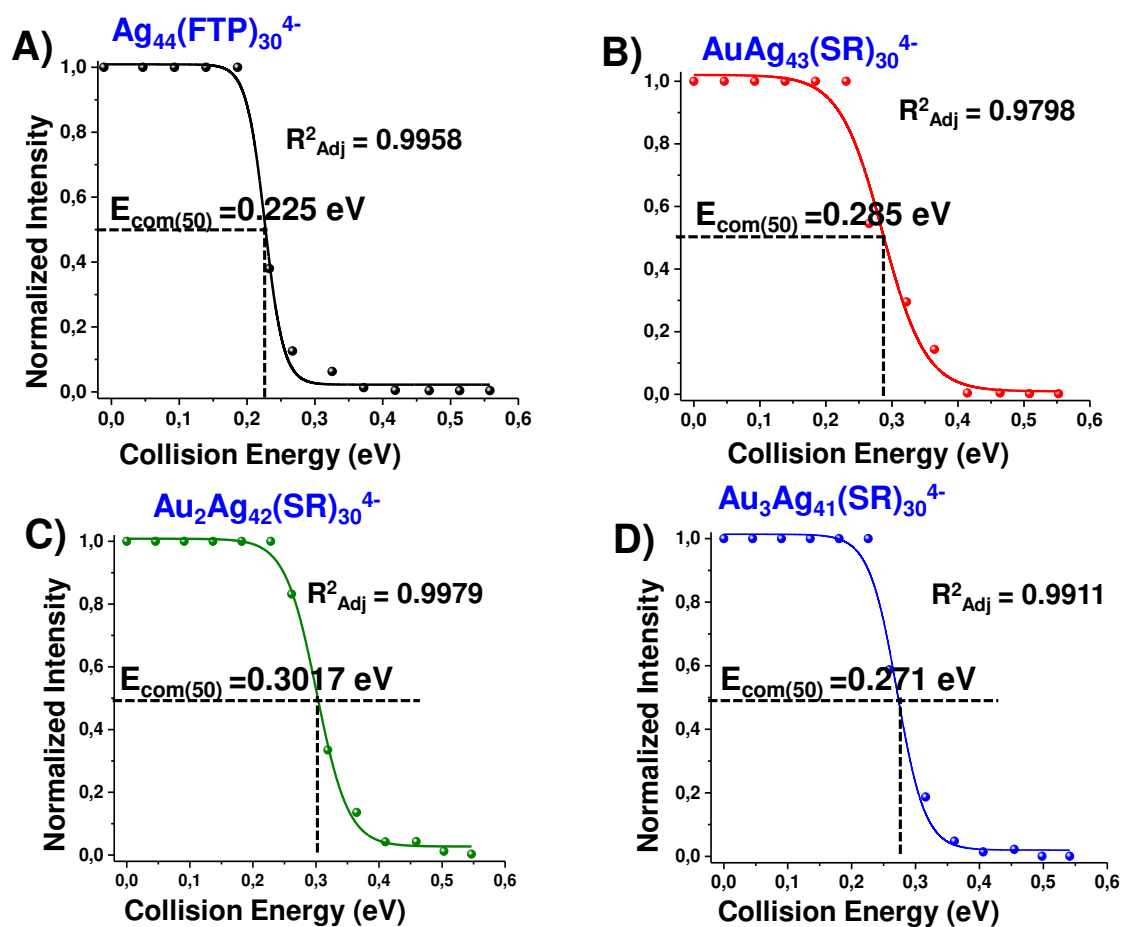


**Figure S13.** Determination of  $E_{\text{com}(50)}$  values for  $\text{Ag}_{44-x}\text{Au}_x(\text{SR})_{30}^{4-}$  ( $x = 0-3$ ) following the same procedure as described in the caption of Figure S10.

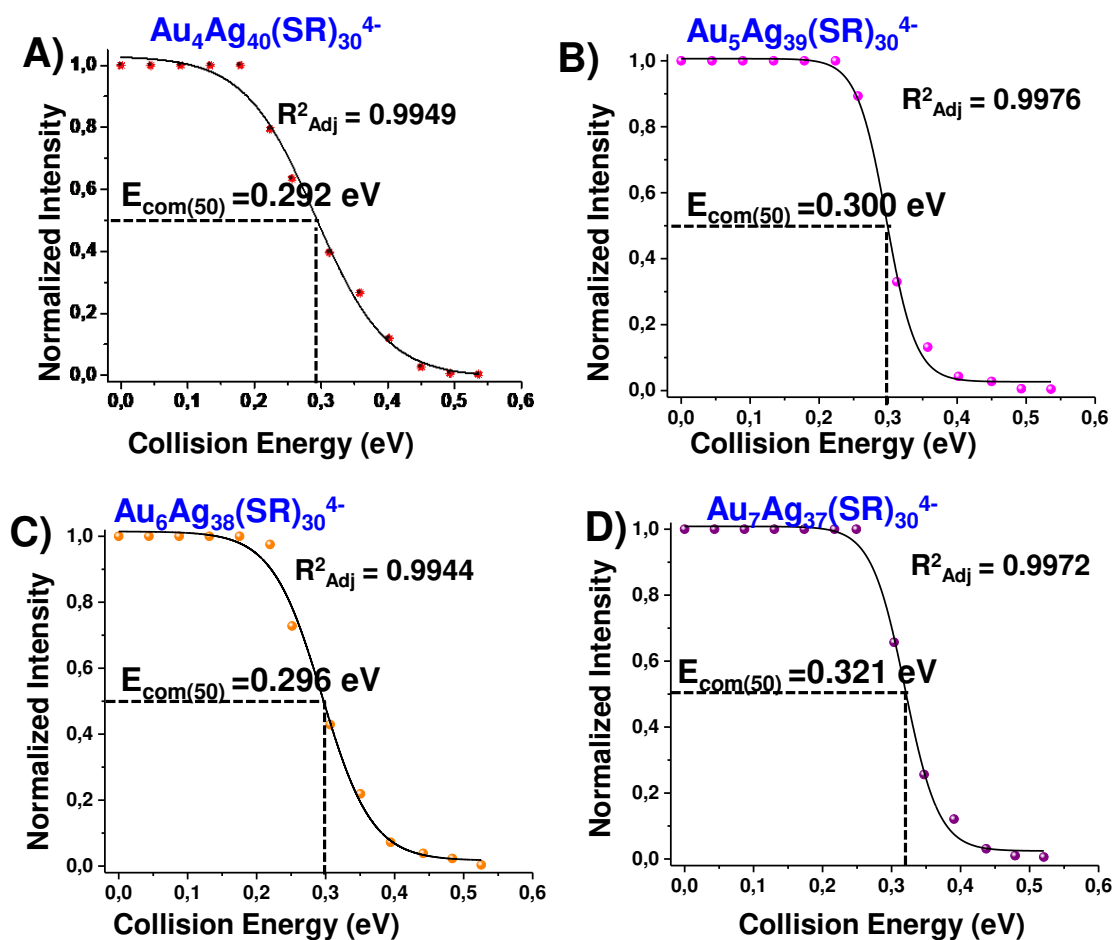


**Figure S14.** Determination of  $E_{\text{com}(50)}$  values for  $\text{Ag}_{44-x}\text{Au}_x(\text{SR})_{30}^{4-}$  ( $x = 4-7$ ) following the same procedure as described in the caption of Figure S10.

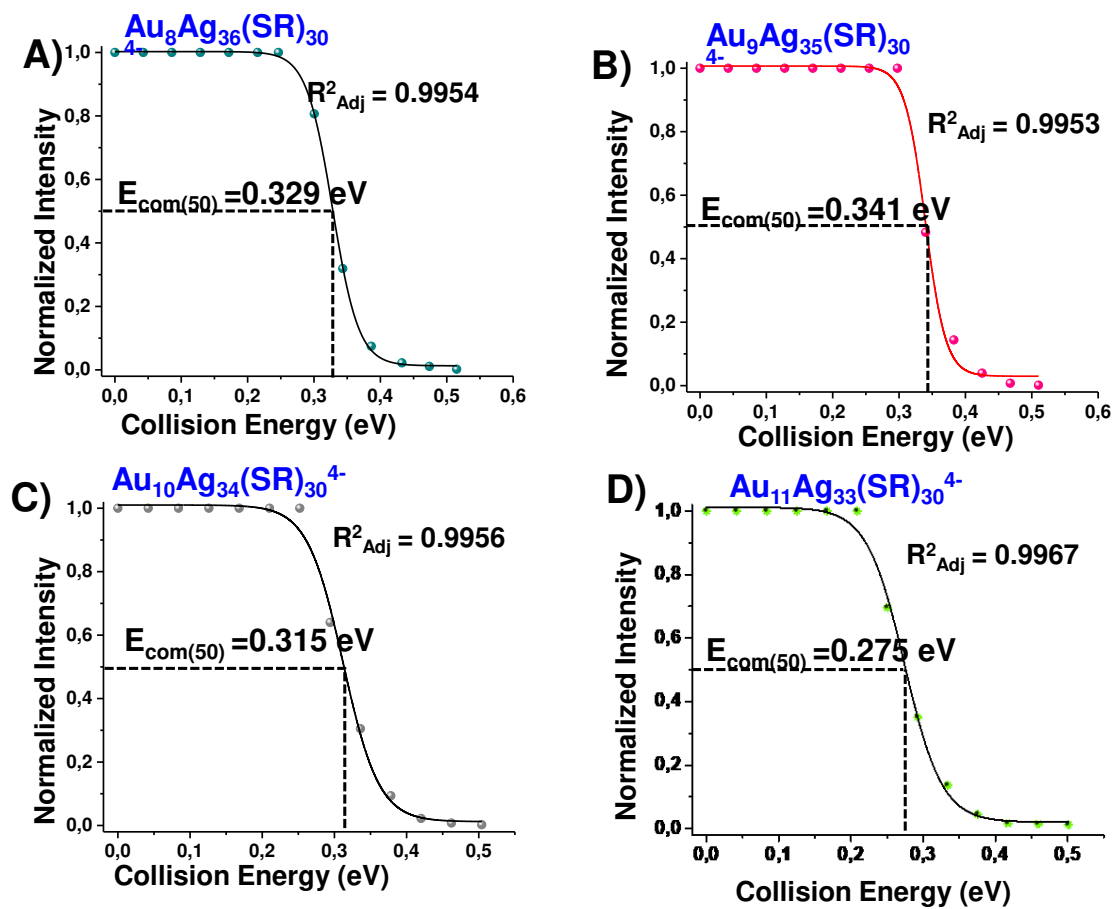


**Figure S15.** Determination of  $E_{\text{com}(50)}$  values for  $\text{Ag}_{44-x}\text{Au}_x(\text{SR})_{30}^{4-}$  ( $x = 8-11$ ) following the same procedure as described in the caption of Figure S10.

**Table S1. Coordinates and NBO-based partial charges of the DFT optimized structures:****Ag<sub>44</sub>(FTP)<sub>30</sub><sup>4-</sup>**

atom	x	y	z	charge
Ag	-0.1982	-2.7379	-0.1630	-0.170
Ag	0.3503	-1.5034	2.4049	-0.174
Ag	2.3196	-1.3859	0.2958	-0.176
Ag	0.1223	2.7607	0.3961	-0.166
Ag	-0.4605	1.5130	-2.1612	-0.175
Ag	-2.4061	1.3861	-0.0464	-0.177
Ag	-1.8946	-0.9596	-1.6951	-0.172
Ag	-2.2631	-1.2186	1.1879	-0.173
Ag	-3.8921	0.8698	2.3742	0.541
Ag	-0.9944	1.0657	2.4792	-0.172
Ag	-4.5128	-0.5322	-0.5813	0.390
Ag	4.4379	0.5083	0.8135	0.395
Ag	2.1158	-3.5896	-1.6419	0.379
Ag	2.1922	1.2256	-0.9467	-0.169
Ag	-2.2351	3.5940	1.8491	0.396
Ag	-0.9074	-0.3656	-4.3393	0.408
Ag	0.7228	3.3213	3.2016	0.517
Ag	1.8742	1.2750	-3.8099	0.374
Ag	1.8284	0.9845	1.9203	-0.177
Ag	-3.2884	1.3210	-2.8243	0.514
Ag	-2.0385	-1.1413	4.0662	0.396
Ag	1.3339	3.7819	-2.0582	0.512
Ag	-2.9623	-3.4007	-0.5667	0.385
Ag	0.9420	-1.0309	-2.2306	-0.173
Ag	-1.8801	3.8912	-1.3888	0.377
Ag	3.8233	-0.8652	-2.1226	0.544
Ag	2.8933	3.4465	0.7554	0.405
Ag	-1.5854	0.7259	6.5902	0.547
Ag	-0.2128	-1.9216	6.5007	0.545
Ag	3.1839	-1.2865	3.0932	0.517
Ag	-1.4161	-3.8053	2.2508	0.516
Ag	-0.7293	-3.2990	-2.9682	0.512
Ag	0.9028	0.3029	4.5685	0.396
Ag	1.7663	-3.8971	1.6505	0.425
Ag	5.8355	3.1516	-0.4328	0.555
Ag	1.7875	-6.4203	-0.3768	0.541
Ag	-5.5441	-2.9435	-2.3481	0.545
Ag	-1.8290	6.4139	0.5229	0.554
Ag	5.5163	2.8891	2.5220	0.546
Ag	1.5779	-0.6113	-6.3256	0.544
Ag	0.1228	1.9855	-6.2906	0.542
Ag	-4.4427	5.0654	0.0049	0.551
Ag	-5.8855	-3.1901	0.6158	0.559
Ag	4.3418	-4.9797	0.0595	0.541
S	0.1133	2.5049	5.7201	-0.432
S	-4.4155	3.7281	-2.1547	-0.410

S	5.8257	0.7176	-1.3559	-0.440
S	-3.9598	-4.5132	1.6025	-0.426
S	3.9047	4.4705	-1.4385	-0.421
S	-4.8064	3.3574	1.9606	-0.434
S	4.7139	-3.3650	-1.8569	-0.427
S	-5.8696	-0.7750	1.6021	-0.436
S	-3.3728	-4.1333	-3.0327	-0.430
S	-0.6770	5.5413	2.6834	-0.442
S	5.2107	0.4346	3.3275	-0.423
S	-2.2902	1.5418	-5.3780	-0.444
S	0.1433	-5.9211	1.6252	-0.437
S	-0.2389	5.9285	-1.4345	-0.430
S	3.5789	-0.4342	-4.7639	-0.428
S	-4.1362	7.4491	0.7937	-0.388
S	-5.2624	-0.4684	-3.1076	-0.428
S	0.5781	-5.6141	-2.4426	-0.403
S	2.2068	-1.7019	5.5975	-0.437
S	3.9570	-7.4460	0.4469	-0.367
S	-7.6913	-3.5363	-1.1404	-0.382
S	-3.6140	0.7117	5.0378	-0.423
S	7.6620	3.4733	1.2800	-0.388
S	-1.4812	-3.5341	4.9840	-0.425
S	1.1672	3.7060	-4.7611	-0.397
S	4.2697	-3.6586	2.3089	-0.433
S	3.3959	4.1309	3.2141	-0.430
S	0.0540	-2.5515	-5.4349	-0.436
S	-0.8099	-0.6104	8.5974	-0.382
S	0.5501	0.5462	-8.3277	-0.368
F	3.6341	4.4082	10.1448	-0.341
F	2.4237	-8.6631	-7.2162	-0.341
F	-2.9500	-4.9697	-9.9817	-0.341
F	6.9956	-10.7338	-3.4956	-0.343
C	-1.2457	6.4260	4.1394	-0.160
F	-5.8642	-6.2349	7.9911	-0.340
C	0.8538	2.7953	8.4000	-0.208
H	-0.0604	2.2268	8.6370	0.240
F	-6.1429	7.1833	-6.6978	-0.340
C	2.2658	-7.4058	-3.7871	-0.208
H	2.7743	-7.5544	-2.8194	0.233
F	4.5167	9.8729	4.3572	-0.340
C	1.2045	-6.4776	-3.8823	-0.159
F	-7.0159	5.7424	6.9527	-0.341
C	-6.8564	0.3077	-3.3935	-0.157
C	-0.8992	-3.2028	-6.8090	-0.156
C	-4.8788	4.8051	-3.5123	-0.158
C	-3.3138	0.9541	-6.7273	-0.152
C	4.4221	-4.2379	-4.5164	-0.195
H	3.3668	-3.9313	-4.4481	0.249
C	5.2717	-4.0967	-3.3952	-0.162
C	7.6002	-1.1618	-0.2406	-0.197



H	6.7567	-1.5201	0.3701	0.246
F	6.7309	-5.6586	-6.9699	-0.338
C	-3.5297	-5.9188	-3.1101	-0.159
C	-5.4229	4.1036	3.4683	-0.153
C	7.4139	-0.0857	-1.1372	-0.153
F	1.0306	-9.9579	5.9193	-0.341
C	2.6827	-8.1420	-4.9070	-0.291
H	3.5112	-8.8634	-4.8327	0.236
F	4.6518	2.7570	-12.0514	-0.343
F	-8.4541	-1.3204	7.8554	-0.340
C	-4.5841	4.4284	4.5574	-0.197
H	-3.4996	4.2498	4.4850	0.244
C	1.6695	3.2592	9.4440	-0.291
H	1.4033	3.0747	10.4968	0.231
C	3.7492	5.8716	3.4779	-0.155
C	-7.4648	0.0273	1.4325	-0.151
C	6.7914	-0.3850	3.5523	-0.157
C	-1.0539	-3.7663	-9.1901	-0.293
H	-0.6428	-3.7455	-10.2118	0.231
C	-0.5956	6.9902	-2.8362	-0.158
C	-5.0648	0.0521	5.8586	-0.160
F	11.1447	-1.8995	-0.7587	-0.342
C	4.9012	-9.7865	-0.6509	-0.217
H	4.3969	-10.2559	0.2093	0.232
C	8.8556	-1.7778	-0.1122	-0.289
H	9.0095	-2.6076	0.5943	0.240
C	6.2538	-5.1497	-5.8067	0.395
C	1.2063	3.0221	7.0492	-0.158
F	-11.2225	1.8004	1.1395	-0.341
C	4.7558	-4.8179	3.5901	-0.155
C	0.4620	-7.1042	2.9353	-0.158
C	2.8438	3.9574	9.1360	0.393
F	-3.8267	-10.0589	-3.4684	-0.338
C	-5.7702	5.8829	-3.3008	-0.213
H	-6.1292	6.0964	-2.2804	0.239
C	8.5111	0.3553	-1.9133	-0.207
H	8.3714	1.1872	-2.6214	0.239
C	8.1303	5.1878	1.4932	-0.162
C	4.2668	8.5701	4.0678	0.395
C	3.2523	-1.1644	6.9526	-0.153
C	4.8117	-8.3810	-0.8157	-0.169
C	-2.1508	-3.8266	-6.5991	-0.220
H	-2.5842	-3.8544	-5.5841	0.245
C	0.5742	-6.2936	-5.1348	-0.200
H	-0.2525	-5.5734	-5.2306	0.240
C	-7.7385	0.9624	0.4100	-0.196
H	-6.9562	1.2194	-0.3220	0.244
C	-6.8136	4.3351	3.5857	-0.206
H	-7.4775	4.0721	2.7469	0.240
C	-5.0076	-5.4163	5.9271	-0.295

H	-5.9012	-5.7944	5.4054	0.237
C	-6.1979	6.6871	-4.3692	-0.291
H	-6.8841	7.5326	-4.2051	0.235
C	6.6262	-4.4891	-3.5103	-0.219
H	7.2998	-4.3633	-2.6478	0.242
C	7.1209	-5.0192	-4.7132	-0.306
H	8.1750	-5.3237	-4.8145	0.230
F	-5.7245	-0.2646	-9.9008	-0.341
C	-6.4953	5.2069	5.8179	0.392
C	2.0327	-7.9448	-6.1318	0.393
C	-5.1160	4.9824	5.7333	-0.292
H	-4.4637	5.2446	6.5804	0.242
C	2.7507	6.8542	3.2853	-0.209
H	1.7562	6.5565	2.9109	0.246
C	0.9853	-7.0242	-6.2608	-0.292
H	0.4943	-6.8836	-7.2363	0.237
C	-0.3651	-3.1770	-8.1188	-0.205
H	0.6015	-2.6806	-8.3007	0.239
F	-5.2150	-3.2527	11.6297	-0.342
C	4.9097	-4.7656	-5.7227	-0.284
H	4.2495	-4.8851	-6.5952	0.244
C	-3.6090	1.8373	-7.7924	-0.214
H	-3.1838	2.8538	-7.7838	0.231
C	-5.4023	-1.3190	5.8386	-0.194
H	-4.7527	-2.0352	5.3109	0.242
C	-9.0033	1.5644	0.3088	-0.288
H	-9.2257	2.2826	-0.4950	0.241
C	-8.4779	-0.2740	2.3723	-0.207
H	-8.2662	-0.9875	3.1845	0.240
C	1.4431	1.6865	-10.6637	-0.219
H	0.3829	1.6229	-10.9585	0.233
C	-2.1696	-1.4170	9.4355	-0.166
C	-3.9850	-4.7603	5.2229	-0.217
H	-4.0816	-4.6153	4.1333	0.246
C	5.0163	0.3780	-5.4650	-0.156
C	-2.7345	-4.4811	7.2911	-0.209
H	-1.8512	-4.1026	7.8319	0.235
C	-4.4239	4.5502	-4.8276	-0.224
H	-3.7261	3.7150	-5.0132	0.247
C	-7.3536	4.8888	4.7570	-0.299
H	-8.4353	5.0721	4.8575	0.228
C	3.5871	-2.0996	7.9595	-0.212
H	3.1925	-3.1262	7.8960	0.231
C	3.7692	0.1470	7.0433	-0.196
H	3.5246	0.8868	6.2655	0.246
C	0.4620	-6.7281	4.2980	-0.205
H	0.2900	-5.6751	4.5748	0.248
C	5.2768	7.6204	4.2624	-0.293
H	6.2626	7.9402	4.6347	0.234
F	-1.3666	9.5527	-6.0294	-0.338

C	3.7332	2.2672	-11.1772	0.385
C	5.6308	-10.5804	-1.5495	-0.301
H	5.7051	-11.6724	-1.4197	0.225
C	-5.2995	10.8771	-1.0763	-0.303
H	-5.8327	11.8020	-0.8026	0.223
C	-4.8298	10.7108	-2.3853	0.387
C	-4.1489	9.5495	-2.7700	-0.285
H	-3.7850	9.4438	-3.8036	0.241
C	-3.9321	8.5353	-1.8238	-0.208
H	-3.3889	7.6261	-2.1263	0.245
C	-4.3877	8.6712	-0.4923	-0.163
C	-5.0769	9.8568	-0.1373	-0.222
H	-5.4377	9.9755	0.8976	0.230
C	-2.2865	-4.3863	-8.9503	0.394
C	5.0135	6.2734	3.9671	-0.216
H	5.8042	5.5184	4.1126	0.238
C	9.7695	-0.2537	-1.7888	-0.298
H	10.6322	0.0875	-2.3829	0.227
C	-2.8331	-4.2902	5.8938	-0.156
C	-6.5465	-1.7864	6.5057	-0.289
H	-6.8010	-2.8577	6.5070	0.241
C	-2.9812	-6.7671	-2.1218	-0.192
H	-2.4649	-6.3327	-1.2514	0.248
C	-5.9128	0.9549	6.5431	-0.207
H	-5.6694	2.0296	6.5451	0.243
C	-2.8894	-2.9287	11.2355	-0.306
H	-2.6594	-3.6254	12.0581	0.225
C	6.2762	-9.9686	-2.6321	0.386
C	1.8239	1.2422	-9.3725	-0.170
C	-7.3574	-0.8725	7.1899	0.389
C	-7.0575	0.4959	7.2137	-0.298
H	-7.7213	1.1910	7.7521	0.231
C	0.6527	-7.6873	5.3055	-0.288
H	0.6459	-7.4022	6.3692	0.234
C	-1.1020	8.7125	-4.9970	0.395
C	-5.7324	6.4097	-5.6605	0.393
C	2.4010	3.7251	6.7678	-0.218
H	2.7038	3.8956	5.7204	0.245
C	3.1896	1.3299	-9.0132	-0.213
H	3.5113	0.9917	-8.0144	0.242
F	5.6712	-0.0627	10.1604	-0.341
C	-3.7536	-5.1334	8.0022	-0.289
H	-3.6867	-5.2719	9.0924	0.234
C	2.3894	2.1963	-11.5666	-0.302
H	2.0954	2.5424	-12.5708	0.225
C	-2.8448	-4.4193	-7.6669	-0.294
H	-3.8176	-4.9119	-7.5103	0.231
C	-3.0791	-8.1621	-2.2387	-0.278
H	-2.6544	-8.8245	-1.4695	0.243
C	4.8899	-0.4220	9.1100	0.398

C	5.4676	-7.7995	-1.9269	-0.217
H	5.4099	-6.7094	-2.0825	0.240
C	3.2200	4.1952	7.8084	-0.296
H	4.1480	4.7473	7.5915	0.237
C	-4.8779	-5.5985	7.3090	0.395
C	-3.7280	-8.7115	-3.3508	0.400
C	9.9257	-1.3138	-0.8863	0.394
C	-4.2255	-2.6509	10.9184	0.388
C	3.0063	8.2027	3.5806	-0.289
H	2.2276	8.9695	3.4435	0.236
C	4.1439	1.8420	-9.9076	-0.291
H	5.2053	1.9108	-9.6219	0.240
C	0.6595	-8.4656	2.6048	-0.210
H	0.6670	-8.7694	1.5459	0.237
C	-4.4220	1.4321	-8.8623	-0.296
H	-4.6507	2.1119	-9.6984	0.227
C	6.1966	-8.5854	-2.8348	-0.292
H	6.7064	-8.1242	-3.6952	0.239
C	-1.8692	-2.3105	10.4941	-0.224
H	-0.8138	-2.5186	10.7359	0.232
C	4.0785	-4.8860	4.8288	-0.207
H	3.2075	-4.2353	5.0095	0.248
C	-3.8528	-0.3516	-6.7590	-0.195
H	-3.6357	-1.0512	-5.9371	0.246
C	-4.8499	5.3494	-5.9014	-0.295
H	-4.5053	5.1505	-6.9285	0.234
C	-9.7447	0.3231	2.2783	-0.298
H	-10.5427	0.0896	3.0013	0.228
C	-4.5574	-1.7720	9.8807	-0.284
H	-5.6151	-1.5847	9.6389	0.239
C	-3.5297	-1.1592	9.1460	-0.203
H	-3.7881	-0.4758	8.3210	0.239
C	-1.6224	7.4131	-5.0190	-0.286
H	-2.2307	7.0793	-5.8735	0.240
C	-0.0740	8.3051	-2.8480	-0.206
H	0.5349	8.6530	-1.9989	0.236
C	0.8534	-9.4292	3.6067	-0.296
H	1.0149	-10.4899	3.3570	0.228
C	-9.9929	1.2319	1.2413	0.394
C	7.3192	0.1754	-6.2734	-0.295
H	8.2172	-0.4274	-6.4822	0.231
C	4.4036	-1.7334	9.0405	-0.296
H	4.6634	-2.4535	9.8327	0.226
C	4.5859	0.5221	8.1221	-0.282
H	4.9796	1.5468	8.2033	0.239
C	-1.3630	6.5538	-3.9391	-0.201
H	-1.7720	5.5312	-3.9501	0.243
C	-4.1810	-6.5031	-4.2221	-0.226
H	-4.6086	-5.8530	-5.0027	0.232
C	-4.6660	-0.7655	-7.8261	-0.283

H	-5.0826	-1.7838	-7.8592	0.237
C	-0.3257	9.1700	-3.9244	-0.293
H	0.0697	10.1980	-3.9372	0.231
C	0.8474	-9.0268	4.9480	0.395
C	-4.9420	0.1319	-8.8646	0.398
C	4.1549	6.3443	-5.7106	-0.292
H	4.7742	7.0938	-5.1939	0.236
C	4.2834	6.1636	-7.0938	0.389
C	3.5100	5.2169	-7.7777	-0.295
H	3.6346	5.0867	-8.8641	0.237
C	2.5839	4.4436	-7.0592	-0.214
H	1.9746	3.6931	-7.5905	0.235
C	2.4240	4.6085	-5.6636	-0.164
C	3.2273	5.5660	-5.0002	-0.199
H	3.1243	5.7035	-3.9128	0.242
F	-2.3347	8.6347	7.5025	-0.342
F	-10.5124	2.1063	-4.2832	-0.342
C	-0.5742	6.2415	5.3709	-0.204
H	0.2437	5.5078	5.4436	0.242
C	-2.3058	7.3591	4.0748	-0.211
H	-2.8500	7.5114	3.1276	0.243
F	6.0650	-7.4114	6.5806	-0.341
C	-0.9401	6.9804	6.5076	-0.292
H	-0.4185	6.8384	7.4669	0.238
C	-1.9839	7.9083	6.4095	0.391
C	3.3431	7.0982	-0.6101	-0.202
H	2.4400	6.6906	-0.1293	0.251
C	8.0077	0.2227	3.1668	-0.209
H	7.9993	1.2016	2.6595	0.243
F	-4.9686	-10.3847	1.4604	-0.341
C	-2.6746	8.1027	5.2068	-0.293
H	-3.5006	8.8298	5.1612	0.232
C	-8.0718	-0.3100	-3.0211	-0.211
H	-8.0605	-1.2756	-2.4891	0.243
C	-6.9048	1.5492	-4.0701	-0.201
H	-5.9675	2.0439	-4.3695	0.240
C	-8.1324	2.1598	-4.3714	-0.292
H	-8.1697	3.1273	-4.8956	0.237
C	5.3769	6.7758	-1.9083	-0.222
H	6.0766	6.1069	-2.4349	0.242
C	-9.3201	1.5217	-3.9936	0.391
C	9.2355	-0.4087	3.4211	-0.294
H	10.1855	0.0575	3.1159	0.232
C	-9.3038	0.2927	-3.3227	-0.294
H	-10.2527	-0.1842	-3.0308	0.233
C	7.2951	6.2894	1.1972	-0.208
H	6.2713	6.1135	0.8307	0.245
C	5.8812	-5.6500	3.3832	-0.208
H	6.4131	-5.6117	2.4194	0.239
F	5.1751	6.9195	-7.7859	-0.341

C	6.8326	-1.6446	4.1949	-0.202
H	5.8941	-2.1303	4.5045	0.243
C	5.6361	-6.5685	5.6056	0.395
C	4.5171	-5.7594	5.8376	-0.290
H	3.9938	-5.8193	6.8047	0.232
C	6.3244	-6.5259	4.3868	-0.295
H	7.1961	-7.1805	4.2295	0.230
C	5.0571	1.7625	-5.7401	-0.205
H	4.1799	2.3916	-5.5192	0.242
C	4.2291	6.2285	-1.2867	-0.165
C	-4.2843	-7.8983	-4.3468	-0.303
H	-4.7829	-8.3615	-5.2132	0.229
F	9.5050	9.1049	1.9728	-0.344
F	10.4346	-2.2688	4.2998	-0.343
F	8.4449	2.1130	-7.0727	-0.340
C	9.0546	7.8307	1.8192	0.386
C	3.5983	8.4779	-0.5515	-0.289
H	2.9181	9.1585	-0.0161	0.238
C	5.6381	8.1544	-1.8548	-0.298
H	6.5339	8.5859	-2.3287	0.233
C	7.7521	7.6079	1.3564	-0.287
H	7.1000	8.4630	1.1208	0.240
C	7.3274	1.5498	-6.5458	0.393
C	6.2098	2.3525	-6.2851	-0.290
H	6.2447	3.4318	-6.4993	0.241
C	9.4416	5.4490	1.9627	-0.220
H	10.1043	4.5999	2.1973	0.230
C	8.0569	-2.2838	4.4484	-0.293
H	8.0901	-3.2660	4.9446	0.237
C	6.1622	-0.4069	-5.7331	-0.203
H	6.1448	-1.4849	-5.5075	0.244
C	9.2458	-1.6559	4.0576	0.391
C	9.9071	6.7632	2.1277	-0.303
H	10.9273	6.9691	2.4907	0.223
C	-7.8135	-7.4580	-2.4227	-0.292
H	-7.2278	-8.1440	-3.0550	0.239
C	-7.3814	-6.1399	-2.2016	-0.214
H	-6.4416	-5.7947	-2.6633	0.240
C	-8.1235	-5.2529	-1.3862	-0.170
C	-9.3147	-5.7358	-0.7875	-0.216
H	-9.9032	-5.0596	-0.1461	0.234
C	-9.7562	-7.0506	-1.0035	-0.300
H	-10.6817	-7.4279	-0.5390	0.226
C	-9.0006	-7.8982	-1.8245	0.386
F	4.9959	10.3221	-1.1155	-0.338
F	-5.0383	11.6979	-3.2962	-0.343
F	-9.4301	-9.1695	-2.0407	-0.342
C	4.7429	8.9902	-1.1751	0.394
C	-4.7305	-9.0475	1.4677	0.393
C	-5.6044	-8.1921	0.7849	-0.289

H	-6.4668	-8.6067	0.2400	0.237
C	-5.3576	-6.8105	0.7994	-0.208
H	-6.0376	-6.1318	0.2592	0.236
C	-4.2467	-6.2808	1.4926	-0.159
C	-3.3791	-7.1689	2.1701	-0.206
H	-2.5027	-6.7746	2.7077	0.243
C	-3.6180	-8.5527	2.1593	-0.292
H	-2.9442	-9.2463	2.6860	0.238

**Table S2. Ag<sub>32</sub>Au<sub>12</sub>(FTP)<sub>30</sub><sup>4-</sup> I isomer: all Au atoms in the inner shell**

atom	x	y	z	charge
Au	-0.1046	0.3495	-2.7301	-0.262
Au	1.1826	2.2893	-0.9803	-0.257
Au	-1.7397	1.9607	-0.8734	-0.264
Au	2.3886	-0.3378	-1.3745	-0.261
Au	-2.3003	-0.8892	-1.2609	-0.261
Au	0.2339	-2.3345	-1.5494	-0.257
Au	-2.3542	0.2763	1.4204	-0.265
Au	-0.1901	2.2766	1.6099	-0.256
Au	-1.1366	-2.3517	1.0342	-0.260
Au	2.3558	0.8460	1.3076	-0.262
Au	1.7672	-2.0277	0.9301	-0.261
Au	0.1684	-0.3760	2.7774	-0.258
Ag	-0.4959	3.2712	-3.1485	0.428
Ag	-2.8498	1.0011	-3.4194	0.457
Ag	2.3980	1.6027	-3.5492	0.587
Ag	1.6590	-1.6004	-3.9629	0.427
Ag	-1.5288	-1.9592	-3.8751	0.557
Ag	-0.5356	4.5421	-0.2189	0.561
Ag	-2.2505	-3.8028	-1.2358	0.440
Ag	-3.0005	3.1223	1.4814	0.434
Ag	4.1197	1.9241	-0.7299	0.440
Ag	-4.4692	0.9426	-0.5111	0.561
Ag	2.2763	3.7795	1.2614	0.449
Ag	-4.0647	-2.0076	0.7705	0.438
Ag	3.0436	-3.1796	-1.4305	0.466
Ag	-1.6852	1.5084	3.9981	0.439
Ag	-2.3347	-1.6388	3.6142	0.584
Ag	4.5044	-1.0121	0.5652	0.563
Ag	2.9467	-1.0818	3.4155	0.446
Ag	0.5747	-4.6208	0.2680	0.565
Ag	0.4858	-3.2357	3.2929	0.440
Ag	1.6173	1.9345	3.9134	0.562
S	0.8069	2.7993	-5.3463	-0.421
S	4.1746	3.4381	-2.8170	-0.432
S	-2.2193	-0.0878	-5.7032	-0.428
S	5.4573	-2.2700	-1.6522	-0.424
S	-4.8809	2.4332	-2.7478	-0.442
S	-4.0511	-3.5409	2.8454	-0.429
S	-1.9735	5.4808	1.8876	-0.426
S	3.7057	-0.3036	-4.9083	-0.420
S	2.0412	-5.5307	-1.8113	-0.436
S	1.8634	5.8553	-0.2656	-0.414
S	-5.9585	-1.2549	-0.8734	-0.426
S	-3.7587	0.2450	4.8732	-0.428
S	-3.6832	-3.6302	-3.3952	-0.425
S	-0.2771	3.4098	5.1229	-0.439
S	-5.4798	2.2718	1.6589	-0.404



S	0.2665	-3.5855	-5.0542	-0.402
S	6.0049	1.1715	0.9265	-0.421
S	-0.7199	-2.6352	5.5240	-0.416
S	-1.7971	-5.9365	0.2122	-0.424
S	2.4599	0.0744	5.6858	-0.429
S	-1.9566	5.3645	-2.3546	-0.396
S	4.9368	-2.5892	2.7247	-0.437
S	3.7371	3.6534	3.4017	-0.424
S	1.7930	-5.3892	2.5932	-0.422
Ag	-1.6530	2.4682	-5.9356	0.546
Ag	4.6141	-2.5528	-4.1118	0.542
Ag	-3.3393	4.0991	-4.0622	0.547
Ag	4.2495	5.1117	-0.8058	0.555
Ag	-2.4489	4.5424	4.2304	0.555
Ag	2.4438	-4.6022	-4.2346	0.548
Ag	-4.1553	-5.2041	0.8273	0.560
Ag	-5.3972	-3.7272	-1.4814	0.547
Ag	5.4555	3.6513	1.5119	0.550
Ag	-4.6865	2.5580	4.0706	0.553
Ag	3.3828	-4.1260	4.1289	0.550
Ag	1.7848	-2.4354	6.0291	0.547
H	1.3831	-0.4513	-6.7666	0.248
H	-1.6849	-5.8261	-3.5130	0.249
H	6.1510	1.2205	-2.9792	0.248
H	-4.4977	5.4955	0.3129	0.244
H	-6.2451	-1.5307	2.8274	0.245
H	-1.5482	0.5754	6.8502	0.245
H	-5.8491	-0.1396	-3.8657	0.248
H	0.9796	6.5340	2.4856	0.251
H	5.8886	-0.0815	4.0115	0.247
H	5.9033	-4.1697	0.5760	0.248
H	3.4109	-6.3800	0.6626	0.248
H	-6.4104	3.5387	-0.8299	0.247
H	-4.2951	-2.1640	-5.5237	0.244
H	-1.0359	-5.4845	4.6854	0.241
H	1.7553	5.0450	5.0604	0.246
H	0.4979	5.6845	-4.6484	0.241
H	4.3533	2.3144	5.5440	0.244
H	-0.5764	-7.0652	2.1606	0.245
C	1.5249	4.3099	-5.9936	-0.159
C	5.7682	3.2703	-3.6215	-0.155
C	3.5408	-0.1338	-6.6851	-0.163
C	-5.6182	-3.4238	3.7091	-0.154
C	-3.6002	-5.1653	-4.3191	-0.161
C	-3.1470	6.7675	1.4572	-0.159
C	-3.6659	0.0924	6.6564	-0.154
C	-6.3098	1.9865	-3.7336	-0.154
H	-0.3247	7.5090	-1.2483	0.241
C	-3.6451	-0.4642	-6.7280	-0.157
C	6.6517	-3.5825	-1.3858	-0.158

C	1.9040	7.3687	0.6959	-0.166
C	2.2943	-0.2296	-7.3443	-0.195
C	7.6073	0.9999	0.1366	-0.157
C	-7.5824	-1.1166	-0.1206	-0.157
C	-1.4622	-4.0746	6.2929	-0.162
C	0.2486	-3.5251	-6.8459	-0.160
C	3.1799	-6.8700	-1.4511	-0.158
H	0.3866	-7.6491	-0.6625	0.243
H	-1.8211	-2.8425	-6.9392	0.240
H	-7.6144	1.0546	-0.3211	0.239
H	7.6100	-1.1700	0.3550	0.242
C	-2.5071	-6.0546	-4.2089	-0.193
H	1.8507	2.6709	6.9606	0.241
C	-0.2107	3.3842	6.9185	-0.160
C	3.9593	0.4459	6.6039	-0.160
C	-1.7893	-7.4864	-0.6922	-0.160
C	-6.7324	3.5123	1.3303	-0.160
C	6.5233	2.0773	-3.5633	-0.198
C	6.3976	-2.1749	3.6790	-0.155
C	-1.4618	6.9511	-3.0232	-0.165
C	3.8184	5.1705	4.3575	-0.157
C	1.2178	-6.8919	3.3907	-0.159
C	-6.5016	-2.3353	3.5350	-0.196
C	-2.4694	0.2882	7.3811	-0.197
C	-4.2957	6.5160	0.6748	-0.202
C	-6.5606	0.6556	-4.1359	-0.196
C	1.3939	7.4380	2.0126	-0.201
C	1.2113	5.5883	-5.4830	-0.203
C	6.6312	-0.8760	4.1823	-0.196
C	6.6623	-4.3537	-0.2018	-0.207
C	-4.4794	-1.5674	-6.4335	-0.217
C	3.6803	-7.0796	-0.1458	-0.205
C	-1.5013	-5.3431	5.6739	-0.194
C	-7.0154	3.9277	0.0076	-0.223
C	4.6716	1.6430	6.3596	-0.217
C	2.7053	5.6040	5.1149	-0.210
C	0.0334	-7.5283	2.9549	-0.214
C	8.1756	-0.2894	0.0125	-0.201
C	-8.1740	0.1623	0.0003	-0.200
C	-0.9374	-3.1512	-7.5187	-0.201
C	-0.6804	7.8317	-2.2388	-0.198
C	-0.5588	-8.1331	-0.9530	-0.206
C	0.9933	3.0125	7.5612	-0.205
S	-3.6782	3.8459	-6.5620	-0.369
H	2.7223	3.2135	-7.4467	0.244
S	4.8674	-4.9188	-4.9616	-0.369
C	2.4595	4.2073	-7.0508	-0.204
H	7.9254	3.1313	-0.2228	0.243
S	6.5965	5.4257	0.0738	-0.386
H	-7.8793	-3.2557	0.2119	0.242

S	-6.5101	-5.5228	-0.0839	-0.382
S	-4.4536	4.4040	5.7889	-0.388
H	2.3062	-4.1970	-7.1034	0.235
S	3.6975	-3.9768	6.6446	-0.380
H	-2.2592	4.0778	7.2336	0.244
H	-3.9543	-7.6226	-0.9035	0.236
C	8.3493	2.1172	-0.3074	-0.209
H	-5.2375	6.0837	3.4007	0.245
C	-8.3190	-2.2482	0.2959	-0.211
C	1.3708	-3.9113	-7.6123	-0.208
C	-1.3061	3.7959	7.7115	-0.210
C	-2.9879	-8.1185	-1.0904	-0.207
H	-2.5028	6.7101	-4.9251	0.237
C	6.2655	4.3563	-4.3790	-0.207
C	-5.9598	-4.4400	4.6316	-0.206
C	-1.8999	7.3867	-4.2952	-0.216
C	4.6951	0.1633	-7.4479	-0.219
C	-3.9063	0.2912	-7.8948	-0.206
C	-2.9007	8.0876	1.9015	-0.207
C	-4.8347	-0.2849	7.3586	-0.206
C	-2.0673	-3.9145	7.5619	-0.207
H	-3.2759	1.1641	-8.1289	0.240
C	7.6451	-3.8223	-2.3637	-0.208
C	-7.2400	2.9916	-4.0876	-0.216
C	-4.6408	-5.4763	-5.2261	-0.226
C	4.4064	-0.4127	7.6342	-0.207
H	4.7082	7.3301	1.4435	0.244
H	-2.0590	-2.9239	8.0446	0.243
H	3.8789	-1.3626	7.8208	0.240
H	7.6440	-3.2313	-3.2931	0.238
C	3.5242	-7.7907	-2.4681	-0.210
H	-5.2690	-5.2838	4.7862	0.240
C	2.4220	8.5454	0.1047	-0.222
C	-7.5155	4.0340	2.3864	-0.212
H	-1.0260	5.1193	-7.1750	0.241
H	4.7575	-2.7565	-7.0479	0.240
H	5.6797	5.2873	-4.4370	0.239
H	-2.0011	8.2973	2.5015	0.238
H	-5.7685	-0.4544	6.7995	0.240
H	3.1487	-7.6322	-3.4918	0.238
H	-7.0485	4.0349	-3.7880	0.232
C	1.9747	-7.4956	4.4211	-0.210
C	7.3680	-3.1784	3.9049	-0.212
H	5.6677	0.2602	-6.9395	0.242
C	5.0251	5.9019	4.4427	-0.215
H	-7.3003	3.7252	3.4231	0.238
H	2.8904	-7.0017	4.7860	0.236
C	2.2014	-0.0458	-8.7333	-0.285
H	5.8981	5.5809	3.8503	0.238
H	2.8242	8.5027	-0.9202	0.242

H	-5.4965	-4.7892	-5.3259	0.233
C	-2.4566	-7.2286	-4.9765	-0.278
H	7.1965	-4.1945	3.5147	0.232
C	7.7490	1.9705	-4.2404	-0.289
H	-5.7988	-6.3916	-2.8631	0.240
H	0.9999	-4.9113	7.5565	0.240
C	-2.4396	0.1226	8.7758	-0.292
C	-5.1906	7.5516	0.3600	-0.287
C	-7.7065	-2.2670	4.2538	-0.289
C	-7.7116	0.3348	-4.8720	-0.282
C	1.7975	6.7435	-6.0260	-0.290
C	1.4074	8.6482	2.7245	-0.288
C	7.8020	-0.5860	4.9003	-0.281
H	1.2332	-0.1271	-9.2509	0.244
C	-2.1188	-6.4332	6.3081	-0.289
C	7.6401	-5.3413	0.0002	-0.290
H	-1.6093	-7.9253	-4.8877	0.243
C	4.4961	-8.1860	0.1399	-0.289
C	-5.5415	-1.9113	-7.2855	-0.294
C	-8.0570	4.8345	-0.2516	-0.296
C	5.7954	1.9804	7.1315	-0.295
H	8.3454	1.0467	-4.1885	0.240
C	2.7968	6.7348	5.9418	-0.291
C	-0.3799	-8.7433	3.5252	-0.295
H	-1.5108	0.2831	9.3447	0.242
C	9.4548	-0.4623	-0.5390	-0.292
H	-6.0924	7.3565	-0.2408	0.240
H	-8.4014	-1.4249	4.1137	0.241
C	-9.4685	0.3122	0.5214	-0.291
C	-1.0047	-3.1699	-8.9211	-0.293
C	-0.5265	-9.3853	-1.5879	-0.292
C	-0.3525	9.1137	-2.7074	-0.293
C	1.1094	3.0640	8.9598	-0.292
H	-7.9100	-0.6997	-5.1919	0.237
C	-5.7517	6.4511	4.3031	-0.208
H	1.0263	8.7035	3.7558	0.240
H	7.9839	0.4225	5.3020	0.239
C	-3.1798	5.3174	-7.4479	-0.171
H	1.5498	7.7414	-5.6323	0.242
C	3.0552	5.3557	-7.5951	-0.295
C	5.0879	-4.8901	-6.7362	-0.170
C	3.1032	-5.4686	7.4326	-0.167
C	-5.5414	5.8054	5.5433	-0.163
C	-1.8339	5.7125	-7.6339	-0.213
C	5.7326	7.7326	1.4822	-0.209
C	5.0199	-3.7159	-7.5241	-0.218
H	-2.1417	-7.4251	5.8304	0.241
H	4.8800	-8.3588	1.1576	0.235
C	-6.7100	-7.0479	-0.9934	-0.169
H	7.6514	-5.9502	0.9177	0.233

H	-8.2860	5.1558	-1.2800	0.235
C	6.7957	6.9919	0.9160	-0.164
H	-6.1929	-2.7714	-7.0644	0.230
C	1.7560	-5.6711	7.8134	-0.204
H	6.3512	2.9129	6.9447	0.236
C	-6.3161	-7.2141	-2.3420	-0.214
H	1.9344	7.0705	6.5393	0.237
C	9.6305	1.9519	-0.8573	-0.293
H	-1.2988	-9.2446	3.1821	0.238
C	-9.6158	-2.1064	0.8157	-0.294
C	1.3127	-3.9337	-9.0143	-0.290
C	-2.9645	-9.3697	-1.7263	-0.290
C	4.6108	0.3471	-8.8380	-0.305
C	-1.1964	3.8502	9.1101	-0.293
C	7.4904	4.2579	-5.0577	-0.299
C	-7.1614	-4.3790	5.3547	-0.298
C	-4.8136	-0.4530	8.7519	-0.299
C	-3.7886	9.1288	1.5903	-0.293
C	-4.5982	-6.6486	-5.9986	-0.304
C	2.7124	6.6122	-7.0780	0.393
C	3.3615	0.2392	-9.4640	0.395
H	9.8967	-1.4655	-0.6410	0.237
C	-2.6868	-4.9987	8.2030	-0.298
H	-9.9282	1.3080	0.6189	0.237
C	-1.5770	8.6677	-4.7718	-0.294
H	0.2525	9.8005	-2.0952	0.236
C	-4.9678	-0.0459	-8.7491	-0.292
H	0.4306	-9.8905	-1.7912	0.237
H	-1.9277	-2.8794	-9.4465	0.237
C	-8.3945	2.6786	-4.8225	-0.296
C	-3.5031	-7.5118	-5.8626	0.399
C	5.5296	-0.0824	8.4078	-0.291
C	8.2177	3.0630	-4.9798	0.394
C	8.6255	-4.8074	-2.1684	-0.295
H	2.0470	2.7759	9.4600	0.238
C	-3.6135	-0.2451	9.4444	0.392
C	2.4388	9.7597	0.8099	-0.301
C	-8.0218	-3.2915	5.1545	0.394
C	4.3403	-8.8988	-2.1893	-0.296
C	-8.5563	4.9415	2.1351	-0.291
C	-4.9274	8.8455	0.8253	0.394
C	8.5422	-2.8963	4.6203	-0.297
C	1.5681	-8.7102	4.9959	-0.289
C	5.1239	7.0340	5.2682	-0.293
C	-8.6155	1.3499	-5.2058	0.399
C	10.1681	0.6638	-0.9670	0.391
C	1.9310	9.7951	2.1150	0.394
C	-2.7042	-6.2468	7.5664	0.391
C	-10.1755	-0.8274	0.9232	0.391
C	-5.7735	-1.1472	-8.4351	0.396

C	0.1222	-3.5645	-9.6530	0.393
C	8.6103	-5.5570	-0.9859	0.396
C	6.2095	1.1143	8.1502	0.393
C	8.7436	-1.5998	5.1104	0.398
C	-1.7317	-9.9910	-1.9643	0.393
C	4.8149	-9.0846	-0.8848	0.396
C	-8.8172	5.3305	0.8155	0.393
C	0.0119	3.4876	9.7187	0.391
C	-0.8077	9.5189	-3.9687	0.390
C	0.3954	-9.3230	4.5368	0.394
C	4.0069	7.4362	6.0110	0.395
H	3.7856	5.2847	-8.4166	0.231
H	10.2105	2.8186	-1.2112	0.231
H	-10.1918	-2.9854	1.1453	0.232
H	2.1893	-4.2295	-9.6116	0.237
H	-3.8984	-9.8595	-2.0428	0.237
H	-2.0481	4.1676	9.7323	0.231
C	-6.6010	7.5651	4.2020	-0.286
C	4.0479	-6.4746	7.7565	-0.223
H	-6.7593	8.0668	3.2347	0.240
H	-1.9172	9.0046	-5.7633	0.237
H	5.5036	0.5809	-9.4398	0.230
H	-5.7191	-0.7472	9.3063	0.228
H	-7.4364	-5.1654	6.0755	0.228
H	7.8874	5.0998	-5.6471	0.227
H	-3.1630	-4.8828	9.1895	0.231
H	-3.6089	10.1581	1.9388	0.230
C	-4.1953	6.1036	-8.0483	-0.219
C	-7.3568	-8.1322	-0.3485	-0.216
H	-5.1783	0.5452	-9.6545	0.230
H	5.8864	-0.7533	9.2054	0.231
C	1.3626	-6.8310	8.5006	-0.286
C	-1.5084	6.8510	-8.3889	-0.290
C	5.4236	-6.1064	-7.3833	-0.217
H	-5.4016	-6.8966	-6.7104	0.230
C	5.2831	-3.7488	-8.9038	-0.293
C	5.9602	8.9780	2.0894	-0.288
H	5.1018	-6.3323	7.4666	0.233
H	9.3971	-5.0047	-2.9294	0.229
H	-9.1226	3.4555	-5.1050	0.227
H	-9.1616	5.3543	2.9570	0.236
H	4.6139	-9.6188	-2.9768	0.228
H	2.8512	10.6769	0.3601	0.233
C	-6.5622	-8.4145	-3.0283	-0.292
C	-6.2125	6.3112	6.6843	-0.221
H	2.1495	-9.1778	5.8054	0.235
C	8.1023	7.5367	0.9849	-0.220
H	6.0605	7.6095	5.3337	0.234
H	-7.6677	-8.0207	0.7031	0.234
H	9.3028	-3.6722	4.8026	0.226

H	-5.2488	5.8080	-7.9145	0.233
H	5.1289	9.5528	2.5261	0.240
H	5.4822	-7.0307	-6.7856	0.232
H	-0.4595	7.1583	-8.5231	0.241
H	5.2270	-2.8307	-9.5097	0.240
H	0.3110	-6.9892	8.7863	0.240
F	3.2790	0.4155	-10.8067	-0.338
F	3.2815	7.7247	-7.6091	-0.340
H	-6.2470	-8.5389	-4.0765	0.239
H	8.9411	6.9707	0.5474	0.231
F	-3.4631	-8.6460	-6.6049	-0.337
F	9.4041	2.9661	-5.6349	-0.342
F	-3.5918	-0.4052	10.7933	-0.341
H	-6.0558	5.8189	7.6581	0.230
F	-9.1861	-3.2330	5.8521	-0.341
F	-5.7978	9.8469	0.5386	-0.339
F	-9.7286	1.0429	-5.9191	-0.340
F	11.4077	0.5038	-1.5008	-0.343
F	1.9581	10.9632	2.8049	-0.338
F	-3.3023	-7.2964	8.1866	-0.340
F	-11.4297	-0.6899	1.4277	-0.342
F	0.0592	-3.5906	-11.0096	-0.341
F	-6.7986	-1.4809	-9.2613	-0.341
F	7.2947	1.4377	8.8999	-0.341
F	9.8767	-1.3242	5.8055	-0.341
F	-1.7044	-11.2048	-2.5729	-0.340
F	9.5575	-6.5106	-0.7935	-0.341
F	-9.8239	6.2069	0.5672	-0.340
F	5.5961	-10.1606	-0.6087	-0.341
F	0.1196	3.5473	11.0719	-0.342
F	-0.4970	10.7616	-4.4209	-0.341
F	-0.0002	-10.5000	5.0863	-0.340
F	4.0991	8.5274	6.8135	-0.340
C	3.6649	-7.6385	8.4427	-0.305
C	2.3231	-7.8009	8.8120	0.387
C	-7.2454	8.0420	5.3502	0.387
C	-2.5365	7.6007	-8.9733	0.385
C	-7.6102	-9.3348	-1.0262	-0.300
C	-3.8806	7.2397	-8.8105	-0.302
C	5.6233	-4.9659	-9.5068	0.386
C	5.6938	-6.1494	-8.7601	-0.301
C	-7.2113	-9.4617	-2.3633	0.386
C	7.2622	9.4902	2.1348	0.386
C	-7.0609	7.4263	6.5944	-0.303
C	8.3404	8.7813	1.5896	-0.303
H	4.3973	-8.4219	8.6968	0.225
H	-8.1136	-10.1788	-0.5273	0.226
H	-4.6684	7.8511	-9.2798	0.225
H	5.9598	-7.0937	-9.2624	0.225
F	1.9521	-8.9230	9.4831	-0.342

F	-8.0643	9.1239	5.2615	-0.343
H	-7.5803	7.8252	7.4810	0.223
H	9.3548	9.2095	1.6408	0.224
F	-2.2283	8.6986	-9.7128	-0.343
F	5.8937	-5.0028	-10.8385	-0.343
F	-7.4595	-10.6239	-3.0233	-0.342
F	7.4867	10.6992	2.7154	-0.344



**Table S3. Ag<sub>32</sub>Au<sub>12</sub>(FTP)<sub>30</sub><sup>4-</sup> M isomer: all Au atoms in the outer shell**

Ag	-0.0958	-2.8535	-0.2800	-0.149
Ag	0.3778	-1.5968	2.3620	-0.192
Ag	2.3699	-1.3614	0.2924	-0.159
Ag	0.1097	2.7141	0.1736	-0.145
Ag	-0.3692	1.3595	-2.3162	-0.144
Ag	-2.3707	1.2477	-0.2286	-0.150
Ag	-1.7664	-1.1087	-1.8540	-0.141
Ag	-2.1868	-1.3208	1.0311	-0.181
Ag	-3.7950	0.7986	2.2823	0.513
Ag	-0.9368	1.0044	2.3048	-0.159
Ag	-4.4954	-0.7168	-0.7146	0.450
Ag	4.5209	0.5487	0.7726	0.428
Ag	2.3832	-3.5645	-1.4781	0.226
Ag	2.2841	1.2023	-1.0329	-0.111
Ag	-2.2148	3.5372	1.6810	0.446
Ag	-0.6105	-0.5966	-4.4991	0.474
Ag	0.6972	3.3687	2.9725	0.509
Ag	1.9910	1.0085	-3.8340	0.214
Ag	1.8570	0.9893	1.8197	-0.189
Ag	-3.1736	1.2184	-3.0305	0.518
Ag	-2.1202	-1.1004	3.8851	0.404
Ag	1.3675	3.6174	-2.3736	0.464
Ag	-2.8860	-3.5062	-0.6714	0.350
Ag	1.1101	-1.1646	-2.2615	-0.154
Ag	-1.9588	3.6699	-1.6764	0.350
Ag	4.0171	-0.9248	-2.0410	0.485
Ag	2.8034	3.4835	0.6092	0.374
Au	-2.0240	-0.1939	6.8159	0.237
Au	0.1814	-2.5208	5.5296	0.297
Ag	3.2677	-1.2848	2.9864	0.518
Ag	-1.4545	-3.9589	1.9476	0.488
Ag	-0.3927	-3.4645	-3.0973	0.470
Ag	0.9592	0.2870	4.4719	0.466
Ag	1.8791	-3.9776	1.5689	0.482
Au	5.6664	4.0706	-0.3082	0.274
Au	1.7830	-6.5093	-1.1278	0.279
Au	-5.4453	-3.2928	-2.4377	0.316
Au	-1.8523	6.2640	0.2886	0.370
Au	5.2250	2.8823	2.6062	0.369
Au	2.4762	-0.3883	-6.2933	0.287
Au	0.9773	2.3795	-6.3357	0.271
Au	-4.4778	5.2977	-0.8917	0.274
Au	-5.8115	-4.0080	0.4528	0.285
Au	4.5973	-5.2387	-0.6666	0.274
S	0.0558	2.4756	5.3285	-0.412
S	-4.6569	3.6179	-2.5729	-0.252

S	5.9072	0.7540	-1.3369	-0.417
S	-4.0354	-4.9380	1.7252	-0.257
S	3.7993	4.7986	-1.6171	-0.300
S	-4.7046	3.2044	1.9154	-0.406
S	5.3881	-3.3355	-1.8330	-0.250
S	-5.5162	-1.0414	1.5873	-0.407
S	-3.3427	-4.1674	-3.2381	-0.312
S	-0.6770	5.6022	2.4584	-0.388
S	5.2474	0.5046	3.3598	-0.356
S	-1.9280	1.4043	-5.3510	-0.433
S	0.2129	-5.9121	1.5139	-0.432
S	-0.4366	5.8012	-1.7307	-0.370
S	4.2095	-0.9370	-4.7708	-0.257
S	-4.2882	7.1386	0.6433	-0.220
S	-5.2033	-0.4430	-3.1439	-0.422
S	0.1081	-6.0608	-2.7459	-0.231
S	2.3892	-1.6153	5.6239	-0.325
S	3.6216	-7.1780	0.3649	-0.148
S	-7.5282	-3.2568	-1.1063	-0.183
S	-3.5701	0.6981	5.2086	-0.275
S	7.4960	3.4616	1.0925	-0.206
S	-1.7582	-3.6200	4.6877	-0.316
S	1.0712	4.2947	-4.9469	-0.225
S	4.3047	-3.5479	2.1580	-0.423
S	3.3453	4.4165	3.0223	-0.351
S	0.3914	-2.7157	-5.5085	-0.421
S	-0.5324	-1.0139	8.4602	-0.220
S	0.9246	0.5174	-7.9122	-0.153
F	3.3633	4.1918	9.9832	-0.344
F	1.6615	-8.5829	-7.9166	-0.342
F	-2.7710	-4.3535	-10.2910	-0.343
F	5.9039	-12.1671	-1.9668	-0.339
C	-1.2967	6.4477	3.9154	-0.162
F	-5.5291	-5.8008	8.7405	-0.340
C	0.6261	2.7797	8.0119	-0.203
H	-0.3314	2.2569	8.1643	0.247
F	-6.0398	6.6107	-7.5454	-0.340
C	1.7516	-7.6769	-4.3739	-0.219
H	2.3409	-7.8978	-3.4680	0.236
F	4.7146	10.1822	3.5772	-0.341
C	0.6588	-6.7840	-4.2878	-0.163
F	-6.7811	5.4661	7.0243	-0.343
C	-6.7638	0.4136	-3.3412	-0.153
C	-0.5961	-3.1977	-6.9191	-0.156
C	-5.0237	4.5667	-4.0552	-0.164
C	-2.9495	0.9362	-6.7474	-0.157
C	4.9970	-4.5286	-4.3706	-0.189
H	3.9193	-4.5580	-4.1434	0.243
C	5.9009	-3.9957	-3.4250	-0.166
C	7.7201	-1.1002	-0.2156	-0.200

H	6.9058	-1.4336	0.4463	0.245
F	7.2801	-5.4407	-7.0748	-0.339
C	-3.6965	-5.9226	-3.4323	-0.165
C	-5.2689	3.8621	3.4795	-0.160
C	7.4814	-0.0741	-1.1601	-0.157
F	1.0114	-10.0000	5.7782	-0.342
C	2.0905	-8.2845	-5.5935	-0.298
H	2.9397	-8.9829	-5.6636	0.230
F	4.0639	2.1949	-12.6991	-0.339
F	-8.8941	-1.3602	6.9261	-0.342
C	-4.4003	4.2427	4.5286	-0.200
H	-3.3128	4.1123	4.4123	0.244
C	1.3837	3.1853	9.1209	-0.293
H	1.0353	2.9942	10.1481	0.233
C	3.7812	6.1536	3.0806	-0.157
C	-7.1297	-0.2766	1.7192	-0.155
C	6.8631	-0.2462	3.5672	-0.157
C	-0.6956	-3.7001	-9.3205	-0.298
H	-0.2121	-3.7833	-10.3073	0.227
C	-0.9494	6.9548	-3.0047	-0.165
C	-5.1549	0.0079	5.7151	-0.160
F	11.2525	-1.8379	-0.8308	-0.345
C	4.0625	-9.8820	0.2087	-0.210
H	3.4354	-9.9087	1.1146	0.241
C	8.9862	-1.6972	-0.1029	-0.293
H	9.1752	-2.4875	0.6397	0.237
C	6.8271	-4.9629	-5.8886	0.397
C	1.0911	3.0061	6.6930	-0.168
F	-10.9172	1.4045	2.1923	-0.344
C	4.8606	-4.6692	3.4360	-0.157
C	0.4718	-7.1010	2.8246	-0.160
C	2.6141	3.8202	8.9098	0.384
F	-4.4195	-9.9746	-4.0512	-0.338
C	-5.8948	5.6814	-4.0135	-0.210
H	-6.3050	6.0122	-3.0456	0.242
C	8.5478	0.3292	-2.0008	-0.209
H	8.3739	1.1239	-2.7431	0.237
C	8.3584	4.9491	1.5674	-0.177
C	4.4089	8.8698	3.4053	0.394
C	2.9847	-1.2521	7.2801	-0.149
C	4.3266	-8.6408	-0.4137	-0.169
C	-1.9777	-3.4891	-6.8245	-0.218
H	-2.4851	-3.4079	-5.8487	0.246
C	-0.0771	-6.5008	-5.4627	-0.202
H	-0.9236	-5.7976	-5.4232	0.244
C	-7.5056	0.8694	0.9813	-0.208
H	-6.7886	1.3333	0.2861	0.250
C	-6.6633	4.0279	3.6644	-0.209
H	-7.3525	3.7233	2.8609	0.238
C	-4.9149	-5.4802	6.4648	-0.298

H	-5.8054	-6.0446	6.1460	0.234
C	-6.2352	6.3731	-5.1856	-0.294
H	-6.9044	7.2476	-5.1570	0.232
C	7.2759	-3.9397	-3.7444	-0.211
H	7.9820	-3.5123	-3.0151	0.247
C	7.7444	-4.4236	-4.9777	-0.306
H	8.8148	-4.3914	-5.2367	0.230
F	-5.2854	-0.0140	-10.0713	-0.342
C	-6.2868	4.9420	5.8714	0.386
C	1.3358	-7.9923	-6.7366	0.391
C	-4.9037	4.7842	5.7224	-0.289
H	-4.2256	5.0824	6.5366	0.241
C	2.7576	7.1051	3.2995	-0.207
H	1.7055	6.7787	3.3308	0.243
C	0.2560	-7.1027	-6.6856	-0.286
H	-0.3124	-6.8729	-7.5999	0.239
C	0.0315	-3.3117	-8.1837	-0.211
H	1.1073	-3.0909	-8.2712	0.238
F	-3.4642	-2.3797	13.4737	-0.348
C	5.4568	-5.0196	-5.6023	-0.286
H	4.7570	-5.4366	-6.3426	0.243
C	-2.8207	1.6643	-7.9553	-0.223
H	-2.0883	2.4858	-8.0118	0.238
C	-5.4100	-1.3762	5.8167	-0.196
H	-4.6161	-2.1017	5.5795	0.241
C	-8.7809	1.4372	1.1376	-0.300
H	-9.0771	2.3292	0.5632	0.238
C	-8.0625	-0.8377	2.6240	-0.206
H	-7.7747	-1.7221	3.2141	0.240
C	1.2596	1.3327	-10.5195	-0.212
H	0.1628	1.2332	-10.5639	0.240
C	-1.4787	-1.3937	9.9151	-0.181
C	-4.0210	-4.9483	5.5223	-0.215
H	-4.2133	-5.0803	4.4440	0.248
C	5.5712	0.1374	-5.2460	-0.163
C	-2.6475	-4.0439	7.3283	-0.214
H	-1.7717	-3.4650	7.6670	0.249
C	-4.5035	4.1585	-5.3044	-0.218
H	-3.8043	3.3066	-5.3548	0.247
C	-7.1756	4.5685	4.8545	-0.306
H	-8.2597	4.7009	5.0018	0.227
C	3.1217	-2.2964	8.2205	-0.200
H	2.7823	-3.3111	7.9599	0.237
C	3.4177	0.0468	7.6188	-0.188
H	3.3017	0.8711	6.8972	0.249
C	0.4852	-6.7442	4.1941	-0.205
H	0.3343	-5.6913	4.4823	0.246
C	5.4386	7.9502	3.1732	-0.289
H	6.4826	8.2967	3.1201	0.234
F	-2.2016	9.7557	-5.8195	-0.340

C	3.3677	1.8323	-11.5923	0.396
C	4.5902	-11.0736	-0.3128	-0.294
H	4.3884	-12.0462	0.1635	0.230
C	-6.0300	10.5879	-0.6527	-0.300
H	-6.8424	11.2544	-0.3204	0.225
C	-5.3261	10.8869	-1.8250	0.392
C	-4.2898	10.0640	-2.2837	-0.285
H	-3.7546	10.3201	-3.2114	0.238
C	-3.9504	8.9168	-1.5503	-0.199
H	-3.1352	8.2660	-1.9049	0.246
C	-4.6488	8.5817	-0.3691	-0.167
C	-5.6881	9.4337	0.0711	-0.218
H	-6.2409	9.1790	0.9903	0.234
C	-2.0617	-3.9799	-9.1934	0.390
C	5.1213	6.5921	3.0099	-0.210
H	5.9241	5.8587	2.8317	0.240
C	9.8160	-0.2636	-1.8964	-0.304
H	10.6506	0.0534	-2.5424	0.225
C	-2.8780	-4.2315	5.9482	-0.163
C	-6.6686	-1.8415	6.2297	-0.292
H	-6.8709	-2.9203	6.3189	0.238
C	-3.3648	-6.8685	-2.4379	-0.191
H	-2.9164	-6.5327	-1.4899	0.248
C	-6.1902	0.9219	6.0120	-0.200
H	-6.0041	2.0037	5.9218	0.243
C	-1.4413	-2.2907	12.2092	-0.303
H	-0.8954	-2.7298	13.0604	0.223
C	5.3896	-11.0177	-1.4610	0.396
C	1.9316	1.0633	-9.3061	-0.169
C	-7.6744	-0.9135	6.5272	0.396
C	-7.4535	0.4641	6.4188	-0.291
H	-8.2673	1.1697	6.6479	0.232
C	0.6651	-7.7166	5.1905	-0.290
H	0.6657	-7.4433	6.2575	0.235
C	-1.7717	8.8322	-4.9206	0.393
C	-5.7102	5.9410	-6.4109	0.390
C	2.3339	3.6564	6.5119	-0.220
H	2.7141	3.8404	5.4929	0.246
C	3.3380	1.1876	-9.2617	-0.209
H	3.8711	0.9747	-8.3197	0.249
F	4.6791	-0.5170	11.0023	-0.340
C	-3.5430	-4.5736	8.2725	-0.286
H	-3.3804	-4.4220	9.3509	0.241
C	1.9738	1.7194	-11.6654	-0.296
H	1.4598	1.9295	-12.6170	0.230
C	-2.7103	-3.8807	-7.9564	-0.294
H	-3.7874	-4.1015	-7.8890	0.230
C	-3.6052	-8.2365	-2.6431	-0.281
H	-3.3491	-8.9775	-1.8708	0.243
C	4.1210	-0.7524	9.7879	0.402

C	5.1392	-8.6135	-1.5682	-0.210
H	5.3531	-7.6480	-2.0564	0.247
C	3.0985	4.0632	7.6190	-0.298
H	4.0696	4.5652	7.4830	0.235
C	-4.6634	-5.2869	7.8297	0.394
C	-4.1806	-8.6547	-3.8487	0.400
C	10.0208	-1.2701	-0.9436	0.385
C	-2.8191	-2.0576	12.3172	0.375
C	3.0697	8.4635	3.4654	-0.294
H	2.2786	9.2091	3.6436	0.235
C	4.0592	1.5735	-10.4020	-0.289
H	5.1559	1.6705	-10.3749	0.237
C	0.6423	-8.4646	2.4806	-0.219
H	0.6227	-8.7549	1.4182	0.239
C	-3.6067	1.3491	-9.0764	-0.302
H	-3.5094	1.9080	-10.0212	0.226
C	5.6716	-9.8009	-2.0954	-0.291
H	6.3060	-9.7897	-2.9958	0.235
C	-0.7808	-1.9580	11.0174	-0.222
H	0.3034	-2.1368	10.9264	0.232
C	4.0924	-4.9933	4.5781	-0.203
H	3.1006	-4.5340	4.7123	0.244
C	-3.8928	-0.1162	-6.6897	-0.205
H	-4.0229	-0.6793	-5.7519	0.250
C	-4.8483	4.8408	-6.4841	-0.292
H	-4.4450	4.5207	-7.4575	0.240
C	-9.3380	-0.2756	2.7873	-0.298
H	-10.0628	-0.7025	3.4986	0.229
C	-3.5399	-1.4990	11.2552	-0.296
H	-4.6229	-1.3266	11.3634	0.231
C	-2.8724	-1.1716	10.0634	-0.225
H	-3.4384	-0.7388	9.2219	0.243
C	-2.2729	7.5269	-4.9839	-0.281
H	-2.9953	7.2506	-5.7674	0.242
C	-0.4386	8.2742	-2.9834	-0.216
H	0.2769	8.5646	-2.1974	0.241
C	0.8281	-9.4427	3.4716	-0.306
H	0.9624	-10.5052	3.2116	0.227
C	-9.6820	0.8568	2.0386	0.391
C	7.9128	0.3093	-5.9381	-0.297
H	8.8773	-0.1550	-6.1982	0.230
C	3.6890	-2.0493	9.4796	-0.298
H	3.8055	-2.8524	10.2249	0.228
C	3.9912	0.3004	8.8753	-0.283
H	4.3225	1.3124	9.1543	0.239
C	-1.8534	6.5895	-4.0270	-0.191
H	-2.2511	5.5634	-4.0628	0.243
C	-4.2708	-6.3745	-4.6429	-0.215
H	-4.5261	-5.6437	-5.4264	0.236
C	-4.6837	-0.4345	-7.8049	-0.288

H	-5.4216	-1.2509	-7.7619	0.235
C	-0.8501	9.2178	-3.9382	-0.300
H	-0.4715	10.2523	-3.9215	0.231
C	0.8381	-9.0554	4.8177	0.392
C	-4.5277	0.2980	-8.9879	0.394
C	3.5721	7.4770	-5.3873	-0.290
H	3.7556	8.4318	-4.8706	0.236
C	4.2998	7.1559	-6.5396	0.390
C	4.0982	5.9443	-7.2113	-0.296
H	4.6885	5.7151	-8.1127	0.231
C	3.1410	5.0408	-6.7223	-0.220
H	2.9695	4.0861	-7.2473	0.237
C	2.3827	5.3416	-5.5672	-0.165
C	2.6199	6.5685	-4.9025	-0.203
H	2.0408	6.8208	-3.9997	0.244
F	-2.4404	8.6146	7.2860	-0.341
F	-10.4257	2.2875	-4.0308	-0.343
C	-0.6741	6.2159	5.1651	-0.210
H	0.1172	5.4542	5.2512	0.244
C	-2.3344	7.4037	3.8371	-0.208
H	-2.8480	7.5732	2.8768	0.242
F	6.3201	-7.3341	6.2966	-0.343
C	-1.0586	6.9418	6.3042	-0.292
H	-0.5741	6.7653	7.2770	0.239
C	-2.0746	7.8985	6.1914	0.392
C	2.7996	7.1805	-0.4971	-0.195
H	2.0309	6.5632	-0.0085	0.252
C	8.0503	0.3515	3.0920	-0.210
H	7.9976	1.2890	2.5148	0.245
F	-4.3474	-10.8856	1.5413	-0.341
C	-2.7240	8.1310	4.9723	-0.292
H	-3.5341	8.8754	4.9186	0.230
C	-7.8622	0.1891	-2.4809	-0.206
H	-7.7551	-0.4895	-1.6214	0.243
C	-6.9313	1.2918	-4.4386	-0.206
H	-6.0851	1.4798	-5.1182	0.242
C	-8.1617	1.9236	-4.6763	-0.292
H	-8.2923	2.6137	-5.5245	0.233
C	4.7636	7.3863	-1.9221	-0.215
H	5.5301	6.9176	-2.5594	0.243
C	-9.2319	1.6772	-3.8074	0.394
C	9.2966	-0.2465	3.3378	-0.293
H	10.2273	0.2064	2.9611	0.232
C	-9.0969	0.8166	-2.7119	-0.294
H	-9.9529	0.6449	-2.0405	0.234
C	8.1366	6.2181	0.9797	-0.221
H	7.3446	6.3274	0.2204	0.244
C	6.1372	-5.2642	3.2889	-0.214
H	6.7445	-5.0201	2.4028	0.239
F	5.2181	8.0367	-7.0162	-0.342

C	6.9449	-1.4638	4.2827	-0.206
H	6.0249	-1.9448	4.6527	0.245
C	5.8456	-6.4632	5.3672	0.391
C	4.5805	-5.8890	5.5430	-0.291
H	3.9825	-6.1495	6.4303	0.232
C	6.6331	-6.1596	4.2500	-0.300
H	7.6226	-6.6310	4.1370	0.227
C	5.4793	1.5471	-5.2605	-0.193
H	4.5323	2.0376	-4.9812	0.235
C	3.7862	6.5742	-1.3028	-0.159
C	-4.5200	-7.7399	-4.8544	-0.300
H	-4.9649	-8.1036	-5.7943	0.229
F	10.6598	8.2583	2.6746	-0.343
F	10.5578	-2.0263	4.2925	-0.342
F	8.8563	2.4578	-6.3173	-0.339
C	9.9068	7.1838	2.3191	0.386
C	2.7887	8.5732	-0.3097	-0.289
H	2.0287	9.0516	0.3267	0.244
C	4.7634	8.7775	-1.7341	-0.303
H	5.5233	9.4206	-2.2060	0.230
C	8.9044	7.3333	1.3531	-0.297
H	8.7305	8.3207	0.8964	0.234
C	7.7865	1.7034	-5.9608	0.397
C	6.5823	2.3350	-5.6237	-0.287
H	6.5148	3.4337	-5.6338	0.243
C	9.3732	4.8366	2.5521	-0.213
H	9.5559	3.8597	3.0286	0.235
C	8.1880	-2.0681	4.5279	-0.293
H	8.2564	-3.0185	5.0794	0.237
C	6.8013	-0.4711	-5.5806	-0.204
H	6.8864	-1.5692	-5.5573	0.241
C	9.3511	-1.4479	4.0548	0.391
C	10.1477	5.9444	2.9268	-0.298
H	10.9361	5.8573	3.6917	0.228
C	-8.7218	-6.8950	-2.6684	-0.289
H	-8.3261	-7.7039	-3.3024	0.237
C	-7.9346	-5.7791	-2.3448	-0.207
H	-6.9025	-5.7030	-2.7272	0.248
C	-8.4477	-4.7469	-1.5281	-0.167
C	-9.7710	-4.8534	-1.0433	-0.212
H	-10.1784	-4.0532	-0.4043	0.239
C	-10.5672	-5.9642	-1.3665	-0.297
H	-11.6004	-6.0560	-0.9948	0.229
C	-10.0316	-6.9719	-2.1783	0.395
F	3.7701	10.6971	-0.7451	-0.337
F	-5.6573	11.9987	-2.5322	-0.342
F	-10.7998	-8.0442	-2.4988	-0.340
C	3.7716	9.3538	-0.9285	0.403
C	-4.2758	-9.5289	1.5544	0.390
C	-5.2588	-8.7849	0.8898	-0.297



H	-6.0732	-9.3045	0.3606	0.232
C	-5.1846	-7.3828	0.9044	-0.219
H	-5.9498	-6.7858	0.3808	0.240
C	-4.1376	-6.7210	1.5859	-0.168
C	-3.1553	-7.4996	2.2434	-0.204
H	-2.3245	-7.0048	2.7701	0.246
C	-3.2220	-8.9013	2.2302	-0.288
H	-2.4545	-9.5050	2.7387	0.240

**Table S4. Ag<sub>32</sub>Au<sub>12</sub>(FTP)<sub>30</sub><sup>4-</sup> S isomer: Au atoms statistically distributed**

Au	-0.0736	0.3640	-2.7385	-0.284
Ag	1.2105	2.2678	-0.9226	-0.069
Ag	-1.7047	1.9354	-0.9093	-0.053
Au	2.4095	-0.3432	-1.3204	-0.300
Ag	-2.2384	-0.9497	-1.3415	-0.009
Ag	0.2952	-2.3174	-1.5746	-0.036
Au	-2.3345	0.1878	1.3461	-0.303
Ag	-0.2517	2.2450	1.6038	-0.127
Ag	-1.0918	-2.3918	1.0006	-0.091
Au	2.3157	0.8293	1.3259	-0.343
Ag	1.7667	-2.0510	0.9552	-0.123
Ag	0.1409	-0.3831	2.7210	-0.122
Au	-0.3581	3.2230	-3.0851	0.122
Ag	-2.8377	1.0170	-3.4612	0.483
Ag	2.4928	1.6247	-3.4809	0.576
Au	1.7668	-1.5809	-3.8900	0.149
Ag	-1.4388	-1.8929	-3.9729	0.548
Ag	-0.5035	4.4675	-0.2309	0.504
Au	-2.1023	-3.7670	-1.2555	0.110
Ag	-3.1190	2.9978	1.3530	0.414
Ag	4.1517	1.9107	-0.7025	0.440
Au	-4.3219	0.8516	-0.6115	0.237
Ag	2.1630	3.7717	1.3080	0.410
Ag	-4.0704	-2.1479	0.7556	0.469
Ag	3.0892	-3.1548	-1.3858	0.430
Ag	-1.7708	1.4459	3.9516	0.417
Ag	-2.2832	-1.6581	3.5606	0.526
Ag	4.5196	-1.0293	0.5677	0.564
Ag	2.8824	-1.0738	3.4576	0.436
Ag	0.6292	-4.6157	0.1569	0.523
Ag	0.4050	-3.1702	3.3015	0.373
Ag	1.5548	1.8801	3.9252	0.518
S	0.9108	2.7927	-5.4713	-0.252
S	4.1077	3.4639	-2.7057	-0.408
S	-2.1868	-0.0763	-5.6832	-0.420
S	5.5283	-2.2679	-1.6368	-0.423
S	-4.8632	2.5019	-2.8166	-0.410
S	-3.9137	-3.6459	2.8626	-0.447
S	-2.0474	5.3438	1.7964	-0.434
S	3.7673	-0.2636	-4.9042	-0.369
S	2.2124	-5.5625	-1.8260	-0.442
S	1.8034	6.1032	-0.1249	-0.291
S	-5.8141	-1.2465	-0.8874	-0.361
S	-3.8548	0.1501	4.7637	-0.428
S	-3.7122	-3.7434	-3.4272	-0.262
S	-0.3852	3.3554	5.0765	-0.435

S	-5.6318	2.2569	1.5826	-0.365
S	0.3745	-3.5841	-5.0266	-0.361
S	6.0361	1.1354	0.9632	-0.428
S	-0.8501	-2.6552	5.7195	-0.282
S	-1.7430	-6.0724	0.0294	-0.382
S	2.3086	0.0492	5.6767	-0.421
S	-1.8074	5.4133	-2.4269	-0.357
S	4.9103	-2.5547	2.7425	-0.446
S	3.6702	3.6866	3.4244	-0.424
S	1.6245	-5.4052	2.5924	-0.428
Au	-1.3668	3.1860	-6.0959	0.266
Ag	4.7323	-2.5099	-4.0951	0.552
Ag	-3.2728	4.1065	-4.0216	0.565
Au	4.1620	5.7100	-0.1320	0.272
Ag	-2.5622	4.4485	4.1468	0.551
Ag	2.5846	-4.5872	-4.2122	0.552
Ag	-3.9800	-5.3049	0.8926	0.568
Au	-5.2180	-4.3631	-1.6531	0.272
Ag	5.3866	3.5392	1.5589	0.567
Ag	-4.8053	2.4747	3.9524	0.548
Ag	3.3147	-4.1309	3.9679	0.569
Au	1.4640	-3.1405	6.1341	0.269
H	1.4251	-0.5938	-6.7179	0.249
H	-1.5667	-5.7246	-3.9257	0.253
H	6.1956	1.3342	-3.0253	0.245
H	-4.5858	5.4694	0.2548	0.244
H	-6.2434	-1.7951	2.8635	0.248
H	-1.7551	0.5441	6.8542	0.246
H	-5.8976	-0.0819	-3.8208	0.249
H	0.8870	6.4218	2.6874	0.253
H	5.6978	-0.0913	4.1955	0.247
H	5.9428	-4.1550	0.6065	0.247
H	3.0244	-6.7230	0.7420	0.244
H	-6.5046	3.5027	-0.9168	0.246
H	-4.2602	-2.2164	-5.4850	0.239
H	-1.0903	-5.4881	4.7721	0.243
H	1.8730	4.8094	5.4139	0.243
H	1.1651	5.5491	-4.3519	0.245
H	4.2537	2.3005	5.5170	0.243
H	-0.4797	-7.3241	1.9459	0.247
C	1.7939	4.2699	-5.9996	-0.162
C	5.6096	3.3345	-3.6691	-0.158
C	3.5451	-0.0822	-6.6731	-0.165
C	-5.4565	-3.6121	3.7768	-0.151
C	-3.6420	-5.2576	-4.4005	-0.162
C	-3.1351	6.6928	1.3290	-0.161
C	-3.8490	0.0147	6.5511	-0.155
C	-6.2654	2.0667	-3.8449	-0.156
H	-0.5203	7.7112	-1.2244	0.242
C	-3.6080	-0.5143	-6.6846	-0.163

C	6.7088	-3.5889	-1.3553	-0.156
C	1.6854	7.5210	0.9820	-0.163
C	2.3002	-0.2814	-7.3104	-0.193
C	7.6277	0.9730	0.1527	-0.155
C	-7.4274	-0.9809	-0.1541	-0.159
C	-1.6954	-4.1135	6.3534	-0.162
C	0.3478	-3.5515	-6.8187	-0.164
C	3.3875	-6.8537	-1.4068	-0.155
H	0.3016	-7.5227	-1.4328	0.245
H	-1.6939	-2.7866	-6.9179	0.242
H	-7.5325	1.1214	-0.7157	0.240
H	7.7558	-1.1529	0.6237	0.243
C	-2.4593	-6.0208	-4.4978	-0.194
H	1.6575	2.5074	6.9717	0.243
C	-0.3694	3.3102	6.8749	-0.160
C	3.7547	0.4955	6.6394	-0.165
C	-1.8450	-7.5042	-1.0398	-0.162
C	-6.7705	3.5986	1.2486	-0.163
C	6.4539	2.2002	-3.6553	-0.203
C	6.3339	-2.1272	3.7474	-0.153
C	-1.2214	6.9443	-3.1415	-0.164
C	3.6956	5.2502	4.2992	-0.158
C	1.0672	-6.8947	3.4241	-0.162
C	-6.4193	-2.5944	3.6010	-0.196
C	-2.6986	0.2461	7.3374	-0.196
C	-4.3052	6.4888	0.5646	-0.196
C	-6.5603	0.7238	-4.1719	-0.195
C	1.1894	7.4064	2.2981	-0.196
C	1.7674	5.4778	-5.2718	-0.191
C	6.4848	-0.8494	4.3292	-0.192
C	6.7056	-4.3505	-0.1646	-0.207
C	-4.4443	-1.6171	-6.3920	-0.217
C	3.5598	-7.2562	-0.0622	-0.207
C	-1.6620	-5.3669	5.7059	-0.192
C	-7.0572	3.9746	-0.0861	-0.226
C	4.5128	1.6615	6.3782	-0.220
C	2.7011	5.5219	5.2683	-0.207
C	0.0234	-7.6691	2.8653	-0.208
C	8.2628	-0.2911	0.1612	-0.201
C	-8.0635	0.2789	-0.2472	-0.199
C	-0.8273	-3.1467	-7.4940	-0.200
C	-0.6383	7.9203	-2.2987	-0.198
C	-0.6592	-8.0372	-1.5983	-0.204
C	0.7991	2.8845	7.5493	-0.207
S	-3.6184	3.8282	-6.6240	-0.238
H	2.6338	3.2293	-7.7184	0.244
S	4.9834	-4.8283	-5.0771	-0.385
C	2.5929	4.1785	-7.1610	-0.203
H	7.8054	3.0536	-0.4792	0.244
S	6.5212	5.3785	0.0041	-0.243

H	-7.6585	-3.0451	0.5224	0.242
S	-6.4881	-5.4317	0.0930	-0.256
S	-4.5615	4.2928	5.7074	-0.388
H	2.3811	-4.2949	-7.0693	0.235
S	3.7175	-3.8545	6.5611	-0.243
H	-2.4000	4.0753	7.1370	0.244
H	-4.0055	-7.7452	-0.8721	0.235
C	8.2898	2.0644	-0.4515	-0.213
H	-4.9216	6.3676	3.5483	0.243
C	-8.1282	-2.0507	0.4505	-0.213
C	1.4533	-3.9908	-7.5809	-0.205
C	-1.4716	3.7559	7.6395	-0.210
C	-3.0725	-8.1578	-1.2915	-0.209
H	-1.8275	6.4884	-5.1858	0.238
C	5.9657	4.4334	-4.4879	-0.207
C	-5.6941	-4.6210	4.7387	-0.205
C	-1.3745	7.2385	-4.5161	-0.209
C	4.6535	0.3346	-7.4476	-0.218
C	-3.8764	0.2430	-7.8514	-0.206
C	-2.7906	8.0101	1.7130	-0.210
C	-5.0477	-0.3752	7.1942	-0.206
C	-2.4463	-3.9701	7.5416	-0.201
H	-3.2417	1.1116	-8.0879	0.242
C	7.7029	-3.8499	-2.3271	-0.208
C	-7.1367	3.0858	-4.2971	-0.219
C	-4.7784	-5.6483	-5.1457	-0.221
C	4.1198	-0.3112	7.7450	-0.206
H	5.4128	7.9078	1.1968	0.246
H	-2.4918	-2.9879	8.0385	0.245
H	3.5495	-1.2298	7.9551	0.242
H	7.7125	-3.2673	-3.2618	0.238
C	4.0942	-7.5408	-2.4202	-0.210
H	-4.9384	-5.4066	4.8975	0.239
C	2.0664	8.7944	0.4990	-0.220
C	-7.4691	4.2420	2.2969	-0.210
H	-1.3508	5.4363	-7.7681	0.245
H	4.9186	-2.5754	-7.0583	0.240
H	5.3130	5.3203	-4.5109	0.238
H	-1.8733	8.1811	2.2987	0.239
H	-5.9455	-0.5728	6.5873	0.240
H	3.9943	-7.2167	-3.4689	0.239
H	-6.9128	4.1367	-4.0515	0.232
C	1.6844	-7.3427	4.6149	-0.212
C	7.3543	-3.0879	3.9342	-0.213
H	5.6223	0.5146	-6.9545	0.243
C	4.7314	6.1925	4.1063	-0.213
H	-7.2454	3.9712	3.3420	0.237
H	2.4901	-6.7426	5.0696	0.235
C	2.1650	-0.0839	-8.6937	-0.282
H	5.5096	5.9990	3.3495	0.236

H	2.4511	8.8877	-0.5293	0.241
H	-5.7035	-5.0534	-5.0761	0.237
C	-2.4116	-7.1563	-5.3228	-0.279
H	7.2487	-4.0864	3.4806	0.232
C	7.6217	2.1628	-4.4351	-0.295
H	-6.1484	-6.8430	-2.5396	0.246
H	1.4465	-5.4515	7.7110	0.247
C	-2.7441	0.1055	8.7345	-0.291
C	-5.1227	7.5714	0.2022	-0.284
C	-7.6022	-2.5892	4.3587	-0.292
C	-7.6983	0.4053	-4.9288	-0.281
C	2.5051	6.5893	-5.7107	-0.287
C	1.0864	8.5397	3.1225	-0.287
C	7.6248	-0.5365	5.0852	-0.280
H	1.1980	-0.2436	-9.1949	0.245
C	-2.3409	-6.4694	6.2505	-0.293
C	7.6704	-5.3486	0.0497	-0.290
H	-1.4942	-7.7590	-5.4028	0.243
C	4.4015	-8.3322	0.2619	-0.291
C	-5.5129	-1.9570	-7.2378	-0.296
C	-8.0268	4.9533	-0.3640	-0.299
C	5.6000	2.0148	7.1950	-0.300
H	8.2836	1.2830	-4.4202	0.238
C	2.7468	6.6965	6.0352	-0.294
C	-0.3876	-8.8649	3.4766	-0.295
H	-1.8514	0.2938	9.3505	0.242
C	9.5339	-0.4611	-0.4088	-0.291
H	-6.0402	7.4147	-0.3858	0.241
H	-8.3591	-1.8019	4.2185	0.241
C	-9.3627	0.4697	0.2480	-0.290
C	-0.9020	-3.1939	-8.8953	-0.293
C	-0.6975	-9.2039	-2.3774	-0.294
C	-0.2183	9.1560	-2.8146	-0.295
C	0.8741	2.9180	8.9515	-0.292
H	-7.9320	-0.6386	-5.1884	0.238
C	-5.6214	6.5657	4.3763	-0.207
H	0.7180	8.4558	4.1562	0.244
H	7.7394	0.4545	5.5501	0.241
C	-3.5158	5.3572	-7.5460	-0.172
H	2.4875	7.5378	-5.1523	0.242
C	3.3360	5.2843	-7.6040	-0.295
C	5.1244	-4.7369	-6.8569	-0.172
C	3.6118	-5.3754	7.4960	-0.174
C	-5.6534	5.6928	5.4890	-0.165
C	-2.3075	5.9265	-8.0146	-0.224
C	6.5010	7.8662	1.3694	-0.221
C	5.0998	-3.5252	-7.5882	-0.212
H	-2.3088	-7.4531	5.7572	0.242
H	4.5317	-8.6543	1.3071	0.235
C	-6.9928	-7.0274	-0.5399	-0.169

H	7.6677	-5.9523	0.9707	0.233
H	-8.2584	5.2426	-1.4015	0.233
C	7.2312	6.7430	0.9149	-0.171
H	-6.1628	-2.8177	-7.0140	0.229
C	2.4022	-5.9378	7.9675	-0.219
H	6.1866	2.9253	6.9939	0.235
C	-6.7361	-7.4789	-1.8562	-0.222
H	1.9778	6.9064	6.7953	0.237
C	9.5627	1.9018	-1.0219	-0.295
H	-1.1978	-9.4722	3.0425	0.237
C	-9.4296	-1.8687	0.9452	-0.299
C	1.3882	-4.0396	-8.9817	-0.290
C	-3.1177	-9.3242	-2.0708	-0.290
C	4.5256	0.5344	-8.8321	-0.307
C	-1.4027	3.7927	9.0412	-0.294
C	7.1309	4.4047	-5.2693	-0.299
C	-6.8733	-4.6231	5.4999	-0.298
C	-5.1021	-0.5171	8.5895	-0.300
C	-3.6002	9.0982	1.3518	-0.296
C	-4.7393	-6.7846	-5.9684	-0.299
C	3.2781	6.4778	-6.8732	0.397
C	3.2801	0.3199	-9.4385	0.393
H	10.0293	-1.4446	-0.4078	0.236
C	-3.1323	-5.0659	8.0895	-0.295
H	-9.8556	1.4525	0.1835	0.236
C	-0.9563	8.4718	-5.0399	-0.292
H	0.2315	9.9198	-2.1610	0.233
C	-4.9445	-0.0891	-8.6994	-0.295
H	0.2229	-9.6254	-2.8118	0.237
H	-1.8163	-2.8809	-9.4229	0.238
C	-8.2751	2.7748	-5.0579	-0.298
C	-3.5519	-7.5247	-6.0461	0.403
C	5.2061	0.0341	8.5637	-0.296
C	7.9461	3.2664	-5.2337	0.388
C	8.6704	-4.8451	-2.1193	-0.295
H	1.7832	2.5850	9.4758	0.238
C	-3.9468	-0.2720	9.3437	0.391
C	1.9704	9.9305	1.3179	-0.300
C	-7.8141	-3.6049	5.2986	0.394
C	4.9385	-8.6165	-2.1019	-0.294
C	-8.4358	5.2229	2.0269	-0.291
C	-4.7594	8.8635	0.6007	0.395
C	8.4993	-2.7824	4.6872	-0.299
C	1.2781	-8.5370	5.2312	-0.292
C	4.7819	7.3717	4.8679	-0.292
C	-8.5419	1.4343	-5.3635	0.398
C	10.1703	0.6409	-0.9925	0.391
C	1.4825	9.7863	2.6237	0.402
C	-3.0638	-6.3043	7.4393	0.396
C	-10.0307	-0.6086	0.8407	0.392

C	-5.7522	-1.1885	-8.3828	0.391
C	0.2071	-3.6437	-9.6226	0.394
C	8.6421	-5.5842	-0.9305	0.394
C	5.9346	1.1962	8.2797	0.390
C	8.6191	-1.5069	5.2535	0.399
C	-1.9270	-9.8362	-2.6012	0.395
C	5.0769	-9.0046	-0.7634	0.394
C	-8.7086	5.5640	0.6965	0.391
C	-0.2283	3.3775	9.6818	0.391
C	-0.3798	9.4167	-4.1812	0.393
C	0.2473	-9.2872	4.6516	0.391
C	3.7900	7.6077	5.8279	0.394
H	3.9654	5.2256	-8.5059	0.231
H	10.0814	2.7472	-1.5009	0.232
H	-9.9785	-2.7002	1.4148	0.231
H	2.2516	-4.3753	-9.5770	0.237
H	-4.0726	-9.8342	-2.2729	0.234
H	-2.2611	4.1362	9.6401	0.231
C	-6.4651	7.6868	4.3107	-0.287
C	4.8288	-6.0202	7.8320	-0.218
H	-6.4361	8.3635	3.4426	0.240
H	-1.0756	8.7021	-6.1100	0.236
H	5.3810	0.8618	-9.4446	0.230
H	-6.0323	-0.8177	9.0978	0.228
H	-7.0668	-5.4036	6.2528	0.229
H	7.4128	5.2575	-5.9073	0.227
H	-3.7207	-4.9668	9.0152	0.231
H	-3.3402	10.1275	1.6457	0.230
C	-4.7339	6.0004	-7.8806	-0.216
C	-7.7453	-7.8638	0.3219	-0.216
H	-5.1601	0.5044	-9.6023	0.228
H	5.4976	-0.5974	9.4184	0.228
C	2.4044	-7.1008	8.7541	-0.294
C	-2.3129	7.0953	-8.7934	-0.295
C	5.3433	-5.9413	-7.5729	-0.218
H	-5.6166	-7.0998	-6.5554	0.229
C	5.2938	-3.5103	-8.9793	-0.290
C	7.1433	8.9234	2.0347	-0.296
H	5.7805	-5.5950	7.4730	0.237
H	9.4424	-5.0577	-2.8757	0.229
H	-8.9576	3.5614	-5.4177	0.226
H	-8.9740	5.7299	2.8429	0.235
H	5.4960	-9.1537	-2.8856	0.228
H	2.2716	10.9267	0.9563	0.230
C	-7.2197	-8.7196	-2.3026	-0.294
C	-6.5701	5.9727	6.5331	-0.220
H	1.7534	-8.8844	6.1618	0.236
C	8.6290	6.7108	1.1482	-0.216
H	5.5879	8.1073	4.7194	0.233
H	-7.9525	-7.5300	1.3517	0.236



H	9.3017	-3.5223	4.8373	0.226
H	-5.6845	5.5702	-7.5252	0.236
H	6.5757	9.7991	2.3877	0.235
H	5.3653	-6.8949	-7.0204	0.231
H	-1.3726	7.5350	-9.1627	0.235
H	5.2667	-2.5635	-9.5414	0.240
H	1.4624	-7.5367	9.1234	0.237
F	3.1571	0.5100	-10.7765	-0.339
F	3.9937	7.5493	-7.3000	-0.339
H	-7.0214	-9.0672	-3.3288	0.236
H	9.2142	5.8429	0.8021	0.235
F	-3.5135	-8.6225	-6.8400	-0.337
F	9.0756	3.2362	-5.9906	-0.344
F	-3.9987	-0.4045	10.6951	-0.342
H	-6.6074	5.3002	7.4056	0.231
F	-8.9560	-3.6055	6.0344	-0.342
F	-5.5462	9.9139	0.2564	-0.338
F	-9.6432	1.1290	-6.0958	-0.340
F	11.4017	0.4829	-1.5454	-0.343
F	1.3991	10.8809	3.4186	-0.336
F	-3.7153	-7.3680	7.9752	-0.339
F	-11.2877	-0.4300	1.3271	-0.343
F	0.1365	-3.6983	-10.9776	-0.340
F	-6.7865	-1.5157	-9.2022	-0.343
F	6.9879	1.5323	9.0707	-0.343
F	9.7238	-1.2089	5.9835	-0.340
F	-1.9647	-10.9681	-3.3495	-0.340
F	9.5765	-6.5486	-0.7274	-0.342
F	-9.6475	6.5097	0.4320	-0.341
F	5.8809	-10.0556	-0.4552	-0.342
F	-0.1599	3.4199	11.0384	-0.342
F	0.0283	10.6115	-4.6813	-0.341
F	-0.1467	-10.4448	5.2430	-0.340
F	3.8397	8.7423	6.5721	-0.340
C	4.8392	-7.1833	8.6170	-0.298
C	3.6236	-7.7105	9.0729	0.386
C	-7.3505	7.9404	5.3655	0.386
C	-3.5339	7.7028	-9.1096	0.388
C	-8.2327	-9.1046	-0.1170	-0.298
C	-4.7476	7.1672	-8.6594	-0.297
C	5.5171	-4.7179	-9.6520	0.385
C	5.5407	-5.9377	-8.9628	-0.302
C	-7.9664	-9.5189	-1.4289	0.388
C	8.5257	8.8611	2.2484	0.387
C	-7.4162	7.0915	6.4779	-0.303
C	9.2777	7.7629	1.8116	-0.297
H	5.7832	-7.6867	8.8810	0.227
H	-8.8192	-9.7567	0.5502	0.228
H	-5.6932	7.6687	-8.9217	0.227
H	5.7132	-6.8731	-9.5194	0.225

F	3.6302	-8.8326	9.8391	-0.342
F	-8.1610	9.0310	5.3159	-0.343
H	-8.1258	7.3151	7.2911	0.224
H	10.3637	7.7390	1.9959	0.228
F	-3.5443	8.8286	-9.8701	-0.342
F	5.7139	-4.7114	-10.9970	-0.342
F	-8.4454	-10.7148	-1.8601	-0.342
F	9.1510	9.8826	2.8898	-0.342

# Lectures Delivered

1. Nanotechnologies for clean water, 9th General Body Meeting distinguished lecture, Water Quality India Association, Renaissance Hotel, Ahmedabad, January 10, 2019.
2. Atomically precise nanoparticles, Indian Association for the Cultivation of Science, Kolkata, January 16, 2019.
3. Clathrate hydrates in interstellar environment, Chemical Research Society of India, 24th NSC, CSIR-CLRI, Chennai February 8-10, 2019.
4. Water for Life – through materials, IIT Madras Technologies for Social Impact, IITM, February 16, 2019.
5. Clathrate hydrates in interstellar environment, ChemPhysMat, SAMat, JNCASR, Bengaluru, February 20-22, 2019.
6. Nanotechnologies for clean water, Centre for Environmental Studies (CES), Anna University, March 8, 2019.
7. Atomically precise nanoparticles, Frontiers in Materials from Basic Science to Real time Applications, Jain University, Bengaluru, March 14, 2019.
8. Science – A way of life, Gemini Ganesan Memorial Lecture, Madras Christian College, March 18, 2019.
9. From Materials to Clean Water: Science, Technology and Industry, National Technology Day Function, CSIR-SERC, CSIR Campus, Taramani, Chennai, May 10, 2019.
10. Materials with atomic precision, Department of Chemistry, Hanyang University, Seoul, May 16, 2019.
11. Atomically precise noble metal nanoparticles, Seoul National University, May 16, 2019.
12. Isotopic Exchange in Nanoparticles, Frontiers of Translational Materials Science,

Department of Chemistry, Hanyang University, Seoul, May 17-18, 2019.

13. From Materials to Clean Water: Science, Technology and Industry, IIT Bombay Institute Colloquium, June 6, 2019.
14. Nanomaterials, clean water and ice, UON-India Symposium at IIT Madras, June 20-21, 2019.
15. Qingdao International Academician Park, Qingdao, China, June 25 – 29, 2019.
16. Nanoparticles with atomic precision, 26th International Symposium on Metastable, Amorphous and Nanostructured Materials, Chennai, July 8-12, 2019.
17. Isotopic Exchange in Nanoparticles, 2nd ACS-CRSI Meeting, IIT Kanpur, July 18, 2019.
18. Nanoparticles with atomic precision, Saint-Gobain Research India, IIT Madras Research Park, July 23, 2019.
19. Water in crisis: Survival, sustainability and opportunities, CSIR HeadQuarters, New Delhi, August 8, 2019.
20. Atomically precise noble metal nanoparticles, 8th ChinaNANO, Beijing, August 17-19, 2019.
21. Isotopic Exchange in Nanoparticles, 2nd Asian Symposium on Nanoscience and Nanotechnology, Beijing, August 18, 2019.
22. Atomically precise noble metal nanoparticles, Tsinghua University, Beijing, August 19, 2019.
23. From small to ultra-small: Nanoparticles to clusters, Science Academies' Lecture Workshop, Ramaiah Institute of Technology, Bengaluru, August 29, 2019.
24. Nanomaterials to clean water: Science, technology and industry, Science Academies' Lecture Workshop, Ramaiah Institute of Technology, Bengaluru, August 29, 2019.

25. From materials to clean water: Science, technology and industry, Tech Fest, SRM University - AP Amaravati, September 28, 2019.
26. Isotopic Exchange in Nanoparticles, Advances in Mass Spectrometry, IISER Tirupati, November 19, 2019.
27. Nanoparticles are Molecules, ISMAS 2019, BARC, Mumbai, November 27-30, 2019.
28. From materials to clean water: Making affordable sensors for clean water, One day interactive session on sensors, ICCW, December 10, 2019.
29. Nanoparticles are Molecules, International Conference on Recent Advances in Nanoscience and Nanotechnology - ICRAN'19, Stella Maris College, Chennai, December 11-12, 2019.
30. Clathrate hydrates in interstellar environment, Emerging Frontiers in Chemical Sciences (EFCS) - 2019, Farook College, December 13-15, 2019.
31. Nanoparticles are Molecules, National Symposium on Convergence of Chemistry & Materials (CCM-2019), BITS-Pilani, Hyderabad Campus, December 17-18, 2019.
32. Nanoparticles are Molecules, National Conference on Recent Trends in Materials Science and Technology (NCMST-2019), Institute of Space Science and Technology, Thiruvananthapuram, December 18-20, 2019.
33. Nanoparticles with atomic precision, National Conference on Nanomaterials for Energy, Environment and Health Care, National Institute of Technology Calicut, December 27-28, 2019.
34. Nanoparticles with atomic precision, International Conference on Nanoscience and Photonics for Medical Applications, MAHE, December 28-30, 2019.

# Patents/Technology

## Patent Applications

### Indian

1. A compact, modular and scalable continuous-flow greywater sink for potable and non-potable uses, Thalappil Pradeep and Ankit Nagar, 201941028155, July 12, 2019.
2. Composition for sustained release of minerals and carbonate in water and a water purification device based on the same, Thalappil Pradeep; Swathy J .R.; Nalenthiran Pugazhenthiran, 201943029174, July 17, 2019.
3. Method for generating different phases of copper sulphide nanostructures using electrospray deposition (ESD) under ambient conditions, Thalappil Pradeep; Arijit Jana; Sourav Kanti Jana; Depanjan Sarkar; 201941032379, August 9, 2019.
4. Tribochemical method for degradation of polymers in water, Thalappil Pradeep. Abhijit Nag, Ananya Bakshi, Jyotirmoy Ghosh, Vishal Kumar, Soumabha Bag, Biswajit Mondal and Tripti Ahuja, TEMP/E-1/34612 /2019-CHE, 201941032757, August 13, 2019.
5. A green method for preparing robust and sustainable cellulose-polyaniline based nanocomposite for effective removal of fluoride from water and a purifier thereof, Thalappil Pradeep; Sritama Mukherjee; Haritha Ramireddy, 201941046691, November 15, 2019.
6. A method for facile, rapid and industrially scalable preparation of metal hydroxide composition, Hydromaterials Private Limited & Indian Institute of Technology Madras (IIT Madras), 201941054546, December 30, 2019.

### PCT

1. A modified surface for condensation, T Pradeep; Ankit nagar; Ramesh Kumar, PCT/IN2019/50078, February 2, 2019.
2. An enhanced carbon dioxide sorbent nanofiber membrane and a device thereof, Thalappil Pradeep; Anagha Yatheendran; Ramesh Kumar; Arun Karthik S, PCT/IN2019/050555, July 30, 2019.

## **Patents Granted**

### **Indian**

1. Anti-gravity water filter cartridge, Design patent number 260460, filed on February 19, 2014, Issued October 18, 2019.
2. Water purification cartridge attached to container, Design patent application, TEMP/D-1/5729/2016-KOL, October 18, 2016 Patent number 287785, Issued June 21, 2019.
3. Composition for sustained release of carbonate and a water purification device based on the same with enhanced biocidal activity, 7026/CHE/2015, December 29, 2015, granted as patent no. 314266 on June 17, 2019.

### **PCT**

1. Detection of quantity of water flow using quantum clusters, T. Pradeep, Leelavathi A, M. Udhaya Sankar, Amrita Chaudhary, Anshup, T. Udayabhaskararao, 1521/CHE/2012, April 17, 2012. Issued in China with patent number CN104520706 B. Issued US patent no. US 10041925 B2, issued on August 7, 2018. Issued in Japan patent no. JP6367182 B2 on August 8, 2018, Issued in Mexico patent no. MX362092 B on October 7, 2019, Issued in Ireland patent no. IL20130235206 on December 31, 2014.

# Media Reports



SCIENCE

## IIT Madras: Breath humidity sensors for wearable electronics



R. Prasad

JULY 27, 2019 18:30 IST

UPDATED: JULY 27, 2019 18:31 IST

**It detects ethanol, acetone in oral breath of alcoholics, diabetics, respectively**

A nanofibre sensor capable of sensing minute variations in relative humidity levels in the exhaled breath has been fabricated by a team led by T. Pradeep from the Department of Chemistry at the Indian Institute of Technology (IIT) Madras. The highly sensitive sensors can be integrated into wearable electronics and might have applications in assessing human metabolism and calorie burn rates.

### Quick response time

The sensors have very quick response time of about one second and can detect a range of relative humidity from 0-95%. The sensor was found to have high stability. "Even after exposing the sensor to ambient conditions for a week, we still found the response time to be about one second and could match the breathing rates quite effectively," says Sathvik Ajay Iyengar who was a short-term student with Prof. Pradeep's team and is one of the first authors of a paper published in the journal *ACS Applied Electronic Materials*.

The breath rate was measured for one-two hours prior to and after exercise. The heart rate is higher soon after exercise and this is reflected in higher breath rate. "We intend collecting breath rate over a period of few days to establish the relationship between heart and breath rate and metabolism," says Pillalamarri Srikrishnarka from IIT Madras, the other first author of the paper.

The nanofibre mat is fabricated by electrospinning poly(vinylidene fluoride) and reduced graphene oxide. Coating the mat with polyaniline turns the mat into a sensor.

The moisture in the breath reduces the resistance of the sensing material thereby allowing more current to flow. So when a fixed voltage (1-2 volts) is applied to the sensor, there is more current that is detected when the sensor comes in contact with moisture in the breath.

"In the presence of humidity, 100-1000 times more current can be detected using our sensor compared with other sensors," says Iyengar. "So when the current measured is in nanoampere range when other sensors are used, we were able to measure it at microampere range using our sensor."

When there are traces of ethanol and acetone in the breath, the resistance of the sensor increases and conductivity reduces. Hence, there is a dip in the current measured from the baseline. "The reduction in conductivity is because of the absence of moisture – the hydrogen bond between the sensor and analyte [ethanol and acetone] is less likely to form," says Srikrishnarka.

"Polyaniline is the major contributor of current conduction, and reduced graphene oxide complements it. The combination of polyaniline coating and reduced graphene oxide allows higher current conduction," says Srikrishnarka. "In the absence of reduced graphene oxide, polyaniline can still conduct current but at a significantly lower level. The reduced graphene oxide alone does not help conduct current."

"The coating of the mat with polyaniline occurs in water and so can be scaled-up to get large-scale coatings. This process also makes it easier, quicker and relatively more eco-friendly than other commercial processes," says Prof. Pradeep. The nanofibre mat obtained is very thin and offers breathability. In order to integrate sensors like this into wearable electronics to monitor breath, resistance-free air flow is the key.

### Portable sensor

To make the sensor truly portable, the researchers are using the popular Arduino prototyping platform coupled with Bluetooth module for collecting data wirelessly.

## Big Breakthrough! IIT Madras degrades plastic in eco-friendly way

By: Ribhu Mishra

Published: September 16, 2019 6:10:11 PM

Arjun Ram Meghwal urged the Indian Institute of Technology, Madras to invent an alternative to the single-use plastic.



Amidst the rising concerns regarding the impact of single-use plastic on nature, a team at Indian Institute of Technology, Madras (IIT Madras) has devised an eco-friendly method to degrade the physically stable and chemically inert plastic fluoropolymer — polytetrafluoroethylene (PTFE). PTFE is used in making Teflon. Following which, the Minister of State (Heavy Industries and Public

According to a report published in The Hindu, a team lead by T. Pradeep from the Department of Chemistry of the esteemed Institution was able to degrade different types of plastic including polypropylene, the results of which were published in the 'ACS Sustainable Chemistry & Engineering' journal.

Minister of State, Heavy Industries and Public Enterprises, Arjun Ram Meghwal who went to attend a conclave while addressing the gathering said, "Hon'ble Prime Minister [Narendra Modi](#) has called for banning single-use plastic. IIT Madras has to invent some alternates, which if available, will be used by people easily in their daily life," according to the Twitter handle of the institution. The institute organised a Tech-Conclave on September 15 of which the MoS was Keynote speaker.

The eco-friendly degradation of the plastic was observed after a scientific process involving metals, glucose, magnetic stirrer coated with Teflon and other sugars.

While talking to The Hindu, Prof T Pradeep said, "While doing the experiment to degrade plastic, We found out that the PTFE polymer might be breaking down into smaller molecules through triboelectric degradation."

Abhijit Nag from IIT Madras said that the amount of glucose dissolved in water is directly proportional to the amount of triboelectric degradation. "Similar results were noted while performing the experiment on polyethylene and polyethylene terephthalate (PET)," added Nag.

This experiment has also given birth to the question of micro and nano-plastics dissolving into our food during cooking as modern cookware are coated with Teflon. The study also suggested that the possibility of generation of microplastics in oceans are high as they have metal ions in abundance and waves provide constant distress.



SCIENCE

## IIT Madras team produces gas hydrates under 'space' conditions

R. Prasad

CHENNAI, JANUARY 08, 2019 01:45 IST

UPDATED: JANUARY 07, 2019 23:03 IST

### IIT Madras team achieve rare feat

Researchers at Indian Institute of Technology (IIT) Madras have experimentally shown that methane and carbon dioxide (CO<sub>2</sub>) can exist as gas hydrates at temperatures and pressures seen in interstellar atmosphere. Gas hydrates are formed when a gas such as methane gets trapped in well-defined cages of water molecules forming crystalline solids. In terrestrial conditions, gas hydrates are formed naturally under the sea bed and glaciers under high pressure, low temperature conditions. Methane hydrate is a potential source of natural gas.

The methane and CO<sub>2</sub> hydrates were produced in the lab at very low pressures (ten thousand billionth of atmospheric pressure) and temperature (as low as -263 degree C) to simulate the conditions of deep space.

### Applications

The carbon dioxide hydrate produced in the lab raises the possibility of sequestering or storing carbon dioxide as hydrates by taking advantage of ice existing in environmental conditions favourable for hydrate formation. "In these environments, the carbon dioxide will have enough energy to interact with ice. So both molecules will have enough mobility to allow interaction to form carbon dioxide hydrate," he said.

"CO<sub>2</sub> hydrate is thermodynamically more stable than methane hydrate. So if methane hydrate has remained stable for millions of years under the sea bed, it would be possible to sequester gaseous CO<sub>2</sub> as solid hydrate under the sea bed," said Prof. Rajnish Kumar, Department of Chemical Engineering, IIT Madras and a co-corresponding author of a paper published in the *Proceedings of the National Academy of Sciences*.

IIT Madras, in collaboration with GAIL, is working to recover methane from methane hydrate from the Krishna-Godavari Basin and sequester CO<sub>2</sub> simultaneously, said Prof. Kumar.

"We have been conducting such experiments for the last five years but have never seen gas hydrates forming," says Prof. T. Pradeep from the Department of Chemistry at IIT Madras who led the team. That was because the researchers conducted the experiments only for a few hours.

Water and methane were originally deposited at -263 degree C (10 K). When the temperature was increased to -243 degree C (30 K), the researchers could observe methane hydrate forming after 25 hours. About 10% of methane present was found in the hydrate form at the end of 25 hours. "By the end of 75 hours, most methane got converted into hydrate," says Jyotirmoy Ghosh from IIT Madras and the first author of the paper.

Though both ice and methane are in a frozen state, prolonging the experiment at a very low temperature enhanced the mobility of methane molecules and led to their insertion into the cage of water molecules to form methane hydrate.



# THE HINDU BusinessLine

www.businessline.in  
businessline  
thehindubusinessline

**EMERGING ENTREPRENEURS**  
The Gensol group is looking to  
hail a ride on the green road by  
introducing electric cabs p2



**DON'T GO LOCAL**  
Data localisation is completely impractical  
and will increase consumer costs, says  
Rajeev Chandrasekhar, MP, Rajya Sabha p8



## Mimicking space, IIT-M scientists cage methane in water

May be a crucible for unique chemical reactions that led to origin of life

**TV JAYAN**

New Delhi, January 7

Mimicking conditions prevailing in interstellar space, a team of Indian researchers has synthesised in a lab tiny water cages containing trace amounts of methane and carbon dioxide at extremely low temperatures and pressure.

These nano cages, also called clathrate hydrates, assume significance because the scientists who created them speculate that various chemical processes on such hydrates in interstellar space may have led to the formation of relevant molecules that eventually gave rise to life on earth.

### New chemistry

Such molecular confinement can result in new chemistry, especially in the presence of cosmic rays present in the interstellar environment. This may have relevance to the origin of life, said the scientists from the Indian Institute of Technology (IIT)-Madras, in a

paper published in the prestigious journal *Proceedings of the National Academy of Sciences*, on Monday.

"For a long time, scientists have been speculating that molecules of life had come from space. Maybe new kinds of molecules were born in space, not normally by a straightforward chemical reaction, but reactions in confinement, like, say, in a hydrate cage. In that sense pre-cursors of carbon-containing molecules could be

hydrates," said Thalappil Pradeep, professor of chemistry at IIT-Madras and a senior author of the paper.

This discovery of hydrates is highly unexpected at extremely low pressures and ultra cold temperatures as cages of water are not expected to form under such conditions as the water molecules are frozen and cannot move at very low temperatures, said Pradeep.

Normally, formation of clathrate hydrates requires high pressures and moderate temperature. On earth, they are found on the ocean floor or the permafrost region of

earth. Such hydrates, especially that of methane, are thought to be the future sources of fuel. Many countries, including India, have already embarked on projects to explore hydrates present on the ocean bed.

The IIT scientists, led by Pradeep and his colleague Rajnish Kumar, created such hydrates in vacuum, one thousand billion times below the atmospheric pressure, called ultra-high vacuum, at temperature close to minus 10°Celsius.

### Pat from French scientist

This is a significant piece of work as the paper for the first time showed that clathrates can be formed at very low temperatures, said Olivier Mousis, a scientist with Laboratoire d'Astrophysique de Marseille, in France.

"Clathrate hydrates were suspected to be part of the building blocks of the ice moons, comets and the material accreted by giant planets. The missing part of the puzzle was the presence of experiments showing that they exist. It is done now," he said.



(From left) Prof Rajnish Kumar, Jyotirmoy Ghosh and Prof T Pradeep around their ultra-high vacuum instrument



## Origin of life: Hydrates in interstellar space may throw new light

Katyan Ray

**NEW DELHI, DHNS:** Gas hydrates, a potential source of energy on Earth, may be present in abundance in interstellar space, suggests new research by scientists at IIT-Madras.

The startling discovery may open up a completely new window to look at a fundamental query in science – how life began on Earth.

Hydrates or clathrate hydrates are molecules like methane, carbon dioxide, etc., trapped in well-defined cages of water molecules forming crystalline solids.

They are formed at places with high pressures and low temperatures such as the ocean floor. They are also found in the glaciers of Siberia.

Such hydrates, especially that of methane, are thought to be the future sources of fuel. Several countries, including India, have government-fund-

ed programmes to explore and harvest the hydrates lying hundreds of metres below the sea level.

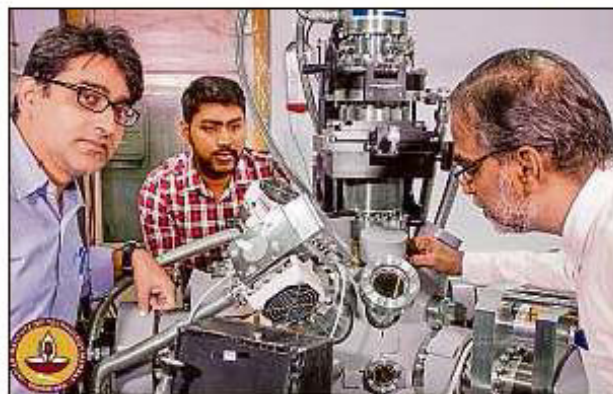
Researchers from IIT-Madras formed such hydrates in a vacuum, 1,000 billion times below the atmospheric pressure called ultra-high vacuum and temperature close to - 263 degree Celsius (10 Kelvin). These are the conditions present in deep space. "The findings open up the possibility of having entirely new chemistry in space. All small molecules in space should now be looked at as caged (hydrate) entity and reaction between two such molecules can give rise to new

chemistry," Thalappil Pradeep, lead author of the study and a professor of chemistry at IIT-Madras, told *DH*. The researchers created an environment in the laboratory to simulate the condition found in interstellar space. "Since cages of water are not expected to form under such conditions, nothing surprising was seen initially. Then I thought why not wait for days and keep observing the changes; after all ice and methane have been sitting in the space for millions of years. The excitement happened after three days when new features started coming. Then of course, several experiments were done under controlled conditions," Pradeep said.

The research has been published on the December 7 issue of the journal *Proceedings of the National Academy of Sciences*. "The findings may have an impact on both as-

tronomy and chemistry," the researchers reported.

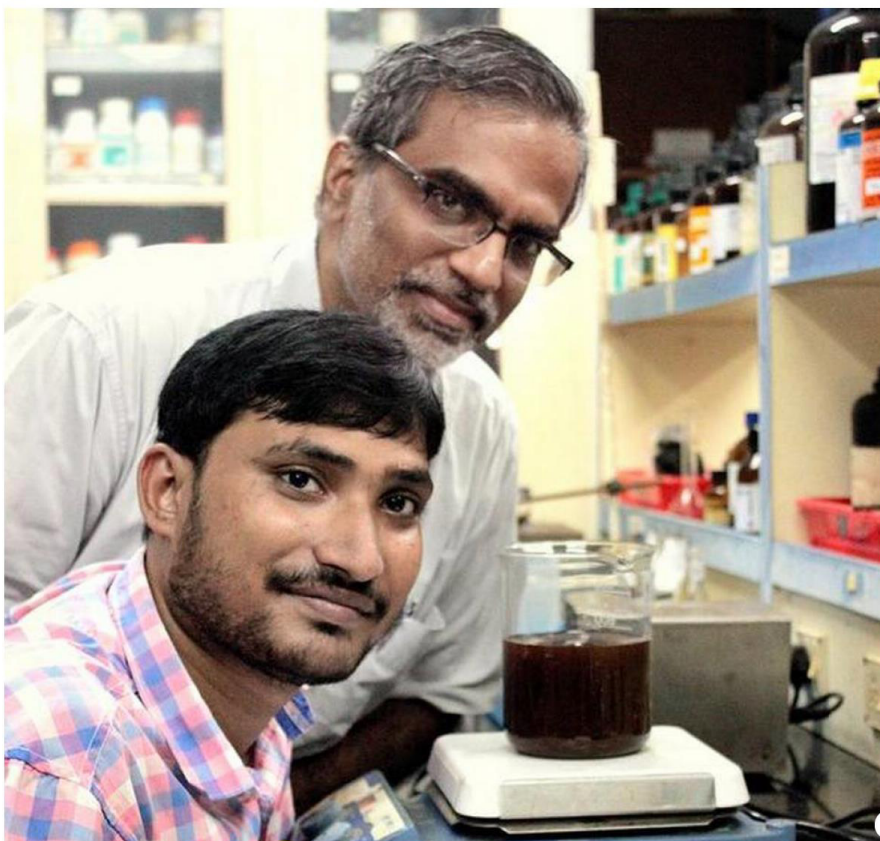
While hydrates are being chased on the Earth as a futuristic source of energy, Pradeep ruled out any such use for an interstellar spacecraft with the current level of technology. Also, the space being too vast, it would be impossible to know where such hydrates can be found. A far more exciting option would be to search for new chemistry and tailor the space-probe instruments like spectrometers to look for those signatures as there is still no answer as to how molecules formed in space and life came into being on Earth, he said.



(From left) Prof Rajnish Kumar, Jyotirmoy Ghosh and Prof Pradeep around their ultrahigh vacuum instrument.



## IIT Madras finds an eco-friendly way to degrade plastics



SEPTEMBER 14, 2019 19:20 IST  
UPDATED: SEPTEMBER 15, 2019 10:57 IST

### The strategy can degrade several varieties of plastic - Teflon, polyethylene, polypropylene

Three years ago researchers from the Indian Institute of Technology (IIT) Madras observed silver slowly dissolving in a glucose solution when heated to 70 degree C. Now, the team has demonstrated an environment-friendly strategy to degrade the chemically inert and physically stable plastic fluoropolymer – polytetrafluoroethylene (PTFE) of which Teflon is made. All that is required to degrade the fluoropolymer into molecules is continuous stirring of it in water containing 1,000 ppm glucose and metal ions for about 15 days at 70 degree C.

Using the same strategy, the team led by T. Pradeep from the Department of Chemistry at IIT Madras was able to degrade polypropylene too. The results were published in the journal *ACS Sustainable Chemistry & Engineering*.

The researchers used a magnetic stirrer coated with Teflon to continuously stir for several days the water mixed with glucose in a glass beaker containing a gold foil. "After a few days we observed something unusual. We found tiny fragments with bright red luminescence floating on the surface," Prof. Pradeep recalls. In earlier studies, they found that gold, too, corrodes slowly due to glucose. This phenomenon was observed when other sugars were tested.

### Hunch that worked

The initial intuition that the bright red luminescent particles should be containing gold turned out to be correct. After all, compounds with gold-carbon bonds showing red luminescence are well known. But to their surprise, besides gold, they found that the tiny

### Teflon

So the team tested Teflon in different forms – pellets, tapes and plates. They repeated the experiment using a Teflon beaker and tried different metals too and still got the same result each time. The only difference was that the particles did not show bright red luminescence when copper, silver and iron were used instead of gold.

"We then got a clue that the PTFE polymer might be breaking down into molecules through triboelectric degradation. An electric potential is produced at the interface of Teflon and water when the polymer is continuously stirred in water," explains Prof. Pradeep.

Glucose added to water first leaches out ions from the metal surface. When the PTFE-coated magnetic pellet is continuously rotated, triboelectric charges get generated on the pellet. The PTFE gets negatively charged. The negative charge on the PTFE surface attracts the metal ions that have been leached out. The interaction between the metal ions and PTFE results in metal-polymer bonding, causing the carbon-carbon bonds to destabilise. This eventually results in PTFEs degrading into molecules.

No such degradation of PTFE was noticed in the absence of stirring, glucose or metal ions. The rate of degradation gets reduced at room temperature.

"The amount of triboelectric degradation depends on the amount of glucose dissolved in water. As the amount of glucose in water increases more metal ions get leached leading to more interaction between PTFE and the metal ions. As more metal ions bind to PTFE, there is enhanced PTFE degradation," says Abhijit Nag from IIT Madras and the first author of the paper.

"Mass spectrometry signatures imply the presence of molecular fragments of PTFE polymer," says Prof. Pradeep. "The fragments seen floating on the water surface might be due to aggregation of molecular fragments or due to fragmentation of the long polymer."

"We have now tested it on polyethylene and polyethylene terephthalate (PET) and got similar results. For a given concentration of dissolved glucose, the reaction is slow as the generation of triboelectric charge is less compared with PTFE," says Nag.

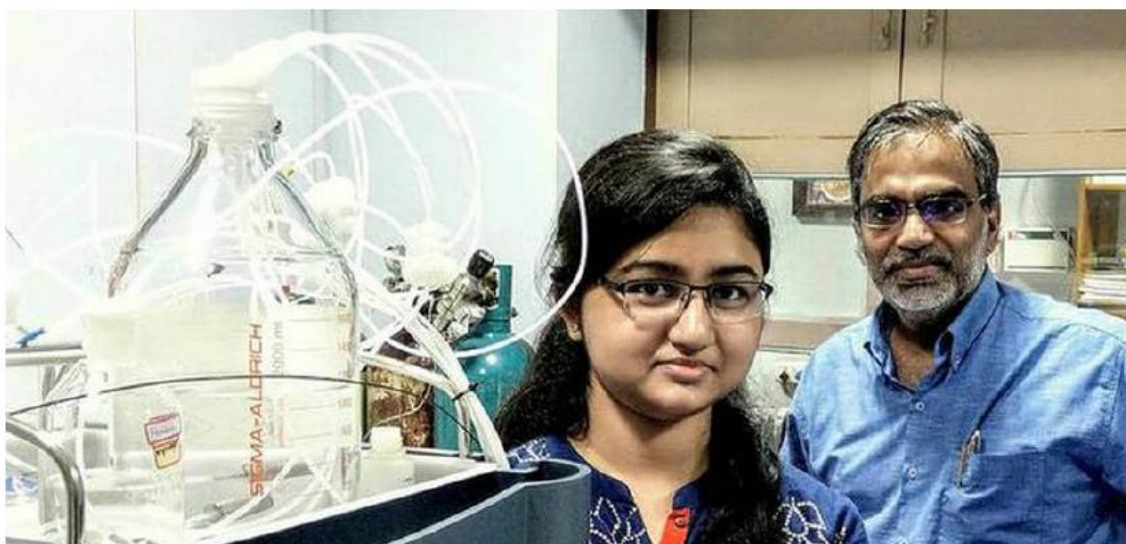
According to the paper, similar chemistry can possibly lead to micro and nanoplastics in food during cooking as many modern cookware are coated with Teflon.

"Triboelectric degradation of PTFE, polypropylene and other polymers might be occurring in nature in large water bodies such as oceans where metal ions are found in abundance and waves provide constant agitation," Prof. Pradeep says. "This must be one of the ways by which microplastics get generated."



SCIENCE

## Silver atoms of nanoparticles are mobile, IIT Madras team finds



R. Prasad

JANUARY 05, 2019 18:34 IST  
UPDATED: JANUARY 05, 2019 18:36 IST

**The rapid exchange of silver atoms in solution might have implications in real-life situations**

While atoms in silver metal remain in their positions forever in bulk material, their behaviour changes completely at the nanoscale, researchers at Indian Institute of Technology (IIT) Madras have discovered.

When nanoparticles made of two silver isotopes ( $^{107}\text{Ag}$  and  $^{109}\text{Ag}$ ) having just 25 atoms each were mixed in solution, a team led by Prof. T. Pradeep of the Chemistry Department found that the atoms from the two particles rapidly exchanged their positions. New particles composed of nearly 50% mixture of both isotopes were formed. This is akin to the exchange of hydrogen and deuterium atoms when normal and heavy water ( $\text{D}_2\text{O}$ ) are mixed. Even in an alloy of silver and gold, a rapid exchange of silver atoms was seen.

"This is a surprising find for the nanoscience community. We have always been thinking that silver and gold particles are rigid, well defined structures even at the nanoscale. But we observed silver atoms undergoing dynamic changes in solution," says Prof. Pradeep. "Unlike bulk silver, silver nanoparticles are not rigid and fixed at specific locations as we thought them to be." The results were published in the journal *Science Advances*.

The rapid exchange of silver atoms in solution might have implications in real-life situations. "The properties of nanoparticles such as catalysis, drug delivery, and biological sensing may all be viewed differently in view of this rapid atom exchange," Prof. Pradeep says. "In homogeneous catalysis involving nanoparticles, the site at which chemistry occurs could be changing continuously," the authors write.

The silver particles composed of 25 atoms were protected by ligands to form clusters. Despite the protection offered by the ligand, the atom exchange between the two clusters happened in millisecond time-scale. The new cluster, which was formed by mixing of atoms belonging to two isotopes, had almost 50:50 ratio of the isotopes.

The researchers found that the rate at which the atoms exchanged could be controlled by changing the temperature. While the exchange was rapid at room temperature, at  $-20$  degree C, the exchange rate was slower and took about 30 seconds to attain equilibrium distribution. The relatively longer time taken to reach equilibrium allowed the researchers to observe the in-between states of atom exchange. They found that the atom transfer rate is similar to that in water.

### Slower exchange rate

The atom exchange rate slowed down drastically when silver nanoclusters were composed of 29 atoms – it took about three hours to reach dynamic equilibrium at room temperature compared with rapid exchange in the case of 25-atom clusters. The slower exchange rates allowed the researchers to study the dynamics in greater detail.

The exchange went through multiple steps. First, there was rapid exchange of atoms at the surface of the nanoparticle. Then the exchanged atoms diffused into the core of the nanoparticle making more exchange at the surface possible. Finally, there was equilibration of the mixed isotope system.

"The difference in the exchange rate between the clusters made of 25 and 29 silver atoms is not due to the difference in the number of atoms but due to the ligand used for binding to the silver atoms," says Papri Chakraborty from the Department of Chemistry at IIT Madras and first author of the paper. "The ligand binds to each silver atom at just one site in the case of the cluster composed of 25 atoms. But it binds at two sites of the silver atoms in the 29-atom cluster thus rendering the structure rigid."

"Such dynamics can occur in any nanosystem. Fundamental insight the study provides is that nanoparticles are indeed molecules," Prof. Pradeep says.





During the visit of Prof. Graham Cooks, Purdue University and Prof. Thomas Thundat, University at Buffalo, December 12, 2019.

## **Acknowledgements**

### **Students and Collaborators**

## **Funding**



सत्यमेव जयते

**Department of Science and Technology**  
**Government of India**